Malaysian Journal of Analytical Sciences
(MJAS)
Published by Malaysian Analytical Sciences Society

Vol 28 No 1 (2024)

Vol 28 No 2 (2024)

Vol 28 No 3 (2024)

Vol 28 No 4 (2024)

Vol 28 No 5 (2024)

Vol 28 No 6 (2024)

2024

Malaysian Journal of Analytical Sciences Vol 28 No 1 2024

		Page
	Nano and Advanced Materials Analysis	1-9
1.	SYNTHESIS AND CHARACTERIZATION OF LIQUID-SILICATE FERTILIZER FROM TREATED AND UNTREATED ASH RICE HUSK *Safari Zainal, Raihan Hanim Tajuddin, and Nur Firdaus Mohamed Yusof*	
	Analytical Method	
2.	PEROXYMONOSULFATE ACTIVATION USING NITROGEN-DOPED BIOCHAR FOR ACID ORANGE 7 REMOVAL IN WATER *Mohamed Faisal Gasim, Nivethah Sivam, and Wen-Da Oh*	10-20
	Organic and Inorganic Analysis	
3.	SPECTROSCOPIC, CRYSTAL STRUCTURE, HIRSHFELD SURFACE AND DFT STUDIES OF 2-AMINO-4-CHLOROBENZONITRILE *Onur Erman Dogan, Erbil Agar, Necmi Dege, Erna Normaya, Siti Syaida Sirat, and Nur Nadia Dzulkifli*	21-32
	Natural Product Analysis	
4.	PHYTOCHEMICALS ISOLATION, ANTIBACTERIAL AND ANTIBIOFILM ACTIVITIES OF MALAYSIAN *Uncaria tomentosa* AGAINST ORAL STREPTOCOCCI *Nor Haslini Wahid, Rohaya Ahmad, Zainon Mohd Noor, Nurul 'Izzah Mohd Sarmin, Norizan Ahmat, Adiez Sapura Azmi, and Fatimah Salim*	33-44
	Nano and Advanced Materials Analysis	
5.	SYNTHESIS OF CARRAGEENAN-BASED BIOCOMPOSITE PLASTICIZED WITH DEEP EUTECTIC SOLVENT AND CHARACTERIZATION OF ITS MECHANICAL PROPERTIES *Nur Amalina Ramli, Fariha Rosli, Mohd Aiman Hamdan, and Fatmawati Adam*	45-56
	Analytical Method	
6.	BUTTERFLY PEA FLOWER-INFUSED QUINOA STARCH FILM AS A pH INDICATOR FOR SHELLFISH FRESHNESS ASSESSMENT *Siti Nur Syahirah Shaikh Ahmad, Nur Nabilah Hasanah, and Mohammad Rashedi Ismail-Fitry*	57-67
	Natural Product Analysis	
7.	ENCAPSULATION OF A MIXTURE OF NONI (*Morinda citrifolia* L.) FRUIT EXTRACT AND PATCHOULI (*Pogostemon cablin*) OIL WITH MALTODEXTRIN AND ITS ANTIOXIDANT ACTIVITY *Ardhianna Salsabilla Puteri, Triana Kusumaningsih, and Desi Suci Handayani*	68-78

Environmental Analysis

8. MICROPLASTICS POLLUTION MITIGATION IN WASTEWATER TREATMENT: CURRENT PRACTICES, CHALLENGES, AND FUTURE PERSPECTIVES 79-96
Rabiatul S. Rusidi, Iwani W. Rushdi, Wan M. Khairul, Sofiah Hamzah, Wan Mohd Afiq Wan Mohd Khalik, Sabiqah Tuan Anuar, Nor Salmi Abdullah, Nasehir Khan E.M. Yahya, and Alyza A. Azmi

Nano and Advanced Materials Analysis

9. INSIGHTS INTO THE STRUCTURAL, MORPHOLOGICAL, AND OPTICAL PROPERTIES OF V_2O_5 CATHODE MATERIAL SYNTHESIZED BY SELF-PROPAGATING COMBUSTION METHOD UNDER VARIED ANNEALING TEMPERATURES 97-105
Mas Fiza Mustafa, Missha Balqis Shariamin, Mohd Sufri Mastuli, Zurina Osman, and Annie Maria Mahat

Environmental Analysis

10. SIZE AND ORGAN-SPECIFIC HEAVY METAL ACCUMULATION PATTERNS IN LONGTAIL TUNA (*Thunnus tonggol*) FROM TERENGGANU 106-115
Norhazirah Abd Aziz, Adiana Ghazali, Sim Siong Fong, Nurul Izzah Ahmad, and Ong Meng Chuan

Analytical Method

11. EXTRACTION OF β-KERATIN FROM POULTRY FEATHER WASTE USING SODIUM METABISULFITE AND SODIUM DODECYL SULFATE 116-126
Soerya Dewi Marliyana, Theresia Inna Sekar Tungga Dewi, and Triana Kusumaningsih

Analytical Method

12. RESPONSE SURFACE METHODOLOGY FOR OPTIMISING CROSS-LINKING CONDITIONS OF UNRIPE BANANA (*Musa balbisiana* VAR. Abu) STARCH 127-140
Nurul Nor Izzuani Nor Sham, Anida Yusoff, Noorlaila Ahmad, and Siti Roha Ab Mutalib

Analytical Method

13. MODIFIED CHRYSIN-BASED BIOSORBENT FOR THE DISPERSIVE MICRO-SOLID PHASE EXTRACTION OF SELECTED PHENOLIC ACIDS FROM STINGLESS BEE HONEY 141-156
NyukTing Ng, Aemi Syazwani Abdul Keyon, Wan Aini Wan Ibrahim, Mohd Marsin Sanagi, and Faridah Mohd Marsin

Analytical Method

14. ANALYTICAL TECHNIQUES OF BIOACTIVE COMPOUNDS FROM MEDICINAL PLANTS WITH THE POTENTIAL TO ADDRESS ALZHEIMER'S DISEASE AND ASSOCIATED SYMPTOMS: A BRIEF OVERVIEW 157-173
Syaza Syazwani Shaifol, Noorfatimah Yahaya, Siti Nurfazilah Awang, Nur Ain Syaheeda Azizan, Nur Nadhirah Mohamad Zain, Nik Nur Syazni Nik Mohamad Kamal, Mazidatulakmam Miskam, and Wan Nazwanie Wan Abdullah

Organic and Inorganic Analysis

15. POTENTIAL GREEN LIQUID FROM TERNARY DEEP EUTECTIC SOLVENT COMPOSED OF GALLIC ACID, UREA, AND ZINC CHLORIDE: CHARACTERIZATION OF THEIR PHYSICOCHEMICAL AND THERMAL PROPERTIES 174-187
Nuraqilah Mohd Hatta and Siti Abd Halim

Organic and Inorganic Analysis

16. A REVIEW ON THE SYNTHESIS STRATEGIES AND FACTORS CONTRIBUTING TO THE FORMATION OF ZEOLITIC IMIDAZOLATE FRAMEWORKS (ZIFs) AND THEIR APPLICATIONS 188-219
Nazhirah Muhammad Nasri, Enis Nadia Md Yusof, Velan Raman, Abdul Halim Abdullah, and Mohamed Ibrahim Mohamed Tahir

Organic and Inorganic Analysis

17. A INHIBITION EFFECTS OF TRIDENTATE HYDRAZONE LIGANDS AS CORROSION INHIBITORS ON MILD STEEL IN SATURATED CO_2 ENVIRONMENT 220-235
Balqis Auni Badrul Hisyam, Zainiharyati Mohd Zain, Nurulfazlina Edayah Rasol, and Amalina Mohd Tajuddin

Nano and Advanced Materials Analysis

18. IONIC TRANSPORT AND STRUCTURAL ANALYSIS OF BIOPOLYMER ELECTROLYTE BASED ON AGAROSE INTEGRATED WITH SODIUM NITRATE 236-246
Nur Farisha Sulthan Hussain, Siti Zafirah Zainal Abidin, Nora Aishah Ahmad Shaharuddin, Raja Nur Qurratu Ain Raja Syiarizzad, and Siti Rudhziah Che Balian

Malaysian Journal of Analytical Sciences (MJAS)
Published by Malaysian Analytical Sciences Society

SYNTHESIS AND CHARACTERIZATION OF LIQUID-SILICATE FERTILIZER FROM TREATED AND UNTREATED ASH RICE HUSK

(Sintesis dan Kajian Sifat-Sifat Baja Cecair-Silikat daripada Abu Sekam yang Dirawat dan Tidak Dirawat)

Safari Zainal[*1], Raihan Hanim Tajuddin[1], and Nur Firdaus Mohamed Yusof[2]

[1]School of Chemical Engineering, College of Engineering,
Universiti Teknologi MARA, 40450 Shah Alam, Selangor, Malaysia
[2]R&D Department, Dibuk Synergy Sdn. Bhd.,
KM 7, Jalan Simpang Empat, 02000, Kuala Perlis, Perlis, Malaysia

[*]Corresponding author: drsafari@uitm.edu.my

Received: 13 September 2023; Accepted: 21 January 2024; Published: 28 February 2024

Abstract

Rice husk ash (RHA) is an agricultural waste material that is abundantly available in all rice-producing Asian countries. The RHA is rich in silica (Si), which can be extracted as silicate sources for many industries, such as fertilizer, building material, insulation material, or fuel. In this research, organic acid, which is a phosphoric acid (H_3PO_4), was used to treat RHA. RHA was treated with H_3PO_4 at various temperatures (60°C, 80°C, and 100°C) and molarity (1 M, 2 M, and 3 M), and followed by an extraction process of untreated and treated RHA using potassium hydroxide (KOH) at 2 and 3 hours of extraction time and 1 M and 2 M of KOH. The extracted liquid-silicate was determined by using Fourier Transfer Infra-Red (FTIR), X-ray fluorescence (XRF), and Particle Size Analyzer (PSA). The highest silica content (40.910%) in liquid-silicate fertilizer (LSF) was recorded for the treatment condition of 2 M H_3PO_4 at 80 °C based on the XRF result. The highest wave number was 1008.78 cm^{-1} from treated RHA at 2 M H_3PO_4 80 °C. According to PSA data, the smallest particle size (1465.9µm) was recorded after leaching with H_3PO_4 at 2 M 80 °C as compared to untreated RHA at 1639.75µm.

Keywords: rice husk ash, liquid-silicate fertilizer, acid leaching, phosphoric acid, silica extraction

Abstrak

Abu sekam padi (RHA) adalah bahan buangan pertanian yang banyak terdapat di semua pengeluar beras untuk negara Asia. RHA kaya dengan silika (Si), yang boleh diekstrak sebagai sumber silikat untuk banyak industri seperti baja, bahan binaan, bahan penebat atau bahan api. Dalam penyelidikan ini, asid organik, iaitu asid fosforik (H_3PO_4) digunakan untuk merawat RHA. RHA dirawat dengan H_3PO_4 pada pelbagai suhu (60 ℃, 80 ℃, dan 100 ℃) dan kemolaran (1 M, 2 M dan 3 M). diikuti dengan proses pengekstrakan RHA yang tidak dirawat dan dirawat menggunakan kalium hidroksida (KOH) pada 2 dan 3 jam masa pengekstrakan dan 1 M dan 2 M KOH. Cecair-silikat yang diekstrak ditentukan dengan menggunakan Inframerah transformasi Fourier (FTIR), pendaflour sinar-X (XRF) dan penganalisa saiz partikel (PSA). Kandungan silika tertinggi (40.910%) dalam baja silikat cecair (LSF) direkodkan untuk keadaan rawatan 2 M H_3PO_4 pada 80 °C berdasarkan keputusan XRF. Nombor gelombang tertinggi ialah

1008.78 cm^{-1} daripada RHA yang dirawat pada 2 M H_3PO_4 80 °C. Menurut data PSA, saiz zarah terkecil (1465.9µm) direkodkan selepas larut lesap dengan H_3PO_4 pada 2 M 80 °C berbanding RHA yang tidak dirawat pada 1639.75µm.

Kata kunci: abu sekam padi, baja cecair-silikat, asid larut lesap, asid fosforik, pengekstrakan silika

Introduction

In 2019, the world's total paddy rice production was estimated to be 757 million tons [1]. China is the world's leading producer of rice and paddy. As of 2019, China's paddy rice production was 211 million tons, accounting for 27.92% of global paddy rice production. The remaining top five countries which account for 71.54% of the production are India, Indonesia, Bangladesh, Vietnam, and Thailand. Malaysia's paddy rice production in 2019 was 2.91 million tons. From the production of paddy rice, about 1.2 million tons per year of agricultural waste is disposed of in Malaysia's landfills [2]. During the paddy rice cultivation, several by-products are also generated such as broken rice, the husk, and the bran layer. Hence, the utilization of these by-products or agricultural solid waste has been done to save the environment. In this study, rice husk ash (RHA) was the targeted waste material from paddy rice cultivation that can be converted into a potential liquid-silicate fertilizer (LSF).

The RHA can be obtained from the combustion process of RH in the furnace under a controlled temperature, which is below 700 ℃. A suitable temperature and burning environment can provide a better quality of RHA as its particle size and specific surface area are dependent on burning conditions. For every 1000 kg of milled paddy, it will produce around 200 kg (20%) of RH, and when this husk undergoes a burning process in the boilers or incinerators, around 50 kg (25%) of RHA is produced [3]. Usually, a completely burnt RHA will be observed in physical color changes from grey to white. From the burning of RH, the ash contains mainly amorphous silica (Si) and carbon black residue, which is also called carbonaceous siliceous material [4]. The silica group minerals are framework silicates with the composition of SiO_2. They belong to the silicate mineral class. The most common silica mineral is quartz. Besides quartz, other silica polymorphs include cristobalite, tridymite, coesite, and stishovite [5].

The burning conditions can affect the amount of silica and carbon black in the ash. As proven by many researchers, RHA has a high content of silica, which is 94% of the total content, while the remaining 6% contains potassium oxide (K_2O), calcium oxide (CaO), magnesium oxide (MgO), aluminum oxide (Al_2O_3), and phosphorus pentoxide (P_2O_5) in decreasing concentrations [2]. Because of that, it has been utilized in many industries such as fertilizer, coating, and paint industries.

To obtain RHA, RH will undergo a carbonization process. Carbonization is a method by which solid residues with increasing carbon element content are produced from organic material in an inert atmosphere, typically by pyrolysis. Mehta proposed that essential amorphous silica can be obtained by holding the temperature for prolonged periods below 500℃ and under oxidizing conditions or the temperature can be increased up to 680 ℃ but with a hold-time of not more than 1 minute [6]. Other researchers have claimed that the burning of RH in extreme temperatures (i.e. high temperature) or long duration of time would result in the formation of crystalline phases [7]. The partially crystalline phase of RHA is caused by burning the RH for more than 1 hour in a temperature range between 973 and 1073 Kelvin. Burning RH at temperatures above 1073 Kelvin for more than 1 hour has been documented to lead to the formation of a complete crystalline phase.

Good quality biogenic silica can be produced by the treatment process. Several researchers have carried out the experiments by using a leaching process with hot acid treatment with inorganic acids such as hydrochloric acid (HCl), nitric acid (HNO_3), and sulfuric acid (H_2SO_4) or hot basic treatment with inorganic bases such as ammonium hydroxide (NH_4OH) and sodium hydroxide (NaOH) [8-11]. Acid leaching treatment of RHA by using organic acid is highly encouraged because it has many economic and ecological benefits compared to a strong acid [12-13]. It is a proper route for silica extraction to remove substances from solid organic

materials via the liquid extraction method. Based on the results obtained from the previous paper, an organic acid solution such as citric acid was considered a more environmentally friendly process during the acid-leaching treatment. However, phosphoric acid (H_3PO_4) was used as a pH adjustor in liquid fish fertilizers, as an inert ingredient in pesticide products, and as a sanitizer for dairy equipment [14].

A method based on acid treatment before the alkaline extraction is developed to produce high-purity silicate with minimal contaminants. This process does not provide any harm to the life of organisms, moreover, it is more economical. In addition, a chelating reaction occurs between the carboxyl group (-COOH) and metal cations, which leads to the removal of metal impurities in the RHA. Conventionally, the removal of metallic impurities is done by using inorganic acids such as HCL, HNO_3, and H_2SO_4. However, the use of inorganic acid has caused harm to human beings and the environment. Furthermore, the expensive materials with corrosion resistance needed for the leaching process using inorganic acid can cause an economic problem. There is also a high consumption of water to remove the acid, as well as the need for a special disposal system [12]. That is the reason why organic acid should be used as the substitute for inorganic acid, to comply with the environmental requirements for less exposure or disposal of hazardous or corrosive chemical waste. For this paper, organic acid which is H_3PO_4 was used to treat the RHA before the liquid-silicate extraction process. This study aimed to synthesize LSF from treated (acid leaching) and untreated RHA and to compare the results of the characterization of LSF by using XRF, FTIR, and PSA techniques for both treated and untreated RHA.

Materials and Methods

Materials

In this experiment, the RHA was obtained from a rice mill, DIBUK Sdn. Bhd., located in Perlis, Malaysia. Chemicals such as 45% potassium hydroxide (KOH) and 85% phosphoric acid (H_3PO_4) were obtained from Reichle & De-Massari (R&M), Switzerland.

Material preparation

An amount of 3 kilograms of RHA was obtained directly from the factory. The rice husk ash (RHA) had already undergone the carbonization process at the factory at 650 °C. After that, RHA was cleansed by using distilled water and dried in the oven to remove any impurities and reduce the moisture content. This was to avoid any effects during the treatment and extraction. The sample was dried at 60 °C for 60 mins [15]. Once the RHA was completely dried, the RHA was grounded using a mechanical grinder until it turned powdery. A few grams of the sample were kept without further treatment process as an untreated sample (blank sample).

Acid leaching treatment process

200 g of RHA were soaked in each beaker containing H_3PO_4 at various molarities (i.e.1 M, 2 M, and 3 M) to undergo acid-leaching treatment. During the treatment process, these acid-treated samples were placed on the hot plate magnetic stirrers to heat the mixture until they reached various temperatures at 60, 80, and 100 °C and were kept constant for 2 hours for each sample [16]. After the acid leaching treatment was completed, each sample was washed using distilled water to neutralize the sample. The pH of the sample must be monitored until it reaches pH 7. After that, all samples were desiccated in an oven at 100 °C for 2 hours.

Extraction process of treated and untreated RHA

100 g of treated and untreated RHA were soaked in beakers containing various molarities of KOH (i.e., 1 M, 2 M, and 3 M) for the extraction process. During the extraction process, each sample was placed on a hot plate magnetic stirrer to heat until the temperature reached a constant 100 °C at 2 and 3 hours for each sample, respectively. Next, the samples were desiccated in an oven at 100 °C for 2 hours.

Chemical composition analysis and characterization of treated and untreated rice husk ashes

Fourier transform infrared (FTIR) spectroscopy, X-ray fluorescence (XRF) spectroscopy, and particle size analyzer (PSA) were used to determine and compare the difference between the composition of silica in treated and untreated RHA in their potential as an LSF. The FTIR technique was used to characterize the major chemical groups present within the LSF using an FTIR spectrometer model L1280044 manufactured by Perkin

Elmer USA. After launching the spectrum software, the sample was placed on the sample holder followed by the operation of the spectrometer, and each spectrum was finally collected until complete spectra were projected on the monitor.

Next, the XRF spectrometer, PAN analytical MiniPAL 4 X-ray (Philips, UK) was used to characterize the number of chemical compounds within the liquid silicate [2]. Each sample was placed in a cup that was covered using a suitable foil, usually Kapton material. After that, the sample was placed into the XRF spectrometer.

Finally, RHA characterization was performed by using PSA Malvern Mastersizer 2000 (Malvern, UK). PSA was used to determine the size and distribution of the particles that comprise a material. The characterization and analysis of the composition of RHA were conducted using the Standard Operation Procedure (SOP) instructions. Then, the sample was added into the water to ensure an adequate amount of sample was aliquoted (one drop at a time) to turn the Laser Obscuration bar green (i.e. until it achieved the mid-value) [17-18]. The sample was measured and the outcome (size distribution) was computed. The recorded measurement was saved to a measurement file automatically.

Results and Discussion

Acid leaching treatment with phosphoric acid (H_3PO_4)

Acid leaching treatment on rice husk ashes was done by using H_3PO_4. The purpose of this treatment is to remove some amounts of metal impurities [15]. Based on the XRF data in Table 1, the highest silica content was at 1 M 60 °C sample with 57.676% and had the lowest potassium (K) and Iron (Fe) content, which are 1.413% and 39.357%, respectively. To proceed with the next stage of the experiment, which was the extraction process, the highest silica content from each proposed molarity was chosen. Hence, 1 M at 60 °C, 2 M at 80 °C, and 3 M at 60 °C were chosen to undergo the extraction process later. From previous studies, it has been demonstrated that the phosphoric acid activation of lignocellulosic [19] precursors produced carbons having not only a well-developed porosity, but also considerable amounts of acid surface groups. [20]

Table 1. XRF data for acid leaching treatment of RHA

Samples	Temperature (°C)	Si (%)	K (%)	Fe (%)	Traces Element (%)
	60	57.676	1.413	39.357	1.554
1 M	80	55.363	1.825	41.176	1.636
	100	54.400	1.758	42.205	1.637
	60	53.835	1.877	42.633	1.655
2 M	80	54.360	1.874	42.107	1.659
	100	53.593	1.754	43.002	1.651
3 M	60	51.378	1.885	45.061	1.676
	80	51.323	1.806	45.248	1.623
	100	51.139	1.731	45.487	1.643

Note: Data are given in mass percentage. The trace elements are Na, Mg, Al, P, Ca, Cu, and Zn

Extraction process using potassium hydroxide (KOH)

The extraction process was done by using KOH for treated and untreated RHAs. The purpose of extraction is to produce LSF. Further characterization was carried out to observe the content, such as silica content in the LSF.

XRF spectroscopy

Two types of sample conditions were tested, which are untreated and treated RHA. The chemical composition was analyzed by using an XRF spectrometer. Table 2 shows the chemical composition of treated and untreated RHA. Untreated RHA recorded the lowest silica content. Meanwhile, treated RHA at 1 M 2 H yielded the highest silica content, which is 40.910% at the treatment

condition of 2 M 80 °C, compared to untreated RHA, in which the silica content was 29.157%.

The other metallic elements such as iron and potassium are presented in the LSF of both treated and untreated RHA. The results indicated that most iron was reduced when the RHA underwent leaching treatment. Similar results were exhibited for the effect of acid-leaching treatment on the potassium content. The removal of these metallic cations after chelating with H_3PO_4 improved the chemical composition of a leached sample to be rich in alkaline metals, which are water-solubles such as potassium. Hence, the unwanted impurities were washed away by the distilled water used in the neutralization process. The impurities in the husk were removed using a chelate reaction between carboxyl groups (-COOH) and metal elements [2]. This is because the majority of elements absorbed during the leaching process were silica which was extracted from RHA. As a result of the strong covalent bond that exists between silicon and oxygen in the properties, silica becomes very hard and rigid [2], which makes it the end product of this leaching process for its useful real-life application as an agricultural fertilizer.

As shown in Table 2, H_3PO_4 leaching treatment was significantly useful and effective in removing impurities and increasing silica purity in RHA. However, the silica content for treated 2 M 2 H and 2 M 3 H was observed to decline from 21.317 to 18.477% and 19.148 to 18.212%, respectively when undergoing the treatment process. As shown in Table 2, the iron content was the highest compared to silica and potassium content. This correlates with the literature finding that, iron is very essential in plant growth. Iron is required for many vital plant functions, including enzyme and chlorophyll production, nitrogen fixation, development, and metabolism. Even though iron is abundant in soil, plants frequently suffer from iron deficiency due to its low solubility, particularly in alkaline calcareous soils. Hence, our liquid silicate fertilizer is very suitable for the plant as it has a high content of iron.

Table 2. XRF data for treated and untreated RHA

Sample (RHA)	Treatment Condition	Si (%)	Fe (%)	K (%)	Traces Element (%)
Untreated Sample (Blank)	-	29.157	52.350	15.164	3.329
Treated 1 M 2 H	1 M 60 °C	37.685	51.053	9.769	1.493
Treated 1 M 2 H	2 M 80 °C	40.910	46.401	11.014	1.675
Treated 1 M 2 H	3 M 60 °C	29.777	50.891	13.906	5.426
Untreated 1 M 3 H	-	28.516	54.098	14.993	2.393
Treated 1 M 3 H	1 M 60 °C	39.285	45.704	13.417	1.594
Treated 1 M 3 H	2 M 80 °C	38.223	49.182	10.905	1.690
Treated 1 M 3 H	3 M 60 °C	34.004	49.943	13.555	2.498
Untreated 2 M 2 H	-	21.317	55.121	21.973	1.589
Treated 2 M 2 H	1 M 60 °C	21.711	55.087	21.680	1.522
Treated 2 M 2 H	2 M 80 °C	22.501	54.454	21.636	1.409
Treated 2 M 2 H	3 M 60 °C	19.477	56.551	22.794	1.178
Untreated 2 M 3 H	-	19.148	58.881	20.276	1.695
Treated 2 M 3 H	1 M 60 °C	27.767	50.150	20.857	1.226
Treated 2 M 3 H	2 M 80 °C	28.073	48.720	22.114	1.093
Treated 2 M 3 H	3 M 60 °C	18.212	52.906	27.465	1.417

Note: Data are given in mass percentage. The samples are from two conditions which are treated and untreated RHA. The trace elements are Na, Mg, Al, P, Ca, Cu, and Zn

FTIR spectroscopy

Figure 1 and Table 3 represent the infrared spectra of treated and untreated RHA at 1 M 2 H. Based on the XRF data tabulated in Table 2, the highest silica can be extracted from 1 M 2 H. Hence, the selected samples were used to further analyze the functional groups in treated and untreated RHA by using FTIR spectroscopy. The peak from 1095 to 1075 cm^{-1} or 1055 to 1020 cm^{-1}

showed the stretching of silicone, Si-O- [21]. Meanwhile, the peak from 1100 to 900 cm^{-1} showed the stretching band of silicate ions [21]. Because of the asymmetric stretching of the silicate ion, it demonstrated a peak at wave number 1006.88, 1001.13, 1008.78, and 1003.34 cm^{-1} for (a) untreated, (b) treated with 1 M 60 °C, (c) treated with 2 M 80 °C, and (d) treated 3 M 60 °C, respectively. The silicate ion present was due to the liquid silicate produced from the extraction process. Based on Table 3, it shows that the highest wavenumber was treated RHA at 2 M 80 °C. This can be proven based on the XRF results as it exhibited the highest silica content in the liquid silicate from the treated RHA of 2 M 80°C (1008.78 cm^{-1}) [22].

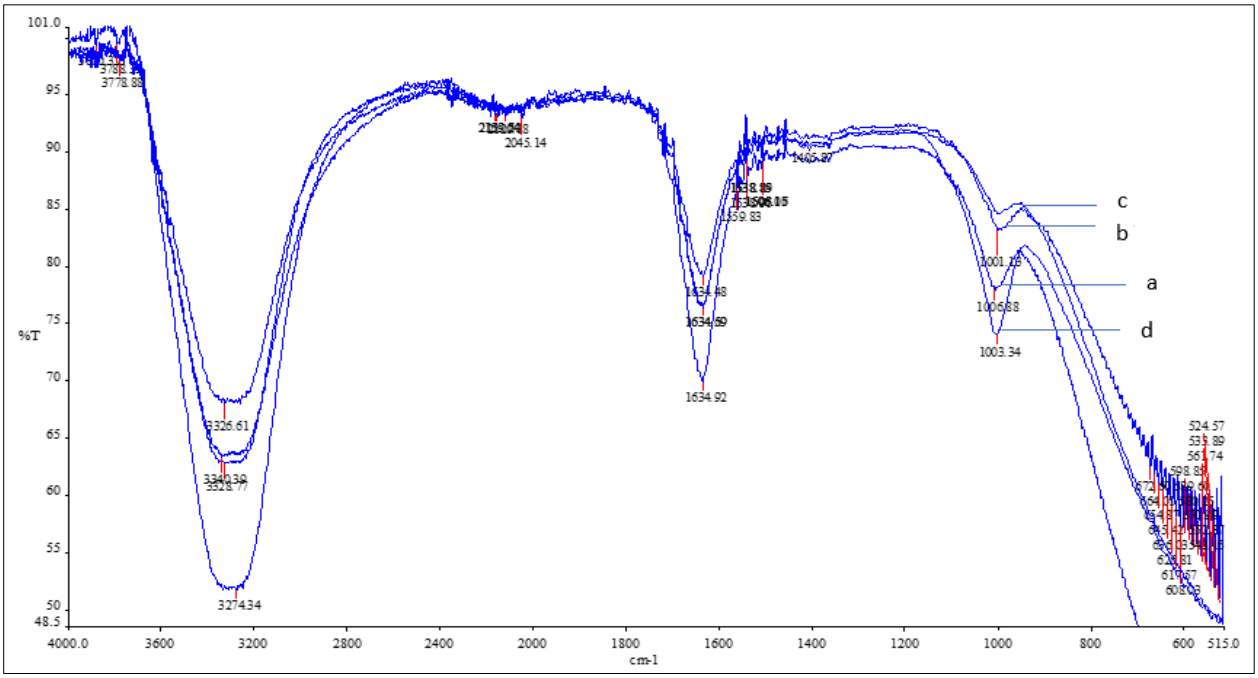

Figure 1. FTIR spectra of treated and untreated RHA of 1M 2H; (a) untreated RHA, (b) treated RHA with 1M 60°C, (c) treated RHA with 2 M 80 °C, and (d) treated RHA with 3 M 60 °C

The presence of O-H stretching was represented by both treated and untreated RHA spectrum, which shows broad characteristic peaks at 3274.34, 3326.61, 3328.77, and 3340.39 cm^{-1} for (a) untreated, (b) treated with 1 M 60 °C, (c) treated with 2 M 80 °C, and (d) treated 3 M 60 °C, respectively (Refer to Table 3). This O-H stretching indicates the presence of phenols and alcohols [23]. The reason for O-H stretching was due to the moisture content in the fibers, which contains hydroxyl groups in the form of lignin, hemicelluloses, and cellulose [24, 25].

Table 3. Wavenumber functional groups identified from treated and untreated RHA at 1M, 2H & 3M

	Wavenumber (cm^{-1})			
Vibration Band Assignment	**Untreated RHA**	**1M 60 °C**	**2M 80 °C**	**3M 60 °C**
Asymmetric stretching of silicate ion	1006.88	1001.13	1008.78	1003.34
O-H	3274.34	3326.61	3328.77	3340.39
O=C=O	2120.18	2155.60	2159.24	2045.14

The presence of O=C=O stretching was represented by both treated and untreated RHA spectrum, which is CO_2 at the wavelength of 2120.18, 2155.60, 2159.24, and 2045.14 cm^{-1} for (a) untreated, (b) treated with 1 M 60

°C, (c) treated with 2 M 80 °C, and (d) treated 3 M 60 °C, respectively (refer to Table 3). Major functional groups of O-H and O=C=O gave rise to bands above ~1500 cm^{-1}. However, the precise pattern of bands seen in the fingerprint region was specific to each compound. The presence of CO_2 in treated and untreated RHA was due to the carbonization process, which produced a gaseous product high in CO_2. However, as shown on the spectrum of treated RHA, the CO_2 formed was present after acid-leaching treatment. This shows that liquid silicate cannot remove volatile materials such as CO_2 [26].

PSA analysis

Table 4 displays the results of the PSA of the treated and untreated RHA at 1 M 2 H. The mean particle diameter decreased with the increase in treatment temperature. The mean particle diameter of H_3PO_4 at 2M 80 °C was recorded as the lowest as compared to other treatments.

Table 4. PSA data for treated and untreated RHA

Component	Untreated	Treated 1 M 60 °C	Treated 2 M 80 °C	Treated 3 M 60 °C
$D_{0.1}$	722.184	878.156	38.975	743.054
$D_{0.5}$	1165.935	1237.355	645.737	1168.995
$D_{0.9}$	1639.751	1645.679	1465.954	1642.913

Note: $D_{0.1}$, $D_{0.5}$, $D_{0.9}$ are the mean diameter for the smallest 10%, 50%, and 90% of the analyzed liquid silicate of untreated RHA, treated RHA at 1 M 60 °C, treated RHA at 2 M 80 °C and treated RHA at 3 M 60 °C.

The particle size was reduced after leaching with H_3PO_4 at 2 M 80 °C before the liquid silicate extraction process. This finding has proven that high temperature is suitable to produce a good small particle size. The temperature has a significant impact on particle size, with lower temperatures producing smaller particles with a larger surface area than higher temperatures [27]. As a result, as the particle size decreases, a greater proportion of the particles are found at the material's surface. Hence, acid leaching treatment is the most suitable method for extracting silica from the rice husk ashes for its application as a fertilizer.

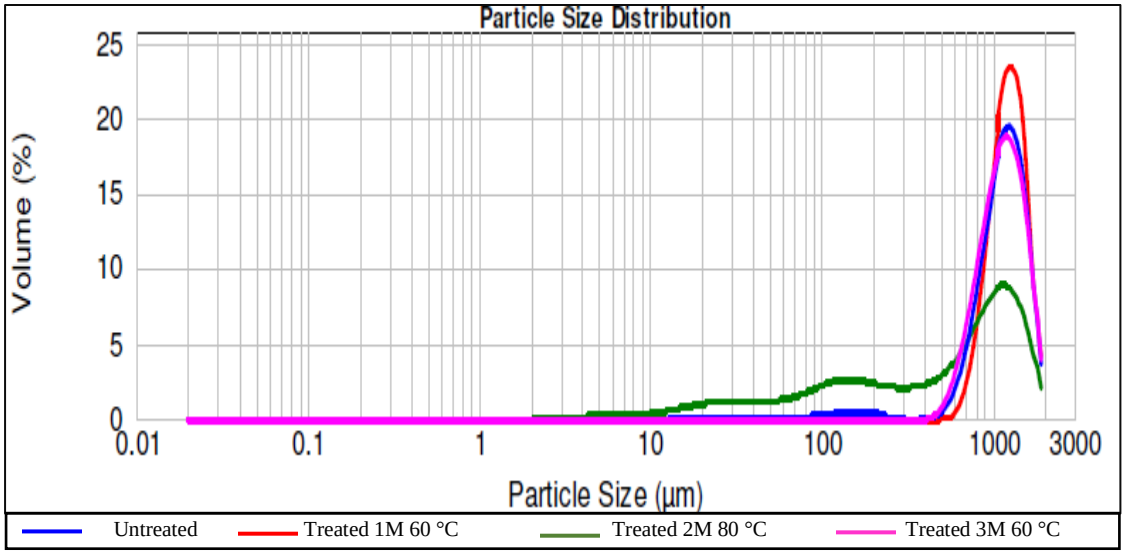

Figure 2. Particle size distributor of treated and untreated RHA at 1M 2H

All organic components dissolve in water, resulting in slow precipitation and small particles forming droplets. The removal of all organic compounds causes more silicate, iron, and potassium ions to be present. Hence, the high amount of silicate particles in the liquid silicate solution of treated RHA at 2 M 80 °C resulted in a decrease in the mean particle diameter.

Figure 2 demonstrates the comparison of particle size distributors between both treated and untreated RHA. As a result, the peak of the treated RHA at 2 M 80 °C was the broadest compared to the rest of the samples as a smaller particle size is preferable as a silicate particle. Besides, the rest of the peak only had a slightly different mean particle diameter. This proved that an acid-leaching treatment process somehow affects the formation of silicate particles.

Conclusion

The characterization of treated and untreated RHA via XRF spectroscopy, FTIR spectroscopy, and PSA of this study has demonstrated that acid leaching treatment using H_3PO_4 produces promising LSF as they contain silica, potassium, iron, and other trace elements, which are deemed to be suitable for plant growth. H_3PO_4 leaching treatment is significantly useful and effective in removing impurities and increasing the silica purity in RHA. Besides that, the alkaline extraction by 1M 2H KOH also exhibits the highest results of silica (40.91%), iron (46.40%), potassium (11.01%), and trace element (1.675%), respectively. These results are correlated with PSA and FTIR analysis. If RHA undergoes suitable treatment such as acid leaching treatment before the extraction process, it will produce high-quality LSF with the addition of other minerals such as iron and potassium.

Acknowledgment

Special gratitude to the School of Chemical Engineering, Universiti Teknologi MARA Shah Alam, Selangor and DIBUK Sdn. Bhd. for their collaboration in this research work.

References

1. Knoema. (2019). Knoema. https://knoema.com/atlas/topics/Agriculture/Crops-Production-Quantity-tonnes/Rice-paddy-production. [Access online August 2022]
2. Abdullah, S. A., Mohd Zarib, N. S. and Jamil, N. H. (2019). Extraction of silica from rice husk via acid leaching treatment. *European Proceedings of Social and Behavioural Sciences EpSBS*, 5: 175-183.
3. Ramezanianpour A. A. (2013). Fly ash. In: Cement replacement materials. *Springer Geochemistry/Mineralogy*, 257 - 298.
4. Sae-Oui, P., Rakdee, C. and Thanmathorn, P. (2002). Use of rice husk ash as filler in natural rubber vulcanizates: In comparison with other commercial fillers. *Journal of Applied Polymer Science*, 83(11): 2485-2493.
5. Mehta, P. K. (1977). Properties of blended cement made from rice husk ash. *American Concrete Institute*, 74(9): 440-442.
6. Earle, S. (2019), Physical geology - Silicate minerals. https://opentextbc.ca/geology/chapter/2-4-silicate-minerals/. [Access online 3 October 2023].
7. Hwang, C. L. and Chandra, S. (1996). The use of rice husk ash in concrete. *Waste Materials Used in Concrete Manufacturing*, pp. 184-234.
8. Hunt, L. P., Dismukes, J. P. Amick, J. A. Schei, A. and Lavsen, K. (1983). Rice hulls as a raw material for producing silicon. *Proceedings - The Electrochemical Society*, 83(11): 106-118.
9. Amick, J. A. (1982). Purification of rice hulls as a source of solar grade silicon for solar cells. *Journal of Electrochem Society*, 129(4): 864-866.
10. Patel, M., Karera, A. and Prasanna, P. (1987). Effect of thermal and chemical treatments on carbon and silica contents in rice husk. *Journal of Material Science*, 22(7): 2457-2464.
11. Umeda, J., Kondoh, K. and Michiura, Y. (2007). Process parameters optimization in preparing high-purity amorphous silica originated from rice husks. *Materials Transactions*, 48(12): 3095-3100.
12. Umeda, J. and Kondoh, K. (2008). High-purity amorphous silica originated from rice husks via carboxylic acid leaching process. *Journal of Material Science*, 43(22): 7084-7090.
13. Umeda, J. and Kondoh, K. (2010). High-purity amorphous silica originated from rice husks by the

combination of polysaccharide hydrolysis and metallic impurities removal. *Industrial Crops and Products*, 32(3): 539-544.

14. Organic Materials Review Institute (2021), OMRI materials review newsletter the winter 2020 issue. https://www.omri.org/phosphoric-acid. [Access online 24 February 2022].
15. Faizul, C. P., Abdullah, C. and Fazlul, B. (2013). Extraction of silica from palm ash using citric acid leaching treatment: Preliminary result. *Advanced Materials Research*, 795: 701–706.
16. Kalapathy, U., Proctor, A. and Shultz, J. (2000). A Simple method for production of pure silica from rice hull ash. *Bioresource Technology*, 73(3): 257-262.
17. Mastersizer (2000). Melvin Instrument. *Pigment Resin Technology*, 27(6): 1-10.
18. Badri, K., Hassan, N. S. and Shen Lim, L. (2015). Silica extraction from rice husk by warm water pretreatment. *Advanced Materials Research*, 1087: 309-315.
19. Puziy, A. M., Poddubnaya, O. I., Martínez-Alonso, A., Castro-Muniz, A., Suárez-García, F. and Tascón, J. M. D. (2007), Oxygen and phosphorus enriched carbons from lignocellulosic material. *Carbon* 45(10): 1941-1950.
20. Puziy, A. M., Poddubnaya, O. I., Martínez-Alonso, A., Castro-Muniz, A., Suárez-García, F. and Tascón, J. M. D. (2007), Oxygen and phosphorus enriched carbons from lignocellulosic material. *Carbon*, 45(10): 1941-1950.
21. Dani Nandiyanto, A. B., Oktiani, R. and Ragadhita, R. (2019). How to read and interpret FTIR spectroscopy of organic material. *Indonesian Journal of Science & Technology*, 4(1): 97-118.
22. Dhaneswara, D., Fatriansyah, J. K., Situmorang, F. W. and Haqoh, A. N. (2020) Synthesis of amorphous silica from rice husk ash: Comparing HCl and CH_3COOH acidification methods and various alkaline concentrations. *International Journal of Technology*, 11(1): 200-208
23. Claoston, N., Samsuri, A. W., Ahmad Husni, M. H. and Mohd Amran, M. S. (2014). Effects of pyrolysis temperature on the physicochemical properties of empty fruit bunch and rice husk biochars. *Waste Management and Research*, 32(4): 331-339.
24. Abdul Khalil, H. P. S., IreanaYusra, A. F., Bhat, A. H. and Jawaid, M. (2010). Cell wall ultrastructure, anatomy, lignin distribution, and chemical composition of malaysian cultivated kenaf fiber. *Industrial Crops and Products*, 31(1): 113-121.
25. Ireana Yusra, A. F, Abdul Khalil, H. P. S., Hossain, M. S., Aziz, A. A., Davoudpour, Y., Dungani, R. and Bhat, A. (2014). Exploration of a chemo-mechanical technique for the isolation of nanofibrillated cellulosic fiber from oil palm empty fruit bunch as a reinforcing agent in composites materials. *Polymers*, 6(10): 2611-2624.
26. Yingjie, L., Changsui, Z., Qiangqiang, R., Lunbo D., Huichao, C. and Xiaoping, C. (2009). Effect of rice husk ash addition on CO_2 capture behavior of calcium-based sorbent during calcium looping cycle. *Fuel Processing Technology*, 90(6): 825-834.
27. Sheard, P. R., Jolley, P. D. and Rush, P. A. J. (1991). Effect of temperature on the particle size distribution of flake-cut meat. *International Journal of Food Science & Technology*, 26(2): 199-205.

Malaysian Journal of Analytical Sciences (MJAS)
Published by Malaysian Analytical Sciences Society

PEROXYMONOSULFATE ACTIVATION USING NITROGEN-DOPED BIOCHAR FOR ACID ORANGE 7 REMOVAL IN WATER

(Pengaktifan Peroksimonosulfat dengan Bioarang Terdop Nitrogen untuk Penyingkiran Asid Oren 7 dalam Air)

Mohamed Faisal Gasim, Nivethah Sivam, and Wen-Da Oh*

School of Chemical Sciences, Universiti Sains Malaysia, 11800 Penang, Malaysia

**Corresponding author: ohwenda@usm.my*

Received: 18 August 2023; Accepted: 21 December 2023; Published: 28 February 2024

Abstract

In this study, N-doped plastic-derived biochar was synthesized at different synthesis temperatures (600, 700 and 800 ºC) using a facile one-pot pyrolysis technique. The as-prepared N-doped biochars were employed to investigate the effect of pyrolysis temperature on the biochar characteristics and catalytic performance as peroxymonosulfate (PMS) activator for acid orange 7 (AO7) removal. The X-ray Diffraction (XRD) analysis indicated that the N-doped biochar consists of amorphous carbon whereas the field emission scanning electron microscope (FESEM) images illustrated that the catalysts have microparticles morphology with porous features. The N-doped biochar synthesized at 800 ºC (N-800) displayed the best performance with 98% AO7 removed in 30 min (pseudo first-order rate constant, k_{app} = 0.211 min^{-1}). The k_{app} was positively affected by increasing the PMS dosage and N-800 loading while neutral condition (pH = 7) was optimum for AO7 removal. The scavenger study suggests that singlet oxygen ($^1O_2$) was the dominant reactive oxygen species (ROS) in this reaction system as sodium azide (NaN_3) scavenger inhibited the AO7 removal by 80%. N-800 catalytic performance in removing AO7 was reduced from 97 to 22% after four consecutive cycles due to irreversible adsorption and oxidation of active sites. Overall, the N-800 was able to activate PMS effectively with a promising potential for sustainable azo dye removal. Future-wise, the employment of co-doping other heteroatoms (such as S, B) into N-doped plastic-derived biochar for synergistic effects should be investigated.

Keywords: advanced oxidation process, peroxymonosulfate, acid orange 7, nitrogen doping, biochar

Abstrak

Dalam kajian ini, bioarang terdop N telah disintesis daripada plastik pada suhu sintesis yang berbeza (600, 700 dan 800 ºC) dengan menggunakan teknik pirolisis satu periuk. Bioarang terdop N yang disediakan telah digunakan untuk menyiasat kesan suhu pirolisis ke atas ciri-ciri bioarang dan prestasi sebagai pemangkin bagi pengaktifan peroksimonosulfat (PMS) untuk penyingkiran asid oren 7 (AO7). Analisa pembelauan sinar-X menunjukkan bioarang terdop N terdiri daripada karbon amorfus manakala mikroskop elektron pengimbasan pelepasan medan (FESEM) menggambarkan bahawa pemangkin mempunyai morfologi mikrozarah dengan ciri berliang. Bioarang terdop N yang disintesis pada 800 ºC (N-800) menunjukkan prestasi terbaik dengan penyingkiran 98% AO7 dalam 30 min (pemalar kadar pseudo tertib pertama, k_{app} = 0.211 min^{-1}). Didapati k_{app} meningkat dengan peningkatan dos PMS dan pemuatan N-800 manakala pH 7 merupakan pH terbaik bagi penyingkiran AO7. Kajian mengunakan perencat radikal natrium azida (NaN_3) menunjukkan bahawa oksigen singlet ($^1O_2$) adalah spesies oksigen reaktif (ROS) yang dominan dalam sistem tindak

balas ini. Prestasi pemangkin N-800 dalam penyingkiran AO7 telah berkurangan daripada 97 kepada 22% selepas empat kitaran berturut-turut disebabkan oleh penjerapan tidak berbalik dan pengoksidaan tapak aktif. Secara keseluruhan, N-800 dapat mengaktifkan PMS dengan berkesan dan menunjukkan potensi penyingkiran pewarna azo yang mampan. Dalam masa hadapan, pendopan bioarang terdop N terbitan plastik bersama heteroatom lain (seperti S, B) perlu disiasat untuk kesan sinergistik.

Kata kunci: proses pengoksidaan lanjutan, peroksimonosulfat, asid oren 7, nitrogen terdop, bioarang

Introduction

Industrialization and population development led to an increase in the usage of water and water pollution. This is predicated on the quality of the water deteriorating and the quantity of hydric resources decreasing, and the world is expected to experience a 40% water shortage by 2030 [1]. Synthetic dyes are widely employed in a variety of industries. Azo dyes are common dyes used in this dyeing industry. Due to the tremendous demand in diverse industries such as pulp and paper, textiles, pharmaceuticals and photo-electrochemical cells, huge amounts of azo dyes are produced globally (about 1 million tons per year) [2]. Acid orange 7 (AO7) is a commonly recognized azo dye since it is low in cost and can be applied rapidly in weakly acidic solutions. Exposure to AO7 has adverse health effects and its consumption is potentially lethal as it is carcinogenic and mutagenic [3]. There are several ways to eliminate AO7 from wastewater including adsorption, biodegradation, and advanced oxidation processes (AOPs). AOPs are chemical treatment procedures designed to remove organic and inorganic materials in wastewater.

Recently, persulfate-based advanced oxidation processes (PS-AOPs) emerged as a viable option for the decontamination of organics in water [1]. The activation of PS can yield strong oxidative species such as sulfate radical ($SO_4^{\bullet-}$), hydroxyl radical ($^{\bullet}OH$) and singlet oxygen ($^1O_2$) [4, 5]. These reactive species can be employed to decompose organic pollutants in wastewater. PS is commercially available as peroxymonosulfate (PMS) and peroxydisulfate (PDS) depending on the number of SO_3^- groups in its structure. Heterogenous catalytic activation of PS is highly preferred over other methods (e.g. heat activation, photoactivation) as no external energy sources are required, making heterogenous catalytic PS activation an economic choice [6]. Between PMS and PDS, the former is more easily activated due to it asymmetricity of structure [7]. Also, PMS is cheaper than PDS [8] making PMS a more advantageous choice of PS to be activated for organic pollutants degradation. Metal-based catalysts are effective in activating PMS, however, the inevitable leaching of metallic ions requiring the need for secondary treatment is a serious drawback [9]. Hence, carbon-based catalysts are emerging as sustainable alternatives. Carbon-based catalysts have preferable characteristics such as excellent specific surface area, microporosity, pore volume, chemical inertness, and stability. Examples of carbon-based catalysts are carbon nanotubes (CNTs), graphene, biochar and nanodiamonds. Among all, biochar is considered as the most economically viable option as it can be prepared directly from biomass waste. The catalytic activity of biochar can be increased by doping with a heteroatom such as nitrogen, sulfur and phosphorus [10]. N is the most compatible heteroatom dopant compared to others (e.g., B, S, P) due to its similar atom size with carbon, high electronegativity, and ability to provide effective active sites for PMS activation [10]. Moreover, the physiochemical properties of the biochar (i.e. thermal stability, functional groups) and the bonding configuration of the N-dopants are dependent on the synthesis temperature of the biochar [11]. These changes affect the overall catalytic performance of the N-doped biochar. Therefore, it is pivotal to study the effects of the synthesis temperature on the catalytic activity of N-doped biochar for PMS activation.

In this study, we aim to prepare and investigate the characteristics of N-doped plastic-derived biochar at different pyrolysis temperatures (600, 700, and 800 ℃). Thereafter, the catalytic performance of the as-prepared N-doped carbon-based catalysts was evaluated as PMS activator for AO7 degradation. The effects of different operational condition (i.e., PMS dosage, catalyst loading, pH) on AO7 removal via PMS activation were evaluated. Chemical scavenging study was employed to

investigate the mechanism of PMS activation by N-doped biochar. Lastly, the reusability of the catalyst was investigated.

Materials and Methods

Chemicals

The disposable vinyl gloves were purchased and used as the precursor in this study. The chemicals employed in this study were urea (QRëC), PMS (as Oxone®, $2KHSO_5 \cdot KHSO_4 \cdot K_2SO_4$, Acros Organics), AO7 (Sigma-Aldrich), sodium hydroxide (NaOH, Fisher Chemical), ethanol (EtOH, 99.7%, QRëC), sodium perchlorate ($NaClO_4$, Sigma-Aldrich), tert-butyl alcohol (TBA, Supelco), and sodium azide (NaN_3, Merck). All experiments were carried out with deionized (DI) water.

Synthesis of N-doped biochar

In this study, the N-doped biochar was synthesized from disposable plastic gloves using a simple one-pot pyrolysis method. Firstly, the plastic gloves were cut into dimension of 1.4×1.4 cm, rinsed several times using DI water and dried in an oven at 60 ℃. Then, the gloves and urea were mixed at a weight ratio of 1:2 (3g of gloves with 6g of urea), respectively, and the mixture was transferred into a crucible. The crucible was closed tightly and wrapped with aluminum foil to produce an oxygen limited atmosphere. Thereafter, the crucible was placed in the furnace (Carbolite Gero Ltd.) and heated to a selected temperature with a heating rate of 10 ℃ min^{-1} for 2 h. The calcination temperature was varied from 600, 700 to 800 ℃. Thereafter, the resultant N-doped biochar was allowed to cool under room temperature, washed several times with DI water and dried in an oven at 60 ℃. The resultant N-doped biochar was labelled as N-600, N-700, and N-800 according to the calcination temperature.

Characterization

The attenuated total reflectance-Fourier transform infrared (ATR-FTIR) spectroscopy (Frontier, Perkin Elmer) was used for the determination of the functional groups of N-doped biochar. The crystal structure/s of the as-prepared N-doped biochar samples were analyzed using the powder X-ray diffraction (XRD) patterns (Bruker D8 Advance diffractometer). Field Emission Scanning Electron Microscope (FESEM, Quanta FEG650, FEI) equipped with energy dispersive X-ray spectroscopy (EDX) were used to analyze the samples' surface morphologies and elemental composition. Thermogravimetric analysis (TGA) was conducted using PerkinElmer thermal analyzer in nitrogen atmosphere (ramping rate = 10 ℃ min^{-1}) to analyze the thermal properties of the as-prepared N-doped biochar samples.

Catalytic performance evaluation

Briefly, a solution containing PMS (0.2 g L^{-1}) and AO7 (10 mg L^{-1}) was prepared in a 250 mL reaction vessel (mole ratio of PMS:AO7 of 1:23). To initiate the catalytic degradation, 0.025 g L^{-1} of the N-doped biochar catalyst was added into the solution mixture mentioned above. At 5 min intervals, 3 mL aliquots of the solution were drawn from the solution and filtered using 0.45 μm cellulose acetate filter to remove the catalyst particles and avoid misleading results. The concentration of AO7 was determined by a calibration curve using a UV-Vis spectrophotometer (Shimadzu 2600 UV–Vis) at $\lambda = 485$ nm. The effects of various operating parameters including initial pH (3-9), catalyst loading (0.01-0.1 g L^{-1}) and PMS dosage (0.1-0.25 g L^{-1}) for AO7 degradation were also studied. To identify the dominant ROS, chemical scavengers were used. TBA (30 mM), NaN_3 (3 mM), $NaClO_4$ (485 mM) and EtOH (2 M), were used as scavengers for $^{\bullet}OH$, $^1O_2$, nonradical electron-transfer, and both $SO_4^{\bullet-}$ and $^{\bullet}OH$, respectively. The degradation tests were performed in duplicates to ensure reproducible results. The reusability of N-800 was studied by conducting four consecutive catalytic cycles in which the N-doped biochar catalyst was recovered using gravitational method, dried and scaled out after each cycle and reused. The total organic carbon (TOC) removal of AO7 by N-800 was measured by using a TOC analyzer (Shimadzu TOC-VCPH).

Results and Discussion

Characterization of biochar catalyst

The crystal structure of the as-synthesized N-800 was investigated using XRD and the results are presented in Figure 1a. In general, the presence of short-range order in the carbon structure is characterized by diffuse and broad bands in XRD patterns, whereas highly crystalline phases with a high degree of long-range order are

confirmed by sharp and distinct peaks. Notably, several diffraction peaks typical of amorphous carbon can be observed at 2θ = 26.2° and 43.9°, representing the (002) and (101) planes, respectively, for N-800. These two planes show the presence of amorphous carbon after the pyrolysis suggesting that the plastic residue has been successfully carbonized into biochar [9]. Apparently, the diffraction peak at 2θ = 26° shows the presence of a crystalline phase with a well-ordered structure produced through calcination and N-doping [12,13]. A sharp peak at 2θ = 29° indicating the existence of crystalline inorganic elements which can be identified as calcium ($CaCO_3$) in plastic residue [14]. The presence of Ca was minimally present in EDX mapping. Other researchers that studied the pyrolysis of other wastes also noted the existence of inorganic elements [15]. Overall, the result showed that the biochar was successfully synthesized.

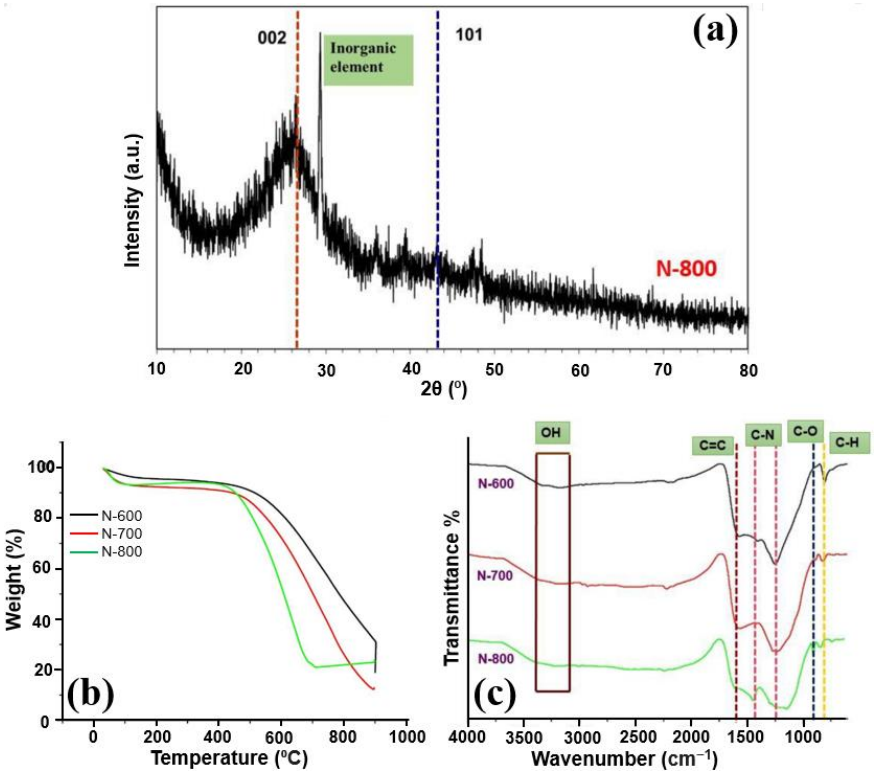

Figure 1. (a) XRD diffractogram, (b) TGA patterns, and (c) FTIR spectra of the as-prepared catalysts

The TGA analysis was carried out to evaluate the thermal stability of N-600, N-700, and N-800 by observing the weight change of the samples with respect to increasing temperature (Figure 1b). All the TGA curves displayed an initial weight loss between 10-30% corresponding to the evaporation of the adsorbed H_2O molecules. There is a continuous drop in weight over a wide temperature range between 500 to 900 °C. Generally, N doping may improve heat tolerance in contrast to normal carbon biochar since N doping induced greater thermodynamic stability of the catalyst against combustion reaction [12]. Furthermore, a larger percent weight/weight inorganic content, which primarily consists of Ca, could increase the proportion of inert components in the carbocatalyst, reducing overall catalytic activity.

The functional groups in the N-doped biochar were analyzed using FTIR and the results are illustrated in Figure 1c. The presence of an absorbance peak at 3250 cm^{-1} is observed signifying -OH bond from hydroxyl and carboxylic groups, and adsorbed water [16]. The broad peaks at the range of 950-1100 cm^{-1} show C-O bond of hydroxyl and alkoxy groups [17]. Several peaks

have appeared at the range of 740-825 cm^{-1} after the thermal treatment indicating the presence of C-H bending vibration (aromatic) while the peak at 1500 cm^{-1} shows that C=C bonding is present. This bonding denotes a higher degree of graphitization [18,19]. Two broad peaks form at 1185 cm^{-1} and 1381 cm^{-1} which shows C-N bond due to the doping of N on the catalyst [20].

The structure and elemental mapping of the synthesized N-800 were characterized using FESEM-EDX (Figure 2). It was observed that N-800 has a morphology consisting of microparticles with porous features. The N-800 displayed a dispersive pore structure making it an effective platform for adsorption and catalysis [10]. The exterior surface of N-800 illustrated roughness with wrinkles and folds suggesting that N doping procedure caused the creation of defective sites. Other than that, N-800 has smooth interior surface indicating that N-doping is limited to the external surface. A possible reason might be the N-doping method where the urea acting as nitrogen precursor will be unable to diffuse into the interior pores implying that adjusting particle size could improve the surface coverage of N species [12]. Besides that, the elemental mapping shows that the N and O atoms are uniformly distributed on N-800. The presence of Ca was also detected in EDX analysis albeit at lower concentration.

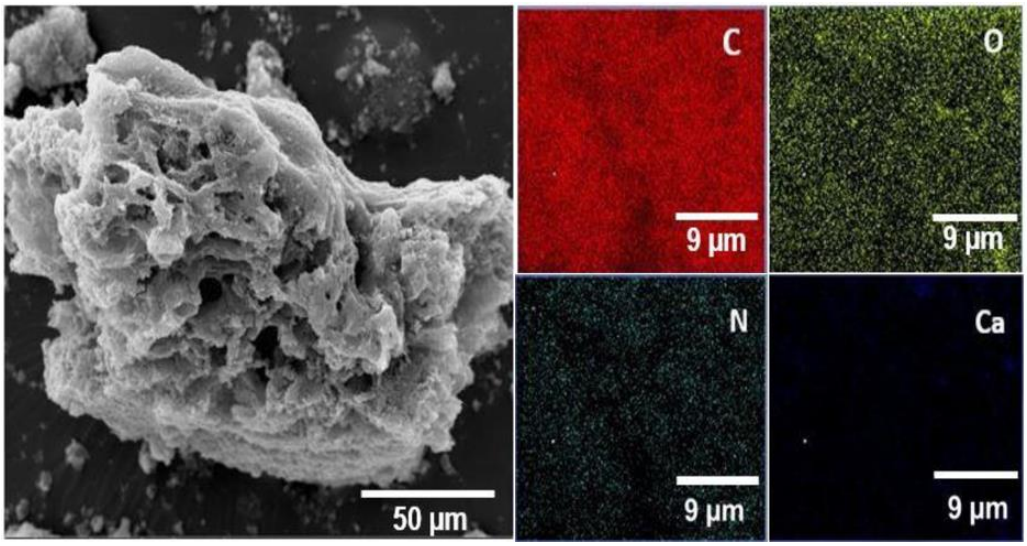

Figure 2. SEM image and elemental mapping of N-800.

Catalytic performance of different catalysts

Figure 3a shows the effect of synthesis temperature of N-doped biochar on the performance of AO7 removal by PMS activation. The control study shows that the AO7 adsorption at 30 min was ~32%. Notably, almost no AO7 degradation was observed in the presence of PMS alone indicating that AO7 is stable to direct PMS oxidation. However, when PMS was activated in presence of N-600, N-700, and N-800, rapid AO7 degradation can be observed. The AO7 degradation by N-doped biochar was evaluated using the pseudo first order kinetics as follows:

$$[AO7]_t = [AO7]_0 \, e^{-kapp\, t} \quad (1)$$

where $[AO7]_t$, $[AO7]_0$, and k_{app} are the AO7 concentration at selected time interval, initial AO7 concentration, and pseudo-first order rate constant (min^{-1}), respectively. Apparently, N-800 displays the best catalytic performance where degradation efficiency of AO7 reached 98% in 30 min while N-600 shows the slowest AO7 removal with only 75% of AO7 removed in 30 min. The obtained k_{app} was in order: N-600 (k_{app} = 0.044 min^{-1}) < N-700 (k_{app} = 0.083 min^{-1}) < N- 800 (k_{app} = 0.211 min^{-1}). While higher calcination temperature will cause the C-N bond to break resulting in the loss of nitrogen, it promotes incorporation of N atoms into the graphitic carbon network as graphitic N [21]. The

graphitic N has been previously identified as the main active site for PMS activation. Hence, N-800 was used in additional degradation studies since it demonstrated the greatest catalytic performance to activate PMS for AO7 degradation.

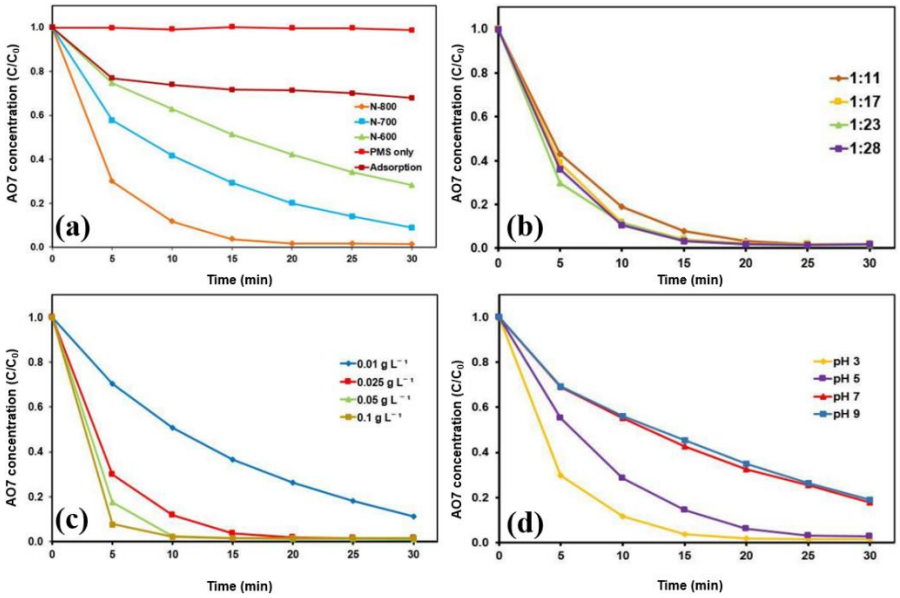

Figure 3. (a) Catalytic degradation of AO7 by different catalysts. Effects of (b) AO7:PMS ratio, (c) catalyst loading, and (d) initial pH

Effect of reaction parameters

Figure 3b shows the effect of PMS dosage on AO7 removal. The k_{app} increased when the ratio of AO7:PMS was decreased in following order: [0.1 g L^{-1} of PMS] 1:11 (k_{app} = 0.155 min^{-1}) < [0.15 g L^{-1} of PMS] 1:17 (k_{app} = 0.161 min^{-1}) < [0.20 g L^{-1} of PMS] 1:23 (k_{app} = 0.170 min^{-1}). However, when the ratio of AO7:PMS was decreased from 1:23 to 1:28 [0.25 g L^{-1} of PMS], the k_{app} decreased to 0.168 min^{-1}. From these results, it can be observed that 1:23 of AO7: PMS shows the highest AO7 degradation rate and optimum rate for AO7 removal. Usually, higher PMS dosage can promote greater interaction between catalyst and PMS for effective AO7 degradation. However, the rate decreased slightly when AO7: PMS was decreased to 1:28 due to the $SO_4^{\bullet-}$ consumption by excessive PMS leading to unproductive $SO_4^{\bullet-}$ use. Excessive PMS could scavenge $SO_4^{\bullet-}$ and produce less reactive $SO_5^{\bullet-}$ (Eq. (2)) [22].

$$HSO_5^- + SO_4^{\bullet-} \rightarrow SO_5^{\bullet-} + SO_4^{2-} + H^+ \quad (2)$$

Figure 3c shows the effect of catalyst loading on the AO7 removal. The degradation efficiency and rate increased linearly with increasing catalyst loading in the following order: 0.01 g L^{-1} (k_{app} = 0.067 min^{-1}) < 0.025 g L^{-1} (k_{app} = 0.211 min^{-1}) < 0.05 g L^{-1} (k_{app} = 0.260 min^{-1}) < 0.1 g L^{-1} (k_{app} = 0.264 min^{-1}). Increasing the catalyst loading increases the concentration of active sites available for PMS activation to produce ROS for AO7 degradation [12,23]. As the catalyst can be reused, modifying the catalyst loading is a more effective strategy to manage the reaction than adjusting PMS dosage. The effect of pH on the degradation of AO7 is presented in Figure 3d. From the figure, the catalytic activity of N-800 is much better achieved under acidic conditions compared with neutral and alkaline conditions. The k_{app} for AO7 removal increased in the following order: pH 3 (k_{app} = 0.170 min^{-1}) > pH 5 (k_{app} = 0.130 min^{-1}) > pH 7 (k_{app} = 0.057 min^{-1}) > pH 9 (k_{app} =0.054 min^{-1}). This observation might be due to the repulsion effect between the surface of the catalyst (pH_{pzc} = 7.4), AO7 (pKa = 10.7) and PMS (pKa_2 = 9.4) [12,23]. Both radical and nonradical routes require PMS

to be in contact with the surface of the catalyst to facilitate the direct electron transfer process. Therefore, this surface repulsion will be detrimental to the reaction, decreasing the overall rate of degradation of AO7 [24,25]. Moreover, the initial pH may have an impact on how much AO7 is adsorbed by the catalyst, causing it to adsorb more AO7 in moderately acidic conditions and increasing the AO7 degradation rate [26].

Identification reactive species and possible catalytic mechanism

For PMS activation using carbocatalysts, there are two activation pathways that have been reported which are the radical and nonradical pathways. These pathways have an impact on the system's performance. Chemical scavengers such as EtOH, TBA, NaN_3 and $NaClO_4$ were used to identify the dominant ROS. EtOH was used to selectively scavenge $^{\bullet}OH$ and $SO_4^{\bullet-}$ ($k_{SO4^{\bullet-}+EtOH}$ = 1.6 × 10^7 M^{-1} s^{-1}; $k_{^{\bullet}OH+EtOH}$ = 1.9 × 10^9 M^{-1} s^{-1}) [12]. As shown in Figure 4, the addition of EtOH into the reaction system shows 48% inhibition and reduced the k_{app} from 0.170 min^{-1} to 0.088 min^{-1}. This suggests that $SO_4^{\bullet-}$ and $^{\bullet}OH$ might be involved in degradation of AO7. To determine the dominant radical, TBA was used to quench $^{\bullet}OH$ because TBA has larger value of reaction rate constant with $^{\bullet}OH$ compared to $SO_4^{\bullet-}$ ($k_{SO4^{\bullet-}+TBA}$ = 4–9.1 × 10^5 M^{-1} s^{-1}, $k_{^{\bullet}OH+TBA}$ = 3.8–7.6 × 10^8 M^{-1} s^{-1}) [12]. TBA shows a minor inhibitory effect in this reaction system. This suggests that the involvement of $^{\bullet}OH$ was limited in degradation of AO7. Next, $NaClO_4$ was employed to reduce the interaction between the catalyst and PMS which decreases the formation of surface complexes for the nonradical pathway. $NaClO_4$ addition into the reaction system shows a 30% inhibition and reduced the k_{app} from 0.170 min^{-1} to 0.119 min^{-1}. $NaClO_4$ can reduce the amount of the nonradical pathway without significantly influencing the radical pathway because it can hinder the surface contact between PMS and the catalyst [27]. Finally, NaN_3 is used to scavenge $^1O_2$. When NaN_3 was employed, the percentage of inhibition was 80% and k_{app} was reduced from 0.170 min^{-1} to 0.034 min^{-1}. The highest inhibitory effect shown by the NaN_3 signifies that $^1O_2$ was dominant in the system.

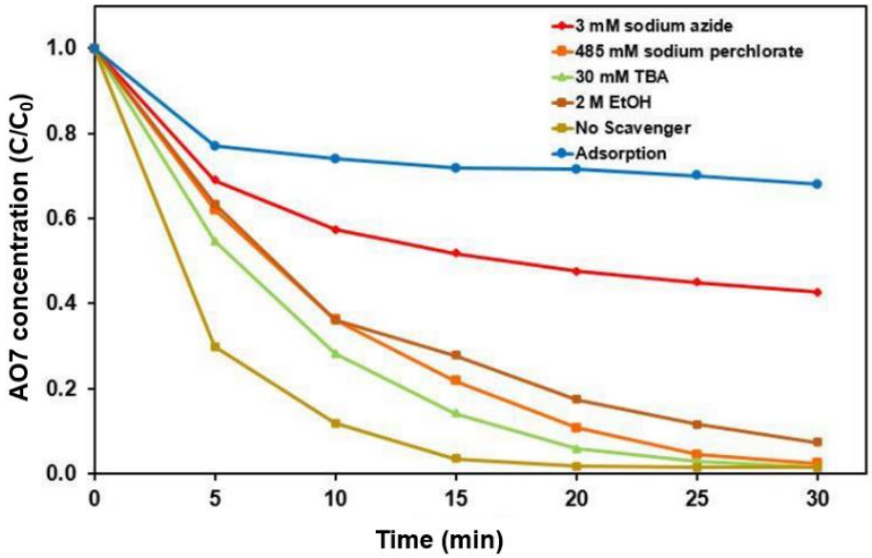

Figure 4. Effect of chemical scavengers on AO7 degradation efficiency by N-800

The results show that there was coexistence between radical and nonradical pathway in this system. Sun et al. proposed that the radical route occurs when the abundant free-flowing electrons from sp^2 carbons conjugate with the lone-pair electrons of N dopants found at Lewis basic sites containing lone-pair electrons such as pyridinic N, pyrrolic N, and ketonic groups. These functional groups can operate as electron donors, transferring electrons to activate PMS by cleaving the O-O bond resulting in production of $SO_4^{\bullet-}$ and $^{\bullet}OH$

[28,29]. Oh et al. proposed that N-doped biochar from biomass waste can be considered as an optimal surface for electron transfer reactions to take place since it has a high concentration of graphitic N and sp^2 hybridized carbon. An electron-deficient environment for the carbon atom is produced when the highly electronegative N atom in the graphitic plane attracts an electron from the less electronegative carbon next to it. Through an electron abstraction process, the electron-deficient carbon may interact strongly with PMS, resulting in the production of $^1O_2$ [30]. The overall results are in consistent with this observation. Hence, it can be speculated that Lewis base group like pyridinic N, pyrrolic N and ketonic groups involved in free radical pathway, while $^1O_2$ formation involves in PMS activation by electron deficient carbon induced by the graphitic N (dominant). The mechanism of PMS activation by N-doped plastic-derived biochar for AO7 degradation is illustrated in Figure 5.

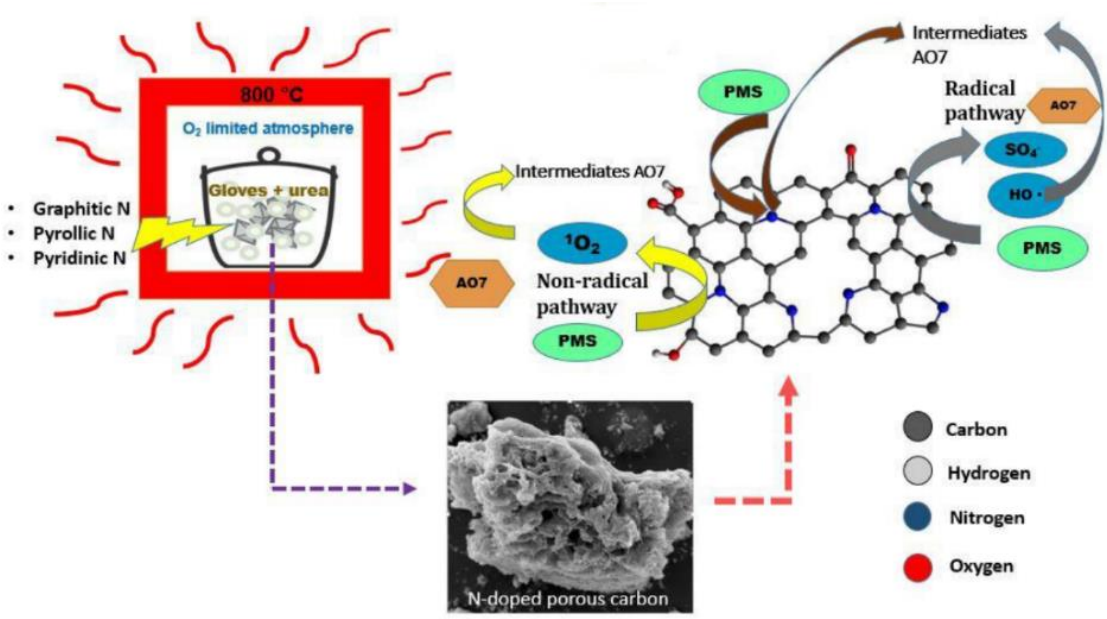

Figure 5. Mechanism of PMS activation for AO7 removal by N-800

Reusability of N-800

In practical applications, stability of N-800 in the PMS system for degradation of pollutant is important. The degradation of AO7 was carried out 4 times using recycled N-800 biochar and the results are presented in Figure 6. In the first cycle, the degradation rate was 97% in 30 min. The removal efficiency was reduced to 89%, 56%, 22% within 30 min in the second, third and fourth cycles, respectively. The N-800 deactivation could be ascribed to the change of configuration of nitrogen bonding and intermediates coverage of catalyst which blocked the PMS interaction with active sites and minimized production of ROS [21]. In short, the N-800 can still efficiently remove AO7 after being used repeatedly. TOC removal of ~5% was achieved in the first 60 min of the oxidation reaction. After 3h, TOC removal reached a 10% suggesting that AO7 can be mineralized by the oxidation processes (Eq. (3)) provided that prolong treatment time was employed.

$$AO7 + ROS \rightarrow CO_2 + H_2O + \text{inorganic ions} \quad (3)$$

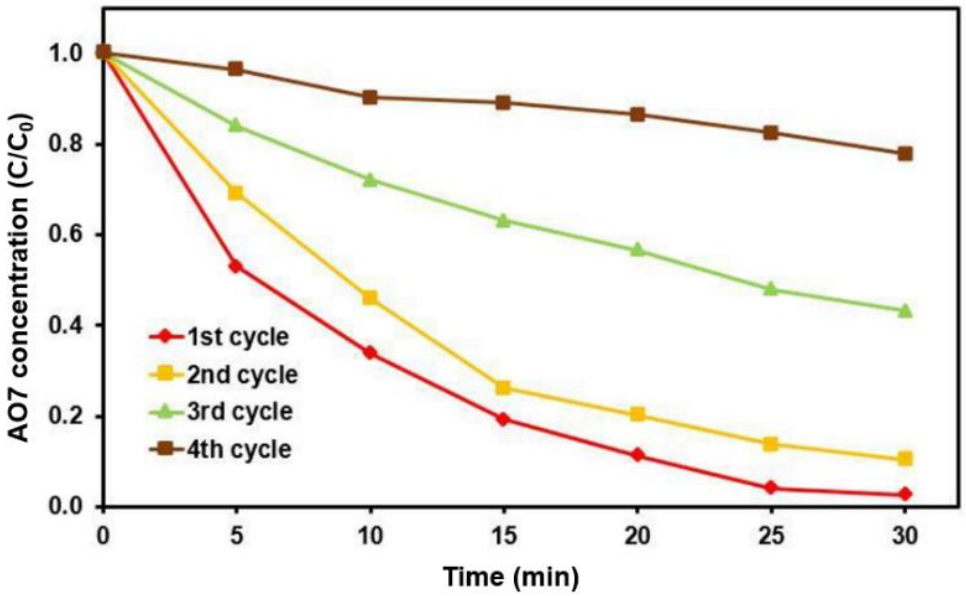

Figure 6. Reusability of N-800 in AO7 removal

Conclusion

In conclusion, N-doped biochar was successfully synthesized by utilizing a thermal calcination approach in an oxygen-limited environment for AO7 degradation by PMS activation. The obtained FTIR spectra of all N-doped biochar and XRD patterns of N-800 proved that the catalysts were successfully synthesized in this study. Through FESEM-EDX, it can be confirmed that N-800 consisted of microparticles with a porous feature with uniform distribution of the N atoms. From effect of synthesis temperature on the performance of AO7 removal by PMS activation, N-800 exhibited the highest efficiency in degrading AO7 and was used for further degradation experiments. About 98% of AO7 was successfully eliminated within 30 min employing N-800/PMS. The catalytic activity of N-800 in terms of PMS activation for AO7 removal with various operating variables (i.e. initial pH, catalyst loading, and PMS dosage) were investigated. The k_{app} values were found to be increasing with the increasing catalyst loading. An AO7: PMS ratio of 1:23 was found to be the optimum ratio for the degradation of AO7. The lower dosage of PMS lowered the k_{app} due to the limited PMS molecules available for activation and ROS formation. Excessively higher dosage of PMS also lowered the k_{app} because it could scavenge $SO_4^{\bullet-}$ and produce less reactive $SO_5^{\bullet-}$. On the other hand, the study on initial pH indicated that the ideal operating pH is found in acidic conditions. This can be explained by the surface repulsion between catalyst, PMS and AO7 at alkaline pH. The TOC removal efficiency by using N-800 was 10% indicating that mineralization of AO7 was achieved. Moreover, the catalyst was able to be reused for four consecutive cycles. Scavenger studies showed that the $^1O_2$ pathway was the prevailing pathway in the degradation of AO7. Overall, it can be inferred that SR-AOPs is a promising technology which can be used effectively to treat organic contaminants in the wastewater.

Acknowledgement

The authors would like to acknowledge the financial support provided by the Ministry of Higher Education Malaysia for Fundamental Research Grant Scheme (FRGS) with project code: FRGS/1/2020/STG04/USM/02/2.

References

1. Guerra-Rodríguez, S., Rodríguez, E., Singh, D. N. and Rodríguez-Chueca, J. (2018). Assessment of sulfate radical-based advanced oxidation processes for water and wastewater treatment: a review. *Water (Switzerland)*, 10(12): 1828.
2. Swain, G., Singh, S., Sonwani, R. K., Singh, R. S., Jaiswal, R. P. and Rai, B.N. (2021). Removal of

acid orange 7 dye in a packed bed bioreactor: process optimization using response surface methodology and kinetic study. *Bioresource Technology Reports*, 13: 100620.

3. Perera, H. J. (2020). Removal of acid orange 7 dye from wastewater: review. *Advances in Science and Engineering Technology International Conferences*, pp. 1-6.
4. Oh, W. Da, Dong, Z. and Lim, T. T. (2016). Generation of sulfate radical through heterogeneous catalysis for organic contaminants removal: current development, challenges and prospects. *Applied Catalysis B: Environmental* 194: 169-201.
5. Xia, X., Zhu, F., Li, J., Yang, H., Wei, L., Li, Q., Jiang, J., Zhang, G. and Zhao, Q. (2020). A Review study on sulfate-radical-based advanced oxidation processes for domestic/industrial wastewater treatment: degradation, efficiency, and mechanism. *Frontiers in Chemistry* 8: 1092.
6. Gasim, M. F., Veksha, A., Lisak, G., Low, S.C., Hamidon, T.S., Hussin, M.H. and Oh, W. Da (2023). Importance of carbon structure for nitrogen and sulfur co-doping to promote superior ciprofloxacin removal via peroxymonosulfate activation. *Journal of Colloid and Interface Science*, 634: 586-600.
7. Song, H., Yan, L., Wang, Y., Jiang, J., Ma, J., Li, C., Wang, G., Gu, J. and Liu, P. (2020). Electrochemically activated PMS and PDS: Radical oxidation versus nonradical oxidation. *Chemical Engineering Journal*, 391: 123560.
8. Gasim, M. F., Choong, Z. Y., Koo, P. L., Low, S. C., Abdurahman, M. H., Ho, Y. C., Mohamad, M., Suryawan, I. W. K., Lim, J. W. and Oh, W. Da (2022). Application of biochar as functional material for remediation of organic pollutants in water: an overview. *Catalysts*, 12(2): 210.
9. Wang, J., Cai, J., Wang, S., Zhou, X., Ding, X., Ali, J., Zheng, L., Wang, S., Yang, L., Xi, S. et al. (2022). Biochar-based activation of peroxide: multivariate-controlled performance, modulatory surface reactive sites and tunable oxidative species. *Chemical Engineering Journal*, 428: 131233.
10. Han, R., Fang, Y., Sun, P., Xie, K., Zhai, Z., Liu, H. and Liu, H. (2021). N-doped biochar as a new metal-free activator of peroxymonosulfate for singlet oxygen-dominated catalytic degradation of acid orange 7. *Nanomaterials*, 11(9): 2288.
11. Gasim, M. F., Lim, J.-W., Low, S.-C., Lin, K.-Y.A. and Oh, W.-D. (2022). Can biochar and hydrochar be used as sustainable catalyst for persulfate activation? *Chemosphere*, 287: 132458.
12. Oh, W. Da, Veksha, A., Chen, X., Adnan, R., Lim, J. W., Leong, K. H. and Lim, T.T. (2019). Catalytically active nitrogen-doped porous carbon derived from biowastes for organics removal via peroxymonosulfate activation. *Chemical Engineering Journal*, 374: 947-957.
13. Ungár, T., Gubicza, J., Ribárik, G., Pantea, C. and Zerda, T. W. (2002). Microstructure of carbon blacks determined by X-ray diffraction profile analysis. *Carbon*, 40(6): 929-937.
14. Ng, W.-Y., Choong, Z.-Y., Gasim, M. F., Khoerunnisa, F., Lin, K.-Y.A. and Oh, W.-D. (2002). Insights into the performance and kinetics of face mask-derived nitrogen-doped porous carbon as peroxymonosulfate activator for gatifloxacin removal. *Journal of Water Process Engineering*, 50: 103239.
15. Lawrinenko, M. and Laird, D. A. (2015). Anion exchange capacity of biochar. *Green Chemistry*, 17(9): 4628-4636.
16. Guo, D., Xin, R., Wang, Y., Jiang, W., Gao, Q., Hu, G. and Fan, M. (2019). N-doped carbons with hierarchically micro- and mesoporous structure derived from sawdust for high performance supercapacitors. *Microporous and Mesoporous Materials*, 279: 323-333.
17. Dey, R. S., Hajra, S., Sahu, R. K., Raj, C. R. and Panigrahi, M. K. (2012). A rapid room temperature chemical route for the synthesis of graphene: metal-mediated reduction of graphene oxide. *Chemical Communications*, 48(12): 1787-1789.
18. Liu, N., Zhang, Y., Xu, C., Liu, P., Lv, J., Liu, Y.Y. and Wang, Q. (2020). Removal mechanisms of aqueous Cr(VI) using apple wood biochar: a spectroscopic study. *Journal of Hazardous Materials*, 384: 121371.
19. Yu, J., Tang, L., Pang, Y., Zeng, G., Wang, J., Deng, Y., Liu, Y., Feng, H., Chen, S. and Ren, X. (2019). Magnetic nitrogen-doped sludge-derived biochar catalysts for persulfate activation: Internal

electron transfer mechanism. *Chemical Engineering Journal*, 364: 146-159.

20. Maiyalagan, T. and Viswanathan, B. (2005). Template synthesis and characterization of well-aligned nitrogen containing carbon nanotubes. *Materials Chemistry and Physics*, 93(2-3): 291-295.
21. Xu, L., Wu, C., Liu, P., Bai, X., Du, X., Jin, P., Yang, L., Jin, X., Shi, X. and Wang, Y. (2020) Peroxymonosulfate activation by nitrogen-doped biochar from sawdust for the efficient degradation of organic pollutants. *Chemical Engineering Journal*, 387: 124065.
22. Fan, Y., Zhou, Z., Feng, Y., Zhou, Y., Wen, L. and Shih, K. (2020). Degradation mechanisms of ofloxacin and cefazolin using peroxymonosulfate activated by reduced graphene oxide-$CoFe_2O_4$ composites. *Chemical Engineering Journal*, 383: 123056.
23. Li, Z., Sun, Y., Yang, Y., Han, Y., Wang, T., Chen, J. and Tsang, D.C.W. (2020). Biochar-supported nanoscale zero-valent iron as an efficient catalyst for organic degradation in groundwater. *Journal of Hazardous Materials*, 383: 121240.
24. Zhang, T., Zhu, H. and Croué, J. P. (2013). Production of sulfate radical from peroxymonosulfate induced by a magnetically separable $CuFe_2O_4$ spinel in water: Efficiency, stability, and mechanism. *Environmental Science and Technology*, 47(6): 2784-2791.
25. Pérez-Urquiza, M. and Beltrán, J. L. (2001). Determination of the dissociation constants of sulfonated azo dyes by capillary zone electrophoresis and spectrophotometry methods. *Journal of Chromatography A* 917(1–2): 331-336.
26. Khan, R., Habib, M., Gondal, M. A., Guan, K., Zhou, P., Zhang, J. and Zhu, L. (2020). Catalytic degradation of acid orange 7 in water by persulfate activated with $CuFe_2O_4$@RSDBC. *Materials Research Express*, 7(1): 016529.
27. Zaeni, J. R. J., Lim, J. W., Wang, Z., Ding, D., Chua, Y. S., Ng, S. L. and Oh, W. Da (2020). *In situ* nitrogen functionalization of biochar via one-pot synthesis for catalytic peroxymonosulfate activation: characteristics and performance studies. *Separation and Purification Technology*, 241: 116702.
28. Sun, P., Liu, H., Feng, M., Guo, L., Zhai, Z., Fang, Y., Zhang, X. and Sharma, V. K. (2019). Nitrogen-sulfur co-doped industrial graphene as an efficient peroxymonosulfate activator: singlet oxygen-dominated catalytic degradation of organic contaminants. *Applied Catalysis B: Environmental*, 251: 335-345.
29. Sun, H., Peng, X., Zhang, S., Liu, S., Xiong, Y., Tian, S. and Fang, J. (2017). Activation of peroxymonosulfate by nitrogen-functionalized sludge carbon for efficient degradation of organic pollutants in water. *Bioresource Technology*, 241: 244-251.
30. Chen, X., Oh, W. Da, Hu, Z. T., Sun, Y. M., Webster, R. D., Li, S. Z. and Lim, T. T. (2018). Enhancing sulfacetamide degradation by peroxymonosulfate activation with n-doped graphene produced through delicately-controlled nitrogen functionalization via tweaking thermal annealing processes. *Applied Catalysis B: Environmental*, 225: 243-257.

Malaysian Journal of Analytical Sciences (MJAS)
Published by Malaysian Analytical Sciences Society

SPECTROSCOPIC, CRYSTAL STRUCTURE, HIRSHFELD SURFACE AND DFT STUDIES OF 2-AMINO-4-CHLOROBENZONITRILE

(Kajian Spektroskopi, Struktur Hablur, Permukaan Hirsfeld dan DFT bagi 2-Amino-4-Klorobenzonitril)

Onur Erman Dogan[1], Erbil Agar[1], Necmi Dege[2], Erna Normaya[4], Siti Syaida Sirat[3,5], and Nur Nadia Dzulkifli[3*]

[1]*Department of Chemistry, Faculty of Arts and Sciences, Ondokuz Mayıs University, Samsun, Turkey*
[2]*Department of Physics, Faculty of Arts and Sciences, Ondokuz Mayıs University, Samsun, Turkey*
[3]*School of Chemistry and Environment, Faculty of Applied Sciences, Universiti Teknologi MARA Cawangan Negeri Sembilan, Kampus Kuala Pilah, Pekan Parit Tinggi, 72000 Kuala Pilah, Negeri Sembilan, Malaysia*
[4]*Experimental and Theoretical Research Laboratory, Department of Chemistry, Kulliyyah of Science, International Islamic University Malaysia, Jalan Sultan Haji Ahmad Shah, Bandar Indera Mahkota, 25200, Kuantan, Pahang, Malaysia*
[5]*Atta-ur-Rahman Institute for Natural Product Discovery (AuRIns), Universiti Teknologi MARA, Kampus Puncak Alam, 42300 Bandar Puncak Alam, Selangor, Malaysia*

**Corresponding author: nurnadia@uitm.edu.my*

Received: 2 July 2023; Accepted: 4 November 2023; Published: 28 February 2024

Abstract

This research concentrates on a summary of the global reactivity parameters on the single crystal structure of 2-amino-4-chlorobenzonitrile, which can be utilised in a wide range of applications. The commercial 2-amino-4-chlorobenzonitrile in light yellow (Sigma-Aldrich) [ACBN] was recrystallized from ethanol. The compound crystallizes in the triclinic, *P-1* space group with unit cell parameters *a* =3.8924 (9) Å, *b* = 6.7886 (15) Å, *c* = 13.838 (3) Å, *α* =77.559 (16)°, *β* = 8.898 (17)° and γ = 83.021 (17)°. The presence of intermolecular interactions was further analyzed via the Hirshfeld Surface analysis. The electronic properties of the compound were investigated via the Density Functional Theory (DFT) using the CIF file of the single crystal. Full geometry optimization was carried out using the DFT at B3LYP with 6- 311++G (d, p) basis set level. The structure of the recrystallized ACBN was confirmed via single crystal X-ray Crystallography, FTIR, and UV-Vis. The IR spectrum showed three main stretching bands namely nitrile, C≡N (2211 cm^{-1}), C-Cl (782 cm^{-1}), and 1° NH (3452 and 3363 cm^{-1}). The UV-Vis analysis showed two main absorption peaks namely $\pi \rightarrow \pi*$ and $n \rightarrow \pi*$ which occured in an aromatic ring and nitrile, C≡N. The compound crystallized in the triclinic system with the space group Pī. Nitrile (C≡N) and C-N have bond lengths of 1.146(4) and 1.369(4) Å, which are less than the theoretical values of 1.160 and 1.470 Å due to the conjugation of the aromatic ring. The intrinsic molecular characteristics analysis showed that the compound has the capability to donate electrons although it is categorized as a hard compound. The exploration of intrinsic molecular features revealed that, despite the fact that ACBN is stable and less reactive, it still has the ability to transfer and accept electrons. Furthermore, the Mulliken analysis revealed that the compound has the capability to function as a nucleophilic agent due to the nitrogen atoms (highly negative charges). As recommendation, the DFT study revealed that the compound can be investigated more thoroughly in terms of reaction kinetics and mechanisms such as corrosion inhibition and biological activities.

Keywords: benzonitrile, density functional theory, mulliken, molecular electrostatic potential, Hirshfeld surface

Abstrak

Kajian ini menumpukan kepada ringkasan parameter kereaktifan global bagi struktur hablur tunggal 2-amino-4-klorobenzonitril, yang boleh diaplikasikan dalam pelbagai kegunaan. Komersial 2-amino-4-klorobenzonitril yang berwarna kuning cair (Sigma-Aldrich) [ACBN] telah dilakukan penghabluran semula daripada etanol. Sebatian tersebut menghablur dalam triklinik, kumpulan ruang P-1 dengan parameter sel unit a =3.8924 (9) Å, b = 6.7886 (15) Å, c = 13.838 (3) Å, α =77.559 (16)°, β = 8.898 (17)° and γ = 83.021 (17)°. Kewujudan interaksi antara molekul dianalisis selanjutnya dengan Permukaan Hirshfeld. Sifat elektronik sebatian telah dikaji dengan Teori Fungsian Ketumpatan (DFT) menggunakan fail CIF hablur tunggal. Pengoptimuman geometri penuh sebatian telah dilakukan menggunakan B3LYP dengan tahap asas 6- 311++G (d, p). Struktur hablur ACBN telah disahkan melalui Kristalografi sinar-X hablur tunggal, FTIR, dan UV-Vis. Spektrum IR menunjukkan tiga jalur regangan yang utama iaitu nitril, C≡N (2211 cm^{-1}), C-Cl (782 cm^{-1}), dan 1° NH (3452 dan 3363 cm^{-1}). Analisis UV-Vis menunjukkan dua puncak serapan utama iaitu $\pi \rightarrow \pi*$ dan $n \rightarrow \pi*$ yang wujud dalam gegelang aromatik dan nitril, C≡N. Sebatian itu terhablur dalam sistem triklinik dengan kumpulan ruang Pī. Nitril (C≡N) dan C-N mempunyai panjang ikatan iaitu 1.146(4) dan 1.369(4) Å di mana kurang daripada nilai teori iaitu 1.160 dan 1.470 Å disebabkan oleh konjugasi dalam gegelang aromatik. Analisis ciri molekul intrinsik menunjukkan bahawa sebatian ACBN mempunyai keupayaan untuk menderma elektron walaupun dikategorikan sebagai sebatian keras. Penerokaan ciri molekul intrinsik mendedahkan bahawa, walaupun hakikatnya ACBN adalah stabil dan kurang reaktif tapi masih mempunyai keupayaan menderma dan menerima elektron. Tambahan pula, analisis Mulliken mendedahkan bahawa sebatian tersebut mempunyai keupayaan untuk berfungsi sebagai agen nukleofilik disebabkan oleh atom nitrogen mempunyai cas negatif yang tinggi. Sebagai cadangan, analisis DFT mendedahkan bahawa sebatian ACBN boleh dikaji lebih teliti dari segi kinetik tindak balas kimia dan mekanisma seperti perencatan kakisan dan aktiviti biologi.

Kata kunci: benzonitril, teori fungsian ketumpatan, Mulliken, potensi elektrostatik molekul, permukaan Hirshfeld

Introduction

Benzonitrile (BN) is produced primarily by heating benzoic acid and theocyanate at 191°C. The liquid benzonitrile smells of almond and is clear and colorless. Due to its properties as an aprotic polar solvent, BN has been widely employed as a solvent in chemistry. In headspace and aqueous extract aromas, it is a powerful odorant. Derivatives of benzonitrile are used in the food preservation business as well as the dye industry to create aniline blue [1]. Besides that, in medicine, the primary byproducts of benzonitrile-benzoic acid are used as urinary antiseptics in salt form and bronchial tube disinfectants in vapor form. Nitrile derivatives have a wide range of industrial applications; for instance, phthalonitrile has been utilized as a precursor to phtalocyanide, a crucial component of dyes [2]. Lacquers, polymers, anhydrous metallic salts as well as medicinal, agrochemical, and other organic chemical intermediates are all generated from benzoinitrile (BN) and its derivatives [3]. Benzonitrile, which features an electron-donor CN substituent, is referred to as being bi-functional since it has the capability to interact with both the CN lone pair and the π-conjugated ring surfaces [4]. The cyano (C≡N) group is a versatile ligand that can serve as both an acceptor and a donor [5]. It is known that the C≡N stretching frequency of the nitrile group changes from low to high depending on whether or not it interacts with a solvent that donates hydrogen bonds [6]. For the re-crystallized compound, Density Functional Theory (DFT) calculations utilizing the B3LYP level of theory and the LANL2DZ basis set were reported, including geometry optimization, vibrational frequency analysis, and electronic structures. This work concentrates on the DFT analysis, with data generated using single crystal data of 2-amino-4-chlorobenzonitrile (CIF format). Although a previous study on DFT analysis by Sudha et al. (2011) was discussed, the researchers employed the proposed structure rather than single crystal data. It is clear that the DFT and Hirshfeld Surface analysis data generated using the CIF file is very different from the previous study. Besides that, the spectroscopic study of ACBN is also discussed in this work. The goal of studying the intrinsic molecular features of ACBN by DFT is to determine its potential to be used in corrosion inhibition, biological activity, energy storage, energy conversion, and other applications.

Materials and Methods

The commercial 2-amino-4-chlorobenzonitrile (Sigma-Aldrich) was recrystallized from ethanol.

Physical measurements

Using a Shimadzu FTIR-8900 spectrophotometer with KBr pellets, the IR spectrum of the compound was recorded in the range 4000-400 cm^{-1}. The ultraviolet absorption spectra of the compound were analyzed in the range 200-400 nm using a Unicam UV-Vis spectrophotometer device with a 10-mm quartz cell. The UV model was taken from a 2×10^{-5} M solution of the compound, dissolved in ethanol at 20°C.

Crystal structure determination

A yellow crystal with dimensions of 0.044 × 0.285 × 0.672 mm was mounted on the goniometer of a STOE IPDS II diffractometer. At room temperature (296 K), measurements were performed using graphite monochromate MoKα radiation (λ = 0.71073 Å). Reflections were gathered in the rotation mode and cell parameters were determined using the X-AREA software [7]. Absorption correction was achieved by the integration method via X-RED32 software [7]. SHELXS 97 [8] was used in the solvation of the structure by direct methods. All atoms except for hydrogens were refined anisotropically by the full-matrix least squares procedure based on F2 using SHELXL-97 [8]. All H atoms were positioned geometrically and treated using a riding model, fixing the bond lengths at 0.86, 0.93, and 0.96 Å for NH, CH and CH_3, respectively. The program ORTEP-3 for windows [9] and MERCURY [10] was used in the preparation of the figures. The crystal data collection and refinement parameters are given in Table 2.

Hirshfeld surface analysis

The Hirshfeld surface analyses were done using the CrystalExplorer17.5 program [11]. The normalized contact distances (dnorm) were mapped into the Hirshfeld surface, which allowed the visualization of intermolecular interactions. The red color represents the closest contact because it indicates the sum of di (the distance from the surface to the nearest nucleus internal to the surface) and de (the distance from the surface to the nearest nucleus external to the surface) whereby de is shorter than the sum of the relevant van der Waals radii. The blue and white color signify the negligible and weak intermolecular interactions, respectively. The two-dimensional fingerprint plots were used to quantify the various intermolecular interactions in the title compound.

Density functional theory

All computations were performed using the Gaussian09 software package. Full geometry optimization was carried out using the Density Function Theory at B3LYP with 6-311++G (d, p) basis set level. The Mullikan charge distributions of the investigated compound was also computed at the same level of method. The GaussView 5.0 program was used to construct the optimized molecular geometry, HOMO and LUMO electron distributions, and the HOMO-LUMO energy gap. The TD-DFT calculation was performed on the ethanol solvent using the IEPCM method.

Results and Discussion

Fourier transform infrared

Nitrile (C≡N) is allotted as a single, typically intense stretching band at 2211 cm^{-1} (for cyano compounds). The C-Cl stretching vibration in the ACBN at 782 cm^{-1} confirms that the halogen group in the para position is highlighted to the aromatic CN group [12]. Geethapriya et al. claimed that the CH in plane bending vibration is typically evident at 1300-1000 cm^{-1} and the CH out-plane is captured at 1000-750 cm^{-1} [13]. The CH in plane and out-plane for the ACBN is displayed in Figure 1. The ACBN's FTIR spectroscopic results show that it has distinctive peaks at 3452 and 3363 cm^{-1}, which refer to the primary NH functional group [14]. Due to the presence of benzene ring C=C stretching vibrational bands, there is significant stretching frequency at 1433 and 1485 cm^{-1}. The stretching bands at 3100–3000 cm^{-1} range is where pure C–H stretching vibrations of aromatic compounds predominate. However, the stretching frequency of the ACBN is slightly different from the report, caused by the presence of withdrawing group Cl at para position.

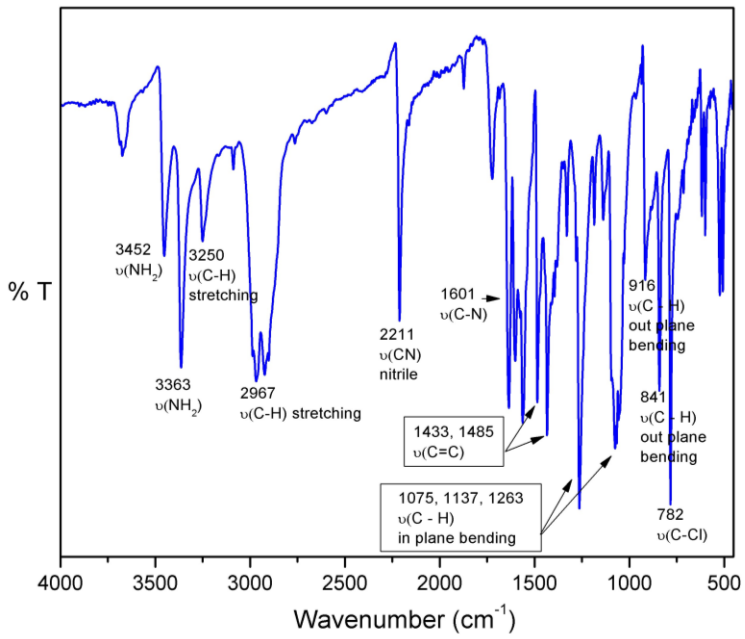

Figure 1. FTIR spectrum of ACBN

Ultraviolet-Visible

The ACBN absorption peak values are depicted in Figure 2. It is commonly perceived that the absorption peak approximately at 328 nm involve transition of n→π* in the C≡N group. In contrast, the aromatic ring of π → π∗ and n → π∗ transitions may be accountable for the absorption peaks in the 210–400 nm range [15]. Figure 6 depicts the B3LYP frontier orbitals of ACBN, demonstrating that the HOMO and LUMO electrons were primarily localized across the whole ACBN where the excitation process occurred. Besides that, based on the experimental and theoretical spectra, there are a slightly different number of absorption peaks. Changes in the geometry of the ACBN in the polar solvent (ethanol) would be associated with the creation of hydrogen bonds between ACBN-Ethanol. Hence, this will influence the electron localization in the HOMO-LUMO regions, causing the early absorption peak (TD-DFT) to be split into two peaks, as shown in Figure 2(a).

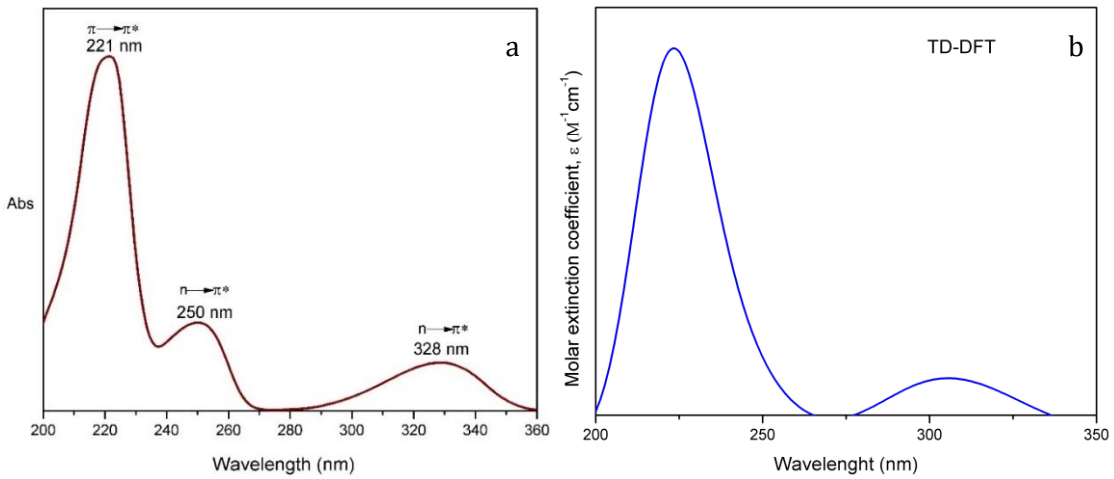

Figure 2. UV-Vis spectrum of ACBN; experimental (a) and theoretical (b)

Single crystal X-ray diffraction

This compound was obtained from the re-crystallization in ethanol. Figure 3 depicts the compound's crystal structure along with an atom-labelling system. The compound crystallized in the triclinic system with the space group Pī. Table 1 summarizes the key crystallographic information, in addition to the bond lengths and angles. Nitrile (C≡N) and C-N have bond lengths of 1.146(4) and 1.369(4) Å, which are less than the theoretical values of 1.160 and 1.470 Å due to the conjugation of the aromatic ring. Furthermore, the presence of the electron-withdrawing group, Cl, in the aromatic ring also led to the reduction of bond lengths. In the crystal structure of BN, the compounds were linked by intermolecular hydrogen bonds, N1---H1A---N2 and N1---H1B—N2 to form 1D chain along a axis as shown in Figure 4 whilst the hydrogen bond geometries are presented in Table 2.

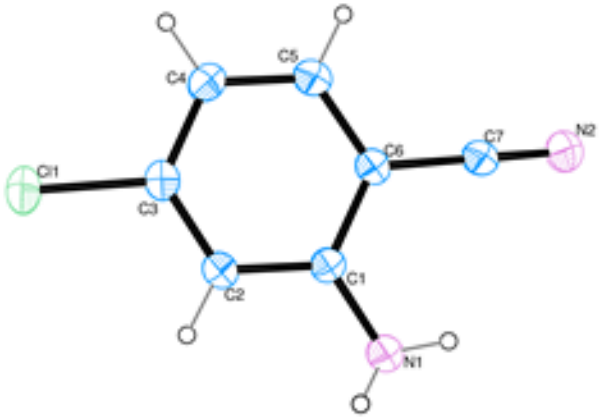

Figure 3. The molecular structure of ACBN with the atom labelling scheme. Displacement ellipsoids are drawn at the 50% probability level

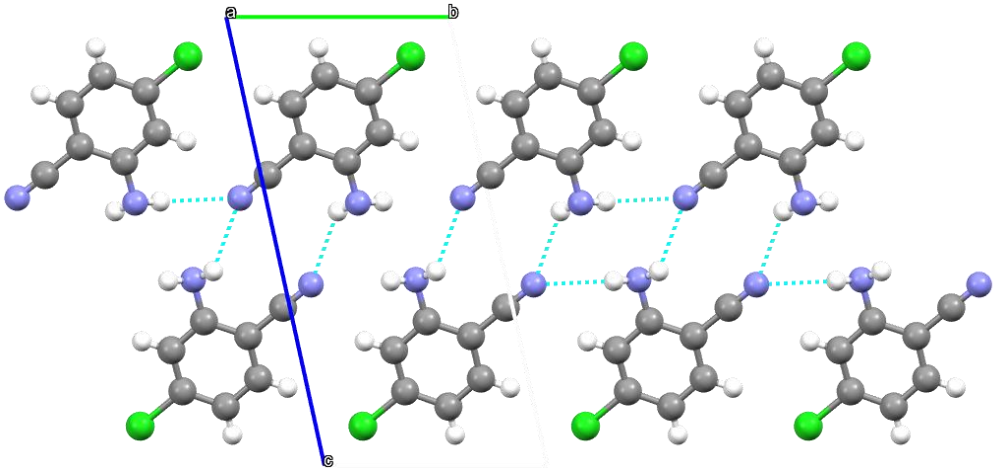

Figure 4. H-bonding view along a-axis

Table 1. Crystallographic data and structural refinement details of ACBN

Crystal Data	
Chemical Formula	$C_7H_5ClN_2$
Molecular mass (gmol^{-1})	152.58
Crystal system, space group	Triclinic, P-1
Temperature (K)	293
a, b, c (Å)	3.8924 (9), 6.7886 (15), 13.838 (3)
α, β, γ (°)	77.559 (16), 88.898 (17), 83.021 (17)
V (Å^3)	354.41 (14)
Z	2
Radiation type	M_o K_α
μ (mm^{-1})	0.45
Crystal size (mm)	0.54 x 0.52 x 0.26
T_{min}, T_{max}	0.243, 0.267
No. of measured, independent and observed [I> 2σ(I)] reflections	6340, 2450, 1033
R_{int}	0.080
(sin θ/λ)max (Å $^{-1}$)	0.750
Refinement R[F^2 > 2σ(F^2)], wR(F ^{2}), S	0.072, 0.158, 1.02
$\Delta\rho_{max}$, $\Delta\rho_{min}$ (e Å^{-3})	0.20, −0.24

Table 2. Hydrogen bond geometries of **ACBN**

D–H···A	**D–H (Å)**	**H···A (Å)**	**D···A (Å)**	**D–H···A (°)**	**Symmetry Codes**
N1–H1A···N2	0.86	2.5	3.166(4)	135	2-x,-y,1-z
N1–H1B···N2	0.86	2.53	3.375(4)	168	x,1+y,z

Hirshfeld surface analysis

The Hirshfeld Surface Analysis was performed to quantify the nature of the intermolecular interactions [16]. Figure 5 presents the Hirshfeld Surface mapped over dnorm. The deep red spots on the dnorm Hirshfeld surfaces represent the close contact interactions, which are mainly responsible for the significant intermolecular N–H···N interactions. The Hirshfeld surfaces mapped over the shape index (Figure 6a) shows comparatively weak interactions involving the phenyl rings represented by the yellowish triangular-shaped regions, which indicate that π···π stacking interactions are present in the crystal packing. The π···π stacking interaction is significant as the *Cg*1-to-*Cg*1 separation ranges from 3.892(2) to 3.893(2) Å [17]. The Cg1 represents the centroid of C1, C2, C3, C4, C5 and C6. The presence of this π···π stacking interactions is also evident by the map of curvedness (Figure 6b) which shows flat surface patches. Two-dimensional fingerprint plots from the Hirshfeld surface analysis of this title compound were calculated to gain quantitative data on the percentage contributions of different intermolecular interactions to the overall Hirshfeld surfaces. The overall two-dimensional fingerprint plot that represents intermolecular contacts are illustrated in Figure 7. The most dominant contribution (26.7%) originates from N···H/H···N contacts which signify the presence of N–H···N interactions. The Cl···H/H···Cl contacts are observed at 21.3% while H···H contacts at 17.9%. The other contacts which are H···C/C···H, C···C, Cl···Cl, N···C/C···N, Cl···C/C···Cl and N···N, show the percentage contributions of 12.3%, 10.8%, 4.2%, 2.6%, 2.3% and 2%, respectively. All these interactions contribute a significant role in crystal packing.

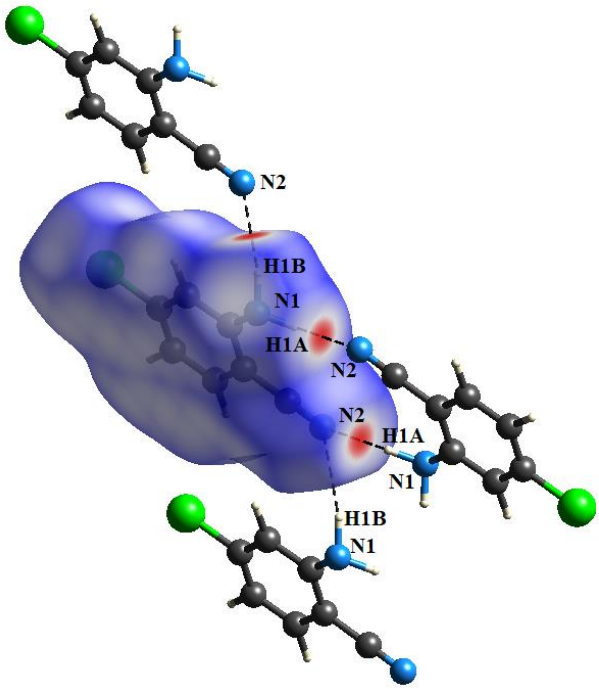

Figure 5. Hirshfeld surfaces mapped over dnorm showing hydrogen-bonding interactions (black dash line) with their neighbouring molecules

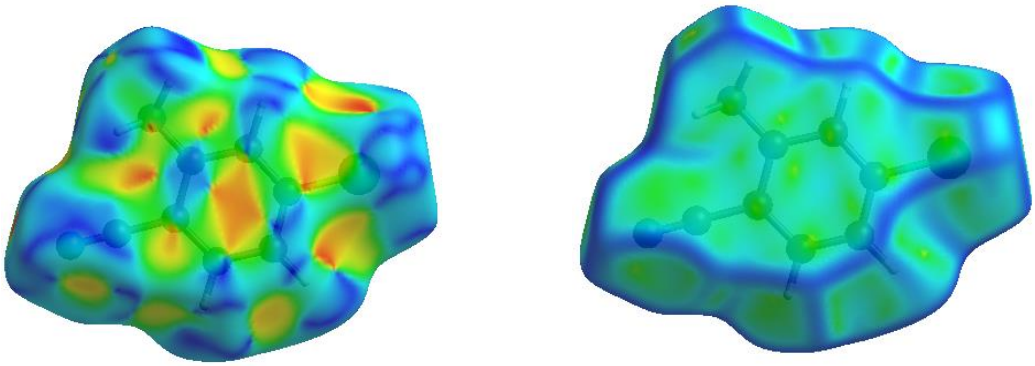

(a) (b)

Figure 6. Hirshfeld surfaces mapped over (a) shape index and (b) curvedness

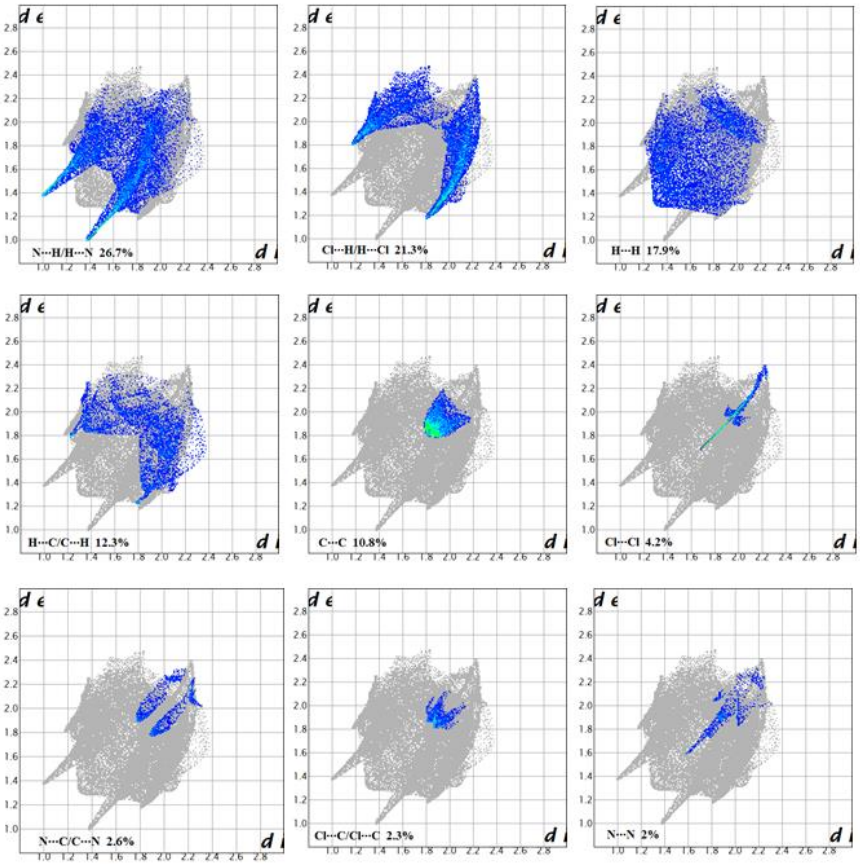

Figure 7. Two-dimensional fingerprint plots of the title compound with their respective contributions

Density functional theory: Mulliken population method

The Mulliken population method using B3LYP/6-311++G(d,p) level of calculation was successfully calculated to obtain the total atomic charge distribution of ACBN. As shown in Figure 8, the 7 atoms from ACBN exhibit negative charges namely 1C, 3C, 4C, 6C, 11N, 14C, and 15N. Positive charges are found in 2C, 5C, 7H, 8H, 9H, 10Cl, 12H, and 13H. The result showed that atom 15N and 11N have a high tendency to act as a nucleophilic atom for the compound as they have negative charges with values of -0.202 and -0.237, respectively.

Intrinsic molecular characteristics

The global reactivity parameters of ACBN are shown in Table 3. The HOMO and LUMO electrons were primarily localized across the whole ACBN. The greater values of ionization potential, I and electron donating capability (ω^-) showed that the ACBN has the capability to donate rather than accept the electrons [18]. Hence, it has the capability to form complexes easier. In comparison to literature, the energy gap value, ΔE, resolved from the crystal data is lower at 3.4988 eV. Sudha et al. [19] generated DFT data using the proposed structure, while this study used crystal data. Calculated ΔE is a crucial stability indicator that aids in defining the compound's chemical reactivity and kinetic stability [20]. As the ΔE value of ACBN is lower than that of the previous study, the reactivity rises with a greater degree of electronic charge transfer from the ACBN as a free ligand to the central metal ion, making it easier to provide electrons to an acceptor. Sherif and Abdel-Kader et al. [21] stated that the ACBN undergoes conjugation, which contributes to the low value of the

energy gap as well. The ACBN has very strong electrophilic properties since the global electrophilicity value is more than 1.5 eV [22]. Global hardness (η) and softness (S) are frequently employed to assess the stability and reactivity of compounds. The ACBN is categorized as a hard compound because the value of global hardness (η) is larger than global softness (S). The high hardness value consistently suggests greater stability and lessened reactivity. It is also consistent with the high value of chemical potential. But despite the high value of ω^-, the ACBN still shows potential to donate electrons to other compounds for specific applications.

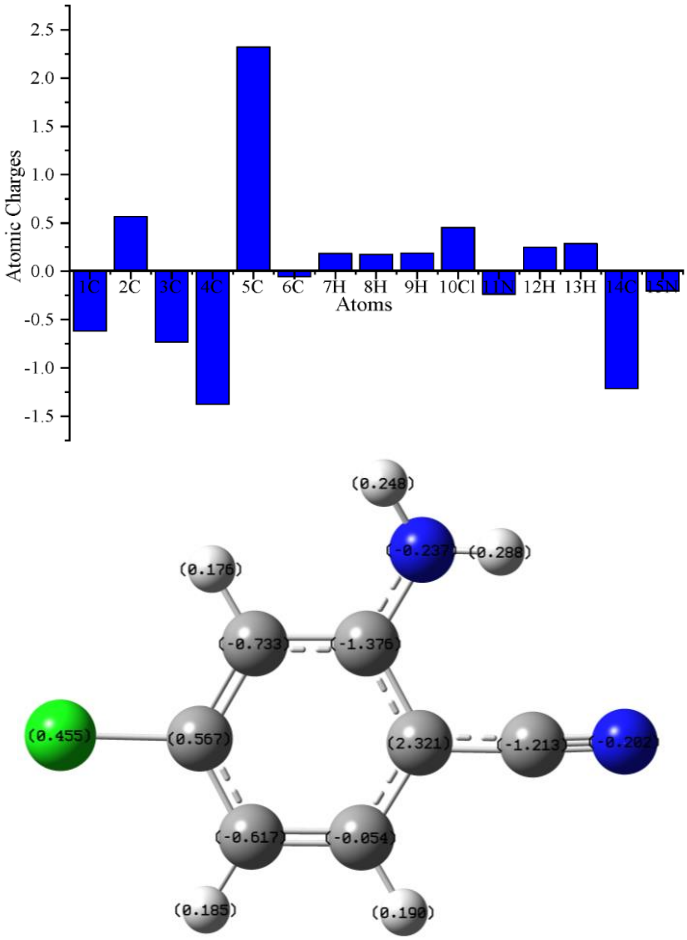

Figure 8. Optimized structure and bar diagram representing the charge distribution of ACBN

Table 3. Global reactivity parameters of ACBN

Molecular energy (eV)	**ACBN**	**Molecular energy (eV)**	**ACBN**
E_{HOMO}	-8.1171 eV	Global Softness (S)	0.1570 eV^{-1}
E_{LUMO}	-4.6183 eV	Chemical potential (μ)	-6.3677 eV
Energy gap (ΔE)	3.4988 eV	Electronegativity (χ)	6.3677 eV
Ionization potential (I)	8.1171 eV	Global electrophilicity (ω)	11.589 eV
Electron affinity (A)	4.6183 eV	Electron donating capability (ω^-)	14.992
Global hardness (η)	1.7494 eV	Electron accepting capability (ω^+)	8.6238

Molecular electrostatic potential

The nitrile (C≡N) is identifiable as a high electron density region as shown in Figure 9, indicating the most preferable reactivity for nucleophilic site. Besides that, the proton of NH_2 has a very noticeable low electron density, which indicates the most preferable reactivity for an electrophilic site [23].

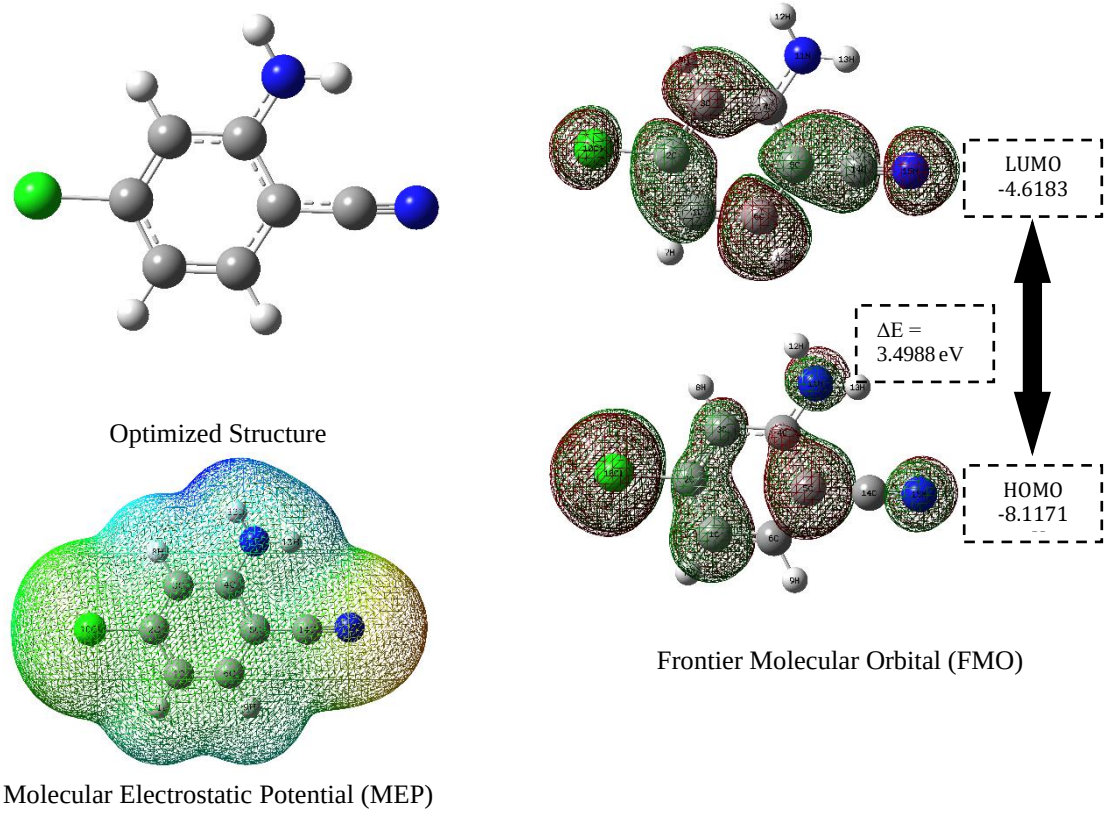

Optimized Structure

Molecular Electrostatic Potential (MEP)

Frontier Molecular Orbital (FMO)

Figure 9. The optimized structure, MEP and FMO of ACBN

Conclusion

The single crystal structure of 2-amino-4-chlorobenzonitrile (ACBN) was successfully confirmed using spectroscopic and single crystal X-ray crystallographic studies. The Hirshfeld Surface analysis revealed that N···H/H···N contacts are the most dominant contributions to the total Hirshfeld surfaces which signify the presence of N–H···N interactions. The intrinsic molecular characteristics analysis showed that although the ACBN is stable and less reactive, the compound still shows a potential in transferring and accepting electrons. Besides that, the Mulliken study showed that the compound has the potential to act as a nucleophilic agent through the nitrogen atoms (highly negative charges). As recommendation, the DFT study revealed that the compound could be investigated more thoroughly in terms of reaction kinetics and mechanisms such as corrosion inhibition and biological activities.

Acknowledgement

The authors thank Ondokuz Mayıs University (Turkey) for the single-crystal X-ray experiment and the Experimental and Theoretical Research Laboratory, International Islamic University Malaysia, for providing the computational facility.

Supplementary Data

CCDC-2224917 contains the supplementary crystallographic data for the compound reported in this paper. These data can be obtained free of charge at

www.ccdc.cam.ac.uk/conts/ retrieving.html [or from the Cambridge Crystallographic Data Centre (CCDC), 12 Union Road, Cambridge CB2 1EZ, UK; fax:+44(0)1223-336033; e-mail: deposit@ccdc.cam.ac.uk].

References

1. Sundaraganesan, N., Elango, G., Sebastian, S. and Subramani, P. (2009). Molecular structure, vibrational spectroscopic studies and analysis of 2-fluoro-5-methylbenzonitrile. *Indian Journal of Pure & Applied Physics*, 47: 481-490.
2. Misra, N., Ahmad Siddiqui, S., Pandey, A. K. and Trivedi, S. (2009). Comparative vibrational spectroscopic investigation of benzonitrile derivatives using density functional theory. *Der Pharma Chemica*, 1(1): 196-209.
3. Kumar, V., Panikar, Y., Palafox, M. A., Vats, J. K., Kostova, I., Lang, K. and Rastogi, V. K. (2010). Ab-initio Calculations, FT-IR and FT-raman spectra of 2-chloro-6-methyl benzonitrile. *Indian Journal of Pure and Applied Physics*, 48: 85-94.
4. Dixon, A. R., Khuseynov, D. and Sanov, A. (2015). Benzonitrile: Electron affinity, excited states, and anion solvation. *Journal of Chemical Physics*, 143(13): 1-12.
5. Karaağaç, D. (2021). Preparation and characterisation of the cyano-bridged transition metal complexes using *n,n′*-diethyl thiourea as a ligand. *South African Journal of Chemistry*, 75: 130-135.
6. Hirose, M. And Torii, H. (2022). Role of the electrostatic interactions in the changes in the CN stretching frequency of benzonitrile interacting with hydrogen-bond donating molecules. *Journal of Molecular Liquids*, 362: 1-7.
7. Stoe and Cie (2002) X-AREA (Version 1.18) X-RED32 (Version 1.04) Stoe & Cie, Darmstadt, Germany.
8. Sheldrick, G. M. (2008) A short history of SHELX, *Acta Crystallographica*, A64: 112-122.
9. Farrugia, L. J. (1997). ORTEP-3 for Windows - a version of ORTEP-III with a Graphical User Interface (GUI). *Journal of Applied Crystallography*, 30(5): 565.
10. Macrae, C. F., Edgington, P. R., McCabe, P., Pidcock, E., Shields, G. P., Taylor, R., Towler, M., van de Streek, J. and Streek, J. V. D. (2006) Mercury: Visualization and analysis of crystal structures. *Journal of Applied Crystallogarphy*, 39: 453-457.
11. Turner, M. J., McKinnon, J. J., Wol, S. K., Grimwood, D. J., Spackman, P. R., Jayatilaka, D. and Spackman, M. A. (2017). Crystal Explorer 17, University of Western Australia: Crawley, Australia.
12. Vhanale, B., Kadam, D. and Shinde, A. (2022) Synthesis, spectral studies, antioxidant and antibacterial evaluation of aromatic nitro and halogenated tetradentate Schiff bases. *Heliyon*, 8(6): 1-7.
13. Geethapriya, J., Devaraj, A. R., Gayathri, K., Swadhi, R., Elangovan, N., Manivel, S., Sowrirajan, S. and Thomas, R. (2023). Solid state synthesis of a fluorescent Schiff base (*E*)-1-(perfluorophenyl)-*N*-(*o*-toly)methanimine followed by computational, quantum mechanical and molecular docking studies. *Results in Chemistry*, 5: 1-11.
14. Nayak, S. G. and Poojary, B. (2019). Synthesis of novel Schiff bases containing arylpyrimidines as promising antibacterial agents. *Heliyon*, 5: 1-7.
15. Đorović, J., Marković, Z., Petrović, Z. D., Simijonović, D. and Petrović, V. P. (2017). Theoretical analysis of the experimental UV-Vis absorption spectra of some phenolic Schiff bases. *Molecular Physics*, 115(19): 2460-2468.
16. Nasaruddin, N. H., Ahmad, S. N., Sirat, S. S., Wai Tan, K., Zakaria, N. A., Mohamad Nazam, S. S., Abd Rahman, N. M. M., Mohd Yusof, N. S. and Bahron, H. (2022). Synthesis, structural characterization, Hirshfeld surface analysis, and antibacterial study of Pd(II) and Ni(II) Schiff base complexes derived from aliphatic diamine. *ACS Omega*, 7(47): 42809-42818.
17. Hema, M. K., García-Santos, I., Castiñeiras, A., Mehrabian, M., Zangrando, E., Ramalingam, R. J., Ramakrishna, B. N., Lokanath, N. K., Karthik, C. S., Mahmoudi, G. (2023) Cg…Cg interactions driven 1D polymeric chains bridged by lattice solvents in N^3-(2-pyridoyl)-4-

pyridinecarboxamidrazone Pb(II) complex. *Journal of Molecular Structure*, 1294(1): 136420-136429.

18. Razali, N. Z. K., Sheikh Mohd Ghazali, S. A. I., Sharif, I., Sapari, S., Abdul Razak, F. I. and Dzulkifli, N. N. (2022). Synthesis, characterisation and corrosion inhibition screening on 2-chloroacetophenone 4-ethyl-3-thiosemicarbazone: Morphology, weight loss and DFT studies. *Chemical Papers*, 76: 5955-5966.
19. Sudha, S., Sundaraganesan, N., Kurt, M., Cinar, M. and Karabacak, M. (2011). FT-IR and FT-Raman spectra, vibrational assignments, NBO analysis and DFT calculations of 2-amino-4-chlorobenzonitrile. *Journal of Molecular Structure*, 985:148-156.
20. Rakha, T. H., El-Gammal, O. A., Metwally, H. M. and Abu El-Reash, G, M. (2014). Synthesis, characterization, DFT and biological studies of (*Z*)-*N*·-(2-oxoindolin-3-ylidene)picolinohydrazide and its Co(II), Ni(II) and Cu(II) complexes. *Journal of Molecular Structure*, 1062: 96-109.
21. Sherif, O. E. and Abdel-Kader, N. S. (2018). DFT calculations, spectroscopic studies, thermal analysis and biological activity of supramolecular Schiff base complexes. *Arabian Journal of Chemistry*, 11(5):700-713.
22. Domingo, L. R., Aurell, M. J., Perez, P. and Contreras, R.́ (2002). Quantitative characterization of the global electrophilicity power of common diene/dienophile pairs in diels-alder reactions. *Tetrahedron*, 58: 4417-4423.
23. Idelfitri, N. I. F., Dzulkifli, N. N., Ash'ari, N. A. N., Sapari, S., Abdul Razak, F. I. and Pungot, N. H. (2023). Synthesis, characterisation and corrosion inhibitory study of meldrum's acid thiosemicarbazone: Weight loss, SEM-EDX and DFT. *Inorganic Chemistry Communications*, 150: 1-11.

Malaysian Journal of Analytical Sciences (MJAS)
Published by Malaysian Analytical Sciences Society

PHYTOCHEMICALS ISOLATION, ANTIBACTERIAL AND ANTIBIOFILM ACTIVITIES OF MALAYSIAN *Uncaria tomentosa* AGAINST ORAL STREPTOCOCCI

(Pengasingan Fitokimia, Aktiviti Antibakteria dan Antibiofilem *Uncaria tomentosa* dari Malaysia terhadap *Streptococci* Oral)

Nor Haslini Wahid[1], Rohaya Ahmad[1], Zainon Mohd Noor[1], Nurul 'Izzah Mohd Sarmin[2,3], Norizan Ahmat[4], Adiez Sapura Azmi[1], and Fatimah Salim[1,2*]

[1]*School of Chemistry & Environment,*
Faculty of Applied Sciences, Universiti Teknologi MARA, 40450 Shah Alam, Selangor, Malaysia
[2]*Atta-ur-Rahman Institute for Natural Product Discovery (AuRIns),*
Universiti Teknologi MARA Selangor Branch, Puncak Alam Campus, 42300 Bandar Puncak Alam, Selangor, Malaysia
[3]*Faculty of Dentistry,*
Universiti Teknologi MARA, Sungai Buloh Campus, 47000 Sungai Buloh, Selangor, Malaysia
[4]*Centre of Foundation Studies,*
Universiti Teknologi MARA Selangor Branch, Dengkil Campus, 43800 Dengkil, Selangor, Malaysia

[*]*Corresponding author: fatimah2940@uitm.edu.my*

Received: 13 September 2023; Accepted: 12 December 2023; Published: 28 February 2024

Abstract

Uncaria tomentosa (Rubiaceae), locally known as 'kait-kait' has long been used for medicinal purposes to heal various diseases, including those related to bacterial infection. In an attempt to search for new antimicrobial agents, the present study was undertaken to evaluate the antibacterial and antibiofilm potentials of hexane (Hx), dichloromethane (DCM), and 80% ethanolic (EtOH) stem extracts of Malaysian *U. tomentosa* against five oral *streptococci* bacteria namely *S. salivarius*, *S. mitis*, *S. uberis*, *S. mutans* and *S. anginosus*. The antibacterial assay employed the agar-well diffusion method where cycloheximide was used as the positive control, while minimum inhibitory concentration (MIC) was determined through resazurin microtiter assay using 96-well microtiter plates. On the other hand, the antibiofilm activity was investigated using a crystal violet assay. The DCM stem extract was found to be active against all tested bacterial strains with ZOI ranging from 10.3±0.6 to 16.0±1.0 mm, and a MIC value of 234.4 µg/mL. Compared to average biofilm growth, the extract reduced biofilm formation by at least 50%. Phytochemical work on the DCM extract afforded four compounds elucidated as isopteropodine (**1**), pteropodine (**2**), β-sitosterol (**3**), and scopoletin (**4**). These four compounds have been previously reported to exhibit antibacterial activity against different bacterial strains. The findings provide evidence to support the plant's traditional use and could be the source of antibacterial and antibiofilm agents for further studies.

Keywords: *Uncaria*, dichloromethane extract, oral bacteria, streptococci, antimicrobial

Abstrak

Uncaria tomentosa (Rubiaceae), yang dikenali sebagai 'kait-kait' telah lama digunakan untuk tujuan perubatan dalam menyembuhkan pelbagai penyakit, termasuk yang berkaitan dengan jangkitan kuman. Dalam usaha mencari agen antimikrob baharu, kajian ini telah dijalankan untuk menilai potensi antibakteria dan antibiofilem ekstrak heksana (Hx), diklorometana (DCM) dan 80% etanol (EtOH) daripada batang *U. tomentosa* dari Malaysia terhadap lima bakteria *streptokokus* oral iaitu *S. salivarius, S. mitis, S. uberis, S. mutans* dan *S. anginosus*. Ujikaji antibakteria menggunakan kaedah ujian peresapan telaga agar di mana sikloheksimida digunakan sebagai kawalan positif, manakala kepekatan perencatan minimum (MIC) ditentukan melalui ujian mikrotiter resazurin dengan menggunakan plat mikrotiter 96 telaga. Ekstrak batang DCM didapati aktif terhadap semua strain bakteria yang diuji dengan ZOI dalam julat 10.3±0.6 - 16.0±1.0 mm, dan nilai MIC 234.4 µg/mL. Berbanding purata pertumbuhan biofilm normal, ekstrak ini dapat mengurangkan pembentukan biofilm sekurang-kurangnya 50%. Kajian fitokimia pada ekstrak DCM menghasilkan empat sebatian yang dikenalpasti sebagai isopteropodine (**1**), pteropodine (**2**), β-sitosterol (**3**), dan scopoletin (**4**). Empat sebatian ini sebelum ini telah dilaporkan mempamerkan aktiviti antibakteria terhadap strain bakteria yang berbeza. Penemuan ini memberikan bukti untuk menyokong penggunaan tradisional tumbuhan dan boleh menjadi sumber agen antibakteria dan antibiofilem untuk kajian lanjut.

Kata kunci: *Uncaria*, ekstrak diklorometana, bakteria oral, streptokokus, aktiviti antimikrob

Introduction

Oral bacteria are an example of an opportunistic human species capable of causing biofilm-related infections. Epithelial cells, dental surfaces, and orthodontic prostheses are some of the many surfaces in the oral cavity that are prone to the formation of multispecies biofilms [1]. In the form of supragingival and subgingival plaque, biofilm is the etiologic agent in dental caries (tooth decay) and periodontal (gum) disease [2]. Furthermore, studies have demonstrated an association between periodontitis and various systemic diseases and conditions in recent years, including cardiovascular disease, diabetes mellitus, respiratory disease, adverse pregnancy outcomes, obesity, pancreatic cancer, and Alzheimer's disease [3].

Uncaria (Rubiaceae) is a flowering woody climber plant. The genus comprises 34 species that distributed mainly in tropical regions, including Southeast Asia, Africa, and South America. Cultivation varies based on the species and region [4,5]. *Uncaria tomentosa* was given the name una de gato (cat's claw) because of hook-like thorns that resemble the claws of a cat. Phytochemical studies of the Peruvian *U. tomentosa* have led to the isolation of numerous constituents including quinovic acid glycosides, oxindole alkaloids, proanthocyanidins, polyphenols, triterpenes and numerous sterols [6-8]. Although there was no literature on the existence of the species in Malaysia, the species has been discovered in Malaysian forests.

The extracts of *U. tomestosa* is also widely studied compared to other species of the genus and they have been found to display multiple biological activities including anti-inflammatory, antioxidant, cytotoxicity, immunostimulant, and antibacterial [9,10]. So far, there is a lack of scientific reports indicating this plant's antimicrobial activities against oral pathogens. Moreover, no study has been published to indicate the potential antibiofilm activities of the plant. Hence, this study aimed to investigate the antibacterial and antibiofilm potentials of the hexane (Hx), dichloromethane (DCM), and 80% ethanol (EtOH) stem extracts of *U. tomentosa* against oral bacteria and to isolate its chemical constituents.

Materials and Methods

Plant material

The plant material was collected from Pasir Raja, Dungun, Terengganu in December 2011. The plant sample was identified by Dr. Shamsul Khamis of Universiti Putra Malaysia. The plant materials were air-dried in the dark at room temperature before being ground with a mechanical grinder.

Preparation of extracts

The dried samples were cut into small pieces and ground into a fine powder with a mechanical grinder. The fine powder of the stems (5 kg) was successively extracted with solvents ranging in different polarities: hexane (nonpolar), dichloromethane (medium polar) and 80% ethanol (polar) solvents by continuous hot extraction

technique using a Soxhlet extractor. The solvents were then evaporated under reduced pressure at a temperature lower than 40 ºC using a vacuum rotary evaporator. The dried extracts were stored in the refrigerator at a temperature of 4 °C until further analysis.

Antibacterial activity

The extracts of stems were prepared by dissolving in 10% dimethyl sulphoxide (DMSO) to a final concentration of 100 mg/mL. As a solvent for all the test samples, DMSO was first tested against bacteria to ensure that it did not contribute to the antibacterial activity of the samples. Then, the extracts were diluted to reach the concentration of 50, 35, and 15 mg/mL. These concentrations of test samples were subjected to an agar well-diffusion assay screening test. The lowest concentration of the test samples showed inhibition activity in the screening test and were chosen for further evaluation of MIC using the resazurin microtiter-plate dilution assay.

Bacterial strains and growth condition

A total of 5 oral bacteria were employed in the study, including *Streptococcus salivarius* (ATCC 13419), *Streptococcus mitis* (ATCC 6249), *Streptococcus uberis* (ATCC 19436), *Streptococcus mutans* (ATCC 25175) and *Streptococcus anginosus* (ATCC 33397). All bacterial strains were purchased from Oxoid (UK). The bacterial strains were grown in brain heart infusion broth (BHI) and were maintained on brain heart infusion agar (BHI) at 4 °C, and subcultures were freshly prepared before being subjected to bioassay.

Antibacterial screening

The agar well-diffusion assay was performed in this study to screen the antibacterial activity of the extracts against the bacteria tested. Briefly, 24 hours of bacterial suspension was adjusted to absorbance reading within the range of 0.08-0.10 at OD625 nm, equivalent to 1-2 x 10^8 CFU/mL [11] that matched the turbidity 0.5 McFarland standards [12]. Liquefied (25 mL) sterile brain heart infusion agar (BHI) at 45 °C was aseptically mixed with 1 mL standardized inoculum and poured immediately into previously labeled sterile petri dishes. Then, the plates were left to solidify in a laminar flow cabinet for 20 minutes. Once the agar hardened, four wells (8 mm) were bored using a sterile cork borer. A 100 µL volume of each extract was introduced into the wells. Chlorhexidine (CHX) of 0.12 % was used as a positive control, while a 10% DMSO was used as a negative control. The extracts were allowed to pre-diffuse at room temperature for 1 hour before the agar plates were incubated at 37 °C for 24 hours. The antibacterial activity was expressed as the average diameter of a clear zone to the nearest millimeter. The tests were performed in triplicate and repeated twice to reduce the possibility of a test error.

Determination of minimum inhibitory concentration (MIC)

Resazurin microtiter-plate assay was used to determine the MIC. The assay was performed according to the procedure described by Gahlaut and Chhillar [13] with some modifications. Under aseptic conditions, a flat bottom sterile 96-well polystyrene tissue culture plate was labeled, and each well was filled with 100 µL of BHI broth. Each extract (100 µL) was then added to the first well, and two-fold serial dilutions were performed so that each well had 100 µL of test extracts in serially descending concentrations. Then, the standardized bacterial culture suspension (50 µL) was added to each well. The final volume in each well was 150 µL. The following controls were prepared: wells containing broth only (sterility control), bacterial strain with no extract (inoculum viability), serial dilution of CHX (positive control), and DMSO (negative control). The plates were incubated at 37 °C overnight. A 30 µL resazurin solution was added to each well, and the plates were incubated for another one to two hours. The MIC was determined as the lowest sample concentration at which no pink color (signifying live growth) appeared.

Antibiofilm activity: Preparation of biofilm development

Preliminary work has been done to determine the optimum growth condition applied to the biofilm formation assay. This work was adopted according to the protocol designed by Stepanović et al. [14]. The standardized bacterial suspension (~1 x 10^8 CFU/mL) was vortexed, 50 µL of the cell solution was then diluted 1:100 by adding to 4950 µL of desired medium [BHI,

BHI+ 1% (w/v) glucose, BHI+ 1% (w/v) sucrose]. These diluted bacteria (~1 x 10^6 CFU/mL) were then vortexed for 30 s to 1 min and transferred to a flat bottomed 96-well polystyrene tissue culture treated plate (200 µL per well). The plates were prepared in triplicates and placed in an incubator shaker at 37 °C for 24 hours. After incubation, the attached biofilm was quantified by measuring the absorbance of the solution at 570 nm [15].

Determination of minimum biofilm inhibitory concentration

The crystal violet (CV) assay was used to investigate the effect of *U. tomentosa* extracts on biofilm formation by adopting the protocol by Stepanović et al. [14]. Briefly,100 µL of fresh BHI supplemented with 1% (w/v) sucrose was distributed into all the wells of the flat bottom 96-well tissue culture plate. In sequence, 100 µL of extracts in a concentration used in the antibacterial activity (MIC) were added to the wells. Serial dilution was performed and followed by adding 100 µL bacterial suspension (1 x 10^6 CFU/mL). The plates were then incubated at 37 °C for 24 hours. After 24 hours of incubation time, the supernatant was discarded. Then, the plates were gently washed thrice with phosphate buffer saline (PBS) solution to remove the remaining planktonic cells, followed by air drying for 30 minutes. The adherent biofilm in the plates was fixed with methanol for 20 minutes, the solution was then removed, and the plates were air-dried. The attached bacterial cells were then stained with 150 µL of 2% crystal violet and left at room temperature for 15 minutes. Following staining, the stains were discarded and rinsed off by placing the plates under running tap water. The plates were blotted on paper towels and air-dried at room temperature. The bound dye was extracted from the stained cells using 150 µL of 95 % EtOH and left at room temperature for 30 minutes. The content's optical density (OD) was measured at 570 nm using a microtiter plate reader. The intensity of staining is directly proportional to the number of biofilms adhering to the 96-well plate. The percentage biofilm inhibition was calculated by the following formula, according to:

$$\%\ inhibition = \frac{OD\ (mean)^{control} - OD\ (mean)^{test\ sample}}{OD\ (mean)^{control}} \times 100\% \quad (1)$$

Where OD control is the mean OD measured for 24 hours bacterial biofilm grown without the extracts, while ODtest samples is the mean OD measured for 24 hours bacterial biofilm grown in the presence of extracts. The minimum biofilm inhibitory concentration ($MBIC_{50}$) was defined as the lowest concentration of the tested extracts required to prevent the formation of ≥50% of the biofilm [16].

Phytochemical work: General procedures

Column chromatography was conducted using silica gel 60, 70-230 mesh ASTM (Merk 7734 packed by slurry packing method. Radial chromatography was carried out using a glass plate with Merck's silica gel (Kieselgel 60 PF254 Merck Art 7749). Preparative TLC was performed using glass-supported silica gel 60 F254 (1.0 mm thickness). TLC was used to monitor the eluates was performed using pre-coated aluminium-backed supported silica gel 60 F254 (0.2 mm thickness). Identification of the spots on the TLC plate was carried out by spraying Dragendorff's reagent for alkaloid and P-anisaldehyde-sulfuric acid for terpenes, sterols, and steroids. Spots and bands for compounds on TLC and PTLC were viewed individually under UV lights (254 and 365 nm). The mass spectrum was recorded with an Agilent1100 series LC/MS ion trap. The infrared (IR) data was obtained on a Perkin Elmer model FT-IR spectrometer as a KBr disc. ^1H and ^{13}C NMR spectra were recorded with a Bruker 300 Ultra shield NMR spectrometer measured at 300 and 75 MHz, respectively.

Isolation and elucidation of compounds

The DCM extract was subjected to an acid-base extraction yielded an alkaloid mixture (3g) and a non-alkaloid mixture (18g). The alkaloid and non-alkaloid mixture was then subjected to column chromatography over silica gel, eluted with Hx:DCM (1:0-0:1) and subsequently DCM:MeOH (1:0-0:1) yielding 30 and 9 fractions, respectively. Based on their TLC profiles, the fractions from the alkaloid mixture were combined together into 9 major subfractions (F1-F9). Subfraction

F7 (40 mg) was subjected to radial chromatography using DCM and EtOAc in an increasing polarity manner to give compounds **1** (20 mg) and **2** (15 mg). Column chromatography on the targeted fraction of non-alkaloid mixture using solvent system Hx:DCM (9.5:0.5) successfully yielded compound **3** (9.4 mg). Another targeted fraction of the mixture using preparative TLC on silica gel using solvent system DCM: EtOAc (8.0:2.0) afforded 2.7 mg of compound **4**. The structure of isolated compounds was elucidated as isopteropodine (**1**), pteropodine (**2**), β-sitosterol (**3**), and scopoletin (**4**) based on spectroscopic data analysis as well as by comparing with the literature values.

Statistical analysis

All the experiments were run in triplicates and were repeated at least twice. The values obtained were analyzed using IBM SPSS Statistics v.22. The replicate absorbance readings were calculated as the mean of individual experiments in triplicate. The significant difference between the means of the test samples and the control group was performed using a Bonferroni post-test. A difference was considered significant when p values ≤ 0.05.

Result and Discussion

Antibacterial activity

The antibacterial activity possessed by extracts of increasing polarity against five oral bacteria is reported in Table 1. From the results obtained, the antibacterial activity of the extracts was greatly affected by solvent polarity. Out of the three extracts, the DCM extract exerted the most pronounced activity. This extract exhibited an inhibitory effect against all tested bacterial strains (*S. mutans*, *S. mitis*, *S. salivarius*, *S. anginosus*, and *S. uberis*). Meanwhile, Hx and 80% EtOH extracts were effective against only two strains (*S. salivarius* and *S. uberis*). The results obtained from this study indicate that the extracts showed varying degrees of antibacterial activity as the extracts were prepared by successive extraction of different polarities. Separating the constituents into nonpolar (Hx), medium polar (DCM), and polar fractions (80% EtOH) is expected to concentrate each extract's antibacterial constituents and enhance their inhibitory ability. The screening test using the agar well-diffusion assay was not a definitive method in detecting the inhibition of the test bacterial because many of the antimicrobial compounds in plant extracts are relatively nonpolar, and these compounds do not diffuse well into the surrounding agar around the wells [17]. This could be the reason for the negative activity shown by the Hx extract.

The test samples were then subjected to the microplate dilution method with resazurin as an indicator to determine the extracts' minimum inhibitory concentration (MIC) because it is more sensitive and provides reproducible results. The results are shown in Table 2. The blue color or the color before pink in the microtitre plates after adding the resazurin dye indicator was determined as the lowest concentration that completely inhibited the microorganism's growth. The MIC values obtained in this study from the extracts tested ranged from 234.4 µg/mL to 937.5 µg/mL. The antimicrobial potential of plant extracts is classified as follows: MIC < 100 µg/mL – strongly active; MIC 100-500 µg/mL – moderately active; MIC 500-1000 µg/mL – weakly active and MIC > 1000 µg/mL – inactive [18]. Based on the criteria given, generally, the extracts of this plant had moderate to low antibacterial activity against the bacteria tested. The strongest (MIC = 234.4 µg/mL) and the weakest (MIC = 937.5 µg/mL) antibacterial activity was shown by the DCM against *S. mutans*, and *S. anginosus*, respectively. In addition, the Hx and DCM extracts showed similar growth inhibitory activity against *S. salivarius*, *S. mitis* and *S. uberis* at a MIC value of 468.8 µg/mL. Meanwhile, no antibacterial activity was observed with the Hx extract against *S. mutans* and *S. anginosus*, and none by the 80% EtOH extract against either bacterial tested.

The difference in the MIC values obtained suggests a varying degree of susceptibility of the microorganisms, as was determined by comparing the MIC values of the test extracts against each bacterial tested. The lower the MIC value, the more susceptible the bacteria tested to the antimicrobial agent and vice-versa. Of the five bacterial tested, *S. mutans* was the most susceptible, as indicated by the lowest MIC values obtained from the DCM extracts (234 µg/mL). The trend in susceptibility to the extracts was *S. mutans* > *S. salivarius*, *S. mitis*, *S. uberis* > *S. anginosus*. In contrast, *S. anginosus* was

found to be less sensitive as only inhibited by the DCM extract. The activity of the extract tested can be ranked as DCM > Hx > EtOH 80% extracts. These results indicated considerable variation in antibacterial activity between extracts obtained with the different polarities of extracting solvents.

Table 1 Inhibition zone diameter of stem extracts against oral bacteria

Extract Type	**Conc. (mg/mL)**	**Zone of Inhibition (mm)**				
		S. mutans	**S. mitis**	**S. salivarius**	**S. uberis**	**S. anginosus**
Hx	50	0	0	12.0±0.0	11.0±0.0	0
	35	0	0	12.0±0.0	10.7±0.6	0
	15	0	0	12.0±0.0	10.3±0.6	0
DCM	50	12.0±1.0	11.0±0.0	15.0±0.0	16.0±1.0	11.3±0.6
	35	11.3±0.6	10.7±0.6	14.3±0.6	13.0±1.0	11.0±0.0
	15	11.0±0.0	10.3±0.6	14.0±1.0	12.3±0.6	10.7±0.6
80% EtOH	50	0	0	15.0±0.0	14.7±0.6	0
	35	0	0	15.0±0.0	14.3±0.6	0
	15	0	0	13.5±0.6	14.0±1.0	0
DMSO	0	0	0	0	0	0
CHX	29.0±1.0	27.0±1.0	29.7±0.6	27.7±0.6	25.3±0.6	29.0±1.0

Table 2. Minimum inhibitory concentration (MIC) of extracts against oral bacteria

Extract Type	**Minimum Inhibitory Concentration (µg/mL)**				
	S. mutans	**S. mitis**	**S. salivarius**	**S. uberis**	**S. anginosus**
Hx	-	468.8	468.8	468.8	-
DCM	234.4	468.8	468.8	468.8	937.5
80% EtOH	-	-	-	-	-

Different solvent extracts showed a different activity level, with DCM extract showing the most pronounced activity against all tested bacteria. It seems that extracts with an intermediate polarity had a much higher antibacterial activity than more polar (80% EtOH) or nonpolar (Hx) extracts. This agrees with the study by Eloff et al. reported that *Melianthus comosus* extract from the intermediate polarity solvent (acetone) had the best activity against fungal pathogens [19]. This has been attributed to more polar compounds being either less or completely inactive against the bacteria tested. It is worth notifying that DMSO (negative control) used as diluents did not affect the bacteria tested. Reports are available on the antibacterial activity of different concentrations of *U. tomentosa* extracts against several microorganisms [20-22]. But a few studies have

investigated the antibacterial activity of *U. tomentosa* against microorganisms frequently found in the human oral cavity. Ccahuana-Vasquez and co-workers employed MIC assay to determine the antimicrobial activity of 0.25% to 5% of micropulverized *U. tomentosa* extract on different strains of microorganisms isolated from the human oral cavity [23]. The authors reported that concentrations of 3% *U. tomentosa* inhibited 52 % of the *S. mutans* strain, which agrees with our findings. On the other hand, different authors reported 2% CC (cat's claw) gel prepared from freeze-dried extract inhibited *Enterococcus faecalis*, *Staphylococcus aureus*, and *Candida albicans* which are microorganisms commonly found in infected root-filled teeth [24].

Antibiofilm activity

The effects of adding alternative carbohydrates, glucose, and sucrose, in the BHI media frequently used to grow oral biofilm were examined to determine the best medium for the subsequent biofilm assays. For this purpose, three different culture media, BHI, BHI + 1% glucose, and BHI + 1% sucrose, was employed in a static biofilm setup to evaluate the best-suited medium for oral biofilm development under in vitro conditions. Biofilm formation of the oral *Streptococci* was assayed and categorized based on the A575 of the crystal violet-stained biofilm: OD570 >2.0, a good biofilm former; OD570 = 1.0 to 2.0, moderate biofilm former and OD570< 1.0, poor biofilm former [15].

As shown in Figure 1, when culture media supplemented with or without glucose were used, the biofilm of the bacteria tested grew poorly (OD570 < 1.0). The results point to the optimal media for simultaneous growth of at least three bacteria to be BHI with 1% sucrose, hence was used for all subsequent experiments. This result is in line with previous findings where sucrose is considered the most cariogenic carbohydrate not only it is being fermented by oral bacteria, but is also a substrate for the synthesis of extracellular polysaccharides which will then promote changes in the composition of the biofilm's matrix [25]. Out of the five bacteria tested, only *S. mutans* was found to be a good biofilm former. Thus, this bacterium was then subjected to a biofilm inhibition assay. The three remaining bacteria, which were found to be poor biofilm formers, were all of the following strains: *S. uberis*, *S. mitis*, and *S. anginosus*.

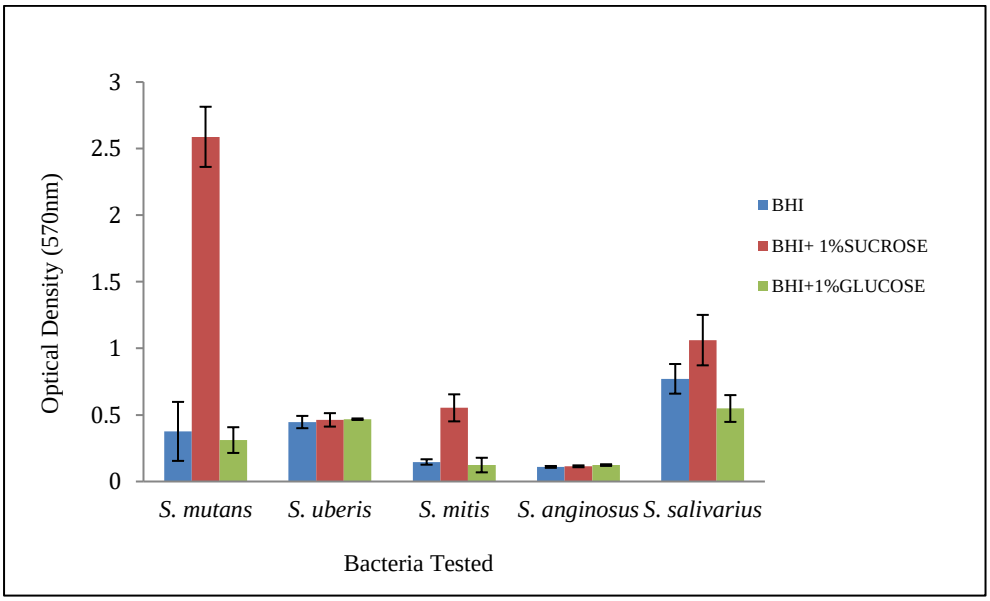

Figure 1. Results from Growth Optimization Assay. Blue, red, and green bars represent bacteria grown in different growth conditions. All assays were performed triplicate, and the data represent the average of 3 or more wells with standard deviations denoted by the error bars

Due to the highest antibacterial activity recorded by the DCM extract, it was further subjected to antibiofilm activity produced by *S. mutans*. As shown in Figure 2, *U. tomentosa* DCM extract showed an increasing ability to inhibit the biofilm by increasing its concentrations evidenced by the reduced absorbance values compared to the control biofilm (no extracts). Inhibition was expressed as percentages, with the extracts exhibiting good antibiofilm activity ≥ 50% inhibition. In this study, the lowest $MBIC_{50}$ reported was at a concentration of 58.6 µg/mL, indicating moderate antibiofilm activity. Higher MBIC (93.21% and 95.36%) was observed for the extract at the higher tested concentrations of 234.4 µg/mL and 468.8 µg/mL, respectively. Perusal the literature value, there are several ways in which natural products execute their antibiofilm activity which include preventing the formation of the polymer matrix, suppressing cell adhesion, interrupting extracellular matrix (ECM) generation, and reducing the production of virulence factors. This, in turn, blocks the quorum sensing (QS) network and hinders biofilm development [26]. The activities here could be contributed by some moderate polarity compounds that work synergically or singularly in the extract. The stem of the plant has been reported to contain a moderate polarity of compounds including coumarins, terpenes, flavonoids and alkaloids that may be responsible for the *U. tomentosa's* medicinal effects [9]. While these compounds may be responsible for the antibacterial activities reported in this study, only flavonoids and an alkaloid had been reported to possess good antibacterial activity [27,28]. In order to have more insight on the possible chemical constituents of the active extract, the DCM extract was subjected to phytochemical study.

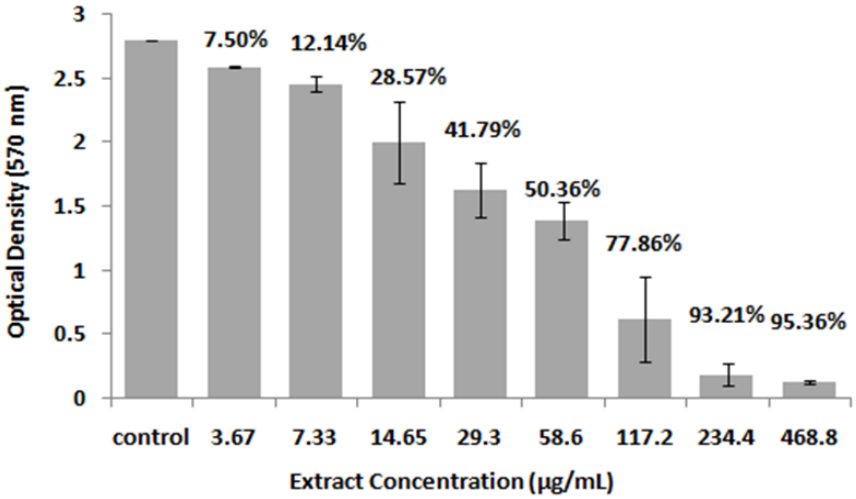

Figure 2. Inhibitory activity towards *S. mutans* biofilm formation by DCM extract. Percent biofilm formation inhibition, shown at the top of each column, was calculated by comparing the absorbance values of test samples with the absorbance of the control biofilm

Phytochemical work

Repeated chromatographic techniques and purification on the DCM extract of the stems of *U. tomentosa* afforded four compounds where two from the alkaloidal [isopteropodine (**1**) and pteropodine (**2**)] and two from the non-alkaloidal [β-sitosterol (**3**) and scopoletin (**4**)]. The structures were determined by spectroscopy particularly extensive NMR analyses as well as by comparison of their spectral data with the literature data [29-32]. The significant spectroscopic characteristics of the compounds are as follows, while their structures are shown in Figure 3.

Isopteropodine (**1**): ESIMS m/z 368 $[M+H]^+$ for $C_{21}H_{24}N_2O_4$; IR (KBR) υ_{max}: 3368 (NH), 1718 (ester C=O), 1657 (amide C=O) cm^{-1}; ^1H NMR ($CDCl_3$, 300 MHz) δ ppm: 8.30 (1H, *s*, N-H), 7.43 (1H, *s*, H-17), 7.29 (1H, *d*, *J* = 7.5 Hz, H-9), 7.20 (1H, *ddd*, *J* = 7.5, 1.2 Hz,

H-11), 7.03 (1H, *ddd*, *J* = 7.5, 1.2 Hz, H-10), 6.89 (1H, *d*, *J* = 7.5 Hz, H-12), 4.36 (1H, *m*, H-19), 3.60 (3H, *s*, OCH_3), 3.33 – 3.20 (2H, *m*, H-21β, H-5β), 2.60 – 2.30 (5H, *m*, H-15, H-21α, H-6β, H-5α, H-3), 2.00 (1H, *m*, H-6α), 1.60 (2H, *m*, H-14α, H-20), 1.43 (3H, *d*, *J* = 6 Hz, H_3-18), 0.89 (1H, *m*, H-14β); ^{13}C NMR ($CDCl_3$, 75 MHz) δ ppm: 181.25 (N-C=O), 167.64 (O-C=O), 155.00 (C-17), 140.96 (C-13), 133.69 (C-8), 127.58 (C-11), 124.07 (C-9), 122.04 (C-10), 109.85 (C-16), 109.43 (C-12), 72.16 (C-19), 71.34 (C-3), 57.09 (C-7), 54.15 (C-5), 53.53 (C-21), 50.99 (OCH_3), 37.90 (C-20), 34.86 (C-6), 30.49 (C-15), 30.19 (C-14), 18.65 (CH_3).

Pteropodine (**2**): ESIMS m/z 368 $[M+H]^+$ for $C_{21}H_{24}N_2O_4$; IR (KBR) υ_{max}: 3206 (NH), 1721 (ester C=O), 1629 (amide C=O) cm^{-1}; ^{1}H NMR ($CDCl_3$, 300 MHz) δ ppm: 8.66 (1H, *s*, N-H), 7.49 (1H, *s*, H-17), 7.22 (1H, *d*, *J* = 7.5 Hz, H-9), 7.19 (1H, *ddd*, *J* = 7.5, 1.2 Hz, H-11), 7.07 (1H, *ddd*, *J* = 7.5, 1.2 Hz, H-10), 6.83 (1H, *d*, *J* = 7.5 Hz, H-12), 4.57 (1H, *m*, H-19), 3.63 (3H, *s*, OCH_3), 3.37 – 3.19 (2H, *m*, H-21β, H-5β), 2.50 – 2.31(5H, *m*, H-15, H-21α, H-6β, H-5α, H-3), 2.03 (1H, *m*, H-6α), 1.74 (1H, *m*, H-14α), 1.61 (1H, *m*, H-20), 1.51 (1H, *m*, H-14β), 1.43 (3H, *d*, *J* = 6 Hz, H_3-18); ^{13}C NMR ($CDCl_3$, 75 MHz) δ ppm: 181.0 (N-C=O), 167.77 (O-C=O), 155.29 (C-17), 140.48 (C-13), 133.41 (C-8), 127.98 (C-11), 123.27 (C-9), 122.74 (C-10), 109.25 (C-12), 109.22 (C-16), 74.42 (C-3), 72.23 (C-19), 56.08 (C-7), 55.17 (C-5), 53.63 (C-21), 50.93 (OCH_3), 37.88 (C-20), 34.59 (C-6), 30.98 (C-15), 29.59 (C-14), 19.0 (CH_3).

β-sitosterol (**3**): ESIMS m/z 414 $[M+H]^+$ for $C_{29}H_{50}O$; IR (KBR) υ_{max}: 3381 (OH), 2934 - 2833 (aliphatic C-H), 1668 (C=C), 1450 (H-C-H) cm^{-1}; ^{1}H NMR ($CDCl_3$, 300 MHz) δ ppm: 5.37 (1H, *t*, *J* = 5.4 Hz, H-6), 3.54 (1H, *m*, H-3), 2.24 (1H, *m*, H-4), 2.00 (2H, *m*, H-7, H-4), 1.83 (1H, *m*, H-25), 1.75 – 1.60 (4H, *m*, H-7, H-20, H-15, H-16), 1.55 – 1.45 (6H, *m*, H-2, H-12, H-11, H-28, H-24, H-17), 1.44 – 1.40 (2H, *m*, H-9, H14), 1.35 – 1.30 (5H, *m*, H-1, H-15, H-16, H-12, H-2), 1.25 – 1.00 (5H, *m*, H-11, H-22, H-23, H-1, H-8), 1.02 (3H, *s*, H_3-19), 0.93 (3H, *d*, *J* = 6.0 Hz, H3-21), 0.94 (3H, *t*, *J* = 6.6 Hz, H_3-29), 0.88 (3H, *d*, *J* = 6.3 Hz, H_3-27), 0.85 (3H, *d*, *J* = 6.3 Hz, H_3-26), 0.75 (3H, *s*, H_3-18); ^{13}C NMR (CDCl3, 75 MHz) δ ppm: 140.76 (C-5), 121.73 (C-6), 71.80 (C-3), 56.76 (C-14), 56.04 (C-17), 50.12 (C-9), 45.82 (C-24), 42.31 (C-13), 42.27 (C-4), 39.76 (C-12), 37.24 (C-1), 36.49 (C-10), 36.14 (C-20), 33.93 (C-22), 31.89 (C-7), 31.89 (C-8), 31.64 (C-2), 29.13 (C-25), 28.24 (C-16), 26.05 (C-23), 24.30 (C-15), 23.05 (C-28), 21.07 (C-11), 19.82 (C-26), 19.39 (C-19), 19.02 (C-27), 18.77 (C-21), 11.98 (C-29), 11.85 (C-18).

Scopoletin (**4**): ESIMS m/z 192 $[M+H]^+$ for $C_{10}H_8O_4$; IR (KBR) υ_{max}: 3350 (OH), 1670 (C=O), 1629 (amide C=O) cm^{-1}; ^{1}H NMR ($CDCl_3$, 300 MHz) δ ppm: 7.86 (1H, *d*, *J* = 9.3 Hz, H-4), 7.12 (1H, *s*, H-5), 6.79 (1H, *s*, H-8), 6.22 (1H, *d*, *J* = 9.3 Hz, H-3), 6.20 (1H, *br s*, OH), 3.92 (3H, *s*, OCH_3); ^{13}C NMR (CDCl3, 75 MHz) δ ppm: 161.46 (C=O), 150.25 (C-6), 149.70 (C-9), 144.01 (C-7), 143.30 (C-4), 113.40 (C-3), 111.49 (C-10), 107.49 (C-5), 103.19 (C-8), 56.41 (OCH_3).

As has been mentioned previously, these alkaloids (**1** and **2**), coumarin **4**, and terpene **3** have been reported to exhibit antibacterial activity against different bacterial strains [9,27,28]. Thus, these compounds are presumably responsible for the antibacterial and antibiofilm activities of the DCM extract in the present study. This is the first report of antibiofilm activity of *U. tomentosa* extracts to the best of our knowledge. The findings provide evidence to support the usage of *U. tomentosa* in microbial infections and could be the source of antibacterial and antibiofilm agents for further studies.

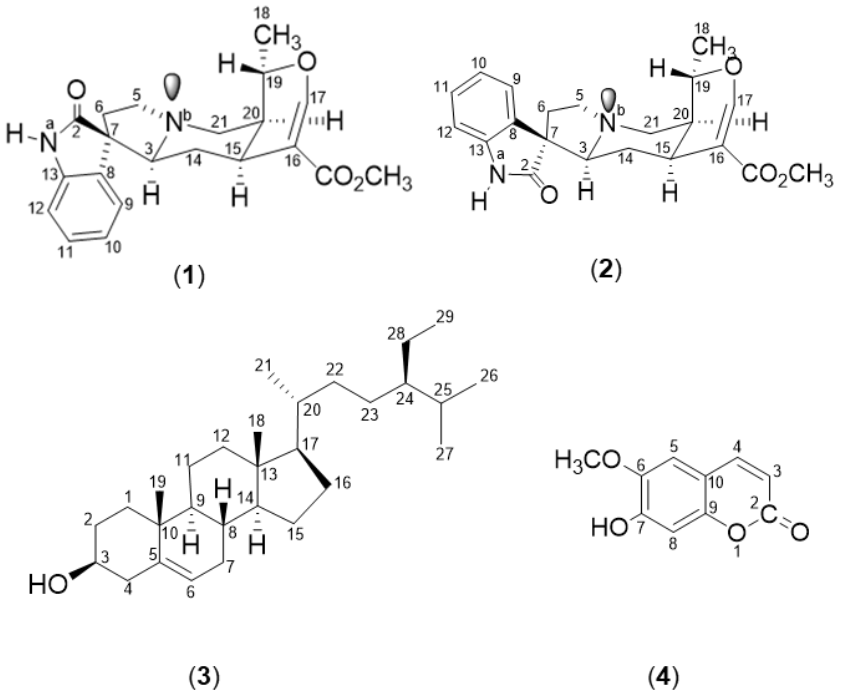

Figure 3. Structure of the isolated compounds: (**1**) pteropodine, (**2**) isopteropodine, (**3**) β-sitosterol and (**4**) scopoletin

Conclusion

The present data suggest that Malaysian *U. tomentosa* extracts exhibited antibacterial and antibiofilm activities against oral bacteria. The isolated phytochemicals namely isopteropodine, pteropodine, and β-sitosterol, scopoletin, are presumably responsible synergically and singularly for the activities of the active DCM extract. However, further research is needed to evaluate these compounds to ensure their contribution. The findings provide evidence to support the plant's traditional use and could be the source of antibacterial and antibiofilm agents for further studies.

Acknowledgment

The authors would like to thank the Universiti Teknologi MARA for providing funding for the research project through Young Talent Researcher (YTR) grant no. 600-RMC/YTR/5/3 (005/2022).

References

1. Sateriale, D., Imperatore, R., Colicchio, R., Pagliuca, C., Varricchio, E., Volpe, M. G., Salvatore, P., Paolucci, M. and Pagliarulo, C. (2020). Phytocompounds vs. dental plaque bacteria: In vitro effects of myrtle and pomegranate polyphenolic extracts against single-species and multispecies oral biofilms. *Frontier Microbiology*, 11: 592265.
2. Kouidhi, B., Al Qurashi, Y. M. and Chaieb, K. (2015). Drug resistance of bacterial dental biofilm and the potential use of natural compounds as alternative for prevention and treatment. *Microbial Pathogenesis*, 80: 39-49.
3. Gao, L., Xu, T., Huang, G., Jiang, S., Gu, Y. and Chen, F. (2018). Oral microbiomes: more and more importance in oral cavity and whole body. *Protein Cell*, 9: 488-500.
4. Salim, F., Yunus, Y. M., Anouar, E. H., Awang, K., Langat, M., Cordell, G. A. and Ahmad, R. (2019). Absolute configuration of alkaloids from *Uncaria longiflora* var. *pteropoda* through experimental and theoretical approaches. *Journal of Natural Products*, 82: 2933-2940.
5. Ahmad, R. and Salim, F. (2015). Oxindole alkaloids of *Uncaria* (Rubiaceae, subfamily Cinchonoideae): A review on its structure, properties and bioactivities. Studies in Natural Products Chemistry, Elsevier, Netherlands. 45, pp. 486-525.

6. Cerri. R., Aquino, R., de Simone, F. and Pizza, C. (1988). New quinovic acid glycosides from *Uncaria tomentosa*. *Journal of Natural Products*, 51(2): 257-261.
7. Laus, G., Brossner, D. and Keplinger, K. (1997). Alkaloids of Peruvian *Uncaria tomentosa*. *Phytochemistry*, 45: 855-860.
8. Senatore, A., Cataldo, A., Iaccarino, F.P. and Elberti, M.G. (1989). Phytochemical and biological study of *Uncaria tomentosa*. *Bollettino della Società Italiana di Biologia Sperimentale*, 65: 17-520.
9. Batiha, G. E., Magdy Beshbishy, A., Wasef, L., Elewa, Y. H., E., M., Taha, A. E., Abdullah, A., Devkota, H. P. and Tufarelli, V. (2019). *Uncaria tomentosa* (Willd. Ex Schult.) DC.: A review on chemical constituents and biological activities. *Applied Sciences*, 10(8): 2668.
10. Blanck, J. J., Huebner, T. M., Rolls, A. M., Cornell, J. S., and Hwang, C. S. (2022). Comprehensive review of the components in Cat's Claw (*Uncaria tomentosa*) and their antibacterial activity. *Applied Chemistry*, 2(1): 1-29.
11. Shafiei, Z., Shuhairi, N. N., Md Fazly Shah Yap, N., Harry Sibungkil, C.-A. and Latip, J. (2012a). Antibacterial activity of *Myristica fragrans* against oral pathogens. *Evidence-Based Complementary and Alternative Medicine*.
12. Das, K., Tiwari, R. and Shrivastava, D. (2010). Techniques for evaluation of medicinal plant products as antimicrobial agents: current methods and future trends. *Journal of Medicinal Plants Research*, 4: 104-111.
13. Gahlaut, A. and Chhillar, A. (2013). Evaluation of antibacterial potential of plant extracts using Resazurin based microtiter dilution assay. *International Journal of Pharmacy and Pharmaceutical Sciences*, 5: 372- 376.
14. Stepanović, S., Vuković, D., Hola, V., Di Bonaventura, G., Djukić, S., Cirković, I. and Ruzicka, F. (2007). Quantification of biofilm in microtiter plates: overview of testing conditions and practical recommendations for assessment of biofilm production by *Staphylococci*. *Apmis*, 115: 891-899.
15. Loo, C.Y., Corliss, D.A. and Ganeshkumar, N. (2000). *Streptococcus gordonii* biofilm formation: identification of genes that code for biofilm phenotypes. *Journal of Bacteriology*, 182(5): 1374-1382.
16. Qaralleh, H.A., Al-Lomoun, O.M., Khlaifat, A., Khleifat, K.M., Al-Tawarah, N., Alsharafa, K.Y. and Abu-Harirah, A.H. (2021). Antibacterial and antibiofilm activities of a traditional herbal formula against respiratory infection causing bacteria. *Tropical Journal Natural Product Research*, 4(9):527-534.
17. Eloff, J. N. (2019). Avoiding pitfalls in determining antimicrobial activity of plant extracts and publishing the results. *BMC Complementary Medicine and Therapies*, 19: 106.
18. Pretto, J., Cechinel Filho, V., Floriani Noldin, V., Sartori, M., Isaias, D. and Cruz, A. (2004). Antimicrobial activity of fractions and compounds from *Calophyllum brasiliense* (Clusiaceae/Guttiferae). *Zeitschrift für Naturforschung. C, Journal of Biosciences*, 59: 657-662.
19. Eloff, J. N., Angeh, I. E. and Mcgaw, L. J. (2017). Solvent-solvent fractionation can increase the antifungal activity of a *Melianthus comosus* (Melianthaceae) acetone leaf extract to yield a potentially useful commercial antifungal product. *Industrial Crops and Products*, 110: 103-112.
20. Kloucek, P., Polesny, Z., Svobodova, B., Vlkova, E. and Kokoska, L. (2005). Antibacterial screening of some Peruvian medicinal plants used in Calleria District. *Journal of Ethnopharmacology*, 99: 309-312.
21. Romero, C.D., Chopin, S.F., Buck, G., Martinez, E., Garcia, M. and Bixby, L. (2005). Antibacterial properties of common herbal remedies of the southwest. *Journal of Ethnopharmacology*, 99: 253-257.
22. Ulloa-Urizar, G., Aguilar-Luis, M. A., De Lama-Odría, M. D. C., Camarena-Lizarzaburu, J. and Del Valle Mendoza, J. (2015). Antibacterial activity of five Peruvian medicinal plants against *Pseudomonas aeruginosa*. *Asian Pacific Journal of Tropical Biomedicine*, 5: 928-931.
23. Ccahuana-Vasquez, R. A., Santos, S. S., Koga-Ito, C. Y. and Jorge, A. O. (2007). Antimicrobial activity

of *Uncaria tomentosa* against oral human pathogens. *Brazilian Oral Research*, 21: 46-50.

24. Herrera, D. R., Tay, L.Y., Rezende, E. C., Kozlowski, V. A., Jr. and Santos, E. B. (2010). In vitro antimicrobial activity of phytotherapic *Uncaria tomentosa* against endodontic pathogens. *Journal of Oral Science*, 52: 473-476.
25. Leme, A. F. P., Koo, H., Bellato, C. M., Bedi, G. and Cury, J. A. (2006). The role of sucrose in cariogenic dental biofilm formation—New insight. *Journal of Dental Research*, 85(10): 878-887.
26. Lu, L., Hu, W., Tian, Z., Yuan, D., Yi, G., Zhou, Y., Cheng, Q., Zhu, J. and Li, M. (2019). Developing natural products as potential anti-biofilm agents. *Chinese Medicine*, 14: 11.
27. White, G., Bourbonnais-Spear, N. and Garner, F. (2011). Antibacterial constituents from *Uncaria tomentosa*. *The Journal of Phytopharmacology*, 1: 16-9.
28. García, R., Cayunao, C., Bocic, R., Backhouse, N., Delporte, C., Zaldivar, M. and Erazo, S. (2005). Antimicrobial activity of isopteropodine. *Zeitschrift für Naturforschung C*, 60: 385-388.
29. Salim, F. and Ahmad, R. (2010). Isopteropodic acid from Malaysian *Uncaria longiflora* var. *pteropoda*. *World Applied Science Journal*, 10(11): 1334-1337.
30. Salim, F. and Ahmad, R. (2011). Alkaloids from Malaysian *Uncaria longiflora* var. *pteropoda*. *Biochemical Systematics and Ecology*, 39(2): 151-152.
31. Sukor, S., Zahari, Z., Rahim, N., Yusoff, J. and Salim, F. (2022). Chemical constituents and antiproliferative activity of *Eleusine indica* (L.) Gaertn. *Sains Malaysiana*, 51 (3): 873-882.
32. Abdullah, N.H., Salim, F. and Ahmad, R. (2016). Chemical constituents of Malaysian *U. Cordata* var. *Ferruginea* and their in vitro α-glucosidase inhibitory activities. *Molecules*, 21(5): 525.

Malaysian Journal of Analytical Sciences (MJAS)
Published by Malaysian Analytical Sciences Society

SYNTHESIS OF CARRAGEENAN-BASED BIOCOMPOSITE PLASTICIZED WITH DEEP EUTECTIC SOLVENT AND CHARACTERIZATION OF ITS MECHANICAL PROPERTIES

(Sintesis Biokomposit Berasaskan Karaginan Diplastikkan dengan Pelarut Eutektik Dalam dan Penyifatan Ciri-Ciri Mekanikal)

Nur Amalina Ramli[1], Fariha Rosli[1], Mohd Aiman Hamdan[2], and Fatmawati Adam[1,3*]

[1]Faculty of Chemical and Process Engineering Technology,
Universiti Malaysia Pahang Al-Sultan Abdullah, 26300 Kuantan, Pahang, Malaysia
[2]School of Food Industry, Faculty of Bioresources and Food Industry,
Universiti Sultan Zainal Abidin, 22200 Besut, Terengganu, Malaysia
[3]Centre for Research in Advanced Fluid and Processes,
Universiti Malaysia Pahang Al-Sultan Abdullah, 26300 Kuantan, Pahang, Malaysia

[*]Corresponding author: fatmawati@umpsa.edu.my

Received: 14 September 2023; Accepted: 12 January 2024; Published: 28 February 2024

Abstract

Carrageenan from seaweed tends to be brittle in the formation of hard capsules. In this study, a carrageenan-based biocomposite was synthesized to provide an alternative to gelatin hard capsules. This study aims to characterize the mechanical properties of carrageenan biocomposite plasticized with a deep eutectic solvent (DES) of choline chloride (ChCl) and glycerol. The carrageenan biocomposite was formulated at varying concentrations (0, 0.2, 0.4, 0.6, 0.8, and 1.0 v/v%) of DES to improve the strength and elasticity of carrageenan biocomposite films and hard capsules. The absence of the ChCl band at 1348 cm^{-1} and the reduced intensity of the C–O glycerol band at 1107 cm^{-1} in the ATR-FTIR spectra of DES were regarded as evidence for the formation of the eutectic mixture. This can be explained by the hydrogen bond donor and acceptor interaction between the DES constituents, which are chloride ions (Cl^-) of ChCl and the hydroxyl group (–OH) of glycerol ($Cl^-\cdots OH$). The highest viscosity of Carra-DES 0.2 at 504.9 mPa·s reflects the improved film tensile strength up to 60.1 MPa, which gives a positive effect after the addition of DES. The capsule loop strength reached its peak at 31.7 N for Carra-DES 0.4. A significant increase in the elongation at break of Carra-DES film was observed at DES concentrations of 0.2–0.6%. However, the concentration of DES should be controlled to achieve high tensile and loop strengths in hard capsule application. In conclusion, the incorporation of DES in carrageenan biocomposite can reduce its brittleness while improving its elasticity and strength in the production of hard capsules.

Keywords: Biocomposite, carrageenan, choline chloride, deep eutectic solvent, plasticizer

Abstrak

Karaginan daripada rumpai laut cenderung menjadi rapuh dalam pembentukan kapsul keras. Dalam kajian ini, biokomposit berasaskan karaginan telah disintesis sebagai alternatif kepada kapsul keras gelatin. Kajian ini bertujuan menyifatkan ciri-ciri mekanikal biokomposit karaginan yang ditambah pemplastik pelarut eutektik dalam (DES) yang diperbuat daripada kolina klorida

(ChCl) dan gliserol. Biokomposit karaginan telah dirumuskan dengan DES menggunakan kepekatan yang berbeza (0, 0.2, 0.4, 0.6, 0.8, dan 1.0 v/v%) untuk meningkatkan kekuatan dan keanjalan filem biokomposit karaginan dan kapsul keras. Ketiadaan jalur penyerapan ChCl pada 1348 cm^{-1} dalam analisis ATR-FTIR dan peralihan jalur getaran C–O dalam gliserol ke arah 1728 cm^{-1} dianggap sebagai bukti pembentukan campuran eutektik. Ini boleh dijelaskan oleh interaksi penderma dan penerima ikatan hidrogen antara konstituen DES, iaitu ion klorida (Cl^-) ChCl dan kumpulan hidroksil (–OH) gliserol ($Cl^{-}\cdots OH$). Kelikatan tertinggi Carra-DES 0.2 pada 504.9 mPa·s mencerminkan kekuatan tegangan filem yang lebih baik sehingga 60.1 MPa dan memberikan kesan positif selepas penambahan DES. Kekuatan gelung kapsul mencapai kemuncaknya pada 31.7 N untuk Carra-DES 0.4. Peningkatan ketara pemanjangan filem Carra-DES semasa putus berlaku pada kepekatan DES 0.2% hingga 0.6%. Walau bagaimanapun, kepekatan DES harus dikawal untuk mencapai kekuatan tegangan filem dan gelung kapsul yang tinggi dalam aplikasi kapsul keras. Kesimpulannya, penggabungan DES dalam biokomposit karaginan dapat mengurangkan kerapuhan di samping meningkatkan keanjalan dan kekuatan dalam menghasilkan kapsul keras.

Kata kunci: Biokomposit, karaginan, kolina klorida, pelarut eutektik dalam, pemplastik

Introduction

A high interest in sustainable polymers from plants has been shown to replace gelatin hard capsules from animal sources due to consumers' dietary restrictions. Carrageenan, a versatile natural polysaccharide, emerges as a promising alternative material for hard capsules with characteristics similar to gelatin, including thermal reversibility and film-forming properties. Derived from seaweed, this resource abounds in Malaysia, particularly in East Malaysia, Sabah [1]. Unveiling superior gelling and high viscosity properties, carrageenan is able to form a biopolymer film, finding widespread application in the pharmaceutical industry as a thickener, stabilizer, and emulsifier [2]. The distinctive attributes of this material have assured its market demand. Despite its film-forming ability, an inherent brittleness limits its application as a hard capsule, presenting an intriguing challenge for further exploration. In order to overcome the shortcomings of carrageenan, formulations of carrageenan biocomposite are thoroughly studied. A biocomposite is a blend of two or more naturally derived materials to develop a reinforced product with improved performance over individual constituent materials. The formulation of carrageenan biocomposite has been modified by incorporating isovanillin as the crosslinker [3] with cellulose nanocrystals (CNCs) and cellulose nanofibers as the reinforcing agents [4, 5]. Thickening agents have also been incorporated, such as gum Arabic [6, 7], hydroxypropyl methylcellulose [8], and carboxymethyl starch [9]. In the application of green bioplastics, *Chlorella vulgaris* microalgae have also been blended into the formulation to improve the hydrophobicity of the carrageenan film [10].

Plasticizer is an additive introduced in polymers to produce more flexible films, increase elasticity, and reduce friction during the manufacturing process. Deep eutectic solvent (DES) has properties that are suitable as a potential plasticizer to improve the mechanical properties of biocomposite films [11]. It is a novel solvent system that can be prepared from a range of anionic and/or cationic chemicals that are commonly available to form an eutectic mixture [12]. Deep eutectic solvent, an analog to ionic liquid (IL), is also utilized as a solvent, reagent, catalyst, and crosslinker in various applications [13]. Deep eutectic solvent is safe and non-toxic as opposed to IL based on its non-volatility and the alleged benign nature of its main constituents [14]. Studies on DES have begun with choline chloride (ChCl) as a hydrogen bond acceptor (HBA), and it is one of the most commonly used compounds in synthesizing DES [12]. Glycerol, the hydrogen bond donor (HBD) used in this study, is a simple natural polyol that is inexpensive, biodegradable, non-toxic, and extensively used in the food industry [15]. The simplicity of DES synthesis, achieved by the precise mixing of HBA and HBD components in specific molar ratios, as well as low toxicity, make it a more viable and safer choice for numerous applications, such as edible biocomposites [16].

In comparison to conventional plasticizers, DES (ChCl and glucose/glycerol/urea) are highly promising plasticizers for cellulose-based biocomposites, with an increase in elongation at break (EAB) up to 81%, while the tensile strength is comparable to that of a single component plasticizer [13]. Furthermore, DES (ChCl/urea) has also been proven to refine film

uniformity and smoothness with only 0.01% of DES, preserving the structural stability and optical properties of the CNC film while significantly reducing film brittleness [17]. The addition of DES (ChCl/lactic acid) with lignin also increased the tensile strength of the chitosan film to 31.6 MPa and effectively increased the plasticity, giving a maximum EAB of 62.6% [18]. The EAB of the gelatin/polyvinyl alcohol composite film reached up to 654% when the mass fraction of DES (sodium acetate trihydrate/urea) was 60% [19]. Most studies reported the advantages of DES for polysaccharides and better plasticizing ability than conventional plasticizers [20,21]. Currently, it is difficult to find research on the influence of DES as a plasticizer for carrageenan biocomposite and the plasticization effect on the carrageenan biocomposite film and hard capsules. This work aimed to synthesize carrageenan biocomposite plasticized with DES (ChCl/glycerol) at different concentrations and to characterize the mechanical properties of the resulting biocomposite films and hard capsules. It was hypothesized that the addition of DES as a plasticizer can reduce the brittleness and increase the carrageenan hard capsule strength when incorporated in an appropriate amount.

Materials and Methods

Materials

Refined carrageenan as the main material of the biocomposite was bought from CV Simpul Agro Globalindo, Indonesia. Hydroxypropyl methyl cellulose (84 kDa) as a thickening agent, 4-methoxybenzyl alcohol (98%) as a crosslinker, and calcium alginic acid (584.5 Da) as a toughening agent were obtained from Sigma-Aldrich (USA). Meanwhile, CNCs for reinforcement were prepared from the microcrystalline cellulose (Avicel PH-101) purchased from Sigma-Aldrich (St. Louis, MO, USA). The DES composed of ChCl (98%, 139.62 Da) and glycerol (99.5%, 104.06 Da) as a plasticizer were obtained from Merck (Darmstadt, Germany). All chemicals used are of analytical grade. Deionized water was used throughout the entire experiment.

Preparation of DES as a plasticizer

Pure ChCl was pretreated to remove any possible moisture by drying in a vacuum oven overnight at 80 °C and was stored in a dry place for further use [22]. Accordingly, ChCl and glycerol were mixed with gentle stirring at a molar ratio of 1:2 at 60 °C for 30 min until homogeneous with no evidence of solid particles [23, 24]. The eutectic mixture of ChCl and glycerol was designated as the DES solution.

Preparation of CNC as a reinforcement agent

The CNC solution was prepared according to Mohd. Amin et al., where 5.0g of microcrystalline cellulose was stirred overnight in 500 mL of deionized water using a hot plate [25]. A QSonica (Q700, USA) ultrasonicator was used to sonicate the cellulose dispersion for 20 min at a 20% amplitude. This process was carried out with 8 s pulsed on and 2 s pulsed off. After resting for 10 min, the bottom layer of the solution was removed, and the solution was left overnight. The top clear layer of the solution was removed to collect 300 mL of the concentrated portion, which was identified as the CNC solution.

Synthesis of carrageenan biocomposite

The biocomposite solution was prepared by dissolving 3.0g of refined carrageenan in 150 mL of deionized water. The solution was heated for 30 min at 60 °C under continuous stirring using a hot plate and a magnetic stirrer. Then, 4-methoxybenzyl alcohol (0.7 w/v%), CNCs (1.6 w/v%), hydroxypropyl methylcellulose (0.8 w/v%), and calcium alginic acid (0.07 w/v%) were added gradually to the biocomposite solution. These concentrations were incorporated into the carrageenan biocomposite following previous research from Hamdan et al. [4] and Ramli et al. [8]. The DES, which composed of ChCl and glycerol, was added to the biocomposite solution at varying concentrations from 0 to 1.0 v/v%, as shown in Table 1. The solution was poured on a round stainless-steel tray with a diameter of 20 cm after 3 h of mixing, while the remaining solution was dipped using the stainless-steel mold pins (size 1) to form the hard capsule. All samples of biocomposite films and hard capsules were dried overnight at room temperature.

Table 1. Sample formulation of carrageenan biocomposite plasticized with DES at various concentrations

Samples	Concentration of Carrageenan (w/v%)	Concentration of DES (v/v%)
Control	2.0	0
Carra-DES 0.2	2.0	0.2
Carra-DES 0.4	2.0	0.4
Carra-DES 0.6	2.0	0.6
Carra-DES 0.8	2.0	0.8
Carra-DES 1.0	2.0	1.0

Functional group determination

The presence of different functional groups in ChCl and glycerol was analyzed by conducting Fourier transform infrared (FTIR) spectroscopy to recognize any potential shifting of the chemical bonds in the formation of DES. The samples were subjected to an attenuated total reflection (ATR)-FTIR spectrometer (Perkin Elmer, Frontier, USA) equipped with OMNIC software within the range of 400-4000 cm^{-1}. Overall, 32 scans were collected with a spectral resolution of 8 cm^{-1} at a rate of 0.15 s/scan [26].

Rheological analysis

The viscosity is a crucial characteristic of a biocomposite as it will affect the mechanical properties of the carrageenan biocomposite. Higher viscosity relates to stronger intermolecular forces between the materials, where the molecules are strongly bonded together. The viscosity and shear stress of the biocomposite solution were measured using a rotational viscometer (Brookfield, Rheo 3000, USA) equipped with LCT 25 4000010 geometry. Approximately 16.5 mL of the biocomposite solution was poured into the cylindrical compartment of the viscometer for each measurement. The sample was evaluated in triplicate at a constant temperature of 40 °C using a preset speed of 300 rpm with 100 MPoints [27].

Mechanical strength evaluation

The mechanical evaluation was carried out to investigate the deformation of the produced films and hard capsules in response to a load or force applied. A texture analyzer (CT3, Brookfield, USA) was used to measure the tensile strength and EAB of the biocomposite films. The analyzer was outfitted with TexturePro CT V1-8 Build 3.1 software and a 5-kN load cell. The tensile strength was measured following the standard method of ASTM D882-12. The biocomposite films were cut into strips with a dimension of 20 × 60 mm^2. The film thickness was calculated as the average of three distinct positions of the film samples measured with Vernier calipers. The analysis was controlled by setting up the texture analyzer with a baseline grip width of 80 mm and a crosshead speed of 30 mm/min to a maximum distance of 15 mm [28]. The tensile strength and the EAB for each sample were calculated as in Equation 1 and Equation 2, respectively. The load at break and the elongation at rupture were collected from the results of the texture analyzer, and the initial gauge length was the set-up value for the crosshead speed used for the measurement.

$$\text{Tensile strength (MPa)} = \frac{\text{Load at break}}{\text{Initial width} \times \text{Initial thickness}} \quad (1)$$

$$\text{Elongation at break (\%)} = \frac{\text{Elongation at rupture}}{\text{Initial gauge length}} \times 100\% \quad (2)$$

The same texture analyzer (CT3, Brookfield, USA) was used to conduct the capsule loop test, but with a capsule loop fixture. A hard capsule was attached to a pair of separating rods, with the lower rod positioned on the stationary platform and centrally beneath the probe. The upper rod gradually went higher at a speed of 0.50 mm/s with a target value of 5.0 mm until the hard capsule was torn apart. [29]. The applied force (N) to break the hard capsule was reported as the capsule loop strength. The analysis was conducted with at least three measurements taken for each sample to calculate the average result.

Moisture content determination

Moisture content can affect the mechanical qualities of a sample. Accordingly, a moisture analyzer (MS70, A&D Japan) was used to measure the moisture content in the biocomposite film. About 0.1 g of the sample was placed on the heating pan of the moisture analyzer [30]. The moisture in the sample would evaporate after air-drying at 30–200 °C. The sample was heated by a halogen lamp for fast and uniform heating to give a quick measurement. When the mass of the sample reached a constant value, the analysis was automatically stopped. The electric balance weighed the sample before and after heating to determine the moisture content, as shown in Equation 3.

$$\text{Moisture content (\%)} = \frac{\text{Initial weight - Dried weight}}{\text{Initial weight}} \times 100\% \qquad (3)$$

Results and Discussion

Functional groups of DES

The formation of the eutectic mixture was analyzed by ATR-FTIR spectroscopy for DES and its pure constituents. The spectra of DES together with ChCl and glycerol are shown in Figure 1. Pure ChCl exhibited vibrational bands at 3223 cm^{-1} and 1200–880 cm^{-1}, corresponding to stretching vibrations of –OH or N–H bonds. The vibrational bands at 3024 cm^{-1} and 1479–1348 cm^{-1} corresponded to alkyl groups or N–H vibrations in quaternary ammonium groups. Other bands in the wavelength ranged from 1273 to 864 cm^{-1}, with the most intense band at 950 cm^{-1}, also showed the existence of hydroxyl and ammonium group characteristics of ChCl. The most prominent group of CH_2 bending was detected at 1479 cm^{-1}. This is comparable to the band at 1482 cm^{-1} from the study by Jakubowska et al. [31].

The most important band in the glycerol spectrum is the typical O–H stretching of the hydroxyl group, which was represented by the vibrational band at 3384 cm^{-1}. The vibrational bands at 2932 and 2878 cm^{-1} corresponded to C–H stretching and 1412 cm^{-1} to CH_2 bending of the alkyl group. The bands at 1107, 1028, and 849 cm^{-1} corresponded to different functional groups, namely C–O stretching, asymmetric C–C–O stretching, and symmetric C–C–O stretching, respectively. An additional band that appeared at 1208 cm^{-1} referred to C–O–H bending. These functional groups are absorbed at a wavelength similar to that reported by Delgado et al. [32].

A few peaks related to ChCl coexisted after the formation of DES. The absence of a ChCl band at 1348 cm^{-1} is consistent with previous results pertaining to the solvent systems of ChCl/malonic acid [33], ChCl/lactic acid [31], and ChCl/acrylic acid [34]. The reduced intensity around 1475 and 1107 cm^{-1}, which indicated CH_2 bending of ChCl and C–O stretching of glycerol, could be interpreted as evidence for the formation of the eutectic mixture of DES. This can be explained by the hydrogen bond donor-acceptor interaction between the constituents of DES, which are chloride ions of ChCl and the –OH group of glycerol ($Cl^{-}\cdots OH$). The absorption band of glycerol at 3293 cm^{-1} was discovered to shift down to 3287 cm^{-1} in the DES, indicating the formation of a hydrogen bond between ChCl and glycerol, such as $Cl^{-}\cdots OH$ and $CH_3\cdots OH$. A similar trend of shifted peaks between the DES constituents was also observed by Sun et al., who synthesized 25 types of ChCl-based DES for cellulose [35].

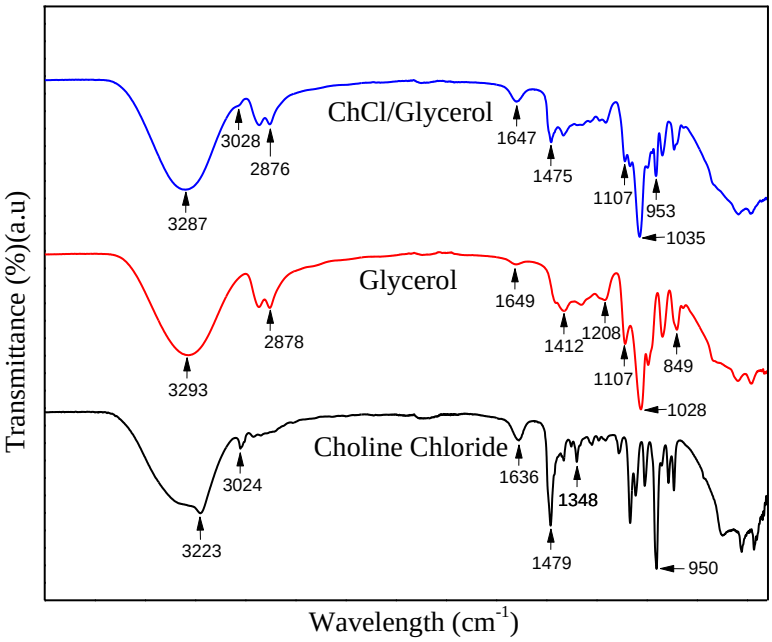

Figure 1. FTIR spectra of DES formation from ChCl and glycerol

Rheological analysis

Viscosity, a property of rheology, is defined as the measure of the resistance of a fluid to gradual deformation by shear stress. Figure 2 presents the relationship between shear stress and viscosity of the carrageenan biocomposite at different DES concentrations, ranging from 0 to 1.0 v/v%. The increase in shear stress between the layers of the biocomposite solution would also increase the viscosity of the solution [36]. The biocomposite without DES had a viscosity of 442.5 mPa·s and a shear stress of 171.2 Pa. The inclusion of 0.2 v/v% DES increased the viscosity and shear stress to their highest values of 504.9 mPa·s and 201.4 Pa, respectively. This increase is due to the rheological complexity of the carrageenan matrix when introduced with DES as a plasticizer. The trend for both plots of viscosity and shear stress fluctuated. It is worth noting that a significant reduction in the viscosity of Carra-DES 0.6 by 16.1% occurs because an excess amount of plasticizer enhances the molecular mobility of the biocomposite, reducing friction force or shear stress, thereby increasing the flowability of the biocomposite [37]. Defining the optimal concentration of a plasticizer in a formulation is crucial, as the viscosity of the biocomposite influences its mechanical properties.

Film tensile strength and EAB

The biocomposite materials used for hard capsules possess high mechanical properties to restrain the load applied, resulting in lower rejection rates during capsule filling. Although carrageenan has good film-forming properties, it is fragile and exhibits poor flexibility. The best concentration of DES as the plasticizer has to be quantified to produce hard capsules with low brittleness. In the mechanical evaluation, tensile strength and EAB were used as indicators for the biocomposite films, while loop strength was assessed for the hard capsules.

Figure 3 presents the tensile strength and EAB of carrageenan biocomposite at different DES concentrations. A significant peak in tensile strength was achieved by Carra-DES 0.2 with an increase of 67.1% from 19.8 to 60.1 MPa. This increase indicates that the addition of DES to the biocomposite film can effectively improve its flexibility and reduce the brittleness of the film. This enables its application as a plasticizer for hard capsules to be exploited. Moreover, the increase is directly related to the increase in viscosity of the biocomposite, as shown in Figure 2. The HBD and HBA of the DES were able to form hydrogen bonds with the hydroxyl groups on the glycosidic moiety of the polysaccharide chains of carrageenan. The increased

intermolecular interaction between DES and carrageenan strengthens the biocomposite film. This is applicable to the lower concentration of DES as the tensile strength gradually decreased with the increasing DES concentration from 0.4 to 0.8 v/v%. The newly formed hydrogen bonds were able to disrupt the intermolecular interactions between the polysaccharide chains, leading to an increase in chain movement and greater flexibility of the biocomposite [19].

In contrast, the EAB of the carrageenan biocomposite film depicted an opposite trend, which was consistent with previous studies [19, 38]. The EAB of the control film gradually increased from 6.1% and reached its maximum value of 45.5% with the addition of DES at a concentration of 1.0 v/v%. The directly proportional relationship between the EAB value and the DES concentration indicated that the DES had a significant plasticizing effect on the biocomposite films. The DES made from ChCl and glycerol was a viable plasticizer as it could significantly increase the percentage of EAB, even at a low volume. At a concentration of 0.6 v/v%, the EAB almost reached a constant value because the excess DES concentration disrupted the intermolecular hydrogen bonding between the polymer chains of carrageenan. This trend was comparable to the study by Zhao et al. in which a high concentration of natural DES was added to the chitosan/zein films [38]. In general, there is an inverse correlation between tensile strength and elongation. The best and most desirable biocomposite films for hard capsule application are those that exhibit both strength and flexibility in an optimal balance. These films would be able to withstand external forces while still being flexible enough to undergo deformation without breaking. Therefore, the amount of DES used in the formulation should be controlled to achieve high physical strength in hard capsule application.

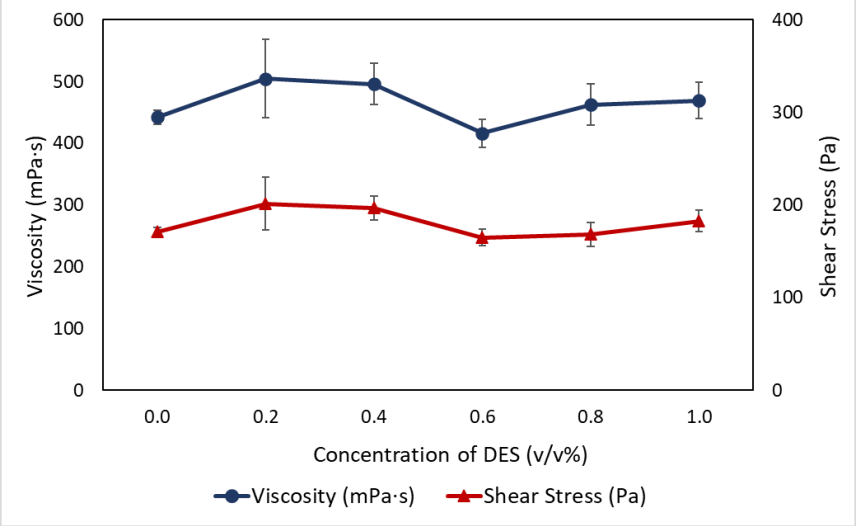

Figure 2. Viscosity and shear stress of carrageenan biocomposite at various DES concentrations

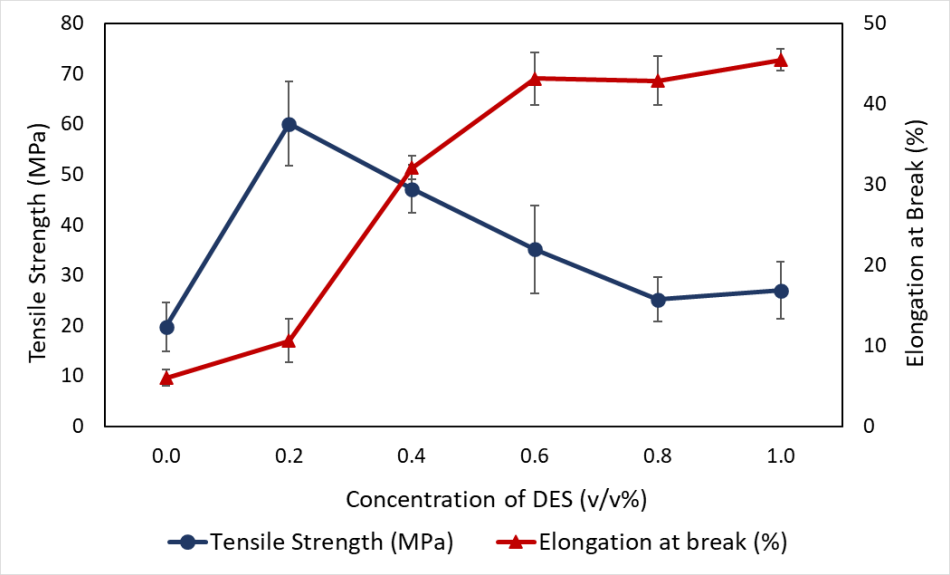

Figure 3. Tensile strength and EAB of carrageenan biocomposite films at various DES concentrations

Capsule loop strength

The loop strength for each carrageenan hard capsule sample at different DES concentrations is shown in Figure 4. The capsule loop strength increased significantly after the addition of DES, up to 35.4% for Carra-DES 0.4. The strength increased to 31.6 N as opposed to the control sample with 20.4 N. As discussed in the tensile strength result, the new hydrogen bond formed between the DES constituents and the carrageenan matrix improved the strength of the capsule loop due to the increased intermolecular interaction. The trend of the graph abruptly declined after the addition of DES at concentrations higher than 0.4 v/v%. The capsule loop strength decreased to 12.8 N in the sample of Carra-DES 1.0. The polar groups of DES made it easy to form hydrogen bonds with carrageenan. However, excessive plasticization weakened the carrageenan hard capsule as it could destroy the existing intermolecular hydrogen bonds between the carrageenan molecules [18]. Therefore, upon adding a higher concentration of DES, the capsule loop strength began to decrease.

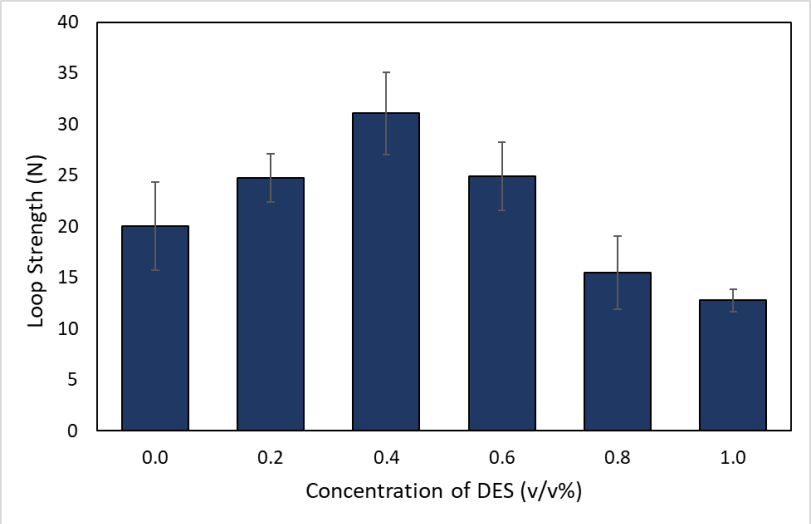

Figure 4. Loop strength of carrageenan hard capsules at various DES concentrations

Film thickness and moisture content

Table 2 presents the film thickness and moisture content of Carra-DES samples at varied concentrations. The control sample without DES was reported to be the thickest film compared to other samples with 0.23 mm. The addition of plasticizer increased the molecular mobility of the carrageenan matrix, which promoted the flowability of the biocomposite solution during film casting and thus reduced the film thickness. The thickness of the biocomposite films with the addition of DES from 0.2 to 1.0 v/v% presented a slight discrepancy, which was around 0.11–0.15 mm.

Table 2. Film thickness and moisture content of carrageenan biocomposite films at various DES concentrations

Samples	Film Thickness (mm)	Moisture Content (%)
Control	0.23 ± 0.02	14.5 ± 0.3
Carra-DES 0.2	0.12 ± 0.02	13.5 ± 0.5
Carra-DES 0.4	0.14 ± 0.01	15.4 ± 0.6
Carra-DES 0.6	0.11 ± 0.04	15.8 ± 0.6
Carra-DES 0.8	0.15 ± 0.01	15.9 ± 0.7
Carra-DES 1.0	0.12 ± 0.03	14.8 ± 0.1

Water can also act as a plasticizer for a biocomposite film, which in excess impairs its mechanical properties. Consequently, the moisture content of the carrageenan biocomposite film should be considered for the development of hard capsules. As shown in Table 2, the moisture content of all tested samples was around 13-15%, indicating that the influence of DES concentration was insignificant in this study. Moreover, these values were comparable to those of commercial gelatin capsules with a moisture content of 13% [39]. Similar results were also found by Hamdan et al., who reported that the moisture content of Carra-CNC biocomposites ranged from 15.5% to 17.5% [4]. However, it is noteworthy that high concentrations of DES at 0.4-0.8 v/v% had the highest moisture content, surpassing 15%. The hygroscopic characteristics of DES likely affect the ability of the film to absorb moisture from the surroundings when a high DES concentration is introduced into the formulation [40].

Physical appearances of films

Figure 5 presents the images of carrageenan biocomposite films at different DES concentrations with a black panel as the background. Based on the observation under natural light, the control sample appears transparent and has a rough surface due to the insoluble solid crystals of CNCs. The addition of the DES to the formulation improved the poor uniformity observed in the control sample. The transparency gradually decreased with increasing DES concentrations. Under the same conditions, Carra-DES 0.8 and Carra-DES 1.0 were observed to be almost opaque. These two samples have a relatively smooth surface compared to the control sample. Higher DES concentrations can improve the appearance of the carrageenan biocomposite film, where the smoothness increases differently. Nevertheless, a higher DES concentration would decrease the mechanical properties of the carrageenan biocomposite film, as discussed in Figure 3 and Figure 4. Wei et al. speculated that a higher DES concentration directly destroys the structure of CNCs, resulting in a loss of optical and mechanical properties of CNC/DES films [17].

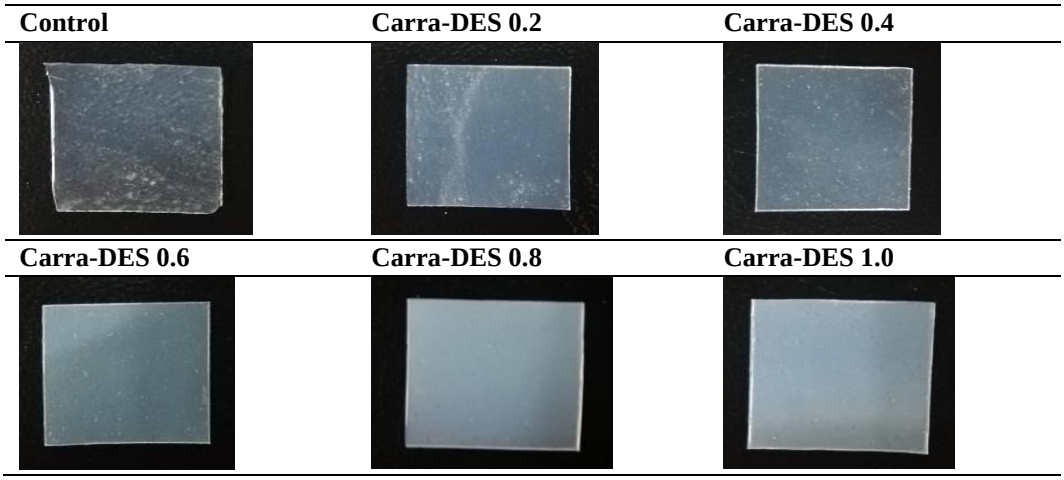

Figure 5. Images of carrageenan biocomposite films at various DES concentrations

Conclusions

In summary, DES has been successfully applied as a new type of plasticizer in the synthesis of carrageenan biocomposite films and hard capsules. The DES, which consists of ChCl and glycerol, is a good and feasible plasticizer because it can significantly increase the flexibility of carrageenan biocomposites even at low concentrations. The EAB of the carrageenan film greatly increased from 6.1% to 45.5% when the DES concentration increased to 1.0 v/v%. Meanwhile, Carra-DES at 0.2 v/v% gave the highest tensile strength of 60.1 MPa, which was the best concentration of Carra-DES biocomposite with a capsule loop strength of 24.8 N. The formation of hydrogen bonds between DES and carrageenan improves the mechanical strength of the biocomposite films. Despite that, an excess concentration of DES could have a detrimental effect on the film tensile and capsule loop strengths of the carrageenan biocomposite. In addition, the hygroscopic characteristics of DES would lead to poor stability of the hard capsule with increased moisture content. For that reason, it should be controlled at an appropriate concentration to achieve high mechanical strength in hard capsule application.

Acknowledgement

The authors would like to express gratitude to Universiti Malaysia Pahang Al-Sultan Abdullah for the research funding through Distinguished Research Grant (RDU223012) and additional financial support under Postgraduate Research Grant (PGRS2003131), as well as for providing laboratory facilities in undertaking this research.

References

1. Phang, S. M., Yeong, H. Y. and Lim, P. E. (2019). The seaweed resources of Malaysia. *Botanica Marina*, 62 (3): 265-273.
2. Dewi, E. N., Darmanto, Y. S. and Ambariyanto. (2012). Characterization and quality of semi refined carrageenan products from different coastal waters based on Fourier transform infrared technique. *Journal of Coastal Development*, 16(1): 25-31.
3. Adam, F., Hamdan, M. A., Hana, S., Bakar, A., Yusoff, M. and Jose, R. (2020). Molecular recognition of isovanillin crosslinked carrageenan biocomposite for drug delivery application for drug delivery application. *Chemical Engineering Communications*, 208(5): 741-752.
4. Hamdan, M. A., Mohd Amin, K. N., Jose, R., Martin, D. and Adam, F. (2021). Tuning mechanical properties of seaweeds for hard capsules: A step forward for a sustainable drug delivery medium. *Food Hydrocolloids for Health*, 1(8): 100023.
5. Wan Yahaya, W. A., Mohd Azman, N. A., M. Krishnnan, P., Adam, F. and Almajano, M. P. (2023). Thermo-mechanical and antioxidant properties of eugenol-loaded carrageenan-cellulose nanofiber films for sustainable packaging applications. *Journal of Applied Polymer Science*: e54943.

6. Adam, F., Jamaludin, J., Abu Bakar, S. H., Abdul Rasid, R. and Hassan, Z. (2020). Evaluation of hard capsule application from seaweed: Gum Arabic-kappa carrageenan biocomposite films. *Cogent Engineering*, 7(1): 1765682.
7. Jamaludin, J., Adam, F. and Abdul Rasid, Z. H. (2017). Thermal studies on Arabic Gum - carrageenan polysaccharides film. *Chemical Engineering Research Bulletin*, 19: 80-86.
8. Ramli, N. A., Adam, F., Mohd Amin, K. N., Nor, A. M. and Ries, M. E. (2023). Evaluation of mechanical and thermal properties of carrageenan/hydroxypropyl methyl cellulose hard capsule. *Canadian Journal of Chemical Engineering*, 101: 1219-1234.
9. Ramli, N. A., Adam, F., Mohd Amin, K. N., Abu Bakar, N. F. and Ries, M. E. (2022). Mechanical and thermal evaluation of carrageenan/hydroxypropyl methyl cellulose biocomposite incorporated with modified starch corroborated by molecular interaction recognition. *ACS Applied Polymer Materials*, 5(1): 182-192.
10. Mat Yasin, N. H., Othman, N. A. and Adam, F. (2022). Evaluation of the properties on carrageenan bio-films with chlorella vulgaris blending. *Chemical Engineering Communications*, 2022: 1-15.
11. Wei, L., Zhang, W., Yang, J., Pan, Y., Chen, H. and Zhang, Z. (2023). The application of deep eutectic solvents systems based on choline chloride in the preparation of biodegradable food packaging films. *Trends in Food Science and Technology*, 139 (2): 104124.
12. Chen, J., Li, Y., Wang, X. and Liu, W. (2019). Application of deep eutectic solvents in food analysis: A review. *Molecules*, 24: 1-12.
13. Sirviö, J. A., Visanko, M., Ukkola, J. and Liimatainen, H. (2018). Effect of plasticizers on the mechanical and thermomechanical properties of cellulose-based biocomposite films. *Industrial Crops & Products*, 122: 513-521.
14. Mbous, Y. P., Hayyan, M., Hayyan, A., Wong, W. F., Hashim, M. A. and Looi, C. Y. (2017). Applications of deep eutectic solvents in biotechnology and bioengineering - promises and challenges. *Biotechnology Advances*, 35 (2): 105-134.
15. Hong, S., Yuan, Y., Li, P., Zhang, K., Lian, H. and Liimatainen, H. (2020). Enhancement of the nanofibrillation of birch cellulose pretreated with natural deep eutectic solvent. *Industrial Crops and Products*, 154(5): 112677.
16. Okwuwa, C. C., Adam, F., Said, F. M. and Ries, M. E. (2023). Cellulose dissolution for edible biocomposites in deep eutectic solvents: A review. *Journal of Cleaner Production*: 139166.
17. Wei, X., Lin, T., Du, H., Wang, L. and Yin, X. (2022). Effect of a trace amount of deep eutectic solvents on the structure and optical properties of cellulose nanocrystal films. *Cellulose*, 29(9): 5235-5249.
18. Li, C., Zheng, C., Huang, H., Su, H. and Huang, C. (2023). Preparation and plasticizing mechanism of deep eutectic solvent/lignin plasticized chitosan films. *International Journal of Biological Macromolecules*, 240 (2): 124473.
19. Wu, T., Dai, R., Shan, Z., Chen, H., Woo, M. W. and Yi, J. (2022). High efficient crosslinking of gelatin and preparation of its excellent flexible composite film using deep eutectic solvent. *Process Biochemistry*, 118 (1): 32-40.
20. Yu, J., Liu, X., Xu, S., Shao, P., Li, J., Chen, Z. and Renard, C. M. G. C. (2023). Advances in green solvents for production of polysaccharide-based packaging films: insights of ionic liquids and deep eutectic solvents. *Comprehensive Reviews in Food Science and Food Safety*, 22(2): 1030-1057.
21. Zdanowicz, M., Wilpiszewska, K. and Spychaj, T. (2018). Deep eutectic solvents for polysaccharides processing. a review. *Carbohydrate Polymers*, 200 (7): 361-380.
22. González-Rivera, J., Mero, A., Husanu, E., Mezzetta, A., Ferrari, C., D'Andrea, F. and Guazzelli, L. (2021). Combining acid-based deep eutectic solvents and microwave irradiation for improved chestnut shell waste valorization. *Green Chemistry*, 23(24): 10101-10115.
23. Thi, S. and Lee, K. M. (2019). Comparison of deep eutectic solvents (DES) on pretreatment of oil palm empty fruit bunch (OPEFB): Cellulose digestibility,

structural and morphology changes. *Bioresource Technology*, 282(3): 525-529.

24. Zhang, H., Lang, J., Lan, P., Yang, H., Lu, J. and Wang, Z. (2020). Study on the dissolution mechanism of cellulose by ChCl-based deep eutectic solvents. *Materials*, 13 (2): 1-12.
25. Mohd Amin, K. N., Annamalai, P. K. and Martin, D. (2017). Cellulose nanocrystals with enhanced thermal stability reinforced thermoplastic polyurethane. *Malaysian Journal of Analytical Sciences*, 21(3): 754-761.
26. Ramli, N. A., Amira Kamaluddin, N. N. and Adam, F. (2022). Mechanical, structural and physical properties of carrageenan-gum Arabic biocomposite film for hard capsule application. *Solid State Phenomena*, 340: 11-18.
27. Hamdan, M. A., Ramli, N. A., Othman, N. A., Mohd Amin, K. N. and Adam, F. (2021). Characterization and property investigation of microcrystalline cellulose (MCC) and carboxymethyl cellulose (CMC) filler on the carrageenan-based biocomposite film. *Materials Today: Proceedings*, 42: 56-62.
28. Adam, F., Othman, N. A., Yasin, N. H. M., Cheng, C. K. and Azman, N. A. M. (2022). Evaluation of reinforced and green bioplastic from carrageenan seaweed with nanocellulose. *Fibers and Polymers*, 23(10): 2885-2896.
29. Hamdan, M. A., Adam, F. and Mohd Amin, K. N. (2018). Investigation of mixing time on carrageenan-cellulose nanocrystals (CNC) hard capsule for drug delivery carrier. *International Journal of Innovative Science and Research Technology*, 3(1): 457-461.
30. Othman, N. A., Adam, F. and Mat Yasin, N. H. (2020). Reinforced bioplastic film at different microcrystalline cellulose concentration. *Materials Today: Proceedings*, 41: 77-82.
31. Jakubowska, E., Gierszewska, M., Nowaczyk, J. and Olewnik-Kruszkowska, E. (2021). The role of a deep eutectic solvent in changes of physicochemical and antioxidative properties of chitosan-based films. *Carbohydrate Polymers*, 255 (10): 117527.
32. Delgado-Mellado, N., Larriba, M., Navarro, P., Rigual, V., Ayuso, M., García, J. and Rodríguez, F. (2018). Thermal stability of choline chloride deep eutectic solvents by TGA/FTIR-ATR analysis. *Journal of Molecular Liquids*, 260: 37-43.
33. Jakubowska, E., Gierszewska, M., Nowaczyk, J. and Olewnik-Kruszkowska, E. (2020). Physicochemical and storage properties of chitosan-based films plasticized with deep eutectic solvent. *Food Hydrocolloids*, 108 (May): 106007.
34. Vorobiov, V. K., Sokolova, M. P., Bobrova, N. V., Elokhovsky, V. Y. and Smirnov, M. A. (2022). Rheological properties and 3D-printability of cellulose nanocrystals/deep eutectic solvent electroactive ion gels. *Carbohydrate Polymers*, 290: 119475.
35. Sun, L., Han, J., Tang, C., Wu, J., Fang, S., Li, Y. and Wang, Y. (2022). Choline chloride-based deep eutectic solvent system as a pretreatment for microcrystalline cellulose. *Cellulose*, 29(15): 8133-8150.
36. Hii, S. L., Lim, J. Y., Ong, W. T. and Wong, C. L. (2016). Agar from Malaysian red seaweed as potential material for synthesis of bioplastic film. *Journal of Engineering Science and Technology*, 11: 1-15.
37. Ghozali, M., Meliana, Y., Fatriasari, W., Antov, P. and Chalid, M. (2023). Preparation and characterization of thermoplastic starch from sugar palm (*Arenga pinnata*) by extrusion method. *Journal of Renewable Materials*, 11(4): 1963-1976.
38. Zhao, P., Wang, J., Yan, X., Cai, Z., Fu, L., Gu, Q. and Fu, Y. (2022). Functional chitosan/zein films with *Rosa Roxburghii Tratt* leaves extracts prepared by natural deep eutectic solvents. *Food Packaging and Shelf Life*, 34: 101001.
39. Smith, A. M., Ingham, A., Grover, L. and Perrie, Y. (2010). Polymer film formulations for the preparation of enteric pharmaceutical capsules. *Journal of Pharmacy and Pharmacology*, 62: 1-6.
40. Wang, S., Li, Z., Wang, H., Yuan, C., Liu, K., Yuan, M. and Wang, Y. (2022). Study on the structure and properties of choline chloride toughened polylactide composites. *Polymer Bulletin*, 80(8): 9237-9252.

Malaysian Journal of Analytical Sciences (MJAS)
Published by Malaysian Analytical Sciences Society

BUTTERFLY PEA FLOWER-INFUSED QUINOA STARCH FILM AS A pH INDICATOR FOR SHELLFISH FRESHNESS ASSESSMENT

(Filem Kanji Kuinoa yang Diserapkan dengan Bunga Telang sebagai pH Indikator untuk Penilaian Kesegaran Kerang-Kerangan)

Siti Nur Syahirah Shaikh Ahmad[1], Nur Nabilah Hasanah[1], and Mohammad Rashedi Ismail-Fitry[1,2*]

[1]*Department of Food Technology,*
Faculty of Food Science and Technology,
Universiti Putra Malaysia, 43400 UPM Serdang, Selangor, Malaysia
[2]*Halal Products Research Institute,*
Universiti Putra Malaysia, 43400 UPM Serdang, Selangor, Malaysia

[*]*Corresponding author:* ismailfitry@upm.edu.my

Received: 15 September 2023; Accepted: 24 December 2023; Published: 28 February 2024

Abstract

The pH indicator film has been utilised in food packaging to guarantee quality and safety as well as to track the freshness of perishable food in real-time. However, previous studies have concentrated on synthetic dyes, so this study investigated the use of butterfly pea flower (BPF) which contains anthocyanin, a natural pigment that is sensitive to a wide pH range. Quinoa starch (QS) contains 10-21% amylose with a small starch granule size of around 1 µm that allows for easier dispersion, making it a promising material to produce pH indicator films. BPF extract was incorporated into QS matrix films as a pH indicator to monitor the freshness of different types of shellfish (blood cockles and short-necked clams) stored at 4°C. The quinoa starch-fish gelatine-butterfly pea flower extract (QS/F-BPF) films were developed with different concentrations of BPF (5% and 10%), and then their characteristics including physical appearance, colour, thickness, water vapour permeability (WVP), moisture content, and colour responses were evaluated at different pH values (pH 1-12). The addition of different concentrations of BPF to the quinoa-gelatine-based film did not significantly affect the thickness, moisture content, and WVP. Meanwhile, the micrograph of the films showed good surface morphology. The colour and pH of the QS/F-BPF film were examined every two days for six days of storage of shellfish at 4°C, with the colour changing from blue to green with increasing pH on day 6, indicating spoilage. In conclusion, the QS/F-BPF pH indicator film is effective for monitoring the freshness of different types of shellfish stored in chiller conditions.

Keywords: butterfly pea flower, quinoa starch, pH indicator, anthocyanin, shellfish

Abstrak

Filem penunjuk pH telah digunakan dalam pembungkusan makanan untuk menjamin kualiti dan keselamatan serta untuk mengesan kesegaran makanan mudah rosak dalam masa nyata. Walaubagaimanapun, kajian lepas tertumpu kepada pewarna sintetik, jadi kajian ini menyiasat penggunaan bunga telang (BPF) yang mengandungi antosianin, pigmen semulajadi yang sensitif kepada julat pH yang luas. Kanji kuinoa (QS) mengandungi 10-21% amilosa dengan saiz butiran kanji kecil sekitar 1 µm yang membolehkan penyebaran lebih mudah, menjadikannya bahan yang berpotensi untuk menghasilkan filem penunjuk pH. Ekstrak BPF telah

dimasukkan ke dalam matriks filem QS sebagai penunjuk pH untuk memantau kesegaran pelbagai jenis kerrang-kerangan (kerang dan lala kepah) yang disimpan pada suhu 4°C. Filem kanji kuinoa-gelatin ikan-ekstrak bunga telang (QS/F-BPF) telah dihasilkan dengan kepekatan BPF yang berbeza (5% dan 10%), dan kemudian ciri-cirinya termasuk rupa fizikal, warna, ketebalan, kebolehtelapan wap air (WVP), kandungan lembapan dan tindak balas warna dinilai pada nilai pH yang berbeza (pH 1-12). Penambahan kepekatan BPF yang berbeza kepada filem berasaskan kuinoa-gelatin tidak menjejaskan ketebalan, kandungan lembapan dan WVP dengan ketara. Sementara itu, mikrograf filem menunjukkan morfologi permukaan yang baik. Warna dan pH filem QS/F-BPF diperiksa setiap dua hari selama enam hari penyimpanan kerrang-kerangan pada suhu 4°C, dengan warna berubah daripada biru ke hijau dengan peningkatan pH pada hari ke-6, menunjukkan kerosakan. Kesimpulannya, filem penunjuk pH QS/F-BPF berkesan untuk memantau kesegaran pelbagai jenis kerrang-kerangan yang disimpan dalam keadaan suhu dingin.

Kata kunci: bunga telang, kanji kuinoa, pH indikator, antosianin, kerang-kerangan

Introduction

Food spoilage is the deterioration of food caused by microbial and biochemical spoilage, and this will lead to changes in food pH [1]. Food spoilage can be detected through smell, touch or sight and is easily detected on perishable foods such as raw chicken, beef, and seafood products. Thus, to ensure the food is safe for human consumption, intelligent packaging made from polymer immobilized with active compounds such as anthocyanin can help identify the changes in food pH through a colour response due to reactions between the anthocyanin and volatile amines produced by bacteria and the enzymes [2].

Anthocyanins are coloured polar pigments that belong to the phenolic group [3]. Anthocyanins have a colour-sensitive characteristic after being applied to a wide pH range. The changes in different colours occur due to the anthocyanins' chemical structure change along with the different pH values. Thus, Anthocyanin is a natural colour pigment that can act as an environment-friendly pH indicator [4]. *Clitoria ternatea* or butterfly pea is known as a perennial herbaceous plant from the Fabaceae family [5]. The butterfly pea flower is well known for its stability and application as a natural food colourant as well as an antioxidant.

Recently, several studies used various sources of anthocyanins and biodegradable polymers to form the solid matrix pH film including butterfly pea with sago (Metroxylon sagu) [6], blackberry pulp with arrowroot starch [7] and mulberry with k-carrageenan [8]. Anthocyanin and starch combined create a smooth and homogeneous surface with an intermolecular hydrogen bond that extends the wavelength of the biopolymer [9]. In addition, the primary biopolymers used in the creation of biodegradable films are proteins and polysaccharides. Carboxymethyl cellulose, starch, and chitosan are the polysaccharides most frequently used for food-based biodegradable films [10]. Proteins have a higher gas barrier and mechanical properties like fish gelatine. Meanwhile, polysaccharides such as quinoa starch can enhance the functionality of films [11].

Quinoa is a flowering plant that is grown as a crop primarily for its edible seeds which are rich in protein, dietary fibre, B vitamins and dietary minerals in higher amounts than many other grains. Most of the dry matter in quinoa grains which is up to 70% is made up of starch [12]. Araujo-Farro et al. [13] reported that quinoa starch contains about 10-21% amylose with a small starch granule size of around 1µm that allows for easier dispersion which is a promising material to produce pH films. To immobilise the natural dyes from butterfly pea flower extract, a solid matrix made from natural and biodegradable polymers, which is quinoa starch, was used in this research as it has better mechanical properties and barrier properties compared to corn and amaranth starch [12]. Although there were many studies on butterfly pea extract with other starch, quinoa starch has not been used as a pH film indicator. Thus, it is the main interest in researching BPF extract incorporated with quinoa starch as a solid matrix of pH indicator films.

Shellfish is a marine life that has a shell and can be categorised as crustaceans, molluscs or echinoderms. Molluscs are divided into three categories, which are bivalves such as cockle, clam, mussel, oyster or scallop, univalves such as abalone, conch or snail and

cephalopods such as octopus or squid. Shellfish that completely seal their shells can be kept for up to seven days except for the storage life of mussels is three to four days [14]. Perishable foods such as shellfish can easily deteriorate and cause biochemical degradation, enzymatic activities, and microbial growth, which will affect the quality characteristics. By developing intelligent film for packaging, where the colour changes from blue to green colour that indicating the spoilage (volatile nitrogenous) of shellfish, the observation of shellfish freshness can be done just using the naked eye in real-time. To the authors' knowledge, limited studies were found to observe the freshness of different types of shellfish using pH indicator films, specifically, films made up of quinoa starch. Therefore, the main objectives of this study were 1) to develop a pH indicator film by incorporating different concentrations of BPF extract into the quinoa starch matrix and determine its physicochemical properties and 2) to evaluate the potential of the developed film for monitoring the freshness and quality characteristics of blood cockles (*Tegillarca granos*a) and short-necked clams *(Paphia undulata*) during storage at 4 °C.

Materials and Methods

Materials

The butterfly pea flower was collected from a local area in Negeri Sembilan. Quinoa flour and fish gelatine were purchased from a bakery supplier in Bangi, Selangor. The blood cockles and short-necked clams were purchased from the Seri Kembangan wet market in Selangor, Malaysia.

Extraction of anthocyanin from butterfly pea flower

The extraction was carried out through ultrasound–assisted extraction of fresh petals. Butterfly pea flower petals were separated from the pods and leaves prior to immersion in 50% ethanol as solvent. A water bath was used to regulate the temperature and was positioned beneath the extraction setup. The solvent containing butterfly pea flowers was submerged completely with the ultrasonic probe and sonicated for 30 mins at 40 °C with 160W [15]. The extracted solution was then gone through a rotary evaporator (Eyela 1L Rotary Evaporator with Water/Oil Bath, N-1001V-WD, China) to remove solvent and will undergo lyophilized for 48 h. Then, the freeze-dried BPF powder was wrapped with aluminium foil and stored in the freezer for further analysis.

Colour responses of anthocyanin in BPF extract to pH change

The colour changes were carried out by adding 0.01g of freeze-dried butterfly pea flower extract to 4 mL of distilled water. The buffer solutions containing different pH of 1, 2, 3, 4, 5, 6, 7, 8, 9, 10, 11, and 12 were prepared with an aqueous solution of 0.1 M HCl and 0.1 M NaOH and distilled water, then checked by a digital pH meter. The BPF extract (1 mL) was mixed in buffer solution (4 mL) ranging from pH values of 1.0 to 12.0 and the colour changes were photographed using a digital camera [4].

Development of quinoa starch films by immobilizing the anthocyanin pigment

The quinoa starch films were developed through solution casting with slight modification [4]. Solution with 100 mL of an aqueous dispersion containing 2.5g of quinoa starch (Q), and 2.5g of fish gelatine was prepared. Then, 30% glycerol was added as the plasticiser on a starch-dry basis. The solution was mixed well using a magnetic stirrer (MS-H280-Pro, DLAB Scientific Inc, Malaysia) which was then heated to 90 °C for 1 hour. Following that, the BPF extract amount (5% and 10% w/w) that corresponded to the weight of starch was added after the solution cooled down to at least 50 °C. The control film (QF) was made without adding BPF extract. The film-forming solution was immediately poured into a petri plate and film hydrogels were formed. Then, the hydrogels were dried to film at room temperature under a fan for 12 hours. After that, the film was peeled from the Petri plate and dried quinoa starch films were preserved in controlled conditions for further use. The films were labelled as QF, Q/F-BPF 5% and Q/F-BPF 10%.

Appearance and colour of film

The colour of the films was measured by a colourimeter (Chroma Meter CR-410, Japan) with L* (light/dark), a* (red/green), and b* (yellow/blue) values in triplicate and the average values were taken [4]. The total colour

difference (ΔE) of the films was calculated according to the following equation (1):

$$\Delta E = \sqrt{(L* - L)^2 + (a* - a)^2 + (b* - b)^2} \quad (1)$$

Where L*, a* and b* were the colour parameters of the BPF incorporated with quinoa starch films while L, a and b were the colour indices of the control film (QF).

Film thickness

The thickness of the films was determined by a digital micrometre (C112XBS, Mitutoyo, Japan) by randomly selecting five different positions on each film with a precision of 0.001 mm [4].

Moisture content

The moisture content of the film was determined using a moisture analyser (SHS AND MX-50, Japan) until it reached constant weight. The analyses were performed in triplicate and the results were recorded.

Water vapour permeability (WVP)

The WVP for BPF incorporated with composite QF films was performed by cutting the films into (7 cm x 7 cm) and then mounted on the top of the 50 ml crucible that contains 6 ml distilled water. The initial weight was recorded prior to being in a desiccator with 55% RH at 25°C. Then, the crucible weight was measured and recorded at 1-hour intervals for 8 hours [16]. WVP was calculated according to the following equation (2):

$$Water\ vapour\ permeability = \frac{W \times X}{t \times A \times \Delta P} \quad (2)$$

Where W is the test tube weight (g), X is the film thickness (m), t is the time for the gain in test tube weight, A is the area of film sample for permeation (m2) and ΔP is the water vapour pressure difference between the two sides of the film (Pa).

pH sensitivity

The films were cut into (2 cm x 2 cm) and then immersed in 9 ml of buffer solutions consisting of different pH values ranging from 1.0–12.0 for around 5 min. The colour changes of the films were photographed with a white background [4, 16].

Microstructural characterization of the film

The morphology of the QF composite films was observed through a Scanning Electron Microscope (SEM) at room temperature. The films were cut into (13 mm x 13 mm), then placed on an aluminium base and covered with a gold layer then observed for the upper surface and the cross-section of films operated at 10kV [7].

Application of quinoa starch films on observing shellfish freshness

The pH films were cut into a square shape (1 cm × 1 cm) and then fixed on the inner lid of each polypropylene container's headspace containing different types of shellfish (cockles and clams). The container was stored in a chiller at 4 °C for 2 to 6 days. Six samples were taken randomly for analysis every 2 days. The changes in the colour of pH indicator films were measured by a hand-held colourimeter (Chroma Meter CR-410, Konica Minolta Inc., Tokyo, Japan) and recorded for triplicate until the end of storage [4].

Determination of pH on shellfish sample

The pH values of the ground cockles and clam samples were measured by homogenizing the sample in distilled water and determined with a pH meter (Eutech pH 700, Thermo Fisher Inc., USA). The pH values of the samples were observed on days 0, 2, 4 and 6.

Statistical analysis

The results obtained from the samples were reported using one-way analysis of variance (ANOVA) from Minitab version 19.1.1.0 and reported by the average values ± standard deviation. The significance of the values was defined at $p < 0.05$.

Results and Discussion

Colour change of butterfly pea flower extract and film

The BPF extract displayed various colour changes after exposure to a wide pH range (Figure 1), turning to pinkish-red colour in a buffer with a pH of 1 and 2 or a strong acid, then to purple or purplish-blue at pH 3 until pH 6 which is slightly acidic and displayed in its original blue colour at natural pH 7. The colour of the BPF extract turned bluish-green at pH 8, greenish at pH 9 and

deep green at pH 10 until pH 12. These colour changes were similar to the previous studies by Hidayati et al. [17] and Hashim et al. [18].

Anthocyanin colour changes are influenced by increasing pH from acidic to alkaline conditions [2] and involve broad values (pH 1.0 to 12.0) with four different stages (flavylium cation, quinoidal base, carbinol pseudobase, and chalcone). Anthocyanins extracted from BPF consist of glycosides which contain flavylium cations that produce the red colour in acidic pH due to the formation of a double bond [19]. The red colour fades at higher pH due to the hydrolysis of the flavylium cation [20], with a slightly higher pH causing the dominance of carbinol, a purplish colour that was perceptible at pH 3-5. At neutral pH, carbinol does not provide any colour with the high abundance of polyacylated anthocyanins being responsible for the pigment's stable blue colour [21]. As the pH increases (pH >8), the colour changes from green to yellow because of chalcone formation [2]. Taken together, BPF is a promising anthocyanin pigment that can be used to develop pH indicator films.

Figure 1. Colour response of BPF extracted in different pH buffer solutions (pH 1.0-12.0)

Figure 2. Colour response of Q/F-BPF 10% films in different pH buffer solutions (pH 1.0-12.0)

Figure 2 shows that the visible colour of the Q/F-BPF films changed due to the response to different pH and were slightly leached after immersing for 5 min in buffer solution (pH 1.0−12.0). The colour gradually changed from red (pH 1) to pink (pH 2) to violet (pH 3) to purple (pH 4−5) to deep blue (pH 6) to original blue (pH 7) to greenish-blue (pH 8) to greenish (pH 9) and darken green (pH 10−12). A previous study reported similar colour changes from pink to yellow of starch BPF films after immersion in pH 1−14 which indicates that the films have a prominent colour response to pH [4]. The response of the pH indicator films is practical and effective for their application in determining the freshness of food products. In addition, the range (pH 1.0−12.0) in this study was sufficient as the colour changing of the film is usually from neutral to acidic or alkaline involving small shifts of pH values when the food deteriorates.

Thickness of Films

Table 1 presents the thickness of the films showing no significant ($p < 0.05$) difference between different concentrations of anthocyanin. The anthocyanins are evenly distributed throughout the solid mass of the film

matrix due to abundant OH groups in BPF, starch and fish gelatine. This mixture of anthocyanin and starch can strongly bond like a bridge with a protein matrix from gelatine through intermolecular interactions [22].

Table 1. Physical properties of the composite films.

Films	Appearance	Colour				Thickness (mm)	Moisture Content (%)	WVP (x 10^{-10} g/m.Pas)
		L^*	a^*	b^*	ΔE			
QF (control)	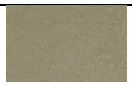	71.01 ± 1.46[a]	1.52 ± 0.15[a]	6.22 ± 0.18[a]	0	0.23 ± 0.023[a]	18.74 ± 5.40[a]	1.40 ± 0.00[a]
Q/F-BPF 5%		33.80 ± 5.83[b]	15.71 ± 0.70[b]	-29.36 ± 5.93[b]	53.40	0.23 ± 0.02[a]	14.22 ± 0.91[a]	1.41 ± 0.00[a]
Q/F-BPF 10%		29.06 ± 0.76[b]	18.51 ± 0.84[c]	-28.39 ± 0.41[b]	56.98	0.24 ± 0.01[a]	16.25 ± 2.17[a]	1.64 ± 0.00[a]

Note: All values are mean ± standard deviation of three replicates. Means that do not share the same letter are significantly different ($p < 0.05$) in the same column.

Film moisture content

Moisture content is an important factor for food packaging material because high moisture is likely to encourage microbial growth on the surface of packaged foods [23]. The moisture content of QF and QF composite indicator films are listed in Table 1 showing no significant difference in moisture content because gelatine is highly hydrophilic and the interaction between the hydrophilic BPF anthocyanin results in more polar groups which can absorb moisture from the surroundings. However, the control film exhibits a slightly high moisture content possibly because the interaction between the hydroxyl group of starch and anthocyanins present in BPF could lower the number of free hydroxyl groups of starch to integrate with moisture during the drying process [24].

Film water vapour permeability

WVP is a crucial measure of application performance and indicates the barrier property which reflects the ability to modulate the flow of moisture [25]. The WVP values are tabulated in Table 1 showing no significant ($p < 0.05$) differences between films. However, the composite film with BPF anthocyanin shows a slightly higher increase than the control film, possibly due to the good solubility of BPF anthocyanin extract. Q/F-BPF 10% had a slightly increased WVP value of 1.64 ×10-10 g/m.Pa.s. because it has a higher concentration of BPF anthocyanin and anthocyanin helped in the transportation of water vapour due to its hydrophilic nature [26]. Therefore, it can be concluded that the quinoa starch and fish gelatine immobilised with BPF had a greater impact on the film WVP

Colour appearance of films

Colour is a crucial parameter for developing pH film indicators. Moreover, colour illustrates the different appearance of the control film and the films immobilised with BPF as shown in Table 1. The QF film was transparent and colourless whereas Q/F-BPF films were opaque and dark blue with the increased BPF concentration. The L* (lightness) of the films was significantly ($p < 0.05$) decreased after immobilised with BPF in the starch matrix. This could be due to the white properties of quinoa starch without any anthocyanin colour. The a* (redness) value significantly ($p < 0.05$) increased from 1.52 to 18.51 while the b* (yellowness) value significantly ($p < 0.05$) decreased along with the increase of BPF concentration. The results indicated that the colour tends to be redder and bluer on Q/F-BPF films.

The colour difference (ΔE) of the films presented in Table 1 increases with the increase in BPF concentration. When the total colour difference (ΔE) was higher than 3, the colour changes are visible to the naked eye [4]. According to Table 2, the (ΔE) values for Q/F-BPF films were above 3 where the lowest was 53.40 and the highest was 56.98, indicating that the colour portrayed by each Q/F-BPF film was visually

discernible. A study by Husin et al. [27] distinguished significant changes in L*, a* and b* of delphinidin-based colour-indicator films coalesced with butterfly anthocyanin. Therefore, these results indicate that Q/F-BPF films are potential indicator films and that the colour changes are visible to the naked eye.

Film microstructure

Figure 3 indicates the surface microstructure as well as the cross-section of QF and Q/F-BPF films. The microstructures are crucial to determining the effect of BPF on the surface and cross-section of the starch gelatine matrix. The QF films exhibited smooth and homogeneous surfaces which demonstrate good compatibility as well as dispersion. The two polymers are very compatible with hydrogen bonding between the carboxyl groups (COO) of the protein and the -OH groups of the polysaccharide, especially when used in the same ratio [28].

The Q/F-BPF film surface was a little rough with a homogeneous and dense structure. Starch and BPF significantly interact, and the anthocyanin extract was thoroughly mixed. The development of hydrogen bonds with the starch matrix is facilitated by the addition of phenolic compounds like anthocyanin [4]. According to Kim et al. [28], although they tended to aggregate in some areas of the film, overall, they were evenly dispersed throughout the polymer matrix. The cross-section specifies the compact and dense surface with the dispersion of the polymers.

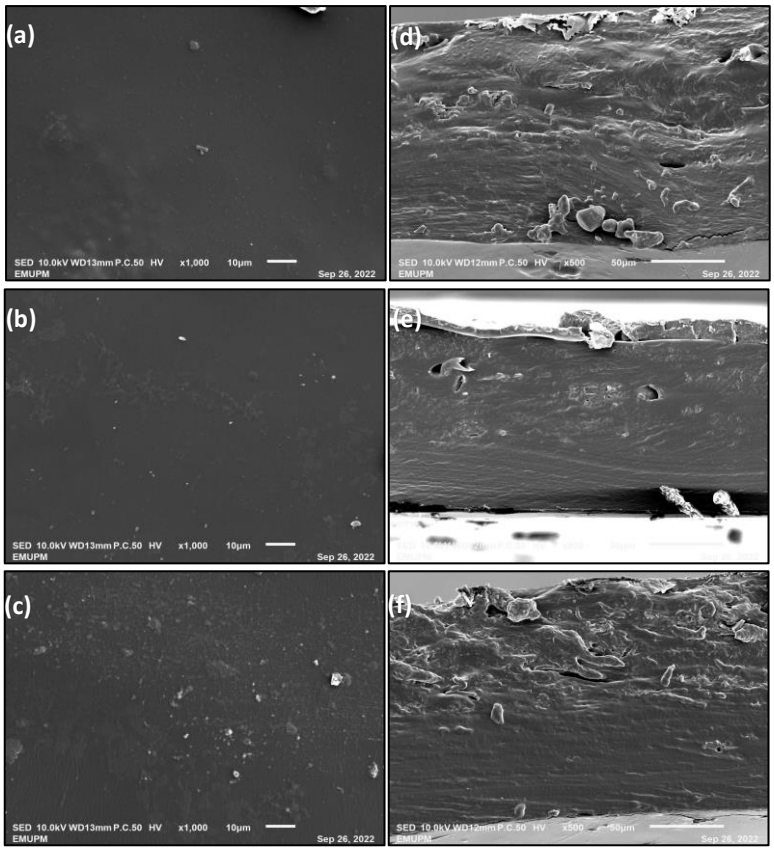

Figure 3. SEM images of the surface of the QF (A), Q/F-BPF 5% (B), and Q/F-BPF 10% (C) indicators and cross sections of the QF (D), Q/F-BPF 5% (E), and Q/F-BP 10% (F) indicators.

Application of Q/F-BPF films to monitor shellfish freshness

The spoilage of seafood products is initially caused by microbes as well as biochemical amine reactions which lead to freshness decline and the release of volatile nitrogenous compounds. Ammonia, trimethylamine, and dimethylamine are volatile foul-smelling gases released by microbial activity and enzyme degradation of proteins in seafood [25]. The pH rises when these volatile nitrogenous compounds accumulate in the headspace of the air-tight containers during extended storage. Thus, pH indicator films are used to detect the shellfish freshness. The Q/F-BPF films were implemented to observe the shellfish freshness under chiller storage (4 °C for 6 days).

The results showed the Q/F-BPF film colour changes indicated shellfish spoilage, with the odour becoming obvious towards the end of the storage. The initial colour of the Q/F-BFE 5% and Q/F-BPF 10% indicator was used as a reference for ΔE calculation and changes in ΔE during storage are presented in Table 3. The ΔE value after 2 days of storage on Q/F-BPF 5% was 5.57 for blood cockles and 7.79 for short-necked clams, indicating an increase in spoilage parameters. The ΔE value of the Q/F-BPF 5% indicator sharply increased to 24.33 for blood cockles and 16.70 for short-necked clams after 6 days of storage and the indicator colour changed from blue to green. Thus, the colour of the Q/F-BPF 5% indicator changed according to the changes in the quality of blood cockles and short-necked clams. The colour changes of the Q/F-BPF films at the end of the storage were visible to the naked eye when the ΔE was more than 3 [4].

Taken together, Q/F-BPF films showed a significant colour change throughout the 6 days of storage of blood cockles and short-necked clams due to the spoilage and the formation of volatile nitrogenous compounds. A previous study reported that the colour of S-BPF films turned to intense green from pink on the 6th day of shrimp storage [4]. Similarly, the recognisable anthocyanin colour changes during storage showed that the quality of the shrimp had declined [28]. The colour changes were more distinct in the Q/F-BPF 10% film which had a higher concentration of BPF extract. These results depicted that BPF immobilised with quinoa starch and fish gelatine has the potential to monitor shellfish freshness and other food samples.

Table 3. The colour response of Q/F-BPF films at different time intervals (0, 2, 4, 6 days) for shellfish freshness

Day	Films	Colour				Films Appearance
		L^*	a^*	b^*	ΔE	
Blood Cockles Sample						
0	Q/F-BPF 5%	53.90 ± 1.54[a]	3.31 ± 0.39[a]	-6.28 ± 2.49[a]	0	
2		57.60 ± 5.03[a]	3.54 ± 0.34[a]	-10.43 ± 1.23[b]	5.57	
4		62.21 ± 4.36[a]	3.87 ± 0.64[a]	-11.51 ± 1.24[a]	9.84	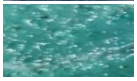
6		65.62 ± 2.32[a]	0.91 ± 2.77[a]	14.90 ± 29.30[a]	24.33	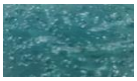
0	Q/F-BPF 10%	55.98 ± 2.96[a]	3.45 ± 0.40[a]	-6.73 ± 1.72[a]	0	
2		64.50 ± 4.64[a]	2.59 ± 0.06[b]	-6.11 ± 0.84[a]	8.59	
4		68.20 ± 4.59[a]	2.63 ± 0.85[a]	-7.86 ± 3.47[a]	12.30	

Day	Films	Colour				Films Appearance
		L^*	a^*	b^*	ΔE	
6		63.20 ± 4.74[a]	0.547 ± 0.61[a]	-3.38 ± 0.21[a]	8.47	
Short-necked Clams Sample						
0	Q/F-BPF 5%	51.94 ± 5.25[a]	3.81 ± 0.55[a]	-8.51 ± 1.46[b]	0	
2		59.44 ± 1.95[a]	3.71 ± 0.19[a]	-10.58 ± 1.58[b]	7.79	
4		66.91 ± 2.26[a]	0.93 ± 1.14[a]	-6.70 ± 1.12[a]	15.35	
6		66.93 ± 2.98[a]	-1.55 ± 2.18[a]	-3.46 ± 0.04[a]	16.70	
0	Q/F-BPF 10%	60.94 ± 2.04[a]	3.07 ± 0.37[a]	-5.41 ± 0.22[a]	0	
2		64.07 ± 3.17[a]	2.95 ± 0.095[b]	-5.66 ± 0.77[a]	3.15	
4		69.73 ± 0.38[a]	2.95 ± 0.09[a]	-5.66 ± 0.77[a]	8.87	
6		66.28 ± 1.84[a]	0.08 ± 0.99[a]	-3.39 ± 0.36[a]	6.44	

Note: All values are mean ± standard deviation of three replicates. Means that do not share the same letter are significantly different ($p < 0.05$) in the same column.

pH as an indicator of shellfish freshness

Table 4 presents a summary of the pH values of blood cockles and short-necked clams. The pH for both shellfish initially was low, 5.8 for blood cockles and 5.9 for short-necked clams, then increased significantly ($p < 0.05$), reaching 8.2 for blood cockles and 8.1 for short-necked clams by day 6. This was due to the accumulation of volatile nitrogenous compounds released by those shellfish [29]. This trend was in line with the significant increase in the pH of mackerel (*Scomber scombrus*) from day 0 to day 15 when stored in a chiller [30]. Hence, the increase in pH of the blood cockles and short-necked clams on day 6 depicted that the freshness and quality of the shellfish declined, and that spoilage had begun.

Table 4. pH value of blood cockles and short-necked clams during storage

Fish Sample	Day	pH
Blood cockles	0	5.83 ± 0.15[d]
	2	6.60 ± 0.10[c]
	4	7.30 ± 0.36[b]
	6	8.22 ± 0.25[a]
Short-necked clams	0	5.97 ± 0.21[d]
	2	6.73 ± 0.21[c]
	4	7.50 ± 0.20[b]
	6	8.20 ± 0.14[a]

Note: All values are mean ± standard deviation of three replicates. Means that do not share the same letter are significantly different ($p < 0.05$) in the same column.

Conclusion

In conclusion, the anthocyanin extract from BPF incorporated into QS solid matrix films produces a good pH film indicator which has good colour intensity, and physical properties, and can be applied to seafood products. The addition of BPF to the quinoa starch and fish gelatine base did not greatly affect the thickness,

moisture content or WVP. The film has good surface morphology with an even dispersion of quinoa starch, fish gelatine, BPF and glycerol. The Q/F-BPF film colour changed from blue to green indicating the spoilage (volatile nitrogenous) of shellfish during storage. The freshness assessment confirmed the shellfish spoilage started on day 1 and corresponded to the colour changes of the Q/F-BPF films on day 6, which were visible to the naked eye. Therefore, Q/F-BPF pH indicator films have promising potential to be used as a pH indicator to monitor shellfish freshness.

Acknowledgement

This study was financially supported by the Malaysian Ministry of Higher Education, grant number FRGS/1/2020/WAB04/UPM/01/3. The authors also thank the Faculty of Food Science and Technology, Universiti Putra Malaysia for the equipment and facilities used for this project.

References

1. Rahim, M. Z. A., Husin, N., Mohd Noor, M. A., Yet, Z. R. and Ismail-Fitry, M. R. (2020). Screening of natural colours from various natural resources as potential reusable visual indicators for monitoring food freshness. *Malaysian Journal of Analytical Sciences*, 24: 288-299.
2. Hasanah, N. N., Mohamad Azman, E., Rozzamri, A., Zainal Abedin, N. H. and Ismail-Fitry, M. R. (2023). A systematic review of butterfly pea flower (*Clitoria ternatea* L.): Extraction and application as a food freshness pH-indicator for polymer-based intelligent packaging. *Polymers*, 15(11): 2541.
3. Khoo, H. E., Azlan, A., Tang, S. T., and Lim, S. M. (2017). Anthocyanidins and anthocyanins: Colored pigments as food, pharmaceutical ingredients, and the potential health benefits. *Food and Nutrition Research*, 61: 1361779.
4. Mary, S. K., Koshy, R. R., Daniel, J., Koshy, J. T., Pothen, L. A., and Thomas, S. (2020). Development of starch based intelligent films by incorporating anthocyanins of butterfly pea flower and TiO_2 and their applicability as freshness sensors for prawns during storage. *RSC Advances*, 10(65): 39822-39830.
5. Oguis, G. K., Gilding, E. K., Jackson, M. A., and Craik, D. J. (2019). Butterfly pea (*Clitoria ternatea*), a cyclotide-bearing plant with applications in agriculture and medicine. *Frontiers in Plant Science*, 10: 645.
6. Ahmad, A. N., Abdullah Lim, S., and Navaranjan, N. (2020). Development of sago (*Metroxylon sagu*) based colorimetric indicator incorporated with butterfly pea (*Clitoria ternatea*) anthocyanin for intelligent food packaging. *Journal of Food Safety*, 40(4): 12807.
7. Nogueira, G. F., Soares, C. T., Cavasini, R., Fakhouri, F. M., and de Oliveira, R. A. (2019). Bioactive films of arrowroot starch and blackberry pulp: Physical, mechanical and barrier properties and stability to pH and sterilization. *Food Chemistry*, 275: 417-425.
8. Liu, Y., Qin, Y., Bai, R., Zhang, X., Yuan, L., and Liu, J. (2019). Preparation of pH-sensitive and antioxidant packaging films based on κ-carrageenan and mulberry polyphenolic extract. *International Journal of Biological Macromolecules*, 134: 993-1001.
9. Erna, K. H., Felicia, W. X. L., Vonnie, J. M., Rovina, K., Yin, K. W., and Nur'Aqilah, M. N. (2022). Synthesis and physicochemical characterization of polymer film-based anthocyanin and starch. *Biosensors*, 12(4): 211.
10. Khan, M. R., and Sadiq, M. B. (2020). Importance of gelatin, nanoparticles, and their interactions in the formulation of biodegradable composite films: A review. *Polymer Bulletin*, 78(7): 4047-4073.
11. Nurdiani, R., Ma'rifah, R. D. A., Busyro, I. K., Jaziri, A. A., Prihanto, A. A., Firdaus, M., Talib, R. A., and Huda, N. (2022). Physical and functional properties of fish gelatin-based film incorporated with mangrove extracts. *PeerJ*, 10: e13062.
12. Li, G. and Zhu, F. (2018). Quinoa starch: Structure, properties, and applications. *Carbohydrate Polymers*, 181: 851-861.
13. Araujo-Farro, P. C., Podadera, G., Sobral, P. J. A., and Menegalli, F. C. (2010). Development of films based on quinoa (*Chenopodium quinoa, Willdenow*) starch. *Carbohydrate Polymers*, 81(4): 839-848.
14. Kontominas, M. G., Badeka, A. V., Kosma, I. S., and Nathanailides, C. I. (2021). Innovative seafood

preservation technologies: Recent developments. *Animals*, 11(1): 92.

15. Salacheep, S., Kasemsiri, P., Pongsa, U., Okhawilai, M., Chindaprasirt, P., and Hiziroglu, S. (2020). Optimization of ultrasound-assisted extraction of anthocyanins and bioactive compounds from butterfly pea petals using Taguchi method and grey relational analysis. *Journal of Food Science and Technology*, 57(10): 3720-3730.
16. Ezati, P. and Rhim, J.W. (2020). pH-responsive pectin-based multifunctional films incorporated with curcumin and sulfur nanoparticles. *Carbohydrate Polymers*, 230: 115638.
17. Hidayati, N. A., Wijaya, M. W., Bintoro, V. P., Mulyani, S. and Pratama, Y. (2021). Development of biodegradable smart packaging from chitosan, polyvinyl alcohol (PVA) and butterfly pea flower's (*Clitoria ternatea L*.) anthocyanin extract. *Food Research*, 5(3): 307-314.
18. Hashim, S. B. H., Elrasheid Tahir, H., Liu, L., Zhang, J., Zhai, X., Ali Mahdi, A., Nureldin Awad, F., Hassan, M. M., Xiaobo, Z., and Jiyong, S. (2022). Intelligent colorimetric pH sensoring packaging films based on sugarcane wax/agar integrated with butterfly pea flower extract for optical tracking of shrimp freshness. *Food Chemistry*, 373: 131514.
19. Kungsuwan, K., Singh, K., Phetkao, S. and Utama-ang, N. (2014). Effects of pH and anthocyanin concentration on color and antioxidant activity of *Clitoria ternatea* extract. *Food and Applied Bioscience Journal*, 2(1): 31-46.
20. Choi, I., Lee, J. Y., Lacroix, M., and Han, J. (2017). Intelligent pH indicator film composed of agar/potato starch and anthocyanin extracts from purple sweet potato. *Food Chemistry*, 218: 122-128.
21. Vidana Gamage, G. C., Lim, Y. Y. and Choo, W. S. (2021). Anthocyanins from *Clitoria ternatea* flower: Biosynthesis, extraction, stability, antioxidant activity, and applications. *Frontiers in Plant Science*, 12: 792303.
22. Koshy, R. R., Reghunadhan, A., Mary, S. K., Pillai, P. S., Joseph, S., and Pothen, L. A. (2022). pH Indicator films fabricated from soy protein isolate modified with chitin nanowhisker and *Clitoria ternate*a flower extract. *Current Research in Food Science*, 5: 743-751.
23. Rawdkuen, S., Faseha, A., Benjakul, S., and Kaewprachu, P. (2020). application of anthocyanin as a color indicator in gelatin films. *Food Bioscience*, 36: 100603.
24. Qin, Y., Liu, Y., Yong, H., Liu, J., Zhang, X. and Liu, J. (2019). Preparation and characterization of active and intelligent packaging films based on cassava starch and anthocyanins from *Lycium Ruthenicum Murr*. *International Journal of Biological Macromolecules*, 134: 80-90.
25. Eze, F. N., Jayeoye, T. J. and Singh, S. (2022). Fabrication of intelligent pH-sensing films with antioxidant potential for monitoring shrimp freshness via the fortification of chitosan matrix with broken riceberry phenolic extract. *Food Chemistry*, 366: 130574.
26. Zhang, K., Huang, T.-S., Yan, H., Hu, X. and Ren, T. (2020). Novel pH-sensitive films based on starch/polyvinyl alcohol and food anthocyanins as a visual indicator of shrimp deterioration. *International Journal of Biological Macromolecules*, 145: 768-776.
27. Husin, D., Rahim, M. Z. A., Noor, M. A. M., Rashedi, I. F. M. and Hassan, N. (2020). Real-time monitoring of food freshness using delphinidin-based visual indicator. *Malaysian Journal of Analytical Sciences*, 24(4): 558-569.
28. Kim, H.-J., Roy, S. and Rhim, J.-W. (2022). Gelatin/agar-based color-indicator film integrated with *Clitoria ternatea* flower anthocyanin and zinc oxide nanoparticles for monitoring freshness of shrimp. *Food Hydrocolloids*, 124: 107294.
29. Bao, Y., Wang, J., Li, C., Li, P., Wang, S. and Lin, Z. (2016). A preliminary study on the antibacterial mechanism of *Tegillarca granosa* hemoglobin by derived peptides and peroxidase activity. *Fish & Shellfish Immunology*, 51: 9-16.
30. Boonsiriwit, A., Lee, M., Kim, M., Inthamat, P., Siripatrawan, U. and Lee, Y. S. (2021). Hydroxypropyl methylcellulose/microcrystalline cellulose biocomposite film incorporated with butterfly pea anthocyanin as a sustainable pH-responsive indicator for intelligent food-packaging applications. *Food Bioscience*, 44: 101392.

Malaysian Journal of Analytical Sciences (MJAS)
Published by Malaysian Analytical Sciences Society

ENCAPSULATION OF A MIXTURE OF NONI (*Morinda citrifolia* L.) FRUIT EXTRACT AND PATCHOULI (*Pogostemon cablin*) OIL WITH MALTODEXTRIN AND ITS ANTIOXIDANT ACTIVITY

Enkapsulasi Campuran Ekstrak Buah Noni (*Morinda Citrifolia* L.) dan Minyak Nilam (*Pogostemon cablin*) Berasaskan Maltodextrin dan Aktiviti Antioksidannya

Ardhianna Salsabilla Puteri, Triana Kusumaningsih*, and Desi Suci Handayani

Department of Chemistry, Faculty of Mathematics and Natural Sciences
Sebelas Maret University, Jl. Ir. Sutami 36A, Surakarta, Central Java, Indonesia 57126

**Corresponding author: triana_kusumaningsih@staff.uns.ac.id*

Received: 13 September 2023; Accepted: 17 December 2023; Published: 28 February 2024

Abstract

Excessive free radical compounds in the human body can cause various dangerous diseases. This can be prevented by consuming antioxidant-rich foods, one of which is noni fruit with its pungent odor and taste that many people dislike. To overcome this issue, noni fruit can be encapsulated. In this study, noni fruit extract was encapsulated with maltodextrin with the addition of patchouli oil. The extraction of noni fruit was done by the maceration method. Research maltodextrin in this study was produced from partial hydrolysis of cassava starch using 0.5% α-amylase enzyme, achieving a Dextrose Equivalent (DE) value below 20. However, as it is insoluble in water, this maltodextrin cannot be used as an encapsulating agent. Therefore, the encapsulation stage was carried out using the freeze-drying method on with commercial maltodextrin as a coating agent, tween 80 as an emulsifier, and noni fruit extract and patchouli oil as the core ingredients in a ratio of 4:1 and 1:1. The highest encapsulation efficiency of 91.35% was achieved in the encapsulation of noni fruit extract without the addition of patchouli oil. Nevertheless, the organoleptic test results showed that patchouli oil positively reduced the unpleasant odor of noni fruit extract. Furthermore, the SEM test results indicated irregular particle shapes and fractures without any pores, while the results of the antioxidant activity test using the DPPH method revealed that the addition of patchouli oil in a ratio of 1:1 made a positive contribution to increasing the antioxidant activity of encapsulated noni extract, with an IC_{50} value of 50.80 µg/mL.

Keywords: antioxidant, encapsulation, maltodextrin, noni, patchouli oil

Abstrak

Sebatian radikal bebas yang berlebihan dalam tubuh manusia boleh menyebabkan berbagai penyakit berbahaya. Ini boleh dicegah dengan pengambilan makanan yang kaya dengan antioksidan, salah satunya ialah buah mengkudu dengan bau dan rasa yang menyengat yang tidak disukai orang ramai. Untuk mengatasi masalah ini, buah mengkudu boleh dikapsulkan. Dalam kajian ini, ekstrak buah mengkudu dikapsulkan dengan maltodekstrin dengan penambahan minyak nilam. Pengekstrakan buah mengkudu dijalankan dengan kaedah maserasi. Maltodekstrin penyelidikan dalam kajian ini dihasilkan daripada hidrolisis separa kanji ubi kayu menggunakan enzim α-amilase 0.5%, mencapai nilai *Dextrose Equivalent* (DE) di bawah 20. Namun, kerana ia tidak larut dalam air, maltodekstrin ini tidak boleh digunakan sebagai agen pengekapsul. Oleh kerana itu, enkapsulasi dijalankan

menggunakan kaedah pengeringan beku dengan maltodekstrin komersial sebagai agen salutan, tween 80 sebagai pengemulsi, dan ekstrak buah mengkudu, dan minyak nilam sebagai bahan teras dalam nisbah 4:1 dan 1:1. Kecekapan enkapsulasi tertinggi iaitu 91.35% dicapai dalam pengkapsulan ekstrak buah mengkudu tanpa penambahan minyak nilam. Namun begitu, keputusan ujian organoleptik menunjukkan bahawa minyak nilam secara positif mengurangkan bau yang tidak menyenangkan daripada ekstrak buah mengkudu. Tambahan pula, keputusan ujian SEM menunjukkan bentuk zarah yang tidak teratur dan patah tanpa sebarang liang, manakala keputusan ujian aktiviti antioksidan menggunakan kaedah DPPH mendedahkan bahawa penambahan minyak nilam dalam nisbah 1:1 memberi sumbangan positif kepada peningkatan aktiviti antioksidan kapsul ekstrak mengkudu, dengan nilai IC_{50} 50.80 µg/mL.

Kata Kunci: antioksidan, enkapsulasi, maltodekstrin, mengkudu, minyak nilam

Introduction

Free radicals are reactive and unstable molecules with one or more unpaired electrons in their outermost orbitals that play a role in oxidative tissue damage and pathological processes in the human body by attacking lipid compounds, proteins, and DNA, thus causing various dangerous diseases such as cancer, cardiovascular diseases, and diabetes mellitus. Therefore, antioxidants are essential for the human body as they can inhibit oxidation through reactions with free radicals to form non-reactive and stable free radicals. One of the antioxidant-rich fruits in Indonesia is noni fruit (*Morinda citrifolia* L.), which is known to contain more than 160 phytoconstituents. One of the antioxidants contained in noni fruit is ascorbic acid, reaching 24-158 mg per 100 grams of noni fruit [1]. This content is higher than that of several other fruits such as tangerine (3.716 mg/100 grams), persimmon (2.878 mg/100 grams), and tamarillo (11.328 mg/100 grams) [2].

However, the caproic acid content in noni fruit produces an unpleasant odor and bitter taste, making people reluctant to consume it. This can be circumvented by encapsulation, a method of coating compounds with certain wall materials to reduce damage to the compounds and improve their characteristics and organoleptic properties [3]. The encapsulating agent used in this study is maltodextrin, which has low viscosity, high solubility, and high binding capacity in forming a microcapsule matrix [3]. Maltodextrin can be produced through enzymatic processes or acid hydrolysis of starch. In Indonesia, one of the extremely abundant sources of starch is cassava. Due to its high starch content, namely around 85%, cassava has the potential to be developed for use in various applications. Further utilization of cassava starch in the industry is expected to increase the economic value of this root vegetable [4]. This study attempts to produce maltodextrin from cassava starch for use in the encapsulation of noni fruit extract.

In this study, encapsulation was performed using the freeze-drying method with the addition of patchouli oil to suppress the unpleasant odor of noni fruit extract and increase the antioxidant activity of the encapsulation results. The use of the freeze-drying method is considered the most suitable for encapsulating compounds that are volatile and sensitive to heat or temperature, such as compounds found in essential oils. When compared with other methods, freeze drying has the advantage of not using high temperatures like other methods so that it can protect sensitive bioactive compounds, the implementation steps are limited compared to other methods and the product can be reshaped quickly and easily. Meanwhile, other methods such as spray drying, extrusion and pan-coating have the disadvantage of removing a lot of material because they use high temperatures during the process and produce a lot of residue [22] This study focuses on changes in the organoleptic properties of noni fruit extract in three different encapsulation variations, especially the decrease in the unpleasant odor and bitter taste of noni fruit extract and the increase in antioxidant activity of the encapsulation results with *freeze drying* method for encapsulation.

Materials and Methods

Materials

Noni (*Morinda cirrifolia* L.) fruit powder, which is the main ingredient in this study, was purchased at Pasar Gede Surakarta, Central Java, Indonesia and macerated

with 96% ethanol solvent (Merck). Commercial patchouli oil was obtained from Happy Green Patchouli Oil e-commerce store. The encapsulation process used Tween 80 and commercial Maltodextrin with DE value of 10-12 purchased from Indoplant e-commerce store. Meanwhile, the alternative maltodextrin in this study was produced from partial hydrolysis of cassava starch and distilled water (Aquadest) with 500 grams of α-amylase enzyme from Micro Bio e-commerce store, D(+)-Glucose anhydrous (Merck), Fehling A or $CuSO_4$ (Merck), Fehling B or KOH and $NaKC_4H_4O_6.4H_2O$ (Merck), n-Hexane (Merck), 200 ppm anhydrous $CaCl_2$ (Merck), 0.1 N Hydrochloric acid or HCl (Merck), 0.1 N Sodium hydroxide or NaOH (Merck), and universal pH paper. Furthermore, the antioxidant testing employed the DPPH method with methanol p.a. (Merck), 2,2-diphenyl-1-picrylhydrazyl or DPPH (Merck), and dimethylsulfoxide ($(CH_3)_2SO$) (Merck).

Instrumentations

This study utilized the following instruments: Scanning Electron Microscope (Jeol JSM-60 SEM), UV-Vis Spectrophotometer (Hitachi UH5300), Particle Size Analyzer (Malvern Zetasizer Nano ZS), GC-MS Spectrophotometer (Shimadzu QP2010S), and Freeze Dryer (Telstar LyoQuest).

Making maltodextrin from cassava starch

Maltodextrin was made based on the literature with several changes to the parameters such as the concentration of the enzyme used. First step is mixing 30% of fine-textured cassava starch in a 200 ppm $CaCl_2$ solution. After that, 0.1 N NaOH was added to the solution to reach pH 7. In the previous method, 0.1% enzyme was used. Meanwhile, in this study, α-amylase enzymes were used at 0.5% of the solution volume. The mixture was heated at 85°C for 120 minutes with a stirring process and cooled rapidly until the temperature dropped to 30 °C. The pH was readjusted to 3-4 by adding 0.1 N HCl. After leaving it at room temperature for 15-30 minutes, 0.1 N NaOH was added to the mixture until the pH became 4.5-6. The maltodextrin obtained was dried in an oven at 50–60 °C for 24 hours [5]. Afterwards, it was crushed and sieved with a 100-mesh sieve to obtain fine maltodextrin. Lastly, an analysis of the Dextrose Equivalent (DE) value and particle size was carried out using Particle Size Analyzer (PSA).

Determination of the physiochemical properties of maltodextrin

The DE value of the maltodextrin was determined by Lane-Eynon Titration based on the SNI 01-2892-1992 standard as a quantitative method of testing reducing sugars. Meanwhile, the solubility of the maltodextrin in water was determined by a solubility test [6], and the results were adjusted to the quality requirements for maltodextrin solubility by the National Standardization Agency of Indonesia (*Badan Standardisasi Nasional*/BSN).

Encapsulation of a mixture of noni fruit extract and patchouli oil

The ratio between encapsulating agent, core ingredients, and Tween 80 in this study is 4:1:1. A total of 30 mL of maltodextrin solution was added to 0.943 mL of Tween 80 then homogenized at a speed of 750 rpm for 15 minutes. Next, comparative modifications were carried out at the stage of adding the core ingredients to determine the effect of the amount of core ingredients on the antioxidant activity and organoleptic properties. Some of these variations are: (1) 100% noni fruit extract without the addition of patchouli oil; (2) 0.8 grams of noni extract and 0.2 grams of patchouli oil in a ratio of 4:1; and (3) 0.5 grams of noni extract and 0.5 grams of patchouli oil in a ratio of 1:1. After that, the mixture was homogenized at a speed of 750-1000 rpm for 30 minutes at room temperature until an emulsion phase was formed. The final stage was drying with a freezer dryer for 3 days. The encapsulation results were then analyzed for yield, organoleptic properties, encapsulation efficiency, microcapsule morphology, and antioxidant activity [7, 8].

Analysis of encapsulation

Changes in the organoleptic properties of noni extract before and after encapsulation with the addition of patchouli oil were determined by carrying out organoleptic tests in the form of observing the taste, color, aroma, texture and overall hedonic test (liking test) which was attended by 15 panelists who had fulfilled the requirements of the Quality Management

Module. Organoleptic Physics (2013). Then, an Encapsulation efficiency analysis was carried out to determine the success of the encapsulation process for noni extract and patchouli oil which was carried out by calculating the percentage of the core ingredients of each noni fruit extract and patchouli oil encapsulated by maltodextrin using the division formula between the difference in total extract used and surface oil content by total extract [10]. The encapsulation results were also analyzed using SEM instruments to compare the morphology of the particles resulting from freeze drying between the encapsulation results without the addition of patchouli oil and with the addition of patchouli oil. Then the particle size was analyzed using PSA to compare the particle size of the maltodextrin before and after encapsulation [14].

Testing of antioxidant activity with the DPPH method

In this study, the positive control was vitamin C, whereas the blank solution was methanol. The concentrations of the test sample solutions were 5, 10, 15, 20, and 25 ppm, prepared by dissolving 100 ppm of test samples in 5 mL of DMSO. Each concentration variation was added to the reagent solution of 0.2 mM DPPH and incubated for 30 minutes in a dark room. The absorbance was then measured using a UV-Vis spectrophotometer at a wavelength of 517 nm [11].

Results and Discussion

Making maltodextrin

Hydrolysis of cassava starch with α-amylase enzyme at a concentration of 0.5% of the solution volume in this study produced maltodextrin with different physical properties from those of commercial cassava starch-based maltodextrin. The differences in the physical properties of the two maltodextrins can be seen in Table 1.

Table 1**.** Physical properties of maltodextrin

Parameter	**Research Maltodextrin**	**Commercial Maltodextrin**
Color	Cream	White
Flavor	No flavor	No flavor
Solubility in water	63%	98.85%
Texture	Rugged and not sticky	Smooth and slightly sticky

According to the National Standardization Agency of Indonesia (BSN), the standard for maltodextrin solubility is in the range of 97-98%. This means that the maltodextrin produced in this study does not meet the specified quality requirement. Maltodextrin's solubility can be affected by its particle size; the larger the particle size, the smaller the surface area, and the longer it takes for water to absorb the starch particles. In other words, if the particle size is smaller, the hydration rate of the flour will increase [12]. Based on the PSA results, the average particle diameters for commercial maltodextrin and research maltodextrin were 214.3 and 415.9 nm, respectively.

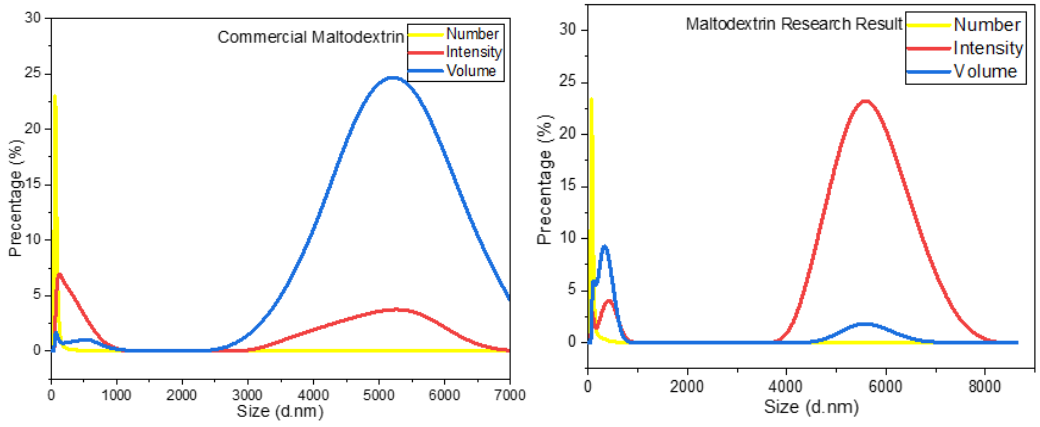

(a) (b)

Figure 1. Graph of particle size distribution in commercial maltodextrin (a) and research maltodextrin (b)

From the PSA results for research maltodextrin (Figure 1b), the highest distribution peak was based on intensity in the particle size range of 5000-6000 nm, signifying that the intensity of photon absorption at these particle sizes is higher than at other particle sizes. Meanwhile, for commercial maltodextrin (Figure 1a), the highest distribution peak was based on volume in the particle size range of 3500-5500 nm, indicating that these particle sizes have a larger total volume than other particle sizes. The presence of larger particles with high intensity can cause the solubility of maltodextrin to decrease. The polydispersity index (Pd index) values of commercial maltodextrin and research maltodextrin were 0.380 and 0.424, respectively. The Pd index value of below 0.5 suggests that the homogeneous dispersion system formed is monodisperse and does not settle. The dispersion results of both maltodextrins are relatively good since these values reflect a fairly narrow particle size distribution and a homogeneous particle size diameter.

Furthermore, based on the analysis results, the DE values of research maltodextrin and commercial maltodextrin were 9.2 and 9.6, respectively. The difference in DE values for the two maltodextrins can be influenced by the concentration of the α-amylase enzyme and the hydrolysis time. With increasing hydrolysis time and α-amylase enzyme concentration, the DE value also increase as more substrates are hydrolyzed over a longer time and at higher enzyme concentrations, thus increasing the numbers of short polymers (monosaccharides, disaccharides, and oligosaccharides) formed in the maltodextrin. Based on the Food and Drug Administration (FDA) standards, maltodextrin has a DE value range of <20 [13]. Hence, the hydrolyzed maltodextrin and commercial maltodextrin in this study have met the FDA standards in terms of their DE values. However, as the maltodextrin produced in this study did not meet the BSN standards for its solubility, it could not be used as encapsulating agent in the encapsulation of noni fruit extract. Therefore, commercial maltodextrin was used as the encapsulating agent in this study.

Compound content of patchouli oil

This study used commercial patchouli oil with the following specifications:

Botanical name : *Pogostemon cablin*
Product Code : 150028
Batch Number : 220408/177366
Appearance : Clear liquid
Color : Yellow-Brown
Smell : Leafy, Earthy, Sweet, and Woody
Production Time : 08 April 2022

Based on its specifications presented in Table 2, the density and color of commercial patchouli oil have met the SNI 06-2385-2006 standards, namely 0.9328-0.9652 g/mL at the same temperature and light yellow to reddish brown.

Table 2**.** Specifications of commercial patchouli oil

Test Item	**Specification**	**Result**
Density (20°C)	0.9328-0.9652	0.9427
Specific Gravity (20°C)	0.9345-0.9669	0.9444
Refractive Index (20°C)	1.4921-1.5225	1.5041
Solubility	Not Soluble in Water	Not Soluble in Water

The results of GC-MS analysis of patchouli oil compounds are displayed in Figure 2 and Table 3.

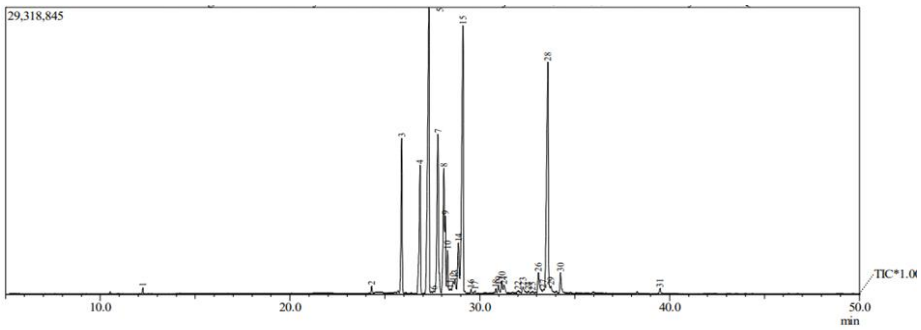

Figure 2. Chromatogram of commercial patchouli oil compounds

Table 3**.** GC-MS analysis of commercial patchouli (*Pogostemon cablin*) oil

RT	Compounds	Area (%)	SI
27.320	Azulene	19.52	92
29.113	delta-Guaiene	16.69	94
33.587	Patchouli Alcohol	16.62	92
27.794	Seychellene	10.03	86
28.104	1H-3a,7-Methanoazulene	7.00	87
25.884	1H-Cyclopropa[a]naphthalene	6.85	91
26.854	trans-Caryophyllene	6.82	93
28.872	Alloaromadendrene	3.11	88
33.090	1H-Cycloprop[e]azulen-4-ol	1.47	84
34.253	2H-Pyran-2,4(3H)-dione	1.08	80
28.690	2,4-Diisopropenyl-1-methyl-1-vinyl-cyclohexane	0.81	90
8.602	1-Iodo-2-methylnonane	0.69	81
31.160	(-)-Caryophyllene oxide	0.63	90
31.273	Pentadecane (CAS) n-Pentadecane	0.59	96
28.439	gamma-Gurjunene	0.30	92
39.497	Octadecanoic Acid	0.27	92

As seen in Table 3, commercial patchouli oil has a patchouli alcohol content of 16.62%, and the highest compound is azulene with a percentage of 19.52%. The chemical structures of patchouli alcohol and azulene compounds are presented in Figure 3.

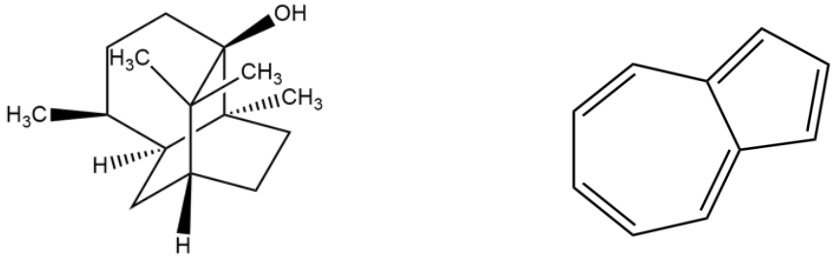

(a) (b)

Figure 3. Chemical structures of patchouli alcohol (a) and azulene (b)

Encapsulation efficiency of a mixture of noni fruit extract and patchouli oil

Encapsulation efficiency states the percentage of noni fruit extract and patchouli oil that can be encapsulated from the total core ingredients used [14]. The yield and efficiency of the encapsulation samples in this study are shown in Table 4.

The decrease in encapsulation efficiency in the three variations can be caused by the increase in encapsulation surface area in each variation. Overall, all encapsulation samples are considered efficient as they range from 80% to 97% [14].

Table 4. Encapsulation yields and efficiencies

Encapsulation Sample	Yield (%)	Encapsulation Efficiency (%)
Noni Fruit Extract	91.35	91.77
Noni Fruit Extract and Patchouli Oil (4:1)	88.03	Noni Fruit Extract: 83.5% Patchouli Oil: 90.78%
Noni Fruit Extract and Patchouli Oil (1:1)	83.51	Noni Fruit Extract: 90.34% Patchouli Oil: 87.15%

Organoleptic test

Organoleptic tests with 15 panelists were carried out on five samples: (1) noni fruit extract before encapsulation; (2) encapsulation of noni fruit extract; (3) encapsulation of a mixture of noni fruit extract and patchouli oil (4:1); and (4) encapsulation of a mixture of noni fruit extract and patchouli oil (1:1). The results of the organoleptic tests show differences in taste, aroma, color, and texture between noni fruit extract before and after being encapsulated together with patchouli oil. After encapsulation, the bitter taste of noni fruit extract is reduced, but the addition of patchouli oil brings back the bitterness because patchouli oil has a bitter taste (*pungent taste*) [15]. Furthermore, the unpleasant odor of noni fruit extract also decreases after encapsulation with the addition of patchouli oil. Meanwhile, based on the results of the favorability test, 15 panelists preferred the encapsulation of pure noni fruit extract (without the addition of patchouli oil) and the encapsulation of noni fruit extract with the addition of patchouli oil in the smallest ratio of 4:1. The results of the organoleptic tests are presented in graphs as displayed in Figure 4.

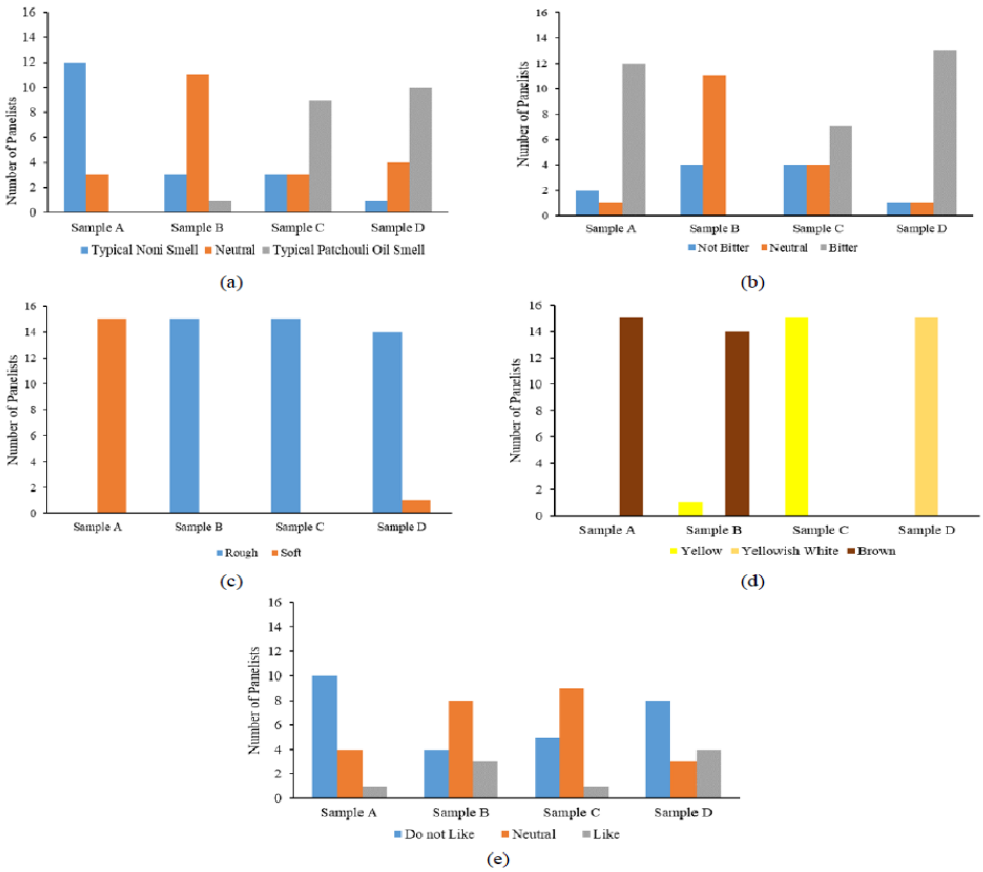

Figure 4. Graphs of organoleptic test results for aroma (a), taste (b), texture (c), color (d), and favorability (e)

Microcapsule morphology using SEM

The morphological analysis results of the microcapsules using SEM reveal an appearance that is not much different from one another at 500x magnification with a scale of 50 μm, as displayed in Figure 5. The resulting microcapsules are irregular, shaped like fractures, and have diverse sizes. This can be caused by incomplete freeze-drying process (the result is not completely dry) and uneven stirring with a magnetic stirrer. Wrinkles formed in the encapsulation of noni fruit extract and patchouli oil may occur due to the inappropriate composition and the lack of emulsifying ability of the maltodextrin used as encapsulating agent [7]. In addition, the particle surface of the three microcapsules did not show detectable pores, signifying that the solvent did not evaporate too quickly during the drying process. The results of the morphological analysis in this study are consistent with those of a previous study that encapsulated cold-pressed seed oils with various unsaturated fatty acids using the same freeze-drying method [16].

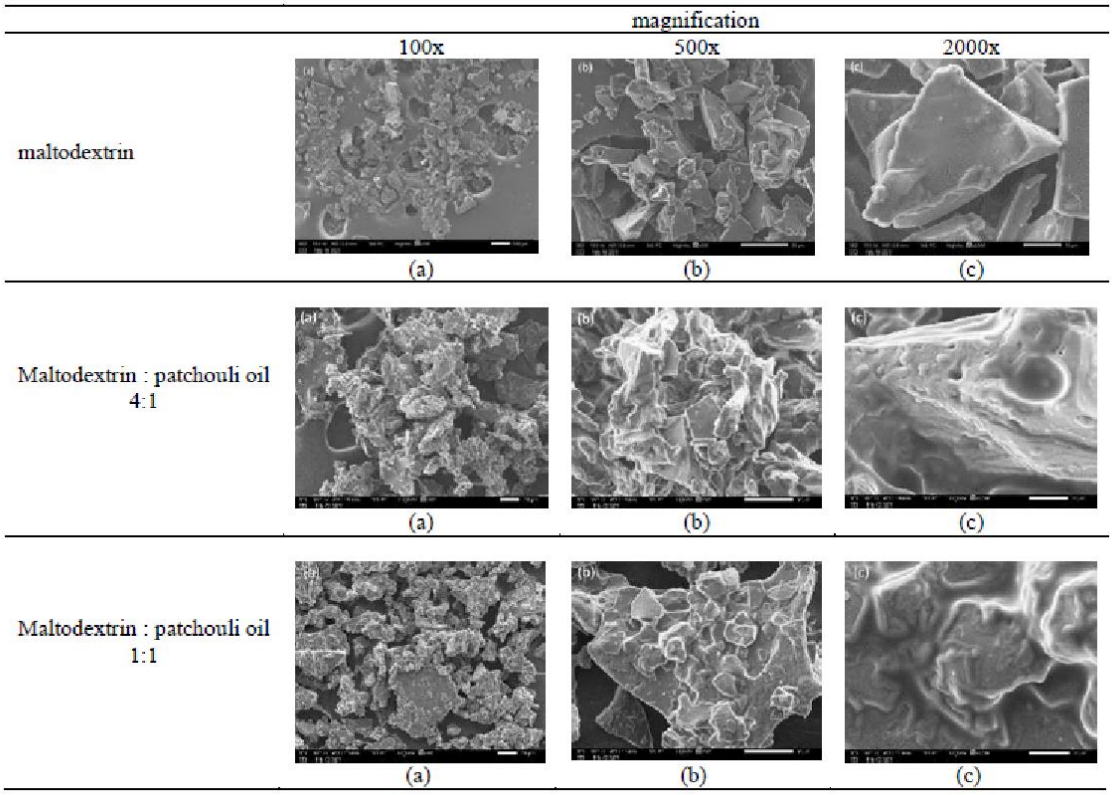

Figure 5. Morphology of noni fruit extract microcapsules with maltodextrin

Antioxidant activity test of the encapsulation

The success of an encapsulation process can be seen from several parameters, i.e., organoleptic properties, encapsulation efficiency, micro-particle characteristics, stability, release after consumption [17], and the antioxidant activity [18]. In this study, the antioxidant activity test was performed using the DPPH method, whose is that antioxidant compounds will donate hydrogen atoms and bond with free electrons in radical compounds, causing the free radical (diphenylpicrylhydrazyl) to change into a more stable non-radical compound (diphenylpicrylhydrazine) [19]. The sample absorbance results are used to determine the IC_{50} values of the encapsulation samples, which are shown in Table 5.

Table 5. IC_{50} values of encapsulation samples

Sample	IC_{50} (µg/mL)	Category
Noni Fruit Extract	61.74	Intermediate
Maltodextrin	1083346.9	Very weak
Encapsulation of Noni Fruit Extract with Maltodextrin	553.24	Very weak
Encapsulation of a Mixture of Noni Fruit Extract and Patchouli Oil (4:1)	88.30	Intermediate
Encapsulation of a Mixture of Noni Fruit Extract and Patchouli Oil (1:1)	50.80	Intermediate
Ascorbic Acid	1.10	Very strong

After encapsulation, the IC_{50} value of noni fruit extract experienced a significant increase. This indicates weak antioxidant activity as maltodextrin encapsulates the noni fruit extract and its active compounds. In this regard, the ratio of the core ingredients greatly influences the antioxidant activity of encapsulation result; the higher the concentration of maltodextrin compared to the core ingredients, the less fruit extract is encapsulated, resulting in the decreased amount of active compounds that act as antioxidants [20]. In this study, the ratio of coating material to core ingredients is 80:20, producing a higher IC_{50} value after encapsulation and resulting in lower antioxidant activity. However, the addition of patchouli oil has been found to contribute positively to increasing the antioxidant activity of encapsulated noni fruit extract. Due to the presence of patchouli alcohol which has hydroxy groups in phenols and terpenes, patchouli oil is known to have high antioxidant properties. As mentioned previously, the patchouli oil used in this study contains 16.62% Patchouli alcohol. Additionally, the patchouli oil also has an IC_{50} value of 22.45 µg/mL, which falls into the 'strong' category [21]. The results of this research indicate that the addition of patchouli oil to the encapsulation of noni extract is able to reduce the unpleasant aroma of noni extract and is able to increase the antioxidant activity of noni extract when combined. In previous research, modifications were also made to the encapsulation of noni extract, namely by adding lemon peel and it gave positive results to eliminate the unpleasant aroma of noni extract. However, this research did not include the antioxidant activity of the encapsulation results so it cannot be said to have potential as an antioxidant [23].

Conclusion

Based on the research that has been carried out, it can be concluded that Maltodextrin with a Dextrose Equivalent (DE) value of less than 20 can be produced through the partial hydrolysis process of cassava starch using the α-amylase enzyme with a concentration of 0.5% of the solution volume. The addition of patchouli oil to the encapsulation process of noni extract with maltodextrin has a positive effect on reducing the unpleasant aroma of noni extract and there is an increase in the antioxidant activity value of noni extract. Therefore, this research can be continued and developed as a solution for consuming noni fruit and preventing diseases caused by free radicals.

Acknowledgement

This study is financially supported by the Institute for Research and Community Services of Sebelas Maret University through the 2023 Applied Research Excellence Grant (PUT-UNS) with contract letter Number: 228/UN27.22/PT.01.03/2023

References

1. Chan-Blanco, Y., Vaillant, F., Mercedes Perez, A., Reynes, M., Brillouet, J. M. and Brat, P. (2006). The noni fruit (*Morinda citrifolia* L.): A review of agricultural research, nutritional and therapeutic properties. *Journal of Food Composition and Analysis*, 19(6-7): 645-654.
2. Elfariyanti, E., Zarwinda, I., Mardiana, M. and Rahmah, R. (2022). Analysis of vitamin c content and antioxidant activity of fruits typical of the Gayo Highlands of Aceh. *Jurnal Kedokteran Dan Kesehatan : Publikasi Ilmiah Fakultas Kedokteran Universitas Sriwijaya*, 9(2): 161-170.
3. Hasna, T., Anandito, B. K., Khasanah, L. U., Utami, R., and Manuhara, G. J. (2019). Effect of maltodextrin and whey combination as wall material on the characteristics of cinnamon

(*Cinnamomum burmanii*) oleoresin microencapsule. *AgriTECH*, 38(3): 259.

4. Suryani, R. and Choirun Nisa, F. (2015). Modification of cassava starch (*Manihot esculenta*) with α-amylase enzyme as a foaming agent and its application in the process of making marshmallows. *Jurnal Pangan dan Agroindustri*, 3(2): 723-733.
5. Krisnitya, W., Darmadji, P. and Pranoto, Y. (2020). Maltodextrin from cassava starch (*Manihot utilissima*) and its application as encapsulating agent of red guava juice extract (*Psidium guajava*). *Journal of Agri-Food Science and Technology*, 1(1): 26.
6. Hasanah, H., Syukri, D. and Ismed, I. (2022). Effect of maltodextrin concentration on antioxidants activity and stability of natural coloring powder of secang wood (*Caesalpinia sappan* L) in various conditions of pH and temperature. *Andalasian International Journal of Agriculture and Natural Sciences*, *3*(02): 1-19.
7. Sulistiyani, I. F. and Prasetya, A. T. (2022). Antibacterial activity of cajuputi oil (*Melaleuca leucadendron*) microcapsules against *Staphylococcus aureus* bacteria applied to cotton fabric fibers. *Indonesian Journal of Chemical Science*, 11(1): 69-80
8. Arifan, F. and Wikanta, D. K. (2020). Formulasi mikroenkapsul oleoresin kayumanis. *Jurnal Ilmu Pertanian*, 4(1): 30-35.
9. Anonim (2013). Pengujian organoleptik. *Modul Penanganan Mutu Fisis (Organoleptik)*. Program Studi Teknologi Pangan Universitas Muhammadiyah Semarang.
10. Mahmoud, K. F., Ibrahim, M. A., Mervat, E. D., Shaaban, H. A., Kamil, M. M. and Hegazy, N. A. (2016). Nano-encapsulation efficiency of lemon and orange peels extracts on cake shelf life. *American Journal of Food Technology*, 11(3): 63-75.
11. Prasetyo, W. E., Kusumaningsih, T., Firdaus, M., Marliana, S. D., Suryanti, V., Artanti, A. N., Apriana, I., and Anggraini, S. D. (2022). Diacylphloroglucinol derivatives as antioxidant agents: green synthesis, optimisation, in vitro, and in silico evaluation. *Natural Product Research*, 36(6): 1460-1466.
12. Imanningsih, N. (2019). Gelatinisation profile of several flour formulations for estimating cooking behaviour. *Penel Gizi Makanan*, 35(1): 13-22.
13. Marta, H., Tensiska, T. and Riyanti, L. (2017). Karakterisasi maltodekstrin dari pati jagung (*Zea mays*) menggunakan metode hidrolisis asam pada berbagai konsentrasi. *Chimica et Natura Acta*, *5*(1): 13.
14. Sahlan, M., Fadhan, A. M., Pratami, D. K., Wijanarko, A., Lischer, K., Hermansyah, H. and Mahira, K. F. (2019). Encapsulation of agarwood essential oil with maltodextrin and gum arabic. *International Journal of Technology*, 10(8): 1541-1547.
15. Muhammad, S., Dirhamsyah, M., Ernawati, E., Lufika, R. D., Khairunnisa, S. and Ledita, N. F. (2022). Innovation of aromatherapy product using Aceh essential oil. *Journal of Patchouli and Essential Oil Products*, 1(2): 47-51.
16. Ogrodowska, D., Tanska, M., Brandt, W. and Czaplicki, S. (2020). Impact of the encapsulation process by spray- and freeze-drying on the properties and composition of powders obtained from cold-pressed seed oils with various unsaturated fatty acids. *Polish Journal of Food and Nutrition Sciences*, 70(3): 241-252.
17. Jayanudin, J. and Heriyanto, H. (2021). A review of encapsulation using emulsion crosslinking method. *World Chemical Engineering Journal*, *5*(2): 37.
18. Santoso, B. S. A., Sudarsono, Nugroho, A. E. and Murti, Y. B. (2018). Hypoglycemic activity and pancreas protection of combination of *Morinda citrifolia* Linn. juice and *Curcuma xanthorrhiza* Roxb. juice on streptozotocin-induced diabetic rats. *Indonesian Journal of Pharmacy*, 29(1): 16-22.
19. Hairunisa, I., Mentari, I. A., Julianti, T., Wikantyasning, E. R., Cholisoh, Z., Ningsih, S. C. and Muslim, M. R. F. (2021). Antioxidant activities in different parts of pulasan (*Nephelium mutabile* Blume) from East Borneo. *IOP Conference Series: Earth and Environmental Science*, 736(1): 1-9.
20. Hasanuddin, A., Anwar, C., Mappatoba, M. and Hafsah, H. (2018). Antibacterial and antioxidant activities of cocoa pod that associated in maltodextrin in various concentration.

AGROLAND: The Agricultural Sciences Journal, *5*(2): 123.

21. Hariyanti, Hanani, E. and Dayatri, D. (2019). Phytochemical identification and antioxidant activity of essential oil of *Pogostemon cablin* Benth. cultivated in Java Island Indonesia. *International Journal of Phytopharmacy*, *9*(6): 1-7.
22. Pudziuvelyte, L., Marksa, M., Sosnowska, K., Winnicka, K., Morkuniene, R. and Bernatoniene, J. (2020). Freeze-drying technique for microencapsulation of *Elsholtzia ciliata* ethanolic extract using different coating materials. *Molecules*, 25(9): 1-16.
23. Julianii, E. and Siregar, S. N. (2020). Noni fruit extract (*Morinda citrifolia*. L) encapsulation using orange peel extract (*Citrus X lomon* L). *AGRINTECH*, 4(1): 1-5.

Malaysian Journal of Analytical Sciences (MJAS)
Published by Malaysian Analytical Sciences Society

MICROPLASTICS POLLUTION MITIGATION IN WASTEWATER TREATMENT: CURRENT PRACTICES, CHALLENGES, AND FUTURE PERSPECTIVES

(Pengurangan Pencemaran Mikroplastik dalam Rawatan Air Sisa: Amalan Semasa, Cabaran dan Perspektif Masa Depan)

Rabiatul S. Rusidi[1,2], Iwani W. Rushdi[1,2], Wan M. Khairul[2], Sofiah Hamzah[3], Wan Mohd Afiq Wan Mohd Khalik[1,2], Sabiqah Tuan Anuar[1,2], Nor Salmi Abdullah[4], Nasehir Khan E.M. Yahya[4], and Alyza A. Azmi[1,2,*]

[1]Microplastic Research Interest Group (MRIG),
Faculty of Science and Marine Environment,
Universiti Malaysia Terengganu, Kuala Nerus, 21030 Terengganu, Malaysia
[2]Faculty of Science and Marine Environment,
Universiti Malaysia Terengganu, Kuala Nerus, 21030 Terengganu, Malaysia
[3]Faculty of Ocean Engineering Technology and Informatics,
Universiti Malaysia Terengganu, Kuala Nerus, 21030 Terengganu, Malaysia
[4]Water Quality Laboratory,
National Water Research Institute of Malaysia (NAHRIM),
Lot 5377, Jalan Putra Permai, Rizab Melayu Sungai Kuyoh,
43300, Seri Kembangan, Selangor, Malaysia

**Corresponding author: alyza.azzura@umt.edu.my*

Received: 17 July 2023; Accepted: 4 November 2023; Published: 28 February 2024

Abstract

The growing attention to microplastics stems from their significant environmental and human impacts. Microplastic accumulation in the environment also contributes to the spread of micropollutants. Daily human activities involving the use of plastics, especially synthetic materials, lead to their eventual presence in wastewater treatment plants (WWTPs). Although WWTPs play a crucial role in removing microplastics during the treatment process, the technologies currently in use are not entirely effective in filtering out all microplastic particles. As a result, WWTPs are recognized as major contributors to microplastic release into the environment. This review delves into the sources and prevalence of microplastics, the methods used for their removal in WWTPs, and the potential risks they pose to human health. Several removal methods are discussed, including sedimentation and flotation, activated sludge and sedimentation, reverse osmosis, and rapid sand filtration. The efficiency of each method is critically assessed, highlighting their strengths and weaknesses in addressing microplastic contamination. Moreover, this review underscores the importance of ongoing comprehensive research and development to improve the removal efficiency of microplastics in WWTPs. Efforts to optimize existing removal techniques and investigate new technologies should be intensified to achieve more holistic microplastic removal. By tackling the microplastics issue at the WWTP level, we can reduce their release into the environment, thereby diminishing potential health risks. In conclusion, the environmental presence of microplastics and their associated micropollutants demands robust removal strategies within WWTPs.

While existing technologies offer some level of effectiveness, there is a need for further advancements to ensure more comprehensive microplastic removal. This review offers valuable insights into the current state of microplastic removal in WWTPs, emphasizing the need for continued research to protect both the environment and human health.

Keywords: microplastics, chemical contaminants, wastewater treatment plants, removal techniques

Abstrak

Mikroplastik telah menjadi tumpuan kerana kesannya yang ketara terhadap alam sekitar dan manusia. Pengumpulan mikroplastik di persekitaran membawa kepada penyebaran bahan pencemar mikro . Aktiviti harian manusia yang melibatkan penggunaan plastik, terutamanya bahan sintetik, mengakibatkan mereka masuk ke dalam loji rawatan air sisa (WWTP). WWTP memainkan peranan penting dalam membuang mikroplastik semasa proses rawatan, Walaubagaimanapun, teknologi sedia ada yang digunakan tidak berkesan sepenuhnya dalam menapis semua zarah mikroplastik. Kajian semula ini memfokuskan kepada sumber dan kewujudan mikroplastik, kaedah semasa yang digunakan untuk penyingkiran mikroplastik di WWTP, dan risiko terhadap kesihatan manusia. Pelbagai kaedah penyingkiran telah dipertimbangkan, termasuk pemendapan dan pengapungan, enap cemar dan pemendapan diaktifkan, osmosis terbalik, dan penapisan pasir pantas. Kecekapan dan keberkesanan setiap kaedah diperiksa secara kritikal, menjelaskan keupayaan dan batasannya dalam mengurangkan pencemaran mikroplastik. Kajian semula ini juga menekankan keperluan untuk penyelidikan dan pembangunan komprehensif yang berterusan untuk meningkatkan keberkesanan penyingkiran mikroplastik dalam WWTP. Strategi untuk mengoptimumkan kaedah penyingkiran sedia ada dan meneroka teknologi baru harus diteruskan untuk mencapai penyingkiran mikroplastik yang lebih komprehensif. Dengan menangani isu mikroplastik di peringkat WWTP, pembebasan zarah ini ke alam sekitar dapat diminimumkan, seterusnya mengurangkan potensi risiko kepada kesihatan manusia. Kesimpulannya, kehadiran mikroplastik dan bahan pencemar mikro yang berkaitan dalam alam sekitar memerlukan strategi penyingkiran yang mantap. Walaupun teknologi semasa menunjukkan beberapa keberkesanan, kemajuan selanjutnya diperlukan bagi memastikan penyingkiran mikroplastik yang lebih cekap dan menyeluruh. Oleh itu, semakan ini memberikan pandangan yang berharga tentang keadaan semasa penyingkiran mikroplastik di WWTP, menekankan kepentingan penyelidikan berterusan untuk menjaga integriti alam sekitar dan kesejahteraan manusia.

Kata kunci: mikroplastik, bahan cemar kimia, loji rawatan air sisa, teknik penyingkiran

Introduction

Plastic is a ubiquitous material that has revolutionized modern life since its inception in 1907 [1]. Its versatility, low cost, and moldability make it an ideal choice for a myriad of applications. One of the primary advantages of plastics is their lightweight nature, which is particularly beneficial in the transportation industry and consumer goods [2]. The chemical structure of plastics is based on long chains of molecules, known as polymers, which consist of repeating units. These units can be tailored to produce plastics with a diverse range of physical and chemical properties, such as transparency, flexibility, and resistance to heat, moisture, and chemicals. Packaging is one of the primary applications for plastics, owing to their exceptional barrier properties. They can be engineered to be impermeable to gases, moisture, and light, making them perfect for safeguarding food, pharmaceuticals, and other delicate materials [3]. According to a 2021 survey in Europe, polypropylene (PP), low-density polyethylene (LDPE), and high-density polyethylene (HDPE) are the three most widely used polymers, as cited by [4]. PP is in high demand, making up roughly 19% of total demand, because of its superior strength, chemical resistance, and recyclability. This makes it apt for a variety of applications, including packaging, automotive, and textiles. Conversely, LDPE and HDPE, which account for about 18% and 12% of the total plastic demand, respectively, also have a significant footprint in the European polymer industry [4]. Figure 1 presents the statistics of plastic demand in Europe in 2021.

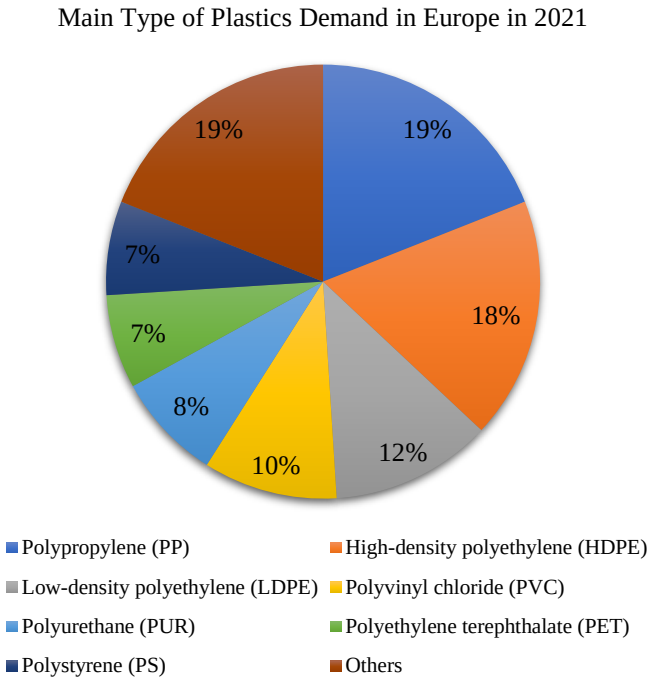

Figure 1. Plastics demand statistics in Europe in 2021

Despite their numerous advantages, the extensive use of plastics has led to significant environmental challenges, notably plastic pollution in oceans and waterways. Plastic waste varies in size from minuscule micrometre-sized particles to large meter-sized items and can originate from diverse sources, including both domestic and industrial [5]. Prior research indicates that domestic plastic production has consistently risen over the past decade, with only a minor fraction being recycled or incinerated [2]. In fact, about 79% of plastic waste either finds its way into landfills or is directly released into the environment, where it accumulates and can persist for centuries [6]. The build-up of plastic waste in aquatic environments is especially alarming due to its potentially detrimental effects on marine life. For instance, marine animals can become entangled in plastic debris, leading to suffocation, or they might ingest it, resulting in health complications or even death [7]. Moreover, plastic waste can release toxic chemicals into water, further jeopardizing the health of aquatic ecosystems [8].

The enduring presence of plastic waste in the environment results in the release of microplastics (MPs) – tiny plastic particles less than 5 mm in size. MPs are divided into two categories: primary and secondary MPs. Primary MPs are deliberately produced in small sizes, such as microbeads in personal care products, plastic pellets in feedstock or plastic manufacturing, and plastic powders for moulding. These particles are inherently small and can linger in the environment for prolonged periods, accumulating in various ecosystems, including oceans. According to Hwang et al. (2020), primary MPs constitute approximately 10% of global plastic waste, equating to 1.5 million metric tons annually [10]. Secondary MPs, conversely, form from the degradation of larger plastic items. They arise from various human activities like textile washing, tire wear, and paint chipping. These particles are minute enough to bypass wastewater treatment plants, eventually entering the environment. The scientific community has increasingly focused on these materials, believed to accumulate in the environment either due to direct discharge or from the fragmentation of larger particles [10].

The potential adverse health implications of microplastic exposure, whether through physical or

chemical pathways in daily life, are becoming a pressing concern. In vivo studies have shown that certain microplastics, especially polystyrene ones, can infiltrate body cells like macrophages, erythrocytes, and rat alveolar epithelial cells, causing intracellular structure damage [11]. The mechanisms by which microplastics enter cells remain elusive, but they are thought to penetrate through various pathways, including phagocytosis, endocytosis, and passive diffusion [12]. Once inside, microplastics can disrupt standard cellular functions, leading to cellular stress and inflammation. This can negatively impact human health and might even play a role in the onset of various diseases. Furthermore, the diminutive size of microplastics allows them to migrate to different organs and tissues in the body, potentially causing more health issues [13]. The accumulation of microplastics in tissues and organs can result in chronic inflammation, tissue damage, and disruption of regular organ function [14].

Additionally, the propensity of MPs to adsorb persistent organic pollutants, metals, and pathogenic microorganisms is alarming, as it can lead to the build-up of these noxious substances in the environment, posing potential risks to humans and other organisms. MPs have a high surface area to volume ratio, making them particularly adept at absorbing and concentrating both organic and inorganic pollutants in the environment [15]. This can happen through various physical and chemical mechanisms, such as electrostatic attraction, van der Waals forces, and hydrophobic interactions [16]. The adsorption of pollutants onto MPs can lead to aggregate formation, which, when ingested by organisms, can induce toxicity. The leaching of chemical additives from microplastics can further amplify their toxic effects [8]. Furthermore, MPs can contain various chemical additives like plasticizers, flame retardants, and pigments, which might be released into the environment as the plastic degrades [17]. These chemical additives can adversely affect both human and environmental health, leading to endocrine disruption, neurotoxicity, and even carcinogenicity [18]. While the potentially harmful effects of microplastics on human health are still debated, several studies have reported alarming findings. For instance, Prata noted an elevated risk of respiratory symptoms in workers exposed to polypropylene flocks compared to their non-exposed counterparts [19]. Chronic inhalation exposure to fine particles has also been associated with gene mutations. Synthetic textile workers exposed to polypropylene for 10-20 years had a higher cancer incidence. Moreover, polyvinyl chloride workers exhibited an increased lung cancer risk, correlated with age, years of work, and exposure duration at the factories [20].

Microplastic sources and occurrence

The widespread presence of microplastics in aquatic ecosystems is a growing concern due to their potential adverse effects on the environment and its inhabitants. Microplastics can be transported globally by various means, including ocean currents, wind, and other environmental factors. This has led to the detection of microplastics in all ocean basins and numerous freshwater systems.

The primary sources of microplastics are diverse, encompassing household sewage, polymeric particles from cosmetics and cleaning products, feedstocks for plastic product manufacturing, and plastic pellets or powders used for air blasting [21]. These sources discharge microplastics directly into the environment, contributing to their accumulation in aquatic ecosystems. Additionally, microplastics can form through the degradation of larger plastic items due to mechanical forces or UV light exposure [22]. This process results in the creation of microplastics that can accumulate in the environment. The fragmentation of larger plastic items into smaller microplastics can occur through various processes, such as photodegradation, thermal degradation, and mechanical abrasion [10]. Once released, microplastics can persist for extended periods due to their resistance to degradation.

The global ingestion of microplastics by a variety of aquatic organisms has unveiled new and concerning environmental threats, as reported by [23]. The consumption of microplastics has been extensively documented in fish, shellfish, and other aquatic creatures, raising concerns about potential adverse

effects on their health and the broader food chain. Microplastics can enter wastewater treatment plants (WWTPs) through various sources, eventually finding their way into water bodies and, subsequently, the wastewater treatment system. Recent research underscores the role of WWTPs in mitigating microplastic presence in the environment. According to Bretas Alvim et al., conventional WWTPs can remove up to 90% of microplastics. However, these systems remain a primary source of microplastic introduction into the environment. This is partly due to the direct release of microplastic-containing skincare products and toothpaste into wastewater from daily human activities [24]. Additionally, during washing, synthetic garments made of polyester and nylon can shed vast quantities of fibers, which can accumulate in WWTPs and contribute to microplastic release [19, 25].

The release of synthetic textile fibers during washing is a significant source of microplastic pollution in oceans. According to Boucher and Friot, about 35% of oceanic microplastics originate from synthetic textile fibers shed during washing [27]. The number of fibers released per wash can vary dramatically, with some studies reporting up to a million fibers shed by a single garment. For instance, Acharya et al. estimated the annual release of polyester and cotton microfibers during washing in Finland to range from 154,000 to 411,000 kg [28].

Several factors influence the release of microplastic fibers from synthetic textiles during washing. Textile properties, such as polymer type and knit structure, can affect fiber shedding [29]. For example, polyester fabrics tend to release more fibers per wash than acrylic fabrics [30]. Washing conditions, including temperature, friction, velocity, and duration, also play a role [30, 31]. Higher washing temperatures and extended durations can increase fiber release [30, 32], as well as mechanical friction and water velocity [31]. Additionally, the use of certain detergents and softeners can influence fiber release. Enzymatic or high-pH detergents can degrade fibers, increasing their release, while fabric softeners can coat fibers, reducing friction and shedding [33].

Microplastics entering WWTPs are typically captured and removed by designed systems. However, some microplastics still find their way into aquatic ecosystems, leading to environmental pollution and potential human health risks. The release of microplastics from WWTPs has garnered increased attention from researchers [34]. Studies have shown that while larger plastic particles are efficiently removed, microplastics can bypass the system and accumulate in aquatic ecosystems [35]. Given that many WWTPs are located near coastal areas and water sources, the discharge of microplastics can pose significant challenges. For example, in mainland China, 1,873 of the 3,340 WWTPs, with a treatment capacity of 78×106 m^3/day, are situated in coastal regions. Their effluents can directly or indirectly enter aquatic ecosystems [36]. To address this issue, researchers are examining the sources, occurrence, and removal of microplastics in WWTPs [21, 37, 38]. Table one summarizes the sources and types of plastics entering WWTPs.

Table 1. Source and type of plastics entering WWTPs

Source	**Type**	**References**
Domestic	Polyethylene (PE)	[39, 40]
	Polyethylene terephthalate (PET)	
	Polyester (PES)	
	Polyacrylate (PAC)	
	Polyamide (nylon)(PA)	
	High-density polyethylene (HDPE)	
	Low-density polyethylene (LDPE)	

Source	Type	References
Landfill	Polyacrylate (PAC)	[41–43]
	Polyimide (PI)	
	Polyethylene terephthalate (PET)	
	Polyoxymethylene (POM)	
	Polystyrene (PS)	
	Polyester (PES)	
	Polypropylene (PP)	
Stormwater runoff	Styrene-butadiene-rubber (SBR)	[44]
	Synthetic rubber (SR)	
Industry	Polyethylene terephthalate (PET)	[45]
	Polyester (PES)	
	Polyacrylate (PAC)	
	Polyamide (nylon)(PA)	
	Polystyrene (PS)	
	Polyvinyl chloride (PVC)	

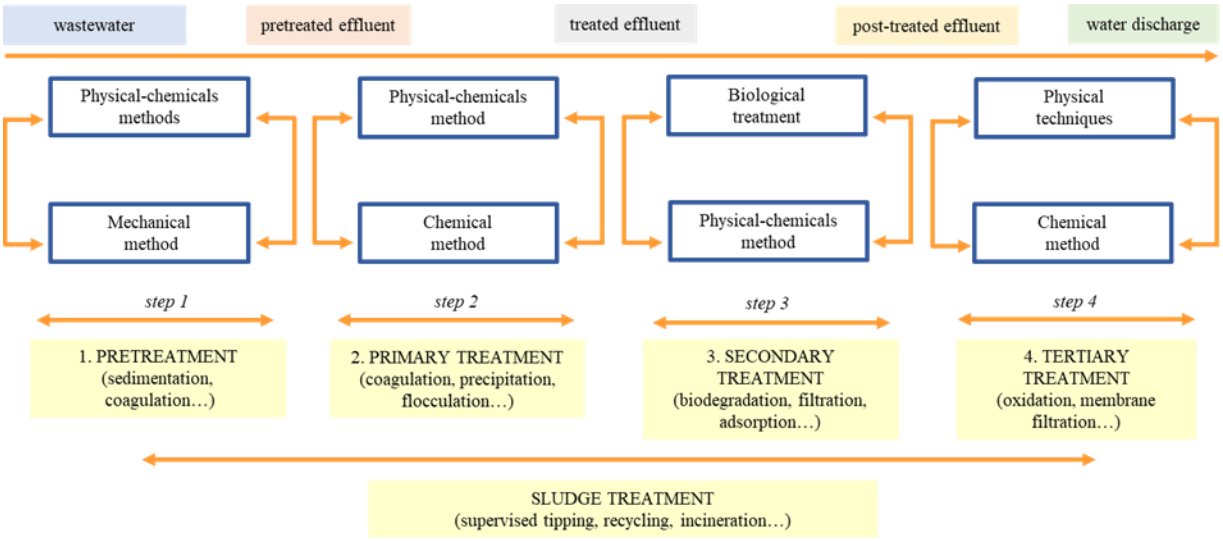

Figure 2. The schematic diagram of general process of WWTPs

Introduction to wastewater treatment plant

Efficient wastewater treatment is essential to maintain a clean and healthy environment and to comply with legal regulations that define decontamination objectives. Typically, conventional wastewater treatment combines physical, chemical, and biological processes to remove solids, including colloids, organic matter, nutrients, and soluble contaminants (e.g., metals, organics) from effluents. Figure 2 provides a comprehensive overview of available technologies for removing various contaminants from wastewater. Conventional methods encompass physical, chemical, and biological processes such as coagulation/flocculation, precipitation, biodegradation, filtration, and adsorption using activated carbon. These methods, established for contaminant removal in wastewater treatment, are widely employed in conventional treatment plants [46].

Besides conventional methods, established recovery processes, including solvent extraction, evaporation, oxidation, electrochemical treatment, membrane

separation, membrane bioreactors, ion exchange, and incineration, have also been utilized for contaminant removal [47]. Emerging removal methods under development and investigation include advanced oxidation, adsorption onto non-conventional solids, biosorption, biomass, and nanofiltration [47]. These methods are gaining popularity due to their high efficiency and ability to treat contaminants challenging to address using conventional methods. Advanced oxidation processes are explained in Tufail et al. [48]. Adsorption onto non-conventional solids, like agricultural waste or biochar, shows promise for contaminant removal, as discussed in Wang et al. [49]. Biosorption and biomass methods utilize microorganisms or plants to remove contaminants from wastewater through absorption or uptake. Nanofiltration, which uses membranes with pore sizes between ultrafiltration and reverse osmosis, effectively removes organic and inorganic compounds and has proven efficient in removing pharmaceuticals and endocrine disruptors, as mentioned in Tufail et al. [48].

The wastewater treatment process generally consists of five steps, as illustrated in Figure 2. The first step, preliminary treatment, uses physical and mechanical methods to remove large solids and debris. The second step, primary treatment, employs physicochemical and chemical processes to remove suspended solids and organic matter. Chemical coagulation or precipitation may enhance particle settling, as discussed in Turan et al. [37]. The third step, secondary treatment or purification, uses chemical and biological methods to degrade organic matter and nutrients with microorganisms. Efrin et al. [50] details the use of activated sludge systems, trickling filters, and other biological reactors for this purpose. Chemical treatments, like disinfection, may also be used to eliminate pathogens and other harmful microorganisms. The fourth step, tertiary or final treatment, uses physical and chemical methods such as filtration, adsorption, or reverse osmosis to remove any remaining contaminants. Advanced treatment methods like membrane filtration and ozonation may also be employed, as discussed in Tufail et al. [48]. The fifth step addresses the treatment of sludge generated during the process, which may involve supervised disposal, recycling, or incineration, as mentioned in Ngo et al. [51].

The first two steps of the wastewater treatment process are often referred to as pre-treatment or preliminary steps, depending on the context. Pre-treatment involves removing large solids and debris that might damage downstream equipment or block pipes, typically using screens or grit chambers, as described in Efrin et al. [50]. Primary treatment focuses on removing suspended solids and organic matter, often through sedimentation or flotation. It may also involve chemical coagulation or precipitation to enhance particle settling, as discussed in Turan et al. [37].

Secondary treatment, the subsequent step, relies on microorganisms to degrade organic matter and nutrients in the wastewater. This can be achieved using activated sludge systems, trickling filters, or other biological reactors, as explained in Enfrin et al. [50]. Chemical treatments, like disinfection, may also be used to eliminate pathogens and other harmful microorganisms. The tertiary or final treatment step typically employs physical or chemical methods, such as filtration, adsorption, or reverse osmosis, to further purify the wastewater. This step might also involve adding chemicals to adjust pH or remove specific contaminants. Enfrin et al. [50] discusses using advanced treatment methods like membrane filtration and ozonation for tertiary treatment. Lastly, treating the sludge generated during the process is crucial. This might involve landfill disposal or specialized techniques like composting, anaerobic digestion, or incineration to convert the sludge into a stable and safe material, as mentioned in [37].

Microplastic removal efficiency in WWTP

Sedimentation and flotation

Two technologies commonly used for MP removal are sedimentation and air flotation. The sedimentation process involves the settling of heavier MPs, such as those with high densities, to the bottom of the tank due to gravity. Concurrently, some MPs might get trapped in the solid flocs that form during the process. The effectiveness of the sedimentation process depends on several factors, including the size, shape, and density of

the MPs. The shape of the MPs can significantly influence their settling velocity, with spherical particles generally settling more slowly than irregularly shaped ones, as discussed in Li et al. [52]. The density of the MPs also affects their settling velocity, with higher-density MPs settling faster than those with lower density. Figure 3 below illustrates the process of flocculation and sedimentation in WWTPs.

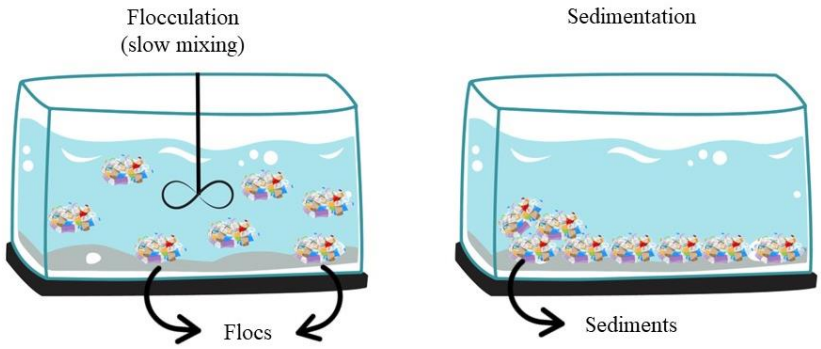

Figure 3. Flocculation and sedimentation process in WWTPs

The efficiency of sedimentation in removing MPs varies, with some studies reporting removal rates as low as 40.7% and others as high as 91.7%. This variation in removal efficiency can be attributed to differences in polymer types, and the size and shape of MPs in the wastewater flow [51, 53]. Polymer types such as PES, PET, and POM, which are denser than wastewater, are more readily removed by physical sedimentation, leading to higher removal efficiency [51]. The natural buoyancy of pollutants in the wastewater environment can also influence the effectiveness of sedimentation technology. Chemical compounds adsorbed onto the surface of MP particles can change their buoyancy, making them harder to remove [54]. The shape and size of the MPs also play a role in their removal efficiency, with fragments and granules being more easily removed than fibers [34].

A study by Liu et al. found that a combination of a coarse and fine grid, aerated grit chamber, and primary settlement tank reduced MPs from 79.9 to 47.4 nL^{-1}, achieving a removal rate of 40.7% [55]. However, another study by Turan et al. discovered that approximately 45% of influent MPs were trapped in the grit and grease fractions of the WWTP, while around 34% were retained within the primary sedimentation tank [37]. This indicates that a total of 80% of MPs accumulated in the primary sludge fraction, also referred to as biosolids. Using biosolids as fertilizer can introduce MPs into the environment, posing a potential risk to human health [56, 57].

Air flotation technology, in contrast, capitalizes on the density difference between the microplastics and the surrounding water. During this process, air bubbles are introduced, allowing MPs with a lower density to attach to them and rise to the water's surface, where they can be skimmed off. The shape and size of the MPs can also affect their removal efficiency in air flotation. Generally, MPs with larger sizes and irregular shapes exhibit higher removal efficiencies, as cited in literatures [51, 58]. Moreover, the presence of surfactants, which can stabilize the MPs and reduce their density, can diminish the effectiveness of air flotation, as noted by Swat et al. [59].

Activated sludge and sedimentation

Activated sludge is a prevalent technology in municipal WWTPs, typically employed after primary treatment processes such as sedimentation tanks, aerated grit chambers, or dissolved air flotation. Figure 4 illustrates the activated sludge and sedimentation process in WWTPs. During the growth phase, sludge flocs or bacterial extracellular polymers assist in accumulating

MPs contaminants in sewage, which are then removed during the sedimentation process. However, the intricate interaction between MPs and microorganisms, as well as the degree to which the process can capture MPs, remains ambiguous and requires further research [60].

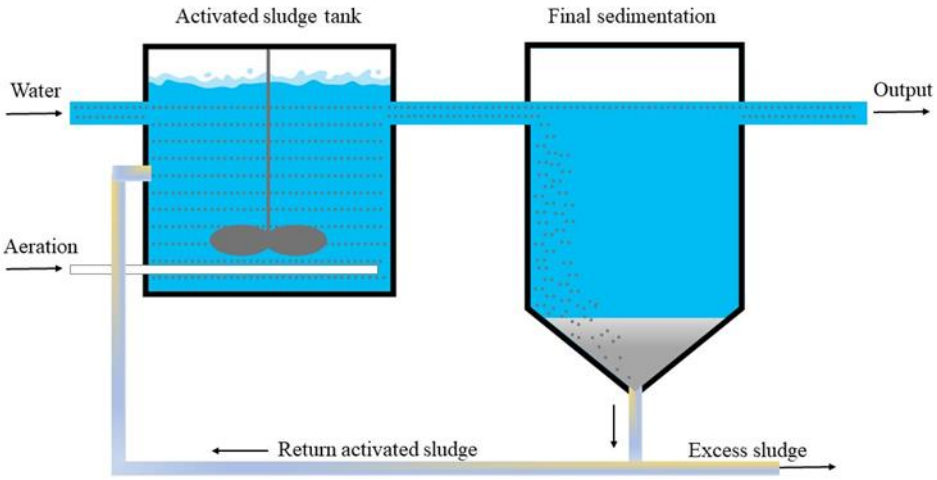

Figure 4. Example of activated sludge and sedimentation process

Ziajahromi et al. [61], Liu et al. [62], and Yang et al. [45] have reported MPs removal rates in activated sludge ranging from 28.1% to 66.7%. This variation is attributed to factors such as retention time and nutrient levels [61]. Extended contact times enhance the likelihood of surface biofilm formation on MPs, altering the surface, size, and relative densities of contaminants. Magni et al. reported that the number of MPs in WWTP sludge was 113 ± 57 MPs/g sludge dry weight (dw), with MPPs/g and MPFs/g accounting for 59.5 ± 21.6 and 53.3 ± 48.9, respectively [63]. The estimated daily accumulation of 3.4 billion MPs in sewage sludge underscores the importance of effective MP removal methods in WWTPs. While WWTPs can mitigate the direct introduction of MPs into aquatic environments by transferring some MPs to sludge during treatment, applying this sludge can introduce MPs into the soil. Li et al. (2018) estimated the total amount of MPs in dry sludge produced by W- and X-WWTP to be 1.64 × 108 and 1.88 × 108 particles per year, respectively [64].

Despite the potential of activated sludge technology to remove MPs, its inconsistent removal rate emphasizes the need for supplementary methods for effective MP removal. Combining sedimentation and air flotation with activated sludge might achieve optimal MP removal efficiency. Additionally, the role of microorganisms in accumulating MPs in sludge flocs, as highlighted by Scherer et al., stresses the significance of studying MPs removal mechanisms in wastewater treatment processes [60]. By understanding these mechanisms, we can pinpoint potential strategies to enhance MP removal in WWTPs, thereby reducing MP pollution in the environment.

Reverse osmosis (RO)

The application of RO (Reverse Osmosis) technology for MP (microplastics) removal has garnered attention as a potential solution to mitigate microplastic pollution in water sources. RO, a method widely employed for desalination and water purification, works by using a semipermeable membrane to separate contaminants based on their size and charge, as depicted in Figure 5. While RO is highly effective in removing dissolved substances, its efficiency in eliminating microplastics is contingent on various factors. This discussion offers an overview of the application of RO technology for microplastics removal, bolstered by pertinent statistical data.

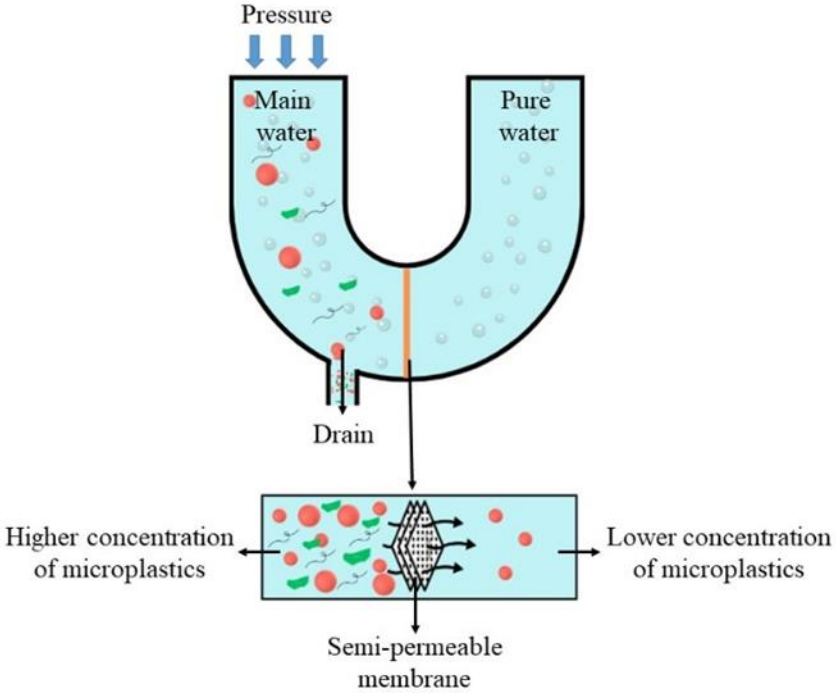

Figure 5. Semipermeable membrane used to separate contaminants

Several studies have evaluated the efficacy of RO in removing microplastics from water sources, yielding invaluable statistical insights. For instance, a study by Liu et al. explored the removal efficiency of RO membranes for microplastic particles ranging from 10-200 μm in size [64]. The research showed that RO achieved a microplastic removal efficiency spanning from 99% to 100% for microplastics of varying sizes. Another study by Ziajahromi et al. centered on the removal efficiency of RO for microplastic particles sized between 25 μm and 100 μm, revealing that RO could effectively eliminate microplastics with removal efficiencies reaching 98% [61].

Other studies have highlighted the impact of specific factors on the efficiency of microplastics removal via RO. Membrane characteristics, such as pore size and surface properties, are pivotal. Mohana et al. delved into the effect of different RO membrane pore sizes on microplastics removal, finding that membranes with tinier pore sizes displayed higher removal efficiencies, achieving 99% for microplastic particles larger than 0.4 μm [65]. The concentration of microplastics in the feedwater also significantly influences RO efficiency. Krishnan et al. assessed the effect of initial microplastic concentration on removal efficiency using RO, determining that higher initial microplastic concentrations resulted in diminished removal efficiencies, with rates ranging from 88% to 97% for initial concentrations from high to low [66].

While RO technology demonstrates the potential for microplastics removal, it is not without challenges and limitations. Fouling of the RO membrane by organic matter and particulate substances can compromise its efficiency. For example, a study referenced as [67] noted that microplastic removal efficiency was higher in tap water samples compared to raw water samples, both spiked with MPs (1 mg/L, 1 μm PS). The raw water sample exhibited a higher TMP value of 74.0 kPa, in contrast to 13.5 kPa for the tap water sample. An increase in the TMP value indicates more severe membrane fouling. Moreover, the energy demands of RO systems warrant consideration, as elevated energy consumption can lead to increased operational costs and environmental repercussions [68].

Rapid sand filtration

Rapid sand filtration is a widely used and economically viable technology for water treatment in various applications, including water supply and sewage treatment. This technique effectively removes impurities from water, making it a preferred choice globally [69, 70]. Within wastewater treatment plants (WWTPs), rapid sand filtration is often employed as a tertiary treatment stage to enhance water quality. Figure 6 illustrates the use of rapid sand filtration in WWTPs. The process works by passing water through a bed of sand, which serves as a filtration medium, removing suspended particles, pathogens, and organic matter. Both physical and biological mechanisms, such as adsorption, sedimentation, and microbial activity, contribute to contaminant removal and water quality improvement. One of the primary benefits of rapid sand filtration is its cost-effectiveness. The technology incurs relatively low operation and maintenance costs, making it an economically attractive choice for water treatment facilities [70]. Additionally, the system's simplicity promotes its broad adoption across various settings.

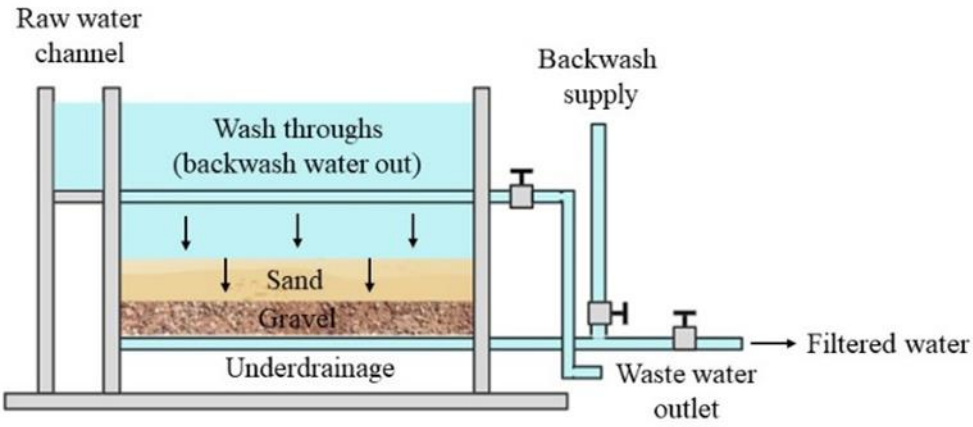

Figure 6. Rapid sand filtration in WWTPs

While rapid sand filtration effectively removes many impurities, its efficacy in MP removal has garnered significant attention. Several studies have explored the capability of rapid sand filtration in this regard, providing insights into its performance and limitations. When comparing the removal efficiency of MPs in different water treatment processes, rapid sand filtration seems to have a slightly lower efficiency than membrane bioreactors (MBRs). Egea-Corbacho et al. reported a removal efficiency of 97.1% for MPs in MBRs, while rapid sand filtration achieved 99.9% [38]. However, some inconsistencies in MP removal rates using rapid sand filtration have been observed. For instance, a study referenced as [71] found that a sand and anthracite coal filtration system in a WWTP in Western New York, USA, achieved only a 15% removal rate for MPs. The reduced efficiency in sand filters might be due to the potential mixing of anthracite coal and sand during filtration, possibly increasing the filter material's porosity over time. This diminished porosity might lead to bypassing or incomplete MP removal, affecting the system's overall efficiency. In contrast, filtration units using alternative methods have shown higher MP removal efficiencies, with several studies reporting rates exceeding 95% [51, 61, 72]. These findings underscore the effectiveness of such filtration units in removing MPs from water sources. Further research by Sembiring et al. identified a trend in MPs removal, indicating a decrease in removal percentages with increasing filtration rates. Their study revealed that the highest MP removal, at 95.5%, occurred at a filtration rate of 6 m/h after one hour of reactor operation. In contrast, the lowest removal, at 77.8%, was observed at a rate of 8 m/h

after five hours of operation [73]. This pattern suggests that as the filtration rate rises, the efficiency of microplastic removal decreases.

Several factors can influence the efficiency of MP removal during rapid sand filtration. One such factor is the MPs' particle size, as removal efficiency may differ based on the size distribution of these particles in the influent water. Different MP sizes might interact uniquely with the sand filtration medium, influencing their capture and removal [74]. A study by Umar et al. reported that smaller microplastics exhibited the highest removal rates by sand filtration compared to larger sizes. Furthermore, the composition of MPs can also affect their removal efficiency. MPs can consist of various polymers, additives, and contaminants, each potentially interacting differently with the sand filtration media [75]. Some MPs might have surface properties that enhance their adhesion to sand particles, leading to better removal, while others might exhibit properties that reduce such interactions, resulting in lower efficiencies.

Operational conditions of the filtration system can also impact MP removal efficiency. Factors like filtration rate, contact time between microplastics and the filtration media, and the filter bed's condition can all influence the process's overall effectiveness [75]. For example, an excessively high filtration rate might reduce the contact time between MPs and the filtration media, limiting removal efficiency [73]. Over time, the accumulation of organic matter and biofilm on the filter bed's surface can alter the sand's pore size and porosity, potentially diminishing the system's ability to capture and retain MPs [76].

Limitations of current technology in WWTPs in removing MPs

All current technological approaches have their limitations in removing MPs. Sedimentation, flocculation, activated sludge, reverse osmosis, and sand filtration are effective existing technologies in WWTPs, but their efficiency in removing microplastics is limited. The small size and buoyancy of microplastics make their removal through sedimentation and flotation challenging due to difficulties in efficient capture. Activated sludge, which can inadvertently break plastic particles into MPs, may contribute to the release of secondary microplastics into the environment. While reverse osmosis has been touted as efficient in removing MPs, its effectiveness depends on several factors. Moreover, it is expensive and energy-intensive. Sand filtration, on the other hand, has limitations in removing MPs, especially those of sub-micron size. Over time, particles can pass through the filter material. These challenges underscore the need for more advanced and specific technologies, such as advanced oxidation processes, membrane filtration techniques, and emerging separation methods. Based on findings from relevant studies, these approaches aim to address the size, density, and efficiency issues inherent in conventional treatment techniques.

Conclusion and future perspectives

In conclusion, the efficiency of MP removal in WWTPs is influenced by variations in design and operational characteristics. While existing technologies predominantly achieve retention of microplastics in sludge and solid waste, they do not offer a comprehensive solution for complete removal. The presence of micropollutants, including pharmaceuticals and additives from cosmetics, poses a significant challenge, as biological treatment processes alone are insufficient for their complete removal. Consequently, WWTPs are increasingly opting to upgrade their facilities by incorporating downstream treatment stages, specifically aimed at the elimination of micropollutants.

Future studies should perform comprehensive investigations into various treatment stages aimed at enhancing the efficiency of MP elimination in WWTPs. These studies should encompass the exploration of various technologies and approaches, considering the intricate characteristics, interactions, and removal mechanisms associated with MPs. Additionally, it is crucial to address the simultaneous presence of micropollutants alongside MPs during treatment processes, as both contaminants necessitate comprehensive and integrated treatment strategies. The findings derived from such studies should be

thoughtfully considered when implementing downstream treatment stages in WWTPs. The objective should be to develop and implement integrated treatment systems that not only target effective MP removal but also demonstrate efficacy in addressing micropollutants. This multidimensional approach may contribute to the realization of more efficient and sustainable wastewater treatment practices, consequently mitigating the release of MPs and micropollutants into the environment.

To achieve these goals, research efforts should focus on the following areas:

Advanced treatment technologies: Further exploration and evaluation of innovative treatment technologies, such as advanced oxidation processes, membrane filtration techniques, and emerging separation methods, should be pursued. In the advanced oxidation process, powerful oxidants are used to break down and remove various contaminants, including MPs present in the WWTPs. Meanwhile, membrane filtering techniques effectively capture and retain small particles of MPs, preventing their discharge into the environment. Emerging separation methods should be studied more since these approaches are continually evolving to offer more effective and focused removal. Therefore, these technologies hold promise for enhanced MP removal and micropollutant control in WWTPs.

Process optimization: Process optimization is a crucial strategy to overcome challenges and increase the effectiveness of MP removal and micropollutant control. Optimal operating conditions for MP removal should be identified through systematic optimization of process parameters such as contact time, filtration rates, and dosing of coagulants or adsorbents. The potential for MPs and micropollutants to interact with treatment agents may be increased by longer contact time, which would increase the effectiveness of removal. The removal efficiency may also increase when the filtration rates are adjusted to achieve a balance between the removal process and system capacity. Chemicals and their dosages used in a process also need to be optimized. Insufficient dosing may result in incomplete removal, while excessive dosing may increase costs and raise potential environmental issues. Therefore, process optimization in WWTPs is essential to help maximize the removal efficiency of MPs and micropollutants, save costs, and protect the environment.

Material development: Research should be dedicated to the development of novel materials with enhanced adsorption or filtration properties specifically designed for MP and micropollutant removal. This includes exploring the use of bio-based materials, nanomaterials, and hybrid composites. Bio-based materials from renewable sources such as agricultural waste, algae, and bacterial byproducts can exhibit good adsorption properties. The development of nanomaterials with a high surface area and reactivity will have a high potential for trapping MPs and micropollutants. Hybrid composites consist of various materials that benefit from their complementary properties. They may be designed to excel at trapping MPs and micropollutants while maintaining structural stability. By developing novel materials, the efficiency of MPs and micropollutant removal will be improved.

Fate and transport studies: Comprehensive investigations into the fate and transport of MPs within WWTPs, including their behaviour during different treatment stages and potential release pathways, should be conducted. Sample collection can be obtained at different stages of WWTPs, enabling the tracking of the movement and fate of MPs within the WWTPs. To ensure the accuracy of the data collected, a consistent methodology for the sampling step for each stage must be established. This will provide valuable insights for designing targeted removal strategies.

Monitoring and analysis: Advancements in analytical techniques and monitoring methodologies should be pursued to accurately quantify and characterize MPs in wastewater, treated effluent, and receiving water bodies. Monitoring will allow the assessment of the effectiveness of each stage of WWTPs. This will aid in assessing the efficiency of treatment processes and the environmental impact of released contaminants.

By focusing on these research directions, the researchers can further contribute to the development of more efficient and sustainable treatment solutions for MPs in WWTPs. This will in turn facilitate the implementation of comprehensive treatment strategies to safeguard water resources and protect environmental and human health.

Acknowledgement

The authors gratefully acknowledge the financial support from the Ministry of Higher Education, Malaysia through the Fundamental Research Grant Scheme (FRGS) (FRGS/1/2020/STG05/UMT/02/1), as well as Universiti Malaysia Terengganu for the research facilities provided.

References

1. Arpia, A. A., Chen, W. H., Ubando, A. T., Naqvi, S. R. and Culaba, A. B. (2021). Microplastic degradation as a sustainable concurrent approach for producing biofuel and obliterating hazardous environmental effects: a state-of-the-art review. *Journal of Hazardous Materials*, 418: 126381.
2. Chen, H. L., Nath, T. K., Chong, S., Foo, V., Gibbins, C. and Lechner, A. M. (2021). The plastic waste problem in Malaysia: management, recycling and disposal of local and global plastic waste. *SN Applied Sciences*, 3: 1-15.
3. Sundqvist-Andberg, H. and Åkerman, M. (2021). Sustainability governance and contested plastic food packaging–An integrative review. *Journal of Cleaner Production*, 306: 127111.
4. Evode, N., Qamar, S. A., Bilal, M., Barceló, D. and Iqbal, H. M. (2021). Plastic waste and its management strategies for environmental sustainability. *Case Studies in Chemical and Environmental Engineering*, 4: 100142.
5. Katare, Y., Singh, P., Sankhla, M. S., Singhal, M., Jadhav, E. B., Parihar, K., ... and Bhardwaj, L. (2021). Microplastics in aquatic environments: sources, ecotoxicity, detection & remediation. *Biointerface Research Applied Chemistry*, 12: 3407-3428.
6. Abdellatif, G., Mahmoud, A. S., Peters, R. W. and Mostafa, M. K. (2021). Waste plastics and microplastics in Africa: Negative impacts and opportunities. In *2021 AIChE Annual Meeting*. New York, NY, USA: AIChE.
7. Kehinde, O., Ramonu, O. J., Babaremu, K. O. and Justin, L. D. (2020). Plastic wastes: environmental hazard and instrument for wealth creation in Nigeria. *Heliyon*, *6*(10): e05131.
8. Nava, V. and Leoni, B. (2021). A critical review of interactions between microplastics, microalgae and aquatic ecosystem function. *Water Research*, 188: 116476.
9. Hwang, J., Choi, D., Han, S., Jung, S. Y., Choi, J. and Hong, J. (2020). Potential toxicity of polystyrene microplastic particles. *Scientific Reports*, 10(1): 7391.
10. Zhang, K., Hamidian, A. H., Tubić, A., Zhang, Y., Fang, J. K., Wu, C. and Lam, P. K. (2021). Understanding plastic degradation and microplastic formation in the environment: A review. *Environmental Pollution*, 274: 116554.
11. Lee, Y., Cho, S., Park, K., Kim, T., Kim, J., Ryu, D. Y. and Hong, J. (2023). Potential lifetime effects caused by cellular uptake of nanoplastics: A review. *Environmental Pollution*, 329: 121668.
12. Liu, L., Xu, K., Zhang, B., Ye, Y., Zhang, Q. and Jiang, W. (2021). Cellular internalization and release of polystyrene microplastics and nanoplastics. *Science of the Total Environment*, 779: 146523.
13. Horvatits, T., Tamminga, M., Liu, B., Sebode, M., Carambia, A., Fischer, L., ... and Fischer, E. K. (2022). Microplastics detected in cirrhotic liver tissue. *EBioMedicine*, 82: 104147.
14. Hu, M. and Palić, D. (2020). Micro-and nano-plastics activation of oxidative and inflammatory adverse outcome pathways. *Redox Biology*, 37: 101620.
15. Khoshmanesh, M., Sanati, A. M. and Ramavandi, B. (2023). Co-occurrence of microplastics and organic/inorganic contaminants in organisms living in aquatic ecosystems: A review. *Marine Pollution Bulletin*, 187: 114563.
16. Wang, F., Zhang, M., Sha, W., Wang, Y., Hao, H., Dou, Y. and Li, Y. (2020). Sorption behavior and mechanisms of organic contaminants to nano and microplastics. *Molecules*, 25(8): 1827.

17. Kitahara, K. I. and Nakata, H. (2020). Plastic additives as tracers of microplastic sources in Japanese road dusts. *Science of the Total Environment*, 736: 139694.
18. Encarnação, T., Pais, A. A., Campos, M. G. and Burrows, H. D. (2019). Endocrine disrupting chemicals: Impact on human health, wildlife and the environment. *Science Progress*, 102(1): 3-42.
19. Prata, J. C. (2018). Airborne microplastics: consequences to human health?. *Environmental Pollution*, 234: 115-126.
20. Girardi, P., Barbiero, F., Baccini, M., Comba, P., Pirastu, R., Mastrangelo, G., ... and Fedeli, U. (2022). Mortality for lung cancer among PVC baggers employed in the vinyl chloride industry. *International Journal of Environmental Research and Public Health*, 19(10): 6246.
21. Jiang, J. Q. (2018). Occurrence of microplastics and its pollution in the environment: A review. *Sustainable Production and Consumption*, 13: 16-23.
22. Ekvall, M. T., Lundqvist, M., Kelpsiene, E., Šileikis, E., Gunnarsson, S. B. and Cedervall, T. (2019). Nanoplastics formed during the mechanical breakdown of daily-use polystyrene products. *Nanoscale Advances*, 1(3): 1055-1061.
23. Sridharan, S., Kumar, M., Bolan, N. S., Singh, L., Kumar, S., Kumar, R. and You, S. (2021). Are microplastics destabilizing the global network of terrestrial and aquatic ecosystem services?. *Environmental Research*, 198: 111243.
24. Alvim, C. B., Mendoza-Roca, J. A. and Bes-Piá, A. (2020). Wastewater treatment plant as microplastics release source–Quantification and identification techniques. *Journal of Environmental Management*, 255: 109739.
25. Schöpel, B. and Stamminger, R. (2019). A comprehensive literature study on microfibres from washing machines. *Tenside Surfactants Detergents*, 56(2): 94-104.
26. Boucher, J. and Friot, D. (2017). Primary microplastics in the oceans: a global evaluation of sources (Vol. 10). Gland, Switzerland: IUCN.
27. Vassilenko, E., Watkins, M., Chastain, S., Mertens, J., Posacka, A. M., Patankar, S. and Ross, P. S. (2021). Domestic laundry and microfiber pollution: Exploring fiber shedding from consumer apparel textiles. *Plos ONE*, 16(7): e0250346.
28. Acharya, S., Rumi, S. S., Hu, Y. and Abidi, N. (2021). Microfibers from synthetic textiles as a major source of microplastics in the environment: A review. *Textile Research Journal*, 91(17-18): 2136-2156.
29. Özkan, İ. and Gündoğdu, S. (2021). Investigation on the microfiber release under controlled washings from the knitted fabrics produced by recycled and virgin polyester yarns. *The Journal of The Textile Institute*, 112(2): 264-272.
30. De Falco, F., Di Pace, E., Cocca, M. and Avella, M. (2019). The contribution of washing processes of synthetic clothes to microplastic pollution. *Scientific Reports*, 9(1): 6633.
31. Šaravanja, A., Pušić, T. and Dekanić, T. (2022). Microplastics in wastewater by washing polyester fabrics. *Materials*, 15(7): 2683.
32. Cotton, L., Hayward, A. S., Lant, N. J. and Blackburn, R. S. (2020). Improved garment longevity and reduced microfibre release are important sustainability benefits of laundering in colder and quicker washing machine cycles. *Dyes and Pigments*, 177: 108120.
33. Periyasamy, A. P. and Tehrani-Bagha, A. (2022). A review on microplastic emission from textile materials and its reduction techniques. *Polymer Degradation and Stability*, 199: 109901.
34. Long, Z., Pan, Z., Wang, W., Ren, J., Yu, X., Lin, L., ... and Jin, X. (2019). Microplastic abundance, characteristics, and removal in wastewater treatment plants in a coastal city of China. *Water Research*, 155: 255-265.
35. Pereao, O., Opeolu, B. and Fatoki, O. (2020). Microplastics in aquatic environment: Characterization, ecotoxicological effect, implications for ecosystems and developments in South Africa. *Environmental Science and Pollution Research*, 27: 22271-22291.
36. Alrbaihat, M. R., & Abu-Afifeh, Q. (2023). Eco-friendly microplastic removal through physical and chemical techniques: A review. *Annals Advance Chemistry*, 7: 014-024.

37. Turan, N. B., Erkan, H. S. and Engin, G. O. (2021). Microplastics in wastewater treatment plants: Occurrence, fate and identification. *Process Safety and Environmental Protection*, 146: 77-84.
38. Egea-Corbacho, A., Martín-García, A. P., Franco, A. A., Quiroga, J. M., Andreasen, R. R., Jørgensen, M. K. and Christensen, M. L. (2023). Occurrence, identification and removal of microplastics in a Wastewater Treatment Plant compared to an advanced MBR technology: Full-scale pilot plant. *Journal of Environmental Chemical Engineering*, 11(3): 109644.
39. Hidalgo-Crespo, J., Álvarez-Mendoza, C. I., Soto, M. and Amaya-Rivas, J. L. (2022). Quantification and mapping of domestic plastic waste using GIS/GPS approach at the city of Guayaquil. *Procedia CIRP*, 105: 86-91.
40. Zhang, Y., Li, Y., Su, F., Peng, L. and Liu, D. (2022). The life cycle of micro-nano plastics in domestic sewage. *Science of The Total Environment*, 802: 149658.
41. He, P., Chen, L., Shao, L., Zhang, H. and Lü, F. (2019). Municipal solid waste (MSW) landfill: A source of microplastics?-Evidence of microplastics in landfill leachate. *Water Research*, 159: 38-45.
42. Joseph, B., James, J., Kalarikkal, N. and Thomas, S. (2021). Recycling of medical plastics. *Advanced Industrial and Engineering Polymer Research*, 4(3): 199-208.
43. Wang, H., Zhang, Y. and Wang, C. (2019). Surface modification and selective flotation of waste plastics for effective recycling-a review. *Separation and Purification Technology*, 226: 75-94.
44. Werbowski, L. M., Gilbreath, A. N., Munno, K., Zhu, X., Grbic, J., Wu, T., ... and Rochman, C. M. (2021). Urban stormwater runoff: a major pathway for anthropogenic particles, black rubbery fragments, and other types of microplastics to urban receiving waters. *ACS ES&T Water*, 1(6): 1420-1428.
45. Yang, F., Li, D., Zhang, Z., Wen, L., Liu, S., Hu, E., ... and Gao, L. (2022). Characteristics and the potential impact factors of microplastics in wastewater originated from different human activity. *Process Safety and Environmental Protection*, 166: 78-85.
46. Rathi, B. S. and Kumar, P. S. (2021). Application of adsorption process for effective removal of emerging contaminants from water and wastewater. *Environmental Pollution*, 280: 116995.
47. Kehrein, P., Van Loosdrecht, M., Osseweijer, P., Garfí, M., Dewulf, J. and Posada, J. (2020). A critical review of resource recovery from municipal wastewater treatment plants–market supply potentials, technologies and bottlenecks. *Environmental Science: Water Research & Technology*, 6(4): 877-910.
48. Tufail, A., Price, W. E., Mohseni, M., Pramanik, B. K. and Hai, F. I. (2021). A critical review of advanced oxidation processes for emerging trace organic contaminant degradation: Mechanisms, factors, degradation products, and effluent toxicity. *Journal of Water Process Engineering*, 40: 101778.
49. Wang, Z., Sedighi, M. and Lea-Langton, A. (2020). Filtration of microplastic spheres by biochar: removal efficiency and immobilisation mechanisms. *Water Research*, 184: 116165.
50. Enfrin, M., Dumée, L. F. and Lee, J. (2019). Nano/microplastics in water and wastewater treatment processes–origin, impact and potential solutions. *Water Research*, 161: 621-638.
51. Ngo, P. L., Pramanik, B. K., Shah, K. and Roychand, R. (2019). Pathway, classification and removal efficiency of microplastics in wastewater treatment plants. *Environmental Pollution, 255:* 113326.
52. Li, J., Shan, E., Zhao, J., Teng, J. and Wang, Q. (2023). The factors influencing the vertical transport of microplastics in marine environment: A review. *Science of the Total Environment*, 870: 161893.
53. Ahmed, R., Hamid, A. K., Krebsbach, S. A., He, J. and Wang, D. (2022). Critical review of microplastics removal from the environment. *Chemosphere*, 293: 133557.
54. Joo, S. H., Liang, Y., Kim, M., Byun, J. and Choi, H. (2021). Microplastics with adsorbed

contaminants: Mechanisms and Treatment. *Environmental Challenges*, 3: 100042.

55. Liu, X., Yuan, W., Di, M., Li, Z. and Wang, J. (2019). Transfer and fate of microplastics during the conventional activated sludge process in one wastewater treatment plant of China. *Chemical Engineering Journal*, 362: 176-182.
56. Naderi Beni, N., Karimifard, S., Gilley, J., Messer, T., Schmidt, A. and Bartelt-Hunt, S. (2023). Higher concentrations of microplastics in runoff from biosolid-amended croplands than manure-amended croplands. *Communications Earth & Environment*, 4(1): 42.
57. Borthakur, A., Leonard, J., Koutnik, V. S., Ravi, S. and Mohanty, S. K. (2022). Inhalation risks of wind-blown dust from biosolid-applied agricultural lands: Are they enriched with microplastics and PFAS?. *Current Opinion in Environmental Science & Health*, 25: 100309.
58. Ziembowicz, S., Kida, M. and Koszelnik, P. (2023). Elimination of a mixture of microplastics using conventional and detergent-assisted coagulation. *Materials*, 16(11): 4070.
59. Swart, B., Pihlajamäki, A., Chew, Y. J. and Wenk, J. (2022). Microbubble-microplastic interactions in batch air flotation. *Chemical Engineering Journal*, 449: 137866.
60. Scherer, C., Weber, A., Lambert, S. and Wagner, M. (2018). *Interactions of microplastics with freshwater biota* (pp. 153-180). Springer International Publishing.
61. Ziajahromi, S., Neale, P. A., Rintoul, L. and Leusch, F. D. (2017). Wastewater treatment plants as a pathway for microplastics: development of a new approach to sample wastewater-based microplastics. *Water research*, 112: 93-99.
62. Liu, W., Zhang, J., Liu, H., Guo, X., Zhang, X., Yao, X., ... and Zhang, T. (2021). A review of the removal of microplastics in global wastewater treatment plants: Characteristics and mechanisms. *Environment International*, 146: 106277.
63. Magni, S., Binelli, A., Pittura, L., Avio, C. G., Della Torre, C., Parenti, C. C., ... and Regoli, F. (2019). The fate of microplastics in an Italian Wastewater Treatment Plant. *Science of the Total Environment*, 652: 602-610.
64. Li, X., Chen, L., Mei, Q., Dong, B., Dai, X., Ding, G. and Zeng, E. Y. (2018). Microplastics in sewage sludge from the wastewater treatment plants in China. *Water Research*, 142: 75-85.
65. Mohana, A. A., Rahman, M., Sarker, S. K., Haque, N., Gao, L. and Pramanik, B. K. (2022). Nano/microplastics: Fragmentation, interaction with co-existing pollutants and their removal from wastewater using membrane processes. *Chemosphere*, 309: 136682.
66. Krishnan, R. Y., Manikandan, S., Subbaiya, R., Karmegam, N., Kim, W. and Govarthanan, M. (2023). Recent approaches and advanced wastewater treatment technologies for mitigating emerging microplastics contamination–A critical review. *Science of the Total Environment*, 858: 159681.
67. Li, J., Wang, B., Chen, Z., Ma, B. and Chen, J. P. (2021). Ultrafiltration membrane fouling by microplastics with raw water: Behaviors and alleviation methods. *Chemical Engineering Journal*, 410: 128174.
68. Cevallos-Mendoza, J., Amorim, C. G., Rodríguez-Díaz, J. M. and Montenegro, M. D. C. B. (2022). Removal of contaminants from water by membrane filtration: A review. *Membranes*, 12(6): 570.
69. Beshr, S., Moustafa, M., Fayed, M. and Aly, S. (2023). Evaluation of water consumption in rapid sand filters backwashed under varied physical conditions. *Alexandria Engineering Journal*, 64: 601-613.
70. Bayo, J., López-Castellanos, J. and Olmos, S. (2020). Membrane bioreactor and rapid sand filtration for the removal of microplastics in an urban wastewater treatment plant. *Marine Pollution Bulletin*, 156: 111211.
71. Marsono, B. D., Yuniarto, A., Purnomo, A. and Soedjono, E. S. (2022). Comparison performances of microfiltration and rapid sand filter operated in water treatment plant. In *IOP Conference Series: Earth and Environmental Science* (Vol. 1111, No. 1, p. 012048). IOP Publishing.

72. Bäuerlein, P. S., Hofman-Caris, R. C., Pieke, E. N. and Ter Laak, T. L. (2022). Fate of microplastics in the drinking water production. *Water Research*, 221: 118790.
73. Sembiring, E., Fajar, M. and Handajani, M. (2021). Performance of rapid sand filter–single media to remove microplastics. *Water Supply*, 21(5): 2273-2284.
74. Koelmans, A. A., Nor, N. H. M., Hermsen, E., Kooi, M., Mintenig, S. M. and De France, J. (2019). Microplastics in freshwaters and drinking water: Critical review and assessment of data quality. *Water Research*, 155: 410-422.
75. Umar, M., Singdahl-Larsen, C. and Ranneklev, S. B. (2023). Microplastics removal from a plastic recycling industrial wastewater using sand filtration. *Water*, 15(5): 896.
76. Pronk, W., Ding, A., Morgenroth, E., Derlon, N., Desmond, P., Burkhardt, M., ... and Fane, A. G. (2019). Gravity-driven membrane filtration for water and wastewater treatment: A review. *Water Research*, 149: 553-565.

Malaysian Journal of Analytical Sciences (MJAS)
Published by Malaysian Analytical Sciences Society

INSIGHTS INTO THE STRUCTURAL, MORPHOLOGICAL, AND OPTICAL PROPERTIES OF V_2O_5 CATHODE MATERIAL SYNTHESIZED BY SELF-PROPAGATING COMBUSTION METHOD UNDER VARIED ANNEALING TEMPERATURES

(Pembelajaran ke atas Ciri-Ciri Struktur, Morfologi, dan Optik V_2O_5 yang Disintesis Melalui Kaedah Pembakaran yang Menyebar Sendiri di Bawah Pelbagai Suhu Pemanasan)

Mas Fiza Mustafa[1,2], Missha Balqis Shariamin[2], Mohd Sufri Mastuli[2,3], Zurina Osman[4,5], and Annie Maria Mahat[2,3*]

[1]*Faculty of Applied Sciences, Universiti Teknologi MARA, 40450 Shah Alam, Selangor, Malaysia*
[2]*Centre of Foundation Studies, Universiti Teknologi MARA, Cawangan Selangor, Kampus Dengkil, 43800 Dengkil, Selangor, Malaysia*
[3]*Institute of Science, Level 3, Kompleks Inspirasi,Universiti Teknologi MARA, 40450 Shah Alam, Selangor, Malaysia*
[4]*Centre for Ionics Universiti Malaya, Universiti Malaya, 50603 Kuala Lumpur, Malaysia*
[5]*Physics Department, Universiti Malaya, 50603 Kuala Lumpur, Malaysia*

[*]*Corresponding author: anniemaria@uitm.edu.my*

Received: 15 September 2023; Accepted: 10 December 2023; Published: 28 February 2024

Abstract

In this study, we report the novel synthesis of V_2O_5 cathode material utilizing the self-propagating combustion (SPC) method, marking the first-ever successful application of this technique for V_2O_5 production. Nonetheless, a thorough examination of the synthesis of V_2O_5 cathode material is required, with a special emphasis on the impact of annealing temperatures. The insufficient examination of the structural, morphological, and optical properties of V_2O_5 produced by the self-propagating combustion method in the current literature impedes the capacity to enhance its synthesis for application in energy storage devices, catalytic systems, and optoelectronic devices. In order to close this information gap, this study will carefully investigate how different annealing temperatures affect the final V_2O_5 material properties by providing comprehensive insights into the structural, morphological, and optical properties of V_2O_5 at varying annealing temperatures. The thermal profile was studied using Simultaneous Thermal Analysis (STA) providing measurement of multiple thermal properties of the sample as a function of time or temperature. The structural characterization was carried out using X-ray diffraction (XRD) analysis, revealing the crystal structure and phase purity of the synthesized V_2O_5 samples. Field emission scanning electron microscopy (FESEM) was employed to examine the morphological features, including particle size, shape, and surface morphology. Additionally, Energy Dispersive X-ray Spectroscopy (EDX) provides elemental composition to further substantiating the synthesis method's efficacy. The optical properties were investigated through UV-Visible (UV-Vis) spectroscopy, providing information on the bandgap energy and optical absorption behavior of the synthesized V_2O_5. The results revealed that the annealing temperature significantly influenced the

structural, morphological, and optical properties of V_2O_5. With increasing annealing temperature, the crystallinity and phase purity of V_2O_5 improved. The morphological analysis indicated variations in particle size, shape, and surface texture as a function of annealing temperature. Moreover, the optical characterization demonstrated that the annealing process influenced the bandgap energy and optical absorption properties of V_2O_5. In this study, it was found that, the optimum annealing temperature is at 600ºC, which gives a single-phase crystal structure with uniform thickness of nano-sheets like appearance.

Keywords: self-propagating combustion method, annealing temperatures, X-ray diffraction, field emission scanning electron microscopy, UV-Visible spectroscopy

Abstrak

Dalam kajian ini, kami melaporkan sintesis V_2O_5 sebagai bahan katod baru dengan menggunakan kaedah pembakaran penyebaran sendiri (SPC), menjadikan ianya laporan pertama penghasilan V_2O_5 menggunakan kaedah ini. Walau bagaimanapun, kajian menyeluruh sintesis bahan katod V_2O_5 diperlukan, dengan penekanan khusus kepada kesan suhu pemanasan. Penyelidikan yang tidak mencukupi mengenai sifat struktural, morfologi dan optik V_2O_5 yang dihasilkan oleh kaedah pembakaran yang menyebarkan diri dalam kajian semasa, menghalang keupayaan untuk meningkatkan sintesisnya untuk aplikasi dalam peranti penyimpanan tenaga, sistem katalis, dan peranti optoelektronik. Untuk menutup jurang maklumat ini, kajian ini akan mengkaji dengan teliti bagaimana suhu pemanasan yang berbeza mempengaruhi sifat bahan V_2O_5 dengan menyediakan konsepsi yang komprehensif ke atas sifat struktural, morfologi, dan optik V_2O_5 pada suhu pemanasan yang berlainan. Profil haba telah dianalisa menggunakan Analisis Terma Serentak (STA) yang menyediakan pengukuran pelbagai sifat haba sampel sebagai fungsi masa atau suhu. Bagi mengkaji struktur kristal dan fasa asli bahan, analisis pembelauan sinar-X (XRD) telah dijalankan ke atas sampel V_2O_5 yang telah disintesis. Mikroskopi Imbasan Elektron Pancaran Medan (FESEM) digunakan untuk mengkaji ciri-ciri morfologi, termasuk saiz partikel, bentuk, dan morfologi permukaan. Selain itu, Spektroskopi Sinar-X Tenagan Serakan (EDX) menyediakan komposisi elemental untuk lebih membuktikan keberkesanan kaedah sintesis. Ciri-ciri optik telah dipelajari melalui spektroskopi UV-Vis, yang menyediakan maklumat mengenai tenaga jurang dan tingkah laku penyerapan optik V_2O_5 yang disintesis. Hasilnya mendedahkan bahawa suhu pemanasan secara signifikan mempengaruhi sifat struktural, morfologi dan optik V_2O_5. Dengan meningkatnya suhu pemanasan, kristaliniti dan kemurnian fasa V_2O_5 meningkat. Analisis morfologi juga menunjukkan perubahan dalam saiz partikel, bentuk, dan tekstur permukaan. Selain itu, sifat optik menunjukkan bahawa proses pemanasan mempengaruhi tenaga jurang dan sifat penyerapan optik V_2O_5. Dalam kajian ini, ia telah ditemui bahawa, suhu pemanasan optimum adalah pada 600ºC, yang memberikan struktur kristal satu fasa dan morfologi denagn permukaan yang sekata serta ketebalan berbentuk lapisan bersaiz nano yang seragam.

Kata kunci: kaedah pembakaran penyebaran sendiri, suhu pemanasan, pembelauan sinar-X, mikroskopi imbasan elektron pancaran medan, spektroskopi UV-cahaya nampak

Introduction

The need for effective electrical energy storage has arisen because of the increasing demand for cleaner energy and the swift expansion of the global economy [1, 2]. Among the various commercialized technologies, batteries have attracted enormous attention due to their relatively high energy density and long cycle life [3]. Rechargeable lithium-ion batteries (LIBs) have been widely used as the most popular energy storage technology in electronic devices and vehicles [4]. It is widely used in the field of portable energy storage due to its long life, without memory effect and environmental toxicity [5, 6]. Nevertheless, some problems including low safety, high cost and lithium resources shortage still hinder its development for large-scale application [5]. Aluminum ion batteries are viewed as practical substitutes for large-scale energy storage devices due to their high theoretical capacity (2980 mAh g^{-1}, 8063 mAh cm^{-3}), abundance, and safety, with aluminum metal anodes being the primary contributing factor [7, 8]. On the other hand, developing cathode materials *via* intercalation reaction seems challenging due to the high charge density of trivalent aluminum ions. Therefore, in recent years, there have been many reports on the cathode materials of aluminum batteries, including carbon-based materials [9-11], oxides [12, 13], sulfides [14, 15], and selenides [16]. Among these cathode materials, vanadium (V) oxide, also known as V_2O_5, is a widely recognized transitional metal oxide (TMO) due to its layered structure, low toxicity, low

cost, and ability to exhibit multiple oxidation valences (V^{2+}, V^{3+}, V^{4+}, and V^{5+}).

V_2O_5 stands as a prominent cathode material in advanced energy storage systems, due to its exceptional redox properties and high theoretical capacity [17]. Despite its appealing features, V_2O_5 has limitations that hinder its performance in certain applications. For example, the material has poor electronic and ionic conductivities, leading to lower reversible capacity and reduced rate capability [18]. To address these limitations and improve the performance of V_2O_5, researchers are actively exploring various synthesis methods for V_2O_5 nanomaterials. Those methods are including the sol-gel method, hydrothermal synthesis, electro-spinning technique and dispersion method [19]. However, based on our current understanding, no prior attempts have been made to utilize the self-propagating combustion (SPC) method for the synthesis of V_2O_5 cathode material. SPC method has emerged as a good choice due to its simplicity, cost-effectiveness, and potential for precise control over material properties [17]. The low electrical and ionic conductivities of V_2O_5 can be ascribed to its crystal structure and morphology, which can be altered by annealing at various temperatures. By manipulating the annealing temperature, one can exert control over the crystal structure, phase purity, and morphology of V_2O_5, hence influencing its electronic and ionic conductivities [20]. Therefore, in this study, we introduce the SPC method as a novel synthesis approach and emphasizes the importance of annealing temperature variation in tailoring material characteristics. The insights garnered herein not only contribute to the fundamental understanding of V_2O_5, as a cathode material but also hold significant implications for the design and fabrication of high-performance energy storage devices. Simultaneous thermal analysis (STA), X-ray diffraction (XRD), field-emission scanning electron microscopy (FESEM), Energy Dispersive X-ray Spectroscopy (EDX) and Ultraviolet-Visible Spectroscopy (UV-Vis) were used to study the thermal, structural, morphological and optical characteristics of the obtained V_2O_5 cathode materials.

Materials and Methods

Preparation of V_2O_5 material

A self-propagating combustion method was used to prepare vanadium(V) oxide, V_2O_5 nanoparticles. The raw material and fuel are crucial components in combustion process. The weight of each materials used was calculated using stoichiometry method. Citric acid (fuel) and the starting material, ammonium metavanadate, NH_4VO_3 was stirred in 15 ml and 200 ml deionized water respectively before the fuel was poured into the NH_4VO_3 solution. The poured solution was vigorously agitated for 25 minutes on a magnetic stirrer to achieve a homogenous mixture. The solution is held on the hot plate at 300 ºC until combustion occurs, and then the material is calcined in a prepared furnace at different temperatures of 500 ºC, 600 ºC and 700 ºC for 6 hours. The materials were removed after the material is allowed to cool in the furnace in off mode resulting in the production of black powder product.

Thermal analysis

Thermal profile of the precursors was carried out using a simultaneous thermogravimetric analyzer (STA; SETARAM SETSYS Evolution 1750, Caluire, France). It means that the thermogravimetric analysis (TGA) and the differential scanning calorimetry (DSC) were measured simultaneously. In this study, about 10-15 mg of each precursor was heated from 30 °C to 700 °C with a heating rate of 10 °C per minute under air atmosphere. The precursors were placed in alumina crucibles which was suitable for heating to high temperatures.

Characterization

The XRD of the samples was obtained by a diffractometer (PANalytical X'pert PRO) with Cu kα radiation. The morphology of cathodes was characterized *via* FESEM. The EDX was used to characterize the composition of the cathode materials. The optical band gap characteristics of the sample were obtained using UV-Vis spectroscopy.

Results and Discussion

Thermal profile

Figure 1 shows the decomposition behavior of the precursor. There are three weight loss occurring on the TGA profile marked as I, II and III. The first weight loss in region I is around 6.5% at the temperature range of 30 °C to 160 °C accompanied by an exothermic peak that

is attributed to the evaporation of water from the sample surface [21]. NH_4VO_3 began to transform into ammonium vanadate ($(NH_4)_2(V_6O_{16})$) with the escape of NH_3 [22]. The abrupt weight loss of 30.8% from ~200 °C to 430 °C period may correspond to the bound water in the structure [23] and it is related to the exothermic process occur at that point. The third region, between 420 °C and 560 °C relates to weight loss of 27.20%. It is correlated with the high and broad exothermic peak on DSC curve at ~540 °C which indicates the releasing of NH_3, O_2 and H_2O [24]. The endothermic peak at 680 °C was attributed to the recrystallization of V_2O_5 materials physical process, which did not affect the vanadium valence of the final products, in facts it involves breaking and reforming intermolecular bonds [23]. This can be related to the TGA graph, where there is no weight loss in the compound at above 600°C, while the endothermic peak may be due to the structural phase transition of V_2O_5 crystals. Consequently, according to the acquired thermal analysis, all samples were annealed at 500 °C, 600 °C and 700 °C. From here, it was suggested that varying the annealing temperature may lead to distinct material characteristics.

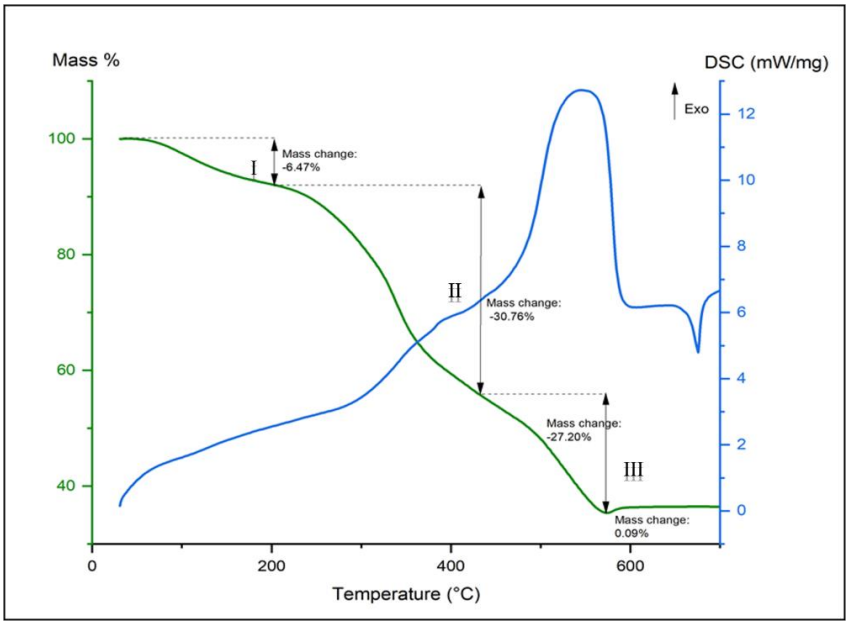

Figure 1. Simultaneous thermogravimetric analyzer (STA) of the V_2O_5 precursor

Structural characterization

Figure 2 displays the XRD patterns of various materials. The annealed sample at a temperature of 500 °C (as shown in Figure 2(a)) exhibits XRD peaks of low intensity, suggesting the existence of orthorhombic and monoclinic crystal structures attributed to vanadium (V) oxide and vanadium (IV) oxide, respectively. The orthorhombic crystal structure of V_2O_5 can be achieved through the process of annealing at temperatures of 600 °C and 700 °C, as depicted in Figure 2(b) and (c) correspondingly. Both samples have a high level of purity and possess an orthorhombic crystal structure system with the Pmmm space group, as validated by the JCPDS reference number 00-041-1426. The augmentation of the annealing temperature results in a corresponding augmentation of the XRD peak intensities. This observation suggests enhancements in the crystallinity of the V_2O_5 material, as well as the production of well-organized crystals. Nevertheless, an abrupt increase in magnitude is noted in the specimen that underwent annealing at a temperature of 700 °C. This increase aligns with the recrystallization peak identified in the STA analysis, which occurs at around 680 °C during the thermogravimetric analysis's stable phase (refer to Figure 1). FESEM micrographs can provide additional evidence to corroborate this condition.

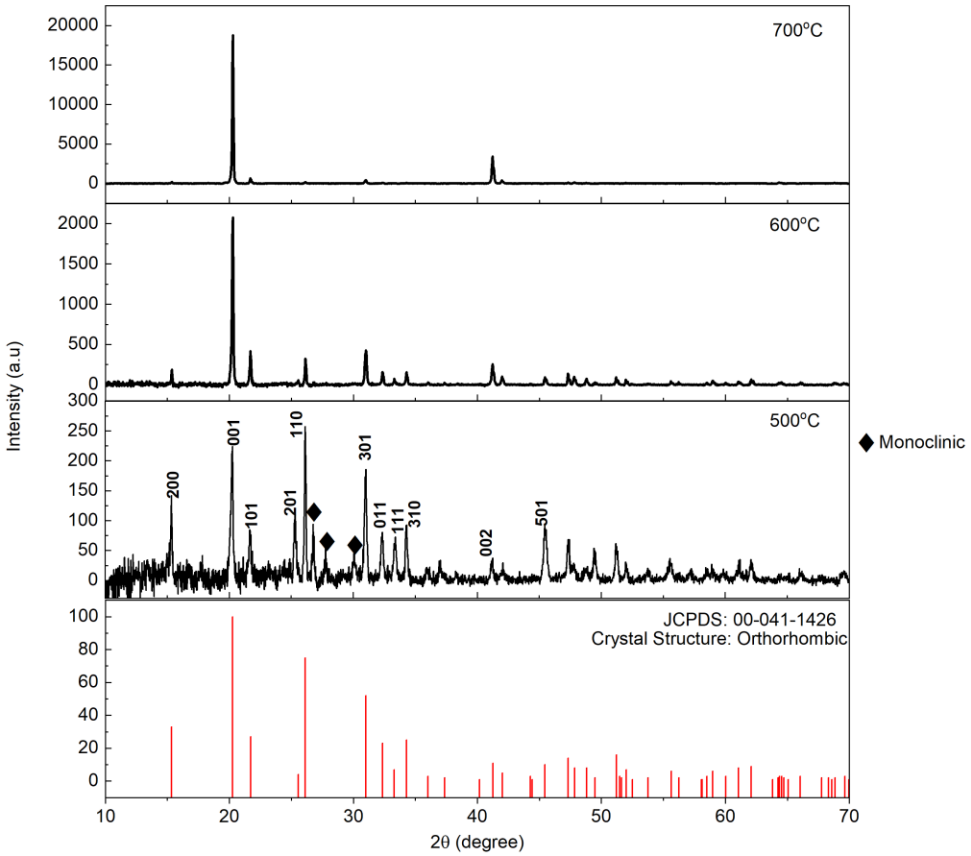

Figure 2 XRD patters of V_2O_5 samples annealed at 500 °C, 600 °C and 700 °C

Morphological characterization

The shape of V_2O_5 at various annealing temperatures is depicted in the FESEM pictures presented in Figure 3(i) and (ii). For the sample annealed at 500 °C, the observed structures exhibit a high degree of agglomeration, forming flake-sheet-like arrangements. These structures possess an average thickness of 196 nm. The flakes have a slender and flat configuration reminiscent of a two-dimensional plane, characterized by a sleek exterior and intermittent protrusions and boundaries. The nano-sheets depicted in sample annealed at 600 °C exhibit a homogeneous thickness spanning 48 nm, accompanied by a regular arrangement of layers while sample annealed at 700 °C shows that the compound displayed prominent bulky flakes with a sheet-like structure. This observation suggests that the compound maintained a constant flaky sheet shape as the annealing temperature was raised. Significantly, the flaky sheets exhibited an increase in size while retaining their characteristic layered structure, as depicted in Figure 3(ii) under a magnification of 50,000x. The observed morphology aligns with the findings of the XRD investigation, which suggests an increase in crystallinity with elevated annealing temperatures. The structures' large aspect ratio is believed to contribute to their possibly improved characteristics in the context of battery applications. The reduced thickness of micro- and nano-sheets facilitates shorter diffusion paths inside the electrode material, leading to enhanced ion transport and improved utilization of the active material. Consequently, this enables faster charge and discharge cycles. The utilization of this data can facilitate the optimization of the annealing temperature to achieve the desired V_2O_5 compound, which serves as an optimal cathode material for usage in aluminum batteries. The compositional atomic percent of the elements obtained by EDX are shown in Table 1 with percentage difference less than ~4%.

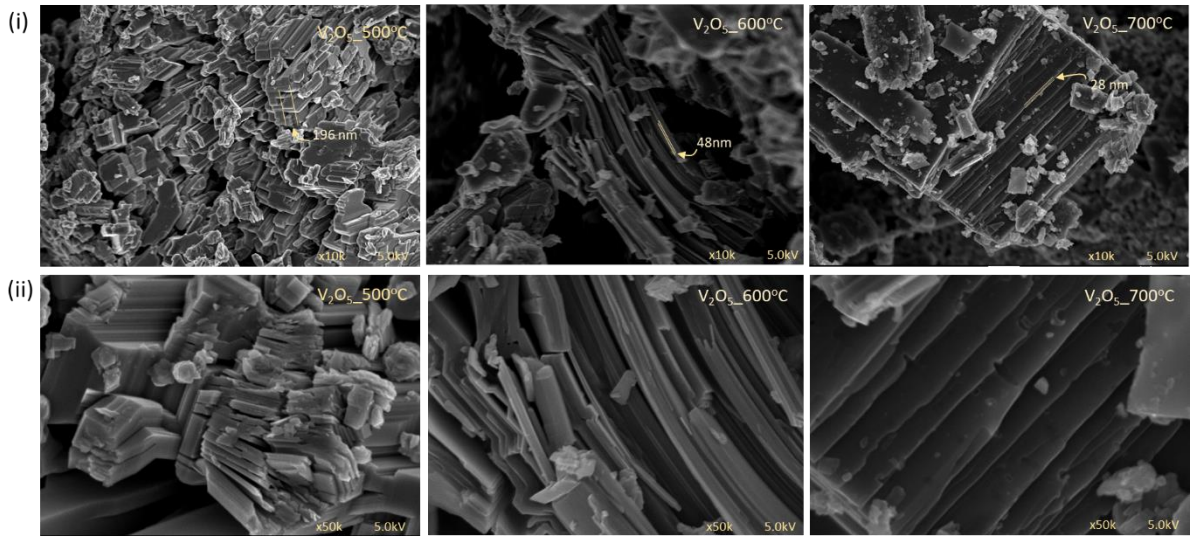

Figure 3. (i) FESEM images of pure V_2O_5 at 10K magnification with annealing temperature of 500ºC, 600ºC and 700ºC and (ii) 50K magnification for each sample

Table 1 Compositional distribution from EDX of the constituent elements for the V_2O_5 at different annealing temperatures.

		Experimental Atomic %					
Elements	**Theoretical Atomic %**	**V_2O_5_ 500ºC**	**% Difference**	**V_2O_5_ 600ºC**	**% Difference**	**V_2O_5_ 700ºC**	**% Difference**
Vanadium	28.6	27.5	3.9	29.7	3.8	29.0	1.4
Oxygen	71.4	72.5	1.5	70.3	1.6	71.0	0.6

Optical characterization

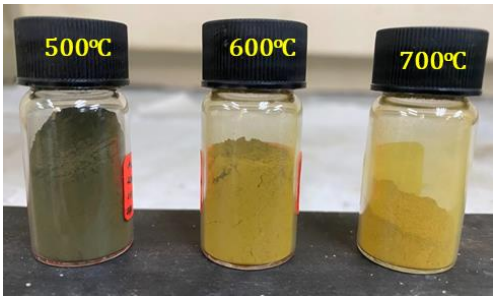

Figure 4. V_2O_5 samples at different annealing temperature

As in Figure 4, the samples of synthesized V_2O_5 were observed at different annealing temperatures. An interesting observation was made as the annealing temperature increased, the colour of the synthesized V_2O_5 became lighter. For optical band gap evaluation, reflectance spectra of all samples were obtained by UV-Vis spectroscopy and further analysed using the Tauc equation (equation (1) [25],

$$(\alpha h\nu) = A(h\nu - Eg)^x \quad (1)$$

where α is the absorption coefficient of the material at a certain value of the wavelength λ, h is the Planck's constant, A is a proportionality constant, υ is the frequency of light, Eg is the band gap energy and x = 1⁄2 (for direct transition mode materials). The absorption coefficient is evaluated using,

$$\alpha = k \ln \left(\frac{R_{max} - R_{min}}{R - R_{min}}\right) \quad (2)$$

where k is a constant, R_{max} is the maximum reflectance and R_{min} is the minimum reflectance.

Consideration of Eqs. (1) and (2) gives,

$$(\alpha hv)^2 = A'(hv - Eg) \quad (3)$$

where A′ is a constant. From Eq. (3), a Tauc plot can be drawn of $(\alpha hv)^2$ versus hv. The band gap energy is obtained by extrapolation of the linear part and the point that meets the abscissa will give the value of the band gap energy of the material. Upon careful analysis using Tauc plots (Figure 5), it was evident that the band gap values experienced a significant reduction as the annealing temperature increased. Specifically, the band gap values were measured to be 3.896 eV, 3.878 eV, and 3.870 eV for annealing temperatures of 500°C, 600°C, and 700°C respectively. These changes indicate the alterations in the electronic structure of the material. Specifically, it points towards a reduction in the band gap [26]. This correlation between the colour of the sample and the band gap is in line with expectations. Lighter colours are associated with lower band gap values. This is because a smaller band gap implies that less energy is required to promote an electron from the valence band to the conduction band. As a result, the material absorbs and reflects light differently, giving rise to the observed colour change. In battery operation, band gap governs charge transfer mechanisms, dictating the efficiency with which charge carriers the electrons and holes are generated and facilitating smooth charge transfer during electrochemical reactions. Moreover, the band gap significantly influences the voltage and energy density of the battery, ensuring compatibility with other components for optimal performance. Furthermore, identifying a suitable band gap contributes to cycling stability, offering insights into the material's durability over numerous charge-discharge cycles, a pivotal factor for the battery's long-term reliability [27].

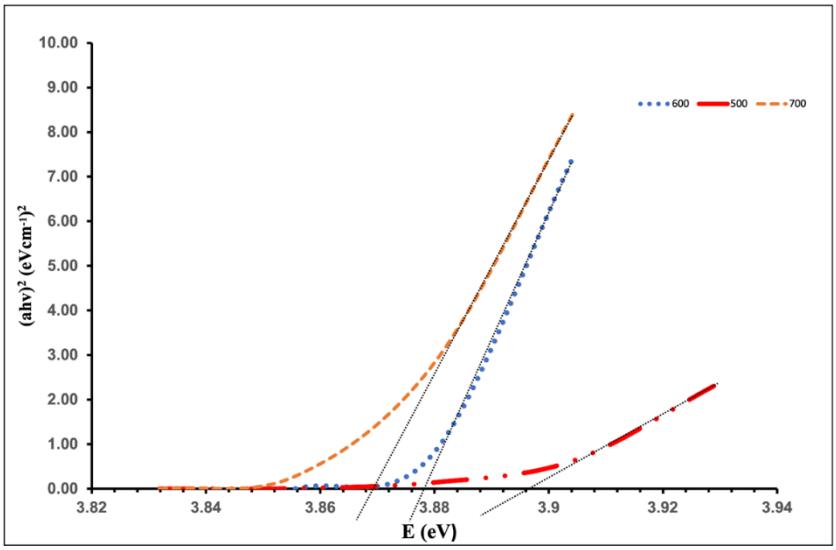

Figure 5. Tauc plots for V_2O_5 powder annealed at 500 ºC, 600 ºC and 700 ºC

Conclusion

Structural, morphological and optical properties of single-phase V_2O_5 powder are synthesized by self-propagating combustion method. XRD results show that the compound is polycrystalline with orthorhombic symmetry structure. After the annealing process, the crystallization was improved by increasing temperature. FESEM images show a highly agglomerated flakes-sheet-like structure for sample annealed at 500 ºC. All flakes exhibited thin and planar structure that resemble a two-dimensional sheet. The surface of the flakes was found to be predominantly smooth, with occasional ridges and edge. Upon increased annealing temperature, the compound exhibited consistent flaky sheet morphology. The flaky sheets grew in dimensions while maintaining their distinct layered appearance as well as

the ridges and edges. This is consistent with the XRD analysis where it is profound that the crystallinity was enhanced at higher annealing temperature. Sample anneals at 600 ^oC gives a single-phase orthorhombic crystal structure with uniform thickness of nano-sheets like appearance and smooth surface suggesting that the optimum annealing temperature was at 600 ^oC. Optically, it was found that lighter colors of V_2O_5 powder associated with lower band gap values. The observed changes in color and band gap values provide valuable insights into how annealing temperatures influence the electronic properties of the synthesized V_2O_5, which in turn can have significant implications for its performance as a cathode material in energy storage applications.

Acknowledgement

This work is financially supported by Special Research Grant (GPK) from Universiti Teknologi MARA (Grant No.600-RMC/GPK 5/3 (140/2020).

References

1. Liu, J., Li, Z., Huo, X. and Li, J. (2019). Nanosphere-rod-like Co_3O_4 as high performance cathode material for aluminium ion batteries. *Journal of Power Sources*, 422: 49-56.
2. Gu, S., Wang, H., Wu, C., Bai, Y., Li, H. and Wu, F. (2017). Confirming reversible Al^{3+} storage mechanism through intercalation of Al^{3+} into V_2O_5 nanowires in a rechargeable aluminum battery. *Energy Storage Materials*, 6: 9-17.
3. Zhang, W., Lu, J. and Guo, Z. (2021). Challenges and future perspectives on sodium and potassium ion batteries for grid-scale energy storage. *Materials Today*, 50: 400-417.
4. Zhou, Y., Chen, F., Arandiyan, H., Guan, P., Liu, Y., Wang, Y., Zhou, C., Wang, D. and Chu, D. (2021). Oxide-based cathode materials for rechargeable zinc ion batteries: Progresses and challenges. *Journal of Energy Chemistry*, 57: 516-542.
5. Zhou, Q., Zheng, Y., Wang, D., Lian, Y., Ban, C. and Zhou, J. (2020). Cathode materials in non-aqueous aluminum-ion batteries: Progress and challenges. *Ceramics International*, 46 (17): 26454-26465.
6. Hwang, J. Y., Myung, S. T. and Sun, Y. K. (2017). Sodium-ion batteries: Present and future. *Royal Society of Chemistry*, 46(12): 3529-3614.
7. Mori, T., Orikasa, Y., Nakanishi, K., Kezheng, C., Hattori, M., Ohta, T. and Uchimoto, Y. (2016). Discharge charge reaction mechanisms of FeS_2 cathode material for aluminum rechargeable batteries at 55^oC. *J Power Sources*, 313: 9-14.
8. Li, J., Luo, W., Zhang, Z., Li, F., Chao, Z. and Fan, J. (2023). ZnSe/$SnSe_2$ hollow microcubes as cathode for high performance aluminum ion batteries. *Journal of Colloid and Interface Science*, 639: 124-132.
9. Debnath, S., Horscheck-Diaz, M., Searles, D. J. and Hankel, M. (2021). Carbon nitrides as cathode materials for aluminium ion batteries. *Carbon,* 183: 546-559.
10. Yang, X., Chen, M., Chai, L., Zhang, C., Zhang, W. and Li, Z. (2022). High-performance carbon-coated hollow nanocube ZnSe as cathode material for aluminum batteries. *Journal of Alloys and Compounds*, 920: 166006.
11. Mączka, M., Mosiałek, M. and Pasierb, P. (2022). Carbon tungsten oxide composite cathode materials for aluminum-ion batteries. *Electrochimica Acta*, 424: 140606.
12. Lahan, H. and Das, S. K. (2019). Al^{3+} ion intercalation in MoO_3 for aqueous aluminum-ion battery. *Journal of Power Sources*, 413: 134-138.
13. Li, Z., Li, J. and Kang, F. (2019). 3D hierarchical AlV_3O_9 microspheres as a cathode material for rechargeable aluminum-ion batteries. *Electrochimica Acta*, 298: 288-296.
14. Hu, Y., Sun, D., Luo, B. and Wang, L. (2019). Recent progress and future trends of aluminum batteries. *Energy Technology*, 7(1): 86-106.
15. Zhuang, R., Huang, Z., Wang,S., Qiao, J., Wu, J. C. and Yang, J. (2021). Binder-free cobalt sulfide @ carbon nanofibers composite films as cathode for rechargeable aluminum-ion batteries. *Chemical Engineering Journal*, 409: 128235.
16. Li, Z., Lv, W., Wu, G. and Zhang, W. (2021). Rhombic dodecahedron hetero-structure Zn/Co–Se @ C as cathode material for aluminum batteries with excellent electrochemical performance. *Journal of Power Sources*, 511: 230455.

17. Sutrave, S., Konda, S., Velpula, D., Volety, S. A., Ravula, S. R., Chidurala, S. C. and Tumma, B. N. (2022). A simple solution combustion method for the synthesis of V_2O_5 nanostructures for supercapacitor applications. *Applied Surface Science Advances*, 12: 100331.
18. Wu, S., Liu, S., Hu, L. and Chen, S. (2021). Constructing electron pathways by graphene oxide for V_2O_5 nanoparticles in ultrahigh-performance and fast charging aqueous zinc ion batteries. *Journal of Alloys Compounds*, 878: 160324.
19. Zeng, M., Yin, H. and Yu, K. (2012). Synthesis of V_2O_5 nanostructures with various morphologies and their electrochemical and field-emission properties. *Chemical Engineering Journal*, 188: 64-70.
20. Lin, T. C., Jheng, B. J., Yen, H. M. and Huang, W. C. (2022). Thermal annealing effects of V_2O_5 thin film as an ionic storage layer for electrochromic application. *Materials*, 15(13): 4598.
21. Li, Z., Liu, G., Guo, M., Ding, L. X., Wang, S. and Wang, H. (2015). Electrospun porous vanadium pentoxide nanotubes as a high-performance cathode material for lithium-ion batteries. *Electrochimica Acta*, 173: 131138.
22. Zhang, T. and Li, Q. (2022). The fabrication of V_2O_3 by using NH_4VO_3 as vanadium source without extra reductant under sealed condition. *Journal of Solid State Chemistry*, 315: 123473.
23. Yilmaz, E and Sonmez, M. S. (2019). The Influence of process parameters on the chemical and structural properties of solution combustion prepared vanadium pentoxide. *Material Letters*, 261: 127095.
24. Zhang, T. and Li, Q. (2022). Facile fabrication of VO_2(M) by thermolysis of ammonium metavanadate (NH_4VO_3) under sealed condition. *Journal of Solid State Chemistry*, 311: 123117.
25. Kamarulzaman, N., Mahat, A. M., Badar, N. and Zhao, C. Z. (2018). Structural and band gaps studies of novel $Al_{2-x}Hf_xO_3$ materials toward MOS applications. *Material Chemistry and Physics*, 216: 237-242.
26. Li, X. F., Cheng, S. L., Wang, R., Yan, Q., Wang, B., Sun, Y., Yan, H., Zhao, Q. and Xin. Y. (2023). Design of novel two-dimensional single-phase chiral phononic crystal assembly structures and study of bandgap mechanism. *Results in Physics*, 48: 106431.
27. Momeni, M., Mashhour, H. Y. and . Kalantarian, M. M. (2019). New approaches to consider electrical properties, band gaps and rate capability of same-structured cathode materials using density of states diagrams: Layered oxides as a case study. *Journal of Alloys and Compounds*, 787: 738-743.

Malaysian Journal of Analytical Sciences (MJAS)
Published by Malaysian Analytical Sciences Society

SIZE AND ORGAN-SPECIFIC HEAVY METAL ACCUMULATION PATTERNS IN LONGTAIL TUNA (*Thunnus tonggol*) FROM TERENGGANU

(Saiz dan Organ-Khusus Corak Pengumpulan Logam Berat dalam Ikan Aya Hitam (*Thunnus tonggol*) dari Terengganu)

Norhazirah Abd Aziz[1], Adiana Ghazali[1,2], Sim Siong Fong[3], Nurul Izzah Ahmad[4], and Ong Meng Chuan[1,2,5]*

[1]*Faculty of Science and Marine Environment, Universiti Malaysia Terengganu, 21030 Kuala Nerus, Terengganu, Malaysia*

[2]*Ocean Pollution and Ecotoxicology (OPEC) Research Group, Universiti Malaysia Terengganu, 21030 Kuala Nerus, Terengganu, Malaysia*

[3]*Faculty of Resource Science and Technology, Universiti Malaysia Sarawak, 94300 Kota Samarahan, Sarawak, Malaysia*

[4]*Environmental Health Research Centre (EHRC), Institute for Medical Research, Setia Alam, Malaysia*

[5]*Institute of Oceanography and Environment, Universiti Malaysia Terengganu, 21030 Kuala Nerus, Terengganu, Malaysia*

**Corresponding author: ong@umt.edu.my*

Received: 15 September 2023; Accepted: 10 December 2023; Published: 28 February 2024

Abstract

Longtail tuna, *Thunnus tonggol*, belongs to the *Scrombidae* family and is commonly served in special Terengganu delicacies, such as in *Nasi Dagang* gravy. Primarily, the predator fish is found in shallow waters. The Terengganu state is located on the east coast of Peninsular Malaysia, where the oil and gas industry is a primary economic bolster. The rapid urbanisation, large-scale developments, and tourist attraction in the area might contribute to the heavy metal pollution in Terengganu waters. The present study was conducted to determine the concentration of six heavy metals, such as copper (Cu), zinc (Zn), cadmium (Cd), lead (Pb), arsenic (As), and mercury (Hg) in longtail tuna muscle, gills, liver, and stomach, by employing inductively coupled plasma-mass spectrometry (ICP-MS). The highest concentration of Cu, Cd, and Pb was recorded in the liver. The muscle samples revealed the highest As and Hg concentrations, while the gills documented the maximum Zn concentration. The results also revealed that the heavy metals possessed a significant positive relationship with the tuna size (p <0.05). For instance, Hg demonstrated a strong positive association with fish size, recording a 0.577 r-value. Conversely, the longtail tuna samples indicated apparent growth dilution effects for Cu and Pb, proved by the negative correlations between their concentrations and the fish length. This study successfully outlined comprehensive approaches to better understand the controlling factors, including fish size and targeted organs in determining the concentration of heavy metals in longtail tuna.

Keywords: heavy metal, inductively coupled plasma-mass spectrometry, pollution, South China Sea, *Thunnus tonggol*

Abstrak

Ikan Aya hitam, *Thunnus tonggol*, dikategorikan dalam keluarga *Scrombidae* dan lazimnya dihidangkan sebagai hidangan istimewa di Terengganu seperti dalam kuah Nasi Dagang. Lazimnya, spesis pemangsa ini dijumpai di kawasan air cetek. Terengganu terletak di Pantai Timur Semenanjung Malaysia yang mana industri minyak dan gas merupakan penyumbang ekonomi utama. Pembandaran yang pesat, pembangunan berskala besar, dan tarikan pelancongan di negeri tersebut mungkin menjadi antara punca pencemaran logam berat dalam perairan Terengganu. Kajian ini dijalankan untuk menentukan kepekatan enam logam berat; kuprum (Cu), zink (Zn), kadmium (Cd), plumbum (Pb), arsenik (As) dan merkuri (Hg) di dalam isi, insang, hati, dan perut ikan

Aya hitam menggunakan ICP-MS. Keputusan menujukkan bahawa kepekatan Cu, Cd dan Pb paling tinggi dicatatkan di dalam hati. Isi ikan merekodkan kepekatan As dan Hg paling tinggi, manakala insang mencatatkan kepekatan Zn yang paling tinggi. Keputusan kajian ini juga menunjukkan bahawa semua logam berat mempunyai hubungan positif yang ketara dengan saiz ikan Aya hitam (p <0.05). Contohnya, Hg mempunyai hubungan positif yang kukuh dengan saiz ikan dengan nilai r ialah 0.577. Sebaliknya, ikan Aya hitam menunjukkan kesan pencairan pertumbuhan untuk Cu dan Pb dengan hubungan negatif antara kepekatan logam berat dengan saiz ikan. Kajian ini telah Berjaya menunjukkan pendekatan menyeluruh dan kefahaman yang lebih mendalam terhadap faktor-faktor yang mempengaruhi kepekatan logam berat di dalam ikan Aya hitam, termasukalah saiz ikan dan organ sasaran.

Kata kunci: logam berat, spektroskopi jisim- plasma gadingan aruhan, pencemaran, laut China Selatan, *Thunnus tonggol*

Introduction

Recently, heavy metal pollution has attracted global attention. Uncontrolled heavy metal contamination could pose critical threats to ecosystems and detrimental health impacts on humans. Increasing levels of heavy metal effluents in marine environments from several anthropogenic sources, such as industrial activities, domestic sewage, and agriculture decreased the quality of fish and other aquatic organisms. Moreover, the growing number of vehicles and metal leachings from various sources, including landfills, waste dumps, and runoffs, could contribute to the increasing heavy metal concentrations in marine environments, which might harm marine life organisms and the ecosystem as a whole [1].

Metals could bioaccumulate and biomagnify in food chains and food webs, posing risks to aquatic organisms and human health [2, 3]. Heavy metals also damage multiple organs, even at low exposure concentrations. Fish in metal-polluted environments could be exposed to metals through food chains or via uptake from contaminated water. The introduction of heavy metals into fish organs is predominantly through adsorption and absorption, hence the accumulation rate is defined by the uptake and depuration rates [4].

In Terengganu, longtail tuna, locally known as *ikan Aya hitam* (*Thunnus tonggol*), is one of the most popular fish. The fish is commonly served in special delicacies, including the gravies for *Nasi Dagang* and *Nasi Lemak* and as *ikan singgang*. A survey documented that the Terengganu locals consumed approximately 437.4 g/person of longtail tuna weekly [5], which constitutes 62.49 g of their daily intake. The consumption rate was slightly higher than the average amount of fish consumed by other Malaysians in 2009 at 60.0 kg/person/day [6].

Longtail tuna is a species belonging to the *Scomberoidae* family and the *Thunnus* genus. The fish could reach a maximum total length of 142 cm and is the second smallest of eight *Thunnus* species [7]. The longtail tuna has a relatively slower growth rate than other tuna species. The species is also considered a suitable indicator of environmental pollution by wastewater, microplastic, or heavy metals as they reportedly accumulate higher concentrations of heavy metals [8, 9].

Heavy metal concentrations in longtail tuna could indicate exposure time and the metal contents in the sediments and water columns of the areas from which the fish are sourced. The size of the tuna emulates the exposure period to the contaminated water. At the same time, the concentrations of heavy metals in their organs allow health condition assessments of the area from which they were collected. This study emphasised the relationship between the accumulation of heavy metals and the size of the longtail tuna and targeted organs.

Materials and Methods

Sampling area

The longtail tuna, *Thunnus tonggol*, samples employed in this study were bought from local fishermen of vessel Class B operating in Kuala Terengganu waters (see Figure 1). The specimens were purchased from the fishermen on the same day of capture and promptly brought to the laboratory on ice before being dissected (see Figure 2).

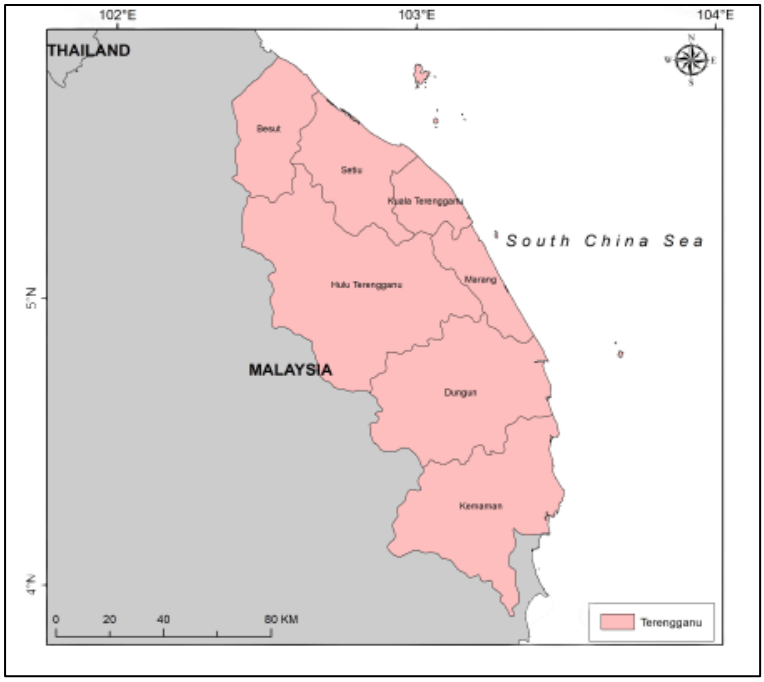

Figure 1. The longtail tuna samples were caught in Kuala Terengganu waters and landed at Lembaga Kemajuan Ikan Malaysia (LKIM) Complex, Pulau Kambing, Kuala Terengganu

Figure 2. The longtail tuna (*Thunnus tonggol*), or locally known as *ikan Aya*, *ikan kayu*, or *ikan tongkol hitam* in Malaysia

Sample collection and preparation

The present study obtained 75 longtail tuna specimens from fishermen before measuring and recording the total length and weight of the samples (see Table 1). Subsequently, the gills, liver, stomach, and muscles were dissected with clean ceramic equipment (see Figure 3). The tissue samples were oven-dried at 60°C for three days or until the samples recorded a constant weight. The dried specimens were then homogenised with mortar and pestle before digestion.

Table 1. The total length and weight ranges of the longtail tuna samples

Location	***n***	**Total length (cm)**	**Total weight (g)**
Terengganu waters	75	21.1–49.5	339–1537

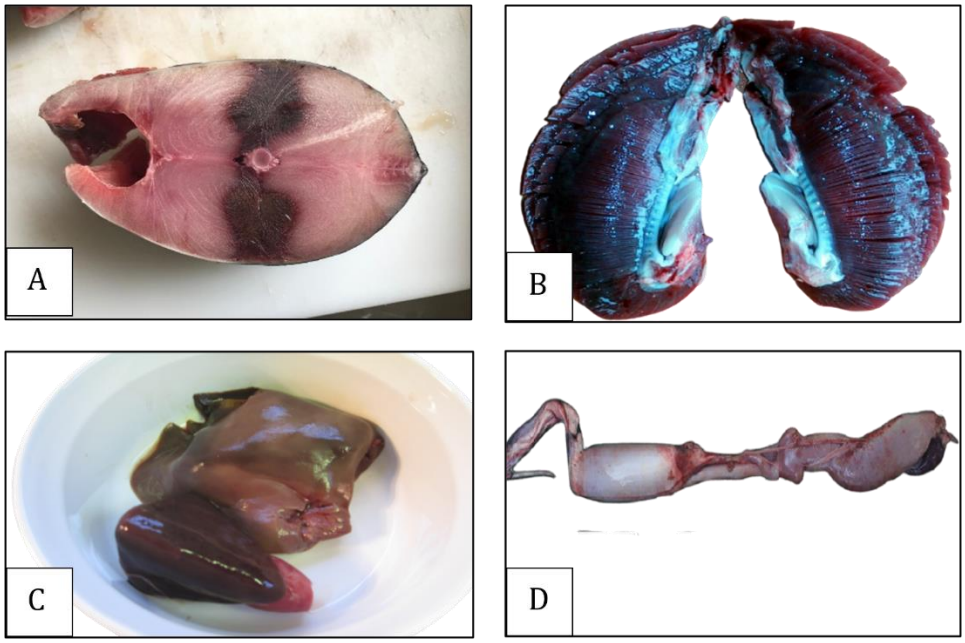

Figure 3. The A: muscle, B: gills, C: liver, and D: stomach samples of the longtail tuna

Samples digestion and heavy metal detection

During the digestion process conducted in this study, 0.05 g of the homogenised dried sample was weighed and mixed with 1.5 mL of Suprapur nitric acid (HNO_3; Merck KGaA, Germany) in an acid-washed Teflon beaker. The Teflon beaker was closed with a cap in a Teflon bomb before being placed into an oven for 8 h at 100 °C to allow complete digestion of the samples [10-12]. The digested samples were cooled to room temperature, transferred into centrifuge tubes, and diluted with deionised water up to 10 mL. Finally, the samples were stored at under 4 °C before selected metal element (Cu, Zn, Cd, Pb, As, and Hg) measurements with inductively coupled plasma-mass spectrometry (ICP-MS) (ELAN 9000) [13].

The standard reference material employed in this study, Dolt-4 Fish Liver SRM 1946 (National Research Council Canada), and blank specimens were digested following a procedure similar to the longtail specimens. The blank samples were prepared with the Suprapur HNO_3 without adding the fish samples. The standard solutions utilised in the present study were yielded via mixing the Suprapur HNO_3 with 0.05 g of DOLT-4 fish liver [14]. The current study constructed the standard to enhance confidence in the levels of heavy metals determined in the longtail tuna samples evaluated.

Statistical analysis

A Shapiro-Wilk (p-value <0.05) normality assessment is conducted to assess the distribution of data before constructing reference intervals and variables. Normality evaluations are required for accurate and reliable conclusions. Generally, non-normally distributed data are subjected to non-parametric assessments. This study applied Friedman and Spearmank's rank, which are non-parametric evaluations, based on the variables involved.

Heavy metal concentrations in the muscle, gills, liver, and stomach of the longtail tuna samples

The present study obtained non-normally distributed data. Accordingly, a Friedman evaluation, which is a non-parametric assessment, was conducted to determine the differences between the independent groups (muscle, gills, liver and stomach) when the dependent criterion (heavy metal concentration) was measured as a continuous parameter (ratio). The employment of the Friedman evaluation was appropriate for the present study, as the concentration of the heavy metals was measured in triplicates or more. The variables also recorded a significant difference when the p-value was under 0.05.

The selected heavy metal concentrations in longtail tuna of different sizes

The data in the present study did not assume normality. Consequently, a non-parametric linear correlation analysis, Spearman's rank, was applied to determine the strength and direction of the associations between two ranked variables: the size of the tuna samples (independent variable) and the concentration of the heavy metals (dependent variable) detected. The non-parametric evaluation was employed as two parameters in this study were continuous (ratio). The Spearman's rank assessment was also utilised to determine the strength of following monotonic relationships.

(i) Increasing longtail tuna size improves the concentration of heavy metals.
(ii) Improving longtail tuna size decreases the concentration of heavy metals.

The Spearman's correlation coefficient, r_s, which might be between +1 and −1, were defined as follows.

(i) A +1 r_s indicates a perfect association of ranks
(ii) A zero r_s zero denotes no association between ranks
(iii) A −1 n r_s demonstrates a perfect negative association of ranks

Results and Discussion

Heavy metal contents in the muscle and target organs of the longtail tuna from Terengganu waters

Heavy metal concentrations (Cu, Zn, Cd, Pb, As, and Hg) in the muscle, gills, stomach, and liver of the longtail tuna (*Thunnus tonggol*) specimens collected caught in Terengganu waters are listed in Table 2. The heavy metals were statistically significant (*p*-value <0.05) to the tissues of the longtail tuna samples, including the muscle, gills, liver, and stomach.

Based on the results, the muscle and organ samples recorded variations in the levels of heavy metal accumulated. For example, the muscle tissues recorded the highest accumulation of As and Hg than the other metals, while Zn demonstrated a higher tendency to accumulate in the gills. On the other hand, Cu, Cd, and Pb were highly concentrated in the liver.

Table 2. The average concentration of heavy metals detected in the muscle, gills, stomach, and liver of the longtail tuna (*Thunnus tonggol*) samples

	The Average Concentration of Heavy Metals (mg/kg) Dry Weight			
Metal	**Muscle**	**Gills**	**Stomach**	**Liver**
Copper	4.46 ± 6.67	1.98 ± 1.81	4.32 ± 5.32	11.2 ± 7.34
Zinc	13.3 ± 18.6	56.1 ± 71.4	31.4 ± 41.5	32.3 ± 22.2
Cadmium	0.060 ± 0.183	0.086 ± 0.129	0.310 ± 0.384	4.73 ± 5.30
Lead	0.075 ± 0.222	0.076 ± 0.118	0.026 ± 0.022	0.087 ± 0.117
Arsenic	10.5 ± 10.2	2.44 ± 1.41	7.98 ± 5.59	7.54 ± 4.90
Mercury	0.114 ± 0.16	0.020 ± 0.023	0.052 ± 0.048	0.080 ± 0.217

Heavy metals could accumulate in most organs in a fish, including the skin, gills, intestine, and kidneys, which might harm the fish physically and internally [15]. Moreover, even trace amounts of heavy metals could be toxic to fish. Heavy metal toxicity in marine organisms depends on several factors, such as exposition routes, nutritional status of the exposed organism, chemical species, genetics, age, and gender [16, 17]. The direct absorption of heavy metals in fish occurs through water columns, while an indirect route is via food chains. Nevertheless, heavy metal concentration variabilities in fish organs could also be due to the types of tissues and organs, which significantly depend on the concentration of heavy metals in the surrounding waters [18, 19].

Among the six elements evaluated in the present study, Hg and As recorded higher concentrations in fish muscle than the other targeted organs. Previous reports hypothesised that the higher tendency of Hg to accumulate in fish muscle is related to its high affinity

to the thiol groups in amino acids, a protein component in muscle tissues [20-22] also suggested that the metals bioaccumulated in muscle tissues could be linked to the feeding habits of the species, contributing to metal level variations [23]. Large predatory fish, such as longtail tuna, consume numerous smaller fish, accumulating Hg in their muscles. Post-Hg assimilation in fish, the contaminant is distributed throughout the organism via blood and stored in various tissues, specifically the muscles [24]. Similarly, this study recorded the highest As levels in the muscle samples. The observations might be due to its diet since longtail tuna have a high feeding rate and are carnivorous and active predators [25].

Besides food, heavy metals could also be absorbed into fish organs via mechanical captures of suspended hydroxide particles in the gills and chemical ion absorptions via membranes [26, 27]. In this study, Zn recorded the highest concentration in fish gills at 56.1 ± 71.4 mg/kg dry weight. Fish gills consist of epithelial membranes primarily containing mucus-covered phospholipids. The gill surfaces are negatively charged, thus providing potential sites for interactions with positively charged metals [27]. Fish also assimilate metals through ionic exchanges across lipophilic membranes in their gills during respiration [28].

Dural et al. [29] found that the accumulation of heavy metals predominantly occurred in metabolically active tissues, such as gills and the liver. A higher metal accumulation in fish liver correlates with the presence of natural protein binding, known as metallothionein (MTs), which stores the metals to fulfil enzymatic and other metabolic demands in the fish [30]. The MTs are small cysteine-rich proteins that are critical in metal homeostasis and protection against heavy metal toxicity, DNA damage, and oxidative stress [30].

Metalloregulatory processes involve MTs by binding the natural proteins to heavy metals through the thiol groups in their cysteine residues. The MTs have a high affinity for heavy metals, hence possessing the ability to bind to xenobiotic heavy metals to protect against metal toxicity, especially Cd [31]. Furthermore, MTs attaching to physiological heavy metals, such as Cu, enable their participation in regulating cell growth and proliferation and protecting the fish against oxidative stress [32]. The MTs also act as an essential metal store to meet enzymatic and other metabolic demands [33]. Nonetheless, higher toxic element concentrations, including Cd and Pb, could lead to adverse health effects as they compete with calcium (Ca^{2+}) at enzymatic locations [34].

The relationship between the selected heavy metal concentrations and the size of the longtail tuna samples caught in Terengganu waters

Generally, the size of a longtail tuna could affect the heavy metal concentration in its muscles. The length of the longtail tuna is commonly considered the fundamental measure as its probability to change considerably is low [35]. The standard length of a fish is the measurement from its closed mouth to the end of the fleshy part of its body [36].

This study assessed the strength of associations between the variables, which were the size of the specimen and the concentration of heavy metals detected. Resultantly, three relationship strength ranks, low, medium, and strong, were obtained (see Table 3). A linear correlation analysis, the Spearman's rank correlation assessment, was employed in the current study to determine the relationship between heavy metal concentration and the longtail tuna size (standard length).

Table 4 demonstrates the relationship value (*r*) that indicates the strength of the correlation between the parameters evaluated. The *p*-values obtained represent the relationship significance between the variables. *r*-values approaching 1 indicated the crucial role of size and strong correlation with heavy metal accumulation.

Table 3. The *r*- and *r* squared (R^2)-values of the linear correlation between the longtail tuna size and the heavy metal concentration

***r*-value**	**R^2-value**	**Indication**
0.1–0.29	0.01–0.084	Low relationship association
0.3–0.49	0.09–0.24	Medium relationship association
0.5–1.0	0.25–1.0	Strong relationship association

Table 4. The Spearman's rank correlation coefficient (*r)* and significance levels (*p*) of the association between heavy metal concentrations in the muscle of the longtail tuna and their size

Element	**Muscle**	
	***r*-value**	***p*-value**
Cu	−0.435	0.000*
Zn	0.353	0.000*
Cd	0.237	0.001*
Pb	−0.192	0.006*
As	0.469	0.000*
Hg	0.577	0.000*

In this study, positive relationships were observed between the fish size and metal levels. Nevertheless, negative associations were demonstrated by Cu and Pb with the longtail tuna muscle samples. The results paralleled a report that documented positive correlations between the size of *Branchiostoma belcheri* with the concentration of Zn, Hg, and Cd [37]. Farkas et al. [32] also found a positive correlation in Hg, Cu, and Zn with the size of *Abramis brama* L. In another report, fish length was positively associated with the concentrations of Cr, Cu, Fe, and Pb but recorded a negative relationship with Cd, Cu, Cr and Pb levels [38].

Typically, increasing fish size reflects the age of the fish [30]. Heavy metal concentration assessments of marine fish from the Oman Gulf found that Hg levels increased with the age and size of the fish [39]. Douben et al. [40] suggested that metal accumulation in fish reaches a steady state after a certain age. Nonetheless, if metal concentrations in the surrounding water are higher than the capacities of growth associated-tissues and lowered metabolic activities in older (larger) organisms, it might not affect the dilution of the metal levels in the fish. Thus, continued metal accumulation might occur, and a positive relationship could be observed. Conversely, the significant negative relationship between Cu and longtail tuna size documented in this study could be due to the slow uptake rates of Cu in muscles compared to other tissue [41]. Furthermore, Cu elimination is reportedly efficient in muscle tissues [41].

Heavy metal concentration could also be affected by environmental contamination and exposure duration [42, 43]. Therefore, larger or older longtail tunas are expected to have accumulated higher metal concentrations than their smaller or younger counterparts. Since longtail tuna is a predator fish, rising heavy metal levels with increasing fish size could also be related to the greater consumption of contaminated prey from higher trophic levels [44].

Conclusion

The concentration of heavy metals in the longtail tuna fish specimens assessed in this study varied significantly. The differences were not only attributable to the size of the specimen but also to the targeted organs. The functions and properties of the organs, such as the presence of natural protein binding, metallothioneins, in fish liver, also influenced the remarkable ability of the organs to absorb more heavy metals. Heavy metal concentrations in the environment, such as sediment and the surrounding water, also affect heavy metal contamination degrees in fish. Nevertheless, the heavy metal levels in the areas were

not measured in the current study.

The findings reported in this study provided the current status of heavy metal contents in longtail tuna from Terengganu waters. The data could assist the Malaysian Environmental Department in evaluating, monitoring, and controlling metal pollutant discharges into marine environments. The information also documents the quality of longtail tuna, which could be beneficial to the Department of Fishery Malaysia (DOF) in enhancing the quality of seafood sources.

Acknowledgement

The present study research was conducted with funding from the Ministry of Higher Education under the Fundamental Research Grant Scheme (FRGS) FRGS/1/2020/WAB05/UMT/02/5. The authors wish to thank the anonymous reviewers for their time and effort and constructive recommendations that enhanced the value of this manuscript. The authors would also like to express appreciation to the staff of Oceanography Laboratory, Faculty of Science and Marine Environment, for their invaluable assistance and the facilities provided to conduct the study. Additionally, the authors are grateful to Mr. Joseph Bidai from the Institute of Oceanography and Environment for supplying the ICP-MS to detect the samples.

References

1. Briffa, J., Sinagra, E. and Blundell, R. (2020). Heavy metal pollution in the environment and their toxicological effects on human. *Heliyon*, 6: e04691
2. Ofukany, A. F., Wassenaar, L. I., Bond, A. L. and Hobson, K. A. (2014). Defining fish community structure in Lake Winnipeg using stable isotopes (ð13C, ð15N, ð34S): Implications for monitoring ecological responses and trophodynamics of mercury and other trace elements. *Science of the Total Environment,* 497: 239-249.
3. Ali, H. and Khan, E. (2019). Environmental chemistry and ecotoxicology of hazardous heavy metals: Environmental persistence, toxicity and bioaccumulation. *Journal of Chemistry*, 2019: 6730305.
4. Annabi, A., Said, K. and Messoudi, I. (2013). Cadmium: bioaccumulation, histopathology and detoxifying mechanism in fish. *American Journal of Research Communication.*,1: 60-79.
5. Norhazirah, A. A., Adiana, G., Yunus, K. B., Annual, Z. F., Ahmad, A. and Ong, M. C. (2020). Longtail tuna (*Thunnus tonggol*) consumption frequency in Terengganu, Malaysia. *Open Journal of Marine Science,* 10:141-148.
6. Irwandi, J and Farida, O. (2009). Mineral and heavy metal contents of marine fin fish in Langkawi Island, Malaysia. *International Food Research Journal* 16: 105-112.
7. Griffiths, S. P. and Fry, G.C. (2010). Age and growth of longtail tuna (*Thunnus tonggol*) in tropical and temperate waters of the central Indo-Pacific. *ICES Journal of Marine Science: Journal du Conseil* 67(1)*:* 125-134.
8. Bonanno, G. and Bonaco, M.O. (2018). Perspectives on using marine species as bio indicators of plastic pollution. *Marine Pollution Bulletin,* 137(2): 209-221.
9. Khristoforova, N. K., Emelyanoz, A. A. and Efimov, A.V. (2018). Bioindication of heavy metal pollution in the coastal marine water of Russky Island (Peter the Great Bay, Sea of Japan). *Russian Journal of Marine Biology* 44(7): 572-579.
10. Ong, M. C., Kamaruzaman, M. I., Norhidayah, S. A. and Joseph, B. (2016). Trace metal in highly commercial fishes caught along coastal water of Setiu, Terengganu Malaysia. *International Journal of Applied Chemistry*, 12(4): 773-784.
11. Ong, M. C., Yong, J. C., Khoo, X. Y., Tan, Y. F. and Joseph, B. (2014). Selected heavy metals and polycyclic aromatic hydrocarbon in commercial fishes caught from UMT enclosed lagoon, Terengganu, Malaysia. *Advances in Environmental Biology* 8(14): 91-98.
12. Ong, M. C., Shazili, N. A. M., Menier, D. and Effendy, A.W.M. (2013). Levels of trace elements in tissue of *Ostrea edulis* and *Crassostrea gigas* from Quiberon Bay, Brittany, France. *Journal of Fisheries and Aquatic Science* 8(2): 378-387.
13. Tengku Nur Alia, T. K. A., Hing, L. S., Sim, S. F., Ahmad, A. and Ong, M.C. (2020). Comparative study of raw and cooked farmed sea bass (*Lates calcarifer*) in relation to metal content and its estimated human health risk. *Marine Pollution*

Bulletin 153: 111009.

14. Ong, M. C. and Gan, S. L. (2017). Assessment of metallic trace elements in the muscles and fins of four landed elasmobranchs from Kuala Terengganu waters, Malaysia. *Marine Pollution Bulletin*, 124(2):1001-1005.
15. Azmat, R., Akhter, Y., Talat, R. and Uddin, F. (2006). Persistent of nematode parasite in presence of heavy metals found in edible herbivores fishes of Arabian sea. *Journal of. Biological Science*, 6: 282-285.
16. Tchounwou, P. B., Clement, G. Y., Anita, K. P. and Sutton, D. J. (2012). Heavy metal toxicity and the environment. *Molecular, Clinical and Environmental Toxicology*: 133-164.
17. Renieri, E. A., Sfakianakis, D. G., Alegakis, A. A., Safenkova, I. V., Buha, A., Matovic, V., Tzardi, M., Dzantiev, B. B., Divanach, P., Kentouri, M. and Tsatsakis, A. M. (2017). Nonlinear responses to waterborne cadmium exposure in zebrafish: an in vivo study. *Environmental Research*, 157: 173-181.
18. Rajkowska, M. and Protasowicki, M. (2013). Distribution of metals (Fe, Mn, Zn, Cu) in fish tissues in two lakes of different trophy in Northwestern Poland. *Environmental Monitoring and Assessment*, 185(4): 3493-3502.
19. Squadrone, S., Prearo, M., Brizio, P., Gavinelli, S., Pellegrino, M., Scanzio, T., Guarise, S., Benedetto, A. and Abete, M. C. (2013). THMs distribution in muscle, liver, kidney and gill of European catfish (*Silurus glarias*) from Italian Rivers. *Chemosphere*, 90(2): 358-365.
20. Leaner, J. J. and Mason, R.P. (2004). Methylmercury uptake and distribution kinetics in sheepshead minnows, *Cryprinodon variegatus*, after exposure to CH_3Hg^- spike food. *Environmental Pollution*, 266(1):115226.
21. Lucyna, P. J. (2018). Distribution of organic and inorganic Hg in the tissues and organs of fish from the southern Baltic Sea. *Enviromental Science and Pollution Research* 25: 451-460.
22. Al-Busaidi, M., Yesudhason, P., Al-Mughari, S., Al-Rahbi, W. A. K., Al-Harthy, K. S. and Al-Mazrooei, N. A. (2011). Toxic metals in commercial marine fish in Oman with reference to national and international standards. *Chemosphere*, 85(1): 67-73.
23. Chirby, M. A. (2016). Bioaccumulation of mercury (Hg) in the brain, muscle and liver tissues of inshore pompano and offshore ambereck from the Gulf of Mexico. Dessertation University of Michigan.
24. El-Moselhy, K. H. M., Othman, A. I., Abd El-Azem, H. and El-Metwally, M. E. A. (2014). Bioaccumulation of heavy metals in some tissues of fish in the Red Sea, Egypt. *Egyptian Journal of Basic and Applied Sciences*, 1: 97-105.
25. Villanueva, R. and Bustamante, P. (2006). Composition in essential and non-essential elements or early stages of cephalopods and dietary effects on the elemental profile of *Octopus vulgaris* paralarvae. *Aquaculture,* 261: 225-243.
26. Shesterin, I. V. (2010). Water pollution and its impact on fish and aquatic invertebrates. *International Food, Agricultural and Environment*, 1: 1-6.
27. Joanna, L., Paszczyk, B. and Marek, J. L. (2018). Fish as a bioindicator of heavy metals pollution in aquatic ecosystem of Pluszne Lake, Poland and risk assessment for consumer's health. *Ecotoxicology and Environmental Safety*, 153: 60-67.
28. Ali, M. and Shakoori, A. R. (2008). Heavy metal accumulation in the gills of an endangered South Asian freshwater fish as an indicator of aquatic pollution. *Pakistan Journal of Zoology,* 40(6): 423-430.
29. Dural, M., Goksu, M. Z. L., Ozak, A. A. and Derici, B. (2006). Bioaccumulation of some heavy metals in different tissues of *Dicentrarchus labrax* L. 1758, *Sparus aurata* L. 1758 and *Mugil cephalus* L. 1758 from the Comlik lagoon of the eastern coast of Mediterranean (Turkey). *Environmental Monitoring and Assessment*, 118 (1-3): 65-74.
30. Yi, Y. J. and Zhang, S. H. (2012). The relationship between fish heavy metal concentration and fish size in the upper and middle reach of Yangtze River. *Procedia Environmental Sciences*, 13: 1699-1707.
31. Yi, Y. J., Yang, Z. F. and Zhang, S. H. (2011). Ecological risk assessment of heavy metals in sediment and human health risk assessment of heavy metals in fishes in the middle and lower reaches of the Yangtze River Basin. *Environmental*

Pollution, 159: 2575-2585.

32. Farkas, A., Salanki, J. and Specziar, A. (2003). Age- and size-specific patterns of heavy metal in the organs of freshwater fish *Abramis brama* L. populating a low-contaminated site. *Water Research*, 37(5): 959-964.
33. Kumari, S., Rahul, A., Neha, J., Mishra, D. and Singh, K. (2020). Recent developments in environmental mercury bioremediation and its toxicity: A review. *Environmental Nanotechnology, Monitoring and Management*, 13: 100283
34. Amiard, J. C., Triquet, C. A., Barka, S., Pellerin, J. and Rainbow, P. S. (2006). Metallothionenins in aquatic invertebrates: Their role in metal detoxification and their use as biomarkers. *Aquatic Toxicology*, 76: 160-202.
35. Rajeshkumar, S. and Li., X. (2018). Bioaccumulation of heavy metals in fish species from the Meiling Bay, Taihu Lake, China. *Toxicology Reports*, 5: 288-295.
36. FWC (2021). How to measure fish. *Florida Fish and Wildlife Conservation Commission.* Retrieved from myfwc.com/fishing/freshwater/fishing-tips/measures. Accessed on 10th January 2021.
37. Guo, J.D. (2005). Assessment of heavy metal concentrations in several ocean endangered fauna. *Shadong University (in Chinese)*
38. Canli, M. and Atli, G. (2003). The relationship between heavy metal (Cd, Cr, Cu, Fe, Pb, Zn) levels and the size of six Mediterranean fish species. *Environmental Pollution*, 121(1): 129-136.
39. De Mora, S., Fowler, S.W., Wyge, E. and Azemard, S. (2004). Distribution of heavy metal in marine bivalves, fish and coastal sediments in the Gulf and Gulf of Oman. *Marine Pollution Bulletin*, 49: 410-424.
40. Douben P. E. (1989). Lead and cadmium in stone loaeh (*Noemacheilus barbatulus* L.) from three rivers in Derbyshire. *Ecotoxicology and Environmental Safety*, 1989; 18: 35-58.
41. Soedarini, B., Klaver, L., Roessink, I. and Gestel, C. A. M. V. (2012). Copper kinetics and internal distribution in the marbled crayfish (*Procambarus* sp.) *Chemosphere*, 87(4): 333-33.
42. Kouba, A, Kanta, J., Buric, M., Policar, T. and Kozak, P. (2010). The effect of water temperature on the number of moults and growth of juvenile noble crayfish, *Astacus astacus* (Linnaeus). *Freshwater crayfish*, 17:37-41.
43. Has-Schon, E., Bogut, I., Vukovic, R., Galovic, D., Bogut, A. and Horvatic,. (2015). Distribution and age-related bioaccumulation of lead (Pb), mercury (Hg), cadmium (Cd), and arsenic (As) in tissues of common carp *(Cyprinus carpio*) and European catfish (*Sylurus glanis*) from the Busko Blato reservoir (Bosnia and Herzegovina). *Chemosphere*, 135: 289-296.
44. Balzani, P., haubrock, P.J., Russo, F., Kaouba, Masoni, A., Tricarico, E. and Haase, P. (2021). Combining metal and isotope analyses to disentangle contaminant transfer in a freshwater community dominated by alien species. *Environmental Pollution*, 268: 115781.

Malaysian Journal of Analytical Sciences (MJAS)
Published by Malaysian Analytical Sciences Society

EXTRACTION OF β-KERATIN FROM POULTRY FEATHER WASTE USING SODIUM METABISULFITE AND SODIUM DODECYL SULFATE

(Pengekstrakan β-Keratin dari Sisa Bulu Ayam Menggunakan Natrium Metabisulfit dan Natrium Dodesil Sulfat)

Soerya Dewi Marliyana*, Theresia Inna Sekar Tungga Dewi, and Triana Kusumaningsih

Department of Chemistry, Faculty of Mathematics and Natural Sciences, Sebelas Maret University, Jl. Ir. Sutami 36A, Surakarta 57126

Corresponding author: msoerya@staff.uns.ac.id

Received: 14 September 2023; Accepted: 18 November 2023; Published: 28 February 2024

Abstract

Environmental contamination due to the disposal of poultry feather waste requires careful attention and management. As poultry feathers are a rich source of keratin protein, this study aims to determine the most efficient reducing agents for extracting β-keratin from chicken and duck feather waste as well as their optimal concentrations. For this purpose, sodium metabisulfite ($Na_2S_2O_5$) and sodium dodecyl sulfate ($NaC_{12}H_{25}SO_4$) at different concentrations, namely 0.2 M, 0.5 M, and 1 M, were utilized as the reducing agents. The results showed that the optimal concentration of reducing agents for extracting β-keratin from both chicken and duck feather waste was 0.2 M. Sodium metabisulfite (SMB) was proven to be the most effective reducing agent for chicken feather waste, with a yield of 76.9%. For duck feather waste, on the other hand, the use of sodium dodecyl sulfate (SDS) resulted in β-keratin extraction of 39.8%.

Keywords: β-keratin, feather waste, chicken feathers, duck feathers, sodium dodecyl sulfate

Abstrak

Pencemaran alam sekitar yang disebabkan oleh sisa bulu unggas memerlukan perhatian dan ditangani secara serius. Bulu unggas dapat dimanfaatkan sebagai salah satu sumber protein keratin. Kajian ini bertujuan untuk menentukan agen penurunan yang paling berkesan dan kepekatan optimum untuk pengekstrakan β-keratin dari sisa bulu unggas (bulu ayam dan bulu itik). Natrium metabisulfit ($Na_2S_2O_5$) (SMB) dan natrium dodesil sulfat ($NaC_{12}H_{25}SO_4$) (SDS) dengan pelbagai kepekatan 0.2 M, 0.5 M, dan 1 M telah digunakan sebagai agen penurunan. Kepekatan yang berkesan untuk pengekstrakan β-keratin dari sisa bulu ayan dan itik adalah 0.2 M. Agen penurunan yang berkesan untuk mengekstrak β-keratin daripada sisa bulu ayam adalah SMB menghasilkan sebanyak 76.9%. Manakala penggunaan SDS dalam sisa bulu itik menghasilkan 39.8% β-keratin.

Kata kunci: β-keratin, sisa bulu, bulu ayam, bulu itik, natrium dodesil sulfat

Introduction

As a global problem that requires careful attention and management, environmental pollution is caused by various contaminants, one of which is poultry feather waste [1]. It is estimated that around 8.5 billion tons of feathers are produced by the poultry processing industry

as waste every year throughout the world [2]. This waste is usually disposed of through incineration and landfilling. Human population growth, increasing income, and changes in lifestyle and diet have caused a rapid increase in livestock production [3]. However, the growth in poultry production also contributes to environmental pollution, especially because the feathers are underutilized in various applications.

Poultry feathers are rich in keratin protein which can be used in various fields, including green chemistry, food science, pharmaceutical industry, biomedicine, hair cosmetics, and composite materials [4]. Keratin is the third most abundant polymer after cellulose and chitin. Due to its unique and non-toxic biodegradability and biocompatibility properties, keratin can be modified and developed into various forms, such as gels, films, beads, and nano/microparticles. Feather keratin is a small and uniform protein with a molar mass of 10-36 kDa. The structure of this keratin is stabilized by various covalent (e.g., disulfide bonds) and non-covalent interactions (e.g., electrostatic forces, hydrogen bonds, hydrophobic forces) [5]. Meanwhile, the high strength and stiffness of keratin are due to the high proportion of cysteine residues in the polypeptide backbone, which are held together by disulfide bonds [4].

The average poultry feather consists of 32.2% α-helix, 53.6% β-sheet, and 14.2% random coils that form turns [3]. Chicken feathers contain more than 85% β-keratin, while duck feathers are an excellent source of β-keratin-based protein comprising around 90% β-keratin [6]. β-keratin can be extracted through hydrolysis, reduction, and oxidation [7]. Among the three, the reduction process is more commonly used for β-keratin extraction owing to its high efficiency. Reducing agents decrease the stability of β-keratin fibers by disassociating disulfide bonds and hydrogen bonds as well as allowing protease access to the polypeptide backbone to dissolve proteins into solution. In the presence of reducing agents, the solubility of β-keratin increases at high temperature [4].

Numerous prior studies have demonstrated the successful extraction of β-keratin from chicken feathers through the application of various reducing agents, namely sodium metabisulfite (SMB), sodium bisulfite ($NaHSO_3$), sodium sulfide (Na_2S), and thioglycolic acid ($HSCH_2COOH$), with respective extraction yields of 87%, 84%, 53%, and 75% [8]. Other reducing agents, such as 2-mercaptoethanol and dithiothreitol (DTT), have also been reported to produce extraction efficiencies of 83.8% and 77.6%, respectively [9]. A mixture of SMB and urea ($CO(NH_2)_2$) with SDS extracted 28.1%, sodium hydroxide (NaOH) yielded 11.8%, cysteine resulted in 17.4% of β-keratin, and a mixture of SMB, urea, and Na_2S obtained 19.5% [10]. Furthermore, a urea-based mixture showed an extraction efficiency of 50.6% for β-keratin, a combination of Na_2S and NaOH yielded 41.5%, while an SDS and $NaHSO_3$mixture achieved an extraction of 18.3% [11]. These findings highlight the potential of utilizing poultry feather waste as an eco-friendly source of β-keratin through an extraction process involving SMB and SDS as reducing agents to minimize the negative impact of this waste on the environment.

Materials and Methods

Materials

In this study, β-keratin was extracted from chicken and duck feather waste collected from the Silir Chicken Market in Surakarta, Central Java on December 2-5, 2021. Sodium dodecyl sulfate (SDS) and sodium metabisulfite (MBS) used for the reduction process were acquired from Merck. The pH of the solution was maintained in the range of 10-13 using sodium hydroxide (NaOH) obtained from Sigma Aldrich. Universal pH paper was utilized for this purpose. Furthermore, the precipitation procedure employed a commercial ammonium sulfate ($(NH_4)_2SO_4$) purchased from the Muda Berkah Jogja e-commerce store, along with deionized water from the One Lab WaterOne brand.

Instrumentations

Several instruments were utilized in this study, namely: ATR-FTIR spectrometer (Agilent Cary 630), HPLC system (Thermo Fisher), and Freeze Dryer (Telstar LyoQuest).

Extraction of β-keratin from chicken and duck feathers

The collected poultry (chicken and duck) feather wastes were washed with soapy water and dried at room temperature. The dried poultry feathers were weighed and crushed with a blender. About 10-50 mL of SDS at various concentrations of 0.2 M, 0.5 M, and 1 M was added to 0.25-1.25g of poultry feathers, then the solution was heated to a temperature of 30 ºC while the pH was maintained at around 10-13. After that, the solution was stirred for 6 hours and filtered using filter paper until a clean filtrate was obtained, which was then centrifuged at 10000 rpm for 5 minutes to form a supernatant liquid. The whole process was repeated using SMB at the same concentration variations, namely 0.2 M, 0.5 M, and 1 M, as the reducing agent.

The $(NH_4)_2SO_4$ solution was added slowly to the resulting chicken feather filtrate with a 1:1 ratio, then this mixture was centrifuged at 10.000 rpm for 5 minutes to isolate solid particles. This procedure was repeated using duck feather filtrate. Next, deionized water was added to the obtained solid particles and stirred until dissolved. The mixture was then freeze-dried until a solid was obtained. The brown-colored β-keratin in the solid particles was separated using a spatula from the remaining white $(NH_4)_2SO_4$.

Yield analysis

The yield is calculated by dividing the weight of β-keratin by the weight of the feather waste sample and expressed in percent (%) as shown in the following equation 1.

$$yield = \frac{(mass\ of\ \beta\text{-}keratin\ obtained)}{(mass\ of\ feathers\ used)} \text{ x } 100\% \quad (1)$$

Identification of β-keratin structures by ATR-FTIR

The chemical structure of β-keratin was analyzed using Attenuated Total Reflectance Fourier-transform Infrared Spectroscopy (ATR-FTIR) at Sebelas Maret University, in Surakarta, Indonesia. The ATR-FTIR analysis was carried out in transmission mode to collect spectra in the wavenumber range of 4000 cm^{-1} to 650 cm^{-1}. The wavelength of β-keratin obtained in previous study was compared with the FTIR spectra of keratin extracted from feathers using sodium sulfite (Na_2S).

Identification of amino acid composition of β-keratin

The amino acid composition of β-keratin can be determined using High-Performance Liquid Chromatography (HPLC). For this purpose, 4 mL of 6 N HCl was added to 60 mg of β-keratin sample, then the mixture was heated for 24 hours at 110 ºC. Afterwards, the mixture was cooled to room temperature and neutralized (pH 7) with 6 N NaOH. Aquabides was then added to the sample to a volume of 10 mL and filtered with 0.2 mm Whatman filter paper. Next, 50 µL of the sample was added to 300 mL of OPA (Orthophalaldehyde) solution and stirred for 5 minutes, then 10 µL of the mixture was inserted into the HPLC injector L. The HPLC instrument was operated at room temperature, LiChrospher 100 RP-18 (5mm) column, an eluent flow rate of 1.5 mL/min, and mobile phases of A= CH_3OH:50 mM CH_3COONa:THF (2:96:2) pH 6.8 and B = 65% CH_3OH using isocratic elution. Furthermore, detection was performed using a Thermo Ultimate 3000 RS Fluorescence Detector, with an excitation wavelength of 300 nm and an emission wavelength of 500 nm.

Results and Discussion

Extraction of β-keratin from chicken and duck feathers

β-keratin is insoluble in water with low chemical reactivity, thereby requiring high temperature and reducing agents to increase its solubility. In the process of reducing β-keratin in poultry feathers, 2 M NaOH needs to be added so that the pH can be maintained at 10-13. NaOH functions to form an alkaline atmosphere needed in the reduction process that cannot occur in an acidic environment; without an alkaline state, protons cannot be released, thus being unable to break ionic bonds. In an alkaline state, on the other hand, protons are removed from the amino group, and the ionic bonds formed by the electrostatic attraction of the NH_3^+ group of the diamino acid and the COOH group of the dicarboxylic acid can be broken [7].

Severe extraction conditions, such as extremely high/low pH at prolonged exposure and high temperature, produce β-keratin with low molecular weight. Conversely, extraction of β-keratin under mild conditions (i.e., at a temperature of 30 ºC) will break the

disulfide bonds of the protein fibers without significantly breaking the polypeptide bonds, resulting in a stable micromolecular structure of β-keratin with a high molecular weight [8]. To extract β-keratin properly, the reduction process takes 6 hours so that the reducing agent can penetrate deeper into the cell wall. An extraction time of 6 hours has a better effect on the yield of β-keratin compared to an extraction time of 4 hours. The longer the extraction time, the higher the yield of β-keratin [12]. In this study, the reduction reaction of β-keratin is shown in equation 2 and Figure 1 [13].

$$SMB \rightarrow 2Na^{+} + SO_3^{2-} + SO_2 \quad (2)$$

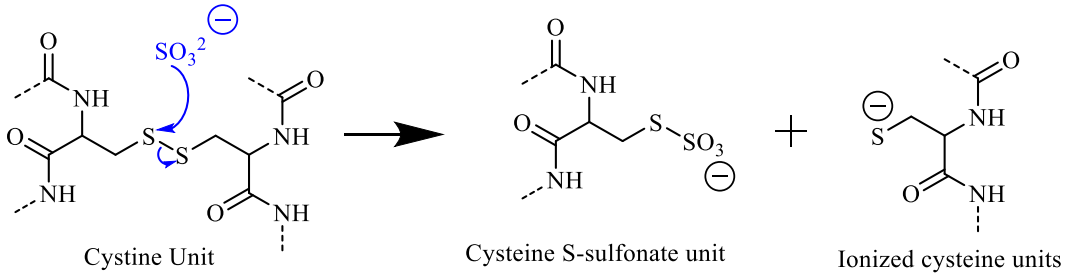

Figure 1. Reduction reaction of β-keratin from poultry feathers using SMB

During the reduction process, β-keratin undergoes heterolytic cleavage of disulfide bonds (-S-S-). The disulfite anion (SO_3^{2-}) is a weak nucleophile, whereas the sulfur atom is a relatively weak reaction center. Nucleophiles must react covalently with electrophilic groups in the protein to become sensitized. The only significant electrophilic groups in proteins are the disulfide bonds of the cystine units that can act as weak electrophiles. The SO_3^{2-} anion attacks one of the sulfur atoms in the S–S bond and breaks it heterolytically, with the thiolate anion of the cysteine unit acting as the leaving group [13].

Reduction process is closely related to a decrease in the oxidation number due to the breaking of disulfide bonds that can affect the structure of the cysteine obtained. In the reduction process of β-keratin, the S atom in the cysteine unit, which has an oxidation number of +4, will experience a decrease in its oxidation number to -1 in the ionized cysteine unit. Disulfide bonds that are disrupted by sulfites will produce cysteine thiols (reduced β-keratin) and cysteine-S-sulfonate residues (Bunte salt), where β-keratin-Cys-S- is reduced keratin and β-keratin-Cys-SSO_3- is Bunte salt [9]. In this study, precipitation of the extracted filtrate was carried out with $(NH_4)_2SO_4$ in high concentration. The addition of salt in high concentrations causes water molecules that were originally bound to the hydrophobic surface of the proteins to bind to the salt. The large number of water molecules that bind to salt ions results in the proteins interacting with each other, aggregating, and precipitating (salting out). In this regard, divalent salts such as $MgCl_2$, $MgSO_4$, and $(NH_4)_2SO_4$ are more effective for protein precipitation than monovalent salts such as NaCl and KCl. $(NH_4)_2SO_4$ is often used in protein precipitation because of its high level of solubility, non-toxicity, and low price [14].

Centrifugation of poultry feathers reduced with SMB produces a brown precipitate at the bottom of the tube, which is β-keratin. Meanwhile, centrifugation of feathers reduced with SDS will form 2 layers; the thick brown liquid in the upper layer is β-keratin, whereas the particle-free supernatant liquid in the lower layer is clear yellow, indicating that β-keratin has been separated from impurities. Additionally, the result of centrifugation of feathers reduced with SDS has a different shape from that of feathers reduced using SMB since the surfactant molecules form a micelle structure on the hydrophobic side of the protein. With the formation of the β-keratin-SDS complex and the prevention of protein aggregation, reduction process using SDS is considered faster and more efficient [9]. SDS prevents the aggregation of polypeptide chains by

blocking the formation of new cross-links, thus increasing the extraction rate and stability of the extracted β-keratin [8]. In this present study, the reduction process was repeated 3 times to increase accuracy; the more reduction processes carried out, the higher the accuracy and validity of the results obtained. The resulting β-keratin solid is brownish white, as presented in Table 1.

Table 1. Extracted β-keratin solids

Chicken Feathers						**Duck Feathers**					
SMB			**SDS**			**SMB**			**SDS**		
0.2 M	0.5 M	1 M	0.2 M	0.5 M	1 M	0.2 M	0.5 M	1 M	0.2 M	0.5 M	1 M

Yield analysis

The yield of β-keratin is influenced by several factors, including the concentration of the reducing agent used in the extraction process. SMB concentrations above 0.2 M will decrease the percentage of β-keratin yield as most of the disulfide bonds are broken [16]. There is also a loss of β-keratin during the extraction process, which can be caused by β-keratin not settling completely or remaining in the container when changing or washing. Furthermore, when the pH is too high or too alkaline, β-keratin typically cannot maintain its structure. In addition, hair removal with hot water (high temperature) causes non-reversible denaturation where β-keratin does not regain its original structure [17]. The yields of β-keratin extracted from chicken and duck feathers in this study can be seen in Table 2.

Table 2. Yields of β-keratin extraction at various concentrations of SMB and SDS

SMB Concentration (M)	**Yield (%)**			
	Chicken Feathers		**Duck Feathers**	
	SMB	**SDS**	**SMB**	**SDS**
0.2	76.9	25.4	37.4	39.8
0.5	32.7	19.3	14.3	38.6
1	45.6	15.3	32.5	10.8

In this study, the highest yield was achieved in the extraction of β-keratin from chicken feathers using 0.2 M SMB, which reached 76.9%. This finding is consistent with a previous study which found that chicken feathers reduced using 0.2 M SMB produced a yield of 87.6% [15]. On the other hand, the yield of β-keratin extracted from duck feathers with SDS at a concentration of 0.2 M as the reducing agent had the largest percentage (39%). Therefore, SDS was proven more effective as a reducing agent for extracting β-keratin from duck feathers.

Identification of β-keratin structures by ATR-FTIR

To measure the effect of the extraction process using SMB, the FTIR spectra of β-keratin extracted from chicken and duck feathers using SMB in different concentrations of 0.2 M, 0.5 M, and 1 M were compared, as shown in Figure 2.

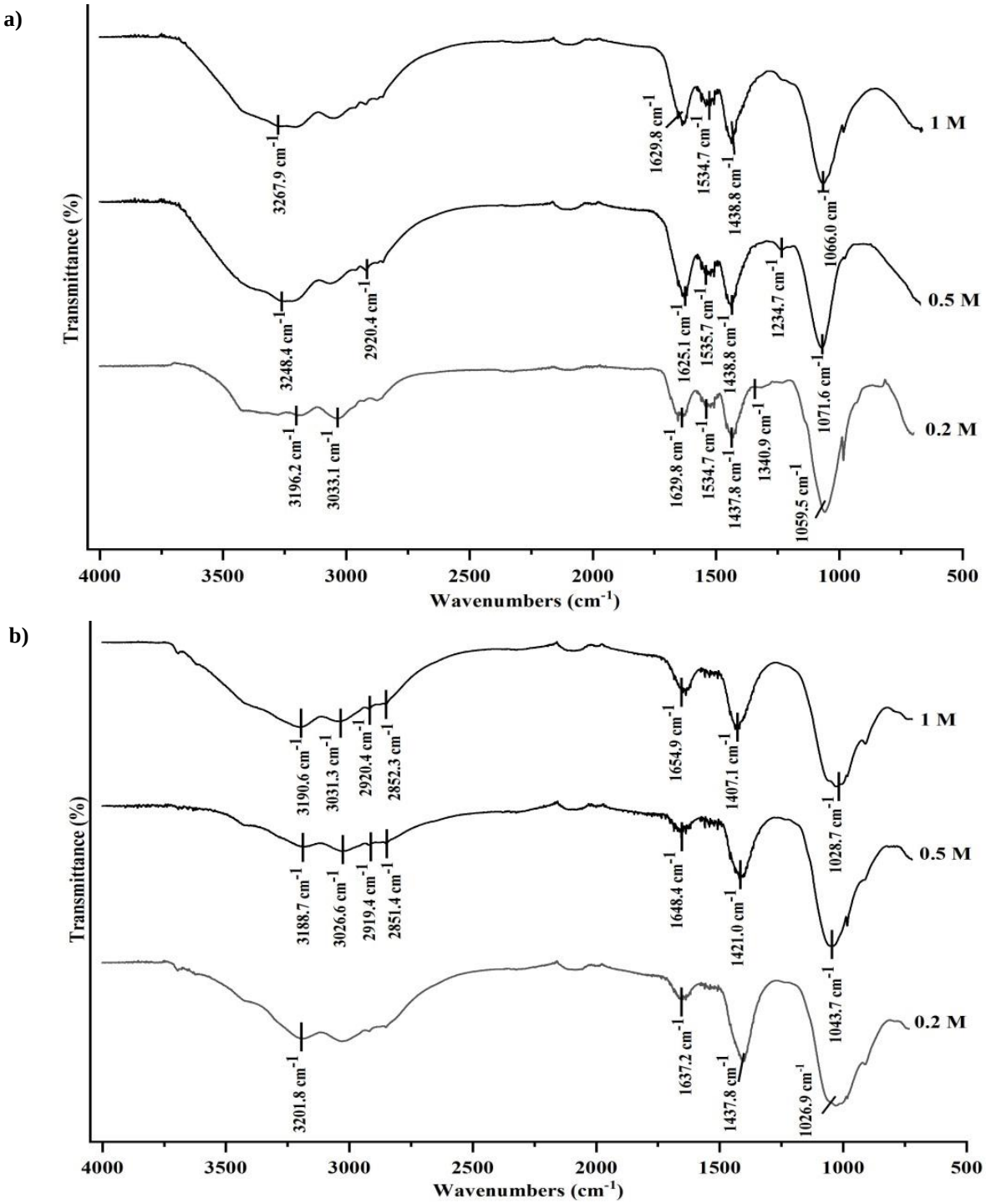

Figure 2. FTIR spectra of β-keratin using SMB reducing agent; a) chicken feathers; b) duck feathers

Similarly, to assess the effects of the extraction process using SDS, the FTIR spectra of β-keratin extracted with SDS in different concentrations of 0.2 M, 0.5 M, and 1 M were compared, as shown in Figure 3.

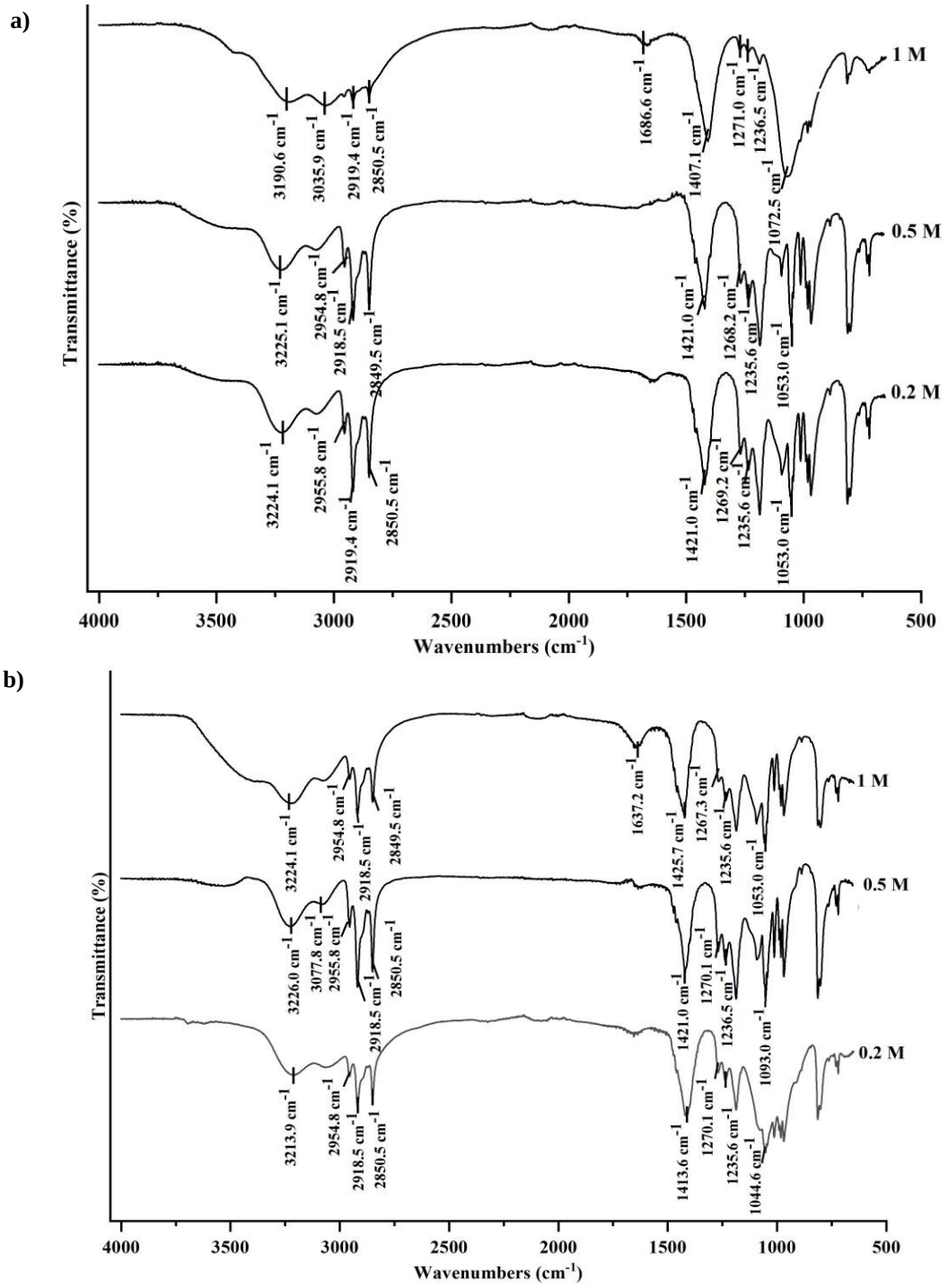

Figure 3. FTIR spectra of β-keratin using SDS reducing agent; a) chicken feathers and b) duck feathers

As seen in Figures 2 and 3, the absorption peaks of β-keratin extracted from chicken and duck feather waste using both SMB and SDS had similar characteristics at the three different concentrations. β-keratin is a protein with unique absorption properties of the peptide bonds (-CONH), and the vibrations of these peptide bonds come from amide A,

amide I, amide II, and amide III bands. The β-sheet structure of β-keratin is displayed in Figure 4.

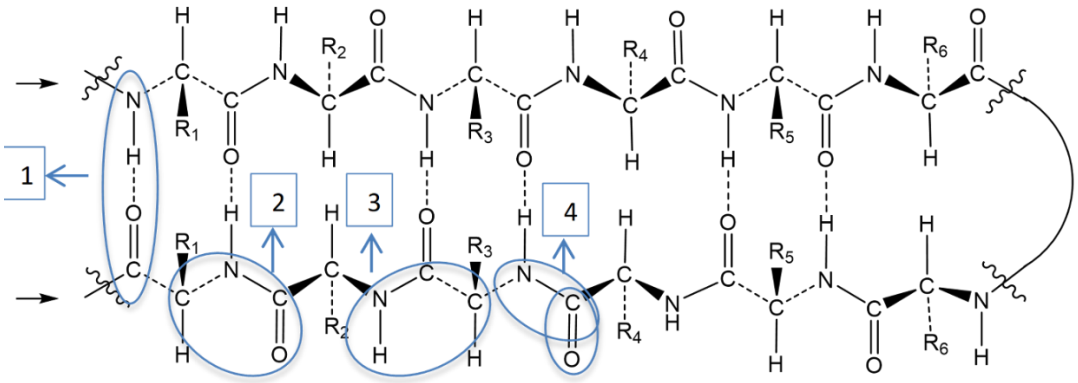

Notes: Amide A = 1; Amide I = 2; Amide II= 3; Amide III= 4

Figure 4. β-sheet structure of β-keratin

The peaks that appear in the wavenumber range of 3200 to 3500 cm^{-1} indicate amide A and an α-helix structure. N-H and O-H stretching vibrations are insensitive to the backbone of β-keratin, but susceptible to the strength of hydrogen bonds [18]. On the other hand, the absorption bands in the range of 3000 to 2800 cm^{-1} exhibit C-H stretching vibrations and are associated with symmetric CH_3 strains. Such absorption is antisymmetric from the C-H bond in CH_3, where the side chains of amino acid residues in the primary protein chain are saturated, thus being insensitive to structural changes [19].

The extraction process affects the chemical structure of β-keratin. In this regard, the use of SMB at higher concentrations (1 M) to extract β-keratin from chicken and duck feathers causes structural damage to β-keratin as shown by the absence of an absorption pattern at wavenumbers ranging from 2800 to 3000 cm^{-1}. Contrarily, in the extraction process with SDS at high concentrations (1 M), an absorption pattern appears because the reaction using surfactants leads to the formation of by-products in the form of C=O groups [20].

Amide bands I–III provide crucial information about the conformation and structure of the protein backbone. The split peak from 1700-1600 cm^{-1} (Amide I region) corresponds to the C=O stretching vibrations and originates from the combination of α-helix and β-sheet [4]. C=O stretching vibrations are the most sensitive part of proteins in determining secondary structure. These bonds are directly related to the conformation of the backbone, and each type of secondary structure has different C=O strains that can change the conformation of proteins and polypeptides [21].

The amide II region which originates from N-H bending and C-H stretching, signifying absorption bands in the range of 1580 and 1480 cm^{-1}, gives information about the vibration bands of the protein backbone and is related to the β-sheet structure by resulting in lower sensitivity to changes in protein conformation, compared to the amide I band [22]. The absorption band with a weak peak of around 1300 to 1220 cm^{-1} is in the amide III region, which is caused by a combination of C-N stretching and N-H in-plane bending as well as some contributions from C-C stretching and C=O bending [4]. The absorption pattern of amide III as shown in Figure 4 is not visible because most of the disulfide bonds have been broken at SMB concentrations above 0.2 M [16].

The absorption band in the range of 1000 to 1200 cm^{-1} is associated with the asymmetric and symmetric S–O stretching vibrations of the cysteine-S-sulfonate residues formed from the reaction of sulfite and cysteine during the protein extraction process [23]. The sharp

peak also indicates an increase in the content of cysteine-S-sulfonate residues in β-keratin [24]. However, because signals from the disulfide bonds (S–S) cannot be detected by FTIR spectroscopy, the use of Raman spectroscopy is highly necessary to verify these bonds. Absorption of disulfide bonds (S–S) in Raman will appear at 510 cm^{-1} [25]. Based on the FTIR spectra of β-keratin above, β-keratin extracted from both chicken and duck feathers using SDS has a better absorption pattern as SDS itself can prevent the aggregation of polypeptide chains by blocking the formation of new cross-links in the protein, thus increasing the extraction rate and structural stability of the extracted β-keratin [8].

Identification of amino acid composition of β-keratin by HPLC

The process of analyzing the amino acid composition of β-keratin using HPLC was carried out in several stages: sample preparation, standard solution preparation, derivatization, and injection. The preparation of β-keratin began with a hydrolysis process using HCl. The data obtained from this process were in the form of area, retention time, and amino acid levels. The Figure 5 displays the chromatograms of β-keratin extracted from chicken and duck feathers.

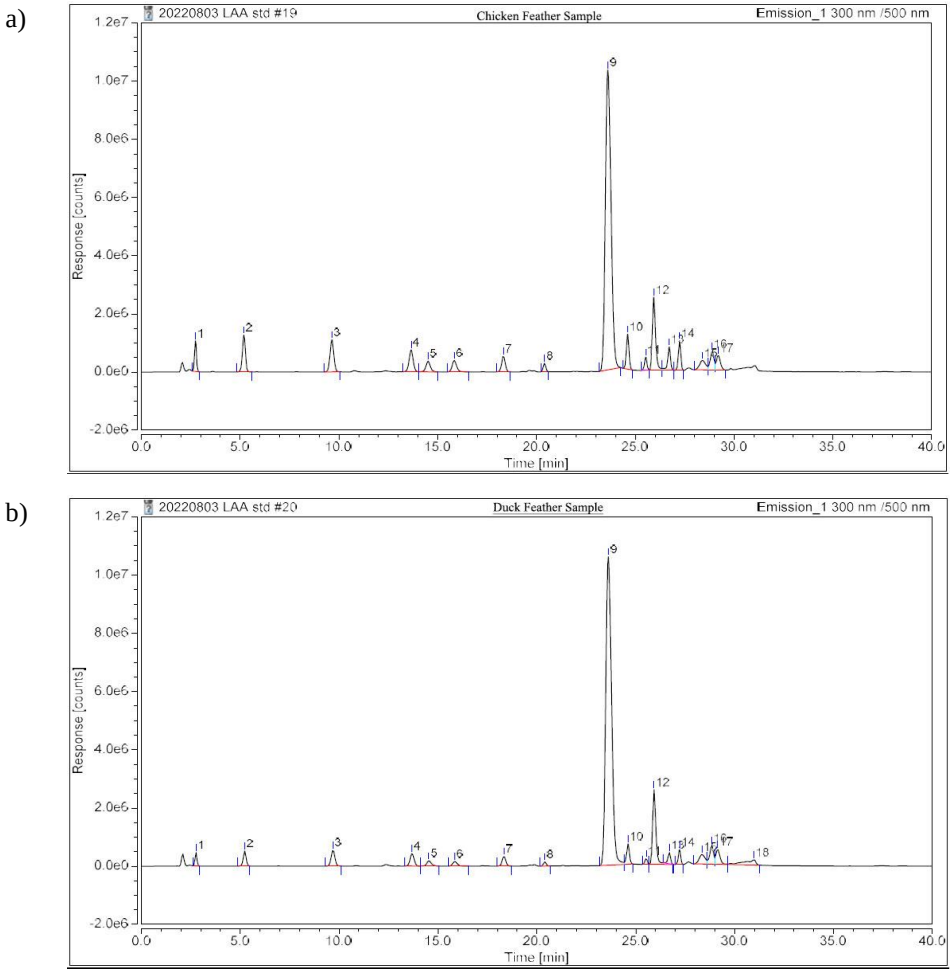

Figure 5. HPLC chromatograms of β-keratin from; a) chicken feathers and b) duck feathers

Based on the chromatograms, the type of amino acids contained in β-keratin in chicken feathers can be determined by comparing the obtained retention time with amino acid standards. Meanwhile, to find out the levels, calculations were carried out using the standard curve functions for amino acids. The amino acids that

make up β-keratin in chicken and duck feathers are: 1) aspartic acid; 2) glutamic acid; 3) serine; 4) glycine; 5) threonine; 6) arginine; 7) alanine; 8) tyrosine; 10) valine; 11) phenylalanine; 13) ileucine; and 14) leucine. The calculation results showed that the highest concentration of amino acids in chicken feathers is glutamic acid at 24.61 ppm. This is in line with a previous study which mentioned that glutamic acid is the most abundant amino acid in chicken feathers [11]. Meanwhile, the highest amino acid content in duck feathers is serine at 11.15 ppm. This finding also supports another prior study which stated that serine is the most abundant amino acid in duck feathers [26]. However, peaks 9, 12, 15, 16, 17, and 18 in Figure 5 do not indicate the types of amino acids that make up β-keratin in chicken and duck feathers but are rather considered as impurities.

Conclusion

The optimal concentration of reducing agent for the extraction of β-keratin was 0.2 M for both chicken feather waste and duck feather waste. The utilization of SMB in the extraction process of β-keratin from chicken feather waste produced the highest yield of 76.9%. Meanwhile, extracting β-keratin from duck feather waste using SDS resulted in a maximum yield of 39.8%. These findings indicate that SMB is preferred as reducing agent for the extraction of β-keratin from chicken feathers, whereas SDS is more effective for duck feathers.

Acknowledgement

This study is supported by the Grant Research Group with contract number 228/UN27.22/PT.01.03/2023

References

1. Mulia, D. S., Yuliningsih, R. T., Maryanto, H. and Purbomartono, C. (2016). Pemanfaatan limbah bulu ayam menjadi bahan pakan ikan dengan fermentasi *Bacillus subtilis*. *Jurnal Manusia dan Lingkungan*, 23(1): 49-57.
2. Jana, A., Kakkar, N., Halder, S. K., Das, A. J., Bhaskar, T., Ray, A. and Ghosh, D. (2022). Efficient valorization of feather waste by *Bacillus cereu*s IIPK35 for concomitant production of antioxidant keratin hydrolysate and milk-clotting metallo-serine keratinase. *Journal of Environmental Management*, 324: 1-11.
3. Qiu, J., Wilkens, C., Barrett, K. and Meyer, A. S. (2020). Microbial enzymes catalyzing keratin degradation: Classification, structure, function. *Biotechnology Advances*, 44: 1-22.
4. Pourjavaheri, F., Ostovar Pour, S., Jones, O. A. H., Smooker, P. M., Brkljača, R., Sherkat, F., Blanch, E. W., Gupta, A. and Shanks, R. A. (2019). Extraction of keratin from waste chicken feathers using sodium sulfide and L-cysteine. *Process Biochemistry*, 82: 205-214.
5. De Silva, R., Wang, X., and Byrne, N. (2016). Development of a novel cellulose/duck feather composite fibre regenerated in ionic liquid. *Carbohydrate Polymers*, 153: 115-123.
6. Peng, Z., Mao, X., Zhang, J., Du, G. and Chen, J. (2019). Effective biodegradation of chicken feather waste by co-cultivation of keratinase producing strains. *Microbial Cell Factories*, 18(1): 1-11.
7. Gupta, A., Kamarudin, N. B., Chua, G. K., Yunus, R. M., Yeo, C., Kee, G., Bin, R. and Yunus, M. (2012). Extraction of keratin protein from chicken feather. *Journal Chemistry and Chemical Engineering*, 6: 732-737.
8. Khumalo, M., Sithole, B. and Tesfaye, T. (2020). Valorisation of waste chicken feathers: Optimisation of keratin extraction from waste chicken feathers by sodium bisulphite, sodium dodecyl sulphate and urea. *Journal of Environmental Management*, 262: 1-7.
9. Sinkiewicz, I., Śliwińska, A., Staroszczyk, H. and Kołodziejska, I. (2017). Alternative methods of preparation of soluble keratin from chicken feathers. *Waste and Biomass Valorization*, 8(4): 1043-1048.
10. Ramya, K. R., Thangam, R. and Madhan, B. (2020). Comparative analysis of the chemical treatments used in keratin extraction from red sheep's hair and the cell viability evaluations of this keratin for tissue engineering applications. *Process Biochemistry*, 90: 223-232.
11. Kamarudin, N. B., Sharma, S., Gupta, A., Kee, C. G., Chik, S. M. S. B. T. and Gupta, R. (2017). Statistical investigation of extraction parameters of keratin from chicken feather using Design-Expert.

3 Biotech, 7(2): 1-9.

12. Welu, K. T., Beyan, S. M., Balakrishnan, S., and Admassu, H. (2020). Chicken feathers based Keratin extraction process data analysis using response surface-box-Behnken design method and characterization of keratin product. *Current Applied Science and Technology*, 20(2): 163-177.
13. Roberts, D. W., Basketter, D., Kimber, I., White, J., McFadden, J. and White, I. R. (2012). Sodium metabisulfite as a contact allergen - An example of a rare chemical mechanism for protein modification. *Contact Dermatitis*, 66(3): 123-127.
14. Sarip. M, T. T. Nugroho, H. Y. T. (2014). Isolasi, uji aktivitas, dan aktivitas spesifik enzim selulase Penicillium sp. LBKURCC27 semimurni melalui pengendapan $(NH_4)_2SO_4$. *Jurnal Online Mahasiswa Fakultas Matematika dan Ilmu Pengetahuan Alam Universitas Riau*, 1(1): 1-6.
15. Na Ayutthaya, I. S., Tanpichai, S. and Wootthikanokkhan, J. (2015). Keratin extracted from chicken feather waste: extraction, preparation, and structural characterization of the keratin and keratin/biopolymer films and electrospuns. *Journal of Polymers and the Environment*, 23(4): 506-516.
16. Khumalo, M., Tesfaye, T., Sithole, B. and Ramjugernath, D. (2019). Possible beneficiation of waste chicken feathers via conversion into international journal of chemical sciences possible beneficiation of waste chicken feathers via conversion into biomedical applications. *International Journal of Chemical Sciences*, 17(1): 1-20.
17. Acharya, V. V. and Chaudhuri, P. (2021). Modalities of protein denaturation and nature of denaturants. *International Journal of Pharmaceutical Sciences Review and Research*, 69(2): 19-24.
18. Valkov, A., Zinigrad, M., Sobolev, A. and Nisnevitch, M. (2020). Keratin biomembranes as a model for studying onychomycosis. *International Journal of Molecular Sciences*, 21: 1-12.
19. Zhao, J., Cui, J. K., Chen, R. X., Tang, Z. Z., Tan, Z. L., Jiang, L. Y. and Liu, F. (2021). Real-time in-situ quantification of protein secondary structures in aqueous solution based on ATR-FTIR subtraction spectrum. *Biochemical Engineering Journal*, 176: 1-12.
20. Silaen, D. S., Herawan, T., Masyithah, Z., and Ginting, H. A. (2017). Optimasi sintesis biosurfaktan lauril amida dari asam laurat dan dietanolamina menggunakan pelarut hexane dan enzim lipase terimobilisasi optimation. *Jurnal Teknik Kimia USU*, 6(2): 19-23.
21. Usoltsev, D., Sitnikova, V., Kajava, A., and Uspenskaya, M. (2019). Systematic FTIR spectroscopy study of the secondary structure changes in human serum albumin under various denaturation conditions. *Biomolecules*, 9(8): 1-17.
22. Sadat, A. and Joye, I. J. (2020). Peak fitting applied to fourier transform infrared and raman spectroscopic analysis of proteins. *Applied Sciences (Switzerland)*, 10(17): 2-16.
23. Shavandi, A., Bekhit, A. E. D. A., Carne, A. and Bekhit, A. (2017). Evaluation of keratin extraction from wool by chemical methods for bio-polymer application. *Journal of Bioactive and Compatible Polymers*, 32(2): 163-177.
24. Alashwal, B. Y., Saad Bala, M., Gupta, A., Sharma, S. and Mishra, P. (2020). Improved properties of keratin-based bioplastic film blended with microcrystalline cellulose: A comparative analysis. *Journal of King Saud University - Science*, 32(1): 853-857.
25. Wang, B., Yang, W., McKittrick, J. and Meyers, M. A. (2016). Keratin: Structure, mechanical properties, occurrence in biological organisms, and efforts at bioinspiration. *Progress in Materials Science*, 76: 229-318.
26. Alphine, J., Lucy, K. M., Maya, S., Sumena, K. B., Indu, V. R. and Vasudevan, V. N. (2019). Comparative studies on the chemical properties of feather barbs in broiler and kuttanad ducks. *Journal of Veterinary and Animal Sciences*, 50(2): 149-153.

Malaysian Journal of Analytical Sciences (MJAS)
Published by Malaysian Analytical Sciences Society

RESPONSE SURFACE METHODOLOGY FOR OPTIMISING CROSS-LINKING CONDITIONS OF UNRIPE BANANA (*Musa balbisiana* VAR. Abu) STARCH

(Kaedah Tindak Balas Permukaan untuk Pengoptimuman Keadaan Penghubung Silang Kanji Pisang Belum Masak (*Musa balbisiana* Var. Abu))

Nurul Nor Izzuani Nor Sham[1*], Anida Yusoff[1], Noorlaila Ahmad[1], and Siti Roha Ab Mutalib[1,2]

[1]*School of Industrial Technology, Faculty of Applied Sciences, Universiti Teknologi MARA, 40450 Shah Alam, Selangor, Malaysia*
[2]*Malaysia Institute of Transport, Universiti Teknologi MARA, 40450 Shah Alam, Selangor, Malaysia*

[*]*Corresponding author: izzuaninorsham@gmail.com*

Received: 5 September 2023; Accepted: 10 January 2024; Published: 28 February 2024

Abstract

Starch is the most abundant organic compound found in nature after cellulose. However, native starch has undesirable properties which could limit its application in food industries. Therefore, starch modification is necessary to enhance its positive attributes and to eliminate the limitations of its specific application in food manufacturing. This study aims to optimize the conditions of the cross-linking of unripe banana (*Musa balbisiana* var. Abu) starch using response surface methodology (RSM). The optimization was conducted using the central composite design (CCD) approach. The extracted unripe banana (*Musa balbisiana* var. Abu) starch was cross-linked with sodium trimetaphosphate (STMP) and sodium tripolyphosphate (STPP) mixture as the cross-linking agent. The two independent variables selected were temperature (40.0- 60.0 ℃) and pH (9.00-11.00). The maximum degree of cross-linking was obtained at the following optimum conditions: temperature 50.57 ℃ and pH 9.52. The degree of cross-linking obtained at the optimum conditions of RSM was verified, and the value obtained was 81.73%. There was no significant difference (p-value >0.05) between the predicted and verified degree of cross-linking values. Thus, it indicated that the predicted optimum condition by RSM can be accepted. These outcomes of this study are very important as they would assist the food industries in developing and designing the process of optimal cross-linking of starch from unripe bananas, which can be used in the future.

Keywords: response surface methodology, unripe banana, banana starch, starch modification, cross-linking

Abstrak

Kanji adalah sebatian organik yang paling banyak ditemui dalam alam semula jadi selepas selulosa. Walau bagaimanapun, kanji semula jadi yang belum diproses mempunyai sifat yang tidak diingini yang boleh mengehadkan penggunaannya dalam industri makanan. Oleh itu, pengubahsuaian kanji adalah perlu untuk meningkatkan kebaikan justeru dapat menghapuskan had penggunaan khususnya dalam pembuatan makanan. Matlamat kajian ini adalah untuk mengoptimumkan keadaan ikatan silang kanji pisang belum masak (*Musa balbisiana* var. Abu) menggunakan kaedah tindak balas permukaan (RSM). Pengoptimuman telah dijalankan dengan pendekatan reka bentuk komposit pusat (CCD). Kanji pisang belum masak (*Musa balbisiana* var. Abu) yang diekstrak telah diikat silang dengan campuran natrium trimetafosfat (STMP) dan natrium tripolifosfat (STPP) sebagai agen

penghubung silang. Dua pembolehubah bebas yang dipilih ialah suhu (40.0-60.0 ℃) dan pH (9.00-11.00). Darjah maksimum penghubung silang diperoleh pada keadaan optimum berikut: suhu 50.57 ℃ dan pH 9.52. Darjah silang yang diperoleh pada keadaan optimum RSM telah disahkan dan nilai yang diperoleh ialah 81.73%. Tidak terdapat perbezaan yang signifikan (nilai p >0.05) antara tahap ramalan dan disahkan nilai silang silang, oleh itu ia menunjukkan bahawa keadaan optimum yang diramalkan oleh RSM boleh diterima. Hasil kajian ini adalah sangat penting kerana ia akan membantu industri makanan untuk membangunkan dan mereka bentuk proses pengikatan silang kanji yang optimum daripada pisang yang belum masak, yang boleh digunakan pada masa hadapan.

Kata kunci: kaedah tindak balas permukaan, pisang belum masak, kanji pisang, pengubahsuaian kanji, penghubung silang

Introduction

Starch, a storage carbohydrate in plants, can be found abundantly in leaves, flowers, fruits, seeds, stems, and roots [1]. It has wide functions and applications in food industries and is commonly used as a thickener, binder, gelling agent, foam stabilizer and texture improver [2]. Starch can be basically manufactured by the combination of the following steps: grinding of the starch-rich crop and wet separation technique to sediment the starch granules in water. Starch has gained much attention due to its usefulness in food and non-food industries, wide availability, low cost of extraction and purification, edibility and total composability without toxic residues [3, 4]. Most of the starches are obtained from cereals such as corn, wheat and various rice, tubers, and roots such as potatoes and cassava. In this regard, unripe bananas have been studied as a potential source of starch [5-7].

Banana, a climacteric fruit that belongs to the *Musaceae* family and *Musa balbisiana*, is the most widely distributed banana in tropical and subtropical regions [8]. The banana fruits were usually harvested at the unripened stage for long handling and transportation because they are perishable fruits that could lead to serious economic losses during maturation [9-11]. The starch content from unripe bananas is between 70-80%, depending on their variety and maturity index, and its starch content is similar to other starches obtained from the endosperm of corn and potatoes [8, 12-14]. Apart from digestible starch, it also contains a high amount of resistant starch and amylose and amylopectin ratio that has potential in diabetes treatment since it contributes to low glycaemic index [7, 15]. Most of the starch obtained from different sources is in its native state. The native starches were found incompetent for industrial use, leading to the least suitability in processing [16] and posing many limitations with regards to their application and functionality that related to the processing conditions; for example-weak-bodied and they produce a cohesive and rubbery paste [16] and undesirable gel upon cooling, easily retrograded, having a lower solubility in cold water, lower viscosity and thickening characteristic after cooking and low shear stress and thermal resistance at higher temperature [17-20]. However, these limitations can be overcome and improved through starch modification treatments [20, 21].

There are several methods of starch modification treatments, which can be classified as physical and chemical methods. Chemical methods involve the use of chemical agents, whereas physical methods involve the application of several physical factors (temperature, pressure, shear, moisture, radiation, ultrasonic wave, and etc). The examples of physical methods include pre-gelatinization, extrusion, heat-moisturizing, annealing, and microwave treatments [22]. These methods are able to change particle size, surface properties, solubility index and functional properties such as water absorption [23]. The most common method for chemical modification is cross-linking treatments. Cross-linking treatment involves the introduction of functional groups to the native starch in the presence of cross-linking agents that are responsible for the formation of the intra or inter-ester or ether linkages between the hydroxyl (-OH) groups in the starch amorphous region [20, 21, 24-26]. The most commonly cross-linking agents used in food industries are phosphorus oxychloride or phosphoryl chloride ($POCl_3$), sodium trimetaphosphate (STMP),

epichlorohydrin (EPCH) and sodium tripolyphosphate (STPP) [26-28]. STMP is the most widely used cross-linking agent as it is non-toxic and has a slow penetration rate [29]. According to Xie et al. [26], chemical modification is usually employed to enhance the mechanical strength of the starch. This method limits the starch swelling to a greater extent because the linkages formed restrict the mobility of the starch molecules in the amorphous region [30]. As a result, it reduces subsequent disintegration during hydrothermal processing [31]. In addition, it also increases resistance to high temperature, shear resistance and the stability of the swollen starch granules [32, 33]. Cross-linking not only alters the chemical and physical properties but also the thermal transition characteristic of the starch. However, its effect depends on the botanical sources of the starch and the cross-linking agent [21].

Cross-linking has been previously performed by many researchers using different temperatures and pH on different starch sources, including porous wheat starches, rice starches, tapioca starches and corn starches [20, 26, 34, 35]. Since the starch modification involves more than one factor to affect the desired response, therefore Response Surface Methodology (RSM) is the most suitable and effective tool to be used since it can provide relevant information in the shortest time with the least number of experimental runs [36]. According to Bambang et al. [37], optimization is a method used to identify and improve the best solution based on specific quality criteria such as process efficiency. It involves a few steps, including the selection of independent variables and responses, choosing of experimental design strategy, running of experiments and data collection, fitting of the model equation to experimental data, verifying the response graph and model (ANOVA), and lastly determining the optimal conditions for the design the possible approaches available in RSM is central composite design (CCD).

Previously, researchers have used RSM to optimize different starch modification processes in various studies. For example, the application of RSM for the pre-gelatinization process of sweet potato and walur starches [37, 38], to modify sago starch through octenyl succinic anhydride (OSA) process [39] and also the cross-linking of corn and wheat starches [40]. Hence, this study aims to optimize the conditions (temperature: 40-60 ℃ and pH value: 9.00-11.00) for unripe banana (*Musa balbisiana* var. Abu) starch modification using the cross-linking method to obtain cross-linked starch with improved physicochemical properties.

Materials and Methods

Materials

An unripe banana (*Musa balbisiana* var. Abu) at maturity index 2 (peel color: green with a trace of yellow) was purchased from a local seller/farmer in Kota Kemuning, Shah Alam. Sodium sulphate, sodium trimetaphosphate (STMP), sodium tripolyphosphate (STPP), sodium hydroxide (NaOH), hydrochloric acid (HCl) and sodium sulphate (Na_2SO_4) used were purchased from Sigma-Aldrich

Flour preparation

Banana flour was prepared by using the method from Ayo-Omogie et al. [41]. The banana was washed, peeled and sliced to 2-3mm thickness using a slicer and was frozen in a freezer (Sanyo, MDF-U5412, Japan) at the temperature of -40 ℃. The frozen samples were then transferred into the freeze dryer (Martin Christ, Alpha 1-4 LD plus), which operated at -50 ℃ and 0.1m Pa. After the drying was completed, dried samples were mashed using a pestle and mortar and kept in an air-tight container for further analysis.

Starch extraction

Agama-Acevedo et al. [42] used the starch extraction method with slight modifications. 100g of banana flour was suspended in 1 L of 1% sodium sulfate solution (pH 4.5), and the suspension was divided into several glass jars. All the glass jars were capped and kept in an incubator shaker at room temperature (27 ℃) for 12 hours. After that, the suspension was centrifuged at 3000 rpm for 15 minutes, and the supernatant was discarded. The sediment was then re-suspended with distilled water, filtered through 200 US mesh to remove the fibre in the solution and rinsed several times to ensure the maximum amount of

starch could be collected. The residue was discarded, and lastly, the filtrate was centrifuged at 3000 rpm for 15 minutes. The white starch sediment obtained was collected and dried in a drying oven (Memmert, Germany) at 45 ℃ for 24 hours.

Experimental design

In this experiment, RSM was used to optimize the cross-linking of banana starch to achieve an optimal degree of cross-linking (%). The experiment was optimized using central composite design (CCD) and conducted in a randomized manner using the Design Expert 12 statistical package. The degree of cross-linking (%) was chosen as the response value, while the temperature (X_1) and pH (X_2) were selected as the independent variables. The ranges for both independent variables were temperature (40-60 ℃) and pH (9.00-11.00), as shown in Table 1.

Table 1. Coded and un-coded table for range and level of independent variables for cross-linking method

Independent Variables		**Factor Level**				
		$-\alpha$	**-1**	**0**	**+1**	**$+\alpha$**
Temperature, (℃)	X_1	30.00	40.00	50.00	60.00	70.00
pH	X_2	8.00	9.00	10.00	11.00	12.00

About 5g of unripe banana starch was dispersed in distilled water (75 mL) containing sodium sulphate (10%, w/w starch basis) and a 99:1 mixture of STMP/STPP (12%) as described by Park et al. [43]. The dispersion was adjusted to various pH (8.59-11.41) with 0.1 N NaOH solution and was kept at different temperatures (35.86-64.14 ℃) in a shaking water bath for 2 hours at 200 rpm. After cooling to ambient temperature, 0.1 N HCl solution was added until the dispersion reached pH 6.0. The starch was recovered by centrifuging at 3,600 rpm for 10 minutes (Kubota 5420, Japan), and the precipitate was washed with 100 mL distilled water (3 times). This sample was dried at 35 ˚C for 24 hours, ground in a mortar, sieved and later stored in a glass jar.

Determination of degree of cross-linking of the cross-linked unripe banana starch

The degree of cross-linking of the modified starch was determined using the method of Kaur et al. [44] with slight modification by using a rheometer (Anton Paar MCR 301). About 5 mL of distilled water was added into the rheometer cell containing 0.6 g of sample and was held at a temperature of 45℃ for 2 minutes. Next, it was heated up to 95℃ at the heating rate of 10℃/min and held for 3 minutes, then cooled to 45℃ at the cooling rate of 10℃/min. The peak viscosity values of the native and cross-linked starch were recorded, and the degree of cross-linking was calculated according to the following formula [45]:

$$\text{Degree of cross-linking, \%} = \frac{A-B}{A} \times 100 \quad (1)$$

Where A is the peak viscosity of the native starch, and B is the peak viscosity of the modified starch.

Swelling power and solubility index of native and modified starches

The swelling power and solubility of native and modified starches were conducted according to the Kittipongpatana and Kittipongpatana methods [46]. About 0.4g (dry basis) of starch samples were mixed with 12.5 mL of distilled water in a 15.0 mL centrifuge tube (pre-weighed). The mixture was equilibrated for 5 minutes at 25 ℃ and heated to 60 ℃ in a shaking water bath for 30 minutes. Next, the samples were cooled in an ice water bath for 1 minute, kept equilibrated at 25 ℃ for another 5 minutes and centrifuged at 3000 rpm for 5 minutes. The supernatant was collected, placed in an evaporating dish and dried at 130 ℃ for 4 hours. The swollen starch sediment was weighed. The swelling power

and solubility of the sample was calculated as follows:

$$\text{Swelling power, (g/g):} \quad \frac{weight\ of\ sediment}{initial\ weight\ of\ dry\ sample} \tag{2}$$

$$\text{Solubility index, (\%)} \quad : \frac{weight\ of\ dried\ supernatant}{initial\ weight\ of\ dry\ sample} \times 100 \tag{3}$$

Results and Discussion

Optimization of cross-linking condition using response surface methodology

Cross-linking of starch is a method that involves the addition of functional groups into the starch molecules, which affects the physicochemical properties of this starch. Response Surface Methodology (RSM) was conducted at different temperatures (40-60 ℃) and pH values (9.00-11.00) (Table 2) to obtain the optimum condition for the cross-linking. Table 2 shows the experimental values (Y) and the predicted values (FITS) of the response generated by the software. The highest experimental and predicted response values were at run number 13, which were 79.70% and 79.27%, respectively, under the temperature of 50 ℃ and pH 10.00 (Table 2). On the other hand, the lowest experimental and predicted response values were at run number 4, which were 35.83% and 35.73%, respectively, at the temperature of 60℃ and pH 11.00. According to Almonaityte et al. [47], natural starches are unstable to changes in pH and temperature. Therefore, minor changes in pH and temperature could influence its degree of cross-linking. Furthermore, different cross-linking agent also have different optimal pH and temperature ranges [48, 49]. In certain conditions, some level of alkalinity can facilitate a reaction by transforming the hydroxyl groups within starch molecules into alkoxide anions through ionization [50]. The response obtained shows that the degree of cross-linking was in the range of 35.83% to 79.70% (Table 2).

Table 2. Full RSM experimental design and the comparison between experimental and predicted values of the degree of cross-linking (%)

Run	Factors		Response (Degree of cross-linking, %)	
	X_1	X_2	Y	FITS
1	40.00	9.00	62.40	62.65
2	60.00	9.00	60.08	60.33
3	40.00	11.00	42.75	42.66
4	60.00	11.00	35.83	35.73
5	35.86	10.00	48.50	48.42
6	64.14	10.00	41.95	41.88
7	50.00	8.59	71.62	71.30
8	50.00	11.41	39.61	39.77
9	50.00	10.00	79.56	79.27
10	50.00	10.00	79.37	79.27
11	50.00	10.00	79.16	79.27
12	50.00	10.00	78.54	79.27
13	50.00	10.00	79.70	79.27
R^2: 0.9997%, R^2 (adj): 0.9995%, CV: 0.65%				

Note: X_1: Temperature (℃), X_2: pH value, Y: Experimental value, FITS: Predicted value, CV: Coefficient of Variation

The goodness of fit of the regression model was defined by determining the R^2 and adjusted R^2, which provides a measure of how much variability in the observed response values can be explained by the experimental factors and their interactions. Theoretically, the R^2 values should be at least 0.8 to have a good fit model.

The value closer to 1.0 shows a better fitting of the model with the actual data and a good correlation between experimental and predicted values. The R^2 value obtained was 0.9997, which means 0.9997 of the variability in the observed response could be explained by the model, and the remaining 0.0003 of the variability cannot be explained by the model obtained due to other factors that are not included in the model (Table 2). It indicated a strong and reasonable fit of the models to the experimental data [51].

The adjusted R^2 is the corrected value for R^2 after the elimination of unnecessary model terms. The adjusted R^2 obtained should not be more than 0.2 difference from the R^2 value [52] and it was observed that the adjusted R^2 value was 0.9995. The smaller difference between the adjusted R^2 and the R^2 shows that there are many non-significant terms included in the model, and it signifies the adequacy of model accuracy [53]. The coefficient of variation (CV) is the ratio of the standard error of estimation to the mean value of the observed response [54] and expressed as percentage (%). The CV of the model was 0.65% (Table 2). Firatligil-Durmus and Evranuz [55] stated that a model can be considered reasonably reproducible if its CV is not more than 10%. Therefore, the obtained CV has good reproducibility for this model and can be employed for the optimization process. A response surface regression analysis was performed, and the result for both regression and coefficient for the optimization of cross-linking of unripe banana starch can be presented as a coded equation at a 5% level:

$$Y_1 = 79.27 - 2.31X_1 - 11.15X_2 - 1.15X_1X_2 - 17.06X_1^2 - 11.86X_2^2$$

Where, Y1 = Degree of cross-linking (%), X_1 = Temperature (°C), and X_2 = pH value

Analysis of variance for the optimization of cross-linking condition of unripe banana starch

The effects of experimental variables on the linear, square and interaction terms were tested for adequacy and fitness by analysis of variance (ANOVA). The summary of the results obtained is presented in Table 3. The p-value is the probability of the factors having a very little or insignificant effect on the response. The larger F-value signifies the better fit of the RSM model to the experimental data. The F-value should be larger, and the p-value should be lower than 0.05 in order for the model to be statistically significant [56]. Therefore, all the regression, linear, square, and interaction models found in this study are highly significant as they have p-values lower than 0.05.

The lack-of-fit test measures the variation of the data concerning the fitted model and is one of the important aspects of a reduced model. If the lack of fit is significant, it means that the model does not fit the data well. The data should be rejected if the results show any significance in the lack-of-fit test. Insignificant lack-of-fit indicates a good model, which means that the p-value must be higher than 0.05. The F-value of the lack-of-fit can be obtained by dividing the lack-of-fit mean square by its pure error mean square. In this study, the lack-of-fit of the selected model showed a non-significant result (*p*-value >0.05) with a *p*-value of 0.7270. Thus, the non-significant p-value indicates that the model is good and fits well with the experimental data, and the parameters have a significant effect on the response value [57].

Table 3. Analysis of variance (ANOVA) of overall effects of test variables on the optimization of cross-linking

Source	Sum of Squares	df	Mean Square	*F*-value	*p*-value	Status
Model	3723.98	5	744.80	4712.63	< 0.0001	Significant.
X_1	42.80	1	42.80	270.79	< 0.0001	Significant
X_2	993.89	1	993.89	6288.73	< 0.0001	Significant.
X_1X_2	5.29	1	5.29	33.47	0.0007	Significant.
X_1X_1	2024.47	1	2024.47	12809.66	< 0.0001	Significant.
X_2X_2	979.20	1	979.20	6195.81	< 0.0001	Significant
Residual	1.11	7	0.1580			
Lack of Fit	0.2824	3	0.0941	0.4570	0.7270	Not Significant
Pure Error	0.8239	4	0.2060			
Total	3725.09	12				

Note: X_1: Temperature (℃), X_2: pH value, df: Degree of freedom

Contour and surface plot

The previously mentioned model was used for the optimization process, and the contour and surface plot was generated as the graphical representation of the response factor based on the regression equation above. The response variable was set to a maximum while both temperature and pH variables were kept in range all the time.

The desirability value was used to determine the optimum combination of the variables for the cross-linking conditions of the starch that leads to the maximized response while satisfying the restriction of the model [58,59]. The value for desirability is between 0.000 and 1.000 for a set of responses [51], and usually, the factor setting/combination that maximized the desirability for the optimization was chosen. The ideal optimum desirability in the RSM model is 1.000, with a value between 0.6 and 0.8 is considered acceptable. The highest desirability value of 1.000 (Figure 1) was obtained at a temperature of 50.57℃ with pH 9.52 **(**these values have been rounded to the nearest integer**)** and was identified as the optimum condition for the cross-linking of the unripe banana starch in this study. A high desirability value signified that the optimized model had high potential in producing the desired outcome aimed for the model.

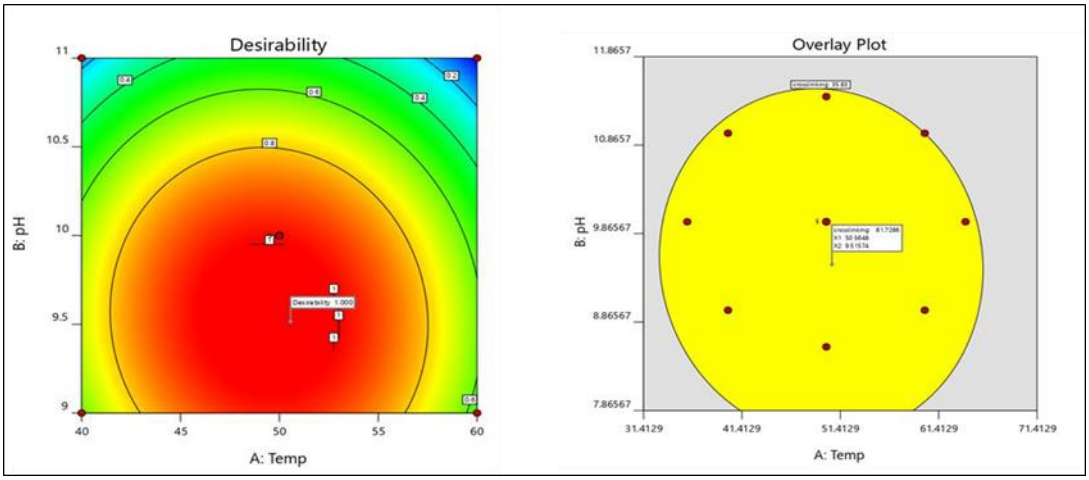

Figure 1. Desirability and overlaid contour plot for the degree of cross-linking (%) at the predicted optimum conditions

The overlaid contour plot is a technique used to combine the variables and response in a similar graph, and the conclusion can be made according to the interaction between the variables and response [60]. The overlaid contour plot is presented in Figure 1 in order to identify the feasibility of the response value at the optimum condition of the variables. The overlaid contour plot showed that the suggested optimum conditions for the temperature (50.57 ℃) and pH (9.52) fell in the yellow region, with the predicted value of the response (degree of cross-linking) of 81.73%. The yellow region means the entire range of all the intervals meets the specified criteria, which indicates that the conditions are feasible to be carried out. On the contrary, the grey region represents the area in which the conditions are not fit to be experimentally done.

The two-dimensional (2D) contour plot and three-dimensional (3D) surface plot (Figure 2) affirmed the effect of both temperature and pH as independent variables towards the degree of cross-linking. The red zone in both 2D and 3D plots represents the higher degree of cross-linking, while the blue zone indicates the lowest. The temperature and pH have greater interaction and also highly contribute to the response, as indicated by the steeper and more curved surface [61] (Figure 2). The 3D plot explained that the increase in temperature and time led to a substantial increase in the response until it achieved the optimal conditions at a temperature of 50.57 ℃ and pH 9.52. However, the response decreased significantly at the point higher than the optimal conditions, which means the variables have a negative impact on the degree of cross-linking. Relatively, the optimal conditions for this experiment correspond to the maximum degree of cross-linking of 81.73%.

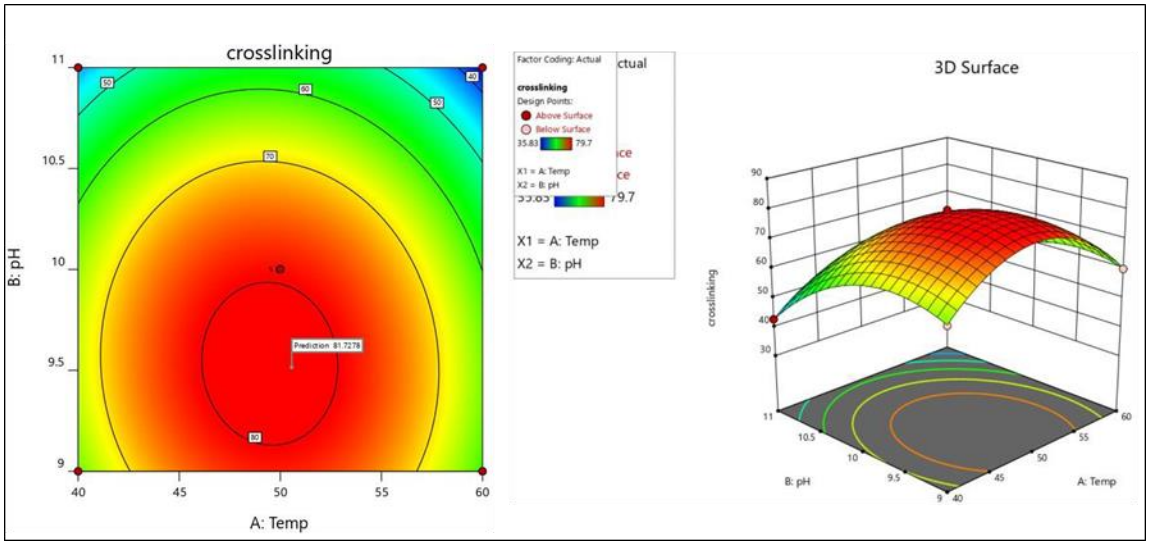

Figure 2. Two-dimensional (2D) contour plot and three-dimensional (3D) surface plot of the degree of cross-linking (%) at the predicted optimum conditions

Verification of the feasible optimum condition

In order to achieve a precise estimation of the optimum condition of all the variables and a prediction of the model fitness, both numerical and graphical validation plays a definite role in deciding the optimum variable combination for a maximum output [62]. The suitability of the model equation for predicting the optimum response values was further evaluated and tested using an independent sample t-test by SPSS between the experimental and predicted values. The result in Table 4 shows that there is no significant difference (p-value>0.05**)** between the experimental values (82.38%) and predicted values (81.73%) for all dependent variables. Therefore, the validation of the model was confirmed, and the mentioned model can be applied for the optimization of the cross-linking of

unripe banana starch.

Table 4. Verification of the experimental and predicted value of the degree of cross-linking (%) at the optimum condition

Optimum Condition		Degree of cross-linking (%)	
X_1	X_2	Y	FITS
50.57	9.52	82.38[a]	81.73[a]

Note: X_1: Temperature (℃), X_2: pH Value, Y: Experimental Value, FITS: Predicted Value. Means with same letters within a column are not significantly different (p >0.05) between experimental and predicted values.

Degree of cross-linking and its effects on swelling and solubility

The degree of cross-linking of the cross-linked starch was measured and calculated using its peak viscosity value. Yin et al. [63] have mentioned that peak viscosity is the most useful property to measure the degree of cross-linking. As shown in Table 5, the peak viscosities obtained are between 8.40 and 18.99 cP, at 35 to 75% degree of cross-linking. It was observed that the peak viscosities of this modified starch decreased significantly as the degree of cross-linking was above 75%, with peak viscosity ranging between 6.01 and 6.35 cP. The highest degree of cross-linking obtained from this study was 79.70%, with a peak viscosity of 6.01 cP. Almonaityre et al. [47] explained that the degree of cross-linking affects the peak viscosity of the cross-linked starch paste, where starch paste with a higher level of cross-linking will show a lower peak viscosity [21]. The findings of this study agree with Babu et al. [64] (Table 5). The presence of an STMP/STPP mixture in an alkaline condition caused a large number of hydrophilic phosphorous groups to react with hydroxyl moieties of starch chains, enabling di-starch phosphate interaction in the inner of the granules [62, 63]. Kou et al. [65] also stated that a higher amount of phosphorous will produce a higher degree of cross-linking, and an increase in the alkalinity of the cross-linking medium will accelerate this reaction [48]. The introduction of the covalent bonds or the cross-links in the granules, therefore, decreased the mobility of the molecules and strengthened the glucose chain [47]. This outcome will inhibit the granular breakdown, producing more stable starch toward thermal and mechanical energy and resulting in a lower peak viscosity value.

Table 5. Peak viscosity and degree of cross-linking (%) of each RSM run order

Run	Factor		Peak viscosity (cP)	Degree of Cross-Linking (%)
	X_1	X_2		
1	40.00	9.00	11.13	62.40
2	60.00	9.00	11.82	60.08
3	40.00	11.00	16.95	42.75
4	60.00	11.00	18.99	35.83
5	35.86	10.00	15.24	48.5
6	64.14	10.00	17.18	41.95
7	50.00	8.59	8.40	71.62
8	50.00	11.41	17.88	39.61
9	50.00	10.00	6.05	79.56
10	50.00	10.00	6.11	79.37
11	50.00	10.00	6.17	79.16
12	50.00	10.00	6.35	78.54
13	50.00	10.00	6.01	79.70

Note: X_1: Temperature (℃), X_2: pH, cP: Centipoise

Table 6 shows the swelling and solubility results for native and cross-linked starches at the optimum conditions suggested by RSM. Swelling is the hydration capacity of starch and the extent of starch granules interaction within both amorphous and crystalline regions [66]. In contrast, solubility is associated with the leaching of amylose from the starch granules during swelling [67]. The results revealed that both swelling, and solubility of native starch were reduced from 2.0528 g/g and 13.17% to 1.9011 g/g and 8.56%, respectively, after the cross-linking treatment at the optimum conditions (temperature: 50.57℃, pH: 9.52) with 81.73% degree of cross-linking. According to Carmona-Garcia et al. [68], a higher degree of cross-linking resulted in a decrease of hydration properties and inhibition of water penetration for swelling, thus lowering swelling of the starch [48, 65] and restricting the starch molecules (mainly amylose) to leach out from the starch granule [66, 67] and reduce the starch solubility [69].

Table 6. Swelling power and solubility index of native and cross-linked starch

Starch Sample	Native	Cross-Linked
Swelling power (g/g)	$2.0528^{a} \pm 0.0008$	$1.9011^{b} \pm 0.0011$
Solubility index (%)	$13.17^{a} \pm 0.0200$	$8.56^{b} \pm 0.0200$

Note: Means with different letters within the row are significantly different (p <0.05) between native and cross-linked samples

Conclusion

The optimisation of starch modification through cross-linking by using RSM was successfully investigated, and the data was systematically interpreted. The optimisation of the present work through CCD revealed that the best optimum conditions for a maximum degree of cross-linking (81.73%) were temperature 50.57 ℃ and pH 9.52. Both variables (temperature and pH) had a significant effect on the response (degree of cross-linking). It was also observed that the degree of cross-linking affects the peak viscosity of the modified starch in the RSM run. The peak viscosity decreased significantly when the degree of cross-linking was higher than 75. It was also observed that cross-linking has significant effects on the swelling power and solubility of the starch, whereby both the swelling power and solubility index of cross-linked starch were significantly decreased. Swelling power decreased from 2.0528 g/g to 1.9011, and the solubility index decreased from 13/17% to 8.56%. This was due to the new linkages created during the cross-linking process that strengthened the starch intermolecular interaction and integrity. Thus, this prevents chain disruption and breakage and reduces swelling power and solubility index by limiting swelling and amylose leaching. As additional covalent bonds were introduced through the cross-linking process, cross-linked starch exhibits higher tolerance to acid, heat, and shear forces and improves its viscosity properties. Therefore, cross-linked starch can be used as a thickening, texturizing and stabilizing agent in foods such as yoghurt, sauces and dairy products.

Acknowledgement

The authors are grateful and would like to thank the Ministry of Higher Education for supporting and funding this research project under Fundamental Research Grant Scheme (600-IRMI/FRGS5/3(195/2019); FRGS/1/2018/WAB01/UITM/02/1

References

1. Alcázar-alay, S. C. and Meireles, M. A. A. (2015). Physicochemical properties, modifications and applications of starches from different botanical sources. *Food Science and Technology*, 35(2): 215-236.
2. Abbas, K. A., Khalil, S. K. and Hussin, A. S. M. (2010). Modified starches and their usage in selected food products: A review study. *Journal of Agricultural Science*, 2(2): 90-100.
3. Gao, F., Li, D., Bi, C. H., Mao, Z. H. and Adhikari, B. (2014). Preparation and characterization of starch crosslinked with sodium trimetaphosphate and hydrolyzed by enzymes. *Carbohydrate Polymers*, 103(1): 310-318.
4. Punia, S., Dhull, S. B., Kunner, P. and Rohilla, S. (2020). Effect of γ-radiation on physico-chemical, morphological and thermal characteristics of lotus

seed (*Nelumbo nucifera*) starch. *International Journal of Biological Macromolecules*, 157: 584-590.

5. Sandhan, S., Thombre, N. and Sagar Aher. (2017). Isolation and evaluation of starch from *Musa Paradisiaca Linn.* as a binder in tablet. *International Journal of Pharmaceutical Sciences and Research*, 8(8): 3484-3491.
6. Wang, J. S., Wang, A. B., Ma, W. H., Xu, B. Y., Zang, X. P., Tan, L., Jin, Z. Q. and Li, J. Y. (2019). Comparison of physicochemical properties and in vitro digestibility of starches from seven banana cultivars in China. *International Journal of Biological Macromolecules*, 121: 279-284.
7. Fida, R., Pramafisi, G. and Cahyana, Y. (2020). Application of banana starch and banana flour in various food product: A review. *International Conference on Food and Bio-Industry* 2019: 443.
8. Pelissari, F. M., Andrade-Mahecha, M. M., Sobral, P. J. D. A. and Menegalli, F. C. (2012). Isolation and characterization of the flour and starch of plantain bananas (*Musa paradisiaca*). *Starch/Staerke*, 64(5): 382-391.
9. Sultan, S. and Rangaraju, V. (2014). Changes in colour value of banana var. Grand Naine during ripening. *Bioscience Trends*, 7(9): 726-728.
10. Mattsson, L., Williams, H., and Berghel, J. (2018). Waste of fresh fruit and vegetables at retailers in Sweden – Measuring and calculation of mass, economic cost and climate impact. *Resources, Conservation Recycling*, 130: 118-126.
11. Karim, R. S. M., Rahmatullah, N., Nordin, M. F. M. and Rajin, S. M. A. K. (2018). Effect of stage of maturity and frying time on the quality of banana springs. *Pertanika Journal of Tropical Agricultural Science*, 41(3): 1097-1110.
12. Zhang, P., Whistler, R. L., N. BeMiller, J. and Hamaker, B. R. (2005). Banana starch: production, physicochemical properties, and digestibility- a review. *Carbohydrate Polymers*, 59: 443-458.
13. Pacheco-Delahaye, E., Maldonado, R., Pérez, E. and Schroeder, M. (2008). Production and characterization of unripe plantain *(Musa paradisiaca L.*) flours. *Interciencia*, 33(4): 290-296.
14. Santana, A. L. and Meireles, M. A. A. (2014). New starches are the trend for industry apllications: A review. *Food and Public Health*, 4(5): 229-241.
15. Zabala, C. C. V. (2020). An overview on starch structure and chemical nature. In *Starch-based Nanomaterials* (1st edition). Springer, Cham: pp. 3-9.
16. Singla, D., Singh, A., Dhull, S. B., Kumar, P., Malik, T. and Kumar, P. (2020). Isolation, morphology, modification and novel applications concern - A review. *International Journal of Biological Macromolecules*, 163: 1283-1290.
17. Waliszewski, K. N., Aparicio, M. A., Bello, L. A. and Monroy, J. A. (2003). Changes of banana starch by chemical and physical modification. *Carbohydrate Polymers*, 52: 237-242.
18. Alimi, B. A., Workneh, T. S. and Sibomana, M. S. (2016). Effect of hydrothermal modifications on functional, pasting and structural properties of false banana (*Ensete ventricosum*) starch. *Food Biophysics*, 11(3): 248-256.
19. Punia, S. (2020). Barley starch modifications: Physical, chemical and enzymatic - A review. *International Journal of Biological Macromolecules*, 144: 578-585.
20. Korkut, A. and Kahraman, K. (2021). Production of cross-linked resistant starch from tapioca starch and effect of reaction conditions on the functional properties, morphology, X-ray pattern, FT-IR spectra and digestibility. *Journal of Food Measurement and Characterization*, 15(2): 1693-1702..
21. Babu, A. S., Naik, G. N. M., James, J., Aboobacker, A. B., Eldhose, A. and Mohan, R. J. (2018). A comparative study on dual modification of banana (*Musa paradisiaca*) starch by microwave irradiation and cross-linking. *Journal of Food Measurement and Characterization*, 12(3): 2209-2217.
22. Compart, J., Singh, A., Fettke, J. and Apriyanto, A. (2023). Customizing starch properties: A review of starch modifications and their applications. *Polymers*, 15(16): 15163491.
23. Nawaz, H., Waheed, R., Nawaz, M. and Shahwar, D. (2020). Physical and chemical modifications in

starch structure and reactivity. Chemical properties of starch. Intechopen Publisher.

24. Souto-Maior, J. F. A., Reis, A. V., Pedreiro, L. N. and Cavalcanti, O. A. (2010). Phosphated crosslinked pectin as a potential excipient for specific drug delivery: Preparation and physicochemical characterization. *Polymer International*, 59(1): 127-135.
25. Majzoobi, M., Hedayati, S., Habibi, M., Ghiasi, F. and Farahnaky, A. (2014). Effects of corn resistant starch on the physicochemical properties of cake. *Journal of Agricultural Science and Technology*, 16(3): 569-576.
26. Xie, Y., Zhang, B., Li, M. and Chen, H. (2019). Effects of cross-linking with sodium trimetaphosphate on structural and adsorptive properties of porous wheat starches. *Food Chemistry*, 289(3): 187-194.
27. Guo, L., Liu, R., Li, X., Sun, Y. and Du, X. (2015). The physical and adsorption properties of different modified corn starches. *Starch/Staerke*, 67(34): 237-246.
28. Sharma, V., Kaur, M., Singh, K. and Kumar, S. (2020). Effect of cross-linking on physicochemical, thermal, pasting, in vitro digestibility and film forming properties of Faba bean (*Vicia faba L.*) starch. *International Journal of Biological Macromolecules*, 159: 243-249.
29. Prompiputtanapon, K., Sorndech, W. and Tongta, S. (2020). Surface modification of tapioca starch by using the chemical and enzymatic method. *Starch - Stärke*, 72(3-4): 1900133.
30. Ding, L., Huang, Q., Xiang, W., Fu, X., Zhang, B. and Wu, J. Y. (2022). Chemical cross-linking reduces in vitro starch digestibility of cooked potato parenchyma cells. *Food Hydrocolloids*, 124: 107297.
31. Roman, L., Reguilon, M. P., Martinez, M. M. and Gomez, M. (2020). The effects of starch cross-linking, stabilization and pre-gelatinization at reducing gluten-free bread staling. *LWT - Food Science and Technology*, 132(7): 109908.
32. Rao, J. S. and Parimalavalli, R. (2019). Effect of cross-linking on structural, chemical and functional properties of corn starch. *International Journal of Food Science and Nutrition*, 4(3): 135-140.
33. Sukarminah, E., Wulandari, E., Lanti, I. and Andrasyifa, D. (2019). Physicochemical characteristics of cross-link modified sorghum flour in Bandung local cultivars. *Scientific Papers Series-Management, Economic Engineering in Agriculture and Rural Development*, 19(3): 569-575.
34. Liu, X., Lan, C., Al, A., Yu, L. and Zhou, S. (2016). Preparation of cross-linked high amylose corn-starch and its effects on self-reinforced starch films. *International Journal of Food Engineering*, 12(7): 673-680.
35. Shen, Y., Zhang, N., Xu, Y., Huang, J., Wu, D. and Shu, X. (2019). Physicochemical properties of hydroxypropylated and cross-linked rice starches differential in amylose content. *International Journal of Biological Macromolecules*, 128: 775-781.
36. Yolmeh, M. and Jafari, S. M. (2017). Applications of response surface methodology in the food industry processes. *Food and Bioprocess Technology*, 10(3): 413-433.
37. Bambang Widjanarko, S., Ulandari, D. and Fibrianto, K. (2023). Response surface methodology in the optimization of walur (*Amorphophallus paeoniifolius* var. Sylvestris) starch pregelatinization process. *Advances in Food Science, Sustainable Agriculture and Agroindustrial Engineering*, 6(1): 62-71.
38. Ulfa, G. M., Putri, W. D. R., Fibrianto, K. and Widjanarko, S. B. (2021). Optimization studies on pre-gelatinized sweet potato starch influenced by temperature and time. *Food Research*, 5: 25-30.
39. Zainal Abiddin, N. F., Yusoff, A. and Ahmad, N. (2015). Optimisation of reaction conditions of octenyl succinic anhydride (OSA) modified sago starch using response surface methodology (RSM). *International Food Research Journal*, 22(3): 930-935.
40. Kahraman, K., Koksel, H. and Ng, P. K. W. (2015). Optimisation of the reaction conditions for the production of cross-linked starch with high resistant starch content. *Food Chemistry*, 174: 173-179.
41. Ayo-Omogie, H. N., Adeyemi, I. A. and Otunola,

E. T. (2010). Effect of ripening on some physicochemical properties of cooking banana (*Musa ABB* Cardaba) pulp and flour. *International Journal of Food Science and Technology*, 45(12): 2605-2611.

42. Agama-Acevedo, E., Nunez-Santiago, M. C., Alvarez-Ramirez, J. and Bello-Pérez, L. A. (2015). Physicochemical, digestibility and structural characteristics of starch isolated from banana cultivars. *Carbohydrate Polymers*, 124: 17-24.
43. Park, E. Y., Ma, J. G., Kim, J., Lee, D. H., Kim, S. Y., Kwon, D. J. and Kim, J. Y. (2018). Effect of dual modification of HMT and crosslinking on physicochemical properties and digestibility of waxy maize starch. *Food Hydrocolloids*, 75: 33-40.
44. Kaur, L., Singh, N. and Singh, J. (2004). Factors influencing the properties of hydroxypropylated potato starches. *Carbohydrate Polymers*, 55(2): 211-223.
45. Mirmoghtadaie, L., Kadivar, M. and Shahedi, M. (2009). Effects of cross-linking and acetylation on oat starch properties. *Food Chemistry*, 116(3): 709-713.
46. Kittipongpatana, O. S. and Kittipongpatana, N. (2011). Preparation and physicochemical properties of modified jackfruit starches. *LWT - Food Science and Technology*, 44(8): 1766-1773.
47. Almonaityte, K., Cizauskaite, G., Bendoraitiene, J. and Peciulyte, L. (2021). Peculiarities of cross-linking degree determination for the starches of different botanical origin. *Starch - Stärke*, 2100041: 1-10.
48. Mulualem, Y., Belete, A. and Gebre-Mariam, T. (2019). Preparation and evaluation of dual modified Ethiopian yam (*Dioscorea abyssinica*) starch for sustained release tablet formulations. *Ethiopian Pharmaceutical Journal*, 34(1): 37-50.
49. Sudheesh, C., Sunooj, K. V., Alom, M., Kumar, S., Sajeevkumar, V. A. and George, J. (2020). Effect of dual modification with annealing, heat moisture treatment and cross-linking on the physico-chemical, rheological and in vitro digestibility of underutilised kithul (*Caryota urens*) starch. *Journal of Food Measurement and Characterization*, 14(3): 1557-1567.
50. Malik, M. K., Kumar, V., Sharma, P. P., Singh, J., Fuloria, S., Subrimanyam, V., Fuloria, N. K. and Kumar, P. (2022). Improvement in digestion resistibility of mandua starch (*Eleusine coracana*) after cross-linking with epichlorohydrin. *ACS Omega*, 7(31): 27334-27346.
51. Jarpa-Parra, M., Bamdad, F., Wang, Y., Tian, Z., Temelli, F., Han, J. and Chen, L. (2014). Optimization of lentil protein extraction and the influence of process pH on protein structure and functionality, *LWT - Food Science and Technology*, 57(2): 461-469.
52. Aziz, N. and Arof, A. K. (2016). A model to investigate extraction parameters for anthocyanin from melastoma malabathricum. *Optical and Quantum Electronics*, 48(3): 7.
53. Manmai, N., Balakrishnan, D., Obey, G., Ito, N., Ramaraj, R., Unpaprom, Y. and Velu, G. (2022). Alkali pretreatment method of dairy wastewater based grown Arthrospira platensis for enzymatic degradation and bioethanol production. *Fuel*, 330: 125534.
54. Lv, C., Jia, X., Li, M., Yang, J. and Zhao, G. (2011). Optimization of extraction process of crude protein from grape seeds by RSM. *Food Science and Technology Research*, 17(5): 437-445.
55. Firatligil-Durmus, E. and Evranuz, O. (2010). Response surface methodology for protein extraction optimization of red pepper seed (*Capsicum frutescens*). *LWT*, 43(2): 226-231.
56. Chen, M., Zhao, Y. and Yu, S. (2015). Optimisation of ultrasonic-assisted extraction of phenolic compounds, antioxidants, and anthocyanins from sugar beet molasses. *Food Chemistry*, 172: 543-550.
57. Shrivastava, A., Tripathi, A. D., Paul, V. and Rai, D. C. (2021). Optimization of spray drying parameters for custard apple (*Annona squamosa L.*) pulp powder development using response surface methodology (RSM) with improved physicochemical attributes and phytonutrients. *LWT - Food Science and Technology*, 151: 112091.
58. Parmar, I., Sharma, S. and Rupasinghe, H. P. V.

(2015). Optimization of β-cyclodextrin-based flavonol extraction from apple pomace using response surface methodology. *Journal of Food Science and Technology*, 52(4): 2202-2210.

59. Roselló-Soto, E., Galanakis, C. M., Brnčić, M., Orlien, V., Trujillo, F. J., Mawson, R., Knoerzer, K., Tiwari, B. K. and Barba, F. J. (2015). Clean recovery of antioxidant compounds from plant foods, by-products and algae assisted by ultrasounds processing. Modeling approaches to optimize processing conditions. *Trends in Food Science and Technology*, 42(2): 134-149.
60. Suseno, S. H., Jacoeb, A. M., Nugraha, R. and Salia. (2021). Bleaching optimization of tuna (*Thunnus sp.*) oil using response surface methodology. *Food Research*, 5(6): 92-103.
61. Zheng, B., Yuan, Y., Xiang, J., Jin, W., Johnson, J. B., Li, Z., Wang, C. and Luo, D. (2022). Green extraction of phenolic compounds from foxtail millet bran by ultrasonic-assisted deep eutectic solvent extraction: Optimization, comparison and bioactivities. *LWT - Food Science and Technology*, 154: 112740.
62. Das, M., Rajan, N., Biswas, P. and Banerjee, R. (2022). A novel approach for resistant starch production from green banana flour using amylopullulanase. *LWT - Food Science and Technology*, 153(8): 112391.
63. Zhang, Y., You, X., Hong, Y., Pu, A., Li, Z. and Li, M. (2014). Investigation of characterization and digestion of banana flour and banana starch. *Food and Machinery*, 30: 50-53.
64. Surendra Babu, A. and Parimalavalli, R. (2014). Effect of starch isolation method on properties of sweet potato starch. *Food Technology*, 38(1): 48-63.
65. Kou, T. and Gao, Q. (2018). New insight in crosslinking degree determination for crosslinked starch. *Carbohydrate Research*, 458-459: 13-18.
66. Reddy, C. K., Suriya, M., Vidya, P. V. and Haripriya, S. (2017). Synthesis and physicochemical characterization of modified starches from banana (*Musa AAB*) and its biological activities in diabetic rats. *International Journal of Biological Macromolecules*, 94: 500-507.
67. Oh, S. M., Kim, H. yun, Bae, J. E., Ye, S. J., Kim, B. Y., Choi, H. D., Choi, H. W. and Baik, M. Y. (2019). Physicochemical and retrogradation properties of modified chestnut starches. *Food Science and Biotechnology*, 28(6): 1723-1731.
68. Carmona-Garcia, R., Sanchez-Rivera, M. M., Méndez-Montealvo, G., Garza-Montoya, B. and Bello-Pérez, L. A. (2009). Effect of the cross-linked reagent type on some morphological, physicochemical and functional characteristics of banana starch *(Musa paradisiaca*). *Carbohydrate Polymers*, 76(1): 117-122.
69. Siroha, A. K. and Sandhu, K. S. (2018). Physicochemical, rheological, morphological, and in vitro digestibility properties of cross-linked starch from pearl millet cultivars. *International Journal of Food Properties*, 21(1): 1371-1385.

Malaysian Journal of Analytical Sciences (MJAS)
Published by Malaysian Analytical Sciences Society

MODIFIED CHRYSIN-BASED BIOSORBENT FOR THE DISPERSIVE MICRO-SOLID PHASE EXTRACTION OF SELECTED PHENOLIC ACIDS FROM STINGLESS BEE HONEY

(Biopenjerap yang Diubahsuai berasaskan Krisin untuk Pengekstrakan Fasa Pepejal-mikro Asid Fenolik Terpilih secara Serakan daripada Madu Lebah Tanpa Sengat)

NyukTing Ng[1], Aemi Syazwani Abdul Keyon[1,2*], Wan Aini Wan Ibrahim[1*], Mohd Marsin Sanagi[1] and Faridah Mohd Marsin[3]

[1]*Department of Chemistry, Faculty of Science, Universiti Teknologi Malaysia, 81310 UTM Johor Bahru, Johor, Malaysia*
[2]*Centre for Sustainable Nanomaterials, Ibnu Sina Institute for Scientific and Industrial Research, Universiti Teknologi Malaysia, 81310 UTM Johor Bahru, Johor, Malaysia*
[3]*Jabatan Kimia Malaysia Negeri Pahang, Jalan Dato' Bahaman, Alor Akar, 25662 Kuantan, Pahang, Malaysia*

[*]*Corresponding author: aemi@utm.my; waini@utm.my*

Received: 13 September 2023; Accepted: 30 December 2023; Published: 28 February 2024

Abstract

This study focuses on the preparation, characterisation, and application of a chrysin-based biosorbent (TA-CHY) for extracting protocatechuic acid (PCA) and vanillic acid (VA) from stingless bee honey (SBH) using a dispersive micro-solid phase extraction method. The extracted analytes were separated using high-performance liquid chromatography and detected using an ultraviolet detector. TA-CHY was prepared by depositing tannic acid onto the amino-functionalized chrysin. Its point of zero charge was determined at pH 6.8. Fourier transform infrared spectroscopy analysis had identified the presence of C=N, C=C, O-H, SiOR and C-O groups in TA-CHY, while aggregate formation was observed on TA-CHY through scanning electron microscopy. Energy dispersive X-ray study revealed the elemental composition of TA-CHY was 52.9% of C, 34.0% of O, 6.80% of Si and 6.3% of N. Its specific surface area was found to be 5.913 m^2/g via Brunauer-Emmett-Teller surface area analysis. Optimised extraction parameters were 1 min extraction time, 300 µL methanol as desorption solvent, 15 min desorption time, sample pH of 2, no NaCl salt addition, 0.20 g biosorbent mass and 2 mL ethanol as dispersant solvent. The developed method was validated using matrix-match calibration where real SBH samples spiked with PCA and VA in the concentration range of 0.5-50 mg/L. The method exhibited satisfactory analytical performance characteristics, with a limit of detection ranging from 0.81 to 1.37 mg/kg, a limit of quantification ranging from 2.69 to 4.56 mg/kg, relative recoveries ranging from 79.38% to 113.38%, and precision with relative standard deviation values ranging from 0.29% to 10.83%. Importantly, the proposed method obtained a score of 71 on the analytical Eco-Scale, indicating its acceptability as a green method.

Keywords: chrysin, biosorbent, dispersive micro-solid phase extraction, phenolic acids, stingless bee honey

Abstrak

Kajian ini memberi tumpuan pada penyediaan, pencirian, dan penggunaan biopenjerap berasaskan krisin (TA-CHY) untuk mengekstrak asid protokatekuik (PCA) dan asid vanillik (VA) daripada madu lebah (SBH) tanpa sengat dengan menggunakan

kaedah pengekstrakan fasa pepejal-mikro secara serakan. Analit yang diekstrak telah diasingkan menggunakan kromatografi cecair berprestasi tinggi dan dikesan menggunakan pengesan ultraungu. Biopenjerap TA-CHY telah disediakan dengan mendepositkan asid tannik pada krisin yang telah diberikan fungsi amino. Cas sifar titiknya telah ditentukan pada pH 6.8. Analisis spektroskopi inframerah transformasi Fourier telah mengenalpasti kehadiran kumpulan C=N, C=C, O-H, SiOR dan C-O dalam TA-CHY manakala pembentukan agregat diperhatikan pada TA-CHY melalui mikroskop pengimbas electron. Kajian tenaga penyerakan sinar-X mendedahkan komposisi unsur bagi TA-CHY ialah 52.9% C, 34.0% O, 6.80% Si dan 6.3% N. Luas permukaan spesifiknya didapati sebanyak 5.913 m^2/g melalui analisis kawasan permukaan Brunauer-Emmett-Teller. Parameter pengekstrakan yang dioptimumkan ialah 1 minit masa pengekstrakan, 300 µL metanol sebagai pelarut desorpsi, 15 minit masa desorpsi, pH sampel 2, tiada penambahan garam NaCl, 0.20 g jisim biopenjerap dan 2 mL etanol sebagai pelarut penyerakan. Kaedah yang dibangunkan telah disahkan menggunakan kalibrasi padanan-matriks dengan sampel SBH tulen dengan menambah PCA dan VA dalam lingkungan kepekatan 0.5-50 mg/L. Kaedah ini menunjukkan ciri prestasi analisis yang memuaskan, dengan had pengesanan antara 0.81 dan 1.37 mg/kg, had kuantitatif antara 2.69 dan 4.56 mg/kg, pemulihan relatif antara 79.38% dan 113.38%, dan ketepatan dengan sisihan piawai relatif, antara 0.29% dan 10.83%. Kaedah yang dicadangkan telah memperoleh markah 71 pada skala-Eko analitik yang menunjukkan kebolehterimaannya sebagai kaedah hijau adalah sangat penting.

Kata kunci: krisin, biopenjerap, pengekstrakan fasa pepejal-mikro secara serakan, asid fenolik, madu lebah tanpa sengat

Introduction

Stingless bee honey (SBH) is a remarkable natural sweetener that possesses several unique physicochemical characteristics, namely high acidity (pH 3.07-3.19), high moisture content (20.00-33.24 g/100 g honey), and low sugar content (50.35-62.38 g/100 g honey) [1, 2]. It is well-known for its unique formulation of bioactive compounds, notably phenolic acids (PAs). PAs are bioactive compounds with potent anti-inflammatory and anti-oxidant properties [3, 4], making their analysis in honey crucial for assessing honey quality and potential health-promoting effects. However, the complicated matrix of the viscous and hygroscopic honey sample makes it difficult to determine the presence of PAs in a direct way. This challenge inspired researchers and thereby promoted the development of more effective and specialized sample preparation methods for SBH [5]. As the search for eco-friendly and sustainable analytical methods has gained prominence, and green analytical chemistry ideas are now more widely acknowledged [6]. It is critical to develop efficient, innovative and environmentally friendly sample preparation procedures for assessing PAs in honey.

Sample preparation methods, such as solvent extraction (SE), liquid-liquid extraction (LLE) and solid-phase extraction (SPE), have been commonly employed for PA analysis [7]. These methods are relatively cheap and simple, without the need of expensive, complicated and specialized instrumentation. Nonetheless, these methods are often associated with drawbacks, including the use of large volumes of organic solvents, which are not environmentally friendly and may pose potential health hazards. For instance, the main disadvantages of LLE are the high volume of solvents used (from a few mL to L of ethyl acetate and diethyl ether) and the emulsion formation, which makes it challenging to recover some phenolic compounds effectively. To overcome emulsion problem, addition of surfactant (methanol and ethanol), the need of ultrasonication, freezing out after separation of phases and gentle sample shaking might be needed. While these solutions are less favorable as addition of surfactant may affect the partition equilibrium between phases, additional steps like shaking, ultrasonication and freezing out could be laborious and may need a longer time to perform extraction. More organic solvent also may be needed for rinsing after the freezing out process.

In SPE, commercial SPE cartridges often require smaller quantities of samples and low amounts of organic solvents while its vacuum manifold and vacuum pumps might be costly for the analysis of a reduced number of samples. The number of stages should be kept to a minimum because each stage or transfer might result in loss of analytes. These limitations motivated analytical chemists to improve and develop new mode of SPE methods and one of these methods is dispersive-micro-solid phase extraction (d-µ-SPE). Furthermore, various analytical approaches have been used to analyze PAs, each with its own set of limitations. Thin-layer chromatography, which employs silica gel, cellulose, or polyamide layers, provides a quick and cost-effective separation process. However, its disadvantage is that it has limited quantitation capabilities due to the loss of analytes during sample processing. The Folin-Ciocalteu reagent, which has traditionally been used for colorimetric measurement of total phenolic content has difficulty in identifying individual phenolic components. This is mostly due to the involvement of other components in food extracts that function as reducing agents. However, employing gas chromatography for

the separation of PAs is challenging as these phenolic compounds have low volatility and derivatisation is necessary. Reversed phase high-performance liquid chromatography (HPLC) provides effective separation of PAs, nevertheless, there were limited studies that focused on PAs. Hence, HPLC was employed for the separation of PAs in this study.

The first d-μ-SPE was developed by Anastassiades et al. [8]. It is one of the desirable methods for sample preparation due to its capacity to offer improved sensitivity, adaptability, and compatibility with automation [9]. When compared to SE, LLE and SPE, d-μ-SPE usually uses far less organic solvent (few μL to mL), making it a greener and a more economical option. It also tends to be quicker than SE and LLE as only few minutes needed for its sorption-desorption process [10]. Besides that, d-μ-SPE may give high selectivity for target analytes by using the right sorbent and experimental conditions. Therefore, sorbent is a core element of this method, facilitating the efficient separation of analytes from complicated matrices. Dispersive mode of SPE typically employs sorbent materials based on silica, layered double hydroxides, magnetic nanomaterials, porous polymers, metal organic framework, and even carbonaceous materials such as activated carbon, graphene, graphite and carbon nanotubes [11]. Furthermore, the development of biosorbents has become imperative in order to make full use of natural resources which includes magnetic cork composites [12], seed [13], tannic acid [14] and many others. Careful sorbent selection is significant in obtaining optimum analytical performances. However, ensuring the high efficiency and effectiveness of an analytical method is equally important as assuring its environmental sustainability.

Flavonoids, which are plentiful in nature, provide a sustainable and biocompatible alternative to traditional sorbents [10, 15]. In this study, d-μ-SPE was developed and combined with a novel chrysin-based biosorbent, TA-CHY for the analysis of vanillic acid (VA) and protocatechuic acid (PCA) in SBH. Chrysin, a natural flavonoid present in propolis and honey in large quantities [16] and shares structural similarities with PAs (benzene rings and hydroxyl groups). The modification of chrysin as a biosorbent which offer numerous advantages, including eco-friendliness, simplicity, and high potential to extract PAs. Since the chrysin biosorbent has remarkable affinity and selectivity towards PAs, it enables effective preconcentration of PAs from difficult matrices like SBH. The distinctive structural characteristics, such as its surface morphology and the presence of functional groups (hydroxyl groups, carbonyl groups, benzene ring), play a key role in increasing its ability to bind analytes, resulting in better analyte recovery and sensitivity [17]. The analysis of PAs in SBH is of great importance for assessing its quality. Therefore, this innovative approach is expected to contribute to the advancement of green analytical practices and provides researchers with a reliable method for the analysis of PAs in SBH. The eco-friendliness of the newly developed method was assessed by analytical Eco-scale metric proposed by Gałuszka et al. [18] to ensure the method align with the principles of green analytical chemistry.

Materials and Methods

Chemicals and reagents

Potassium dihydrogen phosphate, sodium nitrate, sodium hydroxide pellets, ortho-phosphoric acid (85%), nitric acid (65%), sodium chloride and tannic acid were supplied by Merck (Darmstadt, Germany). Analytical grade of toluene, *n*-hexane and acetonitrile were purchased from Thermos Fisher Scientific (Massachusetts, USA), Qrec (Selangor, Malaysia) and Qrec (Selangor, Malaysia), respectively. VA (97%) and PCA were obtained from Sigma-Aldrich (St. Louis, MO, USA). Absolute ethanol used in this study was obtained from VWR International S.A.S. (Fontenay-sous-Bois Cedex, France). Chrysin (99+%) and 3-aminopropyltriethoxysilane (APTES, 99%) were obtained from Acros Organics B.V.B.A. (Geel, Belgium). Methanol and isopropanol were provided by J.T. Baker (Center Valley, PA, USA). The ultrapure water (18.2 MΩ) was collected from Milli-Q gradient water system (Millipore, Massachusetts, USA). All analytical grade chemicals were used without further purification. 1000 mg/L stock solution of each analyte (PCA and VA) were separately prepared in methanol. After that, the stock solution of each analyte was utilized to make their respective single standard solutions of 100 and 10 mg/L. A sample solution was always made fresh before use. When not in use, the stock standard solutions were stored at 4 °C.

Instruments and apparatus

Fourier-transform infrared (FTIR) characterisation was carried out utilizing a PerkinElmer FrontierTM FT-IR spectrometer paired with a polarized UATR (Massachusetts, USA). Surface morphology was studied using a Jeol JSM-IT300LV scanning electron microscopy (SEM) from Essex County, Massachusetts, at 10-15 kV, 1000-2000× magnification, and a working

distance of 10.4-11.1 mm. The elemental composition was investigated using an energy dispersive X-ray spectroscopy (EDX) from Oxford Instrument X-max in Oxford, UK. The *Brunauer-Emmett-Teller* (BET) surface areas of the biosorbent were investigated using a NOVAtouch surface area and pore size analyser acquired from Quantachrome Corporation, Boynton Beach, FL, USA. The pH of the solution was measured using a Eutech pH meter, model pH 700 (Paisley, UK). The sorption equilibration of the biosorbent during point of zero charge measurement (pH_{pzc}) was facilitated by the use of a PROTECH orbital shaker (model 722). A ZX4 vortex mixer was purchased from VELP SCIENTIFICA, Italy for extraction purpose. A FAVORIT stirring hotplate (HS0707V2) was used to stir the solution. A KUBOTA 2420 centrifuge machine, made in Tokyo, Japan, was used for liquor separation. A BRANSON CPX3800H ultrasonicator (Danbury, CT, USA) was used to desorb analytes from the biosorbent surface and to degas the buffer solution. Mass of biosorbent was measured by using a Sartorius ENTRIS224-1S analytical balance (Göttingen, Germany).

The VA and PCA analyses were performed using a reversed phase HPLC (model 1220 Infinity LC) combined with a ultraviolet detector (G4288C). The HPLC was equipped with a 5 m, 2.1×150 mm Eclipse Plus C_{18} separating column. Both HPLC instrument and the separating column were purchased from Agilent Technologies, Santa Clara, CA, USA. The wavelength of detection for VA and PCA was fixed at 280 nm. An isocratic mobile phase, buffer-methanol (90:10) (v/v), was utilized for the chromatographic separation. First, 3.4022 g of potassium dihydrogen phosphate was dissolved in ~480 mL of ultrapure water. Next, the buffer pH was carefully adjusted to 3 using ortho-phosphoric acid or/and sodium hydroxide solution, followed by diluting the buffer to desired volume mark (500 mL) for the making of 0.05 M buffer solution. The prepared buffer was filtered using an LC solvent filter assembly (Agilent technologies, Santa Clara, CA, USA) paired with a 47 mm diameter nylon membrane filter (Whatman, Buckinghamshire, UK). The injection flow rate and volume were set at 0.5 mL/min and 20 µL, respectively. ChemStation software was used to process the chromatographic data. The peaks for PCA and VA showed on the chromatogram at ~4.2 and ~13.25 min, respectively.

Preparation of TA-CHY biosorbent

0.8 g of chrysin was weighed and dispersed in 80 mL of ethanol via stirring. Then, APTES (3%, v/v) prepared in 20 mL ethanol was added dropwise to the stirring mixture, followed by the addition of 2 g of tannic acid to the mixture. The mixture was stirred at room temperature for 24 hours. After that, the solid product was separated from the solvent mixture via filtration. It was rinsed with ethanol and deionized water for several times. At last, the solid product was collected and dried for 24 hours at 60°C.

Point of zero charge determination

Salt addition method was used to determine the pH_{pzc} of TA-CHY. First, initial pH value ($pH_{initial}$) of a 0.1M $NaNO_3$ solution (10 mL) was set at 3, adjusted with nitric acid or sodium hydroxide solutions. Then, in a 50 mL conical flask, 0.1 g of TA-CHY was dispersed uniformly in the $NaNO_3$ solution. The mixture was equilibrated for 24 hours using a mechanical orbital shaker at 200 rpm. At last, final pH, pH_{final} of the $NaNO_3$ solution was measured and recorded. The experiment was repeated with different pHi_{nitial} values (pH 5, 7, and 9), their corresponding pH_{final} values were determined as well.

Dispersive-micro solid phase extraction

A 45 mL of sample solution (pH 5) was poured to a centrifuge tube containing 0.15 g of TA-CHY dispersed in 2 mL of dispersant solvent, ethanol. Then, a vortex mixer was used to extract the analytes, PCA and VA from the sample for one min at 900 rpm. After that, TA-CHY was separated via centrifugation. The collected biosorbent was added with 300 µL of methanol as desorption solvent, followed by ultrasonically desorbed for 15 min. The extract was then separated again via centrifugation and dried under nitrogen flow. The dried sample was added with 150 µL of mobile phase (buffer: methanol at 9:1 ratio) as sample solvent. Finally, the reconstituted extract (20 µL) was injected to the HPLC instrument.

Real sample preparation

Four raw samples of SBH were collected from Alor Gajah (Malacca), Batang Kali, Hulu Selangor (Selangor), Mata Air, Chuping (Perlis) and Taiping (Perak) in Malaysia. Next, 10 g of honey was dissolved in 100 mL of ultrapure water to make the sample. Sodium hydroxide or ortho-phosphoric acid were used to adjust the pH of the diluted sample (~95 mL) to 2. Then, the pH-adjusted sample was diluted to the desired volume, 100 mL. The prepared sample was then readied for further study. When not in use, the SBH samples were kept in a dark, dry area at room temperature.

Method validation

The developed d-μ-SPE was verified using matrix-matched calibration by assessing a series of genuine SBH samples spiked with different levels of analytes. Its analytical characteristics, namely linearity, sensitivity in terms of limits of quantification (LOQ, 10(standard deviation of the response, σ/slope of the calibration curve, S)) and limits of detection (LOD, 3(σ/S)), accuracy in terms of relative standard deviation (RSD), and recovery in terms of relative recovery (RR) were investigated. The linearity ranges of both PVA and VA were 0.5-50 mg/L, and their model fitnesses were assessed through the coefficient of determination, R^2. Three replicate samples were examined on the same day (n=3) and different days (n=9) for intra- and inter-day precision investigations. The percentage of the recovered analyte in the spiked sample vs the known analyte in the spiked sample was expressed as the RR in this study.

Results and Discussion

Biosorbent characterization

A multidisciplinary approach was used to study the properties of TA-CHY such as studying pH_{pzc} using salt addition method, molecular compositions using FTIR, surface morphology and elemental analysis using SEM-EDX, and specific surface area using BET which revealed comprehensive insights into the structural and chemical characteristics of TA-CHY.

Surface morphology, elemental composition and surface area study

The SEM images of chrysin, tannic acid, and TA-CHY are shown in Figure 1. Figure 1(a) depicts pristine tannic acid as spherical with a smooth surface. In contrast, pristine chrysin has a cylindrical form with a rough surface, as seen in Figure 1(b). Figure 1(c) depicts SEM images of TA-CHY with some aggregate formation on the surface of tannic acid, demonstrating that the deposition of chrysin on the tannic acid surface was effective with the aid of APTES. Additional confirmation was obtained in the EDX results (Table 1), where the weight percentages of components changed when compared to the pristine chrysin and tannic acid. The presence of Si and N components in TA-CHY demonstrated that APTES bounded to the biosorbent surface. The surface areas of chrysin, tannic acid and TA-CHY were 5.262, 2.78 and 5.913 m^2/g, respectively.

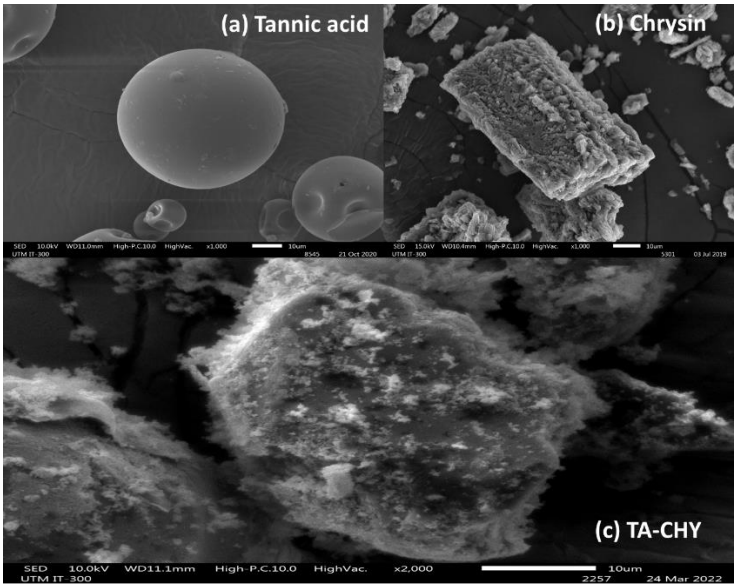

Figure 1. SEM images of (a) tannic acid at ×1000 resolution, (b) chrysin at ×1000 resolution and (c) TA-CHY at ×2000 resolution

Table 1. EDX results of TA-CHY, chrysin and tannic acid

Element	Weight Percentage (%)		
	TA-CHY	Chrysin	Tannic Acid
C	52.9	71.6	55.4
O	34.0	28.4	44.6
Si	6.80	-	-
N	6.30	-	-

Fourier transform infrared spectroscopy (FTIR) study

FTIR spectroscopy is a powerful analytical method that provides useful information on the functional groups that exist in the materials under investigation. The FTIR method was utilized in this investigation to analyze the functional groups of TA-CHY, chrysin, and tannic acid, as shown in Figure 2 (A). The FTIR spectra of chrysin showed multiple peaks at 1447.23-1496.74 and 3006.96 cm^{-1}, which were ascribed to aromatic ring C=C stretching and C-H stretching, respectively. Tannic acid and TA-CHY, on the other hand, displayed multiple C=C stretching bands of aromatic ring with vibration wavelengths of 1444.48-1607.43 and 1447.47-1600.36 cm^{-1}, respectively [19]. Furthermore, the C-O stretching, =C-H bending, C=O stretching, and C-O-C stretching were related with the peaks of chrysin at 1243.55, 839.19, 1649.34, and 1164.63 cm^{-1}, respectively. Many functional groups, including C=O, O-H, O=C-O-C, and C-O, were detected in tannic acid, with peaks emerging at 1703.14 (C=O stretching), 3273.99 (O-H stretching), 1310.56 (aromatic O=C-O-C stretching), and 1181.64 cm^{-1} (C-O stretching of aromatic alcohol). Several notable vibration frequencies were also detected in the FTIR spectra of TA-CHY: Sp^2 C=N double bond stretching measured at 1700.9 cm^{-1}, phenolic O-H bending measured at 1329.74 cm^{-1}, Si-OR stretching measured at 1038.77-1071.21 cm^{-1}, O-H stretching measured at 3152.64 cm^{-1}, and aromatic alcohol C-O stretching measured at 1198 cm^{-1}. This showed that some significant functional groups found in TA-CHY include the benzene ring, the O-H, the C=N, and the C=O groups, may improve the contacts between the sorbent and the sorbate via hydrophobic interaction, cation-π interaction, π-π interaction/aromatic stacking, and hydrogen bonding [20, 21]. Furthermore, the presence of a silanol group in TA-CHY showed that APTES were attached to the biosorbent surface to aid in the deposition of chrysin on tannic acid, as shown in Figure 1 (c). The discussed FTIR data are listed and tabulated in Table 2.

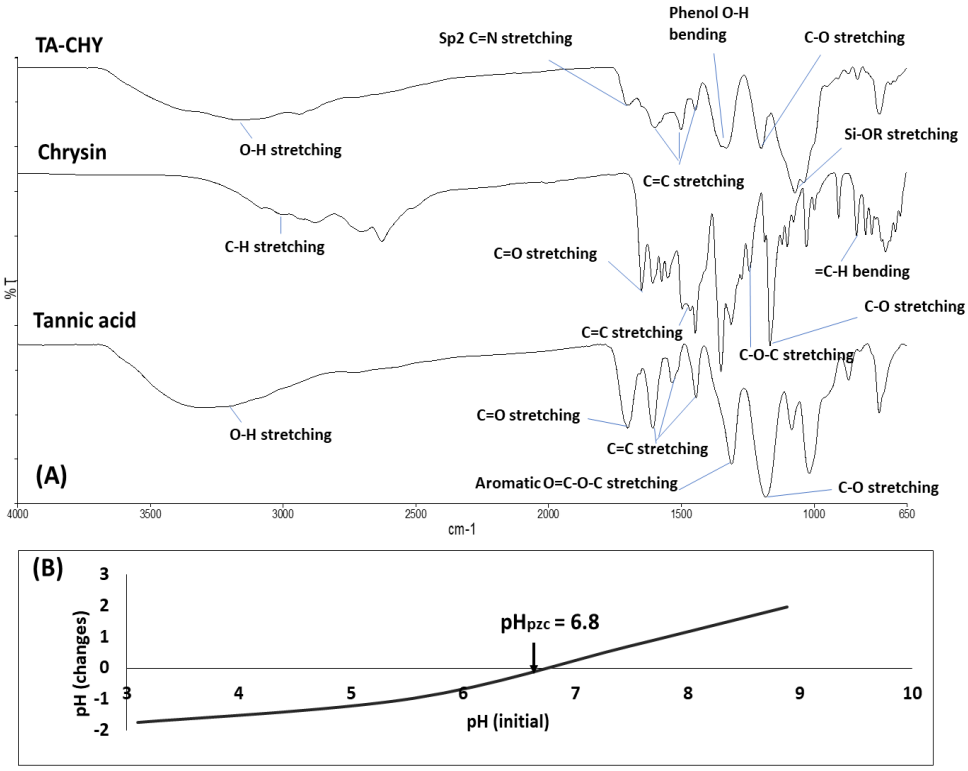

Figure 2. FTIR spectra of TA-CHY, chrysin and tannic acid (A); Graph of point of zero charge (B)

Table 2. FTIR results of chrysin, TA-CHY and tannic acid

Sample	Wavenumber (cm^{-1})	Functional group	Vibration
Chrysin	1243.55	Aromatic alcohol	C-O stretching
	839.19	Alkene	=C-H bending
	1447.23, 1465.50, 1496.74	Aromatic ring	C=C stretching
	3006.96	Aromatic ring	C-H stretching
	1649.34	Ketone	C=O stretching
	1164.63	Ether	C-O-C stretching
TA-CHY	1700.9	Imine	Sp^2 C=N double bond stretching
	1447.47, 1501.12, 1600.36	Aromatic ring	C=C stretching
	1329.74	Aromatic alcohol	Phenol O-H bending
	1038.77, 1071.21	Silanol	Si-OR stretching
	3152.64	Carboxylic acid	O-H stretching
	1198	Aromatic alcohol	C-O stretching
Tannic acid	1310.56	Ester	Aromatic O=C-O-C stretching
	1607.43, 1444.48, 1533.71	Aromatic ring	C=C stretching
	1703.14	Ester	C=O stretching
	1181.64	Aromatic alcohol	C-O stretching
	3273.99	Carboxylic acid	O-H stretching

Point of zero charge (pH_{pzc}) determination

It is vital for scientists to investigate the pH_{pzc} of a biosorbent surface in order to identify its relative surface charges. When the surface charge of a biosorbent surface is thoroughly studied, interactions (mostly electrostatic interactions) between analytes and the biosorbent

surface may be easily manipulated. When the solution pH is greater than pH_{pzc}, the biosorbent surface showed negative charges, and vice versa when the solution pH falls below the pH_{pzc}. When the pH solution was equal to pH_{pzc}, the biosorbent surface was in a neutral condition. Figure 2 (B) depicts a curve formed by graphing $pH_{changes}$ vs $pH_{initial}$. pH_{pzc} of TA-CHY (pH 6.8) which was identified using the intersection point of the curve at axis-x. At solution pH of 6.8, TA-CHY exhibited a neutral charge. Positive charges were present on the biosorbent surface when the solution pH is less than 6.8. The biosorbent surface, on the other hand, exhibited negative charges when the solution pH exceeded 6.8.

Method optimisation

A series of water samples loaded with PCA and VA at a concentration of 0.5 mg/L were prepared and employed for method optimisation. The involved parameters included type of desorption solvent, extraction time, desorption time, solution pH, NaCl addition, biosorbent mass and dispersant solvent. One variable at a time method was used to optimise these parameters.

Effect of type of desorption solvent

In this study, a total of four different organic solvents, including toluene, hexane, ethanol, and methanol, were tested for their potential to desorb PCA and VA. The solvents were then divided into two groups: non-polar solvents (toluene and hexane) and polar solvents (methanol and ethanol). Figure 3(a) demonstrates that methanol has the greatest desorption ability when compared to other solvents. According to Musa et al. [22], methanol was the optimum desorption solvent for PAs with moderate polarity (log P of PCA= 0.82; log P of VA= 1.35 [23]. During this study, the following extraction variables were kept constant: ethanol as the dispersant solvent, solution pH of 8, extraction duration of 1 min, desorption time of 15 min, biosorbent mass of 0.1 g, and 0% NaCl addition (w/v).

Effect of extraction time

Vortex agitation was used for this extraction procedure with the goal to enhance the mass-transfer rate of analytes to the biosorbent surface and shorten the equilibrium period. The extraction time was varied between 0.5 and 4 min with the desorption time set at 15 min whereby methanol was used as the desorption solvent, 0.1 g of biosorbent mass, solution pH 8, 0% NaCl addition (w/v), and ethanol as the dispersant solvent. As seen in Fig. 3 (b), PCA recovery increased from 0.5 to 1 min. The PCA recovery responses decreased and stayed virtually consistent in the 2 to 4 min range. In contrast, VA recovery improved dramatically from 0.5 to 1 min. After that, VA recovery responses fell and stayed steady between 2 and 3 min, followed by another decline at 4 min. The extracted analytes then reached their maximum levels at 1 min. After 1 min, the biosorbent may suffer from active site saturation, resulting in a decline of analyte recovery responses. As a result, 1 min was chosen as the optimal extraction time.

Effect of desorption time

Ultrasonication was utilized to help in the desorption of sorbates from a sorbent by enhancing mechanical agitation and improving mass transfer at the solid-liquid interface. Between 5 and 20 min, the effect of desorption time on sorption recovery was examined (Fig. 3(c)). Other experimental settings were held constant during this study: extraction time was 1 min, desorption solvent was methanol, solution pH was 8, dispersant solvent was ethanol, and the amount of NaCl added was 0% (w/v). Under these conditions, PCA's responses were steady for the first 10 min, then increased at 15 min, followed by a slight decrease at 20 min. The recovery responses for VA climbed gradually from 5 to 15 min, then dropped at 20 min. Both VA and PCA responses decreased after 15 min of desorption processes, suggesting that some of the analytes were re-sorbed by the TA-CHY. Therefore, 15 min was chosen as the desorption time for this research.

Effect of solution pH

As solution pH can have a substantial influence on the existing form of analytes and surface charges of a biosorbent surface which is crucial in an extraction process. The effect of solution pH on PCA and VA recovery was examined in this study throughout a pH range of 1 to 8 (Fig. 3(d)). Other experimental parameters had 15 min of desorption time, methanol as the desorption solvent, 0.1 g of biosorbent mass, 1 min of extraction time, 0% NaCl addition (w/v), and ethanol as the dispersant solvent. Particularly, when the pH increased from 1 to 2, the VA recovery responses increased significantly. The recovery response of VA reduced dramatically and progressively after pH 3 solution. The recovery responses of PCA, on the other hand, were practically consistent from pH 1 to 4. It showed an increasing trend at pH 6 solution before dropping at pH 8 solution. As a result, VA and PCA responded optimally at solution pH levels of 2 and 6, respectively. When compared to PCA (lower hydrophobicity with log P of 0.82 [23], VA (greater hydrophobicity with log P of 1.35 [23] indicated a substantial preference for the positively charged TA-

CHY biosorbent at solution pH 2. This might be attributed to greater cation-π, hydrophobic interactions and π-π interactions between them [24]. In research performed by Musa et al., a higher hydrophobicity analyte, *p*-hydroxybenzoic acid (log P of 2.27) was also found more favorable to a hydrophobic graphene-based adsorbent than a lower hydrophobicity analyte, PCA [22]. In addition, the presence of an extra methyl group in VA might increase electron density in the aromatic ring, resulting in a greater electrostatic affinity with the positively charged biosorbent [25]. This stronger attraction led to a more stable and beneficial cation-π interaction. Other possible interaction mechanisms were primarily driven by hydrogen bonding between the biosorbent's silanol/carbonyl/hydroxyl/amino groups and the analytes' carbonyl/hydroxyl groups. Furthermore, both PCA and VA have pK_a values around 4.2. This might explain why the best solution pH for PCA recovery was pH 6, since there was an electrostatic contact between the deprotonate PCA and the positively charged TA-CHY biosorbent.

Effect of NaCl addition

Salt addition may have a major influence on the sorption process. As salt increases a solution's ionic strength, it may impact the sorbate sorption efficiency and selectivity. For example, when the ionic strength of a solution changed, the electrostatic connections between the analytes and biosorbent were disrupted and weakened. Figure 3(e) shows that when no NaCl salt (0%, v/w) was added to the sample solution, both PCA and VA showed the best recovery responses. Their recovery responses decreased considerably when 1% and 2% (w/v) of NaCl were added to the sample solutions. This is because the additional NaCl salt may compete with the analytes for binding sites on the TA-CHY surface. Therefore, 0% (v/w) NaCl salt addition was set for this method. Other experimental settings used in this optimisation were 1 min of extraction time, 15 min of desorption time, methanol as the desorption solvent, solution pH 2, ethanol as the dispersant solvent and 0.1 g of biosorbent mass.

Effect of mass of biosorbent

The effect of TA-CHY mass on PCA and VA recovery was investigated by increasing the mass from 0.10 g to 0.25 g while keeping the other experimental parameters constant: extraction time = 1 min, desorption solvent = methanol, desorption time = 15 min, solution pH = 2, dispersant solvent = ethanol and NaCl addition = 0% (w/v). The recovery responses of VA indicated an increasing trend from 0.10 to 0.20 g, followed by a drop at 0.25 g in Fig. 3(f). PCA showed a rising tendency from 0.10 to 0.15 g, followed by a drop after 0.20 g. The availability of more analyte sorption sites resulted in an increase in recovery responses with increasing amounts of biosorbent. Therefore, the best biosorbent mass for VA and PCA were 0.20 g and 0.15 g, respectively. The biosorbent mass for the subsequent study was determined to be 0.15 g. The observed reduction in the recovery response of PCA and VA at larger biosorbent mass ranges may be due to the saturation of the TA-CHY adsorption sites and the desorption of analytes back to the bulk phase.

Effect of type of dispersant solvent

In this study, a dispersant solvent was used to promote biosorbent dispersion in a sample solution. Extraction time, desorption solvent, desorption time, solution pH, NaCl addition, and mass of biosorbent were all designated as 1 min, methanol, 15 min, pH 2, 0% (w/v), and 0.15 g biosorbent, respectively. Acetonitrile, ethanol, and methanol were chosen to investigate their potential as dispersant solvents in the newly designed d-μ-SPE (Figure 3(g)). Among these solvents, the use of ethanol as a dispersant solvent provided the highest analyte recovery results. Ethanol, isopropanol, and acetonitrile had log P values of -0.34, 0.05, and -0.54, respectively. The hydrophilicity of these solvents was organized based on their Log P values: isopropanol, ethanol and acetonitrile in ascending order. Since isopropanol is less hydrophilic, it may cause inadequate dispersion of TA-CHY in the sample, thus resulting in unequal interaction between the biosorbent and the analytes. While acetonitrile is more hydrophilic, it may interact negatively with the hydrophobic component of TA-CHY, resulting in poorer biosorbent-analyte interactions. However, because of the modest hydrophilicity, ethanol was able to adequately disseminate the CHT-TA in the sample. The enhanced dispersion was due to its high compatibility with TA-CHY, which enhanced the interaction of TA-CHY with analytes. Therefore, ethanol was chosen as the dispersant solvent.

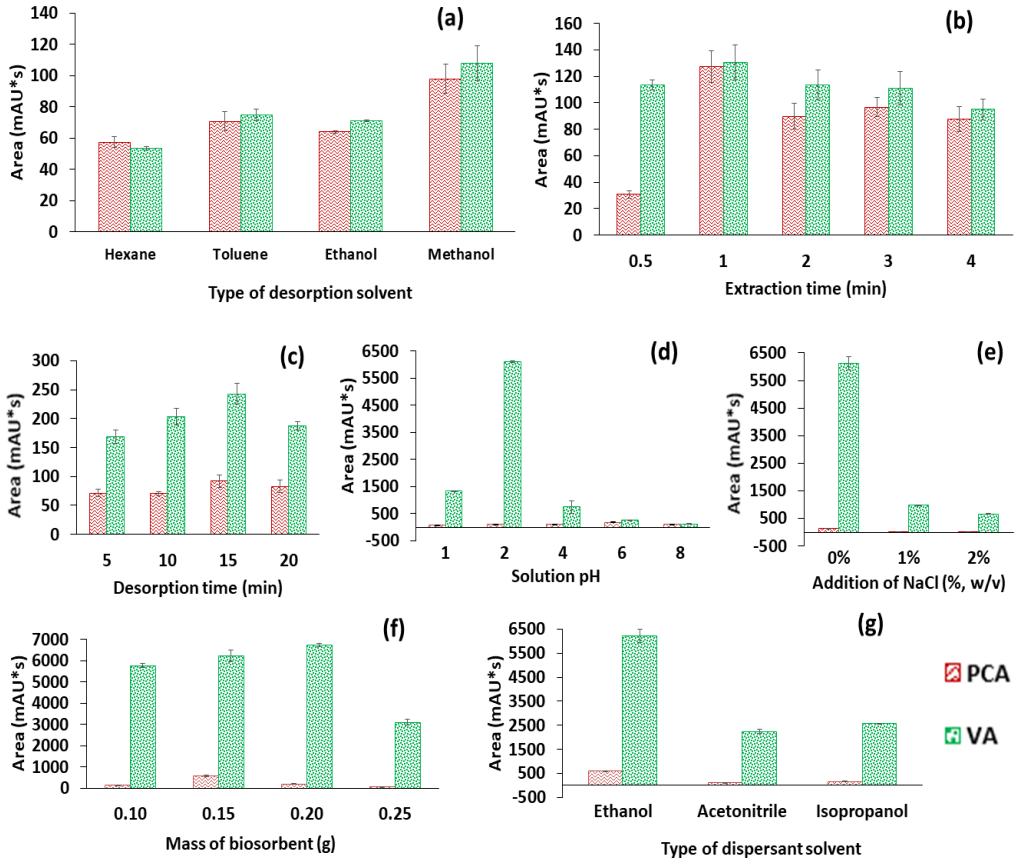

Figure 3. Effects of (a) type of desorption solvent, (b) extraction time, (c) desorption time, (d) solution pH, (e) addition of NaCl, (f) mass of biosorbent and (g) type of dispersant solvent on TA-CHY-d-μ-SPE of VA and PCA

Method validation

Matrix-matched calibration was used to match the matrices of SBH samples and calibration standards to equalize the analyte responses. A series of genuine samples were prepared by spiking PCA and VA in concentrations ranging from 0.5 to 50 mg/L. Both analytes displayed good linearity, with R^2=0.9929 for PCA and 0.9962 for VA (Table 3). LOD values of PCA and VA were 1.37 and 0.81 mg/kg, respectively; while LOQ values of PCA and VA were 4.56 and 2.69 mg/kg, respectively. The approach achieved good RRs and RSDs in the range of 79.38-113.38% and 0.29-9.83%, respectively. To summarize, the approach was shown to be adequate for the determination of PCA and VA in SBH samples with good analytical features.

Table 3. Analytical parameters of the developed method

Analytical Parameter	PCA	VA
Linearity range (mg/L)	0.5-50	0.5-50
LOD (mg/kg), S/N= 3	1.37	0.81
LOQ (mg/kg), S/N= 10	4.56	2.69
Intraday study (*n*=3)		
Spiked concentration at 5 mg/L		
RR (%); RSD (%)	79.38; 2.53	88.88; 0.29
Spiked concentration at 40 mg/L		

Analytical Parameter	PCA	VA
RR (%); RSD (%)	113.12; 9.83	113.38; 7.07
Intraday study (*n*=9)		
Spiked concentration at 5 mg/L		
RR (%); RSD (%)	80.58; 3.01	87.86; 3.43
Spiked concentration at 40 mg/L		
RR (%); RSD (%)	90.49; 9.92	99.45; 10.83

Real sample analysis

The d-μ-SPE approach, which used TA-CHY as a biosorbent, was expanded to analyze PCA and VA in genuine SBH samples collected from Malaysia's Malacca, Perlis, Perak, and Selangor states. Table 4 summarizes the measure quantities of both analytes reported for these SBH samples and their comparison with other honey products. According to the data presented in Table 4, there appears to be a trend showing that SBH samples had greater levels of PCA and VA [26, 27]. The greatest amount of PCA were found in H9 (Greece), SBH sample 2 (Perak, Malaysia), and SBH sample 3 (Perlis, Malaysia), with amount of 16.777, 7.69, and 10.67 mg/kg, respectively. SBH samples 2 (Perak, Malaysia), B and D (Santa Catarina State, Brazil) had the greatest levels of VA, at 11.97, 4.21, and 3.46 mg/kg, respectively. SBHs showed to benefit honey consumers because VA has anti-obesity, anti-diabetic and cardio-protective properties, whilst PCA has anti-inflammatory, antioxidant, anti-microbial, anti-apoptotic, anti-hyperglycemic and anti-proliferative properties [28].

Table 4. Results of PCA and VA analysis in real SBH sample and their comparison with other honey products

Sample, Source	Sample Code	Found Amount (mg/kg ± SD)		Reference
		PCA	VA	
SBH, Malacca, Malaysia	1	2.31±0.26	ND	This study
SBH, Perak, Malaysia	2	7.69±0.86	11.97±1.33	
SBH, Perlis, Malaysia	3	10.67±1.20	ND	
SBH, Selangor, Malaysia	4	3.88±0.43	ND	
SBH, Santa Catarina State, Brazil	A	0.38±0.5	ND	[29]
	B	0.07±0.1	4.21±1.0	
	C	ND	ND	
	D	ND	3.46±0.7	
	E	0.53±1.0	2.78±1.4	
	F	ND	3.36±1.4	
	G	ND	0.96±0.1	
	H	0.4±0.1	ND	
Honey and SBH, different states of Brazil	*Apis mellifera* honey (control)	$0.016\pm0.002\times10^{-3}$	NM	[30]
	SBH1	ND	NM	
	SBH2	ND	NM	
Honey, different regions of Greece	H1	0.649±0.015	0.225±0.006	[31]
	H5	0.346±0.025	0.236±0.002	
	H11	0.300±0.022	0.245±0.011	
	H8	0.590±0.021	0.103±0.001	
	H9	16.777±0.780	0.307±0.014	
	H7	3.258±0.024	0.149±0.002	
	H4	4.140±0.131	0.262±0.008	
	H10	5.967±0.057	0.376±0.002	
	H6	3.058±0.111	0.340±0.013	
	H3	2.394±0.050	0.237±0.007	
	H2	1.046±0.027	0.201±0.005	

Sample, Source	Sample Code	Found Amount (mg/kg ± SD)		Reference
		PCA	VA	
	H12	0.303±0.007	0.092±0.002	
Honey, Xinjiang, China	1	NM	0.042±0.001	[32]
	2	NM	0.021±0.001	
	3	NM	0.031±0.001	
	4	NM	0.052±0.001	
	5	NM	0.031±0.001	
	6	NM	ND	
	7	NM	ND	
	8	NM	0.022±0.001	
	9	NM	0.038±0.001	
	10	NM	ND	

ND= not detectable; NM= not mentioned

Method comparison

Table 5 compares several sample preparation techniques, including this approach, solvent extraction, G-Fe_3O_4-MSPE, and HLB SPE. These techniques were reviewed and compared in terms of LOD, LOQ, linearity range, RSD, and RR. Remarkably, HLB SPE exhibited an outstanding sensitivity with the lowest LOD (0.0002 µg/kg) and LOQ values (0.0006 µg/kg), allowing the reliable detection and quantification of trace VA concentrations. Secondly, G-Fe_3O_4-MSPE allowed for facile sorbent collection by using an external magnetic field while retaining its good analytical properties. Moreover, G-Fe_3O_4-MSPE also used the least amount of toxic organic solvent (~500 µL) during the sample preparation stage, as compared to solvent extraction (>100 mL), HLB SPE (>15mL) and this method, TA-CHY-d-µ-SPE (<4 mL). However, TA-CHY-d-µ-SPE demonstrated comparable sensitivity and accuracy to solvent extraction but used less hazardous organic solvent than solvent extraction. All techniques mentioned in Table 5 demonstrated adequate accuracy, with RSD values of less than 10.83%, thus emphasizing their precision and consistency between replicates. Overall, each technique has its own set of benefits and drawbacks. TA-CHY-d-µ-SPE is considered sufficient and effective in accomplishing its intended purpose in the analysis of PAs in SHB.

Table 5. Comparison with other published sample preparation methods

Method	Sample	Analyte	LOD (µg/kg)	LOQ (µg/kg)	Linearity range	RSD (%)	RR (%)	Reference
TA-CHY-d-µ-SPE	SBH	PCA	1.37	4.56	0.5-50 mg/L	2.53-9.92	79.38-113.12	This study
		VA	0.81	2.69		0.29-10.83	87.86-113.38	
HLB SPE	Honey	PCA	NM	NM	NM	NM	NM	[32]
		VA	0.0002	0.0006	0.001-0.50 mg/L	2.4-5.1	78.5-82.9	
Solvent extraction	Honey	PCA	0.99	3.00	NM	NM	>85	[33]
		VA	0.89	2.71	NM	NM		
G-Fe_3O_4-MSPE	SBH	PCA	0.14	0.46	3-50 mg/kg	0.3-8.5	78.8-107.5	[22]
		VA	NM	NM	NM	NM	NM	

*NM= not mentioned; SPE= solid phase extraction; HLB= Hydrophilic-Lipophilic Balance; G-Fe_3O_4= graphene-magnetite composite; MSPE= magnetic solid phase extraction

Analytical Eco-scale

An analytical Eco-scale calculation [18] was performed to evaluate the eco-friendliness of the developed d-μ-SPE method combined with the use of TA-CHY biosorbent. This covered several stages of a single sample analysis, namely biosorbent preparation, sample preparation and instrumental detection. The calculation was based on the total score obtained from a deduction of total penalty points from 100. The penalty points were given for using less green reagent, instrument, high waste volume and occupational hazard. 100 score of analytical Eco-scale indicated a method as ideal green analysis, whereas score above 75 was excellent, score between 74 and 50 suggested the method as an acceptable green analysis, and score at below 50 indicated inadequate method. This method received a total score of 71, suggesting that it is an acceptable green analytical approach. The calculation details were shown in Table 6.

Table 6. Analytical Eco-scale calculation

Reagent	**Penalty Point**			
	Amount (Point)	**Number of Pictogram (Point)**	**Signal Word (Point)**	**Calculated Point**
Chrysin	<10 g(1)	0(0)	None(0)	1×0×0=0
3-aminopropyltriethoxysilane	<10 mL(1)	2(2)	Danger(2)	1×2×2=4
Tannic acid	10 g(1)	0(0)	None(0)	1×0×0=0
Sodium hydroxide	<10 g(1)	1(1)	Danger(2)	1×1×2=2
Ethanol	10-100 mL (2)	2(2)	Danger(2)	2×2×2=8
Phosphoric acid	<10 mL(1)	2(2)	Danger(2)	1×2×2=4
Methanol	<10 mL(1)	3(3)	Danger(2)	1×3×2=6
Potassium dihydrogen phosphate	<10 g(1)	0(0)	None(0)	1×0×0=0
Water	10-100 mL(2)	0(0)	None(0)	2×0×0=0
Total point				**24**
Instrument		**Energy used per sample (kWh) (point)**		**Calculated point**
HPLC-UV		≤1.5(1)		1
Centrifuge		≤1.5(1)		1
Vortex mixer		≤0.1(0)		0
Vacuum pump		≤0.1(0)		0
Sonicator		≤0.1(0)		0
Total point				**2**
Other				
Waste		<10 mL(3)		3
Occupational hazard		Hermetization in analytical process(0)		0
Total point				**3**
Total penalty point				24+2+3=29
Analytical Eco-Scale total score				100-29=71 **(acceptable)**

Conclusion

In conclusion, our investigation on the newly developed biosorbent, TA-CHY for the extraction of PAs offered substantial insights. CHY-TA had been successfully prepared, characterised and applied for d-μ-SPE of VA and PCA, with higher selectivity towards VA via strong cation-π, hydrophobic interactions and π-π interactions with CHY-TA. The method was extended for the analysis of PCA and VA in Malaysian SBHs. It demonstrated good analytical performance, with LODs ranging from 0.81 to 1.37 mg/kg, LOQs ranging from 2.69 to 4.56 mg/kg, RRs ranging from 79.38% to 113.38%, and RSDs ranging from 0.29% to 10.83%. It also proved its capability to stand alone as a new green analytical method (analytical Eco-scale = 71; acceptable green analysis). This research also contributed to the advancement of analytical methods for studying phenolic acids in stingless bee honey, emphasizing the potential for broader applications in honey analysis and quality assessment.

Acknowledgement

The authors would like to acknowledge the Ministry of Higher Education Malaysia for Fundamental Research Grant Scheme (FRGS) funding with reference code FRGS/1/2019/STG01/UTM/01/2 (Reference No: PY/2019/02237; vote number R.J130000.7854.5F268) and Universiti Teknologi Malaysia (UTM) for the UTM Fundamental Research (UTM FR) funding (Reference No: PY/2019/01834; vote number Q. J130000.2554.21H56). The authors declared no conflict of interest.

References

1. Raja Nurfatin, R. M. Y., Norhayati, M. K., Mohd Fairulnizal, M. N., Hadi, N., Abdul Manam, M., Mohd. Zin, Z. and Yusof, H. M. (2021). The physicochemical, sensory evaluation and glycemic load of stingless bee honey and honeybee honey. *Food Research,* 5(1): 99-107.
2. Najeeb, I. M. A., Norhayati M. K., Zaharah, H., Mohd Isa, N. S., Nur Nadrah, M. R. and Yusof H. M. (2022). Physicochemical properties, sensory acceptance and glycaemic index of processed stingless bee honey and processed honeybee honey. *Food Research*, 6(6): 103-110.
3. Luo, D., Mu, T. H. and Sun, H. N. (2021). Profiling of phenolic acids and flavonoids in sweet potato (*Ipomoea batatas L.*) leaves and evaluation of their anti-oxidant and hypoglycemic activities. *Food Bioscience*, 39: 100801.
4. Saleem, A., Akhtar M. F., Sharif, A., Akhtar, B., Siddique, R., Ashraf, G. M., Alghamdi, B. S. and Alharthy, S. A. (2022). Anticancer, cardio-protective and anti-inflammatory potential of natural-sources-derived phenolic acids. *Molecules*, 27(21): 7286.
5. Valverde, S., Ares, A. M., Stephen Elmore, J. and Bernal, J. (2022). Recent trends in the analysis of honey constituents. *Food Chemistry*, 387: 132920.
6. Gałuszka, A., Migaszewski, Z. and Namieśnik, J. (2013). The 12 principles of green analytical chemistry and the SIGNIFICANCE mnemonic of green analytical practices. *TrAC Trends in Analytical Chemistry*, 50: 78-84.
7. Pascual-Maté, A., Osés, S. M., Fernández-Muiño, M. A. and Sancho, M. T. (2018). Analysis of polyphenols in honey: extraction, separation and quantification procedures. *Separation & Purification Reviews*, 47(2): 142-158.
8. Anastassiades, M., Lehotay, S. J., Štajnbaher, D. and Schenck, F. J. (2003). Fast and easy multiresidue method employing acetonitrile extraction/partitioning and "dispersive solid-phase extraction" for the determination of pesticide residues in produce. *Journal of AOAC international*, 86(2): 412-431.
9. Ghorbani, M., Aghamohammadhassan, M., Ghorbani, H. and Zabihi, A. (2020). Trends in sorbent development for dispersive micro-solid phase extraction. *Microchemical Journal*, 158: 105250.
10. Ng, N. T., Abdul Keyon, A. S., Wan Ibrahim, W. A., Sanagi, M. M., Sutirman, A. A. and Mohd Marsin, F. (2023). Amino-functionalised chrysin as adsorbent in dispersive micro-solid phase extraction of selected heavy metal ions from stingless bee honey. *Journal of Food Composition and Analysis*, 123: 105561.
11. Ścigalski, P. and Kosobucki P. (2020). Recent materials developed for dispersive solid phase extraction. *Molecules*, 25(21): 4869.

12. Hang, N., Yang, Y., Zhang, Y. Y., Zhao, W. N., Tao, J. and Li, S. Q. (2023). Magnetic cork composites as biosorbents in dispersive solid-phase extraction of pesticides in water samples. *Analytical Methods*, 15(29): 3510-3521.
13. Kachangoon, R., Vichapong, J., Santaladchaiyakit, Y. and Srijaranai S. (2022). Green fabrication of *Moringa oleifera* seed as efficient biosorbent for selective enrichment of triazole fungicides in environmental water, honey and fruit juice samples. *Microchemical Journal*, 175: 107194.
14. Adlnasab, L., Ezoddin, M., Shabanian, M. and Mahjoob, B. (2019). Development of ferrofluid mediated CLDH@Fe_3O_4@Tanic acid- based supramolecular solvent: Application in air-assisted dispersive micro solid phase extraction for preconcentration of diazinon and metalaxyl from various fruit juice samples. *Microchemical Journal*, 146: 1-11.
15. Abd Ali, L. I., Wan Ibrahim, W. A., Sulaiman, Azli, Kamboh, M. A. and Sanagi, M. M. (2016). New chrysin-functionalized silica-core shell magnetic nanoparticles for the magnetic solid phase extraction of copper ions from water samples. *Talanta*, 148: 191-199.
16. Shen, N., Wang, T. F., Gan, Q., Liu, S., Wang, L. and Jin, B. (2022). Plant flavonoids: Classification, distribution, biosynthesis, and antioxidant activity. *Food chemistry*, 383: 132531.
17. Pyrzynska, K. and Pękal, A. (2011). Flavonoids as analytical reagents. *Critical Reviews in Analytical Chemistry*, 41(4): 335-345.
18. Gałuszka, A., Migaszewski, Z. M, Konieczka, P. and Namieśnik, J. (2012). Analytical Eco-Scale for assessing the greenness of analytical procedures. *TrAC Trends in Analytical Chemistry*, 37: 61-72.
19. Liu, L. L., Ge, C., Zhang, Y., Ma, W. R., Su, X., Chen, L., Li, S. B., Wang, L., Mu, X. J. and Xu, Y. (2020). Tannic acid-modified silver nanoparticles for enhancing anti-biofilm activities and modulating biofilm formation. *Biomaterials Science*, 8(17): 4852-4860.
20. Abebe, M.W. and Kim, H. (2022). Methylcellulose/tannic acid complex particles coated on alginate hydrogel scaffold via pickering for removal of methylene blue from aqueous and quinoline from non-aqueous media. *Chemosphere*, 286: 131597.
21. Park, S. H., Choi, S. J., Lee, Y. K., Jho, Y. S., Kang, S. T. and Hwang, D. S. (2023). Cation− π interactions contribute to hydrophobic humic acid removal for the control of hydraulically irreversible membrane fouling. *Environmental Science & Technology*, 57(9): 3853-3863.
22. Musa, M., Wan Ibrahim, W. A., Mohd Marsin, F., Abdul Keyon, A. S. and Rashidi Nodeh, H. (2018). Graphene-magnetite as adsorbent for magnetic solid phase extraction of 4-hydroxybenzoic acid and 3,4-dihydroxybenzoic acid in stingless bee honey. *Food Chemistry*, 265: 165-172.
23. Galanakis, C. M., Goulas, V., Tsakona, S. Manganaris, G. A. and Gekas, V. (2013). A knowledge base for the recovery of natural phenols with different solvents. *International Journal of Food Properties*, 16(2): 382-396.
24. Yamada, S. (2020). Cation–π interactions in organic crystals. *Coordination Chemistry Reviews*, 415: 213301.
25. Kim, S. H., Gupta, N. K., Bae, J. Y. and Kim, K. S. (2020). Structural variations and generation of binding sites in Fe-loaded ZSM-5 and silica under the effect of uv-irradiation and their role in enhanced BTEX abatement from gas streams. *Journal of Hazardous Materials*, 384: 121274.
26. Shamsudin, S., Selamat, J., Abdul Shomad, M., Ab Aziz, M. F. and Haque Akanda, M. J. (2022). Antioxidant properties and characterization of *Heterotrigona itama* honey from various botanical origins according to their polyphenol compounds. *Journal of Food Quality*, 2022: 2893401.
27. Zulkifli, N.A., Hassan, Z., Mustafa, M. Z., Wan Azman, W. N., Hadie Hanim, S. N., Ghani, N. and Mat Zin, A. A. (2023) The potential neuroprotective effects of stingless bee honey. *Frontiers in Aging Neuroscience*, 14: 1048028.
28. Rashmi, H. B. and Negi, P. S. (2020). Phenolic acids from vegetables: A review on processing stability and health benefits. *Food Research International,* 136: 109298.
29. Biluca, F. C., da Silva, B., Caon, T., Mohr, E. T., Bramorski, V., Guilherme, N., Gonzaga, L., Valdemiro, V., Luciano, M., Gustavo, F., Roseane,

D. and Eduardo, M. (2020). Investigation of phenolic compounds, antioxidant and anti-inflammatory activities in stingless bee honey *(Meliponinae). Food Research International*, 129: 108756.

30. Moreira, F. I. N., de Medeiros, L. L., de Carvalho, L. M., Olegario, L. S., de Sousa Galvão, M., da Franca, S. A. M., Bezerra, T. K. A., dos Santos Lima, M. and Madruga, M. S. (2023). Quality of brazilian stingless bee honeys: *Cephalotrigona Capitata/Mombucão* and *Melipona Scutellaris Latrelle/Uruçu. Food Chemistry*, 404: 134306.
31. Spilioti, E., Jaakkola, M., Tolonen, T., Lipponen, M., Virtanen, V., Chinou, L., Kassi, E., Karabournioti, S. and Moutsatsou, P. (20140. Phenolic acid composition, antiatherogenic and anticancer potential of honeys derived from various regions in Greece. *PloS One*, 9(4): e94860.
32. Wang, Y., Xing, L. J., Zhang, J. L., Ma, X. N. and Weng, R. (2023). Determination of endogenous phenolic compounds in honey by HPLC-MS/MS. *LWT*, 114951.
33. Puścion-Jakubik, A., Karpińska, E., Moskwa, J. and Socha, K. (2022). Content of phenolic acids as a marker of polish honey varieties and relationship with selected honey-quality-influencing variables. *Antioxidants*, 11(7): 1312.

Malaysian Journal of Analytical Sciences (MJAS)
Published by Malaysian Analytical Sciences Society

ANALYTICAL TECHNIQUES OF BIOACTIVE COMPOUNDS FROM MEDICINAL PLANTS WITH THE POTENTIAL TO ADDRESS ALZHEIMER'S DISEASE AND ASSOCIATED SYMPTOMS: A BRIEF OVERVIEW

(Teknik Analisis bagi Sebatian Bioaktif daripada Tumbuhan Ubatan dengan Potensi untuk Merawat Penyakit Alzheimer dan Gejala Berkaitan: Ulasan Ringkas)

Syaza Syazwani Shaifol[1,2], Noorfatimah Yahaya[1,3*], Siti Nurfazilah Awang[1,2], Nur 'Ain Syaheeda Azizan[1,2], Nur Nadhirah Mohamad Zain[1,3], Nik Nur Syazni Nik Mohamad Kamal[1,3], Mazidatulakmam Miskam[2], and Wan Nazwanie Wan Abdullah[2]

[1]*Department of Toxicology, Advanced Medical and Dental Institute (AMDI), Universiti Sains Malaysia, Bertam, 13200 Kepala Batas, Penang, Malaysia*
[2]*School of Chemical Sciences, Universiti Sains Malaysia, 11800 USM Pulau, Pinang, Malaysia*
[3]*Dementia Multidisciplinary Research Program of IPPT (DMR-IPPT), Advanced Medical and Dental Institute (AMDI), Universiti Sains Malaysia, Bertam, 13200 Kepala Batas, Penang, Malaysia*

[*]*Corresponding author: noorfatimah@usm.my*

Received: 18 August 2023; Accepted: 17 December 2023; Published: February 2024

Abstract

Alzheimer's disease (AD) is a progressive neurological disorder of the brain, named after the German physician Alois Alzheimer, who first documented it in 1906. AD is the most prevalent form of dementia, affecting approximately ten million individuals worldwide. The literature on the extraction and available analytical methods is very helpful in treating AD owing to the diverse and synergistic effects of bioactive compounds. The extraction methodologies allow researchers to concentrate and isolate specific compounds, optimizing their potency and purity for effective treatment. By reviewing these isolated compounds, scientists could have better understanding of their mechanisms, and tailor the dosage and formulation for precise treatments with fewer side effects. This method utilizes the natural qualities of plants and provides a hopeful path for creating safer and more focused treatments for AD. While certain herbal remedies may aid in enhancing brain function, scientific evidence supporting their effectiveness in treating AD remains limited. Thus, the main objective of this review is mainly to provide insight pertaining to AD as well as the analytical techniques of bioactive compounds from medicinal plants that show the potential to treat AD and its associated symptoms.

Keywords: Alzheimer's disease, medicinal plants, analytical techniques, natural products

Abstrak

Penyakit Alzheimer (AD) adalah gangguan neurologi progresif dalam otak, dinamakan sempena doktor Germany, Alois Alzheimer, yang pertama kali mendokumentasikannya pada tahun 1906. AD merupakan bentuk demensia yang paling meluas, memberi kesan

terhadap lebih kurang sepuluh juta individu di seluruh dunia. Kajian literatur mengenai kaedah pengekstrakan dan analisis yang sedia ada amat membantu dalam rawatan AD disebabkan kesan pelbagai dan sinergistik sebatian bioaktif ini. Kaedah-kaedah pengekstrakan membolehkan saintis mengumpul dan mengasingkan sebatian khusus, mengoptimumkan keberkesanan dan ketulenan mereka untuk rawatan yang berkesan. Dengan mengkaji sebatian-sebatian yang diasingkan ini, saintis dapat memahami mekanisme mereka dengan lebih baik, menyesuaikan dos dan rumusan rawatan yang tepat dengan kesan sampingan yang kurang. Kaedah ini menggunakan sifat semula jadi tumbuhan dan kaedah yang boleh digunakan untuk mencipta rawatan yang lebih selamat dan tertumpu untuk AD. Walaupun beberapa ubatan herba mungkin membantu meningkatkan fungsi otak, bukti saintifik yang menyokong keberkesanan mereka dalam merawat AD masih terhad. Oleh itu, objektif utama kajian ini adalah untuk memberikan pandangan ringkas tentang AD serta teknik analisis sebatian bioaktif daripada tumbuhan ubatan yang menunjukkan potensi dalam merawat AD dan gejala yang berkaitan dengannya.

Kata kunci: penyakit Alzheimer, tumbuhan ubatan, teknik analisis, produk semulajadi

Introduction

Neurodegenerative diseases have become one of the most serious health issues worldwide. It is because the development of the first symptoms tends to show up late and the continual aging process of society contributes to the increasing number of these diseases [1]. One of the neurodegenerative diseases includes dementia. Dementia can be defined as a clinical syndrome that can be categorized by a progressive reduction in two or more cognitive abilities which is memory, attention, visual/auditory processing, and reasoning [2]. This leads to loss of functions and inability to perform activities of daily living. According to WHO, dementia influences each person differently, based on the main causes, health conditions, and cognitive functions before getting ill [3]. Study shows that there would be 131 million dementia patients globally by 2050 [4]. Dementia can be broadly classified as primary or secondary dementia. Neurodegenerative dementia is primary, while dementias with underlying systemic or brain diseases are considered secondary dementias [5]. There are many types of primary dementia but the three most common are Alzheimer's disease (AD), vascular dementia, and dementia with Lewy bodies.

Alzheimer's disease

AD is the most common cause of dementia in up to 80% of all dementia cases [2]. AD is a complex neurodegenerative illness that develops slowly over time with symptoms from minor forgetfulness to serious mental disability [6]. The highest number of people with AD is found in the older age group of 65 years and above. According to studies, the number of AD patients will reach 74.7 million by 2030 due to the number of older people increasing all over the world [7]. In the past few years, a significant increase in the exploration and investigation of the benefits of natural products and their bioactive compounds due to the preventive effects against a wide range of illnesses have been documented including neurological diseases [8]. The bioactive compounds in a well-balanced diet have been claimed to have an impact on the mechanisms of AD [9]. Bioactive compounds that can have the potential to treat AD include curcumin, isoflavones, and berberine. The main goal of this review is to offer insights related to AD, focusing on the analytical techniques of bioactive compounds from medicinal plants. These compounds have shown promising potential in treating AD and its related symptoms.

Other types of dementia

In Europe and North America, vascular dementia is estimated to account for 15% to 20% of dementia cases, with slightly higher numbers of roughly 30% in Asia and developing nations. Vascular dementia is generally recognized as the second most common type of dementia after AD. Cognitive deterioration can often happen suddenly in vascular dementia after a stroke that affects vital brain blood arteries. The recorded actual risk of dementia after stroke varies significantly, from less than 7% in population-based studies of first-time stroke in patients who had never had dementia, to over 40% in hospital-based analysis of recurrent stroke with pre-stroke dementia involved [10]. Memory loss that resembles AD may result from a vascular injury that first develops in the parts of the brain that are critical for storing and retrieving information. The pathophysiology of vascular dementia is variable involving interactions between risk factors and alterations to the cerebral blood vessels that lead to pathological events such as infarcts,

white matter ischemia, hemorrhage, thrombosis, and vasospasm [11]. Lewy bodies dementia is an umbrella term that covers dementia with Lewy bodies and Parkinson's disease dementia. This type of dementia has become the third most common type of neurodegenerative dementia. The main protein component that causes Lewy bodies dementia is the abnormalities of alpha-synuclein metabolism [12]. According to clinical criteria, the person with Lewy bodies dementia will have symptoms such as repeated complex visual hallucinations, Parkinsonism, and rapid eye movement sleep disorder. Compared to AD, Lewy bodies dementia confers poorer diagnosis and greater caregiver's stress [13]. Frontotemporal dementia contains a group of health conditions that can be detected by persistent changes in behavior, lack of self-regulation skills, or language [14]. This condition appears due to nerve cell damage in the frontotemporal region of the brain resulting in loss of functions in these brain functional areas. Frontotemporal dementia consists of a few clinical syndromes. Primary progressive aphasia (PPA) is a type of frontotemporal dementia that contain two subgroups which are semantic variant PPA (svPPA) and non-fluent variant PPA (nfvPPA) [15].

Mixed dementia is a combination of AD and vascular dementia. It contributes up to 13% to 17% of all dementia cases worldwide. Researchers also used the term 'mixed dementia' to refer to combinations of any two kinds of dementia [16]. Heavy alcohol consumption has been demonstrated to be both a contributing factor and a required factor in which the disease only exists in the presence of alcohol. Decreasing in rational thinking, physical abilities and also memory are the characteristics of alcohol-related dementia. Due to its links to cardiovascular risk factors and conditions like high blood pressure and stroke, heavy alcohol use is indirectly linked to vascular dementia [17]. Every individual with Down syndrome has the neuropathology of AD by the time they are forty years old, and the majority of them go on to develop AD. It is challenging to spot early signs of dementia because individuals with Down syndrome have different standard functions [18]. According to this interpretation, almost every individual with Down syndrome has amyloid plaques and tau neurofibrillary tangles and their lifetime risk of dementia is more than 90% [19]. As a result, Down syndrome is now recognized as an AD that is caused by genetics. AIDS dementia complex or HIV-associated dementia is the neurocognitive decline linked to HIV [20]. According to epidemiological research, HIV-associated dementia is uncommon (2-4%), with the majority of patients exhibiting milder forms of HIV-associated neurocognitive disorders, such as moderate neurocognitive disorder and asymptomatic neurocognitive impairment [21]. Traumatic brain injury also leads to increased occurrences of dementia, including AD. The probability of having AD, Parkinson's disease, and chronic traumatic encephalopathy will increase by traumatic brain injury resulting from closed head trauma [22]. Childhood trauma such as parental abuse and financial problems is more likely to develop cardiovascular disease and mental disorders. Study shows that childhood trauma can be caused by paternal death before a child is 15 years old which is linked to dementia risk among Aboriginal Australian [23]. Neuronal ceroid lipofuscinoses are the main cause of childhood dementia. It is because in up to 7–8 out of 100 000 births, neuronal ceroid lipofuscinoses are reported to be the major source of childhood dementia globally [24]. Creutzfeldt-Jakob disease (CJD) can be classified as a human prion disease. This disease is rare and can affect both human and non-human mammals [25]. Mad cow disease is unrelated to classic CJD. Additionally, "variant CJD" is another prion disease that is connected to mad cow disease but differs from classic CJD [26].

Causes and risk factors of Alzheimer's disease

There are a lot of biological processes such as oxidative stress, neuroinflammation, excitotoxicity, mitochondrial dysfunction, abnormal protein misfolding and aggregation, and apoptosis that are linked to neurodegeneration [8]. Different types of dementia may be traced to cell damage in specific regions of the brain. The two abnormal proteins that are related to AD are tau and amyloid-β (Aβ). Pathologically, AD is described by the development of amyloid plaques made of aggregated amyloid beta (Aβ), neurofibrillary tangles, which are intraneuronal clusters of hyperphosphorylated tau protein, and brain atrophy due to the loss of neurons and

synapses [27]. The hippocampus is the brain region that has the most impact on AD, followed by degeneration of the association cortices and subcortical structures [28]. Several risk factors can cause AD. A family history of Alzheimer's dementia is a risk factor for late-onset Alzheimer's dementia. Those who have first-degree relatives with Alzheimer's dementia have a high possibility of developing dementia, but it is not a guarantee [29]. The development of AD also appears to be influenced by behavioral factors such as social interactions, sleep patterns, and diet and nutrition. AD and cardiovascular disease also have a strong correlation. The same goes for traumatic brain injury which elevated the risk of dementia [30].

Sign and symptoms of Alzheimer's disease

The most common symptoms of AD are loss of short-term memory, followed by a gradual decline in explicit and implicit memory. People who have the disease also experience neuropsychiatric symptoms and eventually lose the ability to carry out basic activities of daily living. Acetylcholinesterase inhibitors such as donepezil, rivastigmine, galantamine, and the N-methyl-D-aspartate (NMDA) (NMDA) receptor antagonist memantine, are being given to reduce these symptoms [28]. Three stages are linked to AD which are mild stage, moderate stage, and severe stage. Table 1 shows the signs and symptoms linked to AD in the three stages [31].

Table 1. Signs and symptoms according to stages.

No.	Stage	Description	Signs/ symptoms
1	Mild (early)	As a result of the signs and symptoms being rarely seen, dementia's early stages are usually overlooked. Anxiety, apathy, irritability, and depression are examples of neuropsychiatric disorders that can be observed in the mild stage of AD.	• Memory difficulties • Language disturbance • Misplacing or losing things
2	Moderate	The signs and symptoms become clearer and more noticeable. These can be persistent for years.	• Forgetfulness of recent events and people's names • Increasing difficulty with communication • Changes in sleep patterns • Roaming and frequent questioning
3	Severe (late)	It is become close to complete inactivity and reliance. The signs/symptoms become more noticeable. All prior abilities keep getting worse from time to time.	• Need for assistance with everyday tasks and personal care • Loss of capability to handle their movement • Mute, incontinence, and becoming bedridden • Numerous complications

Medicinal herbs to treat Alzheimer's diseases

In the field of science, interest in treating AD has increased. Numerous scientific studies have shown that AD is not an independent illness. This condition is triggered by various metabolic abnormalities brought on by the interaction with multiple pathogenic factors. The cholinergic theory, the -amyloid hypothesis, the tau protein theory, the metal ion issue hypothesis, and the neuroinflammation hypothesis are the five pathogenesis hypotheses that have been presented [32]. Table 2 summarizes the medicinal plants with the potential to treat Alzheimer's and associated symptoms and their analytical methods/ profiling.

Extraction methods

The extraction method is a technique used to separate one or more specific substances from a mixture using suitable solvents. When applying extraction, the choice of methods depends on factors such as the nature of the compounds being extracted. Curcumin, obtained from

Sigma Aldrich, and Rosiglitazone maleate can improve mitochondrial function, potentially leading to positive effects on synapses [33]. Many types of bioactive compounds, such as flavonoids, alkaloids, and phenolic acids, are polar. Therefore, these compounds can be extracted using ethanol or methanol, depending on the polarity of each compound. Before extraction, these compounds need to be made homogeneously through processes like washing, drying, and grinding to form a powder. Subsequently, they are soaked in the extraction solvent, followed by filtration to obtain the desired analyte. In research by Benedec et al. [34], Chlorogenic acid was successfully extracted from four *Amaryllidaceae species*, which is known for its antimicrobial activity. In the research conducted by Eruygur et al. [35] *Achillea cucullata* was extracted using 80% ethanol, and the extracted compounds were identified as phenolic acids and flavonoids. It was found that in *Achillea cucullata*, there were more phenolic acids than flavonoids. Fujimori et al. [36], extracted *Centella Asiatica* using 50% ethanol, yielding araliadiol components that could reduce oxidative stress and endoplasmic reticulum stress, as well as improve cognitive impairment in short-term memory. The concentration of ethanol is determined by the selected target compound class intended for separation. Yu et al. [37] conducted the extraction of macamides from *Lepidium meyenii* Walp, yielding N-benzyl- by soaking dried maca powder in ethanol.

Kumaran et al. [38] used 70% methanol in water to extract *N. nucifera* seed embryo, and the extraction yielded flavonoids. El-Hawary et al. [39] applied high-purity methanol (100% methanol) with no water or impurities to extract *Opuntia ficus-indica* cladode peel and fruits, resulting in an abundance of phenolic acids, flavonoids, and fatty acids. This is because high purity reduces the risk of interferences from impurities, as these compounds were analyzed using HPLC-MS, thus ensuring accurate and reproducible results. A group of researchers [40-42] used methanolic extraction to extract the fruit of *Phyllanthus emblica*, the plant *Indigofera sessiliflora*, and the stem of *Tinospora cordifolia*, respectively. Methanolic fruit extraction of *Phyllanthus emblica* (MFEPE) yields flavonoids, polyphenols, and tannins, possessing antioxidant properties that can reduce damage caused by free radicals. Extraction of phenols and flavonoids from the plant *Indigofera sessiliflora* reduces anxiety behavior and reverses scopolamine-induced amnesia in rats. Rosmarinic acid was extracted from *Salvia fruticose* using methanol [43]. The compound pseudoginsenoside RT8 (PG-RT8) in *Salvia fruticose* contains anti-inflammatory properties that can improve cognitive performance. Rho et al. [44] extracted triterpene saponins and three steroidal saponins from *Panax Ginseng* using methanol extract.

Several flavonoids were extracted from dried *Ginkgo biloba* leaves using 60% w/w acetone [45]. In their research, Ionita et al. [46] and Naseri et al. [47] used hydroalcoholic extract to extract *Matricaria chamomilla L.* and *Melissa officinalis L.,* respectively. The plant extract was prepared using a mixture of water and alcohol (ethanol) as solvents, followed by the evaporation of the solution. The extraction of *Matricaria chamomilla L*. yields flavonoids and polyphenolic carboxylic acid, while the extraction of *Melissa officinalis L.* yields rosmarinic acid, rutin, and apigenin. Callizot et al. [48] used traditional extraction and microwave-assisted extraction to extract huperzine A and two phenolic acids, caffeic acid, and ferulic acid from *Huperzia serrata*. Traditional extraction involves using conventional methods such as soaking, boiling, and cooling to extract compounds from the plant. Microwave-assisted extraction is a modern technique that utilizes microwave energy (Milestone Ethos EX) to heat the sample, accelerating the extraction process of *Huperzia serrata*.

In terms of extraction, solvent extraction or solvent fractionation stands out as the most commonly used technique for preparative separation. Modern extraction methods, often referred to as green extraction methods such as ultrasound-assisted extraction, microwave-assisted extraction, supercritical fluid extraction, and pressurized liquid extraction, have gained significant attention in recent years. However, their application is still limited to extracting bioactive compounds from medicinal plants with the potential to address AD.

Analytical methods (quantitative and qualitative/characterization analysis): Quantitative analysis

Chromatography is a widely used method for the separation and identification of complex mixtures. When choosing the chromatographic technique, the choice depends on the type of sample, the compound to be analyzed, and the sensitivity of the measurement. Chromatographic techniques, such as vacuum liquid chromatography (VLC), are used for the isolation of Tinosporide and 8-hydroxytinosoride from *Tinospora cordifolia (Mernispermaceae)*. Meanwhile, Thin-layer chromatography (TLC) is used to monitor the reaction progress and analyze product mixtures. Based on the study, Tinosporide and 8-hydroxytinosoride can serve as key components for developing new drugs for the treatment of AD [41]. Column chromatography is a separation technique used to isolate a mixture of substances by allowing the mixture to flow through a tube packed with finely divided solid coated with an adsorbent liquid. The different components in the mixture separate at different rates as they travel through the column due to their distinct interactions with the stationary phase. For the study of medicinal plants, column chromatography was used for the separation and analysis of *Nelumbo nucifera (Nelumbonaceae)*, in which reverse-phase silica gels were used as the adsorbent, and a water/methanol mixture (50:50-0:100, v/v) was used as the solvent to elute the extract. After further purification by column chromatography, five flavonoids namely rutin, orientin, isoorientin, isoquercetin, and hyperoside were obtained [38].

High-performance liquid chromatography (HPLC) is the most widely used analytical method for the analysis of bioactive compounds in medicinal plants that have the potential to treat AD. Plant extracts usually contain a combination of bioactive compounds with different polarities, making it difficult to separate them. Fortunately, HPLC is a versatile analytical technique that allows its application to a wide range of compounds with varying polarity and molecular mass. Moreover, it enables the analysis of complex plant matrices with minimal sample preparation, thereby reducing the risk of compound degradation during the analysis. Additionally, HPLC offers high sensitivity, enabling the detection of even trace amounts of bioactive compounds in intricate samples. HPLC analysis is quick, and its system can be automated, allowing for rapid separation when analyzing multiple samples [49, 50].

In the study of AD, HPLC is utilized for the analysis of bioactive compounds in 10 medicinal plants, including the analysis of Araliadiol (C33) in *Centella asiatica L. (Umbelliferae)*. Acetonitrile and 0.1% phosphoric acid are employed as the solvent, revealing the neuroprotective properties of the compound against cognitive impairment. [36]. N-benzyl-(9Z,12Z)-octadecadienamide (M18:3) found in *Lepidium meyenii* Walp (*Brassicaceae*) was examined using UV-Vis detection with a mobile phase composed of 90% acetonitrile. Qualitative identification was achieved by comparing the retention times of macamides with the standards, and peak areas were analyzed to obtain the concentration. The results suggest that macamides and maca extract improve cell adaptability in CORT-induced PC12 cells [37]. In *Nelumbo nucifera (Nelumbonaceae)*, a mobile phase composed of water containing 0.5% acetic acid and methanol, with a gradient program, was used to obtain the major fractions of flavonoids in the seed embryo of *Nelumbo nucifera*. These fractions were determined to be rutin, orientin, isoorientin, isoquercetrin, and hyperoside, detected at a wavelength of 254 nm. The concentrations found to inhibit Aβ1-40 toxicity on dPC-12 cells were in the range of 10–50 µg/mL [38].

Analysis of flavonoids, polyphenols, and tannins, which are bioactive compounds present in Phyllanthus emblica (Euphorbiaceae), was also conducted by injecting filtered samples into the HPLC column for the identification and quantification of glutathione (GSH). This confirmed the excellent antioxidant and radical-scavenging properties, which could be significant in addressing AD [40]. HPLC-MS/MS and HPLC with water and acetonitrile (ACN) as a mobile phase were used to characterize phenolic acids, flavonoids, and fatty acids present in *Opuntia ficus-indica L. (Cactaceae).* Based on the findings, several phenolic acids and flavonoids were detected, with flavonoids as the major compound. However, no betalains were detected due to their low concentration in the extract. This bioactive

compound offers the potential to address various neurological conditions due to its antioxidative properties [39]. HPLC-MS was used to study the antioxidant and microbial properties of phenolic compounds in the extract of *Galanthus nivalis L. (Amaryllidaceae)*. The fingerprint of the polyphenolic compounds was obtained, revealing quantitative analysis surpassing 15 mg/g [34]. *Panax ginseng Meyer (Araliaceae)* was analyzed using HPLC coupled with electrospray-ionization-quadrupole-time-of-flight-mass spectrometry (ESI-Q-TOF-MS), through which the presence and identification of 10 compounds in the extract of P. ginseng seeds were achieved. The retention time obtained was compared with the ion chromatograms (EICs) using the expected theoretical mass-to-charge ratio (*m/z*) of the sodiated pseudomolecular ion from the authentic sample, confirming the presence of the 10 compounds. A new saponin, three known protopanaxatriol saponins, three sterol glycosides, two phenolic glycosides, flavonoid, and three primary metabolites, along with 15 ginsenosides, were expected to be present, but due to a lower concentration of saponin, it could only be observed in the n-butanol extract [44].

Salvia fruticose (Lamiaceae)'s blend, which contained rosmarinic acid, was analyzed utilizing LC-DAD-ESI-MS/MS detection. This helped uncover the underlying neuroprotective properties of the blend for the discovery of new drugs to treat AD [43]. In another study conducted by Naseri et al. [47], the bioactive compound present in the hydroalcoholic extract of *Melissa officinalis L. (Lamiaceae)* was determined using reversed-phase (RP) liquid chromatography, and it was confirmed that the extract was composed of flavonoids and polyphenols, which had antidiabetic effects, inflammation and oxidative stress reduction, and increased insulin secretion. The retention time was used to detect the bioactive compound, and the flavonoid groups were determined to be rutin and apigenin, constituting 9.36% and 0.56% of the extract, respectively. Meanwhile, rosmarinic acid was the main phenolic compound in the extract, composing 4.87% of the extract.

Ultra-high performance liquid chromatography (UHPLC) coupled with mass spectrometry (MS) was used for the analysis of bioactive compounds in two medicinal plants. When compared to HPLC, UHPLC offered the advantage of a shorter analysis time. When the crude extract of *Indigofera sessiliflora (Fabaceae)* was analyzed for the presence of secondary metabolites, eighteen distinct phytocompounds belonging to the flavonoid group were observed. These compounds were found to possess antioxidant characteristics and abilities to participate in cholinergic neuromodulation. [42]. Huperzine A, along with two phenolic acids, caffeic acid and ferulic acid, found in the extract of *Huperzia serrata (Lycopodiaceae)*, was identified as the three major compounds in the extract. This combination has the potential to treat AD and memory loss [48]. A study by Ionita et al. also used HPLC to analyze the photochemical composition of the compound (flavonoids and polyphenolic carboxylic acid) in *Matricaria recutita (Asteraceae)* extract that was administered to the rat model to induce memory impairment. DAD was utilized as a detector, and acetonitrile and water containing 0.1% acetic acid were used as the mobile phase [46].

Qualitative and characterization analysis: Transmission Electron Microscopy

Transmission electron microscopy (TEM) is an advanced imaging technique that involves the interaction of electron beams with atoms in a specimen, enabling the visualization of the specimen's microstructure at an extremely high resolution. This technique permits the study of a specimen's structure and allows observation at the nanometer (nm) scale. In a study conducted by Chen et al. [33], Curcumin (diferuloylmethane), a bioactive component found in *Curcuma longa L. (Zingiberaceae)* was analyzed using TEM. The extract was administered to the mice, and the resulting examination of synapses in the hippocampal CA1 area revealed the promising potential of curcumin in the initial stages of AD.

Electron paramagnetic resonance

Electron paramagnetic resonance (EPR) also known as electron spin resonance (ESR) is a type of spectroscopic technique that is commonly used for the study of the

interaction of atoms or molecules containing unpaired electron with an external magnetic field. EPR spectroscopy can provide information about the electronic structure and bonding of a paramagnetic species. *Galanthus nivalis L. (Amaryllidaceae)* is one of the medicinal plants with potential in the treatment of AD, which uses EPR for the study of its bioactive compounds, specifically chlorogenic acid. Although the extract of *Galanthus nivalis L. (Amaryllidaceae)* contains the highest amount of chlorogenic acid, the EPR signal was revealed not to be dominated by chlorogenic acid. Instead, it is a mixture of isoquercitrin, quercitrin, and chlorogenic acid free radicals [34].

ELISA MRX micro-plate reader

ELISA MRX micro-plate reader is an instrument that can be used for the detection and quantification of specific proteins, antigens, antibodies in a biological sample. It relies on the principle in which the antibodies are bound to a specific antigen, or a target molecule and the measurement of absorbance or fluorescence of samples can then be obtained. Gargouri et al. [45] used ELISA MRX micro-plate reader for the analysis of flavonoids in *Ginkgo biloba L. (Ginkgoaceae)* extract EGb 761 in which the production of pro-inflammatory and cytokines were measured, and the results showed a decrease in neuro-inflammatory activity in primary microglial cells.

Electrospray ionization mass spectrometry

Electrospray ionization mass spectrometry (ESI-MS) is an analytical technique that is used for the identification and quantification of molecules based on their mass-to-charge ratio. The sample solution containing the analyte will be introduced into a mass spectrometer and subjected to an electrospray process which leads to the formation of gas-phase ions in ESI-MS. Flavonoids in *Nelumbo nucifera (Nelumbonaneae)* such as rutin, orientin, isoorientin, isoquercetrin, and hyperoside's chemical structure can be confirmed using ESI-MS's spectral obtained with the published data [38].

UV-Vis spectrophotometer

Two medicinal plants were analyzed by UV as the analytical for the determination of bioactive compounds. UV spectra are useful for the detection of a flavonoid compound due to these compounds having typical chromophoric groups which exhibit characteristics UV profile. In a study conducted by Kumaran et al. [38], extracts of *Nelumbo nucifera (Nelumbonaneae)* were visualized under UV lights at a wavelength of 254 nm and 365 nm and the spectral data were compared with the reported value of the compound. Similarly, Eruygur et al. [35] employed a UV-Vis spectrophotometer to measure the optical density of flavonoids in *Achillea cucullate (Asteraceae)* at 517 nm. The study highlighted the significance of *A. cucullate* aerial parts due to their antioxidant, anticholinesterase, antidiabetic, and moderate antibacterial properties which could be useful as anti-AD agents.

NMR spectroscopy

NMR is an analytical technique to study the magnetic properties of specific atomic nuclei for the determination of their molecular structure and monitor their composition in a mixture. NMR can also be used to study molecular dynamics and interaction. The principle of NMR spectroscopy is based on the absorption and emission of radio waves by the nuclei due to other atoms or molecules bonded to them and the waves are then detected by a detector. For the study of three medicinal plants, the bioactive compounds were determined using NMR spectroscopy. Adib et al. [41] and Kumaran et al. [38] both used the 1H and 13C NMR for the detection of the bioactive compound in *Tinospora cordifolia (Menispermaceae)* and *Nelumbo nucifera (Nelumbonaceae)* respectively. Tinosporide and 8-hydroxytinos oride were isolated from *Tinospora cordifolia (Menispermaceae)* and it is molecular structure was identified and confirmed using proton and carbon NMR. Then, the two bioactive compounds are studied for their acetyl-cholinesterase (AChE) and butylcholinesterase (BuChE) inhibitory activities which it was determined to have anti-AChE activities for treating cognitive impairments in AD. For *Nelumbo nucifera (Nelumbonaceae),* the flavonoid groups that are found that include rutin, orientin, isoorientin, isoquercetrin, and hyperoside is confirmed by obtaining the NMR spectrum and comparing it with the spectrum of the standard that is available commercially [38]. Araliadiol that was isolated from the extract of *Centella*

asiatica L. (Umbelliferae) was determined using proton NMR and the study on neuroprotective effects of *C. asiatica* and Araliadiol shows that cognitive dysfunction can be shielded by the extract (Fujimori et al., 2022).

The combination of chromatographic and spectroscopic techniques, such as LC-MS and LC-NMR, may result in elucidating the structure of natural products without the need for isolation. Using more selective tools in the extraction, fractionation, and purification processes can expedite the time from collecting biological material to obtaining the final purified compound.

Table 2: Medicinal plants with the potential to treat Alzheimer and associated symptoms and their analytical methods/ profiling.

Plant	Bioactive Compounds	Extraction Method	Analytical Methods / Profiling	Experimental Models	Results	Ref
Bacopa monniera Wettst. (Scrophulariaceae)	Alkaloid & Bacoside A	Extracted with chloroform & ethanolic extract	1. HPTLC	In-vitro	Bioactive compounds prevent the activation of N9 microglial cells by inhibiting the release of TNF-α and IL-6. This shows that bioactive compounds proved that they could help with the treatment that focuses on neuroinflammation and have the potential to cure a variety of central nervous system disorders including Alzheimer's disease.	[51]
Rosmarinus officinalis (Lamiaceae)	Nepitrin	Extracted with butanol	1. Column chromatography 2. Thin layer chromatography	In-vivo	Nepitrin has considerable anti-amnesic effects in vivo, inhibits choline esterase enzymes in vitro, and has antioxidant properties. Nepitrin may therefore be a valuable tool in the creation of therapeutics that can help with Alzheimer's disease's short-term and long-term memory loss.	[52]
Urtica dioica L. (Clusiaceae)	Rutin, 2-O-caffeoyl malic acid, and chlorogenic acid	Extracted with ultrasound-assisted extraction technique	1. HPLC	In-vivo	This extract increased antioxidant defense and reduced oxidative stress while also enhancing cardiac performance and hypertension.	[53]
Withania somnifera (Solanaceae)	Withanone	Ethanolic extract	1. HPLC 2. IR 3. NMR	In-vitro and In-vivo	Withanone showed potential for AD cure because of cognitive advantages and mechanisms of action related to the basic pathophysiology of the disease. It has a lot of benefits other than inhibiting AChE, such as modification of Aβ process, decreasing oxidative stress, and reducing inflammation.	[54]
Salvia officinalis (Lamiaceae)	Polyphenols and flavonoids	Methanolic extract	1. HPLC 2. UV-Vis	In-vivo	These findings provide more proof of the effectiveness of S. officinalis extract in the cure of cognitive deficits and may provide a natural treatment for Alzheimer's disease.	[55]
Curcuma longa L. (Zingiberaceae)	Curcumin (diferuloylme	Curcumin was provided by Sigma–	1. Transmission Electron Microscopy	In vivo	Curcumin seems promising as a novel treatment for AD.	[33]

Plant	Bioactive Compounds	Extraction Method	Analytical Methods / Profiling	Experimental Models	Results	Ref
	thane)	Aldrich				
Galanthus nivalis L. (Amaryllidaceae)	Chlorogenic acid	Extracted with 70% ethanol	1. HPLC-MS 2. electron paramagnetic resonance (EPR) spectroscopy	In vitro	The contents of bioactive compounds could be important sources to prevent various diseases associated with oxidative stress including Alzheimer's diseases.	[34]
Ginkgo biloba L. (Ginkgoaceae)	Flavonoids	Extraction solvent (acetone 60% (w/w))	1. ELISA MRX micro-plate reader	Transgenic animal models of AD were used	By targeting PGE2 release and cytokines, gingko biloba extract decreases neuro-inflammatory activity in primary microglial cells.	[45]
Matricaria recutita (Asteraceae)	Flavonoids and polyphenol carboxylic acids	The hydroalcoholic extract	1. HPLC/DAD	A rat model of amnesia	The extract enhanced the scopolamine-induced memory impairments in rats by modulating AChE activity, promoting BDNF, and inhibiting IL1 expression in the hippocampus.	[46]
Nelumbo nucifera (Nelumbonaceae)	Flavonoids (rutin, orientin, isoorientin, isoquercetrin and hyperoside)	70% methanol extract	1. Column chromatography 2. UV 3. ESI-MS 4. 1H, and 13C NMR 5. HPLC	In-vitro assay models	The flavonoid-rich Nn-M-B-VII and Nn-M-B-IX active fractions from N. nucifera seed embryos showed significant reductions in Ab1e40-induced toxicity in dPC-12 cells along with strong radical scavenging activities. It is important to evaluate the optimal concentrations for both the prevention and cure of AD, however, the active fractions indicated cytotoxicity at higher dosages (above 50 mg/mL).	[38]
Phyllanthus emblica (Euphorbiaceae)	Flavonoid, polyphenols, and tannin	Methanolic extract	1. HPLC column	In vitro	Fruit extract from P. emblica has excellent antioxidant and radical-scavenging properties. In the human brain cell line PC12, P. emblica has been shown to have neuroprotective properties.	[40]
Lipidium Meyenii Walp (Brassicaceae)	N-benzyl-(9Z,12Z)-octadecadienamide (M 18:3)	Ethanol extract of maca	1. HPLC	PC12 cells culture using the method described by RuilePan	In PC12 cells, macamides can reduce CORT-induced neurotoxicity, especially M18:3.	[37]
Achillea cucullata (Asteraceae)	Flavonoids are phenolic	Extracted with 80% ethanol	1. UV-Vis spectrophotometer	In vitro	According to this study, A. cucullata's aerial parts have substantial antioxidant,	[35]

Plant	Bioactive Compounds	Extraction Method	Analytical Methods / Profiling	Experimental Models	Results	Ref
	compounds				anticholinesterase, antidiabetic, and moderate antibacterial properties. Therefore, this plant has the potential to serve as a source of naturally occurring anti-AD, anti-diabetic, and anti-inflammatory agents.	
Panax Ginseng (Araliaceae)	Triterpene saponins and three steroidal saponins	Extracted with methanol	1. HPLC-ESI-Q-TOF-MS	In vitro	P. ginseng seeds are a useful natural resource for finding new bioactive compounds, and pseudoginsenoside RT8 has the potential for use in pharmaceuticals as an anti-inflammatory drug.	[44]
Opuntia ficus-indica L. (Cactaceae)	Phenolic acids, flavonoids and fatty acids	Extracted with 100% methanol	1. HPLC-MS/MS 2. HPLC	In vitro and In vivo	Opuntia ficus-indica prevents oxidative stress and may be a promising treatment alternative for a variety of neurological conditions.	[39]
Huperzia serrata (Lycopodiaceae)	Huperzine A and two phenolic acids, caffeic acid and ferulic acid	Traditional extract (NSP01-TE) and the microwave-assisted extract (NSP01)	1. UHPLC-MS	Cell culture of primary rat cortical neurons	Huperzia serrata extract is very potential to cure Alzheimer's disease and loss of ability.	[48]
Indigofera sessiliflora (Fabaceac)	Phenols/flavonoids	Methanolic extract	1. UHPLC-MS	In-vitro, in-vivo & in silico	The phytocompounds in IS.CR have antioxidant characteristics and their capabilities to participate in cholinergic neuromodulation explain why Indigofera sessiliflora has the neuroprotective effects that have been associated with it in traditional uses.	[42]
Melissa officinalis L. (Lamiaceae)	Rosmarinic acid, rutin, and apigenin	Hydroalcoholic extract	1. Reversed phase (RP) liquid chromatography	Diabetic rat model	M. officinalis can improve learning and memory in diabetic rats.	[47]
Salvia fruticose (Lamiaceae)	Rosmarinic acid	Extracted with methanol	1. LC-DAD-ESI-MS/MS	In vitro	Due to its ability to inhibit glycogen synthase kinase 3β CK-1 and β-secretase and increase p-GSK-3 beta protein levels, Salvia fruticosa infusion has a good	[43]

Plant	Bioactive Compounds	Extraction Method	Analytical Methods / Profiling	Experimental Models	Results	Ref
					potential for multipurpose neuroprotective agents for further investigations into the discovery of new anti-drugs Alzheimer's from natural sources.	
Tinospora cordifolia (Menispermaceae)	Tinosporide and 8-hydroxytinosoride	Methanolic extract of the stem of T. cordifolia	1. vacuum liquid chromatography (VLC) 2. 1H and 13C 3. thin-layer chromatography (TLC)	In vitro	These two bioactive compounds could be used as main to develop new drugs for AD.	[41]
Centella asiatica L. (Umbelliferae)	Araliadiol (C33)	Extracted with 50% ethanol	1. NMR spectroscopy. 2. HPLC	In vivo and in vitro	These findings imply that araliadiol has neuroprotective properties that may shield against cognitive impairment.	[36]

Conclusion

Herbal remedies hold promising potential for early-stage treatment of Alzheimer's and similar conditions marked by memory impairment and dementia. A key advantage lies in their comparatively lower toxicity when contrasted with pharmaceutical agents. Comparing the use of herbal medicines in AD treatment with the current pharmacological approaches is essential. These investigations should involve pinpointing the active compounds to enhance clinical trial validation. Additionally, multicenter research is imperative to establish the efficacy of these substances in mitigating cognitive decline in AD. Until such conclusive results are obtained, this review furnishes preliminary evidence of the potential advantages offered by a diverse array of herbs encompassing various traditional medicine systems, including Malay, Indian, Chinese, and European, for AD treatment. The time-consuming and labor-intensive extraction and isolation processes have been a barrier to using natural products in drug development. However, advancements in technology have led to the creation of faster and automated techniques for extracting and separating natural products. These new methods may meet the needs of high-throughput screening in drug development.

Acknowledgement

This study was supported by the Universiti Sains Malaysia, Short Term Grant (Khas) with account code number: 304/CIPPT/6315813. This study also aligned with the mission and vision of the Dementia Multidisciplinary Research Program of IPPT (DMR-IPPT) with grant number: 1001/CIPPT/8070034.

References

1. Grodzicki, W. and Dziendzikowska, K. (2020). The role of selected bioactive compounds in the prevention of alzheimer's disease. *Antioxidants*, 9(3): 1-18.
2. Weller, J. and Budson, A. (2018). Current understanding of Alzheimer's disease diagnosis and treatment. *F1000Research*, 7(0), 1–9.
3. World Health Organization: Dementia. (2023). https://www.who.int/news-room/fact-sheets/detail/dementia (accessed Aug. 18, 2023).
4. Arvanitakis, Z., Shah, R. C. and Bennett, D. A. (2019). Diagnosis and management of dementia: Review. JAMA - *Journal of the American Medical Association*, 322(16): 1589-1599.
5. Wiegmann, C., Mick, I., Brandl, E. J., Heinz, A. and Gutwinski, S. (2020). Alcohol and dementia – What is the link? A systematic review. *Neuropsychiatric Disease and Treatment*, 16: 87-99.
6. Morgan, A. R., Touchard, S., Leckey, C., O'Hagan, C., Nevado-Holgado, A. J., Barkhof, F., Bertram, L., Blin, O., Bos, I., Dobricic, V., Engelborghs, S., Frisoni, G., Frölich, L., Gabel, S., Johannsen, P., Kettunen, P., Kłoszewska, I., Legido-Quigley, C., Lleó, A., … and Mount, H. (2019). Inflammatory biomarkers in Alzheimer's disease plasma. *Alzheimer's and Dementia*, 15(6): 776-787.
7. Gleerup, H. S., Hasselbalch, S. G. and Simonsen, A. H. (2019). Biomarkers for Alzheimer's disease in saliva: A systematic review. *Disease Markers*, 2019: 4761054.
8. Mohd Sairazi, N. S. and Sirajudeen, K. N. S. (2020). Natural products and their bioactive compounds: Neuroprotective Potentials against neurodegenerative diseases. *Evidence-Based Complementary and Alternative Medicine*, 2020: 5-7.
9. Islam, F., Khadija, J. F., Harun-Or-Rashid, M., Rahaman, M. S., Nafady, M. H., Islam, M. R., Akter, A., Emran, T. Bin, Wilairatana, P. and Mubarak, M. S. (2022). Bioactive compounds and their derivatives: An insight into prospective phytotherapeutic approach against Alzheimer's disease. *Oxidative Medicine and Cellular Longevity*, 2022: 5100904.
10. Wolters, F. J. and Arfan Ikram, M. (2019). Epidemiology of vascular dementia: Nosology in a time of epiomics. *Arteriosclerosis, Thrombosis, and Vascular Biology*, 39(8): 1542-1549.
11. Suvarna, A. and Faheem Arshad, A. P. (2022). Encyclopedia of Behavioral Neuroscience, 2nd edition: Vascular Dementia. Elsevier Science.
12. Agbomi, L. L., Onuoha, C. P., Nathaniel, S. I., Coker-Ayo, O. O., Bailey-Taylor, M. J., Roley, L. T., Poupore, N., Goodwin, R. L. and Nathaniel, T. I. (2022). Gender differences in Parkinson's disease

with dementia and dementia with Lewy bodies. *Aging and Health Research*, 2(4): 100096.

13. Amin, J., Erskine, D., Donaghy, P. C., Surendranathan, A., Swann, P., Kunicki, A. P., Boche, D., Holmes, C., McKeith, I. G., O'Brien, J. T., Teeling, J. L. and Thomas, A. J. (2022). Inflammation in dementia with Lewy bodies. *Neurobiology of Disease*, 168(3): 105698.
14. Boeve, B. F., Boxer, A. L., Kumfor, F., Pijnenburg, Y. and Rohrer, J. D. (2022). Advances and controversies in frontotemporal dementia: diagnosis, biomarkers, and therapeutic considerations. *The Lancet Neurology*, 21(3): 258-272.
15. Bruun, M., Koikkalainen, J., Rhodius-Meester, H. F. M., Baroni, M., Gjerum, L., van Gils, M., Soininen, H., Remes, A. M., Hartikainen, P., Waldemar, G., Mecocci, P., Barkhof, F., Pijnenburg, Y., van der Flier, W. M., Hasselbalch, S. G., Lötjönen, J. and Frederiksen, K. S. (2019). Detecting frontotemporal dementia syndromes using MRI biomarkers. *NeuroImage: Clinical*, 22(11): 101711.
16. Moreno Cervantes, C., Mimenza Alvarado, A., Aguilar Navarro, S., Alvarado Ávila, P., Gutiérrez Gutiérrez, L., Juárez Arellano, S. and Ávila Funes, J. A. (2017). Factors associated with mixed dementia vs Alzheimer disease in elderly Mexican adults. *Neurologia (Barcelona, Spain)*, 32(5): 309-315.
17. Rehm, J., Hasan, O. S. M., Black, S. E., Shield, K. D. and Schwarzinger, M. (2019). Alcohol use and dementia: A systematic scoping review. *Alzheimer's Research and Therapy*, 11(1): 1-11.
18. Hamlett, E. D., Ledreux, A., Potter, H., Chial, H. J., Patterson, D., Espinosa, J. M., Bettcher, B. M. and Granholm, A. C. (2018). Exosomal biomarkers in Down syndrome and Alzheimer's disease. *Free Radical Biology and Medicine*, 114(9): 110-121.
19. Fortea, J., Zaman, S. H., Hartley, S., Rafii, M. S., Head, E. and Carmona-Iragui, M. (2021). Alzheimer's disease associated with Down syndrome: a genetic form of dementia. *The Lancet Neurology*, 20(11): 930-942.
20. Kimani, R. W. (2018). Assessment and Diagnosis of HIV-Associated Dementia. *Journal for Nurse Practitioners*, 14(3): 190-195.
21. Rosca, E. C., Tadger, P., Cornea, A., Tudor, R., Oancea, C. and Simu, M. (2021). International hiv dementia scale for hiv-associated neurocognitive disorders: A systematic review and meta-analysis. *Diagnostics*, 11(6): 1124.
22. VanItallie, T. B. (2019). Traumatic brain injury (TBI) in collision sports: Possible mechanisms of transformation into chronic traumatic encephalopathy (CTE). *Metabolism: Clinical and Experimental*, 100: 1-6.
23. Donley, G. A. R., Lönnroos, E., Tuomainen, T. P. and Kauhanen, J. (2018). Association of childhood stress with late-life dementia and Alzheimer's disease: The KIHD study. *European Journal of Public Health*, 28(6): 1069-1073.
24. Dutta, S. S. (2019). Childhood dementia causes. https://www.news-medical.net/health/Childhood-Dementia-Causes.aspx.
25. Iwasaki, Y. (2017). Creutzfeldt-Jakob disease. *Neuropathology*, 37(2): 174-188.
26. Centers for Disease Control and Prevention: Creutzfeldt-Jakob disease, classic (CJD) (2021). https://www.cdc.gov/prions/cjd/index.html (accessed Aug. 18, 2023).
27. Pickett, E. K., Herrmann, A. G., McQueen, J., Abt, K., Dando, O., Tulloch, J., Jain, P., Dunnett, S., Sohrabi, S., Fjeldstad, M. P., Calkin, W., Murison, L., Jackson, R. J., Tzioras, M., Stevenson, A., d'Orange, M., Hooley, M., Davies, C., Colom-Cadena, M. and Spires-Jones, T. L. (2019). Amyloid beta and tau cooperate to cause reversible behavioral and transcriptional deficits in a model of Alzheimer's disease. *Cell Reports*, 29(11): 3592-3604.
28. Götz, J., Bodea, L. G. and Goedert, M. (2018). Rodent models for Alzheimer disease. *Nature Reviews Neuroscience*, 19(10): 583-598.
29. Bird, T. D. (1993). Alzheimer disease overview. Adam, M. P., Ardinger, H. H., Pagon, R. A., Wallace, S. E., Bean, L. J. H., Stephens, K., & Amemiya, A. (Eds.). (1993). Variegate porphyria. GeneReviews®.

30. James, B. D. and Bennett, D. A. (2019). Causes and patterns of dementia: an update in the era of redefining Alzheimer's disease. *Annual Review of Public Health*, 40: 65-84.
31. Zvěřová, M. (2019). Clinical aspects of Alzheimer's disease. *Clinical Biochemistry*, 72(4): 3-6.
32. Du, X., Wang, X. and Geng, M. (2018). Alzheimer's disease hypothesis and related therapies. *Translational Neurodegeneration*, 7(1): 1-7.
33. Chen, F., He, Y., Wang, P., Wei, P., Feng, H., Rao, Y., Shi, J. and Tian, J. (2018). Curcumin can influence synaptic dysfunction in APPswe/PS1dE9 mice. *Journal of Traditional Chinese Medical Sciences*, *5*(2): 168-176.
34. Benedec, D., Oniga, I., Hanganu, D., Gheldiu, A. M., Puşcaş, C., Silaghi-Dumitrescu, R., Duma, M., Tiperciuc, B., Vârban, R. and Vlase, L. (2018). Sources for developing new medicinal products: Biochemical investigations on alcoholic extracts obtained from aerial parts of some Romanian Amaryllidaceae species. *BMC Complementary and Alternative Medicine*, 18(1): 1-12.
35. [35] Eruygur, N., Koçyiğit, U. M., Taslimi, P., Ataş, M., Tekin, M. and Gülçin. (2019). Screening the in vitro antioxidant, antimicrobial, anticholinesterase, antidiabetic activities of endemic Achillea cucullata (Asteraceae) ethanol extract. *South African Journal of Botany*, 120: 141-145.
36. Fujimori, H., Ohba, T., Mikami, M., Nakamura, S., Ito, K., Kojima, H., Takahashi, T., Iddamalgoda, A., Shimazawa, M. and Hara, H. (2022). The protective effect of *Centella asiatica* and its constituent, araliadiol on neuronal cell damage and cognitive impairment. *Journal of Pharmacological Sciences*, 148(1): 162-171.
37. Yu, Z., Jin, W., Cui, Y., Ao, M., Liu, H., Xu, H. and Yu, L. (2019). Protective effects of macamides from: *Lepidium meyenii* Walp. against corticosterone-induced neurotoxicity in PC12 cells. *RSC Advances*, *9*(40): 23096-23108.
38. Kumaran, A., Ho, C. C. and Hwang, L. S. (2018). Protective effect of *Nelumbo nucifera* extracts on beta amyloid protein induced apoptosis in PC12 cells, in vitro model of Alzheimer's disease. *Journal of Food and Drug Analysis*, 26(1): 172-181.
39. El-Hawary, S. S., Sobeh, M., Badr, W. K., Abdelfattah, M. A. O., Ali, Z. Y., El-Tantawy, M. E., Rabeh, M. A. and Wink, M. (2020). HPLC-PDA-MS/MS profiling of secondary metabolites from *Opuntia ficus-indica* cladode, peel and fruit pulp extracts and their antioxidant, neuroprotective effect in rats with aluminum chloride induced neurotoxicity. *Saudi Journal of Biological Sciences*, 27(10): 2829-2838.
40. Rajalakshmi, S., Vijayakumar, S. and Praseetha, P. K. (2019). Neuroprotective behaviour of *Phyllanthus emblica* (L) on human neural cell lineage (PC12) against glutamate-induced cytotoxicity. *Gene Reports*, 17(9): 100545.
41. Adib, M., Islam, R., Ahsan, M., Rahman, A., Hossain, M., Rahman, M. M., Alshehri, S. M., Kazi, M. and Mazid, M. A. (2021). Cholinesterase inhibitory activity of tinosporide and 8-hydroxytinosporide isolated from *Tinospora cordifolia*: *In vitro* and *in silico* studies targeting management of Alzheimer's disease. *Saudi Journal of Biological Sciences*, 28(7): 3893-3900.
42. Sajjad Haider, M., Ashraf, W., Javaid, S., Fawad Rasool, M., Muhammad Abdur Rahman, H., Saleem, H., Muhammad Muneeb Anjum, S., Siddique, F., Morales-Bayuelo, A., Kaya, S., Alqahtani, F., Alasmari, F., and Imran, I. (2021). Chemical characterization and evaluation of the neuroprotective potential of *Indigofera sessiliflora* through in-silico studies and behavioral tests in scopolamine-induced memory compromised rats. *Saudi Journal of Biological Sciences*, 28(8): 4384-4398.
43. Gürbüz, P., Dokumacı, A. H., Gündüz, M. G., Perez, C., Göger, F., Paksoy, M. Y., Yerer, M. B. and Ömür Demirezer, L. (2021). *In vitro* biological activity of Salvia fruticosa Mill. infusion against amyloid β-peptide-induced toxicity and inhibition of GSK-3β, CK-1δ, and BACE-1 enzymes relevant to Alzheimer's disease. *Saudi Pharmaceutical Journal*, 29(3): 236-243.
44. Rho, T., Jeong, H. W., Hong, Y. D., Yoon, K., Cho, J. Y. and Yoon, K. D. (2020). Identification of a novel triterpene saponin from Panax ginseng seeds,

pseudoginsenoside RT8, and its antiinflammatory activity. *Journal of Ginseng Research*, 44(1): 145-153.

45. Gargouri, B., Carstensen, J., Bhatia, H. S., Huell, M., Dietz, G. P. H. and Fiebich, B. L. (2018). Anti-neuroinflammatory effects of *Ginkgo biloba* extract EGb761 in LPS-activated primary microglial cells. *Phytomedicine*, 44(4): 45-55.
46. Ionita, R., Postu, P. A., Mihasan, M., Gorgan, D. L., Hancianu, M., Cioanca, O. and Hritcu, L. (2018). Ameliorative effects of *Matricaria chamomilla* L. hydroalcoholic extract on scopolamine-induced memory impairment in rats: A behavioral and molecular study. *Phytomedicine*, 47(11): 113-120.
47. Naseri, M., Arabi Mianroodi, R., Pakzad, Z., Falahati, P., Borbor, M., Azizi, H. and Nasri, S. (2021). The effect of *Melissa officinalis* L. extract on learning and memory: Involvement of hippocampal expression of nitric oxide synthase and brain-derived neurotrophic factor in diabetic rats. *Journal of Ethnopharmacology*, 276: 114210.
48. Callizot, N., Campanari, M. L., Rouvière, L., Jacquemot, G., Henriques, A., Garayev, E. and Poindron, P. (2021). Huperzia serrata extract 'NSP01' with neuroprotective effects-potential synergies of huperzine a and polyphenols. *Frontiers in Pharmacology*, 12(8): 1-13.
49. Ooh, K.-F., Ong, H.-C., Wong, F.-C., Sit, N.-W. and Chai, T.-T. (2014). High performance liquid chromatography profiling of health-promoting phytochemicals and evaluation of antioxidant, anti-lipoxygenase, iron chelating and anti-glucosidase activities of wetland macrophytes. *Pharmacognosy Magazine*, 10: S443-55.
50. Sasidharan, S., Chen, Y., Saravanan, D., Sundram, K. M. and Yoga Latha, L. (2011). Extraction, isolation and characterization of bioactive compounds from plants' extracts. *African Journal of Traditional, Complementary, and Alternative Medicines, 8*(1): 1-10.
51. Nemetchek, M. D., Stierle, A. A., Stierle, D. B. and Lurie, D. I. (2017). The Ayurvedic plant *Bacopa monnieri* inhibits inflammatory pathways in the brain. *Journal of Ethnopharmacology*, 197: 92-100.
52. Karim, N., Khan, I., Abdelhalim, A., Abdel-Halim, H. and Hanrahan, J. R. (2017). Molecular docking and antiamnesic effects of nepitrin isolated from *Rosmarinus officinalis* on scopolamine-induced memory impairment in mice. *Biomedicine and Pharmacotherapy*, 96(9): 700-709.
53. Vajic, U. J., Grujic-Milanovic, J., Miloradovic, Z., Jovovic, D., Ivanov, M., Karanovic, D., Savikin, K., Bugarski, B. and Mihailovic-Stanojevic, N. (2018). *Urtica dioica* L. leaf extract modulates blood pressure and oxidative stress in spontaneously hypertensive rats. *Phytomedicine*, 46(5): 39-45.
54. Pandey, A., Bani, S., Dutt, P., Kumar Satti, N., Avtar Suri, K. and Nabi Qazi, G. (2018). Multifunctional neuroprotective effect of Withanone, a compound from Withania somnifera roots in alleviating cognitive dysfunction. *Cytokine*, 102(10): 211-221.
55. Gabbas, Z. El, Bezza, K., Laadraoui, J., Makbal, R., Aboufatima, R. and Chait, A. (2018). *Salvia officinalis* induces antidepressant-like effect, anxiolytic activity and learning improvement in hippocampal lesioned and intact adult rats. *Bangladesh Journal of Pharmacology*, 13(4): 367-378.

Malaysian Journal of Analytical Sciences (MJAS)
Published by Malaysian Analytical Sciences Society

POTENTIAL GREEN LIQUID FROM TERNARY DEEP EUTECTIC SOLVENT COMPOSED OF GALLIC ACID, UREA, AND ZINC CHLORIDE: CHARACTERIZATION OF THEIR PHYSICOCHEMICAL AND THERMAL PROPERTIES

(Potensi Cecair Hijau daripada Pelarut Eutektik Terdalam Ternari daripada Asid Galik, Urea, dan Zink Klorida: Pencirian Sifat Fisikokimia dan Termanya)

Nuraqilah Mohd Hatta and Siti Abd Halim*

Universiti Kuala Lumpur, Malaysian Institute of Chemical Engineering Technology, 78000 Alor Gajah, Melaka

**Corresponding author: sitinurulatikah@unikl.edu.my*

Received: 15 September 2023; Accepted: 17 December 2023; Published: 28 February 2024

Abstract

Deep eutectic solvents (DESs) have attracted wide attention due to their cheaper cost, ease of manufacture, lower toxicity, and higher biological compatibility. In this study, we offer a more affordable and adaptable path to similar systems using gallic acid (GA), urea (U), and zinc chloride ($ZnCl_2$). The mixture produced, called GA-based DES, was prepared at varying molar ratios of 1:5:1, 1:6:1, 1:7:1, and 1:8:1 (GA:U:$ZnCl_2$). The eutectic liquid form of the GA-based DES mixture was obtained when heated at an operating temperature of 120 °C, below the melting temperature of each individual chemical. The structural and physicochemical properties of the DESs were studied via Fourier transform infrared spectroscopy, thermogravimetric analysis, and viscosity test. Different molar ratios of the DES mixture affected the hydrogen bond interaction formed between GA and U as the hydrogen bond donors and $ZnCl_2$ as the hydrogen bond acceptor in the DES mixture with the presence of O–H stretching and N–H stretching vibration bands as an association effect of GA, U, and $ZnCl_2$. An increase in the U ratio weakened the hydrogen bond and reduced the viscosity of the liquid in the DES mixture due to an increase in O–H stretching. The current findings provide a potential justification for the viscosity of DES mixtures and aid in tailoring the design and development of new DES mixtures for further applications, such as extraction, separation, conversion to functional porous carbon, and biochemical technology.

Keywords: chemical properties, deep eutectic solvent, gallic acid, urea, physical properties

Abstrak

Pelarut eutektik terdalam (DES) telah menarik perhatian luas kerana kosnya yang lebih murah, kemudahan pembuatan, ketoksikan yang lebih rendah, dan keserasian biologi yang lebih tinggi. Dalam kajian ini, kami menawarkan laluan yang lebih berpatutan dan boleh disesuaikan kepada sistem serupa menggunakan asid galik (GA), urea (U), dan zink klorida ($ZnCl_2$). DES berasaskan GA yang dihasilkan dalam kajian ini adalah daripada campuran GA-U-$ZnCl_2$ yang terdiri daripada empat nisbah molar berbeza iaitu 1:5:1, 1:6:1, 1:7:1, dan 1:8:1. Cecair eutektik campuran DES berasaskan GA diperoleh apabila dipanaskan pada suhu operasi 120 °C di bawah suhu lebur setiap bahan kimia. Sifat struktur dan fizikokimia DES dikaji melalui spektroskopi inframerah transformasi Fourier, analisis termogravimetri, dan ujian kelikatan. Nisbah molar campuran DES yang berbeza mempengaruhi interaksi ikatan

hidrogen yang terbentuk antara GA dan U sebagai penderma ikatan hidrogen dan $ZnCl_2$ sebagai penerima ikatan hidrogen dalam campuran DES dengan kehadiran regangan O–H dan jalur getaran regangan N–H sebagai kesan persatuan GA, U, dan $ZnCl_2$. Peningkatan nisbah U melemahkan ikatan hidrogen dan mengurangkan kelikatan cecair dalam campuran DES disebabkan oleh peningkatan dalam regangan O–H. Penemuan semasa memberikan justifikasi yang berpotensi untuk kelikatan hasil daripada campuran DES dan membantu dalam menyesuaikan reka bentuk dan perkembangan campuran DES baharu untuk aplikasi selanjutnya.

Kata kunci: sifat kimia, pelarut eutektik dalam, asid galik, urea, ciri-ciri fizikal

Introduction

Green chemistry stands at the forefront of scientific endeavors, focusing on creating sustainable procedures and substances. With recent industrial growth causing substantial harm to the environment, various substitutes for processes and solvents have emerged to reduce this adverse impact. Ionic liquids (ILs) were introduced as one such substitute solvent in the past few decades and have increasingly gained attention. Ionic liquids have obtained significant interest, particularly in the realms of catalysis, material chemistry, and preprocessing of biomass [1]. The creation of a liquid-phase product, known as a eutectic mixture, arises from the combination of specific precursor components during the synthesis of ILs. Nevertheless, it has been confirmed that these solvents come with specific disadvantages, such as costly synthesis, purification demands, and toxicity [2]. The claimed environmental friendliness of these modern solvents is currently a subject of considerable debate in existing literature [3]. Numerous reports have highlighted the potentially harmful toxicity and the notably low biodegradability of the majority of ILs [4, 5, 6]. Moreover, their synthesis is far from environmentally friendly, as it typically necessitates a substantial quantity of salts and solvents for complete anion exchange. These shortcomings, coupled with the elevated cost of conventional ILs, regrettably impede their industrial advancement. Consequently, there is a pressing need for innovative approaches to employ these systems in a more judicious manner [1].

Therefore, in recent years, a fresh class of so-called green solvents known as deep eutectic solvents (DESs) has emerged as a promising alternative. Deep eutectic solvents are formed by combining two or more salts, incorporating both hydrogen bond acceptors (HBAs) and hydrogen bond donors (HBDs), such as amides, amines, alcohols, and carboxylic acids [7, 8, 9], which then could be capable of engaging in hydrogen bonds and electrostatic interactions. This combination leads to the formation of a eutectic mixture [6, 10, 11]. Moreover, many HBDs and HBAs have been identified as capable of forming DESs through self-association. The distinctive solvent characteristics of DESs enable a broad spectrum of solutes to exhibit significant solubility in such solvents under certain specific conditions [12]. These properties collectively offer the potential to utilize DESs as an environmentally friendly and effective alternative to traditional methods for synthesizing functional materials. For instance, they can serve as solvent precursors and even contribute to the production of functional carbon material sources. The synthesis of DESs has gained wide attention in numerous literatures. Wang et al. [9] produced DES from different sources of HBAs and HBDs (i.e., tyrosine, urea, and zinc chloride), while Wei et al. [13] applied novelty in synthesizing DES from the mixture of boron acid, choline chloride, and urea. Besides, the key characteristic that sets DESs apart is that their melting point is notably lower than that of the individual components. In some cases, this reduction in melting point can be quite substantial, leading to a liquid mixture even at room temperature.

Furthermore, DESs embody all the favorable attributes of an environmentally friendly and relatively safe solvent [14]. This family of compounds provides numerous benefits, such as straightforward preparation with high levels of purity and yield [15]. Furthermore, DESs are also recognized for their non-toxicity, biodegradability, biocompatibility, and minimal vapor pressure [3, 16]. In addition, DESs hold significant promise in various industrial applications, including organic synthesis, extraction processes,

electrochemistry, enzymatic reactions, and the purification of biodiesel and flavonoids [17, 18, 19]. Some eutectic systems have already demonstrated their ability to dissolve complex lignocellulosic materials like lignin, hemicellulose, cellulose, and starch, yielding successful outcomes.

In this specific context, we introduce a cost-effective and adaptable approach to develop DES systems. This innovative method involves combining gallic acid (GA), urea (U), and zinc chloride ($ZnCl_2$) to create a DES. The inclusion of GA and U, along with $ZnCl_2$ salt, results in a solvent with unique properties. The presence of the amino group ($-NH_2$) in U influences the stretching of O–H bonds, thus impacting the hydrogen bond interaction between the HBD and HBA of $ZnCl_2$ salt in the DES. Luo et al. [20] reported on the synthesis of DES consisting of phenols/ketones, specifically utilizing tannic acid and U. This approach was identified as a favorable pathway for hydrogen bond interaction, with tannic acid serving as the carbon precursor and U as the nitrogen precursor. Carriazo et al. [21] also prepared DES from a phenolic compound, specifically a resorcinol-based DES acting as both a soft template and carbon source. Consequently, drawing inspiration from these previous studies, GA, which is categorized under the phenolic acid group, was chosen as a precursor in this investigation due to its natural origin, cost-effectiveness, and ready availability.

The experimental conditions, including the molar ratio of precursors, were varied to emphasize their impact on bond interaction, composition, morphology, and structural characteristics of the resulting DES. Varied molar ratios of DES mixtures influence hydrogen bond interactions among GA, U (HBD), and $ZnCl_2$ (HBA). This is evident through the O–H and N–H stretching vibration bands, representing the association effect between the individual components. The optimized sample exhibits exceptional solvent and functional performance when utilized as a solvent or other functional materials. This research aims to comprehensively characterize DES systems derived from GA, U, and $ZnCl_2$, providing insights into their physical, chemical, and thermal properties. The ultimate goal is to deepen our understanding of their potential applications, with a specific focus on producing custom porous carbon in future studies.

Materials and Methods

Preparation of des samples at different molar ratios

Chemically pure $ZnCl_2$ and silicone oil were purchased from R&M Chemicals (Selangor, Malaysia), while GA (98%) and U (99.5%) were purchased from Acros Organics (Selangor, Malaysia). The DESs were prepared using various molar ratios of GA, U, and $ZnCl_2$ mixture with GA as a carbonaceous precursor and U as a nitrogen precursor. Zinc chloride was also added as a porogen and activating agent. Figure 1 presents the raw materials used in the synthesis of the DES samples. A round-bottom flask immersed in an oil bath heated by a heating plate was used to prepare the DES mixture. The physical mixture of GA, U, and $ZnCl_2$ in a molar ratio of 1:5:1 was heated at 120 °C with steady stirring until a homogeneous liquid was formed. To investigate the influence of precursor material ratios on the hydrogen bond formation in the synthesized DESs, the molar ratios of GA to U and $ZnCl_2$, designated as Ga:U:$ZnCl_2$, were established at 1:6:1, 1:7:1, and 1:8:1. Figure 2 depicts the experimental set-up.

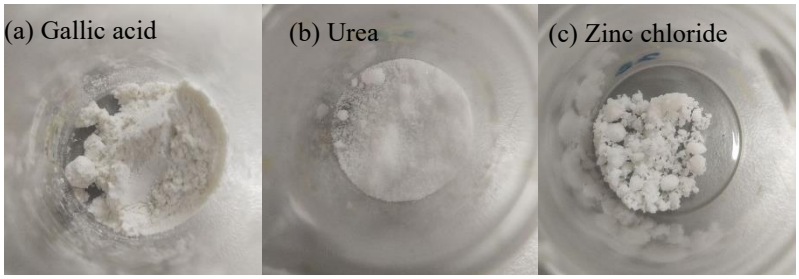

Figure 1. The raw materials of a) gallic acid, b) urea, and c) zinc chloride

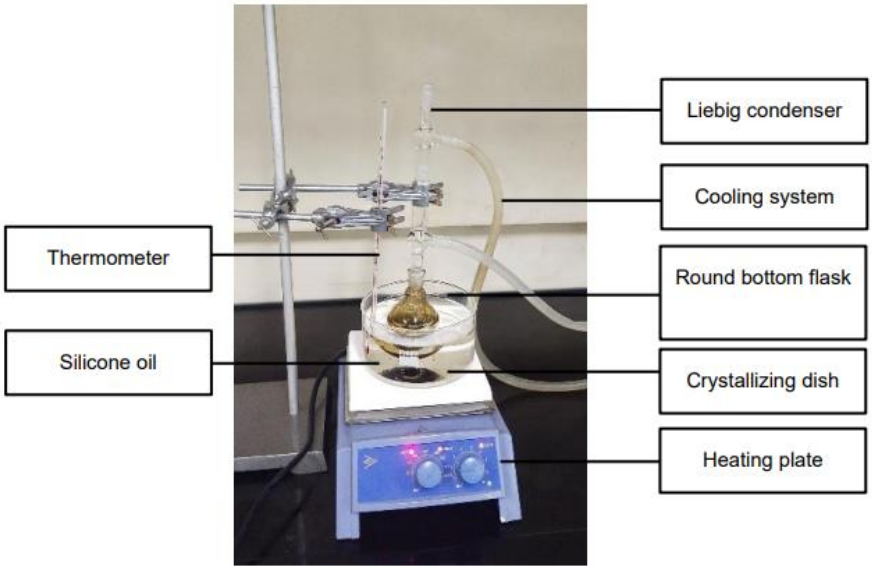

Figure 2. The experimental set-up for DES preparation

Characterization of DESs: The structural and physicochemical properties

The effect of different molar ratios of U content on the structural and physicochemical properties of GA-based DES samples was investigated in depth using viscosity test and Fourier transform infrared (FTIR) spectroscopy analysis. The viscosity test was conducted in this study using a stainless steel digital viscometer (ATAGO VISCO) for each four different molar ratios of DESs. The test was conducted under the operating temperature of 46 °C at 1.0 rpm for each run. Three measurements of the viscosity were taken for each DES sample, and the average values and standard deviations are shown as results. Besides, studies on the chemical structure and functional groups present in the GA-based DES samples produced from four different molar ratios were conducted via FTIR spectroscopy analysis. The wavenumber scans of the FTIR were adjusted to the range 4000–500 cm^{-1}.

Results and Discussion

Physical properties of DESs

To explore the optimal parameters for the formation of DESs, various molar ratios of GA, U, and $ZnCl_2$ were examined. The criteria for assessment included the time required for DES formation, the highest temperature reached during the process, the appearance of the mixture during heating, and the emergence of a homogeneous liquid state. Table 1, Figure 3, and Figure 4 present some physical characteristics of DES mixtures at different molar ratios when subjected to heating in an oil bath.

The evolution of DES formation at the tested ratios was monitored over a 20-min duration at a temperature of 120 °C. Based on visual observations, DESs at various ratios exhibited the formation of highly viscous and adhesive dark brownish liquids, with no apparent color differences among them. However, it was noted that the viscosity of the samples varied, with DES-1:8:1 being the least viscous among the investigated ratios. To validate this finding, viscosity analysis was conducted.

The physical properties of the GA-U- $ZnCl_2$ DES mixtures were determined via the viscosity test for each sample at different molar ratios of DESs using a digital viscometer set at 1.0 rpm. Table *2* presents the data obtained from the viscosity test at different molar ratios of Ga:U:$ZnCl_2$.

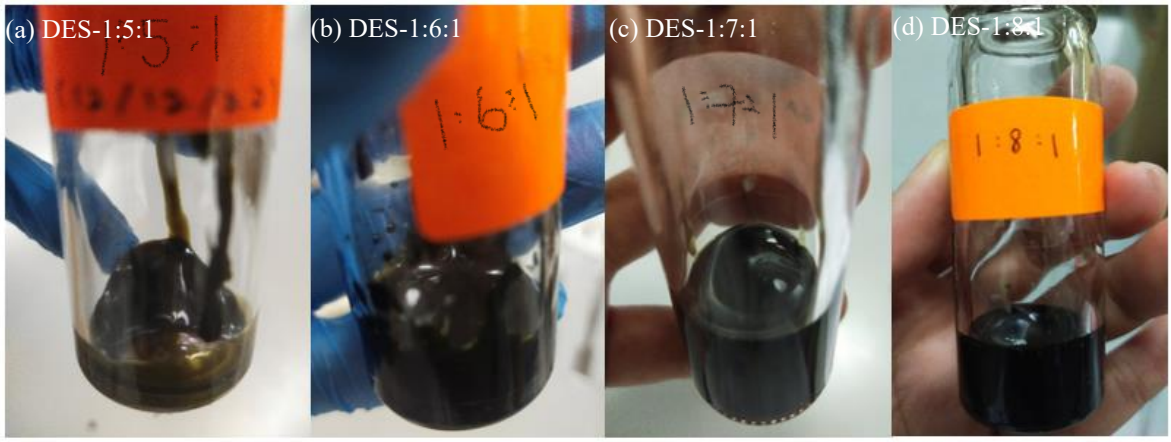

Figure 3. Visual observation of the DES samples at different ratios: a) DES-1:5:1, b) DES-1:6:1, c) DES-1:7:1, and d) DES-1:8:1

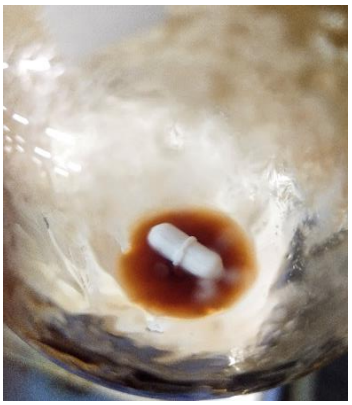

Figure 4. The initial appearance of the DES mixture which turned into a homogeneous brown liquid during heating

Table 1. Properties of DES formation at different molar ratios

Molar Ratio (GA:U:$ZnCl_2$)	**Time (min)**	**Temperature (˚C)**	**Appearance during Heating**	**Appearance at Room Temperature**
1:5:1	15	120	Melts into a brown liquid	Highly viscous mixture with a sticky texture
1:6:1	15	120	Melts into a brown liquid	Highly viscous mixture with a sticky texture
1:7:1	15	120	Melts into a brown liquid	Highly viscous mixture with a sticky texture
1:8:1	15	120	Melts into a brown liquid	Highly viscous brownish liquid with a sticky texture

Table 2. Viscosity of DESs at different molar ratios

Molar Ratio of Ga:U:$ZnCl_2$	**Viscosity Reading (cP)**			
	1st	2nd	3rd	Average
1:5:1	1,400.80	1,399.50	1,400.50	1,400.50 ± 0.89
1:6:1	1,363.60	1,363.20	1,362.10	1,362.97 ± 0.78
1:7:1	1,317.70	1,315.70	1,316.20	1,316.53 ± 1.04
1:8:1	1,063.40	1,062.80	1,063.37	1,063.37 ± 0.55

The interactions between DES components and their macroscopic properties are well-recognized to be strongly connected. Determining the physical characteristics of the DES would therefore be greatly influenced by the hydrogen bond interactions [22] and this statement is aligned with other researchers, in which the hydrogen bonding, van der Waals force, and electrostatic force interaction are the main factors that viscosity is highly dependent on [23, 24, 25]. Viscosity is considered to establish a link between the potency of hydrogen bonds in DESs and their viscosities, which denotes the intrinsic resistance to flow and reflects the intensity of intramolecular interactions within the liquid. *Table 2* illustrates that an increase in the molar ratio, indicating a higher U content in the DESs, results in a decrease in viscosity readings. The sequence of DES-1:5:1 > DES-1:6:1 > DES-1:7:1 > DES-1:8:1 corresponds to a decrease in viscosity.

In this system, U and GA functioned as HBDs, while $ZnCl_2$ acted as a HBA. Increasing the HBD content in the DESs resulted in a reduction in viscosity, primarily due to a decrease in hydrogen bond interactions formed between the chloride ion of salt as HBA and HBD components in the DES mixture. This finding aligns with the results reported by Ghaedi et al. [7], where they observed a similar trend of decreasing viscosity with an increasing amount of HBDs. As the HBD content increases, the hydrogen bonding between the HBD and HBA weakens, which results in an increase in OH stretching bonds, ultimately resulting in lower viscosity [7]. According to Yang et al. [26], one of the major challenges in producing DESs is their typically high viscosity, which can limit mass transfer when used as a solvent. For practical solvent applications, achieving low viscosity in DESs is desirable to enhance mass transfer [7, 27, 28]. Therefore, based on the viscosity test results presented in *Table 2*, DES-1:8:1 can be considered the optimal molar ratio when compared to the other three molar ratios (DES-1:5:1, DES-1:6:1, and DES-1:7:1) because it exhibits the lowest viscosity. Figure 5 depicts the structural elements of GA, U, and $ZnCl_2$ in the synthesis of DES. The precursor components exhibit hydrogen bonding resulting from the interaction between the HBA and HBD.

Chemical properties of DESs

In this study, we formulated and examined newly developed natural DESs. It is common knowledge that DESs comprise HBDs and HBAs. These blends were prepared using a naturally occurring aromatic organic acid, GA, and U as the HBDs, with $ZnCl_2$ as the HBA, and their corresponding spectra are shown in Figure 6a -Figure *6*c. Figure 6d also displays the FTIR spectra of DESs with varying compositions. In accordance with the research by Pena-Solorzano et al. [29], the presence of vibrational bands associated with the NH_2 group is denoted by a peak falling within the range of 3500–3200 cm^{-1}. The peaks located at 1623 and 1461 cm^{-1}, as depicted in Figure 6a, can be attributed to the NH and C-N bending characteristics observed in the pure U sample. Furthermore, a C=O stretching peak is evident at a wavenumber of 1678 cm^{-1}, which aligns with the findings reported by other researchers [30]. Regarding the standard GA depicted in Figure 6b, the spectral region spanning from 3600 to 2500 cm^{-1} is associated with the stretching vibrations of the OH group, and a distinct and sharp OH band is noticeable at 3471 cm^{-1}. Furthermore, the presence of a carbonyl group is indicated by a robust and narrow peak at 1635 cm^{-1}. In addition, the bands appearing at 1635, 1535, and 1431 cm^{-1} are characteristic of stretching vibrations within the C–C bonds present in the aromatic ring of GA. These frequencies closely resemble those previously reported in the literature [31]. Additionally, several other peaks observed in the range of 136–1030 cm^{-1} can be attributed to stretching vibrations associated with the C–O bonds and the bending vibration of the O–H bond within GA. In contrast, the spectra for $ZnCl_2$ (Figure 6c) reveal a vibrational band at 3519 cm^{-1}, which is characteristic of the O–H stretching bond. Furthermore, the spectrum at a wavenumber of 1605 cm^{-1} indicates the presence of O–H bending vibrations in the pure $ZnCl_2$ sample. According to the findings of Pena-Solorzano et al. [29], the occurrence of the O–H bond can be attributed to the presence of water molecules, potentially resulting from the retention of moisture in the sample during analysis. Zinc chloride is known to be hygroscopic, meaning it tends to form hydrates when exposed to water molecules.

Subsequently, FTIR analyses were conducted on various DES samples at different molar ratios, as illustrated in Figure 6d. In general, it can be observed that the four different molar ratios of DESs exhibit minimal variation in the detected peaks and possess relatively similar spectral patterns. The strong C=O band appears distinctly at 1620 cm^{-1} (narrow) and exhibits peaks at 3435 cm^{-1} (broad) in the characteristic bands of DES samples, which can be attributed to the interactions between hydrogen bonds involving the HBD urea, as well as the presence of water content. The stretching vibrations of the C–O bond at 1030 cm^{-1} suggest that the structure of GA remains largely intact within the DES system, demonstrating that the fundamental structural characteristics of GA are preserved in the DESs. When comparing the spectra of pure U (Figure 6a) with the DES samples, a shift in the carbonyl vibration of U is evident, moving from 1678 cm^{-1} to peak wavenumbers at 1573.30, 1573.79, 1572.99, and 1573.11 cm^{-1} for the DES mixtures in Figure 6d. These shifts can be attributed to the formation of coordination bonds primarily between the metal ion and the oxygen atom within the carbonyl group of U [32]. Additionally, Mariappan et al. [30] suggested that these peaks are associated with the C=O stretching vibrations present in the DES samples. Furthermore, the peaks at 1452.06, 1450.34, 1445.35, and 1447.24 cm^{-1} for DES ratios of 1:5:1, 1:6:1, 1:7:1, and 1:8:1 indicate C-N bending attributed to U, as reported.

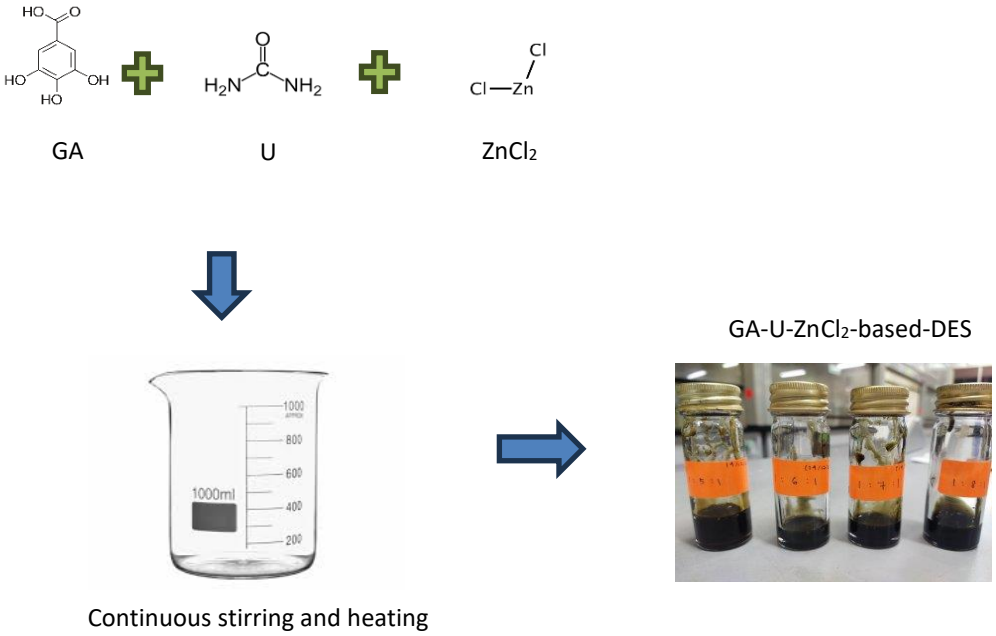

Figure 5. Structural formation of DES from precursor components

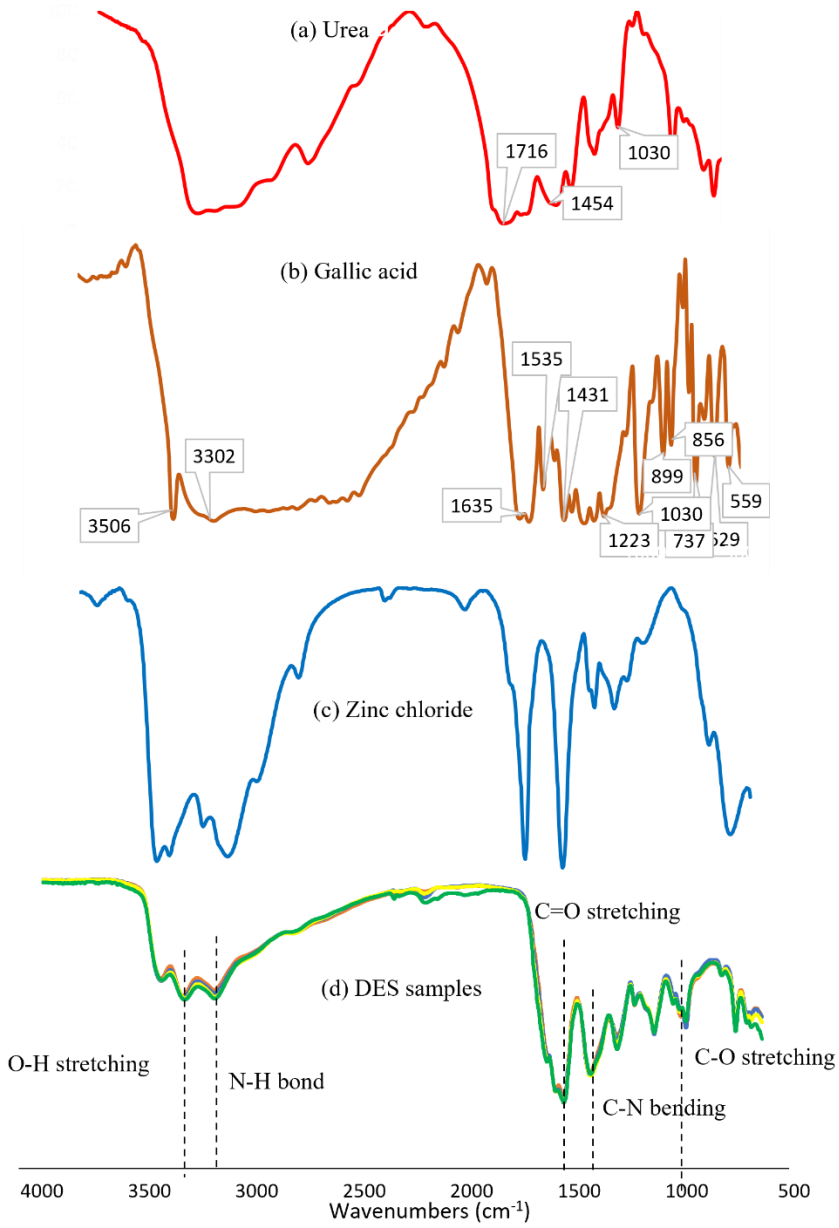

Figure 6. FTIR spectra of DES samples

Thermal properties of DESs

In most cases, hydrogen bond interactions between HBD and HBA result in the formation of homogeneous DES mixture [33]. Hence, the thermal stability of DES was evaluated via thermogravimetric analysis (TGA). Throughout this analysis, the decomposition of HBD and HBA in the investigation at different molar ratios can be determined and studied. According to Chen et. al. [33], at high temperatures, DESs often initially break down into HBDs and HBAs due to the weakening of the hydrogen bond interactions. The volatilization or decomposition of HBA with relatively low boiling points or weak stabilities occurs at a lower temperature than that at which the corresponding HBD occurs [34].

The thermal behavior study of the neat components used in the production of DES is illustrated in thermogravimetric (TG) and differential

thermogravimetric (DTG) thermograms shown in Figure 7. Urea has the lowest boiling point in comparison to GA and $ZnCl_2$. Thus, from Figure 7a, U starts to decompose at an early temperature of 154 °C. Additionally, U shows no further decomposition after 650 °C, which is earlier than the temperatures at which GA (839 °C) and $ZnCl_2$ (723 °C) no longer exhibit decreases in sample weight. The findings from the experiments are aligned with Chen et. al [33], who stated that an HBA generally has poor thermal stability and low boiling temperature, which can cause them to break down or volatilize early during TGA analysis, where U is the HBA in the preparation of the DES sample.

From Figure 7a, the TGA curves demonstrate the first step of weight loss at 86 °C, which might be due to the elimination of crystalline water [35]. The DTG curves show the onset of weight loss at 264 and 320 °C. On the other hand, the initial stage of weight percentage loss for U (Figure 7b) is at 154 °C. The TG thermogram of $ZnCl_2$ shows two steps of the thermal degradation process, where the material had lost around 1.025% and 85.72% in the first and second steps of degradation, respectively, of their total original weight during this process (Figure 7c). The pattern of thermal degradation of $ZnCl_2$ was nearly identical to one of the reported data [35]. The thermogram of the sample disclosed the temperature of the maximum derivative weight loss (T_{max}) at 570 °C. This TG/DTG thermal characteristic information would be helpful for the preparation of eutectic systems.

The thermal stability of DES mixtures can be investigated through TGA and DTG thermal decomposition profiles, which are presented in Figure 8. The TGA and DTG curves extend over the temperature interval (25–900 °C) within which the TGA was conducted. From Figure 8, it can be seen that an initial mass loss (stage A) occurred between the temperature of 25 °C and 110 °C for all samples due to moisture loss. Another peak (stage B) exists in a range of 110–280 °C, which corresponds to the decomposition of U [23]. The mass loss in stage C (from 280 to 400 °C), on the other hand, is due to the decomposition attributed to polymer formation (e.g., monoester and diester) due to the complex reaction among chloride, GA, and U [36]. The onset temperature of sample thermal degradation (T_{onset}), usually defined by 10% mass loss curve, is also a relevant parameter to be investigated through the TGA-DTG thermograms [36]. This temperature establishes the temperature range at which the samples can be utilized without degrading. The values of T_{onset} for DES-1:5:1, 1:6:1, 1:7:1, and 1:8:1 are 180, 181, 176.8, and 175 °C, respectively. These results portray an enhanced thermostability of HBD, particularly U, which initially has a low T_{onset} (154 °C). From the thermal stability point of view between the DES mixture prepared at different molar ratios, $ZnCl_2$ is more heat stable than U; hence, the T_{onset} of DES mixture would decrease with the increased ratio of U. This phenomenon can be ascribed to the surplus U present in the mixture prior to the formation of DES with $ZnCl_2$ (HBA). Overall, the composition appears to resemble a combination of DES and impurities (excess U), indicating that it is not an entirely DES-based system despite the formation of certain hydrogen bonds and the preparation of an approximate eutectic mixture. Additionally, from the TGA and DTG curves, when the U concentration increased, the maximum decomposition temperature (T_{peak}) shifted to higher temperatures. The coordinating nature of the ions, intermolecular interaction, and excess U might explain the rise in thermal decomposition temperatures [27]. These results show that the change in molar ratio has a significant impact on the thermal stability of ternary DES.

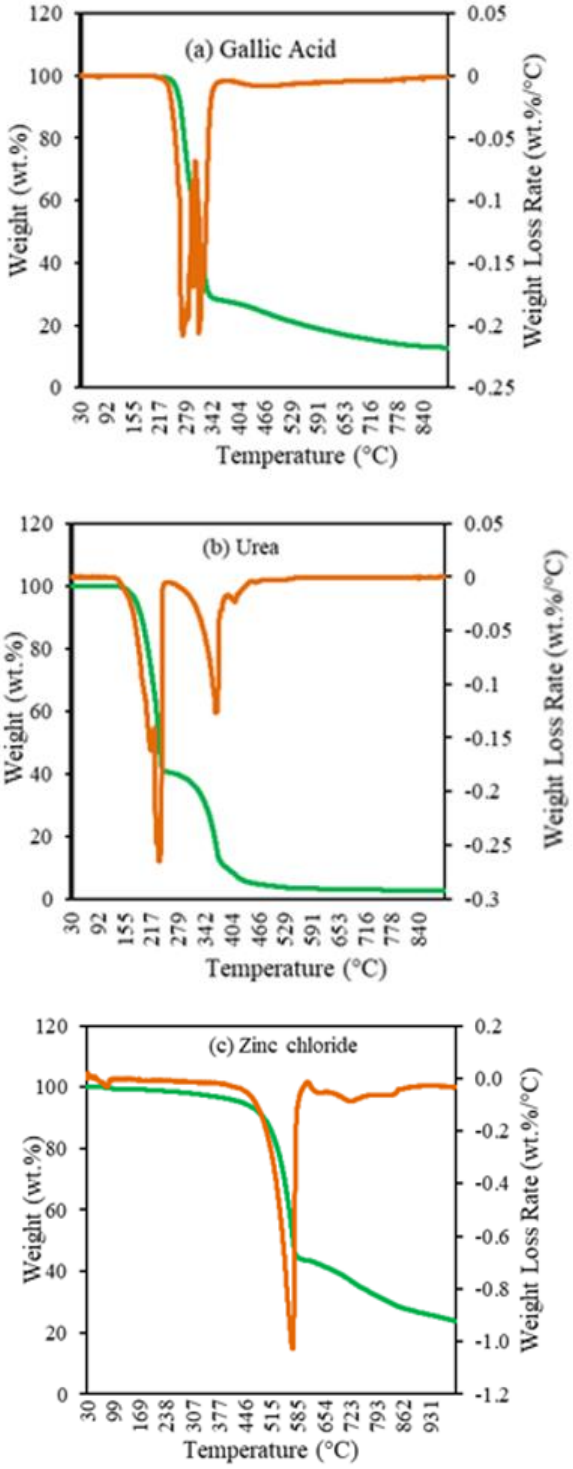

Figure 7. TGA-DTG of the components in DES

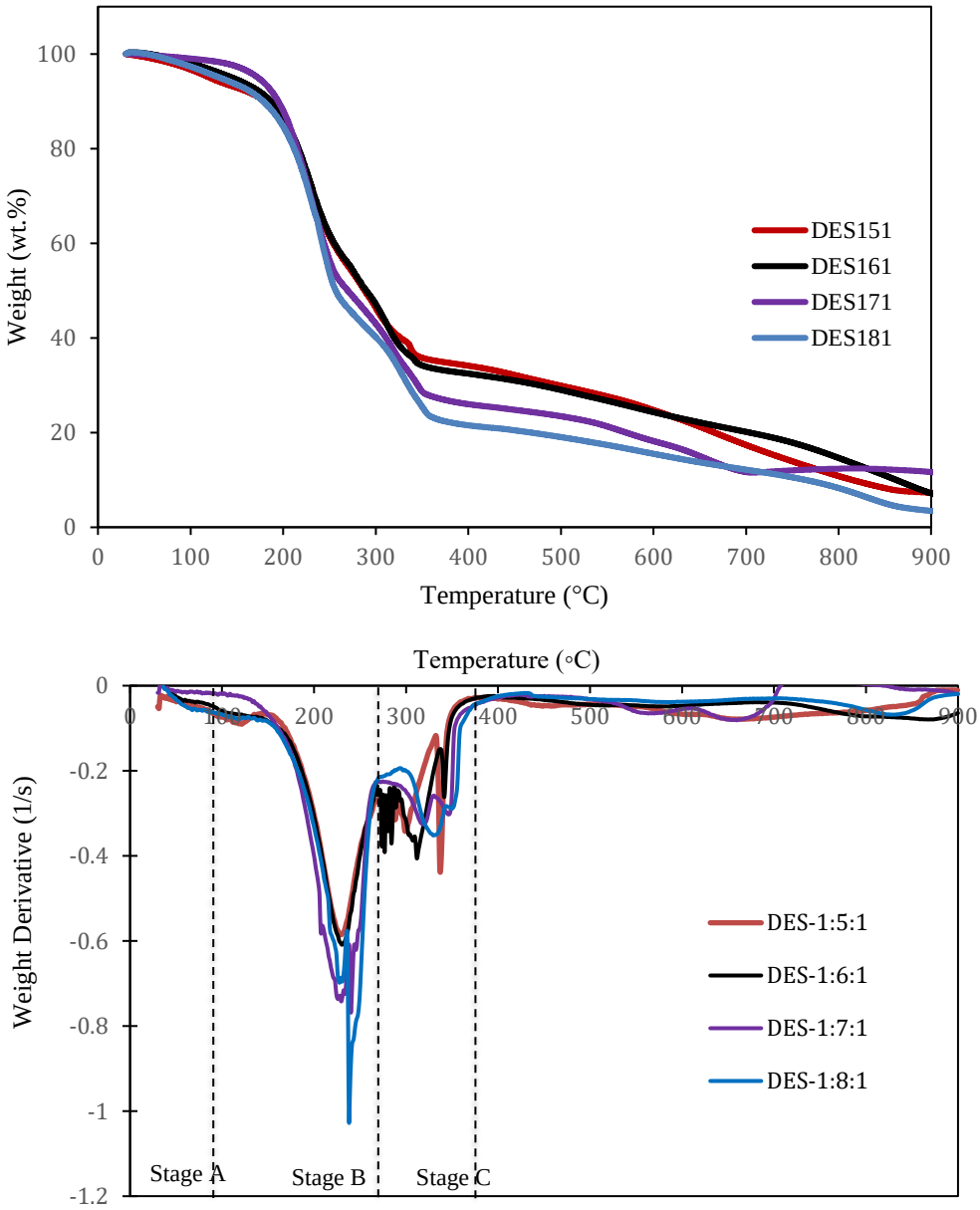

Figure 8. TGA-DTG of the DES samples

Conclusions

In this investigation, a series of DESs was successfully produced using natural components, including GA and U as HBDs, and $ZnCl_2$ as both the salt and HBA. Four different molar ratios, denoted as DES-1:5:1, DES-1:6:1, DES-1:7:1, and DES-1:8:1, were employed for the synthesis. The viscosity results indicated that DES-1:8:1 exhibited the lowest viscosity, suggesting that an increased U (HBD) content led to a reduction in viscosity due to weakened hydrogen bonding resulting from increased O–H stretching during DES synthesis. Furthermore, the FTIR analysis revealed that the GA structure predominantly maintained its integrity within the DES system, as evidenced by the C–O stretching. Additionally, the TGA showed that the thermal stability depended on the molar ratio for the ternary eutectic

mixtures. By carefully choosing an appropriate molar proportion of HBDs and HBAs, particularly focusing on the HBDs, it becomes feasible to synthesize DESs possessing the desired level of thermal stability. This study introduces a novel approach to synthesizing environmentally friendly ternary DESs, showcasing noteworthy properties that hold promise for applications in functional solvents and other materials. The findings not only contribute to advancing the formulation of novel ternary natural DESs but also offer insights for future applications and the customization of formulations in this field.

Acknowledgement

This study was funded by the Ministry of Higher Education, Malaysia under the Fundamental Research Grant Scheme (FRGS) of FRGS/1/2021/STG05/UNIKL/02/1, Majlis Amanah Rakyat (MARA) and Universiti Kuala Lumpur Malaysian Institute of Chemical and Bioengineering Technology (UniKL MICET) for their facilities.

References

1. Zhang, Q., Vigier, K. D. O. and Jerome, F. (2012). Deep eutectic solvents: syntheses, properties and applications. *Chemistry Society Review*, 41: 7108-7146.
2. Hikmawanti, N. P. E., Ramadon, D., Jantan, I. and Mun'im, A. (2021). Natural deep eutectic solvents (Nades): Phytochemical extraction performance enhancer for pharmaceutical and nutraceutical product development. *Plants*, 10(10): 2091.
3. Chandran, K., Kait, C. F., Wilfred, C. D. and Zaid, H. F. M. (2021). A review on deep eutectic solvents: Physiochemical properties and its application as an absorbent for sulfur dioxide. *Journal of Molecular Liquids*, 338: 117021.
4. Smith, E. L., Abbott, A. P. and Ryder, K. S. (2014). Deep eutectic solvents (DESs) and their applications. *Chemical Reviews*, 114(21): 11060-11082.
5. Sekharan, T. R., Chandira, R. M., Tamilvanan, S., Rajesh, S. C. and Venkateswarlu, B. S. (2022). Deep eutectic solvents as an alternate to other harmful solvents. *Biointerface Research in Applied Chemistry*, 12(1): 847-860.
6. El Achkar, T., Greige-Gerges, H. and Fourmentin, S. (2021). Basics and properties of deep eutectic solvents: a review. In *Environmental Chemistry Letters*, 19(4): 3397-3408.
7. Ghaedi, H., Ayoub, M., Sufian, S., Shariff, A. M. and Lal, B. (2017). The study on temperature dependence of viscosity and surface tension of several Phosphonium-based deep eutectic solvents. *Journal of Molecular Liquids*, 241: 500-510.
8. Chen, L., Deng, J., Song, Y., Hong, S. and Lian, H. (2020). Deep eutectic solvent promoted tunable synthesis of nitrogen-doped nanoporous carbons from enzymatic hydrolysis lignin for supercapacitors. *Materials Research Bulletin*, 123: 110708.
9. Wang, T., Guo, J., Guo, Y., Feng, J. and Wu, D. (2021). Nitrogen-doped carbon derived from deep eutectic solvent as a high-performance supercapacitor. *ACS Applied Energy Materials*, 4(3): 2190-2200.
10. Hansen, B. B., Spittle, S., Chen, B., Poe, D., Zhang, Y., Klein, J. M., Horton, A., Adhikari, L., Zelovich, T., Doherty, B. W., Gurkan, B., Maginn, E. J., Ragauskas, A., Dadmun, M., Zawodzinski, T. A., Baker, G. A., Tuckerman, M. E., Savinell, R. F. and Sangoro, J. R. (2021). Deep Eutectic Solvents: A Review of Fundamentals and Applications. *Chemical Reviews*, 121(3): 1232-1285.
11. Wang, B., Cheng, J., Wang, D. D., Li, X., Meng, Q., Zhang, Z., An, J., Liu, X. and Li, M. (2020). Study on the desulfurization and regeneration performance of functional deep eutectic solvents. *ACS Omega*, *5*(25): 15353-15361.
12. Ge, X., Gu, C., Wang, X. and Tu, J. (2017). Deep eutectic solvents (DESs)-derived advanced functional materials for energy and environmental applications: Challenges, opportunities, and future vision. *Journal of Materials Chemistry A*, *5*(18): 8209-8229.
13. Wei, Y., Wu, P., Luo, J., Dai, L., Li, H., Zhang, M., Chen, L., Wang, L., Zhu, W. and Li, H. (2020). Synthesis of hierarchical porous BCN using ternary deep eutectic solvent as precursor and template for

aerobic oxidative desulfurization. *Microporous and Mesoporous Materials*, 293: 109788.

14. Chemat, F., Abert-Vian, M., Fabiano-Tixier, A. S., Strube, J., Uhlenbrock, L., Gunjevic, V. and Cravotto, G. (2019). Green extraction of natural products. Origins, current status, and future challenges. *TrAC Trends in Analytical Chemistry*, 118: 248-263.
15. Singh, S. (2018). Applications of green solvents in extraction of phytochemicals from medicinal plants: A review Promila and Sushila Singh. *The Pharma Innovation Journal*, *7*(3): 238-245.
16. Zainal-Abidin, M. H., Hayyan, M., Hayyan, A. and Jayakumar, N. S. (2017). New horizons in the extraction of bioactive compounds using deep eutectic solvents: A review. *Analytica Chimica Acta*, *979*: 1-23.
17. Ali, M. C., Yang, Q., Fine, A. A., Jin, W., Zhang, Z., Xing, H. and Ren, Q. (2015). Efficient removal of both basic and non-basic nitrogen compounds from fuels by deep eutectic solvents. *Green Chemistry*, 18(1): 157-164.
18. Li, Y., Ali, M. C., Yang, Q., Zhang, Z., Bao, Z., Su, B., Xing, H. and Ren, Q. (2017). Hybrid deep eutectic solvents with flexible hydrogen-bonded supramolecular networks for highly efficient uptake of NH_3. *ChemSusChem*, 10(17): 3368-3377.
19. Chemat, F., Anjum, H., Shariff, A. M., Kumar, P. and Murugesan, T. (2016). Thermal and physical properties of (Choline chloride + urea + l-arginine) deep eutectic solvents. *Journal of Molecular Liquids*, 218: 301-308.
20. Luo, R., Liu, C., Li, J., Wang, C., Sun, X., Shen, J., Han, W. and Wang, L. (2017). Deep-eutectic solvents derived nitrogen-doped graphitic carbon as a superior electrocatalyst for oxygen reduction. *ACS Applied Materials and Interfaces*, 9(38): 32737-32744.
21. Carriazo, D., Gutiérrez, M. C., Ferrer, M. L. and Del Monte, F. (2010). Resorcinol-based deep eutectic solvents as both carbonaceous precursors and templating agents in the synthesis of hierarchical porous carbon monoliths. *Chemistry of Materials*, 22(22): 6146-6152.
22. Li, C., Wang, Y., Xiao, N., Li, H., Ji, Y., Guo, Z., Liu, C. and Qiu, J. (2019). Nitrogen-doped porous carbon from coal for high efficiency CO_2 electrocatalytic reduction. *Carbon*, 151: 46-52.
23. Gutiérrez, M. C., Carriazo, D., Tamayo, A., Jiménez, R., Picõ, F., Rojo, J. M., Ferrer, M. L. and Del Monte, F. (2011). Deep-eutectic-solvent-assisted synthesis of hierarchical carbon electrodes exhibiting capacitance retention at high current densities. *Chemistry - A European Journal*, 17(38): 10533-10537.
24. Haghbakhsh, R., Parvaneh, K., Raeissi, S. and Shariati, A. (2018). A general viscosity model for deep eutectic solvents: The free volume theory coupled with association equations of state. *Fluid Phase Equilibria*, 470: 193-202.
25. Manurung, R., Simanjuntak, G. C., Perez, R. N., Syahputra, A., Alhamdi, M. A., Siregar, H. and Syahputri Zuhri, R. R. (2019). Production of choline chloride-based deep eutectic solvent with hydrogen bond donor d-glucose and ethylene glycol. *IOP Conference Series: Materials Science and Engineering*, 505(1): 012134.
26. Liu, Y., Friesen, J. B., McAlpine, J. B., Lankin, D. C., Chen, S.-N. and Pauli, G. F. (2018). Natural deep eutectic solvents: Properties, applications, and perspectives. *Journal of Natural Products*, 81(3): 679-690.
27. Savi, L. K., Dias, M. C. G. C., Carpine, D., Waszczynskyj, N., Ribani, R. H. and Haminiuk, C. W. I. (2019). Natural deep eutectic solvents (NADES) based on citric acid and sucrose as a potential green technology: a comprehensive study of water inclusion and its effect on thermal, physical and rheological properties. *International Journal of Food Science and Technology*, 54(3): 898-907.
28. Tan, P., Xue, D. M., Zhu, J., Jiang, Y., He, Q. X., Hou, Z. F., Liu, X. Q. and Sun, L. B. (2018). Hierarchical N-doped carbons from designed N-rich polymer: Adsorbents with a record-high capacity for desulfurization. *AIChE Journal*, 64(11): 3786-3793.
29. Penã-Solórzano, D., Kouznetsov, V. V. and Ochoa-Puentes, C. (2020). Physicochemical properties of a urea/zinc chloride eutectic mixture and its improved effect on the fast and high yield synthesis of

indeno[2,1-: C] quinolines. *New Journal of Chemistry*, *44*(19): 7987-7997.

30. Mariappan, M., Madhurambal, G., Ravindran, B. and Mojumdar, S. C. (2011). Thermal, FTIR and microhardness studies of bisthiourea-urea single crystal. *Journal of Thermal Analysis and Calorimetry*, 104(3): 915-921.
31. Sun, Z., Chen, Y., Ke, Q., Yang, Y. and Yuan, J. (2002). Photocatalytic degradation of a cationic azo dye by TiO_2/bentonite nanocomposite. *Journal of Photochemistry and Photobiology A: Chemistry*, 149(1): 169-174.
32. Xu, L., Guo, L., Hu, G., Chen, J., Hu, X., Wang, S., Dai, W. and Fan, M. (2015). Nitrogen-doped porous carbon spheres derived from d-glucose as highly-efficient CO_2 sorbents. *RSC Advances*, *5*(48): 37964-37969.
33. Chen, W., Xue, Z., Wang, J., Jiang, J., Zhao, X. and Mu, T. (2018). Investigation on the thermal stability of deep eutectic solvents. *Wuli Huaxue Xuebao/Acta Physico - Chimica Sinica*, 34(8): 904-911.
34. Jurić, T., Uka, D., Holló, B. B., Jović, B., Kordić, B. and Popović, B. M. (2021). Comprehensive physicochemical evaluation of choline chloride-based natural deep eutectic solvents. *Journal of Molecular Liquids*, 343: 116968.
35. González-Rivera, J., Husanu, E., Mero, A., Ferrari, C., Duce, C., Tinè, M. R., D'Andrea, F., Pomelli, C. S., and Guazzelli, L. (2020). Insights into microwave heating response and thermal decomposition behavior of deep eutectic solvents. *Journal of Molecular Liquids*, 300: 112357.
36. Kadhom, M. A., Abdullah, G. H. and Al-Bayati, N. (2017). Studying two series of ternary deep eutectic solvents (choline chloride–urea–glycerol) and (choline chloride–malic acid–glycerol), synthesis and characterizations. *Arabian Journal for Science and Engineering*, 42(4): 1579-1589.

Malaysian Journal of Analytical Sciences (MJAS)
Published by Malaysian Analytical Sciences Society

A REVIEW ON THE SYNTHESIS STRATEGIES AND FACTORS CONTRIBUTING TO THE FORMATION OF ZEOLITIC IMIDAZOLATE FRAMEWORKS (ZIFs) AND THEIR APPLICATIONS

(Ulasan Strategi Sintesis dan Faktor yang Menyumbang Pembentukan Kerangka Zeolit Imidazolat (ZIFs) dan Aplikasi)

Nazhirah Muhammad Nasri[1,2], Enis Nadia Md Yusof[3], Velan Raman[1,2], Abdul Halim Abdullah[1,4], and Mohamed Ibrahim Mohamed Tahir[1,2*]

[1]*Department of Chemistry, Faculty of Science, Universiti Putra Malaysia, 43400 UPM Serdang, Selangor Darul Ehsan, Malaysia*
[2]*Foundry of Reticular Materials for Sustainability (FORMS), Institute of Nanoscience and Nanotechnology (ION2), Universiti Putra Malaysia, Serdang 43400, Selangor, Malaysia*
[3]*Chemical Sciences Programme, School of Distance Education, Universiti Sains Malaysia, Minden, Penang 11800, Malaysia*
[4]*Institute of Nanoscience and Nanotechnology (ION2), Universiti Putra Malaysia, Serdang 43400, Selangor, Malaysia*

[*]*Corresponding author: ibra@upm.edu.my*

Received: 6 November 2023; Accepted: 5 January 2024; Published: 28 February 2024

Abstract

Zeolitic Imidazolate Frameworks (ZIFs) are a subclass of Metal-Organic Frameworks (MOFs) that have attracted significant attention due to their unique properties such as high surface area, tunable pore size, and excellent thermal and chemical stability. The review aims to discuss reported single and mixed-linker of ZIFs. The synthesis of ZIFs can be achieved through various methods such as solvothermal, hydrothermal, ionothermal, microwave-assisted, sonochemical, contra-diffusion synthesis, and mechanochemical. The review discusses the benefits and disadvantages of each method as well as a critical analysis of their effectiveness. The synthesis factors of ZIFs are classified into several types such as organic solvents, additives, concentration, temperatures, metal salt variations and the reaction time. Furthermore, the paper highlights several applications of ZIFs, including their impact on adsorption of pollutants, catalysis and drug delivery system. The paper concludes by summarising the recent advances in ZIFs research which leads to future directions for further research in this field.

Keywords: zeolitic imidazolate frameworks (ZIFs), method, factors, application

Abstrak

Kerangka kerja zeolit imidazolat (ZIF) adalah subkelas kerangka kerja logam organik (MOF) yang telah menarik perhatian kerana sifat uniknya seperti permukaan yang luas, saiz liang yang boleh dilaraskan dan mempunyai kestabilan terma dan kimia yang sangat baik. Ulasan ini bertujuan untuk membincangkan ZIF dengan satu dan pelbagai penyambung yang telah dilaporkan sebelum ini. Sintesis ZIF boleh dicapai melalui pelbagai kaedah seperti solvoterma, hidroterma, ionoterma, bantuan gelombang mikro, sonokimia, sintesis kontra-resapan dan mekanokimia. Kajian ini membincangkan kelebihan dan kekurangan setiap kaedah serta

menyediakan analisis yang kritikal tentang keberkesanan sesuatu kaedah. Faktor sintesis ZIF juga dikelaskan kepada beberapa jenis seperti pelarut organik, bahan tambahan, kepekatan, suhu, variasi garam logam dan masa tindak balas. Tambahan pula, kertas kerja ini membincangkan beberapa aplikasi ZIF, termasuk kesan ZIF terhadap penjerapan bahan pencemar, pemangkin dan sistem penghantaran ubat. Kertas kajian ini juga meringkaskan kemajuan terkini dalam penyelidikan ZIF yang membawa ke menyerlahkan hala tuju masa depan untuk bidang ini dengan lebih lanjut.

Kata kunci: kerangka zeolit imidazolat, kaedah, faktor, aplikasi

Introduction

ZIFs emerges as a promising subfamily of MOFs that combines the advantages of zeolites and MOFs. ZIFs shows high thermal and chemical stability due to the tetrahedral metal-nitrogen bonds, high porosity, and tunable surface area which is achieved by simple modification of the imidazolate linkers or combined mixed linkers. ZIFs are constructed from transition metals like Zn^{2+} and Co^{2+} bridged to N-donor atoms of the imidazolate linkers in a tetrahedral cluster to form a larger and neutral framework (Figure 1). ZIF structures closely resemble aluminosilicate zeolites, where the tetrahedral metal centres of ZIFs mimic the role of silicon, while the N-donor atoms of the imidazolate linkers replace the function of oxygen in zeolites. It was found that the bonding angle of ZIFs was similar to that of zeolites, Si-O-Si, at 145° [1–3].

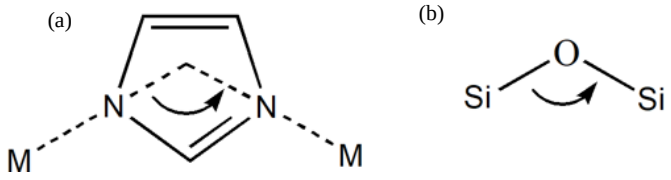

Figure 1. (a) The bond angle in the imidazolate linker, M-Im-M is 145° (b) Tetrahedral arrangement of ZIFs where blue: Metal (Zn, Co) green: imidazolate [3]

Therefore, it is not surprising that ZIFs showed advantages of both zeolites and MOFs. Most ZIF materials demonstrated high thermal stability between 200 to 400 °C under nitrogen. The frameworks also remained stable in various organic solvents at high temperatures and ambient conditions. For example, a chemical stability experiment for ZIF-300, ZIF-301, and ZIF-302 was conducted by immersing the materials in boiling water for seven days. The PXRD patterns of these materials were in good agreement with the simulated PXRD patterns generated from SCXRD [4]. Moreover, the frameworks did not show any compositional changes in organic solvents such as methanol and benzene at 65 and 85 °C within the seven days, indicating that ZIFs were chemically stable materials [1]. The coordination ability between organic linkers and metal centres influenced the formation of ZIFs and offered more controllability and flexibility compared to zeolites. The pore size of ZIFs can be modified by incorporating more than one type of imidazolate linker into the framework along with multiple functional groups. It is also possible to synthesise ZIFs with a wide range of imidazolate linkers and metal centres to create similar topologies. For example, ZIF-8 was synthesised using 2-methylimidazole (2mIM) and zinc nitrate tetrahydrate ($Zn(NO_3)_2.4H_2O$), shared the same sodalite (sod) topology as ZIF-67, which is composed of 2mIM and Co^{2+} centres [5] (Table 1). A similar case occurred with ZIF-90, where this framework was synthesised using 2-imidazolecarboxaldehye (ICA) and ($Zn(NO_3)_2.4H_2O$), resulting in a **sod** topology [6].

In this review, we pay full attention to the research developments in the synthesis and possible applications of ZIFs. We first consider the previously reported single and mixed-linkers of ZIFs, a range of preparation methods (synthetic routes) of ZIFs, encompassing both solvent and solvent-free approaches. In addition, the effects of synthesis conditions on the formation of ZIFs including the main applications in some promising areas

were also highlighted in the write-up. The review is proposed to provide guidance and highlight the significant to the readers for the future development of ZIF materials.

Table 1. Comparison between crystal structures of ZIF-8, ZIF-90 and ZIF-67 with **sod** topology [5]

Metal centre	Linker	Structure	Topology
Zn^{2+}	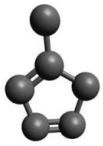 2mIM	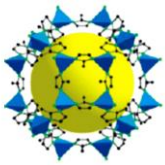 ZIF-8	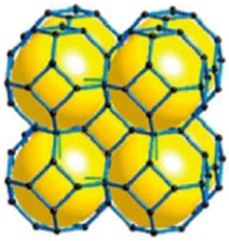 **sod** topology
Zn^{2+}	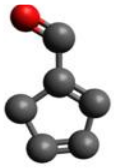 ICA	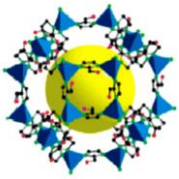 ZIF-90	
Co^{2+}	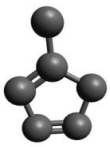 2mIM	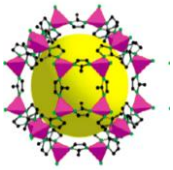 ZIF-67	

Solvent methods of ZIFs

The solvothermal method is a well-known technique to synthesise MOFs and ZIFs by mixing organic linkers and metal ions in a specific reaction solvent such as dimethylformamide (DMF), diethylformamide (DEF) and *N*-methyl-2-pyrrollidone (NMP). The synthesis reaction is conducted in a closed space environment, such as NMR tube, microplates and vials that can withhold high temperatures (80 to 140 ^{o}C) to generate autogenous pressure [7]. These conditions enhance the solubility of reactants and accelerate the interaction between metal centre and organic linker during the reaction. The synthesis of ZIFs typically takes place over a period of 12 to 96 hours [1–4,6,8]. High boiling point solvents may degrade at high temperatures, forming amine as side product that act as nucleophilic bases, facilitating the crystallisation process [3]. Consequently, ZIFs synthesised via the solvothermal method consistently yield highly crystalline products. The synthesis of ZIF-1 to ZIF-12 was reported in 2006 in which the initial development of ZIFs were focused with Zn^{2+} and Co^{2+} as the metal centres, and the different types of imidazolate linkers such as imidazole (IM), benzimidazole (bzIM) and 2mIM). In 2008, a group of researchers introduced two types of imidazolate linkers bonded in a framework which was used to successfully synthesise ZIF-60 to ZIF-80 in different solvents at the reaction temperature beyond 80 ^{o}C [1,5].

Undeniably, the solvothermal method allows the formation of highly crystalline and phase-purified ZIFs by increasing the solubility of reactants [9]. However, organic solvents are not environmental-friendly and cost-redundant for large-scale synthesis of ZIFs. In addition, large solvent molecules are difficult to remove from the framework's pores. Therefore, the hydrothermal synthesis method has been applied to reduce the usage of toxic organic solvents by replacing them with water [10,11]. This method is usually performed after the successful development of established ZIFs through solvothermal method. Several factors that need to be considered before synthesising

ZIFs using the hydrothermal method includes the concentration of imidazolate linkers, the addition of additives and zinc source [12]. These factors are crucial to ensure crystallinity of ZIFs can be achieved.

from solvothermal synthesis methods, the ionothermal method has been employed to produce ZIF material that utilises ionic liquid or eutectic mixtures [13,14]. It should be mentioned that an ionic liquid can act simultaneously as a solvent and a structure-directing agent (template) to avoid the competition between the solvent framework and the template-framework that existed in hydrothermal preparation due to the presence of hydrogen bonding. This method is performed under ambient pressure in an open system, which eliminates the risks of high autogenous pressure in a sealed autoclave [15]. In addition, the advantage of using ionic liquids as solvent is that they can be reused for further synthesis reactions [14]. ZIF-8 was also synthesised under the ionothermal method using a deep eutectic solvent by heating the mixture of $Zn(NO_3)_2.6H_2O$, 2mIM linker, and tetrabutylammonium bromide (TBAB) while stirring at 40 ^oC [16]. The coordination between the 2mIM linker and Zn^{2+} was initiated by the hydrogen bond interaction between the N-H bond of 2mIM linker and the halide ion of TBAB, which promoted the deprotonation of the 2mIM linker. The obtained material possessed a high BET surface area of 1486 $m^2 g^{-1}$, higher than the ZIF-8 material synthesised under the hydrothermal method (460 $m^2 g^{-1}$). The crystallinity of synthesised ZIF-8 under the ionothermal method was also comparable with the simulated PXRD pattern of ZIF-8 [16]. ZIF-67 was synthesised under the same method in 1-ethyl-3-methylimidazolium bromide ([emim])Br ionic liquid. The mixtures of $Co(NO_3)_2.6H_2O$, 2mIM linker, and ([emim])Br ionic liquid were stirred, and the solution was transferred to a 30 mL Teflon-line autoclave at 140 ^oC for several minutes. The PXRD pattern of ZIF-67 synthesised from the ionothermal method was in good agreement with the PXRD pattern of ZIF-67 synthesised from the solvothermal method [17].

Microwave-assisted synthesis is an alternative method that is analogous to conventional synthesis methods. The fundamental concept behind microwave-assisted synthesis is that microwave heating is produced from the interaction of electromagnetic radiation with mobile electrical charges between solid or soluble conducting ions and polar solvent molecules [15]. In the solid phase, the material's electrical resistance produced the electric current, which contributed to the heating effect on conducting or semiconducting materials [18–20]. While in solution phase, high temperatures could increase the collisions between aligned polar molecules with the rapidly changing electromagnetic field, hence increasing the kinetic energy of these molecules [15,18]. This has led to the generation of microwave heating due to molecular friction. The microwave-assisted method is carried out at a temperature above 100 ^oC in a short time within one hour. The feasibility of the microwave-assisted method has been explored for the preparation of ZIF-11. In the first step, bzIM linker and zinc acetate dihydrate ($Zn(OAc)_2.2H_2O$) were dissolved in the solvent mixture (MeOH, toluene and ammonium hydroxide). The solution was placed in a Teflon liner and microwave- heated at 100 ^oC for 60 minutes. ZIF-11 displayed a regular hexagonal shape with an average size of 5.0 μm and possessed high BET surface area of 745 $m^2 g^{-1}$ [21]. ZIF-8 synthesised under this method exhibited good crystallinity and BET surface area, which is consistent with the results obtained from solvothermal and hydrothermal methods. This material also showed good performance as an adsorbent for the adsorption of Congo Red dye (CGR) and Rhodamine B (RhB), with a removal efficiency achieved beyond 87% [22].

The third synthesis method of ZIFs is the sonochemical method, which is related to the molecules' chemical and physical changes after ultrasonic irradiation. The alternate pressure from ultrasonic irradiation is responsible for generating acoustic cavitation. The hot spots around the liquid were developed in the acoustic cavitation and provided extraordinary high temperature and pressure, which initiated the chemical reaction of ZIFs [18,23,24]. This is an eco-friendly method for producing ZIFs over a short period of time. The sonochemical method is performed using a direct immersion ultrasonic horn or ultrasonic cleaning bath. ZIF-8 was obtained under ultrasound radiation with various power settings (98 kHz, 300 kHz, and

1 MHz) and frequencies (10, 20, and 30 watts) [25]. The crystallinity, purity, and yield of ZIF-8 were maintained using this method. However, ultrasound has a significant impact on the nucleation step and contributes to the fast production of the nucleation centre. This resulted in a reduction of the particle size inZIF-8 [25]. Thin film ZIF-8 was prepared under this method by dissolving 2mIM linker in a mixture of deionised water and TEA while stirring for 10 minutes at room temperature [26]. Then, the zinc hydroxide solution was immersed in the respective 2mIM linker solution before being sonicated at room temperature. The frequency and power of the sonicator was set at 40 kHz and 100 watts. The crystal size of ZIF-8 was found to increase as the reaction time proceeded from 5 minutes to 60 minutes. Moreover, the PXRD patterns of ZIF-8 became more sharp and intense, resulting from the prolonged sonication time [26].

Contra-diffusion is another method that can be used to produce existing ZIFs. During the first stage of the reaction, the metal and organic linker solutions are diffused in opposite directions along the support or the defects in the membrane grains, forming a thin membrane layer [27]. Moreover, the contra-diffusion approach is an alternative method for reducing the reaction rate and producing a thin and defect-free membrane. A well-intergrown and continuous ZIF-8 layer is formed on the metal ion side surface of the poly(4-vinylpyridien) brushes as a result of a combination of surface graft and the optimal addition of sodium formate into the ligand. ZIF-8/poly(4-vinylpyridien) membrane demonstrated excellent reusability as an adsorbent material for iodine, with a removal efficiency of 73.4% after five cycles [28]. In 2019, a group of research successfully formed a uniform layer of ZIF-8 on porous polyvinylidene fluoride (PVDF) ultrafiltration membranes. The membranes were separated and filled with solutions of 2-methyl imidazole and zinc nitrate. Both the processes of solution diffusing into the membranes crystallisation took place at room temperature which resulted in an excellent performance of the ultrafiltration process [29]. ZIFs can be synthesised using various methods and it is evident that further development can be undertaken to reduce the reaction time, increase production yield and improve the porosity of the framework.

Solvent-free method of ZIFs

Mechanochemical synthesis is another method that could produce ZIFs. Compared with conventional synthesis methods, mechanochemical synthesis is an approach that uses little solvent and energy and reduces reaction time. This synthesis method uses a ball mill to grind metal salt and organic linker without the involvement of solvent or heat [18]. The mechanical energy generated from grinding would minimise the particle size to promote the interaction between the organic linker and metal ions [15]. Mechanochemical synthesis was conducted at room temperature by converting ZnO to ZIF-8. The solution of ZnO and 2mIM linker were placed in a 300 mL ceramic pot before the ceramic pot was rotated at 100 ppm [30]. The transformation of ZnO to ZIF-8 produced a lower yield product after prolonged milling exposure. The addition of $(Zn(OAc)_2.2H_2O)$ was essential to promote acid dissolution of ZnO and facilitate the complex formation between ionised Zn and the 2mIM linker [30]. Thus, adding a small liquid could promote the formation of ZIF and improve the morphology of ZIF-8 under mechanochemical synthesis from agglomerated amorphous ZIF to dendritic porous architecture (Chen *et al.*, 2014) . The glass-forming ZIF-62 was synthesised by the mechano-synthetic route using liquid-assisted grinding. All starting materials, that are ZnO, 2mIM, and IM linkers, were mixed together in a 10 mL stainless steel grinding jar and was shaken for 30 minutes. In this synthesis method, ZnO was used instead of $Zn(NO_3).2H_2O$ or $ZnCl_2$ to avoid the formation of HNO_3 or HCl by-products that would have resulted from the metathesis of Zn salts with IM and bzIM linkers. This is because the acid by-products would digest ZIF to its starting materials. The mechanochemical method would reduce the amount of starting materials and reaction time for the production of materials compared with the solvothermal synthesis method. Although the crystal size of ZIF-62 obtained from the mechanochemical method is smaller than the conventional synthesis method [31].

Synthesis of single linker ZIFs

Up until 2023, the synthesis and characterisation of ZIFs had been achieved. The pioneering work in this field was led in 2006, when they successfully synthesised 12 ZIFs.

These included ZIFs with Zn^{2+} centres, namely ZIF-1 to ZIF-10, as well as those with Co(II) centres, specifically ZIF-9 and ZIF-11. This achievement was accomplished through the use of a variety of imidazolate linkers, such as IM, bzIM, and 2mIM, resulting in the formation of novel ZIF materials with distinct topological structures [3]. There are six ZIF structures, all composed of Zn^{2+} centres with imidazolate linkers, each displaying different three-dimensional (3D) topologies, including **crb, dft, cag,** and **mer** s depicted in Figure 2.

Notably, ZIF-1, ZIF-2, ZIF-3, ZIF-4, ZIF-10, and ZIF-14 were crystallised in various space groups and crystal systems, which were influenced by the molar composition of the reaction conditions. Consequently, this variance resulted in the formation of diverse topologies. In particular, ZIF-10 was found to crystallise within a tetragonal crystal system with a space group of *I4/mmm. A*mong these ZIFs, ZIF-10 exhibited a notably high crystal volume of approximately 14,211(2) $Å^3$. This exceptional volume can be attributed to the high concentration of imidazolate linker which led to the formation of bigger framework. All the nitrogen atoms from imidazolate are coordinated to Zn^{2+} centres in a tetrahedral geometry resulting in the formation of an 8-membered ring and a 4-membered ring of **mer** and **dft** topology [3,5]. The pore diameter of **mer** topology is 12.12 Å, which is more significant than **dft** topology, 8.02 Å [32]. ZIF-8 and ZIF-67 are well-known frameworks that consist of a similar linker, 2mIM. They adopted the **sod** topology with 4- and 6-membered rings, despite having different kind of metal centres. This topology featured one kind of vertice and edge with a pore diameter of 11.6 Å, which received a considerable attention from many researchers to utilise these frameworks in many promising applications. The surface areas of ZIF-8 and ZIF-67 are 1947 $m^2 g^{-1}$ and 1676 $m^2 g^{-1}$, respectively, surpassing those of other ZIFs with single linker [3,5].

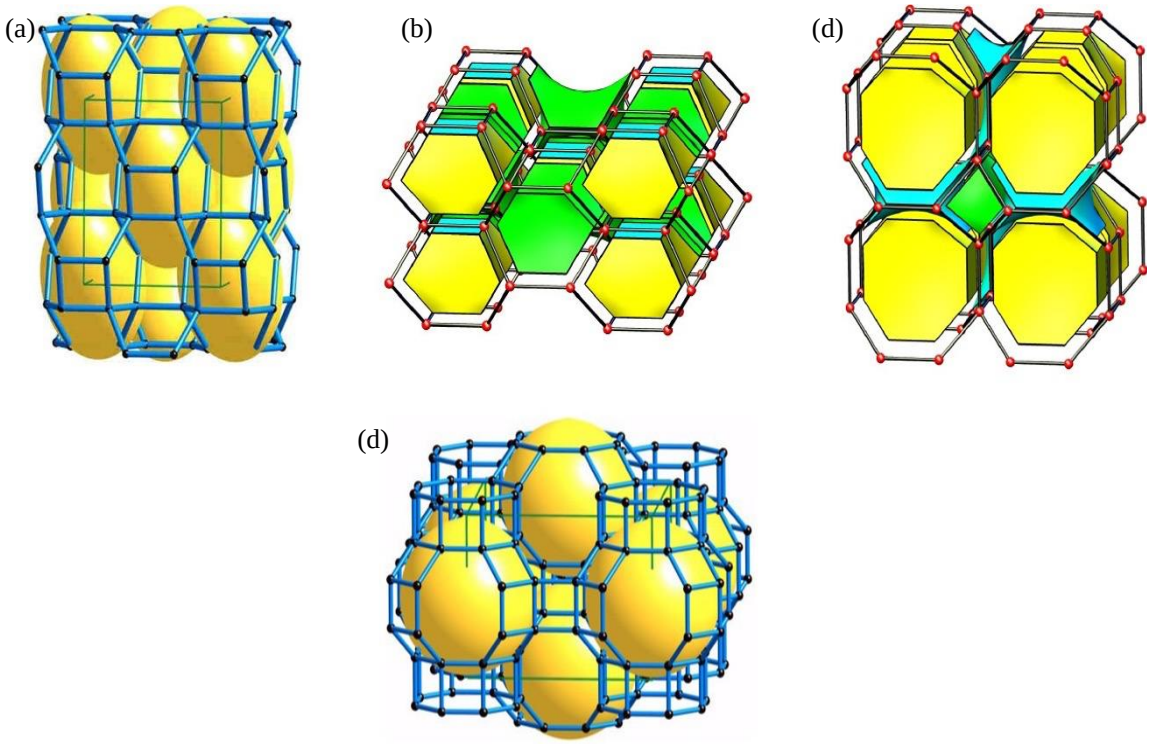

Figure 2. Topologies of the network structures; (a) ZIF-4, **cag**; (b) ZIF-1 and ZIF-2, **crb**; (c) ZIF-3, **dft**; (d) ZIF-10, **mer** [3]

Meanwhile, ZIF-7 and ZIF-11 are comprised of similar metal centres joined by bzIM linkers, but these frameworks adopted different topologies (ZIF-7: **sod and** ZIF-11: **rho),** as shown in Figure 3. The introduction of bzIM in the framework allows for the formation of a larger topology due to the functionalisation of the imidazole linker with benzene rings at 4th and 5th positions. The crystal systems for ZIF-7 and ZIF-11 are hexagonal and cubic, with space groups of $R\bar{3}$ and $Pm\bar{3}m$, respectively. Based on SCXRD results, ZIF-11 was proven to have a high crystal volume of about 23,787(14) Å^3, in contrast to ZIF-7 (7,214(14) Å^3). The topology of ZIF-11 (**rho**) is considered a large topology in the presence of 4-, 6-, and 8-membered rings, compared to the **sod** topology. Therefore, ZIF-11 was successfully crystallised in a larger framework, over longer reaction time and medium temperature of 100 °C, which led to a slow crystallisation process and higher surface area of the framework. Both the ZIFs have exhibited high chemical stability and the crystallinity of the frameworks were maintained after immersing them in boiling benzene, water, methanol, and ethanol for seven days.

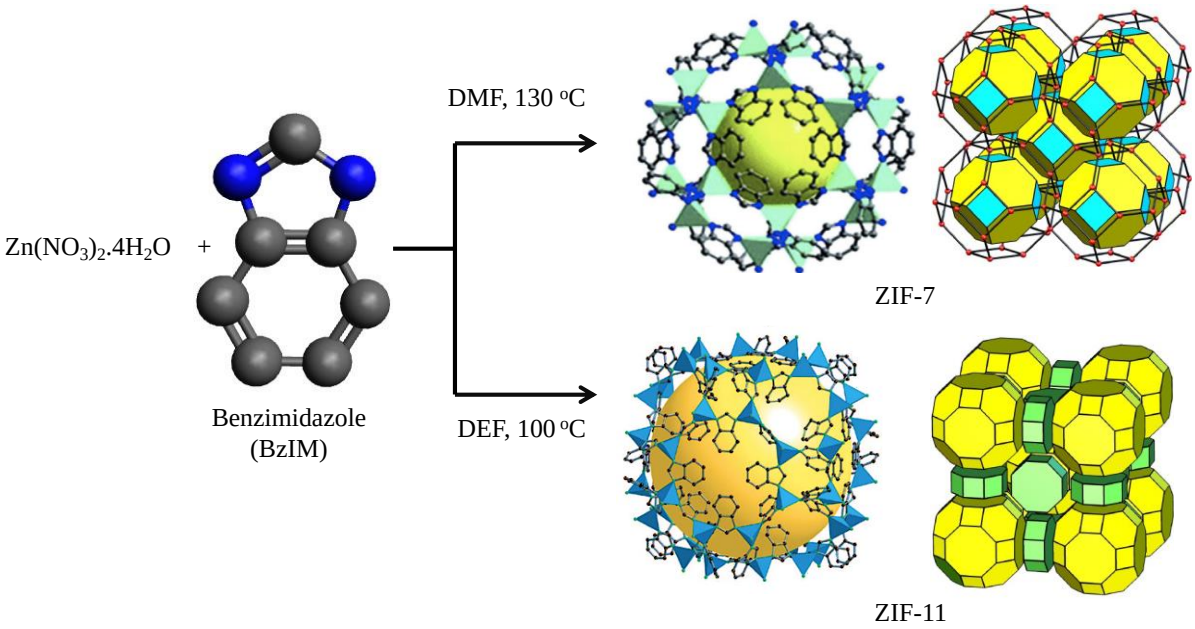

Figure 3. The formation process of ZIF-7 and ZIF-11 which produced different kind of topology [3,5]

In 2008, new porous ZIFs with high surface area were reported, namely ZIF-95 and ZIF-100 (Figure 4). ZIF-95 was constructed using zinc nitrate tetrahydrate ($Zn(NO_3).4H_2O$) and 5-chlorobenzimidazole (5cbIM). ZIF-95 crystallises within the tetragonal space group, displaying *I4/mmm* symmetry, resulting in an underlying net topology symbolised as **poz**. In contrast with ZIF-95, ZIF-100 featured a tetrahedral metal centre with zinc trimethafluorosulfanate ($Zn(O_3SCF_3)_2$). SCXRD results revealed that ZIF-100 shared the same crystal system as ZIF-11 and has $Im\bar{3}$ symmetry, with an extensive cell volume of approximately 372,932(4) Å^3, which proved ZIF-100 to be a large inorganic framework. It is believed that the incorporation of 5cbIM into the framework led to the formation of a new topology, facilitated by the functionalisation of bzIM with a chlorine atom at the 5th position. Figure 4 illustrates the ZIF-100 underlying net topology, denoted as the **moz** topology, with an inner diameter of the framework exceeding that of the faujasite (**fau**) topology, measuring approximately 35.6 Å [2].

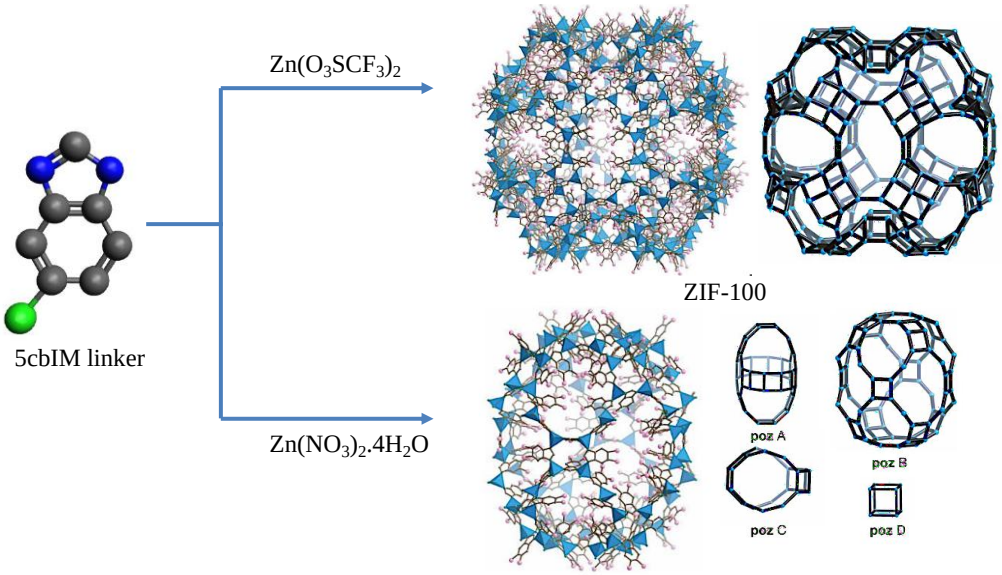

Figure 4. The structure of ZIF-95 and ZIF-100. Both the ZIFs were made up of different kind of metal salts with 5cbIM linker , forming different types of topologies [2].

Notably, ZIF-95 encompasses two distinctive types of cages with varying inner diameters. The initial cage, known as **poz A**, possesses an inner diameter measuring 25.1 x 14.3 Å, making it roughly the same size as the super cage in the **fau** topology. The second cage of ZIF-95 is **poz B** with 30.1 x 20.0 Å of inner diameter, significantly greater than the diameter of the **fau** topology, which is around 14.1 Å. The extended framework was linked by the tetra coordinates of Zn^{2+} centre for ZIF-95, resulting in the creation of an exceptionally expansive **poz** topology. This topology accommodates two large cages, with the first **poz** cage (**poz** A) followed by the second **poz** cage (**poz** B), both cages containing 8-, 10-, and 12-membered rings. Importantly, each imidazolate linker in ZIF-95 exhibits specific steric indexes (δ), as indicated in Figure 5.

The steric index is used to measure the size and shape of imidazolate linkers, taking into account their van der Waals volume and length. Imidazole linkers with increased bulkiness exhibit a higher steric index value (δ) compared to smaller imidazole linkers,. The strategic introduction of bulkiness at the 4^{th} and 5^{th} positions of imidazolate linkers has profound impact, resulting in the formation of large cages containing more than 8-membered rings within the frameworks. This led to the formation of entirely new and extensive underlying net topologies, which is a direct outcome of incorporating imidazolate linkers with high steric indices [8].

Synthesis of mixed-linker ZIFs bearing two different imidazolate linkers

There are several advantages in mixed-linker ZIFs compared to single linker ZIFs. Incorporating two or more different imidazolate linkers in the framework enables the fine-tune of surface area and pore size by selecting imidazolate linkers of varying size and length. For instance, the gas separation efficiency is significantly enhanced in mixed-linker ZIF-7-8, whereas the incorporation of the bulkier bzIM linker, along with the 2mIM linker, results in the formation of a larger aperture [33]. The introduction of different functional groups derived from distinct imidazolate allows for the tailored design of functionality within the frameworks, providing a variable surface environment. This mixed-linker strategy is exemplified by introducing two different imidazolate linkers with diverse functional group, such as combining 2mIM with 2-aminobenzimidazole (2amBzIM) in the ZIF-8 framework [34]. This approach serves to improve the permeability and selectivity for CO_2 capture. Moreover, the frameworks that contained three imidazolate linkers

leads to formation of a substantial topology, as observed in ZIF-412, -413, and -414, generating a novel underlying topology [8]. This unique topology demonstrated capability in capturing large molecules, such as xylene, which further proves the capability of mixed-linker ZIFs to capture molecules like xylene which is comparably difficult to attain in a single linker ZIFs.

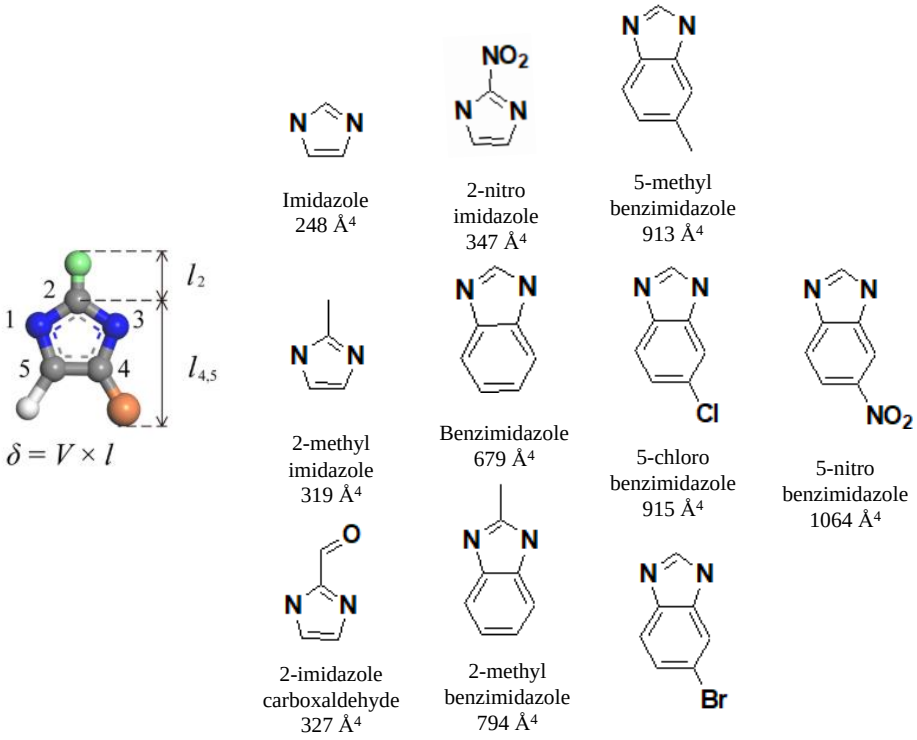

Figure 5. Steric index for imidazolate linkers based on the van der Waals volume (V) and length (*l*) [8]

Incorporating multiple linkers within a single framework proves to be an efficient strategy for the development of novel ZIFs with diverse functionalities, adjustable porosity, customisable topology, and enhanced performance tailored for specific applications. Mixed-linker ZIFs were synthesised based on the chabazite, **cha** topology, which involves the utilisation of bulky imidazolate derivatives such as 5-methylbenzimidazole (5mbIM), ZIF-302; 5-chlorobenzimidazole (5cbIM), ZIF-301; and 5-bromobenzimidazole (5bbIM) for ZIF-300. These derivatives were employed with 2mIM to form coordination bonds with Zn^{2+} centres [4]. ZIF-300 and ZIF-302 were crystallised in trigonal crystal system, and the space group associated with the crystals was *R*-3. Consequently, these ZIFs were classified as part of the isoreticular series of mixed-linker ZIFs.

The isoreticular framework constitutes of a series of compounds sharing the same topology while featuring organic linkers with varying functionalities and sizes [35,36]. Based on NMR analysis, bzIM derivatives were the dominant organic linkers in the frameworks compared to the 2mIM linker, even though the molar composition of metal to organic linkers maintained an equivalent ratio for both ZIF-300 and ZIF-301. This finding was further supported by SCXRD results, demonstrating that all the organic linkers were bound to the tetrahedral Zn^{2+} clusters. The resulting 3-periodic frameworks exhibit the **cha** topology, where the use of water as a co-solvent plays a crucial role in forming specific cavities, as shown in Figure 6. These cavities were composed of two distinct types: a *cha* $[4^{12}6^{2}8^{6}]$ cavity (the symbol $[m^n]$, signifying the presence of n faces with *m*-membered rings), which is described as an 8-membered ring in this topology. Here 5mbIM, 5cbIM

and 5bbIM linkers are situated within this cavity. In contrast, derivatives of 2mIM or bzIM linkers are positioned at the edge of **cha** cavities, connecting to the two 6-membered rings of *hpr* cavities [$4^6 6^2$] (small cage). In addition, all of these frameworks remained stable when subjected to boiling water for seven days, maintaining their crystallinity, as evident from experimental PXRD patterns. Furthermore, these ZIFs demonstrated type-III isotherms as a result of incorporating hydrophobic functionalities into the frameworks, thereby enhancing the overall stability of the frameworks [4].

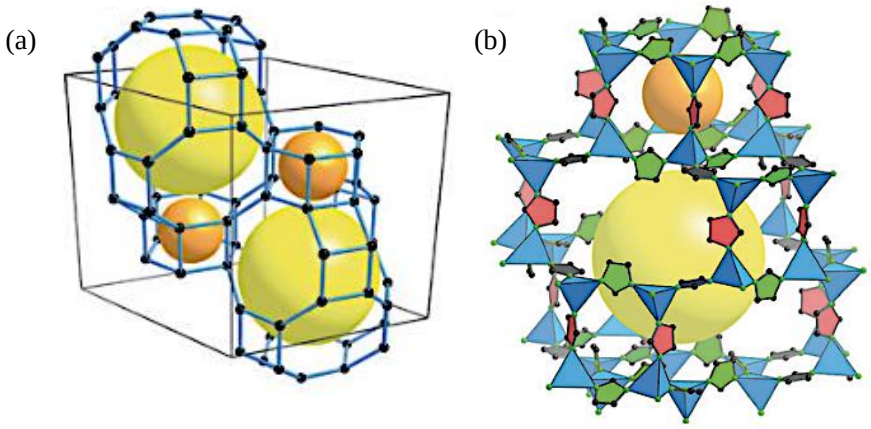

Figure 6. (a) Ball and stick model represent **cha** topology composed of two types of cavities *hpr* (large) and *cha* (small). (b) The **cha** topology of ZIF-300 and ZIF-301. Greyish-blue and red imidazolate linkers represent 2mIM and bulky imidazolates (5bbIM, 5cbIM and 5mbIM) respectively whereas green imidazolate linkers indicated the position for non-specific linkers either 2mIM or bzIM derivatives can occupy in this position [4, 37].

The isoreticular series of ZIFs were successfully synthesised using 2-nitroimidazole (2nIM) with different types of imidazolate derivatives ranging from polar (-CN, ZIF-82; $-NO_2$, ZIF-78) to non-polar functionalities ($-CH_3$, ZIF-79; -Br, ZIF-81; -Cl, ZIF-80). These ZIFs formed definite topology with broad channels and large pore diameter [1]. In particular, the exact topology of the framework structures was constructed with different functionalities of cavities and different sizes of organic linkers, which determined the isoreticular series of ZIFs, as illustrated in Figure 7. ZIF-79, ZIF-80, ZIF-81, ZIF-82 and ZIF-78 were synthesised by solvothermal method using different solvent and period of reactions. These ZIF compounds crystallised in a hexagonal crystal system, sharing the common space group of $P6_3/mmc$. Intriguingly, despite the introduction of diverse functionalities of the imidazolate linkers, these five mixed-linker ZIFs exhibited a gmenilite (**gme**) topology [2,3,5]. As shown in Figure 7, the **gme** topology consists of *hpr* cages where the 2nIM linker occupies along the cage edges, while the imidazolate linker with varying functionalities are within the cavities of *kno* cages with pore diameter ranging from 7.1 Å to 15.9 Å.

Remarkably, functionalised imidazolate linkers found in ZIF-78 and ZIF-79, such as 5-nitrobenzimidazole (nbIM) and 5mbIM contributed to smaller pore diameters around 7.1 Å and 7.5 Å, respectively, achieving a slightly tilted orientation in the topology. ZIF-82 containing smaller imidazolate linkers, 4-cyanoimidazole (cnIM) and 2nIM, featured larger pore diameter around 12.3 Å [1]. In addition, PXRD of these ZIFs remained unchanged even after exposure to boiling benzene, water and methanol. This demonstrated that ZIFs are extremely stable under diverse environmental conditions. The integration of multiple imidazolate linkers within a single framework emerges as an efficient strategy for attaining variable functionalities, larger cages and varying pore sizes of the frameworks.

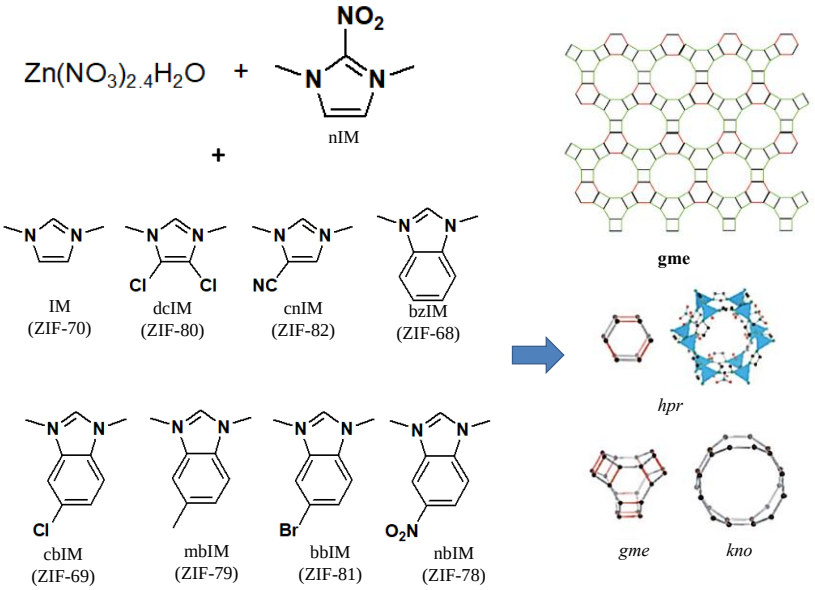

Figure 7. Imidazolate linkers and their abbreviations (IM: Imidazole; dcIM: 4,5-dichloroimidazole; 4cnIM: 4-cyanoimidazole; 5cbIM: 5-chlorobenzimidazole; 5mbIM: 5-methylbenzimidazole; 5bbIM: 5-bromobenzimidazole; 5nbIM: 6-nitrobenzimidazole) reacted with Zn^{2+} and 2-nitroimidazole (2nIM) to form **gme** topology. The **gme** topology consist of several cavities such as *hpr*, *kno* and *gme* as illustrated on the left side [2,3,5].

In 2017, a group of researchers obtained new ZIFs by introducing two bulky imidazolate linkers into the framework, named ZIF-516 and ZIF-586. The crystal structure of ZIF-516 consisted of 5bbIM and 5mbIM linkers, while ZIF-586 featured 5mbIM and 2mbIM linkers, linked together by tetrahedral Zn^{2+} clusters. These ZIFs were crystallised in a tetragonal crystal system; however, both ZIFs were arranged into different space groups (ZIF-516: $P4_32_12$ and ZIF-586: $P4_2/ncm$). Despite the distinct space groups, these frameworks were classified under the same underlying net topology, **ykh,** containing large cages ranging from 22.1 to 22.3 Å. Figure 8 shows the **ykh** and **moz** topology of ZIF-516, ZIF-586 and ZIF-408. The introduction of 5bbIM, 5mbIM, and 5cbIM with functionalised imidazolate linkers at 4th and 5th positions resulted in the formation of large and small cages comprising of 3-, 4-, 10-, 12-, and 14-membered rings, generating large topologies such as **ykh**, **poz**, **moz,** and **zea** [8].

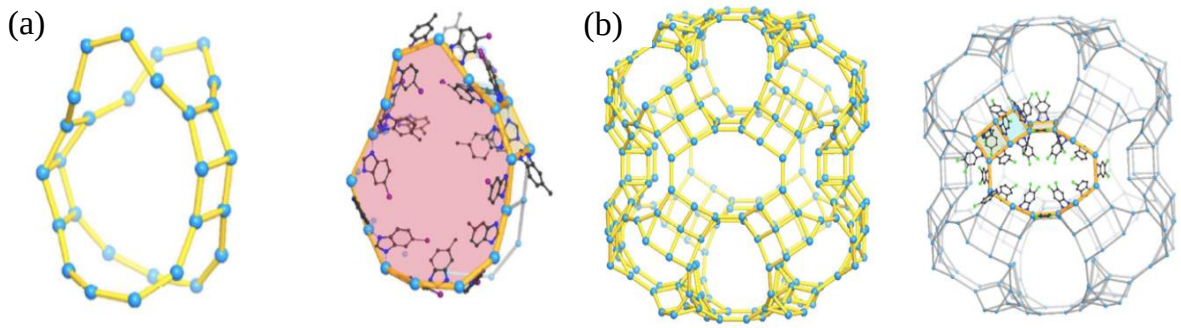

Figure 8. (a) **ykh** topology of ZIF-516 with 3-, 4-, 10-, 12-, and 14-membered rings. (b) **moz** topology of ZIF-408 consists of 4- and 12-membered rings. C: black, N: blue, O: red, Cl: green and Br: violet [8]

ZIF-412, ZIF-413, and ZIF-414 formed a new underlying topology, **ucb**, featuring several types of membered rings ranging from 4-, 6-, 8- to 24-membered rings. The cage size was measured at 45.8 Å, making it the largest cage within the topology (Figure 9). The building units for ZIF-412, ZIF-413, and ZIF-414 was a combination of multiple bulky imidazolate linkers (6nbIM, bzIM, 5mbIM) with small imidazolate linkers (2nIM and IM). These compounds crystallised in a cubic system with the space group, $Fm\bar{3}m$. The combinations of small and large steric indices facilitate the formation of large and small cages in ZIFs, resulting in topologies like **moz** (41.2 Å) and **ucb** (45.8 Å). Therefore, it is important to incorporate small imidazolate linkers like imidazole alongside other bzIM derivatives with high steric index to enable the creation of extensive crystal structures [8].

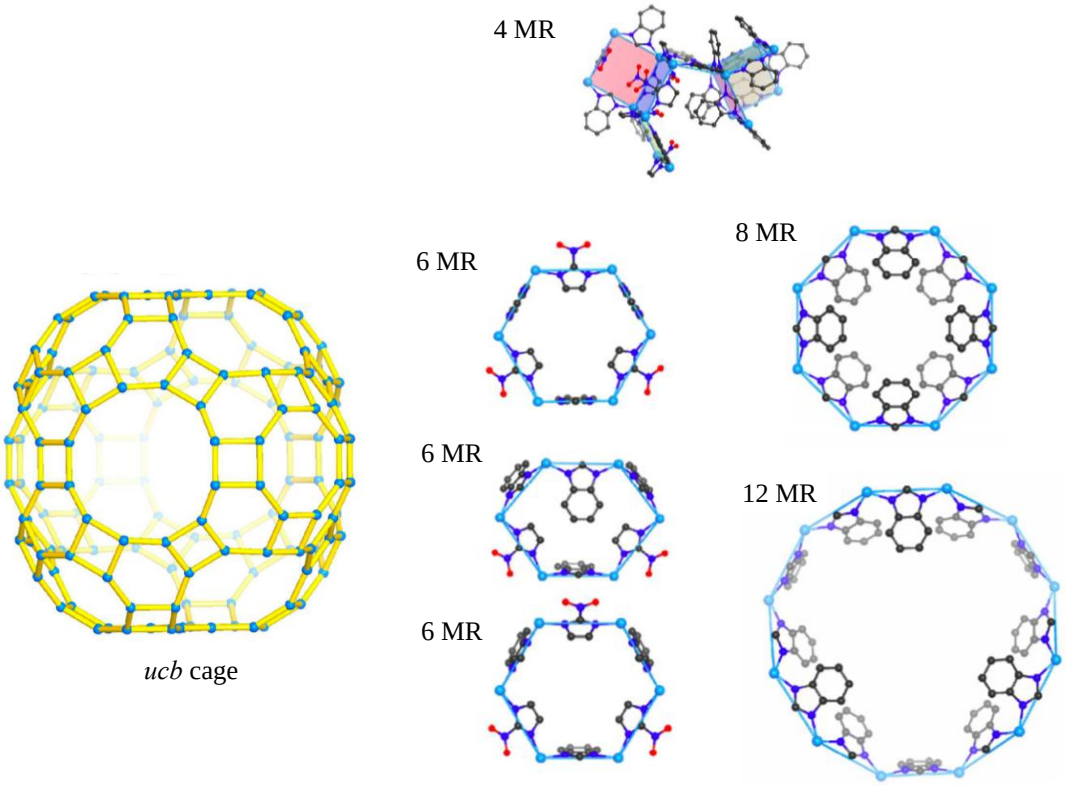

Figure 9. The **ucb** topology of ZIF-412, ZIF-413 and ZIF-414 [8]

Factors in the formation of ZIFs

There are several prevalent factors affecting the formation of ZIFs, such as (i) the effect of organic solvents, (ii) effect of additives, (iii) the effect of concentration, (iv) the effect of temperature, (v) the effect of metal salt variation and (vi) the effect of reaction time on synthesis. Among these, it is believed that the reactant concentration and the type of solvent significantly impact the crystallinity of newly synthesised ZIFs.

Effect of organic solvents

Solvents play a critical role in the deprotonation process of imidazolate linkers, influence the rate of reactions, and affect the size of ZIF crystals. High-boiling-point solvents such as dimethylformamide (DMF), dimethylacetamide, and diethylformamide are widely employed as the primary solvents for the synthesis of ZIFs. The boiling points allow hydrolysis to occur at elevated temperatures, converting them into primary amines. This, in turn, facilitates the deprotonation of imidazole linkers and influences the bonding formation

between metal centres and imidazolate linkers, resulting in the formation of large crystals [4]. The use of DEF for the synthesis of ZIF-11 is due to its high boiling point solvent (178.3 ^{o}C), which allows for control of the nucleation growth of crystals and reduces the formation of cracks in the crystals [38,39].

Dimethylsulfoxide (DMSO) has also been employed as a solvent for synthesizing ZIF-8 and ZIF-67. These frameworks were synthesised at room temperature using DMSO, marking the first synthesis involving DMSO as a solvent. They found that the crystal sizes of ZIF-8 and ZIF-67 obtained using DMSO were smaller compared to those produced in the presence of methanol [40]. For instance, the average particle size of ZIF-67 in DMSO after 30 minutes was only 30 to 50 nm, whereas ZIF-67 in methanol had an average particle size of approximately 306 nm (Figure 10) [41]. Consequently, methanol has been chosen as the primary solvent for the room-temperature synthesis of ZIFs. In addition, ZIF-71, comprising of Zn^{2+} centres and 4,5-dichloroimidazole (dcIM), was synthesized at room temperature in 15 ml of methanol [42]. The precursors were mixed, and the reaction was allowed to proceed for 24 hours at room temperature. A centrifugation process was applied to recover the crystals. Methanol-based ZIF-71 exhibited a higher surface area of approximately 1118.65 m^2 g^{-1} compared to ZIF-71 synthesised with DMF solvent.

Furthermore, ZIF-8 was synthesized at room temperature in the presence of methanol. The mixture solution of $Zn(NO_3)_2.6H_2O$ and 2mIM linker was stirred at 200 rpm for 60 minutes, resulting in an average crystal size of 1 μm. Another ZIF-8 synthesis was conducted at room temperature with the same solvent at 1000 rpm for five minutes. However, the crystal size of ZIF-8 obtained at a higher stirring rate was smaller [43]. This is because the stirring rate influences the rate of crystallisation, which in turn determines the ultimate crystal sizes of ZIFs [44].

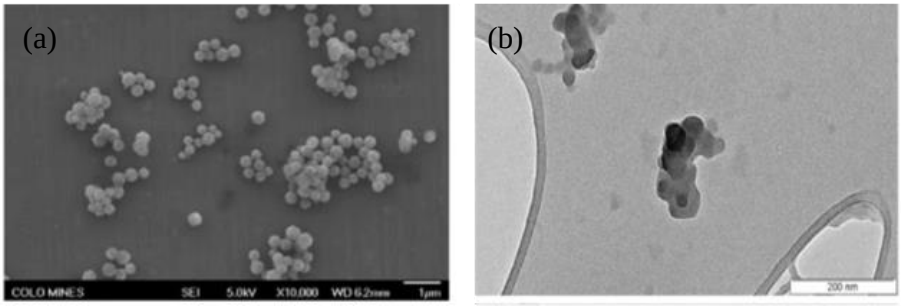

Figure 10. SEM images of ZIF-67 crystals synthesised using (a) methanol and (b) DMSO [41]

Effect of additives

Water is considered an eco-friendly and ideal solvent for the green synthesis method to fabricate ZIFs. However, a high concentration of water in the reaction system can lead to the hydrolysis of Zn^{2+} ions, leading to an increase in by-products of the reaction. Besides, using a high amount of water in the ZIF formation can slow down the crystallisation of ZIF due to the high pK_a value in the aqueous solution. This situation typically occurs when the concentration of imidazolate linkers is lower in the system, slowing down the reaction rate between metal centres and imidazolate linkers [43, 44].

In addition, it can be challenging to synthesise ZIF with a low concentration of precursors in water at room temperature without a base [45, 46]. Therefore, some base agents have been introduced in the synthesis reactions of ZIFs to deprotonate imidazole linkers and accelerate the reaction rate in the water-based synthesis method [47]. ZIF-8 was prepared using an aqueous mixed base, employing ammonium hydroxide (NH_4OH) and triethylamine (TEA) as deprotonating agents. [48]. The mixed base system was believed to have high potential for promoting the formation of ZIF framework at room temperature within several minutes, based on previous works. The synthesis reaction was completed

by stirring the solution mixture for 10 minutes at room temperature [49,50]. As shown in Figure 11, ZIF-8 particles in the presence of TEA formed aggregated sub-micrometer crystals. ZIF-8 particles synthesized without TEA showed a more uniform cubic shape and had a similar morphology to those synthesized using the solvothermal method.

The use of water as a solvent significantly enhances the thermal stability and morphology of the framework. The addition of bases as deprotonation agents in chemical reactions involving organic linkers has resulted in rapid nucleation rates, leading to the formation of small ZIF crystals [51]. The inclusion of additives in the ZIF synthesis is crucial for reactions that use water as the primary solvent. In contrast to solvothermal reactions, these additives serve as deprotonating agents that initiate the crystallisation process, thereby accelerating the reaction and achieving a high yield. Although most of the products are formed within the nanometre size range, they are well-suited for applications requiring nanosized materials, such as catalysts and drug delivery [52].

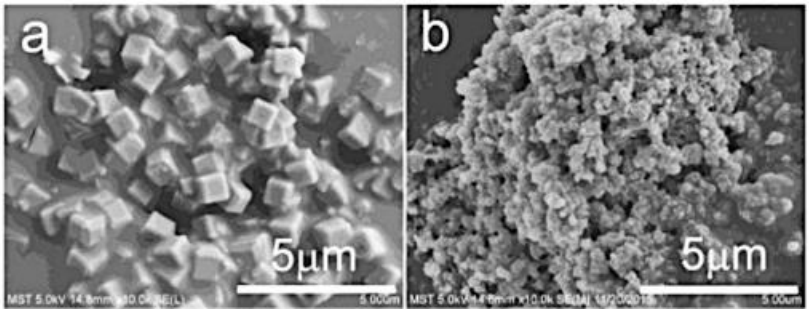

Figure 11. SEM images of ZIF-8 (a) in the absence of TEA and (b) in the presence of TEA [53]

Effect of concentration

The solvothermal method is as well-established as the conventional method to synthesise highly crystalline ZIFs. In this method, a low-molar composition of Zn^{2+} and imidazolate linkers is used to form the framework, with organic amine solvents (DMF, DEF, and DMA) acting as nucleophilic agents in the reaction. Most of the mixed-linker ZIFs were synthesised within the range of 2 to 4 moles under the solvothermal conditions. Pure microcrystals of ZIFs were formed using a low-molar composition of Zn^{2+}:2mIM, demonstrating that a high concentration of imidazolate linkers is not required for the solvothermal method [5]. The presence of organic amine solvents is sufficient to initiate the nucleation process in the synthesis reaction [51]. Despite the promising development of ZIFs, the use of organic solvents contributes to environmental pollution. Therefore, there is a strong desire to use water as a solvent to address the environmental issues and reduce costs.

Nonetheless, using a high amount of water as a solvent can lead to the hydrolysis of Zn^{2+}, increasing the production of by-products and slowing down the rate of deprotonation of the 2mIM linker [45, 47]. To accelerate the reaction rate, a high amount of imidazolate linkers is required in hydrothermal synthesis to increase the basicity of the aqueous solution. The morphology and sizes of crystals heavily depend on the molar composition of metal ions and organic linkers. Thus, conducting multiple synthesis reactions with different concentrations is crucial to obtain ZIF, as determined by SEM and PXRD analysis. In a previous study in 2018, the effect of the molar composition of 2mIM/Zn^{2+} on the properties of ZIF-8 was investigated [44]. ZIF-8 was synthesised with five different molar compositions of 2mIM/Zn^{2+}, ranging from 1, 2, 4, 8, to 16 in 50 mL of methanol at room temperature [44]. Good yield and crystallinity of ZIF-8 were obtained with molar composition of Zn^{2+}/2mIM below 8. Molar compositions of 2 and 4 resulted in ZIF-8 with a truncated dodecahedral morphology. In contrast, different morphologies were observed with higher molar compositions (8 and 16) of 2mIM/Zn^{2+}, as shown in Figure 12.

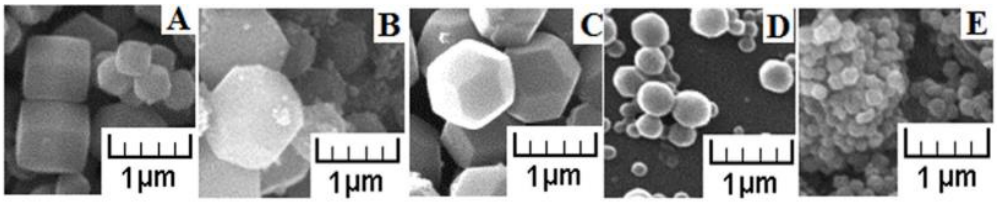

Figure 12. SEM images of different ZIF-8 samples with different molar ratios of Zn^{2+}/2mIM of (a) 1, (b) 2, (c) 4, (d) 8 and (e) 16 [44].

One limitation was that high concentrations of the 2mIM linker led to the formation of a framework with lower surface areas and particles aggregation, as evidenced by SEM analysis. Meanwhile, molar compositions of Zn^{2+}/2mIM in the range of 2 to 4 yielded the highest surface areas for ZIF-8, measuring around 1268 m^2 g^{-1} and 1943 m^2 g^{-1}, respectively. These results indicated that moderate molar compositions of Zn^{2+}/2mIM were capable of producing highly crystalline frameworks with a maximum surface area for ZIFs [3,54]. A higher content of imidazolate linkers in the reaction system accelerated the rate of the nucleation process and also influenced the particle sizes of the frameworks [44]. ZIF-8 was also synthesised in a microemulsion mixture of n-heptane and n-hexanol in TritonX-100, employing different molar compositions of Zn^{2+} to 2mIM (1:2, 1:5, 1:8, and 1:16) at room temperature (Figure 13) [55]. Uniform cubes of ZIF-8 nanoparticles were obtained with a molar ratio of 1:2/Zn^{2+}:2mIM and the particle size decreased from 110 nm to 40 nm as the concentration of the 2mIM linker increased [56,57].

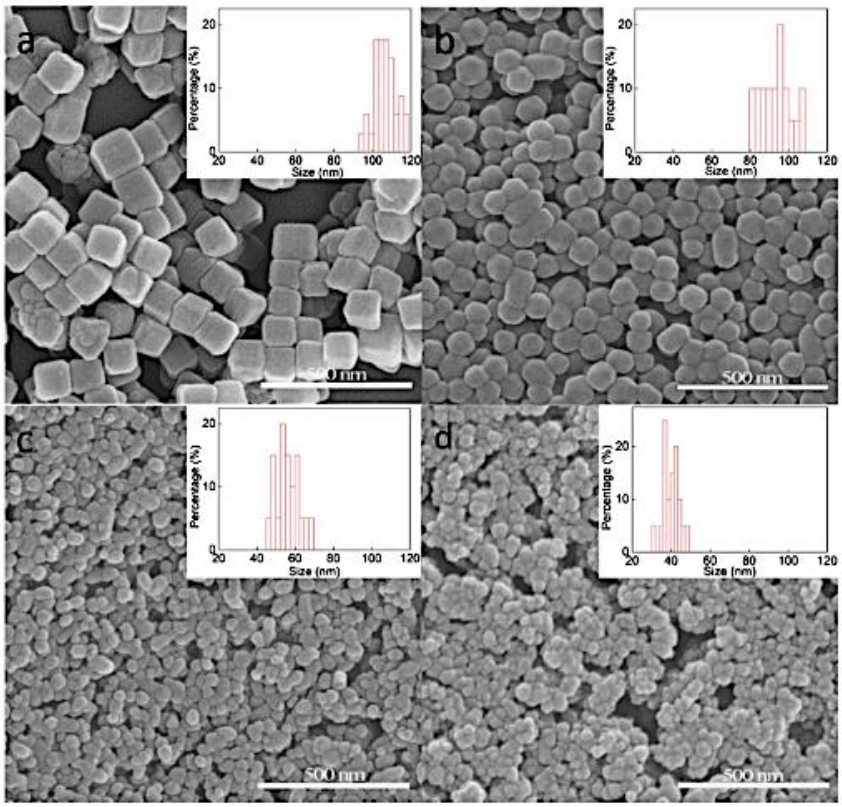

Figure 13. FESEM images of ZIF-8 nanoparticles obtained from different molar compositions of Zn^{2+}:2mIM (a) 1:2 (b) 1:5 (c) 1:8 (d) 1:16 [55]

The broader peak widths of the XRD patterns of ZIF-8-110 and ZIF-8-90 in Figure 14 was attributed to the formation of small crystal size in the samples, as a result from the high concentration of the imidazolate linker [55]. The construction of the framework is a meticulous process that necessitates the use of the appropriate molar composition of organic linkers and metal salts. This parameter is highly dependent on the specific synthesis method employed, as it significantly impacts the crystallinity and particle size of ZIFs.

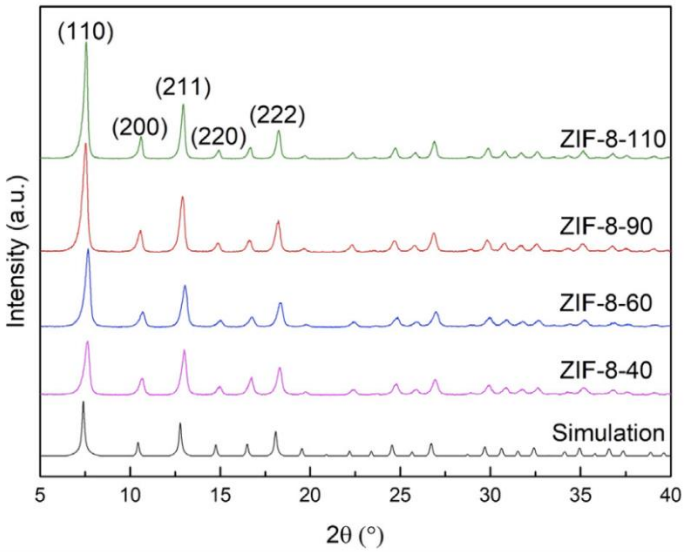

Figure 14. PXRD patterns of ZIF-8 nanoparticles with different sizes based on FESEM images (a) ZIF-8-110, (1:2) (b) ZIF-8-90, (1:5) (c) ZIF-8-60, (1:8) (d) ZIF-8-40, (1:16) [55]

Effect of temperature

The temperature of the chemical reaction is a critical factor in the formation of ZIF particles. Previous studies have reported that synthesis work conducted at different temperatures affects the crystallinity of ZIFs. ZIF-8 was prepared at varying temperatures (80, 100, 120, and 140 ^{o}C) under microwave-assisted solvothermal methods in methanol within 30 minutes [48]. A high crystallinity of ZIF-8 was observed based on PXRD patterns at 120 ^{o}C and 140 ^{o}C, which is close to the reference pattern of ZIF-8 synthesised under the solvothermal method. Meanwhile, the synthesis of ZIF-8 at a temperature lower than 100 ^{o}C was unable to generate a high crystallinity of ZIF-8 [48]. This is because the temperature is directly proportional to the pressure of the reaction under the microwave system and the solvothermal method [55]. In addition, the hydration of the metal salts decreases as the temperature of the reaction increased, as it is associated with entropic gains from the thermodynamic control leading to the release of water molecules from metal sites. This allowed more opportunity for deprotonated linkers to bond with metal sites [48].

Two ZIF-8 compounds were prepared at two different temperature, room temperature (ZIF-8-RT) and 140 ^{o}C (ZIF-8-HT) via hydrothermal synthesis [58]. Sharp peaks were observed in the PXRD patterns of ZIF-8-HT and ZIF-RT. Nonetheless, the full width half maximum values (FWHM) of the PXRD patterns of these ZIFs recorded different values at 7.3° [58]. The FWHM value of ZIF-8-HT was 0.14°, which is smaller than the FWHM value of ZIF-8-RT, which was around 0.20°. A larger FWHM value is responsible for peak broadening in PXRD patterns. The synthesis of ZIF-8 at higher temperature produced better crystallinity, due to the induction of high vapour pressure, as well as increased density, the vacant sites of metal centres, and the dimensionality of the frameworks [58]. The homogeneity in the heating process is a crucial nucleation rate for the construction of ZIFs [59, 60].

Effect of metal salt variations

The construction of ZIFs results from the formation of chemical bonds between the metal ions and the linkers. The types of metal salts used play a crucial role in determining the size of the ZIFs. According to Pearson's acid-base concept, metal salts with different counter ions possessing varying interaction strengths influence the nucleation rate. Higher concentration of metal salts and organic linkers in the reaction system contribute to an increased nucleation rate, leading to the formation of more nuclei which resulted in the production of large amounts of tiny crystals [61, 62]. Zinc acetate, $Zn(OAc)_2$ was the prominent metal salt for synthesising ZIF-8 in the hydrothermal method [47]. The morphology of the synthesised ZIF-8 particles using $ZnSO_4$ and $Zn(OAc)_2$ exhibited a rhombic dodecahedron for molar ratios of 2mIM/Zn^{2+} between 20 and 35. Furthermore, the formation of ZIF crystals is dependent on the molar composition of the precursors in the reactions. When ZIF-8 was synthesised using a high molar ratio of 2mIM/Zn^{2+}, truncated edges with bumpy surfaces were produced. In contrast, low molar ratios of 2mIM/Zn^{2+} resulted in rhombic dodecahedron morphology. As the molar ratio of 2mIM/Zn^{2+} decreased, the average size of ZIF-8 particles using $ZnSO_4$ also decreased from 1.64 μm to 231 nm.

Previous studies have highlighted that the size of ZIF particles depends on the molar ratio of precursors and the type of metal salts in the chemical reaction [47]. The morphology of ZIF-8 particles prepared from $Zn(NO_2)_3$ exhibited spherical and petal shapes, which is opposite to the findings obtained from the synthesis of ZIF-8 using $Zn(OAc)_2$ and $ZnSO_4$. ZIF-8 synthesised using $Zn(NO_2)_3$ showed better crystallinity framework than $Zn(OAc)_2$ and zinc sulphate, $ZnSO_4$, due to the high reaction temperature at 85 ^oC for 60 hours[46]. In terms of crystallinity, previous work has demonstrated that the high crystallinity of ZIF-8 could be obtained in the order of $Zn(NO_3)_2$ > $Zn(OAc)_2$ > $ZnSO_4$ > zinc chloride, $ZnCl_2$. Different metal salts will influence the synthesis process of ZIFs due to variations in pH resulting from the anionic ions of metal salts. Among these metal salts, ZIF-8 using $Zn(NO_3)_2$ recorded high catalytic activity in Knoevenagel condensation reactions due to the high external surface area of the ZIF-8 crystal. $Zn(NO_3)_2$ is composed of a soft acid metal ion, Zn^{2+}, with hard base anion, NO_3^-, which allows for more available vacant sites for the 2mIM linker to coordinate with Zn^{2+} ions, hence forming many nuclei and contributing to the framework's high surface area [46].

Effect of reaction time on synthesis

Another critical parameter to highlight for the formation of ZIFs is the effect of the reaction time on synthesis. It is widely accepted that a longer reaction time will yield higher quantity of products suitable for various promising applications. Previously, ZIF-8 was synthesised within 60 minutes using a sonochemical method under ultrasound irradiation, resulting in fine textural properties, however, with a low yield. The synthesis work conducted within three hours produced a high output of ZIF-8 crystal [25, 26]. Significant differences were observed between the short and long reaction periods of ZIF-8 from 5 minutes to 60 hours conducted in an aqueous medium. A longer reaction period resulted in ZIF-8 having a high surface area of 1027.20 $m^2 g^{-1}$ compared to the surface area obtained at five minutes, which was 878.59 m^2 g^{-1}. It is worth mentioning that reaction time is also interconnected with temperature; as they increase, better morphology is achieved and the product yield is enhanced [46].

ZIF-11 had different morphologies after being synthesised at 60 and 100 ^oC for 12 hours and six hours respectively. These shapes included rhombic dodecahedron shapes. The duration of the reactions strongly depends on the molar composition of the synthesis reaction, as demonstrated previously [40]. ZIF-11 was synthesised using three different molar compositions of Zn^{2+}/bzIM (1:4, 1:8, and 1:12). The same rhombic dodecahedral was formed at low and high concentrations, but the products were formed at different times. ZIF-11 crystals were fully formed after 48 hours for the molar composition of Zn^{2+}/bzIM at 1:4, which was attributed to the slow transition of pure phase crystalline of ZIF-11. In addition, pure crystalline ZIF-11 was achieved within 24 hours for high molar compositions of precursors. This demonstrates that the reaction duration depends on the molar composition and synthesis temperature, which influences the

recrystallisation and dissolution processes for the formation of ZIF [46].

Applications of ZIFs

ZIFs have been utilised in a wide range of applications owing to their exceptional chemical and thermal stability as well as flexible and adaptable frameworks that can be customised to suit specific applications. In this section, some of the significant applications of ZIFs are highlighted and discussed.

Adsorption of pollutants

Adsorption of pollutants is an alternative method for wastewater treatment due to its minimal production of secondary by-products and ease of operation. Activated carbon is a conventional adsorbent in wastewater treatment, and this adsorbent has a few limitations, including weak interactions with pollutants and problems related to regeneration in practical applications. Therefore, MOFs and ZIFs have emerged as promising adsorbents for wastewater treatment [40]. The structures of MOFs and ZIFs are flexible, which allow the incorporation of additional functionalities, such as unsaturated metal centres and active functional groups, to achieve targeted interactions with pollutants. For instance, ZIF-8 demonstrated rapid adsorption of methyl blue (MB), achieving a remarkable adsorption capacity of approximately 1917.5 mg g^{-1} within just 60 minutes. Despite the smaller pore diameter of ZIF-8 compared to the size of MB molecules, the high adsorption of MB is likely attributed to the formation of ionic bonds between the metal centre of ZIF-8, Zn^{2+}, and SO_3^- from MB. Figure 15 shows the proposed adsorption mechanism between SO_3^- from MB and Zn^{2+} from ZIF-8 [63].

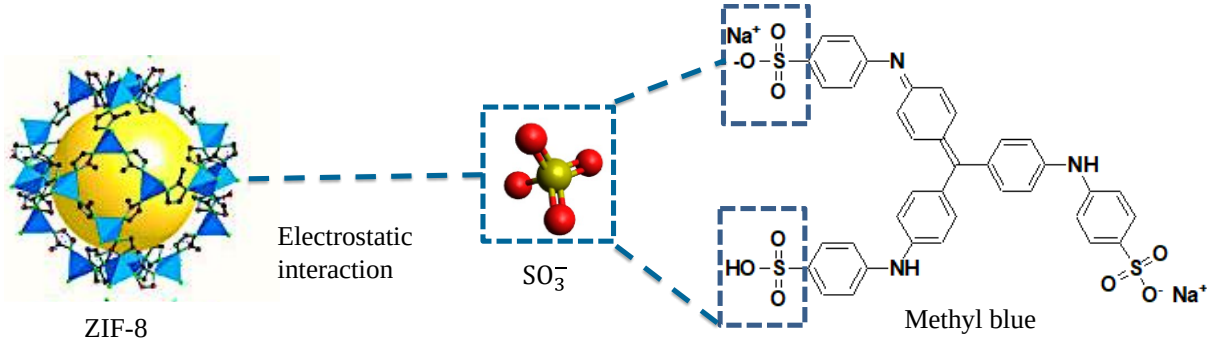

Figure 15. Adsorption mechanism between methyl blue and ZIF-8 [63]

Subsequent studies on the adsorption capabilities of Rhodamine B (RhB) and methylene blue (MB) have been previously explored. ZIF-8 was synthesised using ultrasound and a surfactant (Pluronic* P-123) at room temperature, resulting in ZIF-8 with a surface area of 745 $m^2 g^{-1}$ [64]. Organic dyes such as RhB and MB are classified as larger organic dyes (molecular sizes approximately 1.59 x 1.18 x 0.56 nm and 1.7 x 0.76 x 0.33 nm), preventing them from passing through the pore apertures of ZIF-8. Consequently, adsorption of RhB and MB occured on the external surface of ZIF-8 in between 2 to 48 hours, with adsorption capacities of 25.0 mg g^{-1} and 46.6 mg g^{-1}, respectively [65,66]. This highlights the significance of specific functional groups in organic dyes that enable better adsorption with ZIF, even when the molecule size exceeds the small micropores of ZIF-8.

ZIF-67 showed good adsorption performance with anionic dyes. The adsorption values obtained using ZIF-67 ranged from 37.7 mg g^{-1} for xylene cyanol (XCFF) to 800 mg g^{-1} for Cibacron Blue 3G-A (CB) and fluorescein angiography. High adsorption capacities with anionic dyes are due to the positive surface charges on the surface of ZIF-67, as confirmed zeta-potential values ranged from 2.88 mV to 14.37 mV in a basic solution (pH 7.00-10.00). It is noteworthy that water contact with the surface of ZIF-67 induces the

protonation of imidazolate linkers (2mIM-) and enhances the interaction between anionic dyes and ZIF-67, as depicted in Figure 16 [53, 64, 65]. It should be emphasised that the optimal pH of the aqueous solution for the adsorption studies depends on the types of pollutants.

ZIF-7 was used in the adsorption of trichloroethylene, and it was found that the optimal condition for conducting the adsorption study was low pH solution (pH < 6.00) within 120 minutes [67]. Under these conditions, ZIF-7 achieved a remarkable removal efficiency of approximately 96.29%, highlighting the enhanced removal efficiency of trichloroethylene in an acidic environment [68,69]. It is intriguing to note that the pH of the solution can influence the surface charge of the adsorbents and the degree of ionisation of the solution, which, in turn, affects the adsorption of pollutants. In a separate adsorption study, malachite green (MG) was adsorbed using ZIF-67. Several parameters, such as temperature, time, and concentration, were considered to determine the optimal condition for the adsorption study. Notably, as the temperature increased from 20 to 60 ^{o}C, a substantial increase in adsorption capacity was observed [70]. The maximum adsorption capacity was recorded at 60 ^{o}C with an adsorption capacity value of 2500 m^2 g^{-1}, making it one of the highest adsorption capacities among established adsorbents such as MIL-100 (Fe), chitosan beads, and commercial powder activated carbon [67]. A chemical interaction took place between the imidazole rings and MG via the π–π stacking interaction, which facilitated the adsorption of MG onto the surface of ZIF-67 [71, 72].

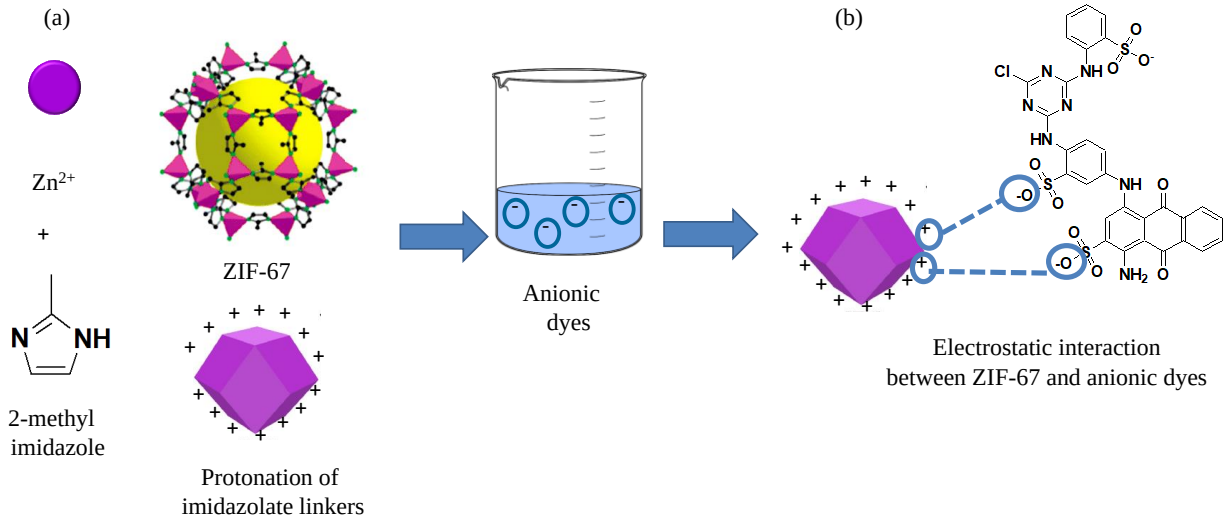

Figure 16. (a) Secondary building unit of ZIF-67 and (b) Interaction of ZIF-67 and anionic dyes [68, 69]

In another adsorption study, ZIF-67 showed excellent adsorption capacity towards Congo Red (CGR) from an aqueous solution, primarily attributed to electrostatic and π–π stacking interactions of the aromatic compound in CGR. Furthermore, the presence of Co^{2+} as the metal centre of ZIF-67 led to coordination between oxygen and nitrogen atoms from CGR, resulting in rapid adsorption in less than 40 minutes, even at a low concentration of 30 ppm. The impact of temperature was also evident, with an increase from 36.9 to 57.9 ^{o}C, leading to a significantly higher adsorption capacity of up to 714.3 mg g^{-1}, indicating the promise of ZIF-67 as an effective adsorbent for CGR [70, 73].

Antibiotics have been extensively used for the treatment of human and animal diseases, owing to their effectiveness. However, a substantial portion of antibiotics is not fully absorbed by humans and animals, resulting in the release of these compounds into the environment [69]. Ofloxacin is a third generation of quinolone that was used in humans, aquaculture, and animal husbandry to prevent livestock disease. ZIF-8 is

used as an adsorbent to remove ofloxacin with an adsorption capacity of approximately ~194.1 mg g^{-1} at pH 7 with an adsorbent amount of 20 mg and 100 ppm of initial concentration [74]. Ofloxacin exists as zwitterionic state within the pH of 8.44 to 9.2, resulting in a strong electric attraction with ZIF-8. Concurrently, ZIF-8 exhibits a positive charge in a basic pH [75,76] as shown in Figure 17. The adsorption of ofloxacin involves various interactions, including strong hydrogen bonding between the fluorine atom in ofloxacin with C-NH bonds in ZIF-8, as well as complexation with unsaturated metal sites that facilitates interaction with ofloxacin. Additionally, the presence of 2mIM rings within the ZIF-8 framework and the benzene ring of ofloxacin further enhance the adsorption capacity through π–π stacking interactions [74].

Similar chemical interactions were observed in the adsorption of norfloxacin using ZIF-8, a quinolone derivative [77]. ZIF-8 exhibited excellent adsorption efficiency at initial norfloxacin concentrations ranging from 10 mg L^{-1} to 30 mg L^{-1}. However, the efficiency of the adsorbent slightly diminished after 30 mg L^{-1} due to increased occupation of the available binding sites on ZIF-8 at higher norfloxacin concentrations. Furthermore, norfloxacin has a lower positive charge at pH levels between 4.5 to 6.2, allowing for enhanced adsorption with the positively charged ZIF-8 adsorbent due to lower electrostatic repulsion [78, 79].

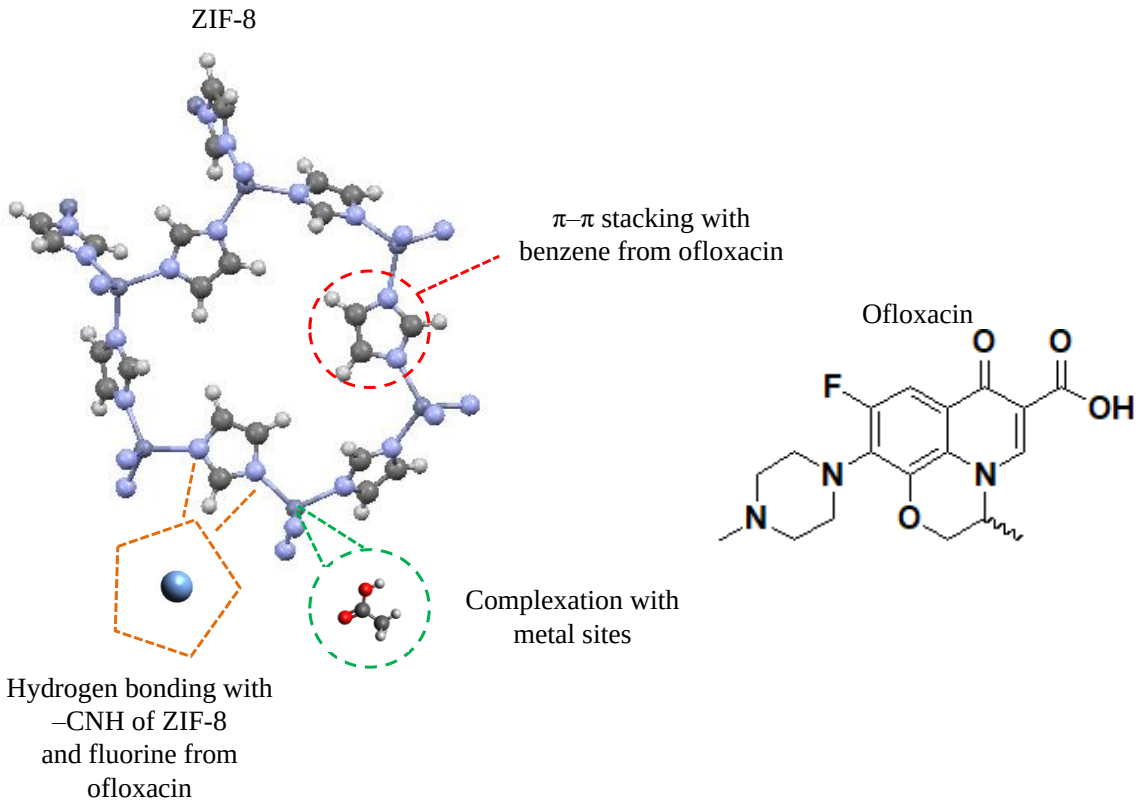

Figure 17. Mechanism of adsorption of ofloxacin with ZIF-8 [73-74]

Tetracycline (TC) and oxytetracycline hydrochloride (OTC) are commonly used antibiotics due to their effectiveness in treating bacterial infections and as veterinary drugs to promote animal growth [80]. However, only 30% of TC and OTC are absorbed by animals, while the remaining antibiotics are discharged into the environment in their original form, posing significant threats to the environment [81]. To address this issue, ZIF-8 was used for the removal of simultaneous mixtures of TC and OTC antibiotics from

wastewater [80]. Fast adsorption was observed within 50 minutes at a pH 4 to 6, with an average simultaneous removal efficiency of 90.7% for TC and 82.5% for OTC at a concentration of 50 ppm. The impact of temperature on the simultaneous adsorption followed a pattern consistent with previous adsorption, indicating the reaction is an endothermic process. Higher temperatures led to rapid adsorption of TC and OTC due to molecular collision, which enabled greater interaction between adsorbates and the adsorbents [75,82].

In conclusion, several ZIFs, particularly ZIF-8, have proven their potential as adsorbents for the removal of organic pollutants such as dyes and antibiotics. The maximum adsorption capacity is determined by the types of organic pollutants and various parameters within the adsorption experiments. These characteristics help to facilitate the chemical interaction that occurs between ZIFs and organic contaminants.

Catalyst

Aluminosilicate zeolites are well-established materials widely explored in many catalysis applications [83]. Owing to similar properties with aluminosilicate zeolites, ZIFs have emerged as efficient catalysts and co-catalysts for various catalytic reactions. Polylactide (PLA) is a widely recognised polymer derived from renewable resources that has received considerable attention due to its biocompatible properties [83–85]. Lactide (LA) is a monomer of PLA and undergoes ring-opening polymerisation (ROP) with a combination of a Lewis acid catalyst and organic bases to obtain cyclic PLA (cPLA) [86, 87]. ZIF-8 stands out as a promising Lewis acid catalyst for the polymerisation of $_L$-lactide. This framework demonstrates exceptional thermal stability up to 400 ^oC based on TGA analysis. In addition, it remains insoluble in many common organic solvents, signifying its chemical stability. In the previous study, ZIF-8 showed excellent catalytic activity at high concentrations ([M]/[I] = 100) and generated a high molecular weight of cyclic poly($_L$-lactide) (PLLA) of approximately 24.5 kg mol^{-1} with a conversion rate of 96%. This outcome aligns with MALDI-TOF mass spectrum results, where strong signals were observed for cyclic PLLA, indicating near complete conversion of L-lactide. The metal centre of ZIF-8, Zn^{2+}, functions as a Lewis acid site based on NMR spectroscopy, initiating chain growth by binding to the monomer. The Lewis acid sites are also working cooperatively with the active basic sites of ZIF-8, specifically the nitrogen atoms from the imidazolate ring, to catalyse the formation of cyclic PLLA via intramolecular transesterification. The PXRD pattern of the recycled ZIF-8 catalyst confirmed that the diffraction peaks remained unchanged after three runs of the ROP reaction, indicating no loss of catalytic activity during the recycling process [88].

The utilisation of CO_2 represents a promising strategy for reducing atmospheric levels of CO_2 caused by human activities. As such, the synthesis of cyclic carbonates using CO_2 offers a particularly alternative pathway to reduce the atmospheric level of CO_2 [89]. Scheme 1 illustrates the application of ZIF-90 as a promising catalyst for cycloaddition, eliminating the need for additional co-catalysts. This approach resulted in 88% of propylene carbonate (PC) with 90% selectivity at 120 ^oC within eight hours. The aldehyde group of ICA within ZIF-90 stimulates CO_2 insertions, leading to the formation of a ring-opening intermediate. ZIF-90 emerges as a truly promising material for catalysis, as it contains ICA linkers that can replace co-catalysts in the catalytic reaction [90].

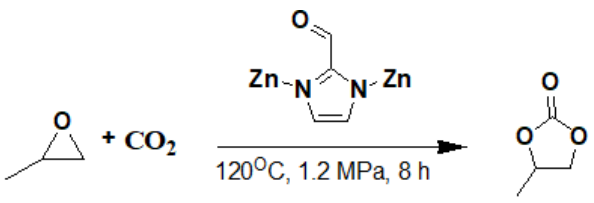

Scheme 1. Cycloaddition of propylene oxide (PO) and CO_2

In contrast with subsequent work in 2017, ZIF-95 showed excellent performance in the cycloaddition reaction, despite its structural similarity to ZIF-90. The maximum conversion of PO achieved with ZIF-95 was notably higher, reaching approximately 91%, with a selectivity exceeding 99% at the same temperature. Tetrabutylammonium bromide (TBAB) was used as a co-catalyst. The diffraction patterns for both frameworks remain unchanged even after they were reused for more than three cycles at higher temperatures, indicating their robust chemical and thermal stability. ZIF-95 featured an unsaturated tetrahedral Zn^{2+} centre that functioned as a Lewis acid site, initiating the reaction on the oxygen atom of PC as an electrophilic attack [91]. In Scheme 2, the bromide anion from TBAB attacks the carbon atom of PO, leading to ring-opening intermediates [92].

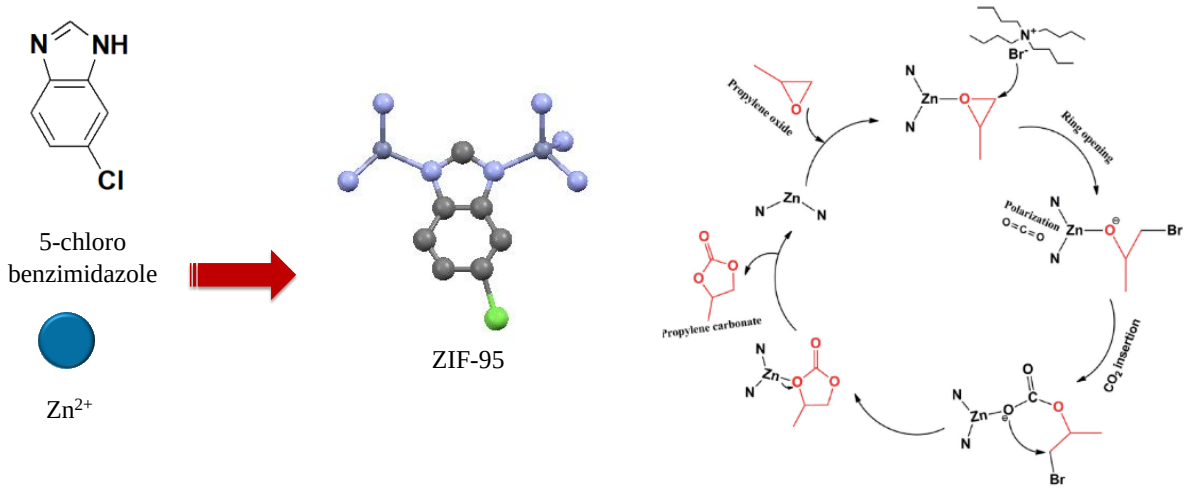

Scheme 2. The mechanism of cycloaddition of propylene oxide (PO) using ZIF-95 as a catalyst to form propylene carbonate (PC), [93]

In addition, ZIF-8 is also used for the epoxidation reaction of menadione with hydrogen peroxide, H_2O_2, achieving a remarkable 90% conversion to menadione-2,3-epoxide. This exceptional catalytic activity can be attributed to the presence of defects on the external surface of the framework, promoting interactions between H_2O_2 and the basic sites of ZIF-8. These basic sites include nitrogen atoms from the 2mIM ring and hydroxyl from methanol, facilitated via hydrogen bonding. The combination of the hydrophobic surface of ZIF-8 and the basic sites of the 2mIM ring contributes to a synergistic effect, resulting in nearly 100% selectivity [93]. Many ZIFs have been used as catalysts in the photodegradation of pollutants. Photodegradation is another alternative way to adsorb contaminants. The potential of ZIF-8 nanocrystals in the photodegradation of RhB was examined under various conditions, such as dark, UV, and visible irradiation conditions [94]. At 430 nm, ZIF-8 nanocrystals exhibited excellent degradation of RhB. This phenomenon is due to as the transition of the excited electrons in ZIF-8 nanocrystals to the conduction band to react with surface oxidants (O*) in order to form hydroxyl radicals (OH*), facilitating the photodegradation of RhB (Scheme 3). The photodegradation process under visible light irradiation was slightly slower due to the large bandgap energy (5.6 eV) of ZIF-8 and the relatively low photon energy of visible light (1.8-3.9 eV) for electron excitation to occur within the framework. Consequently, there is a limitation in the production of the required amount of oxygen radicals for the photodegradation process [94].

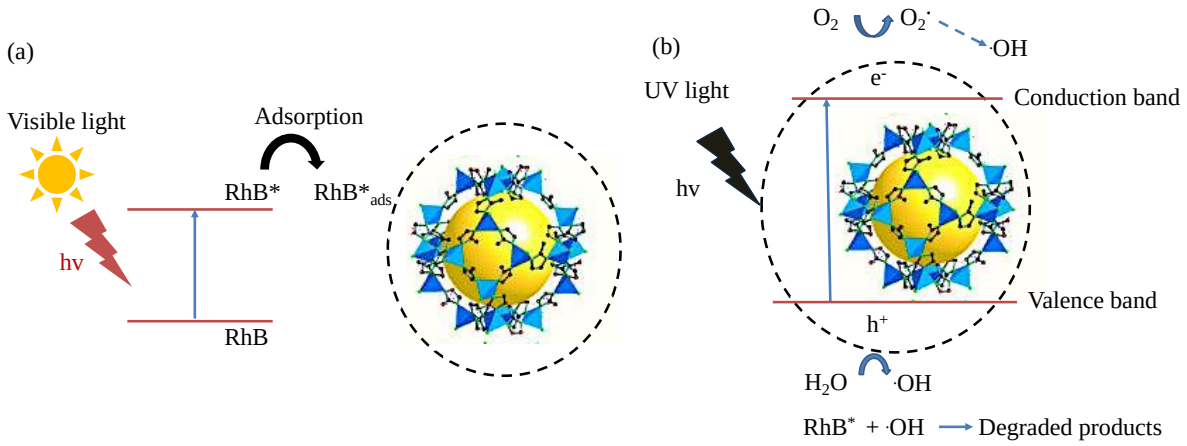

Scheme 3. Proposed mechanism of photodegradation of RhB using ZIF-8 under (a) visible light and (b) UV light [94]

To address these challenges, ZIF-8 was successfully transformed by modifying its framework under thermal treatment to form a visible-light photocatalyst for decomposing gaseous formaldehyde [95]. This thermal treatment involved subjecting ZIF-8 nanocrystals to a temperature of 200 ºC in the presence of air to convert the -N=C of the 2mIM linker into -N=C=O functional groups, thereby expanding the light absorption range from UV to infrared. The presence of the -N=C=O functional group enabled the decomposition of formaldehyde, achieving nearly ~100% efficiency within one hour under simulated sunlight. This result was supported by the optical absorption band of ZIF-8 nanocrystals, which appeared at 715 nm. ZIF-67 also exhibited excellent performance in broadening the absorption spectrum for the photocatalytic activity of Cr^{6+} reduction. The UV-Vis absorption spectra revealed three distinct absorption maxima at 1009 nm, 589 nm, and 265 nm, corresponding to the near-infrared (NIR), visible and UV light regions, with C^{6+} reduction efficiencies of 71.22%, 69.52%, and 40.72% after two hours. It is suggested that the 2mIM ligand in the framework is responsible for absorbing light from different sources, facilitating charge transfer to the metal centre to produce excited electrons for reduction of $Cr^{5+}$to Cr^{3+} [96].

The photocatalytic reduction of CO_2 offers a promising approach for generating hydrocarbon fuels and renewable sources. The mechanism of CO_2 reduction using photocatalysts depends on electron-hole separation, their lifetime, and CO_2 adsorption capacity [96]. ZIF-67 was used as a co-catalyst for CO_2 reduction at room temperature in the presence of photosensitizer ($[Ru(bpy)_3]Cl_3.6H_2O$) and electron donor (Triethanolamine) [97]. This study revealed that two-dimensional ZIF-67 with a leaf-like morphology exhibited a high CO_2 transformation rate and showed high CO_2 adsorption capacity. No decomposition occurred during the photocatalytic activity involving ($[Ru(bpy)_3]Cl_3.6H_2O$) and ZIF-67 at 580 nm, indicating excellent electron transfer efficiency from the photosensitizer to the co-catalyst. Additionally, the strong interaction between CO_2 molecules and Co^{2+} reduced to Co^{+}, which facilitated the production of CO molecules for generating hydrogen gas, H_2 [98]. ZIF-8 was used as a catalyst to promote hydrogen production via sodium borohydride ($NaBH_4$) hydrolysis. ZIF-8 was synthesised using zinc hydroxide nitrate nanosheets ($Zn_5(OH)_8(NO_2)_2$) in the presence of NaCl salt and employed as a catalyst to accelerate hydrogen production. The hydrogen production rate using ZIF-8 (NaCl) was measured at around 3000 mL_{H2} min^{-1} g^{-1} [97,99], proving that ZIF-8 exhibited high catalytic activity without any reduction n performance after several cycles in the presence of $NaBH_4$. In conclusion, ZIFs are exceptional chemical and thermal stable materials to act as catalysts especially ZIF-67 due to its unsaturated metal centre, Co^{2+}.

Drug delivery system

Zinc is an essential micronutrient for human metabolism [100]. The imidazole group is the main functional group that constitutes the amino acid histidine. These combinations are significant for the development of ZIF as a promising biocompatible drug carrier [49]. 6-Mercaptopurine (6-MP) is a cytotoxic drug used to treat acute childhood leukaemia, provide maintenance therapy to prevent concurrent Crohn's disease, and as a treatment drug for autoimmune hepatitis (AH) [101]. ZIF-8 has been identified as a potential biocompatible drug carrier for 6-MP. An *in-situ* synthesis reaction was conducted to encapsulate 6-MP into ZIF-8 in DMSO at room temperature. Two peaks were observed in the UV-visible spectrum, representing ZIF-8 at 216 nm, and another peak at 320 nm which confirmed the presence of 6-MP on ZIF-8. The average particle size of ZIF-8 also increased the encapsulation of 6-MP, as confirmed by SEM analysis (Scheme 4). The drug release works efficiently at pH 5.0 within 10 hours, as the mildly acidic solution leads to the dissolution of ZIF-8 structure [102–104].

In a recent study, ZIF-8 showed potential in the drug delivery system for benznidazole (BNZ), a well-known drug to treat Chagas disease. The purpose of the encapsulation of BNZ into ZIF-8 is to overcome the low bioavailability and solubility of BNZ drugs in the human body [105]. The BNZ into ZIF-8 system was developed by the ex-situ method by mixing BNZ solution and ZIF-8 in acetone with the equimolar ratio of BNZ and ZIF-8. Encapsulation of benznidazole (BNZ) into the ZIF-8 framework exhibited a similar condition as 6-MP inZIF-8, achieving 80% of drug release at pH 4.8 after two days. The disintegration of the framework in an acidic solution allowed the movement of the imidazolate linker within the framework and promoted a greater opening of the pore windows of the framework [106]. Consequently, more diffusion of drug molecules can occur in weak acidic solutions (pH 5.0 – 6.0) [107, 108].

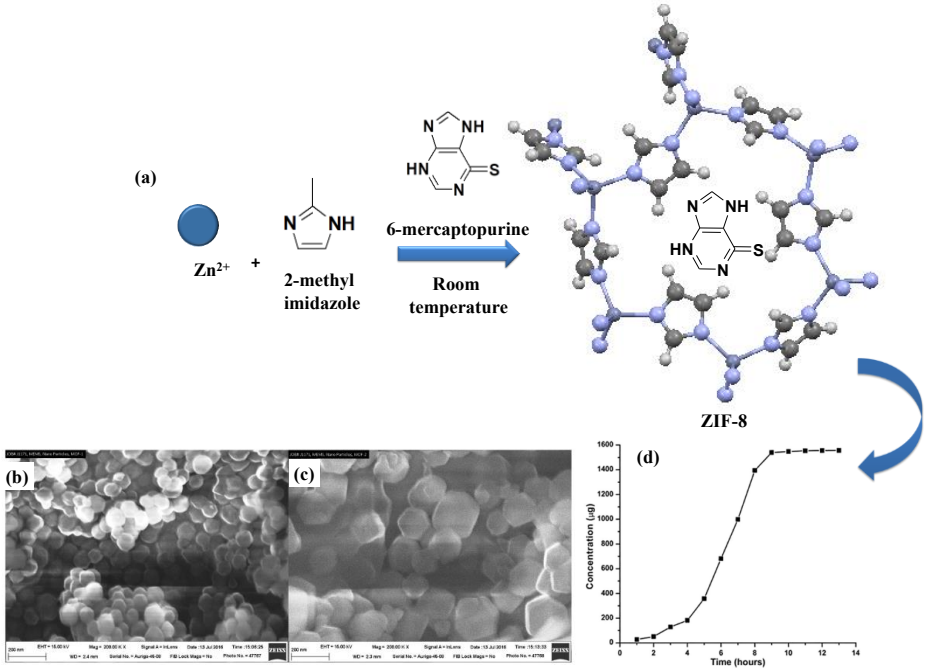

Scheme 4. (a) Encapsulation of 6-mercaptopurine (6MP) into the framework, (b) FESEM analysis of ZIF-8, (c) FESEM analysis of 6MP@ZIF-8 and (d) Drug release study at pH 5.0 [105]

The hydrophobic curcumin drug (CCM) was encapsulated in a ZIF-8 framework (CCM-ZIF-8), achieving a maximum efficiency of 83.3% within 15 minutes at room temperature [109]. CCM-ZIF-8 also exhibited superior stability in MeOH after 30 days, as evidently shown by the TEM image. A high average

drug release, reaching 88%, was recorded in an acidic pH solution within 72 hours, attributed from the protonation of 2mIM linkers. This protonation led to the disintegration of the coordination bond between the metal centre and 2mIM linkers, resulting in drug release. Cytotoxicity studies were conducted using a MTT assay to assess the activity of CCM-ZIF-8 and free CCM against HeLa cell lines. The study found a strong inhibitory effect on cell growth with CCM-ZIF-8 compared to free CCM at higher concentrations. At 62.5 μg mL^{-1}, CCM-ZIF-8 achieved a 57% cell death rate, irrespective to free CCM, which induced only 25% cell death [110].

D-α-Tocopherol succinate (α-TOS) has demonstrated significant cytotoxic effects on various cancer cells via the mitochondrial-dependent pathway while having no toxicity effect on other normal tissue. However, α-TOS has hydrophobic properties that limit its clinical applicability. Therefore, a drug delivery system (DDS) was developed by encapsulating α-TOS into a ZIF-8 framework (α-TOS@ZIF-8) through a one-pot synthesis reaction, followed by functionalisation with hyaluronic acid (HA) on the external surface of α-TOS@ZIF-8 [111]. The function of HA on DDS carriers is to enhance drug accumulation via the CD44 pathway towards the tumour region [109]. The formation of HA/α-TOS@ZIF-8 was confirmed by zeta potential measurements, where the value decreased from 22.1 mV (pure ZIF-8) to -17.9 mV. This negative value indicated that HA was successfully introduced onto the external layer of α-TOS@ZIF-8. The usage of HA/α-TOS@ZIF-8 has led to significant tumour growth inhibition, as demonstrated in *in vivo* and *in vitro* studies [112,113]. Similar studies were conducted with surface functionalisation using folic acid (FA) to reduce the cardiotoxicity of doxorubicin (DOX). DOX is an anticancer drug that was successfully modified using pH-sensitive linker cis-aconitic anhydride (CAA) to enhance drug loading into ZIF-8, forming CAD@ZIF-8. This was due to the lack of surface functional groups such as carbonyl and carboxyl groups on ZIF-8. CAD@ZIF-8 was functionalised with FA to enhance tumour targeting and avoid premature drug release. *In vivo* study revealed that mice treated with CAD@ZIF-8-FA showed a slight increase in weight and drug accumulation in the tumour region at 12 and 24 hours. In contrast, mice treated with DOX experienced a slight weight reduction, and the drug was distributed impartially to various body parts. This implies that CAD@ZIF-8-FA can deliver the drug and accumulate at the tumour region, as opposed to simply encapsulating DOX into ZIF-8. The modification of DOX enables specific targeting of tumour sites in the human body [114].

Conclusion

In conclusion, many new synthesised ZIFs have been successfully synthesised since 2008. It is challenging to incorporate more imidazolate linkers into the framework because different imidazolate linkers have varied reactivities in the synthesis reaction. The synthesis of mixed-linker ZIFs is considered as an interesting development of ZIFs because more functionalities can be added in the frameworks and the materials are suitable for a variety of applications. Instead of employing the solvothermal approach to generate known ZIFs, several methods were developed to produce existing ZIFs to reduce the amount of time needed for the reaction and consumption of hazardous solvents. Therefore, the synthesis strategies of ZIFs such as concentration of precursors, reaction time, the choices of metal salts and solvents must be taken into account as these factors will affect the crystallinity, crystal sizes and the stability of the frameworks. ZIFs have received considerable attention and researchers are currently exploring various applications for ZIF materials. The previous applications of ZIFs were summarised and discussed in detail. Imidazolate linkers provide abundant functionalities in the frameworks and the porous of ZIFs hold great potential across a wide range of applications. The functional properties of ZIFs can be tuneable by the incorporation of imidazolate derivatives linkers in a single framework to enhance the efficiency of ZIFs as catalysts, adsorbents and drug carriers.

Acknowledgement

This research was funded by Universiti Putra Malaysia (UPM) under the Putra Group Initiative (GP-IPB/2017/9581002).

References

1. Banerjee R., Furukawa H., Britt D., Knobler C., O'Keeffe M., and Yaghi O.M. (2009). Control of pore size and functionality in isoreticular zeolitic imidazolate frameworks and their carbon dioxide selective capture properties. *Journal of the American Chemical Society*, 131: 3875-3877.
2. Wang B., Côté A.P., Furukawa H., O'Keeffe M., and Yaghi O.M. (2008). Colossal cages in zeolitic imidazolate frameworks as selective carbon dioxide reservoirs. *Nature*, 453(7192): 207-211.
3. Park K.S., Ni Z., Côté A.P., Choi J.Y., Huang R., Uribe-Romo F.J., Chae H.K., O'Keeffe M., and Yaghi O.M. (2006). Exceptional chemical and thermal stability of zeolitic imidazolate frameworks. *Proceedings of the National Academy of Sciences of the United States of America*, 103(27): 10186-91.
4. Nguyen N.T.T., Furukawa H., Gándara F., Nguyen H.T., Cordova K.E., and Yaghi O.M. (2014). Selective capture of carbon dioxide under humid conditions by hydrophobic chabazite-type zeolitic imidazolate frameworks. *Angewandte Chemie - International Edition*, 53: 10645-10648.
5. Banerjee R., Phan A., Wang B., Knobler C., Furukawa H., O'Keeffe M., and Yaghi O.M. (2008). High-throughput synthesis of zeolitic imidazolate frameworks and application to CO_2 capture. *Science*, 319: 939-944.
6. Morris W., Doonan C.J., Furukawa H., Banerjee R., and Yaghi O.M. (2008). Crystals as molecules: Postsynthesis covalent functionalization of zeolitic imidazolate frameworks. *Journal of the American Chemical Society*, 130(38): 12626-12627.
7. Lee Y.R., Kim J., and Ahn W.S. (2013). Synthesis of Metal-Organic Frameworks: A Mini Review. *Korean Journal of Chemical Engineering*, 30(9): 1667-1680.
8. Yang J., Zhang Y.B., Liu Q., Trickett C.A., Gutiérrez-Puebla E., Monge M.Á., Cong H., Aldossary A., Deng H., and Yaghi O.M. (2017). Principles of designing extra-large pore openings and cages in zeolitic imidazolate frameworks. *Journal of the American Chemical Society*, 139(18): 6448-6455.
9. Kamal K., Bustam M.A., Ismail M., Grekov D., Shariff A.M., and Pré P. (2020). Optimization of washing processes in solvothermal synthesis of nickel-based MOF-74. *Materials*, 13(12): 1-10.
10. Hasan M.R., Paseta L., Malankowska M., Téllez C., and Coronas J. (2022). Synthesis of ZIF-94 from recycled mother liquors: Study of the influence of its loading on postcombustion CO_2 capture with pebax based mixed matrix membranes. *Advanced Sustainable Systems*, 6(1): 2100317.
11. Kenyotha K., Chanapattharapol K.C., McCloskey S., and Jantaharn P. (2020). Water based synthesis of ZIF-8 assisted by hydrogen bond acceptors and enhancement of CO_2 uptake by solvent assisted ligand exchange, *Crystals*, 10(7): 1-23.
12. Wu R., Fan T., Chen J., and Li Y. (2019). Synthetic factors affecting the scalable production of zeolitic imidazolate frameworks. *ACS Sustainable Chemistry and Engineering*, 7(4): 3632-3646.
13. Chen B., Yang Z., Zhu Y., and Xia Y. (2014). Zeolitic imidazolate framework materials: recent progress in synthesis and applications. *Journal of Materials Chemistry A*, 2(40): 16811-16831.
14. Sankar S.S., Karthick K., Sangeetha K., Karmakar A., Madhu R., and Kundu S. (2021). Current perspectives on 3D ZIFs incorporated with 1D carbon matrices as fibers via electrospinning processes towards electrocatalytic water splitting: A review. *Journal of Materials Chemistry A*, 9(20): 11961-12002.
15. Cheong V.F., and Moh P.Y. (2018). Recent advancement in metal–organic framework: synthesis, activation, functionalisation, and bulk production. *Materials Science and Technology*, 34(9): 1025-1045.
16. Hu L., Chen L., Fang Y., Wang A., Chen C., and Yan Z. (2018). Facile synthesis of zeolitic imidazolate framework-8 (ZIF-8) by forming imidazole-based deep eutectic solvent. *Microporous and Mesoporous Materials*, 268: 207-215.
17. Wang Y., Xu Y., Li D., Liu H., Li X., Tao S., and Tian Z. (2015). Ionothermal synthesis of zeolitic imidazolate frameworks and the synthesis dissolution-crystallization mechanism, *Chinese Journal of Catalysis*, 36(6): 855-865.
18. Gangu K.K., Maddila S., Mukkamala S.B., and

Jonnalagadda S.B. (2016). A review on contemporary Metal-Organic Framework materials. *Inorganica Chimica Acta*, 446: 61-74.
19. Wang Q., Sun Y., Li S., Zhang P., and Yao Q. (2020). Synthesis and modification of ZIF-8 and its application in drug delivery and tumor therapy. *RSC Advances*, 10(62): 37600-37620.
20. Xiao T., and Liu D. (2019). Progress in the synthesis, properties and applications of ZIF-7 and its derivatives. *Materials Today Energy*, 14(3): 100357.
21. Lucero J.M., Self T.J., and Carreon M.A. (2020). Synthesis of ZIF-11 crystals by microwave heating. *New Journal of Chemistry*, 44(9): 3562-3565.
22. Tran T. Van, Nguyen H., Le P.H.A., Nguyen D.T.C., Nguyen T.T., Nguyen C. Van, Vo D.V.N., and Nguyen T.D. (2020). Microwave-assisted solvothermal fabrication of hybrid zeolitic-imidazolate framework (ZIF-8) for optimizing dyes adsorption efficiency using response surface methodology, *Journal of Environmental Chemical Engineering*, 8(4): 104189.
23. Hayati P., Rezvani A.R., Morsali A., Molina D.R., Geravand S., Suarez-Garcia S., Villaecija M.A.M., García-Granda S., Mendoza-Meroño R., and Retailleau P. (2017). Sonochemical synthesis, characterization, and effects of temperature, power ultrasound and reaction time on the morphological properties of two new nanostructured mercury(II) coordination supramolecule compounds. *Ultrasonics Sonochemistry*, 37: 382–393.
24. Kukkar P., Kim K.H., Kukkar D., and Singh P. (2021). Recent advances in the synthesis techniques for zeolitic imidazolate frameworks and their sensing applications. *Coordination Chemistry Reviews*, 446: 214109.
25. Nalesso S., Varlet G., Bussemaker M.J., Sear R.P., Hodnett M., Monteagudo-Oliván R., Sebastián V., Coronas J., and Lee J. (2021). Sonocrystallisation of ZIF-8 in water with high excess of ligand: Effects of frequency, power and sonication time. *Ultrasonics Sonochemistry*, 76: 105616.
26. Abuzalat O., Wong D., Elsayed M., Park S., and Kim S. (2018). Sonochemical fabrication of Cu(II) and Zn(II) metal-organic framework films on metal substrates, *Ultrasonics Sonochemistry*, 45: 180-188.
27. Jiang S., Shi X., Zu Y., Sun F., and Zhu G. (2021). Interfacial growth of 2D MOF membranes Via contra-diffusion for CO2 separation. *Materials Chemistry Frontiers*, 5(13): 5150-5157.
28. Long X., Chen Y.S., Zheng Q., Xie X.X., Tang H., Jiang L.P., Jiang J.T., and Qiu J.H. (2020). Removal of iodine from aqueous solution by PVDF/ZIF-8 nanocomposite membranes. *Separation and Purification Technology*, 238: 116488.
29. Karimi A., Vatanpour V., Khataee A., and Safarpour M. (2019). Contra-diffusion synthesis of ZIF-8 layer on polyvinylidene fluoride ultrafiltration membranes for improved water purification. *Journal of Industrial and Engineering Chemistry*, 73: 95-105.
30. Tanaka S., Nagaoka T., Yasuyoshi A., Hasegawa Y., and Denayer J.F.M. (2018). Hierarchical pore development of ZIF-8 MOF by simple salt-assisted mechanosynthesis. *Crystal Growth and Design*, 18(1): 274-279.
31. Thorne M.F., Gómez M.L.R., Bumstead A.M., Li S., and Bennett T.D. (2020). Mechanochemical synthesis of mixed metal, mixed linker glass-forming metal-organic frameworks. *Green Chemistry*, 22(8): 2505-2512.
32. Desai A. V., Sharma S., Let S., and Ghosh S.K. (2019). N-donor linker based metal-organic frameworks (MOFs): Advancement and prospects as functional materials. *Coordination Chemistry Reviews*, 395: 146-192.
33. Utpalla P., Mor J., Sharma S.K., Bahadur J., and Pujari P.K. (2022). Pore interconnectivity and surface accessibility in stiffened mixed linker MOFs: An investigation using variable energy positron spectroscopy, *Journal of Solid State Chemistry*, 307: 122738.
34. Ding R., Zheng W., Yang K., Dai Y., Ruan X., Yan X., and He G. (2020). Amino-functional ZIF-8 nanocrystals by microemulsion based mixed linker strategy and the enhanced CO_2/N_2 separation. *Separation and Purification Technology*, 236: 116209.
35. Eddaoudi M., Kim J., Rosi N., Vodak D., Wachter J., O'Keeffe M., and Yaghi O.M. (2002). Systematic design of pore size and functionality in

isoreticular MOFs and their application in methane storage. *Science*, 295 (5554): 469-472.

36. Furukawa H., Go Y.B., Ko N., Park Y.K., Uribe-romo F.J., Kim J., Kee M.O., and Yaghi O.M. (2011). Isoreticular expansion of metal-organic frameworks with triangular and square building units and the lowest calculated density for porous crystals. *Inorganic Chemistry*, 50: 9147-9152.
37. Gotzias A. (2017). The effect of gme topology on multicomponent adsorption in zeolitic imidazolate frameworks. *Physical Chemistry Chemical Physics*, 19(1): 871-877.
38. Reif B., Fabisch F., Hovestadt M., Hartmann M., and Schwieger W. (2017). Synthesis of ZIF-11 - Effect of water residues in the solvent onto the phase transition from ZIF-11 to ZIF-7-III. *Microporous and Mesoporous Materials*, 243(3):65-68.
39. Pimentel B.R., Parulkar A., Zhou E.K., Brunelli N.A., and Lively R.P. (2014). Zeolitic imidazolate frameworks: Next-generation materials for energy-efficient gas separations. *ChemSusChem*, 7(12): 3202-3240.
40. Reif B., Paula C., Fabisch F., Hartmann M., Kaspereit M., and Schwieger W. (2019). Synthesis of ZIF-11 – Influence of the synthesis parameters on the phase purity. *Microporous and Mesoporous Materials*, 275 (7):102-110.
41. Feng X., Wu T., and Carreon M.A. (2016). Synthesis of ZIF-67 and ZIF-8 crystals using DMSO (Dimethyl Sulfoxide) as solvent and kinetic transformation studies. *Journal of Crystal Growth*, 455(10): 152-156.
42. Lively R.P., Dose M.E., Thompson J.A., McCool B.A., Chance R.R., and Koros W.J. (2011). Ethanol and water adsorption in methanol-derived ZIF-71. *Chemical Communications*, 47(30): 8667-8669.
43. Fu F., Zheng B., Xie L.H., Du H., Du S., and Dong Z. (2018). Size-controllable synthesis of zeolitic imidazolate framework/carbon nanotube composites. *Crystals*, 8(10): 1-12.
44. Zhang Y., Jia Y., Li M., and Hou L. (2018). Influence of the 2-methylimidazole/zinc nitrate hexahydrate molar ratio on the synthesis of zeolitic imidazolate framework-8 crystals at room temperature. *Scientific Reports*, 8(1): 1-7.
45. Kida K., Okita M., Fujita K., Tanaka S., and Miyake Y. (2013). Formation of high crystalline ZIF-8 in an aqueous solution. *CrystEngComm*, 15(9): 1794-1801.
46. Shi Z., Yu Y., Fu C., Wang L., and Li X. (2017). Water-based synthesis of zeolitic imidazolate framework-8 for CO_2 capture, *RSC Advances*, 7(46): 29227-29232.
47. Jian M., Liu B., Liu R., Qu J., Wang H., and Zhang X. (2015). Water-based synthesis of zeolitic imidazolate framework-8 with high morphology level at room temperature. *RSC Advances*, 5(60): 48433-48441.
48. Lai L.S., Yeong Y.F., Lau K.K., and Shariff A.M. (2016). Effect of synthesis parameters on the formation of ZIF-8 under microwave-assisted solvothermal. *Procedia Engineering*, 148: 35-42.
49. Abdelhamid H.N., Huang Z., El-Zohry A.M., Zheng H., and Zou X. (2017). A sast and scalable approach for synthesis of hierarchical porous zeolitic imidazolate frameworks and one-pot encapsulation of target molecules, *Inorganic Chemistry*, 56(15): 9139-9146.
50. Gross A.F., Sherman E., and Vajo J.J. (2012). Aqueous room temperature synthesis of cobalt and zinc sodalite zeolitic imidizolate frameworks, *Dalton Transactions*, 41(18): 5458-5460.
51. Cravillon J., Nayuk R., Springer S., Feldhoff A., Huber K., and Wiebcke M. (2011). Controlling zeolitic imidazolate framework nano- and microcrystal formation: Insight into crystal growth by time-resolved in situ static light scattering, *Chemistry of Materials*, 23(8): 2130-2141.
52. Ebrahimi A., and Mansournia M. (2017). Cost-effective fabrication of thermal- and chemical-stable ZIF-9 nanocrystals at ammonia atmosphere, *Journal of Physics and Chemistry of Solids*, 111: 12-17.
53. Li Y., Zhou K., He M., and Yao J. (2016). Synthesis of ZIF-8 and ZIF-67 using mixed-base and their dye adsorption, *Microporous and Mesoporous Materials*, 234: 287-292.
54. Huang X.C., Lin Y.Y., Zhang J.P., and Chen X.M. (2006). Ligand-directed strategy for zeolite-type metal-organic frameworks: Zinc(II) imidazolates with unusual zeolitic topologies, *Angewandte*

Chemie - International Edition, 45(10): 1557-1559.
55. Zheng W., Ding R., Yang K., Dai Y., Yan X., and He G. (2019). ZIF-8 nanoparticles with tunable size for enhanced CO_2 capture of Pebax based MMMs. *Separation and Purification Technology*, 214: 111-119.
56. Cravillon J., Schröder C.A., Bux H., Rothkirch A., Caro J., and Wiebcke M. (2012). Formate modulated solvothermal synthesis of ZIF-8 investigated using time-resolved in situ X-ray diffraction and scanning electron microscopy. *CrystEngComm*, 14(2): 492-498.
57. Seoane B., Castellanos S., Dikhtiarenko A., Kapteijn F., and Gascon J. (2016). Multi-scale crystal engineering of metal organic frameworks. *Coordination Chemistry Reviews*, 307: 147-187.
58. Oozeerally R., Ramkhelawan S.D.K., Burnett D.L., Tempelman C.H.L., and Degirmenci V. (2019). ZIF-8 metal organic framework for the conversion of glucose to fructose and 5-hydroxymethyl furfural, *Catalysts*, 9(812): 1-14.
59. Zhao X., Fang X., Wu B., Zheng L., and Zheng N. (2014). Facile synthesis of size-tunable ZIF-8 nanocrystals using reverse micelles as nanoreactors, *Science China Chemistry*, 57(1): 141-146.
60. Cheetham A.K., Kieslich G., and Yeung H.H.M. (2018). Thermodynamic and kinetic effects in the crystallization of metal-organic frameworks. *Accounts of Chemical Research*, 51(3): 659-667.
61. Ta D.N., Nguyen H.K.D., Trinh B.X., Le Q.T.N., Ta H.N., and Nguyen H.T. (2018). Preparation of nano-ZIF-8 in methanol with high yield. *Canadian Journal of Chemical Engineering*, 96(7): 1518-1531.
62. Tsai C.W., and Langner E.H.G. (2016). The effect of synthesis temperature on the particle size of nano-ZIF-8, *Microporous and Mesoporous Materials*, 221: 8-13.
63. Feng Y., Li Y., Xu M., Liu S., and Yao J. (2016). Fast adsorption of methyl blue on zeolitic imidazolate framework-8 and its adsorption mechanism, *RSC Advances*, 6(111): 109608-109612.
64. Luan Tran B., Chin H.Y., Chang B.K., and Chiang A.S.T. (2019). Dye adsorption in ZIF-8: The importance of external surface area. *Microporous and Mesoporous Materials*, 277: 149-153.
65. Fan X., Wang W., Li W., Zhou J., Wang B., Zheng J., and Li X. (2014). Highly porous ZIF-8 nanocrystals prepared by a surfactant mediated method in aqueous solution with enhanced adsorption kinetics. *ACS Applied Materials and Interfaces*, 17: 14994-14999.
66. Fernandez-Perez A., and Marban G. (2020). Visible light spectroscopic analysis of methylene blue in water; what comes after dimer? *ACS Omega*, 5(46): 29801-29815.
67. Heydari Moghaddam M., Nabizadeh R., Dehghani M.H., Akbarpour B., Azari A., and Yousefi M. (2019). Performance investigation of Zeolitic Imidazolate Framework – 8 (ZIF-8) in the removal of trichloroethylene from aqueous solutions. *Microchemical Journal*, 150: 104185.
68. Saracco G., Vankova S., Pagliano C., Bonelli B., and Garrone E. (2014). Outer Co(II) ions in Co-ZIF-67 reversibly adsorb oxygen from both gas phase and liquid water. *Physical Chemistry Chemical Physics*, 16 (13): 6139-6145.
69. Tu N.T.T., Thien T.V., Du P.D., Thanh Chau V.T., Mau T.X., and Khieu D.Q. (2018). Adsorptive removal of Congo red from aqueous solution using zeolitic imidazolate framework-67. *Journal of Environmental Chemical Engineering*, 6(2): 2269-2280.
70. Lin K.Y.A., and Chang H.A. (2015). Ultra-high adsorption capacity of zeolitic imidazole framework-67 (ZIF-67) for removal of malachite green from water. *Chemosphere*, 139: 624-631.
71. Bekçi Z., Özveri C., Seki Y., and Yurdakoç K. (2008). Sorption of malachite green on chitosan bead. *Journal of Hazardous Materials*, 154: 254-261.
72. Huo S.H., and Yan X.P. (2012). Metal-organic framework MIL-100(Fe) for the adsorption of malachite green from aqueous solution, *Journal of Materials Chemistry*, 22(15): 7449-7455.
73. Liao S.-M., Du Q.-S., Meng J.-Z., Pang Z.-W., and Huang R.-B. (2013). Evidence for a functionally important histidine residue in human tyrosine hydroxylase, *Chemistry Central Journal*, 7(44): 1-12.
74. Yu R., and Wu Z. (2020). High adsorption for

ofloxacin and reusability by the use of ZIF-8 for wastewater treatment. *Microporous and Mesoporous Materials*, 308 (3): 110494.

75. Daghrir R., and Drogui P. (2013). Tetracycline antibiotics in the environment: A review. *Environmental Chemistry Letters*, 11(3): 209-227.
76. Golet E.M., Alder A.C., and Giger W. (2002). Environmental exposure and risk assessment of fluoroquinolone antibacterial agents in wastewater and river water of the Glatt Valley watershed, Switzerland. *Environmental Science and Technology*, 36(17): 3645-3651.
77. Zhou L., Li N., Owens G., and Chen Z. (2019). Simultaneous removal of mixed contaminants, copper and norfloxacin, from aqueous solution by ZIF-8. *Chemical Engineering Journal*, 362: 628-637.
78. Wu C.S., Xiong Z.H., Li C., and Zhang J.M. (2015). Zeolitic imidazolate metal organic framework ZIF-8 with ultra-high adsorption capacity bound tetracycline in aqueous solution. *RSC Advances*, 5(100): 82127-82137.
79. Xiang Y., Yang X., Xu Z., Hu W., Zhou Y., Wan Z., Yang Y., Wei Y., Yang J., and Tsang D.C.W. (2020). Fabrication of sustainable manganese ferrite modified biochar from vinasse for enhanced adsorption of fluoroquinolone antibiotics: Effects and mechanisms. *Science of the Total Environment*, 709: 136079.
80. Li N., Zhou L., Jin X., Owens G., and Chen Z. (2018). Simultaneous removal of tetracycline and oxytetracycline antibiotics from wastewater using a ZIF-8 metal organic-framework. *Journal of Hazardous Materials*, 366: 563-572.
81. Petkovic H., Lukežic T., and Šuškovic J. (2017). Biosynthesis of oxytetracycline by *streptomyces rimosus*: Past, present and future directions in the development of tetracycline antibiotics. *Food Technology and Biotechnology*, 55(1): 3-13.
82. Ocampo-Pérez R., Rivera-Utrilla J., Gómez-Pacheco C., Sánchez-Polo M., and López-Peñalver J.J. (2012). Kinetic study of tetracycline adsorption on sludge-derived adsorbents in aqueous phase. *Chemical Engineering Journal*, 213: 88-96.
83. Enayati M., Gong Y., and Abbaspourrad A. (2019). Synthesis of lactose lauryl ester in organic solvents using aluminosilicate zeolite as a catalyst. *Food Chemistry*, 279: 401-407.
84. Sarmah B., Satpati B., and Srivastava R. (2017). Highly efficient and recyclable basic mesoporous zeolite catalyzed condensation, hydroxylation, and cycloaddition reactions. *Journal of Colloid and Interface Science*, 493: 307-316.
85. Shalaby N.H., Elsalamony R.A., and El Naggar A.M.A. (2018). Mesoporous waste-extracted SiO_2-Al_2O_3-supported Ni and Ni-$H_3PW_{12}O_{40}$ nano-catalysts for photo-degradation of methyl orange dye under UV irradiation. *New Journal of Chemistry*, 42(11): 9177-9186.
86. Terrade F.G., van Krieken J., Verkuijl B.J.V., and Bouwman E. (2017). Catalytic cracking of lactide and poly(lactic acid) to acrylic acid at low temperatures. *ChemSusChem*, 10(9): 1904-1908.
87. VanWouwe P., Dusselier M., Vanleeuw E., and Sels B. (2016). Lactide synthesis and chirality control for polylactic acid production, *ChemSusChem*, 9(9): 907-921.
88. Kricheldorf H.R. (2001). Syntheses and application of polylactides. *Chemosphere*, 43(1): 49-54.
89. Luo Z., Chaemchuen S., Zhou K., and Verpoort F. (2017). Ring-opening polymerization of $_L$-lactide to cyclicpoly(lactide) by zeolitic imidazole framework ZIF-8 catalyst. *ChemSusChem*, 10(21): 4135-4139.
90. Aresta M., Dibenedetto A., and Angelini A. (2014). Catalysis for the valorization of exhaust carbon: from CO_2 to chemicals, materials and fuels. Technological use of CO_2. *Encyclopedia of Inorganic and Bioinorganic Chemistry*, 3: 1709-1742.
91. Bhin K.M., Tharun J., Roshan K.R., Kim D., Chung Y., and Park D. (2017). Catalytic performance of zeolitic imidazolate framework ZIF-95 for the solventless synthesis of cyclic carbonates from CO_2 and epoxides. *Journal of CO_2 Utilization*, 17: 112-118.
92. Jose T., Hwang Y., Kim D.W., Kim M. Il, and Park D.W. (2015). Functionalized zeolitic imidazolate framework F-ZIF-90 as efficient catalyst for the cycloaddition of carbon dioxide to allyl glycidyl ether, *Catalysis Today*, 245: 61-67.
93. Ivanchikova I.D., Evtushok V.Y., Zalomaeva O. V., Kolokolov D.I., Stepanov A.G., and Kholdeeva O.A.

(2020). Heterogeneous epoxidation of menadione with hydrogen peroxide over the zeolite imidazolate framework ZIF-8. *Dalton Transactions*, 49(36): 12546-12549.

94. Chin M., Cisneros C., Araiza S.M., Vargas K.M., Ishihara K.M., and Tian F. (2018). Rhodamine B degradation by nanosized zeolitic imidazolate framework-8 (ZIF-8). *RSC Advances*, 8(47): 26987-26997.
95. Wang T., Wang Y., Sun M., Hanif A., Wu H., Gu Q., Ok Y.S., Tsang D.C.W., Li J., Yu J., and Shang J. (2020). Thermally treated zeolitic imidazolate framework-8 (ZIF-8) for visible light photocatalytic degradation of gaseous formaldehyde. *Chemical Science*, 11(26): 6670-6681.
96. Park H., Amaranatha Reddy D., Kim Y., Ma R., Choi J., Kim T.K., and Lee K.S. (2016). Zeolitic imidazolate framework-67 (ZIF-67) rhombic dodecahedrons as full-spectrum light harvesting photocatalyst for environmental remediation. *Solid State Sciences*, 62: 82-89.
97. Wang M., Liu J., Guo C., Gao X., Gong C., Wang Y., Liu B., Li X., Gurzadyan G.G., and Sun L. (2018). Metal-organic frameworks (ZIF-67) as efficient cocatalysts for photocatalytic reduction of CO_2: The role of the morphology effect, *Journal of Materials Chemistry A*, 6: 4768-4775.
98. White J.L., Baruch M.F., Pander J.E., Hu Y., Fortmeyer I.C., Park J.E., Zhang T., Liao K., Gu J., Yan Y., Shaw T.W., Abelev E., and Bocarsly A.B. (2015). Light-driven heterogeneous reduction of carbon dioxide: Photocatalysts and photoelectrodes. *Chemical Reviews*, 115(23): 12888-12935.
99. Pattengale B., Santalucia D.J., Yang S., Hu W., Liu C., Zhang X., Berry J.F., and Huang J. (2018). Direct observation of node-to-node communication in zeolitic imidazolate frameworks, *Journal of the American Chemical Society*, 140(37): 11573-11576.
100. Saper R.B., and Rash R. (2009). Zinc: An essential micronutrient. *American Family Physician*, 79(9): 768-772.
101. Karagiaridi O., Lalonde M.B., Bury W., Sarjeant A.A., Farha O.K., and Hupp J.T. (2012). Opening ZIF-8: A catalytically active zeolitic imidazolate framework of sodalite topology with unsubstituted linkers, *Journal of the American Chemical Society*, 134(45): 18790-18796.
102. Aarbakke J., Janka-Schaub G., and Elion G.B. (1997). Thiopurine biology and pharmacology. *Trends in Pharmacological Sciences*, 18(1): 3-7.
103. Hanauer S.B., Korelitz B.I., Rutgeerts P., Peppercorn M.A., Thisted R.A., Cohen R.D., and Present D.H. (2004). Postoperative maintenance of Crohn's disease remission with 6-mercaptopurine, mesalamine, or placebo: A 2-year trial, *Gastroenterology*, 127(3): 723-729.
104. Hübener S., Oo Y.H., Than N.N., Hübener P., Weiler-Normann C., Lohse A.W., and Schramm C. (2016). Efficacy of 6-mercaptopurine as second-line treatment for patients with autoimmune hepatitis and azathioprine intolerance. *Clinical Gastroenterology and Hepatology*, 14(3): 445-453.
105. Kaur H., Mohanta G.C., Gupta V., Kukkar D., and Tyagi S. (2017). Synthesis and characterization of ZIF-8 nanoparticles for controlled release of 6-mercaptopurine drug. *Journal of Drug Delivery Science and Technology*, 41: 106-112.
106. Müller Kratz J., Garcia Bournissen F., Forsyth C.J., and Sosa-Estani S. (2018). Clinical and pharmacological profile of benznidazole for treatment of chagas disease. Taylor & Francis.
107. Coudert F.X. (2017). Molecular mechanism of swing effect in zeolitic imidazolate framework ZIF-8: Continuous deformation upon adsorption. *ChemPhysChem*, 18(19): 2732-2738.
108. Xia Y., Hong Y., Geng R., Li X., Qu A., Zhou Z., and Zhang Z. (2020). Amine-functionalized ZIF-8 as a fluorescent probe for breath volatile organic compound biomarker detection of lung cancer patients. *ACS Omega*, 5(7): 3478-3486.
109. Tiwari A., Singh A., Garg N., and Randhawa J.K. (2017). Curcumin encapsulated zeolitic imidazolate frameworks as stimuli responsive drug delivery system and their interaction with biomimetic environment. *Scientific Reports*, 7(1): 1-12.
110. Moura Ferraz L.R. de, Tabosa A.É.G.A., da Silva Nascimento D.D.S., Ferreira A.S., de Albuquerque Wanderley Sales V., Silva J.Y.R., Júnior S.A., Rolim L.A., de Souza Pereira J.J., and Rolim-Neto P.J. (2020). ZIF-8 as a promising drug delivery system for benznidazole: development, characterization, in vitro dialysis release and

cytotoxicity. *Scientific Reports*, 10(1): 1-14.

111. Sun Q., Bi H., Wang Z., Li C., Wang X., Xu J., Zhu H., Zhao R., He F., Gai S., and Yang P. (2019). Biomaterials hyaluronic acid-targeted and pH-responsive drug delivery system based on metal-organic frameworks for efficient antitumor therapy. *Biomaterials*, 223: 119473.
112. Lin C.W., Lu K.Y., Wang S.Y., Sung H.W., and Mi F.L. (2016). CD44-specific nanoparticles for redox-triggered reactive oxygen species production and doxorubicin release. *Acta Biomaterialia*, 35: 280-292.
113. Song L., Pan Z., Zhang H., Li Y., Zhang Y., Lin J., Su G., Ye S., Xie L., Li Y., and Hou Z. (2017). Dually folate/CD44 receptor-targeted self-assembled hyaluronic acid nanoparticles for dual-drug delivery and combination cancer therapy. *Journal of Materials Chemistry B*, 5(33): 6835-6846.
114. Yan J., Liu C., Wu Q., Zhou J., Xu X., Zhang L., Wang D., Yang F., and Zhang H. (2020). Mineralization of pH-sensitive doxorubicin prodrug in ZIF-8 to enable targeted delivery to solid tumors. *Analytical Chemistry*, 92(16): 11453-11461.

Malaysian Journal of Analytical Sciences (MJAS)
Published by Malaysian Analytical Sciences Society

INHIBITION EFFECTS OF TRIDENTATE HYDRAZONE LIGANDS AS CORROSION INHIBITORS ON MILD STEEL IN SATURATED CO_2 ENVIRONMENT

(Kesan Perencatan Ligan Hidrazon Tridentat Sebagai Perencat Kakisan Pada Keluli Lembut Dalam Persekitaran CO_2 Tepu)

Balqis Auni Badrul Hisyam[1], Zainiharyati Mohd Zain[2], Nurulfazlina Edayah Rasol[1,3] and Amalina Mohd Tajuddin [1,3*]

[1]*Faculty of Applied Sciences, Universiti Teknologi MARA (UiTM), 40450 Shah Alam, Selangor, Malaysia*
[2]*Electrochemical Material and Sensor (EMaS), Universiti Teknologi MARA (UiTM), 40450 Shah Alam, Selangor, Malaysia*
[3]*Atta-ur-Rahman Institute for Natural Product Discovery (AuRIns), UiTM Puncak Alam, 42300, Bandar Puncak Alam, Selangor, Malaysia*

Corresponding author: amalina9487@uitm.edu.my

Received: 15 September 2023; Accepted: 25 November 2023; Published: 28 February 2024

Abstract

Two tridentate hydrazone ligands (AL01, AL02) were synthesized by condensation of an aldehyde and two hydrazides, benzohydrazide and 2-hydroxybenzohydrazide with OH substituent at the *ortho* position of the benzene ring. They were characterized using melting point, FTIR, NMR, elemental analysis, UV-Vis as well as mass spectroscopy. The formation of hydrazone ligands was confirmed by the appearance of *ν*(C=N) peak in the range of 1608 to 1648 cm^{-1}. The significant peak of N-H protons for AL01 and AL02 appeared at 8.82 and 8.41 ppm respectively, while the peak of phenolic proton (O-H) for AL01 was found at 12.28 ppm. Two peaks were observed in the wavelength range of 198-220 nm that can be attributed to π-$\pi^*_{(C=C)}$ and n-$\pi^*_{(C=C)}$ transitions of aromatic benzene, while the peaks for π -$\pi^*_{(C=N)}$ were observed in the range of 297–303 nm. The mass-to-charge (m/z) $[M+H]^+$ values of AL01 and AL02, which are 242.09 and 226.10, respectively, further confirmed their structures. The effectiveness of hydrazone ligands as corrosion inhibitors on mild steel in 3.5% NaCl solution saturated with CO_2 was examined using polarization and electrochemical impedance spectroscopy (EIS). The elemental constituents of the protective layer forms on mild steel immersed in the solution were further observed using scanning electron microscopy (SEM) coupled with energy-dispersive X-Ray (EDX)). Therefore, new corrosion inhibitors of tridentate hydrazone ligands, AL01 and AL02 were successfully synthesized and characterized using FTIR, NMR, elemental analysis, mass spectroscopy and UV-Vis. From polarization and EIS study, AL01 can be concluded to have higher inhibition efficiency, 84.30% at 500 ppm concentration compared to AL02, 74.90%. SEM-EDX analysis has confirmed the formation of the inhibitors' layer on mild steel as the surface of the mild steel immersed in solution with the presence of inhibitors have a smoother surface compared to that of untreated mild steel in 3.5% NaCl solution saturated with CO_2.

Keywords: CO_2, corrosion inhibitor, mild steel, protective layer, tridentate hydrazone

Abstrak

Dua ligan hidrazon tridentat (AL01, AL02) telah disintesis melalui pemeluwapan antara aldehid dan dua hidrazida, benzohidrazida dan 2-hidroksibenzohidrazida, dengan kumpulan pengganti OH pada kedudukan *orto* hidrazida. Mereka dicirikan menggunakan takat lebur, FTIR, NMR, analisis unsur, UV-Vis serta spektroskopi jisim. Pembentukan ligan hidrazon telah disahkan oleh kemunculan puncak *v*(C=N) dalam julat 1608 hingga 1648 $cm^{-1.}$ Puncak utama proton N-H untuk AL01 dan AL02 masing-masing muncul pada 8.82 dan 8.41 ppm, manakala puncak proton fenolik (O-H) untuk AL01 didapati pada 12.28 ppm. Dua puncak diperhatikan dalam julat 198-220 nm yang boleh dikaitkan kepada peralihan π-$\pi^*_{(C=C)}$ dan n-$\pi^*_{(C=C)}$ Kumpulan benzena aromatik manakala pucak bagi peralihan π-π*(C=N) telah diperhatikan dalam julat 297-303 nm. Nilai jisim-ke-cas (m/z) $[M+H]^+$ bagi AL01 dan AL02, iaitu 242.09 dan 226.10, masing-masing, memberikan pengesahan lanjut tentang strukturnya. Keberkesanan ligan hidrazon sebagai perencat kakisan pada keluli lembut dalam larutan NaCl 3.5% tepu dengan CO_2 telah diperiksa menggunakan polarisasi dan spektroskopi impedans elektrokimia (EIS). Kehadiran unsur pada lapisan pelindung yang terbentuk pada keluli lembut yang direndam dalam larutan diperhatikan selanjutnya menggunakan mikroskop elektron pengimbasan (SEM) ditambah dengan X-Ray penyebaran tenaga (EDX). Oleh itu, perencat kakisan baru, ligan hidrazon tridentat, AL01 dan AL02 telah berjaya disintesis dan dicirikan menggunakan FTIR, NMR, analisis unsur, spektroskopi jisim dan UV-Vis. Daripada kajian polarisasi dan EIS, dapat disimpulkan bahawa AL01 mempunyai kecekapan perencatan yang lebih tinggi iaitu, 84.30% pada 500 ppm berbanding AL02 iaitu, 74.90%. Analisis SEM-EDX telah mengesahkan pembentukan lapisan perencat pada keluli lembut kerana permukaan keluli lembut dengan kehadiran perencat mempunyai permukaan yang lebih licin berbanding keluli lembut yang tidak dirawat dengan perencat kakisan dalam larutan 3.5% NaCl tepu dengan CO_2.

Kata kunci: CO_2, perencat kakisan, keluli lembut, lapisan pelindung, hidrazon tridentat

Introduction

Corrosion is a common natural interaction between a pure metal and its surroundings where the metal tends to revert to its stable condition i.e., a compounded state, and the substance deteriorates because of energy being released in the process [1, 2]. It has a significant influence on a variety of machinery, infrastructures, industrial plants, and human life. Many things can suffer serious damage from corrosion, and the costs of the destruction are substantial [3]. A previous study by Tamalmani et al., stated that corrosion has been highlighted as one of the key causes of oil and gas infrastructure problems. Internal pipeline is one of the widely used means for transporting resources in the oil and gas sector, however, internal pipeline corrosion has seemed to represent a substantial threat [4]. It has been acknowledged that pipeline corrosion is primarily brought on by the presence of carbon dioxide (CO_2) as the major corrosive medium which commonly happens during transportation of hydrocarbons in the pipeline. Due to the solubility of CO_2 in water and brine (NaCl solution), the steel and the contacting aqueous phase undergo an electrochemical process resulted in carbonic acid (H_2CO_3) formation, that leads to severe corrosion in pipelines [4–6].

Mild steel is often utilized as a raw material for the construction of pipelines, nevertheless, due to its premature failure and degradation, a gross expenditure of billions of dollars has been incurred worldwide. These costs include replacement, maintenance, and lost productivity since mild steel is an essential component in an infrastructure, which includes pipelines, port facilities, and bridges [7]. This low-carbon steel is widely sought-after for high temperature applications, such as petrochemical processes and pipeline construction, due to its malleability and lack of brittleness. Mild steel is widely used in the oil and gas industries for transporting gases and liquids over long distances in pipelines from their sources to the consumers [8], despite having a low corrosion resistance because of its availability, affordability, and hardness [1]. Moreover, mild steel consists of porous regions within its structure that make it more prone to corrosion, especially in corrosion-aggressive environments such chemical industries, the ocean, and polluted environments [9, 10]. Transportation of crude oil in pipelines for instance, often comes naturally with impurities such CO_2, water, and oxygen, which are thought to be the main causes of corrosion in pipelines. Studies found that since CO_2 dissolves in aqueous solution to generate weak carbonic acid (H_2CO_3) [8, 11, 12], which is considered to be the most hazardous

type of acids to carbon steel, a combination of CO_2 with water indicates a serious corrosion problem. However, the condition gets worsen with the combination of CO_2 with brine solution (NaCl). A study reported by Almeida et al., found that the corrosion rate of steel in distilled water was 28.3 mm/y while in brine solution after being immersed for 30 minutes was 119 mm/y [13].

Therefore, investigations were conducted, and it was discovered that using corrosion inhibitors could be one of the strategies to resolve this problem since it is easy to put into application, affordable, and under control [10]. However, it was also discovered that the inorganic inhibitors used in passivation processes, such as nitrates, chromates, and derivatives of azole and thiourea, were hazardous to both humans and the environment. Additional research on effective, environment-friendly inhibitors that can provide a protective layer on metals is required to address these problems to mitigate the rate of corrosion [14]. Corrosion inhibitors need at least one polar group, such as heteroatoms that can facilitate the process of adsorption in an acidic environment to be able to bond to the metal surface. Additionally, the effect of corrosion inhibition may be enhanced by changing the molecule's size, orientation, and geometry. Aforementioned, organic compounds with unsaturated bonds or heteroatoms like O, N, and S as well as functional groups like -NH, NN, CN-, and CHO frequently work well as corrosion inhibitors [15].

Due to their unique chemical properties, hydrazones, which belong to a special family of organic molecules, have several biological and therapeutic uses. For example, hydrazone-based inhibitors derived from non-steroidal anti-inflammatory medicines (NSAIDs) such mefenamic acid, naproxen, and ibuprofen have been produced, which have shown to be effective against steel corrosion [16]. The most advantageous property of hydrazones is their high reactivity because of the azomethine group, which has two nitrogen atoms with nucleophilic properties and a carbon atom with both electrophilic and nucleophilic properties [17]. In addition, hydrazone-based inhibitors have also been identified as "green corrosion inhibitors" that prevent corrosion by adsorption on the metal surface since they are non-toxic, inexpensive, and biodegradable [18].

Hence, in this study, new corrosion inhibitors of tridentate hydrazone ligands without and with the presence of OH substituent at the *ortho* position of the benzene ring were synthesized, characterized, and evaluated as organic corrosion inhibitors. To the best of our knowledge, no reports on using AL01 and AL02 as corrosion inhibitors are available. Therefore, the relationship between the absence and presence of electron-donating group (-OH) [19] with the inhibition efficiency and corrosion rate of the mild steel is reported.

Materials and Methods

Materials

2-Pyridinecarboxaldehyde, 2-hydroxybenzohydrazide, benzohydrazide, and methanol purchased from commercial suppliers were used without further purification. Melting point determination in triplicate was carried out in glass capillary tubes using Buchii-B454 and the percentage compositions of the elements C, H and N of the compounds were determined by using Thermo Scientific Flash 2000 Elemental Analyzer with sulphanilamide as the standard. Fourier-transform infrared spectra (FTIR) were recorded using Perkin-Elmer FT-IR 1600 spectrometer by preparing samples as KBr discs. ^{1}H NMR spectra were recorded on Bruker Avance 600 MHz NMR spectrometer in deuterated solvents, DMSO and $CDCl_3$. UV-Vis spectra were obtained in acetonitrile ($5x10^{-5}$ M) in the 190-450 nm range Perkin Elmer Lambda 25 UV/Vis Spectrometer. Mass spectral data are measured in 1:1 ratio of acetonitrile: H_2O at concentration of 10 ppm using Thermo Scientific Vanquish Horizon UHPLC system fitted with Thermo Scientific TM Orbitrap Fusion Tribrid. The column used was Accucore TM Vanquish C18 (2.1 x 100 mm, 1.5 μm) at 37 ^{o}C.

Synthesis of tridentate hydrazone ligands

Scheme 1 shows the synthesis reaction for tridentate hydrazone ligands.

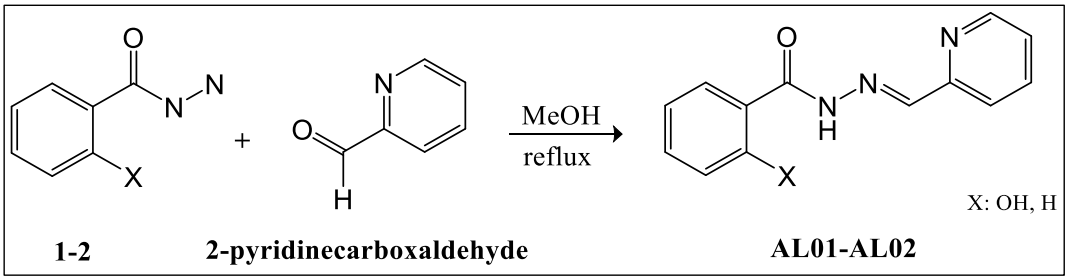

Scheme 1. Overall reaction between hydrazides and aldehyde

Synthesis of *(E)-2-hydroxy-N'-(pyridin-2-ylmethylene)benzohydrazide* (AL01)

2-Pyridinecarboxaldehyde (5 mmol, 0.5356 g) and 2-hydroxybenzohydrazide (5 mmol, 0.7608g) were dissolved in methanol (20 mL), and the mixture was heated under reflux for 30 minutes. The colorless solid obtained was filtered using vacuum pump and washed with ice cold methanol and air dried at room temperature. Yield: 83.5%. IR (KBr pellet, cm^{-1}): *v*(N-H) 3242 cm^{-1}, *v*(C=N) 1608 cm^{-1}, *v*(C=N) (pyridine) 1542 cm^{-1}, *v*(C=O) and 1630 cm^{-1}. ^{1}H NMR (500 MHz, $CDCl_3$) δ 12.28 (s, 1H), 8.82 (s, 1H), 7.97 (td, J = 7.8, 1.8 Hz, 1H), 7.69 (dd, J = 7.6 Hz, 1H), 7.64 – 7.54 (td, 1H), 7.58 – 7.54 (dd, 1H), 7.51 (dd, J = 1.6 Hz, 1H), 7.49 – 7.43 (td, 1H), 7.09 – 7.04 (td, 1H), 7.01 – 6.94 (dd, 1H), 2.19 (s, 1H). Anal. Calc. (%) For $C_{13}H_{11}N_3O_2$: C, 64.72 H, 4.60; N, 17.42. Found (%): C, 65.21; H, 4.66; N, 17.75.

Synthesis of *(E)-N'-(pyridin-2-ylmethylene) benzohydrazide* (AL02)

A mixture of 2-pyridinecarboxaldehyde (5 mmol, 0.5356 g) and bezohydrazide (5 mmol, 0.6808g) was prepared in 20 mL methanol. The reaction mixture was refluxed for 4 hours, and the solvent was concentrated using rotary evaporator. The concentrated product was cooled at room temperature until colorless precipitate formed. Yield: 66.7%. IR (KBr pellet, cm^{-1}): *v*(N-H) 3402 cm^{-1}, *v*(C=N) 1648 cm^{-1}, *v*(C=N) (pyridine) 1572 cm^{-1}, *v*(C=O) and 1651 cm^{-1}. ^{1}H NMR (500 MHz, DMSO) δ 8.57 (d, J = 75.9 Hz, 1H), 8.41 (s, 1H), 8.06 (d, J = 8.0 Hz, 1H), 7.88 (t, J = 6.5 Hz, 3H), 7.60 (t, J = 7.4 Hz, 1H), 7.52 (t, J = 7.6 Hz, 2H), 7.41 (dt, J = 31.4, 15.6 Hz, 1H), 2.06 (s, 1H). Anal. Calc. (%) For $C_{13}H_{11}N_3O$: C, 64.19; H, 5.39; N, 17.27. Found (%): C, 64.16; H, 5.33; N, 17.62.

Inhibition performance of corrosion inhibitors: Materials and electrolytes

Mild steel with surface area of 0.17 cm^2, 3.5% NaCl solution, CO_2 and N_2 to deoxygenate the solution [12]. Every experiment was carried out in unstirred, static solutions. Polishing Material, Potentiostat (Autolab, AUTO302N.FRA2 Netherlands), three electrode system glass cells with platinum electrode as counter electrode (CE), silver/silver chloride (Ag/AgCl) as reference electrode (RE) and mild steel as working electrode (WE). Tridentate hydrazone ligands (AL01 and AL02) were used as corrosion inhibitors.

Preparation of working electrode

The mild steel plate as working electrode was prepared by embedding the plate in epoxy resin, exposing a geometrical surface area of 0.17 cm^2 in 1000 mL of 3.5% NaCl solution saturated with CO_2 gas at pH 4-4.3. The metal plate was polished using various grade of SiC paper (300, 500 and 4000) prior to each experiment and degreased with ethanol and acetone.

Electrochemical impedance spectroscopy measurement (EIS)

Impedance measurements were performed after 15 min immersion of the metal plate in static condition at steady state open circuit potential at 25 ^oC [20] with slight modification. It was conducted in conventional three-electrode cell using platinum as the counter electrode and Ag/AgCl as the reference electrode. The AC current frequency range extended from 10 kHz to 0.1 Hz with 10 mV peak-to-peak amplitude. Electrochemical impedance spectroscopy generated Nyquist and Bode plots where the calculation of corrosion inhibition efficiency (IE %) of the inhibitors were calculated based on the R_p values using Equation 1,

$$IE\% = \left(\frac{R_{p(inh)} - R_{p(blank)}}{R_{p(inh)}}\right) x\ 100 \quad (1)$$

where $R_{p(blank)}$ and $R_{p(inh)}$ are the resistance charge transfer for bare mild steel and after the presence of inhibitor [1].

Polarization measurement

The corrosion behavior was further investigated through potentiodynamic polarization, immediately after the impedance spectra were recorded on the same metal plate without any additional surface treatment. The potentials were scanned at a scan rate of 0.5 mVs^{-1} from the corrosion potential (E_{corr}) in the cathodic direction and subsequently in the anodic direction. Potentiodynamic polarization gave the Tafel plot which was then extrapolated and corrosion inhibition efficiency (IE %) of the inhibitors was calculated based on the corrosion current density (i_{corr}) values using Equation 2,

$$IE\% = \left(\frac{i_{corr(0)} - i_{corr(i)}}{i_{corr(0)}}\right) x\ 100 \quad (2)$$

where $i_{corr(0)}$ and $i_{corr(i)}$ are the corrosion current densities for bare mild steel and after the presence of inhibitor [1].

Surface morphology analysis

The surface morphology and chemical composition were analyzed using scanning electron microscopy (SEM) coupled with energy dispersive X-ray spectroscopy (EDX) on the mild steel surfaces of samples that were immersed for 24 hours in 3.5% NaCl solution saturated with CO_2, with and without the presence of inhibitor at optimal concentration (500 ppm) [21].

Results and Discussion

Physical properties and elemental analysis

Table 1 displays physical characteristics of both ligands, and the experimental percentages of the elements C, H, and N of the compounds are closely corresponded to the theoretical values which proved their stoichiometry.

Table 1. Physical data for tridentate hydrazone ligands

Compound	Molecular Formula	Molecular Weight (g/mol)	Physical Properties	Melting Point (°C)	Elemental Analysis Found (Calculated) (%)		
					C	H	N
AL01	$C_{13}H_{11}N_3O_2$	241.25	White	225.8-227.3	**65.21** (64.72)	**4.66** (4.60)	**17.75** (17.42)
AL02	$C_{13}H_{11}N_3O$	225.25	Brown	111.0-113.6	**64.16** (64.19)	**5.33** (5.39)	**17.62** (17.27)

Infrared spectroscopy

The infrared spectra for AL01 shown in Figure 1, exhibit strong peak for *ν*(N-H), *ν*(C=N), *ν*(C=N) (pyridine), *ν*(C=O) at 3242 cm^{-1}, 1608 cm^{-1}, 1542 cm^{-1} and 1630 cm^{-1}, respectively. For AL02 spectra, the peaks for *ν*(N-H), *ν*(C=N), *ν*(C=N) (pyridine), *ν*(C=O) are at 3402 cm^{-1}, 1648 cm^{-1}, 1572 cm^{-1}, and 1651 cm^{-1}, respectively [22]. The stretching band for *ν*(C=N) of pyridine was at the lower frequency region compared to aliphatic *ν*(C=N) because of the N atom in the ring acts as an activating and electron-donating group which causes the absorption band to move to a lower frequency region by pushing the electron clouds towards the ring and increasing the electron density [21]. There was a broad absorption band of O-H for AL01 that appeared in the region of 3000 cm^{-1} [22]. Other prominent peaks for both ligands observed in Figure 1 are the C=C stretch (1466-1472 cm^{-1}), and the C-H sp^2 stretch (2925-2974 cm^{-1}), which indicate the existence of benzene rings in the structure [23].

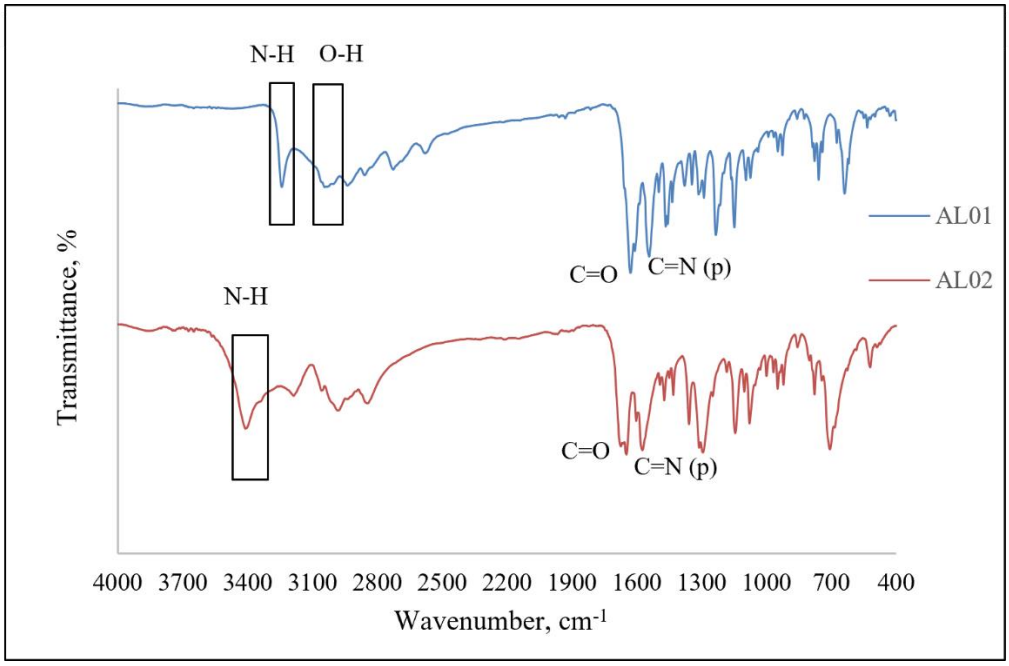

Figure 1. FTIR spectra of AL01 and AL02

Nuclear magnetic resonance spectroscopy

The ^{1}H NMR spectra for the ligand AL01 and AL02 were recorded in $CDCl_3$ and DMSO-d_6 respectively. Both ligands show a singlet peak at downfield region at 8.82 and 8.41 ppm, respectively, due to NH protons [24, 25] as shown in Figure 2(a) and Figure 2(b). For AL01 spectrum (Figure 2a), a singlet peak of phenolic proton appeared at 12.28 ppm strongly confirms the ligand structure [25]. The aromatic protons for benzene ring were observed in the range of 6.95-8.00 ppm for AL01 and in the range of 7.42-8.56 ppm for AL02 [26].

Ultraviolet-visible spectroscopy

The UV-Vis spectra of ligands AL01 and AL02 were measured at 5 x 10^{-5} M in acetonitrile between 190 to 450 nm. Two peaks in the absorption spectra of AL01 and AL02 in the range of 198-201 nm was due to the π-π*(C=C) transitions of aromatic rings [22]. However, for AL01 spectrum, there was a peak in the range of 205-210 nm which was assigned for n- π* transition as OH substituent at the *ortho* position was added to the benzene ring [27]. There was a weak band observed at 319 nm assigned for n-π* transition of C=N for AL01 while the peak for this transition was not found for AL02. There were also peaks of π-π* (C=N) transitions for AL01 at 302 nm and for AL02 at 299 nm. As shown in Figure 3, AL01 absorption is more bathochromic than AL02 because of the conjugated systems' effect from the OH functional group on the benzene ring. Hence, the absorption peaks appear at longer wavelengths compared to that of the benzene peak [27].

Liquid chromatography-mass spectrometry

The ligands AL01 and AL02 were characterized by LC-MS in the positive ion mode. When compared to the hypothesized structure, the mass spectrum of the ligand AL01 (Figure 4) exhibits a strong molecular ion peak at m/z = 242.09, which corresponds to the $[C_{13}H_{11}N_3O_2]+H^+$ (calculated RMM of AL01 = 241.25). Based on AL02 spectrum, an additional support for the structure was provided by the intense molecular ion peak at m/z = 226.10 corresponding to $[C_{13}H_{11}N_3O]+H^+$ which is in agreement with the molecular weight of the compound (225.25 g/mol) [28].

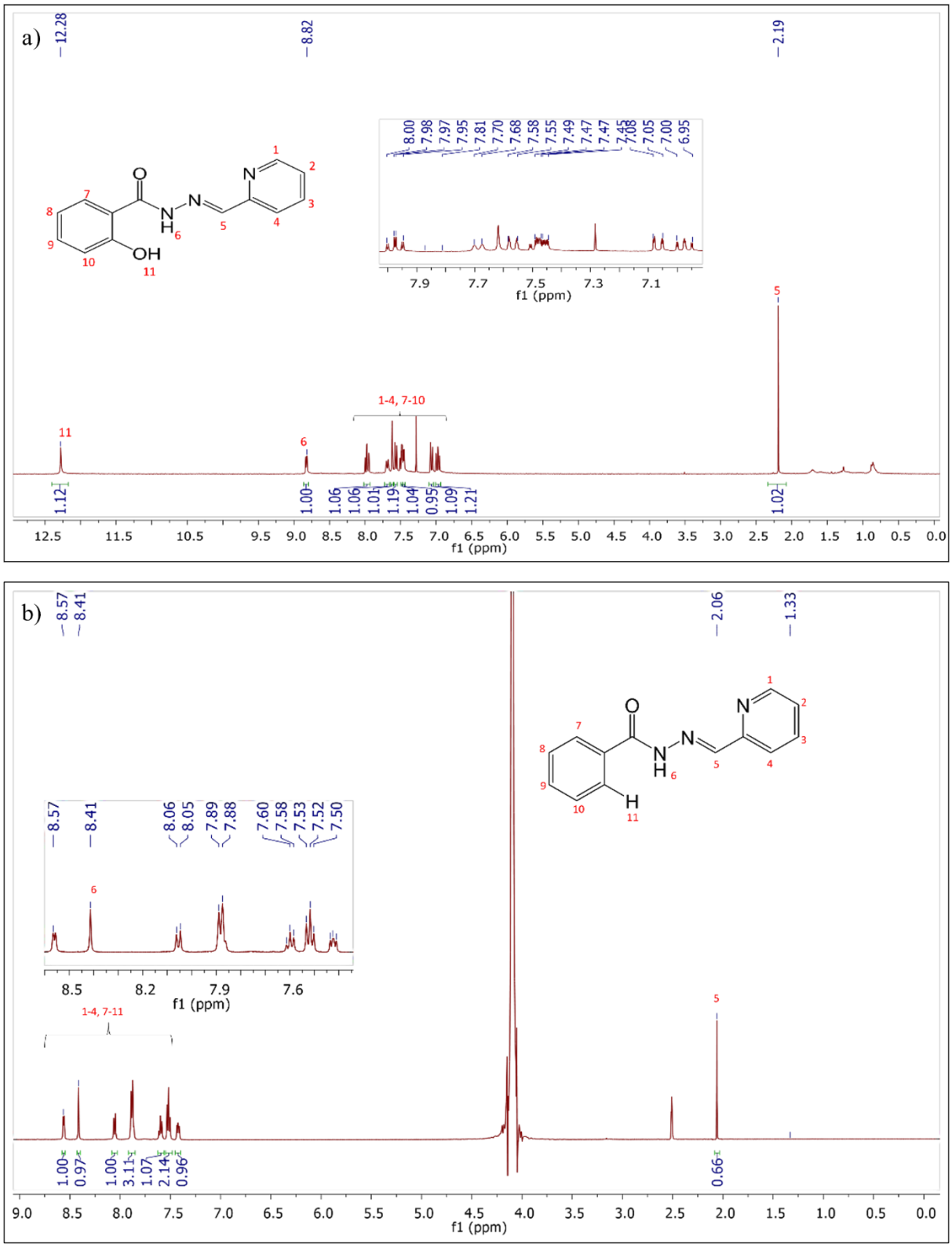

Figure 2. NMR spectra of a) AL01 and b) AL02

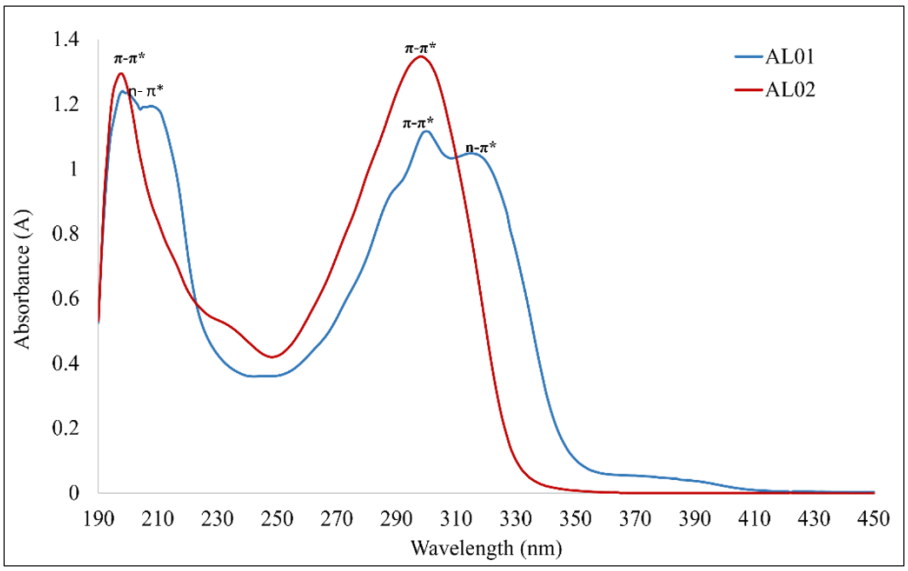

Figure 3. UV-Vis spectra of AL01 and AL02

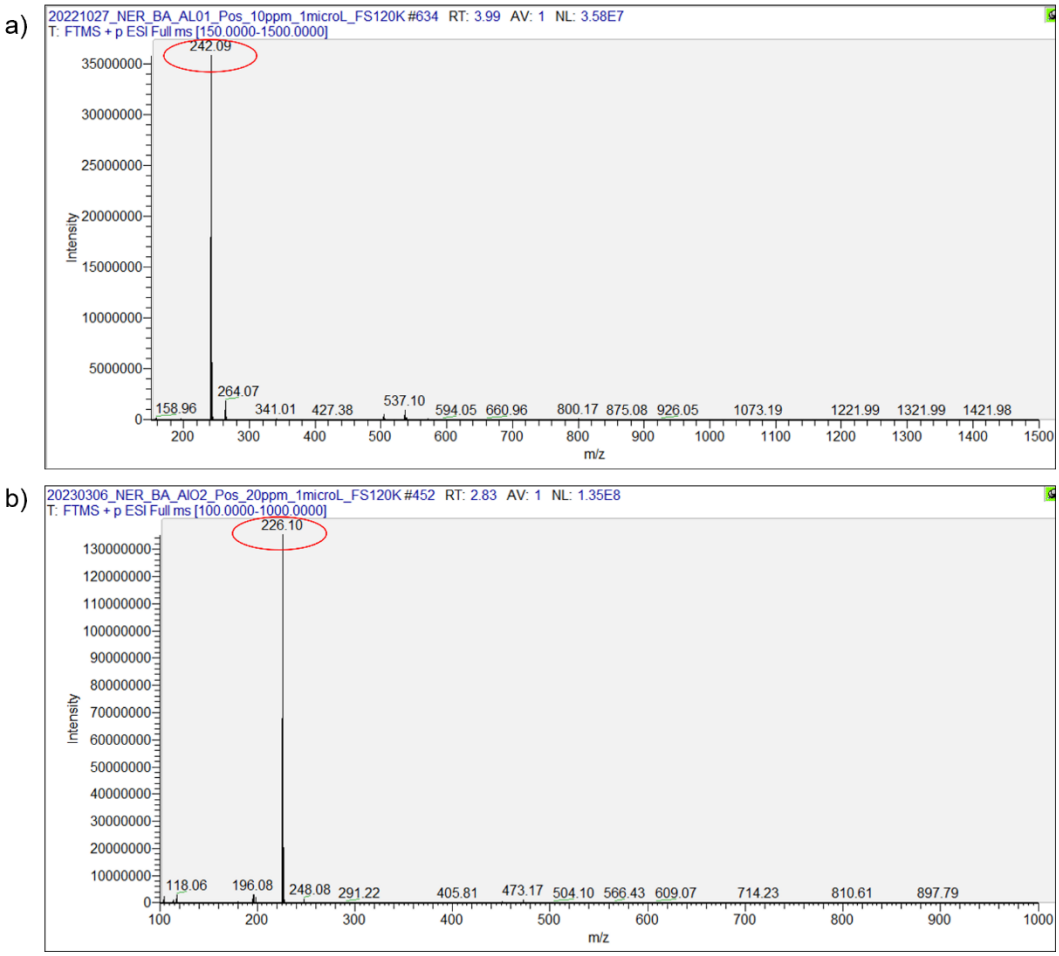

Figure 4. LC-MS spectra of a) AL01 and b) AL02

Inhibition performance of corrosion inhibitors: Potentiodynamic polarization (PDP)

Tafel extrapolation is a polarization technique to estimate corrosion rates that offers a faster alternative to traditional weight-loss method. The Tafel equation can be used to represent mixed potential theory using simple electrochemical kinetics, which can then be used to predict corrosion rate and potential based on the kinetics and thermodynamics of all reactions taking place on an electrode surface [29].

The potentiodynamic polarization parameters were computed using the Tafel extrapolation method. The corrosion rate values may be calculated using Equation 3, which is based on Faraday's equation [29]. Further on, the E_{corr} values were deducted from the intersection of the cathodic and anodic polarization curves [9].

$$\mathrm{CR\ (mpy)} = \frac{0.00327 \times i_{corr} \times EW}{\rho} \quad (3)$$

where i_{corr} is the corrosion current density in μA cm^{-2}, ρ is the density of the metal in g cm^{-3}, EW is the equivalent weight. Table 2 shows the potentiodynamic polarization parameters for the 3.5% NaCl solution, and the solutions with the presence of inhibitors.

Table 2. Potentiodynamic polarization parameters for blank, with presence of inhibitors AL01 and AL02

Compound	Concentration (ppm)	E_{corr} (V)	i_{corr} (μA/cm^2)	βa (V)	βc (V)	Corrosion Rate (mm/year)	Inhibition Efficiency (%)
Blank	3.5% NaCl	-0.6509	83.659	0.0502	-6.3902	0.9834	-
AL01	100	-0.6134	58.795	0.0356	0.1279	0.6912	30.00
	200	-0.5889	47.904	0.0300	0.1602	0.5631	42.74
	300	-0.6177	35.347	0.0618	0.2486	0.4155	57.75
	400	-0.6721	32.938	0.0409	0.3625	0.3872	60.63
	500	-0.6110	13.132	0.0463	0.2081	0.1544	84.30
AL02	100	-0.6583	43.790	0.0607	0.4808	0.5148	47.66
	200	-0.6989	38.570	0.0632	0.2813	0.4534	53.90
	300	-0.6733	34.502	0.0423	0.3106	0.4056	58.76
	400	-0.6729	34.025	0.0665	0.2524	0.4000	59.33
	500	-0.6426	21.002	0.0415	0.3638	0.2469	74.90

All data tabulated in Table 2 were originally obtained from Tafel plot as shown in Figure 5 below. It revealed that uncoated mild steel plate had the highest corrosion current density (i_{corr}), 83.659 μA/cm^2 and was therefore more prone to corrosion (active dissolution) [9]. Table 2 shows that there was a significant reduction in the corrosion current densities (i_{corr}) with increasing inhibitor concentration. In the presence of AL01 inhibitor, the value of i_{corr} decreased from 58.795 μA/cm^2 to 13.132 μA/cm^2, while in the presence of AL02, the value decreased from 43.790 μA/cm^2 to 21.002 μA/cm^2.

This was an obvious indication of how increasing inhibitor concentration resulted in an increasing number of hydrazone molecules to be adsorbed on the mild steel surface, inhibiting all forms of corrosion that were present at the metal-electrolyte interface [30]. The data proved that both inhibitors had an inhibitory impact on the aggressive mild steel solution, which effectively blocked the active site while the inhibitor was adsorbing to the mild steel surface [31]. Additionally, PDP data (Table 2) show that AL01 exhibits the highest level of inhibition, with an inhibition efficiency of 84.30%, followed by AL02 (74.90%).

This result was supported by the presence of OH functional group on the benzene ring in AL01 that could

enhance the adsorption process on the mild steel by increasing the molecule's electron charge density and molecule's binding affinity with the steel surface [12].

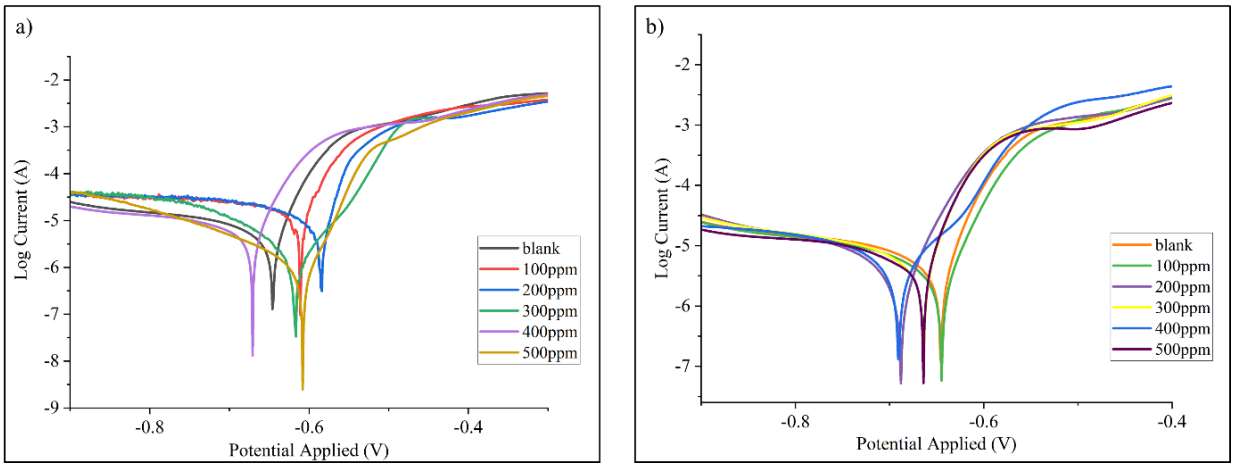

Figure 5. Tafel plots for ligands a) AL01 and b) AL02

The findings from Tafel plots (Figure 5) provided a helpful comparison of changes in potential corrosion values and the degree of corrosion current density reduction. This indicates that the corrosion reactions are inhibited [12]. When carbon dioxide gas dissolved in aqueous media, carbonic acid (H_2CO_3) was produced. Then, the bicarbonate ion (which could further dissociate to produce the carbonate ion) formed when the carbonic acid (H_2CO_3) partially dissociated. It has been widely recognized that, at the same pH, solutions containing H_2CO_3 would corrode mild steel more severely than solutions containing strong acids i.e., hydrochloric (HCl) or sulfuric (H_2SO_4) acids as they act as an additional source of hydrogen ions thus, lead to higher corrosion rates [11, 32].

Electrochemical impedance spectroscopy (EIS)

In addition, electrochemical impedance measurements were carried out to investigate the mechanisms of interaction between the electrode surface and the chemicals being studied, such as charge transfer, diffusion, and adsorption. Inhibitor adsorption on the metal substrate was corroborated by EIS studies, which also showed a rise in polarization resistance as the concentration of inhibitors increased [15]. Figure 6 shows Nyquist plots for mild steel at various concentrations of AL01 and AL02, in 3.5% NaCl solution saturated with CO_2.

Apparently, incomplete single depressed capacitive loops with nearly the same forms, both with and without inhibitors make up Nyquist plots, which show that the corrosion mechanism remains the same [17]. The non-homogeneity or roughness of the metal surface and the resistance to mass movement were the causes of the Nyquist plot's deviation from perfect semicircles, which was known as frequency dispersion. The semi-circle curve's diameter increased as the inhibitor concentration increased, demonstrating the inhibitor's ability to bind to mild steel forming a protective film over the metal surface [12, 31].

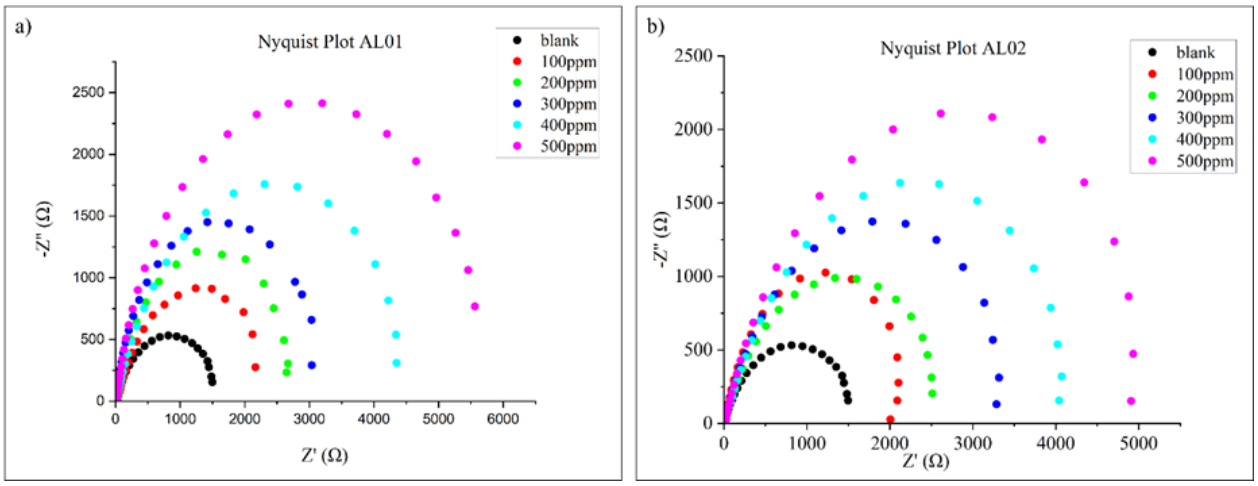

Figure 6. Nyquist plots for ligands a) AL01 and b) AL02

A basic Randle's circuit proposed in Figure 7 can be employed to represent the semi-circle Nyquist plots that were generated through the experiment. This circuit demonstrated that the charge transfer resistance (*Rp*) is parallel to the constant phase element (CPE) in series with the solution resistance (*Rs*) [31].

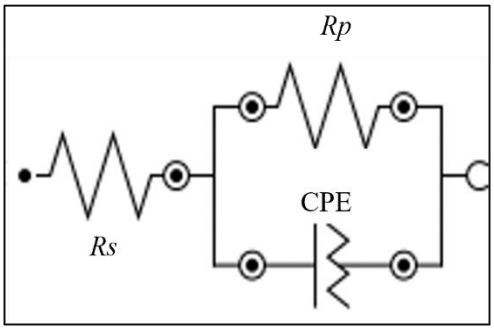

Figure 7. Simple Randle's circuit

Nyquist plots (Figure 6), indicate the samples' capacitive behavior, which consists of a single capacitive loop. The diameter of the Nyquist diagram represents the treated mild steel substrate's corrosion resistance (*Rp*, as indicated in EIS), which is correlated with the rate of corrosion. A greater semicircle diameter is indicative of a higher corrosion resistance, or a lower rate of corrosion. The resultant capacitive loop demonstrates that the charge transfer mechanism and the formation of a corrosion-inhibitory layer on the mild steel surface control the corrosion of mild steel in a 3.5% NaCl solution [9].

The impedance parameters obtained from Nyquist plots are presented in Table 3. The observed *Rp* values exhibited a significant increase in the presence of inhibitors, particularly at higher concentrations, in comparison to the *Rp* value obtained without the presence of an inhibitor. Consequently, the corrosion inhibition efficiency exhibited an increase. This behavior confirmed the formation of the protective film on mild steel. The observed trend in the diameter of the semi-circle curve indicates a positive correlation with the concentration of the inhibitor, hence, suggesting the occurrence of adsorption of the inhibitor on mild steel. This prevents the mild steel from corroding because the adsorbed layer formed hinders charge and mass transfers at the metal-inhibitor solution interface [31].

Table 2. Impedance parameter values for the corrosion of mild steel

Compound	Concentration (ppm)	Rs (Ω)	R_{ct} (Ω)	Inhibition Efficiency (%)
Blank	-	10.8	1596	-
AL01	100	29.8	2461	35.15
	200	35.84	2802	43.04
	300	16.9	3760	57.55
	400	13.1	4749	66.39
	500	19.4	5883	72.87
AL02	100	12.7	2185	26.96
	200	11.0	2781	42.61
	300	11.9	3700	56.86
	400	10.5	4545	64.88
	500	14.7	5529	71.13

The Nyquist plots and impedance data presented in Table 3 indicate that the corrosion resistance of both inhibitors was found to be improved by increasing the concentration to 500 ppm. The mild steel immersed in 3.5% NaCl solution with 500 ppm inhibitors produced the biggest semi-circle diameter, as shown in Figure 6. Furthermore, comparing AL01 and AL02, the diameter of the Nyquist plot was bigger for AL01 at 500 ppm suggesting a better corrosion resistance i.e., a more robust inhibitive layer [9].

SEM-EDX Analysis

Scanning electron microscopy (SEM) was employed to examine the morphology of the metal surface and the development of the protective film on the surface of mild steel. Following the inhibitors' binding, the steel surface was seen to be smoother [33]. Figure 8 shows the SEM micrographs for mild steel after 24 hours immersion in 3.5% NaCl solution with and without the presence of corrosion inhibitors.

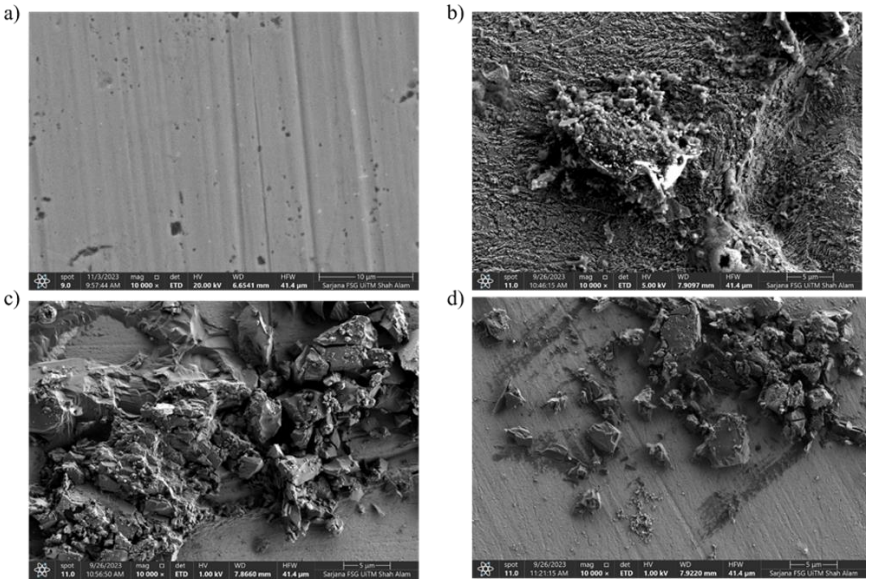

Figure 8. SEM micrographs of a) bare mild steel, (b) 3.5% NaCl solution, c) solution with 500 ppm of AL01 and d) solution with 500 ppm of AL02

Due to the manual abrasion process used during the polishing phase of the panels, scratch marks were apparent on the mild steel's exposed surface [9]. From observation, untreated mild steel plate in 3.5% NaCl solution (blank) (b) had a much rougher surface compared to surfaces with the presence of AL01 and AL02, which were substantially smoother. SEM examination confirmed that the presence of hydrazone ligands in the solution offered efficient corrosion retardation with the least amount of surface damage [9]. This is due to the formation of an adsorption layer that minimizes the effects of corrosion although the steel's surface treatment still left some residual scratches and polishing lines as in Figure 8(a) [34].

Energy dispersive X-ray spectroscopy (EDX) was used to evaluate the protective mechanism of inhibitors to find reductions in peaks related to iron, carbon, and chloride which are markers for metal corrosion [33]. According to the EDX study (Table 4), Fe, C and small traces of Si were detected as elements in bare mild steel. Noticeably, Fe content was decreased when treated with AL01 and AL02 from 97.25% to 82.19 wt.% and 95.35 wt.% respectively. This indicates the adsorption of inhibitors on the surface of the mild steel thus, reducing the Fe content [9]. For untreated mild steel there was a presence of Cl, signifying a corrosion attack from NaCl solution in aggressive environment [35]. However, when comparing the weight percentage (wt.%) (Table 4) of Cl element in the presence of inhibitors with that of the blank, there was no Cl detected when the inhibitors were present. This observation demonstrates the adsorption of inhibitors on the mild steel surface where elements such as C, N and O correspond to the inhibitor's composition, which were found on the mild steel immersed in the presence of AL01 and AL02 inhibitors. These are essential for stabilizing the molecule at the surface, which enhance the ability of the steel to resist corrosion [33, 35]. Hence, compared to AL02, which agrees with the data in Table 4, AL01 had a higher capacity to build a protective film corrosion because of its strong electron-donating ability due to the presence of OH functional group [19].

Table 3. Weight percentage of elements in mild steel specimen obtained from EDX spectra

Mild Steel Specimen	Fe (wt.%)	C (wt.%)	Si (wt.%)	Cl (wt.%)	Na (wt.%)	O (wt.%)	N (wt.%)
Bare mild steel	97.25	2.10	0.65	-	-	-	-
Untreated mild steel	75.51	1.89	-	6.28	15.37	0.95	-
Treated with AL01	82.19	13.60	-	-	-	2.47	1.74
Treated with AL02	95.35	3.23	-	-	-	1.07	0.35

Conclusion

New corrosion inhibitors of tridentate hydrazone ligands, AL01 and AL02 were successfully synthesized via condensation process derived from two different substituents of hydrazides. The ligands were characterized using FTIR, NMR, elemental analysis, mass spectroscopy and UV-Vis. From polarization and EIS study, it can be concluded that AL01 has the highest inhibition efficiency, 84.30% at 500 ppm compared to 74.90% of AL02. SEM-EDX analysis has confirmed the formation of inhibitors' layer on mild steel as the surface of the mild steel with the presence of inhibitors is smoother compared to that of the untreated mild steel in 3.5% NaCl solution saturated with CO_2. Hence, compared to AL02, AL01 has a higher inhibitory efficacy and the compound formed a stronger protective layer on the mild steel as the compound contains electron donating group (OH).

Acknowledgement

The authors express their gratitude to the Malaysian Ministry of Higher Education for providing the research funding under the grant FRGS/1/2021/STG04/UITM/02/21. Additionally, the authors would like to acknowledge the support and research facilities provided by Universiti Teknologi MARA Shah Alam and AuRIns, UiTM Puncak Alam.

References

1. Mashitah A., N., Athena Z., F. and Hazwan H., M.

(2021). The study of electroless Ni-Cu-P plating on corrosion resistance of aluminium in 3.5% NaCl physicochemical characteristics of microcrystalline cellulose and cellulose nanowhiskers from lignocellulosic biomass. *International Journal Electroactive Materials*, 9: 12-26.

2. Sulzer Pumps. (2010). Materials and corrosion. *Centrifugal Pump Handbook*: pp. 227-250.
3. Jafar M. M. A. (2020). Global impact of corrosion: Occurrence, cost and mitigation. *Global Journal of Engineering Sciences*, 5(4): 1-4.
4. Tamalmani, K. and Husin, H. (2020). Review on corrosion inhibitors for oil and gas corrosion issues. *In Applied Sciences*, 10(10): 3389,
5. Adam, M. S. S., Soliman, K. A. and Abd El-Lateef, H. M. (2020). Homo-dinuclear VO^{2+} and Ni^{2+} dihydrazone complexes: Synthesis, characterization, catalytic activity and CO_2-corrosion inhibition under sustainable conditions. *Inorganica Chimica Acta*, 499(9): 119212.
6. Askari, M., Aliofkhazraei, M. and Afroukhteh, S. (2019). A comprehensive review on internal corrosion and cracking of oil and gas pipelines. *Journal of Natural Gas Science and Engineering*, 71: 102971.
7. Oyekunle, D. T., Agboola, O. and Ayeni, A. O. (2019). Corrosion inhibitors as building evidence for mild steel: A review. *Journal of Physics: Conference Series*, 1378(3).
8. Usman, B. J., Umoren, S. A. and Gasem, Z. M. (2017). Inhibition of API 5L X60 steel corrosion in CO_2-saturated 3.5% NaCl solution by tannic acid and synergistic effect of KI additive. *Journal of Molecular Liquids*, 237: 146-156.
9. Hamidon, T. S. and Hussin, M. H. (2020). Susceptibility of hybrid sol-gel (TEOS-APTES) doped with caffeine as potent corrosion protective coatings for mild steel in 3.5 wt.% NaCl. *Progress in Organic Coatings*, 140: 105478.
10. Lin, B., Tang, J., Wang, Y., Wang, H. and Zuo, Y. (2020). Study on synergistic corrosion inhibition effect between calcium lignosulfonate (CLS) and inorganic inhibitors on Q235 carbon steel in alkaline environment with Cl−. *Molecules*, 25(18): 4200.
11. George, K. S. and Nes, S. (1944). Investigation of carbon dioxide corrosion of mild steel in the presence of acetic acid-part 1: basic mechanisms. *Corrosion Science Section Corrosion-February* 2007: 1-30.
12. Singh, A., Ansari, K. R., Xu, X., Sun, Z., Kumar, A. and Lin, Y. (2017). An impending inhibitor useful for the oil and gas production industry: Weight loss, electrochemical, surface and quantum chemical calculation. *Scientific Reports*, 7(1): 14904.
13. Das Chagas Almeida, T., Bandeira, M. C. E., Moreira, R. M. and Mattos, O. R. (2017). New insights on the role of CO_2 in the mechanism of carbon steel corrosion. *Corrosion Science*, 120: 239-250.
14. Chaouiki, A., Chafiq, M., Lgaz, H., Al-Hadeethi, M. R., Ali, I. H., Masroor, S. and Chung, I. M. (2020). Green corrosion inhibition of mild steel by hydrazone derivatives in 1.0 M HCl. *Coatings*, 10(7): 1-17.
15. Saady, A., Rais, Z., Benhiba, F., Salim, R., Ismaily Alaoui, K., Arrousse, N., Elhajjaji, F., Taleb, M., Jarmoni, K., Kandri Rodi, Y., Warad, I. and Zarrouk, A. (2021). Chemical, electrochemical, quantum, and surface analysis evaluation on the inhibition performance of novel imidazo[4,5-b] pyridine derivatives against mild steel corrosion. *Corrosion Science*, 189(7): 109621.
16. Subbiah, K., Lee, H.-S., Al-Hadeethi, M. R., Park, T. and Lgaz, H. (2023). Unraveling the anti-corrosion mechanisms of a novel hydrazone derivative on steel in contaminated concrete pore solutions: An integrated study. *Journal of Advanced Research*, 8: 16.
17. Khamaysa, O. M. A., Selatnia, I., Zeghache, H., Lgaz, H., Sid, A., Chung, I. M., Benahmed, M., Gherraf, N., and Mosset, P. (2020). Enhanced corrosion inhibition of carbon steel in HCl solution by a newly synthesized hydrazone derivative: Mechanism exploration from electrochemical, XPS, and computational studies. *Journal of Molecular Liquids*, 315: 113805.
18. Ansari, K. R., Chauhan, D. S., Singh, A., Saji, V. S. and Quraishi, M. A. (2020). Corrosion inhibitors for acidizing process in oil and gas sectors. *Corrosion Inhibitors in the Oil and Gas Industry*, 2020: 153-

176.

19. Khamaysa, O. M. A., Selatnia, I., Lgaz, H., Sid, A., Lee, H. S., Zeghache, H., Benahmed, M., Ali, I. H. and Mosset, P. (2021). Hydrazone-based green corrosion inhibitors for API grade carbon steel in HCl: Insights from electrochemical, XPS, and computational studies. *Colloids and Surfaces A: Physicochemical and Engineering Aspects*, 626: 127047.
20. Boukazoula, S., Haffar, D., Bourzami, R., Toukal, L. and Dorcet, V. (2022). Synthesis, characterizations, crystal structure, inhibition effects and theoretical study of novel Schiff base on the corrosion of carbon steel in 1 M HCl. *Journal of Molecular Structure*, 1261: 132852.
21. Kamal, N. K. M., Fadzil, A. H., Kassim, K., Rashid, S. H. and Mastuli, M. S. (2014). Synthesis, characterization and corrosion inhibition studies of o, m, p-decanoyl thiourea derivatives on mild steel in 0.1 M H_2SO_4 solutions. *Malaysian Journal of Analytical Sciences*, 18(1): 21-27.
22. Latifah R., H., Bahron, H., Ramasamy, K. and Tajuddin, A. M. (2019). Synthesis and characterization of benzohydroxamic acid and methylbenzohydroxamic acid metal complexes and their cytotoxicty study. *Malaysian Journal of Analytical Sciences*, 23(2), 263-273.
23. Shahrul Nizam, A., Bahron, H. and Tajuddin, A. M. (2019). Effect of temperature on the catalytic activity of new symmetrical tetradentate palladium(II) schiff base complexes in copper-free sonogashira reaction. *Malaysian Journal of Analytical Sciences*, 23(2): 247-254.
24. Gao, H., Li, J. Q., Kang, P. W., Chigan, J. Z., Wang, H., Liu, L., Xu, Y. S., Zhai, L. and Yang, K. W. (2021). N-acylhydrazones confer inhibitory efficacy against New Delhi metallo-β-lactamase-1. *Bioorganic Chemistry*, 114: 105138.
25. Kant, R., Yang, M. H., Tseng, C. H., Yen, C. H., Li, W. Y., Tyan, Y. C., Chen, M., Tzeng, C. C., Chen, W. C., You, K., Wang, W. C., Chen, Y. L. and Chen, Y. M. A. (2021). Discovery of an orally efficacious MYC inhibitor for liver cancer using a GNMT-based high-throughput screening system and structure-activity relationship analysis. *Journal of Medicinal Chemistry*, 64(13): 8992-9009.
26. Singh, Y., Patel, R. N., Patel, S. K., Patel, A. K., Patel, N., Singh, R., Butcher, R. J., Jasinski, J. P. and Gutierrez, A. (2019). Experimental and quantum computational study of two new bridged copper(II) coordination complexes as possible models for antioxidant superoxide dismutase: Molecular structures, X-band electron paramagnetic spectra and cryogenic magnetic properties. *Polyhedron*, 171: 155-171.
27. Bononi, F. C., Chen, Z., Rocca, D., Andreussi, O., Hullar, T., Anastasio, C. and Donadio, D. (2020). Bathochromic shift in the UV-visible absorption spectra of phenols at ice surfaces: Insights from first-principles calculations. *Journal of Physical Chemistry A*, 124(44): 9288-9298.
28. Khaidir, S. S., Bahron, H., Tajuddin, A. M. and Ramasamy, K. (2022). Microwave-assisted synthesis, characterization and anticancer activity of tetranuclear Schiff base complexes. *Journal of Sustainability Science and Management*, 17(4): 32-48.
29. Kakaei, K., Esrafili, M. D. and Ehsani, A. (2019). Graphene and anticorrosive properties. *In Interface Science and Technology*, (Vol. 27, pp. 303-337). Elsevier.
30. Lgaz, H., Chung, I. M., Albayati, M. R., Chaouiki, A., Salghi, R. and Mohamed, S. K. (2020). Improved corrosion resistance of mild steel in acidic solution by hydrazone derivatives: An experimental and computational study. *Arabian Journal of Chemistry*, 13(1): 2934-2954.
31. Hazani, N. N., Mohd, Y., Ghazali, S. A. I. S. M. and Dzulkifli, N. N. (2019). Electrochemical studies of thiosemicarbazone derivative and its tin(IV) complex as corrosion inhibitor for mild steel in 1 M hydrochloric acid. *Chemistry Journal of Moldova*, 14(1): 98-106.
32. Rustandi, A., Adyutatama, M., Fadly, E. and Subekti, N. (2012). Corrosion rate of carbon steel for flowline and pipeline as transmission pipe in natural gas production with CO_2 content. *Makara Journal of Technology*, 16(1): 57-62.
33. Chafiq, M., Chaouiki, A., Al-Hadeethi, M. R., Ali, I. H., Mohamed, S. K., Toumiat, K. and Salghi, R. (2020). Naproxen-based hydrazones as effective corrosion inhibitors for mild steel in 1.0 M HCl.

Coatings, 10(7): 700.

34. Lgaz, H., Chaouiki, A., Albayati, M. R., Salghi, R., El Aoufir, Y., Ali, I. H., Khan, M. I., Mohamed, S. K. and Chung, I. M. (2019). Synthesis and evaluation of some new hydrazones as corrosion inhibitors for mild steel in acidic media. *Research on Chemical Intermediates*, 45(4): 2269-2286.
35. El-Haddad, M. A. M., Bahgat Radwan, A., Sliem, M. H., Hassan, W. M. I. and Abdullah, A. M. (2019). Highly efficient eco-friendly corrosion inhibitor for mild steel in 5 M HCl at elevated temperatures: experimental & molecular dynamics study. *Scientific Reports*, 9(1): 1-15.

Malaysian Journal of Analytical Sciences (MJAS)
Published by Malaysian Analytical Sciences Society

IONIC TRANSPORT AND STRUCTURAL ANALYSIS OF BIOPOLYMER ELECTROLYTE BASED ON AGAROSE INTEGRATED WITH SODIUM NITRATE

(Kajian Pengangkutan Ion dan Struktur kepada Elektrolit Biopolimer Berdasarkan Penggabungan antara Agarose dan Natrium Nitrat)

Nur Farisha Sulthan Hussain[1], Siti Zafirah Zainal Abidin[1,2*], Nora Aishah Ahmad Shaharuddin[1], Raja Nur Qurratu Ain Raja Syiarizzad[1], Siti Rudhziah Che Balian[3]

[1]Faculty of Applied Sciences, Universiti Teknologi MARA, 40450 Shah Alam, Selangor, Malaysia
[2]Ionic Materials and Devices (iMADE) Research Laboratory, Institute of Science, Universiti Teknologi MARA, 40450 Shah Alam, Selangor, Malaysia
[3]Centre of Foundation Studies, Universiti Teknologi MARA, Cawangan Selangor, Kampus Dengkil, Dengkil 43800, Selangor, Malaysia

[*]Corresponding author: szafirah@uitm.edu.my

Received: 15 September 2023; Accepted: 30 December 2023; Published: 28 February 2024

Abstract

The central focus of this paper revolves around investigating biopolymer electrolyte films characterized by exceptional ionic conductivity, a prerequisite for the practical implementation of sodium-ion batteries. This study successfully prepared the agarose-based biopolymer electrolyte using the solution casting method. The effects of adding various weight percentages (0, 10, 20, 30 and 40 wt.%) of sodium nitrate salt ($NaNO_3$) to agarose-based biopolymer electrolytes were characterized. Electrochemical Impedance Spectroscopy (EIS) was adapted to analyze the conductivity and dielectric relaxation phenomena of the agarose-$NaNO_3$ complex. The conductivity of agarose-based biopolymer electrolytes increases with the increasing salt concentration. The increase in ionic conductivity is due to the increase in the number of charge carriers and the mobility of the sodium ions. The highest room temperature conductivity was 3.44×10^{-5} S·cm^{-1} for the agarose-$NaNO_3$ biopolymer electrolytes containing 30 wt.% sodium nitrate. X-ray diffractometer (XRD) spectroscopy was employed to investigate the crystallinity of the agarose-based biopolymer electrolyte. It was confirmed that the agarose-based biopolymer with 30 wt.% of sodium nitrate is the most amorphous compared to the others, as it has the largest full width at half maximum (FWHM) and the smallest crystallite size. This indicated that the amorphousness of the biopolymer electrolyte boosts the Na^+ ions' mobility, increasing the ionic conductivity of the samples.

Keywords: biopolymer electrolyte, agarose, sodium nitrate, conductivity, dielectric constant, crystallite size

Abstrak

Tumpuan utama dalam artikel ini adalah berkisar tentang penyelidikan untuk filem electrolit biopolymer yang dicirikan oleh kekonduksian ionik yang luar biasa, prasyarat untuk pelaksanaan praktikal dalam bateri natrium-ion. Dalam kajian ini, elektrolit biopolimer berasaskan agarosa telah disediakan dengan jayanya menggunakan kaedah penuangan larutan. Kesan penambahan pelbagai peratusan berat (0, 10, 20, 30 dan 40 wt.%) garam natrium nitrat ($NaNO_3$) kepada elektrolit biopolimer berasaskan agarosa

dicirikan. Spektroskopi impedans elektrokimia (EIS) telah disesuaikan untuk menganalisis fenomena masa pengenduran kekonduksian dan dielektrik kompleks agarosa-$NaNO_3$. Kekonduksian elektrolit biopolimer berasaskan agarosa meningkat dengan kepekatan garam yang semakin meningkat. Peningkatan kekonduksian ionik adalah disebabkan oleh peningkatan bilangan pembawa cas dan mobiliti ion natrium. Kekonduksian suhu bilik tertinggi ialah 3.44×10^{-5} $S\cdot cm^{-1}$ untuk elektrolit biopolimer agarose-$NaNO_3$ yang mengandungi 30 wt.% natrium nitrat. Spektroskopi pembelauan sinar-X (XRD) digunakan untuk menyiasat kehabluran elektrolit biopolimer berasaskan agarosa. Telah disahkan bahawa biopolimer berasaskan agarosa dengan 30 wt.% natrium nitrat adalah yang paling amorf berbanding yang lain, kerana ia mempunyai lebar penuh terbesar pada separuh maksimum (FWHM) dan saiz hablur halus terkecil. Ini menunjukkan bahawa amorfus elektrolit biopolimer meningkatkan mobiliti ion-ion Na^+ sekali gus meningkatkan kekonduksian ionik sampel.

Kata kunci: elektrolit biopolimer, agarose, natrium nitrat, kekonduksian, pemalar dielektrik, saiz kristal

Introduction

Sodium-ion batteries offer promise as a feasible choice for large-scale energy storage owing to their advantages, such as the plentiful availability and cost-effectiveness of sodium-based components. The same organic liquid electrolytes used in lithium-ion batteries also contribute to continued safety issues, such as the risk of fire [1]. Polymer electrolytes provide an attractive alternative to liquid electrolytes, boosting sodium-ion batteries' safety. To ensure the success of this technique, all other battery components must be further developed. Electrolytes are essential to sodium batteries since they facilitate the transit of ions inside the cell. Polymers containing amorphous polymer-salt complexes are leading candidates to replace liquid electrolytes. This is because of its good temperature stability, large electrochemical window, and low electrolyte solution leakage.

Biopolymer electrolytes have gained significant attention in the field of sodium battery technology. These electrolytes are composed of natural biopolymers, such as agarose [2], chitosan [3], and alginate [4], which offer several advantages over traditional polymer or liquid electrolytes. Biopolymer electrolytes are environmentally friendly since they are derived from renewable sources. This makes them a sustainable alternative to conventional materials used in batteries. Additionally, these biopolymers possess good mechanical properties and high ionic conductivity, allowing for efficient ion transport within the battery system. A high concentration of functional groups allows for strong coordination interactions between ions and polymers. This leads to improved electrochemical performance, enhanced cycling stability, increased specific capacity retention rates, and low charge transfer resistance at electrode-electrolyte interfaces [5].

Agarose is a biopolymer from seaweed used as a host polymer to conduct ions. Biopolymer electrolytes based on agarose are an excellent potential replacement for synthetic-based polymer electrolytes in electrochemical devices [2]. Fossil fuels play a crucial role in producing synthetic polymers. However, substituting agarose for these synthetic materials can help reduce our reliance on fossil fuels, preserving them for future generations when their scarcity might pose a significant challenge. Fossil fuel formation is a time-consuming process, and our current consumption rate could eventually deplete this finite resource if we do not adopt more sustainable practices [6].

Adding sodium nitrate ($NaNO_3$) improves ionic conductivity in polymer electrolytes because it breaks down into sodium ions (Na^+) and nitrate ions (NO_3^-) when mixed with the polymer. These ions help electric charges move easily through the polymer's ion channels. This addition also boosts bulk and surface conductivities, as shown in X-ray studies revealing a stronger bond between $NaNO_3$ and the polymer, improving ion-polymer interactions and mobility [7]. Using sodium nitrate salts as dopant in polymer electrolytes has much potential to improve their performance in batteries. By interacting with polymers, these additives increase ionic conductivity, making it easier for charges to move while keeping the structure intact at normal temperatures.

This study is about cultivating a biopolymer electrolyte that combines agarose and sodium nitrate. The biopolymer electrolytes that will be utilized in this research are biopolymer electrolytes, which possess a greater conductivity when compared to solid polymer electrolytes. Thin films of biopolymer electrolytes will be produced and studied in this research. The thin films will be subjected to two methods of characterization of biopolymer electrolytes: Electrochemical Impedance Spectroscopy (EIS) to investigate ionic conduction analysis and X-ray Diffractometer (XRD) to determine the structural properties.

Materials and Methods

Preparation of biopolymer electrolyte

The biopolymer, agarose (molecular weight, Mw: 630.5 $g \cdot mol^{-1}$), was acquired from Next Gene in Puchong, Malaysia. Meanwhile, sodium nitrate ($NaNO_3$; Mw: 84.99 $g \cdot mol^{-1}$) as a dopant was attained from Chemiz (M) Sdn. Bhd. in Shah Alam, Selangor. Fisher Scientific, which is in Hampton, NH, USA, was where dimethyl sulfoxide (DMSO) (Mw: 256.41 $g.mol^{-1}$, ≥99.7%), which acts as a solvent, was obtained. The biopolymer electrolyte with a base of agarose and the integration of sodium nitrate was prepared using the method of solution casting. Firstly, 0.5 g of agarose was dissolved in 20 ml of the solvent dimethyl sulfoxide (DMSO). Next, sodium nitrate of different concentrations were added to the solution containing agarose and DMSO. The different concentrations of sodium nitrate are based on the weight percentages of 0, 10, 20, 30 and 40. The solution was stirred continuously at room temperature (300 K) using a magnetic stirrer at room temperature until a homogenous solution was obtained. The solution was cast on a petri dish and the sample was left to dry. The sample was dried in an oven to speed up the process of evaporation. The solvent that underwent evaporation was primarily composed of dimethyl sulfoxide, and upon its complete volatilization, autonomous biopolymer electrolyte films were effortlessly detached from the petri dishes, a visual representation of which is depicted in Figure 1.

Characterization of biopolymer electrolyte

The thin films of biopolymer electrolytes were characterized, and their ionic conductivity and electrical properties were analyzed based on impedance data from Electrochemical Impedance Spectroscopy. The apparatus that was used for this is the HIOKI 3532-50 LCR Hi-tester. The apparatus is consolidated with a computer of the frequency ranging between 100 Hz and 10 MHz at varying temperatures (303-373 K). The ionic conductivity, σ of an electrolyte, can be calculated using the formula in Equation 1. The distance between the electrodes in centimeters (cm) is t. At the same time, A is the contact area of the electrolyte and the electrodes in square centimeters (cm^2), whereas R_b is the bulk resistance of the sample electrolyte. Equation 1 can also be used to determine the ionic conductivity of a polymer electrolyte in the form of a thin film.

$$\sigma = \frac{t}{R_b A} \quad (1)$$

The thin films of the biopolymer electrolytes were characterized using X-ray diffractometer spectroscopy. Other than that, the structural behavior of the thin films was observed to identify the existence of amorphous and crystalline peaks in the thin films. The nature of the thin films, whether crystalline or amorphous, was determined. The apparatus in use for this is the PANalytical X'pert PRO diffractometer. The diffractometer has a copper K-alpha (Cu K-α) radiation of wavelength (λ) equal to 1.5418 Å. The angle of diffraction (2θ) of the diffractometer was set between 5° to 90° at room temperature.

Figure 1. The stand-alone thin film of agarose-$NaNO_3$ biopolymer electrolyte.

Results and Discussion

Conductivity analysis at room temperature

Impedance plot (Figure 2) of biopolymer electrolyte with 30 wt.% $NaNO_3$ shows a smaller depressed semicircle in the high-frequency region by comparing with 40 wt.%, and both samples containing an inclined spike in the low-frequency region. The semicircle indicates ionic conduction within the electrolyte, while the spike is linked to the impact of blocking electrodes. This impedance analysis employed blocking electrodes, creating a double-layer capacitance at the interface between the electrodes and the electrolyte.

The value of the bulk constant, $R_{b,}$ for each sample at different weight percentages was determined by finding the value on the real impedance, the Z_r axis at which the semi-circular arc converges with the spike. The value of the bulk constant is observed to be reduced as the weight percentage of the samples increases from 0 to 30 wt. %. The bulk constant, R_b, then increases as the weight percentage of the sample rises to 40 wt.%.

Table 1 and Figure 3 demonstrate the ionic conductivity of the samples with different weight percentages of $NaNO_3$ at room temperature. The ionic conductivity of the agarose-based biopolymer electrolyte starts at 1.21×10^{-9} $S\cdot cm^{-1}$ when devoid of $NaNO_3$ (0 wt.%), which shows that polymer agarose is the best choice for host polymer as it satisfies the conductivity ranges for pure polysaccharides biodegradable materials from $\sim 10^{-14}$ to 10^{-8} $S.cm^{-1}$ [8]. Steadily escalating to 3.69×10^{-7} $S\cdot cm^{-1}$ at 10 wt.% of $NaNO_3$, with a continuous ascent peaking at the highest conducting of 3.44×10^{-5} $S\cdot cm^{-1}$ at 30 wt. %. However, beyond this concentration, the ionic conductivity experiences a decline, diminishing to 6.84×10^{-7} $S\cdot cm^{-1}$ at 40 wt.%.

The enhancement of ionic conductivity is attributed to the higher number of ion dissociation events obtained because of the addition of $NaNO_3$ from 0 to 30 wt.% into the agarose-based polymer electrolyte system that results in the production of free ions (Na^+ cation and NO_3^- anion) that can be incorporated in the polymer host matrix [9]. Therefore, a high salt concentration promotes the degree of ion dissociation, thus increasing the ionic conductivity of the agarose-$NaNO_3$ biopolymer electrolyte system. On the other hand, the increase in the amorphous nature of the system also affects the enhancement of ionic conductivity. It leads to the flexibility of the agarose polymer chain and promotes segmental motion in this system. However, when ions are abundant in the samples, the viscosity increases, which leads to the formation of ion cluster carriers that cause a decline in both the number of ions and their mobility, which impedes ion movement. Therefore, the ionic conductivity of the samples is reduced to 40 wt.% of $NaNO_3$ because of the change in the flow of charge carriers [2].

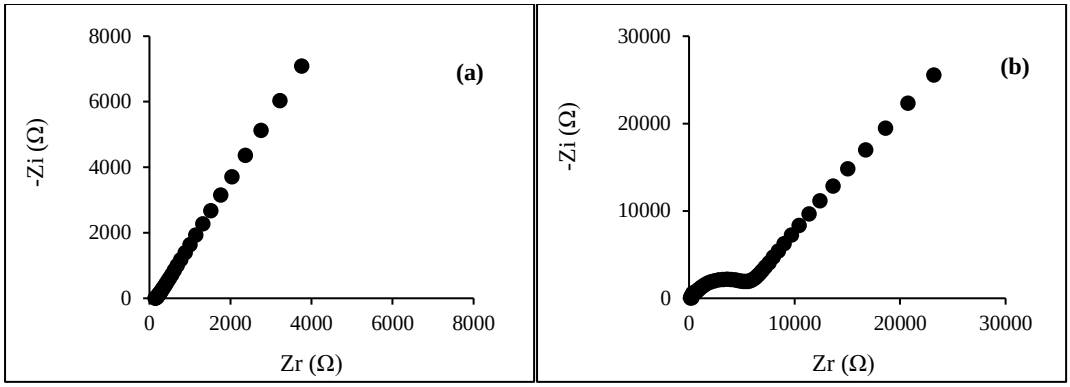

Figure 2. Impedance plot of agarose-based biopolymer electrolyte containing (a) 30 wt.% and (b) 40 wt.% $NaNO_3$ at room temperature.

Table 1. The bulk resistance and conductivity values of respected biopolymer electrolyte

$NaNO_3$ Content (wt. %) in Biopolymer Electrolyte	**Bulk resistance, R_b (Ω)**	**Conductivity, σ ($S \cdot cm^{-1}$)**
0	4.96×10^{7}	1.21×10^{-9}
10	8.33×10^{4}	3.69×10^{-7}
20	2.85×10^{3}	1.67×10^{-5}
30	9.57×10^{1}	3.44×10^{-5}
40	5.58×10^{3}	6.84×10^{-7}

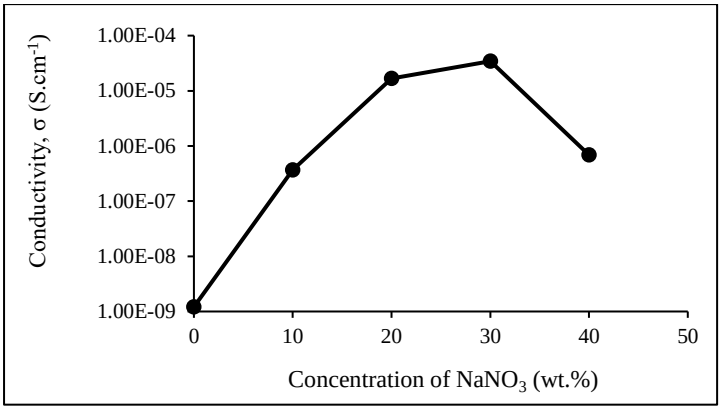

Figure 3. Conductivity plot of agarose-based biopolymer electrolyte containing $NaNO_3$ at room temperature

Temperature dependence conductivity analysis

One of the preliminary indicators for such electrolytes to have good thermal stability is that their ionic conductivity could be measured over a wide range of temperatures. In this work, the temperature dependence of the conductivity of agarose-$NaNO_3$ biopolymer electrolyte was carried out for the highest conducting sample containing 30 wt.% sodium nitrate salt within the temperature range between 303 K and 363 K (Figure 4). The conductivity of polymer electrolyte films is linearly dependent on the temperature, and this relation can be related to the Arrhenius rule as given in the following equation (2), where σ_0 is the pre-exponential factor, k is the Boltzmann constant, and T is the absolute temperature [10].

$$\sigma = \sigma_0 \exp\left(-E_a / k\,T\right) \quad (2)$$

The increase in ionic conductivity of biopolymer electrolytes with temperature can be attributed to the segmental motion of the agarose chain, which provides a higher free volume in the electrolyte upon an increase in temperature. The segmental motion in agarose allows Na^+ ions to hop from one site to another or provides a pathway for its movement. For that reason, it is inferred that the ionic motion in the agarose-$NaNO_3$ biopolymer electrolyte system is due to ion hoping facilitated by the dynamic segmental motion of the agarose. The conductivity amplifies with the temperature. This is due to the fact that the reintegration of ions during the step of solvent desiccation in the formation of thin films is weaker when heat energy is applied to the sample [2]. As a result, when the temperature rises and additional ions become accessible for conduction, it leads to the conductivity being significantly greater [2]. Therefore, at higher temperatures, the amorphous region progressively increases, and agarose chains obtain a faster internal mode in which bond rotations produce segmental motion to favor interchain and intrachain ion hopping. Fortunately, the degree of conductivity becomes appreciable.

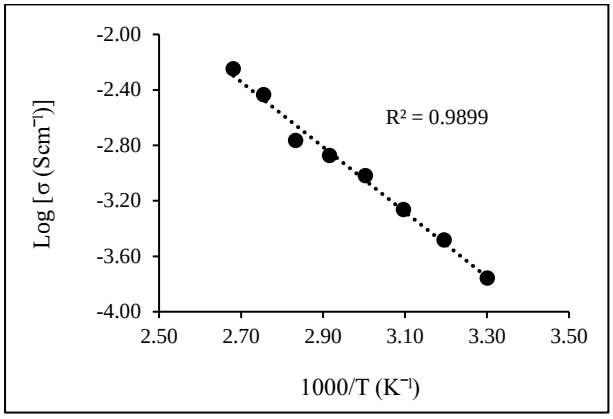

Figure 4. Arrhenius plots for the biopolymer electrolyte containing 30 wt.% of sodium nitrate

Dielectric properties analysis

Their dielectric behaviour is studied to better understand the ionic transport phenomenon in biopolymer electrolyte systems. The dielectric study in electrolyte systems helps us understand the polarization effect of the electrode–electrolyte interface and ionic conduction behaviour. In addition, the dielectric study is favourable due to the contribution of bulk material and interfacial effects at the electrode that are separable. The dielectric constant, ε_r, measures the ability of a material to polarise the amount of dipole alignment in a given volume and correlate with the capacity to store electric charge. Using the impedance data, the real component of complex permittivity is given by equation (3).

$$\varepsilon_r = \frac{Z_i}{\omega C_0 (Z_r^2 + Z_i^2)} \quad (3)$$

Figure 5(a) illustrates the temperature dependence dielectric constant at different frequencies for the highest conducting sample of Agarose-$NaNO_3$ biopolymer electrolyte with 30 wt.% $NaNO_3$ at various temperatures. At low frequencies, the plots rise sharply, indicating that the Na+ ions accumulate at the electrode–electrolyte interface and lead to the formation of an electrical double layer or space charge region in the electrolyte system. Therefore, it contributes to a high dielectric constant value by measuring stored charge directly related to charge carriers. It asserts the non-Debye dependence as the high reversal of the external electric fields [3]. No peak has been seen in the plots of the dielectric constant, which reaffirms that the increase in ionic conductivity is affected by an increase in Na^+ ions density. The increase in dielectric constant supposedly reflects the increase in the density of charge carriers.

A further analysis of the dielectric behavior would be more successfully achieved by using the formulation of

the dielectric modulus. A complex dielectric modulus formalism facilitates the identification and separation of the polarization effect from the bulk relaxation phenomenon in the electrolyte system. The electrical modulus is defined as the [11]:

$$M_r = \frac{\varepsilon_r}{\varepsilon_r{}^2 + \varepsilon_i{}^2} \quad (4)$$

Figure 5(b) demonstrates the real part of electric modulus against log f at different temperatures for the most favorable conductivity sample of Agarose-$NaNO_3$ biopolymer electrolyte containing 30 wt.% of $NaNO_3$. A decreased electric modulus is observed at lower frequencies, linked to the hidden electrode polarization impact. Conversely, at higher frequencies, both the real and imaginary electric modulus show an increase without a clear peak formation, and this rise in values can be attributed to the overall influence of the electrolyte samples. Furthermore, as the temperature rises, the M_r values incline, indicating an increased rate of movement for the charge carriers [2, 4].

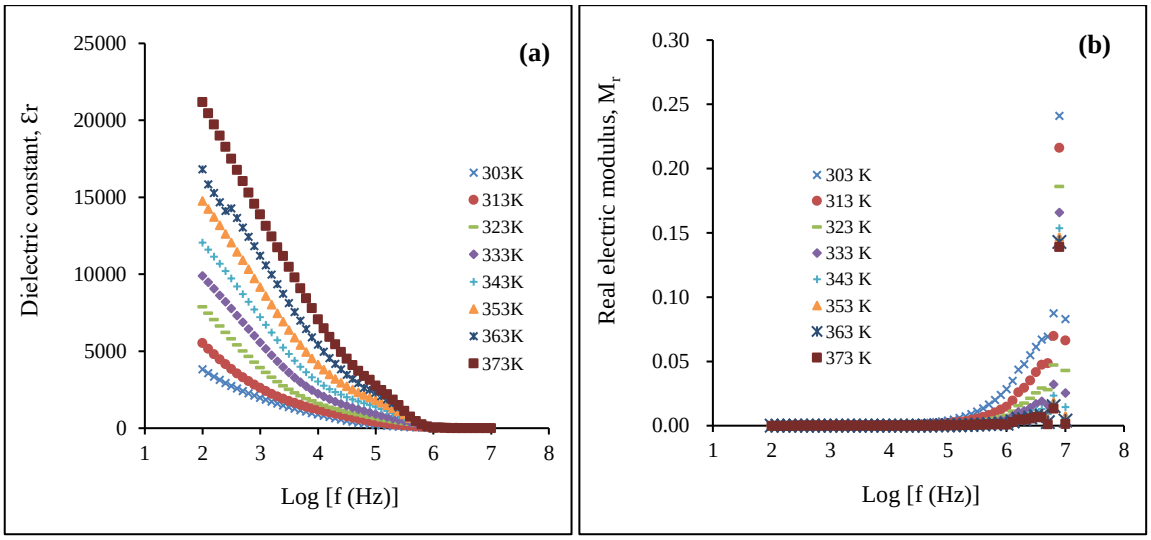

Figure 5. Variation of dielectric constant and real modulus component for optimized Agarose-30 wt.% $NaNO_3$ biopolymer electrolyte as a function of frequencies at various temperatures

The dielectric analysis is further parameterized by the loss tangent (tan $\delta = \varepsilon_i / \varepsilon_r$), and the relaxation time. Relaxation occurs when the loss tangent, tan δ, reaches its peak. The frequency at which the loss tangent, tan δ, reaches its peak is the maximum frequency (relaxation frequency), $f_{max,}$ which is the frequency used to calculate the relaxation time, τ. The relaxation time is calculated using the formula [12]:

$$2\pi f_{max} \tau = 1 \quad (5)$$

Figure 6 shows the plot of loss tangent, tan δ, against the natural logarithm of frequency for selected samples with 20 wt.% $NaNO_3$ best represents the time relaxation trend for the Agarose-$NaNO_3$ biopolymer electrolyte (313 K, 333 K, 353 K and 373 K). It is noticed that the calculated values of relaxation time, as tabulated in Table 2, decrease as the temperature increases. This is caused by the fact that when the temperature rises, ions transition between coordinate sites more quickly, which results in a shorter relaxation time. The results of the relaxation studies in this research correspond with the findings attained by Shetty et al. [13]. Temperature influences the graphs' frequency position and peak intensities, confirming the thermally activated dielectric relaxation process. The relaxation time describes how ionic charge carriers in materials align with the applied field's direction, and at higher temperatures, longer relaxation times are achieved. In high-temperature environments, more mobile ions involved in conduction are generated and undergo relaxation at higher frequencies.

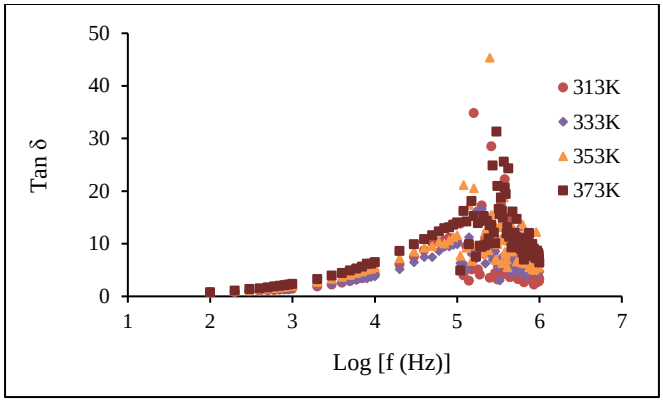

Figure 6. The plot of loss tangent as a function of the logarithm for biopolymer electrolyte with 20 wt.% of $NaNO_3$ at selected temperatures

Table 2. Relaxation time for agarose-$NaNO_3$ biopolymer electrolyte with 20 wt.% of $NaNO_3$

Temperature (K)	Maximum Loss Tangent, tan δ $_{max}$	Maximum Frequency, f $_{max}$ (Hz)	Relaxation Time, τ (s)
313	34.82	5.20	3.06×10^{-2}
333	16.57	5.30	3.00×10^{-2}
353	45.33	5.40	2.95×10^{-2}
373	31.32	5.48	2.91×10^{-2}

Structural properties analysis

The structural or semicrystalline properties of the agarose-$NaNO_3$ biopolymer electrolyte were investigated through XRD analysis. Figure 7(a-c) displays XRD spectra of agarose-$NaNO_3$ biopolymer electrolyte with varying $NaNO_3$ concentrations (0, 30 and 40 wt.%). The presence of amorphous peaks at approximately 2θ = 20° in the absence of $NaNO_3$ (0 wt.%) confirms that agarose exhibits a semicrystalline structure [2]. As more $NaNO_3$ is added to the agarose matrix, the peak broadens, where this broadening indicates an increased amorphous character in the biopolymer electrolyte system, leading to enhanced $NaNO_3$ dissociation into free ions and greater ion migration through the polymer chains. At a 40 wt.% of $NaNO_3$ concentration, the peak narrows compared to the electrolyte with the highest conductivity (30 wt.% $NaNO_3$), suggesting a reduction in the electrolyte's amorphous nature due to the reassociation of ions within the agarose matrix.

The peak was slightly absent in agarose-30 wt.% $NaNO_3$ biopolymer electrolyte indicating the complete dissociation of salts in the electrolytes [8]. The highest conducting sample confirms its characteristic as the most amorphous sample due to the broadest amorphous hump. Elevated amorphous eases the path for the Na^+ ions migration and mobility in the biopolymer electrolyte regions, thus facilitate superior ionic conductivity. A decrease in the degree of crystallinity is also implied by improved amorphousness, which serves as a boost to the ionic conductivity. The dominance of the amorphous region is mathematically confirmed by determining the degree of crystallinity, X_c and crystalline size, L of the electrolyte and evaluated by using equations (6) and (7), respectively [14, 15]:

$$X_c = \frac{A_c}{A_T} \times 100\% \quad (6)$$

$$L = \frac{0.9\,\lambda}{FWHM\,\cos\theta} \quad (7)$$

where A_c is area under the peak of crystalline region while A_T is the total area under the peak, λ is the X-ray wavelength (fixed at 1.5406Å), FWHM is the full width

at half maximum (a measure of the peak broadness) and θ is Bragg's diffraction angle.

In amorphous regions, the polymer chains are less organized, thus making it easier for salt to dissociate into free ions. The detail analysis of degree of crystallinity and crystallite size of 0 wt.%, 30 wt.% and 40 wt.% agarose-$NaNO_3$ biopolymer electrolyte are illustrated in Table 3 and Figure 8. The analysis supports the sample (agarose-30 wt.% $NaNO_3$) which exhibit the broadest XRD peak at 2θ = 20° which also demonstrate its amorphous nature by having the broadest FWHM, lowest degree of crystallinity (16%) and smallest crystallite size (0.0145 nm) among other samples.

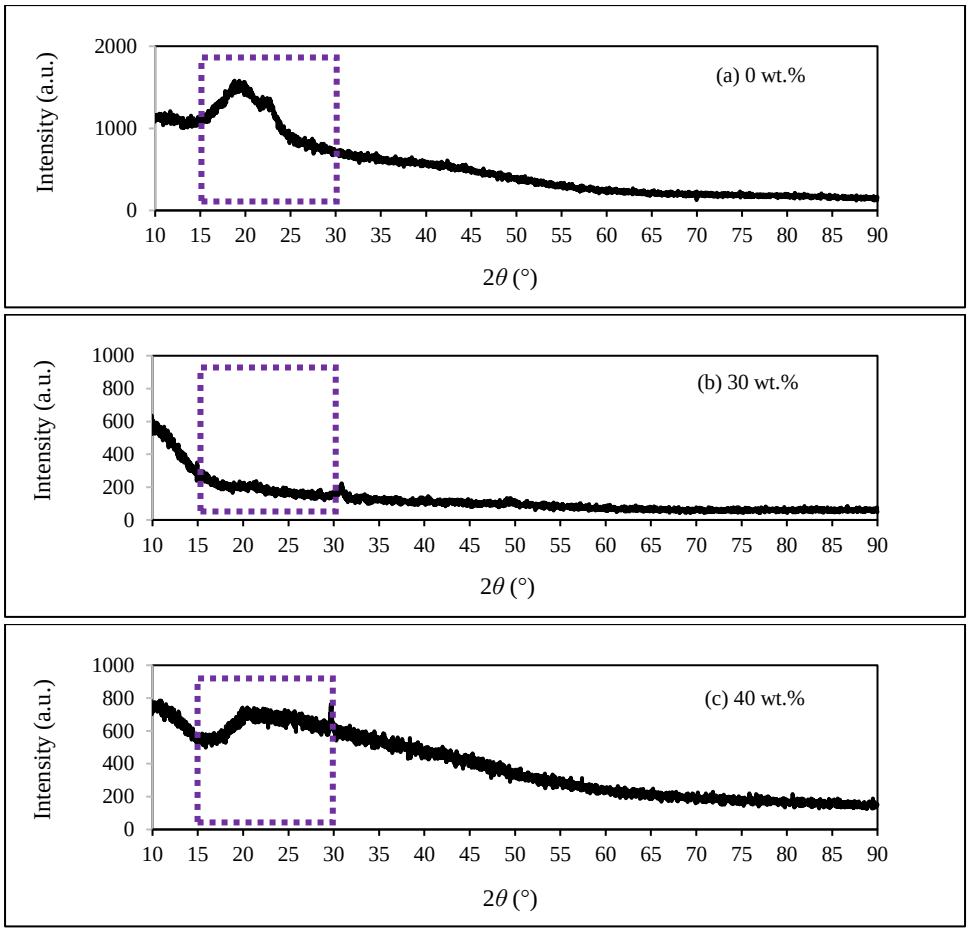

Figure 7. XRD pattern of agarose-$NaNO_3$ biopolymer electrolyte with different concentrations of sodium nitrate

Table 3. The analysis of agarose-$NaNO_3$ biopolymer electrolyte with different concentrations of sodium nitrate

$NaNO_3$ Content (wt.%)	**Full Width Half Maximum (FWHM)**	**Degree of Crystallinity, X_c (%)**	**Crystallite Size, L (nm)**
0	6.70	29	0.0219
30	10.44	16	0.0145
40	9.31	22	0.0161

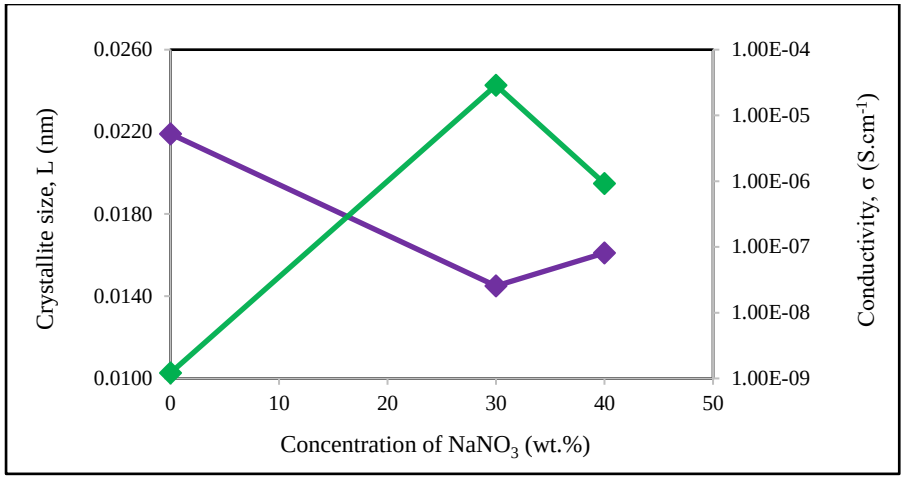

Figure 8. The size of crystallite of selected agarose-$NaNO_3$ biopolymer electrolyte with the respective room temperature conductivity values

Conclusion

In conclusion, Agarose-$NaNO_3$ biopolymer electrolyte was prepared in five different weight percentages of $NaNO_3$ by using the method of solution casting with the weight percentages of 0 wt.%, 10 wt.%, 20 wt.%, 30 wt.% and 40 wt.% $NaNO_3$. Electrochemical Impedance Spectroscopy (EIS) was employed to determine the biopolymer electrolyte's ionic conductivity and electrical properties. In contrast, X-ray diffractometer (XRD) spectroscopy was performed to observe the biopolymer electrolyte's structural behavior and amorphous nature. The conductivity studies at room temperature showed increased conductivity with the increasing sodium salt concentration. The increase in ionic conductivity is due to the increase in the number of charge carriers and the mobility of the sodium ions. The highest room temperature conductivity was 3.44×10^{-5} S·cm^{-1} for the agarose-30 wt.% $NaNO_3$ biopolymer electrolytes and beyond that, the ionic conductivity for agarose-40 wt.% $NaNO_3$ becomes reduced (6.84×10^{-7} S·cm^{-1}) as the aggregation of ions starts to occur. The dielectric properties analysis of the selected biopolymer electrolyte sample indicates a strong dependence on frequency and temperature. The structural properties analysis based on FWHM, degree of crystallinity and crystallite size for agarose-based biopolymer electrolytes confirm that the amorphous regions tend to facilitate higher ion mobility compared to crystalline regions, therefore contributing to higher conductivity, as ions can move more freely through the amorphous parts of the polymer.

Acknowledgement

The authors appreciatively acknowledge the financial support for this work by the Fundamental Research Grant Scheme (FRGS, Sponsorship File No: FRGS/1/2019/STG07/UITM/02/2; and FRGS/1/2019/ STG02/UITM/02/6), Ministry of Higher Education of Malaysia (MOHE), The authors would like to thank iMADE Research Laboratory, Institute of Science and Faculty of Applied Sciences, UiTM for all the support in providing research facilities to carry out this project.

References

1. Zheng, J., Li, W., Liu, X., Zhang, J., Feng, X. and Chen, W. (2023). Progress in gel polymer electrolytes for sodium-ion batteries. *Energy Environment Materials*, 6(4): e12422.
2. Ali, N. I., Abidin S. Z. Z., Majid S. R. and Jaafar N. K. (2021). Role of $Mg(NO_3)_2$ as defective agent in ameliorating the electrical conductivity, structural and electrochemical properties of agarose–based polymer electrolytes. *Polymers*, 13(19): 3357.
3. Rani, M. S. A., Mohamed, N. S., and Isa, M. I. N. (2015). Investigation of the ionic conduction mechanism in carboxymethyl cellulose/chitosan biopolymer blend electrolyte impregnated with ammonium nitrate. *International Journal of*

Polymer Analysis and Characterization, 20(6): 491-503.

4. Fuzlin, A. F., Bakri, N. A., Sahraoui, B. and Samsudin, A. S. (2019). Study on the effect of lithium nitrate in ionic conduction properties based alginate biopolymer electrolytes. *Materials Research Express*, 7: 015902.
5. Lizundia, E., and Kundu, D. (2021). Advances in natural biopolymer-based electrolytes and separators for battery applications. *Advanced Functional Materials*, 31(3): 2005646.
6. Kiruthika, S., Malathi, M., Selvasekarapandian, S., Tamilarasan, K. and Maheshwari, T. (2020). Conducting biopolymer electrolyte based on pectin with magnesium chloride salt for magnesium battery application. *Polymer Bulletin,* 77: 6299-6317.
7. Jinisha, B., Anilkumar, K. M., Manoj, M., Abhilash, A., Pradeep, V. S. and Jayalekshmi, S. (2018). Poly (ethylene oxide) (PEO)-based, Poly (ethylene oxide) (PEO)-based, sodium ion-conducting, solid polymer electrolyte films, dispersed with Al_2O_3 filler, for applications in sodium ion cells. *Ionics*, 24: 1675-1683.
8. Mohd Rafi, N. S., Abidin, S. Z. Z., Majid, S. R. and Zakaria, R. (2022). Preparation of agarose-based biopolymer electrolytes containing calcium thiocyanate: Electrical and electrochemical properties. *International Journal of Electrochemical Science*, 17(7): 220713.
9. Hafiza, M. N. and Isa, M. I. N. (2017). Solid polymer electrolyte production from 2-hydroxyethyl cellulose: Effect of NH_4NO_3 composition on its structural properties. *Carbohydrate Polymers*, 165: 123-131.
10. Leš, K. and Jordan, C.S. (2020). Ionic conductivity enhancement in solid polymer electrolytes by electrochemical in situ formation of an interpenetrating network. *RSC Advances*, 10: 41296-41304.
11. Das, S. and Ghosh, A. (2015). Effect of plasticizers on ionic conductivity and dielectric relaxation of PEO-$LiClO_4$ polymer electrolyte. *Electrochimica Acta*, 171: 59-65.
12. Singh, R., Bhattacharya, B., Tomar, S. K., Singh, V. and Singh, P. K. (2017). Electrical, optical and electrophotochemical studies on agarose based biopolymer electrolyte towards dye sensitized solar cell application. *Measurement*, 102: 214-219.
13. Shetty, S. K., Ismayil and Noor, I. M. (2021). Effect of new crystalline phase on the ionic conduction properties of sodium perchlorate salt doped carboxymethyl cellulose biopolymer electrolyte films. *Journal of Polymer Research*, 28(11): 415.
14. Hafiza, M. N. and Isa, M. I. N. (2020). Correlation between structure, ion transport and ionic conductivity of plasticized 2-hydroxyethyl cellulose based solid biopolymer electrolyte. *Journal Membrane Science*, 597: 117176.
15. Shetty, S. K., Ismayil, Hegde, S. Ravindrachary, V., Sanjeev, G., Bhajantri R. F. and Masti, S. P. (2021). Dielectric relaxations and ion transport study of NaCMC:$NaNO_3$ solid polymer electrolyte films. *Ionics*, 27: 2509-2525.

Malaysian Journal of Analytical Sciences Vol 28 No 2 2024

		Page
	Analytical Method	247-256
1.	FABRICATION AND CHARACTERIZATION OF WATER-IN-PALM OIL NANOEMULSION AS A CARRIER FOR CATECHIN *Nabilah Hauzin, Nursyamsyila Mat Hadzir, Hairul Amani Abdul Hamid, Rosnani Hasham@Hisam, and Wan Nazihah Wan Ibrahim*	
	Nano and Advanced Materials Analysis	
2.	SCREENING OF PROMOTED CeO_2/Al_2O_3 CATALYSTS IN AQUEOUS PHASE GLYCEROL REFORMING AND HYDROGENOLYSIS INTO 1,2-PROPANEDIOL *Norsahida Azri, Ramli Irmawati, Rudy Hakim Danial Leong, Usman Idris Nda-Umar, Mohd Izham Saiman, Yun Hin Taufiq-Yap and G. Abdulkareem-Alsultan*	257-264
	Nano and Advanced Materials Analysis	
3.	CORROSION INHIBITION STUDY OF CARBOXYMETHYL CELLULOSE-IONIC LIQUID VIA ELECTROCHEMICAL AND MACHINE LEARNING TECHNIQUE *Adi Hafizamri Ariffin, Wan Mohd Norsani Wan Nik, Samsuri Abdullah, Mohd Ikmar Nizam Mohamad Isa, Vincent Izionworu, and Mohammad Fakhratul Ridwan Zulkifli*	265-276
	Analytical Method	
4.	ENRICHED SILICA FROM OIL PALM BIOMASS FOR MAGNETIC SOLID PHASE EXTRACTION OF ORGANOCHLORINE PESTICIDE: CHARACTERIZATION AND METHOD DEVELOPMENT *Nur Husna Zainal Abidin, Amir Hisyam Othman, Wan Nazihah Wan Ibrahim, Nordiana Suhada Mohammad Tahirudin, Nor Suhaila Mohamad Hanapi, and Nursyamsyila Mat Hadzir*	277-289
	Analytical Method	
5.	A PORTABLE MICRO-VOLUME COLORIMETRIC ASSAY FOR ALUMINIUM DETERMINATION USING NATURAL REAGENT EXTRACTS FROM SAPPAN HEARTWOOD BY ULTRASOUND-ASSISTED EXTRACTION *Watsaka Siriangkhawut and Yaowalak Khanhuathon*	290-304
	Environmental Analysis	
6.	THE INFLUENCES OF SEASONAL MONSOONS UPON PHOSPHORUS, CHLOROPHYLL-A AND PHYSICAL CHARACTERISTIC OF THE KELANTAN WATERS *Azyyati Abdul Aziz, Suhaimi Suratman, Ku Nor Afiza Asnida Ku Mansor, Fariz Syafiq Mohamad Ali, and Ku Mohd Kalkausar Ku Yusof*	305-321
	Analytical Method	
7.	ANALYSIS OF EFFLORESCENCE OF SPENT BLEACHING CLAY BASED GEOPOLYMER USING ALKALINE LEACHABILITY METHODS *Puuvina Jeyasangar, Mohd Hazwan Hussin, and Shangeetha Ganesan*	322-334

Organic and Inorganic Analysis

8. SYNTHESIS AND CHARACTERIZATION OF PALLADIUM(II) SCHIFF BASE COMPLEXES DERIVED FROM PHENYLAMINES AND THEIR CATALYTIC ACTIVITY FOR STILLE REACTION 335-347
Nur Nabihah Muzammil, Mohd Tajudin Mohd Ali, and Amalina Mohd Tajuddin

Nano and Advanced Materials Analysis

9. FROM TRADITIONAL TO GREEN: EVOLUTION OF SHALE SWELLING INHIBITORS FOR SUSTAINABLE DRILLING 348-364
Siti Qurratu Aini Mahat, Ismail Mohd Saaid, Arina Sauki, Agi Agustine Aja, Norida Ridzuan, and Norasyikin Ismail

Nano and Advanced Materials Analysis

10. PHYSICOCHEMICAL CHARACTERIZATION OF ZNO/G-C_3N_4 FOR PHOTO-REMOVAL OF METHYL ORANGE UNDER LOW UV-LIGHT INTENSITY 365-375
Nurul Izzati Izhar, Zul Adlan Mohd Hir, Hartini Ahmad Rafaie, and Shaari Daud

Nano and Advanced Materials Analysis

11. PHYSICOCHEMICAL STUDY ON ALKOXYLATED AZO-IMINE CHITOSAN-BASED BIOPOLYMER FOR ELECTROLYTE APPLICATIONS 376-387
Tuan Siti Fatimah Tuan Mohd Pauzi, Rafizah Rahamathullah, M. N. Hafiza, and Wan M. Khairul

Nano and Advanced Materials Analysis

12. PERFORMANCE OF MEMBRANE ELECTRODE ASSEMBLY USING Pt/C AND CoFe/N-C CATALYSTS IN PROTON EXCHANGE MEMBRANE FUEL CELLS 388-396
Dedi Rohendi, Edy Herianto Majlan, Dwi Hawa Yulianti, Juwita, Nirwan Syarif, Addy Rachmat, Afriyanti Sumboja, Nyimas Febrika S, and Icha Amelia

Analytical Method

13. AN INSIGHT INTO PINEAPPLE PEEL WASTE ADSORBENT FOR IRON CONTAMINATED WATER THROUGH KINETIC AND ISOTHERM STUDY 397-411
Nurul Faizah Abd Ghapar, Rozaimi Abu Samah, Mohamad Syafiq Abdul Wahab, Sunarti Abd Rahman, and Mohd Hafiz Dzarfan Othman

Analytical Method

14. DETERMINATION OF CELECOXIB IN HUMAN PLASMA BY EFFERVESCENCE-ASSISTED DISPERSIVE LIQUIDâ€"LIQUID MICROEXTRACTION AND HPLC/UV 412-422
Zahra Saharkhiz, Mohammad Reza Hadjmohammadi, and Pourya Biparva

Nano and Advanced Materials Analysis

15. Fe_3O_4-DOPED POLYSULFONE MEMBRANE FOR ENHANCED ADSORPTION OF COPPER FROM AQUEOUS SOLUTION 423-440
Wan Khairunnisa Wan Ramli, Nur Maisyatul Syalina Abdul Wahab, Siti Khalijah Mahmad Rozi, Syumayyah Rasis, Gavin Chew Tiong Chuen, and Lew Guo Liang

Analytical Method

16. PRE-CONCENTRATION OF ORGANOCHLORINE PESTICIDES USING MICRO-SOLID PHASE EXTRACTION BASED ON BIO-SORBENT ALGINATE-SILICA BEADS DERIVED FROM OIL PALM FROND 441-460
Azreen Asyikin Mhd Kamal, Siti Nur Afiqah Binti Mahazan, Nur Husna Zainal Abidin, Fariesha Farha Ramli, and Wan Nazihah Wan Ibrahim

Nano and Advanced Materials Analysis

17. A REVIEW OF THE CURRENT TREND IN THE SYNTHESIS OF NITROGEN-RICH FUNCTIONAL POLYMERS FOR CARBON DIOXIDE ADSORPTION 461-479
Noorhidayah Ishak, Azalina Mohamed Nasir, Chow Wen Shyang, Dai Viet N. Vo, Bassim H. Hameed, Mohd Azmier Ahmad, and Azam Taufik Mohd Din

Malaysian Journal of Analytical Sciences (MJAS)
Published by Malaysian Analytical Sciences Society

FABRICATION AND CHARACTERIZATION OF WATER-IN-PALM OIL NANOEMULSION AS A CARRIER FOR CATECHIN

(Fabrikasi dan Sifat Nanoemulsi Air dalam Minyak Kelapa Sawit sebagai Pembawa Katekin)

Nabilah Hauzin[1], Nursyamsyila Mat Hadzir[1*], Hairul Amani Abdul Hamid[1], Rosnani Hasham@Hisam[2], and Wan Nazihah Wan Ibrahim[1]

[1]*School of Chemistry and Environment, Faculty of Applied Sciences, Universiti Teknologi MARA, 40450 Shah Alam, Selangor, Malaysia*
[2]*Department of Bioprocess and Polymer Engineering, School of Chemical and Energy Engineering, Faculty of Engineering, Universiti Teknologi Malaysia, 81310, Johor Bahru, Johor, Malaysia*

**Corresponding author: nursyamsyila@uitm.edu.my*

Received: 10 September 2023; Accepted: 12 March 2024; Published: 29 April 2024

Abstract

Catechins are known as potent antioxidants with numerous health benefits, including antimicrobial, antiviral, anti-inflammatory, anti-allergenic, and anti-cancer effects. However, there are some challenges to delivering catechins due to their low bioavailability, poor gastrointestinal absorption, and low stability. To overcome the limitations of catechin delivery, nanoemulsion technology with droplet sizes ranging from 10 to 1000 nm was used. In this study, water-in-oil (W/O) nanoemulsion was effectively prepared by employing palm oil (PO) as the oil phase, Span 80 as a lipophilic emulsifier, and Tween 80 as a hydrophilic emulsifier with high-energy approaches (high shear homogenizer). The optimum processing conditions for preparing water-in-palm oil nanoemulsion are as follows: the ratio of the oil phase to the water phase is 60:40, and the total concentrations of emulsifier mixtures are 11 w/w% with a hydrophilic-lipophilic balance (HLB) value of 7.1 using 15,500 rpm for 5 minutes of the high shear homogenizer. The best nanoemulsion showed an average of 185.6 nm particle size and a zeta potential of -38.4 mV. The optimized nanoemulsion containing catechin with a pH value of 6.82, showed a low conductivity value of this nanoemulsion (0.001mS/cm) which means that the continuous phase is oil. The nanoemulsion was stable at centrifugation of 4000rpm for 30 minutes and alongside 28 days of storage tests at 10˚C. Hence, this study successfully developed a stable water-in-palm oil nanoemulsion containing catechins (WPOC-NEs).

Keywords: catechin, nanoemulsion, emulsifiers, formulation, stability

Abstrak

Katekin dikenali sebagai antioksidan kuat yang menawarkan banyak manfaat kesihatan, termasuk kesan antimikrob, antivirus, anti-radang, anti-alergik, dan anti-barah. Walau bagaimanapun, terdapat beberapa cabaran dalam membuat penghantaran katekin disebabkan bioketersediaan mereka yang rendah, penyerapan gastrousus dan kestabilan yang lemah. Untuk mengatasi had penghantaran katekin, teknologi nanoemulsi dengan saiz zarah daripada 10 hingga 1000nm telah digunakan. Dalam kajian ini, nanoemulsi air-dalam-miyak telah disediakan dengan menggunakan minyak kelapa sawit sebagai fasa minyak, Span 80 sebagai pengemulsi lipofilik, dan Tween 80 sebagai pengemulsi hidrofilik dengan pendekatan tenaga tinggi (penghomogenatan ricih tinggi). Keadaan pemprosesan optimum bagi penyediaan nanoemulsi air-dalam-minyak mengandungi katekin adalah seperti

berikut: nisbah fasa minyak kepada fasa air adalah 60:40, dan jumlah kepekatan campuran pengemulsi adalah 11% dengan nilai keseimbangan hidrofilik-lipofilik 7.1 menggunakan penghomogenatan ricih tinggi. Nanoemulsi mengandungi katekin yang terbaik menunjukkan saiz zarah 185.6 nm, dan potensi zeta -38.4mV. Tambahan lagi, nanoemulsi dengan nilai pH 6.82 ini, menunjukkan nilai kondutiviti yang rendah iaitu 0.001mS/cm, yang bermaksud fasa berterusannya adalah minyak. Nanoemulsi ini juga stabil selepas diemparkan pada 4000rpm selama 30 minit dan juga sepanjang ujian simpanan selama 28 hari di suhu 10°C. Oleh itu, kajian ini telah berjaya membangunkan nanoemulsi air-dalam-minyak dengan mengandungi katekin yang stabil.

Kata kunci: katekin, nanoemulsi, pengemulsi, formulasi, kestabilan

Introduction

Catechin is a polyphenol compound found in various fruits, vegetables, and plant-based beverages. Catechins have sparked much interest because of their antiviral, anticancer, antioxidant, antimicrobial, anti-inflammatory, and possible medicinal applications in various viral infections [1]. Catechins have been studied extensively in terms of their biological functions. However, the bioavailability of catechins in vivo has remained limited due to their volatility. As a result of the creation of microemulsions (MEs) or nanoemulsions (NEs) for encapsulation of bioactive chemicals like catechin, it is feasible to improve stability, hence increasing catechin bioavailability and biological activity [2]. Bhushani et al. [3] reported that nanoemulsified catechin can increase their bioaccessibility compared to non-emulsified catechin.

A nanoemulsion is a kinetically stable system composed of two immiscible liquids (oil and water) that are stabilized by surfactants with droplet sizes ranging from 10 to 1000 nm [4]. The advantages of nanoemulsions (NEs) are numerous. Due to a higher surface area, they are suitable for drug administration. This could boost drug absorption through a variety of pathways [5]. A wide surface area also has an impact on the drug's transport characteristics, which is a critical component in ensuring long-term and targeted drug delivery. Drugs are protected from environmental changes, such as pH shifts and enzymatic breakdown, by being encapsulated within the nanoemulsion core [6].

Nanoemulsions consist of two types known as oil-in-water (O/W), where the continuous phase is water, and water-in-oil (W/O), where oil is the continuous phase. W/O nanoemulsion has great potential for pharmaceutical, cosmetic, agricultural, and food applications. This type of nanoemulsion can encapsulate the hydrophilic drugs in the inner water phase by improving the effect of sustained release, maintaining the retention time of the drug in the body, and lowering the metabolic rate [7]. This research applied high-energy emulsification approaches such as high-shear homogenizers to obtain nanodroplet emulsions. The emulsion will be forced into the narrow space between the rotor and stator, causing the droplets to break down and form smaller particles [8].

Overall, this research study aimed to encapsulate the catechin within the water in palm oil nanoemulsion to improve their bioavailability after oral administration or for the fabrication of topical application. Therefore, to form a stable W/O nanoemulsion, the choice of oil and surfactants is essential. Palm oil was chosen in this study since it can help to overcome the issue of low bioavailability, high toxicity, and poor solubility of several drugs, as well as improved drug permeability and shelf life [9]. Non-ionic surfactants were used as they can form a stable nanoemulsion and have a low toxicity potential that helps to reduce irritation [10]. The optimal hydrophilic-lipophilic balance (HLB) surfactant mixtures were first determined to obtain stable water-in-palm oil nanoemulsions containing catechin (WPOC-NEs). Then, the stable nanoemulsions obtained were characterized, including their droplet size, polydispersity index (PDI), zeta potential, and conductivity. To our knowledge, no work has been done on water-in-palm oil nanoemulsion containing catechin.

Materials and Methods

Materials

Catechin Hydrate was purchased from Sigma-Aldrich Co. (St. Louis, MO). Tween 80 and Span 80 were purchased from Chemiz (M) Sdn.Bhd. Palm oil was purchased from a local market. Distilled water was used

to prepare the water-in-palm oil nanoemulsion containing catechin.

Preparation of water-in-oil nanoemulsion

Water-in-palm oil (W/PO) nanoemulsion was prepared according to the method implied by Qonita et al. [11] and Baba Shekh et al. [12] with some modifications. The aqueous phase consisted of distilled water, Tween 80, Span 80, and catechin, which were mixed and stirred using a hotplate stirrer (Model HTS-1003, AB Labmart Malaysia) at 1200 rpm for 10 min. Then, the oil phase was added dropwise into the aqueous phase and homogenized at 15,500 rpm for 5 minutes using a high-shear homogenizer (T25 digital; IKA-Werk, GmbH & Co. KG, Staufen im Breisgau, Germany). All the procedures were standardized, that is (i) 36% water, 11% total surfactants mixture, 0.1% catechin, and 54% palm oil, and (ii) all procedures were performed at room temperature.

Selection of hydrophilic-lipophilic balance (HLB) of mixed surfactants

A range of 4.3-7.1 HLB values was used to prepare water in palm oil nanoemulsion for the HLB value determination. In all samples, the water-to-oil content ratio was maintained constant (40/60, w/w%). The surfactant consists of the mixtures Span 80 and Tween 80. The following calculation calculated calculation of HLB values of mixed surfactants:

$$HLB_{mix} = F_T\, HLB_T + F_S\, HLB_S, \quad (1)$$

where $HLB_{mix,}$ HLB_T, and HLB_S are the HLB values of mixed surfactants, Tween 80 (T80, HLB =15) and Span 80 (S80, HLB=4.3), while F_T and F_S are the weight fractions of Tween 80 and Span 80. All standard conditions were kept constant to prepare the nanoemulsions which were then centrifuged to evaluate their stability. Based on the calculation using Equation (1), a suitable HLB value was investigated until a stable W/PO nanoemulsion containing catechin was obtained for this study.

Fourier transform infrared spectroscopy (FTIR) – based attenuated total reflection (ATR)

Functional groups and chemical structures in the composition of the pure palm oil, span 80, tween 80, catechin, and water in palm oil nanoemulsion containing catechin were evaluated using a Perkin Elmer Fourier Transform Infrared, FTIR-based ATR (Spectrum 400 Perkin Elmer, Waltham, MA, USA) spectrometer in the range of 400 to 4000 cm^{-1}. All the samples were analyzed in their original forms without any kind of preparation.

Droplet size, zeta potential, polydispersity index, conductivity determination, and transmission electron microscopy (TEM) image

The most significant parameter for this study is the measurement of droplet size. The smaller the particle size, the bigger the surface area of the absorption of the drug. The droplet size, zeta potential, conductivity, and polydispersity index of WPOC-NEs were measured using dynamic light scattering, which scattered at an angle of 173˚ and a temperature of 25˚C. This procedure used a droplet-size analyzer (Zetasizer Nano ZS90; Malvern Instruments, Malvern, UK). To certify that the system has reached equilibrium, the droplet size was measured a day after the formulations were made [13].

The TEM image of the WPOC-NEs was obtained using Transmission Electron Microscopy (TEM) (Tecnai G2 Spirit BioTwin). Samples were diluted with deionized water and homogenized. A Formvar-coated copper grid was placed on top of a drop of diluted sample and left at room temperature (25 ± 0.5˚C) for 3 min. The samples on the filled copper grid were then negatively stained using 2% w/w phosphotungstic acid for 2 min and were air-dried before analysis [14].

pH determination

An S20 SevenEasy pH meter (Mettler Toledo, Schwerzenbach, Switzerland) was used to measure the pH of the optimized nanoemulsion containing catechin. The pH meter was calibrated with three pH standard buffer solutions (pH 4.00, 7.00, and 10.00) before taking pH measurements. The pH value was obtained by inserting the electrode directly into the sample.

Viscosity determination

A rotational Physica MCR 300 rheometer (Physica Messtechnic GmbH, Stuttgart, Germany) was used to

determine the viscosity of the optimized nanoemulsion containing catechin, with PP25 plate and plate geometries (gap of 1mm) at 25ºC. A controlled Peltier system (TEK150) with an accuracy of ± 0.1°C was used. The experimental data were fitted to the Power Law Equation:

$$\eta = k\dot{\gamma}^{n-1} \quad (2)$$

Based on the above equation, η is the viscosity (Pa.s), ý is the shear rate (s^{-1}), and k and n are the consistency index and flow behavior index, respectively.

Accelerated stability tests

The stability of nanoemulsions is characterized by their capacity to maintain their physical appearance (in a certain system) without phase separation or physical changes during a specific time of storage and use [15]. The optimized nanoemulsion containing catechin was submitted to two stability tests, namely, the centrifugation test and storage stability at different temperatures (10, 25, 50°C) for 28 days. If the visible appearance of creaming or phase separation occurred, the nanoemulsion containing catechin was said to be unstable.

The centrifugation test was performed using a SIGMA 2-16P centrifuge. The nanoemulsion containing catechin was placed into a centrifugation tube and then centrifuged at 4000 rpm for 30 min. The optimized nanoemulsion was then observed for the presence or absence of phase separation.

The storage stability test was performed at different temperatures and the optimized nanoemulsion was carried out by observing the changes in physical appearance on days 1,7,14, and 28.

Results and Discussion

Formulation and screening of water-in-oil nanoemulsion

Table 1 tabulates the W/PO nanoemulsion containing catechin. This study aimed to encapsulate catechin into water in palm oil nanoemulsion. Water-in-oil nanoemulsions comprise a dispersed aqueous phase with tiny droplets and a continuous oil phase. Oil-in-water nanoemulsions, on the other hand, are the dispersed phase disseminated into the continuous water phase [16]. As reported by Qonita et al. [11], the percentage of oil phase used was more than 50%, to form W/O nanoemulsions which was used in this study.

Tween 80 (T80) and Span 80 (S80), both non-ionic surfactants, were chosen in this study due to their strong biological compatibility, insensitivity to changes in electrolyte concentration or pH, and their established safety and approval for inclusion in specific pharmaceuticals, cosmetics, and food products [12].

Selection of hydrophilic-lipophilic balance (HLB) value of mixed surfactants

An acceptable HLB value of the surfactant utilized in the formulation is one of the primary driving forces for stable nanoemulsions. As it reflects the ideal mixture of surfactants that can produce stable nanoemulsions, it serves as a scale for choosing the suitable surfactants or mixtures of surfactants that are necessary for the oil and water phase [17]. The HLB system predicts the ideal emulsifier when the HLB values of the emulsifier and oil are matched. Well-known non-ionic and ethoxylated sorbitan alkanoates, which are Spans and Tweens, had a wide range of HLB values that helped adjust the HLB [18].

Table 1 shows the result surfactant mixtures (Tween 80/Span 80) of 26.2/73.8 (HLB 7.1) were suitable for producing W/PO nanoemulsion containing catechin, while others show separation. This HLB value did not show any physical separation during centrifugation, supporting the conclusion that the HLB 7.1 of the surfactant mixtures effectively stabilized the W/O nanoemulsion. The selected HLB range (4-9) covers water in oil and wettability agents in the classical HLB scale and was experimentally proven as an effective stabilizer for W/O systems [19].

Table 1. Composition of the water in palm oil nanoemulsion containing catechin for HLB screening

Composition						Observation
Surfactants(w/w%)		HLB	Palm Oil (w/w%)	Distilled Water (w/w%)	Catechin (w/w%)	Centrifugation
Tween 80	Span 80					
0.00	11.00	4.30	60.00	40.00	0.10	X
0.50	10.50	4.70	60.00	40.00	0.10	X
1.00	10.00	5.20	60.00	40.00	0.10	X
1.60	9.40	5.70	60.00	40.00	0.10	X
2.10	8.90	6.10	60.00	40.00	0.10	X
2.70	8.60	6.80	60.00	40.00	0.10	X
2.90	8.10	7.10	60.00	40.00	0.10	/

/ = stable or no physical change X = not stable and physical changes occur

ATR analysis based on FTIR

Figure 1 and Table 2 present the FTIR spectrophotometer and wavenumbers of palm oil (PO), Tween 80, Span 80, catechin, and water in palm oil nanoemulsion containing catechin (WPOC-NEs). FTIR analysis was performed to determine whether catechin was present in the water in palm oil nanoemulsion containing catechin. Figure 1(a), displayed a carbonyl (C=O) stretching peak at 1743.7 cm^{-1} and C–H stretching of alkyl chains at 2854.6 and 2922.9 cm^{-1}, which corresponds to the molecular structure of palm oil [20]. FTIR transmittance spectrum of surfactant Tween 80 was depicted in Figure 1(b) where a broad peak at 3493.3cm^{-1} indicates the presence of the O-H group. The aliphatic CH_2 symmetric and asymmetric stretching vibration is responsible for the 2920.1-2862.9 cm^{-1} band. In the domain 1735.8 cm^{-1}, the presence of C=O stretching methods may be seen. The band from 1349.7 to 1247.4 cm^{-1} is due to C-H bending, whereas the peak at 1097.5 cm^{-1} is attributed to C-O-C in $(CH_2CH_2O)n$.

Figure 1(c) indicates the spectrum of pure Span 80. The OH group is allocated to the peaks at 3410.7 cm-1. It should be noted that the absorption peaks at 1738.8 cm^{-1}, and 1458.8 cm^{-1} are due to C=O and C-H bending in CH_3 and CH_2 [21]. Characteristic IR peaks of catechin in Figure 1(d) were observed at 3355.3 (phenolic hydroxyl group), 1640.3, 1461.2 (phenyl ring), 1155.4, and 1095.8 (stretching vibration of C-O-C) cm^{-1} [22]. From Figure 1(e), the WPOC-NEs spectrum shows all of the distinctive peaks of catechin were attained by WPOC-NEs. The catechin distinctive peak within the WPOC-NEs was observed at 3356.3 (phenolic hydroxyl group), 1640.0, 1460.5 (phenyl ring), 1159.5, and 1096.8 (stretching vibration of C-O-C) cm^{-1}. Based on these findings, it was determined that catechin was present within the core of water in palm oil nanoemulsion containing catechin.

Table 2. Wavenumbers of IR of palm oil, tween 80, span 80, catechin, and W/PO NEs containing catechin

Sample	Wavenumbers (cm^{-1})				
	O-H Stretching	C-H Stretching	C=O Stretching	Phenyl Ring	C-O-C Stretching
Palm Oil	-	2854.6	1743.7	-	1115.3
Tween 80	3493.3	2920.1	1735.8	-	1097.5
Span 80	3410.7	2923.3	1738.8	-	1085.5
Catechin	3355.3	2925.6	-	1640.3	1095.8
WPOC-NEs	3356.3	2925.2	1741.7	1640.0	1159.5

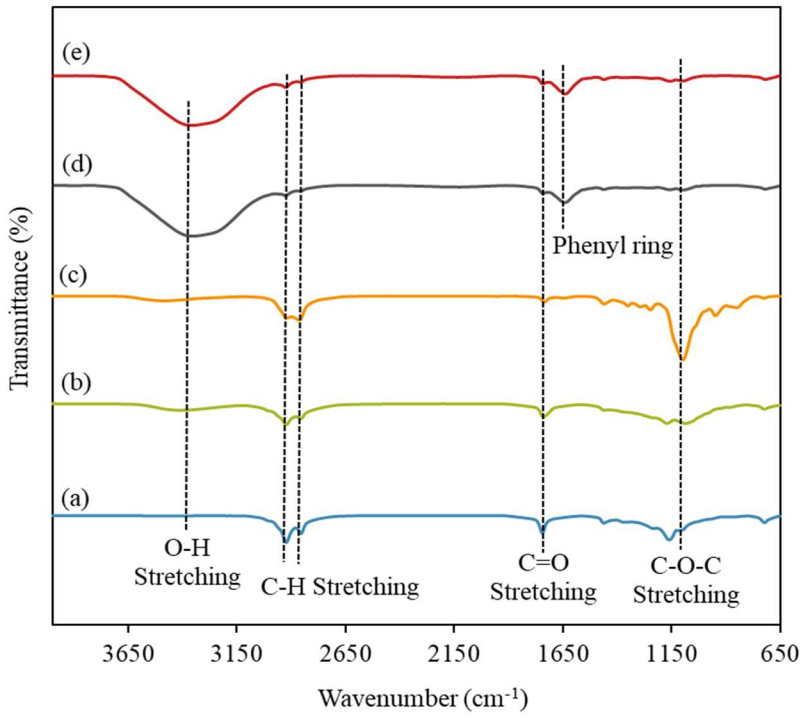

Figure 1. FTIR Spectra of (a)palm oil, (b)tween 80, (c)span 80, (d)catechin, and (e)WPOC-NEs

Droplet size, zeta potential, polydispersity index, conductivity determination, and transmission electron microscopy (TEM) image

The W/PO nanoemulsion containing catechin had mean droplet size, zeta potential, polydispersity index (PDI), and conductivity values of 185.60 nm, -38.4 mV, 0.251, and 0.001 mS/cm, respectively. The droplet size of a nanoemulsion ranging from 20 to 200 nm is substantially smaller than that of conventional colloidal systems. The small droplet size results in a larger colloidal surface area, which increases solubility and the rate of dissolution [23]. The zeta potential, which assesses a particle's electrokinetic potential, was utilized to determine the stability of the nanoemulsion. Readings higher than +30mV or lower than –30mV were said to be stable nanoemulsion [24]. The negatively charged zeta potential was caused by the polyoxyethylene chains in Tween 80, indicating sufficient Van der Waals electrostatic repulsions to stabilize and disperse the w/o system for an extended time [12].

The PDI value was used to examine the particle size distribution in the nanoemulsion. A PDI value close to zero implies a monodispersed system, whereas a PDI value close to one indicates a polydispersed system (a wide range of droplet sizes). Pongsumpun et al.[25] reported that a nanoemulsion system is termed monodispersed (with a restricted size distribution) if the PDI value is less than 0.3. Therefore, in this study, the optimized water in palm oil nanoemulsion containing catechin was found to be stable with a PDI value of 0.251, which conveys it is monodispersed (Figure 2) with a negative zeta potential value.

Conductivity is the measurement of the free amount of water and ions in a solution, as it will respond to any ions present. This parameter aids in determining the type of nanoemulsion produced [26]. The optimized nanoemulsion containing catechin had a low conductivity value of 0.001 mS/cm, indicating that the oil phase was a continuous phase and that the nanoemulsion created was a water-in-oil (W/O) nanoemulsion.

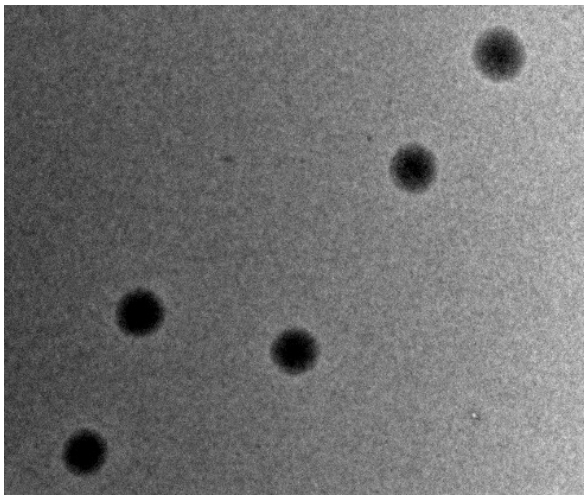

Figure 2. TEM image of WPOC-NEs

pH determination

The pH of the optimized W/PO nanoemulsion containing catechin was 6.82. These features are suitable for pharmaceutical applications, such as topical [27] and oral [28] applications.

Viscosity determination

A steady-state test was used to investigate the behavior of the W/PO nanoemulsion containing catechin. In the steady-state test, the W/PO nanoemulsion containing catechin displayed shear-thinning behavior (non-linear relationship), as shown in Figure 3. The flow behavior index (n) based on Equation (2) can be used to determine the rheological parameters of the W/PO nanoemulsion, as illustrated in Table 3. The value of n is 0.269 (n<1), indicating that the W/PO nanoemulsion was shear-thinning. The W/PO nanoemulsion's viscosity decreased with increasing shear rate, demonstrating that the W/PO nanoemulsion is a non-Newtonian pseudoplastic fluid (n<1). The non-Newtonian pseudo-plastic behavioral features of the W/PO nanoemulsion containing catechin are shown in Table 3. Notably, this type of behavior seen here matches the majority of over-the-counter pharmaceutical applications.

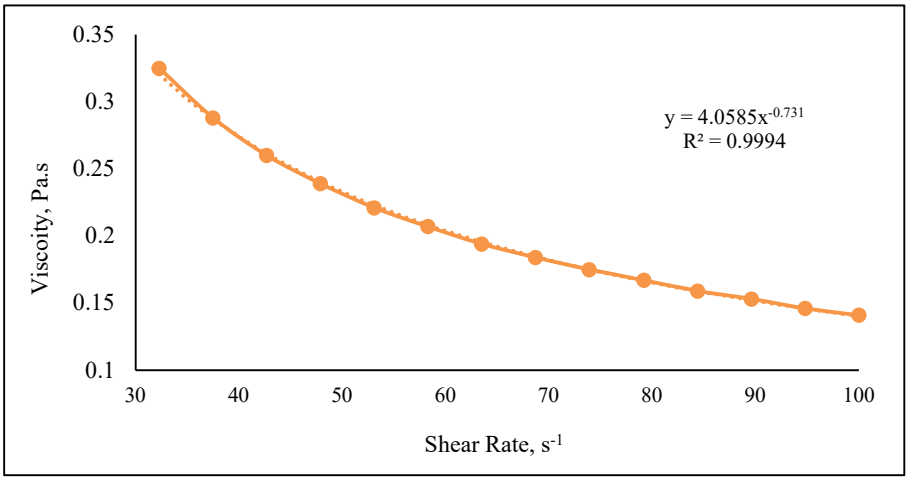

Figure 3. Graph of viscosity (Pa.s) versus shear rate (s^{-1})

Table 3. Flow behavior indices (n), consistency coefficients (k), and regression coefficients (R^2) of the water in palm oil nanoemulsion containing catechin

Sample	k	n	R^2
W/PO nanoemulsion containing catechin	4.0585	0.269	0.9994

Stability tests

For the centrifugation test, the W/PO nanoemulsion containing catechin showed no phase separation after centrifuging at 4000 rpm for 30 min. This indicates the formulation's remarkable stability against creaming or sedimentation and its expected long shelf life.

A storage stability study was conducted by exposing the W/PO nanoemulsion to three different temperatures (10, 25, 50 ℃) for 28 days. Table 4 denotes the physical stability of W/PO nanoemulsion containing catechin under three different storage temperatures. Based on the observations, the optimized nanoemulsion at 10 ℃ remained a homogeneous mixture and exhibited no physical or phase changes for 28 days. This shows that the W/PO nanoemulsion is stable at low temperatures.

However, at 25 and 50 ℃, the W/PO nanoemulsion was unstable after seven days and exhibited physical changes. This is due to the polyoxyethylene head groups of non-ionic surfactants of Tween 80 being known to be dehydrated when exposed to high storage temperatures. This alters the optimal curvature of the surfactant monolayer and reduces the range of steric repulsion, leading to instability [29].

Table 4. Physical stability of water in palm oil nanoemulsion containing catechin under different storage temperatures (10, 25, 50 ℃)

Storage Temperature (℃)	Storage Stability (days)				
	1	7	14	21	28
10	/	/	/	/	/
25	/	X	X	X	X
50	/	X	X	X	X

/ = stable or no physical change X = unstable and physical changes occur

Conclusion

This study successfully developed a stable water in palm oil nanoemulsion containing catechin with 54% palm oil, a ratio of Tween 80: Span 80 (26.2:73.8) with HLB 7.1 and 0.10% of catechin. The physicochemical characterization indicated that the W/PO nanoemulsion containing catechin was in the nanosize range, had a zeta potential of -38.4mV, and a PDI of 0.251, showing that the nanoemulsion produced was stable and monodispersed. The TEM image obtained showed that the monodispersity of the WPOC-NEs was correlated with the PDI value. The pH of the nanoemulsion was 6.82, which was within the acceptable pH range for pharmaceutical products and its conductivity was low, indicating the developed nanoemulsion was a water-in-oil nanoemulsion type. The nanoemulsion produced remained stable and had no phase separation under centrifuge test and during storage at 10℃ over 28 days. These results show that it will be helpful for rationalizing design of water-in-oil nanoemulsion-based delivery systems to encapsulate catechin in food, beverage, cosmetic, and pharmaceutical products.

Acknowledgment

The authors would like to sincerely thank the GIP Grant, Reference code: 600-RMC/GIP 5/3(023/2022), for their financial support for this research. The authors also acknowledge the Faculty of Applied Science of Universiti Teknologi MARA for the facilities provided to carry out this project.

References

1. Bae, J., Kim, N., Shin, Y., Kim, S. Y., and Kim, Y. J. (2020) Activity of catechins and their applications. *Biomedical Dermatology*, 4(1):1-10.
2. Tsai, Y. J., and Chen, B. H. (2016). Preparation of

catechin extracts and nanoemulsions from green tea leaf waste and their inhibition effect on prostate cancer cell PC-3. *International Journal of Nanomedicine*, 11: 1907-1926.

3. Bhushani, J. A., Karthik, P., and Anandharamakrishnan, C. (2016). Nanoemulsion based delivery system for improved bioaccessibility and Caco-2 cell monolayer permeability of green tea catechins. *Food Hydrocolloids*, 56: 372-382.
4. Wilson, R. J., Li, Y., Yang, G., and Zhao, C. X. (2022). Nanoemulsions for drug delivery. *Particuology*, 64: 85-97.
5. Li, P. H., and Chiang, B. H. (2012). Process optimization and stability of d-limonene-in-water nanoemulsions prepared by ultrasonic emulsification using response surface methodology. *Ultrasonics Sonochemistry*, 19(1): 192-197.
6. Tayeb, H. H., Felimban, R., Almaghrabi, S., and Hasaballah, N. (2021). Nanoemulsions: Formulation, characterization, biological fate, and potential role against COVID-19 and other viral outbreaks. *Colloids and Interface Science Communications,* 45: 1-19.
7. Liang, C. X., Qi, D. L., Zhang, L. N., Lu, P., and Liu, Z. D. (2021). Preparation and evaluation of a water-in-oil nanoemulsion drug delivery system loaded with salidroside. *Chinese Journal of Natural Medicines*, 19(3): 231-240.
8. Rai, V. K., Mishra, N., Yadav, K. S., and Yadav, N. P. (2018). Nanoemulsion as pharmaceutical carrier for dermal and transdermal drug delivery: formulation development, stability issues, basic considerations and applications. *Journal of Controlled Release*, 270: 203-225.
9. Maluin, F. N., Hussein, M. Z., and Idris, A. S. (2020). An overview of the oil palm industry: Challenges and some emerging opportunities for nanotechnology development. *Agronomy*, 10(356): 1-20.
10. Goindi, S., Kaur, A., Kaur, R., Kalra, A., and Chauhan, P. (2016). Nanoemulsions: an Emerging technology in the food industry. *Emulsions*, 3: 651-688.
11. Qonita, H. A., Syafika, N., Valensie, V., Kamba, J., Maulana, A., and Permana, A. D. (2022). Development water in oil nanoemulsion of diethylcarbamazine for enhanced the characteristics for lymphatic targeting: A proof of concept study. *Journal of the Indian Chemical Society*, *99*(4): 1-5.
12. Baba Shekh, A. O., Abdul Wahab, R., and Yahya, N. A. (2022). Formulation of roselle extract water-in-oil nanoemulsion for controlled pulmonary delivery. *Journal of Dispersion Science and Technology*, 44(10): 1830-1841.
13. Ahmad, N., Alam, M. A., Ahmad, R., Umar, S., and Jalees Ahmad, F. (2018). Improvement of oral efficacy of irinotecan through biodegradable polymeric nanoparticles through in vitro and in vivo investigations. *Journal of Microencapsulation,* 35(4): 327-343.
14. Roselan M. A., Ashari S. E., Faujan N. H., Faudzi S. M. M., and Mohamad R. (2020). An improved nanoemulsion formulation containing kojic monooleate: optimization, characterization and in vitro studies. *Molecules*. 25(11): 1-23.
15. Shahidan, N. S., Salim, N., and Ashari, S. E. (2019). Preparation and optimization of ibuprofen-loaded nanoemulsion formulation. *Journal of Multidisciplinary Engineering Science and Technology,* 6(12): 89-96.
16. Liu, Q., Huang, H., Chen, H., Lin, J., and Wang, Q. (2019). Food-grade nanoemulsions: Preparation, stability and application in encapsulation of bioactive compounds. *Molecules*, 24(23): 1-37.
17. Genot, C., Kabri, T. H., and Meynier, A. (2013). Stabilization of omega-3 oils and enriched foods using emulsifiers. *Food Enrichment with Omega-3 Fatty Acids*, 252: 150–193.
18. Wang, L., Dong, J., Chen, J., Eastoe, J., and Li, X. (2009). Design and optimization of a new self-nanoemulsifying drug delivery system. *Journal of Colloid and Interface Science*, 330(2): 443-448.
19. Colucci, G., Santamaria-Echart, A., Silva, S. C., Fernandes, I. P. M., Sipoli, C. C., and Barreiro, M. F. (2020). Development of water-in-oil emulsions as delivery vehicles and testing with a natural antimicrobial extract. *Molecules*, *25*(9): 1-15.
20. Sittinun, A., Pisitsak, P., Manuspiya, H., Thiangtham, S., Chang, Y. H., and Ummartyotin, S. (2020). Utilization of palm olein-based polyol for polyurethane foam sponge synthesis: potential as a

sorbent material. *Journal of Polymers and the Environment*, *28*(12): 3181-3191.

21. Branzoi, F., and Branzoi, V. (2017). Investigation of some nonionic surfactants as corrosion inhibitors for carbon steel in sulfuric acid medium. *International Journal of Electrochemical Science*, 12(8): 7638-7658.
22. Ahmad, N., Ahmad, R., Alrasheed, R. A., Almatar, H. M. A., Al-Ramadan, A. S., Amir, M., and Sarafroz, M. (2020). Quantification and evaluations of catechin hydrate polymeric nanoparticles used in brain targeting for the treatment of epilepsy. *Pharmaceutics*, 12(3): 1-34.
23. Danaei, M., Dehghankhold, M., Ataei, S., Hasanzadeh Davarani, F., Javanmard, R., Dokhani, A., Khorasani, S., and Mozafari, M. R. (2018). Impact of particle size and polydispersity index on the clinical applications of lipidic nanocarrier systems. *Pharmaceutics*, 10(2): 1-17.
24. Marzuki, N. H. C., Wahab, R. A., and Hamid, M. A. (2019). An overview of nanoemulsion: concepts of development and cosmeceutical applications. *Biotechnology and Biotechnological Equipment*, 33(1): 779-797.
25. Pongsumpun, P., Iwamoto, S., and Siripatrawan, U. (2020). Response surface methodology for optimization of cinnamon essential oil nanoemulsion with improved stability and antifungal activity. *Ultrasonics Sonochemistry*, 60: 1-27.
26. Jiang, J., Mei, Z., Xu, J., and Sun, D. (2013). Effect of inorganic electrolytes on the formation and the stability of water-in-oil (w/o) emulsions. *Colloids and Surfaces A: Physicochemical and Engineering Aspects*, 429: 82-90.
27. Yahya, N. A., Abdul Wahab, R., Attan, N., Abdul Hamid, M., Mohamed Noor, N., and Kobun, R. (2022). *Ananas comosus* peels extract as a new natural cosmetic ingredient: oil-in-water (o/w) topical nano cream stability and safety evaluation. *Evidence-Based Complementary and Alternative Medicine*, 2022: 1-9.
28. Attebäck, M., Hedin, B., and Mattsson, S. (2022). Formulation optimization of extemporaneous oral liquids containing naloxone and propranolol for pediatric use. *Scientia Pharmaceutica*, 90(1): 1-18.
29. Ryu, V., McClements, D. J., Corradini, M. G., and McLandsborough, L. (2018). Effect of ripening inhibitor type on formation, stability, and antimicrobial activity of thyme oil nanoemulsion. *Food Chemistry*, 245: 104-111.

Malaysian Journal of Analytical Sciences (MJAS)
Published by Malaysian Analytical Sciences Society

SCREENING OF PROMOTED CeO_2/Al_2O_3 CATALYSTS IN AQUEOUS PHASE GLYCEROL REFORMING AND HYDROGENOLYSIS INTO 1,2-PROPANEDIOL

(Penyaringan Mangkin Penggalak CeO_2/Al_2O_3 dalam Fasa Akueus Pembaharuan dan Hidrogenolisis Gliserol Kepada 1,2-Propanadiol)

Norsahida Azri[1,2,3]*, Ramli Irmawati [2,3,5]*, Rudy Hakim Danial Leong[2,3], Usman Idris Nda-Umar[2,3,4], Mohd Izham Saiman[2,3], Yun Hin Taufiq-Yap [2,3] and G. Abdulkareem-Alsultan[2,3].

[1]*Preparatory Centre for Science and Technology, Universiti Malaysia Sabah, 88400 Kota Kinabalu, Sabah, Malaysia*
[2]*Department of Chemistry, Faculty of Science, Universiti Putra Malaysia, 43400 UPM Serdang, Selangor, Malaysia*
[3]*Catalysis Science and Technology Research Centre (PutraCat), Faculty of Science, Universiti Putra Malaysia, 43400 UPM Serdang, Selangor, Malaysia*
[4]*Department of Chemical Sciences, Federal Polytechnic, PMB 55, Bida, Niger State, Nigeria*
[5]*Laboratory of Processing and Product Development, Institute of Plantation Studies, Universiti Putra Malaysia, 43400 UPM Serdang, Selangor, Malaysia*

**Corresponding author: norsahidaazri@ums.edu.my; irmawati@upm.edu.my*

Received: 3 November 2023; Accepted: 16 January 2024; Published: 29 April 2024

Abstract

A series of promoted CeO_2/Al_2O_3 catalysts (10Cu-90CeO_2/Al_2O_3, 10Ni-90CeO_2/Al_2O_3, 10Co-90CeO_2/Al_2O_3) were synthesized via method of impregnation and later calcined at 600 °C. Those catalysts were formerly tested for their physico-chemical properties by X-ray diffraction (XRD), H_2-temperature programmed reduction (H_2-TPR), and NH_3-temperature programmed desorption (NH_3–TPD). After characterized, it was then evaluated in the performance of catalytic glycerol conversion into 1,2-propanediol; propylene glycol (1,2-PDO; PG) via aqueous phase glycerol reforming and hydrogenolysis route under inert N_2 flow. Among the examined catalysts, CeO_2/Al_2O_3 with 10wt% Cu loading (10Cu-90CeO_2/Al_2O_3) showed optimum catalytic activity with 88.5% glycerol conversion (GC) and 35.5% PG selectivity at 300 °C reaction temperature, 2 h duration test, 30 cc/min of N_2 initial pressure, 0.1 g catalyst dosage and 10wt% glycerol concentration. The high catalytic performance of 10Cu-90CeO_2/Al_2O_3 was owing to the good copper-cerium-alumina interaction via its good metal reducibility at low temperature along with good acid capacity for the reaction.

Keywords: copper, cerium, alumina, acid capacity, glycerol conversion

Abstrak

Satu siri mangkin penggalak CeO_2/Al_2O_3 (10Cu-90CeO_2/Al_2O_3, 10Ni-90CeO_2/Al_2O_3, 10Co-90CeO_2/Al_2O_3) telah disintesis menggunakan kaedah pegisitepuan lalu dikalsinkan pada 600 °C. Kesemua mangkin telah dikaji sifat fiziko-kimia dengan menggunakan pembelauan sinar-X (XRD), penuruan suhu terprogram H_2 (H_2-TPR), dan nyahjerapan suhu terprogram NH_3 (NH_3-

TPD). Ia kemudian dinilai dalam penukaran pemangkinan gliserol kepada 1,2-propanadiol; propilena glikol (1,2-PDO; PG) melalui pendekatan pembaharuan dan hidrogenolisis fasa akueus dibawah aliran N_2. Diantara mangkin yang diuji, CeO_2/Al_2O_3 dengan 10wt% muatan Cu ($10Cu\text{-}90CeO_2/Al_2O_3$) telah menunjukkan aktiviti pemangkinan yang optimum dengan 88.5% penukaran gliserol (GC) dan 35.5% keterpilihan PG pada suhu tindak balas 300 °C, tempoh masa 2 jam, 30 cc/min tekanan awal N_2 dan 0.1 g dos mangkin dan 10wt% kepekatan gliserol. Prestasi pemangkinan yang tinggi oleh $10Cu\text{-}90CeO_2/Al_2O_3$ didorong oleh interaksi baik antara kuprum-ceria-alumina melalui penurunan logam yang baik pada suhu rendah dan kapasiti asid yang sesuai untuk tindak balas.

Kata kunci: kuprum, serium, alumina, kapasiti asid, penukaran gliserol

Introduction

The amount of glycerol produced as primary by-product of biodiesel worldwide is far exceeds the current market demand thus resulted in a surplus of crude glycerol, which then impacted the refined glycerol market. It was expected that the global crude glycerol market to provide approximately 680,000 tonnes by 2024 [1-2]. Therefore, one of the opportunities for valorising crude glycerol is by recycling and producing a demanded value-added product from it which is propylene glycol (PG) or 1,2-propanediol (1,2-PDO). This product is essentially used as an industrial solvent, intermediate chemical or multipurpose solvent, additive in food products, unsaturated polyester resins, pharmaceuticals, and cosmetics [3-4]. At present, PG is industrially produced by hydrating propylene oxide to 1,2-PDO from the oxidised propylene via petrochemical route [5-6]. With diminishing returns from petroleum and concerns over detrimental environmental effects on the rise, methods of synthesising PG from renewable sources would significantly desired. Therefore, to cope with uprising production and recycling glycerol from industry, catalytic aqueous phase hydrogenolysis (APH) intertwined with aqueous phase reforming (APR) of glycerol are among the routes that was opted as they can be operated at the same reaction conditions. By coupling both reactions, no external supply of hydrogen is required since in situ generated hydrogen obtained from glycerol reforming process is being utilised in same the reactor. This made the aqueous glycerol hydrogenolysis via reforming route as an alternative to the conventional hydrogenolysis since it can be run even at mild pressure with an inert gas environment without being equipped with external source of hydrogen to the reaction system [7]. However, it could not be denied that conventional hydrogenolysis could offer better product selectivity than the APR approach since the molecular hydrogen supplied could effectively react with the glycerol to give the desired product within low hydrogen pressure [4,6,10].

During aqueous hydrogenolysis process, glycerol is dehydrated and the primary C-OH bonds is cleaved over acid sites to form unstable intermediates such as acetol and it was further hydrogenated by which hydrogen atom was added to acetol over metal sites catalyst to give desired APH product which is propylene glycol [8]. However, formation of lower alcohol such as methanol as side reaction products could happen in the reaction due to the excess C-C cracking of the intermediate acetol [9]. Cerium oxide catalysts have been given more attention due to their effectiveness in various catalytic and hydrogenation reaction used as support, co-catalyst or promoter attributable to its good acid capacity as well as metal reducibility [7,10-11]. As well, a modification of cerium oxide as based-catalyst with promoter/co-catalyst such as Cu and Ni have been reported to improve and strengthen the metal-metal interactions and improved the catalytic performance via their chemical strength, acidity, metallic phase dispersion and reducibility (oxygen ion mobility) [12]. Therefore, the good features of a promoted CeO_2 catalyst would possibly enhance and promote efficiency towards primary C-OH bond cleavage of glycerol which eventually rearranged to activate/break the C=O bond of acetol before it undergoes hydrogenation in a second step to give PG product [13]. Furthermore, Al_2O_3 with high availability, unique acid properties and strong metal-support interaction has been selected as catalyst support to facilitate adequate surface area to allow active phase deposition, prevent sintering and therefore offering hydrogen spill medium for it to moves towards metal surface during reaction. Hence both metal and acid sites surface are the active sites for the reaction. The

performance of a series of promoted CeO_2/Al_2O_3 catalysts were tested in the glycerol conversion to produce PG under 300 ℃ reaction temperature, 2 h reaction time, 30 cc/min of N_2 pressure, 10wt% glycerol concentration, and 0.1 g catalyst dosage to relate the role of catalyst's metal reducibility and acid capacity in the reaction performance.

Materials and Methods

Chemicals

Aluminium oxide beads, Al_2O_3 (3mm) and cerium(II) nitrate hexahydrate ($Ce(NO_3)_2.6H_2O$) with 99% purity was supplied by Sigma-Aldrich. Copper(II) nitrate trihydrate, $Cu(NO_3)_2.3H_2O$ (≥99%) (MW: 241.60 g/mol), nickel(II) nitrate hexahydrate ($Ni(NO_3)_2.6H_2O$) (≥99%) (MW: 290.79 g/mol), and cobalt(II) nitrate hexahydrate ($Co(NO_3)_2.6H_2O$) (≥99%) (MW: 291.03 g/mol) were obtained from R&M Chemicals. Glycerol (≥99.5%) and N-methyl-N (trimethylsilyl)trifluoroacetamide (MSTFA) (≥98.5%) used as derivatizing agent GC derivatization was from Sigma Aldrich while pyridine (C_5H_5N) as binder solvent in derivitization process was from Merck. All chemicals used in this study were of either analytical or of reagent grade.

Preparation of catalyst

The catalysts were prepared by impregnation method. Prior to preparation, monometallic cerium was prepared first using 5g of precursor $Ce(NO_3)_2.6H_2O$ which was discretely dissolved and stirred homogeneously in 5 mL of distilled water. The solution was then added in 5g alumina beads (Al_2O_3) (referred as solution 1). The mixture was then stirred, left dried in drying oven for 24 hours at 90 °C, and calcined at 600 °C for 3 hours in a tube furnace with static air and a ramping rate of 10 ºC/min. The synthesised catalyst was denoted as CeO_2/Al_2O_3 catalyst. For preparing promoted CeO_2/Al_2O_3 catalyst, solution 1 was added with a proper amount of $Cu(NO_3)_2.3H_2O$ at 10wt% copper loading. After which, the similar method as indicated in preparation of Ce/Al_2O_3 was followed. The promoted catalyst was named as $10Cu\text{-}90CeO_2/Al_2O_3$ catalyst. Other promoted catalysts were prepared using similar method indicated by $10Cu\text{-}90CeO_2/Al_2O_3$.

Characterisation of catalyst

The phase composition structure and crystallite size of the catalysts were measured using X-ray diffraction (XRD) using Shimadzu diffractometer model XRD-6000. Hydrogen-temperature programmed reduction (H_2-TPR) was used to evaluate metal reducibility using a Thermo-Finnigan TPD/R/O 1100 SERIES equipped with a TCD (thermal conductivity detector). Typically, catalyst sample of 0.05g was placed in a U-shaped quartz reactor and pre-treated in flowing N_2 ($30cm^3$/min) for 0.5 h at 150 ºC to remove any moisture content followed by cooling it until room temperature. After pretreatment, H_2 chemisorption analysis was performed from temperature 50 ºC to 1000 ºC at a rate 10 ºC/min under $5\%H_2$/He flow ($30cm^3$/min). For determination acid sites of the catalyst, NH_3-temperature programmed desorption NH_3-TPD was used. The experiments were conducted on the same apparatus as the TPR experiments described above. The analysis that was conducted in this present study has already been explained in great detail in our previous study [14].

Set up for experiment

The catalytic reaction was carried out in a mechanically stirred 100 mL two-necked round bottom flask connected to N_2 gas flow (30 cc per min) of semi-batch reactor. In a typical run, 10 wt.% glycerol and 0.1g of catalyst was added into the reactor. Prior to reaction experiment, the reactor contained aqueous mixture was vacuumed and purged with N_2 for 10 min to remove the air inside. The reaction was then performed at 300 ºC and 2 h reaction time. Liquid product from the reaction was collected from the released of vapour species which then undergo condensation using external water-cooling circulator. Once reaction duration was completed, the reactor was cooled down to room temperature before the liquid product was collected and filtered from present catalyst upon analysis.

Product analysis

The liquid product of the experiment was analysed using a gas chromatography–mass spectrometry (GC-MS) coupled with an HP-5 capillary column after it had been extracted thrice using ethyl acetate. Prior for the sample preparation, the liquid product was derivatized with silyl

agent of N-Methyl-N-(trimethylsilyl)trifluroacetamide (MSTFA) and was then dissolved in pyridine (C_5H_5N) as binding solvent at 1:1:1 ratio followed by 30 min heating in oven at 70 ºC to allow complete bonding of silylation reaction. Next, 1 µL sample was injected into the GC inlet at 250 ºC and helium gas was served as the carrier gas. The initial temperature of the oven was set at 40 ºC and held for 6 min, then ramped up to 270 ºC with heating rate of 7ºC min^{-1}. The glycerol conversion and selectivity were determined by comparing the retention time of standard with experimental-based products.

Results and Discussion

Figure 1 shows the XRD analysis of CeO_2/Al_2O_3 and promoted CeO_2/Al_2O_3 catalysts (10Cu-90CeO_2/Al_2O_3, 10Ni-90CeO_2/Al_2O_3, 10Co-90CeO_2/Al_2O_3). As seen in Figure 1, for all catalysts, the intensity of each peak is hardly distinguished could possibly be due to the amorphous character of alumina present in the catalyst. Broad diffraction peaks of CeO_2 (2θ = 29.2º, 32.5º, 48.2º and 57.3º) and Al_2O_3 (2θ = 32º, 38.1º, 47º, 57º and 67.2º) phases were observed with low crystallinity in all catalysts. For promoted catalysts, formation of CuO, NiO and CoO peaks at was detected with the similar peak of CeO_2 and/or Al_2O_3 peak respectively as the oxides could be getting embedded inside the bulk of CeO_2/Al_2O_3 and hard to be distinguished. From Table 1, it was observed that the addition of metal species on CeO_2/Al_2O_3 increased the bulk metal's crystallite of CeO_2 at 2θ = 29.2º due to the metal species filled the interstitial spaces of bulk CeO_2.

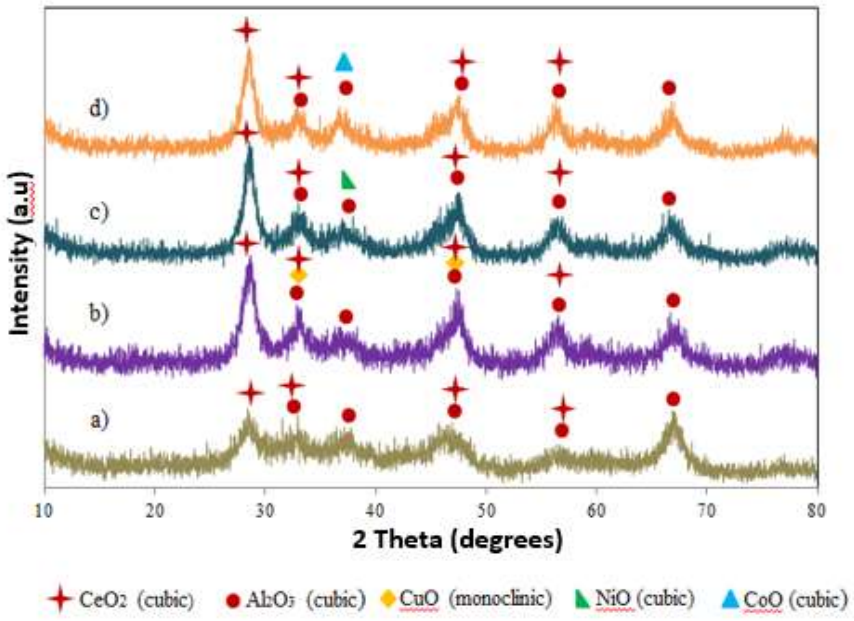

Figure 1. XRD diffractograms of calcined (a) CeO_2/Al_2O_3, (b) 10Cu-90CeO_2/Al_2O_3, (c) 10Ni-90CeO_2/Al_2O_3 and (d) 10Co-90CeO_2/Al_2O_3 catalysts

Figure 2 shows H_2-TPR profile of CeO_2/Al_2O_3 and promoted CeO_2/Al_2O_3 catalysts. From Figure 2, all catalysts gave reduction peak at higher temperature of ~800 ºC. The reduction peak at 800 ºC for all catalysts was indicated by the reduction of bulk ceria from CeO_2 to Ce_2O_3 since the reduction profile for CeO_2/Al_2O_3 was reduced at that temperature [15]. However, when copper was incorporated into CeO_2/Al_2O_3 matrix, a new reduction with high peak appeared at a much lower temperature ~180-330 ºC indicating reduction of the non-associated oxide of dispersed CuO species and the bulk reduction of CuO species, respectively since > 260 ºC was for reduction of CuO species interacted with support of either CeO_2 or Al_2O_3 [16-17]. The peaks could be attributed to the two steps reduction of CuO to Cu^+ and to metallic Cu^0 species [18]. Meanwhile, the

broader reduction peak of 10Ni-90CeO_2/Al_2O_3 than unpromoted CeO_2/Al_2O_3 was noticed at ~900 ºC. This could be due to the reduction of sintered oxide species or bulk nickel oxide interacted strongly with support. Accordingly, the broader reduction profile was caused by the slow diffusion or H_2 adsorption by the interphase due to the presence of clusters of well sintered metal species or alloy cluster [18]. For 10Co-90CeO_2/Al_2O_3, a reduction peak at ~1000 ºC was shifted to higher reduction temperature of CeO_2/Al_2O_3 attributing to the reduction of the metal oxide in complex species, where the interactions with the support were strong [19-20]. The findings in this study indicates that the addition of CuO with 10wt% Cu loading to the CeO_2/Al_2O_3 exhibited a significant promoting effect towards lower reduction temperature. Therefore, embedding Cu species into CeO_2/Al_2O_3 matrix resulted in good interactions between the Cu-Ce-alumina species that enhanced the reduction properties and thus metal reducibility of the catalysts.

Table 1. Physicochemical properties of the catalysts

	XRD	H_2-TPR			NH_3-TPD
Catalyst	**Crystallite Size[a] (nm)**	**H_2 Consumed at Different Temp (µmol/g)**		**Total Amount H_2 Consumed (µmol/g)**	**Total Amount NH_3 Adsorbed (µmol/g)**
		150-550 ºC	**> 550 ºC**		**> 550 ºC**
CeO_2/Al_2O_3	25.6	19	148	167	345
10Cu-90CeO_2/Al_2O_3	43.9	340	84	424	1009
10Co-90CeO_2/Al_2O_3	34.4	-	221	221	1007
10Ni-90CeO_2/Al_2O_3	32.1	-	978	978	1442

[a]The data were estimated according to the Debye Scherrer equation using the FWHM of the CeO_2 peak at $2\theta = 29.2^o$.

As seen from Table 1, amount of H_2 uptake for promoted CeO_2/Al_2O_3 catalysts was increased than the unpromoted catalyst indicating more H_2 was consumed since more oxides species was reducible at larger exposure area which increased H_2 adsorption. This was corroborated with the high and broader reduction peaks profile of the 10Cu-90CeO_2/Al_2O_3 and 10Ni-90CeO_2/Al_2O_3, respectively.

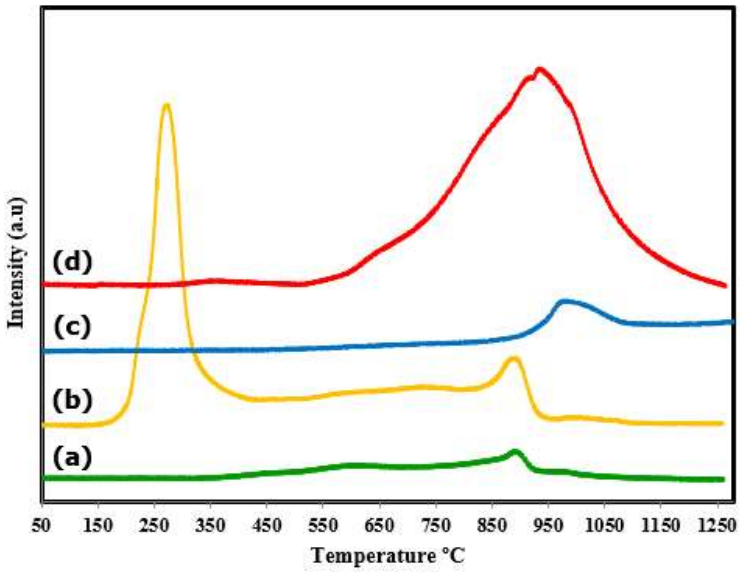

Figure 2. H_2-TPR reduction profile of calcined (a) CeO_2/Al_2O_3, (b) 10Cu-90CeO_2/Al_2O_3, (c) 10Co-90CeO_2/Al_2O_3 and (d) 10Ni-90CeO_2/Al_2O_3 catalysts

According to Zhu et al. [21], the acid sites of catalysts facilitated the activation of the C-OH bonds during dehydration step of glycerol to form unstable intermediate product before formation of PG. Figure 3 depicts the NH_3-TPD profiles of all catalysts while Table 1 lists their corresponding amount NH_3 desorption. The finding showed that the acidity was increased for promoted CeO_2/Al_2O_3 catalysts than the unpromoted CeO_2/Al_2O_3 with the order of CeO_2/Al_2O_3 < 10Co-90CeO_2/Al_2O_3 ≈ 10Cu-90CeO_2/Al_2O_3 < 10Ni-90CeO_2/Al_2O_3. This result demonstrated that the incorporation of copper, cobalt, and nickel oxide species into CeO_2/Al_2O_3 matrix promoted higher acid sites capacity since the presence more oxides species provide larger exposure area for NH_3 adsorption [8].

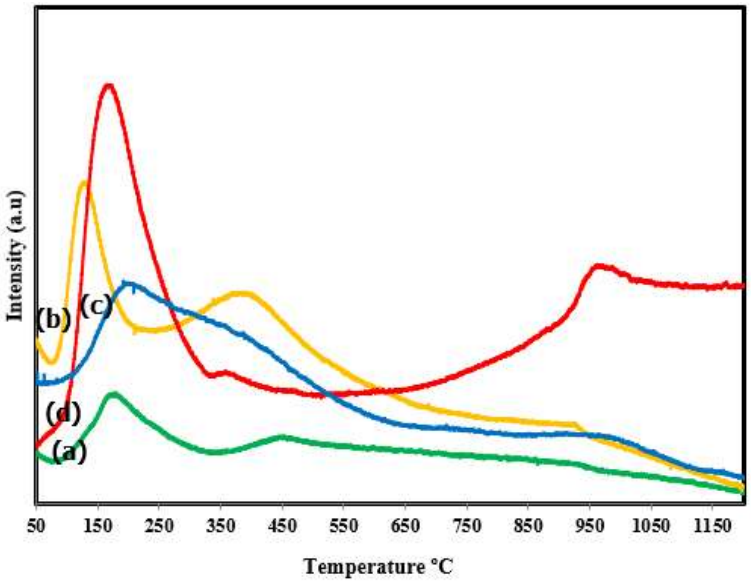

Figure 3. NH_3-TPD profile of calcined (a) CeO_2/Al_2O_3, (b) 10Cu-90CeO_2/Al_2O_3, (c) 10Co-90CeO_2/Al_2O_3 and (d) 10Ni-90CeO_2/Al_2O_3 catalysts

Table 2 shows the catalytic activity of CeO_2/Al_2O_3, and all promoted CeO_2/Al_2O_3 catalysts. All catalysts were evaluated based on their ability to convert glycerol and product selectivity to PG and methanol. From Table 2, the conversion of glycerol and PG selectivity were low with CeO_2/Al_2O_3 catalyst, however the activity was increased with the presence of promoted CeO_2/Al_2O_3 catalysts in the reaction. Among all tested catalysts, 10Cu-90CeO_2/Al_2O_3 contributed the highest glycerol conversion of 88% and 35.5% PG selectivity with the trend of CeO_2/Al_2O_3 < 10Ni-90CeO_2/Al_2O_3 < 10Co-90CeO_2/Al_2O_3 < 10Cu-90CeO_2/Al_2O_3. The high catalytic performance of 10Cu-90CeO_2/Al_2O_3 was attributed to its adequate acid sites (1009 µmol/g) that facilitated the dehydration of glycerol to form unstable intermediates which later converts into PG. The reduction profile of 10Cu-90CeO_2/Al_2O at significantly lower temperature with peak maxima of 260 ºC also contributed to the high activity performance as agreed with other studies suggesting that the reduction of copper oxide species was active at 200-300 ºC [16-17]. At that temperature, copper oxide species was reduced into metallic copper since that temperature was active for CuO reduction. In other words, reduction of copper oxide was occurred in situ by which the presence of metallic species would in turn hydrogenate the unstable intermediate on its surface into desired PG. Formation of of methanol in the reaction was due to the breaking of C-C bond [22]. In addition, when the activity of catalysts in this study was compared with the reported catalyst from literature [23] as shown in Table 2, the catalyst in this study exhibited good glycerol conversion and 1,2-PDO selectivity. This could be due to the catalyst's metal-metal interaction and acidity which contributed to the desired results during catalytic reaction.

Table 2. Performance by catalytic reaction of all catalysts

Sample	GC Conversion (%)	Product Selectivity (%) PG	Methanol	Ref
CeO_2/Al_2O_3	14.8	6.13	93.9	This work
10Cu-90Ce/Al_2O_3	88.0	35.5	64.5	This work
10Co-90Ce/Al_2O_3	84.5	12.3	87.7	This work
10Ni-90Ce/Al_2O_3	63.7	12.9	87.1	This work
Ni/SiO_2–Al_2O_3	40.0	7.9	1.21	[23]

Reaction conditions: 300ºC temperature, 2 h of reaction time, 30cc/min of N_2 initial pressure, 10wt% aqueous glycerol solution and 0.1 g of catalyst dosage

Conclusion

Among all the promoted CeO_2/Al_2O_3 catalysts tested, 10Cu-90CeO_2/Al_2O_3 catalyst gave the highest conversion of glycerol (88%) and PG selectivity (35.5%) over reaction temperature of 300 °C, 2 hours reaction duration, 30 cc/min of N_2 initial pressure, 0.1g of catalyst dosage and 10wt% aqueous glycerol solution. This was attributed to the good Cu-Ce-Al_2O_3 interactions via its adequate acid capacity and the ability to be reduced at lower reduction temperature in the range that close to the experimental reaction temperature of 300 °C.

Acknowledgment

The authors would like to express the highest gratitude to Universiti Putra Malaysia for financial assistance under Financial Research Grant Scheme (Vote No.: 5524811) and Initiative Putra Student Grant (GP-IPS/2018/9619500).

References

1. Attarbachi, T., Kingsley, Martin.D. and Spallina, V. (2023). New trends on crude glycerol purification: A review. *Fuel*, 340: 127485.
2. Ali, S.S., Elsamahy, T., Abdelkarim., E.A. Al-Tohamy., R., Kornaros., M., Ruiz., H. A. Zhao, T., Li, F. and Sun. J. (2022). Biowastes for biodegradable bioplastics production and end-of-life scenarios in circular bioeconomy and biorefinery concept. *Bioresource Technology*, 363: 127869.
3. Yuan, J., Li, S., Yu, L., Liu. Y. and Cao, Y. (2013). Efficient catalytic hydrogenolysis of glycerol using formic acid as hydrogen source. *Chinese Journal of Catalysis*, 342: 2066-2074.
4. Roy, D., Subramaniam, B. and Chaudhari, R.V. (2010). Aqueous phase hydrogenolysis of glycerol to 1, 2-propanediol without external hydrogen addition. *Catalysis Today*, 156: 31-37.
5. Soares, A.V.H. Atia, H., Armbruster, U., Passos, F.B. and Martin, A. (2017). Platinum, palladium and nickel supported on Fe_3O_4 as catalysts for glycerol aqueous-phase hydrogenolysis and reforming. *Applied Catalysis A, General*, 548: 179-190.
6. Zhou, C.H., Denga, K., Serio, M.D., Xiao. S., Tong, D.S., Li, L., Lin, C.X., Beltramini, J., Zhang, H. and Yua, W.H. (2017). Cleaner hydrothermal hydrogenolysis of glycerol to 1,2-propanediol over Cu/oxide catalysts without addition of external hydrogen. *Molecular Catalysis*, 432: 274-284.
7. Roy., D, Subramaniam, B. and Chaudhari, R.V. (2010). Aqueous phase hydrogenolysis of glycerol to 1,2-propanediol without external hydrogen addition. *Catalysis Today*, 156: 31-37.
8. Mallesham. B., Sudarsanam, P., Reddya, B.V.S. and Reddya, B.M. (2016). Development of cerium promoted copper–magnesium catalysts for biomass valorization: Selective hydrogenolysis of bioglycerol. *Applied Catalysis B: Environmental*, 181: 47-57.
9. Zhou, C.H., Deng, K., Serio, M.D., Xiao, Sa., Shen, D., Li, T.Li., Lin, C.X., Beltramini, J., Zhang, H. and Yu, W.H. (2017). Cleaner hydrothermal hydrogenolysis of glycerol to 1,2-propanediol over Cu/oxide catalysts without addition of external hydrogen. *Molecular Catalysis*, 432: 274-284.
10. Yu. W., Zhao. J., Ma. H., Miao, H., Song. Q. and Xu, J. (2010). Aqueous hydrogenolysis of glycerol over Ni–Ce/AC catalyst: Promoting effect of Ce on

catalytic performance. *Applied Catalysis A: General*, 383: 73-78.

11. Ye, L., Duan, X., Lin, H. and Yuan, Y. (2012). Improved performance of magnetically recoverable Ce-promoted Ni/Al_2O_3 catalysts for aqueous phase hydrogenolysis of sorbitol to glycols. *Catalysis Today*, 183: 65-71.
12. Jiang, T., Kong, D., Xu, K. and Cao, F. (2016). Hydrogenolysis of glycerol aqueous solution to glycols over Ni–Co bimetallic catalyst: Effect of ceria promoting. *Applied Petrochemical Research*, 6(2): 135-144.
13. Freitas, I.C., Manfro, R.L. and Souza, M.M.V.M. (2018). Hydrogenolysis of glycerol to propylene glycol in continuous system without hydrogen addition over Cu-Ni catalysts. *Applied Catalysis B: Environmental,* 220: 31-41.
14. Azri, N., Ramli, I., Nda-Umar, U.I., Shamsuddin, M. Razali., Saiman, M. I. and Taufiq-Yap, Y. H. (2020). Copper-dolomite as effective catalyst for glycerol hydrogenolysis to 1,2-propanediol. *Journal of Taiwan Institute and Chemical Engineering,* 112: 34-51.
15. Marinho, A.L.A., Toniolo, F.S., Noronha, F.B., Epron, F., Duprez, D. and Bion, N. (2021). Highly active and stable Ni dispersed on mesoporous CeO_2-Al_2O_3 catalysts for production of syngas by dry reforming of methane. *Applied Catalysis B: Environmental,* 281: 119459.
16. Finger, P.H., Osmari, T.A., Cabral, N.M., Bueno, J.M.C. and Gallo, J.M.R. (2021). Direct synthesis of Cu supported on mesoporous silica: Tailoring the Cu loading and the activity for ethanol dehydrogenation. *Catalysis Today,* 381: 26-33.
17. Xiao, Z., Wang, X., Xiu, J., Wang, Y., Williams, C.T. and Liang, C. (2014). Synergetic effect between Cu^0 and Cu^+ in the Cu-Cr catalysts for hydrogenolysis of glycerol. *Catalysis Today,* 234: 200-207.
18. Soares, A.V.H., Salazar, J.B., Falcone, D.D., Vasconcellos, F.A., Davis, R.J. and Passos, F.B.A. (2016). Study of glycerol hydrogenolysis over Ru–Cu/Al_2O_3 and Ru–Cu/ZrO_2 catalysts. *Journal of Molecular Catalysis A: Chemical,* 415: 27-36.
19. Zhao, Y., Zhang, Y., Wang,Y., Zhang, J., Xu, Y., Wang, S. and Ma, X. (2017). Structural evolution of mesoporous silica supported copper catalyst for dimethyl oxalate hydrogenation. *Applied Catalysis A General,* 539: 59–69.
20. Vargas-Hernández, D., Rubio-Caballero, J.M., Santamaría-González, J., Moreno-Tost, R., Mérida-Robles, J.M., Pérez-Cruz, M.A., Jiménez-López, A., Hernández-Huesca, R. and Maireles-Torres, P. (2014). Furfuryl alcohol from furfural hydrogenation over copper supported on SBA-15 silica catalysts. *Journal Molecular Catalysis A Chemical,* 383-384: 106-113.
21. Zhu, S., Gao, X., Zhu, Y., Zhu, Y., Zheng, H. and Li, Y. (2013). Promoting effect of boron oxide on Cu/SiO_2 catalyst for glycerol hydrogenolysis to 1,2-propanediol. *Journal of Catalysis,* 303: 70-79.
22. Pudi, S.M., Biswa, P., Kumar, S. and Sarkar, B. (2015). Selective hydrogenolysis of glycerol to 1,2 propanediol over bimetallic Cu-Ni catalysts supported on γ-Al_2O_3. *Journal of the Brazilian Chemical Society,* 268 (8): 1551-1564.
23. Seretis, A. and Tsiakaras, P. (2016). Hydrogenolysis of glycerol to propylene glycol by in situ produced hydrogen from aqueous phase reforming of glycerol over SiO_2–Al_2O_3 supported nickel catalyst. *Fuel Processing Technology,* 142: 135-146.

Malaysian Journal of Analytical Sciences (MJAS)
Published by Malaysian Analytical Sciences Society

CORROSION INHIBITION STUDY OF CARBOXYMETHYL CELLULOSE-IONIC LIQUID VIA ELECTROCHEMICAL AND MACHINE LEARNING TECHNIQUE

(Kajian Perencatan Kakisan Menggunakan Karboksimetil Selulosa-Cecairan Ionik Melalui Teknik Elektrokimia dan Pembelajaran Mesin)

Adi Hafizamri Ariffin[1], Wan Mohd Norsani Wan Nik[1], Samsuri Abdullah[1], Mohd Ikmar Nizam Mohamad Isa[2], Vincent Izionworu[3], and Mohammad Fakhratul Ridwan Zulkifli[1*]

[1]*Marine Materials Research Group, Faculty of Ocean Engineering Technology, Universiti Malaysia Terengganu, 21030 Kuala Nerus, Terengganu, Malaysia*
[2]*Energy Storage Research, Advanced Materials Team, Ionic & Kinetic Materials Research (iKMaR) Laboratory, Faculty of Science and Technology, Universiti Sains Islam Malaysia, 71800 Nilai, Negeri Sembilan, Malaysia*
[3]*Department of Chemical/Petrochemical Engineering, Rivers State University, Nkpolu-Oroworukwo, Port Harcourt, Nigeria*

[*]*Corresponding author: fakhratulz@umt.edu.my*

Received: 5 October 2023; Accepted: 25 February 2024; Published: 29 April 2024

Abstract

Corrosion is a natural phenomenon defined as the deterioration of a substance or its properties due to interactions between the substance and the environment. Prolonged exposure to corrosive environment had negative consequences, including increased repair and maintenance costs, decreased structural integrity, and fatalities. An approach to address the issue is to use a corrosion inhibitor. Numerous inhibitors have lately been developed or made accessible on the market. However, some could be dangerous or contain of volatile organic compounds (VOCs). Our study introduces carboxymethyl cellulose (CMC) mixed with 1-ethyl-3-methylimidazolium acetate ([EMIM][Ac]) ionic liquid, also known as CIL, as a corrosion inhibitor on mild steel in seawater. The functional group of combined CIL was examined using Fourier transform infrared spectroscopy (FTIR). The study employed mild steel specimens immersed in varying concentrations of CIL, subject to electrochemical impedance spectroscopy (EIS) measurements at different temperatures. The obtained result of EIS measurement were analyzed to calculate corrosion inhibition efficiency (IE) of CIL. 46 of electrochemical data were fed into a machine learning technique to forecast the effectiveness of the inhibition. Results indicate when inhibition concentration rises, so does inhibition efficiency (IE). The inhibitory efficiency of CIL decreased as the temperature of the test solution rose. At an ambient temperature of 950 ppm, an IE result of 83% was recorded. Levenberg-Marquardt (LM), Bayesian Regularization (BR), and Scale Conjugate Gradient (SCG) training algorithms were compared via Neural Network Fitting Tool (NNTool). LM was found to be the best backpropagation training algorithm, providing the highest regression value (R) of 0.907 and the lowest mean square error (MSE) of 0.006 when compared to BR and SCG. With R value closer to 1 and MSE close to 0, the use of Artificial Neural Networks (ANN) appears to offer a new insight in predicting methods with the goal of easing the hassle and time-consuming of experimental work.

Keywords: carboxymethyl cellulose, corrosion inhibitor, electrochemical, ionic liquid, machine learning

Abstrak

Kakisan adalah fenomena semula jadi yang ditakrifkan sebagai kemerosotan bahan atau sifatnya akibat interaksi antara bahan dan persekitaran. Pendedahan yang berpanjangan kepada persekitaran yang mengkakis memberi kesan yang negatif, termasuk peningkatan kos pembaikan dan penyelenggaraan, penurunan integriti keatas struktur dan mengakibatkan kemusnahan. Salah satu penyelesaian kepada isu ini ialah menggunakan perencat kakisan. Banyak perencat kakisan telah dibangunkan atau boleh didapati di pasaran. Namun, sebahagian daripadanya mungkin berbahaya atau mengandungi banyak sebatian organik meruap (VOC). Kajian ini memperkenalkan karboksimetil selulosa (CMC) dalam 1-etil-3-metilimidazolium asetat ([EMIM][Ac]) cecair ionik, juga dikenali sebagai CIL, sebagai perencat kakisan pada keluli lembut dalam air laut untuk menangani isu alam sekitar. Kumpulan berfungsi kimia hasil dr campuran CIL ini telah diperiksa menggunakan spektroskopi inframerah transformasi Fourier (FTIR). Kajian ini menggunakan spesimen keluli lembut yang direndam dalam kepekatan CIL yang berbeza, diuji menggunakan spektroskopi impedans elektrokimia (EIS) pada suhu yang berbeza. data pengukuran EIS yang diperolehi dianalisis untuk mengira kecekapan perencatan kakisan (IE) CIL. 46 data elektrokimia digunakan di dalam teknik pembelajaran mesin (ML) untuk meramalkan keberkesanan perencatan. Keputusan menunjukkan bahawa apabila kepekatan perencatan meningkat, kecekapan perencatan juga menunjukkan peningkatan. Kecekapan perencatan CIL menurun apabila suhu larutan ujian meningkat. Pada kepekatan 950 ppm pada suhu ambang, keputusan kecekapan perencatan dengan peratusan 83% telah direkodkan. Algoritma latihan Levenberg-Marquardt (LM), Bayesian Regulisasi (BR), dan Gradien Konjugasi Skala (SCG) telah dibandingkan melalui aplikasi Ketepatan Jaringan Saraf (NNtool). LM didapati sebagai algoritma latihan rambatan belakang terbaik, memberikan nilai regresi (R) tertinggi 0.9072580 dan ralat min kuasa dua (MSE) terendah sebanyak 0.0054787 jika dibandingkan dengan BR dan SCG. Dengan nilai R yang menghampiri 1 dan MSE menghampiri 0, penggunaan Rangkaian Saraf Tiruan (ANN) memberi pandangan baharu dalam kaedah peramalam dengan matlamat untuk mengurangkan kerumitan dan penghambatan kerja eksperimen yang memakan masa.

Kata kunci: karboksimetil selulosa, penghambat pengaratan, elektrokimia, cairan ionik, pembelajaran mesin

Introduction

Mild steels are the most extensively used structural materials in a variety of industries due to their good material qualities such as mechanical durability, ease of processing, and low manufacturing cost. This material is frequently utilized in industries as a primary building material for the creation of structural shapes, automobile parts, buildings, plants, pipelines, bridges, and tin cans [1]. Mild steel, on the other hand, is prone to corrosion when exposed to conditions with high moisture levels and corrosive substances [2, 3]. Corrosion is defined as the degradation of a substance or its qualities because of interactions between the substance and its surroundings. It would be more feasible to avoid corrosion rather than strive to entirely eradicate it [4]. Hence, a corrosion inhibitor is utilized by adding it to a closed system to slow down, prevent, and lower the rate of corrosion [5]. Natural products are frequently being researched for corrosion inhibitors as an alternative to conventional corrosion inhibitors due to recent environmental concerns [6, 7, 8].

Carboxymethyl cellulose (CMC) is a cellulose derivative that has been identified as the most abundant and widely used cellulosed derivatives due to the presence of polar functional groups such as carboxyl and hydroxyl groups, which contribute significantly to CMC's strong adsorption ability to metal structures [9, 10]. Despite the fact that CMC is frequently used in the food and pharmaceutical industries [11], some research has indicated that this cellulose derivative is also effective as a corrosion inhibitor [9, 12]. In this project, 1-ethyl-3-methylimidazolium acetate ([EMIM][Ac]) ionic liquid was chosen as the CMC solvent due to its loosely bounded anions, which can strongly interact with the polar functional (-OH, $-NH_2$) groups of polysaccharides, causing them to solubilize and increasing the performance of CMC inhibitor [13]. The objective of this study is to investigate the stability and polarization resistance of carboxymethyl cellulose ionic liquids (CIL) as corrosion inhibitor for mild steel in seawater incorporate ANN for prediction study. Most researchers commonly utilize acidic and artificial NaCl electrolytes in their electrochemical studies involving CMC and CMC with additive [15-24]. In contrast, this research opts for natural seawater. The selection to employ seawater as the electrolyte offers the advantage of investigating the material's behavior in marine environments and offshore applications. This approach aids in gaining insights into the natural corrosion effects

in the environments and contributes to a better understanding, ultimately facilitating the development of strategies to mitigate corrosion in such settings. To reduce the time and effort required for laboratory work, a computational method based on machine learning was used to make predictions.

Artificial Neural Network (ANN) approaches were a viable choice for describing the corrosion inhibition behavior of carboxymethyl cellulose (CMC) in 1-ethyl-3-methylimidazolium acetate ionic liquid (CIL). The Levenberg-Marquardt (LM), Bayesian Regularization (BR), and Scaled Conjugate Gradient (SCG) training algorithms were used, and their performance indicators were analyzed. Furthermore, no machine-learning technique has been used to predict the corrosion inhibition of carboxymethyl cellulose in the ionic liquid ([EMIM][Ac]). By computing the corrosion inhibition efficiency prediction by using machine learning serves as an alternative to extrapolate the experimental data. The establishment of this model would be another new finding where it would beneficial to the research community. This model can be used to determine the corrosion inhibition behavior without the need for replicating the same experiment. This precise and robust model brought a new insight for the researchers parallel with the progression in Industrial Revolution 4.0 (IR 4.0).

Materials and Methods

Sample preparation

the experiment employed a square form of marine grade mild steel-chemical composition-carbon 0.051%, manganese 0.734%, silicon 0.126%, sulphur 0.004%, phosphorus 0.016% and iron remaining [14] with dimensions of 25mm x 25mm x 3mm. Prior to the EIS experiment, the coupons were polished with multiple grits (120, 600, 800, and 1200 grit) of emery paper to remove defects and attain the desired surface roughness. The coupon was then washed with acetone, rinsed with distilled water, quickly dried in air, and stored in desiccators before use. Carboxymethyl cellulose is constantly mixed with 1-ethyl-3-methylimidazolium acetate ([EMIM][Ac]) at 60°C for 30 minutes. Following that, the prepared inhibitor is subjected to Fourier transform infrared (FTIR) spectroscopy utilizing an INVENIO FT-IR Spectrometer with a wavelength range of 400 to 4000 cm^{-1} and a spectra resolution of 4 cm^{-1} to identify and analyze the functional group of a sample based on its interaction with infrared light. Immersion of mild steel in seawater is conducted for three hours to allow the adsorption of CIL onto the mild steel surface. The seawater was collected from Institute of Oceanography and Environment (INOS) Universiti Malaysia Terengganu.

Electrochemical impedance spectroscopy (EIS)

The impedance analysis of the mild steel interface in the presence and absence of CIL in seawater were characterized by using electrochemical impedance spectroscopy (EIS) Gamry 1010E. Three electrodes corrosion cell setup was used where the mild steel was employed as working electrode, Ag/AgCl as reference electrode, and platinum rod as counter electrode. Those electrodes were placed in a 200 mL beaker of seawater as electrolyte solution. For each experiment, volume of the test solutions was maintained to ensure the consistency of the parameter to all experiment. The testing parameters for the EIS are tabulated in Table 1. The ambient temperature was a foundational reference in standard laboratory conditions, establishing a baseline for electrochemical studies [25]. The elevated temperature of 50 °C was chosen to examine the moderate temperature effects on the corrosion inhibitor's behavior. At high temperature, 70 °C was utilized for higher temperature investigations. The decline in inhibition efficiency might happen as temperature rises was a characteristic observed in inhibitors physically adsorbed onto the metal surface resulted in desorption of some adsorbed corrosion inhibitor molecules from the metal surface[22, 26]. Electrochemical impedance spectroscopy (EIS) experiments were performed with a small amplitude perturbation 10 mV (peak-to-peak) for an AC signal where the surface area of the mild steel coupon was 3.125cm^2.

Table 1. Testing parameter of CIL for EIS experiment

Temperature (°C)	Concentration (ppm)	Frequency (Hz)
	0	
Room Temperature	350	
50	550	0.1 – 1000000
70	750	
	950	

The corresponding data then analyzed by using Gamry 1010E EChem Analyst. Determination of the corrosion respond parameters in the Nyquist plot was obtained via construction of equivalent circuit compatible with the Nyquist diagram. To fit the model using simplex method, theoretical transfer function Z(ω) was constructed parallel with the combination of a resistance R_p and a constant phase element (CPE), then, both in series with another solution resistance R_s as shown in Figure 1. To validate the suited equivalent circuit, the experimental data are fitted to the equivalent circuit and the circuit elements are obtained [27].

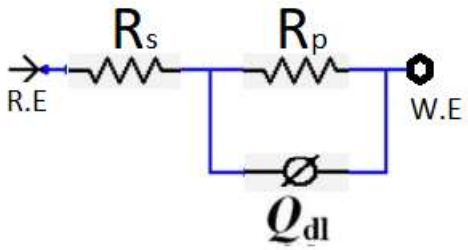

Figure 1. Equivalent circuit for the EIS Analysis

The inhibition efficiency (IE) was determined from Polarization Resistance, R_p according to Equation 1:

$$IE(\%) = \frac{R_{p(inhibited)} - R_{p(uninhibited)}}{R_{p(inhibited)}} \times 100\% \quad (1)$$

Artificial neural network

The Multilayer Feed Forward Neural Network (MFNN) was utilized to estimate the effectiveness of CIL's inhibition using MATLAB® software (R2021b, MathWorks®, Natick, MA, USA). The experimental data obtained from EIS characterization served as the source of the 46 datasets for the modelling investigation. Min-max technique of data normalization was adopted in this study which in the end, the values are between 0 and 1 for an accurate predictive model. The technique is based on the following Equation 2.

$$x = \frac{x_{input} - x_{min}}{x_{max} - x_{min}} \quad (2)$$

where x = (x1, . . ., xn) and x is the normalized data.

A satisfactory normalization is one of the most important aspects of the training process, which represents a direct influence on the model and offers benefits such as suitable results and a considerable decrease in calculation time [28].

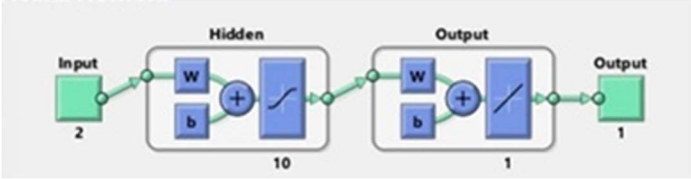

Figure 2. Artificial Neural Network Architecture

To forecast the inhibition efficiency (IE) behavior model of CIL, the Neural Network Toolbox in MATLAB was employed. The default settings of the NNTool were utilized, with 70% (32) of the data allocated for training, 15% (7) for validation, and 15% (7) for testing purposes, chosen randomly from a dataset of 46. The distribution of data between training, validation, and testing in a model of small data range to ensures the chosen subset accurately represents the entire dataset, reducing bias and minimizing the risk of overfitting [29]. As shown in Figure 2, architecture models are composed of three layers with a 2:10:1 structure. Temperature (°C) and Concentration (ppm) were the two parameters that made up the first layer, also known as the input layer. The model is built using 10 nodes in the hidden layer, and the output layer predicts inhibition as IE. As training algorithms, Levenberg-Marquardt (LM), Bayesian Regularization (BR), and Scaled Conjugate Gradient (SCG) were employed. Since there is no established standard procedure, a trial-and-error approach using 10 nodes with one concealed layer is used [30]. Performance Indicator (PI) used to measure the effectiveness and efficiency ANN developed. Here, 2 PI are used. Regression accuracy R is used to measure accuracy and mean square error (MSE) is used to measure error. The accuracy measures evaluate values from 0 to 1, whereby the best model is considered when the evaluated values are close to 1, while the best model for error measures are selected if the evaluated value is close to 0.

Results and Discussion

Fourier transform infrared (FTIR) spectroscopy

Figure 3 depicts the FTIR spectra of the cellulose ionic liquid (CIL). It displays a notable peak in the range of 3600-3100 cm^{-1}, corresponding to the stretching vibration of the O-H (hydroxyl) group [31]. This FTIR range revealed changes in the O-H stretching peak, signifying modifications in the hydrogen bonding pattern. The peak's increased broadening and intensity indicate the development of new formations of hydrogen bonds due to the disruption of the compact structure of the intramolecular hydrogen bonding in the glucose units of CMC [32]. The peak at the range of 1500-1620 cm^{-1} corresponds to the stretching vibration of the C=C group that can be found in the imidazole ring stretch [33]. Based on [34], it is suggested that around 1700 cm^{-1} corresponds to the C=O group and a peak at around 1200 cm^{-1} corresponds to C–N stretching. The peak at 1016 cm^{-1} in the FTIR range is typically associated with the symmetric stretching vibration of C–OC– in CMC [35]. The alkanes functional group exhibited spectral IR bands at around 750 cm^{-1} due to C-H rocking vibrations and at 600 cm^{-1} due to C-H bending vibrations [34]. The FTIR analysis revealed the presence of characteristic functional groups in the CMC mixed with the ([*EMIM*][Ac]) mixture, which was consistent with its expected molecular structure.

.

Electrochemical impedance spectroscopy (EIS)

The corrosion inhibition efficiency of mild steel using CIL at Open Circuit Potential (OCP) was investigated by the area-normalized EIS tested in different concentration and solution temperature. With the different concentration used in the experiment, the result of polarization resistance, R_p shows an increasing trend of value as seen in Figure 4 and Table 2. The R_p for mild steel in the absence of CIL at ambient temperature was recorded with the value of 163.4 $\Omega.cm^2$. The R_p value of inhibited sample at ambient temperature for 350, 550, 750 and 950 ppm were recorded at 274.2, 482.6, 665.4, and 980.0 $\Omega.cm^2$ respectively. The calculated inhibition efficiency, IE were 40.30%, 65.98%, 75.12% and 83.09% for 350, 550, 750 and 950 ppm respectively. The increase of inhibition efficiency with increased concentration of the inhibitor may be attributed to increasing of the number of –O–,–OH, and –COOH groups, which increased the surface coverage of CMC molecules on the metal surface [9]. With the concentration variation, the electrochemical change is indicative of inhibition of corrosion process at increased concentration of the inhibitors by adsorbing on the surface of the metal thereby reducing the active surface area exposed to the aggressive corrosive electrolyte medium [1].

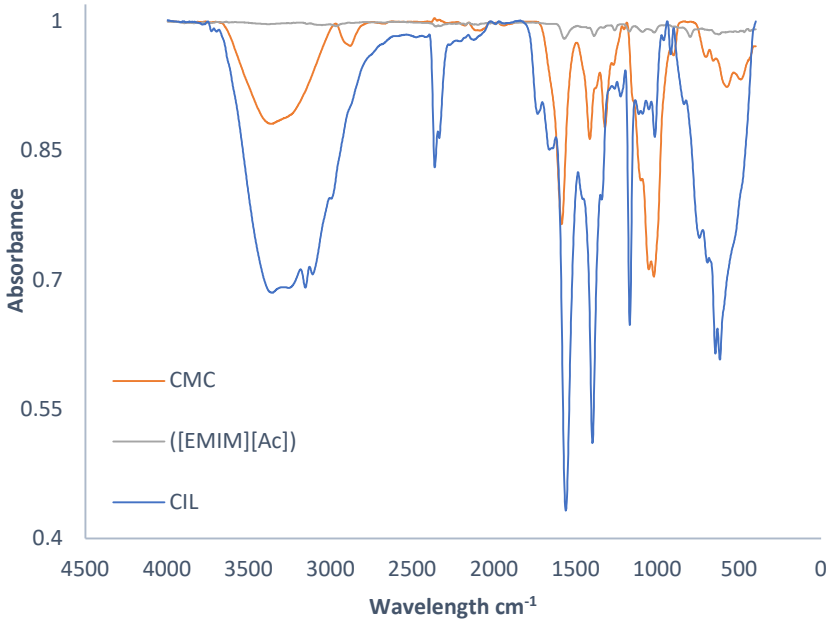

Figure 3. FTIR spectrum of CIL

Table 2. Impedance data for Mild steel in different concentration and temperature effect on CIL in seawater

Concentration (ppm)	Temperature (°C)	R_p (Ω.cm^2)	R_s (Ω.cm^2)	Y_0 (F)	IE %
blank	ambient temperature	163.400	3.129	0.014	0.00
350		274.200	4.739	0.004	40.30
550		482.600	6.856	0.005	65.98
750		665.400	3.914	0.020	75.12
950		980.300	4.231	0.014	83.09
blank	50	120.700	3.063	0.032	0.00
350		157.300	5.233	0.003	23.85
550		217.900	4.677	0.004	44.40
750		391.200	7.068	0.010	68.92
950		340.100	6.993	0.005	64.34
blank	70	85.270	3.111	0.031	0.00
350		155.400	5.465	0.008	45.06
550		201.600	3.239	0.004	56.85
750		295.600	4.876	0.002	70.59
950		249.200	4.876	0.002	65.21

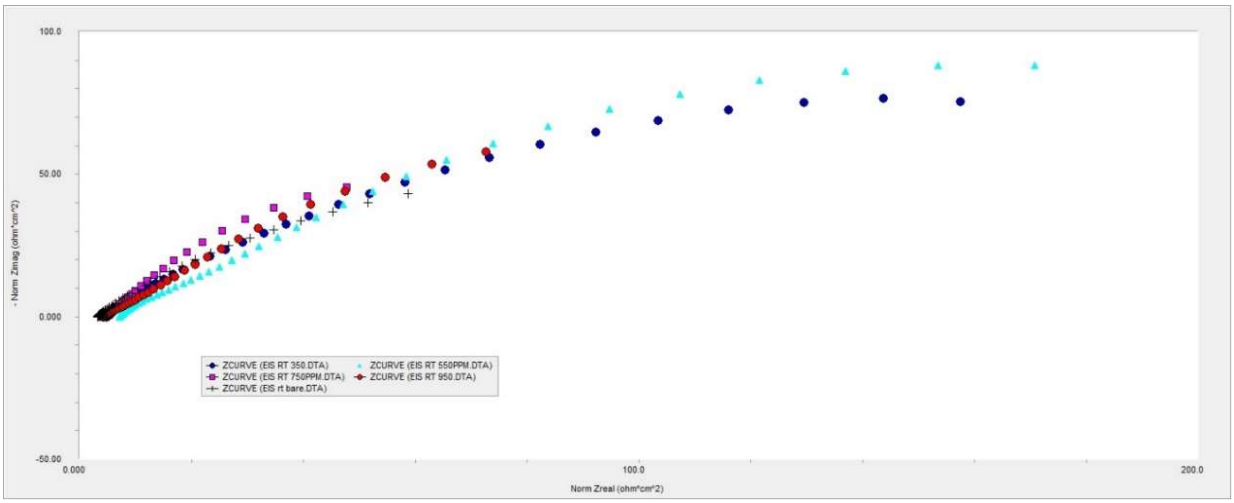

Figure 4. Nyquist Plot at ambient temperature

When testing the sample with a range of different temperatures, as shown in Table 2, the R_p for mild steel in both the presence and absence of CIL was recorded, with lower values obtained compared to the sample tested at ambient temperature. At 50 °C, the R_p recorded for mild steel in the absence of CIL was 120.7 Ω.cm^2. The R_p values of the inhibited sample at 50 °C for 350, 550, 750, and 950 ppm were recorded at 157.30 Ω.cm^2, 217.90 Ω.cm^2, 391.20 Ω.cm^2, and 340.10 Ω.cm^2, respectively. The inhibition efficiency was calculated as 23.85%, 44.40%, 68.92%, and 64.34% for 350, 550, 750, and 950 ppm at 50 °C, respectively, as shown in Table 2.

The Nyquist plot of inhibited and uninhibited samples tested at 70°C is shown in Figure 6. The plot shows a nearly perfect semicircle indicates that the electrochemical process is mainly contributed by the charge transfer process. Charge transfer is the difference in real impedance axis at low and high frequency regions. At 70 °C, the recorded R_p for mild steel in the absence of CIL was 83.27 Ω.cm^2. The inhibited samples record the R_p value at 155.40 Ω.cm^2, 201.00 Ω.cm^2, 295.60 Ω.cm^2, and 249.20 Ω.cm^2 for 350, 550, 750, and 950 ppm respectively. The calculated inhibition efficiency was 45.06%, 56.85%, 70.59% and 65.21% for 350ppm, 550ppm, 750ppm, and 950ppm at 70 °C respectively.

Temperature has a significant impact on corrosion rates and inhibiting efficiency. With the increase in the testing solution temperature from ambient to 70 °C, the inhibition efficiency decreased. At higher temperatures, the adsorption process may be hindered or reversed, leading to reduced inhibitor coverage and decreased corrosion protection due to reduced adsorption**,** as well as faster corrosion reactions because of the higher kinetic energy [36]. However, at temperatures of 50 °C and 70 °C, the inhibition efficiency decreased for both concentrations of 950 ppm. This might suggest a decrease in the effectiveness of the inhibition as the sample experienced the limitation of inhibitor adsorption. This occurs when inhibitor molecules do not have enough opportunities to adsorb onto a metal surface. According to [37], the decreased inhibition efficiency as the temperature increases is due to the physisorption mechanism, which might be attributed to an increase in the solubility of the precipitated inhibitor molecules on the mild steel surface. With the decrease in the number of molecules absorbed on the mild steel surface as the temperature rose, this resulted in a deficiency in the inhibitive performance.

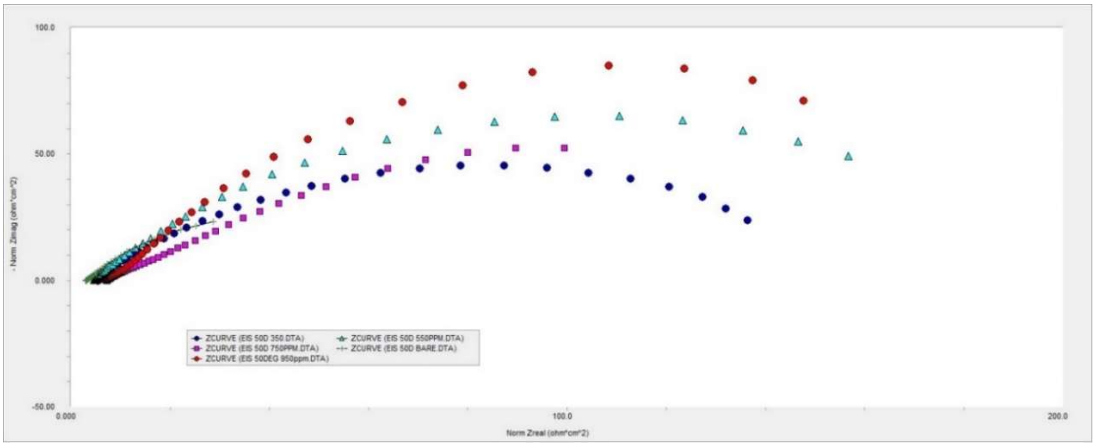

Figure 5. Nyquist Plot of CIL at 50°C testing solution temperature

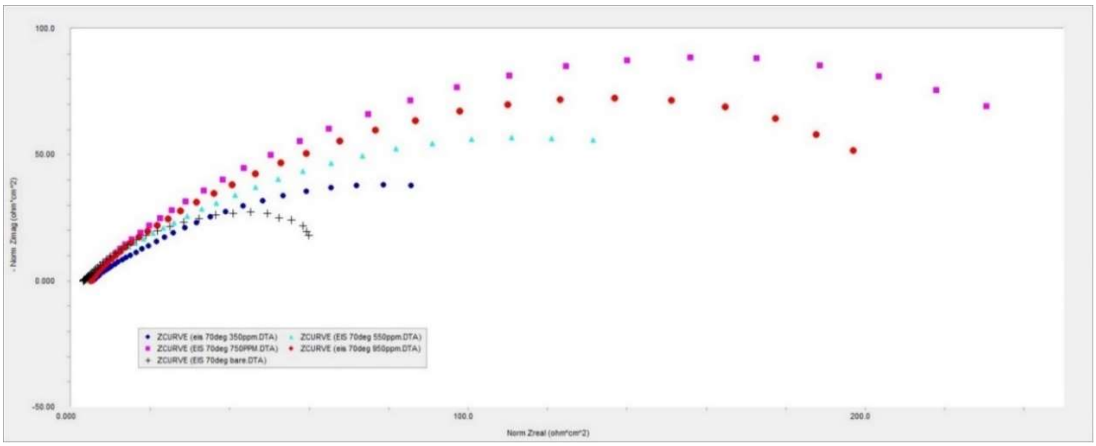

Figure 6. Nyquist Plot of CIL at 70°C testing solution temperature

Artificial neural network

Table 3 shows the values of the performance indicator (PI) obtained from the modelling study via an artificial neural network. The correlation coefficients (R) for the Levenberg Marquardt (LM) training algorithm in the training, validation, and testing phases were 0.907258, 0.887539, and 0.861082, respectively. Based on the fitted line shown in Figure 7a, the fitted slope line falls within the expected range, showing the good relationship between the predicted and observed values obtained for the training, validation, and testing samples. The results from the Bayesian Regularisation (BR) training algorithm showed slightly lower precision as the R values for the training and testing phases were 0.862106 and 0.804661, in comparison to those obtained from LM, as shown in Figure 7b. The Scale Conjugated Gradient (SCG) training algorithm produced R values of 0.359149, 0.828020, and 0.333080 for training, validation, and testing, respectively. The SCG had the lowest precision of all the training algorithms.

Table 3. Performance indicator of training algorithm

Training Algorithm	LM		BR		SCG	
PI	MSE	R	MSE	R	MSE	R
Training	0.005	0.907	0.008	0.862	0.073	0.359
Validation	0.001	0.888	-	-	0.035	0.828
Testing	0.019	0.861	0.002	0.805	0.058	0.333

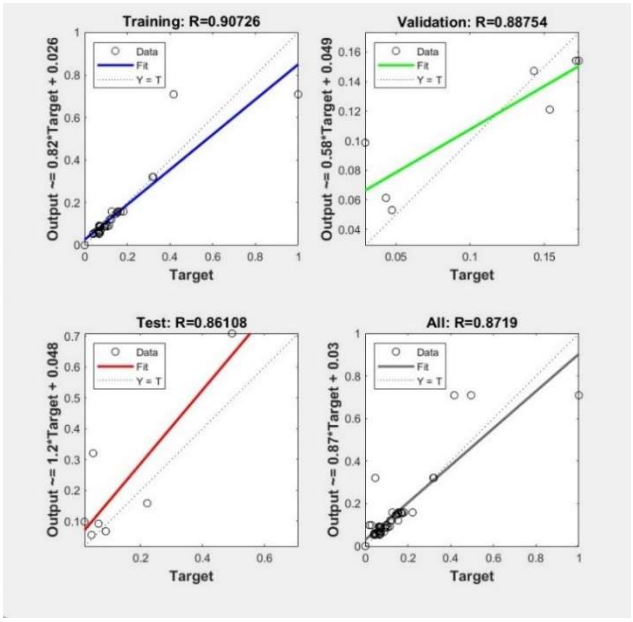

(a)

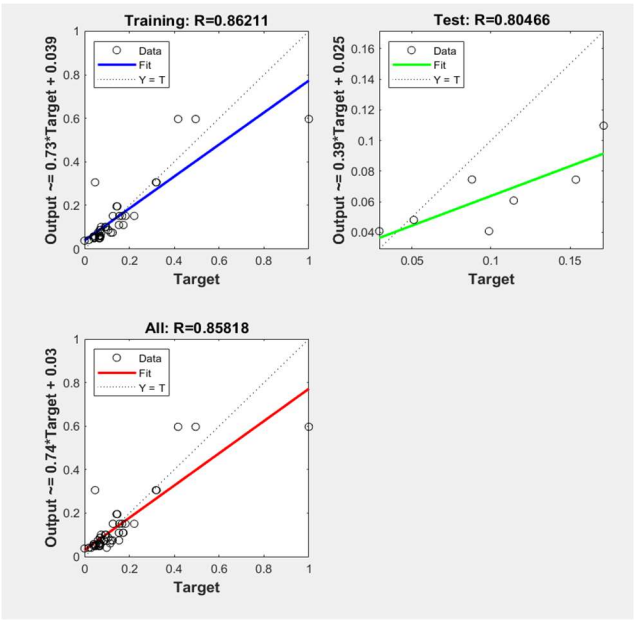

(b)

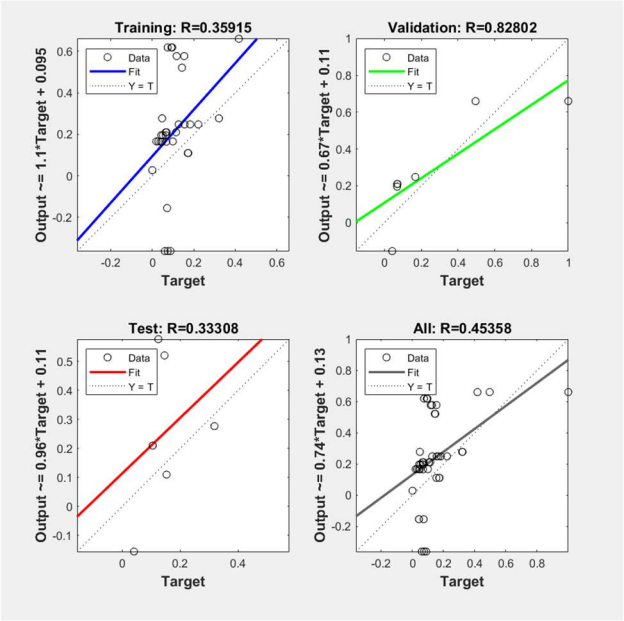

(c)

Figure 7. Correlation of training, validation, testing and overall, between the actual and predicted corrosion rate for (a) Levenberg–Marquardt (LM), (b) Bayesian Regularization (BR) and (c) Scale Conjugate Gradient (SCG training algorithm for CIL inhibition efficiency prediction

Overall, the LM was found to be the best training algorithm. Other study also shows the use of LM gave better outcome [30]. This could be due to the LM backpropagation training algorithm is a modified version of Newton's method. The Levenberg-Marquardt algorithm also designed to approach second-order training speed without having to compute the Hessian matrix [38]. LM was selected as Backpropagation

Learning algorithm as it is known for its efficiency in minimizing the sum of squared errors and its ability to converge faster.

Conclusion

Corrosion inhibition performance of cellulose-ionic liquid (CIL) tested on marine grade mild steel with variation of temperature (°C) and concentration (ppm) using electrochemical analysis and further analyzed using Artificial Neural Network (ANN) has shown the promising result and observation. It was found that FTIR analysis shows the presence of functional groups in CMC mixed with ([EMIM][Ac]) mixture by formation of new hydrogen bonds as result of disrupting and breaking compact structure of intramolecular hydrogen bond of CMC which provides an adsorption site between the inhibitor and the metal. With increasing of CIL concentration, the result gives the higher inhibition efficiency and reducing corrosion rate. With the increase of testing solution temperature from ambient to 70°C, the result of inhibition efficiency is decreasing. LM was found to be the better training algorithm as the regression R is highest and MSE is lowest compared to BR and SCG. With the implication of the research result, CIL has the potential to be used as a natural and environmentally friendly corrosion inhibitor. To drive research forward with innovation and new techniques, the future prospects on enhancing the effectiveness of CIL as corrosion inhibitors should be implemented. This involves exploring various parameters including the immersion period, different CIL concentration or use of different inhibitor formulation. Assessing the corrosion condition under long period of time to simulate realistic conditions, testing CIL performance using different materials, comparing with different combination of ionic liquid, and conducting a thorough environmental impact assessment are possible to be implemented as well. Additionally, an approached of research on CIL interacts and influences marine biofilms on metal surfaces will give significance for the development of new technologies and implementation in marine industries. This feature acknowledges the intricate relationships that exist between corrosion inhibitors and the dynamic of marine environment, providing insights that lead to innovative solutions for effective corrosion protection in real-world marine applications

Acknowledgement

The authors would like to express their gratitude to the Ministry of Higher Education Malaysia for funding this research via Fundamental Research Grant Scheme (FRGS), grant number FRGS/1/2020/STG05/UMT/03/1 (VOT59608).

References

1. Odio, B. O., Chinwuko, E. C., Chukwuneke, J. L. and Sinebe, J. E. (2014). Investigation of the effect of corrosion on mild steel in five different environments. *International Journal Science Technology Research*, 3: 306-310.
2. Li, Z. Liang, Xiao, K., Dong, C. Fang, Cheng, X. qun, Xue, W. and Yu, W. (2019). Atmospheric corrosion behavior of low-alloy steels in a tropical marine environment. *Journal of Iron and Steel Research International,* 26(12): 1315-1328.
3. Hussain, R. R., Alhozaimy, A., Al-Negheimish, A. and Singh, D. D. N. (2022). Role of phosphorus as micro alloying element and its effect on corrosion characteristics of steel rebars in concrete environment. *Scientific Reports,* 12(1): 1-23.
4. Chigondo, M. and Chigondo, F. (2016). Recent natural corrosion inhibitors for mild steel: an overview. *Journal of Chemistry*, 2016: 6208937
5. Kadhim, A., Al-Amiery, A. A., Alazawi, R., Al-Ghezi, M. K. S. and Abass, R. H. (2021). Corrosion inhibitors. A review. *International Journal of Corrosion and Scale Inhibition,* 10(1): 54-67.
6. Zakeri, A., Bahmani, E. and Aghdam, A. S. R. (2022). Plant extracts as sustainable and green corrosion inhibitors for protection of ferrous metals in corrosive media: A mini review. *Corrosion Communications,* 5: 25-38.
7. Medupin, R. O., Ukoba, K. O., Yoro, K. O. and Jen, T. C. (2023). Sustainable approach for corrosion control in mild steel using plant-based inhibitors: a review. *Materials Today Sustainability*, 22: 100373.
8. Badawi, A. K. and Fahim, I. S. (2021). A critical review on green corrosion inhibitors based on plant extracts: Advances and potential presence in the market. *International Journal of Corrosion and Scale Inhibition,* 10(4): 1385-1406.

9. Sovizi, M. R. and Abbasi, R. (2020). Effect of carboxymethyl cellulose on the corrosion behavior of aluminum in H_2SO_4 solution and synergistic effect of potassium iodide. *Journal of Adhesion Science and Technology,* 34(15): 1664-1678.
10. Magalhães, S., Fernandes, C., Pedrosa, J. F. S., Alves, L., Medronho, B., Ferreira, P. J. T. and Rasteiro, M. da G. (2023). Eco-friendly methods for extraction and modification of cellulose: An overview. *Polymers,* 15(14): 1-25.
11. Arefian, M., Hojjati, M., Tajzad, I., Mokhtarzade, A., Mazhar, M. and Jamavari, A. (2020). A review of Polyvinyl alcohol/Carboxymethyl cellulose (PVA/CMC) composites for various applications. *Journal of Composites and Compounds,* 2(3): 69-76.
12. Umoren, S. A., AlAhmary, A. A., Gasem, Z. M. and Solomon, M. M. (2018). Evaluation of chitosan and carboxymethyl cellulose as ecofriendly corrosion inhibitors for steel. *International Journal of Biological Macromolecules,* 117(2017): 1017-1028.
13. Verma, C., Mishra, A., Chauhan, S., Verma, P., Srivastava, V., Quraishi, M. A. And Ebenso, E. E. (2019). Dissolution of cellulose in ionic liquids and their mixed cosolvents: A review. *Sustainable Chemistry and Pharmacy,* 13(7): 100162.
14. Sundjono, S., Priyotomo, G., Nuraini, L. and Prifiharni, S. (2017). Corrosion behavior of mild steel in seawater from northern coast of java and southern coast of Bali, Indonesia. Journal of Engineering and Technological Sciences, 49(6): 770-784.
15. Gabriela, R., Araújo, M. De, Marques, N. and Tonholo, J. (2019). Water-soluble carboxymethylchitosan used as corrosion inhibitor for carbon steel in saline medium. *Carbohydrate Polymers*, 205(6): 371-376.
16. Al-rubaiey, N. A., Kadhim, F. S. and Albrazanjy, M. G. (2019). The effect of adding carboxymethyl cellulose and zinc sulfate on the corrosion characteristics of the drilling fluid. *Al-Khwarizmi Engineering Journal,* 15(1): 125-133.
17. Manimaran, N., Rajendran, S., Manivannan, M., Thangakani, J. A. and Prabha, A. S. (2013). Corrosion inhibition by carboxymethyl cellulose. *European Chemical Bulletin,* 2(7): 494-498.
18. Azeez, R. A., Alrubaiey, N. and Gazi, M. (2022). Investigation of carboxymethyl cellulose and barite additives on the corrosion characteristics of water-based drilling mud. *Engineering and Technology Journal,* 40(3): 451-458.
19. Solomon, M. M., Gerengi, H. and Umoren, S. A. (2017). Carboxymethyl cellulose/silver nanoparticles composite: synthesis, characterization and application as a benign corrosion inhibitor for St37 steel in 15% H_2SO_4 medium. *ACS Applied Materials and Interfaces*, 9(7): 6376-6389.
20. Nwanonenyi, S. C., Obasi, H. C. and Chidiebere, A. M. (2018). Inhibitive performance of carboxymethyl cellulose and additives on corrosion of carbon steel in acidic and alkaline environments. *Journal of Bio- and Tribo-Corrosion*, 4(3): 1-12.
21. Umoren, S. A., Solomon, M. M., Madhankumar, A. and Obot, I. B. (2020). Exploration of natural polymers for use as green corrosion inhibitors for AZ31 magnesium alloy in saline environment. *Carbohydrate Polymers*, 230: 115466.
22. Bayol, E., Gürten, A. A., Dursun, M. and Kayakirilmaz, K. (2008). Adsorption behavior and inhibition corrosion effect of sodium carboxymethyl cellulose on mild steel in acidic medium. *Wuli Huaxue Xuebao/ Acta Physico - Chimica Sinica*, 24(12): 2236-2243.
23. Umoren, S. A., Solomon, M. M., Udosoro, I. I. and Udoh, A. P. (2010). Synergistic and antagonistic effects between halide ions and carboxymethyl cellulose for the corrosion inhibition of mild steel in sulphuric acid solution. *Cellulose*, 17(3): 635-648.
24. Khairou, K. S. and El-Sayed, A. (2003). Inhibition effect of some polymers on the corrosion of cadmium in a hydrochloric acid solution. *Journal of Applied Polymer Science*, 88(4): 866-871.
25. Hu, H., Dong, Y., Li, J., Xiong, C. and Hurley, M. (2018). Investigating electrochemical impedance spectroscopic (EIS) measurement of surrogate oxide at high temperatures. (No. INL/EXT-18-45047-Rev000). Idaho National Lab.(INL), Idaho Falls, ID (United States).
26. Gopiraman, M., Selvakumaran, N., Kesavan, D. and Karvembu, R. (2012). Adsorption and

corrosion inhibition behaviour of N-(phenylcarbamothioyl) benzamide on mild steel in acidic medium. *Progress in Organic Coatings*, 73(1): 104-111.

27. Akbarzade, K. and Danaee, I. (2018). Nyquist plots prediction using neural networks in corrosion inhibition of steel by schiff base. *Iranian Journal of Chemistry and Chemical Engineering,* 37(3): 135-143.
28. Millán-Ocampo, D. E., Parrales-Bahena, A., González-Rodríguez, J. G., Silva-Martínez, S., Porcayo-Calderón, J. and Hernández-Pérez, J. A. (2018). Modelling of behavior for inhibition corrosion of bronze using artificial neural network (ANN). *Entropy*, 20(6): 409
29. Russo, D., & Zou, J. (2020). How much does your data exploration overfit? controlling bias via information usage. *IEEE Transactions on Information Theory*, 66(1): 302-323.
30. Zulkifli, F., Abdullah, S., Suriani, M. J., Kamaludin, M. I. A. and Wan Nik, W. B. (2021). Multilayer perceptron model for the prediction of corrosion rate of aluminium alloy 5083 in seawater via different training algorithms. *IOP Conference Series: Earth and Environmental Science,* 646(1): 012058.
31. Leppänen, I., Vikman, M., Harlin, A. and Orelma, H. (2020). Enzymatic degradation and pilot-scale composting of cellulose-based films with different chemical structures. *Journal of Polymers and the Environment,* 28(2): 458–470.
32. Mateyawa, S., Fengwei, D., Truss, R. W., Halley, P. J., Nicholson, T. M., Shamshina, J. L., Rogers, R. D., Boehm, M. W. and Mcnally, T. (2013). Effect of the ionic liquid 1-ethyl-3-methylimidazolium acetate on the phase transition of starch : Dissolution or gelatinization ? *Carbohydrate Polymers,* 94: 520-530.
33. Rajkumar, T. and Ranga Rao, G. (2008). Synthesis and characterization of hybrid molecular material prepared by ionic liquid and silicotungstic acid. *Materials Chemistry and Physics,* 112(3): 853-857.
34. Yesudass, S., Olasunkanmi, L. O., Bahadur, I., Kabanda, M. M., Obot, I. B. and Ebenso, E. E. (2016). Experimental and theoretical studies on some selected ionic liquids with different cations/anions as corrosion inhibitors for mild steel in acidic medium. *Journal of the Taiwan Institute of Chemical Engineers,* 64: 252-268.
35. Lan, W., Zhang, R., Ji, T., Sameen, D. E., Ahmed, S., Qin, W., Dai, J., He, L. and Liu, Y. (2021). Improving nisin production by encapsulated Lactococcus lactis with starch/carboxymethyl cellulose edible films. *Carbohydrate Polymers,* 251(9): 117062.
36. Haruna, K., Saleh, T. A. and Quraishi, M. A. (2020). Expired metformin drug as green corrosion inhibitor for simulated oil/gas well acidizing environment. *Journal of Molecular Liquids,* 315: 113716.
37. Al-Amiery, A. A., Shaker, L. M., Kadhum, A. H. and Takriff, M. S. (2021). Exploration of furan derivative for application as corrosion inhibitor for mild steel in hydrochloric acid solution: Effect of immersion time and temperature on efficiency. *Materials Today: Proceedings*, 42: 2968-2973.
38. Mammadli, S. (2017). Financial time series prediction using artificial neural network based on Levenberg-Marquardt algorithm. *Procedia Computer Science,* 120: 602-607.

Malaysian Journal of Analytical Sciences (MJAS)
Published by Malaysian Analytical Sciences Society

ENRICHED SILICA FROM OIL PALM BIOMASS FOR MAGNETIC SOLID PHASE EXTRACTION OF ORGANOCHLORINE PESTICIDE: CHARACTERIZATION AND METHOD DEVELOPMENT

(Silika yang Diperkayakan daripada Biomas Kelapa Sawit untuk Pengekstrakan Fasa Pepejal Magnetik Organoklorin Racun Serangga: Ciri dan Pembangunan Kaedah)

Nur Husna Zainal Abidin[1], Amir Hisyam Othman[1], Wan Nazihah Wan Ibrahim[1*], Nordiana Suhada Mohammad Tahirudin [1,2] , Nor Suhaila Mohamad Hanapi[1], and Nursyamsyila Mat Hadzir[1]

[1]*Faculty of Applied Sciences, Universiti Teknologi MARA, 40450 Shah Alam, Selangor, Malaysia*
[2]*Faculty of Applied Science, Universiti Teknologi MARA, Perak Branch, Tapah Campus, 35400, Perak*

[*]*Corresponding author: wannazihah@uitm.edu.my*

Received: 10 September 2023; Accepted: 12 March 2024; Published: 29 April 2024

Abstract

This study focused on preparing magnetic silica bio-sorbent made from oil palm fronds and developing methods for analyzing trace amounts of organochlorine pesticides, including Aldrin, Dieldrin, and Heptachlor. The bio-sorbent, namely Fe_3O_4@SiO_2, was prepared through the sol-gel method by combining silica particles derived from oil palm fronds with commercial ferrous (II) oxide. The physical and chemical properties of the bio-sorbents were analyzed using ATR-FTIR, FESEM, EDX, and XRD. According to ATR-FTIR, the bio-sorbent contained absorption bands at 1100 cm^{-1} and 500-600 cm^{-1}, indicating the functional groups of Si-O and Fe-O. FESEM and EDX studies show the particles have a rough and irregular surface morphology that is composed of 63.9% oxygen, 16.97% silica, and 19.04% ferrous atomic weight. Meanwhile, XRD analysis confirmed that the bio-sorbent was composed of face-centered cubic Fe_3O_4 and amorphous SiO_2, with multiple peaks appearing at 2θ = 22.978 (101), 30.20 (220), 35.60 (311), and 57.50. A magnetic solid-phase extraction method using the synthesized bio-sorbent was developed prior to gas chromatography-mass spectrometry analysis of the selected OCPs. The optimal extraction conditions were determined via one variable at a time (OVAT) and resulted as follows: extraction time, 5 min; desorption solvent, ethyl acetate; desorption time, 5 min; mass of sorbent, 40 mg. The analytical performance of the method was evaluated under these conditions, with a detection limit of 0.1-0.53 mg/L and an extraction recovery of 80-92%. Several linear ranges were obtained for Heptachlor, Aldrin, and Dieldrin, including 0.6-1.8, 0.1-0.3, and 0.2-0.6 mg/L, respectively. The effectiveness of the bio-sorbent was proven by removing pesticides from actual paddy water samples, with calibration curves showing linearity over a wide range of values. The intra- and inter-day precisions were 0.50-1.86% and 0.69-2.54%, respectively.

Keywords: bio-sorbent magnetic silica, organochlorine, paddy water samples, magnetic solid phase extraction

Abstrak

Kajian ini bertujuan untuk menghasilkan biosorbent silika magnetik daripada pelepah kelapa sawit dan membangunkan kaedah untuk menganalisis jumlah jejak racun serangga organoklorin seperti Heptachlor, Aldrin, dan Dieldrin. Bio-sorben iaitu Fe_3O_4-SiO_2 telah disediakan melalui kaedah sol-gel dengan menggabungkan zarah silika yang diperolehi daripada pelepah kelapa sawit

dengan ferus (II) oksida komersial. Sifat fizikal dan kimia bio-sorben telah dianalisis menggunakan ATR-FTIR, FESEM, EDX, dan XRD. Menurut ATR-FTIR, bio-sorben mengandungi julat penyerapan pada 1100 cm^{-1} dan 500-600 cm^{-1}, yang menunjukkan kumpulan fungsi Si-O dan Fe-O. Kajian FESEM dan EDX menunjukkan bahawa partikel mempunyai morfologi permukaan yang kasar dan tidak teratur yang terdiri daripada 63.9% oksigen, 16.97% silika, dan 19.04% berat atom ferus. Sementara itu, analisis XRD mengesahkan bahawa bio-sorben terdiri daripada Fe_3O_4 kubik berpusat muka dan SiO_2 amorfus, dengan pelbagai puncak yang muncul pada 2θ = 22.978 (101), 30.20 (220), 35.60 (311), dan 57.50. Pembangunan kaedah pengekstrakan fasa pepejal magnet dengan menggunakan bio-sorben yang disintesis telah dijalankan diikuti analisis oleh kromatografi gas spektrometri jisim (GC-MS) daripada OCP yang terpilih. Keadaan pengekstrakan optimum ditentukan melalui satu parameter pada satu masa dan hasilnya seperti berikut: masa pengekstrakan 5 min; pelarut desorpsi, etil esitat; masa desorpsi, minit, dan sorbent jisim 40 mg. Prestasi analisis kaedah dinilai di bawah keadaan ini, dengan had pengesanan 0.1-0.53 mg/L dan pemulihan pengekstrakan 80-92%. Beberapa julat linear telah diperolehi untukHeptachlor, Aldrin dan Dieldrin, termasuk 0.6-1.8, 0.1-0.3, dan 0.2-0.6 mg/L masing-masing. Keberkesanan biosorben telah dibuktikan dengan mengeluarkan racun perosak daripada sampel air padi sebenar, dengan lengkung penentukuran menunjukkan kelinearan ke atas julat nilai yang luas.Ketepatan dalam dan antara hari ditemui dalam julat 0.50-1.86% dan 0.69-2.54%, masing-masing.

Kata kunci: bio-sorben silika magnet, organoklorin, sampel air padi, pengekstrakan fasa pepejal magnet

Introduction

In Malaysia, vast areas are devoted to cultivating oil palm, a significant agricultural product [1]. However, oil palm farming is associated with several environmental issues, such as deforestation and the accumulation of agricultural waste in the form of oil palm fronds (OPF). These fronds are often allowed to deteriorate or burn, resulting in greenhouse gas (GHG) emissions and air pollution [2]. Consequently, developing new uses for OPF can help reduce waste, generate economic benefits, and mitigate the negative environmental impact of oil palm farming. Researchers have devised various methods to convert palm oil biomass into valuable goods with added value, thereby decreasing the amount of palm oil biomass produced. One such valuable product is silica, which is found in the frond leaves of oil palms. Commercial silica is typically used as a precursor for other materials in industrial manufacturing that are costly and energy-intensive. Silica, on the other hand, is extracted from agricultural waste at moderate temperatures, resulting in an enormously cost-effective product [3]. Therefore, the production of silica from palm oil biomass can meet industrial demands because it can be used as a precursor in the manufacture of glass and cement, as well as in the biological sector as a catalyst carrier or adsorbent for metal removal. According to a study by Onoja et al. [4], acid-treated OPF ash contains up to 95.30% silica (SiO_2). Their controllable particle size, large surface area, great biocompatibility, and adsorptive properties make them useful in numerous technical applications, including low-loss, subwavelength-diameter single-mode optical waveguides, nanoscale optical sensors, atomic trapping and guiding [5, 6].

In agriculture, pesticides are utilized as plant protection products because they enhance crop quality and productivity. Despite their usefulness, pesticides are immature, environmentally stable, and easily dispersed. In 2016, the overall usage of pesticides, such as herbicides, fungicides, and insecticides, rose by 5.5 million tons per year, according to statistics from the Food and Agricultural Organisation (FAO) [7]. This increase was due to the growing demand for food, as it was anticipated that the world rice output would increase by 42% by 2050 [7]. Unfortunately, only 0.3% of the applied pesticides are necessary to affect the target insect, with the remaining 99.7% being leached into the ground, air, and water [9]. After being sprayed on crops, pesticides can leave the site through multiple mechanisms, including biodegradation, runoff, leaching, and volatilization. Pesticide runoff takes a long time to decompose, leading to soil contamination that could seriously impact human health if people are exposed to it.

Most pesticides have very low allowed residual limits, sometimes in the range of parts per trillion; therefore, enhanced sample collection and extraction methods are required to meet these low concentration levels. The presence of matrix molecules from complex matrices, such as soil, in the extract can interfere with the signal

response of the instrument in detecting the target compound [10]. Conventional sample preparation techniques for OCPs can be laborious and time-consuming because multiple stages are required [11]. A more recent method called Magnetic solid-phase extraction (MSPE) uses magnetic particles as adsorbents. This method is beneficial because it is simpler, more sensitive, and more selective than conventional solid-phase extraction (SPE) approaches [12]. It also allows for the rapid and efficient purification and concentration of pesticide samples. One of MSPE's key benefits is its ability to remove various pesticides from complex samples, owing to the large surface area and strong binding capacity of magnetic particles. The application of MSPE is eco-friendly because it does not utilize harsh chemicals, and the magnetic particles can be easily recycled, reducing the waste produced during analysis.

This study aimed to create and utilize sensitive extraction methods using Fe_3O_4-SiO_2-based magnetic solid phase extraction (MSPE) in combination with gas chromatography-mass spectrometry (GC-MS) for the determination of three organochlorinated (Aldrin, Dieldrin, and Heptachlor) in paddy water samples. The extraction parameters were optimized, including the extraction time, desorption solvent, desorption time, and sorbent mass, using the one-variable-at-a-time (OVAT) approach. The development of Fe_3O_4-SiO_2 from OPF was driven by an environmentally friendly concept, which was to adopt sustainable techniques by converting waste biomass into value-added silica-based adsorbent materials.

Materials and Methods

Chemical and reagents

All HPLC-grade solvents, including n-hexane, acetonitrile, acetone, ethanol, and ethyl acetate, were purchased from Merck (Germany). Additionally, reagents, such as ferrous oxide (Fe_3O_4), were acquired from Sigma-Aldrich. Three organochlorine pesticides, namely Aldrin, Dieldrin, and Heptachlor, with purity assay ≥ 99.9%, were purchased from Sigma-Aldrich. Standard stock solutions of aldrin, dieldrin, and heptachlor at concentrations of 1000 mg/L were prepared in acetonitrile. The prepared stock solutions were stored at 4°C until use. Working solutions of the standard mixtures were prepared by diluting standard stock solutions with acetonitrile.

Instrumentation

The FT-IR spectra were generated using an ATR-FTIR spectrometer (PerkinElmer Spectrum ONE FTIR with Universal ATR Polarization L1250064 ZnSe crystal) in transmittance mode over the wavenumber range of 4000-550 cm^{-1}. FESEM (Zeiss Supra 40VP FESEM) equipped with an EDX spectrometer was used for FESEM-EDX. XRD patterns and crystallinity behavior were obtained through XRD measurements using an X'Pert Pro X-Ray Diffractometer with Cu Kα radiation from 40 kV and 30 mA applied to the sample with a 2θ range of 5–100°.

Chromatographic analysis was conducted using a gas chromatography (Agilent 7890 B) system with a mass spectrometer detector (MS). Chromatographic separations were achieved on an HP-5 fused silica capillary (30 m x 0.32 mm, Agilent Technologies, USA). Helium was the carrier gas with a make-up gas flow rate of 1.1971 mL/min. The column temperature program began at 150 °C for 1 min, then increased to 200 °C at a rate of 30°C/min, held for 2 min, followed by an increase to 250 °C at a rate of 10°C/min, held for 2 min, and finally a ramp increase to 280 °C at a rate of 20°C/min. Splitless injection was maintained throughout the experiment to maintain the GC-MS interface at 250 °C.

Preparation of silica derived from oil palm frond

Oil palm fronds (OPF) were manually separated and washed with water to eliminate impurities. The sample was oven-dried (70 ˚C for 48h) and cut into smaller pieces before ground into fine powder. The following chemical treatment of OPF was adapted from the literature [13]. Briefly, OPF powder (50.0 g) was dispersed in HCl (1.0 M, 500Ml) and constantly stirred (400 rpm) for 2 h. The dispersion was cooled to room temperature and rinsed with distilled water until the washings reached a neutral phase. The neutralized OPF was then filtered and dried in an oven (80) for 24h. The OPF powder was heated in a preheated furnace at 600°C for 14h. The temperature gradually increased over 5 h,

then maintained for 9 h. The rate of temperature increase was 2°C/min. White ash from the treated OPF-Si was collected and stored in airtight containers at room temperature for further examination.

Preparation of sodium silicate (Na_2SiO_3)

Sodium silicate (Na_2SiO_3) was prepared using a modified procedure reported by Onoja et al. [14] by mixing OPF-SiO_2 (10.0 g) and 3.5M NaOH (82 mL) in a paraffin oil bath at 100 °C for 4 hours with constant stirring (200 rpm). The resulting sodium silicate solution was filtered using Whatman 41 filter paper at room temperature, and the filtrate was placed in a polypropylene vial with a screw-on cover for analysis.

Preparation of magnetic silica Fe_3O_4@SiO_2

The preparation of magnetic OPF-Silica was based on the developed method by Azmayawati et al. (2018) with minor modifications [14]. First, 1 g of Fe_3O_4 was diluted in 20 mL distilled water and ultrasonicated for 10 min. Subsequently, 5 mL of Na_2SiO_3 was diluted in 80 mL of distilled water and mixed with the Fe_3O_4 solution. The mixture was then ultrasonicated for an additional 20 min. Next, hydrochloric acid (HCl) was added dropwise while stirring the mixture at room temperature until the pH reached 7. The gel was aged and left at room temperature for 24 hours. The solution was then washed and vacuum-filtered to remove the gel. The sorbent was oven-dried for 24 h at 80°C and stored in a desiccator until needed.

Collection and pre-treatment of paddy water samples

Water samples from the paddy fields were collected in propylene bottles from Sawah Padi Bukit Gambir, Johor. The bottles were protected from UV by being covered with aluminum foil and kept at 4ºC. The samples were filtered twice using Whatman 125 mm filter papers to remove colloidal particles, and the filtered solutions were stored in glass bottles before analysis.

Magnetic solid phase extraction procedure

A 50 mg sample of Fe_3O_4@SiO_2 powder was added to a 10 mL aqueous solution containing 3 ppm of heptachlor, 0.5 ppm Aldrin, and 1 ppm of dieldrin. The mixture was vortexed in 5 min to allow the adsorption process. The solution was then separated by magnetic force and discarded. 1 mL of the desorption solvent acetonitrile (ACN) was added for the desorption of the targeted analytes and further sonicated for 5 minutes. The sorbent was separated by magnetic force, and the remaining ACN was concentrated to 0.5 mL via nitrogen before GC-MS analysis.

Results and Discussion

Characterization of the prepared adsorbent

The characteristics of the synthesized adsorbents were studied using ATR-FTIR, FESEM-EDX, and XRD. An ATR-FTIR study was conducted to compare the spectral data and discern any changes in the chemical characteristics of the prepared bio-sorbent. The origin of the Fe_3O_4 spectrum (Figure 1(a)) shows the vibrational mode at 586 cm^{-1} (stretching vibrations of the Fe−O bonds) and 1648 cm^{-1} (bending vibrations of Fe_3O_4 bound water), which is similar to a previous study reported by Lesiak et al. [1]. In contrast, the spectrum of SiO_2 -OPF (Figure 1 (b)) exhibits a wide peak at 3430 cm^{-1}, indicating the presence of silanol (Si-OH) groups and antisymmetric and symmetric stretching vibrations of siloxane groups at wavenumbers of 1073 cm^{-1} and 805 cm^{-1}, respectively [Onoja et al. (2017)]. The spectrum of Fe_3O_4@SiO_2 (Figure 1(c)) exhibits distinct peaks at 3366 cm^{-1}, 1629 cm^{-1}, 1088 cm^{-1}, 809 $cm^{-1,}$ and 577 cm^{-1}, which correspond to the stretching vibrations of the O-H, Fe-O, and siloxane groups, respectively, as reported by Zhang et al. [15]. In addition, the exhibited peaks were similar to those seen in the Fe_3O_4 and SiO_2-OPF spectra but with significantly reduced intensities. This suggests that SiO_2 was effectively integrated into Fe_3O_4, as supported by the corresponding EDX analysis as shown in Figure 2(b).

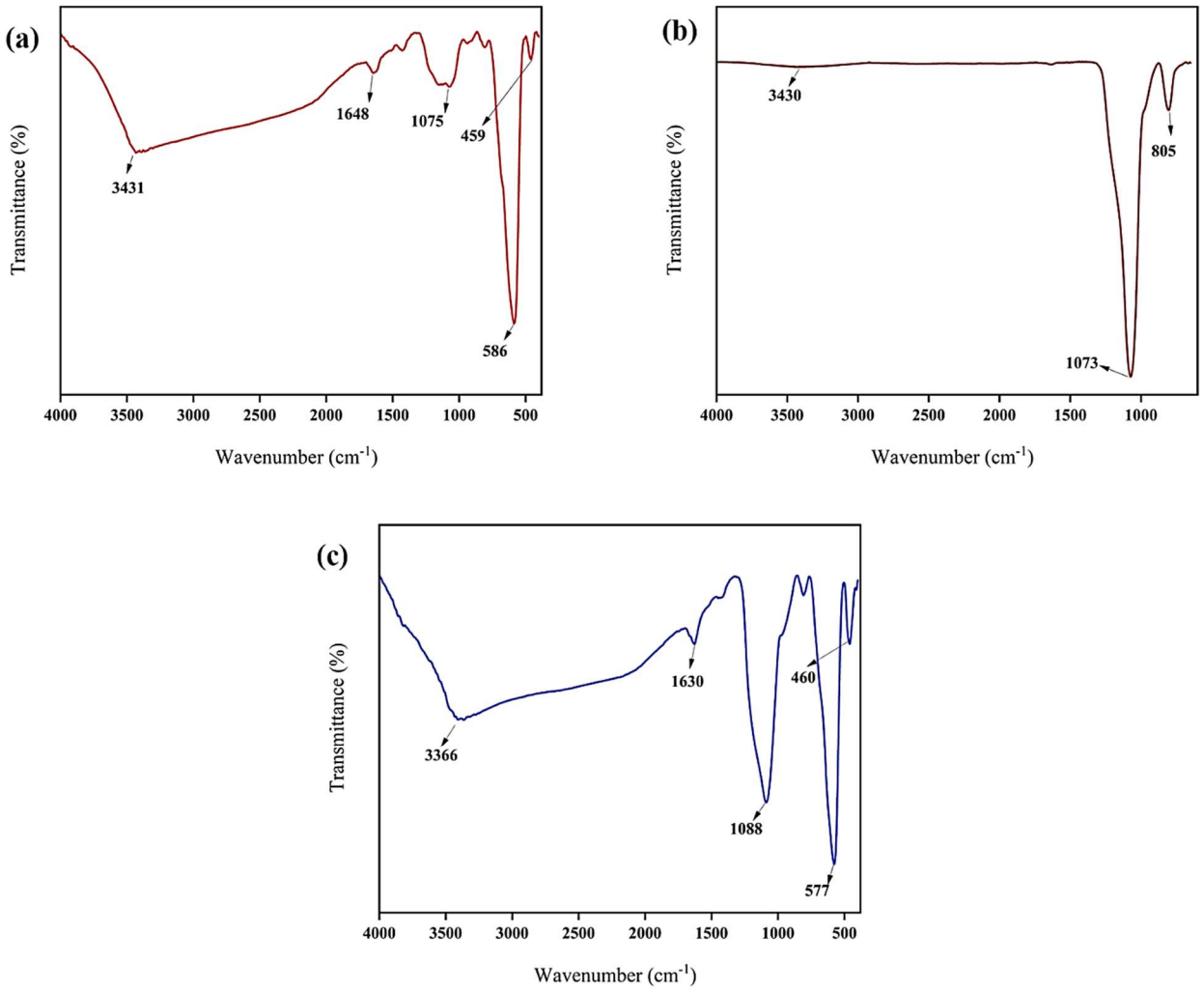

Figure 1. The ATR-FTIR spectra of the as-prepared (a) Fe_3O_4, (b) SiO_2 and (c) Fe_3O_4@SiO_2

Figure 2(a) depicts the FESEM micrographs of Fe_3O_4-SiO_2. As shown in Figure 2(a), the particles were obtained in agglomerated particles, rough surface structure, and the presence of cavities [14, 17]. Fe_3O_4 particles have a cubic shape and aggregate because of their high surface energy and adhesion properties. Nonetheless, the absence of a cubic structure in the FESEM images suggests that SiO2 has coated the magnetite and acted as a core to protect the magnetite from oxidation under acidic conditions, similar to a description by previous work [17].

The FESEM micrograph of Fe_3O_4-SiO_2 was further analyzed by mapping the elemental composition using energy-dispersive X-ray (EDX) analysis, as shown in Figure 2(b). Based on the result, the prepared bio-sorbent mainly consisted of 41.5 wt. % iron (Fe), 39.9 wt.% oxygen (O), and 18.6 wt.% silicon (Si), which correlated with the expected elements in Fe_3O_4-SiO_2. The high percentage of O could be from ferrous oxide and Si-OH in the silica layer, which acts as a shell for the core of the sorbent. The presence of Si can be interpreted as evidence of the successful synthesis of magnetic silica.

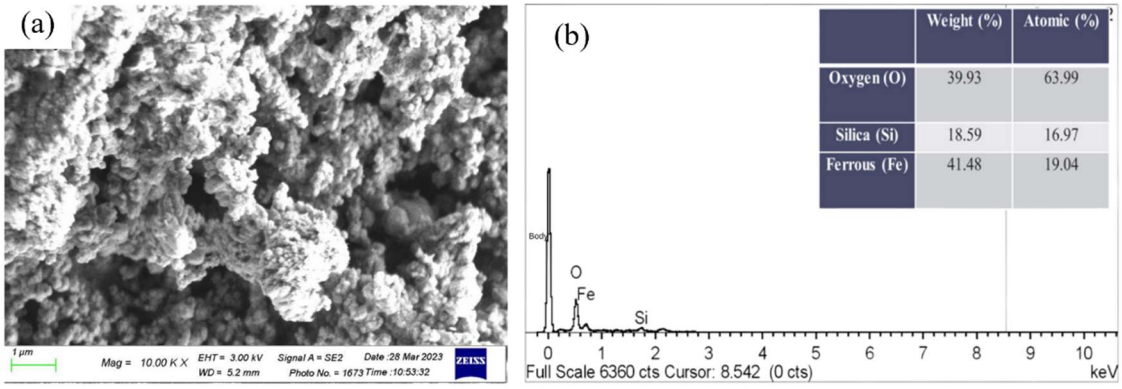

Figure 2. FESEM micrographs of the (a) $Fe3O_4$-SiO_2 and (b) EDX spectrum from specific regions of Fe_3O_4@SiO_2

The XRD diffractograms of each sample were analyzed to evaluate the impact of crystallinity on the sorbents. The diffractograms of Fe_3O_4@SiO_2, Fe_3O_4, and SiO_2 are shown in Figure. 3. The SiO_2 sample in Figure 3(a) displays a broad peak and a Bragg angle of $2\theta = 22.978°$ corresponding to the (101) Miller indices (ICDD No. 01-083-2300), indicating that it is in an amorphous form, which is consistent with previous studies [18]. While, the diffraction peaks seen at angles 2θ~ 30.20 (220), 35.60 (311), and 57.50 can be attributed to the face-centered cubic structure of Fe_3O_4 as documented in the JCPDS file number 85-1436 [19]. The diffraction pattern depicted in Figure 3c indicates a displacement of the peak, signifying that the presence of Fe_3O_4 has resulted in the shift. This alteration suggests that Fe_3O_4@SiO_2 particles have been formed successfully, with the magnetite phase being integrated into the silica surface [20]. With comparison, both peaks were present on the diffractogram of Fe_3O_4-SiO_2.

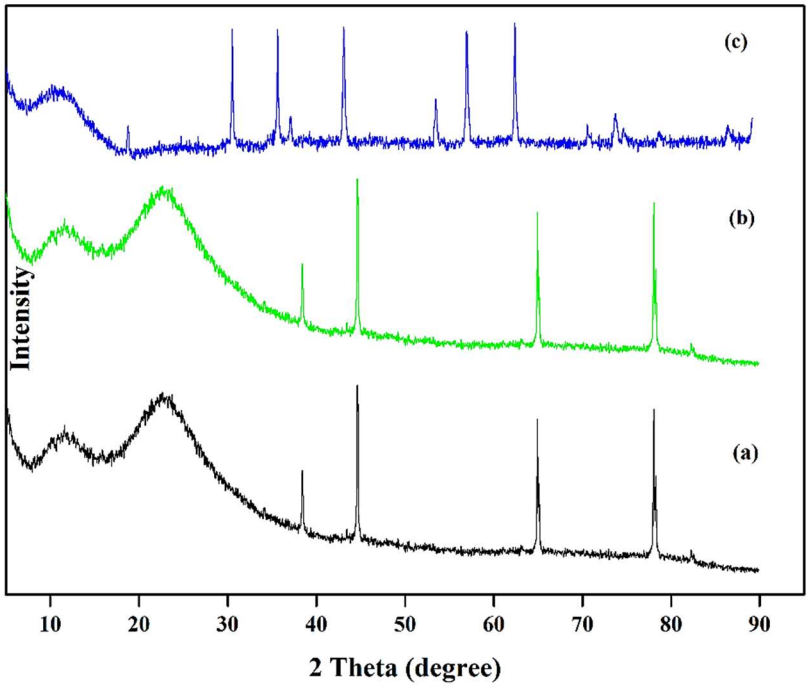

Figure 3. XRD patterns of (a) SiO_2, (b) Fe_3O_4 and (c) Fe_3O_4-SiO_2

Optimization of extraction conditions

The performance of the sorbent was assessed by MSPE for OCPs analysis in aqueous samples to determine the optimum extraction parameters. The one-variable-at-time (OVAT) approach was used to optimize the following MSPE parameters: extraction time, desorption solvent type, desorption time, and amount of sorbent. This approach reduces the use of chemicals, labor, and time. The optimization process involved utilizing distilled water spiked with heptachlor, aldrin, and dieldrin solutions. These solutions were prepared to achieve final concentrations of 3, 0.5, and 1 mg/L in 10 mL of water.

Effect of extraction time

The parameter of extraction time in analytical chemistry pertains to the period during which the extraction process isolates specific analytes from a sample matrix. The efficiency and effectiveness of the extraction procedure can be significantly influenced by critical factors. Precise optimization of the extraction time is crucial for obtaining reliable and accurate analytical results. This study focused on the impact of various extraction durations, ranging from 2.5 to 10 min, on the peak area of the analytes. Figure 4(a) illustrates the correlation between the peak area and extraction time, showing a significant increase in analyte extraction from 2.5 minutes to 5 min. However, the trend gradually decreases from 7.5 minutes to 10 minutes. This suggests that the most efficient extraction time for analyte adsorption onto the magnetic silica was 5 min. The decrease in trend may be because as the extraction time prolongs, there is an increased probability of analyte degradation or instability, leading to loss or alteration of the analyte and inaccurate, unreliable analytical outcomes [21]. Thus, 5 minutes of extraction time was selected for further experiments.

Effect of desorption solvent

The selection of the desorption solvent is crucial for facilitating the elution of the desired analytes from the sorbent material, which ultimately affects the overall efficiency and selectivity of the extraction process. As shown in Figure 4(b), ethyl acetate demonstrated the most favorable performance compared with other solvents such as n-hexane, acetonitrile, ethanol, and acetone. Ethyl acetate may have a greater selectivity towards chlorinated analytes than less polar solvents such as n-hexane, ethanol, acetonitrile, and acetone. This method enables the selective separation of heptachlor, aldrin, and dieldrin, reducing interference from other constituents in the sample matrix. Ethyl acetate is a solvent with moderate polarity (4.4) with favorable solubility characteristics for various organic molecules. Heptachlor, aldrin, and dieldrin are examples of chlorinated organic compounds. Owing to its moderate polarity (with dieldrin having a relative polarity of 5.40, heptachlor at 6.10, and aldrin at 6.75), ethyl acetate effectively dissolves these analytes from the sorbent material [22]. Therefore, ethyl acetate was selected as the desorption solvent for the subsequent analysis.

Effect of desorption time

Desorption time is a crucial parameter in extraction processes in analytical chemistry because it affects the efficiency and completeness of eluting target analytes from the extraction medium. The time range between 2.5 minutes and 10 min was examined, and the results showed that at 5 min, heptachlor and dieldrin were desorbed the most, while 7.5 minutes was required for aldrin. Proper control and optimization of desorption time are essential to achieve accurate and reproducible analytical results. The optimum desorption time was chosen as the one that was standardized for all three analytes. The differences in aldrin levels at 5 and 7.5 minutes were insignificant; therefore, the latter was accepted. A declining trend was observed as the sonication time was increased (from 7.5 to 10 minutes). This phenomenon may be attributed to the thermal effects caused by the sonicator, leading to the degradation of the analyte over time [23]. Therefore, 5 min was selected as the optimal desorption time.

Effect of mass sorbent

The adsorption capacity of the target analytes is influenced by the mass of the sorbent and its effect on both the adsorption capacity and the equilibrium between the sorbent and the sample matrix. The optimal sorbent mass for this extraction was 30 mg, as shown in Figure 4(d), with the highest extraction efficiency. This is because 30 mg of sorbent offers sufficient surface area

for the target analytes (heptachlor, aldrin, and dieldrin) to bind. Increasing the sorbent mass beyond this limit might not result in improved extraction effectiveness, as it could cause the sorbent particles to become overcrowded and limit mass transfer, thereby decreasing the extraction efficiency. Additionally, higher sorbent masses can saturate the active binding sites in the sorbent, leading to declining returns in extraction efficiency [24].

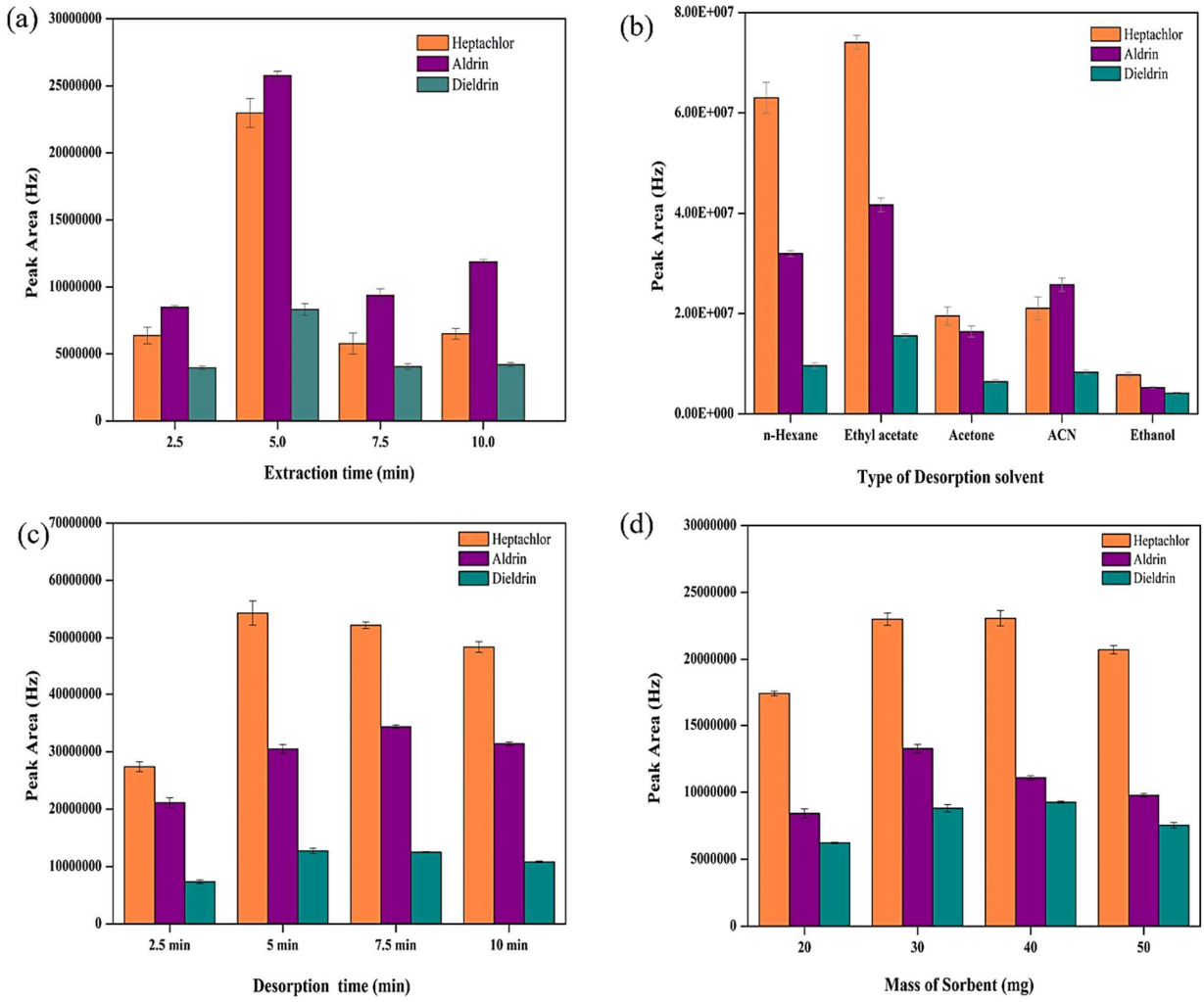

Figure 4. MSPE optimization conditions. (a) Extraction time (b) type of desorption solvent (c) desorption time (d) mass of sorbent

Method validation: Analytical performance

The accuracy of the proposed method for the magnetic solid-phase extraction of Fe_3O_4@SiO_2 was evaluated by analyzing certain organic pollutants in a water sample obtained from a paddy field. To determine the reliability of Fe_3O_4@SiO_2 for extracting three specific pollutants (heptachlor, aldrin, and dieldrin), a matrix-matched calibration approach was employed. The method was validated by calculating the limit of detection (LOD) and limit of quantification (LOQ) using the linear regression approach, standard deviation, and slope of the calibration curve. Calibration curves were generated using the least-squares approach, and peak areas were plotted against concentration. A strong linear relationship was observed between heptachlor, aldrin, and dieldrin, with R^2 values ranging from 0.98 to 0.99.

The limit of detection (LOD) was found to be 0.53-1.50 mg/L. The mean squared prediction error (MSPE) of Fe_3O_4-SiO_2 was evaluated in the context of pesticide analysis of paddy water samples.

Table 1. Performance of the proposed method under optimized conditions

Samples	Analytes	Linearity (mg/L)	Regression coefficient, R^2	LOD (mg/L)	LOQ (mg/L)
Paddy water	Heptachlor	0.6-2.4	0.99	0.53	1.62
	Aldrin	0.1-0.4	0.98	0.10	4.59
	Dieldrin	0.2-0.8	0.99	0.16	1.89

Analysis of real sample

The MSPE method, which utilizes Fe_3O_4@SiO_2, has been effectively used to analyze paddy water samples. The experiment involved adding spiked water samples to achieve final concentrations of 0.1 and 2.4 mg/L for heptachlor, 0.1 and 0.4 mg/L for aldrin, and 0.2 and 0.8 mg/L for dieldrin to conduct relative recovery tests. The results (Table 2) showed that the relative recoveries of the pesticides were within the standard range specified by AOAC International (2016), ranging from 80% to 95%. The intra- and inter-day precisions exhibited relative standard deviations within 0.50-1.86% and 0.69-2.54%, respectively. These results demonstrated the effectiveness of Fe_3O_4@SiO_2-MSPE as a technology for extracting pesticides from aqueous matrices. This study compared the new Fe_3O_4@SiO_2-MSPE method to conventional SPE methods that have already been published [25]. The results showed that the SPE method has recoveries ranging from 75.9 to 112.1 %, upon comparison with previous studies that used magnetic solid phase extraction to identify OCPs, the extraction time was shorter than that of conventional SPE. Figure 5 displays the gas chromatograms showing the presence of heptachlor, aldrin, and dieldrin in water samples from paddy fields.

Table 2. Method precision for intra-day and inter-day (%RSD) and percent recovery (%ER)

Analytes	Concentration (mg/L)	Inter-day RSD (%, n=9)	Intra-day RSD (%, n=3)	ER (%)
Heptachlor	0.6	1.86	2.54	80%
	1.8	0.93	1.93	90%
Aldrin	0.1	1.43	1.98	81%
	0.3	1.12	1.83	90%
Dieldrin	0.2	0.50	1.71	88%
	0.6	1.69	0.69	92%

Green assessment profile

New microextraction techniques are being developed to meet the demand for analytical sample preparation methods that are faster, less invasive, more selective, and require fewer resources. The AGREE calculator (shown in Figure 6) was used to evaluate the long-term feasibility of the proposed Fe_3O_4@SiO_2-MSPE procedure. The evaluation is considered eco-friendly because it meets a set of standards, such as reducing the number of extra sample treatments (4), avoiding derivatization during analysis and extraction (6), and using less energy (9), and fewer potentially harmful solvents (12). However, its primary limitation is that the target analytes must be determined offline, which means that Fe_3O_4@SiO_2 must be integrated into online or inline procedures.

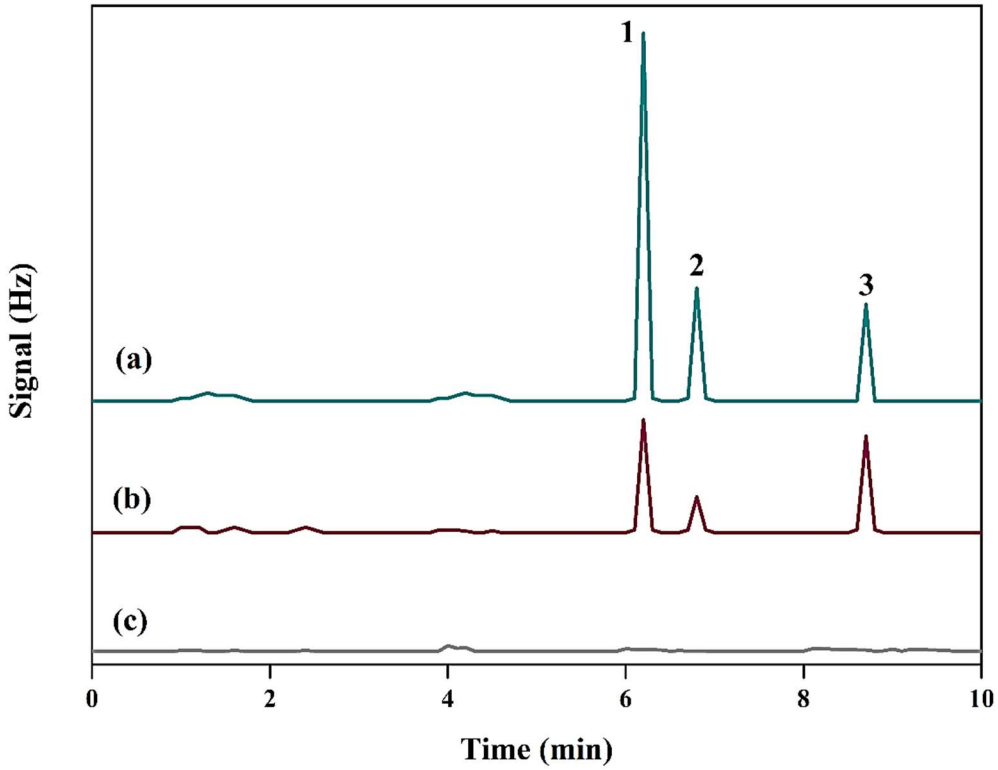

Figure 5. Chromatogram obtained from Fe_3O_4@SiO_2 MSPE-GC-MS of (a) blank of paddy water (b) and (c) paddy water spiked with at range 0.1 mg/L to 2.4 mg/L of analytes respectively. Chromatographic peaks: (1) Heptachlor, (2) Dieldrin, and (3) Aldrin.

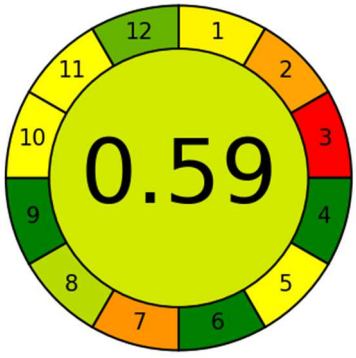

Figure 6. AGREE analysis of the method developed in this study

Proposed adsorption mechanism

Various interactions can occur between the sorbent and sorbate compounds, potentially affecting the extraction efficiency. These interactions, including electrostatic forces, hydrogen bonding, and hydrophobicity, can either attract or repel compounds involved. The properties of the sorbent materials, such as surface area, porosity, and sorption surface morphology, may also influence the extraction process of sorbate compounds [26]. The possible interactions between Fe_3O_4@SiO_2 and the OCPs include hydrogen bonding and van der Waals interactions, as schematically illustrated in Figure

7. Fe_3O_4@SiO_2 is sensitive to chlorinated groups of OCPs in its structure (aldrin and heptachlor) via van der Waals forces. Furthermore, silica has a polar functional group that interacts with the OCP molecule in a manner that makes it stick together, and the hydroxyl group of silica and the chlorine atom in the OCP compounds form strong hydrogen bonds. This interaction is facilitated by forming hydrogen bonds between the hydroxyl groups on silica and the anionic groups present in heptachlor molecules [27].

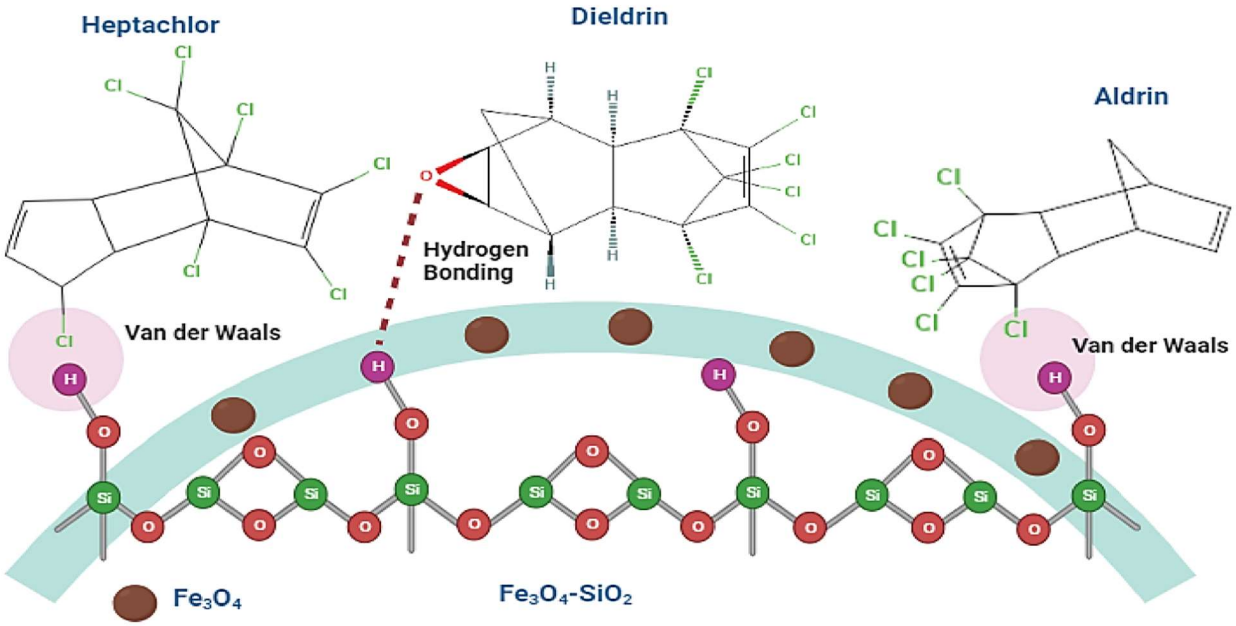

Figure 7. Schematic diagram of proposed interactions between sorbent and analytes

Conclusion

In summary, the present study included synthesizing a Fe_3O_4@SiO_2 composite material, which was then used as a magnetic sorbent in the magnetic solid-phase extraction (MSPE) method. This approach was coupled with gas chromatography-mass spectrometry (GC-MS) to quantify trace amounts of organochlorine pesticides (OCPs) in water samples collected from paddy fields. The main aim of this study is to develop a material that exhibits both environmentally friendly properties and magnetic sensitivity. The synthesizing and fabricating of a composite material consisting of Fe_3O_4@SiO_2 was successfully achieved via the sol-gel technique. The successful synthesis of Fe_3O_4 and its efficient extraction of organochlorine pesticides (OCPs) within a short timeframe was confirmed by the use of Fourier transform infrared spectroscopy (FTIR), field emission scanning electron microscopy (FESEM), and X-ray diffraction (XRD) methods. Significantly, the MSPE procedure offers efficient extraction within a short time frame (5 min) and only uses a small quantity of sorbent (40 mg). In addition, the suggested methodology demonstrated a low limit of detection (LOD), a broad range of linearity, and satisfactory accuracy. The use of the MSPE approach, combined with the GC-MS method, proved to be successful in analyzing organochlorine pesticide (OCP) residues in paddy samples. The findings obtained in this study exhibited good values for recoveries, enrichment factors, and relative standard deviations (RSDs), which significantly improved the sensitivity and simplicity of the sample preparation technique. Furthermore, the Fe_3O_4-SiO_2 adsorbent may be conveniently synthesized using abundant biomass sources, presenting supplementary benefits like cost-efficiency and ecological sustainability.

Acknowledgment

The authors are grateful to the Organisation Prohibited Chemical Warfare for financial aid through the

research grant No: L/ICA/ICB-17/21 (100-TNCPI/INT 16/6/2 (022/2021) and Universiti Teknologi MARA (UiTM) for their facilities support.

References

1. Lesiak, B., Rangam, N., Jiricek, P., Gordeev, I., Tóth, J., Kövér, L., ... and Borowicz, P. (2019). Surface study of Fe_3O_4 nanoparticles functionalized with biocompatible adsorbed molecules. *Frontiers in chemistry*, 7: 642.
2. Vijay, V., Pimm, S. L., Jenkins, C. N., and Smith, S. J. (2016). The impacts of oil palm on recent deforestation and biodiversity loss. *PloS one*, 11(7), e0159668.
3. Kamaraj, M., Sudarshan, K., Sonia, S. V. R. K. N., Chidambararajan, P., and Bekele, A. (2020). Upgradation of maize stalk waste as an alternate agrarian raw material for the production of amorphous silica composites. *Journal of Analytical and Applied Pyrolysis*, 151: 104908.
4. Onoja, E., Attan, N., Chandren, S., Razak, F. I. A., Keyon, A. S. A., Mahat, N. A. and Wahab, R. A. (2017). Insights into the physicochemical properties of the Malaysian oil palm leaves as an alternative source of industrial materials and bioenergy. *Malaysian Journal of Fundamental and Applied Sciences*, 13(4): 623-631.
5. Chen, L., Liu, J., Zhang, Y., Zhang, G., Kang, Y., Chen, A., ... and Shao, L. (2018). The toxicity of silica nanoparticles to the immune system. *Nanomedicine*, 13(15): 1939-1962.
6. Nguyen, V. H., Vu, C. M., Choi, H. J. and Kien, B. X. (2019). Nanosilica extracted from hexafluorosilicic acid of waste fertilizer as reinforcement material for natural rubber: Preparation and mechanical characteristics. *Materials*, 12(17): 2707.
7. Sharma, A., Kumar, V., Shahzad, B., Tanveer, M., Sidhu, G. P. S., Handa, N., ... and Thukral, A. K. (2019). Worldwide pesticide usage and its impacts on ecosystem. *SN Applied Sciences*, 1: 1-16.
8. Fukase, E. and Martin, W. (2020). Economic growth, convergence, and world food demand and supply. *World Development*, 132: 104954.
9. van der Werf, H. M. (1996). Assessing the impact of pesticides on the environment. *Agriculture, Ecosystems & Environment*, 60(2-3): 81-96.
10. Tsagkaris, A. S., Pulkrabova, J., and Hajslova, J. (2021). Optical screening methods for pesticide residue detection in food matrices: advances and emerging analytical trends. *Foods*, 10(1): 88.
11. Ranveer, S. A., Harshitha, C. G., Dasriya, V., Tehri, N., Kumar, N., and Raghu, H. V. (2023). Assessment of developed paper stripbased sensor with pesticide residues in different dairy environmental samples. *Current Research in Food Science*, 6: 100416.
12. Alam, S., Srivastava, N., Iqbal, N., Saini, M. K., and Kumar, J. (2021). Magnetic solid-phase extraction (MSPE) using magnetite-based core-shell nanoparticles with silica network (SiO2) coupled with GC-MS/MS analysis for determination of multiclass pesticides in water. Journal of AOAC International, 104(3): 633-644.
13. Tahiruddin, N. S. M., Abidin, N. H. Z., Kamal. A. A. M., Hanapi. N. S. M., Hadzir. N. S. M., Sheela Chandren S. and Ibrahim. W. N. W., (2023). Optimising the operating parameters of oil palm frond silica-based dispersive solid phase extraction for determination of organochlorine pesticides. *Malaysian Journal of Chemistry*, 25: 26-35.
14. Azmiyawati, C., Pratiwi, P. I. and Darmawan, A. (2018). New silica magnetite sorbent: the influence of variations of sodium silicate concentrations on silica magnetite character. In *IOP Conference Series: Materials Science and Engineering*, 349(1): 012012.
15. Zhang, Y., Qi, S., Xing, X., Yang, D., Devi, N. L., Qu, C., ... and Zeng, F. M. (2018). Legacies of organochlorine pesticides (OCPs) in soil of China—a review, and cases in Southwest and Southeast China. *Environmental Geochemistry*, 2018: 543-565.
16. Tarley, C. R., Scheel, G. L., Ribeiro, E. S., Zappielo, C. D., and Suquila, F. A. (2018). Synthesis of chelating agent free-solid phase extractor (CAF-SPE) based on new $SiO_2/Al_2O_3/SnO_2$ ternary oxide and application for online preconcentration of Pb^{2+} coupled with FAAS. *Journal of the Brazilian Chemical Society*, *29*: 1225-1236.
17. Ansari, S. (2017). Application of magnetic

molecularly imprinted polymer as a versatile and highly selective tool in food and environmental analysis: Recent developments and trends. *TrAC Trends in Analytical Chemistry*, 90: 89-106.

18. Liu, J. C., Tsai, P. J., Lee, Y. C., and Chen, Y. C. (2008). Affinity capture of uropathogenic *Escherichia coli* using pigeon ovalbumin-bound Fe_3O_4@Al_2O_3 magnetic nanoparticles. *Analytical chemistry*, 80(14): 5425-5432.
19. Duhan, S., Aghamkar, P., and Singh, M. (2008). Synthesis and characterization of neodymium oxide in silica matrix by solgel protocol method. *Physics Research International*, 4: 1-4.
20. Cai, L., Gao, Y., Chu, Y., Lin, Y., Liu, L., and Zhang, G. (2023). Green synthesis of silica-coated magnetic nanocarriers for simultaneous purification-immobilization of β-1, 3-xylanase. *International Journal of Biological Macromolecules*, 233: 123223.
21. Wan Ibrahim, W. N., Sanagi, M. M., Mohamad Hanapi, N. S., Kamaruzaman, S., Yahaya, N., and Wan Ibrahim, W. A. (2018). Solid-phase microextraction based on an agarose-chitosan-multiwalled carbon nanotube composite film combined with HPLC–UV for the determination of nonsteroidal anti-inflammatory drugs in aqueous samples. *Journal of Separation Science*, 41(14): 2942-2951.
22. Merhi, A., Kordahi, R., and Hassan, H. F. (2022). A review on the pesticides in coffee: Usage, health effects, detection, and mitigation. *Frontiers in Public Health*, 10: 1004570.
23. Othman, N. Z., Hanapi, N. S. M., Ibrahim, W. N. W. and Saleh, S. H. (2020). Alginate incorporated multi-walled carbon nanotubes as dispersive micro solid phase extraction sorbent for selective and efficient separation of acidic drugs in water samples. *Nature Environment and Pollution Technology*, 19(3): 1155-1162.
24. Nodeh, H. R., Ibrahim, W. A. W., Kamboh, M. A., and Sanagi, M. M. (2017). New magnetic graphene-based inorganic–organic sol-gel hybrid nanocomposite for simultaneous analysis of polar and non-polar organophosphorus pesticides from water samples using solid-phase extraction. *Chemosphere*, 166: 21-30.
25. Liu, S., Huang, X., Hu, K., Jin, Q., and Zhu, G. (2020). Development of a multiresidue method for endocrine-disrupting pesticides by solid phase extraction and determination by UHPLC-MS/MS from drinking water samples. *Journal of Chromatographic Science*, 58(3): 195-202.
26. Md Badrul Hisham, N. H., Ibrahim, M. F., Ramli, N., and Abd-Aziz, S. (2019). Production of biosurfactant produced from used cooking oil by Bacillus sp. HIP3 for heavy metals removal. *Molecules*, 24(14): 2617.
27. Latif, S., Rehman, R., Imran, M., Hira, U., Iqbal, S., Akram, M., ... and Al-thagafi, Z. T. (2022). Use of green chemistry for amputation of chromium ions from wastewater by alkali-treated composts of fruit peels in economical way. *Journal of Chemistry*, 2022: 9924164.

Malaysian Journal of Analytical Sciences (MJAS)
Published by Malaysian Analytical Sciences Society

A PORTABLE MICRO-VOLUME COLORIMETRIC ASSAY FOR ALUMINIUM DETERMINATION USING NATURAL REAGENT EXTRACTS FROM SAPPAN HEARTWOOD BY ULTRASOUND-ASSISTED EXTRACTION

(Satu Kaedah Uji Warna Isipadu-Mikro yang Mudah Alih untuk Penentuan Aluminium Menggunakan Ekstrak Bahan Semulajadi dari Teras Kayu Sappan Melalui Pengekstrakan Dibantu Ultrasonik)

Watsaka Siriangkhawut[1*] and Yaowalak Khanhuathon[2]

[1]*Creative Chemistry and Innovation Research Unit, Department of Chemistry and Center of Excellence for Innovation in Chemistry, Faculty of Science, Mahasarakham University, Maha Sarakham 44150, Thailand*
[2]*Chemistry Program, Faculty of Education, Chiang Rai Rajabhat University, Chiang Rai 57100, Thailand*

[*]*Corresponding author: watsaka@hotmail.com*

Received: 18 December 2023; Accepted:12 February 2024; Published: 29 April 2024

Abstract

An environmentally friendly small-scale ultrasound-assisted extraction and portable micro-volume colorimetry was proposed for the determination of aluminium in pharmaceutical formulations by extraction of Sappan heartwood in acetate buffer pH 5.5. Sonication parameters influencing the extraction of non-synthetic reagents from Sappan heartwood for quantification of aluminium including type of solvent, mass/volume ratio of solvent, extraction time and temperature were investigated. Efficiency of the ultrasound-assisted extraction procedure of aluminium from aluminium hydroxide gel was evaluated by comparing label values and the official method for pharmaceutical formulations. Under optimal conditions, a linear calibration graph ranging from 0.5 to 10 mg L^{-1} was obtained from micro-volume colorimetric determinations (at 530 nm) with limits of detection and quantification of 0.07 and 0.37 mg L^{-1}, respectively. Relative standard deviations were 2.3 and 1.3% for 1 and 3 mg L^{-1}, respectively. The developed system was successfully applied for the analysis of various forms of aluminium in pharmaceutical formulations (suspension and tablet). Good recoveries between 91 and 107% were obtained.

Keywords: Micro-volume colorimetry, ultrasound-assisted extraction, natural reagent, Sappan heartwood, aluminium

Abstrak

Satu kaedah pengekstrakan dibantu ultrasonik berskala kecil yang mesra alam dan uji warna isipadu-mikro mudah alih telah dicadangkan untuk penentuan aluminium dalam formulasi farmaseutikal dengan mengekstrak teras kayu Sappan dalam penimbal asetat pH 5.5. Parameter sonikasi yang mempengaruhi pengeluaran bahan kimia bukan sintetik dari teras kayu Sappan untuk pengukuran aluminium termasuk jenis pelarut, nisbah jisim/isipadu pelarut, masa pengekstrakan, dan suhu telah disiasat. Kecekapan prosedur pengekstrakan bantuan ultrasonik aluminium dari gel hidroksida aluminium di nilai dengan membandingkan

nilai label dan kaedah rasmi untuk formulasi farmaseutikal. Di bawah keadaan optimum, graf pemilihan linear dengan julat dari 0.5 hingga 10 mg L^{-1} diperolehi dari penentuan warna isipadu-mikro (pada 530 nm) dengan had pengesanan dan pengukuran masing-masing adalah 0.07 dan 0.37 mg L^{-1}. Sisihan piawai relatif adalah 2.3 dan 1.3% untuk 1 dan 3 mg L^{-1}, secara berturut-turut. Sistem yang dibangunkan telah berjaya digunakan untuk analisis pelbagai bentuk aluminium dalam formulasi farmaseutikal (ampaian dan tablet). Perolehan semula yang baik antara 91 dan 107% telah diperolehi.

Kata kunci: Uji warna isipadu-mikro, pengekstrakan dibantu ultrasonik, bahan semulajadi, teras kayu Sappan, aluminium

Introduction

Aluminium (Al), an abundant metal in the earth's crust, is a non-essential element commonly used to make aluminium-containing packaging for food/drink and cooking utensils [1]. It is also used for cosmetics production and pharmaceutical products [2]. Aluminium compounds are less toxic than heavy metals but excessive intake of Al has been associated with various diseases such as Alzheimer's, anaemia, osteomalacia and neurological syndrome [3-4]. Therefore, it is important to develop detection methodologies to monitor and quantify different matrices containing this metal.

Conventional methods for the determination of aluminium include flame atomic absorption spectrometry (FAAS) [5], graphite furnace atomic absorption spectrometry (GFAAS) [6], inductively coupled plasma-optical emission spectrometry (ICP-OES) [7], inductively coupled plasma-mass spectrometry (ICP-MS) [8], spectrophotometry [9-12], and fluorometry [13]. However, these methods require tedious pre-treatment as time-consuming processes that require professional operation with high instrumentation and maintenance costs. The development of green analytical techniques or procedures which provide economical and environmentally friendly advantages has now become an important aspect of sustainable analytical chemistry [14]. The use of a portable miniaturized system with green analytical methods involves stocking fewer samples, with reduced transport and analytical risks of contamination or analyte losses, together with positive environmental benefits [15].

Natural reagent extracts from various sources including vegetables, plant-based, animals, or bacteria require minimal treatment [16]. Natural reagents may be used instead of high purity chemical reagents when a reagent is only required in excess, or a crude extract contains the necessary active compound [17]. The use of crude plant extracts such as Indian mulberry (*Morinda citrifolia*) root extract [18], Indian almond (*Terminalia catappa* L.) leaf extract [19] and heartwood of Sappan wood (*Ceasalpinia sappan* L.) [20, 21] as chromogenic agents for analysis of Al in combination with flow-based analysis techniques [18-20] and paper-based analytical devices [21] have been reported as green analytical approaches. Contained plant compounds can be extracted by classical solvent extraction processes that include maceration with an organic solvent or boiling with water; however, these methods are time consuming and generate high waste production.

Sappan heartwood extracts are popular used for Al determination due to their high sensitivity and selectivity. The red homoisoflavonoid, brazilein is one of the main compounds found in the extracts of Sappan heartwood. In aqueous solution at pH 4.5, aluminium and pure brazilein extracted from Sappan heartwood form a 1:2 ratio complex via the ionized 10-hydroxyl group and 9-carbonyl oxygen of two molecules of brazilein bidentate ligands as shown in Figure 1 [22]. Traditional extraction methods of red dye from Sappan wood involve boiling the wood in water [23]. Various extraction methods have been proposed for the extraction of brazilein from Sappan heartwood such as maceration with ethanol [24], methanol [25], microwave-assisted extraction (MAE) [26-28] and ultrasound-assisted extraction (UAE) [29-30]. Among these, the ultrasound-extraction method is popular as a green analytical technique with clean protocol, safety, short operation time (less than 1 h) and moderate volume/concentration consumption of solvents and energy [31].

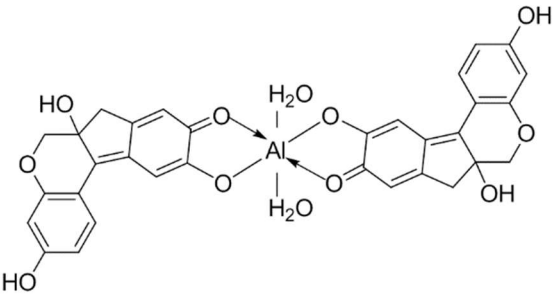

Figure 1. The proposed chemical structure of the Al(brazilein)$_2$ complex at pH 4.5

This study presented a new green analytical approach for Al determination based on simple small-scale ultrasound-assisted treatment procedures for (1) extraction of natural reagent from Sappan heartwood for complexation with Al, and (2) dissolution of Al in pharmaceutical products (suspension and tablet). A portable micro-volume colorimeter with an LED light was utilized to minimize the consumption of chemicals/reagents as a cost-effective device.

Materials and Methods

Chemicals and reagents

All chemicals used were of analytical reagent grade. Deionized water from Simplicity 185 (Millipore, Billerica, MA, USA) with resistivity 18.2 MΩ cm was used throughout the experiments. A 1000 mg L^{-1} aluminium (Al) standard solution (Merck, Darmstadt, Germany) was used in all the experiments. Working standard solutions of Al with different concentrations were prepared by appropriately diluting the stock solution. Hydrochloric acid (HCl, 37%) (Univar, Ingleburn, New South Wales, Australia) was used to digest the samples. Acetate buffer solutions at different pH were prepared from sodium acetate and acetic acid (Carlo Erba, Milano, Italy).

Instrumentation

A photo absorbance sensor, PiCOEXPLORER™ Model PAS-110 (Ushio Inc., Japan), controlled by a PAS-110 application via a smart phone/tablet mobile device was used for micro-scale colorimetric determination. A visible spectrophotometer, Genesys™ 20 (Thermo Fisher Scientific, USA) with Thermo Scientific VISIONlite 5 software was used for scanning the absorbance wavelength. Ultrasound-assisted extraction was carried out using a high power ultrasonic cleaning unit, Sonorex Digitec DT 100/H (Bandelin Electric GmbH & Co. KG, Berlin, Germany) with technical specifications: timer 0-30 min, 230 V, 50/60 Hz, frequency 35 kHz, and built-in heater 20 - 80 °C. All pH measurements were conducted using a pH meter (Model 713, Metrohm, Switzerland).

Preparation of natural reagent: Plant materials

Sappan heartwood powder (> 5 kg) was purchased from a local retail shop and dried in an oven at 50 °C for 24 h, storing in a dry place until use.

Ultrasound-assisted extraction method

Plant powder (0.5g) was accurately weighed into centrifuge tubes with caps (15 mL capacity) and 10 mL of 1 M acetate buffer solution pH 5.5 was added. The resulting solution were then mixed by a vortex and allowed to stand for 10 min at room temperature, termed as presonication time. The tubes were then immersed in an ultrasonic water bath and subjected to ultrasonic energy at 35 kHz for 30 min, termed as sonication time. The ultrasonic bath was set at 80 °C using a built-in heater. After sonification, the extract was centrifuged at 6000 rpm for 5 min, then passed through a filter paper (Whatman® No.1, UK) and made up to a volume of 10 mL with 1 M acetate buffer solution pH 5.5.

Conventional extraction method

Plant powder (5.0g) and deionized water (100 mL) were mixed in an extraction flask and heated on a hotplate until boiling. The extract was boiled for 10 min. After cooling, the extract was passed through a filter paper (Whatman® No.4, UK) and made up to a volume of 100 mL with deionized water.

Sample preparation: Pharmaceutical samples

Twelve aluminium hydroxide ($Al(OH)_3$) gel samples as suspensions (S1 – S6) and tablets (T1 – T6) were bought from local drug stores in Maha Sarakham Province, Thailand. Before analysis, 20 tablets were manually ground to powder and homogenized with an agate mortar and pestle.

Ultrasound-assisted extraction method

An accurately measured quantity of gel or fine powder (in case of tablet) as 0.024 to 0.030g of aluminium hydroxide (0.4-0.8 mL of aluminium hydroxide gel suspension, 0.010-0.020 g of aluminium hydroxide gel tablet) was transferred to a glass test tube. Then, 0.3 mL of hydrochloric acid was added and the mixture was immersed in an ultrasonic water bath for 10 min at 40 °C using a built-in heater. After sonification, the solution was cooled, filtered (in case of tablet) and diluted with 10 mL of deionized water.

Official method

A stock solution of the suspension was prepared following the pharmacopoeia procedures [32]. Briefly, the method involved the transfer of an accurately measured quantity of gel or fine powder (in case of tablet), equivalent to 1.2 to 1.5 g of aluminium hydroxide into a beaker. Then, 15 mL of hydrochloric acid was added and the mixture was heated gently until completely dissolved. The solution was then cooled, filtered (in case of tablet) and diluted with deionized water in a 500 mL volumetric flask.

Micro-volume colorimetric assay

This assay was performed in a micro-centrifuge tube (200 µL capacity), with reactive solutions measured by a portable colorimeter. For the construction of standard curves, 90 µL of natural reagent was added to each micro-centrifuge tube, followed by aliquots of eight different concentrations (0, 0.5, 1, 2, 4, 6, 8, and 10 mg/L) of aluminium standard solutions. Deionized water was used to make up the volume to 150 µL per tube. The contents were then mixed by shaking and kept at room temperature for 20 min, followed by reading at 530 nm (green LED) using PiCOEXPLORER™.

Results and Discussion

Ultrasound-assisted extraction of natural reagent from Sappan heartwood: Type of solvent

Normally, the extraction solvent has a strong impact on extraction yield by the solubility of the target analytes and also by physical parameters such as viscosity, vapor pressure and surface tension of the solvent [33]. From our previous study [20], the extraction solvent types (boiling with water, and maceration with different polar solvents, such as methanol, ethanol, and acetone) were optimized. An aqueous extract by boiling Sappan heartwood with water was chosen due to its simplicity and reduced chemical usage. After aqueous extraction, the extracts were mixed with sodium acetate and acetic acid to make a buffer solution of pH 5.5. This pH was chosen from its high sensitivity when comparing to other studied pH ranges from 3.0-6.0 [20]. However, the disadvantages of this method include tedious preparation steps and high consumption of water and chemicals (≈100 mL per batch per extraction). Therefore, ultrasound-assisted extraction (sonication time 30 min, temperature 80 °C) using 0.5 g of plant powder with water and acetate buffer pH 5.5 (10 mL) as extraction solvent was investigated for extraction efficiency compared to the conventional extraction method at the same mass ratio per extractant volume. Absorption spectra at 400-700 nm were recorded for the obtained solutions as shown in Figure 2. The conventional extraction method by boiling with water gave the highest absorbance of reagent extracts and reagent-Al complex. The decrease in absorption of the reagent and reagent-Al complex spectra obtained from ultrasound-assisted extraction was due to mass transfer limitation of soluble constituents from the material to the solvent by diffusion [34]. The absorption spectra obtained from ultrasonic energy with buffer solution were higher than with water. Therefore, acetate buffer pH 5.5 was chosen as the solvent for ultrasound-assisted extraction.

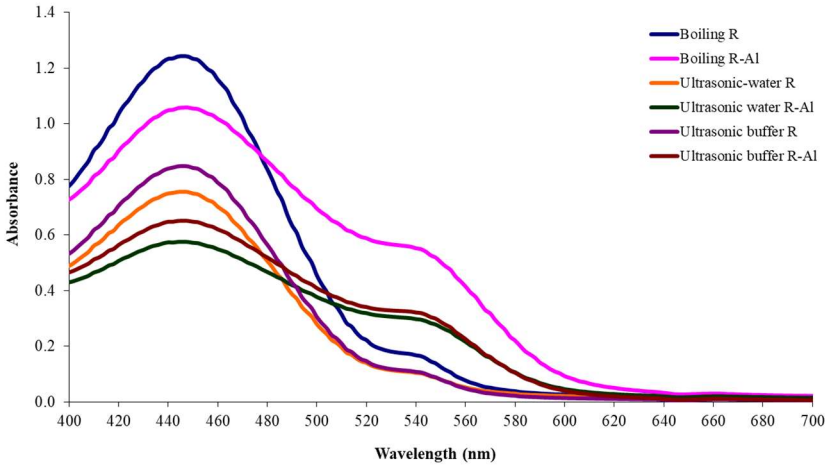

Figure 2. Absorption spectra of extracts from Sappan heartwood using different extraction procedures (boiling with water and ultrasonic-assisted extraction) and different extraction solvents (water and acetate buffer pH 5.5)

Effect of Sappan heartwood mass

In general, an increase in the solid sample mass improves sensitivity due to the transfer of higher amounts of analyte to the liquid phase. In this experiment, the volume of the extractant solvent was kept constant at 10 mL, while the mass of Sappan heartwood powder utilized in the extraction was varied from 0.1 to 1g. All other conditions were set according to the previous optimization experiments, with results shown in Figure 3. The absorbance of the reagent (at 446 nm) and reagent-Al complex (at 530 nm) increased with increasing amounts of plant powder from 0.1-0.5g, then slightly increased before remaining constant. A ratio of 0.5g of plant material per 10 mL of acetate buffer was selected as suitable for the extraction procedure from its high extraction reproducibility.

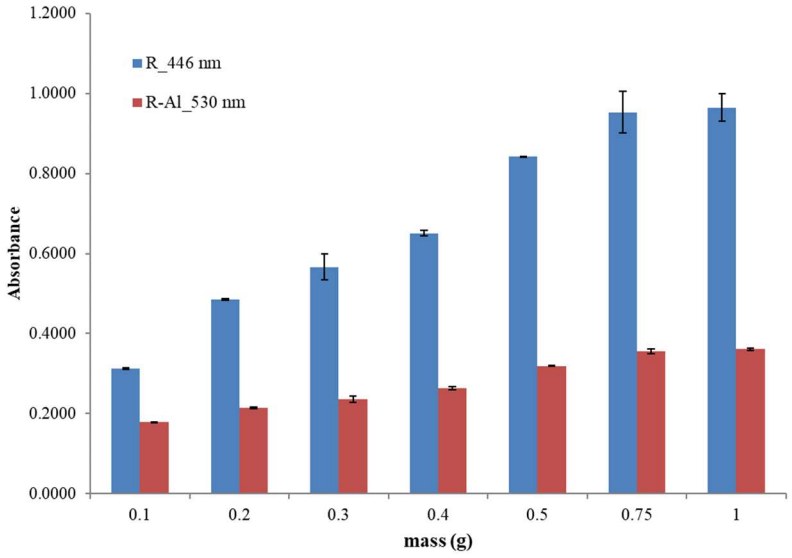

Figure 3. Effect of plant powder mass on the extraction of natural reagent performed in 10 mL of acetate buffer pH 5.5 with sonication time 30 min and temperature 80 °C

Extraction time

Long extraction time enhances extraction yields, but long extraction time may induce undesirable changes in the extracted compounds [35]. The influence of sonication time (10, 20, 30, 40, 50, and 60 min) on the yield of natural reagent extracts from Sappan heartwood using buffer pH 5.5 as extraction solvent was investigated with results shown in Figure 4. The yields of brazilein gradual increased from 10 to 30 min. After 30 min, there was a slight decrease in the yield, possibly due to degradation of the extracts at longer extraction times. This result indicated that ultrasonic irradiation played an important role in the extraction process. The increasing of the absorbance at 60 min might be due to the absorption of other species during degradation or the low reproducibility of the extraction process. An extraction time of 30 min was selected as suitable.

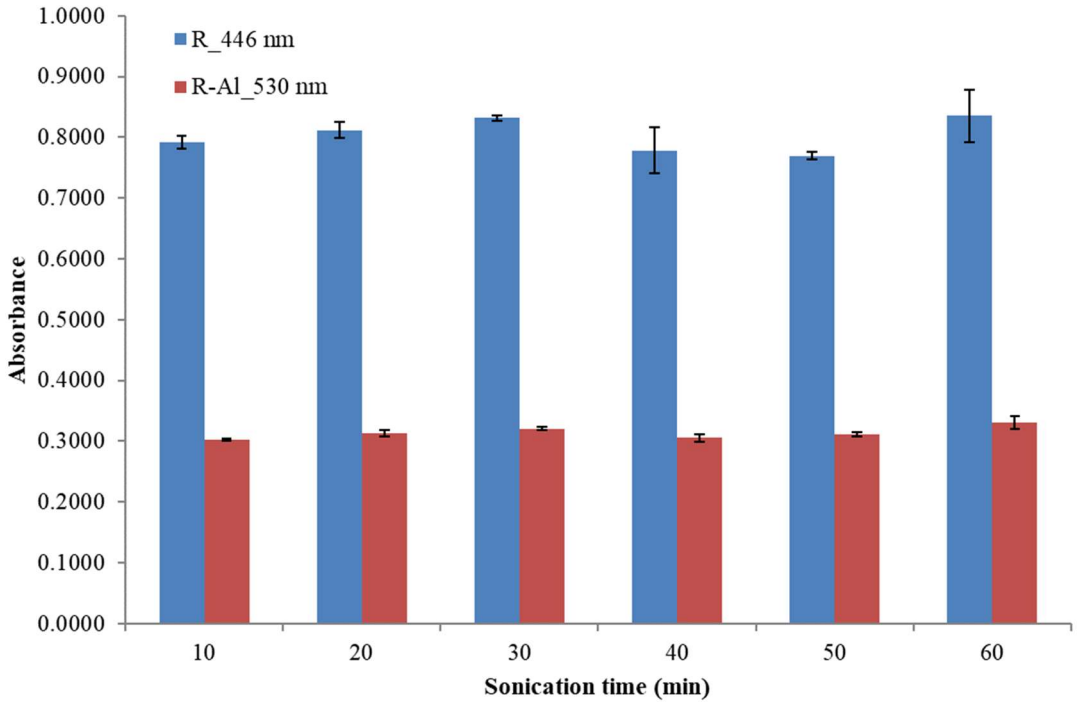

Figure 4. Effect of sonication time on the extraction of natural reagent performed with 0.5g of plant powder and 10 mL of acetate buffer pH 5.5 at 80 °C

Temperature

The extraction temperature is also important. Temperature contributes to efficiency of extraction. Usually, increase of temperature leads to an increase of extraction yield [33]. In this study, using an ultrasonic cleaning bath with built-in heater from 20-80 °C, the effect of different temperatures (30, 40, 50, 60, 70, and 80 °C) on the extraction yield was investigated. All other conditions were set according to the optimal parameters obtained above. Results are displayed in Figure 5. Extraction yield increased as temperature increased from 30 to 80 °C, showing that sonication temperature had a profound influence on the extraction of active ingredients from plant materials. Extraction temperature at 80 °C was selected as suitable.

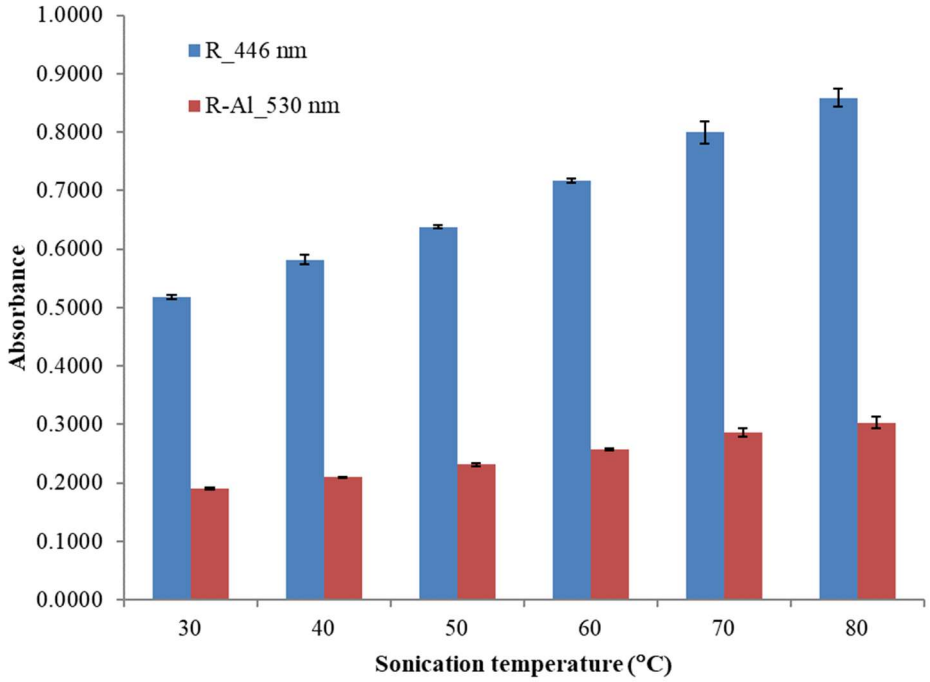

Figure 5. Effect of sonication temperature on the extraction of natural reagent performed with 0.5g of plant powder and 10 mL of acetate buffer pH 5.5 for 30 min

Extraction efficiency and reproducibility of crude plant extracts

After optimization, the extraction efficiency of the proposed small-scale ultrasonic-assisted extraction was lower than the conventional extraction by boiling with water (relative absorbance of 50%). However, the crude plant extracts contained sufficient active compounds to reacts with Al. To ensure the reproducibility of the various batches of natural reagent extracts for future use, the precision of absorbance of 10 batches of extracts prepared independently was evaluated. The relative standard deviation (%RSD) for the 10 batches was 3.8% and lower than the conventional extraction procedure [20]. The proposed small-scale ultrasonic-assisted extraction procedure had advantages over the conventional extraction procedure such as ease of operation, low chemical consumption, and high precision.

Determination of Al by micro-scale colorimetric procedure

Aluminium analysis was conducted using crude plant extracts containing brazilein. The complexation ratio of Al with brazilein in the crude plant extracts was 1:2 [22] with 530 nm the maximum complexation absorption wavelength. A marked change in color of the natural reagent with Al from yellow to reddish was observed.

Effect of mixing volume ratio of sample and reagent

The concentration of natural reagent extract used was 0.5g of heartwood /10 mL of buffer pH 5.5. The effects of sample and reagent volumes on the sensitivity of the system were studied at mixing volume ratios of Al:reagent 1:9, 2:8, 3:7, 4:6, 5:5, 6:4, 7:4, 8:2, and 9:1 for a total volume of 150 µL. As shown in Figure 6, the mixing volume ratio of Al:reagent at 4:6 (60:90 µL) gave the highest sensitivity and was selected as the optimal condition.

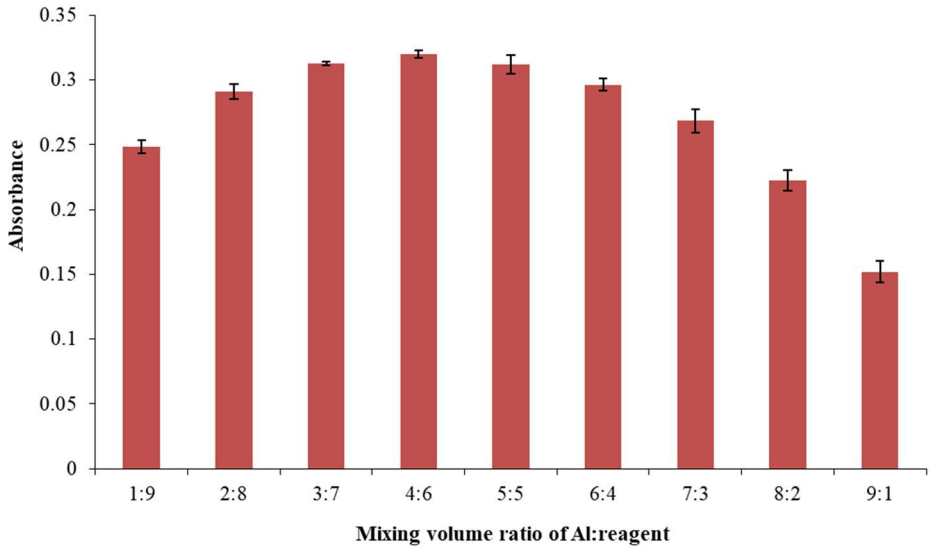

Figure 6. Effects of mixing volume ratios of sample (Al) and natural reagent extracts from Sappan heartwood at pH 5.5 on the sensitivity of the proposed micro-volume colorimetric measurement at 530 nm

Analytical features of the proposed system

The analytical characteristics of the proposed colorimetric assay were investigated. Using the optimal extraction conditions and the mixing volume ratio described above, standard calibration in the range 0.5-10 mg L^{-1} was constructed by plotting the absorbance against Al concentration. A linear graph was obtained with the calibration equation y = (0.0528±0.0024)x + (0.0111±0.0032) and R^2 = 0.9977, as shown in Figure 7. The limits of detection and quantification for Al were 0.07 and 0.37 mg L^{-1}, respectively with relative standard deviations for ten replicate determinations of 1 and 3 mg L^{-1} 2.3 and 1.3%.

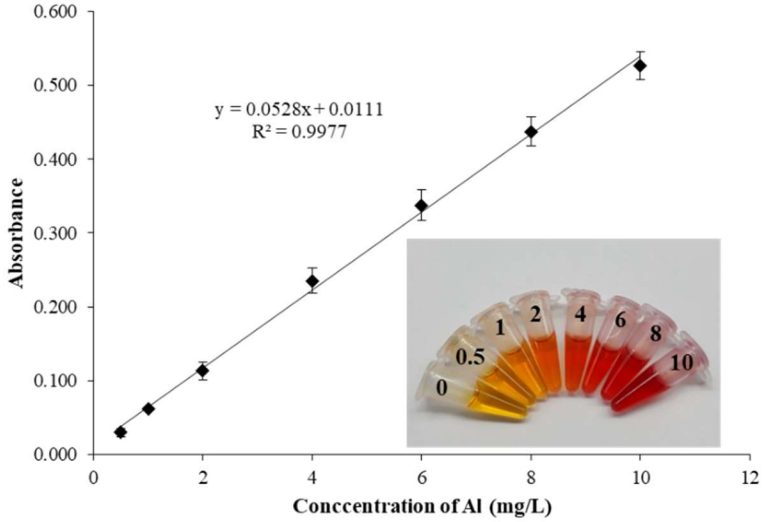

Figure 7. Visual detection and calibration curve of the aluminium standard with natural reagent extracts from Sappan heartwood at pH 5.5 obtained from micro-volume colorimetric measurement at 530 nm

The analytical performance of the proposed method was compared with previous methods using various natural reagents, as summarized in Table 1. The proposed method was not as sensitive as some other flow-based systems but the sensitivity was sufficient to measure Al in pharmaceutical samples (2.4-3.0 g/L). Our proposed micro-volume colorimetric assay consumed only 150 µL of each sample/standard and reagent solution per analysis. This assay also reduced contamination risk and analysis time and allowed portable on-field measurements.

Table 1. Analytical characteristics of the colorimetric determination method for Al using various natural reagents

Method	Natural Reagent	Extraction Method	Linear Range (mg L^{-1})	LOD (mg L^{-1})	Sample Volume (µL)	Ref.
Flow injection	Indian mulberry root extract	Maceration with 80%v/v acetone	0.1 – 1.0	0.05	75[a]	[18]
Flow injection	Indian almond leaf extract	Blending with acetate buffer pH 4.8	0 – 100	0.8	100[a]	[19]
Sequential injection	Sappan heartwood extract	Boiling with water	0.075 – 1.0	0.021	300[b]	[20]
Naked-eye detection	Cyanidin extracted from red cabbage	Extracted with MeOH and 2 M HCl (85:15 v/v)	1.35 – 2.70 (detection range)	1.35	1300[b]	[36]
Naked-eye and Vis-spectrophotometry	Pectin-rich apple extract-based gold nanoparticles	-	0 – 2.7	0.54	-	[37]
Naked-eye detection	Anthocyanin from black rice immobilized in carboxymethylcellulose/starch film	-	0 - 10	3.0	30 mL	[38]
Smartphone-based	Commercially fermented black carrot juice	-	1 – 50	0.2	2500[b]	[39]
Micro-volume colorimetry	Sappan heartwood extract	Small scale UAE	0.5 – 10.0	0.07	150[b]	This work

[a] sample volume only

[b] total analysis volume (sample+reagent+other solutions)

The effects of interfering species on the Al-natural reagent complex were investigated using the proposed method under optimal conditions. Various concentrations of foreign ions (Na^{+}, Ca^{2+}, Mg^{2+}, Zn^{2+}, Ni^{2+}, Cu^{2+}, Mn^{2+}, and Fe^{3+}) were spiked into a standard solution of 3 mg L^{-1} Al. An interfering concentration was considered as the value that caused signal variations higher than ±10%. Results showed that the system tolerated spiked cations up to at least a 1:1 concentration ratio of Al to interfering cations. Higher interference ratios were not studied since these minerals are normally

found in pharmaceutical formulations at lower amounts than Al compounds.

Ultrasound-assisted extraction of Al in pharmaceutical formulations

Aluminium hydroxide gel in suspension and tablet forms was used for optimization. The extraction efficiency or percentage label values (by comparing the amounts of aluminium found in aluminium hydroxide gel samples with their label values) of the results provided by ultrasonic variable parameters were evaluated under the optimal conditions. The mass of the sample, volume of the solvent, and type of solvent followed the standard method [32].

Sonication time

The influence of sonication time (1, 5, 10, 15, and 20 min) on the extraction efficiency of aluminium from aluminium hydroxide gel using hydrochloric acid as the extraction solvent and temperature 80 °C was investigated with results shown in Figure 8. Normally, long extraction time enhances extraction yields [35]. High percentage label of aluminium was obtained within 1 min for aluminium hydroxide gel suspension, while 10 min was required for the aluminium hydroxide gel tablet. Results indicated that sonication time played an important role in the extraction process of aluminium, especially in the form of aluminium hydroxide gel tablet. Therefore, an extraction time of 10 min was selected as suitable.

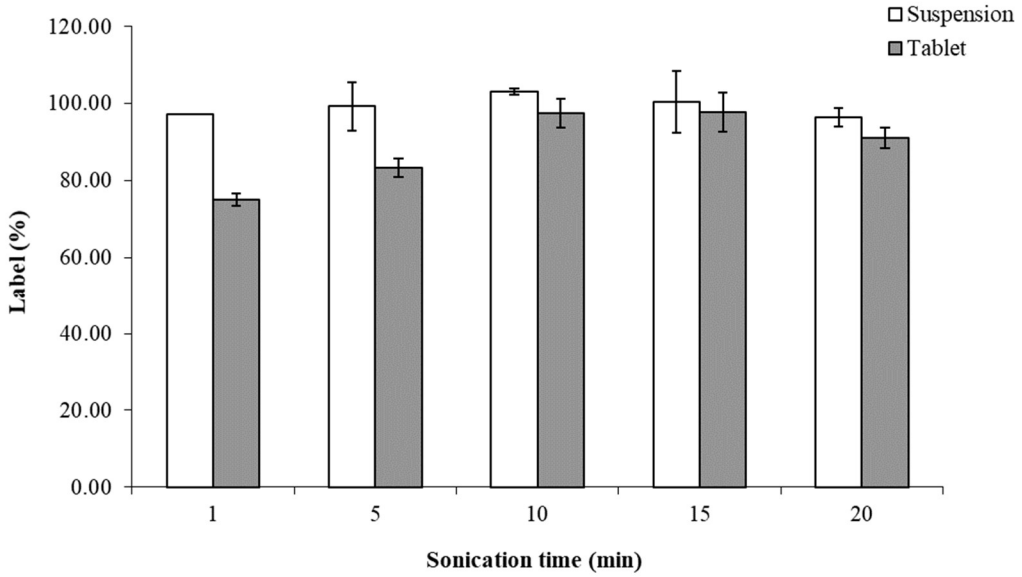

Figure 8. Effect of sonication time on the extraction of aluminium performed with 0.4 mL of $Al(OH)_3$ gel suspension or 11 mg of $Al(OH)_3$ gel tablet powder and 0.3 mL of concentration HCl at 80 °C

Temperature

The choice of extraction temperature is also important. The temperature strongly impacts the solvent's properties [33]. High temperature enhances solvent diffusion rates, while, low temperature enhances cavitation [35]. In this study, different temperatures (40, 50, 60, 70, and 80 °C) were investigated for extraction efficiency. All the other conditions were set according to the optimal parameters, with results displayed in Figure 9. High temperature during sonication did not influence the extraction of aluminium from aluminium hydroxide gel suspension and tablet. It might be due to aluminium ions were easily to dissolve from aluminium hydroxide gel under the acidic condition. Therefore, an extraction temperature of 40 °C was selected.

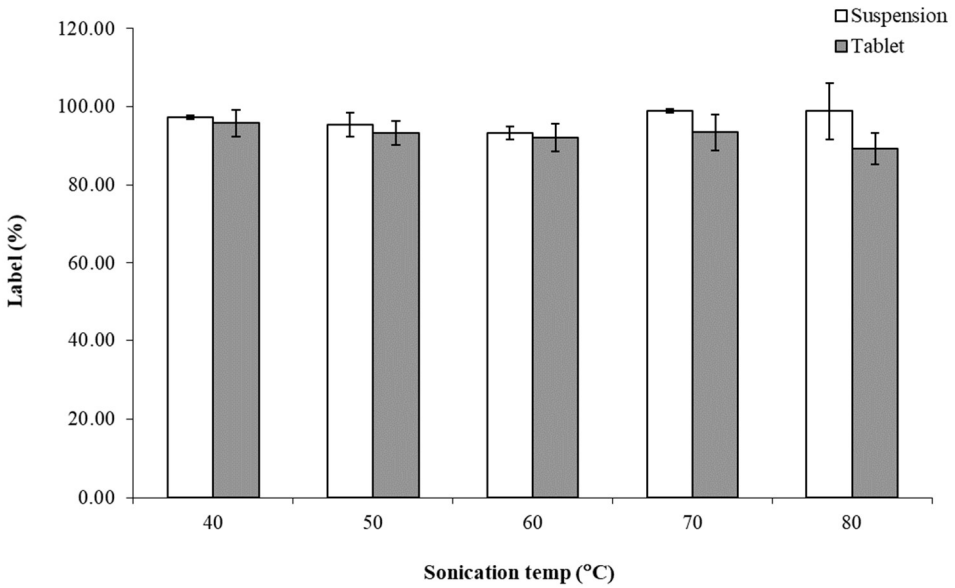

Figure 9. Effect of sonication temperature on the extraction of aluminium performed with 0.4 mL of $Al(OH)_3$ gel suspension or 11 mg of $Al(OH)_3$ gel tablet powder and 0.3 mL of conc. HCl for 10 min

Extraction efficiency

Small-scale ultrasound-assisted extraction efficiency was evaluated by comparing the results obtained from the official method for pharmaceutical formulations, as presented in Table 2. Satisfactory recoveries for both procedures were obtained at 103.3 and 96.8% for suspension and tablet forms, respectively. Results indicated that the extraction efficiency of the proposed small-scale ultrasound-assisted extraction procedure was comparable to the official procedure. Relative standard deviations of the aluminium concentration obtained after extraction by the proposed procedure were lower than for the official procedure.

Table 2. Extraction efficiency of the proposed ultrasound-assisted extraction procedure under optimal conditions

Pharmaceutical Form	Amount of Aluminium Hydroxide (mg) in 15 mL of Suspension or 1 Tablet		% Recovery[a]
	Reference Method (n = 10)	Proposed Method (n = 10)	
Suspension (960 mg Al / 15 mL)	960.5 ± 36.9 (3.8% RSD)	992.4 ± 12.9 (1.3% RSD)	103.3
Tablet (188.8 mg Al / tablet)	186.0 ± 9.4 (5.1% RSD)	180.0 ± 6.4 (3.6% RSD)	96.8

[a]Recovery (%) = [proposed method / reference method] x 100

Application to pharmaceutical samples

The proposed assay was used to determine aluminium content in pharmaceutical preparations, and the amounts of aluminium found in aluminium hydroxide gel samples were compared with their label values. Results are presented in Table 3. The aluminium contents in aluminium hydroxide gel suspension and tablet samples were acceptable at 90.0 to 110.0 % of the labeled amount of aluminium hydroxide [32]. Satisfactory recoveries ranging 91 to 107% for pharmaceutical samples were obtained.

Table 3. Determination of aluminium in pharmaceutical formulations (n = 3)

Sample[a]	Amount of aluminium hydroxide (mg) in 15 mL of suspension or 1 tablet		% Relative error[b]	%Recovery
	Label value	Found		
S1	960	986.3 ± 13.5	2.7	97.2 ± 3.4
S2	918	938.1 ± 6.9	2.2	101.2 ± 2.7
S3	900	910.7 ± 8.8	1.2	100.6 ± 3.5
S4	900	930.9 ± 7.4	3.4	104.0 ± 4.7
S5	600	603.4 ± 13.1	0.6	103.8 ± 3.6
S6	459	465.5 ± 6.6	1.4	106.6 ± 1.2
T1	188.8	183.8 ± 3.0	-2.7	90.9 ± 2.6
T2	191.3	188.7 ± 2.7	-1.4	91.2 ± 1.2
T3	248.6	235.2 ± 6.5	-5.4	95.2 ± 9.1
T4	191.3	179.8 ± 1.1	-6.0	101.0 ± 4.8
T5	188.8	184.6 ± 15.8	-2.2	104.4 ± 6.2
T6	153	147.6 ± 4.3	-3.5	94.6 ± 10.1

[a]S1-S6 : aluminium hydroxide gel suspension, T1-T6 : dried aluminium hydroxide gel tablet
[b]relative error = [(found - label value) / label value] x 100

Greenness assessment

The greenness of the proposed method was compared with the official method for Al in pharmaceutical sample [32] according to Analytical GREEnness (AGREE) metrics approach as seen in Figure 10. The calculation of the AGREE metrics software carried out by the application depends on 12 parameters that correspond to the 12 green analytical chemistry (GAC) principles [40]. Every principle or factor has a score range. According to the AGREE method, the proposed method scored 0.84 and stood out with portable miniaturized system, less amount of samples/reagent, less amount of waste, low energy consumption for sample pretreatment, high sample throughput and the use of bio-based reagents, while the reference method scored 0.42.

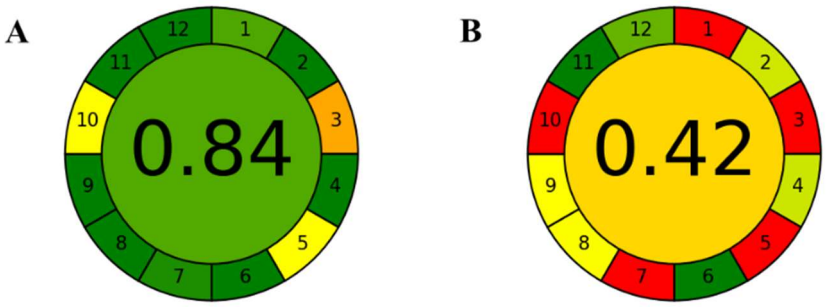

Figure 10. Results of AGREE analysis for the proposed micro-volume colorimetric assay (a) and the official method (b) for Al in pharmaceutical sample

Conclusions

A simple, reliable, cost-effective, and green analytical approach for the colorimetric determination of aluminium in pharmaceutical samples was presented. High efficiency sample preparation procedures based on ultrasound-assisted extraction were successfully applied

for small-scale extraction of natural reagent from Sappan heartwood, and also for aluminium from aluminium hydroxide gel samples. High throughput of more than 12 samples treated simultaneously was achieved using only a simple ultrasonic bath with a built-in temperature control. Our proposed micro-volume colorimetric assay significantly increased performance for the determination of aluminium in terms of cost-effectiveness, field-portability, and low chemical consumption. Satisfactory recoveries and high sample measurement frequency suggested that our proposed system showed high potential as a good alternative assay for the quality assurance of antacid suspensions and tablet products in the pharmaceutical industry. The "naked-eye" detection of this green approach can be used as a screening method for high aluminium content in wastewater samples from factories to improve environmental safety for the local residents.

Acknowledgements

The authors gratefully acknowledge financial support from Mahasarakham University, and the Center of Excellence for Innovation in Chemistry (PERCH-CIC), Office of the Higher Education Commission, Ministry of Education. Thanks are also due to Ushio Inc., and Thai Unique Co., Ltd. for supplying and lending the PiCOEXPLORER™. Additional support from the Center of Excellence for Innovation in Analytical Science and Technology (I-ANALY-ST), Chiang Mai University was also greatly appreciated. The authors wish to thank Ms. Patcharee Sittichan and Ms. Pirom Didpinrum for laboratory assistance.

References

1. Müller, J.P., Steinegger, A. and Schlatter, C. (1993). Contribution of aluminium from packaging materials and cooking utensils to the daily aluminium intake. *Zeitschrift für Lebensmittel-Untersuchung und Forschung*, 197: 332-341.
2. Schäfer, U. and Seifert, M. (2006). Oral intake of aluminum from foodstuffs, food additives, food packaging, cookware and pharmaceutical preparations with respect to dietary regulations. *Trace Elements and Electrolytes*, 23 (7): 150-161.
3. Campbell, A., Becaria, A., Lahiri, D. K., Sharman, K. and Bondy, S. C. (2004). Chronic exposure to aluminium in drinking water increases inflammatory parameters selectivity in the brain. *Journal of Neuroscience Researches*, 75: 565-572.
4. Zatta, P., Lucchini, R., van Rensburg, S. J. and Taylor, A. (2003). The role of metals in neurodegenerative processes: aluminium, manganese, and zinc. *Brain Research Bulletin*, 62: 15-28.
5. Antunes, G. A., dos Santos, H. S., da Silva, Y. P., Silva, M. M., Piatnicki, C. M. S. and Samios, D. (2017). Determination of iron, copper, zinc, aluminum, and chromium in biodiesel by flame atomic absorption spectrometry using a microemulsion preparation method. *Energy Fuels,* 31(3): 2944-2950.
6. Jalbani, N., Kazi, T. G., Jamali, M. K., Arain, B. M., Afridi, H. I. and Baloch, A. (2007). Evaluation of Aluminum contents in different bakery foods by electrothermal atomic absorption spectrometer. *Journal of Food Composition and Analysis,* 20: 226-231.
7. Rezaee, M., Yaminia, Y., Khanchib, A., Farajia, M. and Saleha, A. (2010). A simple and rapid new dispersive liquid–liquid microextraction based on solidification of floating organic drop combined with inductively coupled plasma-optical emission spectrometry for preconcentration and determination of aluminium in water samples. *Journal of Hazardous Materials,* 178: 776-770.
8. Albals, D., Al-Momani, I. F., Issa, R. and Yehya, A. (2021). Multi-element determination of essential and toxic metals in green and roasted coffee beans: a comparative study among different origins using ICP-MS. *Science Progress,* 104(2): 1-17.
9. Nihan, S. and Elmas, K. (2022). A simple and rapid determination of Al(III) in natural water samples using dispersive liquid–liquid microextraction after complexation with a novel antipyrine-based Schiff Base reagent. *Environmental Monitoring and Assessment,* 194: 47.
10. Ammar, J. W., Khan, Z. A., Ghazi, M. N. and Naser, N. A. (2021). Synthesis of a new organic probe 4-(4 acetamidophenylazo) pyrogallol for spectrophotometric determination of Bi(III) and Al(III) in pharmaceutical samples. *Reviews in Analytical Chemistry,* 40: 108-126.

11. Renedo, O. D., Cunado, A. M. N., Romay, E. V. and Lomillo, M. A. A. (2019). Determination of aluminium using different techniques based on the Al(III)- morin complex. *Talanta,* 196: 131-136.
12. Hafez, E. M., Sheikh, R. E., Fathallah, M.., Sayqal, A. A. and Gouda, A. A. (2019). An environment-friendly supramolecular solvent-based liquid–phase microextraction method for determination of aluminum in water and acid digested food samples prior to spectrophotometry. *Microchemical Journal,* 150: 104100.
13. Yıldız, E., Saçmacı, S., Saçmacı, M. and Ülgen, A. (2017). Synthesis, characterization and application of a new fluorescence reagent for the determination of aluminum in food samples. *Food Chemistry,* 237: 942-947.
14. Armenta, S., Garrigues, S. and de la Guardia, M. (2008). Green analytical chemistry. *Trends in Analytical Chemistry,* 27 (6): 497-511.
15. Chemat, F., Garrigues, S. and de la Guardia, M. (2019). Portability in analytical chemistry: A green and democratic way for sustainability. *Current Opinion in Green and Sustainable Chemistry,* 19: 94-98.
16. Grudpan, K., Hartwell, S. K., Lapanantnoppakhun, S. and McKelvie, I. (2010). The case for the use of unrefined natural reagents in analytical chemistry—a green chemical perspective. *Analytical Methods,* 2: 1651-1661.
17. Kiwfo, K., Woi, P. M., Saenjum, C., Sukkho, T. and Grudpan, K. (2022). Initiatives in utilizing natural reagents and natural materials for chemical analysis: talent and challenge for asian in new normal chemical analysis. *Malaysian Journal of Analytical Sciences,* 26(2): 399-414.
18. Tontong, S., Khonyoung, S. and Jakmunee, J. (2012). Flow injection spectrophotometry using natural reagent from *Morinda citrifolia* root for determination of aluminium in tea. *Food Chemistry,* 132: 624-629.
19. Insain, P., Khonyoung, S., Sooksamiti, P., Lapanantnoppakhun, S., Jakmunee, J., Zajicek, K. and Hartwell, S. K. (2013). Green analytical methodology using indian almond (*Terminalia Catappa* L.) leaf extract for determination of aluminium ion in waste from ceramic factories. *Analytical Sciences,* 29: 655-659.
20. Siriangkhawut, W., Khanhuathon, Y., Chantiratikul, P., Ponhong, K. and Grudpan, K. (2016). A green sequential injection spectrophotometric approach using natural reagent extracts from heartwood of *Caesalpinia sappan* Linn. for determination of aluminium. *Analytical Sciences,* 32: 329-336.
21. Anugerah, M. D. A., Daud, A., Sulistyarti, H., Sabarudin, A. and Retniwati, R. (2012). Method development for the determination of aluminum by μPAD using sappan wood extract (*Caesalpinia sappan*). *AIP Conference Proceedings,* 2638(1): 050003.
22. Wongsooksin, K., Rattanaphani, S., Tangsathitkulchai, M., Rattanaphani, V. and Bremmer, J. B. (2008). Study of an Al(III) complex with the plant dye brazilein from *Caesalpimia sappan* Linn. *Suranaree Journal of Science and Technology*, 15 (2): 159-165.
23. Nirmal, N. P., Rajput, M. S., Prasad, R. G. S. V. and Ahmad, M. (2015). Brazilin from *Caesalpinia sappan* heartwood and its pharmacological activities: A review. *Asian Pacific Journal of Tropical Medicine,* 8(6): 421-430.
24. Lioe, H. N., Adawiyah, D. R. and Anggraeni, R. (2012). Isolation and characterization of the major natural dyestuff component of brazilwood (*Caesalpinia sappan* L.). *International Food Research Journal,* 19(2): 537-542.
25. Sirirak, J., Suppharatthanya, P., Chantha, K., Girdthep, S. and Chayabutra, S. (2021). Eco-friendly lake pigment from Sappanwood: Adsorption study and its application as natural colorant for natural rubber toy balloon. *Journal of Metals, Materials and Minerals,* 31(2): 27-37.
26. Thanayutsiri, T., Patrojanasophon, P., Opanasopit, P., Ngawhirunpat, T., Laiwattanapaisal, W. and Rojanarata, T. (2023). Rapid and efficient microwave-assisted extraction of *Caesalpinia sappan* Linn. heartwood and subsequent synthesis of gold nanoparticles. *Green Processing and Synthesis,* 12: 20228109.
27. Chowdhury, M. A., Choi, M., Ko, W., Lee, H., Kim, S. C., Oh, H., Woo, E. R., Kim, Y. C. and Lee, D. S. (2019). Standardized microwave extract of sappan

lignum exerts anti-inflammatory effects through inhibition of NF-κB activation via regulation of heme oxygenase-1 expression. *Molecular Medicine Reports,* 19: 1809-1816.

28. Badami, S., Geetha, B., Sharma, S. V., Rajan, S. and Suresh, B. (2007). Microwave-assisted rapid extraction of red dye from *Caesalpinia sappan* heartwood. *Natural Product Research,* 21 (12): 1091 – 1098.
29. Djaeni, M., Kumoro, A. C., Utari, F. D. and Septiani, I. E. (2021). Enhancement of the sappanwood extract yield by aqueous ultrasound-assisted extraction using water solvent. *International Journal on Advanced Science, Engineering and Information Technology,* 11(4): 1514-1520.
30. Kurniasari, L., Djaeni, M. and Kumoro, A. C. (2023). Ultrasound-assisted extraction (UAE) of sappan wood (*Caesalpinia sappan* L.): Effect of solvent concentration and kinetic studies. *Brazilian Journal of Food Technology,* 26: e2022140.
31. Bendicho, C., De La Calla, I., Pena, F., Costas, P. M., Cabaleiro, N. and Lavilla, N. (2012). Ultrasound-assisted pretreatment of solid samples in the context of green analytical chemistry. *Trends in Analytical Chemistry,* 31 (1): 50 – 60.
32. The United States Pharmacopoeia (2007). 24th ed., US Pharmacopoeia Convention, Rockville, MD, 86.
33. Chemat, F., Rombaut, N., Sicaire, A. G., Meullemiestre, A., Fabiano-Tixier, A. S. and Abert-Vian, M. (2017). Ultrasound assisted extraction of food and natural products. mechanisms, techniques, combinations, protocols and applications: a review. *Ultrasonics Sonochemistry*, 34: 540-560.
34. Vinatoru, M. (2001). An overview of the ultrasonically assisted extraction of bioactive principles from herbs. *Ultrasonics Sonochemistry*, 8: 303-313.
35. Tiwari, B. K. (2015). Ultrasound: A clean, green extraction technology. *Trends in Analytical Chemistry*, 71: 100-109.
36. Khaodee, W., Aeungmaitrepirom, W. and Tuntulani, T. (2014). Effectively simultaneous naked-eye detection of Cu(II), Pb(II), Al(III) and Fe(III) using cyanidin extracted from red cabbage as chelating agent. *Spectrochimica Acta Part A: Molecular and Biomolecular Spectroscopy*, 126: 98-104.
37. Park, H., Kim, W., Kim, M., Lee, G., Lee, W. and Park, J. (2021). Eco-friendly and enhanced colorimetric detection of aluminum ions using pectin-rich apple extract-based gold nanoparticles. *Spectrochimica Acta Part A: Molecular and Biomolecular Spectroscopy*, 245: 118880.
38. da Silva, H. M., Mageste, A. B., e Silva, S. J. B., Ferreira, G. M. D. and Ferreira, G. M. D. (2020). Anthocyanin immobilization in carboxymethylcellulose/starch films: a sustainable sensor for the detection of Al(III) ions in aqueous matrices. *Carbohydrate Polymers*, 230: 115679.
39. Yardımcı B. (2023). Spectrophotometric and smartphone-based dual monitoring method for the determination of Al(III) ions using fermented black carrot juice (şalgam/shalgam) as a green chromogenic agent. *Journal of the Turkish Chemical Society Chemistry Section A*, 10 (1): 161-76.
40. Pena-Pereira, F., Wojnowski, W. and Tobiszewski, M. (2020). AGREE—Analytical GREEnness Metric approach and software. *Analytical Chemistry*, 92(14): 10076-10082.

Malaysian Journal of Analytical Sciences (MJAS)
Published by Malaysian Analytical Sciences Society

THE INFLUENCES OF SEASONAL MONSOONS UPON PHOSPHORUS, CHLOROPHYLL-A AND PHYSICAL CHARACTERISTIC OF THE KELANTAN WATERS

(Kesan Monsun Bermusim ke atas Fosforus, Klorofil-a dan Ciri-ciri Fizikal di Perairan Kelantan)

Azyyati Abdul Aziz[1], Suhaimi Suratman[1*], Ku Nor Afiza Asnida Ku Mansor[1], Fariz Syafiq Mohamad Ali[1], and Ku Mohd Kalkausar Ku Yusof[2]

[1]*Institute of Oceanography and Environment, Universiti Malaysia Terengganu, 21030 Kuala Nerus, Terengganu, Malaysia*
[2]*Faculty of Science and Marine Environment, Universiti Malaysia Terengganu, 21030 Kuala Nerus, Terengganu, Malaysia*

[*]*Corresponding author: miman@umt.edu.my*

Received: 5 October 2023; Accepted: 9 January 2024; Published: 29 April 2024

Abstract

The influences of seasonal monsoons on the variability of phosphorus (phosphate (PO_4^{3-}), dissolved organic phosphorus (DOP), total particulate phosphorus (TPP)), chlorophyll-a, and physical characteristics in the water columns of Kelantan Waters were investigated based on the datasets collected by three cruises during the southwest monsoon (SWM), inter-monsoon (IM), and northeast monsoon (NEM) seasons. Concentrations of PO_4^{3-} were determined using a discrete analyzer and standard colorimetric techniques. DOP and TPP were measured using an indirect method that involved a UV digestion system. This system utilizes UV light to oxidize organic phosphorus and total phosphorus compounds into PO_4^{3-}, thereby making them measurable. Surface and vertical profiles were investigated and showed that almost all parameters measured showed significant differences ($p < 0.05$) among seasons. The seasonal trends in the surface and vertical distributions of PO_4^{3-}, DOP, and chlorophyll-a concentrations were found to have peaked during the NEM, followed by the SWM and IM periods. The combination factors of heavy rainfalls, large river discharges, and stronger wind-induced processes during the NEM created conditions conducive for the enhancement of PO_4^{3-}, DOP, and chlorophyll-a concentrations in the study area. Principal Component Analysis (PCA) demonstrated a strong correlation between chlorophyll-a and PO_4^{3-}, suggesting that PO_4^{3-} supply was the dominant source for phytoplankton biomass (chl-a) survival during our sampling period. This study has provided valuable information about phosphorus dynamics in the Kelantan Waters, establishing a baseline for future studies.

Keywords: intermonsoon, northeast monsoon, phosphate, dissolved organic phosphorus, South China Sea

Abstrak

Pengaruh musim monsun ke atas kepelbagaian fosforus (fosfat (PO_4^{3-}), organik terlarut fosforus (DOP), jumlah partikulat fosforus (TPP)), klorofil-a, dan ciri fizikal dalam turus air di perairan Kelantan telah dikaji berdasarkan dataset yang dikumpul oleh tiga pelayaran semasa monsun barat daya (SWM), peralihan-monsun (IM), dan monsun timur laut (NEM). Kepekatan PO_4^{3-} ditentukan menggunakan pengnalisis automatik diskret dan kaedah kolorimetrik piawai. DOP dan TPP diukur menggunakan kaedah tidak langsung yang melibatkan sistem pencernaan UV. Sistem ini menggunakan cahaya UV untuk mengoksida fosforus organik dan

sebatian jumlah fosforus menjadi PO_4^{3-}, menjadikannya boleh diukur. Profil permukaan dan menegak telah dikaji, dan menunjukkan hampir semua parameter yang diukur adalah berbeza secara signifikan ($p < 0.05$) di antara musim. Kami dapati trend musim dalam taburan permukaan air dan menegak kepekatan PO_4^{3-}, DOP, dan klorofil-a mencapai puncaknya semasa monsun timur laut, diikuti oleh monsun barat daya dan tempoh perlihan-monsun. Gabungan faktor hujan lebat, sungai besar, dan proses yang diperkuatkan oleh angin semasa monsun timur laut mencipta keadaan yang menyokong peningkatan konsentrasi PO_4^{3-}, DOP, dan klorofil-a di kawasan kajian. Analisis komponen utama (PCA) menunjukkan korelasi kuat antara klorofil-a dan PO_4^{3-}, menunjukkan bahawa bekalan PO_4^{3-} adalah sumber dominan untuk fitoplankton (chl-a) biojisim semasa tempoh penyempelan kami. Kajian ini memberikan maklumat berharga mengenai dinamik fosforus di perairan Kelantran and sebagai garis asas untuk kajian masa depan.

Kata kunci: monsun peralihan, monsun timur laut, fosfat, fosforus organik terlarut, Laut China Selatan

Introduction

Phosphorus (P) is long-recognized as an essential nutrient for life, required by all living organisms for growth, energy transport, and membrane synthesis [1, 2]. Phosphorus is present in oceans as inorganic phosphate (i.e., orthophosphate (PO_4^{3-}) and condensed phosphate) and organic phosphate in both dissolved and particulate forms (i.e., dissolved organic phosphorus (DOP) and particulate phosphorus (PP) [3, 4]. Microbial organisms can access a variety of P sources to satisfy nutritional P demands and preferentially utilize orthophosphate, as it can be directly consumed and assimilated, whereas DOP generally requires more energy for conversion into PO_4^{3-} before its metabolic assimilation [5, 6]. However, PO_4^{3-} is present in low concentrations, which is potentially limiting for microbial organisms in the oligotrophic oceans (tropical and subtropical) [1, 7]. These oligotrophic oceans are subject to smaller variations of seasonal temperature than temperate waters and are permanently underlain by a strong thermocline, which is considered the least variable and the least productive in the oceans' surface waters [8]. Microbes actively utilize DOP as an alternative P source when PO_4^{3-} is depleted in the ocean [7, 9-12]. DOP is a complex mixture of organic compounds in the ocean, and is predominantly mediated by phytoplankton through cell excretion, exudation, death, and autolysis [11], and can also be derived from organic compounds discharged from industrial, agricultural, and domestic sewage [12]. The recycling and utilization of DOP play a significant role in primary productivity, which may support approximately 90% of gross primary productivity [13, 14]. Meanwhile, most of the P is transported to the ocean by mainly being attached to the particles phase as total particulate phosphorus (TPP) through riverine input [15, 16], where TPP includes clay and silt-associated organic and inorganic P [9]. Additionally, living microorganisms attached in TPP (98%) are higher than that in particulate C (60%) and N (49%), and thereby result in low TPP in particular detrital sedimentary fractions as evidence of preferential utilization of P [7]. Thus, P availability in the ocean has significantly impacted primary productivity.

The Kelantan waters are located in the east coast of Peninsular Malaysia (ECPM), and lie in the southern region of the South China Sea, bordering the Gulf of Thailand. Kelantan Waters form a system that has a high variability of hydrographical factors predominantly based on its monsoon season. Four different monsoon seasons affect this region, i.e., the northeast (Nov–Feb), southwest (May–Aug), and two transitional shorter inter-monsoon (Mar–Apr and Sep-Oct) periods, which can be distinguished based on their wind flow [17, 18]. The northeast monsoon (NEM) is associated with the strong north-easterly winds that generate a strong southward current along the ECPM, and usually bring heavier rainy seasons and rough seas over this region [17, 19]. Meanwhile, the southwest monsoon (SWM) season generates weaker south-westerly winds and drives northward currents along ECPM, and typically receives minimum rainfall and drier weather regions [17, 19]. The prevailing SWM winds with the north-south orientation of the coastline induce offshore Ekman transport, thus being favourable for upwelling along the ECPM, and unfortunately, less favourable in Kelantan Waters [20,21]. The two inter-monsoons (IM) are referred to as the first IM period (March-April) and the second IM period (Sept-Oct), and have unique features of wind direction and surface current, which are characteristics similar to SWM and NEM accordingly,

but are relatively slow and driven by limited mixing [17, 22].

The selected parameters of phosphorus (PO_4^{3-}, DOP, and TPP), chlorophyll-a, and physical characteristics (salinity and temperature) are interlinked, forming a complex web of relationships that govern nutrient dynamics and ecosystem health. PO_4^{3-}, DOP, and TPP collectively provide a comprehensive view of phosphorus cycling, where PO_4^{3-} concentration in the water column directly affects the nutrient availability for phytoplankton biomass (Chl-a), establishing a fundamental link between phosphate levels and overall ecosystem productivity. Furthermore, DOP, represented as an organic form of phosphorus, is intricately linked to nutrient dynamics, and DOP measurement provides insights into the bioavailability of phosphorus, impacting microbial and algal communities. It is also important to measure TPP concentrations, which are associated with suspended particles and sediments, reflecting the interactions between nutrients and the physical environment. Moreover, chl-a serves as a proxy for primary productivity. The relationship between chl-a levels and nutrient concentrations, especially phosphate, is crucial for understanding the impact of nutrient availability on algal biomass and the overall ecosystem health in the study area. Meanwhile, salinity and temperature contribute to the physical context that influences nutrient distribution and biological processes in the water column. The existing knowledge regarding nutrient distribution in Kelantan Waters, particularly in terms of vertical distribution, remains notably scarce.

While previous studies have explored phosphorus (P) nutrient distribution in Peninsular Malaysia Waters during the southwest monsoon (SWM) [21, 23, 24], northeast monsoon (NEM) [23], and inter-monsoon (IM) [25], the focus on nutrient distribution within Kelantan Waters, especially in the vertical profiling in the water column, is still limited. Recognizing this critical gap, our study has aimed to comprehensively investigate the spatial distribution of P-based nutrients (PO_4^{3-}, DOP, and TPP), chlorophyll-a, and the physical characteristics (temperature and salinity) across both, the surface and vertical profiles in Kelantan Waters. In addition, this research has also sought to evaluate the temporal patterns of nutrient variations in response to the three monsoon seasons (IM, SWM, and NEM), and identify the key environmental factors governing these patterns. By addressing this research gap, our study contributes essential insights crucial for the effective and robust monitoring of nutrient dynamics in the Kelantan Waters. The interplay between all parameters measured would help researchers and environmental managers grasp the intricate relationships within the water column.

Materials and Methods

Study area and sampling activity

The study area of Kelantan Waters is located between 102° to 105° E longitude (Figure 1), which lies within the shallow continental shelf with less than 100 m in water depth. This study was part of the cruise expedition "HICOE 2017". Three cruises to the Kelantan Waters aboard the RV Discovery occurred from 1-2 April, 4-8 July, and 16-18 November 2017, respectively. A total of 7 sampling stations were sampled, which were in the transect that is oriented perpendicular to the coast of Kelantan and is about 260 km towards the offshore region (Figure 1). The sampling area is influenced by anthropogenic activities from its adjacent city of Kota Bharu, mainly discharged through the Kelantan River [21, 23]. Seawater samples were collected in Niskin bottles attached to a CTD (Conductivity-Temperature-Depth, Sea-Bird) probe frame. At each sampling station, surface water samples (~ 0.5 m) were collected for surface distribution, while water samples for vertical profiling were taken at 5, 10, 20, 30, 45, and 60 m depths, respectively. The seawater samples for PO_4^{3-}, DOP, and chlorophyll-a analyses were vacuum filtered onboard, through pre-combusted (5 hours at 450ºC) and pre-weighed GF/F filters (0.7 µm pore-size, Whatman). The filtrate samples were transferred into acid-washed polyethylene bottles and immediately kept frozen at –20 °C to reduce all the activities and metabolism of the organisms in the water. Meanwhile, unfiltered samples were used for TPP determination. Chlorophyll-a filters were folded in half twice, and placed in a 15 mL centrifuge tube wrapped in aluminium foil to protect the phytoplankton from light. Both the filtrate samples and the chlorophyll-a filters were immediately stored at –20 °C until laboratory analyses.

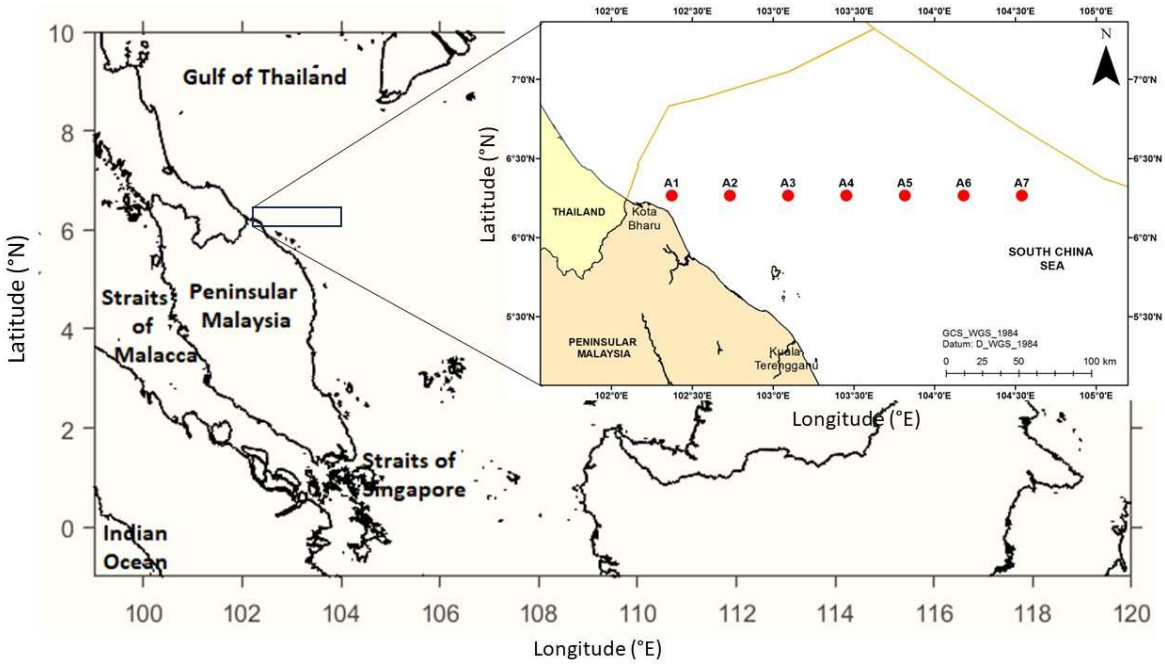

Figure 1. Map of the study area. Transect and stations are shown in the inset

Physical measurement

The physical data measurements began with temperature and salinity using a CTD sensor, and were displayed on a computer screen in the labs onboard. The sea surface current data were retrieved from the global ocean model, and the HYbrid Coordinate Ocean Model (HYCOM) global reanalysis (https://www.hycom.org/). The monthly means near-surface currents (u and v components of the current, unit: m/s) averaging over the top 10 m were used to investigate the influence of monsoons on the seasonal ocean circulation of the Kelantan Waters.

Laboratory analysis

In the laboratory, PO_4^{3-} samples were analysed based on standard colorimetric methods [26] using a SmartChem 200 discrete autoanalyzer (AMS Alliance), and were detected spectrophotometrically as a coloured complex. Basically, a water sample reacts with molybdate under acidic conditions (pH < 2) to form phosphomolybdic acid; the formed heteropolyacid is then reduced by ascorbic acid to produce a blue colour complex and detected at 880 nm using a SmartChem 200 discrete autoanalyzer. The determination of DOP relies upon the measurement of total dissolved phosphorus (TDP) and PO_4^{3-}, where DOP is calculated by subtracting PO_4^{3-} from TDP (DOP= TDP - PO_4^{3-}). TDP was first converted to measurable PO_4^{3-} by UV oxidation techniques using a Metrohm 909 UV digestion system, without the addition of any reaction initiators, catalysts, or oxidants. This process breaks down complex organic phosphorus forms, simplifying their quantification through analytical methods for inorganic phosphate PO_4^{3-}, which was subsequently measured using the same method as used for PO_4^{3-} determination above. This UV oxidation method is sufficient to oxidise 60–70% of DOP in the sample to PO_4^{3-} [27]. The unfiltered waters were used to determine the concentrations of TPP. The concentration of TPP measurement depends on the analyses of total phosphorus, TDP, and PO_4^{3-} (TPP = TP – TDP). TP was measured by converting all P forms to PO_4^{3-}, and the same method as used for TDP determination was applied. The Chl-a was determined using a UV-VIS spectrophotometer (Shimadzu 1201) after chlorophyll pigment was extracted from filters under subdued light in 90% (v/v) acetone and refrigerated at ~4 °C for 24 h [28].

Quality control (QC) measures were applied to ascertain the precision and accuracy of phosphorus determination

in this study, aligning with the EPA standard method [26]. These measures encompassed the analysis of duplicate samples, examination of blanks (utilizing deionized water treated as a sample), and the analysis of standard additions. Precision was evaluated through duplicate samples by estimating the standard deviation based on the results of a set of duplicate samples. The accuracy of measurements was assessed through the analysis of standards with known concentrations, reported as a percentage error. The percentage error was calculated using the following equation:

Percentage error = ((measured concentration – actual concentration) / actual concentration) x 100 (1)

Samples with error > 10% were reanalysed. The midrange standard concentrations and blanks were analysed periodically and simultaneously with the samples run at the beginning, intermediately and at the end of the run to confirm that instrument performance. The analyses yielded satisfactory results, with a percent measurement error staying consistently at less than 5%. Triplicates of every sample were analysed, and the concentrations of PO_4^{3-}, DOP, and TPP used here were the average of two measurements, and the overall analytical precision was within ± 2%. The detection limit was determined by calculating three times the standard deviations (DL=3SDb) of the blank measurement. The detection limit for phosphorus-based nutrients was found to be 0.05 μM P (n = 20).

Estimation of river nutrient input

Nutrient input from the Kelantan rivers, which were directly discharged to the study area, was estimated and calculated according to the following equation [23]

F = c x f (2)

where c is the nutrient concentration and f is the river flow. The information presented in this paper was calculated from data collected during the period of January-December 2017. The daily river flows in the Kelantan River are gauged and recorded by the Malaysian Department of Irrigation and Drainage (DID) and summed as monthly totals. Riverine nutrient concentrations were acquired from the Malaysian Department of Environment (DOE) for the Kelantan River estuary station, with sampling done at every two-three months of 2017. Unfortunately, load data is unavailable for the northeast monsoon season.

Statistical analysis

Statistical analyses were implemented by using the Xlstat 2019 (Addinsoft, France) software. We opted to apply a non-parametric test since most data distribution deviates from normality through the Shapiro-Wilk test (p<0.05, two-tailed). The Kruskal – Wallis with Bonferroni correction was employed as the post hoc analysis (at p<0.05), to test the significant differences of all parameters measured between stations (spatial pattern) and between monsoon seasons (temporal pattern). The degrees of potential correlations among the variables were identified through Spearman correlation analysis. The correlation was considered statistically significant when p-value < 0.05, and the strength of correlation was determined in three different classes (strong (r ≥ 0.60), moderate (r = 0.30 ≤, 0.59), weak r ≤ 0.29). Additionally, the compressed information of many correlated variables was further investigated through principal component analysis (PCA) to identify latent information generated from the spatiotemporal difference variations. In preparation for PCA, all variables were log-transformed to normalise their distributions, and eigenvalues >1 were considered significant principal components. Furthermore, to ensure the appropriateness of the data for PCA, Bartlett's test and Kaiser–Meyer–Olkin (KMO) was conducted. Bartlett's test should have a significance measure of less than 0.05 to indicate significant relationships among variables, and the minimum score of 0.60 was suggested for the KMO value. The high KMO values indicate a PCA with few errors [29].

Results and Discussion

Surface current

The surface current movement is largely controlled by wind, and Kelantan Waters' current circulation pattern is strongly influenced by monsoon winds. Figure 2 shows the sea surface current retrieved from the HYCOM in April, July, and November 2017, respectively, to represent current circulation during (A) IM, (B) SWM, and (C) NEM, respectively. In general,

the current direction during IM and NEM is similar, which moves towards the southward direction along Peninsular Malaysia; but both show different current patterns due to the stronger north-easterly winds occurring during NEM compared to IM. The variability of current circulation in the coastal area during IM due to winds is much weaker, which causes slow current movements, and which may be interrupted by tidal currents. Earlier research has proven that features of IM periods in East Coast Peninsular Malaysia include relatively weak winds as it is in prior monsoon seasons [17, 30], affected by local winds from the coast [17]. Strong north-easterly winds during NEM produce a stronger current that contributes to rough seas and brings colder water to Peninsular Malaysia [17, 31], with the current speed reaching up to 1.33 m/s during the sampling period. In contrast, surface currents during SWM showed a reverse direction, with the current circulation pattern flowing in the northward direction along the coast, with a maximum current speed recorded at 0.8 m/s. The prevailing winds during the SWM with the north-south orientation of the coastline are favourable for upwelling along the east coast of Peninsular Malaysia [20, 21]. However, so far, there has been no evidence of upwelling that can reach Kelantan Waters, because, as can be seen, the current movement diverts near 6˚N (Figure 2b) north-eastward towards the Vietnam coast [21, 32]. The variability of surface current circulation is an important factor to understand the oceanic environment. Strong water current causes water column mixing that may supply nutrients into the photic zone and vice versa.

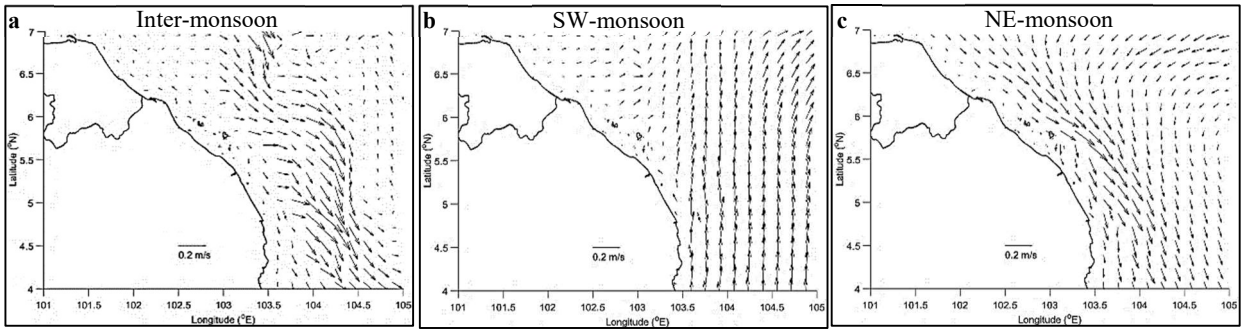

Figure 2. The seasonal variation of the mean surface current from HYCOM (unit: m/s) in Kelantan Waters

Kelantan river nutrient input

Kelantan River Nutrient Input in terms of PO_4^{3-} concentration was estimated based on the F = c x f equation. The results of Kelantan River Nutrient Input in terms of PO_4^{3-} concentration for April (IM) and July (SWM) were found to be 0.09 x 10^6 and 390 x 10^6 g per year, respectively. There were expectations of higher PO_4^{3-} inputs during November (NEM) based on higher rainfall and increased river discharge during NEM. Literature [23] recorded PO_4^{3-} riverine input from the river along the ECPM as 76% of its total annual input to ECPM waters in NEM, compared to SWM, where it was only 24%.

Surface distribution

The surface distribution of temperature, salinity, Chl-a, PO_4^{3-}, DOP, and TPP during three monsoon seasons for the seven stations area are illustrated in Figures 3 (a)-(r). The surface temperature in the study area exhibited relatively warm temperatures with a very slight variation, which was ubiquitous, with the surface temperatures reaching as high as 30 °C for all monsoon seasons. A clear decreasing gradient of surface temperatures toward the offshore region was recorded in the IM (28.26-30.4 °C; 29.13 ± 0.61 °C) (Figure 3a), while an opposite pattern was observed in SWM (29.56-30.7 °C; 30.08 ± 0.34 °C) (Figure 3b), with a few areas having a high temperature. Surface temperature measurements in NEM (Figure 3c) recorded low temperature values reaching 28 °C, especially in the coastal and middle areas (28-30.14 °C; 29.1 ± 0.52 °C). Figures 3d-f shows a surface salinity distribution pattern with low-salinity patches in the coastal area, which increase towards the open ocean. The lowest and the

highest salinity values of 28.18 psu and more than 34.16 psu were recorded during IM (31.98 ±2.0 psu), respectively. Meanwhile, the salinity pattern was slightly homogenous in the offshore areas during SWM and NEM, ranging from 29.69 – 33.38 psu (32.58 ± 1.3 psu) and 30.81 – 32.30 psu (31.81 ± 0.5 psu), respectively. The strong low-salinity distribution pattern observed in the coastal areas indicated the influence of freshwater from the adjacent river (Kelantan River) to our sampling area. This observation agrees well with existing studies in ECPM [21, 23, 25]. Overall, surface Kelantan Waters were characterised by relatively low salinity, and the warm temperature was variable between seasons. The Kruskal-Wallis test showed that salinity and temperature distributions were significantly different between seasons (p <0.05), but not significant among the stations (p>0.05).

The Chl-a gives an overview of phytoplankton biomass featuring monsoonal season influence. Surface Chl-a levels were significantly low with concentrations less than 0.2 µg/L, which varied from 0.03 to 0.17 µg/L (0.07 ±0.05 µg/L) during IM (Figure 3g), and 0.03-0.14 µg/L (0.07 ±0.04 µg/L) during SWM (Figure 3h), respectively. Both monsoon seasons were noticed with relatively uniform distribution, with a gradual decrease in Chl-a concentrations from coastal toward offshore stations. Meanwhile, high chlorophyll patches were observed in the coastal area during NEM, with concentrations ranging between 0.05 to 0.57 µg/L (0.14 ±0.2 µg/L). In NEM, particularly, the highest total rainfall (Figure 4) resulted in greater discharges from Kelantan rivers into nearshore areas. These discharges might have carried more domestic sewage from anthropogenic activities into the coastal seawater, leading to the higher nutrient concentrations and Chl-a observed in that season. Similarly, previous study [33] also found peak and extreme Chl-a concentrations (7.74 µg/L) along the coastal area of ECPM during NEM, and indicated that heavy rainfall and strong river discharge were the factors that affected the higher availability of Chl-a. Moreover, other previous studies also reported a similar pattern of Chl-a concentrations higher in coastal areas and lower towards offshore areas in Peninsular Malaysia Waters [21, 23, 34]. Statistically, the Kruskal–Wallis test shows that Chl-a concentrations were significantly different among the studied stations (p <0.05) and during monsoon season (p <0.05).

The concentrations of PO_4^{3-} (Figures 3 j-l) were measured to be low at less than 1 µM, and some were almost undetectable as the lowest concentration was below the detection limit (bdl) (bdl, <0.05 µM). Across the IM, SWM, and NEM, the following range of concentrations were recorded – bdl-0.22 µM (0.17 ± 0.07 µM), bdl-0.32 µM (0.14 ± 0.10µM), and 0.14-0.34 µM (0.29 ± 0.07 µM), respectively. The highest concentrations of DOP also have been estimated during NEM (Figure 3o), with concentrations ranging between 0.17-0.6 µM (0.38 ± 0.14 µM), followed by DOP concentrations during SWM (0.11-0.42 µM; 0.23 ± 0.10 µM) and IM (bdl-0.20 µM; 0.08 ± 0.07 µM). Generally, the DOP distribution patterns show large variations among monsoon seasons, with a uniform distributed pattern during IM (Figure 3m). TPP showed a similar trend with DOP, where a uniform distribution pattern was found in the IM (bdl-0.14 µM; 0.07 ± 0.05 µM) season, but irregular TPP distributions were found during SWM (0.23-0.59 µM;0.36 ± 0.16 µM) and NEM (0.12-0.44 µM; 0.29 ± 0.11 µM). Seasonally, the general trends of surface PO_4^{3-} and DOP show higher concentrations in NEM, probably attributed to the strong monsoonal winds that are associated with strong sea surface currents, resulting in increased nutrient input to the surface waters. The strong monsoon current was able to exchange Kelantan Waters and the adjacent bodies of water, since the surface current direction moves in the southward direction along Peninsular Malaysia, suggesting higher DOP and PO_4^{3-} during NEM, especially in the middle region, which could be transported from the Gulf of Thailand. Previous studies have found that the Gulf of Thailand-derived nutrients dominated the northern area of peninsular Malaysia [21, 23]. However, an unclear surface trend of TPP was observed in this study, with higher TPP during SWM. In terms of spatial distribution, PO_4^{3-}, DOP, and TPP showed a strong concentration onshore-offshore gradient, decreasing seaward. Except for TPP, the highest concentration was recorded at the nearshore station (A1) during NEM. The higher nutrients input during NEM at the nearshore station is in relation to the strong riverine input from Kelantan River due to higher

rainfall (900 mm) associated with greater river discharge (665 m^3/s), resulting in more PO_4^{3-} and DOP input to this station. Even so, there were still non-significant differences between stations (Kruskal Wallis $p > 0.05$), which were significant among the monsoons ($p < 0.05$).

The comparison of the data obtained in this study with previous studies in Peninsular Malaysia is useful in providing information on Chl-a and P distributions in Peninsular Malaysia (Table 1). Overall, the Chl-a concentration in this present study is much lower than in the previous study in ECPM [25] and coastal areas in Peninsular [6], but higher than the latest study in ECPM [23]. Surface PO_4^{3-} in this present study (0.14-0.34 µM) was recorded as slightly higher than other ECPM areas i.e., <0.10-0.11 µM [24] and <0.02-0.20 µM [23], but lower than coastal areas around Peninsular Malaysia (0.02-0.84 µM). Meanwhile, DOP concentrations (<0.11-0.60 µM) in this study were within the range previously reported for Peninsular Malaysia, by Lim et al. [6] (<0.01-0.61 µM) and Hee et al. [23] (<0.1-0.7 µM). However, as far as we know, no previous research has investigated TPP in Peninsular Malaysia Waters.

Depth-profile Distribution

The vertical profiles of temperature, salinity, and concentration of Chl-a, PO_4^{3-}, DOP, and TPP during all monsoon seasons are visualised in the contour plot, Figure 4. In IM, the temperature ranged from 26.32 - 30.04 °C, with an average of 28.24 ± 1.18 ºC, and salinity values were spread between 28.18-34.29 psu (33.11 ± 1.29 psu). The temperature (Figure 4a) and salinity (Figure 4d) profiles show similar stratification as observed at depths of 10-20 m, and there are significant differences between the depths ($p < 0.05$). The temperature and salinity profiles during SWM were already discussed in our previous work [21]. Briefly, the isotherm of 29.5 °C (Figure 4b) and isohaline of 32.5 psu (Figure 4e) was shoaled until 10 m in the region of 103 °E and bent downward towards the coast. This well-stratified water column was due to the Kelantan River plume and strong solar radiation during both IM and SWM. Both seasons of IM and SWM show a similar distribution pattern of warm temperatures and low salinities at ~10 m above the layer. This pattern indicated the typical features of riverine discharge that are influenced by the nearest adjacent river, i.e., the Kelantan River's direct input into the study area. The river outflow restricted the movement of water underneath from reaching the surface layer. Similar features were also observed in ECPM by [25], where these were studied during IM and SWM, and [20], during SWM. Moreover, weak water column mixing is mainly due to large surface water heating on the surface and weak surface current, which also explains why the underneath water did not reach the surface. In contrast, well-mixed water columns during NEM for temperature and slightly mixed for salinity, varied from 28.51- 30.14 °C (29.08 ± 0.26 ºC) and 30.81-33.10 psu (32.34 ± 0.5 psu), respectively. Temperature is vertically homogeneous with a mean of 29 °C occupied by all water columns (Fig. 4C), and offshore water of > 40 m depth showing a colder temperature (28.51°C). Thus, the temperature did not show any significant difference against the depth ($p > 0.05$). However, significant differences were observed in different depths ($p < 0.05$) for salinity, where salinity is more saline at the bottom layer, especially in offshore water (33.10 psu). The well-mixed water column was expected as a result of the large river discharge and strong water current, which increased the vertical mixing from the bottom to reach the surface layer. Although this study did not emphasise vertical water current, the river discharge and rainfall data obtained from the DID reveal that there was an increased rainfall amount associated with strong river discharge during November 2017 (NEM) as compared to April (IM) and July (SWM) 2017 (Figure 4). This is in agreement with previous studies in ECPM [17, 23], where NEM tends to have well-mixed water columns due to higher freshwater influence and strong wind speeds associated with the strong vertical current. The Kruskal-Wallis test results indicate significant differences among the monsoonal seasons regarding temperature and salinity ($p<0.05$). Seasonally, the vertical profile of Chl-a varied remarkably from the surface to the bottom, where Chl-a concentration showed a similar pattern with high concentration in the bottom and low concentration in the surface layers. Chl-a concentration varied from 0.02 to 0.73 µg/L (0.16±0.18 µg/L) during IM, with a weak trend of Chl-a movement towards the surface. Meanwhile, Chl-a concentration was recorded as 0.01 to 0.60 µg/L

(0.16±0.16 µg/L) during SWM, and 0.02 to 0.75 µg/L (0.22±0.17 µg/L) during NEM, respectively. The Chl-a variability shown in NEM slightly fluctuates and is higher in the middle of the water column. The strong vertical mixing mechanism induced by strong winds during NEM led to the re-suspension of bottom sediment and facilitates the release of nutrients. Consequently, this has supported increased phytoplankton biomass, reflected in higher Chl- a. concentration toward middle water. Previously, [35] revealed the occurrence of higher Chl-a concentration at the bottom water of the shallow region attributed to resuspension and turbulent water mixing, which modify the vertical dispersion rates of phytoplankton and the upward flux of nutrients and further promote the phytoplankton growth. Moreover, [36] also found higher Chl-a concentration at the bottom water due to the occurrence of turbulent vertical mixing that resulted in more efficient transport of nutrients from bottom to the water column and subsequently increased phytoplankton abundance and the chlorophyll-a content. Additionally, when there are low nutrients available in the surface water, phytoplankton tends to survive in bottom water without light limitations, especially in shallow water, due to the sediments releasing an abundant amount of nutrients [37]. Thus, in agreement with this study, where limited surface P availability in the surface water (except for PO_4^{3-} in NEM) and water depth was less than 60 m, phytoplankton (Chl-a) tended to grow in bottom layers. The Kruskal-Wallis test showed significantly different ($p < 0.05$) Chl-a levels among the monsoon seasons.

Table 1. The variability of the surface concentrations ranges of Chl-a, PO_4^{3-}, DOP, and TPP measured in different areas of Peninsular Malaysia

Location	Chl-a (µg/L)	PO_4^{3-} (µM)	DOP (µM)	TPP (µM)	Ref.
Current study	0.02-0.57	0.14-0.34	<0.11-0.60	0.01-0.69	
ECPM	0.068-7.744			-	[33]
ECPM	-	<0.10-0.11		-	[24]
ECPM	<0.01-0.06	<0.02-0.20	<0.1-0.7	-	[23]
Coastal around Peninsular Malaysia	2.77 ± 3.36	0.02-0.84	<0.01-0.61	-	[6]
ECPM	0.076-1.27	0.54-1.68			[25]

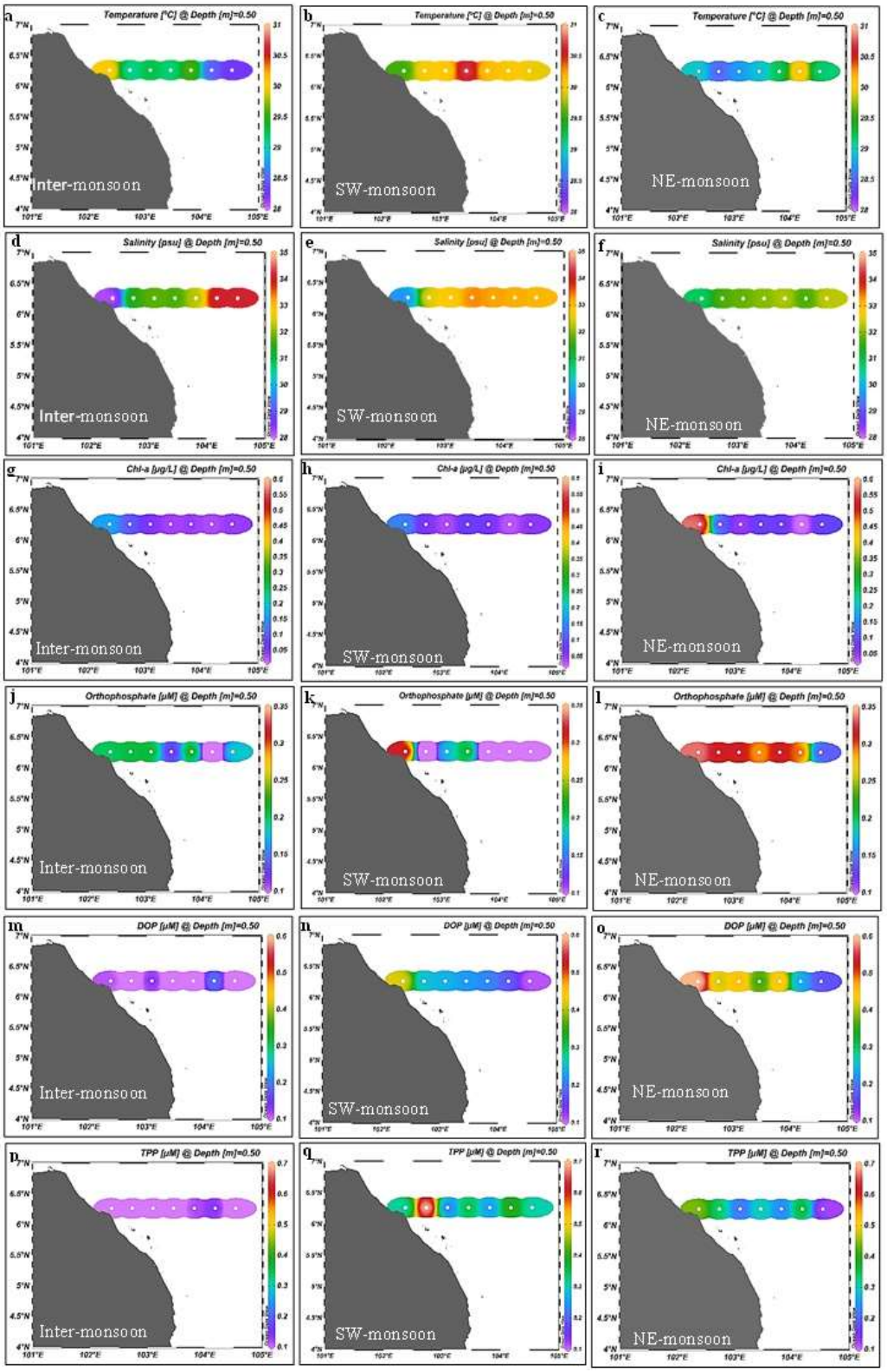

Figure 3. Seasonal variation of the surface physical characteristics, Chl-a, and P-based nutrients in Kelantan Waters

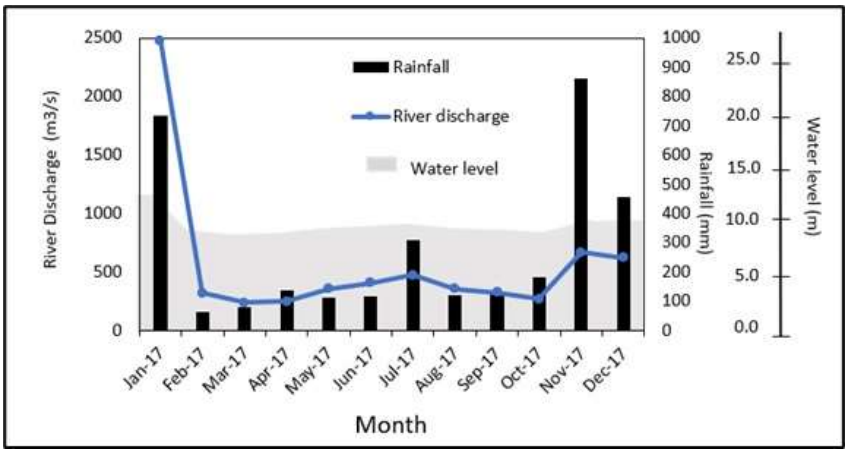

Figure 4. Monthly river discharge and rainfall in Kelantan River

The vertical profile of PO_4^{3-} during IM ranged between bdl to 0.44 µM (0.23 ± 0.09 µM), showing a large fluctuation, and an irregular variation for the entire water column (Figure 5d). Meanwhile, in SWM, PO_4^{3-} was exhausted or near the detection limit in most of the offshore area; nevertheless, higher concentrations were observed in the coastal area (bdl to 0.45 µM; 0.20 ± 0.13 µM). However, the Kruskal-Wallis test indicated that no significant depth change was noted (p >0.05) during both seasons. Conversely, the PO_4^{3-} distribution patterns showed a vertically uniform pattern in NEM (Figure 5F), and recorded concentrations of 0.20-0.45 µM (0.33 ± 0.05 µM), where a significant variability of PO_4^{3-} in the water columns was apparent (p <0.05). Uncommon PO_4^{3-} concentrations were notably higher in the offshore bottom water rather than in the coastal water, possibly due to stronger wind-induced vertical mixing during NEM; hence causing re-suspension of bottom sediments that brings up PO_4^{3-}-rich bottom water to the water column. PO_4^{3-}-rich bottom water is derived from remineralization processes of organic matter and sediment as a buffer to release nutrients to the water column when wind-induced currents disturb the water-sediment interface, especially in the shallow region [38]. However, this situation was not observed in the bottom water of the coastal area, which could be due to the lack of PO_4^{3-} resources in the bottom water, as a consequence of biological uptake or a strong river influence which transported PO_4^{3-} away to the offshore region. Earlier studies indicated that no matter how efficient the re-suspension event, the re-suspending of materials in the bottom also depends on the availability of the resources due to earlier re-suspension and/or benthic predation, which reduces the resources [35].

Overall, all monsoonal seasons have displayed a significant influence on PO_4^{3-} variation in the study area (p < 0.05). DOP was both seasonally and spatially significantly different (p <0.05). Vertically, the DOP distribution exhibited a general pattern of increased concentration with depth for all seasons ranging between 0.18 and 0.76 µM (0.39 ± 0.15 µM) in IM, 0.11 and 0.71 µM (0.41 ± 0.17 µM) in SWM, and 0.17 and 0.79 µM (0.51 ± 0.11 µM) in NEM, respectively. The DOP enrichment in the bottom depends on organic matter export processes, i.e., gravitational settling of living and dead cells or plankton biomass that can be remineralized into DOP. The DOP rapidly cycled and created a balance between local DOP production and utilisation processes occurring in the bottom water, leading to high DOP in the bottom water [39, 2]. However, DOP functioning in the bottom could not be clarified completely in this study, which can be clarified by further studying about P recycling in the future. Seasonally, the higher DOP concentrations have been estimated in the NEM, likely due to higher riverine run-offs induced by higher precipitation. According to [40], it was estimated that 61% of DOP in the Yellow Sea was mainly from riverine input, and [41] found peak DOP concentrations during wet seasons compared to dry seasons due to greater run-offs associated with higher precipitation. Thus, DOP distribution may vary depending on physical and chemical environmental conditions. Vertically, TPP distribution exhibited a

similar pattern with DOP, where concentration increased with depth. TPP was present in significant concentrations with depth ($p < 0.05$) for all seasons, and the concentrations ranged from 0.21-0.87 µM (0.54 ± 0.16 µM) during IM, 0.11-0.95 µM (0.46 ± 0.21 µM) during NEM, and 0.21-0.86 µM (0.54 ± 0.18 µM) during SWM, respectively. Monsoonal weather is an important factor that controls the distribution of Chl-a and nutrients measured in this present study, but plays a relatively insignificant ($p > 0.05$) role in TPP distribution.

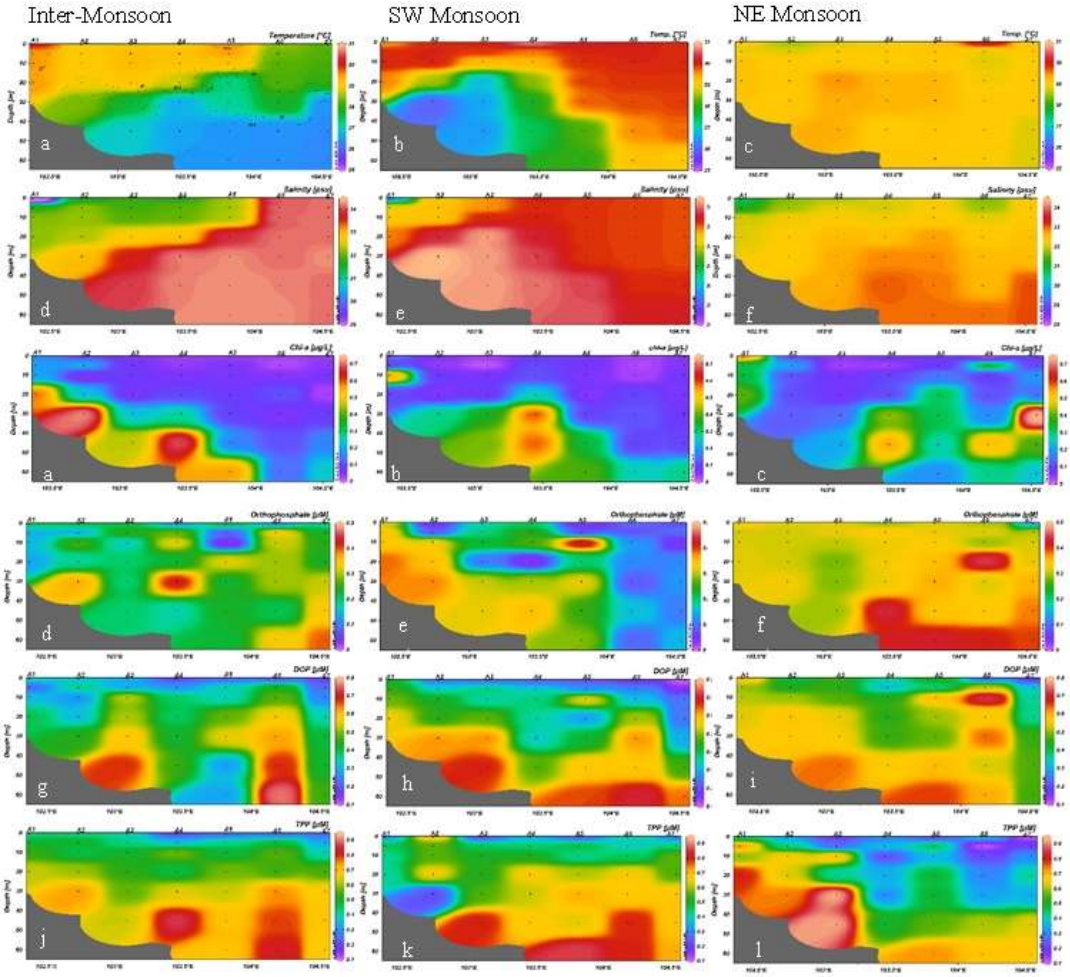

Figure 5. The seasonal cross-sectional profile of physical characteristics, Chl-a and P-based nutrients in Kelantan Waters

Principal component analysis (PCA)

The phosphorus species distribution within the Kelantan Waters is subject to influences not solely attributable to physical determinants but also governed by biological parameters, specifically chlorophyll-a (chl-a). This interplay is potentially modulated by the monsoonal fluctuations prevalent in the Southern South China Sea [21, 23]. The Kaiser-Meyer-Olkin (KMO) correlation coefficient, registering at 0.60, and the statistically significant Bartlett's sphericity test (p <0.001) collectively affirm the adequacy of the dataset for principal component analysis (PCA). The utilization of PCA proves instrumental in discerning the most salient variables in our investigation, facilitating a comprehensive understanding of the dataset while minimizing the loss of original information.

Consequently, PCA is applied to ascertain the potential influence of variables such as temperature, salinity, and Chl-a on the distribution of phosphorus variables throughout the study. The outcome of the PCA analysis reveals the acquisition of Principal Component 1 (PC1, denoted as F1 in Figure 6) for this study, possessing eigenvalues exceeding 1 (2.456) and accounting for 40.9% of the total variance in the dataset. This suggests a substantial explanatory power of the identified factors. The findings further suggest a strong correlation between salinity and Chl-a in determining the variability of phosphorus within the Kelantan Waters

The results of factor loading obtained from the PCA, as presented in Table 2, reveal distinctive contributions of various variables to the overall variability in phosphorus distribution within the Kelantan Waters. Specifically, phosphate exhibits the highest factor loading at 0.853, succeeded by DOP at 0.765, salinity at -0.698, and Chl-a at 0.687. These numerical values elucidate the respective influences of these variables on the observed fluctuations in phosphorus levels in the study area. Figure 6a visually elucidates the interrelationships between phosphorus species and other environmental factors in the Kelantan Waters. Notably, the concentration of phosphate demonstrates an inverse correlation with both salinity and temperature, while Chl-a stands as the singular variable deviating from this observed trend. The identified inverse relationships imply that regions characterized by lower salinity and temperature are prone to exhibit higher concentrations of phosphate. In contrast, the positive correlation between phosphate levels and Chl-a concentrations suggests that elevated phosphate availability contributes to increased phytoplankton biomass, subsequently augmenting Chl-a production. These findings align with prior research [21, 43], underscoring a significant correlation between Chl-a and phosphate, thereby emphasizing the essential role of phosphate in phytoplankton production. Consequently, the availability of phosphate emerges as a pivotal factor influencing Chl-a levels during the studied period.

Principal component analysis (PCA) was applied to delineate the distinctions in phosphorus distribution during the monsoon seasons, as elucidated in Figure 6b. This graphical representation underscores the statistically significant disparities ($p < 0.05$), previously ascertained through the Kruskal–Wallis test. The PCA results manifested as ellipses, characterizing the phosphorus distribution during the NEM, SWM, and IM seasons. Each ellipse encapsulated distinctive features corresponding to the respective monsoon seasons, except A1 during SWM. The discerned differences among the ellipses underscore the pivotal role played by monsoon seasons in shaping the observed variability in phosphorus distribution. Each monsoon season exhibited specific patterns and trends in phosphorus distribution, as delineated by the individual characteristics of the ellipses. Notably, the overlapping ellipses for SWM, IM, and NEM implied shared characteristics in phosphorus distribution during these seasons. This overlapping pattern suggests the persistence of certain factors and conditions, such as nutrient cycling, that influence phosphorus levels across SWM, IM, and NEM, highlighting the interconnected nature of phosphorus dynamics. The larger size of the ellipse for the SWM indicates its predominant influence on the observed phosphorus variability in the study area. This observation underscores the heightened impact of the SWM on shaping the phosphorus dynamics during the study period.

Table 2. Factor loading, eigenvalue, and percent of variance for 6 variables on the first two factor

Variables	Factor 1	Factor 2
Temperature	-0.173	**0.626**
Salinity	**-0.698**	0.396
Chlorophyll-a	**0.687**	-0.210
PO_4^{3-}	**0.853**	-0.169
DOP	**0.765**	0.441

Variables	Factor 1	Factor 2
TPP	0.392	**0.856**
Eigenvalue	2.456	1.526
Variability (%)	40.94	25.81
Cumulative	40.94	66.75

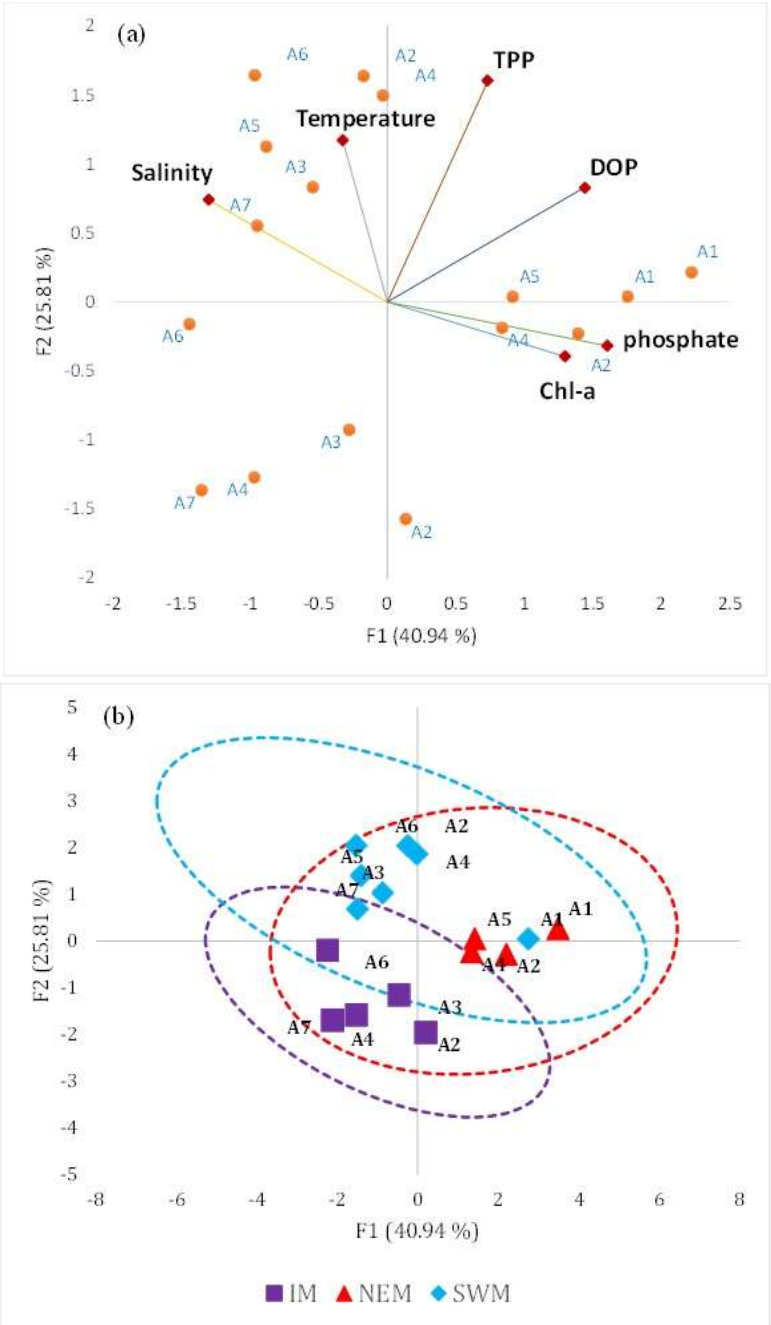

Figure 6. The correlation biplot using PCA of (a) phosphorus concentration and environmental factors and (b) phosphorus abundance

Conclusion

In this study, both surface and vertical distributions of PO_4^{3-}, DOP, TPP, Chl-a, and their physical characteristics in the Kelantan Waters were evaluated. Surface distributions of the most distinguished parameters demonstrated higher concentrations in the coastal waters compared to the offshore region, which indicates the influence of freshwater from the adjacent river of Kelantan River to our studied area. Supporting the warmer water with low salinity in the coastal area has proved the features of riverine discharge from the Kelantan River into the ocean. The influence of Kelantan riverine input is localized to the nearshore station (≤20 km), where further offshore areas may be influenced by the Gulf of Thailand-derived water. Offshore areas have their own ecological dynamics and biological processes, including nutrient cycling and phytoplankton activity, which can influence phosphorus levels. Vertical profiling showed higher concentrations of P-based nutrients and Chl-a in the deeper layer as compared to the surface layer, potentially derived from biological activities of remineralization processes and sediment as a buffer to release nutrients to the water column when wind-induced currents disturb the water-sediment interface. A direct link between the monsoon wind forcing with nutrients and Chl-a was noticed. Based on PCA, Chl-a strongly correlated with phosphate, which suggested that phosphate supply was the dominant source during our sampling. The monsoon weather pattern significantly acts as a key factor in controlling all the variables measured in Kelantan Waters, with SWM having a dominant influence on the variability observed in the study. Even though the obtained data are limited to one transect, the information provided an oceanographically meaningful spatial and temporal pattern of field data during all three monsoon seasons, which is vital for this study area, where a very limited amount of field data is available.

Acknowledgement

This work was supported by the Higher Institution Centre of Excellence (HICoE) Research Grant (Vote No. 66928) and National Scientific Cruise Expedition (Vote No. 53209) awarded to the Institute of Oceanography and Environment, Universiti Malaysia Terengganu (UMT). The authors would like to thank the Ministry of Education Malaysia (MOE) for funding these research grants.

References

1. Sosa, O. A., Repeta, D. J., DeLong, E. F., Ashkezari, M. D. and Karl, D. M. (2019). Phosphate-limited ocean regions select for bacterial populations enriched in the carbon–phosphorus lyase pathway for phosphonate degradation. *Environmental Microbiology*, 21(7): 2402-2414.
2. Duhamel, S., Diaz, J. M., Adams, J. C., Djaoudi, K., Steck, V. and Waggoner, E. M. (2021). Phosphorus as an integral component of global marine biogeochemistry. *Nature Geoscience*, 14(6), 359-368.
3. Dodds, W. K., and Whiles, M. R. (2010). Chapter 14 - Nitrogen, Sulfur, Phosphorus, and Other Nutrients. In Freshwater Ecology (Second Edition). Academic Press, London: pp. 345-373.
4. Ruttenberg, K. C., and Dyhrman, S. T. (2012). Dissolved organic phosphorus production during simulated phytoplankton blooms in a coastal upwelling system. *Frontiers in Microbiology*, 3: 1-12.
5. Lin, S., Litaker, R. W. and Sunda, W. G. (2016). Phosphorus physiological ecology and molecular mechanisms in marine phytoplankton. *Journal of Phycology*, 52(1): 10-36.
6. Lim, J. H., Lee, C. W., Bong, C. W., Affendi, Y. A., Hii, Y. S., and Kudo, I. (2018). Distributions of particulate and dissolved phosphorus in aquatic habitats of Peninsular Malaysia. *Marine Pollution Bulletin*, 128: 415-427.
7. Hashihama, F., Saito, H., Shiozaki, T., Ehama, M., Suwa, S. and Sugiyama, T. (2020). Biogeochemical controls of particulate phosphorus distribution across the oligotrophic subtropical Pacific Ocean. *Global Biogeochemical Cycles*, 34(9): e2020GB006669.
8. Raimbault, P., Garcia, N., and Cerutti, F. (2008). Distribution of inorganic and organic nutrients in the South Pacific Ocean - evidence for long-term accumulation of organic matter in nitrogen-depleted waters. *Biogeosciences*, 5: 281-298.
9. Worsfold, P., Mckelvie, I. and Monbet, P. (2016). Determination of phosphorus in natural waters: A

historical review. *Analytica Chimica Acta*, 918: 8-20.

10. Nausch, M., Achterberg, E. P., Bach, L. T., Brussaard, C. P. D., Crawfurd, K. J., Fabian, J., Riebesell, U., Stuhr A., Unger, J. and Wannicke, N. (2018). Concentrations and uptake of dissolved organic phosphorus compounds in the Baltic Sea. *Frontiers in Marine Science*, 5: 386.
11. Yamaguchi, T., Sato, M., Hashihama, F., Kato, H., Sugiyama, T., Ogawa, H., Takahashi K. and Furuya, K. (2021). Longitudinal and vertical variations of dissolved labile phosphoric monoesters and diesters in the subtropical North Pacific. *Frontiers in Microbiology*, 11: 570081.
12. Yang, Y., Shi, J., Jia, Y., Bai, F., Yang, S., Mi, W., He, S. and Wu, Z. (2020). Unveiling the impact of glycerol phosphate (DOP) in the dinoflagellate Peridinium bipes by physiological and transcriptomic analysis. *Environmental Sciences Europe*, 32(1): 38
13. Karl, D. M. (2014). Microbially mediated transformations of phosphorus in the sea: New views of an old cycle. *Annual Review of Marine Science*, 6: 279-337.
14. Diaz, J. M., Holland, A., Sanders, J. G., Bulski, K., Mollett, D., Chou, C. W., Phillips, D., Tang Y., and Duhamel, S. (2018). Dissolved organic phosphorus utilization by phytoplankton reveals preferential degradation of polyphosphates over phosphomonoesters. *Frontiers in Marine Science*, 5: 1-17.
15. Scharler, U. M. and Baird, D. (2003). The nutrient status of the agriculturally impacted Gamtoos estuary, South Africa, with special reference to the river-estuarine interface region (REI). *Aquatic Conservation: Marine and Freshwater Ecosystems*, 13(2): 99-119.
16. Meng, J., Yu, Z., Yao, Q., Bianchi, T. S., Paytan, A., Zhao, B., Pan, H., and Yao, P. (2015). Distribution, mixing behavior, and transformation of dissolved inorganic phosphorus and suspended particulate phosphorus along a salinity gradient in the Changjiang estuary. *Marine Chemistry*, 168: 124-134.
17. Akhir, M. F. M., Zakaria, N. Z., and Tangang, F. (2014). Intermonsoon variation of physical characteristics and current circulation along the east coast of Peninsular Malaysia. *International Journal of Oceanography*, 2014: 1-9.
18. Syafrina, A. H., Zalina, M. D., and Juneng, L. (2015). Historical trend of hourly extreme rainfall in Peninsular Malaysia. *Theoretical and Applied Climatology*, 120; 259-285.
19. Daud, N. R., Akhir, M. F. and Muslim, A. M. (2019). Dynamic of ENSO towards upwelling and thermal front zone in the east coast of Peninsular Malaysia. *Acta Oceanologica Sinica*, 38(1): 48-60.
20. Kok, P. H, Akhir, M. F., Tangang, F. and Husain, M. L. (2017). Spatiotemporal trends in the southwest monsoon wind-driven upwelling in the southwestern part of the South China Sea. *PLoS ONE* 12(2): e0171979.
21. Aziz, A. A., Suratman, S., Kok, P. H., and Akhir, M. F. (2019). Distribution of nutrients concentration in the upwelling area off the east coast of Peninsular Malaysia during the southwest monsoon. *Malaysian Journal of Analytical Sciences,* 23(6): 1030-1043.
22. Akhir, M. F. (2012). Surface circulation and temperature distribution of southern South China Sea from global ocean model (OCCAM). *Sains Malaysiana*, 41(6): 701-714.
23. Hee, Y. Y., Suratman, S., and Weston, K. (2020). Nutrient cycling and primary production in Peninsular Malaysia Waters; regional variation and its causes in the South China Sea. *Estuarine, Coastal and Shelf Science*, 245: 106947.
24. Uning, R., Suratman, S., Nasir, F. A. M. and Latif, M. T. (2021). Spatial and temporal variations in nutrients during upwelling season off the east coast of Peninsular Malaysia. *Bulletin of Environmental Contamination and Toxicology.* 108(1): 145-150.
25. Zainol, Z. and Akhir, M. F. (2016). Coastal upwelling at Terengganu and Pahang coastal waters: Interaction of hydrography, current circulation and phytoplankton biomass. *Jurnal Teknologi*, 78(8): 11-27.
26. Environment Protection Agency (1993). Method 365.1, revision 2.0: Determination of phosphorus by semi- automated colorimetry.
27. Mahaffey, C., Williams, R. G., Wolff, G. A. and Anderson, W. T. (2004). Physical supply of

nitrogen to phytoplankton in the Atlantic Ocean. *Global Biogeochemical Cycles*, 18(1): 1-13.
28. Parsons, T. R., Maita, T. and Lalli, C. M. (1984). Plant pigment. In: a manual of chemical and biological method for seawater analysis. Oxford: Pergamon Press: pp. 173.
29. Shrestha, S. and Kazama, F. (2007). Assessment of surface water quality using multivariate statistical techniques: a case study of the Fuji River Basin, Japan. *Environmental Modelling and Software*, 22(4): 464-475.
30. Marghany, M. (2012). Intermonsoon water mass characteristics along coastal waters off Kuala Terengganu, Malaysia. *International Journal of the Physical Sciences*, 7(8): 1294-1299.
31. Akhir, M. F. M., Sinha, P. C. and Husain, M. L. (2011). Seasonal variation of South China Sea physical characteristics off the east coast of Peninsular Malaysia from 2002-2010 datasets. *International Journal of Environmental Science*, 2(2): 569-575.
32. Kok, P. H., Akhir, M. F. and Qiao, F. (2019). Distinctive characteristics of upwelling along the Peninsular Malaysia's east coast during 2009/10 and 2015/16 El Niños. *Continental Shelf Research*, 184: 10-20.
33. Idris, M. S., Sidik, M. J. and Hing, L. S. (2021). Optical characterisation and classification of water types in the southern South China Sea and straits of Malacca. *Estuarine, Coastal and Shelf Science*, 262: 107594.
34. Shaari, F. and Mustapha, M. A. (2017). Factors influencing the distribution of chl-a along coastal waters of east peninsular Malaysia. *Sains Malaysiana*, 46(8): 1191-1200.
35. Zhao, C., Maerz, J., Hofmeister, R., Röttgers, R., Wirtz, K., Riethmüller, R. and Schrum, C. (2019). Characterizing the vertical distribution of chlorophyll a in the German bight. *Continental Shelf Research*, 175: 127-146.
36. Ooi, S. H., Samah, A. A. and Braesicke, P. (2013). Primary productivity and its variability in the equatorial South China Sea during the northeast monsoon. *Atmospheric Chemistry and Physics Discussions*, 13(8): 21573-21608.
37. Yu, Y., Song, J., Li, X., Yuan, H. and Li, N. (2012). Distribution, sources and budgets of particulate phosphorus and nitrogen in the East China Sea. *Continental Shelf Research*, 43: 142-155.
38. Provoost, P., Braeckman, U., Van Gansbeke, D., Moodley, L., Soetaert, K., Middelburg, J. J. and Vanaverbeke, J. (2013). Modelling benthic oxygen consumption and benthic-pelagic coupling at a shallow station in the southern North Sea. *Estuarine, Coastal and Shelf Science*, 120: 1-11.
39. Karl, D. M., and Björkman, K. M. (2015). Dynamics of dissolved organic phosphorus. In biogeochemistry of marine dissolved organic matter, Academic Press Burlington: pp. 233-334.
40. Liu, S., Li, X., Zhang, J., Wei, H., Ren, J. and Zhang, G. (2007). Nutrient dynamics in Jiaozhou Bay. *Water, Air, & Soil Pollution: Focus*, 7(6): 625-643.
41. Hee, Y. Y., Suratman, S., Tahir, N. M., and Jickells, T. (2018). Seasonal variability and Fractionation of P-based nutrients in Sungai Setiu basin, Terengganu, Malaysia. *Sains Malaysiana*, 47(5): 883-891.
42. Huang, Y.-C. A., Huang, S.-C., Meng, P.-J., Hsieh, H. J., and Chen, C. A. (2012). Influence of strong monsoon winds on the water quality around a marine cage-culture zone in a shallow and semi-enclosed bay in Taiwan. *Marine Pollution Bulletin*, 64(4): 851-860.
43. Nausch, M., Achterberg, E. P., Bach, L. T., Brussaard, C. P. D., Crawfurd, K. J., Fabian, J., … Wannicke, N. (2018). Concentrations and uptake of dissolved organic phosphorus compounds in the Baltic Sea. *Frontiers in Marine Science*, 5: 386.

Malaysian Journal of Analytical Sciences (MJAS)
Published by Malaysian Analytical Sciences Society

ANALYSIS OF EFFLORESCENCE OF SPENT BLEACHING CLAY BASED GEOPOLYMER USING ALKALINE LEACHABILITY METHODS

(Analisa Peroian Geopolimer Berasaskan Tanah Liat Terluntur Menggunakan Kaedah Kelarutlesapan Alkali)

Puuvina Jeyasangar, Mohd Hazwan Hussin, and Shangeetha Ganesan*

School of Chemical Sciences, Universiti Sains Malaysia, 11800 USM, Pulau Pinang, Malaysia

**Corresponding author: shangeetha@usm.my*

Received: 1 September 2023; Accepted: 15 February 2024; Published: 29 April 2024

Abstract

Geopolymers are a class of inorganic amorphous polymeric materials made up of silica, alumina and alkali- metal oxides. The presence of alkali in the geopolymer formulation aids in the dissolving of aluminosilicate precursors, resulting in the creation of microstructures and increases geopolymer strength. However, the alkali content is the most critical factor influencing efflorescence production. Therefore, this study evaluated the effects of curing parameters on efflorescence formation on spent bleaching clay based geopolymer. The efflorescence effects were analysed by alkaline leachability methods using atomic absorption spectroscopy (AAS) and electrochemical impedance spectroscopy (EIS). Neat geopolymer as well as cured geopolymer with different liquid/solid (L/S) ratio effects were studied. Alkaline leaching studies revealed water-cured geopolymers with liquid/solid (L/S) ratio of 2:1 shows that 974.9 ppm Na^+ ions leached from the geopolymer. This method helps to prevent efflorescence from reoccurring as most of the free Na^+ ions has already been leached from the geopolymer sample. The EIS analysis also showed that a 2:1 ratio had excellent resistance which reflects the mobility of the other ions such as silicon, aluminium and chloride ions. Functional group analysis using FTIR demonstrated the key peaks involved in development of geopolymer from spent bleaching clay (SBC) such as v(Si-O-Si / Si-O-Al) (bending & stretching), v(Al-O)(symmetrical), v(Si-O / Al-O) (asymmetrical) and v(O-H). Surface morphology analysis using SEM-EDX indicates that adequate silica-rich components were required to increase the mechanical strength of geopolymers by densifying their microstructure with more bulk and compact layers. From the examination of thermal stability of neat and treated geopolymer compositions decomposed at 700 °C confirming the thermal resistance of the material. Therefore, for more sustainable cements, alkali leachability can be performed on SBC-based geopolymer by water-curing as it revealed to have an exceptional performance on total Na leached, resistance and thermal stability as shown in this study.

Keywords: geopolymer, spent bleaching clay, efflorescence, leachability

Abstrak

Geopolimer adalah kelas bahan polimer amorfus tidak organik yang terdiri daripada silika, alumina dan logam-alkali oksida. Kehadiran alkali dalam formula geopolymer membantu dalam pelarutan bahan pemula aluminosilika, menghasilkan mikrostruktur serta menguatkan struktur geopolimer. Akan tetapi, kandungan alkali adalah faktor yang paling kritikal yang mempengaruhi pembentukan peroi. Oleh itu, kajian ini adalah untuk menilai sintesis geopolimer daripada tanah liat terluntur dan menganalisa peroian dengan kaedah kelarutanlesapan menggunakan AAS dan EIS. Geopolimer tulen serta geopolimer yang

dirawat dengan kesan nisbah cecair/pepejal (L/S) yang berbeza telah dikaji. Kajian kelarutlesapan alkali menunjukkan geopolimer yang diawet dengan air pada nisbah air/pepejal (L/S) 2:1 menghasilkan 974.9 ppm Na^+ ions melarutlesap daripada geopolimer tersebut. Cara ini mencegah pembentukkan peroi daripada berulang kerana kebanyakkan ion Na^+ bebas telah dilarutlesap daripada geopolimer. Analisa EIS menunjukkan bahawa nisbah 2:1 juga mempunyai rintangan yang baik yang mencerminkan pergerakan ion-ion yang lain seperti silicon, aluminium dan klorida. Analisa kumpulan fungsi menggunakan FTIR menunjukkan puncak-puncak utama yang terlibat dalam penghasilan geopolimer berasaskan tanah liat (SBC) yang terdiri daripada v(Si-O-Si / Si-O-Al) (bengkok & regangan), v(Al-O) (simetri), v(Si-O / Al-O) (tidak simetri) dan v(O-H). Analisis morfologi permukaan mengunakan SEM-EDX menunjukkan bahawa komponen kaya silika yang mencukupi diperlukan untuk meningkatkan kekuatan mekanikal geopolimer dengan memadatkan struktur mikronya dengan lebih banyak lapisan pukal dan padat. Daripada pemeriksaan kestabilan terma komposisi geopolimer yang asal dan dirawat itu terurai pada suhu 700°C menunjukkan kerintangan haba mereka. Oleh itu, untuk simen yang lebih mampan, kelarutlesapan alkali boleh dilakukan pada geopolimer berasaskan SBC dengan pengawetan air kerana ia menunjukkan prestasi yang luar biasa berdasarkan jumlah Na yang kelarutlesapan serta kestabilan termanya seperti yang dibuktikan dalam penyelidikan ini.

Kata kunci: geopolimer, tanah liat terluntur, peroian, kelarutlesapan

Introduction

Geopolymers or inorganic polymers, have excellent potential for industrial applications as they are both environmentally friendly and possess unique physico-chemical characteristics [1]. Geopolymers are alternative binder for fibre composites and cement for concrete that have outstanding physical, chemical, and mechanical prospects. They can also be employed in a variety of applications due to their outstanding physical properties, which include fire, heat, acid, and corrosion resistance, as well as high compressive strength. Fire-resistant and thermal-insulating materials, also low-tech and low- energy materials like cements, concretes and tiles are amongst them [2]. The appearance of efflorescence on geopolymer surfaces, independent of the precursor utilised, is a significant impediment to the application of geopolymer products. The formation of efflorescence might cause the geopolymer structure to deteriorate. The formation of efflorescence is linked to the leaching of sodium ion from geopolymers when the product encounters moisture or water. The material leaches alkali ions and transport them to the surface via capillary forces. These ions combine with carbon dioxide (CO_2) in the environment to generate hydrated sodium carbonate (Na_2CO_3) when the water evaporates. This takes effect notably when the material contains an excessive amount of alkaline substances which also has a high porosity [3]. Sodium hydroxide (NaOH) is extensively utilised during geopolymer synthesis as compared to potassium hydroxide (KOH) as NaOH optimises the dissolution procedure along with the combination of silicate solution [4]. This process is important since the solubility of aluminosilicate increases as the concentration of hydroxide increases. Geopolymer concrete with a greater NaOH concentration has a better compressive strength [5].

Numerous aluminosilicate substances are present in nature and some of them are also produced from industry wastes [6]. Spent bleaching clay (SBC) is a solid waste product from the refinement of palm oil where the disposal of bleaching clay as a byproduct from refining plants causes several environmental issues as well as financial losses to the country [7]. Spent bleaching clay (SBC) contains between 20-40% residual oil that may be a fire hazard [8]. Spent bleaching clay (SBC) is mostly made of SiO_2 followed by Al_2O_3, MgO, Fe_2O_3 and CaO, whilst its elemental components are C, Ca, O, Fe, Mg, Al, Si, P and K [9,10]. Besides, the main component utilised in this research is montmorillonite, which is a bentonite clay, with the potential to absorb several times its size, taking on a jelly-like consistency due to the hydration upon contact with aqueous solutions. Therefore, giving it a capacity for ion sorption, which can be improved by conducting an alkaline activation that results in the formation of a geopolymer or inorganic polymer.

As afore mentioned, the alkali concentration is vital to produce geopolymeric gels and to enhance the strength of the synthesised geopolymer [11]. Nevertheless, the alkali metals are weakly attached in the matrix and can readily be leached away in water. Thus, resulting in development of white efflorescence (Na_2CO_3) on the surface of the geopolymer, when it is in contact with water and moisture. This subsequently has a major

effect on degradation of geopolymer cements [12]. Furthermore, efflorescence on geopolymer surfaces, whether made of montmorillonite, metakaolin, fly ash, volcanic tuff, or other aluminosilicate precursors, is a significant hurdle for their utilisation [3]. Therefore, this work strategises towards the target of studying efflorescence formation by evaluating the amount of Na^+ leached using AAS and EIS are vital for future construction science.

It is hypothesised that the SBC-based geopolymer demonstrates greater physicochemical properties. However, excess efflorescence may disrupt the stability of the binder microstructure, which has been a persistent drawback in the development of geopolymers as reported in previous studies [3,12]. The characterisation techniques are used to support the formation of geopolymer from spent bleaching clay. This work develops the variation in curing conditions as the principal motive to study the development of efflorescence for the novel spent bleaching clay based geopolymer which has not been reported elsewhere.

Materials and Methods

Reagents and raw materials

Chemicals, reagents, and solvents employed in this investigation, specifically sodium hydroxide (NaOH), sodium silicate (Na_2SiO_3), sodium chloride (NaCl) were commercially purchased from local suppliers as analytical reagents such as Systerm, QReC and R&M Chemicals. They were utilised exactly as they are, with no further purification. Furthermore, all reactions were carried out in an ambient environment. While, spent bleaching clay was contributed by KL Kepong Oleomas Sdn Bhd, Selangor.

Geopolymer synthesis

Geopolymer was synthesised with starting materials, 15.6633g of NaOH and 54.8213g of Na_2SiO_3 mixed in 150 mL distilled water respectively. The ratio of the starting materials were NaOH : Na_2SiO_3 = 1 : 3.5, also known as the alkaline activator solution. The geopolymer paste and composites were attained by mixing the alkaline activator solution into 160.0g of SBC gradually. Empirically, the geopolymer composite complied to the ratio of alkaline activating solution (NaOH + Na_2SiO_3) : SBC of 1 : 2.27 [11,13]. Then, the composite was poured into molds and left in the oven at 70°C for 24 hours; conducive for curing process in to accelerate the gel formation [13,14]. Then, the geopolymer paste was left to undergo a hardening process for a week before proceeding with subsequent steps.

Characterisation of geopolymer

Perkin Elmer 100 FT-IR spectroscopy was utilised for FT-IR analysis by employing potassium bromide (KBr) pellets within spectral range 4000-400 cm^{-1} for determination of functional group in the synthesised geopolymer. In addition, for image analysis, Zeiss GeminiSEM 360 Field Emission Scanning Electron Microscope (FESEM) was utilised to examine the morphological phases. The characterisation techniques are important to showcase the formation of the geopolymer before the leaching study can be conducted.

Alkaline leaching test

Leaching test was conducted on the geopolymers to determine the alkaline leachability after 28 days of immersion test via AAS and EIS [15]. The leaching process was examined in two different conditions which were ambient curing and water curing, as per Table 1. Demolded geopolymers were placed in larger containers and sealed for ambient curing meanwhile, for water curing, the study progressed by immersing demolded geopolymer into distilled water in sealed containers for 28 days. The liquid/solid (L/S) for water curing varied from 2:1, 4:1, 10:1 and 20:1 to fully get rid of sodium ions from geopolymer sample. Ambient cured sample was immersed in water to collect the leachate for testing. The ratio of L/S was calculated based on previous study [11]. Thermogravimetric-differential thermal analysis (TGA-DTA) was explored to examine the mass loss as temperature rises. The test proceeded with a heating rate of 10°C/min from ambient temperature to 900°C. All untreated and treated geopolymer samples were evaluated for thermal stability.

Alkaline leachability study via AAS

After 28 days, the samples were analysed by Atomic Absorption Spectroscopy (AAS) for total amount of sodium ions (Na^+) leached. Initially, AAS instrument

was calibrated by using standard solution of 1, 2, 3, 4 and 5 ppm of NaCl, prepared from stock solution of 100 ppm. The standards were run, and a calibration graph was plotted. It is ensured that the $R^2 \geq 0.99$ prior to sample readings. Then, all the leachate of the water cured samples were examined and evaluated.

Table 1. Alkaline leaching sample details according to its curing condition

Curing Conditions	Liquid-to-Solid Ratio (L/S)	Sample
Water curing	2:1	A
	4:1	B
	10:1	C
	20:1	D
Ambient curing	N/A	E

Alkaline leachability study via AAS

After 28 days, the samples were analysed by Atomic Absorption Spectroscopy (AAS) for total amount of sodium ions (Na^+) leached. Initially, AAS instrument was calibrated by using standard solution of 1, 2, 3, 4 and 5 ppm of NaCl, prepared from stock solution of 100 ppm. The standards were run, and a calibration graph was plotted. It is ensured that the $R^2 \geq 0.99$ prior to sample readings. Then, all the leachate of the water cured samples were examined and evaluated.

Alkaline leachability study via EIS

Impedance of the geopolymer samples from different curing conditions as per Table 1 were measured by the electrochemical impedance spectroscopy (EIS), Gamry Reference 600 electrochemical workstation with three electrode setups. First, the electrodes utilised were platinum as counter electrode (CE), graphite as working electrode (WE) and saturated calomel electrode (SCE) as reference electrode (RE). These electrodes were immersed in a beaker which contained a leached liquid sample of geopolymers from different curing conditions. Then, the Gamry Reference600 electrochemical workstation was opened to test the EIS with the frequency range set at 10^{-1} to 10^5 while AC amplitude of 10mV. The resulted Nyquist plots were analysed further.

Results and Discussion

Synthesis of geopolymer

Geopolymer was synthesized and characterized as an alternate new cement for concrete instead of ordinary Portland Cement (OPC). The preparation of geopolymer was accomplished via geopolymerisation process through aluminosilicate material dissolved in 0.39 mol of sodium hydroxide and 0.45 mol of sodium silicate to attain geopolymer and a by-product which is water molecules as shown in Figure 1.

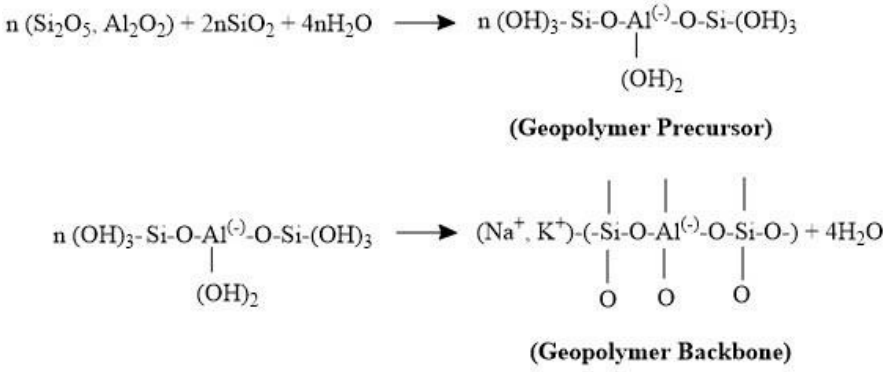

Figure 1. Mechanism of geopolymer synthesis [15]

Principally, the geopolymerisation technique consists of three main mechanisms [16]. Firstly, the dissolution of aluminosilicate materials in alkaline media by the breaking of covalent Si-O-Si and Al-O-Al bonds, resulting in the production of silicate and aluminate species. The hydroxyl (OH-) groups commence this process by attaching to the silicon atom, making the Si-O-Si bond more prone to breaking. At high pH, reactive aluminosilicates will dissolve quickly. Then, condensation of silicate and aluminate monomers will develop a gel until the solution approaches saturation, resulting in the release of NaOH, which reacts again. Finally, the gel undergoes polycondensation and structural rearrangement, resulting in a 3-D aluminosilicate structure of geopolymers. The final compound attained in this study is medium deep brown as shown in Figure 2. Physically, the cementitious geopolymer showed slight amount of efflorescence on its surface after aging for 28 days. There is no visible pore spotted on the surface of synthesised geopolymer.

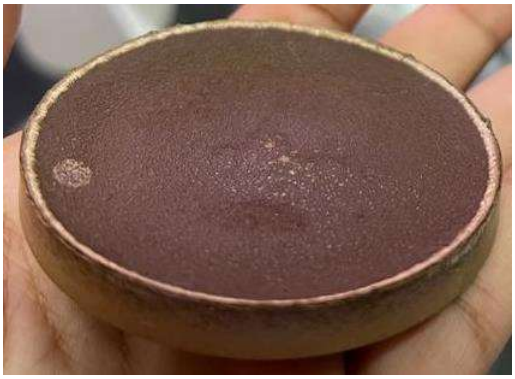

Figure 2. Geopolymer synthesized and aged for 28 days at room temperature

Functional group analysis

Functional group analysis of SBC and SBC-based geopolymer revealed all the expected bands of interest namely v(Si-O-Si / Si-O-Al) (bending), v(Si-O-Si / Si-O-Al) (stretching), v(Al-O) (symmetrical), v(Si-O / Al-O) (asymmetrical) and v(O-H) as seen in Figure 3. The spectrum ranging from strong intensity of SBC to moderate intensity of SBC-based geopolymer synthesised in this study showed a noticeable displacement. It is due to improvised geopolymer network organisation and there is more alkali cations present making the bonds to be less polar [18].

From the geopolymer spectra, the absorption band for v(Si-O-Si / Si-O-Al) strong bending vibration was observed at 523.94 cm^{-1} while a moderate IR band at 692.20 cm^{-1} was assigned as stretching vibrations of v (Si-O-Si/Si-O-Al) in geopolymer which is in close agreement with previous reported studies, as it is contributed to the stretching bands of tetrahedral aluminium [18]. Strong peaks from SBC around wavenumbers of 461.56 cm^{-1} and 531.33 cm^{-1} indicated montmorillonite structure which was then deconstructed and dissolved into Si-O and Al-O tetrahedral; characteristic of an amorphous aluminosilicate for geopolymer [20, 21].

Additionally, the presence of symmetrical v(Al-O) moderate vibration peak in AlO_4 with tetrahedral coordination can be observed at 789.88 cm^{-1} from the spectra of geopolymer [20]. Meanwhile, Li et al. highlighted that this modest peak can be attributed to Al-O-H bending vibrations or minor anionic ions such as silicate monomer, SiO^-. This is because the source material is rapidly dissolved forming small silicate monomers. The small peak seen in SBC spectra at 796.44 cm^{-1} disappeared in the geopolymer spectra, indicating that silicate monomers were consumed in favor of bulkier species [22].

The intense absorption band of asymmetrical Si-O/Al-O assigned at 1027.09 cm^{-1} is considered as the main absorption band. As the polycondensation process progresses, this band gets more concentrated, producing more aluminosilicates matrix. The band at 1027 cm^{-1} was likely due to an increase in the amount

of functional group attached to the molecular bond resulting in less non-bridging oxygen and Al being substituted in the silicate sites [18]. An absorption peak near 1600 cm^{-1} is attributed to bending vibration of (H-O-H) bonds, perhaps because the NaOH residue in the geopolymer which consequently produces Na_2CO_3 by interacting with CO_2 in the air [23].

Furthermore, the two absorption peaks in the 2800-3200 cm^{-1} range were the stretching vibrations of v(-Al-OH) and v(-Si-OH), indicating that tetrahedral structure was not damaged. This is mostly due to the evaporation of water in the paste that limited soluble ion movement, resulting in an inadequate reaction between clay precursor and the alkali activator [20]. It appeared that the band at approximately 3443.50 cm^{-1} is related to the stretching vibration of the O-H bond of geopolymer, whereas a comparable peak emerged at 3345.83 cm^{-1} for the SBC. The bands shifted likely because the usage of water during preparation of alkaline activator solution added with geopolymer slurry for geopolymerisation process. Considering water is a main byproduct of geopolymers, the results were comparable [24].

Carbon dioxide (CO_2) stretching vibration band at around 1300-1400 cm^{-1} was also discovered. These bands defined the geopolymer material [25]. These distinct peaks mostly indicate the presence of geopolymer compounds. The small-scale difference in intensity for the influence of carbonates was recorded at 1429.30 and 1387.02 cm^{-1}, corresponding to the stretching vibrations of O-C-O bonds in the carbonate group (CO_3^{2-}) caused by the carbonation reaction between carbon dioxide from the air and the geopolymer. The slight detected rise was caused by increased carbonation as a result of the high number of free ions. Carbonates contributed more to samples activated with sodium solution, which can react with atmospheric CO_2 to form Na_2CO_3 species [18].

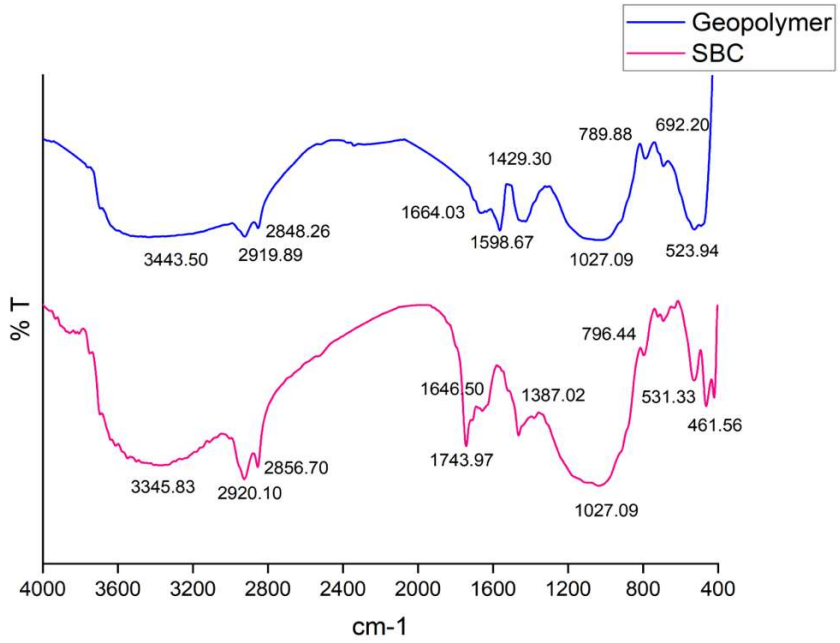

Figure 3. FTIR spectrum of geopolymer synthesized in this study and spent bleaching clay (SBC)

Surface morphology and elemental analysis

Figure 4 shows the SEM images of SBC and geopolymer. Figure 4 (a) shows that bulk, compact, and sponge-like structure are well formed for SBC. In contrast to other precursors, montmorillonite has a mainly fluffy and lumpy morphology, which may be characterised by the material's very amorphous structure caused by the dissolution of the multilayered plates structure [21,26]. This lumpy microstructure could be attributed to chemical modification in the clay galleries during palm oil refinement process. As a result, the composite is altered by an ionic liquid

(which is entrained oil and metallic contaminant) filled with aggregated montmorillonite particles that act as thickeners, and the ionic liquid completely form a thin film spread over the clay particles [27,28]. It also has a structure similar to illite, except that isomorphous substitution commonly occurs in the octahedral sheet, where every sixth aluminium is replaced by magnesium [21]. Figure 4 (b) shows an amorphous appearance with a rough, flaky, mild porous and less dense condition.

Additionally, the big lumps present in Figure 4 (b) exposes the homogenous part of sample. The aggregate seemed strongly bonded and a transition layer developed between SBC and the geopolymer matrix phase, indicating that a polymerisation process took place, generating a (-Al-O-Si-) chemical link. Thus, when a geopolymer substitutes the concrete, the alkali aggregated reaction does not induce product cracking [20]. Besides, the morphology of clay based geopolymer shifted to layer-like structure after geopolymerization process despite the curing temperature [19]. Meanwhile, the pores in geopolymers are mostly generated by water evaporation in the precursor. Pore structure parameters such as pore diameter, porosity, pore morphology and pore diameter uniformity have been shown to influence the microstructure and mechanical properties of geopolymers [29]. The rise of water absorption in geopolymer composition causing the microstructural deterioration, allowing water to exit the geopolymer network and be retained [30].

Spent bleaching clay (SBC) and geopolymer elemental composition were examined by using EDX analysis as per Table 2. The semi-quantitative elemental composition exposed the primary elements characterised were oxygen, carbon, silicon and aluminium with proportion values of 40.09%, 36.00%, 10.02% and 2.16% respectively, with traces of Ca, Fe, Mg, K and S. Based on these findings, the microstructure is primarily made up of amorphous sodium aluminosilicate binder (N- A-S-H) [31]. It is noteworthy that the composition of Na comprised almost 7% of the geopolymer's structure. Due to the alkali activator utilised during the geopolymerization reaction, the proportion of Na elements rose drastically [32,33]. Whilst, the Si molar ratios revealed the significance of binder phases in alkali activated geopolymers [31].

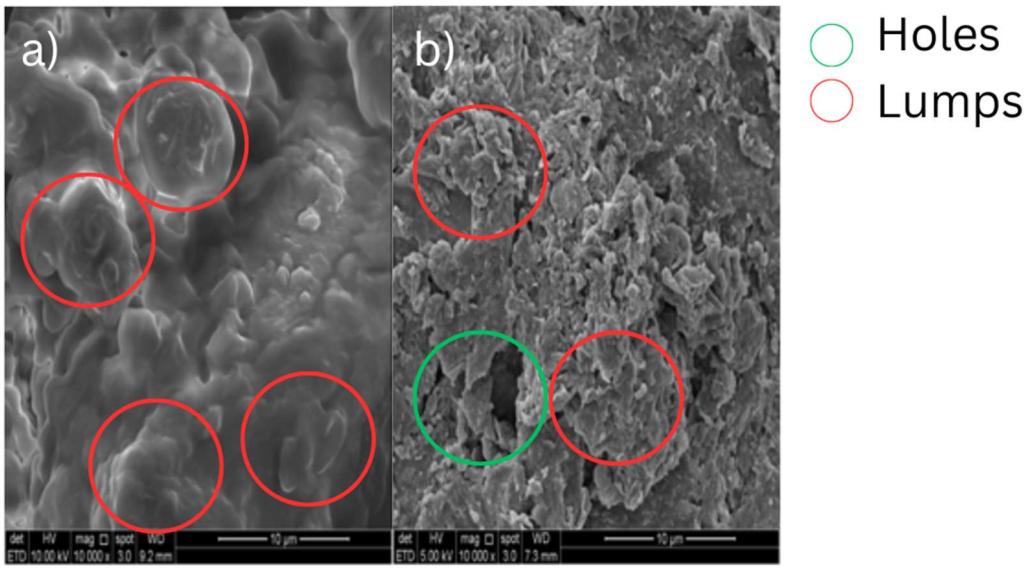

Figure 4. SEM image of (a) SBC and (b) geopolymer at 10,000x magnification

Table 2. EDX analysis of SBC and Geopolymer

Element	SBC (wt.%)	Geopolymer (wt.%)
O	22.95	40.09
C	64.40	36.00
Si	6.08	10.02
Na	NA	6.77
Al	1.57	2.16
Ca	0.81	1.85
Fe	3.57	1.74
Mg	0.62	0.64
K	NA	0.39
S	NA	0.34

Thermal analysis of neat and treated geopolymers

Figure 5 displays the thermogravimetric analysis and their differential curves for the neat and treated geopolymers developed in this work. From Figure 5, it was discovered that there is no discernible difference in the weight loss regardless of the curing method utilised. According to Gultekin and Ramyar, the geopolymers' free and weakly bonded-absorbed water caused the abrupt weight loss in the region of 0-200°C [34]. Another phenomenon, leading to the second weight loss, which occurs around 350°C, is the loss of hydroxyl from clay and organic residual oil, which makes up roughly 10-30% of the mass respective to the geopolymers. At 700 °C, this phase denotes the amorphization of the clay and the elimination of the montmorillonite precursor [1]. Dehydroxylation of the illite phase, the endothermic peak, begins at 600°C and concludes at 700°C, as can be shown in Figure 5 [35]. Besides, Marsh et al. stated that the continued curve is the formation of activated montmorillonite system [36].

Eventually, the presence of carbonates might also increase the compressive strength of geopolymer [37]. Besides, the unburnt organic carbon might be responsible for a mass loss of roughly < 1%, which were measured at the DTA peak of 170-180°C. Thermal analysis demonstrated that the clay-based geopolymers exhibited a thermally stable structure when heated up to 900°C. As a result of its improved thermal characteristics, SBC-based geopolymer may be more beneficial for manufacturing components that are stable at high temperatures than Portland cement systems. All in all, it can be summarised that all treated and untreated geopolymer samples possess good heat resistance, where it all decomposed only after 700°C.

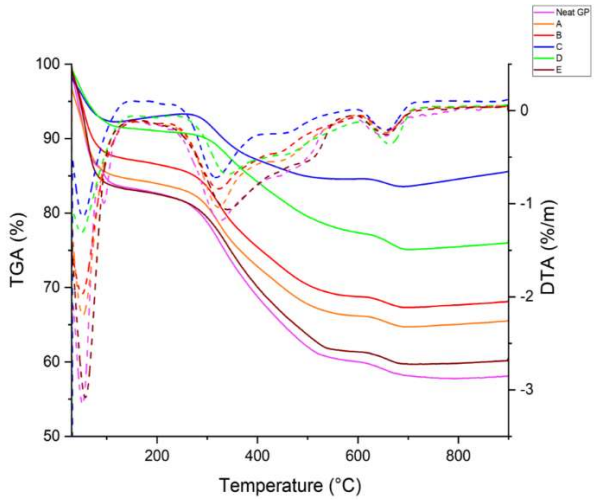

Figure 5. TGA-DTA of neat and treated geopolymer at different curing condition; water-cured (A-D) and ambient-cured (E)

Alkaline leachability via AAS

Geopolymer of same batch was tested for alkaline leachability from ambient curing and various liquid/solid (L/S) ratio as per Table 1 for water curing. Figure 6 depicts the concentration of sodium in the leachate after 28 days of leaching.

It is noticed that with increasing L/S ratio, there was a further drop in Na^+ leaching. This is because the increased of soluble silicate content in the geopolymer matrix probably results in less alkali leaching, which is consistent with water absorption values [38]. The less compact microstructure leads to fewer sodium associated in charge balancing sites. As a result of the porosity effects, the leaching of Na^+ is substantially enhanced [39]. This shows that resistance to efflorescence requires both decreased porosity and sodium incorporation in charge balancing sites [38].

As per Figure 6, alkaline leaching ability of geopolymer samples treated with L/S ratio of 2:1 is greater than for other samples with higher L/S ratios. Despite having a variable L/S ratio, samples C and D released nearly less Na^+ and at a slower rate in the leaching tests. Meanwhile, for all water-cured specimens, the leaching process significantly reduced the total alkali leaching after 28 days of immersion as compared to ambient-cured specimen. This is possibly due to the NaOH concentration in the sample and solution leveled off more slowly when pouring higher quantities of sample, in other words, more effective diffusion [3].

Besides, leaching behavior reduced for water-cured samples according to the L/S ratio from 2:1 to 20:1. Due to the high solution concentration of water content, the diffusion and mass transfer velocity were quick during the initial stage of leaching. The specimen surfaces begin to be progressively covered in residue as the reaction goes on and the concentration of the solution also starts to decrease. On account to this, the diffusion and mass transfer velocity slowed down, which given the lesser concentration that was leached out, indicated that the leachate solubility was also decreased [40]. Overall, water-cured specimen, sample A, with L/S ratio of 2:1 exhibited the most sodium ions leached from geopolymer as compared to other specimens.

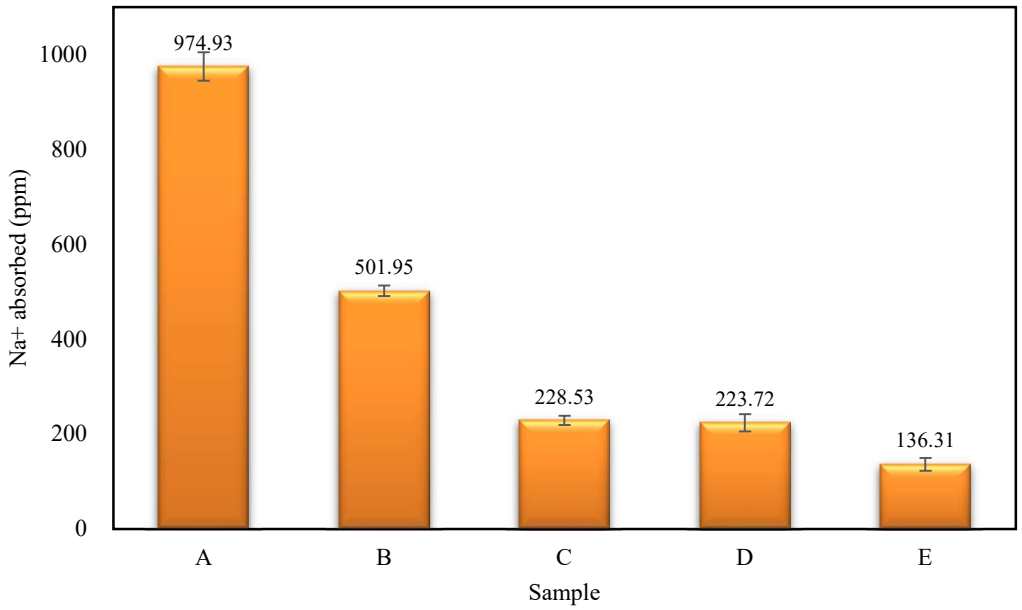

Figure 6. Sample A-D are water-cured specimens while E is ambient-cured specimen. Liquid/solid (L/S) ratio for water-cured specimens of A is 2:1, B is 4:1, C is 10:1 and D is 20:1

Alkaline leachability via EIS

The AC impedance spectra, also known as Nyquist plot, of treated geopolymers after 28 days of curing shown in Figure 7. It illustrates the oblique lines, which increases gradually due to ion diffusion effect. The resultant Nyquist plot shifts from left to right as curing age grows, and the value of resistance, which refers to the actual impedance of the junction, also rises. The elevation in resistance reflects the mobility of ions in the individual specimens, which in accordance with the L/S ratio [41]. On account to this, Biondi et al. reported that when immersed in water, Na^+ ions, as well as silicon and chloride ions, migrate in small amounts from the geopolymer [42]. According to Song et al., the parameter, θ linked to the surface condition of the montmorillonite particles and the applied voltage, E are the two key factors affecting the current of the geopolymer slurry. The θ represents the relationship between the dissolved surface area and the combined surface area of the montmorillonite particles. Consequently, an increase in θ will cause a rise in plasma current [43]. Therefore, the Nyquist plot from sample D with L/S ratio of 20:1 reflected highest impedance real part data to those of other ratios. This is because during the soaking phase, oxygen vacancies that have diffused from the solution interface to the geopolymer interface essentially promotes the formation of the leachates with high ion concentrations [44].

Charges in pore solution could be conveyed over the surface of the solid phase due to the differing resistance characteristics of solid and liquid phases [41]. Also, the concentration of ions in the geopolymer slurry rises as Si and Al dissolve, progressively increasing the resistance value of the sample. Furthermore, ambient-cured specimen, sample E, yield increased impedance response due to excellent electrolyte interfacial contact, probably anticipated to OH^- concentration solubility [45]. Potentially, the sample should have developed more aluminosilicate bonds during the curing phase. Therefore, sample A is considered to indicate excellent resistance in alkaline leaching since the other samples likely to have charge transferred in its solution.

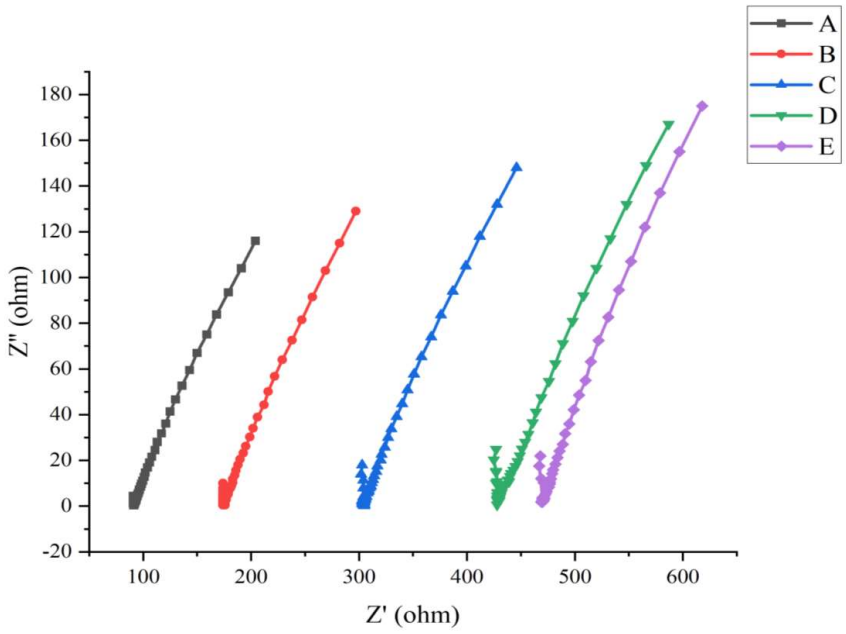

Figure 7. EIS responses in Nyquist curve at various curing condition; water-cured (A-D) and ambient-cured (E)

Conclusion

Aluminosilicates polymerised in an alkaline media at elevated temperature, produce a substance with cementitious characteristics. Spent bleaching clay-based geopolymer has been successfully designed by geopolymerisation, characterised and evaluated towards investigating the efflorescence development by using the leachability methods. This study details an

effort to investigate the alkaline leachability which causes the efflorescence phenomena on geopolymers using AAS and EIS. Mineralogically, the efflorescence still has impact on the main amorphous gels and residual crystalline phases formed from montmorillonite, which make up the majority of the clay-based geopolymers. According to this finding, free alkali concentration is significantly influenced by the alkalinity of the activating solution. Despite favouring the mechanical strength of the goods, higher alkalinities tend to enhance the leachability. Hence, sample A (L/S ratio 2:1) was analysed to have the most prominent curing condition to work towards efflorescence formation. In addition, the compound was analysed via several spectroscopic and analytical techniques, namely infrared (FT-IR), scanning electron microscopy (SEM-EDX), and thermogravimetric-differential thermal analysis (TGA-DTA). The montmorillonite based geopolymer in this study have significant thermal stability, as for both water and ambient-cured specimens yielded less weight loss as compared to neat geopolymer indeed. It is compatible with the outcome that high water and NaOH concentration reduces the strength of geopolymers to yield low compressive strength and a mild porous structure. On the other hand, studies on efflorescence propensity via AAS and EIS have demonstrated that curing geopolymers in water conditions is an efficient way to reduce efflorescence formed on their surface. This is due to the most Na^+ being leached away in sample A, liquid/solid (L/S) 2:1 ratio, with also an adequate thermal stability and impedance response. It is also demonstrated that ambient curing could not act preferably as a suggested curing condition with utmost exhibition.

Acknowledgement

This work was supported by the Research University (RUI) Grant (1001/PKIMIA/8011137) from Universiti Sains Malaysia.

References

1. Majdoubi, H., Haddaji, Y., Mansouri, S., Alaoui, D., Tamraoui, Y., Semlal, N., Oumam, M., Manoun, B. and Hannache, H. (2021). Thermal, mechanical and microstructural properties of acidic geopolymer based on moroccan kaolinitic clay. *Journal Building Engineering*, 35:102078.
2. Janošević, N., Đorić-Veljković, S., Topličić-Ćurčić, G. and Karamarković, J. (2018). Properties of geopolymers. *Facta Universitatis, Series: Architecture and Civil Engineering,* 16(1): 045-056.
3. Łach, M., Korniejenko, K., Walter, J., Stefańska, A. and Mikuła, J. (2020). Decreasing of leaching and improvement of geopolymer properties by addition of aluminum calcium cements and titanium oxide. *Materials,* 13(3): 495.
4. Abdul Rahim, R. H., Rahmiati, T., Azizli, K. A., Man, Z., Nuruddin, M. F. and Ismail, L. (2015). Comparison of using NaOH and KOH activated fly ash-based geopolymer on the mechanical properties. In Materials science forum (Vol. 803, pp. 179-184). Trans Tech Publications Ltd.
5. Memon, F. A., Nuruddin, M. F., Khan, S., Shafiq, N. A. S. I. R. and Ayub, T. (2013). Effect of sodium hydroxide concentration on fresh properties and compressive strength of self-compacting geopolymer concrete. *Journal Engineering Science Technology,* 8(1): 44-56.
6. Tuyan, M., Andiç-Çakir, Ö. and Ramyar, K. (2018). Effect of alkali activator concentration and curing condition on strength and microstructure of waste clay brick powder-based geopolymer. *Composites Part B: Engineering,* 135: 242-252.
7. Hatami, A. M., Sabour, M. R. and Amiri, A. (2018). Recycling process of spent bleaching clay: Optimization by response surface methodology. *Global Journal of Environmental Science and Management,* 4(1): 9-18.
8. Sedghamiz, M. A., Attar, F. and Raeissi, S. (2019). Experimental investigation of acid regeneration of spent bleaching clay de-oiled by the in-situ transesterification process at various operating conditions. *Process Safety and Environmental Protection,* 124: 121-127.
9. Loh, S. K., Cheong, K. Y. and Salimon, J. (2017). Surface-active physicochemical characteristics of spent bleaching earth on soil-plant interaction and water-nutrient uptake: A review. *Applied Clay Science,* 140: 59-65.
10. Zhang, C., Yu, M., Li, X., Li, X., Siyal, A. A., Liu, Y., ... and Li, Y. (2022). Disposal, regeneration and

pyrolysis products characterization of spent bleaching clay from vegetable oil refinery in a fluidized bed pyrolyser. *Journal of Cleaner Production,* 346: 131157.

11. Saludung, A., Azeyanagi, T., Ogawa, Y. and Kawai, K. (2021). Alkali leaching and mechanical performance of epoxy resin-reinforced geopolymer composite. *Materials Letters,* 304: 130663.
12. Škvára, F., Kopecký, L., Šmilauer, V. and Bittnar, Z. (2009). Material and structural characterization of alkali activated low-calcium brown coal fly ash. *Journal of Hazardous Materials*, 168(2-3): 711-720.
13. Ying, M. W., Azmi, M. and Ganesan, S. (2022). Synthesis and characterization of spent bleaching clay-based geopolymer: an effort towards palm oil industry waste reutilization. *Chemistry–An Asian Journal,* 17(14): e202200286.
14. Shehata, N., Sayed, E. T. and Abdelkareem, M. A. (2021). Recent progress in environmentally friendly geopolymers: A review. *Science of the Total Environment,* 762: 143166.
15. Zhang, Z., Provis, J. L., Reid, A. and Wang, H. (2014). Fly ash-based geopolymers: The relationship between composition, pore structure and efflorescence. *Cement and Concrete Research*, 64: 30-41.
16. Liew, Y. M., Heah, C. Y. and Kamarudin, H. (2016). Structure and properties of clay-based geopolymer cements: A review. *Progress in Materials Science,* 83: 595-629.
17. Tchadjie, L. N. and Ekolu, S. O. (2018). Enhancing the reactivity of aluminosilicate materials toward geopolymer synthesis. *Journal of Materials Science*, 53(7): 4709-4733.
18. Finocchiaro, C., Barone, G., Mazzoleni, P., Leonelli, C., Gharzouni, A. and Rossignol, S. (2020). FT-IR study of early stages of alkali activated materials based on pyroclastic deposits (Mt. Etna, Sicily, Italy) using two different alkaline solutions. *Construction and Building Materials,* 262: 120095.
19. Abdullah, M. M. A. B., Ming, L. Y., Yong, H. C. and Tahir, M. F. M. (2018). Clay-based materials in geopolymer technology. *Cement Based Materials,* 239: 77438.
20. Shi, H., Ma, H., Tian, L., Yang, J. and Yuan, J. (2020). Effect of microwave curing on metakaolin-quartz-based geopolymer bricks. *Construction and Building Materials,* 258: 120354.
21. Okashah, A. M., Zainal, F. F., Hayazi, N. F., Nordin, M. N. and Abdullah, A. (2021). Pozzolanic properties of calcined clay in geopolymer concrete: A review. In AIP Conference Proceedings (Vol. 2339, No. 1). AIP Publishing.
22. Li, Z., Zhang, S., Zuo, Y., Chen, W. and Ye, G. (2019). Chemical deformation of metakaolin based geopolymer. *Cement and Concrete Research,* 120: 108-118.
23. Feng, B., Liu, J., Chen, Y., Tan, X., Zhang, M. and Sun, Z. (2022). Properties and microstructure of self-waterproof metakaolin geopolymer with silane coupling agents. *Construction and Building Materials,* 342: 128045.
24. Zawrah, M. F., Sawan, S. A., Khattab, R. M. and Abdel-Shafi, A. A. (2020). Effect of nano sand on the properties of metakaolin-based geopolymer: Study on its low rate sintering. *Construction and Building Materials,* 246: 118486.
25. Zidi, Z., Ltifi, M. and Zafar, I. (2021). Synthesis and attributes of nano-SiO_2 local metakaolin based-geopolymer. *Journal of Building Engineering,* 33: 101586.
26. Salahudeen, N. (2018). Metakaolinization effect on the thermal and physiochemical propperties of kankara kaolin. *Applied Science and Engineering Progress,* 11(2): 127-135.
27. Cecilia, J. A., García-Sancho, C. and Franco, F. (2013). Montmorillonite based porous clay heterostructures: Influence of Zr in the structure and acidic properties. *Microporous and Mesoporous Materials,* 176: 95-102.
28. Alekseeva, O., Noskov, A., Grishina, E., Ramenskaya, L., Kudryakova, N., Ivanov, V. and Agafonov, A. (2019). Structural and thermal properties of montmorillonite/ionic liquid composites. *Materials,* 12(16): 2578.
29. Chen, X., Zhu, G., Zhou, M., Wang, J. and Chen, Q. (2018). Effect of organic polymers on the properties of slag-based geopolymers. *Construction and Building Materials,* 167: 216-224.

30. Boum, R. B. E., Kaze, C. R., Nemaleu, J. G. D., Djaoyang, V. B., Rachel, N. Y., Ninla, P. L., ... and Kamseu, E. (2020). Thermal behaviour of metakaolin–bauxite blends geopolymer: microstructure and mechanical properties. *SN Applied Sciences,* 2(8):1358.
31. Nemaleu, J. G. D., Bakaine Djaoyang, V., Bilkissou, A., Kaze, C. R., Boum, R. B. E., Djobo, J. N. Y., ... and Kamseu, E. (2022). Investigation of groundnut shell powder on development of lightweight metakaolin based geopolymer composite: mechanical and microstructural properties. *Silicon,* 14(2): 449-461.
32. Aouan, B., Alehyen, S., Fadil, M., Alouani, M. E., Khabbazi, A., Atbir, A. and Taibi, M. H. (2021). Compressive strength optimization of metakaolin-based geopolymer by central composite design. *Chemical Data Collections,* 31:100636.
33. El Alouani, M., Alehyen, S. and El Achouri, M. (2019). Preparation, characterization, and application of metakaolin-based geopolymer for removal of methylene blue from aqueous solution. *Journal of Chemistry,* 2019: 4212901.
34. Gultekin, A. and Ramyar, K. (2022). Effect of curing type on microstructure and compressive strength of geopolymer mortars. *Ceramics International,* 48(11): 16156-16172.
35. Nmiri, A., Hamdi, N., Yazoghli-Marzouk, O., Duc, M. and Srasra, E. (2017). Synthesis and characterization of kaolinite-based geopolymer: Alkaline activation effect on calcined kaolinitic clay at different temperatures. *Journal Materials Environmental Sciences,* 8(2): 276-290.
36. Marsh, A., Heath, A., Patureau, P., Evernden, M. and Walker, P. (2018). Alkali activation behaviour of un-calcined montmorillonite and illite clay minerals. *Applied Clay Science,* 166: 250-261.
37. Jaradat, Y. and Matalkah, F. (2021). Olive biomass ash-based geopolymer composite: development and characterisation. *Advances in Applied Ceramics,* 120(1): 1-9.
38. Longhi, M. A., Zhang, Z., Walkley, B., Rodríguez, E. D. and Kirchheim, A. P. (2021). Strategies for control and mitigation of efflorescence in metakaolin-based geopolymers. *Cement and Concrete Research,* 144: 106431.
39. Zhang, Z., Provis, J. L., Ma, X., Reid, A. and Wang, H. (2018). Efflorescence and subflorescence induced microstructural and mechanical evolution in fly ash-based geopolymers. *Cement and Concrete Composites,* 92: 165-177.
40. Tigue, A. A. S., Malenab, R. A. J., Dungca, J. R., Yu, D. E. C. and Promentilla, M. A. B. (2018). Chemical stability and leaching behavior of one-part geopolymer from soil and coal fly ash mixtures. *Minerals,* 8(9): 411.
41. Hu, X., Shi, C., Liu, X. and Zhang, Z. (2020). Studying the effect of alkali dosage on microstructure development of alkali-activated slag pastes by electrical impedance spectroscopy (EIS). *Construction and Building Materials,* 261: 119982.
42. Biondi, L., Perry, M., McAlorum, J., Vlachakis, C. and Hamilton, A. (2020). Geopolymer-based moisture sensors for reinforced concrete health monitoring. *Sensors and Actuators B: Chemical,* 309: 127775.
43. Song, Q., Wang, J., Dong, T., Hel, L. and Lu, S. (2019). Study of the Alkali activated Geopolymer by AC Impedance Spectroscopy. *In IOP Conference Series: Earth and Environmental Science* (Vol. 267, No. 2, p. 022001). IOP Publishing.
44. Fan, L. F., Zhong, W. L. and Zhang, Y. H. (2022). Effect of the composition and concentration of geopolymer pore solution on the passivation characteristics of reinforcement. *Construction and Building Materials,* 319: 126128.
45. Pengou, M., Ngouné, B., Tchakouté, H. K., Nanseu, C. P. and Ngameni, E. (2020). Utilization of geopolymer cements as supercapacitors: influence of the hardeners on their properties. *SN Applied Sciences,* 2: 1-7.

Malaysian Journal of Analytical Sciences (MJAS)
Published by Malaysian Analytical Sciences Society

SYNTHESIS AND CHARACTERIZATION OF PALLADIUM(II) SCHIFF BASE COMPLEXES DERIVED FROM PHENYLAMINES AND THEIR CATALYTIC ACTIVITY FOR STILLE REACTION

(Sintesis dan Pencirian Palladium(II) Bes-Schiff Kompleks Dari Fenilamina dan Aktiviti Sebagai Pemangkin untuk Tindak Balas Stille)

Nur Nabihah Muzammil[1], Mohd Tajudin Mohd Ali[1], and Amalina Mohd Tajuddin[1,2*]

[1]*Faculty of Applied Sciences, Universiti Teknologi MARA, Shah Alam, 40450 Shah Alam, Selangor, Malaysia*
[2]*Atta-ur-Rahman Institute for Natural Product Discovery (AuRIns), Universiti Teknologi MARA Puncak Alam, 42300, Bandar Puncak Alam, Selangor, Malaysia*

[*]*Corresponding author: amalina9487@uitm.edu.my*

Received: 10 September 2023; Accepted: 25 February 2024; Published: 29 April 2024

Abstract

Schiff bases with hydrogen and methyl at the *para*-position of phenylamines (B1H and B1Me) and their palladium(II) complexes, (PdB1H and PdB1Me) were synthesized and characterized by elemental analysis, FTIR, ^{1}H and ^{13}C NMR, magnetic susceptibility measurement and UV-Visible spectroscopy. The shifting of the *v*(C=N) and *v*(C-O) bands to lower frequencies in FTIR indicated that the complexation to palladium(II) occurred through these moieties. All complexes are diamagnetic and displayed low molar conductivity in acetonitrile, indicating non-electrolytic behaviour. B1H and B1Me are structurally characterized using single crystal X-ray diffraction. B1H and B1Me crystallize in orthorhombic space group $P2_12_12_1$, with a = 6.0879(2) Å, b = 9.1847(2) Å, and c = 21.0661(5) Å and a = 5.9051(9) Å, b = 9.2389(13) Å, and c = 23.297(3) Å, respectively. The palladium(II) complexes were screened for their catalytic activity in the Stille reaction. The reaction was monitored by measuring the % conversion of iodobenzene using GC-FID, where the reaction conditions used were 1.0 mmol% catalyst loading in the presence of triethylamine as the base and DMSO as the solvent at 80°C within 6 hours of the reaction time. It was observed that PdB1Me displayed the best catalytic performance for the Stille reaction, as indicated by the 80% conversion of iodobenzene.

Keywords: catalysis, palladium(II), Schiff base, Stille reaction, single crystal X-ray crystallography

Abstrak

Bes-Schiff dengan hidrogen dan metil pada fenilamina posisi *para* (B1H dan B1Me), dan kompleks paladium(II) (PdB1H dan PdB1Me), telah disintesis dan dicirikan oleh analisis unsur, FTIR, ^{1}H dan ^{13}C NMR, ukuran kerentanan magnet dan sinar ultraungu spektroskopi. Peralihan jalur *v*(C=N) dan *v*(C-O) kepada frekuensi yang lebih rendah dalam FTIR menunjukkan bahawa kompleksasi kepada paladium(II) berlaku melalui gugusan ini. Semua kompleks adalah diamagnet dan menunjukkan kekonduksian molar rendah dalam asetonitril yang menunjukkan tingkah laku bukan elektrolitik. B1H dan B1Me dicirikan secara struktur menggunakan pembelauan sinar-X kristal tunggal. B1H dan B1Me menghablur dalam ortorombik dengan kumpulan ruang $P2_12_12_1$, dengan a = 6.0879(2) Å, b = 9.1847(2) Å, dan c = 21.0661(5) Å dan a = 5.9051(9) Å, b = 9.2389(13) Å, dan c = 23.297(3) Å. Kompleks paladium(II) telah disaring untuk aktiviti pemangkinnya dalam tindak balas Stille. Tindak balas dipantau dengan mengukur % penukaran iodobenzena menggunakan GC-FID, di mana keadaan tindak balas yang digunakan ialah 1.0 mmol%

pemangkin dengan kehadiran trietilamina sebagai bes dan DMSO sebagai pelarut pada 80°C selama 6 jam. PdB1Me memaparkan prestasi pemangkin terbaik di kalangan kompleks untuk tindak balas Stille, ditunjukkan oleh penukaran 80% iodobenzena.

Kata kunci: pemangkinan, paladium(II), Bes-Schiff, tindak balas Stille, kristalografi sinar-X kristal tunggal

Introduction

The Schiff base complexes have received great attention in recent years because of their highly considered as stereochemical models in coordination chemistry, their easy mode of preparation and their structural diversity [1]. Schiff bases and their complexes have a wide range of applications such as bioactive agents [2], catalysts [3], medicines [4], and anti-corrosion agents [5]. Schiff base complexes play a key role in various homogeneous catalytic reactions and the activity of these complexes changes with the types of ligands, coordination sites and metal ions [6].

Schiff bases that are derived from amines and carbonyl compounds belong to a class of ligands involved in the coordination of metal ions via azomethine nitrogen [7]. Phenylamines, through the condensation reaction with various types of organic reagents such as aldehydes, ketones, thiosemicarbazides, carbazides, and similar compounds, are able to form flexible ligand systems that are able to coordinate with a variety of metals [8]. Schiff bases derived from phenylamines and their respective transition metal complexes exhibit potential catalytic activity [9].

Palladium is considered a very important metal from a coordination point of view and it plays a key role as a catalyst in a variety of catalytic activities by varying the ligand environment [10]. Palladium complexes are excellent and versatile catalysts in many important chemical reactions such as carbon-carbon coupling, alkylation, carbonylation, and oxidation [11]. Palladium(II) Schiff base complexes are mostly used to catalyse these couplings reactions as they offer high product yields, high regioselectivity, high stereoselectivity, and compatibility with many functional moieties.

The palladium-catalysed Stille cross-coupling reaction represents one of the most important transformations in constructing carbon-carbon bonds in organic synthesis [12, 13]. Generally, the combination of palladium catalysts with various phosphine ligands is commonly used in the Stille reaction [14]. However, phosphine ligands are air-sensitive and expensive, which places significant limits on their synthetic applications [15].

This paper aims to report the synthesis and characterization of bidentate Schiff base ligands with hydrogen and methyl at the *para*-position of phenylamines with *o*-vanillin and their palladium(II) complexes. Scheme 1 shows the synthesis of the Schiff base ligands and their palladium(II) complexes. The molecular structures of all compounds were elucidated through elemental analysis, magnetic susceptibility, molar conductivity, FTIR, ^{1}H NMR, ^{13}C NMR, UV−Visible analysis, and single crystal X-ray diffraction. The palladium(II) complexes were screened for their catalytic activity in the Stille reaction.

Materials and Methods

Materials and physical measurements

All chemicals and solvents received from commercial suppliers were used. Microanalyses for C, H and N were conducted on Thermo Finnigan Flash Elemental Analyzer 2000. Melting point determination was carried out in glass capillary tubes using Buchii-B454. The IR spectra were obtained using Perkin Elmer 1750X FTIR spectrophotometer (4000-400 cm^{-1}) with samples prepared as KBr discs. Proton (^{1}H) and carbon (^{13}C) NMR (600 MHz) spectra were recorded on Bruker Varian spectrometer in $CDCl_3$ and reported in ppm (δ) relative to TMS, used as the internal reference. The UV-Vis spectra were obtained on Perkin Lambda 35 in chloroform ($CHCl_3$) 1×10^{-4} M solution at room temperature, in the range of 200-800 nm, using a quartz cuvette. Magnetic measurements were carried out using the Guoy method with distilled water as a calibrant on the Sherwood Auto Magnetic Susceptibility Balance. A single crystal X-ray diffraction investigation was carried out on Bruker D8 QUEST CCD diffractometer with PHOTON III 7 detector, using graphite-monochromated Mo-Kα radiation (λ = 0.71073 Å) at 298 K. The collected frames were processed with the

software SAINT. Structures were solved by the direct methods and refined by full-matrix least-squares on F^2 using the SHELXTL software package. Mercury [16] software was utilized for the graphical representation of the X-ray results. Gas chromatographic analyses were performed on Agilent 7890A Network GC System using ethyl laurate as standard. The column used is HP-5 capillary columns with a temperature increment of 15°C per minute, and the final temperature was 300°C.

Synthesis of ligands

The Schiff base ligands were synthesized by condensation reactions between *o*-vanillin and phenylamine derivatives using a 1:1 molar ratio (Scheme 1) in hot ethanol, under reflux for 3 hours. The mixture was allowed to cool slowly to room temperature. Upon cooling, orange precipitate formed. The precipitate was filtered off, washed with ice-cold ethanol, and air-dried at room temperature. The crystals were obtained through slow evaporation of the filtrate solutions.

Synthesis of palladium(II) complexes

The ligands and palladium(II) acetate were dissolved in hot ethanol in a round-bottom flask using a 2:1 molar ratio. The mixture was stirred and refluxed for 6 hours. The mixture was allowed to cool slowly to room temperature. Upon cooling, brown precipitate formed. The precipitate was filtered off, washed with ice-cold ethanol, and air-dried at room temperature.

General procedure for the Stille reaction

The general procedure (Scheme 2) is as follows: Iodobenzene (1 mmol, 0.2 g), tributylphenyltin (1.5 mmol, 0.55 g), triethylamine (Et_3N, 2.0 mmol, 0.20 g), palladium(II) complex (1 mmol%) (PdB1H, PdB1Me) and dimethylsulfoxide (DMSO, 7 mL) were mixed in Radley's 12-placed reaction carousel and refluxed at 80 °C for 6 hours. The reaction was monitored regularly using GC-FID.

Results and Discussion

Elemental analysis

The physicochemical data of the compounds are presented in Table 1. According to the elemental analysis of C, H, and N for the compounds, the experimental values were in accordance with the calculated values of the proposed structure. The melting points of the parent ligands were typically lower than those of the complexes, which is likely due to the increased molecular sizes and the presence of stronger dative covalent bonds between C-N-Pd and ionic bonds between C-O-Pd [16].

Molar conductivity measurement for complexes revealed that the non-conductivity nature of the solution at room temperature indicating the absence of any electrolytes [17]. These values show that there are no ions existing in the outer-sphere coordination of the complexes. As expected, the magnetic susceptibility measurements showed diamagnetic behaviour reflected in the zero effective magnetic moment, $\mu_{eff} = 0$, in all complexes consistent with the 0 unpaired electrons of Pd(II) d^8 species having square planar geometry [18].

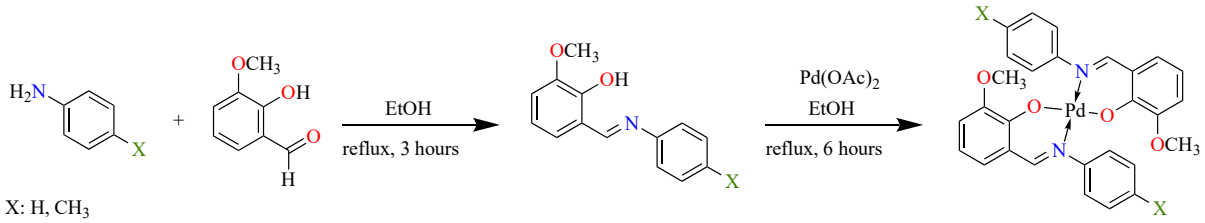

Scheme 1. Synthesis of the Schiff base ligands and their Pd(II) complexes

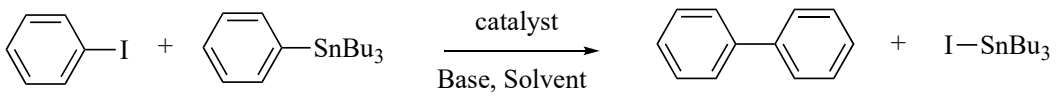

Scheme 2. General reaction of Stille reaction

Table 1. Physicochemical data of ligands and their complexes

Compounds	Empirical Formula	Colour	Melting Point (°C)	Elemental Analysis (%)			Magnetism	Molar Conductivity ($\Omega^{-1}cm^2mol^{-1}$)
				C	H	N		
B1H	$C_{14}H_{13}NO_2$	Orange	227.26	73.99 (**73.29**)	5.77 (**5.68**)	6.16 (**6.05**)	-	-
PdB1H	$C_{28}H_{24}N_2O_4Pd$	Brown	558.93	60.17 (**59.39**)	4.33 (**4.19**)	5.01 (**4.84**)	Diamagnetic	1.275
B1Me	$C_{15}H_{15}NO_2$	Orange	241.29	74.67 (**73.79**)	6.27 (**6.24**)	5.81 (**5.71**)	-	-
PdB1Me	$C_{30}H_{28}N_2O_4Pd$	Brown	586.98	61.39 (**60.55**)	4.81 (**4.74**)	4.77 (**4.58**)	Diamagnetic	0.874

FTIR spectroscopy

The FTIR spectra of the ligands and palladium(II) complexes are shown in Figure 1. There is an absence of ν(OH) peak in the FTIR spectra of the ligands (Figure 1). This can be attributed to the formation of hydrogen bonding between the hydrogen and nitrogen atoms in the solid state. This is supported by the discovery of an intramolecular hydrogen bond in the X-ray crystallography analysis. The strong bands around 1615-1618 cm^{-1} are assignable to the azomethine ν(C=N) group for the ligands. This band was observed to be shifted slightly to lower frequencies of 1601– 1602 cm^{-1} in the complexes, likely due to the coordination of the imine nitrogen atom through the sharing of the N lone pair of electrons in a dative manner with the metal centre [19]. The involvement of deprotonated phenolic oxygen atoms in chelation was indicated by the shifting to lower frequencies of the $\nu(C\text{-}O)_{phenolic}$ band. The medium intensity $\nu(C\text{-}O)_{phenolic}$ band that was observed at 1253-1258 cm^{-1} in ligands shifted to lower wavenumbers of 1237-1240 cm^{-1} in complexes.

The coordination of the imine nitrogen and phenolic oxygen atoms to the metal centres was supported by the appearance of new peaks of ν(Pd-O) and ν(Pd-N) bands in palladium(II) complexes, which appeared in the regions of 507-572 cm^{-1} and 446-473 cm^{-1}, respectively [20].

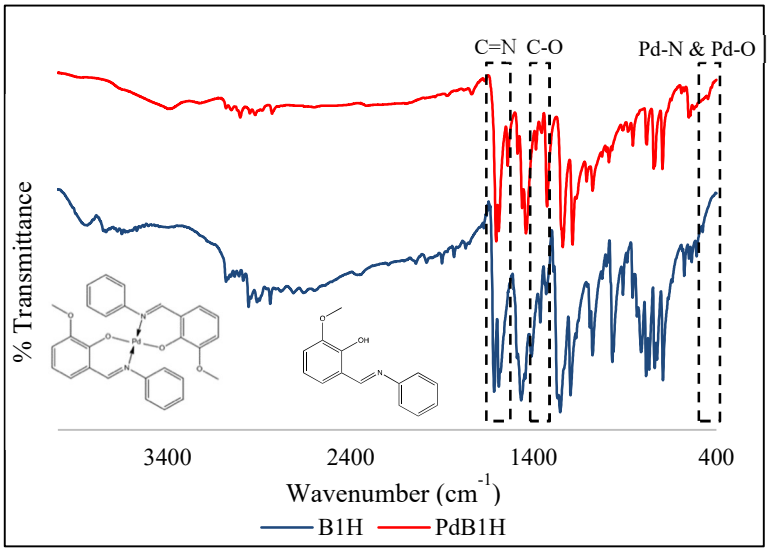

(a)

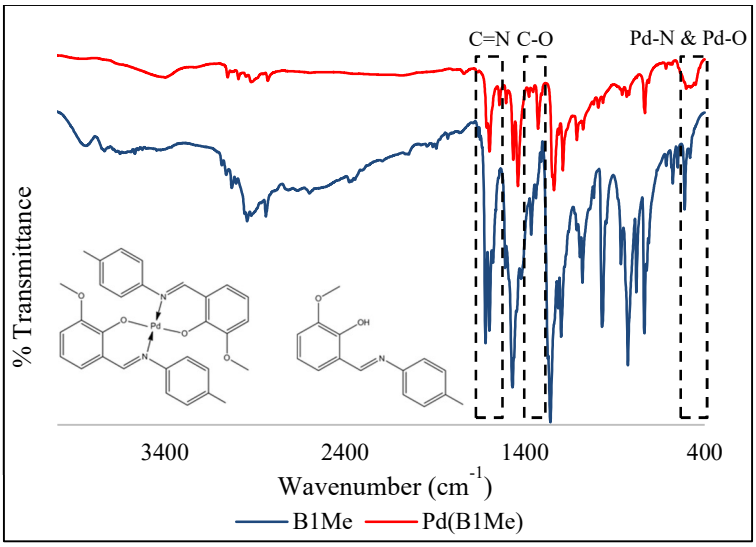

(b)

Figure 1. Infrared Spectra of (a) B1H and PdB1H and (b) B1Me and PdB1Me

Nuclear magnetic resonance (NMR) spectroscopy

The ^{1}H spectra of the ligands and palladium(II) complexes are presented in Figure 2. The ^{1}H NMR spectra showed integrations and multiplicities consistent with the proposed structures. The phenolic proton in ligands appears as a singlet in the downfield region in the range of 13.70 to 13.84 ppm [21]. Upon complexation, the peak of the phenolic proton was absent in both spectra of the complexes suggesting the deprotonation of the phenolic proton [22]. The chemical shift of the azomethine proton (-HC=N-) was shielded at the range of 7.69-7.72 ppm in the complexes compared to the ligands at 8.63 ppm, inferring coordination of the palladium(II) ion to the ligand through the azomethine nitrogen atom [23]. The metal donates the π electrons to the ligands π* orbital, adding the electron density to an antibonding molecular orbital, and this results in weakening of the C-O bond and C=N bond [24]. The spectra of the ligands and complexes show aromatic hydrogen appearing in the ranges of 6.88-7.44 and 6.41-7.32 ppm, respectively. The presence of the methyl groups attached to the structure of B1Me was confirmed by the appearance of singlet peaks at 2.38 ppm and 2.45 ppm at PdB1Me.

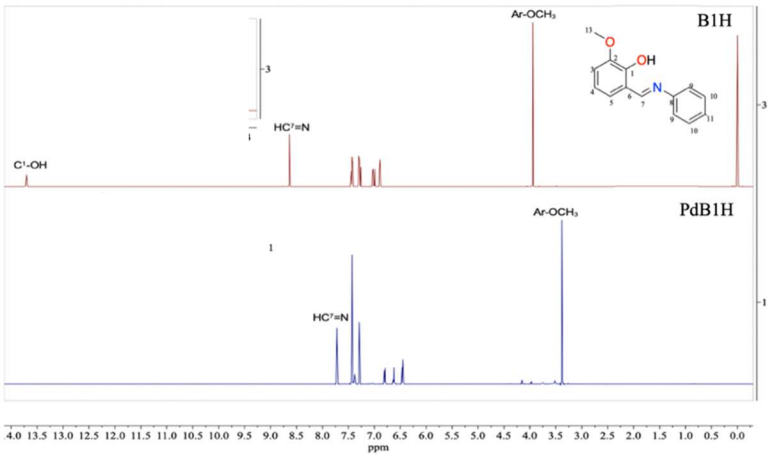

(a)

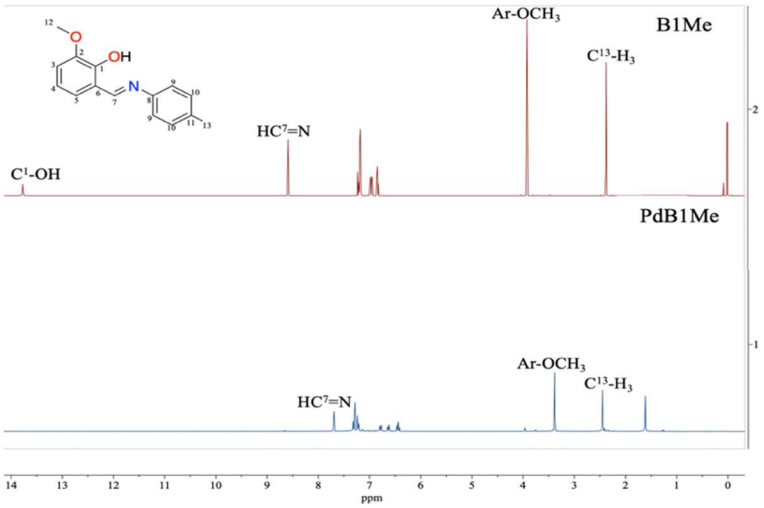

(b)

Figure 2. ^{1}H NMR spectra of (a) B1H and PdB1H and (b) B1Me and PdB1Me

The ^{13}C NMR spectra of the ligands and palladium(II) complexes in Figure 3, respectively recorded signals of sharp peaks representing the chemically non-equivalent carbon atoms in the compound. The phenolic carbon for the ligands was found in the range of 148.5-151.5 ppm and upon complexation, they appeared in the downfield region for complexes. The shifting indicates the establishment of new bond between metal centre and phenolic oxygen. The presence of the methyl group was detected at 22.7 and 19.6 ppm for B1Me and PdB1Me, respectively.

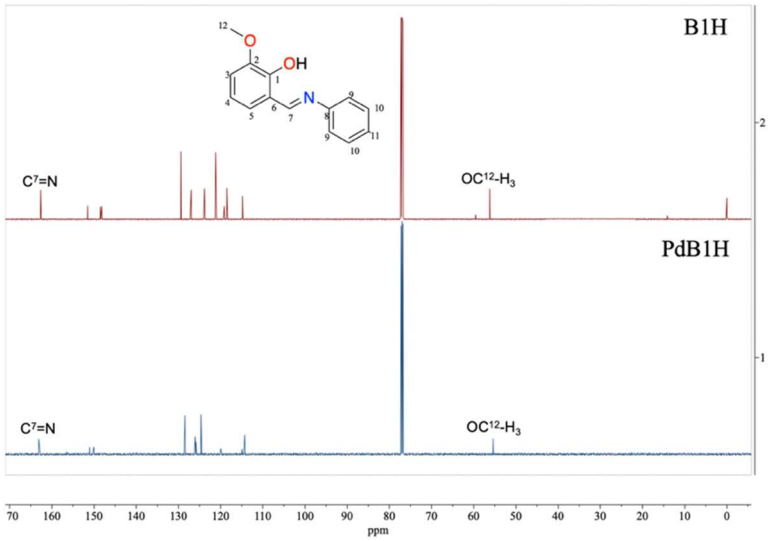

(a)

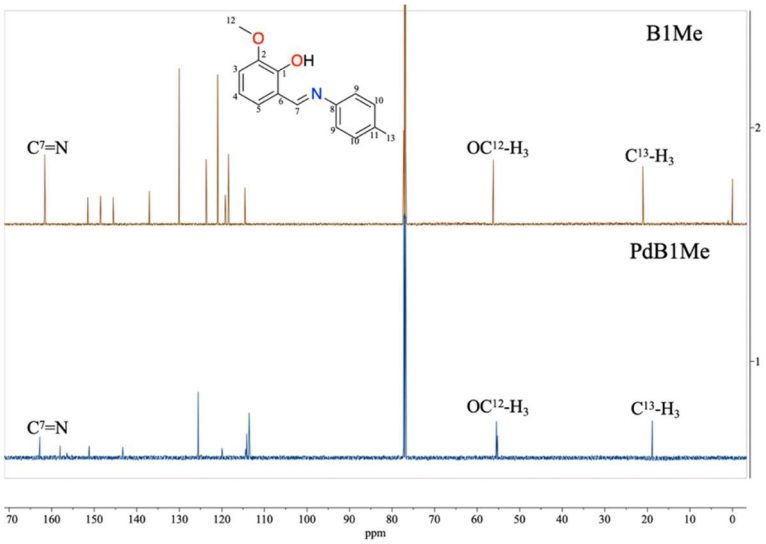

(b)

Figure 3. ^{13}C NMR spectra of (a) B1H and PdB1H and (b) B1Me and PdB1Me

UV-visible spectroscopy

The UV−vis spectroscopy spectra and data of the ligands and palladium(II) complexes are shown in Figure 4 and Table 2. The electronic transitions result in three main characteristic absorption peaks, i.e., π−π*(C=C), π−π*(C=N), and n−π*(C=N). The π−π*(C=C) peak of the ligand was observed at 210-229 nm, and the peak shifted to a bathochromic shift in the complexes, appearing at 220-253 nm for palladium(II) complexes. Besides, the π−π*(C=N) peak at 271-279 nm of the ligands underwent a bathochromic shift upon complexation, appearing at 301-305 nm. It arises due to the coordination of the lone pair of electrons with the metal ion [25]. The n−π* transitions of imine in the complexes were not found in the complexes, possibly due to the stabilization of the electron pair on the nitrogen atom upon the formation of the metal-nitrogen bond [26]. Upon complexation, there is the appearance of ligand to metal charge transfer at 420-421 nm, which suggests the square planar geometry around the Pd(II) centre [27]. Thus, it could be said that the magnetic susceptibility measurements for the PdB1H and PdB1Me, which show diamagnetic behaviour with square planar geometry, are complimentary to the UV-visible data obtained in Table 2.

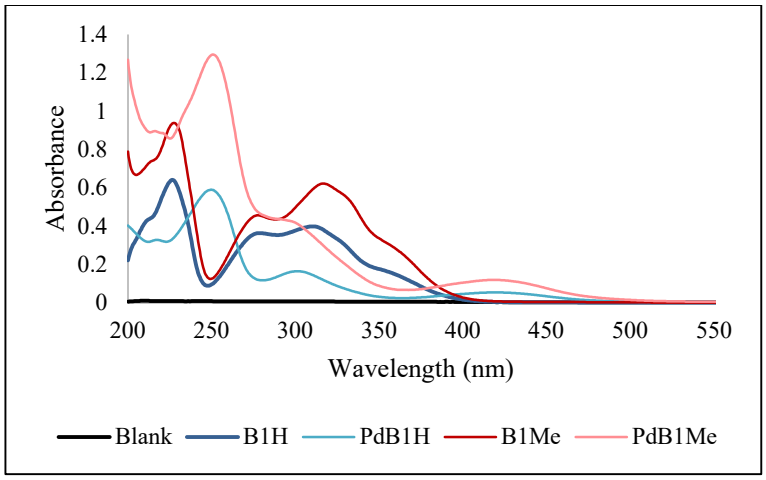

Figure 4. UV-visible spectra of ligands and complexes

Table 2. UV-Visible Data of Ligands and Their Pd(II) Complexes

Compounds	π→π* (C=C)	π→π* (C=N)	n→π*	Ligand to Metal Charge Transfer
B1H	210 (1386), 225 (2108)	271 (1102)	310 (1331)	-
PdB1H	220 (1080), 253 (1918)	305 (539)	-	421 (183)
B1Me	213 (2441), 229 (3104)	279 (1517)	317 (2074)	-
PdB1Me	220 (2953), 253 (4274)	301 (1379)	-	420 (400)

Single X-ray crystallography

Suitable single crystals of B1H and B1Me were subjected to X-ray crystallography investigation to determine the structure. Both crystals were obtained through slow evaporation of their filtrate solutions. Crystallographic data collection parameters for the compounds are shown in Table 3. B1H and B1Me crystallize in orthorhombic space group $P2_12_12_1$, with a = 6.0879(2) Å, b = 9.1847(2) Å, and c = 21.0661(5) Å. and a = 5.9051(9) Å, b = 9.2389(13) Å, and c = 23.297(3) Å, respectively. The ORTEP diagrams of the compounds drawn at 50% probability ellipsoids are depicted in Figure 5.

Table 3. Crystallographic Data Collection Parameters for B1H and B1Me

Compounds	B1H	B1Me
CCDC number	2233459	2233467
Empirical formula	$C_{14}H_{13}NO_2$	$C_{15}H_{14}NO_2$
Formula weight	227.27	240.27
Temperature (K)	298.50	299.50
Crystal system	Orthorhombic	Orthorhombic
Space group	$P2_12_12_1$	$P2_12_12_1$
Unit cell dimensions		
a (Å)	6.0879(2) Å	5.9101(14) Å
b (Å)	9.1847(2) Å	9.235(2) Å
c (Å)	21.0661(5) Å	23.303(6) Å
Volume (Å^3)	1177.92 (5) Å^3	1271.9(5) Å^3
Z	4	4
D_{calc} (Mg/m^3)	1.282 Mg/m^3	1.255 Mg/m^3
Absorption coefficient (mm^{-1})	0.086	0.084
F (000)	480.0	512.0
Crystal size (mm^3)	0.500 × 0.320 × 0.150 mm^3	0.39 × 0.27 × 0.13 mm^3
Theta range for data collection	6.96 to 56.6	6.854 to 56.582
Index ranges	$-7 \le h \le 8$, $-12 \le k \le 12$, $-27 \le l \le 28$	$-7 \le h \le 7$, $-10 \le k \le 12$, $-29 \le l \le 30$
Reflections collected	35437	22568
Independent reflections	2933 [R_{int}= 0.0603]	3145 [R_{int}= 0.0532]
Data/restraints/parameters	2933/0/159	3145/0/165
Goodness-of-fit on F^2	0.974	1.031
Final R indices [I > 2sigma(I)]	R1= 0.0400, wR2= 0.1189	R_1 = 0.0434, wR_2 = 0.1187
R indices (all data)	R1= 0.0524, wR2= 0.1314	R_1 = 0.0583, wR_2 = 0.1296
Largest diff. peak and hole	0.15/-0.17	0.29/-0.14

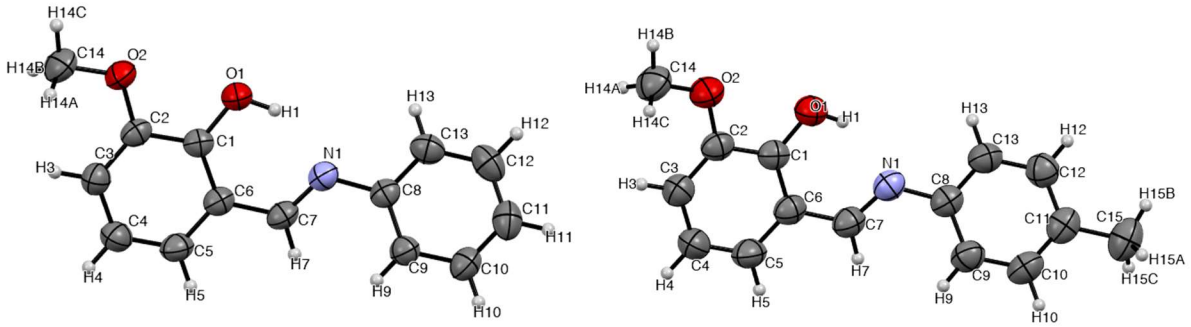

B1H B1Me

Figure 5. The ORTEP diagrams of compounds with the atom labelling scheme drawn at 50% probability ellipsoids

For B1H, the two benzene rings C1-C6 and C8-C13 are each non-planar with a maximum deviation of 0.010(2) and 0.015(2) Å for atoms C1 and C8, respectively, from their mean square planes. Both planes make a dihedral angle of 30.58°. The C-O bond length ranges from 1.352(2) to 1.419(3) Å in the B1H molecule. The C-N and C=N bond lengths of B1H are 1.279(2) and 1.396(3) Å, respectively (Table 4). The bond length values correspond to the previously reported values [28].

For B1Me, the two benzene rings C1-C6 and C8-C13 are each non-planar with maximum deviation of 0.018(2) and 0.012(2) Å for atom C1 and C8, respectively from their mean square planes. Both planes make a dihedral angle of 26.84°. The bond lengths and angles of B1Me are in normal ranges and the values in Table 4 are similar to those in a previous study [29].

Table 4. Selected Bond Lengths (Å) and Bond Angles (°) of B1H and B1Me

	B1H	**B1Me**
Bond Lengths (Å)		
O1—C1	1.352(2)	1.348(2)
O1—C2	1.368(2)	1.362(2)
O2—C14	1.419(3)	1.420(3)
N1—C7	1.279(2)	1.275(3)
N1—C8	1.396(3)	1.414(2)
Bond Angles (°)		
O2—O2—C14	117.12(16)	117.03(18)
C7—N1—C8	120.64(15)	121.31(16)

The packing diagram for B1H view down the crystallographic a-axis is shown in Figure 6. There is an intramolecular hydrogen bond O1—H1···N1 and the intermolecular hydrogen bond is drawn as dashed lines at C10—H10···O2 in the compound, as shown in Table 5. The packing diagram for the B1Me view along the a-axis is shown in Figure 6. There is an intramolecular hydrogen bond O1—H1···N1, and the intermolecular hydrogen bond at C10—H10···O1 is drawn as dashed lines in the compound (Table 5).

Table 5. Intramolecular and intermolecular hydrogen bonds of B1H and B1Me (Å, °)

D—H···A	**D—H**	**H···A**	**D ···A**	**D—H···A**
B1H				
O1—H1···N1	0.90(3)	1.83(3)	2.619(2)	146(2)
C10—H10···O2[(a)]	0.93	2.57	3.488(2)	167

D—H···A	D—H	H···A	D ···A	D—H···A
B1Me				
O1—H1···N1	0.82	1.90	2.621(2)	146
C10—H10···O1$^{(b)}$	0.93	2.47	3.365(3)	162

Symmetry code= (a): -x,1/2+y,3/2-z, (b): 1-x,-1/2+y,1/2-z

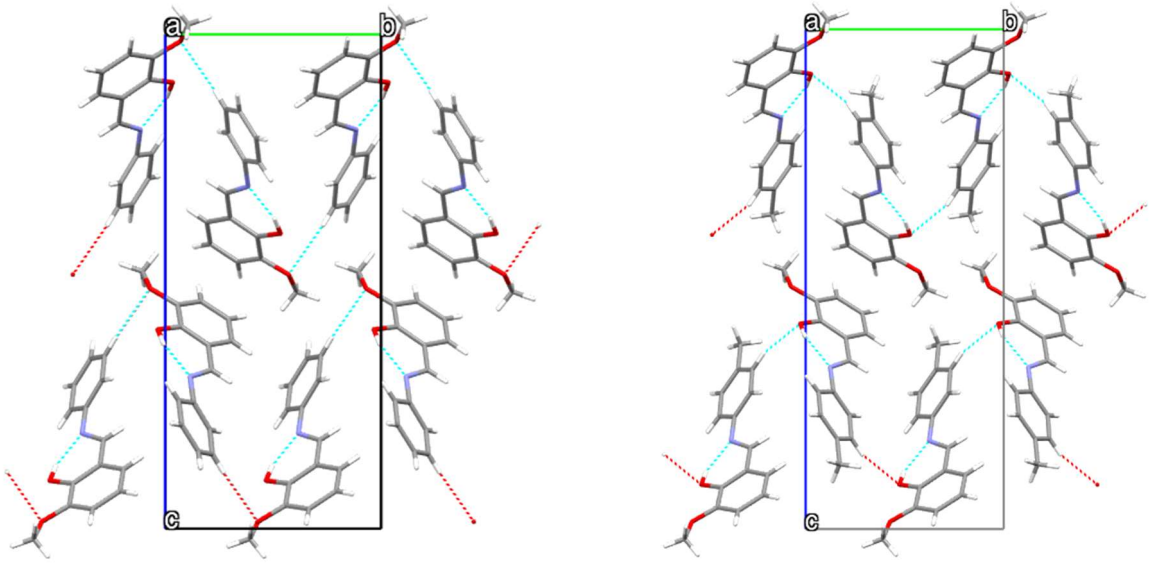

B1H B1Me

Figure 6. Packing B1H and B1Me view down crystallographic a-axis

Catalytic studies

The palladium(II) complexes in this study were screened for their catalytic activity in Stille reaction. The reaction was conducted by reacting iodobenzene with tributylphenyltin. The reaction conditions used were 1.0 mmol% catalyst loading in the presence of triethylamine as a base in dimethyl sulfoxide at 80 °C within 6 hours of the reaction time. Scheme 3 proposes the mechanism of the palladium-catalysed cross-coupling Stille reaction. The three key basic steps involved in the catalytic cycle are oxidative addition, transmetallation and reductive elimination. The mechanism begins with the oxidative addition of the organohalide to the Pd(0) in order to form a Pd(II) complex. Transmetallation with the organotin then proceeds where the R group of the organotin reagent replaces the halide anion on the palladium complex. Reductive elimination then gives the final coupled product, regenerates the palladium catalyst, and the catalytic cycle can recommence.

The reaction was monitored by measuring the % conversion of the aryl iodide starting material using gas chromatography [30]. The results are summarized in Figure 7. It was observed that PdB1Me displayed a better catalytic performance compared to PdB1H for the Stille reaction, as indicated by the 80% conversion of iodobenzene (PdB1Me) while for PdB1H, the % conversion is only 73%, this could be due to the presence of the electron donating group (-CH_3) [31, 32]. The presence of an electron-donating group in ligands will activate the benzene ring, thus as the π system in the benzene ring is activated, the electron density will increase [33]. By increasing the electron density, the formed metal-N bond will be shorter and stronger, thus this will improve the catalytic performance.

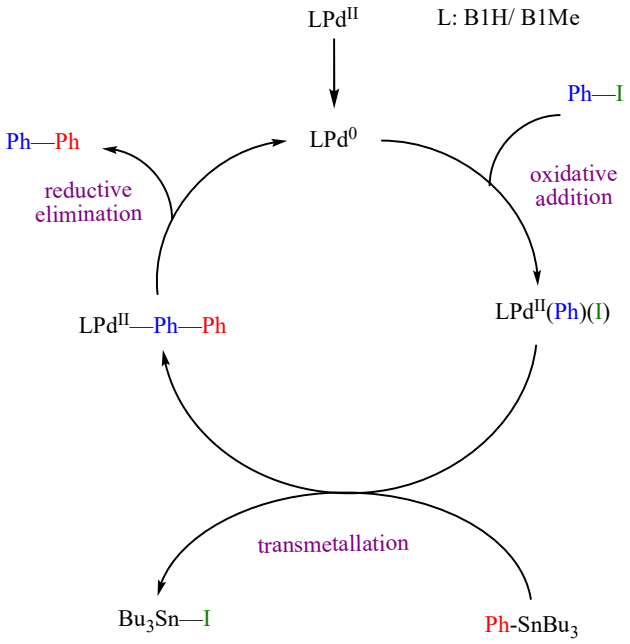

Scheme 3. Mechanism of palladium-catalyzed Stille reaction

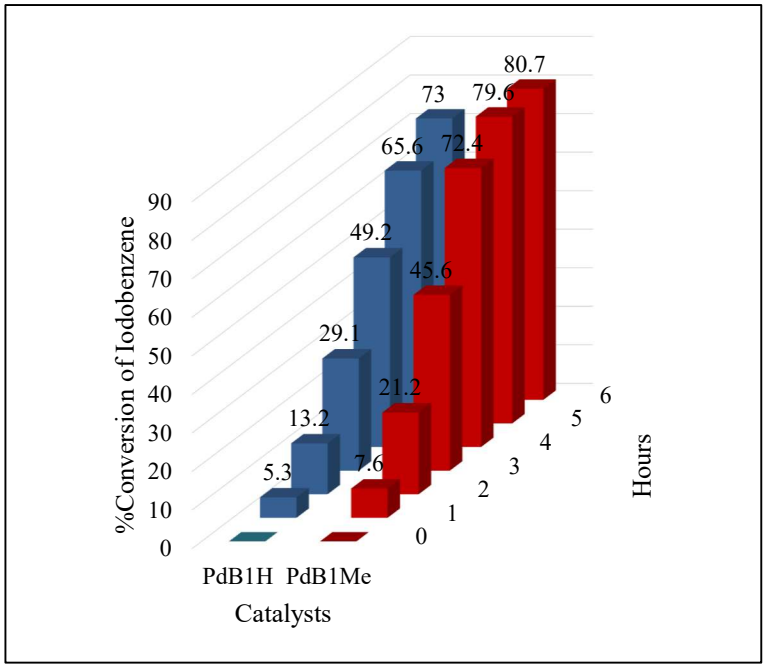

Figure 7. Activity of palladium catalysts on the Stille reaction between iodobenzene and tributylphenyltin

Conclusion

Two ligands and their palladium(II) complexes have been successfully synthesized and confirmed by characterization via various physico-spectral techniques. It can be concluded that the ligands act as bidentate chelators coordinated to the Pd(II) ion upon complexation based on the spectroscopic results and exhibited a square planar geometry. The good agreement between experimental and predicted spectral data of the Schiff bases strongly supported the elucidation of Pd(II) complexes. It was observed that both Pd(II) complexes displayed the properties of good catalysts for the reaction. PdB1Me was the most efficient catalyst for the

Stille reaction, which could be due to the presence of an electron donating group ($-CH_3$).

Acknowledgement

The authors would like to acknowledge the Ministry of Higher Education (MoHE) for the MyBrainSc scholarship, and Universiti Teknologi MARA for research funding via the grant 600-RMC/YTR/5/3 (007/2020).

References

1. Xiao, Y. and Cao, C. (2020). Influence of substituents on the structure of Schiff bases Cu(II) complexes. *Journal of Molecular Structure,* 1209: 127916.
2. Da Silva, C. M., Da Silva, D. L., Modolo, L. V., Alves, R. B., De Resende, M. A., Martins, C. V. B. and De Fátima, Â. (2011). Schiff bases: A short review of their antimicrobial activities. *Journal of Advanced Research*, 2(1): 1-8.
3. Gupta, K. C. and Sutar, A. K. (2008). Catalytic activities of Schiff base transition metal complexes. *Coordination Chemistry Reviews*, 252(12–14): 1420-1450.
4. Tsacheva, I., Todorova, Z., Momekova, D., Momekov, G. and Koseva, N. (2023). Pharmacological activities of Schiff bases and their derivatives with low and high molecular phosphonates. *Pharmaceuticals*, 16(7): 938.
5. Verma, C. and Quraishi, M. A. (2021). Recent progresses in Schiff Bases as aqueous phase corrosion inhibitors: Design and applications. *Coordination Chemistry Reviews*, 446: 214105.
6. El-Ajaily, M. M., Maihub, A. A., Mahanta, U. K., Badhei, G., Mohapatra, R. K. and Das, P. K. (2018). Mixed ligand complexes containing schiff bases and their biological activities: A short review. *Rasayan Journal of Chemistry*, 11(1): 166-174.
7. Sheikhshoaie, I., Lotfi, N., Sieler, J., Krautscheid, H. and Khaleghi, M. (2018). Synthesis, structures and antimicrobial activities of nickel(II) and zinc(II) diaminomaleonitrile-based complexes. *Transition Metal Chemistry,* 43: 555-562.
8. Sobola, A. O., Watkins, G. M. and Van Brecht, B. (2014). Synthesis, characterization and antimicrobial activity of copper(II) complexes of some ortho-substituted aniline schiff bases; Crystal structure of Bis(2-methoxy-6-imino)methylphenol copper(II) complex. *South African Journal of Chemistry*, 67: 45-51.
9. Patil, C. J. and Salve, S. B. (2022). Catalytic studies on complexes of organic compounds: Part-5. Review on use of chiral Schiff base complexes as catalyst. *International Journal of Pharmaceutical Sciences Review and Research*, 74(2): 9-22.
10. Czajkowska-Szczykowska, D., Morzycki, J. W. and Wojtkielewicz, A. (2015). Pd-catalyzed steroid reactions. *Steroids*, 97:13-44.
11. Herrmann, W. A., Bo, V. P. W., Gsto, C. W. K., Grosche, M., Reisinger, C. and Weskamp, T. (2001). Synthesis, structure and catalytic application of palladium(II) complexes bearing. *Journal of Organometallic Chemistry*, 618: 616-628.
12. Davis, J. L., Dhawan, R., & Arndtsen, B. A. (n.d.). Imines in Stille-type cross-coupling reactions: A multicomponent synthesis of a-substituted amides. 590-594.
13. Carrera, N., Salinas-Castillo, A., Albéniz, A. C., Espinet, P. and Mallavia, R. (2011). Fluorene-based stannylated polymers and their use as recyclable reagents in the Stille reaction. *Journal of Organometallic Chemistry*, 696(21): 3316-3321.
14. Ghammamy, S. and Sedaghat, S. (2012). Determination and characterization of new palladium complexes and study of their properties. *Middle East Journal of Scientific Research*, 12(2): 264-269.
15. Mpungose, P. P., Vundla, Z. P., Maguire, G. E. M. and Friedrich, H. B. (2018). The current status of heterogeneous palladium catalysed Heck and Suzuki cross-coupling reactions. *Molecules*, 23(7): 1676.
16. Prakash, A. and Adhikari, D. (2011). Application of Schiff bases and their metal complexes-A review. *International Journal Chemical Technology Research,* 3(4): 1891-1896.
17. Aggoun, D., Fernández-garcía, M., López, D., Bouzerafa, B., Ouennoughi, Y., Setifi, F. and Ourari, A. (2020). New nickel(II) and copper(II) bidentate Schiff base complexes, derived from dihalogenated salicylaldehyde and alkylamine: synthesis, spectroscopic, thermogravimetry, crystallographic determination and electrochemical studies. *Polyhedron*, 187: 114640.

18. Aslantaş, M., Kendi, E., Demir, N., Şabik, A. E., Tümer, M. and Kertmen, M. (2009). Synthesis, spectroscopic, structural characterization, electrochemical and antimicrobial activity studies of the Schiff base ligand and its transition metal complexes. *Spectrochimica Acta - Part A: Molecular and Biomolecular Spectroscopy*, 74(3): 617-624.
19. Buta, I., Shova, S., Ilies, S., Manea, F., Andruh, M. and Costisor, O. (2022). Mono- and oligonuclear complexes based on a o-vanillin derived Schiff-base Ligand: Synthesis, crystal structures, luminescent and electrochemical properties. *Journal of Molecular Structure*, 1248: 131439.
20. Kargar, H., Ardakani, A. A., Tahir, M. N., Ashfaq, M. and Munawar, K. S. (2021). Synthesis, spectral characterization, crystal structure and antibacterial activity of nickel(II), copper(II) and zinc(II) complexes containing ONNO donor Schiff base ligands. *Journal of Molecular Structure*, 1233: 130112.
21. Soliman, A. A. and Linert, W. (1999). Investigations on new transition metal chelates of the 3-methoxy-salicylidene-2-aminothiophenol Schiff base. *Thermochimica Acta*, *338*(1-2): 67-75.
22. Ansari, R. M., Kumar, L. M. and Bhat, B. R. (2018). Air-stable cobalt(II) and nickel(II) complexes with Schiff Base ligand for catalyzing Suzuki–Miyaura cross-coupling reaction. *Russian Journal of Coordination Chemistry/Koordinatsionnaya Khimiya*, 44(1): 1-8.
23. Singh, K., Thakur, R. and Kumar, V. (2016). Co(II), Ni(II), Cu(II), and Zn(II) complexes derived from 4-[{3-(4-bromophenyl)-1-phenyl-1h-pyrazol-4-ylmethylene}-amino]-3-mercapto-6-methyl-5-oxo-1,2,4-triazine. *Beni-Suef University Journal of Basic and Applied Sciences*, *5*(1): 21-30.
24. Ghorbani-Choghamarani, A., Derakhshan, A. A., Hajjami, M. and Rajabi, L. (2016). Copper-Schiff base alumoxane: A new and reusable mesoporous nano catalyst for Suzuki-Miyaura and Stille C-C cross-coupling reactions. *RSC Advances*, 6(97): 94314-94324.
25. Kondori, T., Akbarzadeh-t, N., Fazli, M. and Mir, B. (2020). A Novel Schiff Base Ligand and its Copper Complex: Synthesis, Characterization, X-ray Crystal Structure and Biological Evaluation. *Journal of Molecular Structure*, 1226: 129395.
26. Bartyzel, A. (2017). Synthesis, thermal study and some properties of N_2O_4—donor Schiff Base and its Mn(III), Co(II), Ni(II), Cu(II) and Zn(II) complexes. *Journal of Thermal Analysis and Calorimetry*, 127(3): 2133-2147.
27. Abu-khadra, A. S., Farag, R. S. and Abdel-hady, A. E. M. (2016). Synthesis, characterization and antimicrobial activity of Schiff Base phenylsulfonyl acetamide metal complexes. *American Journal of Analytical Chemistry*, 3: 233-245.
28. Yu, Y. Y. (2011). 6-Methoxy-2-[(E)-phenyliminomethyl]-phenol. *Acta Crystallographica Section E: Structure Reports Online*, 67(4): 421-424.
29. Yeap, G. Y., Ha, S. T., Ishizawa, N., Suda, K., Boey, P. L. and Mahmood, W. A. K. (2003). Synthesis, crystal structure and spectroscopic study of para substituted 2-hydroxy-3-methoxybenzalideneanilines. *Journal of Molecular Structure*, 658(1–2): 87-99.
30. Brayton, D. F., Larkin, T. M., Vicic, D. A. and Navarro, O. (2009). Synthesis of A bis(phenoxyketimine) palladium(II) complex and its activity in the Suzuki-Miyaura reaction. *Journal of Organometallic Chemistry*, 694(18): 3008-3011.
31. Rosnizam, A. N., Hamali, M. A., Low, A. L. M., Youssef, H. M., Bahron, H. and Tajuddin, A. M. (2022). Palladium (II) complexes bearing N, O-bidentate Schiff base ligands: Experimental, in-silico, antibacterial, and catalytic properties. *Journal of Molecular Structure,* 1260: 132821.
32. Denmark, S. E., Smith, R. C. and Chang, W. T. T. (2011). Probing the electronic demands of transmetalation in the palladium-catalyzed cross-coupling of arylsilanolates. *Tetrahedron*, 67(24): 4391-4396.
33. Rufino-Felipe, E., Valdés, H. and Morales-Morales, D. (2022). C−S cross-coupling reactions catalyzed by well-defined copper and nickel complexes. *European Journal of Organic Chemistry*, *2022*(31): e202200654.

Malaysian Journal of Analytical Sciences (MJAS)
Published by Malaysian Analytical Sciences Society

FROM TRADITIONAL TO GREEN: EVOLUTION OF SHALE SWELLING INHIBITORS FOR SUSTAINABLE DRILLING

(Daripada Tradisional Ke Hijau: Evolusi Pencegahan Pembengkakan Syal Untuk Penggerudian Lestari)

Siti Qurratu' Aini Mahat[1*], Ismail Mohd Saaid[2], Arina Sauki[3], Agi Agustine Aja[1], Norida Ridzuan[1] and Norasyikin Ismail[1]

[1]*Faculty of Chemical and Process Engineering Technology, Universiti Malaysia Pahang Al-Sultan Abdullah, Lebuh Persiaran Tun Khalil Yaakob, 26300, Kuantan, Pahang, Malaysia*
[2]*Petroleum Engineering Department, Universiti Teknologi Petronas, 32610, Seri Iskandar, Perak, Malaysia*
[3]*School of Chemical Engineering, Universiti Teknologi MARA, 40450, Shah Alam, Selangor, Malaysia*

[*]*Corresponding author: sitiqurratu@umpsa.edu.my*

Received: 1 November 2023; Accepted: 11 March 2024; Published: 29 April 2024

Abstract

The occurrence of shale swelling during water-based drilling operations poses substantial challenges to the stability of shale formations. Clay layer expansion is the primary cause of shale swelling, which results from interactions between clay minerals and drilling fluid components. The degree of expansion is determined by variables such as clay composition, ion exchange processes, osmotic pressure, ionic strength, temperature, and pressure. Therefore, this study explores various shale swelling inhibitors and meticulously investigates the underlying mechanisms. The effectiveness of conventional inhibitors, such as potassium chloride (KCl), ammonium chloride (NH_4Cl), and amine-based inhibitors, is well-established. However, it is important to note that these inhibitors do have certain limitations. Hence, the present work investigates a range of environmentally friendly inhibitors, including graphene oxide, ionic liquids, deep eutectic solvents, nanoparticles, nanocomposites, and biosurfactants. Graphene oxide exhibits notable efficacy in mitigating shale swelling and producing extensive, unbroken protective coatings. Ionic liquids, represented by 1-butyl-3-methylimidazolium chloride (BMIMCl), have demonstrated enhanced inhibitory characteristics in comparison to KCl, resulting in a reduction in bentonite swelling rates by 19.38%. Furthermore, it has been observed that deep eutectic solvents (DESs), such as NADES, exhibit remarkable inhibitory characteristics, resulting in a 49.1-62.8% reduction in the rate of swelling in clay samples. Nanocomposites, which involve the integration of single-walled carbon nanotubes (SWCNTs) and polyvinylpyrrolidone (PVP), have demonstrated successful mitigation of shale swelling and regulation of fluid loss. Moreover, biosurfactants such as chitosan-grafted l-arginine, flaxseed protein (FP), and flaxseed mucilage (FM), have exhibited potential as shale inhibitors that are both biodegradable and environmentally friendly. These findings contribute to ongoing efforts to improve the environmental sustainability of drilling operations and adhere to rigorous environmental protection standards. Nevertheless, more investigation, refinement, and practical application analysis are needed before they can be widely used.

Keywords: water-based drilling fluid, shale formation, shale swelling, inhibitors, environmentally friendly

Abstrak

Kejadian pembengkakan syal semasa operasi penggerudian berasaskan air menimbulkan cabaran besar kepada kestabilan pembentukan syal. Pengembangan lapisan tanah liat adalah punca utama pembengkakan syal, yang terhasil daripada interaksi antara mineral tanah liat dan komponen bendalir penggerudian. Tahap pengembangan ditentukan oleh pembolehubah seperti komposisi tanah liat, proses pertukaran ion, tekanan osmotik, kekuatan ion, suhu, dan tekanan. Oleh itu, kajian ini meneroka pelbagai perencat pembengkakan syal dan menyiasat dengan teliti mekanisme asas. Keberkesanan perencat konvensional, seperti kalium klorida (KCl), ammonium klorida (NH_4Cl), dan perencat berasaskan amina, adalah mantap. Walau bagaimanapun, adalah penting untuk ambil perhatian bahawa perencat ini mempunyai batasan tertentu. Oleh itu, kajian ini menyiasat pelbagai perencat mesra alam, termasuk graphene oksida, cecair ionik, pelarut eutektik dalam, nanopartikel, nanokomposit dan biosurfaktan. Grafin oksida mempamerkan keberkesanan yang ketara dalam mengurangkan pembengkakan syal dan menghasilkan salutan pelindung yang luas dan tidak pecah. Cecair ionik, yang diwakili oleh 1-butil-3-metilimidazolium klorida (BMIMCl), telah menunjukkan ciri-ciri perencatan yang dipertingkatkan berbanding dengan KCl, mengakibatkan pengurangan kadar pembengkakan bentonit sebanyak 19.38%. Tambahan pula, telah diperhatikan bahawa pelarut eutektik dalam (DES), seperti NADES, mempamerkan ciri-ciri perencatan yang luar biasa, mengakibatkan pengurangan 49.1-62.8% dalam kadar bengkak dalam sampel tanah liat. Nanokomposit, yang melibatkan penyepaduan tiub karbon berdinding tunggal (SWCNTs) dan polivinilpirolidon (PVP), telah menunjukkan kejayaan pengurangan bengkak syal dan pengawalan kehilangan bendalir. Selain itu, biosurfaktan seperti kitosan yang dicampurkan bersama l-arginin, protein biji rami (FP), dan lendir biji rami (FM), telah mempamerkan potensi sebagai perencat syal yang boleh terbiodegradasi dan mesra alam. Penemuan ini menyumbang kepada usaha berterusan untuk meningkatkan kelestarian alam sekitar operasi penggerudian dan mematuhi piawaian perlindungan alam sekitar yang ketat. Namun begitu, lebih banyak penyiasatan, penghalusan, dan analisis aplikasi praktikal diperlukan sebelum ia digunakan secara meluas.

Kata kunci: cecair penggerudian berasaskan air, batuan syal, pembengkakan syal, perencat, mesra alam sekitar

Introduction

Oil drilling is a challenging industrial process for finding and extracting hydrocarbon resources such as crude oil and natural gas. It entails drilling a borehole or wellbore through the earth's crust to reach reservoirs containing these valuable resources. The fundamental goal of oil drilling is to extract these resources safely and efficiently for use in a variety of applications such as energy production, transportation, and petrochemical manufacturing. To facilitate this process, drilling fluids plays a pivotal role. Drilling fluids, often known as drilling muds, are multipurpose fluids that are essential to the oil and gas drilling industry. These specialty fluids are painstakingly designed to accomplish a variety of critical duties during the drilling operation. Drilling fluids operate as cooling and lubricating agents while the drill bit bores into the earth's crust, minimizing the adverse effects of heat and friction on the drill bit. At the same time, they efficiently transport the rock cuttings generated during drilling, preventing obstructions, and keeping a clear wellbore. Drilling fluids also play an important role in preserving wellbore stability by exerting hydraulic pressure on the wellbore walls, preventing the entrance of formation fluids, which could cause well control concerns and blowouts. By preserving the integrity of cuttings for examination, they enable geologists and geophysicists to examine subsurface formations. Additionally, drilling fluid density is altered to give the drill string buoyancy, preventing it from getting stuck in the wellbore and promoting efficient drilling operations. In addition, these fluids contain corrosion inhibitors to protect drilling equipment and minimize formation damage, making them essential to the oil and gas industry's pursuit of safe, efficient, and environmentally responsible drilling practices.

Essential to the oil and gas drilling process, drilling fluids comprise a wide variety of formulations tailored to specific well conditions. These fluids are divided into three primary categories. First, water-based drilling fluids use water as their primary base fluid, which is frequently combined with additives. These compounds, which may include clays, polymers, and salts, serve to improve the viscosity, lubrication, and shale inhibition properties of the fluid. Second, oil-based drilling fluids use oil as their base fluid. These fluids are highly valued for their resistance to high-temperature and high-pressure drilling environments and their ability to provide superior lubrication for the drill bit. Lastly, gas-based drilling fluids, such as air or nitrogen, employ gases as the base fluid. They excel in specific drilling

scenarios, such as excavating coalbed methane. The selection of drilling fluid type is influenced by geological formations, well conditions, and environmental factors, and selecting the optimal formulation is essential for optimizing drilling performance and ensuring wellbore stability [1]. Each type provides a distinct combination of ingredients and functions to address the difficulties encountered during drilling operations.

In addition to the three main categories of drilling fluids, there is another important category known as synthetic drilling fluids. Synthetic drilling fluids, also known as synthetic-based muds (SBMs), are composed of synthetic or man-made base fluids as opposed to conventional oil or water. These base fluids can include esters, olefins, and other hydrocarbons that are synthetic. Drilling operations benefit from several advantages when synthetic drilling fluids are used. They are highly stable at elevated temperatures, making them ideal for excavating in high-temperature environments, such as offshore deep wells. Additionally, synthetic fluids have excellent lubricating properties, reducing equipment wear and extending their lifespan. Moreover, they have less of an impact on the environment than oil-based lubricants because they do not contain crude oil. When drilling through sensitive formations where contamination from conventional drilling fluids could cause significant damage, synthetic drilling fluids are particularly advantageous [2]. Synthetic drilling fluids are a valuable option for optimizing drilling performance while mitigating environmental impact in certain drilling scenarios due to their adaptability, stability, and environmental benefits. However, synthetic drilling fluids can be more expensive than their conventional equivalents, which can impact their selection based on the budget and drilling conditions of a project.

Particularly when considering the sustainability and environmental impact of drilling operations, the significance of water-based drilling fluids which consist predominantly of water as their base fluid, has risen in popularity. As industry endeavors to reduce its carbon footprint and minimize drilling's environmental impact, water-based fluids have emerged as a sustainable solution. However, water-based drilling fluids present their own set of challenges particularly when drilling through shale formations, where problems such as shale swelling can compromise wellbore stability [3]. Shale formations are characterized by their high concentration of clay minerals, notably smectite and montmorillonite clay minerals, which are recognized for their swelling properties. When drilling fluids containing water meet clay minerals, the water is absorbed, causing the clay to expand. This expansion, also known as shale swelling, can exert pressure on the wellbore walls and result in a few problems. Increased pore pressure within the formation can result in wellbore instability, which can lead to wellbore expansion and other problems such as blocked pipe incidents, lost circulation, and decreased drilling efficiency. Inefficient cuttings conveyance may also exacerbate drilling challenges. To combat these issues, shale inhibitors or shale stabilizers are added to water-based drilling fluids by the drilling industry. These additives are designed to minimize the interaction between the drilling fluid and shale minerals, thereby reducing swelling and sustaining the stability of the wellbore.

Shale swelling inhibitors are chemical additives used to combat the swell of clay minerals in shale formations during drilling operations. Potassium chloride (KCl) and amine-based inhibitors are two popular types of traditional shale swelling inhibitors. KCl prevents clay swelling by increasing the ionic strength of the drilling fluid, thereby decreasing the water absorption capacity of clay minerals. On the other hand, amine-based inhibitors function by adsorbing onto clay surfaces and modifying their chemical properties to render them less susceptible to hydration. Although these inhibitors have historically played a role in sustaining the stability of the wellbore, they have significant limitations related to conventional drilling methods. The release of KCl and certain amine-based inhibitors can contaminate soil and water, raising environmental concerns about the sustainability of these conventional approaches. In addition, these inhibitors may not function optimally under high-temperature or high-pressure drilling conditions, restricting their applicability for modern unconventional resources. There is also limited compatibility with some drilling fluid formulations

containing polysaccharides or polyanionic cellulose, further reducing the scope of usable formulations. The high cost of these traditional inhibitors additionally influences selection criteria, driving demand for more affordable shale swelling options.

To mitigate these drawbacks, the industry has shifted focus toward more sustainable and environmentally friendly approaches that align with stringent environmental regulations. The "green criteria" for new shale swelling inhibitors place priority on reduced toxicity, biodegradability, and minimizing environmental impact. This context encompasses not only environmental sustainability but also improved performance and adaptability under diverse drilling conditions. Alternatives like Graphene Oxide (GO) demonstrate promise for reducing shale swelling with less risk of ecological damage. Ionic Liquids (ILs) boast superior inhibition properties and a lower environmental footprint compared to conventional options. Emerging solvents like Deep Eutectic Solvents (DESs) effectively prevent swelling. Furthermore, biosurfactants, nanomaterials, and natural biomolecules offer environmentally conscious solutions to promote wellbore stability with minimal toxicity.

Shale swelling mechanism

The enlargement of shale during drilling with water-based drilling fluids is a complex process governed by several interrelated factors. Shale swelling is triggered when shale is exposed to drilling fluid with a different chemistry that causes clay minerals to absorb and adsorb water [4]. This typically occurs when shale formations that were confined in situ underground at high stresses are excavated and exposed to surface conditions or water infiltration. At the molecular level, as pore waters and moisture infiltrate into the shale, water molecules first get attracted to and bonded to the surfaces of clay mineral particles like montmorillonite or illite. These clays have an affinity for water and the additional mass intake causes them to expand their layered structures. These interactions between water and clay minerals are crucial to the phenomenon of shale expansion [5]. According to Alcázar-Vara and Cortés-Monroy, shale swelling occurs in three distinct stages: stage 1: surface hydration and inter-crystalline swelling; stage 2: intra-crystalline swelling from moisture ingress between mineral layers and stage 3: osmotic swelling from diffused double-layer expansion [6].

When shale comes into contact with water, the first stage of swelling occurs through capillary absorption of the water into the pores between the clay mineral particles (inter-crystalline pores) as shown in Figure 1. This stage corresponds to inter-crystalline swelling. As the water molecules enter the pores, they become attached to the surface of the clay mineral particles through hydrogen bonding and other surface forces. In sodium montmorillonite clay, the water dipoles readily attach to the siloxane cavities exposed on the edges of the clay mineral layers, as well as to cations like Na^+ adsorbed on the surface. The affinity for water absorption depends on the specific surface area available for bonding and the nature of the interchangeable cations present. Cations like Ca^{2+} attract fewer water molecules than cations like Na^+. The absorbed water forms a hydration shell around the particles, forcing them apart and leading to volumetric expansion and inter-crystalline swelling. The rate and amount of swelling depend on factors like the permeability of the shale, the availability of surface area for water bonding, shale mineralogy, and cation exchange capacity. Tight shales with low permeability and surface area tend to absorb less water and swell less. Highly reactive shales containing montmorillonite as the predominant clay mineral, with high cation exchange capacity, tend to imbibe larger amounts of water and exhibit greater inter-crystalline swelling.

The second stage of swelling occurs as water penetrates between the layered structural packets within the clay mineral particles themselves, known as intra-crystalline swelling. This process is most significant in smectite group clay minerals like montmorillonite, where the layered packets are held together only by relatively weak van der Waals forces. For instance, in montmorillonite clay, water dipoles can penetrate between the 2:1 layered silicate sheets that make up its structure. The extent of penetration and separation of the sheets depends heavily on the exchangeable cations present. Sodium montmorillonite will hydrate extensively, with unlimited swelling possible as water freely enters the interlayer spaces. On the other hand,

calcium montmorillonite has limited swelling due to the stronger binding of Ca^{2+} ions holding the sheets more tightly together. The intrusion of water leads to an increase in the basal spacing between the stacked sheets and a many-fold volumetric expansion - the intra-crystalline swelling. The presence of even small amounts of swelling clays like montmorillonite in shale can result in substantial overall swelling behavior.

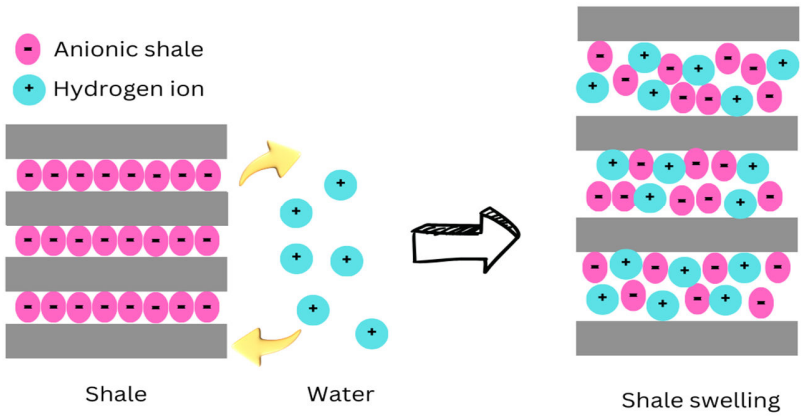

Figure 1. Surface hydration or inter-crystalline swelling

For the last stage, the introduction of water into the shale also induces osmotic pressure within the clay structure [7]. This osmotic pressure forces more water into the interlayer spaces, causing the clay layers to separate and swell. The degree of swelling increases as the osmotic pressure created by the drilling fluid rises, which is affected by variables including water content and salt concentration [8]. The ionic strength of the drilling fluid, which is determined by the concentration of salts such as potassium chloride (KCl) and calcium chloride ($CaCl_2$), can substantially influence the behavior of shale swelling [9]. The negatively charged surfaces of shale minerals attract positively charged ions or cations present in the drilling fluid. This exchange process results in the adsorption of cations onto the surfaces of clay minerals, which causes the clay strata to expand. Due to this, the distance between the strata grows, which contributes to the swelling effect [10]. Nevertheless, it was reported that higher salt concentrations in the drilling fluid somehow diminish the water's ability to permeate clay layers, thereby mitigating swelling to some extent [11]. Moreover, it was found that temperature and pressure also play a significant role in shale swelling. In a wellbore, elevated temperatures and pressures can intensify the absorption of water by shale minerals and the concurrent expansion of clay layers. These downhole conditions can have a significant effect on the amount of shale swelling encountered during drilling [12, 13]. Therefore, chemical inhibitors, such as surfactants or polymers, are frequently included in drilling fluid formulations to combat shale expansion issues. These shale inhibitors alter the surface properties of the shale, reduce water absorption, and prevent clay layers from expanding, as shown in Figure 2. By understanding the relevant factors, drilling engineers and fluid specialists can devise more effective strategies for combating shale swelling and preserving wellbore stability. It was concluded that the rate and magnitude of volume expansion depend on shale mineralogy, permeability to water, and pore pressures. This information guides the selection and formulation of drilling fluid additives intended to inhibit shale swelling. In addition, it permits the optimization of drilling parameters, such as temperature and pressure, to minimize the amount of edema encountered during operations. The ultimate objective is to improve drilling efficiency, reduce operational difficulties, and ensure the safety and integrity of wellbore systems. In addition, this understanding contributes to ongoing efforts in the oil and gas industry to develop environmentally sustainable drilling practices by minimizing the environmental impact of shale swelling and the use of drilling fluid

additives.

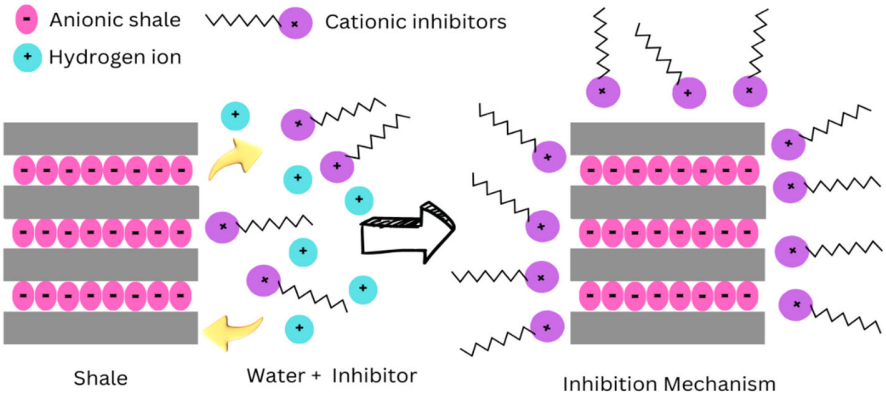

Figure 2. Shale inhibition mechanism by shale swelling inhibitors

Traditional shale swelling inhibitors

Potassium chloride (KCl) is the earliest and most extensively used shale swelling inhibitor for water-based drilling fluids. KCl inhibits the swelling of shale through an ion exchange mechanism. It does this by exchanging the Na^+ ions in the montmorillonite clay layers with K^+ ions that are weakly hydrated, as shown in Figure 3. This exchange of ions decreases the clay's affinity for water, preventing expansion and preserving the wellbore's integrity. Previously, it was found that by using KCl as the shale inhibitor, the activity of the drilling fluid increased, and the contact angles between the fluid and the shale increased, indicating a higher absorption rate [14]. According to the study, the ability of the drilling fluid to inhibit was inversely proportional to its ability to hydrate the surface. Osmotic hydration data showed that the shale had the lowest negative extreme swelling ratio with KCl, indicating its superior inhibitory effect, while the KCl drilling fluid displayed the highest surface adsorption rate. Moreover, another study found that KCl had an inhibitory effect on the mechanical properties of the samples, increasing their compressive strength and elastic modulus while decreasing their Poisson's ratio [15]. However, the results demonstrated that the clay content and presence of microcracks and bedding fissures in shale had a significant impact on the inhibitory effect of KCl on hydration. In addition, it was found that the relationship between KCl concentration and expansion rate is negatively exponential [16]. As the KCl concentration increased, the swelling rate decreased. When the concentration of KCl was 6%, the rate of swelling tended to be stable. The ultimate rate of swelling decreased from roughly 2% to 0.5% as shown in Figure 4. This high concentration increased the density of the drilling fluid, making it less suitable for use under specific drilling conditions.

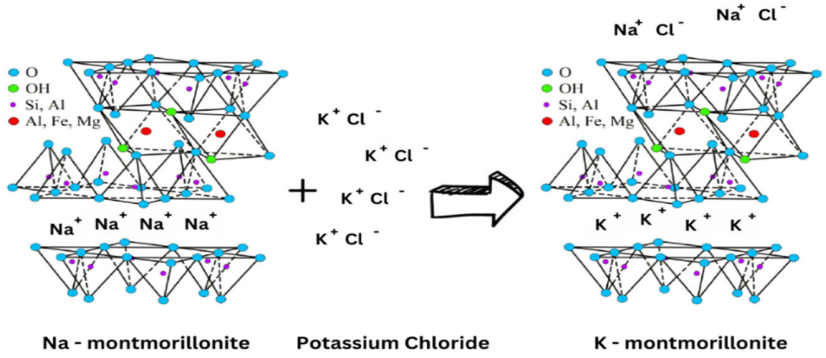

Figure 3. The replacement of Na^+ with K^+ within the montmorillonite structure

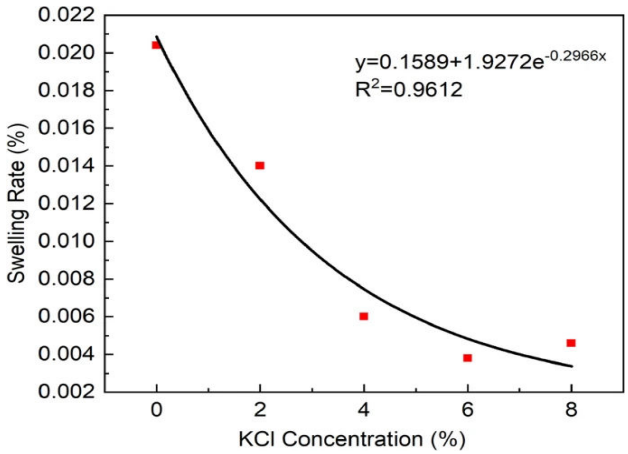

Figure 4. Final swelling rate of mudstone samples in relation to KCl concentration [16]

As a result of these limitations, various possible replacements for KCl have been investigated. Ammonium chloride (NH_4Cl), in contrast, functions as a shale inhibitor by facilitating the exchange of ammonium ions with the cations present on the surface of clays [17]. This ion exchange aids in preventing clay hydration and subsequent swelling. The NH_4^+ ion from NH_4Cl can replace Na^+ and other cations between the layers of the clay minerals. Since NH_4^+ has a lower hydration energy and tendency to attract water molecules compared to Na^+, the overall water uptake by the clay is reduced, thereby diminishing the swelling potential. According to a previous study, NH_4Cl is notably effective in stabilizing clays that are sensitive to potassium ions [18]. Moreover, NH_4Cl helps to establish an osmotic balance between the drilling fluid and the shale formation [19]. By controlling the water activity in the drilling fluid, the drive for water molecules to move into the shale and cause swelling is reduced. The presence of NH_4^+ ions also stabilized the clay structure by reducing the repulsive forces between the clay platelets [20]. This contributes to a reduction in the swelling and dispersion of the clays. Nevertheless, despite its benefits, the environmental impact of NH_4Cl, particularly its potential to contribute to eutrophication, and its corrosive nature are significant concerns. To surmount these issues, NH_4Cl is often used alongside corrosion inhibitors and advanced waste management techniques to minimize its environmental footprint.

The investigation of ammonium cations with similar hydration volumes to potassium ions (K^+) is a prominent strategy. This research led to the development of a variety of amine-based shale inhibitors, including polyetheramine, polyetherdiamine, polyvinylamine, and quaternary amine compounds. Amine-based shale inhibitors have emerged as a prospective alternative to potassium chloride (KCl) in water-based drilling fluids due to their ability to inhibit shale swelling effectively while mitigating some of the environmental concerns associated with KCl. Polyamines are particularly effective in inhibiting the swelling of smectite clays commonly found in shale formations. They work by adsorbing onto clay surfaces and neutralizing the charges that cause clay particles to repel each other and swell. In addition, amine-based inhibitors can inhibit shale at lower concentrations than KCl, which can aid in mitigating problems associated with drilling fluid density and disposal. Previously, the function of polyether amine as a shale inhibitor in the production of shale hydrocarbons has been studied [21]. The study demonstrated that the pH of polyether amine solution can influence its shale-inhibiting properties. Besides, it was found that polyether amine-derived bis-quaternary ammonium salt demonstrated superior shale inhibition performance compared to conventional stabilizers. The mechanism entails strong adsorption, an increase in hydrophobicity, and the reduction of clay particle repulsion by positive charges. This research provided an effective shale inhibitor, which is crucial for the efficient and sustainable development of shale gas and hydrocarbons. Moreover, the application of ammonium-

malic salts (AMS) as inhibitors for shale swelling has also been investigated [22]. The compound AMS-9, which was synthesized using malic acid and tetraethylenepentamine, demonstrated remarkable effectiveness in inhibiting the expansion of bentonite hydration. The addition of this substance resulted in a notable decrease in both the swelling and dispersion of bentonite within the water-based drilling fluid with the swelling rate dropping to 57.14% at a concentration of 0.5% AMS-9. According to this study, the inhibitory mechanism of AMS-9 on bentonite is likely attributed to the process of ion exchange between ammonium and Ca^{2+}, as well as the formation of hydrogen bonds and surface modifications. Furthermore, the potential of ammonium adipate solutions (AASs) as inhibitors for the phenomenon of shale swelling has also been studied [23]. The results showed that AAS-8 exhibited significant inhibitory effects on the hydration and swelling of clay. The substance exhibited the ability to regulate alterations in particle size inside bentonite and showed compatibility with additives such as carboxymethyl cellulose (CMC) and modified starch in water-based drilling fluids.

Nonetheless, the disposal of significant quantities of amine-containing drilling fluid can have negative environmental effects, including the disruption of ecosystems and the contamination of groundwater. In addition, certain amine compounds may have adverse effects on the rheological properties of the drilling fluid, which may affect drilling performance. Proper disposal procedures and monitoring are required to ensure that the use of amine-based inhibitors does not result in environmental contamination or damage to ecosystems. In response to the environmental and toxicity issues associated with amine-based inhibitors, there has been a growing interest in researching environmentally benign and low-toxicity shale inhibition alternatives over the past few years. As prospective shale inhibitors, researchers and industry are investigating various materials, including nanomaterials, ionic liquids, natural plant extracts, and other innovative compounds. These options seek to inhibit shale effectively while minimizing toxicity and environmental impact. The ongoing research in this area reflects a broader commitment to enhancing the environmental sustainability of drilling operations and conforming to more stringent environmental protection policies.

Green shale swelling inhibitors

Graphene oxide

Graphene oxide (GO) is a notable environmentally friendly shale swelling inhibitor that has garnered prominence in recent years. Graphene oxide is an oxidation of graphene that has demonstrated potential for mitigating shale expansion while minimizing environmental impact. In shale formations, GO particles readily adsorb onto shale clay mineral surfaces due to their hydrophilic groups and large area. Once adsorbed, the graphene oxide forms extensive hydrogen bonds and van der Waals forces, adhering tightly to the shale. This also allows the graphene oxide to act as a physical barrier that obstructs nano-sized pores and interlayer spacing between clay mineral platelets. By hindering water molecule intrusion, graphene oxide mitigates the swelling and dispersion of clay components. Additionally, graphene oxide imparts hydrophobicity to the shale surface, further diminishing the affinity of clays to hydrate and swell when contacting aqueous drilling fluids. Through this multipronged mechanism of physical obstruction of nanopores, hydrogen bonding, and hydrophobic modification, graphene oxide can effectively suppress shale swelling when used as an inhibitor additive. Significant reductions in shale swelling have been observed in various studies utilizing GO as a shale inhibitor, yielding encouraging results, as shown in Figure 5. The study demonstrated the ability to plug nano-sized pores, prevent water intrusion into shale, and prevent clay mineral swelling [24]. According to the findings of his study, GO exhibited superior performance to conventional inhibitors, forming a large, uninterrupted film to protect shale and adapting to various shale pore morphologies. Based on this foundation, glucopyranose-modified graphene (Glu-Gr) as a shale swelling inhibitor has also been studied [25]. The study revealed the exceptional dispersion recovery and inhibition durability of Glu-Gr, which surpasses conventional drilling mud. The mechanism of Glu-Gr, which is characterized by scanning electron microscopy (SEM) and X-ray diffraction spectroscopy (XRD), relies on establishing hydrogen bonds, physically obstructing clay nanopores, and preventing water penetration,

thereby diminishing shale swelling.

Moreover, *Janus amphiphilic* graphene oxide (JAGO) has also been used as a high-performance and dual-functionality shale swelling inhibitor [26]. It was found that the distinctive amphiphilic structure of JAGO, obtained by dodecylamine modification, has exceptional chemical inhibition and physical plugging properties. The effectiveness of JAGO derives from its capacity to adsorb onto clay surfaces, expel water molecules, and generate hydrophobic shields. In addition, choline chloride-modified graphene (Ch-G) has also been used as an eco-friendly and effective shale inhibitor [27]. The study demonstrated the inhibition mechanism, which includes hydrogen bonds, coordination, and electrostatic interactions with clay surfaces, thereby inhibiting shale expansion. Because of graphene's high performance, it has also been employed as a fluid additive [28, 29]. The use of silica nanoparticles (SiO_2-NPs) and graphene nanoplatelets (GNPs) as additives in drilling fluids exhibited synergistic effects, improving filtration properties, enhancing thermal stability, and increasing the fluid's ability to inhibit shale-related challenges. Collectively, these studies demonstrate the transformative potential of nanomaterial-based shale inhibitors, which offer innovative and environmentally friendly methods for ensuring wellbore stability in shale formations while minimizing environmental impact. While graphene oxide offers a novel approach to inhibiting shale swelling by physically blocking water absorption and chemically interacting with clay minerals, there remain significant economic and environmental challenges to its widespread adoption in the field. Research is ongoing to overcome the cost barriers, ensure environmental safety, and maintain operational stability and compatibility within drilling fluid systems. Through innovation and rigorous testing, the goal is to optimize the use of GO in drilling operations, harnessing its unique properties to enhance wellbore stability and efficiency.

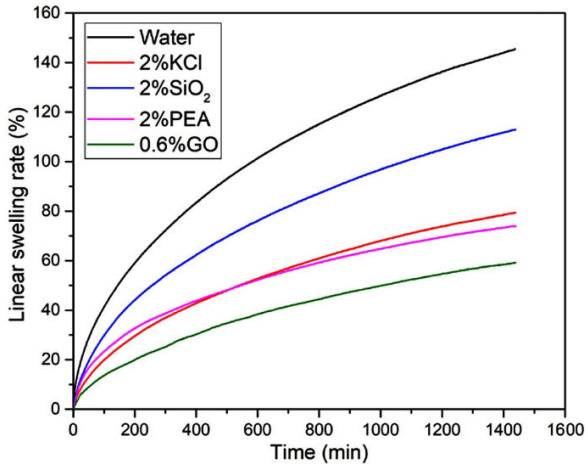

Figure 5. Linear swelling rate of Na-BT pellets in pure water, KCl, nano-SiO_2, PEA, and GO aqueous solutions [24]

Ionic liquids (ILs)

Aside from that, ionic liquids (ILs) have also emerged as an environmentally favorable option for reducing shale swelling in water-based drilling fluids. The mechanism by which ionic liquids inhibit shale swelling involves several interactions. They can replace water in the interlayer spaces of clay minerals through cation exchange, thus reducing the clay's ability to absorb water and swell. Additionally, the hygroscopic nature of ionic liquids can lower the activity of water in the drilling fluid, and their adsorption onto clay surfaces can alter the surface chemistry to further reduce swelling. In addition, ILs have garnered attention for their low toxicity and eco-friendly properties, making them a desirable option for sustainable drilling practices. Previously, the use of 1-butyl-3-methylimidazolium chloride (BMIMCl) as an inhibitor of clay expansion has been investigated [30]. It was found that BMIMCl exhibited superior inhibitory properties than the conventional stabilizer KCl, decreasing bentonite

swelling rates by 19.38%. FT-IR analysis confirms that this enhanced performance is due to the unique structure of BMIMCl, which features a hydrophilic head for adsorption on bentonite surfaces, hydrogen bonding, and a hydrophobic tail to create a water-repellent shield. Besides, the use of hydrophobic ILs in conjunction with gemini surfactants to prevent clay expansion has also been studied [31]. A novel combination of hydrophobic ionic liquid (trihexyltetradecyl phosphonium bis(2,4,4-trimethyl pentyl) phosphinate) and cationic gemini surfactant (GB) enhanced inhibition efficiency.

Contact angle measurements revealed a highly hydrophobic surface and linear swelling experiments indicate that the combined solution reduces bentonite swelling. This innovative technique improves wellbore integrity in drilling applications involving high temperatures. Besides, the used of multibranched ionic liquid (Trihexyltetradecyl phosphonium bis(2,4,4-trimethyl pentyl) phosphinate, Tpb-P) in water-based drilling fluid exhibited enhanced shale recovery and reduced linear swelling compared to conventional drilling fluids [32]. Contact angle measurements confirmed decreased shale surface hydrophilicity, and Tpb-P demonstrated the potential to maintain wellbore stability under high-temperature and high-pressure conditions. The results of these experiments demonstrated that the adsorption of ILs on clay minerals is dependent on their structure and concentration, leading to intercalation between clay layers. XRD analysis revealed increased basal spacing, implying IL intercalation, which was corroborated by FT-IR spectral data. The study provides insight into the inhibitory mechanisms and adsorption behavior of ILs on clay surfaces. Due to the unique properties of ILs, they have also been proposed as completion fluids to reduce formation damage. Moreover, experiments with core-flooding on confined sandstone formations with a high clay content demonstrated that completion fluids comprised of ionic liquids effectively stabilized clays, thereby preserving in-situ permeability [32]. These results indicated that completion fluids based on ionic liquids can be used for well completion without causing formation injury. This study was supported by using tetramethylammonium chloride (TMACl) and 1-ethyl-3-methylimidazolium chloride (EMIMCl). It was found that TMACl and EMIMCl ionic liquids outperformed the conventional inhibitor potassium chloride (KCl) [33]. TMACl exhibited superior inhibition due to its more positive charge, which facilitated adsorption and decreased clay enlargement. This study emphasized the importance of cationic and anionic components in ILs for shale inhibition.

SEM images revealed fewer cavities and a smoother clay surface when ILs were added, while XRD results indicated intercalation of ILs in clay layers. The type of anion also affected rheological properties, but clay swelling was not substantially affected. In comparison to a commercial clay inhibitor, ILs exhibited superior performance with fewer adverse effects on drilling fluid properties. These studies illuminate the diversity of ionic liquids and inhibitors, shedding light on their potential to revolutionize shale inhibition strategies, assure wellbore stability, and reduce environmental impact. Nevertheless, increasing the length of the alkyl chain increased the hydrophobicity of ILs, making it more challenging for ILs to minimize layer spacing and reduce water activity as shown in Figure 6.

Deep eutectic solvents (DESs)

Building upon the promising attributes of graphene and ionic liquids as environmentally benign swelling inhibitors for shale, numerous studies explore the effectiveness of deep eutectic solvents (DES) in a similar capacity. Deep Eutectic Solvents (DESs) are a class of fluids like ionic liquids but composed of a mixture of a hydrogen bond donor and a hydrogen bond acceptor, which can form a eutectic mixture with a melting point much lower than either of the individual components. DESs interact with clay minerals via solvation and ion exchange mechanisms, thereby decreasing the tendency of shale to swell. DESs can inhibit shale swelling effectively while exhibiting low toxicity and environmental impact. Previously, the novel deep eutectic solvent CU-DES as a potential shale inhibitor was studied [34]. From the study, it was seen that CU-DES exhibits remarkable inhibitory properties, outperforming conventional inhibitors such as KCl and PDA, especially at high temperatures (160°C). CU-DES substantially reduces the swelling rate of clay samples, increases the recovery of shale cuttings after hot-rolling,

and inhibits clay hydration and dispersion. Analytical techniques, such as particle size distribution measurement, Zeta potential measurement, SEM, FTIR, and XRD, demonstrated that CU-DES exerts its inhibitory effects via electrostatic attraction and hydrogen bonding with clay minerals. The findings of this study indicated that CU-DES is a prospective and cost-effective shale inhibitor for water-based drilling fluids, addressing wellbore instability issues. Recent research on DESs as shale swelling inhibitors has also been thoroughly studied [35].

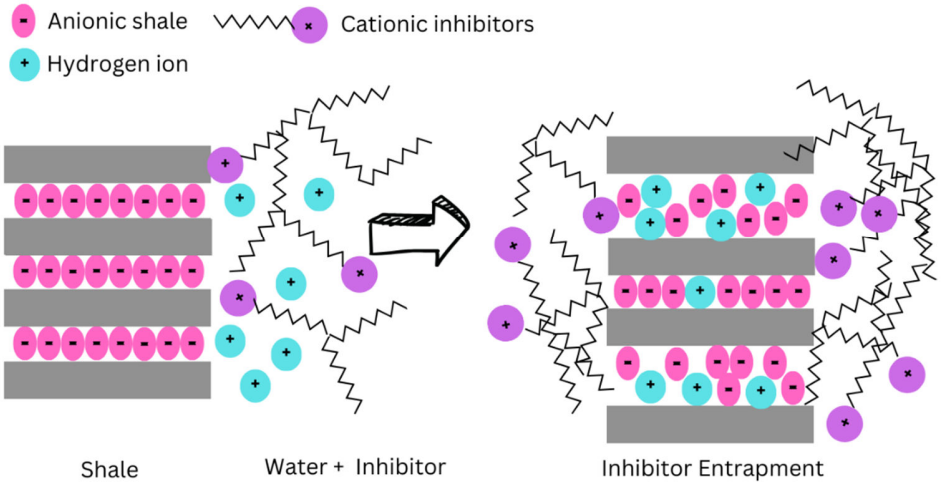

Figure 6. Inhibitor entrapment due to the length of the alkyl chain

Even at low concentrations, DESs exhibit extraordinary inhibitory performance, effectively reducing shale swelling. This study emphasizes the electrostatic attraction, hydrogen bonding mechanisms, and charge neutralization of clay surfaces. It highlighted the significance of comprehending DES-clay interactions for effective shale stabilization. As a drilling fluid adjuvant, a Natural Deep Eutectic Solvent (NADES) based on Epsom salt and glycerine was also introduced [36]. The results indicated that NADES significantly enhances the properties of drilling fluids. NADES reduces mudcake thickness by 26% and filtrate volume by 30.1% at a concentration of 1%. It inhibited the shale swelling by an impressive 49.14% due to hydrogen bonding and clay structure modification. The results of this study suggest that NADES could replace conventional inhibitors that are toxic and non-biodegradable. An extensive study using calcium chloride with NADES as a versatile drilling mud additive has also been done [37]. It was found that NADES improved mud rheology and inhibited hydrate formation by up to 80%, according to the findings. Moreover, it inhibited shale swelling by a remarkable 62.8% and enabled an 84.1% enhancement in shale recovery. These results are supported by surface tension, d-spacing, zeta potential, and FESEM analyses. This paper suggests that NADES is an environmentally favorable alternative to conventional additives, effectively addressing drilling operations' cost, biodegradability, and environmental impact issues. In comparison to conventional inhibitors, the results consistently demonstrate DES' superior inhibitory properties, cost-effectiveness, and environmental advantages. These results contribute to the advancement of environmentally sustainable drilling practices and highlight the need for additional research and optimization to realize their maximum potential in the industry.

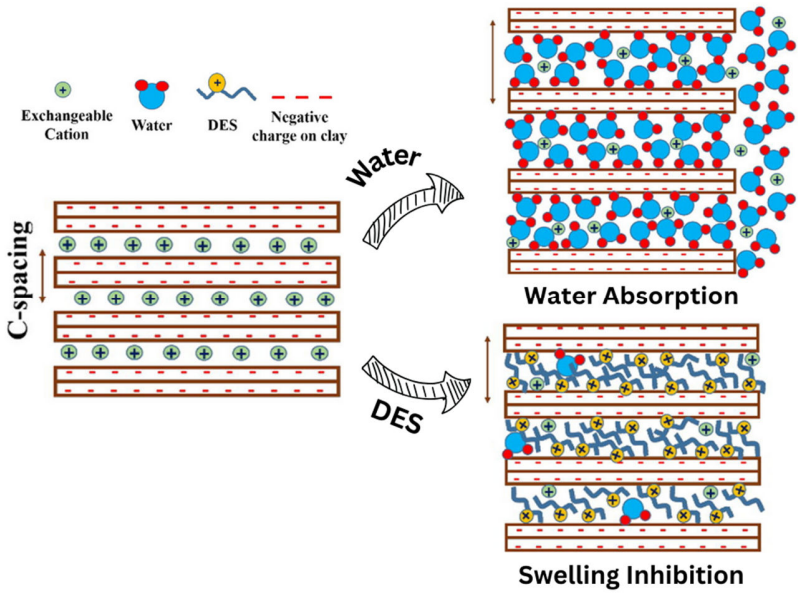

Figure 7. Shale swelling inhibition mechanism by using DES inhibitor [38]

Nanoparticles and nanocomposites

Similarly, numerous researchers have also conducted extensive studies on nanomaterials such as nanoparticles and nanocomposites. Nanoparticles and nanocomposites frequently perform their functions by adhering to clay surfaces and preventing water absorption. Figure 8 shows the surface of the shale sample using SEM. Their effectiveness in inhibiting shale swelling has been demonstrated, and their low environmental impact is encouraging. A novel method for enhancing the effectiveness of water-based drilling muds through the utilization of nanocomposites consisting of single-walled carbon nanotubes (SWCNTs) and polyvinylpyrrolidone (PVP) has been proposed [39]. The findings of their research demonstrated that the presence of 5-SWCNTs/PVP in the drilling fluid resulted in greater control of fluid loss and effectively reduced shale swelling. The combination of single-walled carbon nanotubes (SWCNTs) with polyvinylpyrrolidone (PVP) resulted in enhanced shale stability through the establishment of a protective barrier that effectively hindered the penetration of water. Additionally, the synergistic effect of ZnO nanoparticles and polymer additives in drilling fluids has also been investigated [40]. This study provided important insights into how the combination of these additives improves rheological properties, filtration control, and shale stability. The results indicated that this synergistic strategy significantly reduces shale swelling and enhances drilling fluid performance. Alternatively, the addition of two-dimensional nanoparticles, such as graphene and nanosheets, to water-based drilling fluids demonstrated that these nanomaterials significantly improve the rheological, viscoelastic, and filtration properties of drilling fluids while contributing to the stability of the wellbore [41]. In a recent study, the researchers examined the role of different nanoparticles in completion fluids [42]. The study specifically focused on the dual impact of these nanoparticles, which included both enhancing well stimulation and inhibiting clay swelling damage. The results of the study revealed that specific nanoparticles, specifically those possessing positive charges, could significantly enhance the mobility of crude oil and inhibit the swelling of clay. The study highlighted the importance of both the chemical composition and dosage of nanoparticles. Nevertheless, the necessity for further investigation to assess a broader range of nanoparticle categories and their performance in dynamic reservoir circumstances must be emphasized [43]. The study suggested delving deeper into the interactions between various nanoparticles and polymers to optimize their formulations for particular

downhole conditions. Therefore, to fully exploit the benefits of nanoparticles in drilling fluids, future research should strive to bridge the gap between laboratory experiments and actual drilling operations.

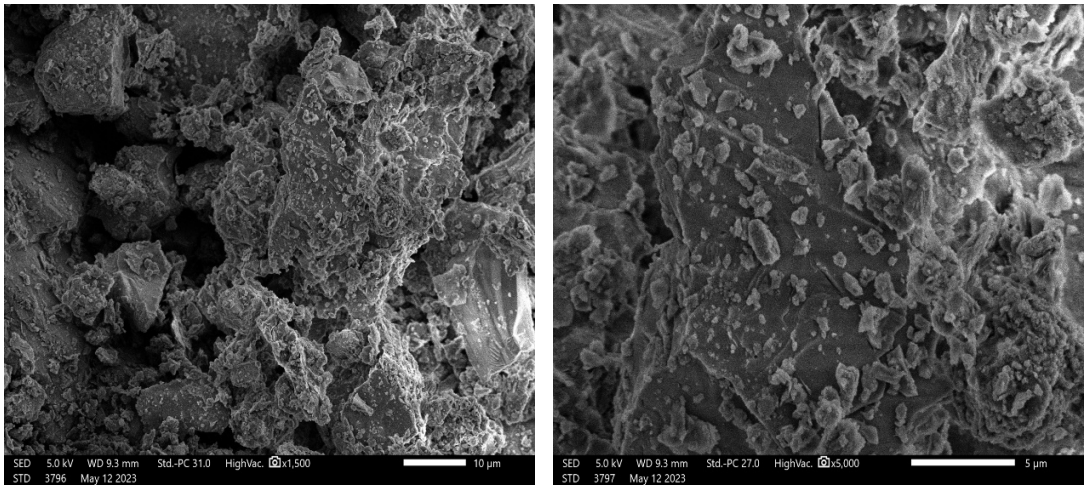

Figure 8. SEM images of the surface of shale taken at (a) 1500x resolution and (b) 5000x resolution

Biosurfactants

As eco-friendly shale inhibitors, biomolecules and biosurfactants derived from natural sources such as plants and microorganisms have been explored. Previously, a biodegradable and environmentally benign shale inhibitor based on chitosan-grafted l-arginine (CA) for shale formation was synthesized and used as a shale swelling inhibitor [44]. The results demonstrated that the inhibition of CA was superior to that of KCl, HPA, and SIAT, and that it can recover more than 90% of hot-rolled shale at 150 °C, indicating that CA has greater temperature resistance and prolonged durability. It was found that the positively charged CA effectively adhered to the surfaces of both MMT and shale, achieving multiple beneficial effects. It neutralized the negative charge associated with MMT, compacted the diffused electric double layer, and simultaneously enhanced the contact angle of both MMT and shale surfaces. This dual action resulted in an increased hydrophobicity of MMT and shale, effectively impeding their hydration enlargement and dispersion. Furthermore, compatibility experiments revealed that CA displayed compatibility with widely used treatment agents, demonstrating no impact on the rheology of water-based drilling fluids, and contributing to reduced fluid loss due to degradation.

Moreover, a fascinating investigation into the potential use of green and biodegradable surfactants, namely *Flaxseed Protein* (FP) and *Flaxseed Mucilage* (FM), as shale inhibitors in water-based drilling fluids has also been presented [45]. This research showed that these surfactants have the potential to reduce clay swelling and enhance drilling efficacy. The compatibility of these surfactants with salt (KCl) and their survivability under varying temperature conditions qualify them for further study. Nevertheless, the study suggests that future research should concentrate on optimizing the extraction methods to increase the yield and functionality of these surfactants, paving the way for more environmentally friendly drilling fluid additives. In addition, field-scale testing and compatibility evaluations with other drilling fluid components would shed light on the practical implementation of these surfactants in real-world drilling operations. Similarly, the feasibility of using Korean Red Ginseng root extract, rich in non-ionic surfactants, as a clay swelling inhibitor in water-based drilling muds has also been widely studied [46]. The research emphasized several distinctive properties of mud systems prepared with biosurfactants, including a low rheological profile, good sedimentation, and high recovery of shale cuttings. These characteristics demonstrated the efficacy of the biosurfactant in inhibiting clay swelling. The study also examined the

mechanisms underlying this inhibition, proposing that the biosurfactant produces a hydrophobic layer on clay surfaces, thereby decreasing water absorption and clay swelling. Optimizing the performance of the biosurfactant and investigating its potential as an environmentally friendly drilling fluid additive could be the focus of future research. Future research could entail scaling up the use of plant or food waste extract biosurfactants to assess their performance under field conditions. For practical applications, investigating its long-term stability and potential interactions with other drilling fluid additives would also be essential. Additionally, investigating cost-effective methods for obtaining the biosurfactant on a larger scale would make its industrial application more feasible.

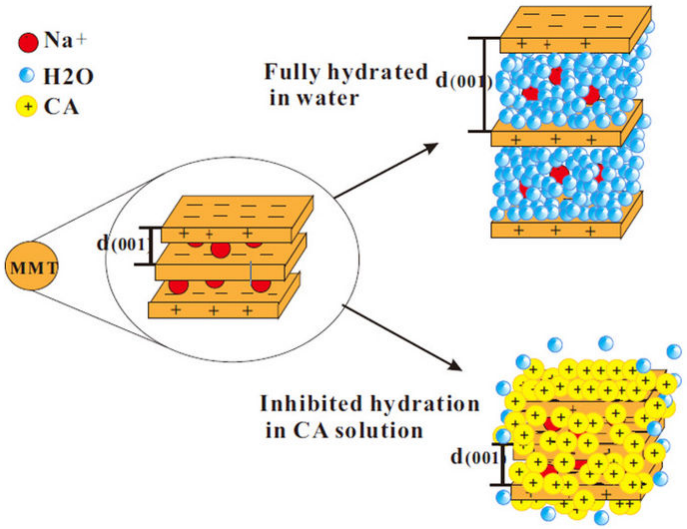

Figure 9. Inhibition mechanism of CA on shale surface [45]

Conclusion

In summary, the transition from conventional shale swelling inhibitors to environmentally friendly alternatives represent a significant paradigm shift within the drilling industry, highlighting the industry's commitment to conservation and environmental sustainability. Shale swelling, a common issue in drilling operations, is increasingly being handled using environmentally friendly inhibitors, which are replacing conventional options such as potassium chloride (KCl). The study has examined a range of environmentally friendly inhibitors, such as graphene oxide, ionic liquids, deep eutectic solvents, nanoparticles, nanocomposites, and biosurfactants. Graphene oxide, with its high surface area and functional groups, can interact with clay particles in shale to prevent water uptake. Ionic liquids and deep eutectic solvents (DESs) offer tunable properties that can be designed to reduce water activity and clay swelling without the environmental harm associated with inorganic salts like KCl. Nanoparticles and nanocomposites act at the nanoscale to block the pathways for water molecules or alter the surface chemistry of the clay minerals, preventing them from swelling. Biosurfactants, derived from biological processes, offer a biodegradable and less toxic alternative to traditional surfactants.

The transition to these greener inhibitors is not without challenges. There are concerns about cost, effectiveness under a range of geological conditions, potential health impacts, and long-term environmental effects. However, through ongoing research and development, improvements in these inhibitors are being made. Innovations in material science, chemistry, and engineering are leading to more effective and environmentally sustainable drilling practices. The use of environmentally friendly shale swelling inhibitors is a testament to the drilling industry's commitment to reducing its environmental footprint while still meeting global energy demand. By investing in these

technologies, industry not only adheres to stricter environmental regulations but also contributes to the broader goal of sustainable development. Attention may also turn to the life cycle analysis of these inhibitors to ensure their sustainability from production to disposal. Additionally, the integration of digital technologies like AI and machine learning could revolutionize the selection and application of swelling inhibitors by optimizing their performance in real time and predicting their behavior under various geological conditions. Furthermore, collaborative efforts between industry, academia, and regulatory bodies will likely be pivotal in establishing standardized protocols for the assessment and implementation of these green inhibitors.

Acknowledgments

The authors would like to acknowledge the Faculty of Chemical and Process Engineering Technology, Universiti Malaysia Pahang Al-Sultan Abdullah, and UMP Fundamental Grants (RDU 220376) for providing the funds and facilities to accomplish the experimental work for this research.

References

1. Ahmed, A. W., and E. Kalkan, E. (2019). Drilling fluids; Types, formation choice and environmental impact. *International Journal of Latest Technology in Engineering, Management & Applied Science,* 8(12): 66-71
2. Davoodi, S., Al-Shargabi, M., Wood, D. A., Rukavishnikov, V. S., and Minaev, K. M. (2024). Synthetic polymers: A review of applications in drilling fluids. *Petroleum Science*, 21(1): 475-518.
3. Li, Y., Xia, C., and Liu, X. (2023). Water-based drilling fluids containing hydrophobic nanoparticles for minimizing shale hydration and formation damage. *Heliyon*, 9(12): e22990.
4. Saleh, T. A. (2022). Advanced trends of shale inhibitors for enhanced properties of water-based drilling fluid. *Upstream Oil and Gas Technology*, 8: 100069.
5. Zhang, C., Gamage, R. P., Perera, M. S. A., and Zhao, J. (2017). Characteristics of clay-abundant shale formations: Use of CO_2 for production enhancement. *Energies*, 10(11): 1887.
6. Alcázar-Vara, L. A., and Cortés-Monroy, I. R. (2018). Drilling fluids for deepwater fields: An overview. *Recent Insights in Petroleum Science and Engineering*, InTech Publication.
7. Xianyu, Y., Jihua, C., Guosheng, J., Shuya, C., Ye, Y., Yanping, S., and Zhaohui, W. (2021). A method of determining osmotic pressure for low-clay shale with different salt ions considering effect of dynamic permeability on flow. *Engineering Geology*, 295: 106434.
8. Xianyu. Y, Zhenxiao, S., Yanping, S., Yangdong, P., Ye, Y., Shuya, C., Guosheng, J., and Jihua, C. (2018). Influence of salt solutions on the permeability, membrane efficiency and wettability of the Lower Silurian Longmaxi shale in Xiushan, Southwest China. *Applied Clay Science,* 158: 83-93.
9. Dankwa, O. K., Appau, P. O., and Broni-Bediako, E. (2018). Evaluating the effects of monovalent and divalent salts on the rheological properties of water based mud. *Open Petroleum Engineering Journal*, 11(1): 98-106.
10. Sun, C., Li, G., Sun, Y., He, J., and Rong, H. (2019). Modelling hydration swelling and weakening of montmorillonite particles in mudstone. *Processes,* 7(7): 428.
11. Al-Sarraf, H., Albazali, T., and Garrouch, A. (2022). Role of diffusion osmosis on the mechanical and petrophysical alterations of shale when interacting with aqueous solutions. *Geosystem Engineering,* 25(1-2): 13-24.
12. Yang, L., Lu, L., Li, X., Shan, Y., Mo, C., Sun, M., Hu, J., Liu, W., Liang, B., and Xu, J. (2023). Clay mineral transformation mechanism modelling of shale reservoir in Da'anzhai Member, Sichuan Basin, Southern China. *Frontier Earth Sci (Lausanne)*, 11: 1205849.
13. Liu, J., Yang, Z., Sun, J., Dai, Z., Lv, K., and Yo, Q. (2021). Experimental investigation on hydration mechanism of Sichuan shale (China). *Journal of Petroleum Science and Engineering*, 201: 108421.
14. Cao, H., Zhang, Z., Bao, T., Sun, P., Wang, T., and Gao, Q. (2019). Experimental investigation of the effects of drilling fluid activity on the hydration behavior of shale reservoirs in northwestern Hunan, China. *Energies (Basel)*, 12(16): 3151.
15. Shi, X., Wang, L., Guo, J., Su, Q., and Zhuo, X.

(2019). Effects of inhibitor KCl on shale expansibility and mechanical properties. *Petroleum*, 5(4): 407-412.
16. Chen, X., Yi, H., Gao, L., Shi, X., and Liu, Y. (2020). Effects of inhibitor KCl on hydration swelling and softening of a smectite-poor mudstone. *Journal of Petroleum Exploration and Production Technology*, 10(7): 2685-2692.
17. Wysocki, S., Gaczoł, M., and Wysocka, M. (2018). Drilling mud with addition of new hydration inhibitor for clay rocks', in *E3S Web of Conferences*, EDP Sciences, 7: 100013.
18. Lopez-Hernandez, D., Mahia-Masip, M., Melendez, W., and Lopez-Contreras, A. (2022). NH_4^+ Fixation and ionic competition with K^+ in a clayey soil from Ocumare Del Tuy, Venezuela. *Canadian Journal of Agriculture and Crops*, 7(2): 38-45.
19. Mo, S., Song, J., Lu, X., Chen, J., and He, L. (2010). The application of ammonium calcium chloride drilling fluid in the shale section in Sudan. *Engineering, Environmental Science, Geology,* 27(3): 47-50.
20. Chen, W. L., Grabowski, R. C., and Goel, S. (2022). Clay swelling: Role of cations in stabilizing/destabilizing mechanisms. *ACS Omega*, 7(4): 3185-3191.
21. Fu, L., Liao, K., Ge, J., He, Y., Huang, W., and Du, E. (2020). Preparation and inhibition mechanism of bis-quaternary ammonium salt as shale inhibitor used in shale hydrocarbon production. *Journal of Molecular Liquids*, 309:113244.
22. Zhang, R., Wang, X., Sun, Y., Zhang, J., Hu, W., Du, W., and Chen, G. (2020). Preparation and performance of ammonium-malic salts as shale swelling inhibitor and a mechanism study. *Inorganic and Nano-Metal Chemistry*, 50(10): 1027-1031.
23. Xian, S., Chen, S., Lian, Y., Du, W., Song, Z., and Chen, G. (2021). Preparation and evaluation of ammonium adipate solutions as inhibitors of shale rock swelling. *Minerals*, 11(9):1013.
24. Wang, K., Jiang, G., Li, X., and Luckham, P. F. (2020). Study of graphene oxide to stabilize shale in water-based drilling fluids. *Colloids and Surfaces A: Physicochemical and Engineering Aspects*, 606: 125457.
25. Rana, A., Arfaj, M. K., and Saleh., T. A. (2020). Graphene grafted with glucopyranose as a shale swelling inhibitor in water-based drilling mud. *Applied Clay Science*, 199:105806.
26. Lv, K., Huang, P., Zhou, Z., Wei, X., Luo, Q., Huang, Z., Yan, H., and Jia, H. (2020). Study of Janus amphiphilic graphene oxide as a high-performance shale inhibitor and its inhibition mechanism. *Frontiers in Chemistry*, 8: 201.
27. Zhu, H., Li, D., Zhao, X., Pang, S., and An, Y. (2022). A novel choline chloride/graphene composite as a shale inhibitor for drilling fluid and the interaction mechanism. *RSC Advances*, 12(47): 30328-30334.
28. Ma, J., Pang, S., Zhang, Z., Xia, B., and An, Y. (2021). Experimental study on the polymer/graphene oxide composite as a fluid loss agent for water-based drilling fluids. *ACS Omega*, 6(14): 9750-9763:
29. Aramendiz, J. and Imqam, A. (2020). Silica and graphene oxide nanoparticle formulation to improve thermal stability and inhibition capabilities of water-based drilling fluid applied to Woodford shale. *SPE Drilling and Completion*, 35(2): 164-179.
30. Ahmed Khan, R., Murtaza, M., Abdulraheem, A., Kamal, M. S., and Mahmoud, M. (2020). Imidazolium-based ionic liquids as clay swelling inhibitors: Mechanism, performance evaluation, and effect of different anions. *ACS Omega*, 5(41): 26682-26696.
31. Khan, R. A., Ahmad, H. M., Murtaza, M., Abdulraheem, A., Kamal M. S., and Mahmoud, M. (2021). Impact of multi-branched ionic liquid on shale swelling and hydration for high temperature drilling applications in *Proceedings of the SPE/IADC Middle East Drilling Technology Conference and Exhibition*, Society of Petroleum Engineers.
32. Khan, R. A., Tariq, Z., Murtaza, M., Kamal, M. S., Mahmoud, M., and Abdulraheem, A. (2022). Ionic liquids as completion fluids to mitigate formation damage. *Journal of Petroleum Science and Engineering*, 214:110564.
33. Rahman, M. T., Negash, B. M., Danso, D. K., Idris,

A., Elryes, A. A., and Umar, I. A. (2022). Effects of imidazolium- and ammonium-based ionic liquids on clay swelling: experimental and simulation approach. *Journal Petroleum Exploration Production Technology*, 12(7): 1841-1853.

34. Jia, H., Huang, P., Han, Y., Wang, Q., Jia, K., Sun, T., Zhang, F., Yan, H., and Lv, K. (2022). Investigation for the novel use of a typical deep eutectic solvent as a potential shale inhibitor. *Energy Sources, Part A: Recovery, Utilization and Environmental Effects*, 44(1): 1402-1415.
35. Sultana, K., Rahman, M. T., Habib, K., and Das, L. (2022). Recent advances in deep eutectic solvents as shale swelling inhibitors: A comprehensive review. *ACS Omega*, 7(33): 28723-28755.
36. Rasool, M. H. and Ahmad, M. (2023). Epsom salt-based natural deep eutectic solvent as a drilling fluid additive: A game-changer for shale swelling inhibition. *Molecules*, 28(15): 5784.
37. Rasool, M. H., Ahmad, M., Siddiqui, N. A., and Junejo, A. Z. (2023). Eco-friendly drilling fluid: Calcium chloride-based natural deep eutectic solvent (NADES) as an all-rounder additive. *Energies (Basel)*, 16(14): 5533.
38. Beg, M., Haider, M. B., Thakur, N. K., Husein, M., Sharma, S., and Kumar, R. (2021). Clay-water interaction inhibition using amine and glycol-based deep eutectic solvents for efficient drilling of shale formations. *Journal of Molecular Liquids*, 340: 117134.
39. Rana, A., I. Khan, A., Ali, S., Saleh, T. A., and Khan, S. A. (2020). Controlling shale swelling and fluid loss properties of water-based drilling Mud via ultrasonic impregnated SWCNTs/PVP nanocomposites. *Energy and Fuels*, 34(8): 9515-9523.
40. Ahmad, H. M., Iqbal, T., Al Harthi, M. A., and Kamal, M. S. (2021). Synergistic effect of polymer and nanoparticles on shale hydration and swelling performance of drilling fluids. *Journal of Petroleum Science and Engineering*, 205: 108763.
41. Zamora-Ledezma, C., Narváez-Muñoz, C., Guerrero, V. H., Medina, E., and Meseguer-Olmo, L. (2022). Nanofluid formulations based on two-dimensional nanoparticles, their performance, and potential application as water-based drilling fluids. *ACS Omega*, 7(24): 20457-20476.
42. López, D., Chamat, N. M., Galeano-Caro, D., Páramo, L., Ramirez, D., Jaramillo, D., Cortés, F. B., and Franco, C. A. (2023). Use of nanoparticles in completion fluids as dual effect treatments for well stimulation and clay swelling damage inhibition: an assessment of the effect of nanoparticle chemical nature. *Nanomaterials*, 13(3): 388.
43. Abdullah, A. H., Ridha, S., Mohshim, D. F., Yusuf, M., Kamyab, H., Krishna, S., and Maoinser, M. A. (2022). A comprehensive review of nanoparticles: Effect on water-based drilling fluids and wellbore stability. *Chemosphere*, 308: 136274.
44. Ma, J., Yu, P., Xia, B., An, Y., and Wang, Z. (2019). Synthesis of a biodegradable and environmentally friendly shale inhibitor based on chitosan-grafted l-arginine for wellbore stability and the mechanism study. *ACS Applied Bio Materials*, 2(10): 4303-4315.
45. Fakhari, N., Bing, C. H., Bennour, Z., and Gholami, R. (2023). Green and biodegradable surfactant based shale inhibitors for water based fluids. *Journal of Molecular Liquids*, 371: 121106.
46. Ghasemi, M., Moslemizadeh, A., Shahbazi, K., Mohammadzadeh, O., Zendehboudi, S., and Jafari, S. (2019). Primary evaluation of a natural surfactant for inhibiting clay swelling. *Journal of Petroleum Science and Engineering*, 178: 878-891.

Malaysian Journal of Analytical Sciences (MJAS)
Published by Malaysian Analytical Sciences Society

PHYSICOCHEMICAL CHARACTERIZATION OF ZnO/G-C_3N_4 FOR PHOTO-REMOVAL OF METHYL ORANGE UNDER LOW UV-LIGHT INTENSITY

(Pencirian Fizikokimia ZnO/g-C_3N_4 untuk Penyingkiran Metil Oren di Bawah Lampu UV Berkeamatan Rendah)

Nurul Izzati Izhar[1], Zul Adlan Mohd Hir[1,2*], Hartini Ahmad Rafaie[3] and Shaari Daud[1]

[1]*Faculty of Applied Sciences, Universiti Teknologi MARA Pahang, 26400 Bandar Tun Abdul Razak Jengka, Pahang, Malaysia*
[2]*Catalysis for Sustainable Water and Energy Nexus Research Group, School of Chemical Engineering, College of Engineering, Universiti Teknologi MARA, 40450 Shah Alam, Selangor, Malaysia*
[3]*Centre of Foundation Studies, Universiti Teknologi MARA, Selangor Branch, Dengkil Campus, 43800 Dengkil, Selangor, Malaysia*

[*]*Corresponding author: zuladlan@uitm.edu.my*

Received: 14 September 2023; Accepted: 12 February 2024; Published: 29 April 2024

Abstract

UV light-active photocatalyst of ZnO/g-C_3N_4 was synthesized by a facile mixing method with different ratio of g-C_3N_4 (0.01, 0.03, 0.05, 0.07, and 0.09 g). The photocatalytic activity of ZnO/g-C_3N_4 was tested towards methyl orange (MO) dye in aqueous solution using a low UV light intensity (7W). FTIR spectroscopic results obtained show the functional groups spectrum corresponding to the ZnO and g-C_3N_4. Besides, SEM results also show the formation of heterogenous photocatalysts as irregular shape particles of ZnO interlink with g-C_3N_4 surface. EDX analysis confirms the presence of Zn, C, O, and N elements correspond to ZnO/g-C_3N_4 photocatalyst. From the results obtained, ZG3 (0.1:0.03) photocatalysts exhibit almost complete removal of methyl orange under UV irradiation in a period of 60 min (~95%). The highest degradation rate constant of 5.26×10^{-2} min^{-1}, based on pseudo-first-order kinetics is estimated. The best photocatalyst (ZG3) showed high potential in degrading MO under low UV light intensity which can be used for photocatalytic water remediation application.

Keywords: g-C_3N_4, methyl orange, photocatalysis, UV light, ZnO

Abstrak

Fotomangkin cahaya UV-aktif ZnO/g-C_3N_4 telah disintesis dengan kaedah pencampuran mudah dengan nisbah g-C_3N_4 yang berbeza (0.01 g, 0.03 g, 0.05 g, 0.07 g dan 0.09g). Aktiviti fotomangkin ZnO/g-C_3N_4 telah diuji terhadap pewarna metil oren (MO) dengan menggunakan cahaya UV berkeamatan rendah (7W). Analisa FTIR spektroskopik yang diperoleh menunjukkan spektrum kumpulan berfungsi yang sepadan dengan ZnO dan g-C_3N_4. Selain itu, analisa SEM juga menunjukkan pembentukan fotomangkin heterogen ZnO sebagai zarah bentuk tidak sekata ZnO bersaling paut dengan permukaan g-C_3N_4. Analisa EDX mengesahkan kehadiran unsur Zn, C, O dan N sepadan dengan fotomangkin ZnO/g-C_3N_4. Melalui keputusan yang diperoleh, fotomangkin ZG3 (0.1:0.03) menunjukkan penyingkiran hampir lengkap pewarna metil oren di bawah penyinaran UV dalam tempoh 60 minit (~93%). Pemalar kadar degradasi yang tertinggi adalah 5.26×10^{-2} min^{-1} berdasarkan kinetik pseudo-tertib pertama telah dianggarkan. Fotomangkin terbaik (ZG3) menunjukkan potensi yang tinggi untuk degradasi MO dibawah keamatan cahaya UV

yang rendah yang boleh digunakan untuk aplikasi pemulihan air fotomangkin.

Kata kunci: g-C_3N_4, metil oren, fotokatalisis, cahaya UV, ZnO

Introduction

Since the last few decades, industrialization, technologies, and consumption of non-renewable resources have grown at a rapid pace, owing to the constant increase in demand for textile, dye, fertilizer, domestic, and plastic materials. As a result, environmental pollution and energy crises have already reached alarming proportions. Industrial wastes are more toxic and nonbiodegradable than municipal wastes because they contain fats, oil, grease, heavy metals, phenols, and ammonia, among other things [1]. The negative effects of these pollutants on human and wildlife reproductive health have become a major source of public concern [2]. Though since traditional wastewater treatment methods aren't designed to remove toxic organic pollutants, these toxins have ended up in aquatic life, where they can subsequently make their way into the human food chain [3].

In the fight against the accumulation of organic wastes in the environment and aquatic life, heterogeneous semiconductor photocatalysis has been proposed as an effective method of removing this pollution. Zinc oxide (ZnO) is a semiconductor metal oxide and widely regarded as the most potential photocatalytic materials for the abatement of pollutant in water. It has a wide bandgap of 3.37 eV, good mechanical, thermal, and chemical stability, nontoxic, cost-efficient, and can also absorb a large portion of the light spectrum (UV/solar) [4–6]. However, the photo-corrosion of pure ZnO caused by the photoinduced holes is found to be severe during the reaction, which could affect the stability and photocatalytic activity of ZnO [7]. Furthermore, the rapid recombination of photoinduced electrons and holes limits its practical application due to its weak photocatalytic activity. Several initiatives, such as metal doping, have been made to enhance its charge separation efficiency and prevent photo-corrosion [8], as well as non-metal doping [9], and heterojunction formation [10].

Recently, graphitic carbon nitride (g-C_3N_4) has proved to be a promising candidate to form heterojunctions with ZnO [11, 12]. The material in question is a metal-free, n-type polymeric semiconductor with a narrow bandgap of 2.7 eV that could provide a viable solution to increase charge separation [13]. Previous research has revealed that the heterostructure formation and synergistic interaction between ZnO and g-C_3N_4 continue to improve photocatalytic activity. Ismael, for example, synthesized ZnO/g-C_3N_4 using a simple calcination process, and the photocatalytic enhancement was attributed to an increase in the quantity of the surface hydroxyl group [11]. Alternately, Le et al. synthesized ZnO/mesoporous g-C_3N_4 using a hard-templating technique, which then discovered that those composite photocatalysts exhibited remarkable photocatalytic activity due to effective charge carrier separation at the heterojunction interfaces [14]. The charge recombination rate can be reduced with an appropriate band alignment, resulting in improved high electron transfer and increased photocatalytic activity. However, not many studies proposed the photocatalytic activity of ZnO through n-n heterojunction with g-C_3N_4 under low UV light intensity. Accordingly, an improved surface area and visible light absorption capacity of the g-C_3N_4-ZnO composite resulted in more active sites, photogenerated electron-hole pairs, and a lower frequency of photo-induced charge recombination, all of which improved the photoactivity potential [12]. On the other hand, the band adjustment at the interface was responsible for the type-II heterojunction formation and the subsequent charge transfer process from g-C_3N_4 to ZnO at the interface [15]. Direct addition of g-C_3N_4 to ZnO nanocomposite results in a decrease in crystalline size, an increase in optical bandgap, and a modification in nanocomposite morphology. When compared to pure ZnO, g-C_3N_4 significantly improves the photocatalytic performance of g-C_3N_4@ZnO nanocomposites under visible light irradiation [16].

In this work, ZnO/g-C_3N_4 composite photocatalysts were synthesized by a simple mixing approach with the use of commercially available ZnO and dicyanamide as the precursor for g-C_3N_4. By only changing the mass of g-C_3N_4, a variety of composites with various ratios were created. Utilizing X-ray diffraction (XRD), scanning

electron microscopy (SEM), energy dispersive spectroscopy (EDX), and Fourier transform infrared (FTIR), we looked at the structural, morphological, surface compositions, and functional groups of the ZnO/g-C_3N_4 photocatalysts. In order to assess the photocatalytic activity of ZnO/g-C_3N_4 under low UV light intensity (7 W), the probe molecule methyl orange (MO) dye was chosen. Grafting of non-metal materials like g-C_3N_4 onto a wide bandgap ZnO photocatalyst could be an alternative strategy to prepare a stable and efficient photocatalyst for water remediation process.

Materials and Methods

Materials

Commercial zinc oxide (ZnO, 99%) and dicyanamide ($C_2H_4N_4$, 99%) were purchased from Sigma-Aldrich (Selangor, Malaysia). Methyl orange dye was obtained from Bendosen Laboratory Chemicals (Selangor, Malaysia). All chemicals were used as received and deionized water was used throughout the experimental procedures.

Preparation of g-C_3N_4

Dicyandiamide (0.1 mol) was dissolved in a deionized water (50 mL) and magnetically stirred for 1 hour. Next, the solution was dried in the oven at 80 °C overnight, followed by calcination in a muffle furnace at 500 °C for 2 hours (heating rate: 5°C/min) in a close crucible. The obtained yellow powder of g-C_3N_4 was grounded and stored for later use.

Preparation of ZnO/g-C_3N_4 composite photocatalyst

ZnO/g-C_3N_4 composite photocatalyst was prepared by mixing the two materials through different mass ratios of g-C_3N_4. First, 0.01g of previously prepared g-C_3N_4 was mixed with 0.10g ZnO and dispersed in a deionized water (50 mL) with continuous stirring for 1 h. The collected light-yellow sample was dried in the oven at 80 °C overnight and labelled as ZG1. The same procedure was repeated with different masses of g-C_3N_4. The composition of the prepared photocatalysts is presented in Table 1.

Table 1. Compositions for the preparation of ZnO/g-C_3N_4

Photocatalyst	ZnO (g)	g-C_3N_4 (g)
ZG1	0.10	0.01
ZG3	0.10	0.03
ZG5	0.10	0.05
ZG7	0.10	0.07
ZG9	0.10	0.09

Physicochemical characterization of ZnO/g-C_3N_4 composite photocatalyst

The XRD patterns were recorded using a powder X-ray diffractometer (XRD6000, Shimadzu) with Cu Kα radiation (λ = 1.540 Å, 30 kV, and 30 mA) in the *2θ* range of 10–70° with a scanning speed of 2°/min. The structural and elemental compositions were characterized using a scanning electron microscope equipped with an electron dispersive X-ray analyzer (SEM-EDX, TESCAN VEGA3). The presence of functional groups in the ZnO/g-C_3N_4 photocatalysts were analyzed by Fourier transform infrared (FT-IR) between 4000 to 500 cm^{-1} on a Perkin Elmer Infrared Spectrometer.

Photocatalytic evaluation of ZnO/g- C_3N_4 composite photocatalyst

The calibration plot of the selected pollutant methyl orange (MO) dye in aqueous solution under normal condition was carried out prior to the photocatalytic activity. The calibration curve was plotted based on different concentrations of the selected pollutant ranging from 5 to 25 mg/L. The linear equation was calculated from this calibration plot by measuring the absorbance of each sample at maximum wavelength (λ_{max} = 464 nm). Figure 1 shows the photodegradation of methyl orange in aqueous solution in a 250 mL glass photoreactor with a low intensity of UV-C light (7 W). A preliminary test which is photolysis was done on MO without the addition of photocatalyst to determine that no degradation of MO occurs when irradiated with low-intensity UV light. The system received a predetermined

amount of the powder photocatalyst. To assure the presence of dissolved oxygen in the solution, the photoreactor was then constantly supplied with air at a flow rate of 4 L/min. First, the working solution was agitated for 30 minutes in the absence of light to achieve adsorption-desorption equilibrium. The solution was then exposed to UV light for 60 minutes while being continuously stirred. The liquid (5-10 mL) was collected at predefined time intervals and filtered to remove the photocatalyst and the concentration left was monitored using a Perkin Elmer UV–vis spectroscopy (UV-2550, Shimadzu). In this study, the percentage of degradation was calculated using Equation (1) [17].

$$\text{Percentage of degradation (\%)} = \left[\frac{(C_t - C_0)}{C_0}\right] X\ 100\% \quad (1)$$

where C_o is the concentration of pollutant before irradiation and C_t is the concentration of pollutant at 't' min.

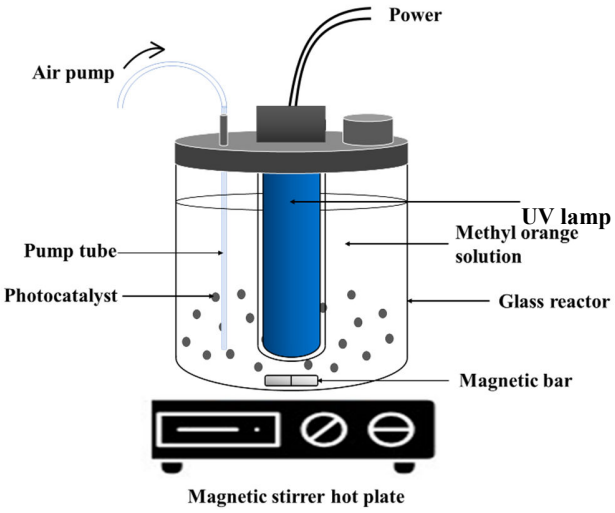

Figure 1. Schematic illustration of photoreactor set up for degradation of MO dye in aqueous solution using ZnO/g-C_3N_4 composite photocatalyst

The kinetics of the MO degradation by the prepared photocatalysts was studied based on the Langmuir–Hinshelwood (L–H) kinetic model using the following equation:

$$r = \left(\frac{dC}{dt}\right) = k_{obs}C \quad (2)$$

which can be rewritten as

$$ln\left(\frac{C_o}{C_t}\right) = k_{obs}t \quad (3)$$

where r is the reaction rate, k_{obs} is the rate constant (min^{-1}), and C_o and C_t are the concentration (mg/L) of MO initially and at different irradiation times, respectively.

Results and Discussion

Physicochemical characterization of ZnO/g-C_3N_4 composite photocatalyst: XRD analysis

The XRD patterns of pure g-C_3N_4, pure ZnO, and ZnO/g-C_3N_4 composite photocatalysts are shown in Figure 2. The pure g-C_3N_4 pattern (Figure 2a) shows some peaks as the (002) lattice planes' most strong peak, which corresponds to the interplanar stacking peak of conjugated aromatic rings, is identified at 28.16° [18–20]. The peak of 13.27° locates (100) lattice plane attributed to the in-plane structural repeating unit of N-bridged tri-s-triazine [18, 21]. In the meantime, ZnO's typical diffraction peaks are found at 31.78°, 34.40°, 36.25°, 47.54°, 56.58°, 62.82°, 67.94°, and 69.04°, with corresponding crystal indices of (100), (002), (101), (102), (110), (103), (200), (112), (201), and (202)

(Figure 2b), indicating that ZnO is the wurtzite as confirmed from the standard (JCPDS card 36–1451) [22, 23]. Next, the samples of ZG composite photocatalysts exhibit associated diffraction peaks for ZnO and g-C_3N_4 (Figure 2c-g). The presence of g-C_3N_4 diffraction peaks becomes more noticeable as the content of g-C_3N_4 was increased up to 0.09 g. It can be clearly observed that the ZG7 and ZG9 composite exhibits two-phase compositions of both ZnO and g-C_3N_4, as demonstrated by their diffraction peaks and the absence of any further peaks (Figure 2f and g). Comparing all composite photocatalysts to pure ZnO and pure g-C_3N_4, the positions of the distinctive peaks are often unchanged. This demonstrates that the ZnO/g-C_3N_4 combination has no effect on the stability of the lattice structures of individual ZnO and g-C_3N_4 [24].

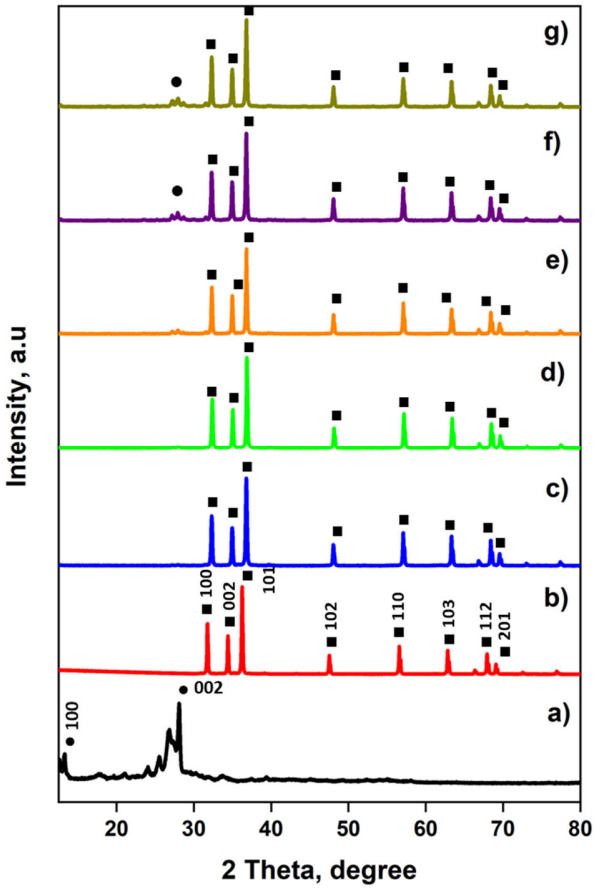

Figure 2. XRD patterns of a) pure g-C_3N_4, b) pure ZnO, c) ZG1, d) ZG3, e) ZG5, f) ZG7 and g) ZG9 photocatalysts

SEM-EDX analysis

Scanning electron microscopy (SEM) was used to examine the morphology of the prepared photocatalysts. At a magnification of 2000x, the photocatalyst images are noticed. The SEM morphology for pure ZnO, pure g-C_3N_4, and ZnO/g-C_3N_4 composite photocatalysts with various ratio compositions are shown in Figure 3. Pure ZnO reveals that it is made up of agglomerated and irregularly shaped particles (Figure 3a). It was previously reported that pure g-C_3N_4 depicted shape of irregular sheet-like meanwhile other researcher reported that pure g-C_3N_4 showed layered morphology and this is consistent with the results obtained in this study; pure g-C3N4 has a sheet-like surface and layered structure (Figure 3b) [25, 26]. Figure 3c)–d) depicts the morphology of ZnO/g-C_3N_4 composites with various g-C_3N_4 compositions. Figure 3c-g shows that ZnO are dispersed across the graphitic carbon nitride (g-C_3N_4)

surface, which helps the two phases form a heterojunction, improving charge transfer and separation as well as the photocatalytic activity of the composites [27]. This demonstrates the interactions between ZnO and g-C_3N_4 at the interface, which could help with internal electron migration to the photocatalyst surface and the effective separation of photoinduced excited photons [26].

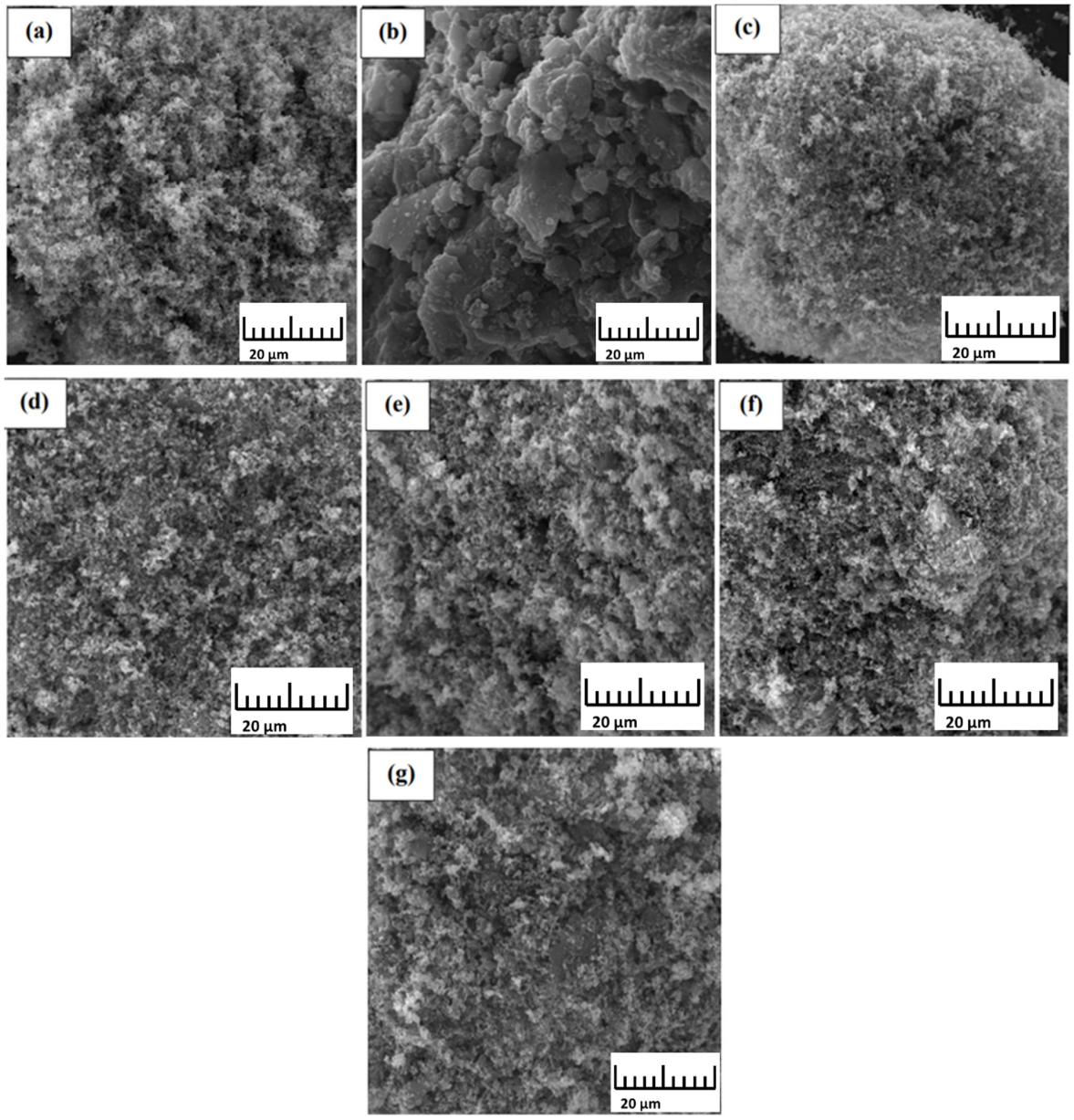

Figure 3. SEM images of (a) pure ZnO, (b) pure g-C_3N_4, (c) ZG1, (d) ZG3, (e) ZG5, (f) ZG7, and (g) ZG9

The EDX study was conducted to support the results from the SEM examination and to further confirm the presence of ZnO and g-C_3N_4 in the ZnO/g-C_3N_4 composite photocatalyst. The existence of zinc, carbon, oxygen, and nitrogen has been established for the ZG1 and ZG9 photocatalyst, confirming the composition of ZnO/g-C_3N_4, as illustrated in Figure 4a) and 4b) below.

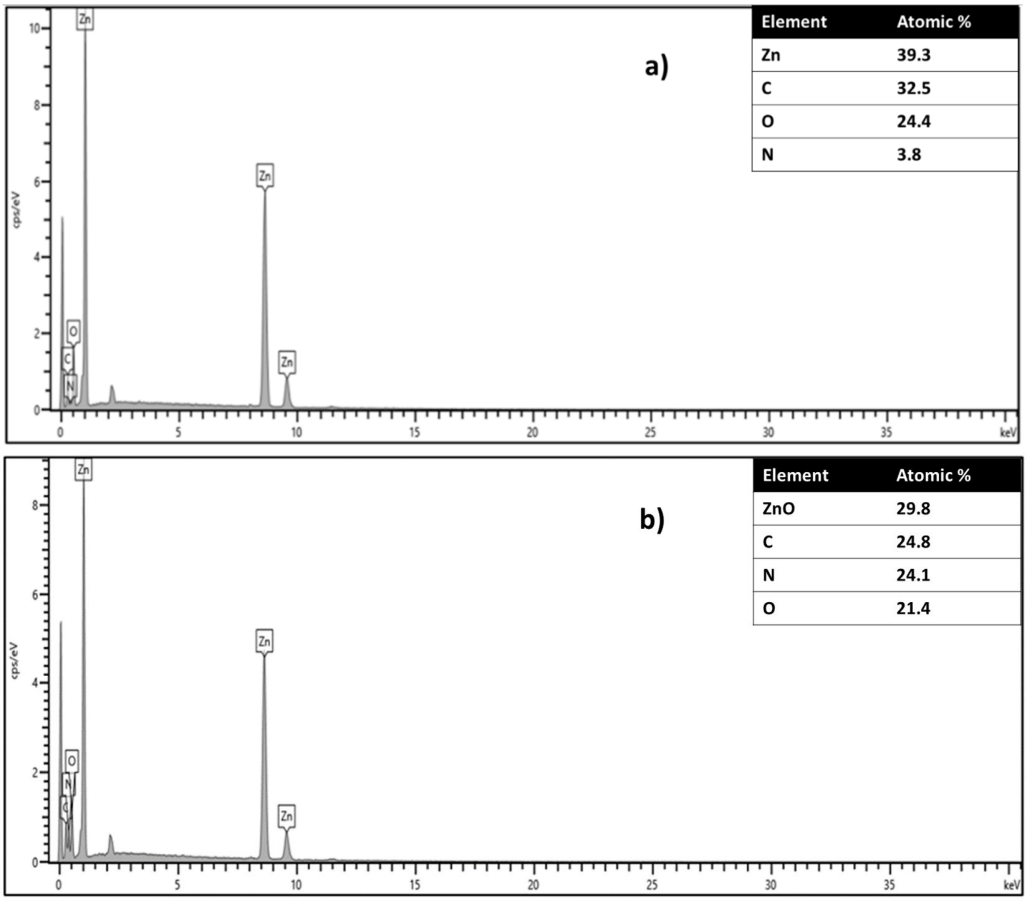

Figure 4. EDX analysis of a) ZG1, and b) ZG9

FTIR analysis

The distinct functional groups and chemical bonds present in the pure ZnO, pure g-C_3N_4, and ZnO/g-C_3N_4 composite photocatalysts were determined using the Fourier transform infrared spectroscopy (FTIR) analysis (Figure 5). From the spectrum, Zn-O bond vibrational modes can be detected in the band at the 560.80 cm^{-1} region. It is also possible to see a peak at 3348.90 cm^{-1}, which indicates the existence of a hydroxyl group in the ZnO component resulting from water molecules adhering to the oxide's surface [28]. The prepared g-C_3N_4 exhibits peaks between 1240 and 1640 cm^{-1} that indicates the presence of C_3N_4 heterocycle stretching modes. While aromatic C-N stretching vibration modes are responsible for the peak at 1463.47 cm^{-1}, C=N stretching is represented by the peak at 1613.81 cm^{-1} [29]. The triazine units of g-C_3N_4 have out-of-plane bending vibration modes that are associated to the peak at 797.32 cm^{-1} area [12]. Additionally, the N-H stretching modes are responsible for the absorption peak at 3098.56 cm^{-1}, which is between 2900 and 3400 cm^{-1} [15]. The spectrum of the ZnO/g-C_3N_4 composite photocatalyst are similar to the main peaks of g-C_3N_4, indicating that the component's structure was preserved even after combining with ZnO (subset a) and b) of Figure 5). Plus, the characteristics peaks of ZnO can also be seen in the spectrum because of its high content in the photocatalyst (subset c) of Figure 5). Moreover, the conjugated system of the g-C_3N_4 is stretched because the band red-shifted and the band strengths also diminished [30]. Thus, a broader conjugated system is generated between the ZnO and g-C_3N_4 [30]. The interfacial interaction between the ZnO and g-C_3N_4 will improve the photocatalytic performance as it will enable the transportation of photoinduced charges [26].

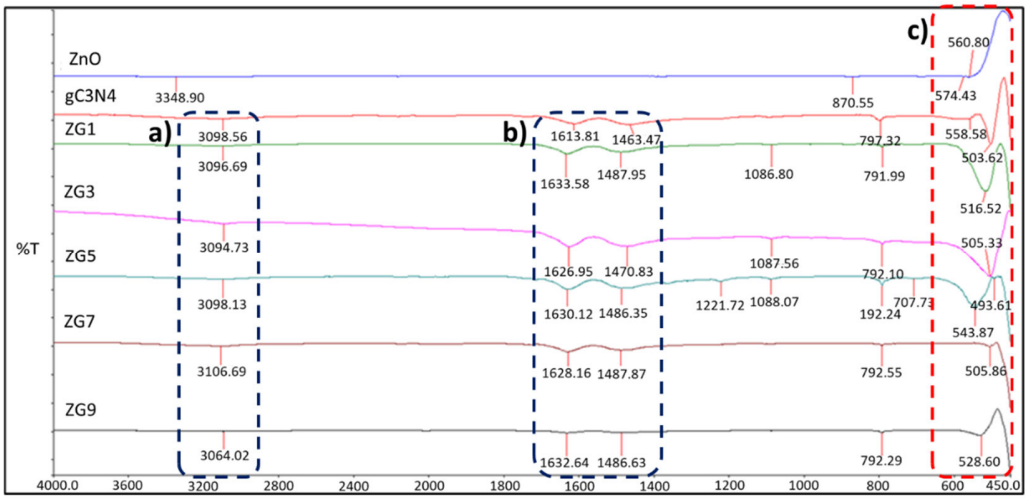

Figure 5. FTIR spectra of all prepared photocatalysts

Photocatalytic performance of ZnO/g-C_3N_4 photocatalyst

The photocatalytic degradation of MO dye by pure ZnO, pure g-C_3N_4, and ZnO/g-C_3N_4 composite photocatalysts with varied mass ratios is shown in Figure 6a). According to preliminary investigations, no degradation of MO was found throughout the photolysis process, indicating that MO was stable against UV light irradiation, with a negligible effect. In 60 minutes, pure ZnO shows 2.2 times the percentage of degradation greater than pure g-C_3N_4 (33%). In degrading MO, all generated ZnO/g-C_3N_4 composite photocatalysts demonstrate a higher percentage of degradation than pure ZnO (Figure 5a). Interestingly, with a maximum percentage of degradation of 95%, the ZG3 photocatalyst with a ratio of 0.1:0.03 is shown to be the best. It can be seen that the photocatalytic activity and degradation rate increase with an increasing amount of g-C_3N_4 up to 0.03g. As previously reported, the heterojunction that formed between ZnO and g-C3N4 is what led to the improved photocatalytic activity [11], [31–33]. However, as the g-C_3N_4 percentage increase (> 0.03), the photocatalytic activity and degradation rate falls dramatically due to the presence of aggregated particles, which lowers the surface area and light absorption capacity of the composite photocatalysts. When subjected to UV light, the photocatalyst may not function as well due to the reduced capacity of the photoinduced electrons to transfer electrons from ZnO to the g-C_3N_4 surface [34]. These results reveal the fact that there is a limitation to the amount of g-C_3N_4 that can be integrated into the ZnO surface without negatively impacting the percentage of degradation and the rate of deterioration. Therefore, ZG3 contains the appropriate ratio for the degradation of MO dye when exposed to low intensity of UV light irradiation. Given the strong synergistic interactions between ZnO and g-C_3N_4, it is clear that both elements are crucial for the enhanced photocatalytic activity.

As depicted in Figure 6b), the degradation of MO follows pseudo first-order kinetics. Likewise, the degradation percentage, the ZG3 has the greatest rate constant of 5.26 x 10^{-2} min^{-1} and, as a result, the highest rate of MO deterioration. Table 2 shows the degradation percentage and pseudo first-order kinetics for all produced photocatalysts.

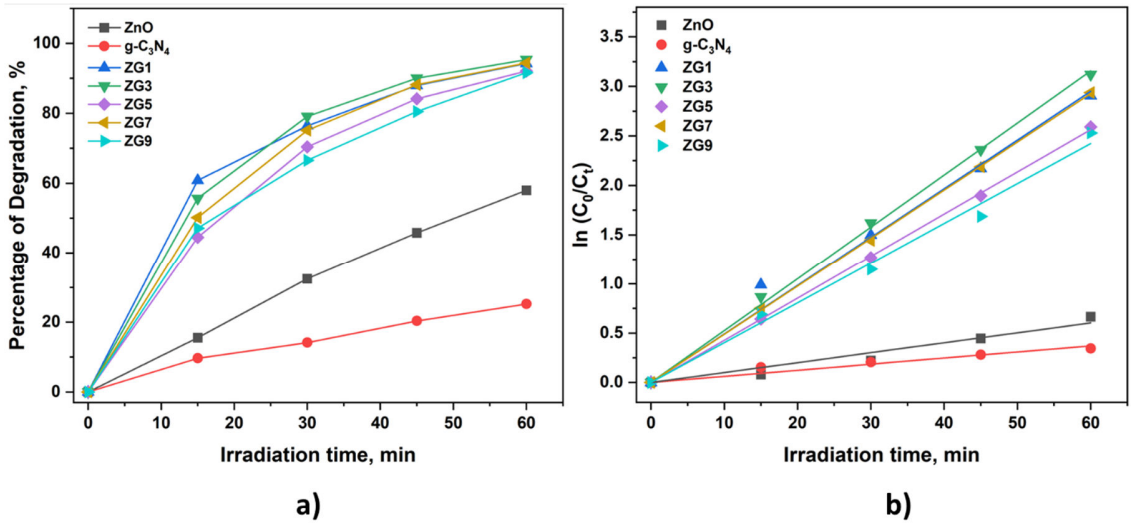

Figure 6. a) Degradation percentages and b) kinetics of the degradation of MO by all prepared photocatalysts

Table 2. Percentage of degradation and pseudo first-order kinetic for all prepared photocatalysts

Photocatalyst	Percentage of Degradation (%)	Rate Constant, K_{obs} (min^{-1}) × 10^{-2}	Rate (mg/L ·min)	Correlation Factor, R^2
Pure ZnO	57.97	1.01	0.1038	0.9782
Pure g-C_3N_4	25.20	0.62	0.0637	0.9809
ZG1	94.23	4.92	0.5057	0.9958
ZG3	95.35	5.26	0.5407	0.9995
ZG5	92.10	4.27	0.4389	0.9999
ZG7	94.41	4.88	0.5016	0.9999
ZG9	91.60	4.04	0.4153	0.9964

Conclusion

A simple mixing method was used to prepare the ZnO/g-C_3N_4 composite photocatalyst, resulting in an efficient photocatalytic removal of methyl orange (MO) dye under low UV light intensity. The findings demonstrate that the synthesized photocatalysts showed aggregated semi-spherical ZnO particles interlink with g-C_3N_4 surface. This can aid in achieving effective charge separation and lowering the rate of recombination of photoinduced charge carriers. Since ZG3 had the best photocatalytic performance which displayed ~95% photodegradation efficiency in a period of 60 min compared to other photocatalysts, it had the optimal ratio of ZnO and g-C_3N_4 contents. Overall, this research not only offers a different approach to construct ZnO/g-C_3N_4 photocatalysts through heterostructure synthesis, but also encourages simple and inexpensive processing methods.

Acknowledgements

The authors would like to thank the Ministry of Higher Education (MOHE) for financial supports under the Fundamental Research Grant Scheme (FRGS) (Project Number: FRGS/1/2021/STG05/UITM/02/17), Turn Thesis to Paper Research Grant (GT2P)(Project Number: 600-TNCPI 5/3/DDN (06) (014/2023), Universiti Teknologi MARA (UiTM) Pahang and UiTM Shah Alam for the services and facilities to carry out the laboratory work.

References

1. Mutamim, N. S. A., Noor, Z. Z., Hassan, M. A. A.,

and Olsson, G. (2012). Application of membrane bioreactor technology in treating high strength industrial wastewater: a performance review. *Desalination,* 305: 1-11.

2. Ohore, O. E., and Zhang, S. (2019). Endocrine disrupting effects of bisphenol A exposure and recent advances on its removal by water treatment systems. A review. *Scientific African,* 5: e00135.
3. Balabanič, D., Rupnik, M. and Klemenčič, A. K. (2011). Negative impact of endocrine-disrupting compounds on human reproductive health. *Reproduction, Fertility and Development,* 23(3): 403-416.
4. Kumar, S., Dhiman, A., Sudhagar, P., and Krishnan, V. (2018). ZnO-graphene quantum dots heterojunctions for natural sunlight-driven photocatalytic environmental remediation. *Applied Surface Science,* 447: 802-815.
5. Qi, K., Cheng, B., Yu, J., and Ho, W. (2017). Review on the improvement of the photocatalytic and antibacterial activities of ZnO. *Journal of Alloys and Compounds,* 727: 792-820.
6. Pullagurala, V. L. R., Adisa, I. O., Rawat, S., Kim, B., Barrios, A. C., Medina-Velo, I. A., ... and Gardea-Torresdey, J. L. (2018). Finding the conditions for the beneficial use of ZnO nanoparticles towards plants-A review. *Environmental Pollution,* 241: 1175-1181.
7. Zhou, J., Zhang, M., and Zhu, Y. (2014). Preparation of visible light-driven gC 3 N 4@ ZnO hybrid photocatalyst via mechanochemistry. *Physical Chemistry Chemical Physics,* 16(33): 17627-17633.
8. Rafaie, H. A., Nor, R. M., Azmina, M. S., Ramli, N. I. T., and Mohamed, R. (2017). Decoration of ZnO microstructures with Ag nanoparticles enhanced the catalytic photodegradation of methylene blue dye. *Journal of Environmental Chemical Engineering,* 5(4): 3963-3972.
9. Roza, L., Fauzia, V., Rahman, M. Y. A., Isnaeni, I., and Putro, P. A. (2020). ZnO nanorods decorated with carbon nanodots and its metal doping as efficient photocatalyst for degradation of methyl blue solution. *Optical Materials,* 109: 110360.
10. Mousa, H. M., Alenezi, J. F., Mohamed, I. M., Yasin, A. S., Hashem, A. F. M., and Abdal-Hay, A. (2021). Synthesis of TiO_2@ ZnO heterojunction for dye photodegradation and wastewater treatment. J*ournal of Alloys and Compounds,* 886: 161169.
11. Ismael, M. (2020). The photocatalytic performance of the ZnO/g-C_3N_4 composite photocatalyst toward degradation of organic pollutants and its inactivity toward hydrogen evolution: the influence of light irradiation and charge transfer. *Chemical Physics Letters,* 739: 136992.
12. Paul, D. R., Gautam, S., Panchal, P., Nehra, S. P., Choudhary, P., and Sharma, A. (2020). ZnO-modified g-C_3N_4: a potential photocatalyst for environmental application. *ACS Omega*, 5(8): 3828-3838.
13. Mukhair, H., Abdullah, A. H., Hir, Z. A. M., Osman, N. S., Zainal, Z., and Ngee, L. H. (2023). In-depth investigation on the photostability and charge separation mechanism of Ag_3PO_4/g-C_3N_4 photocatalyst towards very low visible light intensity. *Journal of Molecular Liquids,* 376: 121494.
14. Le, S., Jiang, T., Li, Y., Zhao, Q., Li, Y., Fang, W., and Gong, M. (2017). Highly efficient visible-light-driven mesoporous graphitic carbon nitride/ZnO nanocomposite photocatalysts. *Applied Catalysis B: Environmental,* 200: 601-610.
15. Bayan, S., Gogurla, N., Midya, A., and Ray, S. K. (2016). White light emission characteristics of two dimensional graphitic carbon nitride and ZnO nanorod hybrid heterojunctions. *Carbon,* 108: 335-342.
16. Luu Thi, L. A., Neto, M. M., Van, T. P., Nguyen Ngoc, T., Nguyen Thi, T. M., Nguyen, X. S., and Nguyen, C. T. (2021). In situ g-C_3N_4@ ZnO nanocomposite: one-pot hydrothermal synthesis and photocatalytic performance under visible light irradiation. *Advances in Materials Science and Engineering,* 2021: 1-10.
17. Hir, Z. A. M., Alam, N. M. F. H. N. B., Shaari, A. S., and Rafaie, H. A. (2022). One-pot sol-gel synthesis of a zinc oxide-reduced graphene oxide composite: Photocatalysis and kinetics studies using a fuzzy inference system. *Malaysian Journal Chemistry,* 24(2): 37-46.
18. Zhao, Z., Wang, X., Shu, Z., Zhou, J., Li, T., Wang, W., and Tan, Y. (2018). Facile preparation of

hollow-nanosphere based mesoporous g-C3N4 for highly enhanced visible-light-driven photocatalytic hydrogen evolution. *Applied Surface Science,* 455: 591-598.

19. Si, Y., Sun, Z., Huang, L., Chen, M., and Wu, L. (2019). A "ship-in-a-bottle" strategy to fabricate highly crystallized nanoporous graphitic C_3N_4 microspheres under pressurized conditions. *Journal of Materials Chemistry A*, 7(15): 8952-8959.
20. Li, Y., Yang, M., Xing, Y., Liu, X., Yang, Y., Wang, X., and Song, S. (2017). Preparation of carbon-rich g-C_3N4 nanosheets with enhanced visible light utilization for efficient photocatalytic hydrogen production. *Small,* 13(33): 1701552.
21. Lia, J., Wang, Y., Li, X., GaO, Q., and Zhang, S. (2021). A facile synthesis of high-crystalline g-C_3N_4 nanosheets with closed self-assembly strategy for enhanced photocatalytic H_2 evolution. *Journal Alloys Compounds*, 881: 1-9.
22. Cai, J., Zhang, A., Tao, H., Li, R., Han, J., and Huang, M. (2022). In situ growth TiO_2 nanoparticles on mxene (Ti_3C_2) decorated with nio quantum dots for enhanced photocatalytic performance. *SSRN*, 2022: 4045349.
23. Chen, Z., Fang, Y., Wang, L., Chen, X., Lin, W., and Wang, X. (2021). Remarkable oxygen evolution by Co-doped ZnO nanorods and visible light. *Applied Catalysis B: Environmental,* 296: 120369.
24. Li, L., Sun, S. Q., Wang, Y. X., and Wang, C. Y. (2018). Facile synthesis of ZnO/g-C_3N_4 composites with honeycomb-like structure by H_2 bubble templates and their enhanced visible light photocatalytic performance. *Journal of photochemistry and photobiology A: Chemistry*, 355: 16-24.
25. Ma, X., Huo, X., Hao, K., Song, L., Yu, Q., Liu, T., and Wang, Z. (2021). Visible light driven VO_2/g-C_3N_4 Z-scheme composite photocatalysts for selective oxidation of DL-1-phenylethyl alcohol under Vis-LEDs irradiation and aerobic oxidation. *ChemistrySelect,* 6(9): 2101-2110.
26. Alfaifi, M. Q. and Bagabas, A. A. (2019). Preparation, characterization, and application in water purification of gC_3N_4/I-TiO_2 composite photocatalysts. *Advance Material Sciences,* 4: 1-10.
27. Ismael, M. (2020). The photocatalytic performance of the ZnO/g-C_3N_4 composite photocatalyst toward degradation of organic pollutants and its inactivity toward hydrogen evolution: the influence of light irradiation and charge transfer. *Chemical Physics Letters,* 739: 136992.
28. Goulart, L. A., Alves, S. A., and Mascaro, L. H. (2019). Photoelectrochemical degradation of bisphenol A using Cu doped WO_3 electrodes. *Journal of Electroanalytical Chemistry,* 839: 123-133.
29. Brasileiro, I. L. O., Madeira, V. S., Lopes-Moriyama, A. L., and de Almeida Ramalho, M. L. R. (2023). Addition of g-C_3N_4 to ZnO and $ZnFe_2O_4$ to improve photocatalytic degradation of emerging organic pollutants. *Ceramics International,* 49(3): 4449-4459.
30. Zhu, Y. P., Li, M., Liu, Y. L., Ren, T. Z., and Yuan, Z. Y. (2014). Carbon-doped ZnO hybridized homogeneously with graphitic carbon nitride nanocomposites for photocatalysis. *The Journal of Physical Chemistry C*, 118(20): 10963-10971.
31. Sundaram, I. M., Kalimuthu, S., and Ponniah, G. (2017). Highly active ZnO modified g-C_3N_4 nanocomposite for dye degradation under UV and visible light with enhanced stability and antimicrobial activity. *Composites Communications,* 5: 64-71.
32. Yang, P., Wang, J., Yue, G., Yang, R., Zhao, P., Yang, L., ... and Astruc, D. (2020). Constructing mesoporous g-C_3N_4/ZnO nanosheets catalyst for enhanced visible-light driven photocatalytic activity. *Journal of Photochemistry and Photobiology A: Chemistry,* 388: 112169.
33. Garg, R., Gupta, R., and Bansal, A. (2021). Synthesis of g-C_3N_4/ZnO nanocomposite for photocatalytic degradation of a refractory organic endocrine disrupter. *Materials Today: Proceedings,* 44: 855-859.
34. Sun, J. X., Yuan, Y. P., Qiu, L. G., Jiang, X., Xie, A. J., Shen, Y. H. and Zhu, J. F. (2012). Fabrication of composite photocatalyst gC_3N_4–ZnO and enhancement of photocatalytic activity under visible light. *Dalton Transactions,* 41(22): 6756-6763.

Malaysian Journal of Analytical Sciences (MJAS)
Published by Malaysian Analytical Sciences Society

PHYSICOCHEMICAL STUDY ON ALKOXYLATED AZO-IMINE CHITOSAN-BASED BIOPOLYMER FOR ELECTROLYTE APPLICATIONS

(Kajian Fizikokimia ke atas Biopolimer Alkoksi Azo-Imina Berasaskan Kitosan bagi Aplikasi Elektrolit)

Tuan Siti Fatimah Tuan Mohd Pauzi[1], Rafizah Rahamathullah[1*], M. N. Hafiza[2], Wan M. Khairul[3]

[1]*Faculty of Chemical Engineering & Technology, Universiti Malaysia Perlis, 02600 Arau, Perlis, Malaysia*
[2]*Faculty of Maritime Studies, Universiti Malaysia Terengganu, 21030, Kuala Nerus, Terengganu, Malaysia*
[3]*Faculty of Science and Marine Environment, Universiti Malaysia Terengganu, 21030, Kuala Nerus, Terengganu, Malaysia*

[*]*Corresponding author: fizah@unimap.edu.my*

Received: 15 September 2023; Accepted: 25 February 2024; Published: 29 April 2024

Abstract

The performance of electrolytes in electronic applications are in decline due to low ionic conductivity, leakage, and inadequate thermal stability. Overcoming these challenges necessitates innovative approaches which includes electrolyte design, and materials selection, that should be taken into consideration. In this study, new additive alkoxylated azo-imine (**AZ**) material containing hybrid moieties of azo (-N=N-) and imine (-CH=N-) groups was successfully synthesized, characterized, and doped in biopolymer matrix. Chitosan-based biopolymer was formulated with **AZ** additive material as solid biopolymer electrolyte (SBE) through the concept of Donor (D) - π- Acceptor (A). The prepared **AZ** additive was characterized by selected spectroscopic and thermal analyses using FTIR, 1D NMR, and TGA before integration as SBE. The thermogram of **AZ** additive revealed good thermal stability up to 300 °C, making it suitable for application as electrolytes. Several weight percentages (2%-8%) of additive were doped with chitosan biopolymer as new SBEs (**F1-F4**). The conductivity of prepared SBE was measured via electrochemical impedance spectroscopy (EIS) which achieved the highest ionic conductivity of 8.22 x 10^{-3} S cm^{-1} at room temperature (303K). The preliminary findings suggest that this organic material has significant potential as an additive material in electrolyte application.

Keywords: additive, azo-imine, biopolymer electrolyte, conductivity, chitosan

Abstrak

Prestasi elektrolit dalam aplikasi elektronik semakin merosot kerana konduktiviti ion yang rendah, kebocoran, dan ketidakstabilan terma. Bagi mengatasi cabaran ini, pendekatan inovatif termasuk reka bentuk elektrolit dan pemilihan bahan perlu diberi perhatian. Dalam kajian ini, bahan tambah baharu azo-imina alkoksi (**AZ**) yang mengandungi moieti campuran azo (-N=N-) dan imina (-CH=N-) telah berjaya disintesis, dicirikan, dan dicampurkan ke dalam matriks biopolimer. Biopolimer berasaskan kitosan telah diformulasikan dengan bahan tambah **AZ** sebagai elektrolit pepejal biopolimer (SBE) melalui konsep Penderma (D) - π - Penerima (A). Bahan tambah **AZ** yang disediakan telah dicirikan menggunakan analisis spektroskopi dan terma yang terpilih menggunakan FTIR, 1D NMR, dan TGA sebelum digabungkan sebagai SBE. Termogram bahan tambah **AZ** menunjukkan kestabilan terma yang baik sehingga 300 °C, menjadikannya sesuai untuk digunakan sebagai elektrolit. Beberapa peratusan berat (2-8 wt. %) bahan

tambah telah dicampurkan dengan biopolimer kitosan sebagai SBE baharu (**F1-F4**). Kekonduksian SBE yang sediakan telah diukur melalui spekstroskopi impedans elektrokimia (EIS) dan mencapai konduktiviti 8.22 x 10^{-3} S cm^{-1} pada suhu bilik (303 K). Keputusan awal menunjukkan bahawa bahan organik ini mempunyai potensi yang baik sebagai bahan tambah dalam aplikasi elektrolit.

Kata kunci: bahan tambah, azo-imina, biopolimer elektrolit, kekonduksian, kitosan

Introduction

Electrolytes are a crucial component in energy storage devices, and these includes capacitors, batteries, and fuel cells [1]. The properties of the electrolyte, such as potential window, resistivity, conductivity, viscosity, stability, and flexibility, provides a huge impact on device performance [2]. A wide variety of electrolytes have been explored, including liquid electrolytes (aqueous, organic, and ionic liquid) [3] and solid-state electrolytes [4] as the potential ideal electrolyte. In this context, there is a high demand on liquid electrolytes-based alkali metals, lithium salts and organic solvent due to their performance in high ionic conductivity, capability to form stable contact with electrode, and the ability to reach high-rate performance in devices [5, 6]. Despite its superior performance, electrolytes have their own set of shortcomings as they are susceptible to corrosion and leakage issues, leading to device degradation and the possibility of self-discharge to electronic waste (e-waste) [7]. To mitigate the risks associated with liquid electrolytes and harmful material, solid-state electrolytes have been considered as a promising alternative.

Solid-state electrolytes offer various advantages properties including non-flammable, no flowing and corrosion after damage, and higher operation temperature [8]. The development of sustainable and eco-friendly materials for electrolyte applications has initiated a growing demand for new materials that can enhance performance. Thus, biopolymers have emerged as a promising candidate for polymer matrix due to their abundant availability, biodegradability, and excellent physicochemical properties [9]. Specifically, the preceding research employed biopolymers such as cellulose, alginate, and starch as solid-state electrolytes with the conductivity of these biopolymers is in the magnitude range of 10^{-5} - 10^{-10} S cm^{-1} [1, 10, 11]. Among various biopolymers materials, chitosan has garnered considerable interest in biopolymer-based electrolytes, primarily because of its unique characteristics including high mechanical strength, good thermal stability, and excellent film-forming ability [12]. Nonetheless, its ionic conductivity is often restricted, posing a challenge for its optimal use in high-performance applications [13].

In this context, researchers focus on effective methods to boost up the ionic conductivity of electrolytes by incorporating small portion of additives into the biopolymer matrix [14]. Some of the strategies to achieve an ideal ionic conductivity of at least 10^{-3} S/cm in electrochemical application includes utilizing ionic liquids [15], increasing the amounts of inorganic salts [16], and incorporate the organic liquid plasticizers [17] into biopolymer. Nevertheless, plasticization can result in deterioration of the mechanical integrity of the film and increased corrosive reactivity of polymer electrolyte as it requires large amounts of plasticizers [18]. Recently, the functional additives containing nitrogen (N), oxygen (O), carbon (C), and hydrogen (H) have been extensively explored to enhance the ionic conductivity of biopolymer electrolytes which consequently improve the electrolyte performance [19, 20]. Hence, this study aims to prepare new organic functional additives for polymer-based electrolyte application. The new hybrid moiety of azo (-N=N-) and imino (-C=N-) with alkoxy chain has been tested to act as an additive in the attempts to explore their suitability in chitosan biopolymer matrix. Individually, the moiety of (-N=N-) and (-C=N-) have soft and hard donor functionalities, offer π-system that highly desirable for various applications in electrolyte [20, 21], optoelectronic [22], and sensor [23]. These conjugated π-systems provide electron delocalization and π-π stacking interactions, resulting in improved charged transport properties [24]. Thus, in this study, azo-imine additive has been incorporated with chitosan-based biopolymer and in turn, the performance is tested on electrolyte application. The combination of the mixed

soft-hard donor character and the intriguing properties of these compounds should open a new avenue for electrolyte application. The mixing of prepared **AZ** additive in biopolymer matrix system is expected to support the ion dissociation; and as a result, a greater number of migrating ions may become available for charge transport.

Materials and Instrumentations

The reagents, 4-nitroaniline, 4-acetamidophenol, 1-bromohexane, chitosan powder (high molecular weight (M_w), 310,000-375,000, salicylaldehyde, glacial acetic acid, potassium carbonate and ethanol were purchased from commercial suppliers. It was used without further purification. Fourier transform infrared (FTIR) spectroscopy was performed in the wavenumber range of 4000 – 400 cm^{-1} using the Bruker Invenio-S instrument via the Attenuated total reflectance (ATR) method. 1D Nuclear magnetic resonances (NMR) of ^{1}H and ^{13}C were conducted using the Varian NMR System 500 MHz instrument using tetramethylsilane (TMS) as internal standard in deuterated chloroform ($CDCl_3$). Thermogravimetric Analysis (TGA) was conducted using the Perkin Elmer analyzer, with a heating temperature ranging from 30 to 600 °C and a flowrate of 10 °C/min under nitrogen atmosphere. The conductivity of the prepared SBE were run using electrical impedance spectroscopy (EIS) within the frequency range of 1 MHz to 50 Hz, employing the HIOKI 3532-50 LCR Hi-Tester.

Synthesis of alkoxylated azo-imine additive (AZ)

Prior to obtain **AZ** additive, azo salicylaldehyde (**1**), *N*-4-hexyloxy phenyl acetamide (**2a**) and *N*-4-hexyloxy aniline (**3a**) acting as precursors were attained via different designated reactions. The experimental details on the precursors (**1**, **2a** & **3a**) have been reported in previous studies [24–26]. Several modifications in term of synthetic pathway and characterization were carried out and are discussed further in this contribution. The precursor **1** was synthesized via diazotization process, using 4-nitroaniline (0.015 mole, 2g) and salicylaldehyde (0.015 mole, 1.8g). The progress of the compound's reaction completion was monitored using Thin Layer Chromatography (TLC) performed under ethyl acetate: n-hexane (2:3) as a mobile phase. Then, the product obtained was filtered and washed with ethanol. The precipitate was then dried over silica gel until fully dried. For precursor **2a**, it was accomplished via Williamson ether reaction using 4-acetamidophenol (0.018 mole, 3g), 1-bromohexane (0.018 mole, 2.5g) and potassium carbonate (0.018 mole, 2.5g). The reaction resulted in a white precipitate and a colorless solution. TLC technique was used to determine the completion of the reaction. After cooling to room temperature and vacuum removal of the solvent, white solid was obtained. Then, the obtained white solid of **2a** was refluxed with constant stirring in a mixture of ethanol and concentrated acid for *ca.* 2 hours. This reaction has afforded **3a**, along with light brown solution. To obtain the **AZ** additive, the precursor of **1** (0.0018 mole, 0.5g) was fully dissolved in ethanol (100 mL) whilst, the precursor of **3a** (0.0018 mole, 0.35g) was completely dissolved in ethanol (30 mL) before being added dropwise to the precursor of **1**. Once both compounds were fully dissolved, reflux process was initiated. The reaction was refluxed for approximately 6 hours at 70 °C, the boiling point of ethanol. When adjudged completion also via TLC, the orange precipitate obtained was filtered and collected. The overall chemical pathway for the synthesis of **AZ** additive is represented in Scheme 1.

Preparation of solid biopolymer electrolyte (SBE)

An amount of chitosan (2g) was dissolved in 2% acetic acid and stirred continously for 4 hours. The obtained **AZ** additive was dissolved in 1 mL acetic acid and added into chitosan solution until a clear solution was achieved. The composition of **AZ** additive (2 wt.% to 8 wt.%) were added into the chitosan solution to obtain new SBE (**F1** – **F4)** is presented in Table 1. The solution was then casted into glass petri dishes, followed by drying in an oven at 50°C for 30 hours. In this work, a maximum amount of 8 wt. % was tested to form clear solution and film.

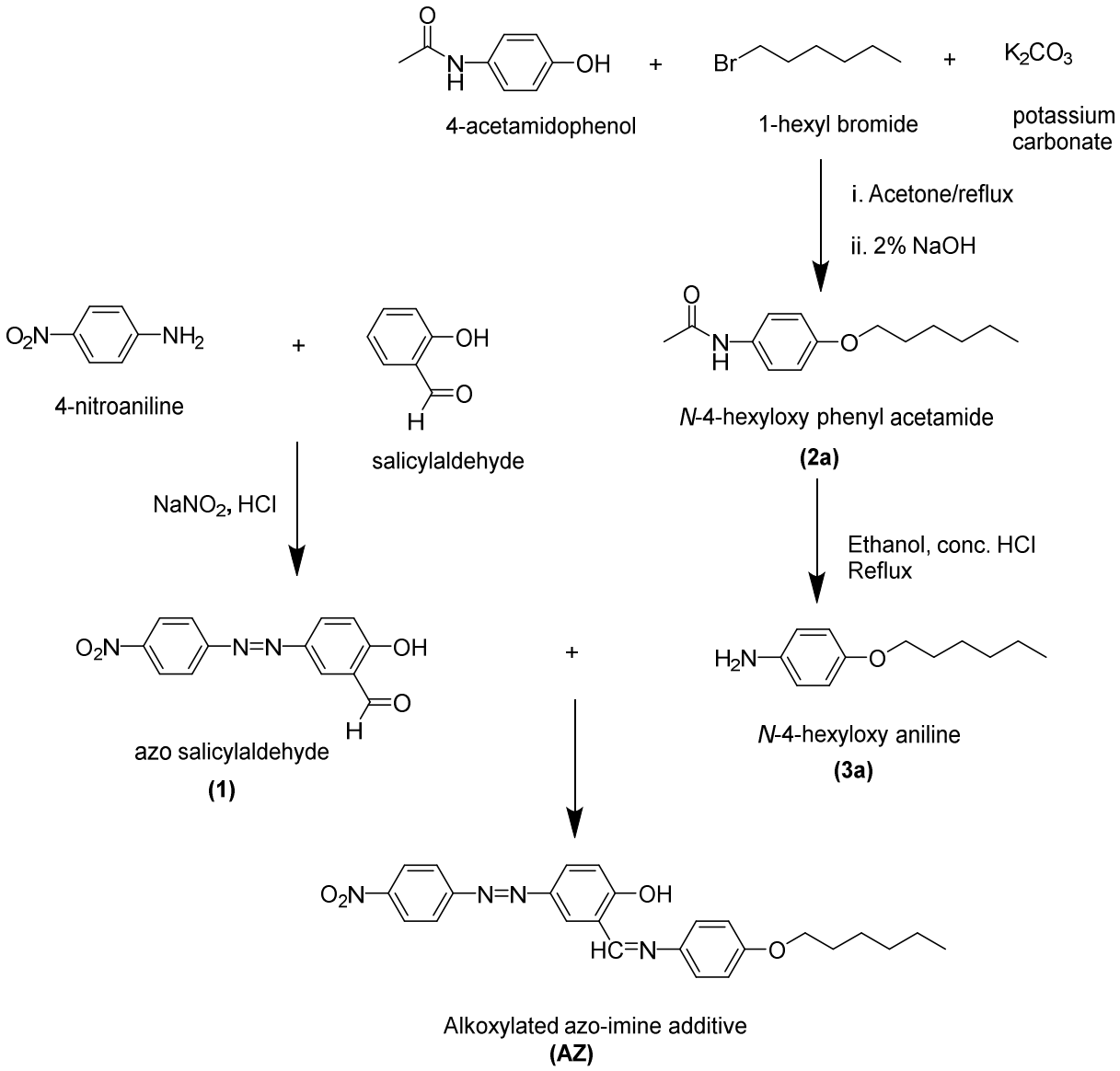

Scheme 1: Preparation of **AZ** additive

Table 1. Formulation of solid biopolymer electrolyte

Coding	Additive, wt.%	Weight percentage of additive, g	Chitosan, g
F0	0	0	2
F1	2	0.04	2
F2	4	0.08	2
F3	6	0.12	2
F4	8	0.16	2

Electrical impedance spectroscopy (EIS)

The prepared SBE was evaluated using EIS model HIOKI 3532-50 LCR Hi-Tester to determine its conductivity. For EIS measurement, 2 cm diameter of SBE was sandwiched between two stainless steel electrodes and tested in room temperature at a frequency range of 1 MHz to 50 Hz. The data was presented in the Cole-Cole plot form. The ionic conductivity, σ, of the electrolyte was calculated by using equation 1 [28] .

$$\sigma = \frac{t}{R_b \cdot A} \quad (1)$$

From eq. 1, t is the thickness of the electrolyte, R_b is the bulk resistivity and A is the (cm^2) electrode-electrolyte contact area. The value of R_b is retrieved from the Cole–Cole plot.

Results and Discussion

Spectroscopy technique

Figure 1 shows the IR spectra of precursors (**1**, **2a** & **3a**) and targeted compound of **AZ** additive. **AZ** additive revealed all the bands of interests namely ν(C-H), ν(C=N), ν(N=N), and ν(NO_2). The aliphatic C-H stretching vibrations arise at 2921 and 2856 cm^{-1} of the alkoxy substituent. The assignment of the stretching mode was made by comparison to their precursors **2a** and **3a** which indicates that the intensities of these bands increased. The absence of the stretching modes of residual amino, ν(NH_2) from precursor (**3a**) and aldehyde ν(CHO) groups from **1** together with the appearance of a typical band of imine bonds, ν(C=N) at 1614 cm^{-1} have provided strong evidence to the Schiff base formation reaction for **AZ** additive [29]. Two bands of ν(N=N) occur at 1500 cm^{-1} and 1440 cm^{-1} represent the asymmetric and symmetric N=N stretching vibrations of azo moiety [30, 31]. The shifting of ν(N=N) band to the higher wavenumber compared to **1** is due to the enhanced of mesomeric and inductive effect of the substituents. The characteristics of nitro group shifted to a slightly lower wavenumber at 1343 cm^{-1} due to stretching vibrations of ν(NO_2).

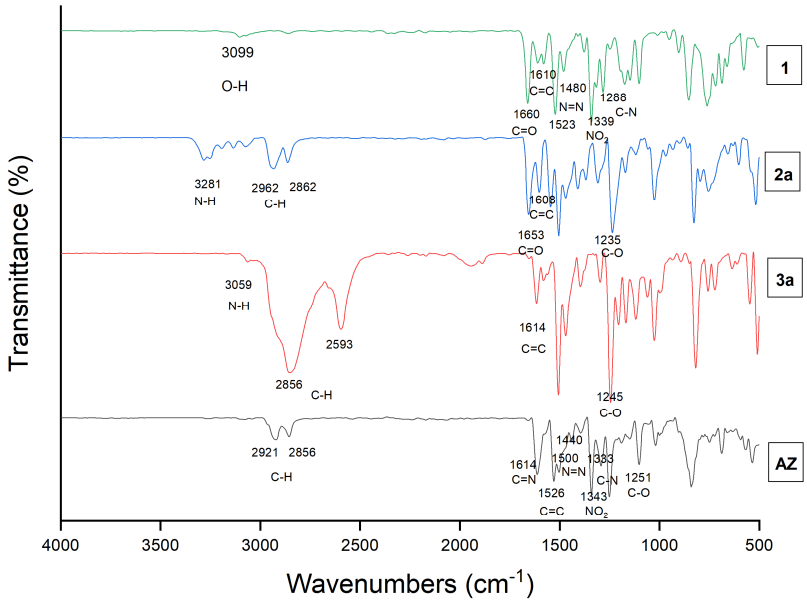

Figure 1. IR spectra of precursors and **AZ** additive

From Figure 2, the ^1H NMR spectrum for **AZ** additive reveals the methyl protons at δ_H 0.92 ppm while protons for methylene group were detected in the region of δ_H 1.35-1.82 ppm. The signal of R-O-CH_2 deshielded at δ_H 4.00 ppm due to the contribution of electronegativity of the oxygen atom. The closer the proton

approaches the electronegative oxygen atom, the greater the deshielding effect and therefore the resonance of R-O-CH_2 shifted towards downfield as compared to CH_3 which is located further from the oxygen atom. The values are in good agreement with the previous literature reported by Nakum and team [32]. The resonance of aromatic protons of *para*-substituted aromatic ring can be clearly observed as a pseudo-doublet resonance in the range of δ_H 6.82 ppm − 6.98 ppm and δ_H 7.66 ppm − 7.82 ppm and is considerably downfield due to large anistropic effect. The CH=N and hydroxyl protons found at around δ_H 8.06 ppm and δ_H 8.71 ppm respectively, are characterized by their unique singlet resonance at downfield [33], thus confirming the targeted compound.

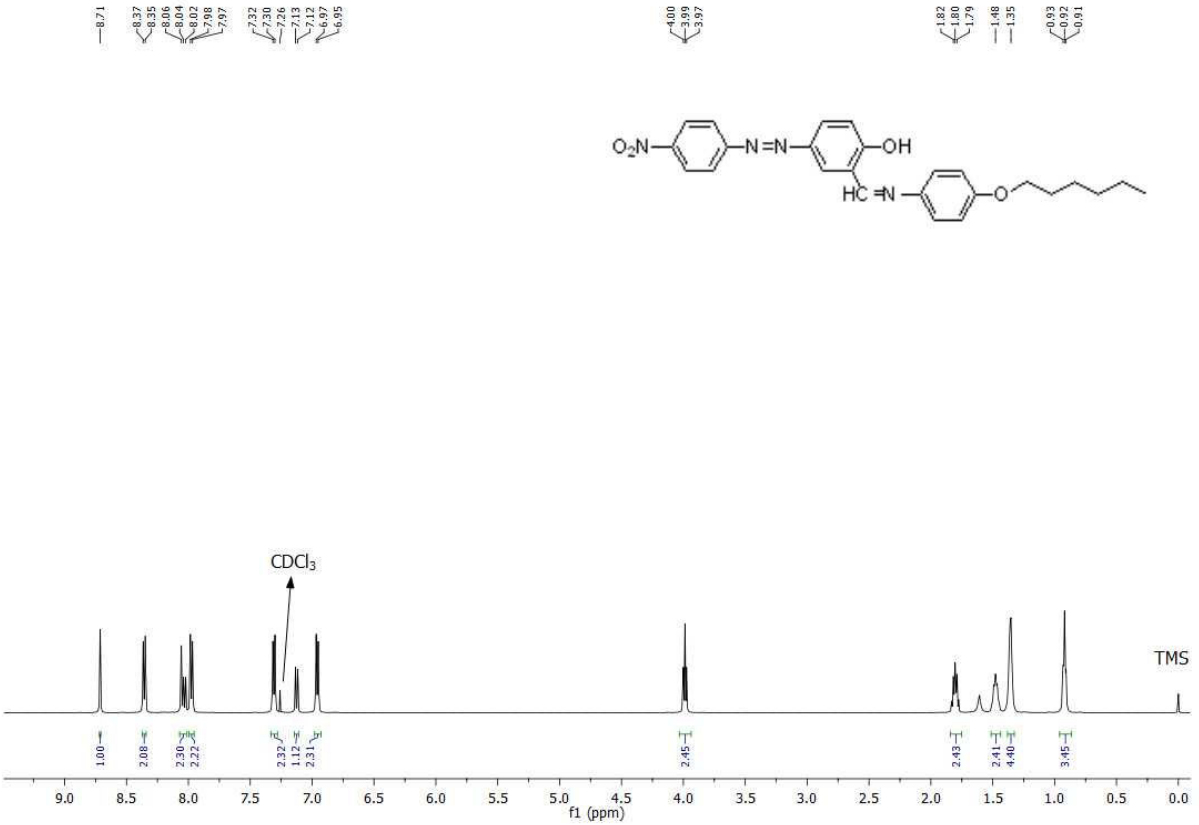

Figure 2. ^{1}H NMR for the **AZ** additive

Based on ^{13}C NMR spectrum of **AZ** additive, all expected resonances are at appropriate and expected chemical shifts. The carbon resonance of the terminal methyl group (CH_3) appears around δ_C 14.03 ppm, while for alkyl chain length, it appeared in the range of δ_C 22.60-35.57 ppm. The chemical shift for R–CH_2-O- can be found at δ_C 62.69 ppm due to the deshielding effect and is similar to Nakum et al. [34]. The resonances of aromatic ring carbon were assigned in the range of δ_C 115.29-155.85 ppm. The signal observed at δ_C 165.57 ppm is attributed to the C=N carbon atom which indicates the presence of imino linkage in the **AZ** additive.

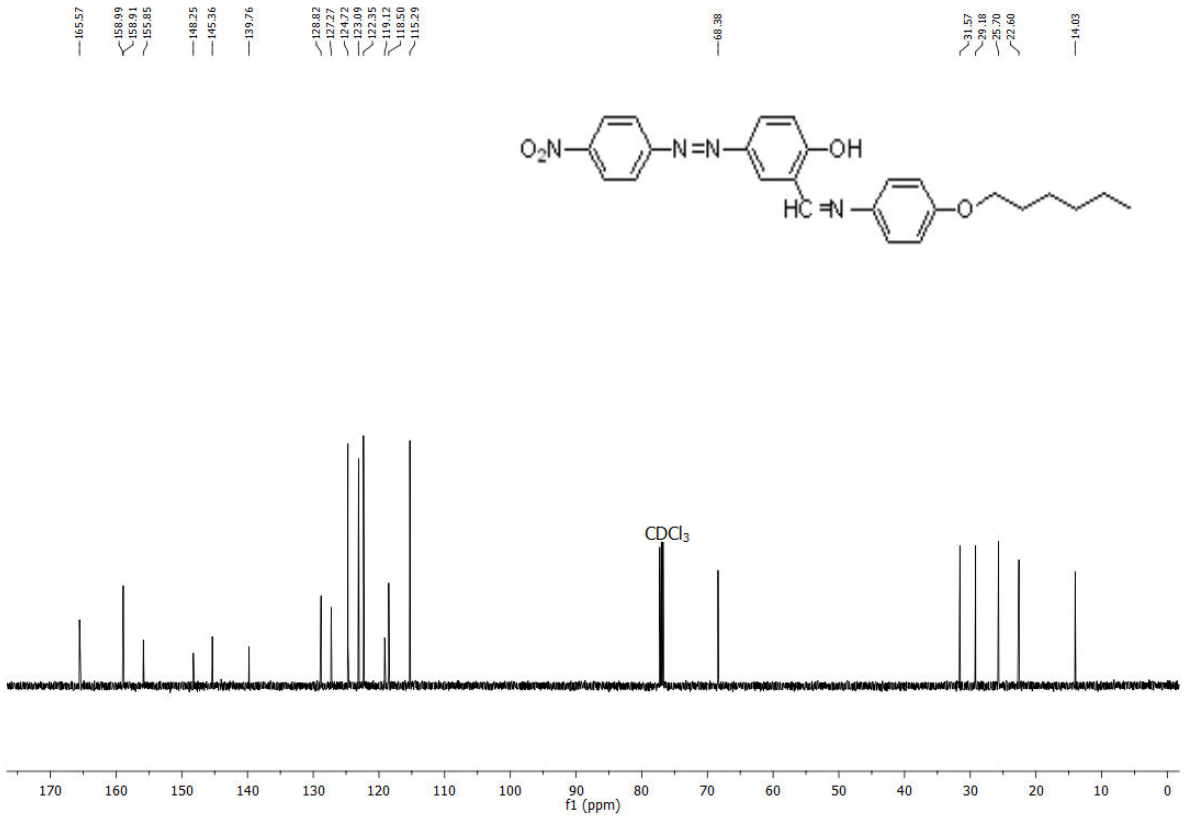

Figure 3: ^{13}C spectrum of the **AZ** additive

Thermogravimetric analysis (TGA)

TGA of precursors (**1**, **2a**, and **3a**) and **AZ** additive were carried out to investigate their thermal property. Based on the thermograms shown in Figure 4, no weight loss was observed at temperature below 120 °C. This indicated absence of water or solvent molecules that are left or trapped during the synthetic reaction and recrystallization. All synthesized compounds exhibited only one step of thermal degradation with different onset and offset values. By comparing the onset temperature of each compound, **AZ** additive was found to be stable up to 300 °C indicating that it has higher thermal stability compared to its precursor and therefore chosen as the additive to be tested in this study. The degradation of **AZ** additive was not complete at 600 °C, with 42.55% of residue left. This value coincides with the reported value by Ahmed et al. [35]. This may be due to the degradation of azo moiety which occurred through the cleavage of the azo bond by reductive process as suggested by previous studies [35, 36]. The trend of the thermal stability can be clearly observed by the presence of azo and alkoxy group in **AZ** additive. Ultimately, it can be concluded that the stability of additive increases as the degradation increases and it also depends on the substituent and molecular weight of the material. The thermal degradation parameters are given in Table 2.

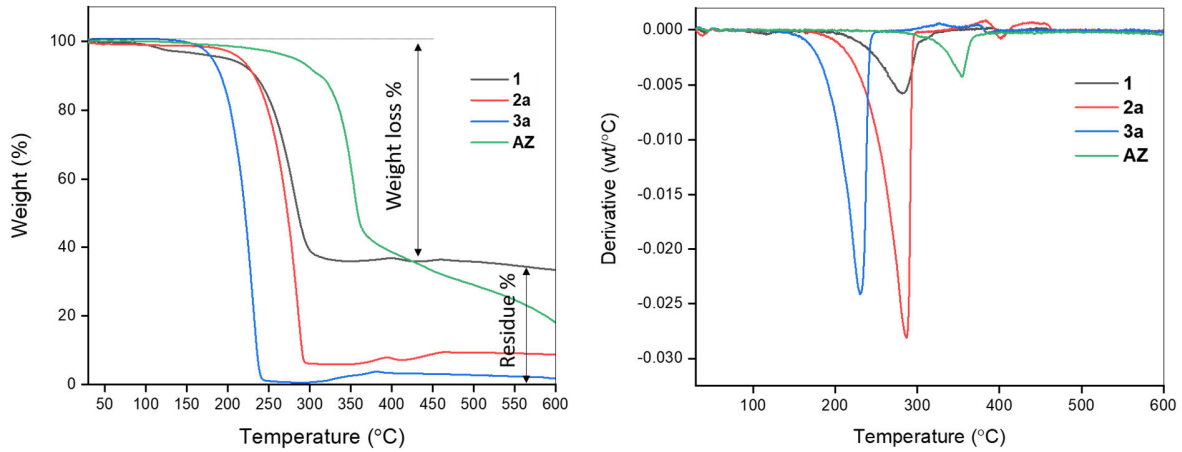

Figure 4. TGA and DTG of precursors and **AZ** additive

Table 2. Thermal degradation parameters of precursors and **AZ** additive

Compound	**T_{onset} (°C)**	**T_{max} (°C)**	**Weight Loss (%)**	**Residue (%)**
1	243	300	62.91	37.09
2a	254	289	92.6	7.4
3a	204	235	99.83	0.17
AZ additive	319	348	57.45	42.55

Ionic conductivity analysis

Impedance spectroscopy is typically used to study the electrical properties of the electrolytes. The Cole-Cole plot for the prepared SBE system is illustrated in Figure 5. From the plots, chitosan-based solid biopolymer electrolyte shows high-frequency region semicircle arc and low-frequency region inclination spike, where both are related to ionic conduction in the bulk of sample. Upon the addition of additives, the semicircle of chitosan disappeared and bulk resistance (R_b) decreases. The SBE with the incorporation of 4% additive (**F2**) gives the highest ionic conductivity value of 8.22 x 10^{-3} S/cm.

Figure 6 shows the ionic conductivity of the prepared SBE. The ionic conductivity value for chitosan SBE (without addition of additive) is 7.38 x 10^{-10} S/cm which is comparable with reported results by Rahman et al. [13]. The value shows the significant trends where it shows the increment of values upon the addition of **AZ** additive in the polymer host matrix of up to 8.22 x 10^{-3} S/cm for SBE containing 4 wt.% **AZ** additives. The increment in ionic conductivity can be attributed to the enhancement in the number density of charge carriers and efficiency of synthesized additives in dissociating chitosan matrix [37]. However, the value decreases after 6 wt.% because it has already reached the optimum concentration, thus leading towards sample aggregation [11]. From the preliminary result, **AZ** additive reveals good potential as an additive agent in SBEs as it can improve the ionic conductivity of the system with a potential in electrolyte application.

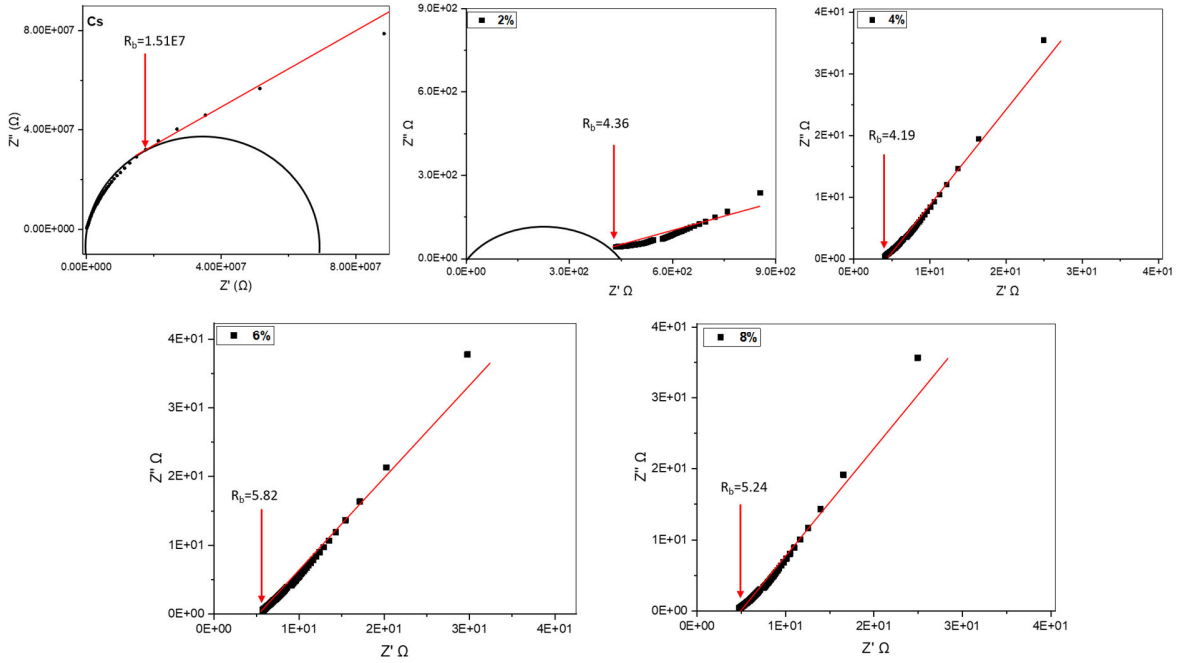

Figure 5. Cole-Cole plot of chitosan and variation weight percent of additive

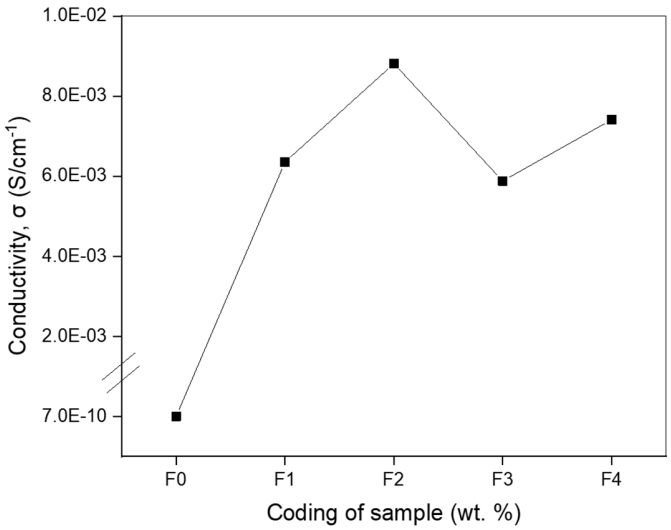

Figure 6. Conductivity of SBE system

Conclusion

This present work has successfully introduced a new **AZ** additive material integrated into chitosan biopolymer electrolyte to enhance charge carrier mobility and conductivity performance. All synthesized compounds including the precursors and **AZ** were analyzed via FTIR, 1D NMR, and TGA. TGA studies show that the effect of **AZ** influenced the thermal stability of the SBEs system by increasing the temperature decomposition (T_d) and is stable up to 300 °C. The ionic conductivity of the prepared SBEs system have been successfully evaluated using EIS and shows an increment in the order of 10^{-7} S/cm to 10^{-3} S/cm with the addition of **AZ** additive.

The maximum conductivity at ambient temperature (303 K) achieved up to 8.22 x 10^{-3} S/cm at 4% of additive. The preliminary finding reveals that the presence of active group of hydroxyl (-OH) and azo (N=N) can significantly affect the conductivity performance. Hence, the output from this work creates an alternative approach to initiate further investigation on new, efficient, stable additive materials in various optoelectronic application.

Acknowledgement

We would like to acknowledge the research grant support from Ministry of Higher Education, Malaysia for Fundamental Research Grant Scheme, FRGS/1/2021/STG05/UNIMAP/03/1 (9003-00914) and Faculty of Chemical engineering & Technology, Universiti Malaysia Perlis for facilities and research aids.

References

1. Li, X., Ding, C., Li, X., Yang, H., Liu, S., Wang, X., Zhang, L., Sun, Q., Liu, X. and Chen, J. (2020). Electronic biopolymers: From molecular engineering to functional devices. *Chemical Engineering Journal,* 397: 125499.
2. Mirzaeian, M., Abbas, Q., Ogwu, A., Hall, P., Goldin, M., Mirzaeian, M., and Jirandehi, H. F. (2017). Electrode and electrolyte materials for electrochemical capacitors. *International Journal of Hydrogen Energy,* 42(40): 25565-25587.
3. Pan, Q., Gong, D., and Tang, Y. (2020). Recent progress and perspective on electrolytes for sodium/potassium-based devices. *Energy Storage Materials*, 31: 328-343.
4. Hakari, T., Yoshimi, S., Nagao, K., Sakuda, A., Tatsumisago, M., and Hayashi, A. (2022). Thermally stable bulk-type all-solid-state capacitor with a highly deformable oxide solid electrolyte. J*ournal of Power Sources,* 543: 231821.
5. Zeng, Q., Lv, Z., Li, S., Yang, B., He, J., and Song, J. (2023). Electrolytes for liquid metal batteries. *Materials Research Bulletin,* 2023: 112586.
6. Sun, J., Yuan, H., Yang, J., Zhang, Y. W., and Wang, J. (2023). Electrolytes for better and safer batteries: Liquid, solid or frameworked, what's next?. *Next Materials,* 1(3): 100024.
7. Taneja, N., Kumar, A., Gupta, P., Gupta, M., Singh, P., Agrawal, N., Bocchetta, P. and Kumar, Y. (2022). Advancements in liquid and solid electrolytes for their utilization in electrochemical systems. *Journal of Energy Storage,* 56: 105950.
8. Varshney, P. K., and Gupta, S. (2011). Natural polymer-based electrolytes for electrochemical devices: a review. *Ionics,* 17(6): 479-483.
9. Yusuf, S. N. F., Yusof, S. Z., Kufian, M. Z., and Teo, L. P. (2019). Preparation and electrical characterization of polymer electrolytes: A review. *Materials Today: Proceedings,* 17: 446-458.
10. Abdulwahid, R. T., Aziz, S. B., and Kadir, M. F. (2023). Environmentally friendly plasticized electrolyte based on chitosan (CS): Potato starch (PS) polymers for EDLC application: Steps toward the greener energy storage devices derived from biopolymers. *Journal of Energy Storage,* 67: 107636.
11. Khairul, W. M., Rahamathullah, R., Joni, J. R., and Isa, M. I. N. (2022). Density functional theory (DFT) calculations, synthesis and electronic properties of alkoxylated-chalcone additive in enhancing the performance of CMC-based solid biopolymer electrolyte. *International Journal of Hydrogen Energy,* 47(65): 27866-27876.
12. El-Hefian, E. A., Nasef, M. M., and Yahaya, A. H. (2014). Chitosan-based polymer blends: Current status and applications. *Journal of the Chemical Society of Pakistan,* 36(1): 11-27.
13. Rahman, N. A., Hanifah, S. A., Mobarak, N. N., Ahmad, A., Ludin, N. A., Bella, F., and Su'ait, M. S. (2021). Chitosan as a paradigm for biopolymer electrolytes in solid-state dye-sensitised solar cells. *Polymer,* 230: 124092.
14. Shaari, N., and Kamarudin, S. K. (2019). Recent advances in additive-enhanced polymer electrolyte membrane properties in fuel cell applications: An overview. *International Journal of Energy Research*, 43(7): 2756-2794.
15. Kumar, S., Dhapola, P. S., Pandey, S. P., Singh, P. K., and Chauhan, M. (2021). Corn-starch based porous carbon and IL based electrolyte for high efficient supercapacitor. *Materials Today: Proceedings,* 34: 842-845.
16. Aziz, S.B., Nofal, M.M., Abdulwahid, R.T., Kadir,

M.F.Z., Hadi, J.M., Hessien, M.M., Kareem, W.O., Dannoun, E.M. and Saeed, S.R. (2021). Impedance, FTIR and transport properties of plasticized proton conducting biopolymer electrolyte based on chitosan for electrochemical device application. *Results in Physics,* 29: 104770.

17. Perumal, P., and Selvin, P. C. (2021). Boosting the performance of electric double layer capacitor via engaging pectin macromolecular electrolyte with elevated ionic conductivity and potential window stability. *Chemical Engineering Journal Advances,* 8: 100178.
18. Marturano, V., Cerruti, P., and Ambrogi, V. (2017). Polymer additives. *Physical Sciences Reviews,* 2(6): 20160130.
19. Baran, T., and Menteş, A. (2016). Polymeric material prepared from Schiff base based on O-carboxymethyl chitosan and its Cu (II) and Pd (II) complexes. *Journal of Molecular Structure,* 1115: 220-227.
20. Shanavas, A., Vanjinathan, M., Nasar, A. S., Amudha, S., and Suthanthiraraj, S. A. (2012). Synthesis, thermal and solar cell application of novel hyperbranched polyurethanes containing azomethine and aryl-ether connectivities. *High Performance Polymers,* 24(7): 561-570.
21. Rahamathullah, R., Low, J. K., Khairul, W. M., Osman, R. A. M., and Isa, M. I. N. (2023). Fused aromatic disubstituted azomethine as organic additives in NH_4SCN doped CMC based electrolyte film. In AIP Conference Proceedings (Vol. 2703, No. 1). AIP Publishing.
22. Sarswat, P. K., Sathyapalan, A., Zhu, Y., and Free, M. L. (2013). Design, synthesis, and characterization of TPA-thiophene-based amide or imine functionalized molecule for potential optoelectronic devices. *Journal of Theoretical and Applied Physics*, 7: 1-9.
23. Kamali, S., Orojloo, M., Arabahmadi, R., and Amani, S. (2022). Design and synthesis of a novel azo-Schiff base ligand: Its application as a colorimetric chemosensor for selective detection of Ni^{2+} and CN^{-} in aqueous-organic media, computational studies, antimicrobial properties, and molecular logic circuits. *Journal of Photochemistry and Photobiology A: Chemistry,* 433: 114136.
24. Liu, M., Yin, L., Wang, L., Miao, T., Cheng, X., Wang, Y., Zhang, W. and Zhu, X. (2019). Synthesis of monodisperse aromatic azo oligomers toward gaining new insight into the isomerization of π-conjugated azo systems. *Polymer Chemistry,* 10(14): 1806-1811.
25. Rahamathullah, R., and Khairul, W. M. (2017). Evaluation on the electrochemically deposited alkoxy thiourea as liquid crystalline semiconductor film. *Applied Surface Science,* 424: 45-51.
26. Menati, S., Azadbakht, A., Azadbakht, R., Taeb, A., and Kakanejadifard, A. (2013). Synthesis, characterization, and electrochemical study of some novel, azo-containing Schiff bases and their Ni(II) complexes. *Dyes and pigments,* 98(3): 499-506.
27. Ma, I. W., Ammar, S., Bashir, S., Selvaraj, M., Assiri, M. A., Ramesh, K., and Ramesh, S. (2020). Preparation of hybrid chitosan/silica composites via ionotropic gelation and its electrochemical impedance studies. *Progress in Organic Coatings,* 145: 105679.
28. Kotatha, D., Torii, Y., Shinomiya, K., Ogino, M., Uchida, S., Ishikawa, M., Furuike, T. and Tamura, H. (2019). Preparation of thin-film electrolyte from chitosan-containing ionic liquid for application to electric double-layer capacitors. *International Journal of Biological Macromolecules,* 124: 1274-1280.
29. Purtas, F. Sayin,K. Ceyhan, G., Kose, M. and Kurtoglu, M. (2017). New fluorescent azo-Schiff base Cu(II) and Zn(II) metal chelates, spectral, structural, electrochemical, photoluminescence and computational studies. *Journal Molecular Structure,* 1137: 461-475.
30. Eskikanbur, S., Sayin, K., Kose, M., Zengin, H., McKee, V., and Kurtoglu, M. (2015). Synthesis of two new azo-azomethines; spectral characterization, crystal structures, computational and fluorescence studies. *Journal of Molecular Structure,* 1094: 183-194.
31. Gür, M., Kocaokutgen, H., Kandemirli, F., Özkinali, S., and Yerlikaya, Z. (2016). Synthesis, spectral and thermal characterization of some azo-polymers containing acrylate derivatives. *Research & Reviews: Journal of Chemistry,* 5(2):1-9.

32. Nakum, K. J., Katariya, K. D., Savani, C. J., and Jadeja, R. N. (2022). The influence of molecular flexibility on the mesogenic behavior of a new homologous series based on azo-azomethine: Synthesis, characterization, photoisomerization and DFT study. *Journal of Molecular Structure,* 1249: 131586.
33. Ozkinali, S., Cavus, M. S., and Sakin, B. (2018). Synthesis, structural characterization and theoretical investigations of new azo-azomethine compounds bearing acryloyl moiety. *Hittite Journal of Science and Engineering,* 5(4): 259-269.
34. Nakum, K. J., Katariya, K. D., Hagar, M., and Jadeja, R. N. (2022). The influence of lateral hydroxyl group and molecular flexibility on the mesogenic behaviour of a new homologous series based on thiophene-chalcone: Synthesis, characterization, crystal structure and DFT study. *Journal of Molecular Structure,* 1261: 132891.
35. Ahmed, N. H., Saad, G. R., Ahmed, H. A., and Hagar, M. (2020). New wide-stability four-ring azo/ester/Schiff base liquid crystals: Synthesis, mesomorphic, photophysical, and DFT approaches. *RSC Advances,* 10(16): 9643-9656.
36. Mali, H., Sharma, V. S., Rathod, S. L., Sharma, A. S., Shrivastav, P. S., and Prajapati, H. R. (2023). Synthesis, characterization and photophysical study of cholesterol functionalized azo-based room temperature liquid crystals. *Journal of Molecular Structure,* 1289: 135776.
37. Ismail, N. I., Saidin, S. N., RA, N. H., Ahmad, A., and NaiiM, N. (2022). The Effects of monosaccharides on the physico-electrochemical properties of chitosan based solid polymer electrolytes (SPEs). *Sains Malaysiana*, 51(8): 2461-2472.

Malaysian Journal of Analytical Sciences (MJAS)
Published by Malaysian Analytical Sciences Society

PERFORMANCE OF MEMBRANE ELECTRODE ASSEMBLY USING Pt/C AND CoFe/N-C CATALYSTS IN PROTON EXCHANGE MEMBRANE FUEL CELLS

(Prestasi Pemasangan Elektrod Membran Menggunakan Pemangkin Pt/C dan CoFe/N-C dalam Sel Bahan Api Membran Pertukaran Proton)

Dedi Rohendi[1,2], Edy Herianto Majlan [4*], Dwi Hawa Yulianti[2], Juwita[1], Nirwan Syarif[1,2], Addy Rachmat[1,2], Afriyanti Sumboja[3], Nyimas Febrika S.[2], and Icha Amelia[2]

[1]*Department of Chemistry, Faculty of Mathematic and Natural Sciences, Universitas Sriwijaya, Jl. Palembang-Prabumulih Km 32, Indralaya, Ogan Ilir 30862, Indonesia*
[2]*Center of Research Excellent in Fuel Cell and Hydrogen, Universitas Sriwijaya, Jl. Srijaya Negara, Palembang 30128, Indonesia*
[3]*Chemistry Program, Faculty of Computer and Science, Universitas Indo Global Mandiri,, Palembang, 30129, Indonesia*
[4]*Materials Science and Engineering Research Group Institut Teknologi Bandung, Faculty of Mechanical and Aerospace Engineering, Jl. Ganesha 10, Bandung, Indonesia*
[5] *Fuel Cell Institute, Universiti Kebangsaan Malaysia, Bangi 43600, Selangor, Malaysia*

[*]*Corresponding author: edyhm71@gmail.com*

Received: 16 October 2023; Accepted: 15 February 2024; Published: 29 April 2024

Abstract

The performance of membrane electrode assembly (MEA) hinders fuel cell commercialisation. MEA is greatly affected by humidification, temperature and hydrogen flow rate. In this study, the effects of operating conditions on MEA were determined using Pt/C and CoFe/N-C catalysts in proton exchange membrane fuel cells. Herein, two types of MEAs using the Nafion-212 membrane were prepared and tested. The anode and cathode of the first MEA were coated with Pt/C and CoFe/N-C catalysts, respectively, whereas the second MEA utilised a Pt/C catalyst on both electrodes. The electrode with Pt/C and CoFe/N-C catalysts was characterised using cyclic voltammetry and electrochemical impedance spectroscopy to obtain the electrochemical surface area (ECSA) and electrical conductivity of the electrode, respectively. The performance of two MEAs was tested under different operating conditions, such as various humidifier temperatures (40 °C, 60 °C, 80 °C and 100 °C) and hydrogen flow rates (100, 200, 300 and 400 mL/min). The electrode with a Pt/C catalyst exhibited higher ECSA (0.245 m^2/g) than the CoFe/N-C electrode (0.018 m^2/g). Similarly, the Pt/C electrode possessed higher conductivity (7.2×10^{-3} S/cm) than the CoFe/N-C electrode (4.4×10^{-3} S/cm). Consequently, the open-circuit voltage (OCV) of the second MEA with a Pt/C catalyst on both electrodes showed a higher value (0.890 V) than the OCV of the first MEA (0.790 V). Furthermore, the humidifier temperature was optimum at 80 °C, and it achieved power density levels as high as 10.14 and 3.43 mW/cm^2 for the second and the first MEA, respectively. In addition, the performance of MEA was affected by the hydrogen flow rate. At the optimum hydrogen flow rate of 400 mL/min for the first MEA, a power density of 4.93 mW/cm^2 was achieved. Meanwhile, the second MEA required a lower hydrogen flow rate (200 mL/min) to achieve a maximum power density of 10.14 mW/cm^2.

Keywords: proton exchange membrane fuel cells, MEA performance, Co-Fe/N-C, humidification temperature, hydrogen flow rate

Abstrak

Prestasi pemasangan elektrod membran (MEA) membawa kepada kesesakan pengkomersialan sel bahan api. MEA sangat dipengaruhi oleh pelembapan, suhu, dan kadar aliran hidrogen. Dalam kajian ini, menentukan kesan keadaan operasi pada MEA menggunakan pemangkin Pt/C dan CoFe/N-C dalam sel bahan api membran pertukaran proton (PEMFC). Di sini, dua jenis MEA yang menggunakan membran Nafion-212 telah disediakan dan diuji. Anod dan katod MEA pertama disalut dengan pemangkin Pt/C dan CoFe/N-C, manakala MEA kedua menggunakan pemangkin Pt/C pada kedua-dua elektrod. Elektrod dengan pemangkin Pt/C dan CoFe/N-C dicirikan menggunakan voltammetri kitaran dan spektroskopi impedans elektrokimia (EIS) untuk mendapatkan kawasan permukaan elektrokimia (ECSA) dan kekonduksian elektrik elektrod. Prestasi dua MEA diuji dengan keadaan operasi yang berbeza, seperti pelbagai suhu humidifier (40 °C, 60 °C, 80 °C, dan 100 °C) dan kadar aliran hidrogen (100, 200, 300, dan 400 mL/min). Elektrod dengan pemangkin Pt/C mempamerkan ECSA yang lebih tinggi (0.245 m^2/g) daripada elektrod CoFe/N-C (0.018 m^2/g). Begitu juga, elektrod Pt/C mempunyai kekonduksian yang lebih tinggi (7.2 x 10^{-3} S/cm) daripada elektrod CoFe/N-C (4.4 x 10^{-3} S/cm). Akibatnya, voltan litar terbuka (OCV) MEA kedua dengan pemangkin Pt/C pada kedua-dua elektrod menunjukkan nilai yang lebih tinggi (0.890 V) daripada OCV MEA pertama (0.790 V). Tambahan pula, suhu humidifier adalah optimum pada 80 °C dan mencapai tahap ketumpatan kuasa setinggi 10.14 dan 3.43 mW/cm^2 masing-masing untuk MEA kedua dan pertama. Di samping itu, prestasi MEA dipengaruhi oleh kadar aliran hidrogen. Dengan kadar aliran hidrogen optimum 400 mL/min untuk MEA pertama, ketumpatan kuasa 4.93 mW/cm^2 telah dicapai. Sementara itu, MEA kedua memerlukan kadar aliran hidrogen yang lebih rendah (200 mL/min) untuk mencapai ketumpatan kuasa maksimum 10.14 mW/cm^2.

Kata kunci: sel bahan api membran pertukaran proton, prestasi MEA, Co-Fe/N-C, suhu pelembapan, kadar aliran hidrogen

Introduction

Proton exchange membrane fuel cells (PEMFCs) have high efficiency, high power density, pollution-free properties because they use hydrogen as fuel [1] and flexible source of hydrogen [2]. PEMFCs can be used in electric vehicles [3] and maritime applications [4], as well as for portable and stationary applications [5]. The membrane electrode assembly (MEA) is the most important component in PEMFCs. The performance of MEA's is determined by the catalytic activity, the method of placing the catalyst at the catalyst layer (CL) [1], the effect of supporting a material for the CL [6] and the design structure of the flow field [7]. The ideal catalyst for PEMFCs has good conductivity and high stability [8], particularly the activity and stability of the catalyst at the cathode [9]. In general, the catalyst used in PEMFCs is Pt-based because it is optimum for the hydrogen oxidation reaction at the anode [10], [11]. However, the weakness of the Pt/C catalyst lies in its high cost and susceptibility to CO poisoning, which accelerates platinum particle growth, causing aggregation and structural changes. This phenomenon negatively impacts catalytic activity, which leads to gradual deactivation, thereby reducing fuel cell lifespan and efficiency [12].

Meanwhile, oxygen reduction at the cathode in PEMFCs is relatively slow [13]. Thus, a catalyst that can accelerate the reduction reaction at the cathode is necessary. Pt catalyst alloys with other transition metals is commonly used at the cathode to reduce the interatomic distance in the lattice and energy variations in the d-orbitals, which can facilitate the adsorption of oxygen on the cathode surface [9]. Moreover, the slow reaction at the cathode will lead to the improper occurrence of the stoichiometric equilibrium between the hydrogen and oxygen reactions that are supplied, thereby decreasing the performance of the PEMFC. The oxygen reduction reaction (ORR) of the CoFe/N-C catalyst makes it a good catalyst for the cathode because it increases the reduction reaction in rechargeable zinc–air batteries [14].

Meanwhile, the use of nitrogen graphene with iron fibre can increase the ORR on the membrane, whereas the N-doped cobalt carbon (Co/C) can reduce the oxygen evolution reaction (OER). Thus, the performance of the CoFe/N-C catalyst in PEMFC can be compared with that of the Pt/C catalyst that is often used in the PEMFC cathode. Using a non-platinum FeCo-based catalyst at the cathode has also been carried out using the printing method for catalyst synthesis [15]. Several studies have shown that the alloys of transition metals, nitrogen and carbon synergise with one another to obtain ORR electrocatalytic activity and high performance durability [16]. Based on the evaluation using the rotating disk electrode technique, a significant increase in ORR activity is observed in CoFe/N-C compared with Co/N-C and Fe/N-C (Table 1). This finding indicates a synergistic coupling effect between Co and Fe in alloy

metal nanoparticles supported on nitrogen-doped Vulcan carbon. The CoFe/N-C catalyst demonstrates higher current density at the same overpotential, indicating greater electrocatalytic activity [14].

Apart from the catalytic activity, the performance of MEA also depends on operating conditions. Humidification and gas flow rate are the operating conditions of MEA that can affect its performance [8, 17]. In MEA, humidification is important because it will affect the supply of water vapor to the membrane. If the water vapor supply is less, then the membrane will be dehydrated, and the evaporation of water in the membrane increases [18]. Meanwhile, increasing the temperature can increase the reaction kinetics [19]. Increasing the temperature of the humidifier keeps the water passing through the electrode in a vapor state to avoid condensation, which can create a flood condition on the electrode [20].

Table 1. Electrocatalytic data at a current density of 10 mA·cm^{-2} (E@10 mA·cm^{-2} for OER)

Materials	ORR		
	$E_{on\ set}$ (V vs RHE)	$E_{1/2}$ (V vs RHE)	Tafel slope (mV dec^{-1})
CoFe/N-C	1.03	0.821	86
Pt/C	1.01	0.817	93
Fe/N-C	0.95	0.764	80
Co/N-C	0.91	0.776	54

Source: [14]

Materials and Methods

Herein, we compared the performance of two MEAs. The electrodes of the first MEA used Pt/C 40 wt.% (Fuel Cell Store) and CoFe/N-C (self-synthesised, refer to paper [14]) catalysts at the anode and cathode, respectively, with catalyst loading of 1 mg/cm^2 of each electrode, whereas the second MEA used a Pt/C catalyst on both electrodes. The electrode size was 5 cm × 5 cm, and the electrolyte membrane used was Nafion-212 (Fuel Cell Store). A pin type flow field and gold-plated current collectors (Electrochem/Fuel Cell Store) were also used. The electrode structure consisted of a backing layer in the form of a carbon paper (Gashub, Singapore) and a microporous layer (MPL) comprising a mixture of carbon Vulcan XC-72R (Fuel Cell Store), ammonium bicarbonate (Sigma-Aldrich) and Teflon DISP 30 Fluoropolymer dispersion (Fuel Cell Store). The electrode structure also consisted a CL comprising a Pt/C catalyst (40 wt%, Fuel Cell Store) at the anode (for both MEA types) and Pt/C and Co-Fe/C-N catalysts (self-synthesised) for each cathode at two types of MEAs. Catalyst loading was 1 mg/cm^2, and the catalyst ink on the catalyst and MPL was stirred using an ultrasonic homogeniser for 15 min. The electrodes were characterised using an Autolab PGSTAT 204 by cyclic voltammetry and electrochemical impedance spectroscopy to determine electrochemically active surface area (ECSA) and electrical conductivity. ECSA and electrical conductivity are calculated using Equations (1) and (2) with modifications.

$$\text{ECSA (cm}^2\text{/g)} = \frac{q}{\Gamma . L} \quad (1)$$

where q is the charge density (C/cm^2), Γ is the equivalent constant (μC/cm^2), and L is the catalyst loading (mg/cm^2) [21, 22].

$$\text{EIS } (\sigma)\ \text{(S/cm)} = \frac{1}{Z_R} \times \frac{1}{A}, \quad (2)$$

where Z_R is the total resistance = Rp + Rs (Ω) (note: Rp, and Rs are obtained from Nyquist curve fitting), l is the thickness (cm), and A is the surface area (cm^2) [23, 24].

CV and EIS analyses were performed using Potentiostat/Galvanostat PGSTAT204 from Methrom with Nova 2.1.4 software to process the data. CV and EIS were performed by placing Pt/C or Co-FeN/C electrodes, Ag/AgCl and platinum rods as working, reference and supporting electrodes, respectively. In addition, NaOH solution with a concentration of 1 M served as the electrolyte with a potential range of −0.2 V to 0.6 V and a scan rate of 100 mV/s. The measurements were repeated for 5 cycles.

MEA was fabricated from two electrodes and Nafion 212 (NR 212) (Fuel Cell Store) as an electrolyte membrane with hot pressing at 135 °C of 2000 psi for 3 min. The performance of MEA (I-V and I-P's performance) was tested using the fuel cell test station SMART2 WonAtech (South Korea) with varying flow rates of hydrogen gas (UHP, Samator, 100, 200, 300 and 400 mL/min) and oxygen gas (UHP, Samator) at 100 mL/min. The humidifier temperature varied from 40 °C, 60 °C, 80 °C and 100 °C.

Results and Discussion

Electrochemical characterisation

MEAs consisting of Pt/C (anode) and Co-Fe/N-C (cathode), as well as Pt/C catalysts on both electrodes, were arranged in a stack. Before making the MEA, the electrodes were characterised using CV and EIS. These methods were used in electrode characterisation to determine catalytic activity based on the ECSA values from CV analysis and electrical conductivity from EIS analysis. Determining the ECSA value from the voltammogram is a common procedure, and the value depends on the area of the electrode as well as the kinds and the loading of the catalyst [25, 26].

EIS is a well-established diagnostic method in electrochemistry [27]. The voltammogram and Nyquist curve of the electrodes are shown in Figure 1. As shown in Figure 1, the performance of the electrode with a Pt/C catalyst was better than that with a CoFe/N-C catalyst. Figure 1(a) shows a voltammogram from CV analysis with a scan rate of 100 mV/s. The electric charge can be determined on the basis of the area of the peak curve of the voltammogram and the scan rate data. If the electric charge is observed from the voltammogram curve in Figure 1(a), then the area of the electrode with the CoFe/N-C catalyst is smaller than that with the Pt/C catalyst. This result was confirmed through a smaller ECSA value compared with the Pt/C catalyst.

Figure 1(b) represents the impedance characteristics of the electrode with Pt/C and CoFe/N-C catalysts. Electrodes with a Pt/C catalyst had an impedance value of 3.12 Ω, whereas CoFe/N-C electrodes had a real impedance value of 5.54 Ω. The electrical conductivity of the electrode can be determined with the known equation based on the impedance values [24]. The ability of an electrode to conduct electricity can be determined from the conductivity value. The electrical conductivity value in electrodes coated with Pt/C was 7.2×10^{-3} S/cm, whereas that in electrodes coated with CoFe/N-C catalysts was 4.4×10^{-3} S/cm (Table 2).

.

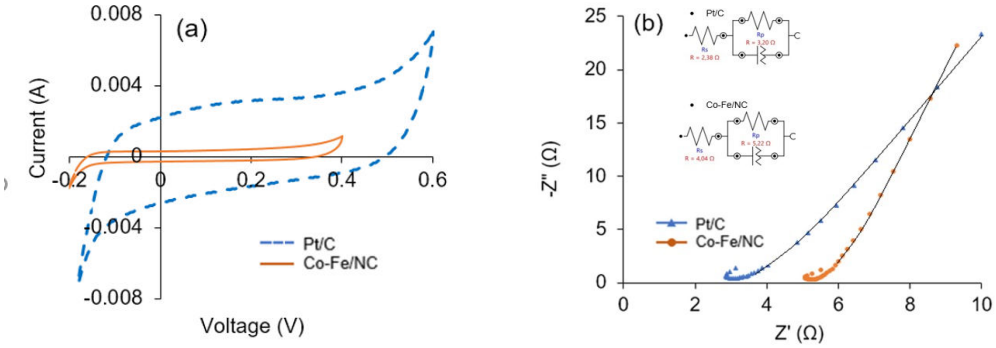

Figure 1. Electrode characterisation result using (a) CV and (b) EIS

Table 2. The electrical conductivity with Pt/C and CoFe/N-C catalysts

No.	Electrode	Impedance Parameters		Electrical Conductivity (S/cm)
		Rs (Ω)	Rp (Ω)	
1.	Pt/C	4.0357	5.2236	7.2×10^{-3}
2.	CoFe/N-C	2.3826	3.2046	4.4×10^{-3}

ECSA shows the active surface area of the catalyst, which is the response of the electrode in the form of current to the applied voltage. In turn, ECSA can be determined through the existing equations [28, 29] by considering the loading of the catalyst and the surface area of the electrode. Apart from the catalyst loading and surface area, ECSA also used a correction factor [30]. Moreover, based on the calculations, the ECSA value of the electrode with Pt/C and CoFe/N-C catalysts was 0.245 and 0.019 m^2/g, respectively. The distribution and surface area of the catalyst in the CL are the factors influencing the ECSA value of an electrode. Adding conductive carbon to the catalyst can lead to the even distribution of the catalyst [31, 32]. The even distribution of the catalyst in carbon may increase the active site of the catalyst. The carbon matrix in the catalyst is a factor affecting the ECSA value on a fuel cell electrode, which can make the catalyst spread more evenly. The more even the distribution of the catalyst in the carbon is, the larger the active site of the catalyst will be. A large surface area allows the distribution of Pt and CoFe metals amongst the carbon pores and even distribution on the surface of the CL [30].

The particle size of CoFe/N-C was more than 10 nm and uneven [14], whereas the particle size of Pt/C was approximately 3–4 nm [33]. The relatively smaller particle size of Pt/C led to a larger surface area of the Pt/C catalyst. Thus, it became a factor that led to a larger Pt/C ECSA value. Electrodes with Pt/C catalysts have an impedance value of 3.12 Ω, whereas CoFe/N-C electrodes have a real impedance value of 5.54 Ω. A high impedance value indicates the low conductivity of the electrodes. Moreover, EIS was used to analyse the electrochemical performance of an electrode, which will produce data from the sample response to a given frequency range in the form of real independence (Z′) and imaginary independence (Z″) values [34, 35]. The Nyquist curve can determine the impedance of electrodes through fitting to simulate the equivalent circuits.

Measurement of open-circuit voltage (OCV)

The OCV testing of the two MEAs showed their initial performance. The MEA with a Pt/C catalyst on both electrodes had a higher OCV of 0.890 V compared with that with a CoFe/C-N catalyst on one of the electrodes, which had an OCV of 0.720 V. Although the OCV value suggests an opportunity to use CoFe/C-N catalyst as a catalyst for PEMFC, the performance of the MEA is largely determined by its ability to maintain voltage with increasing load and not just under OCV conditions.

Performance testing of MEA at various humidifier temperatures

The performance of MEA was measured by testing the influence of humidifier temperature at 40 °C, 60 °C, 80 °C and 100 °C with a hydrogen flow rate of 200 mL/min. In addition, MEA treatment at high temperatures can increase the electrochemical kinetics, reduce the susceptibility to contamination and facilitate good water management [8]. Moreover, the performance of MEA at various humidifier temperatures is shown in Figure 2.

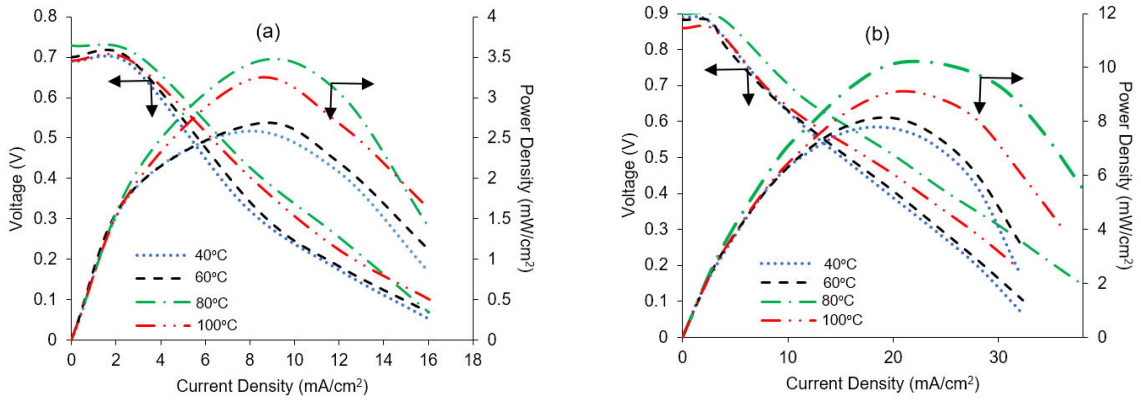

Figure 2. Effects of humidifier temperature on the performance of MEA with (a) CoFe/N-C and (b) Pt/C catalysts

The polarisation curve shows that the voltage decreases with the increase of load implemented as the electric current density [36]. Figure 2 shows that 80 °C is the optimum humidifier temperature because it can maintain voltage against an increase in current density, which is greater than those of other humidifier temperatures. The performance of MEA with CoFe/NC and Pt/C catalysts on the cathode and anode side (Figure 2[a]) was lower than that with a Pt/C catalyst on both sides (Figure 2[b]). This fact strengthened the OCV data. The MEA with a COFe/N-C catalyst in the cathode (Figure 2[a]) cannot support the performance of the Pt/C catalyst in the anode. However, in zinc–air batteries [14], the COFe/N-C catalyst is superior to Pt/C. The MEA shown in Figure 2(a) produced a maximum power density of 3.42 mW/cm^2 at a current density of 8.04 mA/cm^2, whereas the MEA with a Pt/C catalyst on both sides (Figure 2[b]) obtained a maximum power density of 10.14 mW/cm^2 at a current density of 20.04 mA/cm^2. Prior studies have investigated the impact of humidifier temperature on the performance of MEA in PEMFCs, using Pt catalysts on the anode and cathode. The humidifier temperature set at 80 °C delineates the boundary for high-temperature PEMFCs [37].

MEA performance test on various hydrogen flow rates

After obtaining the optimum humidifier temperature of 80 °C, the performance of MEA on PEMFCs was continuously tested on the basis of the effect of varying hydrogen flow rates (100, 200, 300 and 400 mL/min). The I-P and I-V performances are shown in Figure 3.

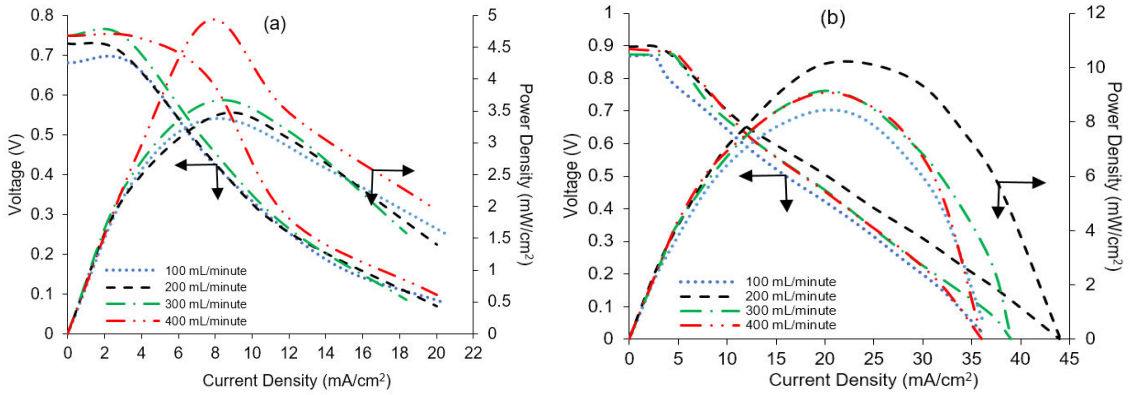

Figure 3. Effects of the hydrogen flow rate on the performance of MEA with (a) CoFe/N-C and (b) Pt/C catalysts

The ability of MEA to maintain a high voltage for a given current at a hydrogen flow rate of 400 mL/min compared with other hydrogen flow rates was shown on the basis of the I-V curve depicted in Figure 3(a) (MEA with CoFe/N-C and Pt/C catalysts). The hydrogen flow rate can well maintain the voltage during activation and ohmic polarisation; hence, the voltage does not decrease drastically with the increase of current density. However, MEA with a Pt/C catalyst on both sides (Figure 3[b]) at a hydrogen flow rate of 400 mL/min could not maintain the resulting voltage with increasing current density. This result was particularly true in the region of concentration polarisation because of an imbalance in the ratio between the supply of reactants and the supply of products. Meanwhile, at a hydrogen flow rate of 200 mL/min, MEA in PEMFC can better maintain the resulting voltage with increasing current density. The resulting I-V curve was gentler than the curves of other hydrogen flow rates.

Figure 3(a) shows that MEA with a CoFe/N-C catalyst on the cathode side had a fairly good performance with increasing hydrogen flow rate. This result was due to the maximally distributed hydrogen supply on the anode side, which increased the number of protons produced. The increase can be seen from the resulting power density of 4.93 mW/cm^2 at a current density of 7.72 mA/cm^2. However, it did not affect MEA with Pt/C catalysts on both sides (Figure 3[b]). Thus, this finding indicated that a hydrogen flow rate of 400 mL/min produced a lower power density than a hydrogen flow rate of 200 mL/min, that is, 10.14 mW/cm^2 at a current density of 20.04 mA/cm^2. MEA with a Pt/C catalyst on both sides of the electrode showed better performance than MEA with CoFe/N-C and Pt/C catalysts at the

cathode and anode side, respectively. Thus, Pt/C was the best catalyst for MEA of PEMFCs, and adequate hydrogen flow rate can lead to a good performance.

Conclusion

The characterisation of electrodes with a Pt/C catalyst showed a higher ECSA and electrical conductivity value compared with electrodes with a CoFe/N-C catalyst. Furthermore, a humidifier temperature of 80 °C produced the best performance on PEMFC for both MEAs with a Pt/C catalyst on both sides as well as Pt/C and CoFe/N-C catalysts on the anode and cathode sides, respectively. Meanwhile, increasing the hydrogen flow rate improved the performance of MEA. A hydrogen flow rate of 400 mL/min produced the highest performance for MEA with Pt/C and CoFe/N-C catalysts on the anode and cathode side, respectively. However, for MEA with a Pt/C catalyst on both sides (anode and cathode), the optimum hydrogen flow rate was 200 mL/min. Therefore, the CoFe/N-C catalyst can be an alternative for a Pt/C catalyst in fuel cells, especially PEMFCs.

Acknowledgement

We would like to thank Sriwijaya University for facilitating this research and the authors who assisted in the research and publication process, especially to Prof. Dr. Edy Herianto Majlan and Dr. Afriayanti Sumboja for the best collaboration in this research.

References

1. Toudret, P., Blachot, J. F., Heitzmann, M., and Jacques, P. A. (2021). Impact of the cathode layer printing process on the performance of MEA integrating PGM free catalyst. *Catalysts,* 11(6): 669.
2. Giuliano, A., Catizzone, E., and Freda, C. (2021). Process simulation and environmental aspects of dimethyl ether production from digestate-derived syngas. *International Journal of Environmental Research and Public Health,* 18(2), 807.
3. Matulić, N., Radica, G., Barbir, F., & Nižetić, S. (2019). Commercial vehicle auxiliary loads powered by PEM fuel cell. *International Journal of Hydrogen Energy,* 44(20): 10082-10090.
4. Van Biert, L., Godjevac, M., Visser, K., and Aravind, P. V. (2016). A review of fuel cell systems for maritime applications. *Journal of Power Sources,* 327: 345-364.
5. Wang, Y., Chen, K. S., Mishler, J., Cho, S. C., and Adroher, X. C. (2011). A review of polymer electrolyte membrane fuel cells: Technology, applications, and needs on fundamental research. *Applied Energy,* 88(4): 981-1007.
6. Kumar Mohanta, P., Ripa, M. S., Regnet, F., and Jörissen, L. (2021). Effects of supports BET surface areas on membrane electrode assembly performance at high current loads. *Catalysts,* 11(2): 195.
7. Wang, Y., Guan, C., Zhang, P., Zhu, T., Wang, S., Zhu, Y., and Wang, X. (2022). Optimal design of a cathode flow field with a new arrangement of baffle plates for a high clean power generation of a polymer electrolyte membrane fuel cell. *Journal of Cleaner Production,* 375:134187.
8. Rohendi, D., Majlan, E. H., Mohamad, A. B., Daud, W. R. W., Kadhum, A. A. H. and Shyuan, L. K. (2015). Effects of temperature and backpressure on the performance degradation of MEA in PEMFC. *International Journal of Hydrogen Energy,* 40(34): 10960-10968.
9. Falina, I., Pavlets, A., Alekseenko, A., Titskaya, E., & Kononenko, N. (2021). Influence of PtCu/C catalysts composition on electrochemical characteristics of polymer electrolyte fuel cell and properties of proton exchange membrane. *Catalysts,* 11(9): 1063.
10. Zhou, Y., Yu, F., Lang, Z., Nie, H., Wang, Z., Shao, M., ... and Kang, Z. (2021). Carbon dots/PtW_6O_{24} composite as efficient and stable electrocatalyst for hydrogen oxidation reaction in PEMFCs. *Chemical Engineering Journal,* 426: 130709.
11. Briega-Martos, V., Ferre-Vilaplana, A., Herrero, E., and Feliu, J. M. (2020). Why the activity of the hydrogen oxidation reaction on platinum decreases as pH increases. Electrochimica Acta, 354, 136620.
12. Molochas, C., and Tsiakaras, P. (2021). Carbon monoxide tolerant Pt-based electrocatalysts for H_2-PEMFC applications: Current progress and challenges. *Catalysts,* 11(9): 1127.
13. Chung, S., Ham, K., Kang, S., Ju, H., and Lee, J. (2020). Enhanced corrosion tolerance and highly durable ORR activity by low Pt electrocatalyst on unique pore structured CNF in PEM fuel cell. *Electrochimica Acta,* 348: 136346.

14. An, T., Ge, X., Tham, N. N., Sumboja, A., Liu, Z., & Zong, Y. (2018). Facile one-pot synthesis of CoFe alloy nanoparticles decorated N-doped carbon for high-performance rechargeable zinc–air battery stacks. *ACS Sustainable Chemistry & Engineering,* 6(6), 7743-7751.
15. Rao, P., Deng, Y., Fan, W., Luo, J., Deng, P., Li, J., ... and Tian, X. (2022). Movable type printing method to synthesize high-entropy single-atom catalysts. *Nature Communications,* 13(1): 5071.
16. Hao, Z., Ma, Y., Chen, Y., Fu, P., and Wang, P. (2022). Non-noble metal catalysts in cathodic oxygen reduction reaction of proton exchange membrane fuel cells: recent advances. *Nanomaterials,* 12(19): 3331.
17. Chang, Y., Qin, Y., Yin, Y., Zhang, J., and Li, X. (2018). Humidification strategy for polymer electrolyte membrane fuel cells–A review. *Applied Energy*, 230: 643-662.
18. Houreh, N. B., Ghaedamini, M., Shokouhmand, H., Afshari, E., and Ahmaditaba, A. H. (2020). Experimental study on performance of membrane humidifiers with different configurations and operating conditions for PEM fuel cells. *International Journal of Hydrogen Energy,* 45(7): 4841-4859.
19. Zhang, J., Wang, C., and Zhang, A. (2022). Experimental study on temperature and performance of an open-cathode PEMFC stack under thermal radiation environment. *Applied Energy,* 311: 118646.
20. Xia, Z., Chen, H., Zhang, T., and Pei, P. (2022). Effect of channel-rib width ratio and relative humidity on performance of a single serpentine PEMFC based on electrochemical impedance spectroscopy. *International Journal of Hydrogen Energy,* 47(26): 13076-13086.
21. Cooper, K. R. (2009). In situ PEM fuel cell electrochemical surface area and catalyst utilization measurement. *Fuel Cell Magazine,* 9: 28.
22. Eris, S., Daşdelen, Z., and Sen, F. (2018). Enhanced electrocatalytic activity and stability of monodisperse Pt nanocomposites for direct methanol fuel cells. *Journal of Colloid and Interface Science,* 513: 767-773.
23. Wang, C., Feng, Z., Zhao, Y., Li, X., Li, W., Xie, X., ... and Hou, H. (2017). Preparation and properties of ion exchange membranes for PEMFC with sulfonic and carboxylic acid groups based on polynorbornenes. *International Journal of Hydrogen Energy*, 42(50): 29988-29994.
24. Zhang, F., Cheng, F., Cheng, C., Guo, M., Liu, Y., Miao, Y., ... & Wang, X. (2022). Preparation and electrical conductivity of (Zr, Hf, Pr, Y, La) O high entropy fluorite oxides. *Journal of Materials Science & Technology,* 105: 122-130.
25. Arroyo-Ramírez, L., Montano-Serrano, R., Luna-Pineda, T., Román, F. R., Raptis, R. G., and Cabrera, C. R. (2013). Synthesis and characterization of palladium and palladium–cobalt nanoparticles on vulcan XC-72R for the oxygen reduction reaction. *ACS Applied Materials & Interfaces,* 5(22): 11603-11612.
26. Wu, K., Wang, Z., Zhang, G., Fan, L., Zhu, M., Xie, X., ... and Jiao, K. (2022). Correlating electrochemical active surface area with humidity and its application in proton exchange membrane fuel cell modeling. *Energy Conversion and Management,* 251: 114982.
27. Niya, S. M. R. and Hoorfar, M. (2013). Study of proton exchange membrane fuel cells using electrochemical impedance spectroscopy technique–A review. *Journal of Power Sources,* 240: 281-293.
28. Shiva Kumar, S., Ramakrishna, S. U. B., Rama Devi, B., and Himabindu, V. (2018). Phosphorus-doped graphene supported palladium (Pd/PG) electrocatalyst for the hydrogen evolution reaction in PEM water electrolysis. *International Journal of Green Energy*, 15(10): 558-567.
29. Andrews, J., and Doddathimmaiah, A. K. (2008). Regenerative fuel cells. In Materials for Fuel Cells (pp. 344-385). Woodhead Publishing.
30. Brightman, E., Hinds, G., and O'Malley, R. (2013). In situ measurement of active catalyst surface area in fuel cell stacks. *Journal of Power Sources*, 242: 244-254.
31. Binninger, T., Fabbri, E., Kötz, R. and Schmidt, T. J. (2013). Determination of the electrochemically active surface area of metal-oxide supported platinum catalyst. *Journal of The Electrochemical Society,* 161(3): H121.
32. Li, Y., Xiong, D., Liu, Y., Liu, M., Liu, J., Liang, C., ... and Xu, J. (2019). Correlation between electrochemical performance degradation and catalyst structural parameters on polymer electrolyte membrane fuel cell. *Nanotechnology Reviews,* 8(1): 493-502.

33. Rohendi, D., Majlan, E. H., Mohamad, A. B., Daud, W. R. W., Kadhum, A. A. H., and Shyuan, L. K. (2013). Characterization of electrodes and performance tests on MEAs with varying platinum content and under various operational conditions. *International Journal of Hydrogen Energy*, 38(22): 9431-9437.
34. Asghari, S., Mokmeli, A., and Samavati, M. (2010). Study of PEM fuel cell performance by electrochemical impedance spectroscopy. *International Journal of Hydrogen Energy*, 35(17): 9283-9290.
35. Ruiz-Camacho, B., Vera, J. B., Medina-Ramírez, A., Fuentes-Ramírez, R., and Carreño-Aguilera, G. (2017). EIS analysis of oxygen reduction reaction of Pt supported on different substrates. *International Journal of Hydrogen Energy,* 42(51): 30364-30373.
36. Zhu, D., Yang, Y., Pei, F., and Ma, T. (2022). High-precision identification of polarization processes of distribution of relaxation times by polarization curve model for proton exchange membrane fuel cell. *Energy Conversion and Management,* 268: 115994.
37. Rohendi, D., Majlan, E. H., Mohamad, A. B., Daud, W. R. W., Kadhum, A. A. H., and Shyuan, L. K. (2015). Effects of temperature and backpressure on the performance degradation of MEA in PEMFC. *International Journal of Hydrogen Energy,* 40(34): 10960-10968.

Malaysian Journal of Analytical Sciences (MJAS)
Published by Malaysian Analytical Sciences Society

AN INSIGHT INTO PINEAPPLE PEEL WASTE ADSORBENT FOR IRON CONTAMINATED WATER THROUGH KINETIC AND ISOTHERM STUDY

(Tinjauan Terhadap Penjerap daripada Sisa Kulit Nanas bagi Air Tercemar dengan Ferum Melalui Kajian Kinetik dan Isoterma)

Nurul Faizah Abd Ghapar[1], Rozaimi Abu Samah[1]*, Mohamad Syafiq Abdul Wahab[2], Sunarti Abd Rahman[1], and Mohd Hafiz Dzarfan Othman[3]

[1]*Faculty of Chemical & Process Engineering Technology, Universiti Malaysia Pahang Al-Sultan Abdullah, Lebuh Persiaran Tun Khalil Yaakob, 26300 Kuantan, Pahang, Malaysia.*
[2]*EMZI-UiTM Nanoparticles Colloids and Interface Industrial Research Laboratory (NANO-CORE), School of Chemical Engineering, College of Engineering, Universiti Teknologi MARA, Cawangan Pulau Pinang, Kampus Permatang Pauh,13500 Permatang Pauh, Penang, Malaysia.*
[3]*Advanced Membrane Technology Research Center (AMTEC), School of Chemical and Energy Engineering, Universiti Teknologi Malaysia, 81310 UTM Johor Bahru, Johor, Malaysia*

[*]*Corresponding author: rozaimi@umpsa.edu.my*

Received: 17 November 2023; Accepted: 12 February 2024; Published: 29 April 2024

Abstract

The swift growth of sectors like steel and coal mining leads to a higher release of heavy metals like iron into aquatic ecosystems, resulting in water pollution. In this study, the kinetics and isotherms studies were applied to pineapple peel waste based adsorbent for iron removal. An adsorbent derived from discarded pineapple peels was created through a chemical activation process, employing zinc chloride ($ZnCl_2$) as the activator. By examining the effects of various experimental parameters, including contact duration (30–240 min), concentration of iron (5–80 ppm), and the amount of adsorbent (2–24 g/L), the behaviour of the adsorbent for iron adsorption was carefully studied. Maximum iron removal of 99.24% efficiency with adsorbent dosage of 20 g/L was achieved through this study. The iron removal process was most accurately represented by the Freundlich isotherm model, exhibiting an R^2 value of 0.985. Furthermore, the kinetics investigation demonstrated an excellent fit with the pseudo-second-order model for iron adsorption, yielding an R^2 value of 0.999. These findings strongly indicate that pineapple peel waste holds promise as a viable adsorbent for eliminating iron from water bodies.

Keywords: Pineapple peel waste, iron removal, adsorption isotherm, adsorption kinetic

Abstrak

Pertumbuhan pesat sektor-sektor seperti keluli dan perlombongan arang menyebabkan peningkatan pelepasan logam berat seperti ferum ke dalam ekosistem akuatik, yang mengakibatkan pencemaran air. Dalam kajian ini, kajian kinetik dan isoterma telah digunakan bagi penyingkiran ferum menggunakan penjerap berasaskan sisa kulit nanas. Penjerap yang diperoleh daripada kulit nanas yang dibuang telah dihasilkan melalui proses pengaktifan kimia dengan menggunakan zink klorida ($ZnCl_2$) sebagai pengaktif. Dengan mengkaji kesan pelbagai parameter eksperimen, termasuk tempoh penjerapan (30–240 minit), kepekatan ferum (5–80 ppm), dan jumlah penjerap (2–24 g/L), tingkah laku penjerap untuk penjerapan ferum telah dikaji dengan teliti. Penyingkiran ferum maksimum sebanyak 99.24% dengan dos penjerap 20 g/L telah dicapai melalui kajian ini. Proses penyingkiran ferum paling tepat

diwakili oleh model isoterma Freundlich, dengan nilai R^2 sebanyak 0.985. Selain itu, penyiasatan kinetik menunjukkan kesesuaian yang sangat baik dengan model pseudo-tertib kedua untuk penjerapan ferum, menghasilkan nilai R^2 sebanyak 0.999. Penemuan ini menunjukkan bahawa sisa kulit nanas berpotensi sebagai penjerap yang berkesan untuk menyingkirkan ferum dari air.

Kata kunci: sisa kulit nenas, penyingkiran ferum, isoterma penjerapan, kinetik penjerapan

Introduction

Iron stands as one of the most plentiful elements in the earth's crust, occurring naturally in water in two primary forms: soluble ferrous iron, Fe(II) or $Fe(OH)^+$, and complexed ferric iron, Fe(III), which precipitates as $Fe(OH)_3$ [1]. Iron can also be found in water because of industrial activities like metal plating, mining, the iron and steel industry, and the corrosion of metal materials [1, 2]. As reported by Al-Anber, the safe level for Fe(III) ions for the human body is not more than 0.3 ppm and excessive iron ions may cause anorexia and oliguria. The high amount of iron can also give the water a metallic taste and odour [3]. To overcome these problems, special attention should be given to removing or reducing the amount of iron ions from industrial water effluents or water supply.

Liquid-phase adsorption is one of the most common methods used to remove heavy metals from wastewater due to the proper design of the adsorption process that will produce a high-quality treated effluent [2]. However, the adsorption of heavy metals such as iron by commercial adsorbent is expensive; therefore, research studies focus on developing adsorbents from agricultural waste to remove iron from the aqueous system [3]. Among these various adsorbents, including rice hull [2], rice husk ash [4], orange peel [5], olive stones [1, 6], wild jack, and jambul barks [7] have been employed for the purpose of eliminating iron ions from aqueous solutions. Based on recent works, adsorbent from pineapple peel waste can be considered an agricultural waste that shows remarkable potential towards the adsorption of toxic heavy metals from the aqueous solutions. For instance, Zn, Cr, Cd, Pb, Mn, and Cu ions have been removed from aqueous solutions [8–11].

Malaysia's pineapple (*Ananas comosus*) industry was ranked 18th world's largest pineapple producer with 334,400 metric tonnes produced by 13,733 hectares of planted area. As reported by Ahmad Zamri et al., about 335,488 tonnes of pineapple produced in Malaysia yielded 137,550 tonnes of pineapple peel [12]. Pineapple fruit typically consists of around 60% edible flesh and approximately 35% skin or peel, which is considered waste material. This peel is primarily composed of cellulose, hemicellulose, lignin, and pectin substances. With certain modifications, pineapple peel can be repurposed and utilised as an adsorbent material [10, 11]. Previous studies reported adsorbent from pineapple peel waste showed very high removal efficiencies of heavy metals such as Cd(II), Pb(II), Cu(II), Zn(II), and Cr(VI). For example, Turkmen et al. reported that the pineapple peel waste which was carbonised using microwave at 800 W yielded a maximum Zn(II) removal efficiency of 93% for both types of activating agent: $ZnCl_2$ and H_2SO_4 [13]. The similar result reported by Olowu et al. (2022) when pineapple peel adsorbent was used to remove Zn(II) and Cr(VI) from the aqueous solution with the maximum percentage removals of 89% and 91.2%, respectively [8]. Hence, considering both economic and environmental aspects, pineapple peel waste may serve as an effective adsorbent for the removal of iron from aqueous solutions.

Solid waste derived from processed pineapple peel waste has previously been employed as an adsorbent, demonstrating considerable potential for adsorbing harmful pollutants, including heavy metals. In this study, we assessed the capability of pineapple peel waste as an adsorbent for capturing Fe(III) ions from aqueous solutions. The investigation involved the assessment of various operational factors such as contact time, adsorbent quantity, and initial iron concentration through a batch adsorption study. Furthermore, we delved into the sorption mechanism by examining different kinetic models, including the pseudo-first- and pseudo-second-order models. To evaluate various isotherms and their capacity to correlate with experimental data, three isotherm models—Langmuir, Freundlich, and Temkin—were employed.

Materials and Methods

Materials

Iron standard solution, $Fe(NO_3)_3$, sulfuric acid, H_2SO_4, and zinc chloride, $ZnCl_2$, of analytical grade were procured from Merck chemicals. A stock iron solution

with a concentration of 1,000 mg/L was employed as the adsorbate, and different concentrations were prepared by diluting the stock solution with distilled water. pH measurements were conducted using the pH meter pH 150 from Eutech Instruments.

Preparation of adsorbent from pineapple peel waste

The adsorbent was prepared using a method reported by Rozaidi & Abu Samah with some modifications [14]. Pineapple peel waste collected from Pekan Pina Sdn. Bhd. was washed with distilled water. The peels were oven-dried at 80 °C for 24 h. Then, the dried peels were ground and sieved using a sieve with 300 µm size to obtain the particle size of less than 300 µm. After that, chemical activation was performed by mixing 30 g of sieved pineapple peels with 1.0 M of $ZnCl_2$. The procedure involved stirring the mixture for 24 h at room temperature using a magnetic stirrer, followed by filtration. The filtered peels were then dried in an oven at 80 °C overnight. Subsequently, the sample was placed in a sealed crucible and subjected to carbonisation at 800 °C for 1 h, with a heating rate of 10 °C per min. After cooling to room temperature, the sample was immersed in a 0.5 M H_2SO_4 solution for 30 min to remove the excess $ZnCl_2$. Following this, the sample was once again dried in an oven at 80 °C for 24 h after being filtered and washed with distilled water until the wash water reached a pH of 7. The samples were then transferred to a desiccator and stored in sealed plastic bags for future use [15].

Characterisation of adsorbent

To identify the primary functional groups, present in the adsorbent, Fourier transform infrared spectroscopy (FTIR) was employed, utilising a Nicolet AVATAR 370 DTGS, UK instrument. The analysis covered the functional groups within the samples across a range of 500–4500 cm^{-1}. FTIR analysis allows the samples to be absorbed at different wavelengths with characteristic beams produced at different wavelengths which will later be analysed and computerised in the form of wave numbers, expressed in cm^{-1}. All spectra included the wave numbers from 4000 to 500 cm^{-1} with 128 scans at a resolution of 2.0 cm^{-1}.

Furthermore, the adsorbents were pretreated by degassing at 200 °C for 2 h, in a vacuum condition, then the specific Brunauer–Emmett–Teller analysis (BET, Micromeritics ASAP 2010, USA) was used to determine the surface area (S_{BET}) of the samples.

Additionally, the morphology of the adsorbent was examined through scanning electron microscopy (SEM, JEOL JSM-7800F, Japan). The adsorbent was mounted using a carbon conductive pad on a metal stub and silver metals were placed at both sides of the samples. In a vacuum condition of an argon atmosphere, the samples were coated with gold for observation and analysis. When the scanning completed, the results were shown based on image formed at SEM display unit.

Batch adsorption study

Batch adsorption experiments were performed under standard conditions, where 2 g/L of the pineapple peel waste adsorbent was mixed with an iron-containing aqueous solution. The stirring process took place at ambient temperature and pressure. The mixture was continuously stirred magnetically for a duration of 240 min. To monitor the adsorption process over time, 10 mL of the mixture were withdrawn at 30-min intervals, and the amount of iron in these samples was analysed. The iron content was determined by using an atomic absorption spectrometer (AAS AAnalyst 400, Perkin Elmer). The experiment was repeated with different amounts of adsorbent (2–24 g/L) and different initial concentrations of iron (5–30 ppm). The removal of iron by the adsorbent was calculated using Equation 1.

$$Removal\ (\%) = \frac{C_i - C_t}{C_i} \times 100\ \% \quad (1)$$

C_i represents the initial iron concentration in the sample (measured in mg/L), while C_t denotes the concentration of iron at a particular time during the experiment (also measured in mg/L).

The amount of iron adsorbed on the adsorbent at certain time was calculated using Equation 2:

$$q_t = \frac{(C_i - C_t)V}{M} \quad (2)$$

Here, q_t represents the iron adsorption on the adsorbent at any given time (measured in mg/g), V indicates the volume of the solution in litres (L), and M signifies the mass of the adsorbent in grams (g).

Kinetic modeling

Pseudo-first- and pseudo-second-order kinetic models are commonly used to describe the adsorption kinetics [16]. The pseudo-first-order equation is given by Equation 3:

$$\frac{dq_t}{dt} = k_1 (q_e - q_t) \quad (3)$$

where q_t and q_e are the amount of solute adsorbed (mg/g) at time t and equilibrium, respectively and k_1 is the rate constant of the kinetic model (min^{-1}). The linearised equation of pseudo-first-order can by expressed by Equation 4:

$$\log(q_e - q_t) = \log\ q_e - \frac{k_1}{2.303} t \quad (4)$$

A plot of $\log(q_e - q_t)$ versus t can be used to obtain the rate constant.

The pseudo-second-order equation is expressed by Equation 5:

$$\frac{dq_t}{dt} = k_2(q_e - q_t)^2 \quad (5)$$

where k_2 is the pseudo-second-order rate constant (g/mg·min) and the linearised form is expressed in Equation 6:

$$\frac{t}{q_t} = \frac{1}{k_2 {q_e}^2} + \frac{1}{q_e} t \quad (6)$$

A plot of t/q_t versus t gives the pseudo-second-order rate constant.

Adsorption Isotherms

Langmuir, Freundlich, and Temkin isotherms are commonly used to determine the adsorption isotherms. These equations explain the relationship between the solute concentrations in both liquid and adsorbent surface equilibrium. Equation 7 represents the Langmuir isotherms:

$$q_e = \frac{q_m K_L C_e}{1 + K_L C_e} \quad (7)$$

where q_e is the quantity of the adsorbed adsorbate bound per unit amount of adsorbent (mg/g), q_m is the maximum adsorption capacity, K_L is the affinity constant for Langmuir isotherm (L/mg), and C_e is the adsorbate equilibrium concentration (mg/L).

To determine the values of maximum adsorption capacity (q_m) and the Langmuir affinity constant (K_L), Equation 7 can be linearised into several form as shown in Equation 8.

$$\frac{C_e}{q_e} = \frac{C_e}{q_m} + \frac{1}{q_m K_L} \quad (8)$$

A plot of C_e/q_e versus C_e was plotted to determine the values of q_m and K_L.

Freundlich isotherm does not predict the saturation binding of the adsorption. It assumes a logarithmic relationship between the adsorption equilibrium and the solute concentration as shown in Equation 9.

$$q_e = K_F {C_e}^{1/n} \quad (9)$$

where K_F is known as the Freundlich constant (mg/g) and 1/n is a constant reflecting the solute affinity towards the adsorbent.

By taking logarithmic on both sides of the equation, a linearised form of Freundlich isotherm can be used as shown in Equation 10 to determine the adsorption constant (K_F) and its affinity (1/n) by plotting log q_e versus log C_e.

$$log\ q_e = log\ K_F + \frac{1}{n} \log C_e \quad (10)$$

The Temkin isotherm model infers that the adsorption energy decreases linearly with the surface coverage caused by adsorbent–adsorbate interactions [3]. The Temkin isotherm is described in Equation 11:

$$q_e = B\ lnA + B \ln C_e \quad (11)$$

where C_e is the adsorbate equilibrium concentration (mg/L) and q_e is the quantity of metal adsorbed per gram of the adsorbent (mg/g).

The Temkin isotherm equation can be linearised to Equation 12:

$$q_e = \frac{RT}{b}\ lnC_e + \frac{RT}{b} lnK_T \quad (12)$$

where RT/b = B (J/mol) and K_T = A (L/g) are the Temkin constants. R (8.314 J/mol·K) represents the universal gas constant at T (K) which is the absolute solution temperature.

A plot q_e versus ln C_e was plotted to determine the Temkin constant.

Results and Discussion

Characterisation of pineapple peel waste adsorbent: BET analysis

The Brunauer–Emmett–Teller (BET) surface area measurement was utilised to assess the adsorption capacity of the adsorbent. This measurement operates on the principle that a greater surface area of the adsorbent corresponds to a higher adsorption capacity. In other words, as the surface area of the adsorbent increases, its ability to adsorb substances, in this case, iron, also increases. This relationship underscores the importance of surface area in determining the effectiveness of the adsorbent in adsorbing the target substance [17]. After chemical treatment followed by carbonisation at 800 °C for 1 hour, the surface area of pineapple peel waste adsorbent obtained was 1080.91 m^2/g. A prior study documented that following the activation and carbonisation procedures applied to raw pineapple peel waste, there was a noteworthy enhancement in the surface area of the prepared adsorbent [18]. Besides, the surface area of raw pineapple peel waste was 7.9348 m^2/g [14]. The carbonisation process conducted at 800 °C had the effect of improving the elimination of volatile compounds. Additionally, the inclusion of $ZnCl_2$ as an impregnation agent heightened the heat energy within the process. This, in turn, led to the creation of new pores and an accelerated development of porosity in the adsorbent. Consequently, these factors collectively contributed to an increase in the surface area of the adsorbent. [19].

The N_2 adsorption isotherms for the adsorbent are depicted in Figure 1. The behaviour of the adsorbent corresponds to a Type I isotherm, indicating that the adsorbent possesses microporous characteristics. A Type I isotherm typically exhibits a convex curve, and its plateau is either horizontal or nearly horizontal. In this type of isotherm, the adsorption curve directly intersects with the line $P/P_0 = 1$ [18]. The amount of adsorption experienced a rapid increase in a region of low relative pressure ($P/P_0 < 0.2$) during the initial stages of adsorption. This observation suggests that the primary location for nitrogen molecule adsorption was within the microporous structure of the adsorbent [18].

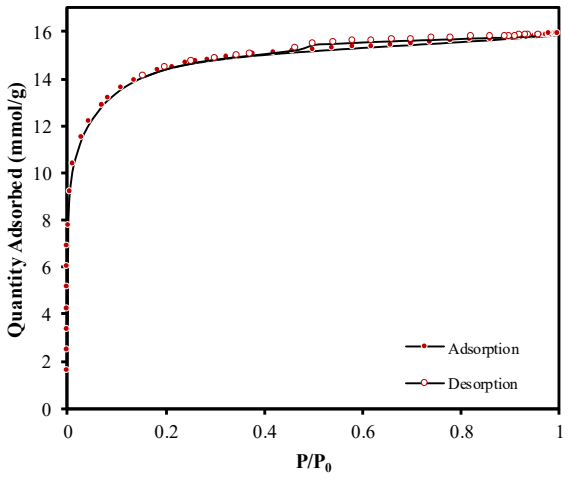

Figure 1. N_2 adsorption–desorption isotherms of adsorbent

Scanning electron microscopy (SEM) of adsorbent

Figure 2 shows the SEM images of raw pineapple peel waste, the prepared pineapple peel waste adsorbent, and the adsorbent after the adsorption process. SEM analysis was employed to observe the surface morphologies of the raw pineapple peel waste, the prepared adsorbent at 800 °C for 1 h, and the adsorbent after adsorption. The surface of raw pineapple peel waste is naturally uneven and features creases. However, the surface of the adsorbent exhibits a more intricate and porous structure after the modification process. This transformation can be attributed to the removal of volatile substances during carbonisation and activation, resulting in a stable carbon mass and the widening of pore networks within the

adsorbent sample, as documented in reference [20]. The porous nature of the adsorbent plays a significant role in facilitating the adsorption of heavy metals in wastewater. These pores serve as active sites for adsorption and increase the overall surface area of the adsorbent, as discussed in reference [21]. Furthermore, in this study, it was noted that the adsorbent's surface featured densely packed bundles of elongated cylindrical pores, signifying a strong adsorption capacity. This configuration provides an abundance of sites for capturing heavy metal ions, such as iron. This could be explained by the morphology of the adsorbent after adsorption where the surface morphology became rougher or more irregular due to the formation of metal ion complexes or precipitates on the surface of the adsorbent. It was observed that there are some cavities on the surface of the adsorbents [22].

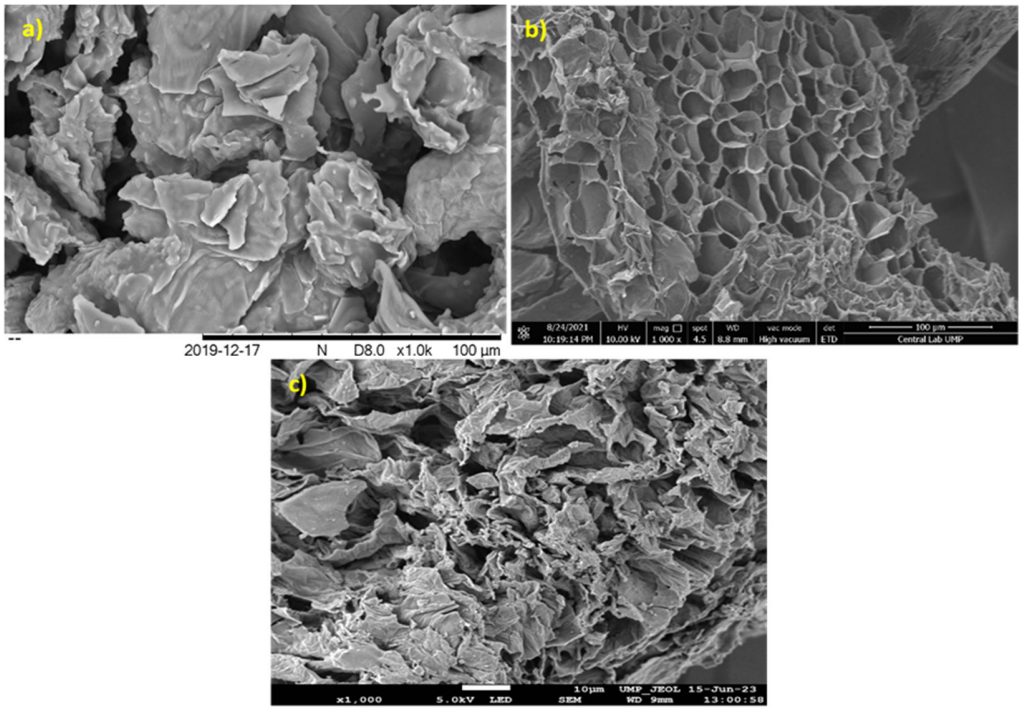

Figure 2. SEM images (1000× magnification) of (a) raw pineapple peel waste, (b) pineapple peel waste adsorbent and (c) adsorbent after adsorption

FTIR analysis

FTIR analysis was conducted to qualitatively identify the primary functional groups present on the surface of the adsorbent derived from pineapple fruit peel. Figure 3 displays the FTIR spectra of both the adsorbent and the raw pineapple peel. In the spectrum of the raw pineapple peel, a broad band appearing around 3,300 cm^{-1} is primarily associated with hydrogen bonds (O–H or NH_2) symmetrical stretching variations. Additionally, the peak at 2,917 cm^{-1} corresponds to aliphatic CH groups. However, after the modification process, several peaks within the range of 1,560–1,300 cm^{-1} can be attributed to CH_2 bending vibrations, O–H bending, and O–H stretching or C-– bending vibrations. Furthermore, a strong band at 1,089 cm^{-1} is attributed to the C–O of the $–OCH_3$ group, aligning with the lignin structure present in pineapple fruit peel [10] and [21]. The slight shift in absorption bands indicates the successful transformation of the raw pineapple peel into the adsorbent.

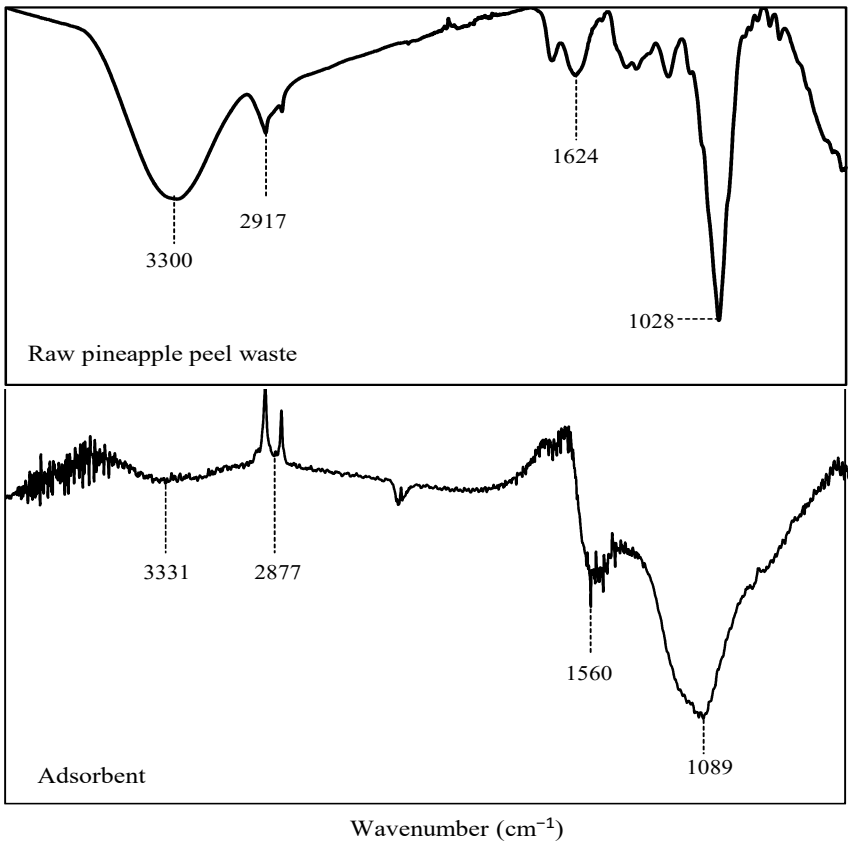

Figure 3. FTIR spectra for the raw pineapple peel waste and pineapple peel waste adsorbent

Batch adsorption studies: The effect of contact time

One of the most critical factors affecting adsorption performance is the contact time, as it illustrates the removal percentage of metal ions from the solution over time [24]. The effect of contact time on iron adsorption onto the pineapple peel waste adsorbent is shown in Figure 4(a). In the initial stages, the rate of adsorption exhibited a substantial increase and gradually reached equilibrium around the 150-min mark, achieving an efficiency of approximately 48.86% removal. Then, the final Fe(III) ions concentration became almost similar until 240 min. Therefore, the process was at steady state at 150 min. This situation happened when the metal ions rapidly adsorbed onto the adsorbent at the beginning caused by the availability of the empty active sites. In addition, the uptakes were gradually slower due to the decrease in vacant active sites [10]. It was reported that the properties of the adsorbent and its existing active sites are known to affect the time needed to reach equilibrium [23, 24].

The effect of adsorbent dosage

The impact of adsorbent dosage on the adsorption of iron onto the pineapple peel waste adsorbent was explored, as adsorbent dosage is recognised as another key factor influencing the adsorbent's capacity to adsorb metal ions at a given initial concentration [25–27]. In Figure 4(b), the removal percentage of Fe(III) ions and the adsorption capacity of the pineapple peel waste adsorbent are depicted across various dosages, all while maintaining a constant initial concentration of 5 ppm Fe solution. The graph demonstrates that 20 g/L gave the highest iron removal up to 99.24% and remained constant till 24 g/L. A higher amount of adsorbent dosage will increase the number of active sites since the adsorption depends on the availability of binding sites for iron [30].

The effect of initial iron concentration

In batch adsorption processes, the adsorption rate is a function of the initial concentration of heavy metal ions; hence it is a principal factor for a successful adsorption

process [31]. The percentage removal of iron at different initial concentrations from 5 to 80 ppm is shown in Figure 4(c). The removal efficiency increased drastically at 5 ppm before increasing gradually until 80 ppm with the highest removal of 80.13%. It shows that the pineapple peel waste adsorbent had a higher magnitude for Fe(III) ions adsorption. This may also be related to an increase in the concentration gradient driving force with the increase in metal ions concentration [4]. A comparable result was also reported where the adsorption of iron using rice husk ash gave higher iron adsorption capacity than manganese, which means that increasing the initial concentration of iron also improves the removal efficiency of iron [4].

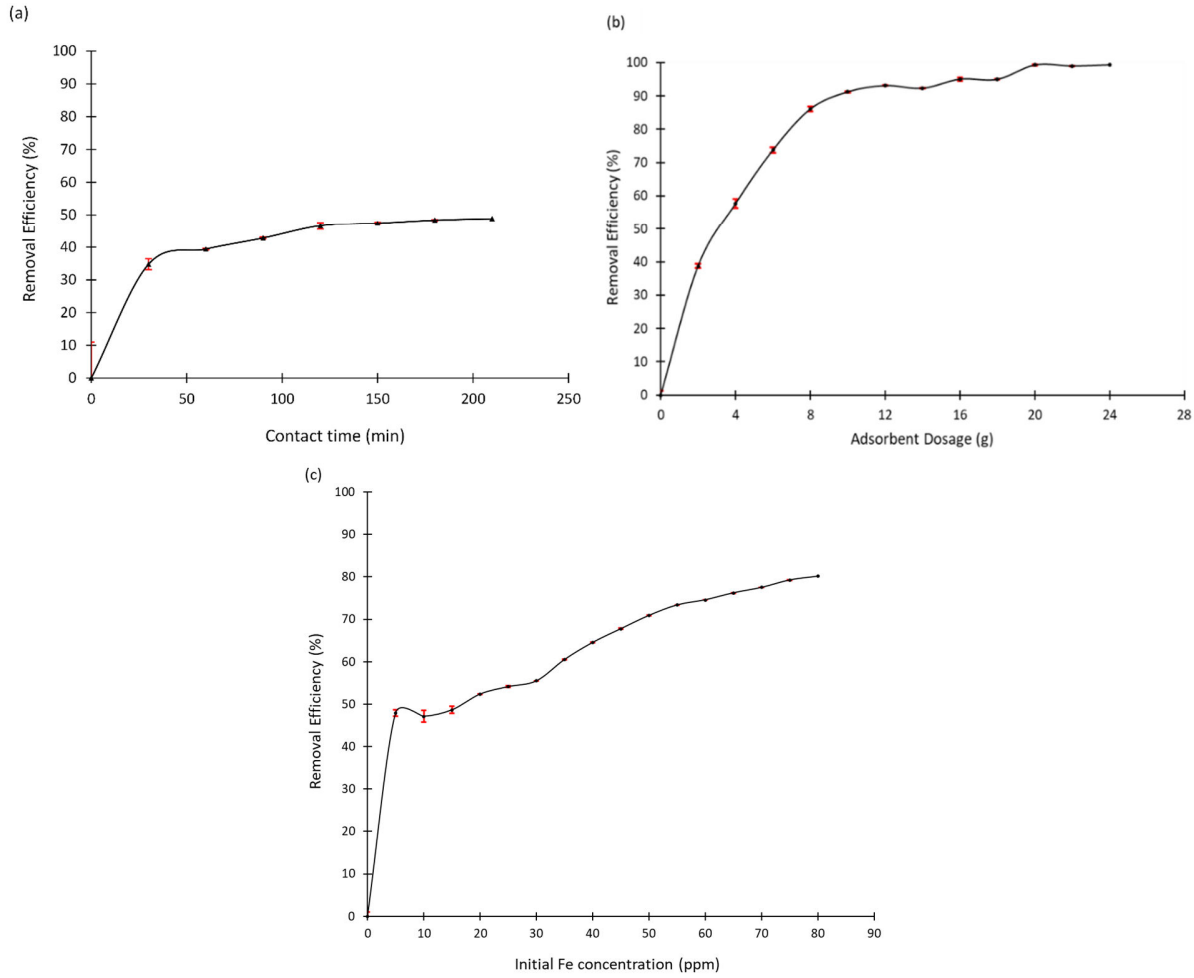

Figure 4. The effect of (a) contact time, (b) adsorbent dosage, and (c) initial iron concentration on the iron removal efficiency

Adsorption kinetic

Adsorption kinetics are used to explain the adsorption mechanism and characteristics. The pseudo-first- and pseudo-second-order kinetics models were applied to the adsorption data to specify the rate of adsorption of iron onto the pineapple peel waste adsorbent. Constants of pseudo-first- and pseudo-second-order were determined from the slope and intercept of the linear plots as shown in Figure 5(a) and 5(b), respectively.

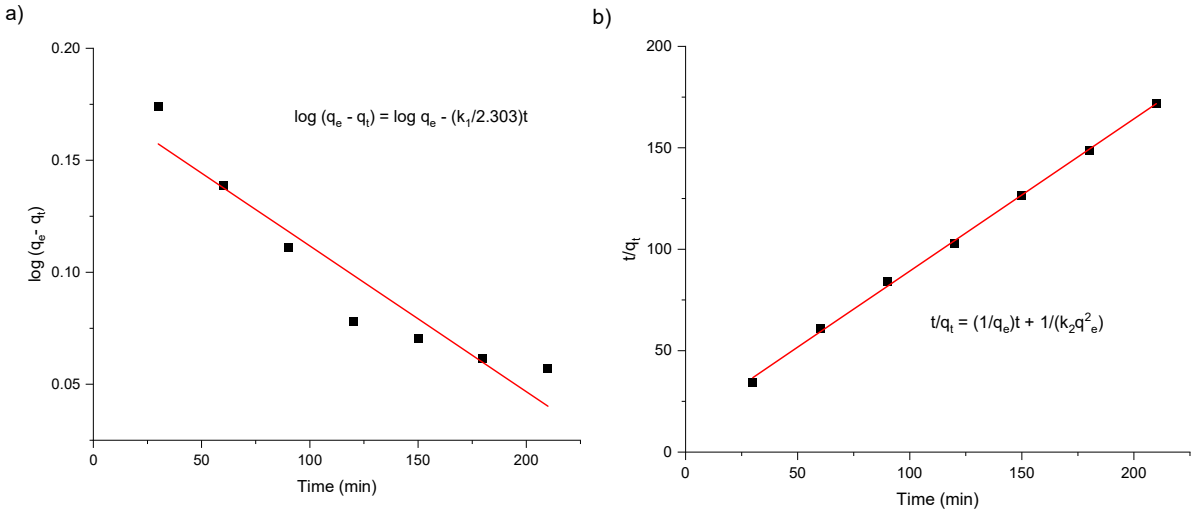

Figure 5. The plots of (a) pseudo-first- and (b) pseudo-second-order kinetic models for iron removal

Table 1. Pseudo-first- and pseudo-second-order parameters for iron removal

Model	Intercept	Slope	$q_{e\,(exp)}$ (mg/g)	$q_{e\,(cal)}$ (mg/g)	q^2_e	k	R^2
Pseudo-first-order	0.01535	−0.01228	1.198	−4.17664		0.028281	0.93689
Pseudo-second-order	14.19527	0.75037		1.332676	1.776025	0.039665	0.99872

Table 1 presents the parameters and regression coefficients (R^2) for both the pseudo-first-order and pseudo-second-order kinetic models. It is noteworthy that the pseudo-second-order model demonstrates a notably higher correlation coefficient ($R^2 > 0.9987$) in comparison to the pseudo-first-order model. This high R^2 value, close to unity, signifies a robust relationship between the parameters and underscores the suitability of the pseudo-second-order kinetic equation for describing the uptake of Fe(III) by the pineapple peel waste adsorbent [32]. Meanwhile, the equilibrium removal capacity calculated ($q_{e,\,cal}$) of the pseudo-second-order model was much closer to the equilibrium removal capacity experimental ($q_{e,\,exp}$) representing that the pseudo-second-order rate model gives a better summary of iron removal from solution to the pineapple peel waste adsorbent. This conveys that the pseudo-second-order model can assume a chemically rate-controlling removal process [33].

The comparison of kinetics results with values from other studies is listed in Table 2. Iron adsorption onto the pineapple peel waste adsorbent was inferred to follow pseudo-second-order kinetics. These findings suggest that the rate-limiting step in the adsorption process is chemisorption, which entails valency forces, including the sharing or exchange of electrons between the adsorbent and the adsorbate [31, 34]. These results are consistent with previous literature, which also indicated that the adsorption kinetics of Fe(III) ions by distinct types of adsorbents typically adhere to the pseudo-second-order model [4, 32].

Table 2. Kinetic parameters comparison of iron adsorption onto various adsorbents

Adsorbent	Pseudo-first-order model		Pseudo-second-order model			References
	k_1 (min^{-1})	R^2	k_2 (g/mg·min)	q_e	R^2	
Pineapple peel	0.0283	0.9369	0.0397	1.33	0.9987	This study
Natural Clay	0.056	0.986	0.02	7.42	0.998	[35]
Acid–activated clay	0.058	0.991	0.007	11.41	0.994	[35]
Natural zeolite	4.9	0.8558	0.22	8.70	0.9985	[36]
Orange peel	0.001	0.032	0.068	13.44	0.996	[5]

Adsorbent	Pseudo-first-order model		Pseudo-second-order model			References
	k_1 (min^{-1})	R^2	k_2 (g/mg·min)	q_e	R^2	
Limestone	0.069	0.919	5.913	0.019	0.997	[37]
Rice hull	0.017	0.90	0.000813	22.73	0.99	[2]
Natural feldspar	0.0283	0.83	0.0352	8.72	0.9987	[3]
Rice husk ash	-	-	0.033	1.340	0.995	[4]

Adsorption isotherms

An isotherm characterises the equilibrium association between the solute molecules bound to the adsorbent's surface and those remaining unbound in the liquid phase. In this study, Langmuir, Freundlich, and Temkin isotherms were employed to elucidate the equilibrium relationship between the concentration of solute in the liquid phase and its interaction with the adsorbent's surface. Batch adsorption isotherm experiments were conducted to investigate iron adsorption using the pineapple peel waste adsorbent at room temperature. The results of these adsorption isotherms are visually presented in Figure 6(a-c).

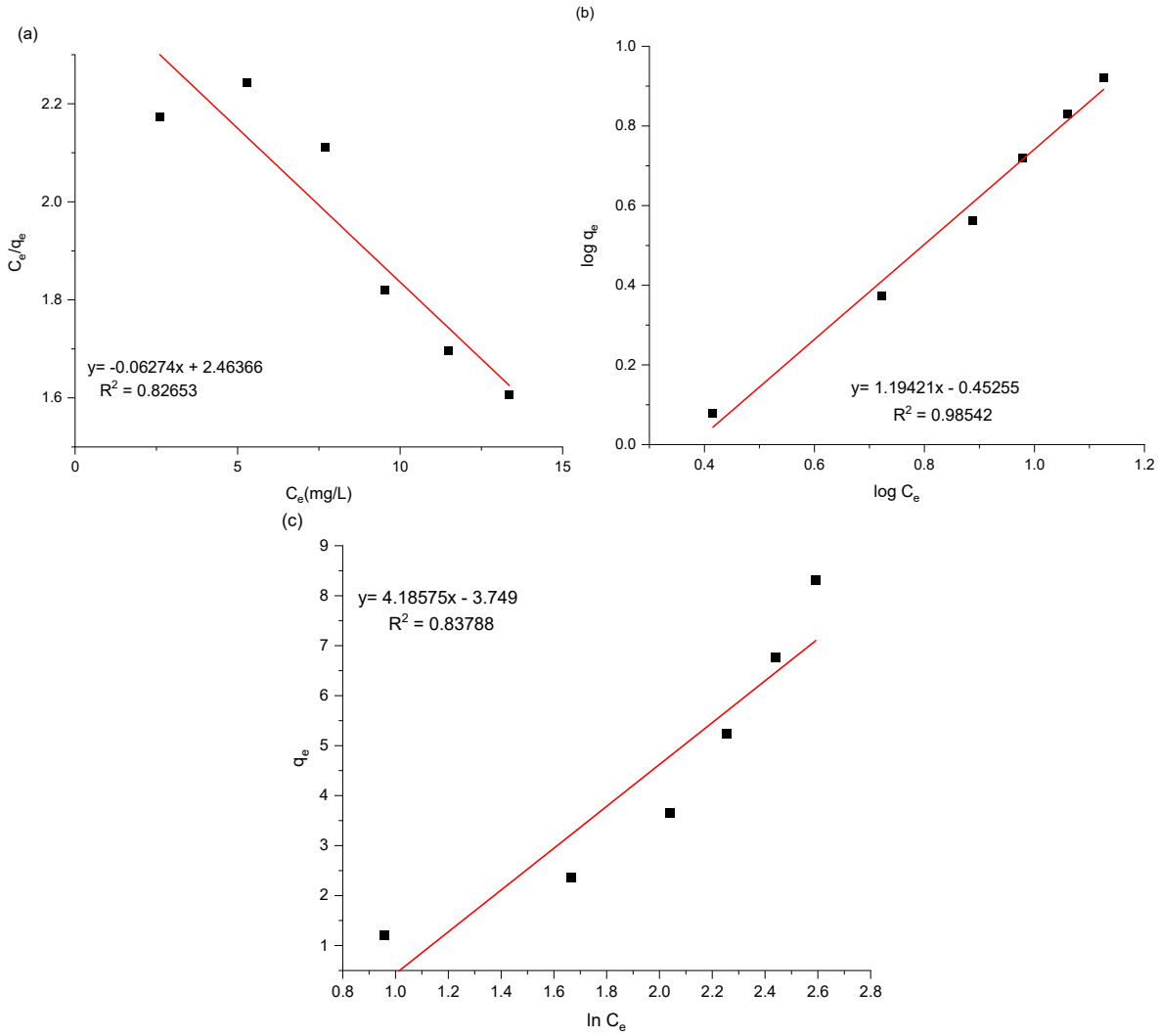

Figure 6. The plots of (a) Langmuir, (b) Freundlich, and (c) Temkin isotherms

Table 3. Langmuir, Freundlich, and Temkin isotherms parameters for iron removal

Isotherms	Constants	Value
Langmuir	$1/q_m$	0.0624
	q_m (mg/g)	15.9288
	K_L (L/mg)	0.0255
	R_L	1.1459
	R^2	0.8265
Freundlich	1/n	1.1942
	n	0.83737
	log K_F	0.4526
	K_F (L/mg)	2.8349
	R^2	0.9854
Temkin	Slope = RT/B	4.1858
	Intercept = RT/B (ln A)	−3.749
	B	597.8651
	A (L/mol)	0.3274
	R^2	0.8379

The results for all the parameters obtained from the Langmuir, Freundlich, and Temkin isotherms are summarised in Table 3. The Langmuir isotherm model was employed to fit the experimental data, yielding a correlation regression coefficient (R^2) of 0.8265. The maximum sorption capacity (q_m) was determined to be 15.94 mg/g using this model. However, it is evident that the data does not align well with the Langmuir model. This deviation may be attributed to interactions between the adsorbate or the fact that the adsorption process is not monolayer adsorption involving just one adsorbate molecule per adsorption site [38]. In this case, iron can be said to be adsorbed in inhomogeneous distribution to the adsorbent surface due to the irregular surface. So, there might be a 'favoured' point of strong adsorption side. The results indicate that the Freundlich isotherm best fitted the iron adsorption on pineapple peel waste adsorbent with R^2 of 0.9854. However, with $1/n > 1$, it is best described by the S-type isotherm. This experiment agrees with the hypothesis that at low concentrations, such compounds compete with water for the adsorption sites. It means that the surface has a low affinity for the adsorptive at low concentrations, which then increases at higher concentrations [39]. On the other hand, the Temkin isotherm model moderately fitted the experimental data for iron adsorption onto pineapple peel waste adsorbent as the R^2 value is 0.84. The comparison of the adsorption capacity of other adsorbents for iron removal from aqueous solutions is tabulated in Table 4.

Table 4. Comparison of adsorption isotherms for iron removal using other adsorbents

Adsorbents	Langmuir			Freundlich			Temkin			References
	q (mg/g)	K_L (L/mg)	R^2	K_f (L/mg)	1/n	R^2	A	B	R^2	
Pineapple peel	15.93	0.0255	0.827	2.835	1.194	0.985	0.327	597.87	0.838	This study
Natural Clay	18.86	0.044	0.990	0.805	0.543	0.985				[35]
Acid–activated clay	25.00	0.09	0.998	5.96	0.312	0.993	-	-	-	[35]

Adsorbents	Langmuir			Freundlich			Temkin			References
	q (mg/g)	K_L (L/mg)	R^2	K_f (L/mg)	1/n	R^2	A	B	R^2	
Natural zeolite	6.13	17.92	0.977	6.04	0.3497	0.945	-	-	-	[36]
Spent coffee grounds	0.615	2.803	0.999	0.530	0.6606	0.991	-	-	-	[28]
Chitosan	133.3	0.0643	0.93	3.807	0.388	0.979	-	-	-	[40]
Limestone	0.018	140.31	0.923	0.029	0.216	0.753	-	-		[37]
Rice hull	45.45	0.03	0.99	1.07	0.68	0.97	32.27	28.36	0.79	[2]
Natural feldspar	25.00	0.046	0.936	1.701	0.622	0.997	-	-	-	[3]
Orange peel	8.35	0.15	0.998	4.97	0.0937	0.900	-	-	-	[5]
Rice husk ash	66.66	0.026	0.927	1.0739	0.916	0.908	54.5	101.76	0.93	[4]
Palm oil mill effluent	1.116	0.25	0.998	0.376	0.281	0.966	-	-	-	[41]

Proposed mechanisms of iron adsorption

Adsorbent from pineapple peel waste consists of three main components: cellulose, hemicellulose, and lignin. These cellulosic components contain a majority of the oxygen functional groups, such as hydroxyl, ether, and carbonyl, that influence the adsorption properties of the iron onto the adsorbent [42]. The adsorbent after adsorption was examined using SEM analysis in Figure 2 and showed that the morphology of the adsorbent changed with the presence of some precipitation. The binding mechanism of the adsorbent and iron ions is proposed in Figure 7.

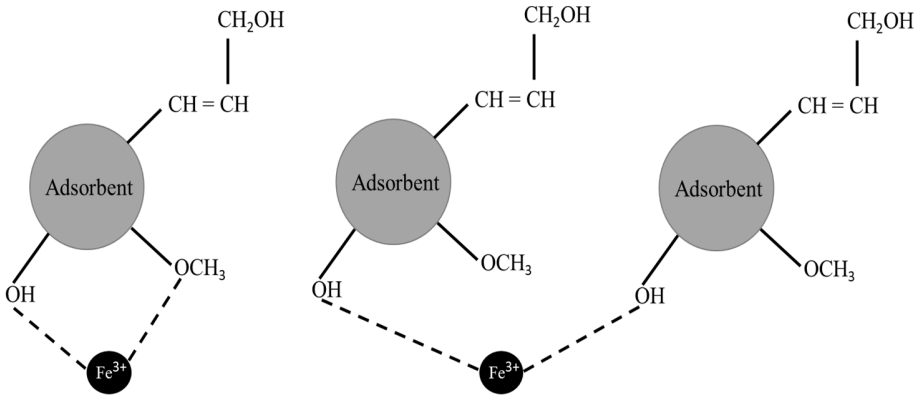

Figure 7. Binding mechanism of adsorbent and Fe(III) ions

Conclusion

In this study, the adsorbent from pineapple peel waste can potentially remove iron from wastewater. The results show that the adsorbent could remove 48.86% iron when 2 g/L of the adsorbent was used and increased to 99.24% when 20 g/L of the adsorbent was used. The adsorption isotherm study shows that iron adsorption fitted the experimental data of the Freundlich isotherm rather than Langmuir and Temkin isotherms due to the highest R^2 value of 0.985. From the Langmuir model, the maximum iron adsorption capacity of the adsorbent was 15.93 mg/g. The adsorption kinetics study shows that iron adsorption followed the pseudo-second-order kinetics model, indicating that chemisorption was the mechanism of adsorption that contributed to the iron removal from the aqueous solution. Based on the results

of this study, pineapple peel waste adsorbent was found to be effective in removing iron from an aqueous solution.

Acknowledgements

The Ministry of Education Malaysia funded this study through the Fundamental Research Grant Scheme (FRGS) (RDU190126;FRGS/1/2018/TK02/UMP/02/8). Appreciations to Pekan Pina Sdn. Bhd. for providing the pineapple peel. We are grateful for the assistance from all the laboratory staff of the Faculty of Chemical & Process Engineering Technology, UMP.

References

1. Hodaifa, G., Ochando-Pulido, J. M., Ben Driss Alami, S., Rodriguez-Vives, S. and Martinez-Ferez, A. (2013). Kinetic and thermodynamic parameters of iron adsorption onto olive stones. *Industrial Crops Product*, 49: 526-534.
2. Abdel-ghani, N. T., El-chaghaby, G. A. and Zahran, E. M. (2015). Cost effective adsorption of aluminium and iron from synthetic and real wastewater by rice hull activated carbon (RHAC). *American Journal of Analytical Chemistry*, 6: 71-83.
3. Al-Anber, M. A. (2015). Adsorption of ferric ions onto natural feldspar: kinetic modeling and adsorption isotherm. *International Journal of Environmental Science and Technology*, 12(1): 139-150.
4. Adekola, F. A., Hodonou, D. S. S. and Adegoke, H. I. (2014). Thermodynamic and kinetic studies of biosorption of iron and manganese from aqueous medium using rice husk ash. *Journal of Applied Water Science*, 6: 319-330.
5. Surovka, D. and Pertile, E. (2015). Sorption of iron, manganese, and copper from aqueous solution using orange peel: Optimization, isothermic, kinetic, and thermodynamic studies. *Polish Journal of Environmental Study*, 26(2): 795-800.
6. Akl, M. A., Yousef, A. M. and AbdElnasser, S. (2013). Removal of iron and manganese in water samples using activated carbon derived from local agro-residues. *Journal of Chemical Engineering Process Technology*, 4(4):1-10.
7. Rose, E. P. and Rajam, S. (2012). Equilibrium study of the adsorption of iron (II) ions from aqueous solution on carbons from wild jack and jambul. *Advances in Applied Science Research*, 3(2): 1889-1894.
8. Olowu, R. A., Osundiya, M. O., Oyewole, T. S., Onwordi, C. T., Yusuff, O. K., Osifeko, O. L. and Tovide, O. O. (2022). Equilibrium and kinetic studies for the removal of Zn(II) and Cr(VI) ions from aqueous solution using pineapple peels as an adsorbent. *European Journal of Applied Sciences*, 10(5):34-47.
9. Mopoung, R. and Kengkhetkit, N. (2016). Lead and cadmium removal efficiency from aqueous solution by NaOH treated pineapple waste. *International Journal of Applied Chemistry*, 12(1): 23-35.
10. Ahmad, A., Khatoon, A., Mohd-Setapar, S. H., Kumar, R. and Rafatullah, M. (2016). Chemically oxidized pineapple fruit peel for the biosorption of heavy metals from aqueous solutions. *Desalination of Water Treatment*, 57(14): 6432-6442.
11. Hu, X., Zhao, M., Song, G. and Huang, H. (2011). Modification of pineapple peel fibre with succinic anhydride for Cu^{2+}, Cd^{2+} and Pb^{2+} removal from aqueous solutions. *Environmental Technology*, 32(7): 739-746.
12. Ahmad Zamri, M. F. M., Akhiar, A., Mohd Roslan, M. E., Mohd Marzuki, M. H., Saad, J. M. and Shamsuddin, A. H. (2020). Valorisation of organic fraction municipal solid waste via anaerobic co-digestion of Malaysia tropical fruit for biogas production. *IOP Conference Series: Earth & Environmental Sciences*, 476(1):1-8.
13. Turkmen Koc, S. N., Kipcak, A. S., Moroydor Derun, E. and Tugrul, N. (2021). Removal of zinc from wastewater using orange, pineapple and pomegranate peels. *International Journal of Environmental Sciences & Technology*, 18(9): 2781-2792.
14. Rozaidi, N. I. M. and Abu Samah, R. (2018). Peel wastes of *Ananas comosus* (L.) Merr as biosorbent for Fe(II) Ions removal from aqueous solution. *Research Communication: Engineering Science & Technology Special issue Regional Chemical Engineering Undergraduate Congress (RCEUC)*, 1:8.
15. Abd Ghapar, N. F., Abu Samah, R. and Abd Rahman, S. (2020). Pineapple peel waste adsorbent for adsorption of Fe (III). *IOP Conferences Series: Materials & Science Engineering*, 991(012093): 1-5.

16. Liu, Y. and Shen, L. (2008). A general rate law equation for biosorption. *Biochemical Engineering Journal*, 38: 390-394.
17. Reddy, K. S. K., Al Shoaibi, A. and Srinivasakannan, C. (2015). Preparation of porous carbon from date palm seeds and process optimization. *International Journal of Environmental Sciences & Technology*, 12(3): 959-966.
18. Fu, B., Ge, C., Yue, L., Luo, J., Feng, D., Deng, H. and Yu, H. (2016). Characterization of biochar derived from pineapple peel waste and its application for sorption of oxytetracycline from aqueous solution. *BioResources*, 11(4): 9017-9035.
19. Saadia, M., Nazha, O., Abdlemjid, A. and Ahmed, B. (2012). Preparation and characterization of activated carbon from residues of oregano. *Journal of Surface Sciences & Technology*, 28(3): 91-100.
20. Das, D., Samal, D. P. and BC, M. (2015). Preparation of activated carbon from green coconut shell and its characterization. *Journal of Chemical Engineering Process Technology*, 6(5):1-12.
21. Ashtaputrey, S. D. and Ashtaputrey, P. D. (2016). Preparation, characterization and application of pineapple peel activated carbon as an adsorbent for water hardness removal. *Journal of Chemical and Pharmaceutical Research*, 8(8): 1030-1034.
22. Hossain, M. A., Kumita, M. and Mori, S. (2010). SEM characterization of the mass transfer of Cr(VI) during the adsorption on used black tea leaves. *African Journal of Pure Applied Chemistry*, 4(7): 135-141.
23. Mahamad, M. N., Ahmad Zaini, M. A. and Zakaria, Z. A. (2015). Preparation and characterization of activated carbon from pineapple waste biomass for dye removal. *International Biodeterioration & Biodegradation*, 102: 274-280.
24. Sazali, N., Harun, Z. and Sazali, N. (2020). A review on batch and column adsorption of various adsorbent towards the removal of heavy metal. *Journal of Advanced Research in Fluid Mechanics and Thermal Sciences*, 67(2): 66-88.
25. El-Sayed, G. O., Dessouki, H. A. and Ibrahiem, S. S. (2011). Removal of Zn(II), Cd(II) and Mn(II) from aqueous solutions by adsorption on maize stalks. *Malaysian Journal of Analytical Sciences*, 15(1): 8-21.
26. Sekhararao Gulipalli, C., Prasad, B. and Wasewar, K. L. (2011). Batch study, equilibirum and kinetics of adsorption of selenium using rice husk ash (RHA). *Journal of Engineering Science & Technology*, 6(5): 590-609.
27. Desta, M. B. (2013). Batch sorption experiments: Langmuir and Freundlich isotherm studies for the adsorption of textile metal ions onto teff straw (eragrostis tef) agricultural waste. *Journal of Thermodynamic*, 1(1): 1-6.
28. Mohamed, K. N. and Yee, L. L. (2019). Removal of Fe Ion from polluted water by reusing spent coffee grounds. *Pertanika Journal of Science & Technology*, 27(3): 1077-1090.
29. Renu, Agarwal, M. and Singh, K. (2018). Removal of copper, cadmium, and chromium from wastewater by modified wheat bran using Box–Behnken design: Kinetics and isotherm. *Separation Science and Technology*, 53(10):1476-1489.
30. Nayeem, A., Mizi, F., Ali, M. F. and Shariffuddin, J. H. (2023). Utilization of cockle shell powder as an adsorbent to remove phosphorus-containing wastewater. *Environmental Research*, 216:1-8.
31. Kaur, R., Singh, J., Khare, R., Cameotra, S. S. and Ali, A. (2013). Batch sorption dynamics, kinetics and equilibrium studies of Cr(VI), Ni(II) and Cu(II) from aqueous phase using agricultural residues. *Applied Water Science*, 3(1): 207-218.
32. Seliem, M. K. and Komarneni, S. (2016). Equilibrium and kinetic studies for adsorption of iron from aqueous solution by synthetic Na-A zeolites: Statistical modeling and optimization. *Microporous Mesoporous Materials,* 228: 266-274.
33. Chen, J., Cai, Y., Clark, M. and Yu, Y. (2013). Equilibrium and kinetic studies of phosphate removal from solution onto a hydrothermally modified oyster shell material. *PLoS One*, 8(4):1-10.
34. Sahu, M. K., Mandal, S., Yadav, L. S., Dash, S. S. and Patel, R. K. (2016). Equilibrium and kinetic studies of Cd(II) ion adsorption from aqueous solution by activated red mud. *Desalination Water Treatment*, 57(30): 14251-14265.
35. Khalfa, L., Cervera, M. L., Souissi-Najjar, S. and Bagane, M. (2021). Removal of Fe(III) from synthetic wastewater into raw and modified clay: Experiments and models fitting. *Separation Science and Technology*, 56(4): 708-718.

36. Neag, E., Török, A. I., Tanaselia, C., Aschilean, I. and Senila, M. (2020). Kinetics and equilibrium studies for the removal of Mn and Fe from binary metal solution systems using a Romanian thermally activated natural zeolite. *Water (Switzerland)*, 12(6):1-13.
37. Akbar, N. A., Aziz, H. A. and Adlan, M. N. (2016). Potential of high quality limestone as adsorbent for iron and manganese removal in groundwater. *Jurnal Teknologi*, 78(9-4):77-82.
38. Doran, P. M. (2013). Bioprocess engineering principles. Chapter 11, John Wiley. pp: 445-595.
39. Younes, A. A., Abdulhady, Y. A. M., Shahat, N. S. and El-Din El-Dars, F. M. S. (2021). Removal of cadmium ions from wastewaters using corn cobs supporting nano-zero valent iron. *Separation Science and Technology*, 56(1):1-13.
40. Ali, M. E. A., Aboelfadl, M. M. S., Selim, A. M., Khalil, H. F. and Elkady, G. M. (2018). Chitosan nanoparticles extracted from shrimp shells, application for removal of Fe(II) and Mn(II) from aqueous phases. *Separation Science and Technology*, 53(18): 2870-2881.
41. Shavandi, M. A., Haddadian, Z., Ismail, M. H. S., Abdullah, N. and Abidin, Z. Z. (2012). Removal of Fe(III), Mn(II) and Zn(II) from palm oil mill effluent (POME) by natural zeolite. *Journal of the Taiwan Institute of Chemical Engineers*, 43(5): 750-759.
42. Al-Ghouti, M. A., Li, J., Salamh, Y., Al-Laqtah, N., Walker, G. and Ahmad, M. N. M. (2010). Adsorption mechanisms of removing heavy metals and dyes from aqueous solution using date pits solid adsorbent. *Journal of Hazardous Materials*, 176: 510-520.

Malaysian Journal of Analytical Sciences (MJAS)
Published by Malaysian Analytical Sciences Society

DETERMINATION OF CELECOXIB IN HUMAN PLASMA BY EFFERVESCENCE-ASSISTED DISPERSIVE LIQUID–LIQUID MICROEXTRACTION AND HPLC/UV

(Penentuan Celecoxib dalam Plasma Manusia dengan Bantuan Buih Berbuak Pengekstrakan Mikro Penyebaran Cecair-ke-Cecair dan HPLC/UV)

Zahra Saharkhiz[1*], Mohammad Reza Hadjmohammadi[1], and Pourya Biparva[2]

[1]*Department of Analytical Chemistry, Faculty of Chemistry, University of Mazandaran, NirooHavayii Boulevard, 47416-95447 Babolsar, Iran*
[2]*Department of Basic Sciences, Sari Agricultural Sciences and Natural Resources University, Sari, India*

[*]*Corresponding author: z_saharkhiz@yahoo.com*

Received: 15 November 2023; Accepted: 29 February 2024; Published: 29 April 2024

Abstract

In this study, effervescence-assisted dispersive liquid–liquid microextraction was utilized for rapid, simple, and inexpensive microextraction of celecoxib followed by HPLC/UV. In the proposed method, carbon dioxide microbubbles were produced by the reaction between oxalic acid and sodium bicarbonate. Various factors such as type and volume of extraction solvent, pH of the sample solution, content of the acidic and basic promoters, and type and volume of auxiliary solvent were optimized. Under optimum conditions, 60 µL chloroform (as an extraction solvent) was added to 2 mL methanol and 0.4g oxalic acid. The mixture was added to the test tube containing 0.8g sodium bicarbonate and 10 mL of sample solution (pH 6). The presented method offered wide linear dynamic range of 0.5-1000 µg L^{-1} with satisfactory extraction recovery of 94.4%, high pre-concentration factor of 206, and normal RSD% (2.15, n=3). Finally, the proposed method was successfully applied for the analysis of celecoxib in plasma samples.

Keywords: effervescence-assisted liquid-microextraction, celecoxib, plasma, acid-base reaction, carbon dioxide microbubbles

Abstrak

Dalam kajian ini, pengekstrakan mikro cecair-ke-cecair yang dibantu buih berbuak telah digunakan untuk pengekstrakan celecoxib yang cepat, mudah, dan murah diikuti oleh HPLC/UV. Dalam kaedah yang dicadangkan, buih mikro karbon dioksida dihasilkan oleh tindak balas antara asid oksalik dan natrium bikarbonat. Pelbagai faktor seperti jenis dan isipadu pelarut pengekstrakan, pH larutan sampel, kandungan penggalak asid dan bes, dan jenis dan isipadu pelarut bantu telah dioptimumkan. Di bawah keadaan optimum, 60 µL kloroform (sebagai pelarut pengekstrakan) ditambahkan ke dalam 2 mL metanol dan 0.4g asid oksalik. Campuran tersebut ditambahkan ke dalam tabung uji yang mengandungi 0.8g natrium bikarbonat dan 10 mL larutan sampel (pH 6). Kaedah yang dikemukakan menawarkan julat dinamik linear yang luas dari 0.5-1000 µg L^{-1} dengan pulihkan pengekstrakan yang memuaskan sebanyak 94.4%, faktor pra-pemekatan tinggi sebanyak 206, dan RSD% normal (2.15, n=3). Akhirnya, kaedah yang dicadangkan telah berjaya digunakan untuk analisis celecoxib dalam sampel plasma.

Kata kunci: pengekstrakan cecair-mikro yang dibantu buih berbuak, celecoxib, plasma, tindak balas asid-bes, buih mikro karbon dioksida

Introduction

Non-steroidal anti-inflammatory drug (NSAID), celecoxib (CEL) has been extensively prescribed for the treatment of inflammation and pain in osteoarthritis, rheumatoid arthritis, and painful menstruation [1]. Furthermore, the therapeutic effect of this drug on renal and pancreatic functions, as well as its chemo-preventive effect on various cancer types have been recently investigated and reported [2]. In spite of the excellent therapeutic effect of CEL, its high dosage can enhance the risk of heart attack. Some recent reports have also mentioned the distribution of CEL into human breast milk [3, 4]. In this context, the development of an efficient technique for the measurement of CEL concentration in biological matrices can contribute to optimizing the CEL dosage based on medical strategies and therapeutics for serious intoxication. The most common analytical method for measuring the CEL in bio-fluid samples is based on high-performance liquid chromatography (HPLC) [5-8]. The quality of analysis usually decreases due to the complexity of bio-fluids matrices and trace concentration of CEL. Hence, the development of a sample preparation technique to reduce the matrix interference and enrich the trace values of CEL is the main challenge.

The structure and corresponding log P value (octanol–water partition coefficient) and dissociation constant value (pKa value) of CEL are presented in Figure 1.

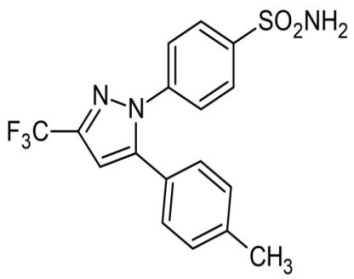

Log p= 3.5 pKa= 11.1

Figure 1. Chemical structure, Log p and pKa of Celecoxib

Extraction of trace contents of chemical compounds that can be analyzed by analytical instruments has found increasing popularity among the scientists. This extraction should be able to concentrate analytes and also sample cleanup contemporaneously. This process is called sample preparation [9, 10]. Liquid- liquid extraction (LLE) and Solid phase extraction (SPE) are among the earliest sample preparation methods [11, 12]. Scientists have also attempted to minimize the consumption of organic solvents and simplify this type of extraction. Liquid–liquid microextraction (LLME) and Solid phase microextraction (SPME) are really useful in the extraction of the analytes from various matrixes [13-15]. Liquid phase microextraction (LPME) is an interesting and applicable method capable of extracting analytes from an aqueous phase in mL to an organic solvent in μL [16, 17].

Among the conventional solvent-minimized extraction methods, dispersive liquid liquid microextraction (DLLME) is frequently applied due to its outstanding benefits such as fast microextraction process, high enrichment factor, and low consumption of organic reagents as extraction solvents [18-21]. In spite of the excellent performance of this method, there are several disadvantages in the initial version of DLLME method. The low partition coefficient of the target analytes due to use of the organic disperser solvents and inadequate contact surface between the organic extractor and sample solution are the shortcomings of the DLLME method. The use of hazardous chlorinated extractors and toxic disperser solvents increases the operational and environmental pollution risks which it is the other drawback of the mentioned method [22]. In recent years, effervescence-assisted dispersive liquid–liquid microextraction (EADLLME) method has been proposed as a new assisted technique with promising potential for pre-concentration of target analytes without using the disperser solvent [23-27].

The present study is focused on the development of EADLLME technique based on gas-generation reaction which could be an appropriate alternative for organic disperser solvent in DLLME method. In this method, CO_2 microbubbles are formed as disperser by the reaction between acid and base source in the sample solution. The produced CO_2 microbubbles enhance the dispersibility of organic extraction solvent which promotes the transfer of CEL to the organic phase. Also, the gas bubbles provide the large contact surface between CEL and extractant, a high extraction efficiency and rapid extraction equilibrium. The effect of several important factors on the extraction efficiency was investigated by utilizing one-at-a-time process to achieve the optimum micro-extraction conditions.

Finally, the developed EADLLME method was successfully applied to isolate and pre-concentration of CEL in the plasma samples. The analysis of target analyte was accomplished by high-performance liquid chromatography with ultraviolet detection (HPLC/UV). Precise and repeatable data were obtained to find further high pre-concentration factor and extraction recovery.

Materials and Methods

Materials and standard

Celecoxib was supplied from Arasto Pharmaceutical Chemicals Inc (Tehran, Iran). Oxalic acid, sodium bicarbonate, HPLC grade methanol (MeOH), and acetonitrile (ACN) were provided from Merck (Darmstadt, Germany). N-hexane, dichloromethane, carbon tetrachloride, chloroform, methanol and ethanol were also purchased from Sigma-Aldrich (St. Louis, MO, USA). Plasma samples were obtained from Blood Transfusion Organization (Babol, Iran). Standard stock solution of CEL (500 ppm) was prepared by dissolving 50 mg of reference material into 100 mL of HPLC grade methanol which was refrigerated before use. Working solutions were prepared by diluting the stock solution in water.

Apparatus

HPLC analysis of CEL was carried out using an Alliance HPLC system from waters Company (Milford, USA). The HPLC instrument included a 2695 pump, an online degasser, a UV/vis detector (Model 2487), and a 6-port/3-channel injection valve encompassing a high-pressure manual injection valve (20 µL loop). The detector was adjusted at 252 nm. C_{18} (150 mm × 4.6 mm I.D., 5 µm) MZ-Analysentechnik GmbH HPLC column (Mainz, Germany) was also utilized for chromatographic separation. Empower software was employed for data processing. Isocratic elution was also conducted by a mixture of acetonitrile: water (75:25) at the flow rate of 1mL/min.

Effervescence-assisted dispersive liquid–liquid microextraction procedure

2 mL methanol (auxiliary solvent), 0.4g oxalic acid (acidic promoter), and 60 µL Chloroform (Extraction solvent) were mixed and then added to a conical test tube containing 0.8g sodium bicarbonate(basic promoter) in 10 mL water with the concentration of 1 µg mL^{-1} of CEL (pH 6). The acid-base reaction occurred rapidly upon adding the acidic promoter to the basic promoter solution (Eq. 1) and CO_2 (one of the reaction products) generated bubbles inside the test tube, resulting in a cloudy solution. After one minute, the mixture was centrifuged for 5 min at 5000 rpm and the dispersed droplets of organic phase were gathered at the conical bottom of the test tube. The extract was withdrawn using a micro-syringe and analyzed by HPLC/ UV.

$$2NaHCO_3 + (COOH)_2 \longrightarrow (COONa)_2 + 2CO_2 + 2H_2O \quad (1)$$

Results and Discussion

This work addressed the effects of various parameters such as type and volume of extraction solvent, content of acidic and basic promoters, pH of sample solution and type and volume of auxiliary solvent for the optimization of EADLLME procedure of CEL.

Extraction solvent

The following criteria should be considered in the selection of an extraction solvent for EADLLME: It should be immiscible with water and compatible with chromatographic systems and also have good efficiency for extraction of the analyte. Dichloromethane, chloroform, carbon tetrachloride (higher density than water), and n-hexane (lower density than water) were examined. Among these solvents, chloroform showed the highest Extraction recovery and was used for further studies (Figure 2).

Content of acidic and basic promoter

Four contents of oxalic acid (acidic promoter) and sodium bicarbonate (basic promoter) were examined for optimizing the promoter's content. The molar ratio of $NaHCO_3$: $C_2H_2O_4$ was set to 2:1. The Extraction recovery of celecoxib increased by raising the oxalic acid content to 0.4 g (Figure 3). So 0.4g of oxalic acid and 0.8g of sodium bicarbonate are considered as the optimized amount in the further studies.

Type and volume of auxiliary solvent

An auxiliary solvent dissolves the oxalic acid, promoting the dispersion of the extraction solvent in the aqueous phase. Methanol, ethanol, and acetonitrile were studied for this purpose. Extractions were conducted with oxalic acid (0.4g) and 1 mL methanol, ethanol and acetonitrile. Based on Figure 4, methanol

was the best auxiliary solvent. According to Figure 5, 2 mL methanol led to the highest extraction recovery in the extraction of CEL.

Volume of extracting solvent

Volume of extraction solvent is one of the main parameters that should be optimized. For this purpose, 60, 70, 80, 90, and 100 µL of chloroform were applied. Based on the results, extraction with 60 µL showed the greates extraction recovery, thus, this value was selected for further analyses (Figure 6). Under this volume, no organic solvent sedimented at the bottom of the test tube.

Effect of pH

The pH of the sample solution is another important parameter in the EADLLME method. The effect of this factor was explored on the extraction recoveries of CEL in the ranges of 3.0-8.0. Based on the obtained results (Figure 7), the extraction recovery of CEL decreased by decrementing the pH of sample to 3.0. The target analyte appeared into its ionic form at low pH value which reduced transferring into the organic phase and decreased extraction efficiency. At higher pH levels, the reaction between acid and base is likely to be disrupted, decreasing CO_2 production, followed by a reduction in the dispersion of the organic phase in the sample solution and extraction recovery. Therefore, pH of 6.0 was chosen as the optimum pH for the following experiments.

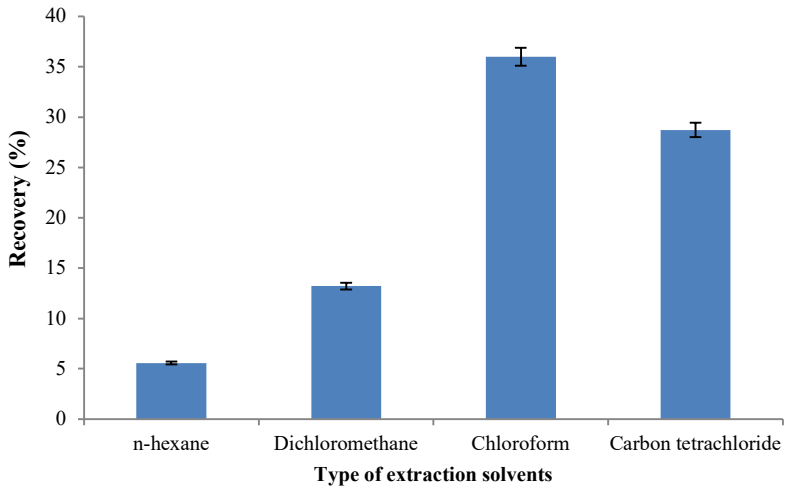

Figure 2. Effect of extraction solvent on the extraction recovery of CEL. Extraction condition: CEL 1µg mL^{-1}; sample volume 10 mL; extraction solvent volume: 100 µL; acidic promoter 0.3g; basic promoter 0.6g; auxiliary solvent; methanol, 1 mL; centrifuging time: 2 min at 4000 rpm. All experiments were done at triplicate and the mean value of the results is reported

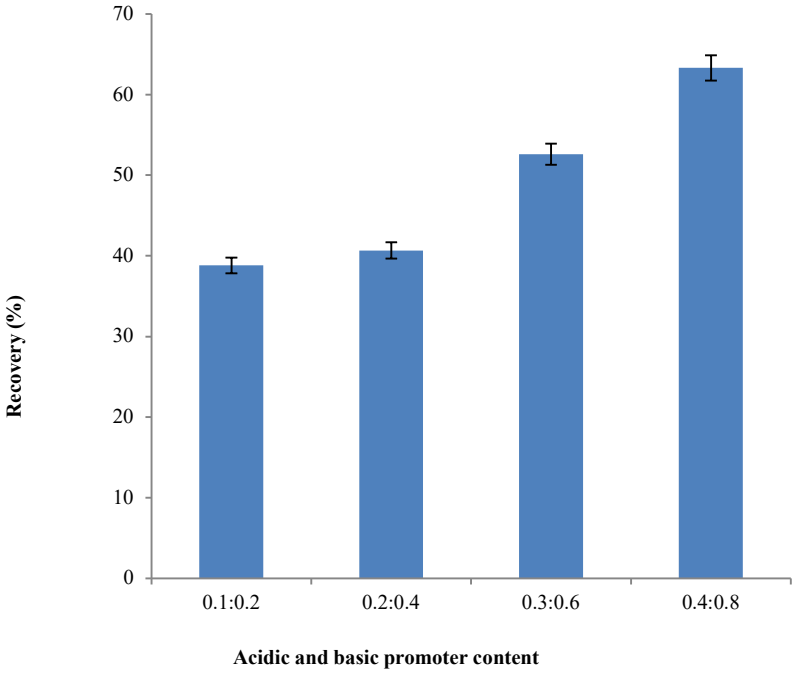

Figure 3. Effect of the content of acidic and basic promoter on extraction recovery. Extraction condition: CEL 1µg mL^{-1}; sample volume 10 mL; extraction solvent: $CHCl_3$, 100 µL; auxiliary solvent; methanol, 1 mL; centrifuging time: 2 min at 4000 rpm. All experiments were done at triplicate and the mean of results is reported

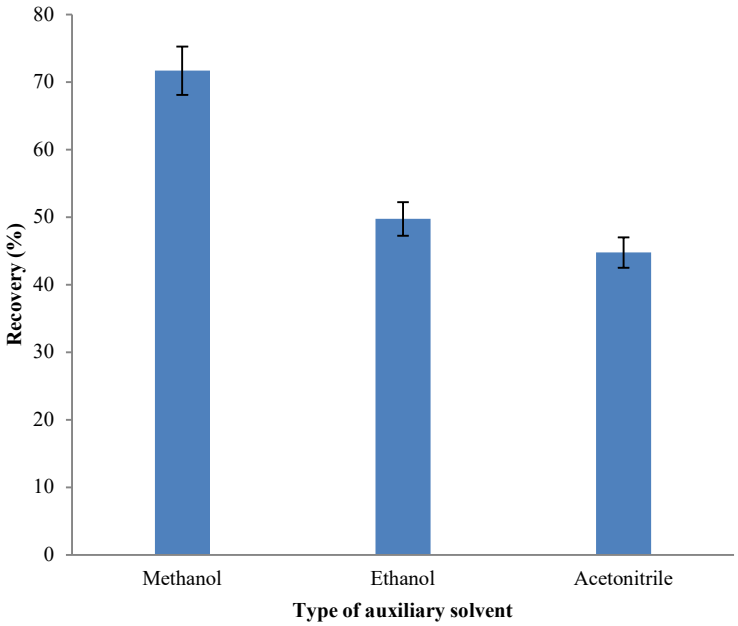

Figure 4. Effect of the type of auxiliary solvent on extraction recovery. Extraction condition: CEL 1 µg mL^{-1}; sample volume: 10 mL; extraction solvent: $CHCl_3$, 100 µL; acidic promoter: 0.4g; basic promoter 0.8 g; volume of auxiliary solvent: 1 mL; centrifuging time: 2 min at 4000 rpm. All experiments were performed in triplicate and the mean values of results are reported

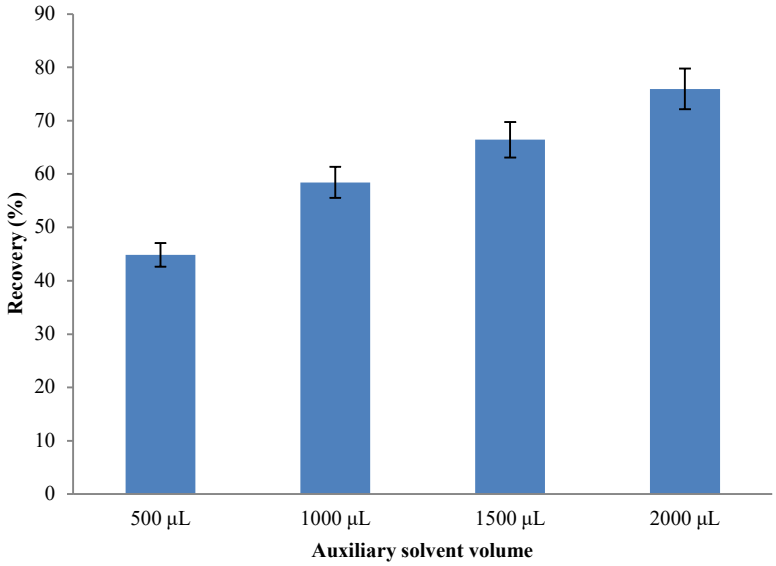

Figure 5. Effect of the volume of auxiliary solvent on extraction recovery. Extraction condition: CEL 1µg mL^{-1}; sample volume: 10 mL; extraction solvent: $CHCl_3$, 100 µL; acidic promoter: 0.4g; basic promoter: 0.8g; auxiliary solvent: methanol; centrifuging time: 2 min at 4000 rpm. All experiments were performed in triplicate and the mean values of results are reported

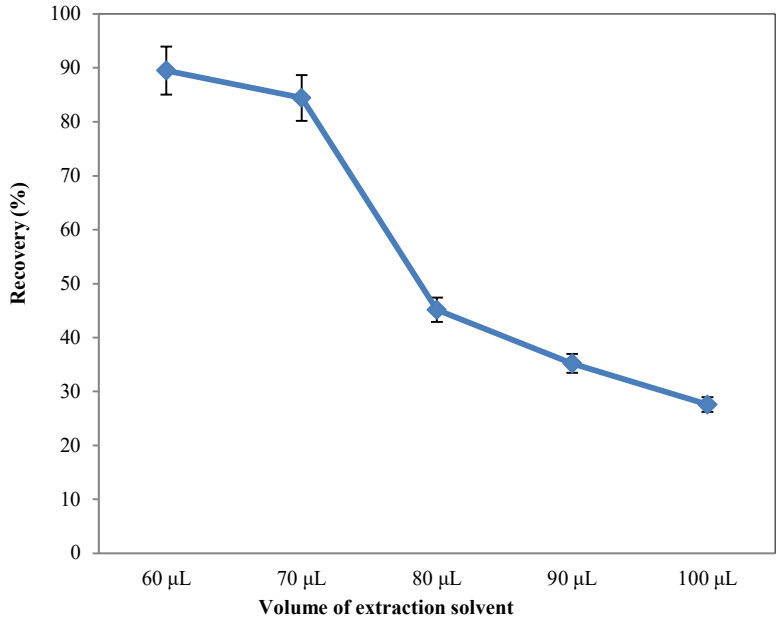

Figure 6. Effect of the volume of extraction solvent on extraction recovery. Extraction condition: CEL 1 µg mL^{-1}; sample volume: 10 mL; extraction solvent: $CHCl_3$; acidic promoter 0.4g; basic promoter 0.8g; auxiliary solvent: methanol, 2 mL; centrifuging time: 2 min at 4000 rpm, pH of sample solution, 6. All experiments were performed in triplicate and the mean value of the results are reported

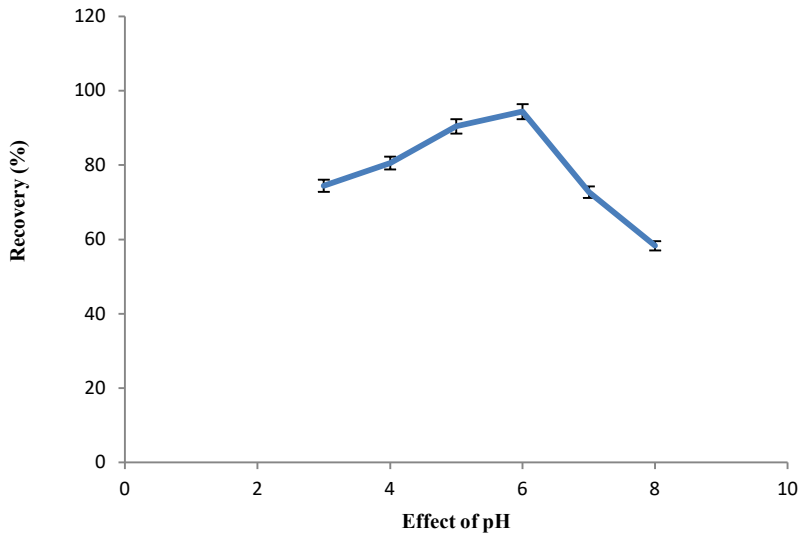

Figure 7. Effect of pH of sample solution on extraction recovery. Extraction condition: CEL 1 µg mL^{-1}; sample volume: 10 mL; acidic promoter: 0.4g; basic promoter: 0.8g; auxiliary solvent: methanol, 2 mL; extraction solvent: $CHCl_3$, 60 µL; centrifuging time: 2 min at 4000 rpm. All experiments were done in triplicate and the mean value of results is reported.

Method performance

The performance of EADLLME was investigated in optimal conditions. The limit of detection (LOD), linear dynamic range (LDR), correlation coefficient (r^2), Enrichment factors (EF), and extraction recovery (ER %) were evaluated which can be calculated using the following equations:

$$\text{LOD} = \frac{3\text{Sb}}{\text{m}} \quad (2)$$

Where S_b is the standard deviation of three replicates in the blank solution and m shows the slope of calibration curve.

Table 1 summarizes the performance of the EADLLME as an approach for extraction of celecoxib.

$$\text{EF} = \frac{Co}{Caq} \quad (3)$$

Where C_o denotes the concentration of the analyte in the organic phase (settled at the conical end of test tube) and C_{aq} represents the concentration of analyte in the aqueous phase.

$$\text{ER}=(\frac{Vo}{Vaq}) \times EF \times 100 \quad (4)$$

Where V_o and V_{aq} are the volume of the organic phase and aqueous phase, respectively [28].

The figures of merits of EADLLME method and other extractions of celecoxib are compared in Table 2.

Table 1. Figures of merit of the presented method

LDR (µg L^{-1})	Correlation Equation	R^2	PF[a]	LOD (µg L^{-1})	RSD %, n=3
0.5- 1000	$Y = 38.82C^{b} + 4221.1$	0.9912	206	0.1	2.15

[a] Preconcentration factor was calculated at 100 µg L^{-1}.
[b] Concentration in µg L^{-1}.

Table 2. Comparison of presented method with other extraction method applied for the extraction and quantification of Celecoxib

Methods	LOD (μg L^{-1})	LDR (μg L^{-1})	Recovery (%)	RSD	Ref.
EADLLME –HPLC/UV[a]	0.1	0.5-1000	94.4	2.15	The current method
LLE-HPLC/UV[b]	3.0	10- 2000	96.0	≤ 10	[6]
LLE-HPLC/UV	6.0	20-2000	85.0	≤ 10.7	[29]
LC-MS/MS[c]	-	5-4000	82.2	≤ 13.0	[30]
SPE-HPLC/UV[d]	7.5	25-2000	91.0	≤ 5.7	[31]
SPE-MIP-HPLC/UV[e]	8.0	50-100000	96.0	≤ 1.1	[5]

[a] Effervescence-Assisted Dispersive Liquid–Liquid Microextraction-high performance liquid chromatography with ultraviolet detection
[b] Liquid- liquid microextraction-high performance liquid chromatography with ultraviolet detection
[c] Liquid chromatography mass mass spectrometry
[d] Solid phase extraction- high performance liquid chromatography with ultraviolet detection
[d] Solid phase extraction- molecular imprinted polymer- high performance liquid chromatography with ultraviolet detection

Comparison of the extraction efficiency of presented method with ultrasonic/vortex/air- dispersive liquid-liquid microextraction methods

In this method, the use of CO_2 bubbles enhanced the dispersibility of organic phase into the sample solution. To confirm this claim, other DLLME techniques such as Air assisted-DLLME (ADDLME), Ultrasound assisted-DLLME (UADLLME), and vortex- assisted DLLME (VADLLME) were examined at optimum conditions. The obtained recoveries (Table 3) showed the high extraction recovery of the presented method with excellent repeatability.

Real sample analysis

The isolation and quantification of CEL in plasma sample was studied to investigate the applicability and accuracy of EADDLE method. The 3 mL of plasma sample were deproteinized by 5 mL of acetonitrile and diluted at the ratio of 1:3 by water and analyzed to assess the EADLLME method at optimal conditions (methanol as an auxiliary solvent; 2 mL, oxalic acid as an acidic promoter; 0.4g, sodium bicarbonate as basic promoter; 0.8g, pH of sample solution 6, chloroform as extraction solvent; 60 μL, and centrifugation time; 5 min). Table 4 lists the recoveries achieved for the plasma spiked at three different concentration levels (10, 50, and 100 μg L^{-1}). The obtained results demonstrated an admissible relationship between the obtained relative recoveries and spiked amount of CEL standards. Fig. 8 shows the data obtained from the proposed method of CEL existing in plasma samples.

Table 3. Comparison of the proposed method with other dispersive liquid-liquid microextraction methods applied for the extraction and quantification of CEL (50 μg L^{-1})

Methods	Recovery (%)	RSD
EADLLME-HPLC/UV[a]	94.4	2.15
UADLLME-HPLC/UV[b]	90.9	3.7
ADLLME-HPLC/UV[c]	96.2	3.1
VDLLME-HPLC/UV[d]	87.5	4.9

[a] Effervescence-Assisted Dispersive Liquid–Liquid Microextraction-high performance liquid chromatography with ultraviolet detection
[b] Ultrasound-assisted liquid-phase microextraction-high performance liquid chromatography with ultraviolet detection
[c] Air-assisted liquid-liquid microextraction- high performance liquid chromatography with ultraviolet detection
[d] Vortex-assisted liquid-liquid microextraction- high performance liquid chromatography with ultraviolet detection

Table 4. Analytical performance of presented method for plasma sample (n=3)

C_{added} (µg L^{-1})	$C_{founded}$ (µg L^{-1})	RR%[a]	RSD[b]	RSD[c]
10	9.8	98	1.87	2.13
50	50.3	100.6	2.27	1.84
100	101.6	101.6	2.05	2.46

[a] Relative recovery
[b] Relative standard deviation, interday (n=3)
[c] Relative standard deviation, intraday (n=3)

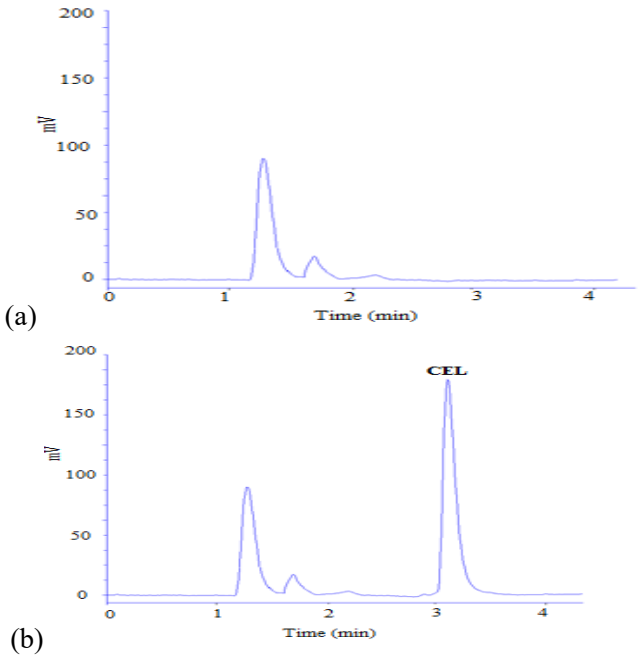

Figure 8. Chromatograms of blank plasma (a) and spiked plasma (b) at 100 µg L^{-1} of CEL

Conclusion

This study addressed the application of effervescence-assisted dispersive liquid–liquid microextraction (EADLLME) through acid-base reaction promotion for the extraction of CEL in the plasma sample and further determination through HPLC/UV. The carbon dioxide produced in the acid-base reaction distributes the extraction solvent throughout the aqueous phase with no complex apparatus. The method offered several advantages over other extraction methods. EADLLME is a simple, fast, accurate, and inexpensive approach with high extraction recovery.

References

1. Clemett, D. and Goa, K. L. (2000). Celecoxib: a review of its use in osteoarthritis, rheumatoid arthritis and acute pain. *Drugs*, 59: 957-980.
2. Abdel-Hamid, M., Novotny, L. and Hamza, H. (2001). Liquid chromatographic–mass spectrometric determination of celecoxib in plasma using single-ion monitoring and its use in clinical pharmacokinetics. *Journal Chromatography B Biomedical Applied*, 753(2): 401-408.
3. Knoppert, D. C., Stempak, D., Baruchel, S. and Koren, G. (2003). Celecoxib in human milk: a case report. *Pharmacotherapy*, 23(1): 97-100.
4. Hale, T. W., McDonald, R. and Boger, J. (2004). Transfer of celecoxib into human milk. *Journal Human Lactose*, 20(4): 397-403.
5. Ansari, S., and Ghorbani, A. (2017). Molecularly imprinted polymers (MIP) for selective solid phase extraction of celecoxib in urine samples followed by high performance liquid

chromatography. *Journal Chemical Health Risks*, 7(3): 225-237.

6. Chamkouri, N., Zare-Shahabadi, V., Niazi, A. and Ramezani, M. (2004). Ibuprophen, diclofenac, and celecoxib quantification in human urine samples with ultrasound assisted emulsification microextraction–HPLC and chemometrics. *Bulgaria Chemical Communication*, 49: 281-289.
7. Jalalizadeh, H., Amini, M., Ziaee, V., Safa, A., Farsam, H. and Shafiee, A. (2004). Determination of celecoxib in human plasma by high-performance liquid chromatography. *Journal Pharmaceutical Biomedical Analysis*, 35(3): 665-670.
8. Zhang, M., Moore, G. A., Gardiner, S. J. and Begg, E. J. (2006). Determination of celecoxib in human plasma and breast milk by high-performance liquid chromatographic assay. *Journal Chromatography B*, 830(2): 245-248.
9. Zhao, E., Zhao, W., Han, L., Jiang, S. and Zhou, Z. (2007). Application of dispersive liquid–liquid microextraction for the analysis of organophosphorus pesticides in watermelon and cucumber. *Journal Chromatography A*, 1175(1): 137-140.
10. Ranjbari, E., and Hadjmohammadi, M. R. (2012). Magnetic stirring-assisted dispersive liquid–liquid microextraction followed by high performance liquid chromatography for determination of phthalate esters in drinking and environmental water samples. *Talanta*, 100: 447-453.
11. Jayachandran, J., and Dhadke, P. M. (1997). Liquid-liquid extraction separation of iron (III) with 2-ethyl hexyl phosphonic acid mono 2-ethyl hexyl ester. *Talanta*. 44(7): 1285-1290.
12. Thurman, E. M., and Mills, M. S. (1998). Solid-phase extraction. Principles and Practice, *Wiley, New York*, 1998.
13. Korta, E., Bakkali, A., Berrueta, L. A., Gallo, B. and Vicente, F. (2001). Study of semi-automated solid-phase extraction for the determination of acaricide residues in honey by liquid chromatography. *Journal of Chromatography A*, 930 (1-2): 21-29.
14. Jeannot, M. A., and Cantwell, F. F. (1996). Solvent microextraction into a single drop. *Analytical Chemistry,* 68(13): 2236-2240.
15. Pedersen-Bjergaard, S., and Rasmussen, K. E. (1999). Liquid− liquid− liquid microextraction for sample preparation of biological fluids prior to capillary electrophoresis. *Analytical Chemistry*, 71(14): 2650-2656.
16. Shen, G., and Lee, H. K. (2003). Headspace liquid-phase microextraction of chlorobenzenes in soil with gas chromatography-electron capture detection. *Analytical Chemistry*, 75(1): 98-103.
17. Šrámková, I. H., Horstkotte, B., Fikarová, K., Sklenářová, H. and Solich, P. (2018). Direct-immersion single-drop microextraction and in-drop stirring microextraction for the determination of nanomolar concentrations of lead using automated Lab-In-Syringe technique. *Talanta*, 184: 162-172.
18. Rezaee, M., Assadi, Y., Hosseini, M. R., Aghaee, E., Ahmadi, F. and Berijani, S. (2006). Determination of organic compounds in water using dispersive liquid–liquid microextraction. *Journal of Chromatography A*, 1116(1-2): 1-9.
19. Ferrone, V., Genovese, S., Carlucci, M., Tiecco, M., Germani, R., Preziuso, F., Epifano, F., Carlucci, G. and Taddeo, V. A. (2018). A green deep eutectic solvent dispersive liquid-liquid micro-extraction (DES-DLLME) for the UHPLC-PDA determination of oxyprenylated phenylpropanoids in olive, soy, peanuts, corn, and sunflower oil. *Food Chemistry*, 245: 578-585.
20. Bala, S. S., Sireesha, G., Ramya, Th. and Mohana, K. R. M. (2023). Experimental design of non-ionic hydrophobic DES-DLLME coupled with injector port silylation-GC–MS/MS for the quantitative determination of 13 bisphenols in food samples. *Food Chemistry*, 405(A): 134778.
21. Elik, A., Özlem, A., Hameed, U. H., Grzegorz, B. and Nail, A. (2023). Combination of homogeneous liquid–liquid extraction and vortex assisted dispersive liquid–liquid microextraction for the extraction and analysis of ochratoxin A in dried fruit samples: Central composite design optimization. *Journal Food Composition Analysis,* 124: 105656.
22. Florindo, C., Branco, L. C. and Marrucho, I. M. (2017). Development of hydrophobic deep eutectic solvents for extraction of pesticides from aqueous environments. *Fluid Phase Equilibria*, 448: 135-142.
23. Jiang, W., Chen, X., Liu, F., You, X. and Xue, J. (2014). Effervescence-assisted dispersive liquid–liquid microextraction using a solid effervescent

agent as a novel dispersion technique for the analysis of fungicides in apple juice. *Journal Separation Sciences*, 37(21): 3157-3163.

24. Jafarinejad, M., Ezoddin, M., Lamei, N., Abdi, K., Babhadi-Ashar, N., Pirooznia, N. and Akhgari, M. (2020). Effervescent tablet-assisted demulsified dispersive liquid–liquid microextraction based on solidification of floating organic droplet for determination of methadone in water and biological samples prior to GC/flame ionization and GC/MS. *Journal Separation Sciences*, 43(16): 3266-3274.
25. Kirill, B., Irina, T. and Andrey, B. (2022). An effervescence-assisted dispersive liquid-liquid microextraction based on three-component deep eutectic solvent for the determination of fluoroquinolones in foods. *Talanta*, 250: 123709.
26. Rajendran, S., Loh, S. H., Ariffin, M. M., and Khalik, W. M. A. W. M. (2022). Magnetic effervescent tablet-assisted ionic liquid dispersive liquid–liquid microextraction employing the response surface method for the preconcentration of basic pharmaceutical drugs: Characterization, method development, and green profile assessment. *Journal of Molecular Liquids,* 367: 120411.
27. Sepideh, S., Ramin, A. and Mohammad, R. A. M. (2022). Combination of microwave-assisted solvent extraction and effervescence-assisted deep eutectic solvent-based in-syringe dispersive liquid-liquid microextraction and its application in the extraction of triazine pesticides from apple samples. *Journal Separation Sciences*, 45(19): 3735-3744.
28. Aghaie, A. B., and Hadjmohammadi, M. R. (2006). Fe_3O_4@p-Naphtholbenzein as a novel nano-sorbent for highly effective removal and recovery of Berberine: Response surface methodology for optimization of ultrasound assisted dispersive magnetic solid phase extraction. *Talanta*, 156: 18-28.
29. Hamama, A. K., Ray, J., Day, R. O. and Brien, J. A. E. (2005). Simultaneous Determination of rofecoxib and celecoxib in human plasma by high-performance liquid chromatography. *Journal of Chromatographic Sciences*, 43(7): 351-354.
30. Oh, H. A., Kim, D., Lee, S. H., and Jung, B. H. (2015). Simultaneous quantitative determination of celecoxib and its two metabolites using liquid chromatography–tandem mass spectrometry in alternating polarity switching mode. *Journal Pharmaceutical Biomedicine*, 107: 32-39.
31. Rose, M. J., Woolf, E. J. and Matuszewski, B. K. (2000). Determination of celecoxib in human plasma by normal-phase high-performance liquid chromatography with column switching and ultraviolet absorbance detection. *Journal Chromatography B*, 738(2): 377-385.

Malaysian Journal of Analytical Sciences (MJAS)
Published by Malaysian Analytical Sciences Society

Fe_3O_4-DOPED POLYSULFONE MEMBRANE FOR ENHANCED ADSORPTION OF COPPER FROM AQUEOUS SOLUTION

(Membran Polisulfon Berdop Fe_3O_4 untuk Peningkatan Penjerapan Kuprum daripada Larutan Akues)

Wan Khairunnisa Wan Ramli[1*], Nur Maisyatul Syalina Abdul Wahab[1], Siti Khalijah Mahmad Rozi[1,2], Syumayyah Rasis[1], Gavin Chew Tiong Chuen[1], and Lew Guo Liang[1]

[1]*Faculty of Chemical Engineering and Technology, Universiti Malaysia Perlis, Kompleks Pusat Pengajian Jejawi 3, 02600 Arau,Perlis, Malaysia*
[2]*Centre of Excellence for Biomass Utilization, Universiti Malaysia Perlis, 02600 Arau, Perlis, Malaysia*

[*]*Corresponding author: wankhairunnisa@unimap.edu.my*

Received: 3 November 2023; Accepted: 12 February 2024; Published: 29 April 2024

Abstract

Water pollution, especially from industrial wastewater has become one of the major global environmental problems. As the result of rapid industrialization, the expansion of industries such as the electroplating industry has resulted in an increase in heavy metals effluent, especially copper, in the wastewater, and this poses detrimental effects on the biodiversity and environment. The abatement of copper pollution has received widespread attention, and continuous research advancement has been observed in adsorption and membrane technology. Nanofiltration membranes with nanopores recorded higher suitability to remove ions but at the expense of membrane fouling as a result of the formation of contaminants on the surface layer that blocks the diffusion of contaminants into the membrane substructure. This research highlights the incorporation of Fe_3O_4 nanoparticles into the polysulfone (PSf) membrane matrix as an adsorptive membrane and their possible adsorption mechanism towards Cu, which can manifest the combined characteristics of both removal techniques. Fe_3O_4 nanoparticles were synthesized using the co-precipitation method. Fe_3O_4-doped PSf membranes were then synthesized with various concentrations of Fe via the Non-solvent Induced Phase Separation (NIPS) technique. The physicochemical properties of the Fe nanoparticles and the membranes were evaluated using X-ray diffraction (XRD), Scanning Electron Microscope (SEM), water contact angle and porosity testing. Crystal phase analysis confirmed the formation of magnetite Fe_3O_4 in a cubic structure. Agglomerations of Fe NPs on the membrane surface were observed for membranes with lower Fe concentrations, suggesting the possibility of poor blending and this contributed to the lower adsorption capability of these membranes. Membranes with 2 wt.% Fe concentration (Fe-2.0) exhibited the highest Cu(II) ions adsorption capacity of 637 mg/g, which is trifold of those recorded for pristine PSF membrane (Fe-0.0). The adsorption data of Cu adsorption were best fitted into the Temkin isotherm and pseudo-second-order models, suggesting an adsorption mechanism involving an exothermic chemical interaction between Cu ions and the Fe_3O_4 NPs within the membrane. This research confirms the potential of incorporating Fe_3O_4 in the PSf membrane backbone to enhance Cu removal as an adsorptive membrane, even at lower NP concentrations.

Keywords: adsorptive membrane, copper removal, iron oxide, adsorption kinetics

Abstrak

Pencemaran air, terutamanya daripada air sisa industri telah menjadi salah satu masalah alam sekitar yang utama di seluruh dunia. Berikutan pengindustrian yang pesat, peluasan industri seperti industri penyaduran elektrik telah mengakibatkan peningkatan dalam efluen logam berat, terutamanya kuprum, dalam air buangan, dan ini menimbulkan kesan buruk kepada biodiversiti dan alam sekitar. Pengurangan pencemaran kuprum telah mendapat perhatian yang meluas, dan kemajuan penyelidikan berterusan telah diperhatikan dalam teknologi penjerapan dan membran. Membran penapisan nano dengan liang bersaiz nano mencatatkan kesesuaian yang lebih tinggi untuk menyingkirkan ion tetapi dengan mengorbankan penyisikan membran akibat pembentukan lapisan permukaan bahan cemar yang menghalang resapan bahan cemar ke dalam substruktur membran. Penyelidikan ini menekankan penggabungan nanopartikel Fe_3O_4 ke dalam matriks membran polisulfon (PSf) sebagai membran penjerap dan mekanisme penjerapan yang mungkin terhadap Cu, yang boleh menunjukkan ciri gabungan kedua-dua teknik penyingkiran tersebut. Nanozarah Fe_3O_4 disintesis menggunakan kaedah pemendakan bersama. Membran PSf terdop Fe kemudiannya disintesis dengan pelbagai kepekatan Fe melalui teknik pemisahan fasa teraruh bukan pelarut (NIPS). Sifat fizikokimia nanopartikel Fe dan membran dinilai menggunakan pembelauan sinar-X (XRD), mikroskop elektron pengimbasan (SEM), sudut sentuhan air dan ujian keliangan. Analisis fasa kristal mengesahkan pembentukan magnetit Fe_3O_4 dalam struktur kubus. Aglomerasi NP Fe pada permukaan membran diperhatikan untuk membran dengan kepekatan Fe yang lebih rendah, menunjukkan kemungkinan pengadunan yang lemah dan ini menyumbang kepada keupayaan penjerapan yang lebih rendah bagi membran ini. Membran dengan kepekatan Fe 2% berat (Fe-2.0) mempamerkan kapasiti penjerapan ion Cu(II) tertinggi sebanyak 637 mg/g, iaitu tiga kali ganda daripada yang direkodkan untuk membran PSF murni (Fe-0.0). Data penjerapan penjerapan Cu paling baik dipadankan ke dalam model isoterma Temkin dan pseudo-second-order, mencadangkan mekanisme penjerapan yang melibatkan interaksi kimia eksotermik antara ion Cu dan NP Fe_3O_4 dalam membran. Penyelidikan ini mengesahkan potensi menggabungkan Fe_3O_4 dalam tulang belakang membran PSf untuk meningkatkan penyingkiran Cu sebagai membran penjerap, walaupun pada kepekatan NP yang lebih rendah.

Kata kunci: membran penjerap, penyingkiran kuprum, ferum oksida, isoterma penjerapan, kinetik penjerapan

Introduction

The rapid growth of urban industrialization, including the chemical industries, uses enormous amounts of water and produces large amounts of waste effluent during the production processes. Copper (Cu), chromium (Cr), zinc (Zn), and cadmium (Cd) are the most common heavy metals present in these industrial effluents, making the release of heavy metals from such operations far more dangerous [1]. In fact, the electroplating industry alone produces a high amount of copper, in the range of 8.8 g/L [2]. These heavy metals are stable, non-biodegradable, toxic, and carcinogenic. They accumulate in living organisms and can cause severe problems for public health and the environment. The Environmental Protection Agency (EPA) has set the acceptable standard concentrations of Cu that can be discharged from industries to the environment, which falls within the range of 0.2 and 1.0 mg/L. Therefore, the remediation of water contaminated by Cu is critical to protect the environment as well as to promote water reuse.

Increased interest was observed towards membrane filtration, mainly ultrafiltration (UF) and nanofiltration (NF). UF is replacing the conventional method for water treatment and is becoming universally accepted due to the lower operating pressure and the simple membrane preparation, among others. However, small compounds and toxic ions cannot be removed using UF. Meanwhile, nanofiltration (NF) is used to remove heavy metals from water, but the performance of the NF membrane, is restricted by the species of the targeted heavy metal and the fact that it degrades as heavy metal concentrations increase up to 2000 mg/L [3]. In addition, NF membranes require higher mechanical strength, owing to the higher operating pressure and the functional surface layer that is critical to ensure the efficacy of the membrane separation. These often require complicated preparation of the functional surface layer such as interfacial polymerization and surface coating [4]. Polysulfone (PSf) membrane is often used in NF membrane formation due to its high chemical and mechanical resistance, but its hydrophobic nature often results in low flux and membrane fouling [5]. This has triggered the rapid development of efficient and cost-effective membranes for heavy metal removal, particularly Cu, which can overcome the limitations of NF and other common remediation techniques. The

invention of adsorptive membranes that combine the advantages of both adsorption and membrane filtration can also overcome the drawbacks of both techniques. The impregnation of prospective nano adsorbents into polymeric membranes can be achieved by characterizing them based on their affinity towards pollutants in the forms of ions and molecules [6].

Hydrophilic nanoparticles are often used to boost the hydrophilicity and flux of the PSf membrane, especially in removing Cu. The findings of Ayaz et al. [7] indicated that adding hydrophilic nanoparticles such as alumina into the PSf membrane matrix can increase the hydrophilicity of the membrane. This subsequently increases the water flux and Cu rejection from 40% for the nascent PSf membrane to 75% for PSf membrane with 1 wt.% alumina. Zeolite is also used in the PSf membrane to remove Cu. Hamid et al. [8] reported that the highest Cu adsorption capacity of 101 mg/g for PSf membrane doped with 15 wt.% of zeolite at an optimum pH of 5 as well as the anionic character of zeolite, attract the positive Cu ions for the adsorption process. Iron oxide nanoparticles have been amalgamated into membrane matrix due to their strong affinity towards Cu and hydrophilic nature, which can increase the hydrophilicity of PSf membranes in order to enhance the membrane performance towards not only Cu but other heavy metals. This includes lead [9], phosphate [10] and other contaminants such as protein. Said et al. [11] reported increased water flux and protein rejection with the addition of iron oxide into their PSf membrane, attributed to the higher porosity and hydrophilicity. Even though iron oxide has been reported as a popular nano adsorbent in many reports involving polymeric adsorptive membranes to remove heavy metals, the adsorption mechanism towards Cu (II) ions in highly concentrated copper aqueous solution has never been reported previously.

In this present work, the adsorption capability and mechanism of the Fe_3O_4-doped PSf membrane were evaluated. A set of adsorptive membranes was synthesized by incorporating various concentrations of Fe_3O_4 NPs into the PSf membrane matrix to remove Cu from the aqueous solution. The Fe_3O_4 NPs were prepared via the common co-precipitation method and the membranes were synthesized via the simple nonsolvent induced phase separation (NIPS) technique. The Fe_3O_4 NPs were characterized using XRD and the membranes were evaluated using FTIR, SEM, contact angle measurement and porosity analysis. The adsorption performance of the membranes was evaluated in terms of contact time and initial Cu concentrations. Subsequently, the adsorption mechanism of these membranes was also evaluated.

Materials and methods

Chemicals

Metal precursors such as $FeCl_2.6H_2O$, $(NH_4)_2Fe(SO_4)_2.6H_2O$ and $CuSO_4$ powders were procured from R&M chemicals. Polysulfone (PSf) polymer pellets were procured from Solvay Solexis (France). Dimethylacetamide (DMAc, 99.5%), used as the solvent, was purchased from Sigma-Aldrich (Germany). Ultrapure deionized water was used as the coagulant. All solvents and precursors were used as received.

Instrumentation

X-ray diffraction (XRD) pattern of the synthesized Fe nanoparticles was recorded using a diffractometer (Bruker AXS Inc., 30 kV, 10 mA), and equipped with a Cu-Kα radiation source (λ = 1.5412 Å). The samples were scanned from 15° to 70° (2θ). Surface morphological analysis of Fe_3O_4-doped PSf membranes was carried out using Hitachi SU8220 Scanning Electron Microscopy (Oxford Instrument, Oxford Shire, UK). FTIR spectra were recorded on Perkin Elmer FTIR spectrophotometer (Massachusetts, USA) with a crystal diamond universal ATR sampling accessory at room temperature. All spectra were recorded in the wavenumber range of 4000 to 500 cm^{-1}. The membrane porosity was measured using the gravimetric method. The membrane was immersed in ethanol for 2 hours. The wet membrane was then slightly patted to remove excess liquid on the surface and weighed to get the weight of the wet membrane, w_m. The membrane was then dried in an oven for an additional 2 hours and the weight of the dried membrane, w_d was weighed. The membrane porosity can be calculated using Equation 1:

$$\varepsilon = \frac{(w_m - w_d)/\rho_e}{((w_m - w_d)/\rho_e) + (w_d/\rho_p)} \quad (1)$$

where w_m is the weight of the wet membrane (g), w_d is the weight of the dry membrane (g), ρ_e is the density of ethanol and ρ_p is the density of the polymer, PSf. The water contact angle of the membrane surface was evaluated using the sessile drop method. A water droplet of 2 µL was dropped on the membrane surface and images of the droplet were taken after 5 s. The images were analysed using the ImageJ software to get the water contact angle of the membrane [12,13].

Synthesis of Fe_3O_4 nanoparticles

The Fe_3O_4 nanoparticles were synthesized via the co-precipitation method. High-purity precursors including $FeCl_2.6H_2O$ (3.9 g) and $Fe(SO_4)_2.6H_2O$ (5.4 g) were used in appropriate stoichiometric molar ratios. The precursors were dissolved in 200 mL of deionized water under vigorous stirring until a suspension solution was formed. A concentrated NaOH solution was then added dropwise until the pH of the suspension achieved 7 (Neutral). The suspension was vigorously stirred for 2 h before repeatedly washing with deionized water to remove the excess NaOH. The formed suspension was then filtered and dried in the oven at 110 °C for 5 h. The dried nanoparticle powders were kept in a desiccator prior to characterization and testing [3,14].

Synthesis of Fe_3O_4-doped PSf membranes

The Fe_3O_4-doped PSf membranes were prepared following the formulation shown in Table 1, via the phase separation method, particularly the Nonsolvent Induced Phase Separation (NIPS) method (Figure 1). Dope solutions with various wt.% of nanoparticles were prepared. DMAc was first heated to 60 °C, with constant stirring and pre-weighed PVP at 1 wt.% was added to the solvent as a pore former. Next, various wt.% of nanoparticles prepared in the previous subsection were added slowly to the solution [15]. Dried PSf granules at 18 wt.% were then gradually added and dissolved into the solution for 6 h. After mixing, the dope solution was degassed prior to casting, to remove any bubbles formed during the stirring process. The dope solution was then cast onto a glass plate using a casting machine, with a membrane thickness of 250 µm. The casted solution was then immediately immersed into a coagulation bath, containing deionized water for the phase inversion process to occur. The membrane formed was then washed to remove any excess solvent and dried at ambient temperature. The membrane was then placed in fresh DI water prior to characterization and performance tests.

Table 1. Composition of the synthesized Fe_3O_4-doped PSf membranes

Membrane	PSf, (wt.%)	PVP, (wt.%)	DMAc, (wt.%)	Fe NPs, (wt.%)
Fe-0.0	18	1	81.0	0.0
Fe-0.5	18	1	80.5	0.5
Fe-1.0	18	1	80.0	1.0
Fe-2.0	18	1	79.0	2.0

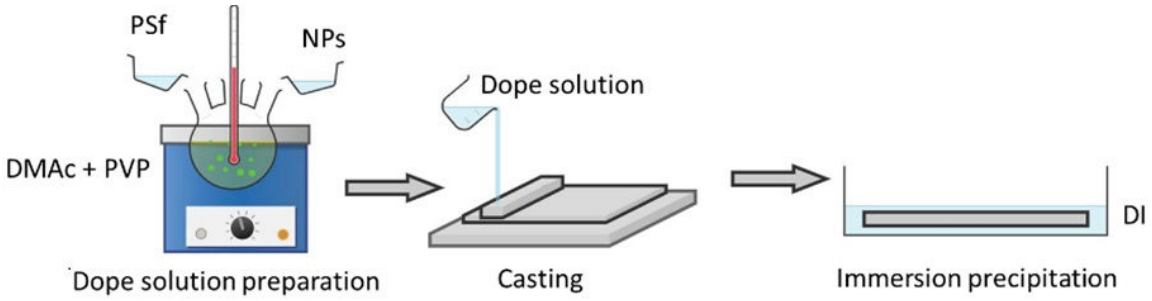

Figure 1. Fe_3O_4-doped PSf membrane preparation via NIPS

Batch adsorption studies

The batch adsorption study was performed to evaluate the adsorption characteristics of Fe_3O_4-doped PSf membranes towards copper. Effects of contact time and initial concentration on the adsorption capacity, q and copper rejection, R of the synthesized membranes were evaluated using Equation 2 and 3.

$$q_e = \frac{(C_o - C_e)V}{m} \quad (2)$$

$$R = \left[1 - \left(\frac{C_e}{C_o}\right)\right] \times 100\% \quad (3)$$

where q is the adsorption capacity (mg/g), Co and Ce are the initial and equilibrium concentration of metal ions in solution (mg/L), V is the volume of the solution (L) and m is the membrane dry mass (g).

The adsorption experiments were performed in batches and the effects of Cu initial concentration and contact time on Cu removal were evaluated. 12.5 mg of the membranes with various wt.% of Fe nanoparticles were cut into smaller pieces and placed into several centrifuge tubes containing 12.5 mL of various initial concentrations of Cu solution; from 0.05 to 1.2 M. The tubes were agitated at 160 rpm for 30 minutes. To study the effect of contact time, the membranes were placed into 0.05 M of Cu solution and were removed from the solution after 5, 10, 15, 20, 25 and 30 minutes, respectively. The final concentration of the Cu solution was measured using a UV-Vis spectrophotometer.

Adsorption Isotherm and Kinetic

The mechanism of Cu adsorption onto the Fe_3O_4-doped PSf membranes was further evaluated based on three isotherms models;1. Langmuir, 2. Freundlich and 3. Temkin. These isotherm models are best described based on the following linear equations as shown in Equations 4 to 6, respectively:

$$\frac{C_e}{q_e} = \frac{1}{q_{max}K_L} + \frac{C_e}{q_{max}} \quad (4)$$

$$lnq_e = \ln K_f + \frac{1}{n} lnC_e \quad (5)$$

$$q_e = \frac{RT}{b_T} lnK_T + \frac{RT}{b_T} lnC_e \quad (6)$$

where q_e is the equilibrium adsorption capacity (mg/g), q_{max} is the maximum adsorption capacity (mg/g), C_e is the equilibrium concentration of metal ions (mg/L) and K_L is the Langmuir adsorption constant (L/mg), n is the adsorption intensity constant, K_f is the Freundlich adsorption constant (L/g), R is the gas constant (8.314 J/mol), T is the absolute temperature (K), K_T is the Temkin equilibrium constant (L/g) and b_T (J/mol) is the constant associated with the adsorption heat. For the Langmuir model, an important parameter, known as the separation factor or equilibrium parameter, denoted as R_L, shown in Equation 7, is used to check the favourability of Cu adsorption onto the Fe_3O_4-doped PSf membranes.

$$R_L = \frac{1}{1+K_L C_0} \quad (7)$$

where K_L and C_o are the Langmuir constant and the highest initial concentration of Cu, respectively.

The kinetics of the adsorption were also evaluated based on these two common kinetic models; the pseudo-first-order and pseudo-second-order models. The pseudo-first-order and pseudo-second-order models are described in linear forms as Equation 8 and 9, respectively:

$$log\ (q_e - q_t) = logq_e - K_1 t \quad (8)$$

$$\frac{t}{q_t} = \frac{1}{K_2 \cdot q_e^2} + \frac{t}{q_e} \quad (9)$$

where K_1 (1/min) is defined as the pseudo-first-order adsorption rate constant, q_e (mg/g) and q_t (mg/g) are the adsorption capacities for Cu adsorption at equilibrium and at respective contact time and K_2 (g/mg min) is the pseudo-second-order rate constant.

Results and Discussion

Characterizations

The XRD pattern of the synthesized nanoparticles, shown in Figure 2 shows well-defined Bragg reflection characteristics of Fe_3O_4. The data shows diffraction peaks at 2θ = 30.2306°, 35.59°, 43.4167°, 57.3511° and 56.998° which can be indexed to the (220), (311), (400), (422) and (511) planes of Fe_3O_4 in a cubic phase, respectively which is consistent with the standard pattern for magnetite Fe_3O_4 (JCPDS no.- 96–900-7645) [16]. Based on the XRD pattern, the highest peak is approximately 35.59°, indicating that the (311) plane is the most ordered plane in the crystal lattice. The crystallite size was around 15 nm to 42 nm which agrees

with the findings by Upadhyay et al. [17], which reported a crystallite size ranging from 27 nm to 53 nm for Fe_3O_4 nanoparticles.

Figure 3a displays the FTIR spectra of the synthesized membranes. All membranes showed similar peaks at 1585 cm^{-1}, 1488 cm^{-1}, 1242 cm^{-1} and 1150 cm^{-1} [18]. These peaks confirm the presence of PSf as the backbone of these membranes although the reduced intensity of the absorption peaks for Fe_3O_4-doped PSf membranes suggested that the weight percentage of PSf was affected by the addition of Fe into the membrane matrix [19]. The presence of the carbonyl and sulfone group within the PSf polymer was confirmed by the characteristic peaks observed at approximately 558 cm^{-1}, 1242 cm^{-1}, 1150 cm^{-1} and 1585 cm^{-1} which correspond to the asymmetric stretching, symmetric stretching, and bending vibrations of the sulfone group, including the C-O-C, O=S=O and C=C aromatic, respectively [20, 21]. Peaks for the C-S stretching vibrations were also observed at 635 cm^{-1} for all membrane [22]. After the addition of Fe_3O_4 NPs, the intensity of the C-S peak increases (Figure 3b), due to the presence of Fe-O bond at around 635 cm^{-1}, confirming the succesful incorporation of the Fe_3O_4 nanoparticles on the PSf membrane [23].

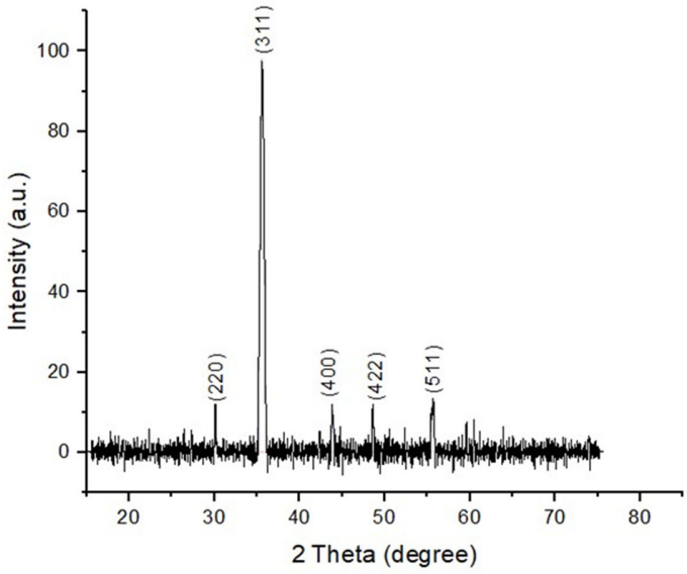

Figure 2. XRD pattern of the synthesized Fe nanoparticles

The surface morphology of Fe_3O_4-doped PSf membranes was appraised under SEM (Figure 4). Figure 4a indicates some pores on the surface of the Fe-0.0 membrane, with other visible pores, hidden under a very thin skin layer and uniformly distributed across the surface. As the concentration of Fe nanoparticles increased from 0.5 wt.% to 1.0 wt.% (Figure 4b and c), the dense skin layer thickens, evidenced by the less visible pores on the surface but at the expense of increasing Fe agglomeration on the surface layer. The blending of 2 wt.% of Fe into the PSf membrane (Figure 4d) also induced some nonsolvent penetration through the thick dense layer, forming pores on the surface and with less Fe agglomeration. These top surface morphologies also revealed that the blending of Fe nanoparticles in the membrane matrix was improved with increasing concentration of Fe. The top surfaces of the Fe-0.5 and Fe-1.0 membranes (Figure 4b and c) were covered by white particle agglomeration and this agglomeration was significantly reduced when the Fe concentration was increased to 2 wt.%. This observation can be explained by the miscibility of PSf with PVP and Fe nanoparticles. Since PVP is hydrophilic in nature and is not miscible with PSf, thermodynamically, it facilitated the penetration into the membrane during the solvent/ nonsolvent exchange. However, kinetically,

this can also increase the viscosity of the solution. Without the addition of the Fe nanoparticles (Fe-0.0), the thermodynamic effects are more dominant, resulting in a rapid demixing process, whereby the polymer precipitates very quickly, forming a very thin skin layer and presumably with a finger-like substructure [24, 25]. The addition of Fe NPs reduces the shear force of the dope solution due to the restricted shear flow of polymer chains by the NPs thus increasing the viscosity of the dope solution. This then potentially delayed the demixing process by slowing down the exchange between the solvent and nonsolvent in the sublayer, thus delaying the solvent polymer demixing, forming a denser skin layer before the demixing occurs [10, 26].

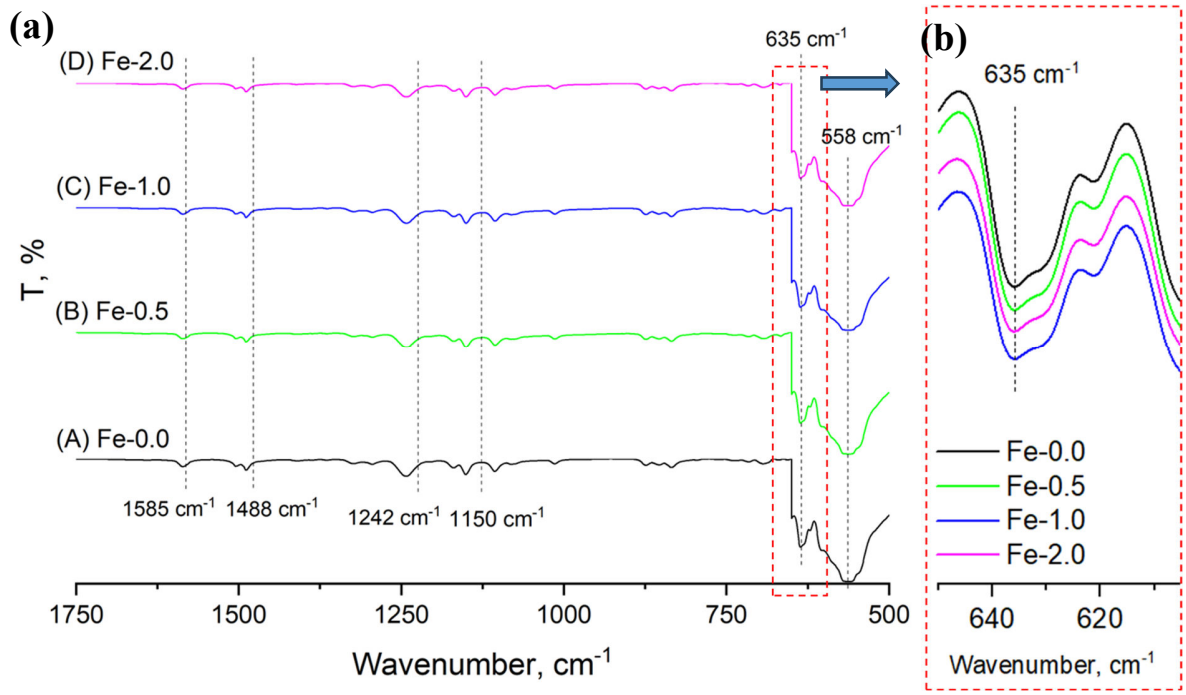

Figure 3. (a) FT-IR spectra of (A) Fe-0.0 (B) Fe-0.5, (C) Fe-1.0 and (D) Fe-2.0, and (b) FT-IR spectra of Fe-0.0, Fe-0.5, Fe-1.0 and Fe-2.0 at the Fe-O stretching band (635 cm^{-1})

The surface hydrophobicity or the wetting capability of the membrane is considered one of the important requirements for water filtration, specifically to improve the pure water flux and prevent membrane fouling. In addition, the surface hydrophilicity of a membrane also depends on the porosity, surface roughness, and chemical composition of the surface. Lower water contact angle measurements are a sign of higher hydrophilicity, which is preferable for wastewater treatment purposes because it can draw in water molecules and prevent foulants from adhering to or interacting with the surface of the membrane, improving its antifouling abilities and water flux [27]. Figure 5 shows the water contact angle (WCA), measured using the sessile drop method and the porosity of the membranes. As shown in Figure 5, the pristine PSf membrane exhibited a WCA of 77.40˚, showing a rather hydrophobic trait against water, while other membranes revealed a decreasing trend of WCA values than that of the pristine PSf membrane (Fe-0.0) with increasing Fe concentration. Fe-0.5, Fe-1.0 and Fe-2.0 recorded WCA values of 71.96˚, 53.99˚ and 50.93˚, respectively. The hydrophilicity of the membranes improved significantly due to the hydrophilicity nature of the Fe NPs, owing to the higher surface energy and the presence of the oxygen element in the Fe NPs [28], in the form of Fe_3O_4, as corroborated by the XRD result, albeit at lower concentration of Fe NPs into the membrane matrix. This subsequently promotes chemisorption and makes it attractive as an adsorptive membrane [29].

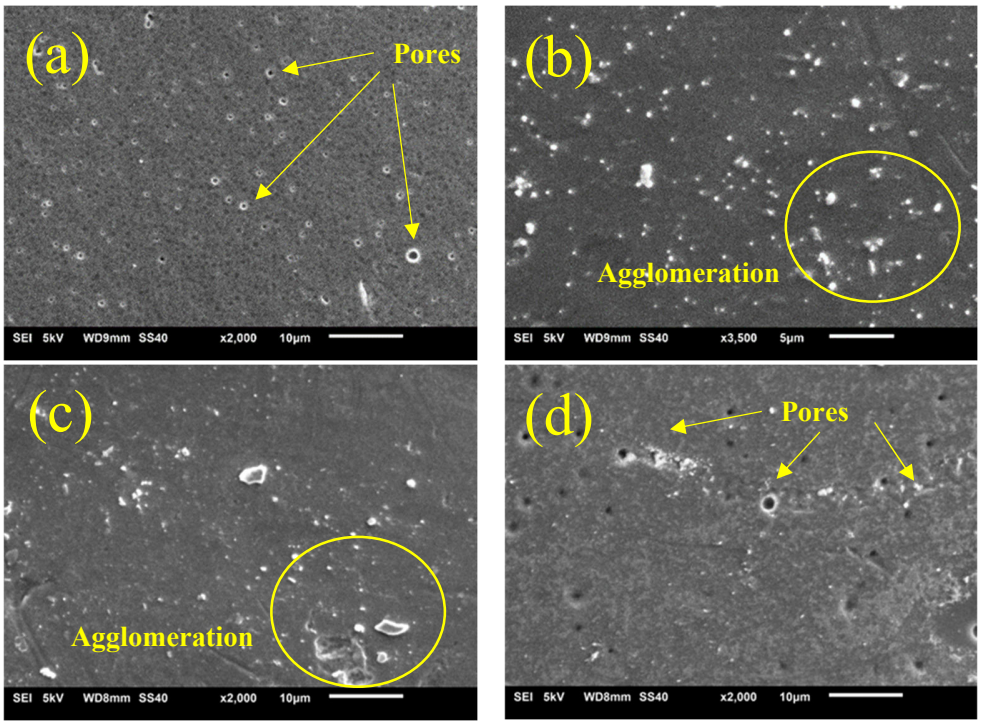

Figure 4. SEM images of the surface region of Fe_3O_4-doped PSf membranes at 2000x magnification: (a) Fe-0, (b) Fe-0.5, (c) Fe-1.0, and (d) Fe-2.0

In terms of the porosity of the membrane, a substantial decline was observed after the addition of Fe NPs, with Fe-0.5 membrane recorded the lowest porosity at 14%. This was more than half than the porosity recorded for the pristine PSf membrane (Fe-0.0) which was at 38%. Granting that the porosity of the Fe_3O_4-doped PSf membranes was lower compared to the pristine PSf membrane, the porosity immediately picks up the trend and shows a positive increase of porosity with increasing Fe concentrations. The formation of the denser skin layer at the top of the Fe-0.5, Fe-1.0 and Fe-2.0 membranes, resulting from the polymer-rich phase formation at the nonsolvent-film interface hindered the diffusion of solvent/nonsolvent of the membrane film after immersion into water. The closer porous substructure formed due to the delayed demixing subsequently increases the thickness of the top dense layer, reducing the porosity of the membrane [13]. The lower porosity of Fe-0.5 and Fe-1.0 membranes can also be attributed to the ineffective blending of Fe NPs in the membrane matrix causing the NPs to agglomerate. The formation of larger Fe agglomerates can reduce the free space of the membrane, thus reducing the porosity [26].

Batch adsorption study fo Cu

The synthesized Fe_3O_4-doped PSf membrane was evaluated as the adsorptive membrane for Cu removal. The adsorption capacity (mg/g) and the Cu removal percentage (%) of the membranes were established under two main adsorption parameters, such as the initial Cu concentrations and the contact time. The adsorption process was evaluated with a membrane mass of 12.5 mg, and 12.5 mL of Cu solutions at 27 ˚C and pH 7 except otherwise stated.

Effect of Fe_3O_4 doping

Figure 6 illustrates the effect of blending Fe_3O_4 into the PSf membrane matrix on the adsorption capacity. It is evident that the adsorption capacity was improved from below 267 mg/g to almost double (514 mg/g) when only 0.5 wt.% of Fe_3O_4 was blended into the membrane. The Cu removal increases almost trifold after 30 minutes of contact with the PSf membrane with 2 wt.% of Fe (Fe-

2.0) as compared to the pristine membrane (Fe-0.0). The data revealed a clear increasing trend of adsorption capacity with increasing Fe_3O_4 concentration with the Fe-2.0 membrane recording the highest Cu adsorption capacity of 670 mg/g. The root cause of this enhancement can probably be traced back to the higher Fe_3O_4 loading with less agglomeration, hence providing more available adsorption sites for Cu ions adsorption. Agglomerations observed for Fe-0.5 and Fe-1.0 might obstruct the potential adsorption sites for Cu ions, lowering the adsorption capacity of the membranes [3].

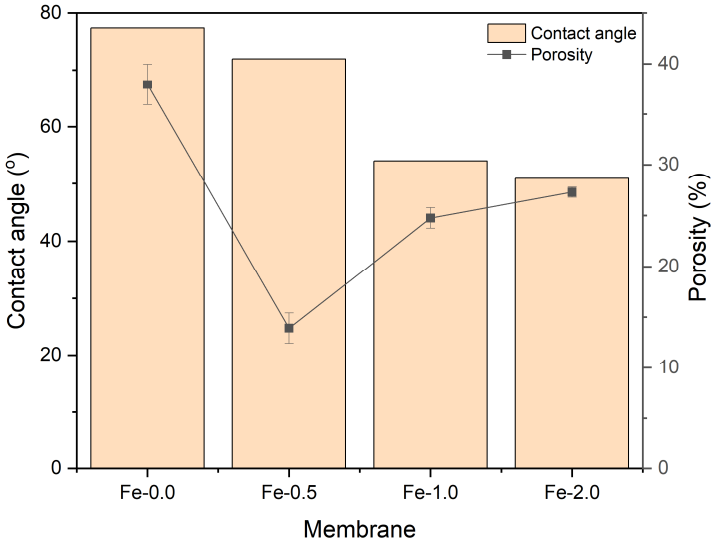

Figure 5. Water contact angle (˚) and porosity of the Fe_3O_4-doped PSf membranes

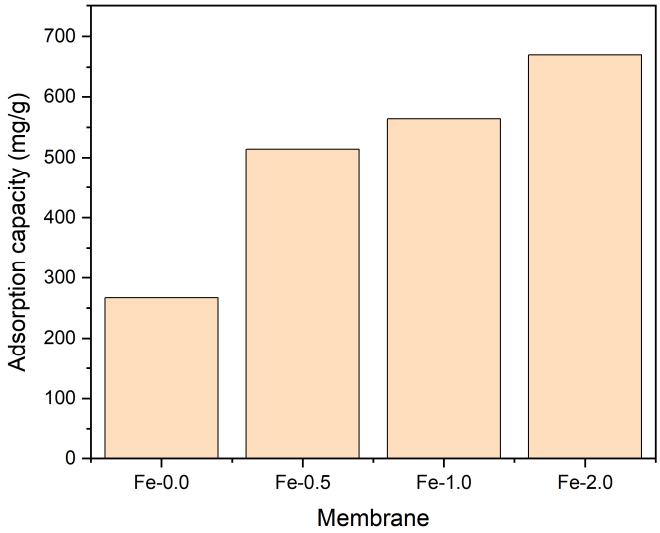

Figure 6 Effect of Fe_3O_4 doping into PSf membrane in terms of the adsorption capacity

Table 2 presents the comparison between the current work, Fe_3O_4-doped PSf membrane with previously reported adsorptive membrane for the adsorption of Cu ion from aqueous solution in terms of the adsorption capacity. The results revealed that the proposed Fe_3O_4-doped PSf membrane is a highly efficient adsorptive

membrane with the highest adsorption capacity for the treatment of Cu ions from aqueous solution. The Fe_3O_4-doped PSf membrane exhibited the highest adsorption capacity of Cu ions with a comparable NP concentration and contact time to other reported adsorbents.

Table 2. Comparison of the synthesized adsorptive membrane with other published adsorptive membranes for adsorption of Cu ions

Membrane	Adsorbent	Concentration of Adsorbent (wt.%)	Adsorption Capacity	References
PSf	$NiFe_2O_4$	3	42 mg/g	[30]
PES	PEG-coated $CoFe_2O_3$	2-6	-	[31]
PES	PANI/ Fe_3O_4	0.01-1	1.6 mg/g	[32]
PSf	Fe_3O_4	0.5-2	670 mg/g	This work

Effect of Cu initial concentration

Figure 7 depicts the removal of Cu(II) by Fe_3O_4-doped PSf membranes at different Cu initial concentrations (0.05, 0.06, 0.07 and 0.08 M). A steady increase in Cu adsorption can be seen for all membranes with respect to increasing Cu initial concentration ranging from 0.05 to 0.08 M. This occurred as a consequence of the increasing concentration gradient, which increased the driving force for the molecules to slit into the membrane pores and adhere to the surface of the NP [15]. Additionally, a higher number of Cu ions to be adsorbed onto the NPs can also facilitate the adsorption. At a lower Cu concentration of 0.05 M, the increasing Cu adsorption capacity was in the order of Fe-1.0 <Fe.0.5<Fe-2, while at higher Cu concentrations of 0.08 M, Fe-0.5 membrane recorded the lowest adsorption capacity of around 4613 mg/g. For membranes with lower adsorption capacity such as Fe-0.5 and Fe-1.0 membranes, the ineffective blending of the Fe NPs which results in particle agglomeration, observed in the SEM images might cause the uneven distribution of NPs in the membrane matrix subsequently reducing the number of readily available adsorption sites. These large agglomerates can also restrict the access of Cu(II) ions to the active sites on the surface of the membrane and in the membrane matrix.

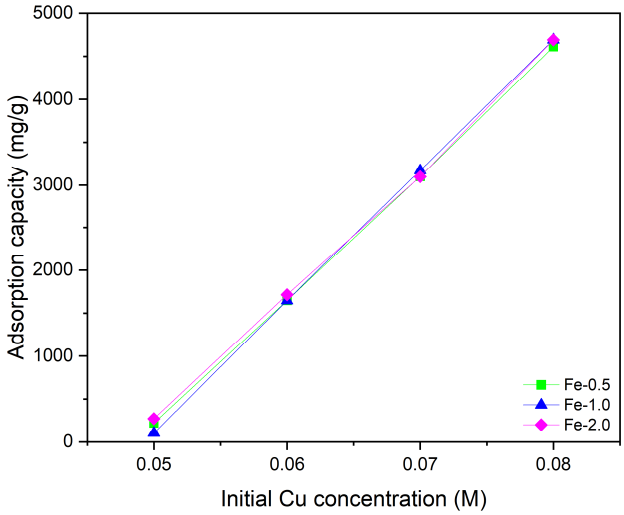

Figure 7. Effect of initial Cu concentration (M) on Cu adsorption capacity and rejection of the Fe_3O_4-doped PSf membranes (pH =7.0±0.1, membrane dosage = 1.0 g/L, contact time = 120 min, volume of feed solution = 12.5 mL)

Effect of contact time

The effects of contact time on the adsorption capability of the synthesized Fe_3O_4-doped PSf membranes are shown in Figure 8. In general, within 30 minutes, two distinct main stages were observed in the adsorption process for all three membranes. Following the common trend of any adsorption process, the adsorption was rapid in the first 5 minutes of contact time. The adsorption capacity of the membranes increases with increased concentration of Fe in the PSf membrane with 394 mg/g, 586 mg/g and 637 mg/g for Fe-0.5, Fe-1.0 and Fe-2.0, respectively. This rapid trend was due to the bulk diffusion of Cu ions into the membrane pores followed by the sorption of the ions onto the abundant vacant Fe nanoparticles in the pores. The higher number of adsorption sites at the beginning of the adsorption process was believed to be the driving force of this rapid Cu removal. No further increment of Cu removal was observed for the Fe-1.0 membrane as the vacant adsorption sites decreased and became saturated over time [33]. A slight difference can be observed in the adsorption process trends for Fe-0.5 and Fe-2.0 which can be attributed to the difference in morphologies of the membranes. Fe particle aggregates on the Fe-0.5 surface can also promote the adsorption of Cu on the surface particles which then blocks the penetration of more Cu into the membrane pores, slowing down the adsorption process altogether [9]. The adsorption activity of the Fe-2.0 membrane was further increased after 20 minutes, indicating that there are more available sites for Cu to adsorb hence improving the Cu removal even more.

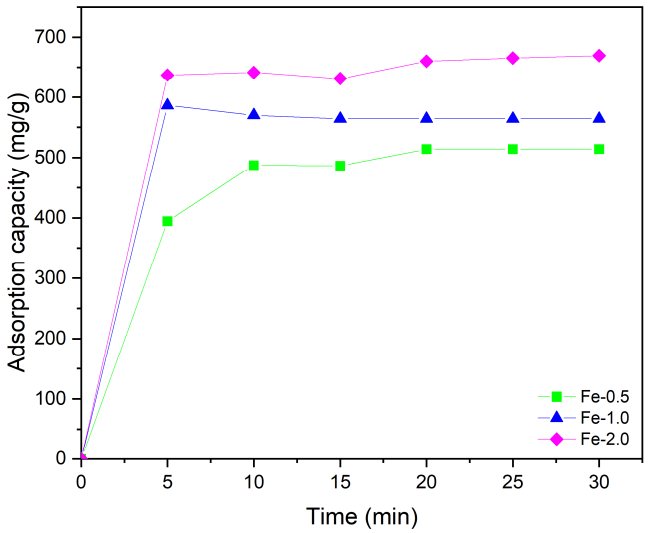

Figure 8. Effect of contact time (min) on Cu adsorption capacity and rejection of the Fe_3O_4-doped PSf membranes (pH =7.0±0.1, membrane dosage = 1.0 g/L, contact time = 60 min, volume of feed solution = 12.5 mL)

Evaluation of adsorption isotherm models and kinetics

In order to gain an understanding of the sorption mechanism of Cu ions onto these Fe_3O_4-doped PSf membranes, the experimental data were fitted into three main adsorption isotherms, specifically the Langmuir, Freundlich and Temkin models. The Langmuir isotherm model assumes that the adsorbate molecules are adsorbed onto a surface in a single layer, with each adsorption site having the same affinity for the adsorbate. The model also assumes that there is no transmigration of adsorbate molecules within the plane of the surface [34]. The Freudlich isotherm model describes the adsorption of a substance onto a heterogeneous surface with active sites having different binding energies. The adsorption favours the chemical adsorption process if the value of n is <1. However, if the value of n is >1, the adsorption then adopts the physical adsorption process [35]. The Temkin isotherm model focuses on the effect of adsorbate-adsorbent

interactions and the heat of adsorption on the adsorption process. It assumes a linear decrease in adsorption energy with increasing surface coverage, indicating that the adsorbate-adsorbent interactions weaken as the adsorption progresses [36].

Table 3 tabulates the isotherm parameters for all three models of all three membranes. In general, the equilibrium data of all membranes demonstrated stronger correlations with the Temkin isotherm model (Figure 9), evidenced by the higher correlation coefficients, R^2 of around 0.90-0.97, compared to those of the Langmuir and Freundlich isotherm models. The values obtained for the maximum adsorption capacity, q_{max} of Fe_3O_4-doped PSf membranes reveal that the adsorption of Cu onto these membranes does not follow the Langmuir isotherm. The corresponding R^2 for the Freundlich isotherm was higher than those of Langmuir showing a good linearity to the model. Still, the values of n did not fall within the range for favourable adsorption of between 1 to 10 [37]. Low values of n were observed for all membranes in the range of 0 to 1 indicating lower affinity between Cu ions and Fe NPs on the membrane [38], although this also suggests the adsorption involves chemisorption. The strength of the adsorption can also be described by the values of 1/n. All membranes demonstrated 1/n values above 1 indicative of cooperative adsorption whereby the adsorbed Cu ions can influence the adsorption of free Cu ions [39]. These results show that the linearized Langmuir and Freundlich models alone cannot properly describe the adsorption of Cu ions onto these membranes. As for Temkin, the variation of the adsorption energy, b_T was positive for all membranes, suggesting an exothermic sorption process between the Cu ions and the Fe_3O_4 NPs. This isotherm also validates the influence of Cu ions-Fe_3O_4 NPs interaction on the linear decrease of adsorption energy with increasing surface coverage [40].

It can also be inferred that these isotherms on their own might be underestimating the adsorption capability of these Fe_3O_4-doped PSf membranes, which contradicts the experimental data that suggests a higher performance of these membranes in removing Cu. However, the underestimation might also be due to the poor blending of the NPs resulting in huge agglomerates on the surface and in the membrane substructure. These agglomerates also occupied larger surface areas, reducing the available active sites for adsorption, hindering the proper adsorption of Cu ions onto the adsorption sites and consequently reducing the Cu removal and the misinterpretation of these isotherms [41].

Table 3. Isotherm parameters for Cu adsorption onto the Fe_3O_4-doped PSf membranes

Isotherm	**Parameter**	**Fe-0.5**	**Fe-1.0**	**Fe-2.0**
Langmuir	q_{max}	-12.3457	-8.3472	-16.1031
	b	-8119.07	-8039.9	-8077.29
	R^2	0.7814	0.8540	0.7686
Freundlich	K_f	2.53×10^{-19}	5.23×10^{-24}	3.43×10^{-18}
	1/n	5.4230	6.5660	5.1493
	n	0.1844	0.1523	0.1942
	R^2	0.8968	0.8484	0.8808
Temkin	K_T	0.00012	0.00015	0.00013
	b	0.0292	0.0218	0.0316
	R^2	0.9722	0.9441	0.9081

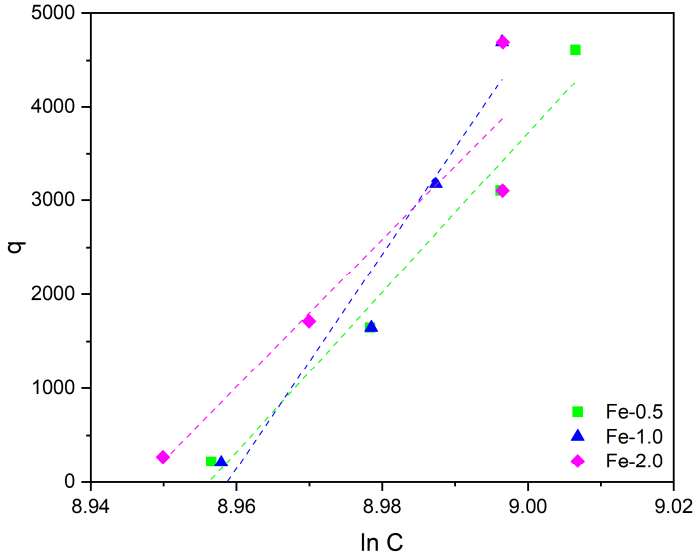

Figure 9. Temkin adsorption equilibrium of Cu onto Fe_3O_4-doped PSf membranes (pH =7.0±0.1, membrane dosage = 1.0 g/L, contact time = 60 min, volume of feed solution = 12.5 mL)

To investigate the controlling mechanism of the adsorption kinetics, two kinetic models were used; the Lagergren's pseudo-first-order and pseudo-second-order linear models. Table 4 revealed the kinetic parameters for both models and the linear regression of the Pseudo-second-order kinetics for the adsorption of Cu(II) onto all three membranes is shown in Figure 10, respectively. From the table, it can be seen that the correlation coefficient of the linear regression (R^2) for the pseudo-second-order model was higher for all membranes (0.98-1), suggesting that the adsorption kinetics of Cu ions onto these PSf membranes obeyed the Pseudo-Second order model. In this kinetic model, the adsorption of Cu ions onto the Fe_3O_4-doped PSf membranes adopts the chemisorption process and this chemical reaction is considered the rate-limiting step. It also depends on the concentration of the Cu ions and the NPs.

Table 4. Kinetic parameters for Cu adsorption onto the Fe_3O_4-doped PSf membranes

Membrane	Parameter	Fe-0.5	Fe-1.0	Fe-2.0
Pseudo 1st order	K_1	0.0320	0.0442	0.0574
	q_e	9.2452	6.6866	2.8115
	R^2	0.2980	0.7361	0.9912
Pseudo 2nd order	K_2	0.0013	0.0025	0.0274
	q_e	666.6670	666.6670	270.27
	R^2	0.9812	0.9991	1

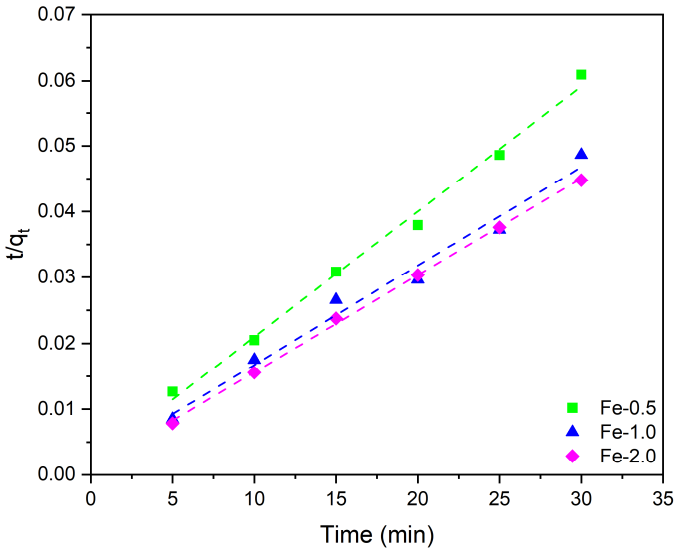

Figure 10. Linear regression of the Pseudo-second-order kinetics for the adsorption of Cu (II) onto Fe_3O_4-doped PSf membranes with various Fe_3O_4 NPs concentrations (pH =7.0±0.1, membrane dosage = 1.0 g/L, contact time = 60 min, volume of feed solution = 12.5 mL)

The adsorption of Cu ions onto Fe_3O_4-doped PSf membranes is believed to follow four general steps; (1) bulk diffusion of Cu ions into pores of PSf membrane; (2) sorption of Cu ions onto Fe_3O_4 NPs inside the pores; (3) chemical interaction between Cu ions and Fe_3O_4 NPs through electrostatic interaction; and (4) Adsorption equilibrium reached. Figure 11 illustrates the possible electrostatic interaction between the Cu ions and the NPs. The adsorption of Cu ions onto these Fe_3O_4 NPs that were incorporated into the PSf membrane was facilitated by the electrostatic interaction between the positive charges of Cu ions and negative charges on the Fe_3O_4 nanoparticle surface [30].

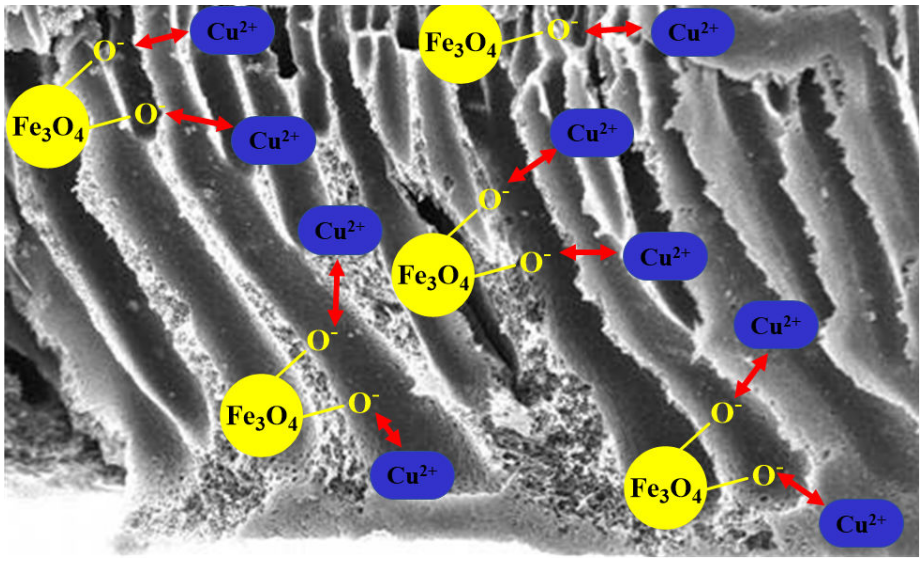

Figure 11. Schematic illustration of the possible mechanism for Cu adsorption on Fe_3O_4-doped PSf membrane

Conclusion

This work reported the synthesis of Fe_3O_4-doped PSf membranes for the removal of Cu(II) from wastewater, particularly from the electroplating industry. XRD analysis confirmed the successful synthesis of Fe_3O_4 NPs with crystallite sizes ranging from 15 to 42 nm. The Fe_3O_4-doped PSf membranes were successfully synthesized and the experimental results show a trifold increase in adsorption capability towards Cu, from 262 to 637 mg/g, proving that the Fe NPs help in improving the removal process of Cu. Membrane with 2 wt.% Fe_3O_4 showed the highest adsorption activity, credited to the easiness of Cu ions to travel to the adsorption sites, through the thicker dense layer with less agglomerations. The research also revealed that the adsorption process fitted well with the Temkin isotherm and the Pseudo-second order models with coefficient correlation, R^2 of around ~0.98, suggesting that the adsorption process adopts the chemisorption process and is exothermic in nature. This research demonstrated the potential of incorporating Fe_3O_4 NPs into the PSf membrane matrix to improve the adsorption of Cu ions and ultimately increase Cu removal as an adsorptive membrane in membrane filtration. Further research in this direction can contribute to the development of polymeric adsorptive membranes with embedded single and alloyed transition metals, including nickel and cobalt, for effective copper and any heavy metal removal.

Acknowledgement

The authors would like to acknowledge the support from the Centre of Excellent of Biomass Utilization (CoEBU) and Centre of Excellence for Frontier Materials Research (CFMR), Universiti Malaysia Perlis (UniMAP) for assisting in sample characterizations throughout this work.

References

1. Ahmed Basha, C., Bhadrinarayana, N. S., Anantharaman, N., and Meera Sheriffa Begum, K. M. (2008). Heavy metal removal from copper smelting effluent using electrochemical cylindrical flow reactor. *Journal of Hazardous Materials*, 152(1): 71-78.
2. Bai, D.-K., Ying, Q.-H., Wang, N., and Lin, J.-H. (2016). Copper removal from electroplating wastewater by coprecipitation of copper-based supramolecular materials: Preparation and application study. *Journal of Chemistry*, 2016: 5281561.
3. Nasir, A. M., Goh, P. S., and Ismail, A. F. (2019). Highly adsorptive polysulfone/hydrous iron-nickel-manganese (PSF/HINM) nanocomposite hollow fiber membrane for synergistic arsenic removal. *Separation and Purification Technology*, 213, 162–175.
4. Liu, Y., Wang, H., Cui, Y., and Chen, N. (2023). Removal of copper ıons from wastewater: A review. *International Journal of Environmental Research and Public Health*, 20(5): 3885.
5. Dashtbozorg, A., Saljoughi, E., Mousavi, S. M., & Kiani, S. (2022). High-performance and robust polysulfone nanocomposite membrane containing 2D functionalized MXene nanosheets for the nanofiltration of salt and dye solutions. *Desalination*, 527: 115600.
6. Qalyoubi, L., Al-Othman, A. and Al-Asheh, S. (2021). Recent progress and challenges on adsorptive membranes for the removal of pollutants from wastewater. Part I: Fundamentals and classification of membranes. *Case Studies in Chemical and Environmental Engineering*, 3: 100086.
7. Ayaz, M., Muhammad, A., Younas, M., Khan, A. L., and Rezakazemi, M. (2019). Enhanced water flux by fabrication of polysulfone/alumina nanocomposite membrane for copper(II) removal. *Macromolecular Research*, 27(6): 565-571.
8. Hamid, S. A., Azha, S. F., Sellaoui, L., Bonilla-Petriciolet, A., and Ismail, S. (2020). Adsorption of copper (II) cation on polysulfone/zeolite blend sheet membrane: Synthesis, characterization, experiments and adsorption modelling. *Colloids and Surfaces A: Physicochemical and Engineering Aspects*, 601: 124980.
9. Abdullah, N., Gohari, R. J., Yusof, N., Ismail, A. F., Juhana, J., Lau, W. J., and Matsuura, T. (2016). Polysulfone/hydrous ferric oxide ultrafiltration mixed matrix membrane: Preparation, characterization and its adsorptive removal of lead

(II) from aqueous solution. *Chemical Engineering Journal*, 289: 28-37.

10. Zainol Abidin, M. N., Goh, P. S., Ismail, A. F., Said, N., Othman, M. H. D., Hasbullah, H., Abdullah, M. S., Ng, B. C., Sheikh Abdul Kadir, S. H., and Kamal, F. (2019). Polysulfone/ıron oxide nanoparticles ultrafltration membrane for adsorptive removal of phosphate from aqueous solution. *Journal of Membrane Science and Research*, 5(1): 20-24.
11. Said, N., Mansur, S., Zainol Abidin, M. N., and Ismail, A. F. (2023). Fabrication and characterization of polysulfone/ıron oxide nanoparticle mixed matrix hollow fiber membranes for hemodialysis: Effect of dope extrusion rate and air gap. *Journal of Membrane Science and Research*, 9(1): 1972553.
12. Rosli, A., Ahmad, A. L., and Low, S. C. (2019). Anti-wetting polyvinylidene fluoride membrane incorporated with hydrophobic polyethylene-functionalized-silica to improve CO_2 removal in membrane gas absorption. *Separation and Purification Technology*, 221: 275-285.
13. Wan Ramli, W. K., Liang, L. G., Othman, S., Yusri, N. A. M., and Che Lah, N. F. (2022). Phase separation behaviour modification using co-solvents on PVDF membranes for water filtration. *AIP Conference Proceedings*, 2541(1): 040012.
14. Jannah, N. R., and Onggo, D. (2019). Synthesis of Fe_3O_4 nanoparticles for colour removal of printing ink solution. *Journal of Physics: Conference Series*, 1245(1): 12040.
15. Mansur, S., Othman, M. H. D., Abidin, M. N. Z., Ismail, A. F., Abdul Kadir, S. H. S., Goh, P. S., Hasbullah, H., Ng, B. C., Abdullah, M. S., and Mustafar, R. (2021). Enhanced adsorption and biocompatibility of polysulfone hollow fibre membrane via the addition of silica/alpha-mangostin hybrid nanoparticle for uremic toxins removal. *Journal of Environmental Chemical Engineering*, 9(5): 106141.
16. Dawn, R., Zzaman, M., Faizal, F., Kiran, C., Kumari, A., Shahid, R., Panatarani, C., Joni, I. M., Verma, V. K., Sahoo, S. K., Amemiya, K., and Singh, V. R. (2022). Origin of magnetization in silica-coated Fe_3O_4 nanoparticles revealed by soft X-ray magnetic circular dichroism. *Brazilian Journal of Physics*, 52: 99.
17. Upadhyay, S., Parekh, K., and Pandey, B. (2016). Influence of crystallite size on the magnetic properties of Fe_3O_4 nanoparticles. *Journal of Alloys and Compounds*, 678: 478-485.
18. Singh, K., Devi, S., Bajaj, H. C., Ingole, P., Choudhari, J., and Bhrambhatt, H. (2014). Optical resolution of racemic mixtures of amino acids through nanofiltration membrane process. *Separation Science and Technology*, 49(17): 2630-2641.
19. Mansur, S., Othman, M. H. D., Abidin, M. N. Z., Ismail, A. F., Abdul Kadir, S. H. S., Goh, P. S., Hasbullah, H., Ng, B. C., Abdullah, M. S., and Mustafar, R. (2021). Enhanced adsorption and biocompatibility of polysulfone hollow fibre membrane via the addition of silica/alpha-mangostin hybrid nanoparticle for uremic toxins removal. *Journal of Environmental Chemical Engineering*, 9(5): 106141.
20. Gohain, M. B., Pawar, R. R., Karki, S., Hazarika, A., Hazarika, S., and Ingole, P. G. (2020). Development of thin film nanocomposite membrane incorporated with mesoporous synthetic hectorite and MSH@UiO-66-NH_2 nanoparticles for efficient targeted feeds separation, and antibacterial performance. *Journal of Membrane Science*, 609: 118212.
21. Kumar, R., Isloor, A. M., Ismail, A. F., Rashid, S. A., and Matsuura, T. (2013). Polysulfone–chitosan blend ultrafiltration membranes: preparation, characterization, permeation and antifouling properties. *RSC Advances*, 3(21): 7855-7861.
22. Muntha, S. T., Ajmal, M., Naeem, H., Kausar, A., Zia, M. A., and Siddiq, M. (2019). Synthesis, properties, and applications of polysulfone/polyimide nanocomposite membrane reinforced with silica nanoparticles. *Polymer Composites,* 40(5): 1897-1910.
23. Rozi, S. K. M., Berhanundin, K. M., Ishak, A. R., Mohd, F. L., Rasdi, N. C. D., Rahim, N. Y., Aziz, M. Y., Shafie, F. A., and Abdullah, A. M. (2023). Novel magnetıc eggshell membrane functıonalızed wıth waste palm fatty acıd for selectıve adsorptıon

of oıl from aqueous solutıon. *Malaysian Journal of Analytical Sciences*, 27(1): 74-86.

24. Mansur, S., Othman, M. H., Ismail, A., Zainol Abidin, M. N., Said, N., Goh, P., Hasbullah, H., Sheikh Abdul Kadir, S. H., and Kamal, F. (2018). Study on the effect of spinning conditions on the performance of PSf/PVP ultrafiltration hollow fiber membrane. *Malaysian Journal of Fundamental and Applied Sciences*, 14: 343-347.
25. Kim, J. H., Kim, Y., Kim, C. K., Lee, J. W., and Seo, S. B. (2003). Miscibility of polysulfone blends with poly(1-vinylpyrrolidone-co-styrene) copoly mers and their interaction energies. *Journal of Polymer Science Part B: Polymer Physics*, 41(12): 1401-1411.
26. Said, N., Abidin, M. N. Z., Hasbullah, H., Ismail, A. F., Goh, P. S., Othman, M. H. D., Abdullah, M. S., Ng, B. C., Kadir, S. H. S. A., and Kamal, F. (2019). Iron oxide nanoparticles improved biocompatibility and removal of middle molecule uremic toxin of polysulfone hollow fiber membranes. *Journal of Applied Polymer Science*, 136(48): 48234.
27. Makhetha, T. A., and Moutloali, R. M. (2018). Antifouling properties of Cu(tpa)@GO/PES composite membranes and selective dye rejection. *Journal of Membrane Science*, 554: 195-210.
28. Said, N., Hasbullah, H., Ismail, A. F., Othman, M. H. D., Goh, P. S., Zainol Abidin, M. N., Sheikh Abdul Kadir, S. H., Kamal, F., Abdullah, M. S., and Ng, B. C. (2017). Enhanced hydrophilic polysulfone hollow fiber membranes with addition of iron oxide nanoparticles. *Polymer International*, 66(11): 1424-1429.
29. Salar-García, M. J., Walter, X. A., Gurauskis, J., de Ramón Fernández, A., and Ieropoulos, I. (2021). Effect of iron oxide content and microstructural porosity on the performance of ceramic membranes as microbial fuel cell separators. *Electrochimica Acta,* 367: 137385.
30. Mondal, M., Dutta, M., and De, S. (2017). A novel ultrafiltration grade nickel iron oxide doped hollow fiber mixed matrix membrane: Spinning, characterization and application in heavy metal removal. *Separation and Purification Technology*, 188: 155-166.
31. Chan, K. H., Wong, E. T., Idris, A., and Yusof, N. M. (2015). Modification of PES membrane by PEG-coated cobalt doped iron oxide for improved Cu(II) removal. *Journal of Industrial and Engineering Chemistry*, 27: 283-290.
32. Daraei, P., Madaeni, S. S., Ghaemi, N., Salehi, E., Khadivi, M. A., Moradian, R., and Astinchap, B. (2012). Novel polyethersulfone nanocomposite membrane prepared by PANI/Fe_3O_4 nanoparticles with enhanced performance for Cu(II) removal from water. *Journal of Membrane Science*, 415: 250-259.
33. Mandal, S., Calderon, J., Marpu, S. B., Omary, M. A., and Shi, S. Q. (2021). Mesoporous activated carbon as a green adsorbent for the removal of heavy metals and Congo red: Characterization, adsorption kinetics, and isotherm studies. *Journal of Contaminant Hydrology*, 243: 103869.
34. Fita, G., Djakba, R., Mouhamadou, S., Duc, M., Rao, S., Popoola, L. T., Harouna, M., and Benoit, L. B. (2023). Adsorptive efficiency of hull-based activated carbon toward copper ions (Cu^{2+}) removal from aqueous solution: Kinetics, modelling and statistical analysis. *Diamond and Related Materials*, 139: 110421.
35. Subhransu Sahoo Uma, S. B. and Sharma, Y. C. (2014). Application of natural clay as a potential adsorbent for the removal of a toxic dye from aqueous solutions. *Desalination and Water Treatment*, 52(34–36): 6703-6711.
36. Elzain, A. A., El-Aassar, M. R., Hashem, F. S., Mohamed, F. M., and Ali, A. S. M. (2019). Removal of methylene dye using composites of poly (styrene-co-acrylonitrile) nanofibers impregnated with adsorbent materials. *Journal of Molecular Liquids*, 291: 111335.
37. Zand, A. D., and Abyaneh, M. R. (2020). Adsorption of Lead, manganese, and copper onto biochar in landfill leachate: implication of non-linear regression analysis. *Sustainable Environment Research*, 30(1): 18.
38. Boparai, H. K., Joseph, M., and O'Carroll, D. M. (2011). Kinetics and thermodynamics of cadmium ion removal by adsorption onto nano zerovalent iron particles. *Journal of Hazardous Materials*, 186(1): 458-465.

39. Nandiyanto, A. B. D., Girsang, G. C. S., Maryanti, R., Ragadhita, R., Anggraeni, S., Fauzi, F., Sakinah, P., Astuti, A. P., Usdiyana, D., Fiandini, M., Dewi, M. W., and Al-Obaidi, A. S. M. (2020). Isotherm adsorption characteristics of carbon microparticles prepared from pineapple peel waste. *Communications in Science and Technology*, 5(1): 31-39.
40. Karim, K. H. (2020). Copper adsorption behavior in some calcareous soils using Langmuir, Freundlich, Temkin, and Dubinin-Radushkevich models. *Journal of Soil Sciences and Agricultural Engineering,* 11(1): 27-34.
41. van den Berg, T. and Ulbricht, M. (2020). Polymer nanocomposite ultrafiltration membranes: The influence of polymeric additive, dispersion quality and particle modification on the integration of zinc oxide nanoparticles into polyvinylidene difluoride membranes. *Membranes,* 10(9): 197.

Malaysian Journal of Analytical Sciences (MJAS)
Published by Malaysian Analytical Sciences Society

PRE-CONCENTRATION OF ORGANOCHLORINE PESTICIDES USING MICRO-SOLID PHASE EXTRACTION BASED ON BIO-SORBENT ALGINATE-SILICA BEADS DERIVED FROM OIL PALM FROND

(Pra-Kepekatan Racun Organoklorin Menggunakan Pengekstraksi Fasa Mikro-Pepejal Berasaskan Bio-sorben Alginat-Silika Komposit yang Diperoleh daripada Daun Pelepah Kelapa Sawit)

Azreen Asyikin Mhd Kamal[1], Siti Nur Afiqah Binti Mahazan[1], Nur Husna Zainal Abidin[1], Fariesha Farha Ramli[1,2], and Wan Nazihah Wan Ibrahim[1*]

[1]*Faculty of Applied Science, Universiti Teknologi MARA, 40450 Shah Alam, Selangor, Malaysia*
[2]*Faculty of Applied Science, Universiti Teknologi MARA, Perak Branch, Tapah Campus, 35400, Perak*

[*]*Corresponding author: wannazihah@uitm.edu.my*

Received: 27 September 2023; Accepted: 16 January 2024; Published: 29 April 2024

Abstract

This study focuses on the extraction of organochlorine pesticides (OCPs) contained in environmental water samples by using encapsulated alginate-silica (Alg-SiO_2) composite beads. The composite beads were made by ionic crosslinking interaction between polymeric alginate and silica particles derived from oil palm fronds and were characterized by ATR-FTIR, FESEM, and EDX to study their chemical and physical properties. The Alg-SiO_2 composite beads were then used as the sorbent material for the micro-solid phase extraction (μ-SPE) to extract OCPs from aqueous samples. Optimization of method development for extraction of targeted analytes (heptachlor, aldrin, and dieldrin) was done by varying the extraction time, extraction solvent, desorption time, and sorbent mass before the gas chromatography-mass spectrometry analysis. Analytical figures of merit for μ-SPE were calculated under the optimized extraction conditions. Under the optimum conditions of 50 mg of sorbent extracted for 5 mins and desorbed using n-hexane for 7 mins, good linearity was achieved based on the data from method validation, linear ranges of 1–10 mg/L for heptachlor, 0.1–1.0 mg/L for aldrin, and 0.2–1.4 mg/L for dieldrin, with a limit of detection of 0.09–0.85 mg/L. The proposed method was successfully applied to determine organochlorine pesticides in paddy water samples. The wide range of the calibration curves was linear, and the coefficients of regression were all around 0.979-0.993. The recoveries were obtained in a satisfactory range of 82-98%, and the precision RSD value was in the range of 0.19-4.52%.

Keywords: alginate, silica sorbent, organochlorine, oil palm, micro solid phase extraction

Abstrak

Kajian ini memfokuskan kepada pengekstrakan racun perosak organoklorin (OCP) yang terkandung dalam sampel air persekitaran dengan menggunakan kapsulan manik komposit alginat-silika (Alg-SiO_2). Manik komposit dibuat melalui interaksi pertautan silang ion antara polimer alginat dan zarah silika yang diperoleh daripada pelepah kelapa sawit, dan dicirikan oleh ATR-FTIR, FESEM, dan EDX untuk mengkaji sifat kimia dan fizikalnya. Manik komposit Alg-SiO_2 kemudiannya digunakan sebagai bahan

penjerap untuk pengekstrakan fasa pepejal mikro (μ-SPE) untuk mengekstrak OCP daripada sampel akueus. Pengoptimuman pembangunan kaedah untuk pengekstrakan analit yang disasarkan (heptaklor, aldrin, dan dieldrin) dilakukan dengan mempelbagaikan masa pengekstrakan, pelarut pengekstrakan, masa nyahjerapan dan jisim penjerap sebelum analisis spektrometer jisim gas kromatografi. Angka analisis merit untuk μ-SPE dikira di bawah keadaan pengekstrakan yang dioptimumkan. Di bawah keadaan optimum 50 mg penjerap yang diekstrak selama 5 min dan nyahjerap menggunakan n-heksana selama 7 min telah menghasilkan julat linear yang baik. Berdasarkan data yang diperoleh daripada pengesahan kaedah, julat linear 1–10 mg/L untuk heptaklor, 0.1–1.0 mg/L untuk aldrin, dan 0.2–1.4 mg/L untuk dieldrin, dengan had pengesanan 0.09–0.85 mg/L. Kaedah yang dicadangkan telah berjaya digunakan untuk menentukan racun perosak organoklorin dalam sampel air padi. Julat luas keluk penentukuran adalah linear, dan pekali regresi adalah sekitar 0.979-0.993. Pemulihan diperolehi dalam julat yang memuaskan iaitu 82-98% dan nilai ketepatan RSD dalam julat 0.19-4.52%.

Kata kunci: alginat, silika sorben, organoklorin, kelapa sawit, pengekstraksi fasa mikro-pepejal

Introduction

Oil palm plants have contributed to Malaysia's gross domestic product by around 37.9% compared to other agriculture plants [1]. As stated in the statistic report, 77% of all residues come from oil palm production, which includes its frond, empty fruit bunch, trunks, kernel, and shells. As the number of oil palm plants increases, the waste undeniably increases. Dry oil palm fronds (OPF) only generated 44-47 million tons, which were burned as one of the disposal methods. This causes air pollution to the environment. In contrast, agricultural wastes are renewable resources that can be utilized to create energy, bio-based products, and items with additional value [2]. Consequently, numerous research and reviews exist on how these agricultural wastes can be utilized as useful resources rather than discarded [3, 4]. Oil palm fronds have numerous underutilized natural polymers, including cellulose, hemicellulose, and lignin. According to Roslan et al., OPF may contain siliceous material, attracting the attention of many researchers to the potential of silica extracted from this biomass [5]. Silica is an inorganic substance with excellent mechanical strength, high chemical stability, and thermal stability. Its internal connection is composed of siloxane, while the surface is abundant in silanol. This provides silica with excellent hydrophilicity. Furthermore, this silica is environmentally tolerant, which makes it widely used as an adsorbent carrier [6]. Thus, this study utilized silica extracted from oil palm fronds, which follows the government's announcement on "Zero Waste Initiatives" by reusing the oil palm fronds' wastes into silica powders. A study by Onoja et al. showed that ash from acid-treated OPF could produce about 95.30% silica (SiO_2), which is employed in many applications such as in diverse array applications, enzyme immobilization carriers, as well as functional biomaterial [7]. The hydroxyl groups on the surface of silica particles make it easy to chemically modify the surface and introduce functional groups [8] by controlling the pore volume, pore size, and tortuosity, and surface chemistry on the particle allows for tunable release profiles in controlled release applications involving silica particles [9]. However, the light and fine particles of obtained silica properties make it complicated to collect and reuse after extraction. Hence, encapsulating the silica with tensile polymeric alginate proves to be a favorable option for improving their recyclability without the loss of any of the fine particles [10].

Alginate (Alg) is a biomaterial with several uses in biomedical science and engineering due to its advantageous features, such as biocompatibility and ease of gelation [11], with the presence of hydrophilic and reactive functional groups providing superior adsorption [12]. This biopolymer is rich in D-mannuronic acid (M block) and L-guluronic acid (G block), which can be easily cross-linked utilizing bivalent ions such as calcium ions to create hydrogels during the gelation process [13]. Hence, it is frequently used to create a gel-phase adsorbent material that is easier to manipulate than the raw precursor material [14]. Nevertheless, this biomaterial has high rigidity, fragility, and weak elasticity, as well as weak mechanical properties [15]. Organic and inorganic alginate-based composites have been produced to improve the mechanical and thermal stability, as well as the swelling

properties of pure alginate polymers, which have been intensively studied for the removal of pollutants from aqueous solution over the past decade [15]. One of the materials studied was inorganic silica matrices that provided several benefits regarding chemical and mechanical stability [16]. These combined characteristics of silica and alginate composites have drawn interest since they may be superior compared to their individual compounds [17], which enhances their high biocompatibility and reasonable physical and chemical durability [18]. Thus, alginate-silica composites were proposed in the study as a new class of materials with promising applications in a variety of disciplines, including biomedicine, bio-catalysis, bio-separation, and bio-sensing [19]. The proposed synthesis mechanism of alginate-silica adsorbent is shown in Figure 1 [20].

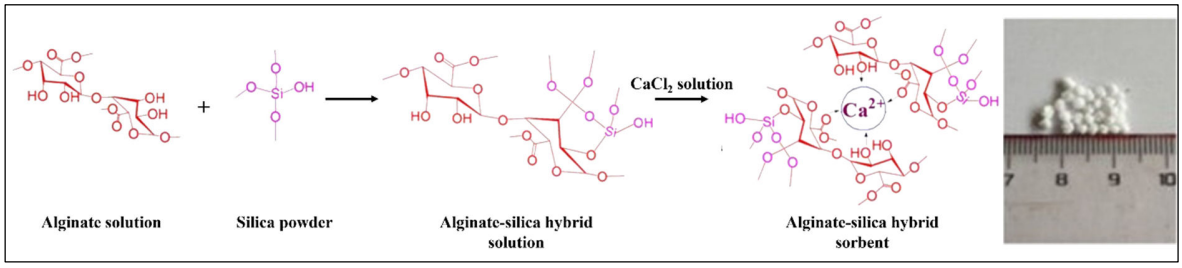

Figure 1. Synthesis mechanism of alginate-silica hybrid adsorbent

Amongst the aforementioned applications, very few studies of modification biowaste-silica for the pre-concentration of organochlorine pesticides have been investigated, as summarized in Table 1. Most of them applied different types of sorbents for OCPs or organophosphorus pesticides (OPPs). Organochlorine pesticides (OCPs) are one of the major pesticides that are used to manage insect pests on various types of crops. These OCPs are in the persistent organic pollutants (POPs) class, which are poisonous, bio-accumulative, and bio-magnified. The widespread adoption of these pesticides causes accumulation in the environment and food chains, and the incidence of OCP contamination in the human body can cause cancer, neurological system damage, generative diseases, and immune system disruption. The usage of OCPs is usually for pest and vector control in agricultural plantations such as oil palm, cocoa, and rubber in Malaysia [21]. However, the usage of OCPs has declined over the previous decade, as shown by various environmental monitoring studies [22, 23]. It is still possible to find OCPs and the products of their decomposition in the water, soil, sediment, and aquatic species in some regions of the world due to human activity. This is confirmed by several studies that have found the existence of OCPs in various samples in Malaysia. This includes the presence of OPCs (heptachlor and aldrin) in the surface water of Bertam and Terla River in Cameron Highland [24] and the detection of other types of OCPs such as endosulfan sulfate, 4-4'-DDT, and hexachlorocyclohexane isomers (α, β, γ, δ) in paddy soil situated in Machang, Kelantan [25] as well as detection of another group of OCPs, benzenehexachlorides (BHCs) in fish and sediment distributed in numerous countries including Malaysia [26].

These OCPs are present at the trace level, which needs sensitive, accurate, and efficient analytical procedures, which include sample preparation for their detection, identification, and quantification. Few sample preparations include liquid-liquid extraction (LLE) and solid phase extraction (SPE), which consume enormous volumes of toxic organic solvents and generate a substantial amount of waste that is unsafe for users and the environment [39]. Until today, SPE has mainly been used as sample preparation, especially on aqueous matrices, which mostly employ cylindrical cartridges packed with sorbent as SPE devices [40]. Countless researchers studied the miniaturization and solventless of SPE, such as dispersive SPE, or coined as μ-SPE. It is explained that this procedure implements loose

sorbent dispersed in the aqueous sample to allow the extraction of analytes and separated physically by magnetism, filtration, or centrifugation before the elution of analytes using solvent for the analysis [40]. This extraction method is favorable since it applies small amounts (microgram or milligram quantities) of sorbent, which allows the dispersion to occur and facilitates rapid and uniform interaction between sorbent and target analytes, resulting in faster equilibrium and enhancing the extraction efficiency [40]. Basheer et al. presented membrane-protected micro-solid-phase extraction (μ-SPE) as a replacement for classical multistep SPE, which allowed a reduction in the volumes of sorbent and desorption solvent as well as smaller sample volume and lower overall cost [41]. Sev eral studies implementing numerous types of μ-SPE techniques with results are summarized in Table 1. Therefore, the research aimed to investigate the use of the first-ever attempt of alginate-silica beads derived from oil palm frond as a promising bio-sorbent for the determination of OCPs in water samples with the aid of μ-SPE. Besides, this method works well for matrices that are moderately difficult to process by protecting the hydrophobic membrane and improving the sorbent as well as matrix influence to a greater extent.

Table 1. Summaries on analytical performance and extraction conditions of the developed procedure with other recently published works

Extraction Technique	**Sorbent Type**	**Sample Vol. (mL)**	**Desorption Solvent**	**Desorption Solvent Vol. (mL)**	**Total Extraction Time & Desorption Time (min)**	**LOQ (μg L^{-1})**	**RR (%)**	**Ref.**
d-μ-SPE	C18/Florisil/ Chromosorb G/AW-DCMS	100	EtAc	0.5	54	0.0017–0.0745	62.3-123	[27]
SBSE	SMNMa	60	ACN	1.50	57	0.23 – 2.94	82.6-104	[28]
d-μ-SPE	Zn-MOFb	20	ACN	0.20	~12	0.099 – 0.693	91.9-99.5	[29]
d-μ-SPE/ MSPE	Fe_3O_4@PDA-DES	100	ACN	1.50	~23	0.03 – 0.036	72.5-108	[30]
d-μ-SPE/ MSPE	Fe_3O_4@SiO_2 @KIT-6	100	ACN	2.00	~12	0.04 – 0.018	86.6-98.8	[31]
MIP-SPE	MIP	50	MeOH/HAc	1.50	-	0.23 – 0.41	79-104	[32]
d-μ-SPE	Fe_3O_4@TGA @TMU6	25	1-ButOH	0.10	35	1.65 – 3.30	88-107	[33]
SPE	PDMAT microbeads	100	DCM	10.0	-	0.006 – 1.99	69-139	[34]
SPE	PEG-CNT	70	ACN	0.80	-	0.033 – 0.099	95.2-99.8	[35]
d-μ-SPE/ MSPE	Fe_3O_4@APTES-GO /ZIF-8	30	MeOH	1.50	18	0.033 – 0.363	71.2-111	[36]
d-μ-SPE	MIL-101	10	EtAc	0.10	55	0.0083 – 0.053	87.6-98.6	[37]
d-μ-SPE/ MSPE	KHA/Fe_3O_4	30	MeOH	0.25	10	0.099 – 0.330	93.4-99.3	[38]
d-μ-SPE	Alginate – silica	10	n-hexane	1.00	22	0.27 – 2.55 (mg/L)	82 - 98	This work

Materials and Methods

Chemicals and materials

Three organochlorine pesticide standards: heptachlor ($C_5H_{10}Cl_7$, ≥ 98%), aldrin ($C_{12}H_8Cl_6$, ≥ 98%), dieldrin ($C_{12}H_{16}O$, ≥ 95%), Acetonitrile (C_2H_3N, 99.9%), and ethanol (C_2H_6, 99.9%, HPLC grade) were purchased from Sigma-Aldrich. Acetone (CH_3COCH_3, ≥ 99.5%) ACS reagent, ethyl acetate ($C_4H_8O_2$, 98%), n-hexane (C_6H_{12}, 99%), anhydrous calcium chloride ($CaCl_2$, ≥ 97%) and sodium alginate were all purchased from Sigma Aldrich (St. Louis, USA). Ultrapure water was collected from Barnstead Nanopure (Thermo Scientific).

Preparation of standard and sample solutions

A series of working solutions from stock solution, 1000 mg/L, were diluted in acetonitrile to prevent the decomposition of analytes and stored in amber glass at 4°C when not in use. Paddy water samples were collected from Bukit Gambir, Johor, and filtered through 0.45 µm nylon filter paper to remove any suspended particles. The samples were stored in a pre-cleaned bottle with acetone polyethylene at 4°C prior to the extraction. The sample was spiked with a standard mixture to give a final concentration of 5 mg/L of heptachlor, 0.5 mg/L of aldrin, and 1 mg/L of dieldrin common solution into a solution for a final volume of 10 mL for the precision and accuracy studies.

Preparation of silica derived from oil palm fronds

The method of synthesis was adapted from the literature [42]. Freshly harvested oil palm fronds (OPF) were then dried in the oven at 70 °C for 48 hours and ground into fine powder. The OPF powder was dispersed into 1 M HCl and constantly stirred for 2 hours at 400 rpm. The dispersion was allowed to cool at room temperature. The wet powder was washed with distilled water until the acid-treated OPF reached neutrality at pH 7. The neutralized OPF was filtered and dried in an oven at 80 °C for 24 hours. Then, the OPF powder was calcined in the furnace at 600 °C for 14 hours with a ramping time of 5 hours and a hold time of 9 hours at the rate of 2 °C/min. The white ash of silica was harvested and stored in capped vials at room temperature for further analysis.

Preparation of alginate-silica composite beads (Alg-Si)

Experimental methods for the preparation of alginate-silica were adapted and modified from the previous studies with minor modifications [43]. Alginate-silica (Alg-Si) composites were prepared by adding 2g of sodium alginate into 100 mL of distilled water and stirring using a magnetic stirrer at 60 °C to produce 2% (w/v) of sodium alginate solution until no longer coagulated. The heat was turned off, and the solution was left stirred. In the meantime, 10 mL of distilled water was added to 0.1g of silica powder and ultrasonicated with parafilm covered onto the beaker's mouth for approximately 10 mins. The silica solution was then added to the 2% (w/v) sodium alginate solution and stirred thoroughly. In the separated beaker, 4% (w/v) of $CaCl_2$ was prepared and diluted with distilled water. The Alg-Si mixture was then dropped wisely into the prepared $CaCl_2$ solution and left for 30 mins. The Alg-Si beads formed were filtered and rinsed with distilled water before being dried in an oven overnight at 80 °C to remove any excess cation solution. The Alg-Si was then stored and tested for the extraction procedure.

Characterization of alginate-silica composite beads

Several characterization methods were applied to study the physical and chemical properties of Alg-Si beads formedAttenuated Total Reflectance Fourier Transform Infrared spectroscopy (ATR-FTIR) with a resolution of 4 cm^{-1} and a total of 8 scans in the range of 500-4000 cm^{-1}. Scanning Electron Microscope (SEM) was used to determine the qualitative characteristics of the physical organization and morphology of pure alginate beads and alginate-silica beads as well as energy-dispersive X-ray spectroscopy (EDX) analyzer TEAM ™ EDS to measure the micro-area elements and the condition of element distribution in beads.

Micro-solid phase extraction (µ-SPE)

Several parameters were optimized by changing one variable at a time (OVAT), including extraction time, desorption solvent, desorption time, and mass of sorbent. OVAT was chosen because of the simplicity of the system and the limited number of parameters under consideration. With only four parameters to be examined, OVAT provides a practical and

straightforward approach, allowing for a focused exploration of individual factors while ensuring resource efficiency. This OVAT method was adapted from Othman et al. with minor modification, where 50 mg of the beads were added to 10 mL of spiked aqueous sample and agitated at 900 rpm for 15 mins to allow the desorption process to occur in 12-Radley carousel system. The supernatant was discarded, and 1 mL of desorption solvent (acetonitrile) was added to the beads before sonicated for 7 mins. Under a gentle stream of nitrogen gas, the collected solvent was pre-concentrated to 500 µL and transferred to the vial for GC-MS analysis [44]. The schematic flow diagram of µ-SPE is illustrated in Figure 3.

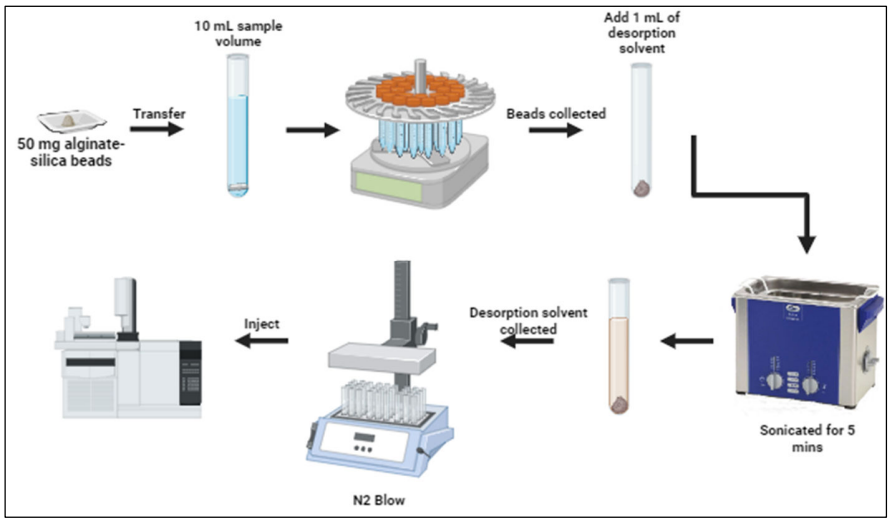

Figure 2. Micro-Solid Phase Extraction (µ-SPE)

Chromatographic conditions

The analysis was conducted using GC-MS, Shimadzu's (Kyoto, Japan) QP2010 GC-MS system, and a Shimadzu AOC-20i autosampler. The flow rate was set at 1.2 mL/min with pressure at 16 kPa at an average velocity of 41.633 cm/sec using helium as carrier gas. The injection was set without any intermediate splits. The separation was carried out on a silica capillary column (30 x 250 µm x 0.25 µm). The chromatographic conditions were optimized by varying the temperature. The temperature in the oven was increased from 150 °C (held for 1 min) to 200 °C at a rate of 30 °C per min (held for 2 mins), then to 250 °C at a rate of 10 °C per min, and finally to 280 °C at a rate of 20 °C per min. The data was collected in full scanning mode from 50 to 500 m/z to verify retention times. Selective ion monitoring (SIM) analysis was performed on all standards and sample extracts.

Method validation

Prior to sample analysis, the linearity (R^2), limit of detection (LOD), limit of quantification (LOQ), precision (RSD%), and accuracy (relative recovery%) of the method were evaluated.

Green analytical calculator (AGREE)

This analytical green calculator is a simple software applied in various research to evaluate the greenness of the analysis method. This calculator evaluated the greenness of the developed method when the AGREE metric values are near 1, correlated to a dark green. Meanwhile, a red color implies the least environmentally friendly, which is close to 0. This calculator has 12 scales, each of which corresponds to fundamental principles of green analytical chemistry, and the weight of each scale represents the importance of the principles of the analytical procedure [45]. The principle of the scale includes (1) the implementation of direct analytical techniques to avoid sample treatment, which can reduce the safety issues and health and environmental problems related to the methodology. However, direct analysis is usually inexecutable as the

appropriate form of the sample is required to increase its sensitivity; (2) the minimal usage of sample size and samples are recommended; (3) preferable *in situ* measurements whereby the location of analytical device should be close to the measurement location; (4) reduction usage of reagents and saves energy by the integration of analytical process and operations such as sampling with pre-concentration, simultaneous performance of derivatization with extraction or chromatographic determination; (5) automated and miniaturized methods; (6) no derivatization should be employed; (7) the proper management of analytical waste and a small volume of analytical waste should be implemented; (8) the multianalyte or multiparameter methods are preferred compared to methods using one analyte at a time; (9) the minimization of energy consumption in detection steps, sample preparation and analytical separation; (10) reagents obtained from renewable sources should be preferred; (11) toxic reagents should be eliminated or replaced by greener alternatives whenever possible; (12) the safety of the operator and environment whereby the several threats that are not avoidable should be selected [46].

Results and Discussion

Physical properties

Digital photographs were captured to examine the visual structure of the composite beads (Figure 4). Alg-Si beads, before drying, were obtained in asymmetrical white color and have a texture resembling hydrogel due to water content, as shown in (a). However, the size of Alg-Si shrunk to half after the drying process and turned to a yellowish color. In comparison, the pure alginate bead was prepared with a similar method and obtained as dark yellow beads.

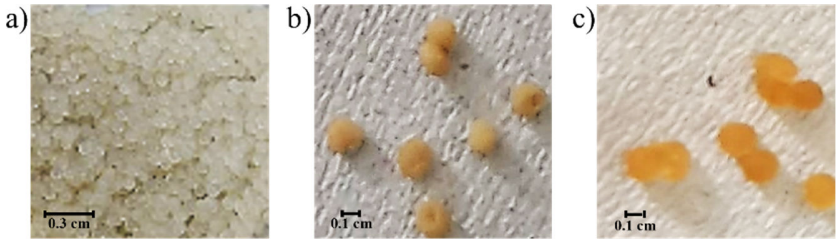

Figure 3. Digital photograph using phone camera with the scale of (a) Alg-Si beads before dried, (b) Alg-Si beads after dried overnight, (c) pure alginate beads after dried overnight

ATR-FTIR analysis

Figure 5 shows the spectra of OPF-silica powder, Alg-Si beads, and pure alginate beads. In the spectrum of OPF-silica powder, the existence of a broad band around 3407 cm^{-1} is attributed to the -OH stretching vibration of the silanol on the silica surface. The strong band at 805-1079 cm^{-1} corresponds to the asymmetric vibration of the Si-O-Si siloxane bond, which forms the silica matrix backbone [7]. The FTIR spectra of Alg-Si beads demonstrate that the absorption peaks at 3326 cm^{-1} correspond to the O-H absorption band, which is due to the stretching vibration of residual -OH groups and free hydrogen bonds [47]. The absorption peaks at 824 and 1029 cm^{-1} correspond to symmetric and asymmetrical stretching vibrations of Si-O-Si bonds, respectively. The bands at 1419 and 1598 cm^{-1} in the spectrum of the Alg-Si beads may be assigned to asymmetric and symmetric COO- deformation, respectively, confirming the interaction of carboxylate groups with silanol [48]. The FTIR spectra of pure alginate beads display characteristic bands at 3331 $cm^{-1,}$ which correspond to the OH stretching vibrations of hydrogen-bonded OH groups. Other distinctive peaks of pure alginate beads can be detected at 1424 cm^{-1} and 1598 cm^{-1}. They are caused by the asymmetric and symmetric stretching peaks of carboxylate (-COO), respectively. Table 2 summarizes the comparison of major absorption bands for OPF-silica powder, pure alginate beads, and alginate-silica beads with all the spectra in Figure 5.

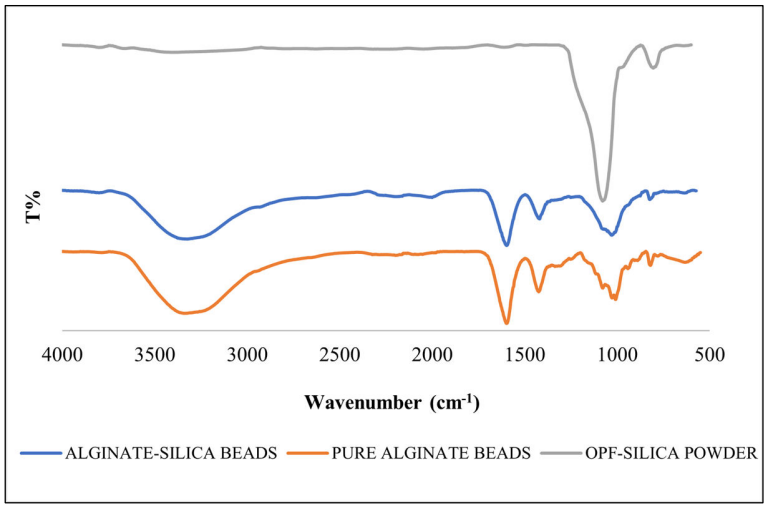

Figure 4. ATR-FTIR spectra of OPF-silica powder, Alg-Si beads, and pure alginate beads

Table 2. Comparison of major absorption bands for OPF-silica powder, Alg-Si beads, and pure alginate beads

Major Functional Groups	OPF-Si powder	Alg-Si beads	Pure alginate beads
	Wavenumber (cm^{-1})	Wavenumber (cm^{-1})	Wavenumber (cm^{-1})
Stretching of O-H	3407	3326	3331
Antisymmetric stretching of COO-groups	-	1598	1598
Symmetric stretching of COO-groups	-	1419	1424
Asymmetric stretching of Si-O-Si	1079	1029	-
Symmetric stretching of Si-O-Si	805	824	-

Field emission scanning electron microscopy

The morphology of Alg-Si beads and pure alginate beads was investigated by field emission scanning electron microscopy (FESEM). Under magnification 45X, 1000X, 3000X, and 5000X, micrographs of pure alginate and Alg-Si beads were viewed. Alginate and calcium chloride can form a rigid structure due to the sequential placement of G units on alginate, which generates a space for calcium ions to bind, with each ion able to link to four G units [49]. In accordance with Figure 4 (a-b), the surface of pure alginate beads was rough, irregular in shape, and possessed a deep and extensive fissure span. At the same time, the morphology study of Alg-Si beads in Figure 6 (c-d) found that the gully and folds on the surface of the hybrid material diminished after interaction with SiO2; the surface of the "wrinkles" ring shrunk and progressively became more regular, with no discernible fold ring appearing. Briefly, the surface structure of Alg-Si beads was more homogeneous and regular than that of pure alginate composite beads. In addition to having a rough surface, the Alg-Si beads have cavities created during the cross-linking process. The formation of cavities during sonication, in which alginate and silica combine to produce a homogenous web [50]. Moreover, these cavities facilitate pore diffusion during adsorption due to the significance of the inner specific surface with a low diffusion resistance in the composite beads (involving increased adsorption potential and rate). In conclusion, the composite particles of alginate and silica exhibited a porous network structure. A large number of hydroxyl and carboxyl groups in sodium alginate provided numerous chemical and physical cross-linking and reactive sites, which enhanced the deformation of resistance of cross-linked structures [51].

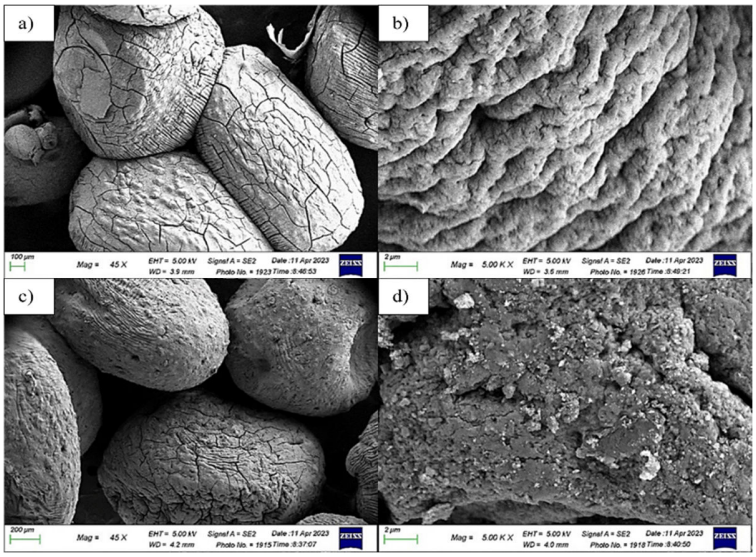

Figure 5. FESEM images for pure alginate beads at a) 45X, b) 1KX and Alg-Si beads at c) 45X, d) 5KX

Energy dispersive X-ray (EDX) analysis

In conjunction with energy dispersive X-ray (EDX), energy spectra of Alg-Si beads and pure alginate beads were measured to characterize the beads. It permits the quantification of the active molecules retained within the beads. Figures 7 a) and b) depict the EDX analysis of pure alginate and Alg-Si beads, respectively. EDX analysis revealed that pure alginate beads consisted primarily of oxygen (68.83%), calcium (28.55%), and a minor amount of sodium (2.62%) by weight. There were no additional impurity peaks in the EDX spectra, and this was consistent with the results obtained in the FTIR. Details of the chemical composition of pure alginate and Alg-Si beads were tabulated in Table 3.

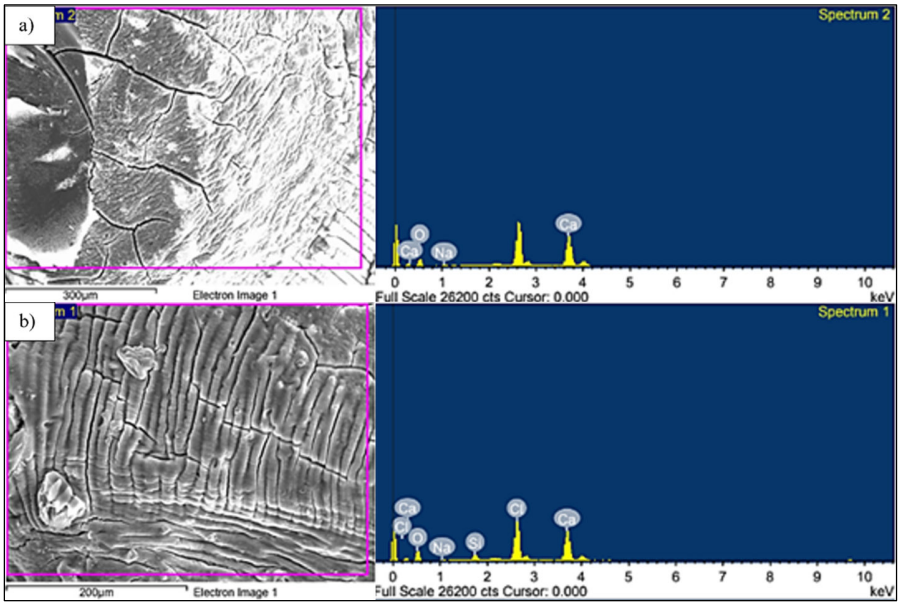

Figure 6. a) The EDX analysis of pure alginate beads and b) the EDX analysis of Alg-Si beads

Table 3. Chemical composition of pure alginate beads and alginate-silica beads based on EDX analysis

Element	Pure Alginate Beads		Alginate-Silica Beads	
	Weight (%)	Atomic (%)	Weight (%)	Atomic (%)
O	68.83	83.89	59.05	76.64
Na	2.62	2.23	0.71	0.64
Ca	28.55	13.89	18.16	9.41
Cl	-	-	19.55	11.45
Si	-	-	2.53	1.87

Optimization parameters of µ-SPE

Heptachlor, aldrin, and dieldrin were chosen as the target analytes for this analysis since they are the most frequently used OCPs in the agriculture industry due to their excellent efficacy in pest control and cost-effectiveness [52]. In order to find the optimal conditions for the extraction of OCPs performance from aqueous samples, several significant variables that can affect the extraction performance, including extraction time, desorption solvent, desorption time, and sorbent mass, were studied. Optimization was conducted by using OVAT (one variable at a time) in which the distilled water samples were spiked with each OPC at a concentration of 1 mg/L in a 10 mL solution. Triplicate extractions were performed for every parameter optimized in this analysis using gas chromatography-mass spectroscopy (GC-MS).

Effect of extraction time

In the µ-SPE principle, the sorbent is encapsulated in a polysaccharide alginate matrix; as a result, its sorption behavior is based on the equilibrium of mass transfer between the sample matrix and the sorbent, as opposed to the exhaustive extraction as in cartridge- or disc-based SPE. The sorption time was one of the most important parameters for enhancing the precision and sensitivity of the extraction procedure, as it is vital to allow enough time to ensure the equilibrium between the aqueous phase and sorbent [53]. Thus, various extraction times were evaluated in the range of 2.5 to 15 minutes to study the optimum time for the sorbent-analyte to achieve an equilibrium state. The impact of contact time between the sorbent and target analytes is depicted in Figure 6. It was discovered that the adsorption efficiency of OCPs was significantly increased up to 15 minutes, especially for heptachlor and aldrin. However, the adsorption of dieldrin was practically constant after 10 minutes. This could be due to the saturation of the surface area of the sorbent as time progressed and the competitive adsorption rate of the analytes [54]. Further extraction time after 15 minutes was not advisable as a few studies show that it will cause back extraction of analytes from the acceptor into the sample solution [55]. Thus, the optimal extraction time was determined to be 15 mins and was employed in subsequent experiments. The average was reported with associated error bars representing the standard deviation (n=3) in Figure 8.

Effect of desorption solvent

According to the principle of “like dissolves like”, compounds dissolve in a solvent when their chemical properties, particularly their polarities, are similar [56]. Polar and non-polar solvents are able to dissolve polar and non-polar compounds, respectively [57]. In this analysis, the desorption solvents n-hexane, ethyl acetate (EA), acetone, acetonitrile (ACN), and ethanol were assessed, with increasing polarity from n-hexane to ethanol to determine which one provided the maximum analyte recovery using µ-SPE technique. Figure 9 demonstrates that n-hexane performed better than the other solvents regarding desorption. N-hexane, which is non-polar with a polarity index of 0.1, provides a more favorable performance in desorbing the target analytes due to the hydrophobicity properties of the OCPs [58]. Meanwhile, due to its reduced compatibility with the hydrophobic OCPs in terms of polarity, ethanol exhibited the lowest desorption efficiency. Hence, the principle “like dissolves like” was applicable and produced the greatest results among various solvents used, and n-hexane was regarded as the optimal desorption solvent for further analysis.

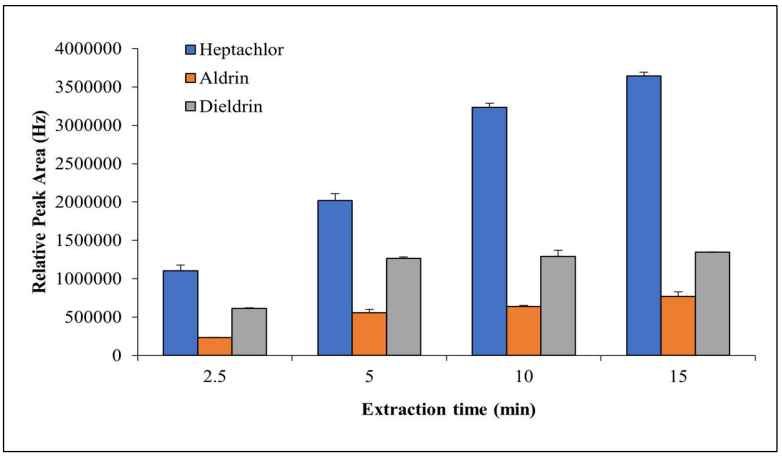

Figure 7. Graph of average relative peak height (Hz) against extraction time (min)

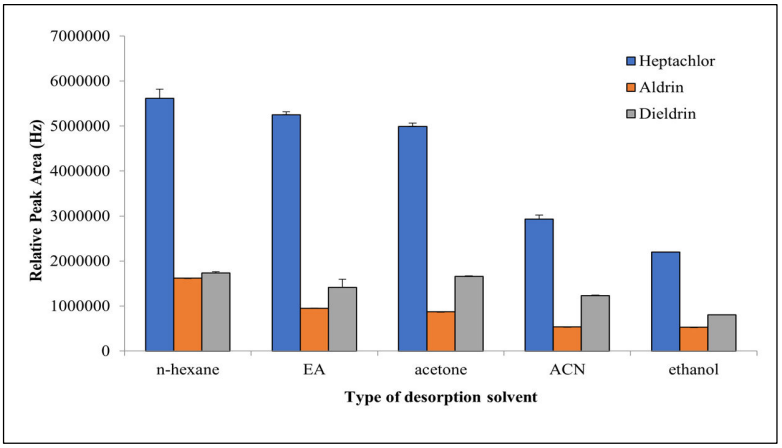

Figure 8. Graph of average relative peak height (Hz) against desorption solvent

Effect of desorption time

Desorption time was an additional significant element that could influence the peak area of the analytes. It has been determined that ultrasonication is an effective method for enhancing the desorption procedure [59]. The effectiveness of ultrasonic-assisted desorption is dependent on the parameters that influence the acoustic cavitation created during the process [60]. In addition to the ultrasonic power, the total amount of analytes eluted is also influenced by the time consumed. As depicted in Figure 10, there were only minor changes in desorption efficiency between 1,3,5,7 and 10 mins of ultrasonication. As the ultrasonic time increased from 3 to 7 minutes, a modest increase in the desorption of heptachlor, aldrin, and dieldrin was detected. Regardless of the result, at 1 and 10 mins, the trend of the graph appears to increase, although the data appears to be consistent at 3,5 and 7 mins, which are the span of time in the middle. Adding to this, extended ultrasonication decreased the efficacy of the OCP desorption. This result can be attributed to its comparatively high hydrophobicity among these analytes, indicating that the analyte prefers to diffuse into the hydrophobic pores of alginate-silica. It has been shown that ultrasonication can facilitate the desorption of adsorbed molecules and boost pore diffusion in the sorption process [60]. As a result of the re-adsorption of the target analytes, the peak area of each target OCP steadily decreased after a 7-minute desorption time [61]. Thus, the optimal desorption time for further analysis was determined to be 7 minutes.

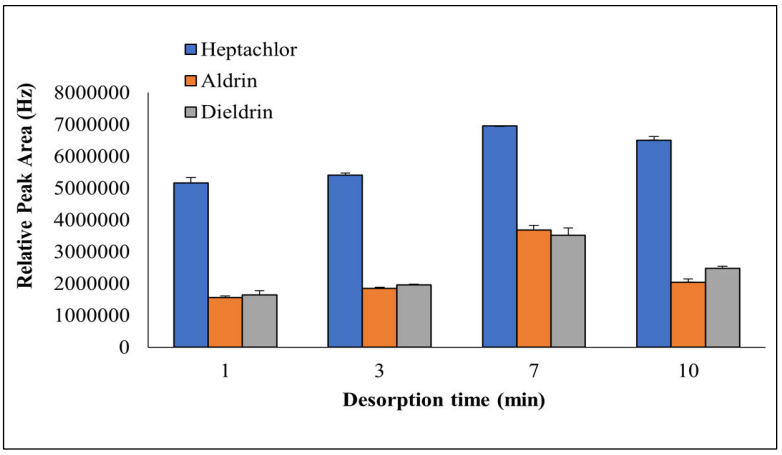

Figure 9. Graph of average relative peak height (Hz) against desorption time (min)

Effect of sorbent mass

In this study, 20, 30, 40, 50, and 60 mg of Alg-Si beads were used to optimize the sorbent mass. The results in Figure 11 demonstrate that the maximum peak area of analytes is attained with 50 mg of sorbents. With increasing sorbent mass, no discernible increase in peak area was seen; instead, the peak areas continued to diminish. This may be owing to the saturation of Alg-Si beads as the primary sorption site; hence, the use of an excessive amount of sorbent (more than 50 mg) made desorption more difficult and demanded a larger volume of desorption solvent [62]. Since the peak area for the analytes was at its maximum at 50 mg, 50 mg of sorbent was used for the following analysis.

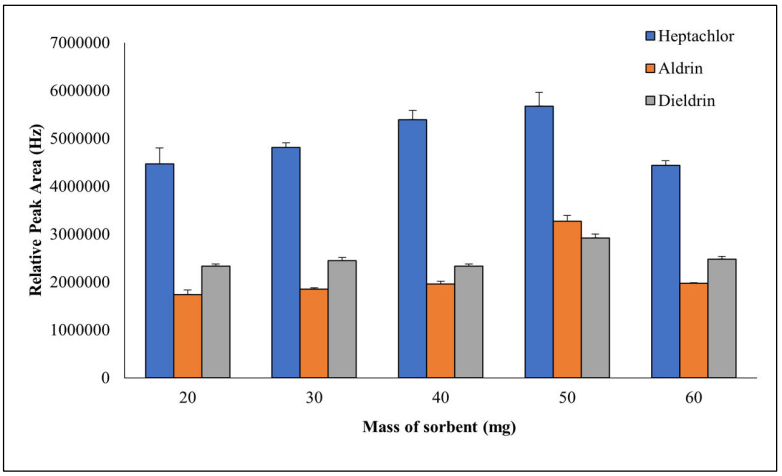

Figure 10. Graph of average relative peak height (Hz) against mas of sorbent (mg)

Optimum µ-SPE conditions.

The final adopted Alg-Si-µ-SPE conditions were: 15 min extraction time; n-hexane as desorption solvent; 7 min of desorption time; sorbent mass, 50 mg. Hence, these optimum extraction conditions were applied for subsequent studies.

Matrix-matched calibration

In analytical procedures, matrix effect (ME) can manifest as an undesired enhancement or suppression of the analytical response due to the eco-elution of interfering matrix components. Therefore, ME is a source of error in quantitative chromatography analyses of complex matrices such as pesticides, and it may be

compound or matrix-dependent. Commonly, ME is determined by comparing the slope of the calibration curve of analytes spiked into a blank paddy water sample to the slope of the calibration curve derived by spiking analytes into the solvent. In this study, matrix-matched calibration was performed on blank pesticides of varying concentrations of the OCPs.

Method validation

The proposed µ-SPE-GC-MS analytical method for the determination of three pesticides in paddy water samples under optimized experimental conditions was deemed valid. The analytical figures of merit, including the limit of detection (LOD), the limit of quantification (LOQ), the linear range, the relative recoveries (RR), the determination coefficient (R^2), and the precision (as relative standard deviation, RSD), were therefore determined. A calibration curve for each pesticide was constructed by adding six concentration levels of each analyte to a blank sample of paddy water. Heptachlor at 1, 4, 7, 10, and 13 ppm; aldrin at 0.3, 0.5, 0.7, 1, and 1.3 ppm; and dieldrin at 0.2, 0.6, 1, 1.4, 1.8 mg/L. Using least-squares linear analysis, the contours and corresponding regression equations were determined and subsequently validated by R^2 values. The spiked concentration differs because of the varying detection limits and anticipated ambient concentrations of the analytes [63], in which the calculated values indicate the expected levels of a particular substance or analyte in the surrounding environment. The optimized, developed µ-SPE procedure was validated to determine the adsorption capacity of Alg-Si particles as a functional bio-sorbent using paddy water as a sample, as shown in Table 4.

For each of the analytical curves, good R^2 values for each analyte were obtained in the range of 0.9796 to 0.9935. The LOD varied between 0.85 mg/L for heptachlor, 0.09 mg/L for aldrin, and 0.19 mg/L for dieldrin, as presented in Table 4, while the LOQ varied between 2.55 mg/L for heptachlor, 0.27 mg/L for aldrin, and 0.57 mg/L for dieldrin. Concerning precision, the examined OCPs exhibited intraday precision values of 10% or less. The intraday precision RSD% ranged from 2.52 – 2.78% for heptachlor, 2.34 – 3.29% for aldrin, and 3.52 – 4.52% for dieldrin. Meanwhile, the interday precision ranged from 1.82 – 2.31%, 0.30 – 1.91%, and 0.19 – 2.11% for heptachlor, aldrin, and dieldrin, respectively. Enrichment factor (EF) and extraction recovery (ER%) were also determined to evaluate the method's effectiveness. All the target pesticides provide RR (%) values above 80%, ranging from 82 – 84%, 90 – 91%, and 95 – 98%, for heptachlor, aldrin, and dieldrin, respectively. This result is comparable with another study conducted by Huang et al., which obtained a range of 87.6 – 98.6% for the same method with the application of different sorbents [64]. The EF values for the pesticides ranged between 6.74 – 16.87 for heptachlor, 9.64 – 34.73 for aldrin, and 4.38 – 20.25 for dieldrin. The results are summarized in Table 5. Meanwhile, Figure 12 shows the chromatogram of blank paddy water sample in three different analyses (blank, spiked at 1 mg/L and 10 mg/L, 0.1 mg/L and one mg/L, and 0.2 and 1.4 mg/L for heptachlor, aldrin, and dieldrin, respectively). All targeted analytes were detected in less than 10 minutes.

Table 4. Performance of the proposed method under optimized conditions

Sample	Analytes	Linearity (mg/L)	Correlation Coefficient	Regression Coefficient, R^2	LOD (mg/L)	LOQ (mg/L)
Paddy water	Heptachlor	1-10	y = 1246479x + 102580	0.9796	0.85	2.55
	Aldrin	0.1-1	y = 710263x + 166656	0.9908	0.09	0.27
	Dieldrin	0.2-1.4	y = 469676x + 62885	0.9935	0.19	0.57

Table 5. Method precision for intra- and inter-day (RSD), relative recovery (RR%), and enrichment factor (EF)

Analytes	Concentration (mg/L)	Intra-day RSD (%, n=3)	Inter-day RSD (%, n=9)	%RR	EF
Heptachlor	1	2.52	1.82	84	6.74
	10	2.78	2.31	82	16.87
Aldrin	0.1	2.34	0.30	90	9.64
	1	3.29	1.91	91	34.73
Dieldrin	0.2	3.52	0.19	95	4.38
	1.4	4.52	2.11	98	20.25

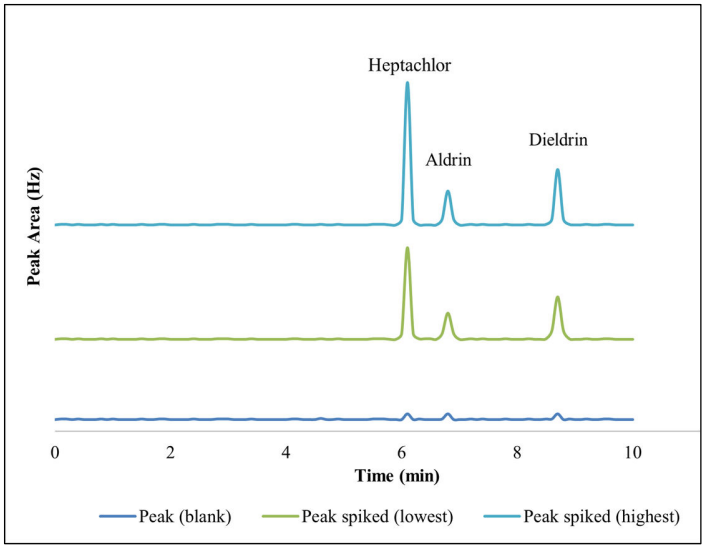

Figure 11. Chromatogram of paddy water sample at unspiked (blank), spiked (lowest concentration), and spiked (higher concentration)

Figure 12 shows the proposed interaction mechanism between the targeted analytes' OCPs and the obtained alginate-silica sorbent in this study. The extraction of OCP on alginate-silica sorbent is based on adsorption, whereby it possesses a porous structure comprising a substantial number of active sites accessible for binding with analytes [65]. It is explained that the binding type is contingent upon the nature of interactions between the adsorbent's surface and the molecular species of the analyte. For this interaction between OCP and alginate-silica composite, the interaction is physical, primarily governed by weak van der Waals forces, which is known as physisorption [65].

Green analytical calculator (AGREE)

The greenness of the developed method was evaluated using the AGREE metric calculator, which falls under a score (Figure 13) of 0.56. According to Rajendran et al., the determination of green classification lacks a predefined scale or metric; it hinges on the number of segments exhibiting a green color, with the value on the central pictogram approaching 1.0 [45]. The assessment implied an adequate green analytical methodology as it meets specific criteria, including (4) the integration of analytical processes for simultaneous steps, such as extraction and sonication (6), no derivatization agent was used during analysis and extraction, (10) no reagent used in the procedure, (12) the threats to the operator and environment were minimum due to minimum organic solvent consumption which approximately less than 1mL. The other two criteria represented by red are (3) the offline position of the analytical device and (9) the high consumption of energy-intensive techniques as the analysis was performed using GC-MS. The red colors of

the assessment will be improved for future work. Nevertheless, by concentrating solely on the advancement of sample preparation techniques, this study can be regarded as an environmentally friendly method in comparison to conventional SPE and LLE techniques.

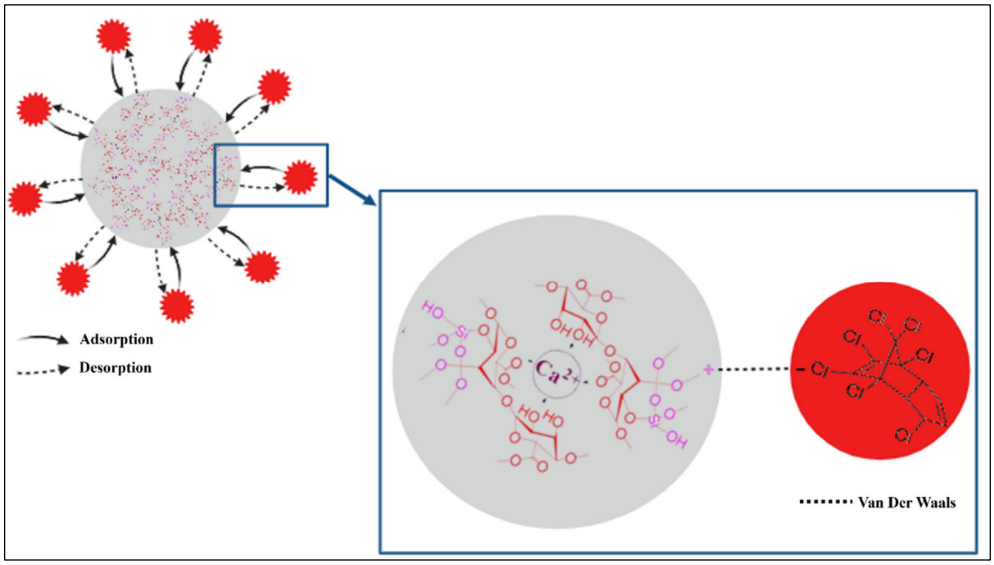

Figure 12. Interaction mechanism of extraction between alginate-silica sorbent with OCP (heptachlor) by van der Waals interaction

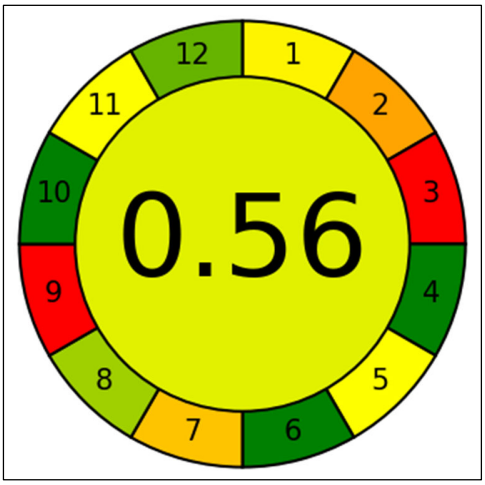

Figure 13. AGREE metric for greenness assessment of method developed

Conclusion

In conclusion, the chemical and physical properties of Alg-Si beads prepared by the encapsulation method were examined by characterization with ATR-FTIR and FESEM and showed that the functional groups of O-H, Si-O-Si, and COO^- groups contribute to the van der Waals, the interaction between prepared Alg-Si beads sorbent with targeted analytes. An uneven, rough surface area from the FESEM analysis of the sorbents could be attributed to the porosity of the beads obtained. The performance of Alg-Si-µ-SPE to extract OCPs from paddy water samples using alginate-silica beads was optimized, which included extraction time, desorption solvent, desorption time, and mass of sorbent.

Furthermore, the high adsorption capacity of the sorbent is demonstrated by the data obtained from method validation, which reveals linear ranges of 1-10 mg/L, 0.1-1.0 mg/L, 0.2-1.4 mg/L, for heptachlor, aldrin, and dieldrin, respectively with LOD and LOQ in between of 0.09-0.85 mg/L and 0.27-2.55 mg/L, respectively. The relative recoveries (RR) have been found in the range of 82-98% for all targeted analytes. OCPs were extracted from genuine paddy water samples, demonstrating the effectiveness of the developed sorbent. Most of the calibration curves were linear, and all regression coefficients were in the range of 0.97-0.99. The intra-day precision varied from 2.34-4.52% while the inter-day ranged from 0.30-2.31% by spiking the three analytes into a sample solution. The miniaturized solvents volume (μL) and sorbents mass (mg) utilized in this method could be considered a green method and safe for the environment. Furthermore, the silica produced from oil palm fronds (OPF) is likely to evolve considerably in various applications and not limited to analytical and material chemistry only.

Acknowledgment

The authors would like to convey their sincere appreciation to the Kurita Oversea Research Grant, Reference number: 22pmy058-K1 [100-TNCPI/INT 16/6/2 (065/2022)], for their financial support for this research. The authors also acknowledge the Faculty of Applied Science of Universiti Teknologi MARA for the facilities provided to carry out this project.

References

1. Department of Statistics Malaysia (2019). Gross domestic product. https://www.dosm.gov.my/portal-main/release-content/e37cf376-8b79-11ed-96a6-1866daa77ef9. [Access online 02 July 2023].
2. Marsin, F. M., Wan Ibrahim, W. A., Nodeh, H. R., and Sanagi, M. M. (2020). New magnetic oil palm fiber activated carbon-reinforced polypyrrole solid phase extraction combined with gas chromatography-electron capture detection for determination of organochlorine pesticides in water samples. *Journal of Chromatography* A, 1612: 460638.
3. Sulaiman, F., Abdullah, N., Gerhauser, H., and Shariff, A. (2011). An outlook of Malaysian energy, oil palm industry and its utilization of wastes as useful resources. *Biomass and Bioenergy,* 35(9): 3775-3786.
4. Ozturk, M., Saba, N., Altay, V., Iqbal, R., Hakeem, K.R., Jawaid, M. and Ibrahim, F. H. (2017). Biomass Bioenergy: An overview of the development potential in Turkey and Malaysia. *Renewable Sustainability Energy Reviews,* 79: 1285-1302.
5. Roslan, A. M., Zahari, M. A. K. M., Hassan, M. A., and Shirai, Y. (2014). Investigation of oil palm frond properties for use as biomaterials and biofuels. *Tropical Agriculture and Development,* 58(1): 26-29.
6. Zhong, L. B., Yin, J., Liu, S. G., Liu, Q., Yang, Y. S., and Zheng, Y. M. (2016). Facile one-pot synthesis of urchin-like Fe–Mn binary oxide nanoparticles for effective adsorption of Cd(II) from water. *RSC Advances,* 6(105): 103438-103445.
7. Onoja, E., Chandren, S., Razak, F. I. A., and Wahab, R. A. (2018). Extraction of nanosilica from oil palm leaves and its application as support for lipase immobilization. *Journal of Biotechnology*, 283: 81-96.
8. McCarthy, S. A., Davies, G. L., and Gun'ko, Y. K. (2012). Preparation of multifunctional nanoparticles and their assemblies. *Nature Protocols*, 7(9): 1677-1693.
9. Barbé, C. J., Kong, L., Finnie, K. S., Calleja, S., Hanna, J. V., Drabarek, E., … and Blackford, M. G. (2008). Sol–gel matrices for controlled release: from macro to nano using emulsion polymerization. *Journal of Sol-Gel Science and Technology,* 46: 393-409.
10. Chiew, C. S. C., Yeoh, H. K., Pasbakhsh, P., Poh, P. E., Tey, B. T., and Chan, E. S. (2016). Stability and reusability of alginate-based adsorbents for repetitive lead (II) removal. *Polymer Degradation and Stability,* 123: 146-154.
11. Lee, K. Y. and Mooney, D. J. (2012). Alginate: properties and biomedical applications. *Progress in Polymer Science,* 37(1): 106-126.
12. Crini, G. (2005). Recent developments in polysaccharide-based materials used as adsorbents

in wastewater treatment. *Progress in Polymer Science*, 30(1): 38-70.

13. Vijayalakshmi, K., Devi, B. M., Sudha, P. N., Venkatesan, J., and Anil, S. J. J. N. N. (2016). Synthesis, characterization and applications of nanochitosan/sodium alginate/microcrystalline cellulose film. *Journal Nanomedicine Nanotechnology,* 7(6): 419.
14. Cataldo, S., Gianguzza, A., Milea, D., Muratore, N., and Pettignano, A. (2016). Pb (II) adsorption by a novel activated carbon alginate composite material. A kinetic and equilibrium study. *International Journal of Biological Macromolecules,* 92: 769-778.
15. Thakur, S., Pandey, S., and Arotiba, O. A. (2016). Development of a sodium alginate-based organic/inorganic superabsorbent composite hydrogel for adsorption of methylene blue. *Carbohydrate Polymers*, 153: 34-46.
16. Pannier, A., Soltmann, U., Soltmann, B., Altenburger, R., and Schmitt-Jansen, M. (2014). Alginate/silica hybrid materials for immobilization of green microalgae *Chlorella vulgaris* for cell-based sensor arrays. *Journal of Materials Chemistry B*, 2(45): 7896-7909.
17. Singh, V., Srivastava, P., Singh, A., Singh, D., and Malviya, T. (2016). Polysaccharide-silica hybrids: design and applications. *Polymer Reviews*, 56(1): 113-136.
18. Jaganathan, H., and Godin, B. (2012). Biocompatibility assessment of Si-based nano-and micro-particles. *Advanced Drug Delivery Reviews*, 64(15): 1800-1819.
19. Choudhari, S. K., Premakshi, H. G., and Kariduraganavar, M. Y. (2016). Development of novel alginate–silica hybrid membranes for pervaporation dehydration of isopropanol. *Polymer Bulletin,* 73: 743-762.
20. Shi, J., Zhang, H., Yu, Y., Zou, X., Zhou, W., Guo, J., ... and Zhao, Y. (2020). Adsorption properties of calcium alginate-silica dioxide hybrid adsorbent to methylene blue. *Journal of Inorganic and Organometallic Polymers and Materials,* 30: 2114-2125.
21. Santhi, V. A., and Mustafa, A. M. (2013). Assessment of organochlorine pesticides and plasticisers in the Selangor River basin and possible pollution sources. *Environmental Monitoring and Assessment,* 185: 1541-1554.
22. Borrell, A., and Aguilar, A. (2007). Organochlorine concentrations declined during 1987–2002 in western Mediterranean bottlenose dolphins, a coastal top predator. *Chemosphere,* 66(2): 347-352.
23. Hernandez, F., Bakker, J., Bijlsma, L., De Boer, J., Botero-Coy, A. M., de Bruin, Y. B., and Hogendoorn, E. A. (2019). The role of analytical chemistry in exposure science: Focus on the aquatic environment. *Chemosphere,* 222: 564-583.
24. Abdullah, M. P., Abdul Aziz, Y. F., Rozali Othman, M., and Wan Mohd Khalik, W. M. A. (2015). Organochlorine pesticides residue level in surface water of Cameron Highlands, Malaysia. *Iranica Journal of Energy & Environment,* 6(2): 141-146.
25. Osman, B. E., and Khalik, W. M. A. W. M. (2018). Data on organochlorine concentration levels in soil of lowland paddy field, Kelantan, Malaysia. *Data in Brief*, 20: 999-1003.
26. Mat Saad, A., and Hassan Asari, F. F. A. (2019). Distributions of organochlorine pesticides in sediment and aquatic biota: Benzenehexachlorides (BHCS). *Proceedings of the International Conference on Design Industries & Creative Culture:* pp. 28-39.
27. Nascimento, M. M., da Rocha, G. O., and de Andrade, J. B. (2021). Customized dispersive micro-solid-phase extraction device combined with micro-desorption for the simultaneous determination of 39 multiclass pesticides in environmental water samples. *Journal of Chromatography A,* 1639: 461781.
28. Gorji, S., Bahram, M., and Biparva, P. (2019). Optimized stir bar sorptive extraction based on self-magnetic nanocomposite monolithic kit for determining bisphenol A in bottled mineral water and bottled milk samples. *Analytical and Bioanalytical Chemistry Research*, 6(1): 137-156.
29. Amiri, A., Tayebee, R., Abdar, A., and Sani, F. N. (2019). Synthesis of a zinc-based metal-organic framework with histamine as an organic linker for the dispersive solid-phase extraction of organophosphorus pesticides in water and fruit juice samples. *Journal of Chromatography*

A, 1597: 39-45.

30. Wang, D. D., Lu, Z. H., Guan, X. Y., Yang, M. N. O., Guo, H. M., and Yang, Z. H. (2021). Magnetic polydopamine modified with choline-based deep eutectic solvent for the magnetic solid-phase extraction of sulfonylurea herbicides in water samples. *Journal of Chromatographic Science,* 59(1): 95-102.
31. Zhang, M., Mei, J., Lv, S., Lai, J., Zheng, X., Yang, J., and Cui, S. (2020). Simultaneous extraction of permethrin diastereomers and deltamethrin in environmental water samples based on aperture regulated magnetic mesoporous silica. *New Journal of Chemistry,* 44(37): 16152-16162.
32. Arias, P. G., Martínez-Pérez-Cejuela, H., Combès, A., Pichon, V., Pereira, E., Herrero-Martínez, J. M., and Bravo, M. (2020). Selective solid-phase extraction of organophosphorus pesticides and their oxon-derivatives from water samples using molecularly imprinted polymer followed by high-performance liquid chromatography with UV detection. *Journal of Chromatography A,* 1626: 461346.
33. Shakourian, M., Yamini, Y., and Safari, M. (2020). Facile magnetization of metal–organic framework TMU-6 for magnetic solid-phase extraction of organophosphorus pesticides in water and rice samples. *Talanta,* 218: 121139.
34. Özer, E. T., Osman, B., and Parlak, B. (2020). An experimental design approach for the solid phase extraction of some organophosphorus pesticides from water samples with polymeric microbeads. *Microchemical Journal,* 154: 104537.
35. Amiri, A., Baghayeri, M., and Vahdati-Nasab, N. (2020). Effective extraction of organophosphorus pesticides using sol–gel based coated stainless-steel mesh as novel solid-phase extraction sorbent. *Journal of Chromatography A,* 1620: 461020.
36. Senosy, I. A., Guo, H. M., Ouyang, M. N., Lu, Z. H., Yang, Z. H., and Li, J. H. (2020). Magnetic solid-phase extraction based on nano-zeolite imidazolate framework-8-functionalized magnetic graphene oxide for the quantification of residual fungicides in water, honey and fruit juices. *Food Chemistry*, 325: 126944.
37. Huang, Z., and Lee, H. K. (2015). Micro-solid-phase extraction of organochlorine pesticides using porous metal-organic framework MIL-101 as sorbent. *Journal of Chromatography A,* 1401: 9-16.
38. Chahkandi, M., and Amiri, A. (2019). Hydroxyapatite/Fe_3O_4 nanocomposite as efficient sorbent for the extraction of phthalate esters from water samples. *Inorganic Chemistry Research,* 3(1): 50-64.
39. Sajid, M., Khaled Nazal, M., Rutkowska, M., Szczepańska, N., Namieśnik, J., and Płotka-Wasylka, J. (2019). Solid phase microextraction: apparatus, sorbent materials, and application. *Critical Reviews in Analytical Chemistry,* 49(3): 271-288.
40. Naing, N. N., Tan, S. C., and Lee, H. K. (2019). Micro-solid-phase extraction 16. Solid-Phase Extraction, 443.
41. Basheer, C., Alnedhary, A. A., Rao, B. M., Valliyaveettil, S., and Lee, H. K. (2006). Development and application of porous membrane-protected carbon nanotube micro-solid-phase extraction combined with gas chromatography/mass spectrometry. *Analytical Chemistry*, 78(8): 2853-2858.
42. Abidin, N. H. Z., Ibrahim, W. N. W., Raharjo, Y., Nodeh, H. R., Wahab, R. A., Yaakob, M. K., and Hanapi, N. S. M. (2024). Microextraction experimental and forcefield theoretical modelling study on exploring a silica-enriched oil palm frond biomass for the determination of polycyclic aromatic hydrocarbons in *Psidium guajava*. *Microchemical Journal*, 197: 109885.
43. Zaini, N., Hanapi, N. S. M., Ibrahim, W. N. W., and Anis, A. L. (2020). Selective determination of acidic drugs in water samples using online solid phase extraction liquid chromatography with alginate incorporated multi-walled carbon nanotubes as extraction sorbent. *Indonesian Journal of Chemistry,* 20(5): 987-999.
44. Othman, N. Z., Hanapif, N. S. M., Ibrahim, W. N. W., and Saleh, S. H. (2020). Alginate incorporated multi-walled carbon nanotubes as dispersive micro solid phase extraction sorbent for selective and efficient separation of acidic drugs in water samples. *Nature Environment and Pollution*

Technology, 19(3): 1155-1162.

45. Rajendran, S. (2022). Formulating and evaluation of magnetic effervescent tablets containing ionic liquid used as microextraction tool for multi-analytes pharmaceutical active compounds analysis. Thesis of Master of Science, Universiti Malaysia Terengganu.
46. Pena-Pereira, F., Wojnowski, W., and Tobiszewski, M. (2020). AGREE—Analytical GREEnness metric approach and software. *Analytical Chemistry,* 92(14): 10076-10082.
47. Yang, M., Xia, Y., Wang, Y., Zhao, X., Xue, Z., Quan, F. and Zhao, Z. (2016). Preparation and property investigation of crosslinked alginate/silicon dioxide nanocomposite films. *Journal of Applied Polymer Science*, 133(22).
48. Xu, S. W., Jiang, Z. Y., Lu, Y., Wu, H., and Yuan, W. K. (2006). Preparation and catalytic properties of novel alginate− silica− dehydrogenase hybrid biocomposite beads. *Industrial & Engineering Chemistry Research,* 45(2): 511-517.
49. Draget, K. I., Stokke, B. T., Yuguchi, Y., Urakawa, H., and Kajiwara, K. (2003). Small-angle X-ray scattering and rheological characterization of alginate gels. 3. Alginic acid gels. *Biomacromolecules,* 4(6): 1661-1668.
50. Amouzgar, P., Chan, E. S., and Salamatinia, B. (2017). Effects of ultrasound on development of Cs/NAC nano composite beads through extrusion dripping for acetaminophen removal from aqueous solution. *Journal of Cleaner Production,* 165: 537-551.
51. Pawar, S. N., and Edgar, K. J. (2012). Alginate derivatization: A review of chemistry, properties and applications. *Biomaterials,* 33(11): 3279-3305.
52. Fosu-Mensah, B. Y., Okoffo, E. D., Darko, G., and Gordon, C. (2016). Assessment of organochlorine pesticide residues in soils and drinking water sources from cocoa farms in Ghana. SpringerPlus, 5: 1-13.
53. Asgharinezhad, A. A., Ebrahimzadeh, H., Mirbabaei, F., Mollazadeh, N., and Shekari, N. (2014). Dispersive micro-solid-phase extraction of benzodiazepines from biological fluids based on polyaniline/magnetic nanoparticles composite. *Analytica Chimica Acta*, 844: 80-89.
54. Zaini, N., Hanapi, N. S. M., Ibrahim, W. N. W., Osman, R., Kamaruzaman, S., Yahaya, N., and Anis, A. L. (2022). Dispersive micro-solid-phase extraction (D-μ-SPE) with polypyrrole-graphene oxide (PPy-GO) nanocomposite sorbent for the determination of tetracycline antibiotics in water samples. *Malaysian Journal of Analytical Sciences*, 26(5): 953-964.
55. Hernando, M. D., Mezcua, M., Fernández-Alba, A. R., and Barceló, D. (2006). Environmental risk assessment of pharmaceutical residues in wastewater effluents, surface waters and sediments. *Talanta,* 69(2): 334-342.
56. Abidin, N. N. Z., Sanagi, M. M., Ibrahim, W. A. W., Endud, S., and Shukri, D. S. M. (2014). Portable micro-solid phase extraction for the determination of polycyclic aromatic hydrocarbons in water samples. *Analytical Methods,* 6(15): 5512-5518.
57. Deshmukh, S., Kumar, R., and Bala, K. (2019). Microalgae biodiesel: A review on oil extraction, fatty acid composition, properties and effect on engine performance and emissions. *Fuel Processing Technology*, 191: 232-247.
58. Zarrinmehr, M. J., Daneshvar, E., Nigam, S., Gopinath, K. P., Biswas, J. K., Kwon, E. E., ... and Bhatnagar, A. (2022). The effect of solvents polarity and extraction conditions on the microalgal lipids yield, fatty acids profile, and biodiesel properties. *Bioresource Technology*, 344: 126303.
59. Hamdaoui, O., Naffrechoux, E., Tifouti, L., and Pétrier, C. (2003). Effects of ultrasound on adsorption–desorption of p-chlorophenol on granular activated carbon. *Ultrasonics Sonochemistry*, 10(2): 109-114.
60. Breitbach, M., and Bathen, D. (2001). Influence of ultrasound on adsorption processes. *Ultrasonics Sonochemistry*, 8(3): 277-283.
61. Rozaini, M. N. H., Yahaya, N., Saad, B., Kamaruzaman, S., and Hanapi, N. S. M. (2017). Rapid ultrasound assisted emulsification micro-solid phase extraction based on molecularly imprinted polymer for HPLC-DAD determination of bisphenol A in aqueous matrices. *Talanta,* 171: 242-249.
62. Dahane, S., García, M. G., Bueno, M. M., Moreno,

A. U., Galera, M. M., and Derdour, A. (2013). Determination of drugs in river and wastewaters using solid-phase extraction by packed multi-walled carbon nanotubes and liquid chromatography–quadrupole-linear ion trap-mass spectrometry. *Journal of Chromatography A,* 1297: 17-28.

63. Batt, A. L., Furlong, E. T., Mash, H. E., Glassmeyer, S. T., and Kolpin, D. W. (2017). The importance of quality control in validating concentrations of contaminants of emerging concern in source and treated drinking water samples. *Science of the Total Environment*, 579: 1618-1628.
64. Huang, Z., and Lee, H. K. (2015). Micro-solid-phase extraction of organochlorine pesticides using porous metal-organic framework MIL-101 as sorbent. *Journal of Chromatography A*, 1401: 9-16.
65. Ponnuchamy, M., Kapoor, A., Senthil Kumar, P., Vo, D. V. N., Balakrishnan, A., Mariam Jacob, M., and Sivaraman, P. (2021). Sustainable adsorbents for the removal of pesticides from water: a review. *Environmental Chemistry Letters,* 19: 2425-2463.

Malaysian Journal of Analytical Sciences (MJAS)
Published by Malaysian Analytical Sciences Society

A REVIEW OF THE CURRENT TREND IN THE SYNTHESIS OF NITROGEN-RICH FUNCTIONAL POLYMERS FOR CARBON DIOXIDE ADSORPTION

(Sorotan Terhadap Trend Semasa Dalam Sintesis Polimer Fungsional Kaya Nitrogen Untuk Penjerapan Karbon Dioksida)

Noorhidayah Ishak[1], Azalina Mohamed Nasir[2], Chow Wen Shyang[3], Dai Viet N. Vo[4], Bassim H. Hameed[5], Mohd Azmier Ahmad[1], and Azam Taufik Mohd Din[1*]

[1] *School of Chemical Engineering, Engineering Campus, Universiti Sains Malaysia, 14300 Nibong Tebal, Pulau Pinang, Malaysia*
[2] *Faculty of Chemical Engineering and Technology, Kompleks Pusat Pengajian Jejawi 3, Kawasan Perindustrian Jejawi, Universiti Malaysia Perlis (UniMAP) 02600 Arau, Perlis, Malaysia*
[3] *School of Materials and Mining Resources Engineering, Engineering Campus, Universiti Sains Malaysia, 14300 Nibong Tebal, Pulau Pinang, Malaysia*
[4] *Institute of Environmental Technology and Sustainable Development, Nguyen Tat Thanh University, 298-300A Nguyen Tat Thanh, District 4, Ho Chi Minh City, 755414, Viet Nam.*
[5] *Department of Chemical Engineering, College of Engineering, Qatar University, P.O. Box: 2713, Doha, Qatar*

[*] *Corresponding author chazam@usm.my*

Received: 1January 2024; Accepted: 19 March 2024; Published: 29 April 2024

Abstract

The consumption of fossil fuels (oil, coal, and natural gas) has increased due to the increasing demand for energy from various industries. The International Energy Agency, in its World Energy Outlook 2022, has noted a steady increase in global energy demand from fossil fuels from 350 EJ in 2000 to over 500 EJ in 2030. This increase has contributed significantly to the emission of greenhouse gases, mainly carbon dioxide (CO_2), leading to global warming and climate change. Carbon capture by adsorption on polymeric adsorbents is a strategic approach to mitigate climate change by reducing CO_2 concentration in the atmosphere. This review focuses on the preparation of various nitrogen-rich functional polymers, mainly polyamine, polyamide/polyimide, and covalent triazine framework. This article provides important information on improving the functionality of nitrogen-rich functional polymers for CO_2 adsorption. Brief insights into the CO_2 adsorption mechanism and molecular modeling using density functional theory are also included. The challenges and future recommendations are also addressed in this review.

Keywords: carbon capture, adsorbent, climate change, density functional theory

Abstrak

Penggunaan bahan api (minyak, arang, dan gas asli) telah meningkat kerana pertambahan permintaan untuk tenaga dalam pelbagai sektor industri. Agensi Tenaga Antarabangsa (IEA) dalam Tinjauan Tenaga Dunia 2022 telah mencatatkan pertambahan yang mantap dalam permintaan global tenaga daripada bahan api fosil dari 350 EJ pada tahun 2000 hingga melebihi 500 EJ pada tahun 2030. Peningkatan ini telah menyumbang kesan yang ketara pada pembebasan gas hijau terutamanya karbon dioksida (CO_2) yang

membawa kepada pemanasan global dan perubahan iklim. Penangkapan karbon menggunakan kaedah penjerapan ke atas bahan penjerap daripada polimer ialah satu strategi bagi mengatasi perubahan iklim dengan cara mengurangkan kepekatan CO_2 dalam atmosfera. Sorotan ini memfokuskan kepada penyediaan beberapa jenis polimer fungsional kaya nitrogen, antaranya poliamina, poliamida/poliimida, dan kerangka kovalen triazina. Artikel ini menyediakan maklumat penting bagi menambah baik kefungsian polimer kaya nitrogen bagi tujuan penjerapan CO_2. Pemahaman ringkas mengenai mekanisma penjerapan CO_2 serta pemodelan molekul menggunakan teori ketumpatan berfungsi turut disertakan. Cabaran dan cadangan masa hadapan turut disampaikan dalam sorotan ini.

Kata kunci: penangkapan karbon, bahan penjerap, perubahan iklim, teori ketumpatan berfungsi

Introduction

The increasing demand for energy due to population growth has led many countries to explore their natural resources to strengthen their economy. The increase in greenhouse gas emissions is mainly contributed by carbon dioxide (CO_2) generated from the combustion of fossil fuels and natural resources, impacting the environment, and causing global warming and climate change [1]. To address this issue, the Paris Agreement was adopted on 12th December 2015 by 196 parties at the United Nations Climate Change Conference 21 in Paris. It aims to reduce global warming to below 2 °C, if possible, to 1.5 °C compared to the pre-industrial level [2]. Carbon capture, utilization, and storage is considered one of the strategic climate mitigation options to meet this international goal. It refers to technologies that capture CO_2 emissions from main contributors, such as energy production and manufacturing facilities that utilize either non-renewable or renewable energy sources (e.g., biomass) [3]. If the captured CO_2 is not consumed, it is compressed and transported through pipelines, ships, rails, or trucks for use in various applications, or injected into deep geological formations, such as a gas reservoir or saline formation that traps CO_2 for permanent storage [4].

An increasing number of publications have reported on carbon capture using various methods, including absorption, adsorption, membrane separation, and cryogenic distillation [5]. However, the conventional CO_2 capture technology using liquid amine systems has some drawbacks. For instance, the regeneration and desorption of captured CO_2 from aqueous amine scrubbing systems can be energy-inefficient due to the high regeneration temperature. The significantly inefficient energy consumption requirements can lead to economic inefficiency. Other shortcomings, such as equipment corrosion and concerns about amine leakage into the environment, are frequently encountered in these conventional aqueous amine schemes [6]. If a system experiences amine leakage and is exposed to atmospheric oxidants, it can lead to a degradation reaction, producing toxic compounds (e.g., nitrosamines, nitramines, and amides) that pose a threat to human health and environmental safety [7]. Adsorption using solid materials is a practical technology that can be applied for CO_2 capture. Adsorption offers low energy requirements and low operating costs, including controlled waste generation, high CO_2 adsorption uptake in ambient conditions, high specific surface area, high mechanical durability, adequate pore size distribution, and accessibility for regeneration [8].

Adsorption is a sorption process of CO_2 molecules onto the surface of a solid adsorbent that has residual surface energy due to unbalanced forces. These unbalanced forces will attract CO_2 molecules colliding with the solid surface, causing them to remain on the solid surface. The attraction that forms between gaseous CO_2 and the adsorbent can be classified as a weak physical interaction (i.e., physical adsorption) and a stronger chemical bond (i.e., chemical adsorption) [9]. Several solid materials, such as zeolites and silica, have been reported for CO_2 capture. These materials possess high CO_2 capture capacity and high selectivity of CO_2 over nitrogen (N_2) under atmospheric conditions. Nevertheless, the adsorption capacity of zeolites can be affected by the presence of water. Hence, dehumidification would be necessary in such conditions prior to CO_2 capture. This additional step would significantly increase the investment cost, total energy consumption, and the difficulty of the operation [10].

Mesoporous carbon-based materials offer promising potential for CO_2 capture due to their widely available resources, high chemical and thermal stability, and inexpensive and tunable porous structure [11].

On the other hand, polymeric materials are great adsorbents for CO_2 adsorption due to the presence of different functional groups on their backbone. The adsorption capacity and selectivity of a polymeric adsorbent can be improved when these functional groups form specific interactions with CO_2. Surface morphology and tunable porosity can enhance the intraparticle transport of CO_2 toward the active sites of the adsorbent, thereby increasing its performance [12]. Recently, porous polymeric adsorbents have been receiving attention due to the increasing number of publications on the functionalization of polymers with various functional groups to improve the performance of adsorbents. A previous study reported the introduction of nitrogen- and oxygen-based functional groups that could enhance the CO_2 adsorption capacity of the adsorbent [13]. The functionalization of polymers has also led to the development of various combinations of porous support materials, such as zeolite and mesoporous silica, with functional polymeric materials. The functionalized polymeric solid sorbent can overcome the issue of low stability caused by the leaching of amines over repeated capture/regeneration cycles and the limited transportation of CO_2 to the active sites in an amine-impregnated CO_2 sorbent system [13]. Hassan et al. [14] also synthesized triptycene-based nitrogen-rich hyper-cross-linked polymer (HCP). Their results indicated a higher adsorption capacity of 160 mg/g at 273 K and 1 bar, and a lower specific surface area of 848 m^2/g. The specific surface area decreased as a result of the functionalization with the nitrogen functional group; however, this modification did not affect the performance of CO_2 adsorption. The inclusion of a nitrogen heteroatom in HCP has increased the affinity of the material toward CO_2 due to their dipole-quadrupole interaction [14].

Tremendous efforts have been dedicated to designing porous materials with different channel geometries, pore sizes, and chemical compositions to improve the effectiveness of sorbents. These design variations have considered several criteria, such as high adsorption capacity, cost-effectiveness, fast kinetics, energy efficiency, and long-term stability [15,16]. This review presents a comprehensive discussion of the current trends in the development of polymeric adsorbents for CO_2 adsorption. The introduction is presented in the first section, elaborating on the background study on CO_2 adsorption. This includes the main sources of CO_2 production, the current policies being applied, and carbon capture methods. In the second section, the preparation of nitrogen-functional polymers for CO_2 adsorption is discussed. The structure of CO_2 and the mechanisms of interaction with CO_2 are elaborated in the subsequent section. This review ends with conclusions and recommendations for future studies.

Preparation of nitrogen-rich functional polymer

Nitrogen-rich porous solid adsorbents have been widely explored for their CO_2 chemisorption ability under low CO_2 concentrations. Figure 1 shows nitrogen moieties like amine, amide, imide, triazine, melamine, imidazole, and hydrazine, which are often used to produce nitrogen-rich functional polymers in CO_2 capture applications [17–20]. This section presents a brief discussion on the preparation of nitrogen-rich polymers, mainly focusing on polyamine, polyamide/polyimide, and covalent triazine frameworks.

Preparation of amine-functionalized polymer

Polyethyleneimine (PEI) or polyaziridine is a polymer composed of an amino group and two carbon aliphatic CH_2CH_2 spacers, and it is widely applied as an adsorbent in CO_2 adsorption [21, 22]. This amine-bearing polymer is well known for its highly positive charge, and it can exist in a linear and branched chain with different properties. Linear PEIs are composed of secondary amines, whereas branched PEIs are composed of primary, secondary, and tertiary amino groups that can be found on the polymeric backbone [23]. For CO_2 adsorbent application, PEIs are commonly combined with different porous inorganic supports to achieve cost-effectiveness and high amine content through chemical grafting of amine reagent, physical impregnation, and impregnation-cross-linked method [24–26].

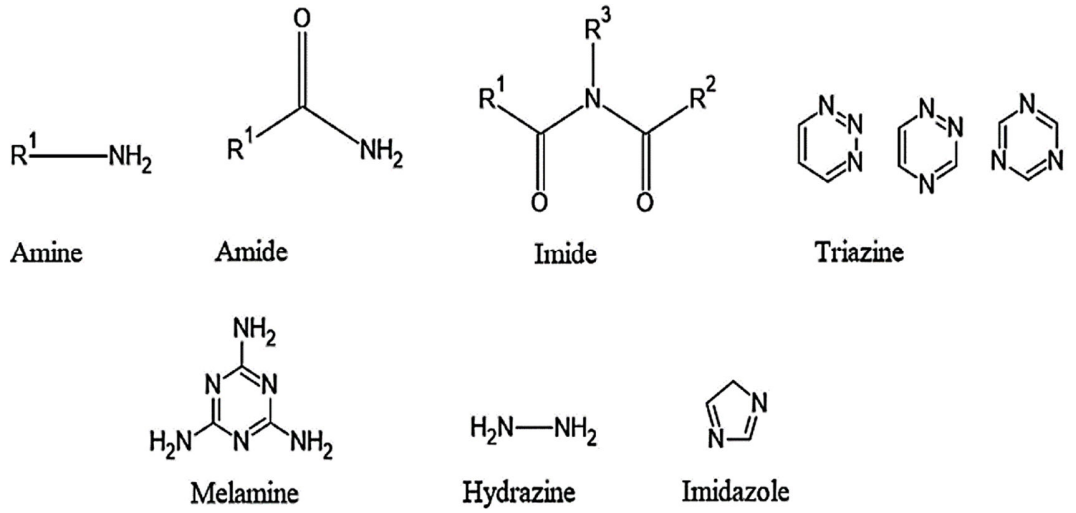

Figure 1. Nitrogen functional groups are commonly used in nitrogen-rich functional polymers

Physical impregnation onto porous materials

Physical impregnation of low vapor pressure amine polymers onto porous support materials is an easy and more scalable method [54, 60]. Li et al. [30] used the wet impregnation method by dissolving PEI in the solvent to obtain a homogeneous solution. Then, the porous material (Al_2O_3) was added to the solution, and the mixture was stirred until the solvent evaporated. The obtained material was dried in a vacuum oven overnight. The synthesized 50%PEI@Al_2O_3 adsorbent exhibited high adsorption stability for up to ten cycles with an adsorption capacity of 136 mg/g. The high operating temperature increased the kinetic effect, reduced the viscosity of PEI molecules, and increased the diffusion of CO_2 molecules, thereby increasing the likelihood of molecular collisions between CO_2 and PEI molecules. Nonetheless, this method also suffered from several drawbacks, such as amine leaching during the capture and regeneration cycles, and low active site accessibility after impregnation, which reduced the performance of the adsorbent [31]. Li et al. [32] reported a simplified and environmentally friendly method to prepare amine-modified amorphous silica to overcome the issue of particle agglomeration between PEI and silica by introducing a solventless mechanical grinding method. The CO_2 adsorption capacity of 70% PEI/SiO_2 was approximately 2.47 mmol/g at 70 °C and 1.5 bar. These results show that the absorbents have a remarkable CO_2 adsorption capacity at high temperatures.

In addition to infusion into porous solid supports, porous polymer supports are also used to enhance CO_2 performance. This approach will increase CO_2 adsorption performance with low mass transfer limitation caused by clogged pores by maximizing amine loading and improving the accessibility of gas through the sorbent [24]. Choi et al. [33] prepared metal-organic frameworks (MOFs) and immobilized polyacrylonitrile (PAN) fiber mats with PEI impregnation for CO_2 capture. The PEI was impregnated into the PAN-MOF electrospun mats using the wet impregnation method. They selected two types of MOFs, namely ZIF-8 and HKSUT-1, to prepare the PAN/MOF electrospun mats. The impregnation of PEI into the PAN/ZIF-8 electrospun mats enhanced their adsorption capacity by 45% and improved the CO_2/N_2 sorption selectivity due to the strong intermolecular interactions between the amine group in PEI and CO_2 molecules. However, a further increase in PEI loading reduced the adsorption capacity due to the reduction of surface area and pore volume.

Chemical grafting

A functional adsorbent with specific amine group and functional group densities suitable for investigating the

CO_2 adsorption mechanism can be obtained using the surface grafting method. However, this method is expensive and involves a complex procedure. Yin et al. [34] successfully synthesized PEI-modified poly(melamine)-polyacrylamide (MF/PAM-g-PEI), which demonstrated higher CO_2 adsorption of 2.8 mmol/g (10% CO_2 and 90% N_2; 30 mL/min) at 273 K compared to non-modified MF and PAM polymer networks. The polymer network was synthesized by interpenetrating PAM between the molecular chains of MF and functionalizing it with PEI to attain a solid amine adsorbent, as shown in Figure 2. The interpenetration of PAM into the porous amino resin improved its swelling capacity and provided amine grafting sites for the amine agents. Consequently, the adsorption capacity and the regeneration performance of the adsorbents increased.

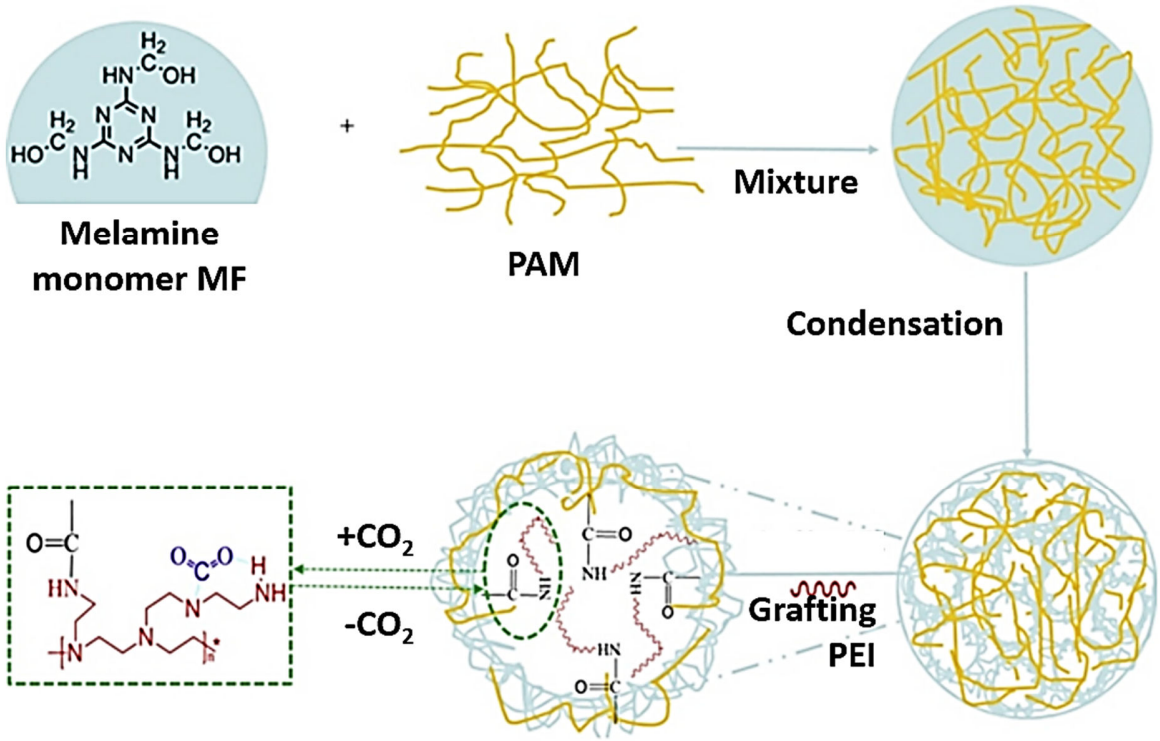

Figure 2. Schematic diagram of the synthesis of MF/PAM polymer network [34]

The grafting method was applied by Wang et al. [35] using nucleophilic substitution reaction without a catalyst to prepare the precursor for PEI-based polymers. The surface of the precursor was evenly coated with amine groups, while its internal side has a dual role of a pore-forming agent through self-decomposition and in creating nitrogen sites that can enhance surface polarity. The formation of narrowly distributed ultramicropores (d = ~0.6 nm) can attract CO_2 by relying on the van der Waals force as affinity attraction. This material achieved a CO_2 uptake of 4.92 mmol/g. The polymers exhibited the typical adsorption-desorption patterns of Type-I isotherms. Alongside the distribution of pore sizes, the polymers exhibited a recognizable microstructural feature, with ultramicropore sizes ranging from 0.6 to 0.9 nm [35]. Yang et al. [36] also synthesized an amine-functionalized polymer for CO_2 adsorption from flue gas under the pressure swing adsorption operating mode. Linear pentaethylenehexamine (PEHA) was functionalized on the open-cell foams of low-density and high-porosity polypropylene/polyolefin elastomer (PP/POE), which served as a support material.

Impregnation-cross-linking method

Porous poly(divinylbenzene) (PDVB) was synthesized using the high internal phase emulsion (HIPE) template. The porous structure was further tailored by adding a pore-forming agent and applying the post-cross-linking method. The adsorption capacity of meso-PDVB increased with the introduction of PEHA to 4.52 and 4.99 mmol/g at a 10% CO_2 concentration, with higher N efficiency observed under wet conditions [25]. The same group also reported the preparation of porous polyHIPE with silica hydroxyl groups that act as a silane coupling agent via the copolymerization of styrene, divinylbenzene, triethoxyvinylsilane (VTEO), and tetraethyl orthosilicate (TEOS), as illustrated in Figure 3. The surface morphology of polyHIPE in Figure 3 shows the formation of a thin layer of TEOS and VTEO compared to the surface morphology of polyHIPE without the presence of both silane groups. The material can be easily functionalized with aziridine via the Friedel-Crafts cross-linking reaction through the silanol group of polyHIPE, as shown in Figure 3, thus increasing the specific surface area and enriching the CO_2 chemical adsorption sites [37]. This group also synthesized a novel amine-functionalized adsorbent with an interconnected porous structure. The adsorbent was prepared using HIPE polymerization of styrene and divinylbenzene, and then functionalized with PEI in a one-step synthesis. The 4.0PEI70k@polyHIPE adsorbent showed a maximum adsorption capacity of 4.18 mmol CO_2 per gram of adsorbent at 20 °C (CO_2:N_2 = 1:9; volume ratio of 30 mL/min) under humid conditions. The monolithic structure produced from the HIPE template on a macroscopic scale of the materials offers a better advantage in industrial applications compared to powder adsorbent [38]. This is also supported by Haorui, who synthesized cross-linked polyHIPE with PEI, producing a sponge-like PEI-based solid amine adsorbent that exhibited a record high CO_2 adsorption capacity of 14.22 mmol/g with stable regeneration performance; hence, the adsorbent holds great potential in CO_2 adsorption and separation [39].

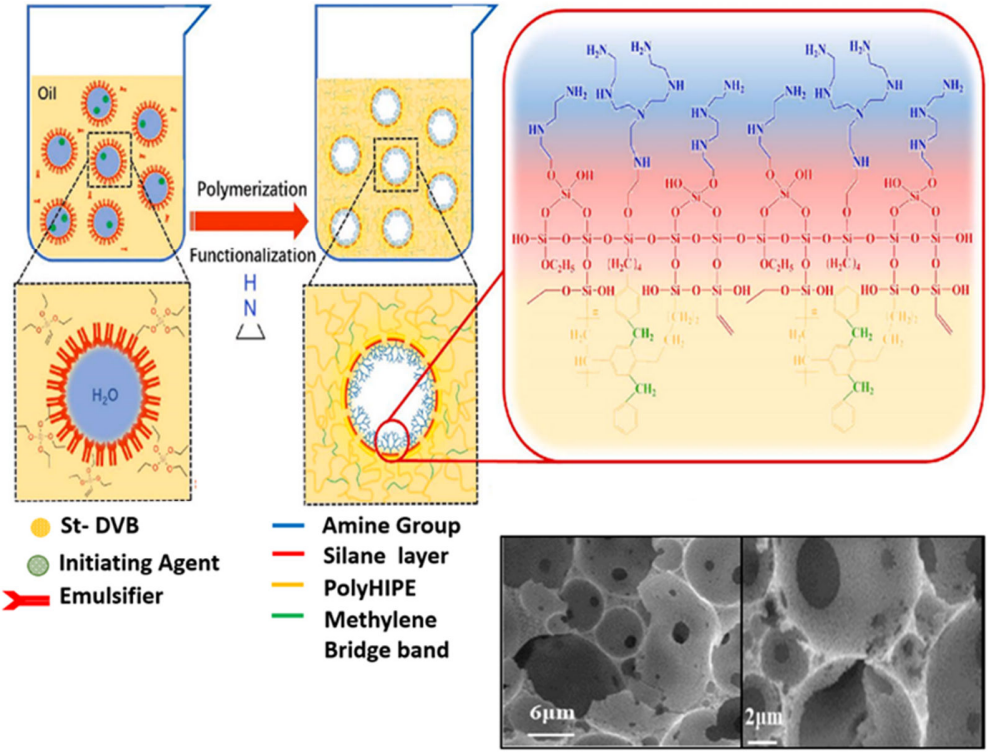

Figure 3. Synthesis of the hierarchically porous solid amine adsorbent and scanning electron microscopy images of cross-linked polyHIPE [37]

Table 1. Summary of different methods used for introducing amine group in polymer

No.	Polymer	Amine Introduction Method	Support	Adsorption Capacity	Advantages	Disadvantage	Ref
1	Polyethyleneimine/ tetraethylenepentamine (PEI/TEPA)	Physical impregnation	Macroporous silica	TEPA/SIO: 5.36 mmol/g PEI-1200: 3.75 mmol/g	• A simple, effective, and inexpensive method	• Low accessibility toward active sites after impregnation • The use of organic solvent during impregnation increases production cost • High amine loading can lead to agglomeration	[40]
2	PEI	Physical impregnation	Colloidal silica and ceramic fiber honeycomb monolith	PEI-SS (50%): 1.79 mmol/g			[41]
3	PEI	Physical impregnation	Silica support	2.3 mmol/g			[22]
4	TEPA grafted on polyethylene/ polypropylene (PE/PP) grafted with poly(glycidyl methacrylate) (PGMA)	Chemical grafting	PGMA-grafted fiber	117 mg/g	• Improved swelling capacity • Improved regeneration performance • The functionalization method can be tailored and the functional group on the surface porous material can be controlled	• Require complex sample preparation	[42]
5	Poly(aminoethyl methacrylate)	Chemical grafting	N/A	2.4 mmol/g			[43]
6	PEI	Chemical grafting	Poly(acrylic acid) foam	5.91 mmol/g			[44]
7	Molecular imprinted polymer (PEI and glycol diglycidyl ether)	Impregnation cross-linked	Molecular imprinted polymer	MIP: 6.58 mmol/g; NIP: 5.87 mmol/g.	• Improved regeneration stability • The monolithic structure of polyHIPE offers a greater advantage in industrial applications • Avoid high resistance to mass transfer during adsorption	• Complex synthesis processes	[45]
8	PolyHIPE-PEI	Impregnation-cross-linking method	PolyHIPE	6.22 mmol/g			[46]

Preparation of amide- and imide-functionalized polymers

Both amide- and imide-based polymers, which are commonly synthesized for CO_2 capture applications, consist of a carbonyl group and nitrogen atoms. These polymers can be prepared for CO_2 capture using several methods, such as polycondensation, polymerization, and radical copolymerization.

Radical copolymerization of polyacrylamide

Polyacrylamide is a polymer obtained from the radical copolymerization of acrylamide (AAm) or methacrylamide (MAAM), which demonstrated great potential in CO_2 adsorption and separation [45, 47, 48]. Yoo et al. [49] synthesized an MOF (MIL-101) loaded with polymethacrylate (PM). This polymer was synthesized using radical copolymerization in the presence of azobisisobutyronitrile as an initiator, while ethylene glycol dimethacrylate (EGDMA) and MAAM were used as monomers to produce PM@MOF, which was further reduced to R-PM@MOF to introduce free –NH_2 group. The CO_2 adsorption capacity and selectivity performance of this adsorbent increased under optimum PM loading and the reduction of PM to R-PM due to the introduction of an amine functional group [49].

In another work, Fayemiwo et al. [50] synthesized three different HCPs using radical bulk polymerization, whereby EGDMA was used as the monomer cross-linker, while MAAM, AAm, and triallylamine (TAAm) were used as the functional monomers. The results showed that the maximum CO_2 uptake was obtained by HCPMAAM-2 (1.45 mmol/g), followed by HCP-AAm and HCP-TAAm at 273 K. The highest CO_2/N_2 selectivity (15/85) was achieved by HCPMAAM. Meanwhile, HCP-TAAm showed low adsorption performance and selectivity, possibly attributed to the weak attraction between tertiary amine and CO_2. In comparison, HCP-MAAM-2 and HCP-Aam have NH_2 functional groups that can form strong interactions with CO_2 molecules. The same group also reported the life cycle assessment of HCP-MAAM as an adsorbent. The results indicated that this adsorbent has lower environmental impacts compared to molecularly imprinted polymers, as the latter used solvents sourced from fossil fuels [50]. Su et al. [51] reported an improved molecular imprinting polymerization method using the surface imprinting technique to produce CO_2 molecular imprinting polymer (CO_2-MIP). As shown in Figure 4, the porous polymer was prepared using surface radical polymerization with continuous stirring using acrylamide as a monomer, EGDMA as a cross-linker, and activated carbon (AC) synthesized from sunflower heads (biomass waste) acted as a carrier. The MIP was polymerized onto the surface of the AC. The results showed that the macropores of the carrier decreased after molecularly imprinted polymerization, whereas its micropores and mesopores increased, leading to a decrease in the average pore size. The results obtained indicated better performance than other CO_2-MIP samples prepared using suspension polymerization [51].

Polycondensation polymerization of polyimide

Polycondensation is a polymerization method that produces a long-chain polymer from single or multiple monomers by releasing water or any related by-products. Aromatic polyimide has gained attention in CO_2 capture applications as this microporous material has outstanding thermal stability, excellent chemical resistance, and abundant heteroatoms [52]. The polycondensation of an aromatic dianhydride and tridimensional geometry amine can produce microporous polyimide with a high specific surface area for excellent CO_2 adsorption.

Ning et al. [53] introduced a new composite adsorbent named PI-UiO/GO-1, which was synthesized using a chemical in situ knitting method involving the reaction among 4,4'-oxydiphthalic anhydride, 2,4,6-trimethyl-1,3-phenylenediamine, UiO-66-NH_2, and graphene oxide (GO). Compared to pristine UiO-66-NH_2, the PI-UiO/GO-1 adsorbent exhibited superior performance, including higher CO_2 capacity, higher CO_2/N_2 selectivity (64.71 compared to 15.43), and significantly improved acid-base resistance stability. Interestingly, grafting polyimide onto UiO-66-NH_2 had no impact on the microporous structure. However, the introduction of C-N covalent bonds and secondary amines in PI-UiO/GOs enhanced the selective adsorption of CO_2. This enhancement was achieved through the interaction between the negative charge of N and O atoms in polyimide and the electrophilic C in CO_2, thereby

enhancing the selectivity and CO_2 adsorption capacity of the adsorbent [53].

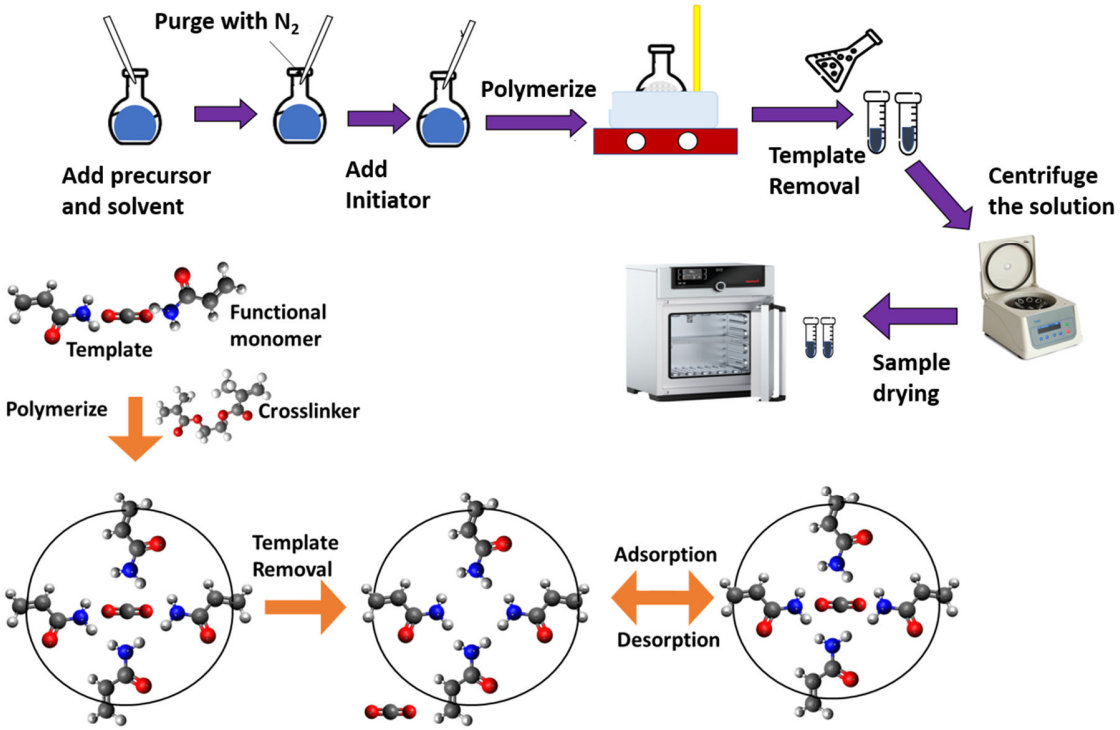

Figure 4. Schematic diagram of the steps in MIP preparation for CO_2 adsorption

Song et al. [54] reported a more simplified and economical method for preparing cross-linkable hyperbranched polyimide for CO_2 capture using polycondensation and thermal cross-linking. The cross-linked structure served as a scaffold that restricted the movement of polyimide chains, thus preventing the polymer skeleton from collapsing and facilitating the formation of micropores [54, 55].

Earlier research described the synthesis of two cross-linked microporous polyimides (i.e., TAPM-PEPA-CL and TAPA-PEPA-CL) using aromatic alkynyl monomers through thermal cross-linking polymerization in diphenyl sulfone [56]. The former exhibited a higher Brunauer-Emmett-Teller (BET) surface area and microporous volume (736 m^2/g and 0.175 cm^3/g, respectively) compared to the latter (351 m^2/g and 0.018 cm^3/g, respectively). Additionally, the adsorption capacity of TAPM-PEPA-CL was significantly enhanced. These results indicate that adjusting the topological structure of cross-linked microporous polyimides can influence their microporosity and CO_2 adsorption performance [56]. Wang et al. [57] also introduced cross-links to linear polyimide by synthesizing linear cross-linked polyimides with porous structures. This adsorbent showed higher porosity with improved CO_2 adsorption (5.7–9.3 wt.%) and good CO_2/N_2 selectivity (34.4–58.5) at 273 K compared to the other linear polyimide [57].

Preparation of covalent triazine framework

A covalent triazine framework (CTF) is often classified as a type of covalent organic framework (COF). It is synthesized through the classical ionothermal cyclotrimerization of a precursor containing carbonitrile groups. Covalent triazine frameworks possess distinctive attributes, including exceptional stability and robustness due to the presence of conjugated aromatic

C=N linkages, making them suitable for various adsorption applications [58, 59]. The design of CTFs allows for controlling the textural, structural, and physicochemical characteristics of the framework by manipulating the geometry, dimensions, and functionalities of the organic building units [60, 61]. Chen et al. [62] reported the preparation of four pyrene-based CTF materials using one-pot ionothermal polymerization. Pyrene units were chosen as the building blocks for forming CTFs due to their strong π–π interactions, which contribute to the dense structure of COFs. Additionally, the π-conjugated system derived from the pyrene group contributed to the overall structural rigidity of the CTFs. These newly developed materials exhibited remarkably high BET surface areas ranging from 1,415 to 1,753 m^2/g, along with notable CO_2 uptake capacities. The triazine-based frameworks have garnered significant interest in CO_2 adsorption research because their carbon backbones contain higher nitrogen content than other frameworks, leading to higher porosity characterized by both micropores and mesopores [62]. Liu et al. [17] prepared triazole-functionalized triazine-based porous organic polymer using copper-catalyzed azide-alkyne cycloaddition (Cu-AAC) polymerization, as shown in Figure 5. The presence of triazine and triazole rings in the CTF chain enriched the nitrogen content, thus enhancing the interaction between CO_2 and this porous material. A triazine ring with a pre-decorated azide functional group was used as the key building block for the synthesis of CTF. The Cu-AAC reaction led to the formation of 1,4-triazole, which showed a considerable CO_2 adsorption capacity of 52.0 cm^3/g at 273 K and 1 bar. They also reported a lower adsorption capacity due to the lower permanent porosity [17]. The CTF can also be prepared through the polycondensation of formamide and triazine-based amine to produce nitrogen-rich microporous polyaminals [63, 64]. The outcome of this reaction yielded various geometric configurations and functionalities, depending on the initial monomers used. As a result, it allowed for the tuning of BET surface areas and pore sizes within a range of 842–1,227 m^2/g and 0.53–3.82 nm, respectively [63]. The adsorption capacity of CO_2 can also be influenced by the pore size and BET surface area [63].

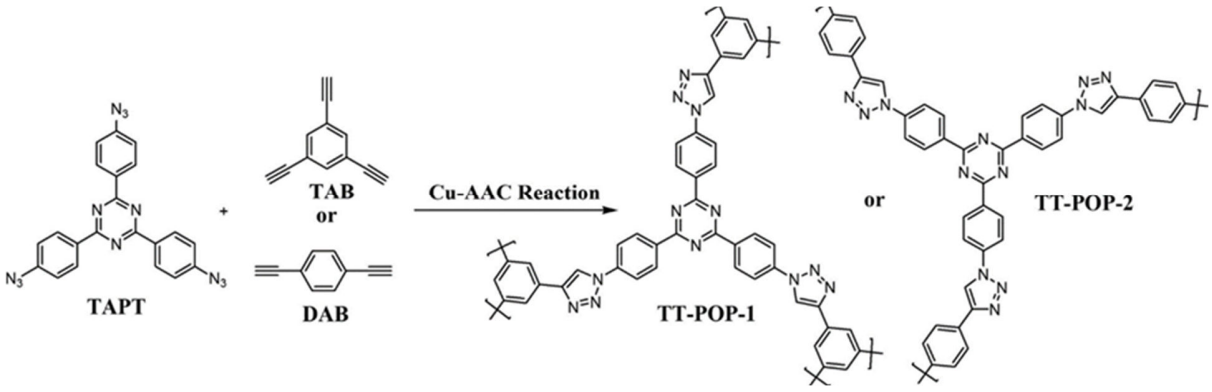

Figure 5. Schematic diagram of the synthesis of triazine-based porous organic polymer [17]

Carbon dioxide adsorption mechanism

Carbon dioxide has two oxygen atoms bonded to a central carbon atom through a covalent double bond. Its linear geometry causes the net molecular dipole moment to be zero, making it a non-polar molecule. Quadrupole interaction, or London dispersion interaction, can form between CO_2 molecules, where the middle carbon carries a partial positive charge and both terminal oxygens carry partial negative charges. The opposite charge that comes into contact forms the quadrupole interaction or electrostatic interaction (+/−). Figure 6 shows the electrostatic potential surfaces of CO_2, illustrating the distribution of charges on the molecular surface. The surfaces plotted in pink indicate the negative potential regions, while the surface in green indicate the most positive region. The surface potential site of CO_2 shows the carbon atom with a positive charge (poor electron) and the oxygen atoms at both ends with

a negative potential (rich electron). The potentials of the positive and negative regions can form electrostatic interactions with electrophilic and nucleophilic regions of other molecules [65, 66].

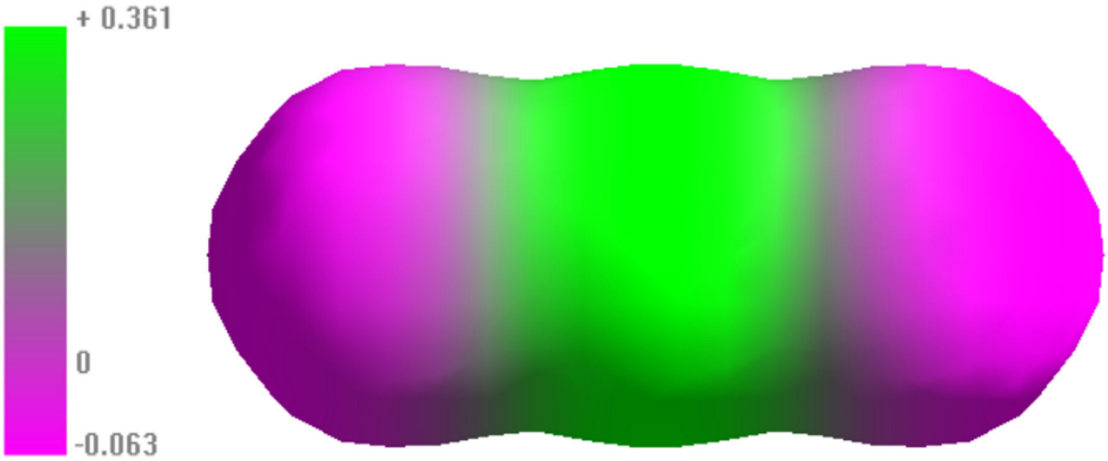

Figure 6. Electrostatic potential surfaces generated for two molecules.

The interaction between CO_2 and an amine (primary or secondary) functional group can lead to the formation of a zwitterion. Faisal et al. [67] reported the mechanism of the reaction between the primary amine of ethylenediamine (RNH_2), which was functionalized onto the surface of mesoporous carbon and reacted with CO_2 to form carbamate ions, as shown in Equation (1). Meanwhile, mesoporous carbon triethylenetetramine, which contains both primary and secondary amines (RNH_2 and R_2NH, respectively), reacted with CO_2, as illustrated in Equation (1) and (2) [67].

$$CO_2 + 2RNH_2 \rightarrow RNH_3^+ + RNHCOO^- \quad (1)$$

$$CO_2 + 2R_1R_2NH \rightarrow R_1R_2NH_2^+ + R_1R_2NCOO^- \quad (2)$$

$$CO_2 + RNH_2 + H_2O \rightarrow HCO_3^- + RNH_3^+ \quad (3)$$

$$RNH_3^+RNHCOO^- + H_2O \rightarrow RNH_2 + HCO_3^-RNH_3^+ \quad (4)$$

$$CO_2 + RN_3 + H_2O \rightarrow HCO_3^- + R_3NH^+ \quad (5)$$

This mechanism is supported by another study that used a different support-free cross-linked PEI sorbent [68]. They reported that primary and secondary amines reacted rapidly with CO_2 to form carbamates, as shown in Equations (1) and (2). This mechanism, which was proposed by Caplow et al. [69], is initiated by the nucleophilic attack of an amine that acts as a Lewis base to form a zwitterion. Later, this zwitterion is deprotonated by another amine acting as a Bronsted base, resulting in the formation of an ammonium carbamate ion [69]. The reaction between an amine and CO_2 in the presence of water can lead to the formation of ammonium bicarbonate, as shown in Equation (3). This reaction involves the interaction between zwitterion and water molecules, whereby only one amino group is needed to interact with one CO_2 molecule instead of two amino groups, as shown in Equations (1) and (2) [68]. The formation of ammonium carbonate can also occur through the hydrolysis of ammonium carbonate, as presented in Equation 4 [70]. In the case of tertiary amines, which possess no hydrogen atom or any weak amine nucleophiles, such as sterically hindered amines, this group of amines does not directly react with CO_2. Hence, water or other strong nucleophiles will attack the electrophilic CO_2 and generate bicarbonate/carbonate, as shown in Equation

(5) [68–71]. The reaction mechanism between CO_2 and amine, whether in a solution or solid adsorbent under dry or humid conditions, depends on the type of nucleophile, the Bronsted base, and the stabilizing component. The strong, stable interaction that forms between CO_2 and amine is the main reason why amine polymer is widely used. Numerous studies have reported the use of amine polymers combined with other porous materials, highlighting their remarkable potential as CO_2 adsorbents. However, extensive research must be done to modify the adsorbents so that they can fulfill this application. Suresh et al. [72] reported that based on an electron density difference map analysis, CO_2 was capable of interacting with oxygen molecules in amide carbonyl via Lewis acid-base reaction. They also reported weak H bonds with phenyl C−H and π−π interactions with the aromatic phenyl group [72]. An intermolecular interaction can form between CTF and CO_2 through the nitrogen-based functional group. Lee et al. [73] and Tan et al. [74] each reported a theoretical study of the intermolecular interaction between melamine and CO_2. The nitrogen atoms in the melamine molecule and the C in the CO_2 molecule (N-C) can interact, including the hydrogen bonds between the H-amine and the O-CO_2 molecule [73,74]. Tumnantong et al. [75] suggested that the adsorption mechanism of the synthesized modified natural rubber (MNR) composite was a combination of physisorption and chemisorption. This was further proven by the kinetic study conducted by the group, where Avrami's kinetic model fitted well with the adsorption kinetics data, showing a high R^2 value (>0.95). The Avrami exponent, n_a reflects the changes in the mechanism during adsorption. In the MNR foam composites, the values ranged from 1.0535 to 1.2469, indicating a complex reaction mechanism.

Application of molecular modeling in adsorption mechanisms

The Hohenberg-Kohn principle is the foundation of the density functional theory (DFT) approach. The electron density function is utilized in molecular simulation. This approach has low computing complexity and can determine the chemical bond energy, forecast the structures of compounds, and predict reaction processes. Table 2 presents a summary of DFT applications in studying the interaction between CO_2 and the polymer. Schukraft et al. [76] conducted a study on the interaction of adsorption sites in triazine-biphenyl HCP with CO_2 adsorption using DFT and in situ diffuse reflectance infrared Fourier transform spectroscopy. The study indicated that the strong intermolecular interaction between HCP and CO_2 was confirmed and compared using experimental infrared spectra and theoretical vibrational bands during CO_2 adsorption.

A study by Dash [66] involved the calculation of binding energy (BE) to study the interaction between a COF polymer containing a triazine group building block and CO_2 using DFT simulation. The results indicate that the BE between the triazine benzene and CO_2 complex is higher than the BE of the triazine benzene and N_2 complex, with approximately 18.1 kJ/mol and 13.47 kJ/mol, respectively. These differences are due to electrostatic interactions. These electrostatic interactions can be classified as dipole-quadrupole and dipole-induced dipole interactions. Moreover, the formation of hydrogen bonds can be explained by the interaction between the hydrogen atom of the aromatic ring and the oxygen atom of CO_2. The strength of the hydrogen bond increases with a greater number of aromatic rings [66]. Xu et al. [77] described the interaction between CO_2 and a polyimide matrix through molecular dynamic simulations. Their analysis through the radial distribution function revealed that CO_2 has greater intermolecular affinity with the polyimide chain; in addition, O and N atoms in the imide groups are identified as the preferred sorption sites for CO_2 molecules [77]. Zhang et al. [78] used four organic amines with different properties to prepare amine-functionalized X-5 adsorbents using the impregnation method. The study involved the strategy of matching mechanisms between different organic amines and porous resins for CO_2 adsorption using DFT calculations to investigate the interaction between the amine and CO_2.

Table 2 Summary of DFT applications in investigating CO_2 interaction mechanism.

Polymer	Purpose	Approach	Software	Ref
Amide-functionalized microporous organic polymer	To analyze CO_2 molecule interactions with amide functional groups via Lewis acid-base type interactions	DFT, geometry optimization by M06-2X/cc-pVTZ level of theory	Gaussian 09 program	[72]
Poly(1-vinylimidazole)	To study how CO_2 interacts with oligomers of n-VIm, where 'n' represents the number of monomers (from 1 to 4)	DFT, geometry optimization by B3LYP–D3/6–311++G* (d, p) level	Gaussian 03 program	[79]
α- and β-Polyvinylidene fluoride (PVDF)-supported imidazolium and pyridinium	To investigate the interaction of PVDF/ionic liquid (IL)-based system with binary mixtures of CO_2, CO, CH_4, and H_2 gases (the gas adsorption interactions involving PVDF tetramers, ILs, and the combinations of PVDF/IL complexes are elucidated by considering various quantum chemical descriptors)	DFT, geometry optimization by B3LYP, along with triple zeta basis set 6-311+G (d, p)	Gaussian 16 program and Gaussview 6.0	[80]
Polyvinyl chloride (PVC)/ polyvinyl imidazole (PVIm)	To analyze the interaction of CO_2 and methane gases with PVC and PVIm	DFT, geometry optimization by B3LYP–D3/6–311++G* (d, p) level	Gaussian 03 program	[81]
Graphene oxide/ polymer composite	To analyze the interaction of CO_2 and nitrogen gases with GO/polymer composite complex	Geometry optimization by DFT using the long-range corrected ωB97XD functional 39 together with the 6–31+G(d) basis set	Gaussian 16 package	[82]

Conclusion and future direction

This review discusses the preparation methods for three types of nitrogen-rich polymers, namely amine-functionalized polymer, amide- and imide-functionalized polymer, and covalent triazine framework. Several limitations, as well as advantages, have been identified in the implementation of these methods. Impregnating silica with high amine loading can cause agglomeration of the adsorbent, which may impact its adsorption capacity. This impregnation method can also suffer from leaching and degradation of amine during the regeneration cycle, which can affect the stability of the adsorbent. Despite these drawbacks, the sample preparation is easy and uses inexpensive chemicals (silica and PEI) compared to other methods. On the other hand, surface grafting is quite costly and requires complex preparation procedures. Nonetheless, this technique can overcome amine leaching, dissolution, and deactivation of the adsorbent. In-depth modification and cross-linking of amine can improve the stability of the adsorbent, even after ten regeneration cycles. Meanwhile, the use of HIPE template during polymerization can produce excellent, stable porous solid amine adsorbents with a three-dimensional interpenetrating network. The monolithic polymer produced from the HIPE template has a greater potential for industrial applications compared to powder adsorbent. This polymer also possesses a high pore

volume and specific surface area. However, the abundance of specific surface area will not benefit CO_2 adsorption as mesopore structures are favored for CO_2 adsorption. Free radical polymerization in the preparation of molecularly imprinted polymer can produce simple and highly selective tailor-made polymers. However, the use of solvents during the washing step can have an impact on the environment. This issue can be addressed by using a greener solvent or reducing the consumption of fresh solvent through recycling or using tools that can assist in the washing step. The use of imide-functionalized polymers in the polycondensation method can produce highly porous polymers with improved adsorption capacity and stability. The disadvantage of this method is that the chemical used is quite expensive and the preparation is complex. In the future, more research related to the formulation and design of materials on a large scale should be emphasized. In-depth analysis should also be considered to determine the cost of preparing the materials and the process involved during the adsorption of CO_2 onto adsorbents. The long-term stability and life-cycle assessment of adsorbents should be studied to determine their environmental impact before undergoing scalable production. Molecular modeling has proven to be a valuable approach for studying CO_2 adsorption and its interaction with various functional materials. The findings reveal that investigations at the molecular level can enhance the understanding of CO_2 interaction mechanisms. This study can greatly contribute to designing and optimizing functional polymers for carbon adsorption and storage purposes.

Acknowledgment

This work was co-supported by the Ministry of Higher Education Malaysia through the Fundamental Research Grant Scheme (FRGS/1/2023/TK05/USM/02/4), with financial support under the SLAB scholarship, and Universiti Sains Malaysia through the Bridging Grant (304/PJKIMIA/6315719). The authors are also thankful to Universiti Malaysia Perlis for providing laboratory facilities.

References

1. Martins, T., Barreto, A.C., Souza, F.M. and Souza, A.M. (2021). Fossil fuels consumption and carbon dioxide emissions in G7 countries: Empirical evidence from ARDL bounds testing approach. *Environmental Pollution*, 291:118093.
2. Nations, U. (2015) Paris Agreement. Paris.
3. Vannak, H., Osaka, Y., Tsujiguchi, T. and Kodama, A. (2024). The efficacy of carbon molecular sieve and solid amine for CO_2 separation from a simulated wet flue gas by an internally heated/cooled temperature swing adsorption process. *Applied Thermal Engineering*, 239: 122145.
4. Energy Technology Perspectives 2020 - Special report on carbon capture utilisation and storage. *Energy Technology Perspectives 2020 - Special Report on Carbon Capture Utilisation and Storage*.
5. Ma, C., Bai, J., Hu, X., Jiang, Z. and Wang, L. (2023). Nitrogen-doped porous carbons from polyacrylonitrile fiber as effective CO_2 adsorbents. *Journal of Environmental Sciences (China)*, 125: 533-543.
6. Wang, X. and Song, C. (2020). Carbon capture from flue gas and the atmosphere: A perspective. *Frontiers in Energy Research*, 2020: 560849.
7. Gelles, T., Lawson, S., Rownaghi, A.A. and Rezaei, F. (2020). Recent advances in development of amine functionalized adsorbents for CO_2 capture. *Adsorption*, 2020: 151.
8. Borhan, A., Yusup, S., Lim, J.W. and Show, P.L. (2019) Characterization and modelling studies of activated carbon produced from rubber-seed shell using KOH for CO_2 Adsorption. *Processes*, 7: 110855.
9. Hu, H. and Xu, K. (2020). Physicochemical technologies for HRPs and risk control. *High-Risk Pollutants in Wastewater*, Elsevier: pp. 169-207.
10. Kwon, D. il, Kim, J.C., Lee, H., Lee, W. and Jo, C. (2022). Engineering micropore walls of beta zeolites by post-functionalization for CO_2 adsorption performance screening under humid conditions. *Chemical Engineering Journal*, 427: 131461.
11. Mochizuki, Y., Bud, J., Byambajav, E. and Tsubouchi, N. (2022). Influence of ammonia treatment on the CO_2 adsorption of activated carbon. *Journal of Environmental Chemical Engineering*, 10: 107273.

12. Ansari, K.B., Gaikar, V.G., Trinh, Q.T., Khan, M.S., Banerjee, A., Kanchan, D.R., Mesfer, M.K. and Danish, M. (2022). Carbon dioxide capture over amine functionalized styrene divinylbenzene copolymer: An experimental batch and continuous studies. *Journal of Environmental Chemical Engineering*, 10: 106910.
13. Varghese, A.M. and Karanikolos, G.N. (2020). CO_2 capture adsorbents functionalized by amine – bearing polymers: A review. *International Journal of Greenhouse Gas Control*, Elsevier, 96: 103005.
14. Hassan, A., Goswami, S., Alam, A., Bera, R. and Das, N. (2021). Triptycene based and nitrogen rich hyper cross linked polymers (TNHCPs) as efficient CO_2 and iodine adsorbent. *Separation and Purification Technology*, 257: 117923.
15. Chen, J., Jiang, L., Wang, W., Shen, Z., Liu, S., Li, X. and Wang, Y. (2022). Constructing highly porous carbon materials from porous organic polymers for superior CO_2 adsorption and separation. *Journal of Colloid and Interface Science*, 609: 775–784.
16. Barbarin, I., Politakos, N., Serrano-Cantador, L., Cecilia, J.A., Sanz, O. and Tomovska, R. (2022). Towards functionalized graphene/polymer monolithic structures for selective CO_2 capture. *Microporous and Mesoporous Materials*, 337: 111907.
17. Liu, X., Du, J., Ye, Y., Liu, Y., Wang, S., Meng, X., Song, X., Liang, Z. and Yan, W. (2022). Boosting selective C_2H_2/CH_4, C_2H_4/CH_4 and CO_2/CH_4 adsorption performance via 1,2,3-triazole functionalized triazine-based porous organic polymers. *Chinese Journal of Chemical Engineering*, 42: 64-72.
18. Shang, Q., Cheng, Y., Gong, Z., Yan, Y., Han, B., Liao, G. and Wang, D. (2022). Constructing novel hyper-crosslinked conjugated polymers through molecular expansion for enhanced gas adsorption performance. *Journal of Hazardous Materials*, 426: 127850.
19. Li, L., Luo, Z., Zou, W., Liang, S., Wang, H. and Zhang, C. (2024). Physicochemical synergistic adsorption of CO_2 by PEI-impregnated hierarchical porous polymers. *Greenhouse Gases: Science and Technology*, 2024: 2263.
20. Liu, Y., Li, S., Pudukudy, M., Lin, L., Yang, H., Li, M., Shan, S., Hu, T. and Zhi, Y. (2024). Melamine-based nitrogen-heterocyclic polymer networks as efficient platforms for CO_2 adsorption and conversion. *Separation and Purification Technology*, 331: 125645.
21. HaiyanYang, Wang, X., Liu, J., Liu, W., Gong, Y. and Sun, Y. (2022). Amine-impregnated polymeric resin with high CO_2 adsorption capacity for biogas upgrading. *Chemical Engineering Journal*, 430: 132899.
22. Liu, L., Jin, S., Park, Y., Kim, K.M. and Lee, C.H. (2021). Sorption equilibria, kinetics, and temperature-swing adsorption performance of polyethyleneimine-impregnated silica for post-combustion carbon dioxide capture. *Separation and Purification Technology*, 266: 118582.
23. Chen, Z., Lv, Z., Sun, Y., Chi, Z. and Qing, G. (2020). Recent advancements in polyethyleneimine-based materials and their biomedical, biotechnology, and biomaterial applications. *Journal of Materials Chemistry B*. 8(15): 2951-2973.
24. Rosu, C., Narayanan, P., Leisen, J.E. and Jones, C.W. (2022). Sequential polymer infusion into solid substrates (SPISS): Impact of processing on sorbent CO_2 adsorption properties. *Separation and Purification Technology*, 292: 121042.
25. Wang, S., Liu, H. and Chen, S. (2022). A strategy to synthesis amine-functional poly(divinylbenzene)HIPEs with controllable porous structure for effective CO_2 adsorption. *Fuel*, 322: 124120.
26. Chen, X., Quan, H., Yu, J., Hu, Y. and Huang, Z. (2024). Development of composite amine functionalized polyester microspheres for efficient CO_2 capture. *Environmental Science and Pollution Research*, 31: 7027–7042.
27. Meng, Y., Ju, T., Meng, F., Han, S., Song, M. and Jiang, J. (2021). Insights into the critical role of abundant-porosity supports in polyethylenimine functionalization as efficient and stable CO_2 adsorbents. *ACS Applied Materials & Interfaces*, 13: 54018–54031.
28. Hack, J., Frazzetto, S., Evers, L., Maeda, N. and Meier, D.M. (2022). Branched versus linear

structure: Lowering the CO_2 desorption temperature of polyethylenimine-functionalized silica adsorbents. *Energies*, 15: 31075.

29. Mohamad, N.A., Nasef, M.M., Nia, P.M., Zubair, N.A., Ahmad, A., Abdullah, T.A.T. and Ali, R.R. (2021). Tetraethylenepentamine-containing adsorbent with optimized amination efficiency based on grafted polyolefin microfibrous substrate for CO_2 adsorption. *Arabian Journal of Chemistry*, 14: 103067.
30. Li, C., Yan, F., Shen, X., Qu, F., Wang, Y. and Zhang, Z. (2021). Highly efficient and stable PEI@Al_2O_3 adsorbents derived from coal fly ash for biogas upgrading. *Chemical Engineering Journal*, 409: 128117.
31. Irani, V., Khosh, A.G. and Tavasoli, A. (2020). Polyethyleneimine (PEI) functionalized metal oxide nanoparticles recovered from the catalytic converters of spent automotive exhaust systems and application for CO_2 adsorption. *Frontiers in Energy Research*, 8: 196.
32. Li, C., Wang, X., Yang, A., Chen, P., Zhao, T. and Liu, F. (2021). Polyethyleneimine-modified amorphous silica for the selective adsorption of CO_2/N_2 at high temperatures. *ACS Omega*, 6: 35389-35397.
33. Choi, C., Kadam, R.L., Gaikwad, S., Hwang, K.S. and Han, S. (2020). Metal organic frameworks immobilized polyacrylonitrile fiber mats with polyethyleneimine impregnation for CO_2 capture. *Microporous and Mesoporous Materials*, 296: 110006.
34. Yin, F., Zhuang, L., Luo, X. and Chen, S. (2018). Simple synthesis of nitrogen-rich polymer network and its further amination with PEI for CO_2 adsorption. *Applied Surface Science*, 434: 514-521.
35. Wang, H., Chen, C., Chen, Y., Wan, H., Dong, L. and Guan, G. (2021). Construction of ultramicropore-enriched N-doped carbons for CO_2 capture: Self-decomposition of polyethyleneimine-based precursor to promote pore formation and surface polarity. *Journal of Environmental Chemical Engineering*, 9: 105046.
36. Yang, C., Xiong, Y., Chen, J., Jin, J. and Mi, J. (2021) Amine-functionalized micron-porous polymer foams with high CO_2 adsorption efficiency and exceptional stability in PSA process. *Chemical Engineering Journal*, Elsevier, 420: 129555.
37. Wang, S., Qiu, X., Chen, Y. and Chen, S. (2022). Preparation and structure tuning of CO_2 adsorbent based on in-situ amine-functionalized hierarchical porous polymer. *Microporous and Mesoporous Materials*, 330: 111585.
38. Wang, S., Wu, J., Ma, N. and Chen, S. (2021). High molecular weight polyethylenimine encapsulated into a porous polymer monolithic by one-step polymerization for CO_2 capture. *New Journal of Chemistry,* 45: 12538-12548.
39. Liu, H., Wang, X., Chen, S. and Chen, S. (2024). Sponge-like polyethyleneimine adsorbents with interconnected open channels enabling ultra-high CO_2 adsorption and separation capacity. *Separation and Purification Technology*, 330: 125528.
40. Choi, W., Park, J., Kim, C. and Choi, M. (2021). Structural effects of amine polymers on stability and energy efficiency of adsorbents in post-combustion CO_2 capture. *Chemical Engineering Journal*, 408: 127289.
41. Wu, J., Zhu, X., Yang, F., Ge, T. and Wang, R. (2021). Easily-synthesized and low-cost amine-functionalized silica sol-coated structured adsorbents for CO_2 capture. *Chemical Engineering Journal*, 425: 131409.
42. Mohamad, N.A., Nasef, M.M., Nia, P.M., Zubair, N.A., Ahmad, A., Abdullah, T.A.T. and Ali, R.R. (2021). Tetraethylenepentamine-containing adsorbent with optimized amination efficiency based on grafted polyolefin microfibrous substrate for CO_2 adsorption. *Arabian Journal of Chemistry*, 14: 103067.
43. Tiainen, T., Mannisto, J.K., Tenhu, H. and Hietala, S. (2022). CO_2 capture and low-temperature release by poly(aminoethyl methacrylate) and derivatives. *Langmuir*, 38: 5197-5208.
44. Deng, J., Liu, Z., Du, Z., Zou, W. and Zhang, C. (2019). Fabrication of PEI-grafted porous polymer foam for CO_2 capture. *Journal of Applied Polymer Science*, 136: 2-8.
45. Liu, F., Kuang, Y., Wang, S., Chen, S. and Fu, W. (2018). Preparation and characterization of molecularly imprinted solid amine adsorbent for

CO_2 adsorption. *New Journal of Chemistry*, 42: 10016-10023.

46. Liu, H., Wang, S., Wang, X., Feng, X.J. and Chen, S. (2022). A stable solid amine adsorbent with interconnected open-cell structure for rapid CO_2 adsorption and CO_2/CH_4 separation. *Energy*, 258: 124899.
47. Nabavi, S.A., Vladisavljević, G.T., Wicaksono, A., Georgiadou, S. and Manović, V. (2017). Production of molecularly imprinted polymer particles with amide-decorated cavities for CO_2 capture using membrane emulsification/suspension polymerisation. *Colloids and Surfaces A: Physicochemical and Engineering Aspects*, 521: 231-238.
48. Nabavi, S.A., Vladisavljević, G.T., Wicaksono, A., Georgiadou, S. and Manović, V. (2017). Production of molecularly imprinted polymer particles with amide-decorated cavities for CO_2 capture using membrane emulsification/suspension polymerisation. *Colloids and Surfaces A: Physicochemical and Engineering Aspects*, 521, 231-238.
49. Yoo, D.K., Yoon, T.U., Bae, Y.S. and Jhung, S.H. (2020). Metal-Organic Framework MIL-101 loaded with polymethacrylamide with or without further reduction: Effective and selective CO_2 adsorption with amino or amide functionality. *Chemical Engineering Journal*, 380: 122496.
50. Fayemiwo, K.A., Chiarasumran, N., Nabavi, S.A., Manović, V., Benyahia, B. and Vladisavljević, G.T. (2020). CO_2 capture performance and environmental impact of copolymers of ethylene glycol dimethacrylate with acrylamide, methacrylamide and triallylamine. *Journal of Environmental Chemical Engineering*, 103536.
51. Su, W., Wang, R. and Zhao, T. (2020). CO_2-imprinted sustainable carbon derived from sunflower heads for highly effective capture of CO_2 from flue gas. *Aerosol and Air Quality Research*, 20: 180-192.
52. Liu, Y., Zhao, X.-Y., Sun, Y.-G., Li, W.-Z., Zhang, X.-S. and Luan, J. (2023). Synthesis and applications of low dielectric polyimide. *Resources Chemicals and Materials*, 2: 49-62.
53. Ning, H., Yang, Z., Yin, Z., Wang, D., Meng, Z., Wang, C., Zhang, Y. and Chen, Z. (2021). A novel strategy to enhance the performance of CO_2 adsorption separation: grafting hyper-cross-linked polyimide onto composites of UiO-66-NH_2 and GO. *ACS Applied Materials & Interfaces*, 13: 17781-17790.
54. Song, N., Ma, T., Wang, T., Li, Z., Yao, H. and Guan, S. (2020). Microporous polyimides with high surface area and CO_2 selectivity fabricated from cross-linkable linear polyimides. *Journal of Colloid and Interface Science*, 573: 328-335.
55. Song, N., Wang, T., Ma, T., Li, J., Yao, H. and Guan, S. (2022). Microporous polyimide networks with tunable micropore size constructed through side-chain engineering of linear precursors. *Polymer*, 255: 125161.
56. Wang, T., Yang, Y., Song, N., Zhu, S., Yao, H., Zhang, Y. and Guan, S. (2021). Thermal crosslinking polymerization of aromatic alkynyl monomers to microporous polyimides in diphenyl sulfone. *Microporous and Mesoporous Materials*, 328: 111447.
57. Wang, T., Yao, H., Song, N., Yang, Y., Shi, K. and Guan, S. (2021). Microporous polymer networks constructed from cross-linkable linear polyimides for CO_2 adsorption. *Microporous and Mesoporous Materials*, 311: 110708.
58. Huang, Q., Zhan, Z., Sun, R., Mu, J., Tan, B. and Wu, C. (2023). Light triggered pore size tuning in photoswitching covalent triazine frameworks for low energy CO_2 capture. *Angewandte Chemie - International Edition*, 62: 5500.
59. Ping, R., Ma, C., Shen, Z., Zhang, G., Wang, D., Liu, F. and Liu, M. (2023). Metalloporphyrin and triazine integrated nitrogen-rich frameworks as high-performance platform for CO_2 adsorption and conversion under ambient pressure. *Separation and Purification Technology*, 310: 123151.
60. Pourebrahimi, S. and Pirooz, M. (2022). Functionalized covalent triazine frameworks as promising platforms for environmental remediation: A review. *Cleaner Chemical Engineering*, 2: 100012.
61. Ngo, H.M., Pal, U., Kang, Y.S. and Ok, K.M. (2023). DFT-based study for the enhancement of

CO_2 adsorption on metal-doped nitrogen-enriched polytriazines. *ACS Omega*, 8: 8876-8884.

62. Chen, Y., Hu, X., Guo, J., Guo, Z., Zhan, H. and Du, S. (2022). Optimizing CO_2 capture and separation in pyrene derived covalent triazine frameworks. *European Polymer Journal*, 171: 111215.
63. Li, G., Zhou, X. and Wang, Z. (2020). Highly nitrogen-rich microporous polyaminals using n, n-dimethylformamide and formamide as the starting monomers for CO_2 adsorption and separation. *Journal of Physical Chemistry C*, 124: 3087-3094.
64. Zhang, B., Yan, J., Li, G. and Wang, Z. (2019). Cost-effective preparation of microporous polymers from formamide derivatives and adsorption of CO_2 under dry and humid conditions. *Polymer Chemistry*, 10: 3371-3379.
65. Alkorta, I. and Legon, A.C. (2018) An ab initio investigation of the geometries and binding strengths of tetrel-, pnictogen-, and chalcogen-bonded complexes of CO_2, N_2O, and CS_2 with simple Lewis bases: some generalizations. *Molecules*, 23: 92250.
66. Dash, B. (2018). Carbon dioxide capture using covalent organic frameworks (COFs) type material-a theoretical investigation. *Journal of Molecular Modeling*, 24: 3646.
67. Faisal, M., Pamungkas, A.Z. and Krisnandi, Y.K. (2021). Study of amine functionalized mesoporous carbon as CO_2 storage materials. *Processes*, 9: 1-13.
68. Wang, F., Yu, L., Li, Y. and Huang, D. (2021). CO_2 adsorption capacity of organic alkali sorbent CPEI from polyethyleneimine. Adsorption Science and Technology, 2021: 6629365.
69. Caplow, M. (2002). Kinetics of carbamate formation and breakdown. *Journal of the American Chemical Society*, 90: 6795-6803.
70. Said, R. ben, Kolle, J.M., Essalah, K., Tangour, B. and Sayari, A. (2020). A unified approach to CO_2 −amine reaction mechanisms. *ACS Omega*, 5: 44.
71. v. Kortunov, P., Siskin, M., Saunders Baugh, L. and C. Calabro, D. (2015). In situ nuclear magnetic resonance mechanistic studies of carbon dioxide reactions with liquid amines in aqueous systems: New insights on carbon capture reaction pathways. *Energy & Fuels*, 29: 5919-5939.
72. Suresh, V. M., Bonakala, S., Atreya, H. S., Balasubramanian, S., and Maji, T. K. (2014). Amide functionalized microporous organic polymer (Am-MOP) for selective CO_2 sorption and catalysis. *ACS Applied Materials & Interfaces,* 6(7): 4630-4637.
73. Lee, H.M., Youn, I.S., Saleh, M., Lee, J.W. and Kim, K.S. (2015). Interactions of CO_2 with various functional molecules. *Physical Chemistry Chemical Physics*, 17: 673.
74. Tan, M.X., Zhang, Y. and Ying, J.Y. (2013). Mesoporous poly(melamine-formaldehyde) solid sorbent for carbon dioxide capture. *ChemSusChem*, 6: 107.
75. Tumnantong, D., Panploo, K., Chalermsinsuwan, B., Prasassarakich, P. and Poompradub, S. (2021). Carbon dioxide adsorption of diallylamine-modified natural rubber with modified silica particles. *Express Polymer Letters*, 15: 899-909.
76. Schukraft, G.E.M., Itskou, I., Woodward, R.T., Van Der Linden, B., Petit, C. and Urakawa, A. (2022). Evaluation of CO_2 and H_2O adsorption on a porous polymer using DFT and in situ DRIFT spectroscopy. *Journal of Physical Chemistry B*, 126: 3912.
77. Xu, Y., Zhou, Z., Guo, Y., Liu, L., Xu, Y., Qiao, C. and Jia, Y. (2022). Carbon dioxide detection using polymer-coated fiber bragg grating based on volume dilation mechanism and molecular dynamics simulation. *Applied Surface Science*, 584: 152616.
78. Zang, P., Tang, J., Zhang, H., Wang, X., Zhao, P., Cui, L., Chen, J., Zhao, P. and Dong, Y. (2024). Insights into amine-resin matching strategy for CO_2 capture: Adsorption performance tests and mechanistic investigation. *Separation and Purification Technology*, 331: 125622.
79. Mehrdad, A. and Noorani, N. (2019). Study of co_2 adsorption onto poly(1–vinylimidazole) using quartz crystal microbalance and density functional theory methods. *Journal of Molecular Liquids*, 291:111288.
80. Sarkar, R. and Kundu, T.K. (2021). Density Functional theory-based analyses on selective gas separation by β-PVDF-supported ionic liquid

membranes. *Journal of Molecular Graphics and Modelling*, 108: 108004.

81. Noorani, N. and Mehrdad, A. (2019). Adsorption, permeation, and DFT studies of PVC/PVIm blends for separation of CO_2/CH_4. *Journal of Molecular Liquids*, 292: 111410.
82. Stankovic, B., Barbarin, I., Sanz, O. and Tomovska, R. (2022). Experimental and theoretical study of the effect of different functionalities of graphene oxide / polymer composites on selective CO_2 capture. *Scientific Reports*, 2022: 1-13.

Malaysian Journal of Analytical Sciences Vol 28 No 3 2024

Nano and Advanced Materials Analysis 480-488

1. THE CONVERSION OF CELLULOSE TO GLUCOSE USING NOBLE METAL PLATINUM SUPPORTED ON ZEOLITE
Puteri Nurain Syahirah Megat Muhammad Kamal, Nor Farisha Farhana Mohd Zaid, and Amin Safwan Alikasturi

Organic and Inorganic Analysis

2. SYNTHESIS AND MODELLING OF FUNCTIONALIZED UiO-66 METALORGANIC FRAMEWORKS FOR GAS ADSORPTION 489-499
Tuan Nurul Azura Tuan Kob@Yaakub, Mohd Basyaruddin Abdul Rahman, Felipe Gandara, and Muhammad Alif Mohammad Latif

Nano and Advanced Materials Analysis

3. NANOCRYSTALLINE CELLULOSE EXTRACTED FROM DISCARDED CIGARETTE BUTTS 500-511
Muhammad Hafiz Azlan, Khairatun Najwa Mohd Amin, and Noraziah Abu Yazid

Organic and Inorganic Analysis

4. SYNTHESIS AND CHARACTERISATION OF REUSABLE PVA-SODIUM ALGINATE-Ni CATALYST IN HECK REACTION 512-521
Norul Azilah Abdul Rahman, Nurul Afiqah Mohd Haris, Karimah Kassim, Mazni Musa, and Nur Rahimah Said

Environmental Analysis

5. METHANOGEN INHIBITOR EFFECT ON ANAEROBIC DEGRADATION OF 1,2-DICHLOROETHANE BY SUNGAI ULAR SEDIMENT 522-529
Nur Intan Shaheera Nuralhuda, Muhammad Haikal Muhaimin Ariza Fattah, Nur Kholis Zulkifli, and Siti Hatijah Mortan

Computational Analysis

6. INVESTIGATIONS ON THE INCLUSION OF BETULINIC ACID INTO CDMOF-1 PERFORMED BY QUANTUM MECHANICS CALCULATIONS AND MOLECULAR DOCKING SIMULATION 530-542
Saurelle Kenfack Tiofack, Mostafa Yousefzadeh Borzehandani, Patrice Kenfack Tsobnang, Muhammad Alif Mohamad Latif, Bimo Ario Tejo, Haslina Ahmad, Jean Ngoune, and Mohd Basyaruddin Abdul Rahman

Nano and Advanced Materials Analysis

7. UNVEILING THE IMPACT OF BACTERIAL CELLULOSE DERIVED FROM NATA DE COCO AND SORBITOL ON BIOCOMPOSITE FILM PROPERTIES FOR POTENTIAL FOOD PACKAGING 543-554
Sharifah Fathiyah Sy Mohamad, Nur Fikriyah Yaacob, and Intan Anak Ekong

Organic and Inorganic Analysis

8. GLYCEROL ACETYLATION INTO ACETINS OVER SnO_2-BASED BIMETALLIC OXIDE CATALYST 555-568
Ain Arisya Azami, Irmawati Ramli, Shera Farisya Mohamad Rasid, Muhammad Shamirul Khairu Lail, Mohd Rafein Zakaria, and Sarwat Iqbal

Environmental Analysis

9. MICROPLASTIC POLLUTION IN MALAYSIA: STATUS AND CHALLENGES - A BRIEF OVERVIEW 569-585
Nurul Shahfiza Noor, Noorfatimah Yahaya, Nur Nadhirah Mohamad Zain, Nik Nur Syazni Nik Mohamed Kamal, Mohd Syahir Mansor, Mohd Yusmaidie Aziz, and Maisarah Nasution Waras

Organic and Inorganic Analysis

10. SYNTHESIS AND MOLECULAR DOCKING SIMULATION OF CINNAMIC ACIDS DERIVATIVES AGAINSTS DENV2 NS2B/NS3 586-602
Nadia Mohamed Yusoff, Siti Nor Khadijah Addis, Nurul Huda Abdul Wahab, Fauziah Abdullah, and Asnuzilawati Asari

Analytical Method

11. FORMULATION AND EVALUATION OF BODY SCRUB USING PINEAPPLE WASTE AS NATURAL EXFOLIATOR 603-610
Nur Aisha Ahmi, and Siti Fatimah Sabran

Analytical Method

12. A REVIEW ON CONVERSION OF MICROPLASTICS INTO VALUE-ADDED PRODUCTS: CHALLENGES AND PERSPECTIVES 611-631
Nurul Mohd Ridzuan Afifah, Jennifer Janani Sathiaseelan, Seng Hon Kee, Tan Suet May Amelia, Wei Yien Lua, Nazli Aziz, Wan Mohd Afiq Wan Mohd Khalik, Sevakumaran Vigneswari, and Kesaven Bhubalan

Analytical Method

13. INNOVATOVE ECO-FRIENDLY WOOD ADHESIVE FORMULATIONS:EXPLORING THE EFFICACY OF GELATINIZED CASSAVA STARCH AND POLYVINYL ALCOHOL CROSSLINKED WITH CITRIC ACID 632-644
Bima Prasetya Pancasakti, Danang Tri Hartanto, Vincent Sinarta, Masyta Dinda Riani, and Budhijanto

Analytical Method

14. EXPLORING DEEP EUTECTIC SOLVENTS AS A POTENTIAL SOLVENT FOR THE EXTRACTION OF FOOD ADDITIVE ALLURA RED IN FOOD TECHNOLOGY APPLICATION 645-663
Thanussha Elangovan, Nor Munira Hashim, Nurina Izzah Mohd Husani, Noorfatimah Yahaya, Farhanini Yusoff, and Nur Nadhirah Mohamad Zain

Analytical Method

15. AUTHENTICATION OF CLOVE LEAF OIL IN PRODUCTS (*Syzygium aromaticum* (L.) Merr. & L. M. Perry) USING GC-MS AND FTIR METHODS COMBINED WITH CHEMOMETRIC 664-680
Any Guntarti, Laela Hayu Nurani, Putri Lestari, Citra Ariani Edityaningrum, Lalu Muhammad Irham, and Abdul Rohman

Organic and Inorganic Analysis

16. SYNTHESIS OF TIN DOPED ZINC OXIDE (TZO) NANOWIRES: EFFECT ON DYE ADSORPTION 681-693
Nur Fairuz Rostan, Mohd Firdaus Malek, Maryam Mohammad, Nurul Zulaikha Mohd Zambri, Nurfatini Atiqrah Khairul Azhar, Zahidah Othman, Kevin Alvin Eswar, Irmaizatussyehdany Buniyamin, Noor Asnida Asli, Mohd Yusri Abdul Rahman, Mohamad Hafiz Mamat and Mohamad Rusop Mahmood

Analytical Method

17. MEMBRANE-PROTECTED MICRO-SOLID PHASE EXTRACTION OF CARCINOGENIC AROMATIC AMINES IN WATER SAMPLES PRIOR TO GC-FID ANALYSIS 694-710
Anjalee Pushpika Patabendi, Mohamad Shariff Shahriman, Hemavathy Surikumaran, Nur Nadhirah Mohamad Zain, Noorfatimah Yahaya, Faizah Mohammad Yunus, Usman Abdullahi Usman, Kavirajaa Pandian Sambasevam, and Muggundha Raoov

Organic and Inorganic Analysis

18. SYNTHESIS, CHARACTERIZATION AND BIOLOGICAL EVALUATION OF NOVEL THIAZOLIDINEDIONE DERIVATIVES AS EMERGING ANTIDIABETIC AGENTS 711-723
Shaik Munwar, M K Kathiravan, and Ilango K

Malaysian Journal of Analytical Sciences (MJAS)
Published by Malaysian Analytical Sciences Society

THE CONVERSION OF CELLULOSE TO GLUCOSE USING NOBLE METAL PLATINUM SUPPORTED ON ZEOLITE

(Penukaran Selulosa kepada Glukosa Menggunakan Mangkin Logam Adi Platinum Disokong pada Zeolit)

Puteri Nurain Syahirah Megat Muhammad Kamal, Nor Farisha Farhana Mohd Zaid, and Amin Safwan Alikasturi*

Universiti Kuala Lumpur Branch Campus Malaysian Institute of Chemical and Bioengineering Technology, Lot 1988 Vendor City, Taboh Naning, 78000 Alor Gajah, Melaka, Malaysia

Corresponding author: aminsafwan@unikl.edu.my

Received: 15 September 2023; Accepted: 31 March 2024; Published: 29 June 2024

Abstract

Today, the chemical industry faces tremendous pressure to make breakthroughs in green materials, biofuels, and sustainable chemicals. In fact, the goal is to move industrial methods and technologies toward those that are cost-effective and environmentally friendly. Chemical transformation of renewable resources is essential to ensure the long-term sustainability of chemicals and to make sure that energy is sufficient for society in the future. The focus of this study was on the conversion of cellulose to glucose using platinum supported on zeolite as a catalyst. Wet impregnation method was employed to synthesize the catalyst, which was then characterized by thermogravimetric analysis (TGA), Fourier transform infrared (FTIR) spectroscopy, and Brunauer-Emmett-Teller (BET) analysis. According to the catalyst characterization performed using TGA, the nitrate precursors of the catalyst decomposed at temperatures between 200 and 280 °C. The finding was verified by FTIR, which showed a diminishing intensity of the peak around 1450–1300 cm^{-1}, indicating that the catalyst was free of precursors. Subsequently, the catalyst was calcined at 500 °C for 5 h. It is noteworthy that this catalyst has a large surface area of up to 648.13 m^2/g. A catalytic reaction study on the conversion of cellulose to glucose was carried out to investigate several factors, including substrate loading and catalyst loading. It was discovered that 0.4 g of cellulose and 0.1 g of platinum supported on zeolite contributed to a high yield of glucose and conversion of cellulose (22.07% and 54.9%, respectively). The study shows that the chemical transformation of cellulose to glucose is possible with the supported noble metal catalyst.

Keywords: cellulose, glucose, heterogeneous catalyst, platinum supported on zeolite, supported noble metal catalyst

Abstrak

Industri kimia pada masa kini menghadapi tekanan yang sangat besar untuk melakukan penemuan dalam bahan hijau, bahan bakar-bio, dan bahan kimia yang mapan. Malah, matlamatnya adalah untuk menggerakkan kaedah dan teknologi perindustrian ke arah yang kos efektif dan mesra alam. Transformasi kimia bagi bahan boleh diperbaharui adalah penting untuk memastikan keberlanjutan jangka panjang bahan kimia dan tenaga yang mencukupi untuk masyarakat pada masa hadapan. Oleh itu, fokus kajian ini adalah kepada penukaran selulosa kepada glukosa menggunakan platinum yang disokong pada zeolit sebagai mangkin. Kaedah pengisitepuan basah digunakan untuk mensintesis mangkin, dan ia kemudiannya dicirikan oleh analisis termogravimetri

(TGA), spektroskopi inframerah transformasi Fourier (FTIR), dan analisis Brunauer-Emmett-Teller (BET). Menurut pencirian mangkin yang dilakukan menggunakan TGA, prekursor nitrat daripada mangkin boleh diuraikan pada suhu antara 200 dan 280 °C. Penemuan ini telah disahkan oleh FTIR yang menunjukkan keamatan puncak yang semakin berkurangan sekitar 1450–1300 cm^{-1}, menunjukkan mangkin adalah bebas daripada prekursor. Seterusnya, mangkin dikalsin pada 500 °C selama 5 jam. Selain itu, mangkin ini didapati mempunyai luas permukaan yang besar sehingga 648.13 m^2/g. Kajian tindak balas mangkin mengenai penukaran selulosa kepada glukosa telah dijalankan untuk menyiasat beberapa faktor, termasuk pemuatan substrat dan pemuatan mangkin. 0.4 g selulosa dan 0.1 g platinum yang disokong pada zeolit didapati menyumbang kepada hasil glukosa dan penukaran selulosa yang tinggi (masing-masing 22.07% dan 54.9%). Kajian menunjukkan bahawa transformasi kimia selulosa kepada glukosa menunjukkan potensi dengan pemangkin logam adi yang disokong.

Kata kunci: selulosa. glukosa, mangkin heterogen, platinum disokong pada zeolit, mangkin logam adi sokongan

Introduction

The conversion of cellulose, the most abundant biomass on Earth, into valuable chemicals such as glucose, has gained significant attention in recent years due to its potential as a sustainable alternative to traditional fossil fuel-based processes [1]. The preference for utilizing biomass-derived resources is because these feedstocks do not compete with the food supply [2].

Glucose is utilized as a starting chemical in the chemical industry to produce various valuable compounds through biochemical and chemical processes. It serves as a renewable and abundant source for the synthesis of numerous products, including 5-hydroxymethylfurfural, levulinic acid, ethanol, organic acids (e.g., citric acid and gluconic acid), amino acids (e.g., lysine and glutamic acid), and polyols (e.g., sorbitol and xylitol) [3]. Glucose is also a key precursor in the synthesis of pharmaceuticals, polymers, and bio-based materials. Its versatility and availability make it an important starting material for diverse applications in the chemical industry, contributing to sustainable and environmentally friendly production processes.

Catalytic systems play a crucial role in facilitating this conversion, and researchers are continually exploring new catalysts to enhance the efficiency and selectivity of the reaction. One promising approach is the utilization of supported noble metal catalysts as heterogeneous catalysts, which have demonstrated remarkable performance in various biomass conversion reactions. Previously, homogeneous catalysts such as mineral acids, acidic ionic liquids, heteropolyacids, and Lewis acids (e.g., Al, Zr, and Cr salts) were utilized for cellulose degradation. Despite their high efficiency in catalyzing cellulose conversion, homogeneous catalysts pose several challenges, including equipment corrosion, high separation costs, and environmental pollution. Although homogeneous catalysts are extensively utilized in industry, they have inherent drawbacks that add complexity to the process. These drawbacks include low stability, difficulties in isolating and separating the final product from the reaction mixture, and the need for recycling expensive noble metals or ligands [4].

Zeolites are crystalline aluminosilicates with well-defined nanoporous structures, which possess both Brønsted and Lewis acid sites, provide a high surface area and shape-selective properties, and offer excellent support for catalytic species [5]. Due to their adjustable acidity, exceptional thermal stability, and impressive shape-selective properties, zeolites have proven effective in dehydrating cellulose in water. The porous nature of zeolites also allows for easy access to reactants and products, facilitating efficient mass transfer. The incorporation of noble metals, such as platinum (Pt), palladium (Pd), and gold (Au) onto zeolite, on the other hand, results in unique catalytic properties, such as high activity, selectivity, and resistance to deactivation, making them ideal candidates for biomass conversion [6].

Several recent journal articles have highlighted the effectiveness of noble metals supported on zeolite catalysts for cellulose conversion. For example, Negoi et al. investigated the catalytic performance of noble metal-supported zeolites in the hydrolysis of cellulose to sorbitol [7]. The authors demonstrated that the catalyst exhibited remarkable activity and selectivity (85%) toward sorbitol production, with a yield of over 50%

under mild reaction conditions. In another study, Ya'Aini et al. employed zeolite as the catalyst for converting glucose to levulinic acid (LA) [8]. The researchers observed that the catalyst exhibited excellent stability and selectivity, achieving a high LA yield of 65% under optimized reaction conditions. The catalyst also demonstrated good recyclability, making it a promising candidate for industrial-scale applications.

These recent findings underscore the potential of noble metals supported on zeolite as heterogeneous catalysts for the conversion of cellulose to glucose. The combination of noble metals' unique catalytic properties with the advantageous features of zeolite support holds great promise for the development of efficient and sustainable processes for biomass utilization. Hence, in this study, we investigated the impact of catalyst and cellulose loading on the conversion of cellulose to glucose, utilizing Pt supported on zeolite. Further research and optimization of these catalyst systems are expected to pave the way for the commercial production of valuable chemicals from cellulose, contributing to the advancement of green chemistry and the transition toward a more sustainable future.

Materials and Methods

Materials

The catalyst was synthesized using platinum (IV) nitrate ($Pt(NO_3)_2$) with 15% w/w of Pt and zeolite Y purchased from Sigma-Aldrich. For the reaction work, microcrystalline cellulose (extra pure, 100%) from Acros Organics and glucose (>99.9%) were employed as the substrate and for standard reference calibration purposes, respectively. All the chemicals were of analytical grade and used without further purification unless otherwise stated. Distilled water was utilized for all the experiments.

Catalyst synthesis

The catalyst was synthesized through the wet impregnation method, which aimed to bind the active sites to the support material. $Pt(NO_3)_2$ and zeolite Y were employed for catalyst preparation. The objective was to achieve a Pt content of 4 wt.% on the zeolite support. Initially, the zeolite was weighed using an analytical balance and evenly distributed on a Petri dish. Subsequently, 1.3g of $Pt(NO_3)_2$ was diluted with 2 mL of distilled water. The Pt solution was then dropped onto the zeolite sample in four separate batches using a syringe. During each application, the first 0.5 mL of the Pt solution was dropped in a circular motion, and the dispersion was carefully spread using a spatula. These steps were repeated until the entire Pt solution had been used. Following the impregnation process, the catalyst was dried in an oven at 120 °C overnight to eliminate any residual water content. Subsequently, the catalyst underwent calcination in a furnace for a duration of 5 h at a temperature of 500 °C. Finally, the catalyst was allowed to cool in a desiccator and then stored in a vial for future use.

Catalyst characterization

The catalyst underwent characterization through several analytical techniques, including thermogravimetric analysis (TGA), Fourier transform infrared (FTIR) spectroscopy, and Brunauer-Emmett-Teller (BET) analysis. A Mettler-Toledo STARe software system was used for TGA. Approximately 5–10 mg of the catalyst was weighed using an analytical balance and placed in an alumina crucible. The analysis was conducted over a temperature range from ambient (30 °C) to 600 °C, utilizing a heating rate of 15 °C/min and a continuous flow of high-purity air at 20 mL/min. The FTIR analysis was carried out using a Nicolet iS10 FTIR spectroscopy instrument, with a spectral range from 4000 cm^{-1} to 400 cm^{-1}. The spectral resolution was set at 8 cm^{-1}, and five scans were accumulated under an open-beam air background at room temperature. A Micromeritics 3Flex surface characterization analyzer was used to determine the surface area and pore volume of the catalyst. Prior to analysis, the catalyst was degassed for 12 h at 150 °C in nitrogen (N_2).

Reaction study

The pre-reduction of the catalyst was conducted in a 20 mL stainless steel batch reactor. Initially, 0.1g of catalyst and 10 mL of distilled water were loaded into the reactor. The pre-reduction process was carried out under conditions of 1 bar of hydrogen (H_2) at a temperature of 150 °C for a duration of 1 hr. Following the pre-reduction of the catalyst, 0.4g of cellulose was introduced into the reactor in preparation for the

subsequent reaction. The reactor was purged three times with N_2 to remove any residual air. Subsequently, the reactor was placed in an oil bath on a magnetic stirring hot plate. Once the desired temperature was reached, the stirrer and timer were set to initiate the catalytic reaction. The reactor was rapidly cooled by immersing it in a water bath to halt the reaction. The resulting product was collected and subjected to filtration. Liquid products were filtered using cotton wool, while solid products were filtered through filter paper. Following the filtration process, the liquid product was stored in a vial in preparation for high-performance liquid chromatography (HPLC) analysis. For the solid product, the filter paper was dried in an oven for 12 h at 80 °C, and the weights of the filter paper before and after drying were recorded to calculate cellulose conversion.

Product analysis

The liquid products obtained from the reaction were identified and quantified through HPLC with a refractive index detector. For this analysis, a mobile phase of 0.005 M sulfuric acid with a flow rate of 0.5 mL/min was utilized. The column temperature was maintained at 40 °C throughout the analysis.

Results and Discussion

Catalyst characterization: TGA

Based on the TGA data presented in Figure 1, two distinct weight losses were observed in the temperature ranges of 50–100 °C (I) and 210–280 °C (II) for the catalyst prior to calcination. The initial weight loss can be attributed to the removal of adsorbed water [9, 10], while the subsequent weight loss is associated with the decomposition of nitrates and the elimination of organic compounds [11, 12]. Notably, beyond 300 °C, no additional weight loss was noted, indicating the absence of further decomposition. Consequently, a calcination temperature of 500 °C was selected to ensure complete decomposition of nitrate precursors.

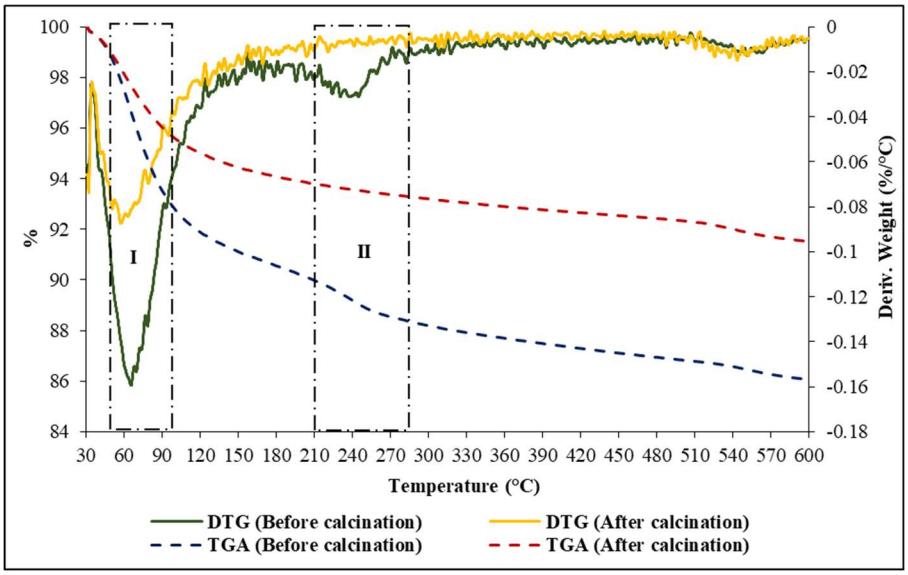

Figure 1. TGA and DTG of Pt/zeolite (before and after calcination)

Following the calcination process, the catalyst exhibited a single weight loss, which occurred within the temperature range of 50–100 °C, as indicated by the TGA pattern in Figure 1. Importantly, no weight loss was detected at temperatures exceeding 100 °C, signifying the complete decomposition of nitrates. Therefore, it is noteworthy that the optimal calcination temperature for achieving a precursor-free catalyst is 500 °C [13]. This observation aligns with the FTIR analysis results, which reveal the absence of nitrate peaks in the catalyst after calcination.

Catalyst characterization: FTIR

According to the FTIR spectra presented in Figure 2, the

spectral region from 3600 to 3200 cm^{-1} (I) is associated with the stretching and bending modes related to water molecules and their hydrogen bonding [14,15]. The O–H stretch bands observed at 3600–3200 cm^{-1} in the catalyst before calcination appear broader compared to those in the catalyst after calcination, owing to the expansion and contraction absorption of hydrogen bonds. This finding is supported by Jamal et al. [16], who also observed widened bands in their study. They examined various calcination temperatures and noted that lower temperatures resulted in broader bands at 3600–3200 cm^{-1}. This broadening effect is attributed to a decrease in the peak mode of O–H bond elongation and bending as the calcination temperature rises, which could reduce the absorption of water molecules on the catalyst surface.

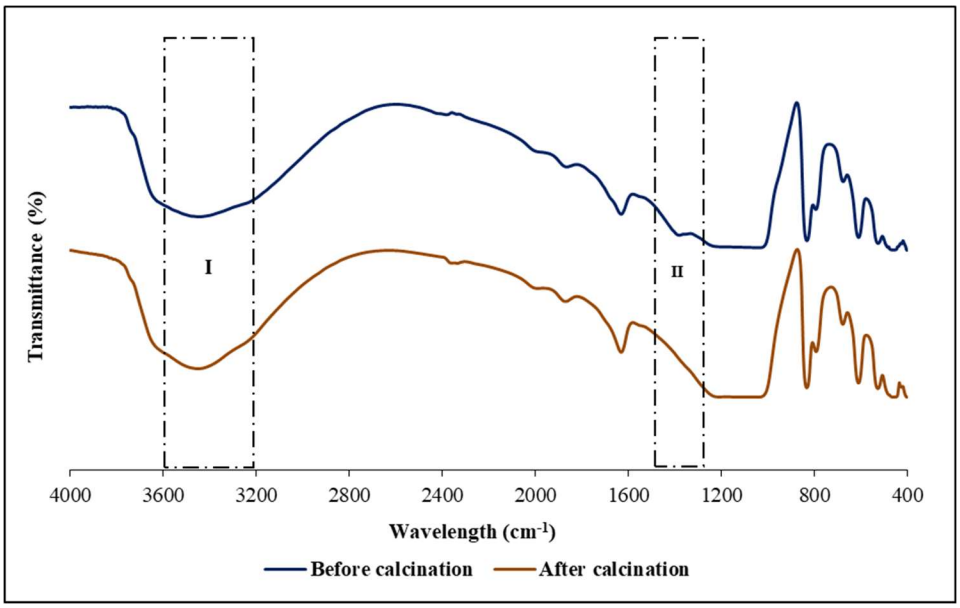

Figure 2. FTIR spectra of Pt/zeolite (before and after calcination)

In contrast, the spectral region between 1450 and 1300 cm^{-1} (II) signifies the presence of nitrate precursor ions (NO_3^-) within the catalyst prior to calcination [15,17]. Significantly, these NO_3^- bands were observed to disappear in the catalyst after undergoing calcination, providing clear evidence that nitrate decomposition was effectively accomplished at the calcination temperature of 500 °C. Consequently, it is important to highlight that the optimal temperature for eliminating the nitrate precursor is 500 °C.

Catalyst characterization: BET

Based on Table 1, the surface area and pore volume of the catalyst before calcination were notably high (665.40 m^2/g and 0.3575 cm^3/g, respectively). However, these values experienced a slight decrease after catalyst calcination. Nevertheless, the reduction observed in both surface area and pore volume amounted to only 17.21 m^2/g and 0.0128 cm^3/g, respectively. According to the findings by Baharudin et al., this decrease in surface area can be attributed to particle aggregation during calcination [18]. It is worth noting that despite the reduction in surface area and pore volume due to calcination, this process has the potential to maintain the structural stability of the catalyst [19]. Furthermore, it is important to highlight that even after calcination, the catalyst still retains a substantial surface area and pore volume, measuring up to 648.13 m^2/g and 0.3447 cm^3/g, respectively, in comparison to previous research [13].

Table 1. BET surface area and pore volume of catalysts

Sample	Surface Area[a] (m^2/g)	Pore Volume[b] (cm^3/g)
Pt/zeolite (Before calcination)	665.40	0.3575
Pd/zeolite (After calcination)	648.13	0.3447

[a]: Surface area was obtained from the BET method, [b]: Pore volume was obtained from the BET method.

Effect of cellulose loading on the yield of glucose and conversion of cellulose

As illustrated in Figure 3, it becomes evident that as the cellulose loading increases from 0.2g to 0.3g, both the yield of glucose and the conversion of cellulose exhibit a consistent increase. However, when cellulose loading further increased from 0.4g to 0.5g, there is a noticeable decrease in glucose yield and cellulose conversion. This observed trend aligns with the outcomes of prior studies conducted by Joshi et al. and Zhang et al. [12,20]. Several factors may contribute to this condition, including potential product feedback inhibition, a reduction in reactivity, or an insufficient dosage of catalyst for increased cellulose content. Moreover, higher cellulose loading might increase the likelihood of reactive compounds colliding and initiating cross-polymerization, leading to the formation of undesired products [21]. Consequently, the increase in cellulose loading ultimately results in the saturation of the catalyst's optimal surface area and active site availability.

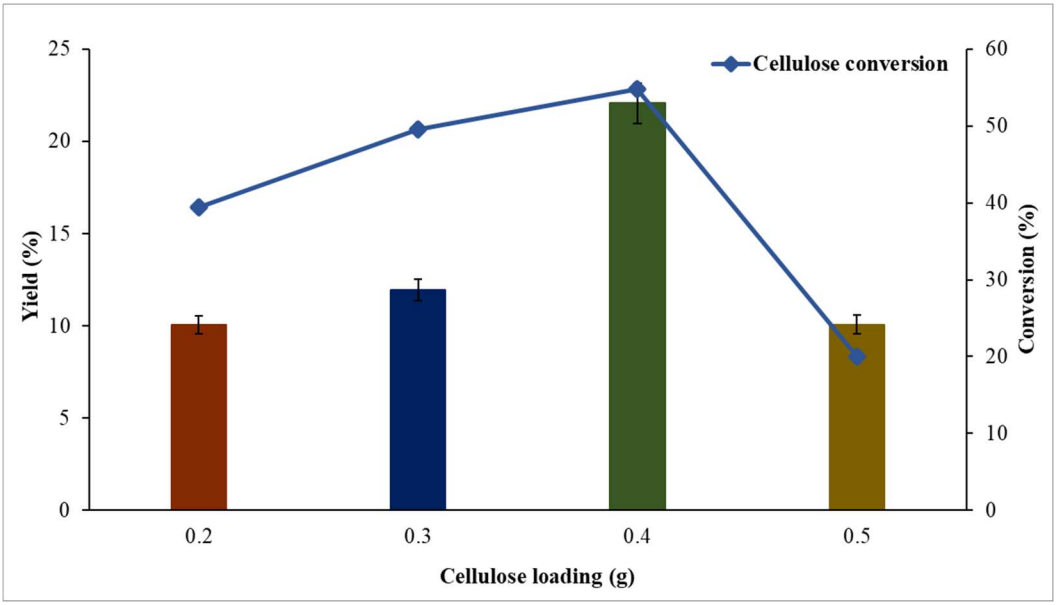

Figure 3. Effect of cellulose loading on the yield of glucose and cellulose conversion at 15 min

Note: a) Pre-reduction of catalyst conditions: 10 mL of distilled water, agitation speed of 1300 rpm, and 1 bar of H_2 for 1 h at 150 °C, b) Reaction conditions: 0.1 g of cellulose, reaction temperature of 210 °C, agitation speed of 1100 rpm, and reaction time of 15 min.

Effect of catalyst loading on the yield of glucose and conversion of cellulose

As shown in Figure 4, the highest cellulose conversion and glucose yield were 54.9% and 22.1%, respectively, when 0.1g of catalyst was employed in the reaction. It is worth noting that as the catalyst loading increased from 0.04g to 0.1g, both glucose yield and cellulose conversion also exhibited an increasing trend. This condition can be attributed to the increasing availability of active sites on the catalyst, which allows more

cellulose to enter and break down into the desired product at an accelerated rate. The lowest glucose production was observed when using 0.04g of the catalyst due to the limited number of active sites available to efficiently convert cellulose into glucose. This observation aligns with findings from other studies, such as those conducted by Wang et al. [21] and Zhang et al. [20], which demonstrated that increasing catalyst loading favored higher product yields. However, Kamal et al. found an opposite trend, where an increase in catalyst loading led to a decrease in glucose yield and cellulose conversion [22]. This might be attributed to unwanted side reactions occurring at higher catalyst loadings. Additionally, high catalyst loading could increase the viscosity of the reaction mixture, resulting in a slower reaction [23]. This leads to reduced mixing efficiency and increased mass transfer resistance within the mixture, ultimately limiting the availability of cellulose for the reaction. Consequently, it is important to refrain from adding additional catalyst once the required amount for the reaction has been reached.

The introduction of the catalyst accelerates the progress of the reaction. The use of the catalyst does not alter the equilibrium constant of the reaction; instead, it accelerates both the forward and reverse processes. This is achieved by providing an alternative pathway with a lower energy barrier, thus facilitating the production of the desired product [24]. As a point of reference, a control experiment without the use of a catalyst was conducted under the optimal conditions outlined in this paper. Without the catalyst, the glucose yield and cellulose conversion were at their lowest levels, which were 4.2% and 2.8%, respectively.

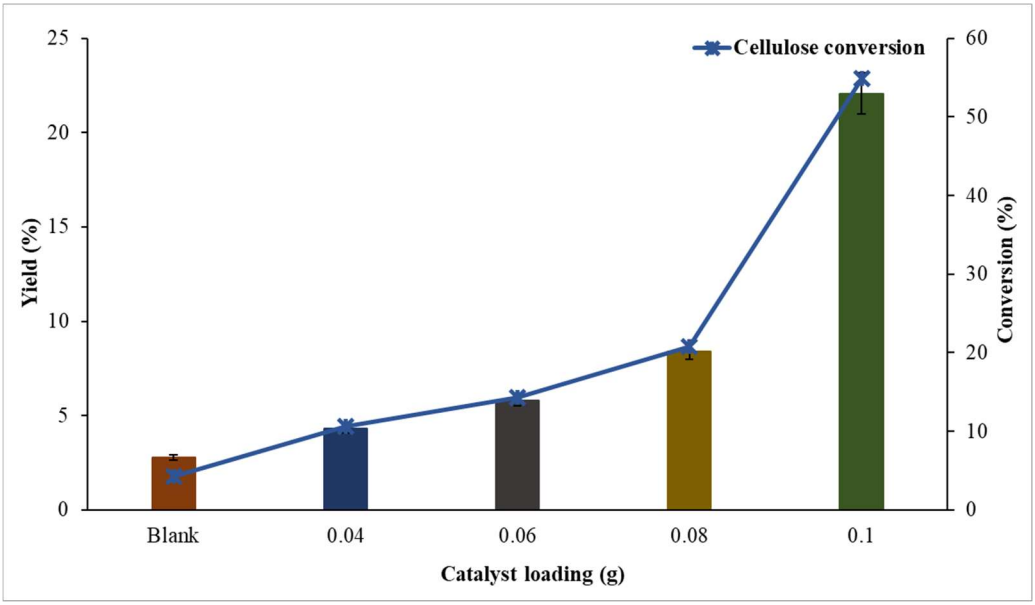

Figure 4. Effect of catalyst loading on the yield of glucose and cellulose conversion at 15 min

Note: a) Pre-reduction of catalyst conditions: 10 mL of distilled water, agitation speed of 1300 rpm, and 1 bar of H_2 for 1 h at 150 °C, b) Reaction conditions: 0.4 g of cellulose, reaction temperature of 210 °C, agitation speed of 1100 rpm, and reaction time of 15 min.

Conclusion

The catalyst synthesis involved $Pt(NO_3)_2$ and zeolite, aiming for a Pt content of 4 wt.% on the zeolite support prepared via the wet impregnation method. Catalyst characterization was performed using TGA, FTIR, and BET analysis. First, TGA was conducted from 30 °C to 600 °C, and the results revealed that the weight losses are attributable to water and nitrate decomposition. Subsequently, the FTIR analysis detected nitrate bands prior to calcination, which disappeared after calcination, confirming successful nitrate decomposition. Despite minor decreases, the catalyst maintained a substantial surface area and pore volume of up to 648.13 m^2/g and 0.3447 cm^3/g, respectively, affirming its stable structure.

In addition, the influence of cellulose and catalyst loading on glucose yield and cellulose conversion was explored. The results revealed that the optimal conditions for maximizing glucose yield and cellulose conversion were achieved when employing 0.4g of cellulose and 0.1g of catalyst, resulting in yield and conversion of 22.1% and 54.9%, respectively. These findings underscore the important role of catalyst selection and loading in achieving efficient biomass conversion processes, which contribute to the advancement of sustainable and eco-friendly chemical production.

Acknowledgement

The authors would like to express their highest gratitude for the financial support from the Ministry of Higher Education (MOHE) (under the Fundamental Research Grant Scheme, FRGS/1/2018/TK02/UNIKL/02/3), Universiti Kuala Lumpur Malaysian Institute of Chemical and Bioengineering Technology (UniKL MICET), and Majlis Amanah Rakyat Malaysia (MARA).

References

1. Merklein, K., Fong, S. S., and Deng, Y. (2016). Chapter 11 – biomass utilization.
2. Rackemann, D. W., and Doherty, W. O. (2011). The conversion of lignocellulosics to levulinic acid. *Biofuels, Bioproducts and Biorefining*, 5(2): 198-214.
3. Lee, J., Jung, S., Kim, Y. T., Kim, H. J., and Kim, K. H. (2023). Catalytic and electrocatalytic conversion of glucose into value-added chemicals. *Renewable and Sustainable Energy Reviews*, 181: 113337.
4. Wasie, A. T., Getachew, M., Asselefech, T., Wotango, S., and Bachheti, R. K. (2024). Heterogeneous catalytic conversion of lignocellulose: towards green and renewable chemicals. *Discover Applied Sciences*, 6: 37.
5. Xiang, M., Liu, J., Fu, W., Tang, T., and Wu, D. (2017). Improved activity for cellulose conversion to levulinic acid through hierarchization of ETS-10 Zeolite. *ACS Sustainable Chemistry and Engineering*, 5(7): 5800-5809.
6. Yoshimura, A., Tochigi, S., and Matsuno, Y. (2021). Fundamental study of palladium recycling using "dry aqua regia" considering the recovery from spent auto-catalyst. *Journal of Sustainable Metallurgy*, 7(1): 266-276.
7. Negoi, A., Triantafyllidis, K., Parvulescu, V. I., and Coman, S. M. (2014). The hydrolytic hydrogenation of cellulose to sorbitol over M (Ru, Ir, Pd, Rh)-BEA-zeolite catalysts. *Catalysis Today*, 223: 122-128.
8. Ya'Aini, N., Amin, N. A. S., and Endud, S. (2013). Characterization and performance of hybrid catalysts for levulinic acid production from glucose. *Microporous and Mesoporous Materials*, 171: 14-23.
9. Ayad, Z., Hussein, Q. H., and Al-Tabbakh, B. A. R. (2020). Synthesis and characterization of high silica HY zeolite by basicity reduction. *AIP Conference Proceeding*. 2213: 020168.
10. Azan, M. N. I. N., Kamal, P. N. S. M. M., Rasmadi, M. A. A., Adzhar, M. H., Zakaria, M. A., Taufek, A. S. A., Nasir, N. S. M., and Alikasturi, A. S. (2020). Production of biodiesel from palm oil refinery pilot plant waste using Ni/CaO (ES) catalyst. *Materials Today: Proceedings*, 31: 292-299
11. Małecka, B., Łącz, A., Drożdż, E., and Malecki, A. (2015). Thermal decomposition of d-metal nitrates supported on alumina. *Journal of Thermal Analysis and Calorimetry,* 119(2): 1053-1061.
12. Joshi, S. S., Zodge, A. D., Pandare, K. V., and Kulkarni, B. D. (2014). Efficient conversion of cellulose to levulinic acid by hydrothermal treatment using zirconium dioxide as a recyclable solid acid catalyst. *Industrial and Engineering Chemistry Research*, 53(49): 18796-18805.
13. Kamal, P. N. S. M. M., Sapawe, N., and Alikasturi, A. S. (2022). Characterization and performance of supported noble metal (pt) on the production of levulinic acid from cellulose. *Materials Science Forum*, 1077: 193–202.
14. Kamal, P. N. S. M. M., Mohamad, N. I., Serit, M. E. A., Rahim, N. S. A., Jimat, N. I., and Alikasturi, A. S. (2020). Study on the effect of reaction and calcination temperature towards glucose hydrolysis using solid acid catalyst. *Materials Today: Proceedings,* 31: 282-286.
15. Kamal, P. N. S. M. M., Sapawe, N., and Alikasturi,

A. S. (2022). Catalytic conversion of cellulose to levulinic acid using supported noble metal palladium catalyst. *Malaysian Journal of Analytical Sciences*, 26(1): 119-129.

16. Jamal, S., Rosid, M., Toemen, S., Azelee, W., Abu Bakar, W., Rosid, S. M., Nazwanie, W., Abdullah, W., & Maisarah Aziz, S. (2021). Characteristics of praseodymium oxide doped manganese/ruthenium catalyst in methanation: effect calcination temperature. *Journal of Academia*, 9(1): 49-55.
17. Ashok, A., Kumar, A., Bhosale, R. R., Saleh, M. A. H., and Van Den Broeke, L. J. P. (2015). Cellulose assisted combustion synthesis of porous Cu-Ni nanopowders. *RSC Advances,* 5(36): 28703-28712.
18. Baharudin, K. B., Abdullah, N., and Derawi, D. (2018). Effect of calcination temperature on the physicochemical properties of zinc oxide nanoparticles synthesized by coprecipitation. *IOP Publishing*, 5: 125018.
19. Al-Fatesh, A. S. A., and Fakeeha, A. H. (2012). Effects of calcination and activation temperature on dry reforming catalysts. *Journal of Saudi Chemical Society*, 16(1): 55-61.
20. Ramli, N. A. S., and Amin, N. A. S. (2014). Catalytic hydrolysis of cellulose and oil palm biomass in ionic liquid to reducing sugar for levulinic acid production. *Fuel Processing Technology*, 128: 490-498.
21. Zhang, X., Zhang, X., Sun, N., Wang, S., Wang, X., and Jiang, Z. (2019). High production of levulinic acid from cellulosic feedstocks being catalyzed by temperature-responsive transition metal substituted heteropolyacids. *Renewable Energy*, 141: 802-813.
22. Wang, K., Ye, J., Zhou, M., Liu, P., Liang, X., Xu, J., and Jiang, J. (2017). Selective conversion of cellulose to levulinic acid and furfural in sulfolane/water solvent. *Cellulose*, 24(3): 1383-1394.
23. Kamal, P. N. S. M. M., Zabidi, M. D. H. M., and Alikasturi, A. S. (2023). Hydrolysis of cellulose to glucose catalyzed by noble metal palladium (Pd) supported on silica-alumina. *Malaysian Journal of Analytical Sciences*, 27: 261-270.
24. Zarin, M. A. A., Zainol, M. M., and Amin, N. A. S. (2020). Optimizing levulinic acid from cellulose catalyzed by HY-zeolite immobilized ionic liquid (HY-IL) using response surface methodology. *Malaysian Journal of Fundamental and Applied Sciences*, 16(6): 625-629.
25. Mufrodi, Z., Astuti, E., Aktawan, A., and Purwono, S. (2018). The effect of recycle stream on the selectivity and yield of the formation of triacetin from glycerol. *IOP Conference Series: Earth and Environmental Science*, 175(1): 012013.

Malaysian Journal of Analytical Sciences (MJAS)
Published by Malaysian Analytical Sciences Society

SYNTHESIS AND MODELLING OF FUNCTIONALIZED UiO-66 METAL-ORGANIC FRAMEWORKS FOR GAS ADSORPTION

(Sintesis dan Pemodelan Rangkaian Organik-Logam UiO-66 Terfungsi bagi Penjerapan Gas)

Tuan Nurul Azura Tuan Kob@Yaakub[1,2], Mohd Basyaruddin Abdul Rahman[1,2], Felipe Gándara[4], and Muhammad Alif Mohammad Latif[1,2,3*]

[1]*Integrated Chemical BioPhysics Research, Faculty of Science, Universiti Putra Malaysia, 43400 UPM Serdang, Selangor, Malaysia*
[2]*Department of Chemistry, Faculty of Science, Universiti Putra Malaysia, 43400 UPM Serdang, Selangor, Malaysia*
[3]*Centre of Foundation Studies for Agricultural Science, Universiti Putra Malaysia, 43400 UPM Serdang, Selangor, Malaysia*
[4]*Department of New Architectures in Materials Chemistry, Materials Science Institute of Madrid – CSIC, Sor Juana Inés de la Cruz 3, Madrid, Spain*

[*]*Corresponding author: aliflatif@upm.edu.my*

Received: 15 September 2023; Accepted: 25 April 2024; Published: 29 June 2024

Abstract

In this article, we present our experimental and computational findings on the adsorption of ethylene gas within variations of UiO-66 metal-organic frameworks (MOFs). UiO-66 MOF was functionalized with 2-vinylbenzoic acid (2VBA), 3-vinylbenzoic acid (3VBA), and 4-vinylbenzoic acid (4VBA) and characterized using powder X-ray diffraction techniques, FT-IR analysis and ^{1}H NMR. Based on structural analysis, the functionalized UiO-66 MOFs were found to possess the same structural stability as the 3D porous crystalline lattices of UiO-66, with hexanuclear zirconium oxyhydroxide clusters ($Zr_6O_4(OH)_4(RCO_2)_{12}$. Grand Canonical Monte Carlo simulation showed that the average loading of ethylene gas in UiO-66 and functionalized UiO-66 were relatively close. The adsorption was further investigated using radial distribution function analysis and it was found that the most favorable interactions were between the adsorbate and the carbon atom of the MOFs. These interactions were crucial for ethylene stabilization inside UiO-66 pore channels. The results presented here supported the viability of ethylene adsorption in UiO-66's modified terephthalate linker by demonstrating that functionalized UiO-66 not only retain structural integrity, but also have comparable ethylene adsorption at different pressures with stronger interactions with ethylene gas.
.

Keywords: metal organic framework, gas adsorption, UiO-66, Grand Canonical Monte Carlo

Abstrak

Dalam artikel ini, kami melaporkan kerja eksperimen dan hasil pengiraan untuk penjerapan gas etilena dalam rangkaian logam organik (MOF) UiO-66. UiO-66 MOF difungsikan dengan asid 2-vinilbenzoik (2VBA), asid 3-vinilbenzoik (3VBA), dan asid 4-vinilbenzoik (4VBA) serta dicirikan menggunakan teknik pembelauan sinar-X serbuk, analisis FT-IR dan ^{1}H NMR. Berdasarkan analisis struktur, UiO-66 MOF yang difungsikan didapati mempunyai kestabilan struktur yang sama seperti kekisi kristal berliang 3D UiO-66, dengan gugusan zirkonium oksihidroksida heksanuklear ($Zr_6O_4(OH)_4(RCO_2)_{12}$. Grand Canonical Monte Carlo simulasi menunjukkan purata pemuatan gas etilena dalam UiO-66 dan UiO-66 yang difungsikan adalah agak hampir hasilnya.

Penjerapan disiasat lebih lanjut menggunakan analisis fungsi taburan jejari dan didapati bahawa interaksi yang paling baik adalah antara penjerap dan atom karbon MOFs. Interaksi ini adalah penting untuk penstabilan etilena di dalam saluran liang UiO-66. Keputusan yang dibentangkan di sini menyokong daya maju penjerapan etilena dalam penyambung tereftalat yang diubah suai UiO-66 dengan menunjukkan bahawa UiO-66 yang difungsikan bukan sahaja dapat mengekalkan integriti struktur, tetapi juga mempunyai penjerapan etilena yang setanding pada tekanan yang berbeza dengan interaksi yang lebih kuat dengan gas etilena.

Kata kunci: rangkaian logam organik, penjerapan gas, UiO-66, Grand Canonical Monte Carlo

Introduction

Fast ripening and pest attack are the two most common causes of food loss in climacteric fruits. Food losses can also occur as a result of insect pest attacks in stored agricultural products. Every season, the Muda Agricultural Development Authority (MADA) estimates that RM 980 million is lost in postharvest rice crop losses [1]. As a result, solutions for controlling the ripening process and securing product storage prior to consumption are in great demand. Ethylene gas usage causes fast ripening and promotes fungal growth during storage, reducing fruit quality and shelf life [2]. As a result, for effective long-distance transportation and subsequent storage, many fruits must be kept in a low ethylene concentration environment due to its adverse effect on postharvest fruit. This has led to a great deal of research on ways to enhance ethylene adsorption and storage.

Materials used for reducing postharvest losses must be applied carefully to the targeted climacteric fruits and staple foods. Furthermore, the material's biocompatibility must be considered and created from non-toxic materials. The environmental implications, including the synthesis technique and disposal features, must also be acknowledged. For the material to be employed in food storage applications, it should ideally be water soluble or biodegradable. Ethylene gas adsorption is frequently based on extremely porous adsorbents with large surface areas, such as clays and zeolites [3]. The first porous material known to be capable of encapsulating ethylene was zeolite [4]. However, the tiny pore size of zeolite creates a significant limitation in its application on gaseous molecule exchange and release [5].

Reticular materials, or metal-organic frameworks (MOFs), are a class of functional material with unique chemical and physical characteristics. It has long been known that MOFs, a kind of crystalline, porous material, are ideal host platforms for gas adsorption [6]. For example, copper-terephthalate (CuTPA) MOF has a total pore capacity of 0.39 cm^3/g and can encapsulate 654 L/L ethylene gas in a 50 mg section of the material. When stored in a 4 L container, CuTPA loaded with ethylene dramatically accelerated the ripening of bananas and avocados [7]. One of the most used MOFs for adsorption studies is UiO-66 (Figure 1a). Numerous studies have been conducted on the adsorption of CO_2 on UiO-66, and the results have been promising [8,9]. At 298 K and 100 kPa, Le et al. (2021) discovered that UiO-66 modified with 10% PABA had the greatest CO_2 absorption capacity of 2.47 mmol g^{-1} and ideal adsorbed solution theory (IAST)-based CO_2/N_2 selectivity, outperforming several other CO_2 benchmark adsorbents [10].

The UiO-66 metal-organic framework (MOF) has high surface area, variable pore size, and good chemical stability, making it a promising material for a wide range of applications. UiO-66 consists of 1,4-benzenedicarboxylic acid (BDC) as ligands connected by Zr_6O_8 as a metal cluster. Additionally, UiO-66 possesses easily accessible metal sites, which indicates that this material has potential applications in gas storage and separation. Due to its large specific surface area, which ranges from 1,000 to 1,500 m^2/g, UiO-66 is a great choice for gas adsorption such as ethylene gas [11]. Furthermore, UiO-66 has been shown to be resistant to high temperatures (up to 500°C) and a broad range of chemical conditions, making it perfect for the adsorption of gases. By altering the metal ions or organic linkers, UiO-66's pore size may also be changed, allowing for the selective adsorption of different gas molecules [11]. Additionally, the functionalized UiO-66 can also help to increase the gasses loading and adsorption capacity. Due to UiO-66 unique properties, a great deal of research has been conducted on UiO-66

and UiO-66 mixed linker, which have been used for a range of gas adsorption and separation techniques, such as the storage of gasses, and the capture of numerous gases including ethylene, carbon dioxide, and many others. For a variety of gas-related applications, UiO-66 is a good choice due to its versatility and tunable properties.

Here, to improve adsorption capability, the UiO-66 terephthalate linker was modified with 2-vinylbenzoic acid, 3-vinylbenzoic acid and 4-vinylbenzoic acid (Figure 1c-1e). UiO-66 and functionalized UiO-66 MOFs were synthesized by using solvothermal method. Powder X-ray diffraction techniques, FTIR analysis and ^{1}H NMR were used to elucidate the resulting structures. The adsorption capacity and host-guest interactions were studied using Grand Canonical Monte Carlo (GCMC) simulation. We were able to illustrate the characteristics and behaviour of ethylene adsorption within UiO-66 and functionalized UiO-66 MOFs using appropriate computational approaches to this system. Modifying the UiO-66 terephthalate linker should boost the ethylene adsorption while simultaneously increasing the number of interactions between host and guest molecules i.e., improved storage.

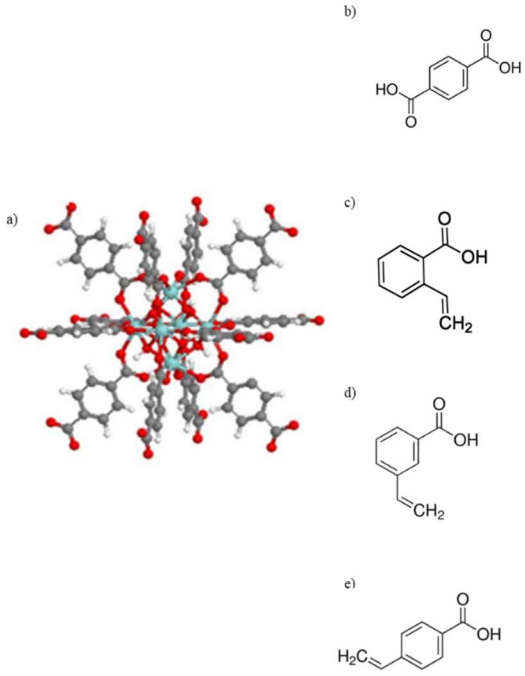

Figure 1. a) Unit cell of UiO-66, b) parent organic linker, c) 2-vinylbenzoic acid d) 3-vinylbenzoic acid, and e) 4-vinylbenzoic acid

Materials and Methods

Materials

All chemicals were obtained commercially (Aldrich) and used without further purification.

Preparation of UiO-66 and functionalized UiO-66

A standard synthesis of UiO-66 was performed by dissolving zirconium tetrachloride, $ZrCl_4$ (0.0625g, 6.4 mmol) in formic acid (2.5mL) and DMF (2.5mL) at room temperature in a volumetric flask. The mixture was stirred for 20 minutes and (0.05g, 0.05mmol) 1,4-dibenzenedicarboxylicacid was added into the mixture. The mixture was stirred again for another 20 minutes. The resulting mixture was placed in an oven at 120 ^{o}C for 24 h. After the solution cooled to room temperature in the air, the resulting solid was filtered and repeatedly washed with absolute ethanol for 3 days. Thus, the resulting white powder was filtered and dried under vacuum at ambient temperature. UiO-66 modified linker with 2-vinylbenzoic acid, 3-vinylbenzoic acid and 4-

vinylbenzoic acid were synthesized analogously by replacing 1,4-dibenzenedicarboxylicacid with ratio of 4:1 of 1,4-dibenzenedicarboxylicacid and modified linker, respectively.

Characterization

Approximately 3 mg of UiO-66 and modified samples were soaked in ethanol dispersed and dried as a thin layer on a glass plate before the PXRD measurements. PXRD data were collected at ambient atmosphere and temperature on a Bruker D5000 instrument with monochromatic Cu Kα radiation (λ=1.540 A˚) operated in Bragg-Bretano geometry. The IR experiments were performed in transmission mode on a FTIR Bruker VERTEX 80 spectrometer equipped with two detectors: a cryogenic MCT detector (spectral range 4000-600 cm^{-1}) for UiO-66 and modified UiO-66 MOFs. The MOFs under study was analyzed in the form of a thin film deposited on a silicon wafer. The thin film was prepared from an ethanol suspension of the samples. Solvent removal spectra were obtained by introducing the silicon wafer in a quartz cell that allowed *in situ* spectrum collection in a controlled atmosphere, and the sample was degassed at 373 K under dynamic vacuum (residual pressure). For the ^{1}H-NMR analysis, 20 mg of the sample were dissolved in a solution of natrium hydroxide, NaOH, and D_2O for a duration of 24 hours. The resultant solution was then utilized using a Bruker Advance DRX-300 NMR Spectrometer (300 MHz) to obtain the ^{1}H-NMR spectra.

Computational details

The UiO-66(Zr) crystal information file (.cif) with deposition number 733458 was obtained from the Cambridge Crystallographic Data Center [12]. The .cif file was utilised to carry out preliminary geometry-based analysis, such as pore sizes, using the BIOVIA Material Studio tool [13]. UiO-66 has the chemical formula [C39.36H23.52O34.80Zr6], and the metal centers, zirconium, Zr were completely coordinated. The unit cell lengths of a, b, and c UiO-66 were 20.7343, 20.7343, and 20.7343, respectively, and the atom arrangement in the unit cell produced a triclinic symmetry. Next, using Material Studio, 2-vinylbenzoic acid, 3-vinylbenzoic acid, and 4-vinylbenzoic acid were used to modify the terephthalate acid UiO-66 linker. Structures were modified by replacing one of the terephthalate linkers with 2-, 3-, or 4-vinylbenzoic acid using the Material Studio's "modify element" tool. The Forcite module was used to carry out energy minimization with a convergence tolerance of 10^{-4} kcal/mol. Furthermore, geometry optimization was performed using the Smart method with maximum iteration numbers of 1000 for all the MOFs series [14].

For geometry optimization, the convergence tolerances for displacement, energy, and force were set to 10^{-6}, 10^{-5}, and 10^{-4} kcal/mol, respectively. The cell parameters of the frameworks were also allowed to be relaxed at this stage. The Universal Force Field potential parameters were used to optimize UiO-66 and the functionalized UiO-66 MOFs [14]. In order to compute the electrostatic interactions between MOF atoms and the gas molecules, partial charge of the framework atoms was calculated using the Qeq (charge equilibration technique) and EQeq (extended charge equilibration method) methods, depending on the existing metal type [15]. GCMC simulations were used to examine the ethylene gas adsorption isotherms in UiO-66 and functionalized UiO-66 MOFs. All simulations were performed using the RASPA [16] package at 293 K [17] with pressures ranging from 0 to 100 kPa. The accessible pore volume and helium (He) void percentage of UiO-66, UiO-66-2VBA, UiO-66-3VBA, and UiO-66-4VBA were determined to be at 0.43, 0.44, 0.44 and 0.44 cm^3/g, respectively. Widom particle insertion was also used to calculate the He void fraction for UiO-66 and functionalized UiO-66, and the resulting values were set in the input file for adsorption simulations. A 12.0 Å cut-off was set for electrostatic and van der Waals interactions. The adsorption simulations used up to 2.5 x 10^5 Monte Carlo cycles, with 5 x 10^4 cycles for the initial equilibrium phase and 2 x 10^5 cycles for the production phase [18-20]. Each Monte Carlo (MC) move was set to having an equal chance of being translated, rotated, inserted, or deleted.

Results and Discussion

Characterizations of UiO-66 and functionalized UiO-66

The powder X-ray diffraction (PXRD) pattern of the synthesized UiO-66 and functionalized UiO-66 MOFs

are shown in Figure 2. The peaks are identical to the one previously reported research [21]. The identical XRD patterns of UiO-66 and functionalized UiO-66 show that these functionalized UiO-66 have the same 3D porous crystalline lattices as UiO-66, with hexanuclear zirconium oxyhydroxide clusters ($Zr_6O_4(OH)_4(RCO_2)_{12}$) and octahedral cages assembled with these modified terephthalate linkers. It was determined that the functionalization did not alter the framework topology of UiO-66(Zr) MOFs. The peak at $2\theta = 7.3°$ corresponds to the (111) crystal plane of the UiO-66 structure. This peak is one of the important peaks for UiO-66 and this peak was considered as fingerprint peak that indicates whether a sample has the UiO-66 framework. When compared to another UiO-66 sample, the peak for UiO-66-2VBA at 7.3° is sharper and more intense, indicating that the UiO-66-2VBA sample has good crystallinity properties. A second notable low-angle peak is seen at approximately $2\theta = 8.4°$, which is the crystal plane (200). Additionally, mid-angle peaks were noted at around $2\theta = 12.0°$, which is the peak associated with the (220). The (311) crystal plane is assigned a peak at about $2\theta = 14.0°$. The (222) crystal plane is thought to be responsible for the peak at about $2\theta = 15.8°$.

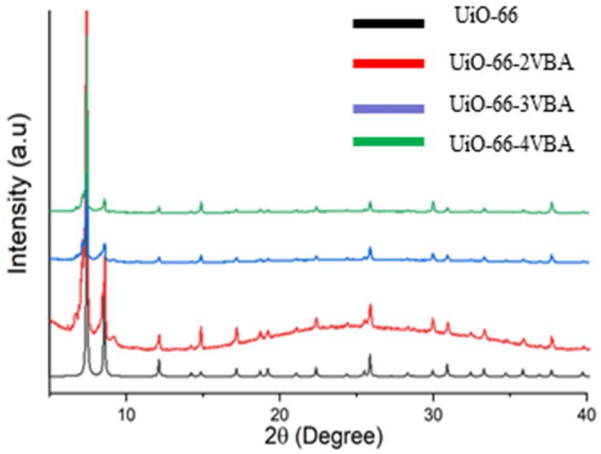

Figure 2. PXRD pattern for UiO-66 and functionalized UiO-66

The FT-IR spectra of UiO-66 and functionalized UiO-66 MOFs is shown in Figure 3. These four UiO-66 samples have IR spectra with comparable distinctive peaks. UiO-66 sample FTIR spectra show multiple major wavelengths. We can see a large peak around 3419 cm^{-1} that indicated -OH group present in the structure. Two highly linked C–O bonds in the carboxylate group of the ligand, BDC, result in two distinct peaks: an asymmetric C–O stretching band at 1586 cm^{-1} and a symmetric C–O stretching band at 1398 cm^{-1}. The C=C of the benzene ring of the ligand in the structure could be the source of the tiny bands at 1504 cm^{-1}. After synthesizing UiO-66 using a mixed linker, the peaks show that the ligand at 1586 cm^{-1} changed somewhat and widened. The existence of several functional groups with various vibrational frequencies, which cause overlapping bands and a broadening effect, is one potential explanation.

Solid state ^1H NMR of the three UiO-66-2VBA, UiO-66-3VBA and UiO-66-4VBA samples also exhibit similar characteristic peaks with the one previously reported [22]. According to Ky Vo et al. (2020) ^1H NMR spectra, UiO-66 had a single signal that was 7.84 ppm in strength and was attributed to the phenyl proton of the BDC ligand [23]. On the other hand, our research indicates that functionalized UiO-66 show three distinct peaks (Figure 4). The ^1H NMR spectra of functionalized UiO-66 show two notable peaks: one at 1.9 ppm, which is related to the vinyl chain, and another at 7.8 ppm, which is related to the aromatic protons in the ligand. The addition of vinyl groups to the UiO-66 framework is linked to the different peaks observed in the ^1H NMR spectra of the functionalized UiO-66. A noteworthy

peak was noted for the functionalized UiO-66. The result of bridging hydroxyl (OH) protons is a wide singlet at 5.5 ppm, which represents the four hydroxyl protons that bridge the zirconium clusters.

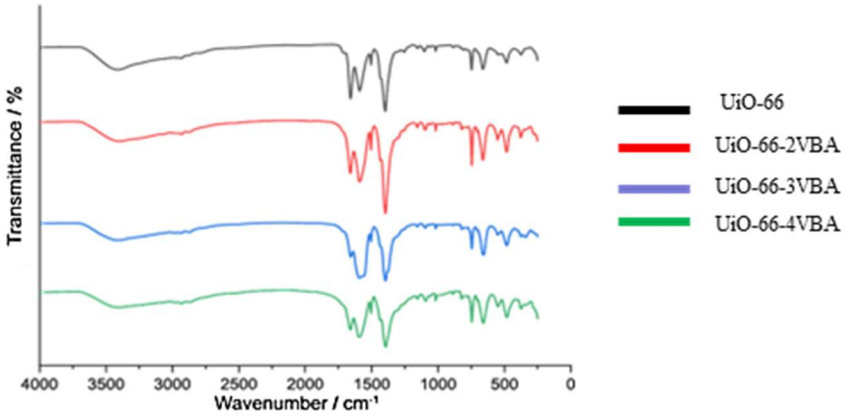

Figure 3. FT-IR spectra for UiO-66 and UiO-66 with mixed linker

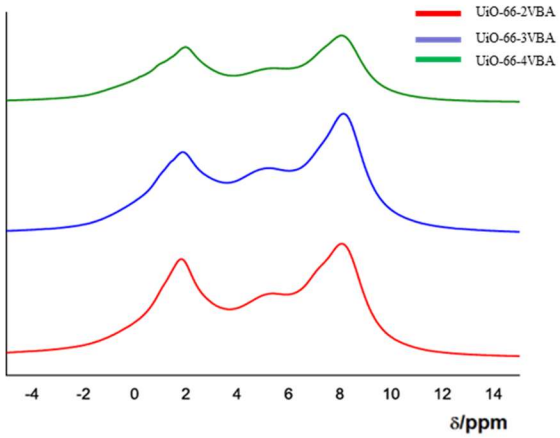

Figure 4. [1] H NMR Spectra of UiO-66 functionalized

Adsorption isotherm

Figures 5(a) and 5(b) show the ethylene gas adsorption isotherms in UiO-66 and functionalized UiO-66 at 293 K. Force fields mentioned in the method section were used and the ethylene uptake was simulated at pressures ranging from 0 to 100 kPa. The average loading for UiO-66 and functionalized UiO-66 rose as the pressure increased from 0 kPa to 100 kPa. When the MOFs are sorted according to the average loading for molecule per unit cell, the following order were produced; UiO-66-2VBA > UiO-66-4VBA > UiO-66-3VBA > UiO-66. At 100kPa, the maximum ethylene gas loading was 14.45 molecules per unit cell in UiO-66-2VBA, as compared to 14.05, 14.37, and 14.40 molecules per unit cell in UiO-66, UiO-66-3VBA, and UiO-66-4VBA, respectively. Although the highest loading was found for UiO-66-2VBA, the values between all MOFs were closely spaced. The present of the guest-guest interactions, which played a key role at higher pressures resulting in larger loadings, may explain the small variation in the average ethylene loading. The observations at higher pressures do not truly reflect the functionalized UiO-66's remarkable sensitivity to isotherms. Hence, the intermolecular interactions analysis was carried out to better understand the influence of functionalization on ethylene gas

adsorption.

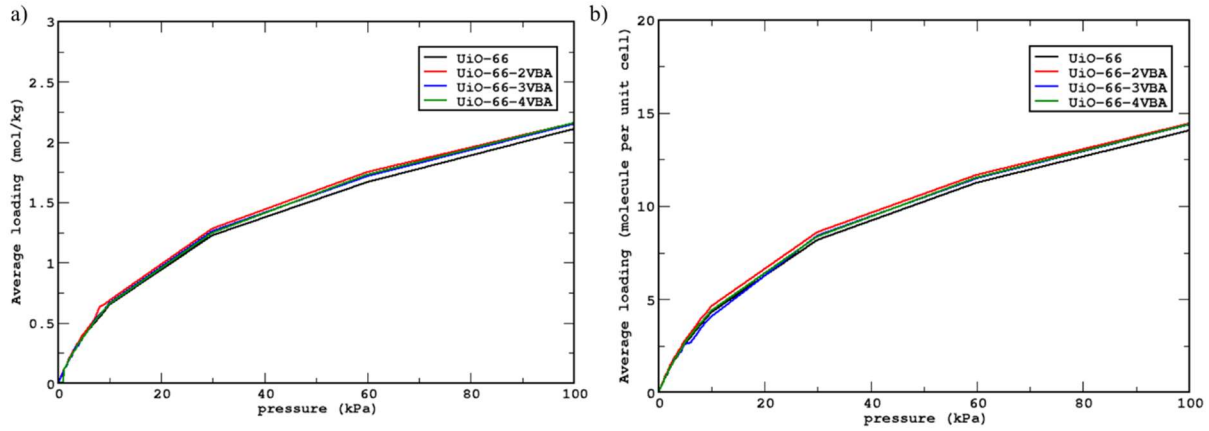

Figure 5. Simulated adsorption isotherms of ethylene molecule in UiO-66 and functionalized UiO-66: (a) pressure(kPa) versus average loading (mol/kg) and (b) pressure(kPa) versus average loading (molecule per unit cell)

Radial Distribution Function (RDF)

To study the interactions of the ethylene gas with UiO-66 and functionalized UiO-66 MOFs, the radial distribution function (RDF) was calculated using the following equation:

$$g_{ij}(r) = \frac{N_{ij}\,(\mathrm{r}, \mathrm{r} + \Delta\mathrm{r}).\ V}{4\pi r^2.\,\Delta r.N_i.N_j} \quad (1)$$

In this equation, N_{ij} (r, r + Δr) represents the number of particles *j* around particle *i* inside the area from r to r + Δr. *V* and *N* denote the volume of the system and the number of particles, respectively. Analyzing RDF allowed for assessing the distribution of ethylene gas molecules on the interaction sites of UiO-66 and functionalized UiO-66 MOFs. In general, the greatest distribution of gas molecules in the UiO-66 pores must follow the adsorbed quantity. The RDF plots for ethylene gas (Figure 6) showed an acceptable distribution of oxygen, hydrogen, carbon and zirconium atoms based on the adsorbed quantities and van der Waals surfaces of UiO-66 and functionalized UiO-66 MOFs. Although the ethylene gas adsorption quantity in UiO-66 and functionalized UiO-66 MOFs is not significantly different, the difference in terms of RDF values is noticeable. The level of distribution for the gas molecules was found in the order of UiO-66-2VBA < UiO-66-4VBA < UiO-66 < UiO-66-3VBA (Figure 6). Except for UiO-66, these results show an agreement with the adsorption isotherm results. Carbon, C and Zr atoms in the UiO-66-2VBA were discovered to be the most favorable sites for ethylene gas. C and Zr atoms have distribution *g*(*r*) values of 3.1 and 3.5 in UiO-66-2VBA, respectively. In comparison, the *g*(*r*) distributions for C and Zr atoms in UiO-66 are only approximately 2.0 and 3.1, respectively. These findings show that functionalizing UiO-66 with vinyl benzoic acid increased the interaction of ethylene gas with the C of the organic linker, while decreasing the interaction with H atoms.

Simulation snapshot analysis

The simulation snapshots for the adsorption of the ethylene gas in UiO-66, UiO-66-2VBA, UiO-66-3VBA and UiO-66-4VBA at 100 kPa along the y-axis is presented in Figure 7. As illustrated, all gas molecules were contained within pores of UiO-66. The simulated snapshots show molecules of ethylene gas adsorbed in UiO-66's porous structure. The ethylene molecules are located at the centre of the huge channels, where they interact with the framework via van der Waals forces. UiO-66's huge pore size enable effective ethylene adsorption, which results in a high adsorption capacity. The snapshots also indicate that ethylene gas molecules were adsorbed on the exposed zirconium metal sites. This Lewis's acid sites, which are made from coordinatively unsaturated zirconium atoms, facilitate robust interactions with the ethylene molecules. The

figure further shows that ethylene gas molecules are also dispersed throughout the framework, taking up the available pore space of UiO-66. It also can be observed that the functionalization of UiO-66 with vinyl benzoic acid helps to enhance the active sites for ethylene gas interactions. More ethylene gasses were adsorbed in the framework's pore in UiO-66-2VBA, UiO-66-3VBA, and UiO-66-4VBA. This might be owing to increased interactions between ethylene and the linker in the framework. It was clear that functionalizing UiO-66 had a positive effect on the adsorption of ethylene. As the pressure increased, the framework was gradually loaded with ethylene molecules at the metal sites. Hence, interactions between ethylene gas and Zr metal ions also increase. In comparison, the ethylene molecules' interaction with the Uio-66-2VBA framework is stronger than that of UiO-66, UiO-66-3VBA, and UiO-66-4VBA adsorption. This suggests that the ethylene gas adsorption inside UiO-66 MOF is enhanced by the mixed linker techniques.

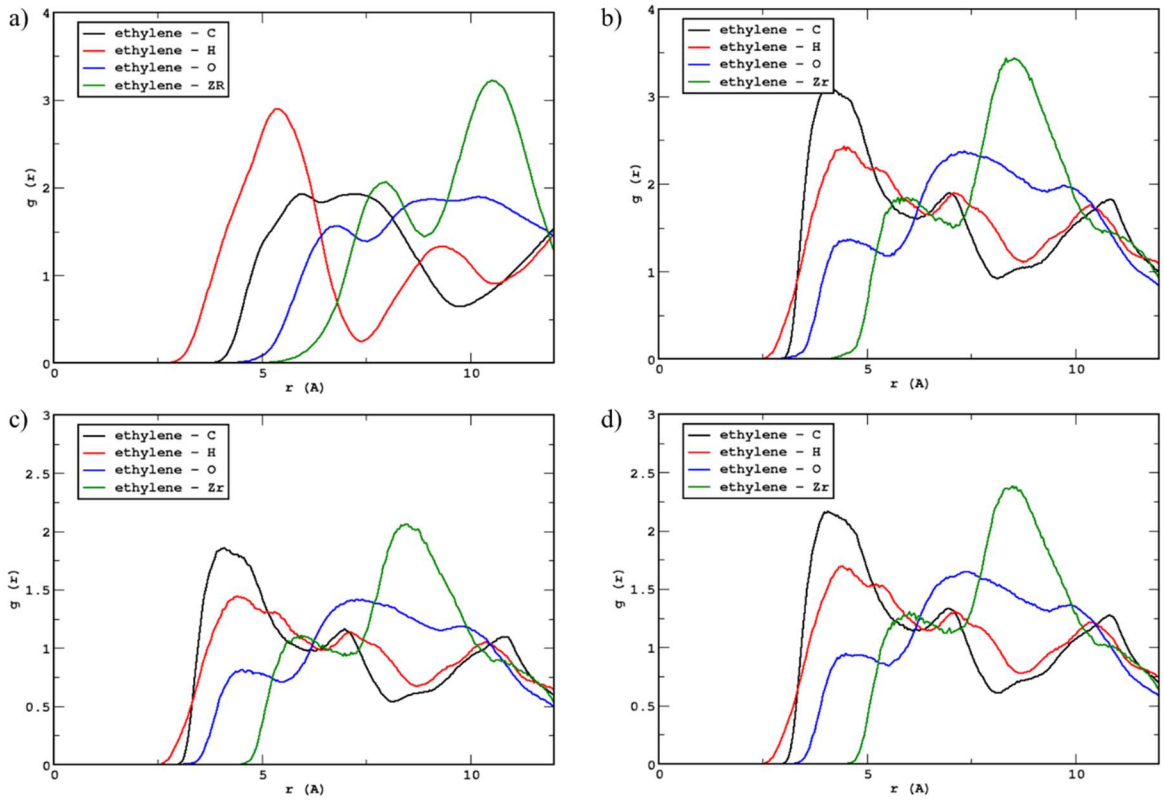

Figure 6. Radial distribution plots for (a) UiO-66, (b) UiO-66-2VBA, (c) UiO-66-3VBA, and (d) UiO-66-4VBA

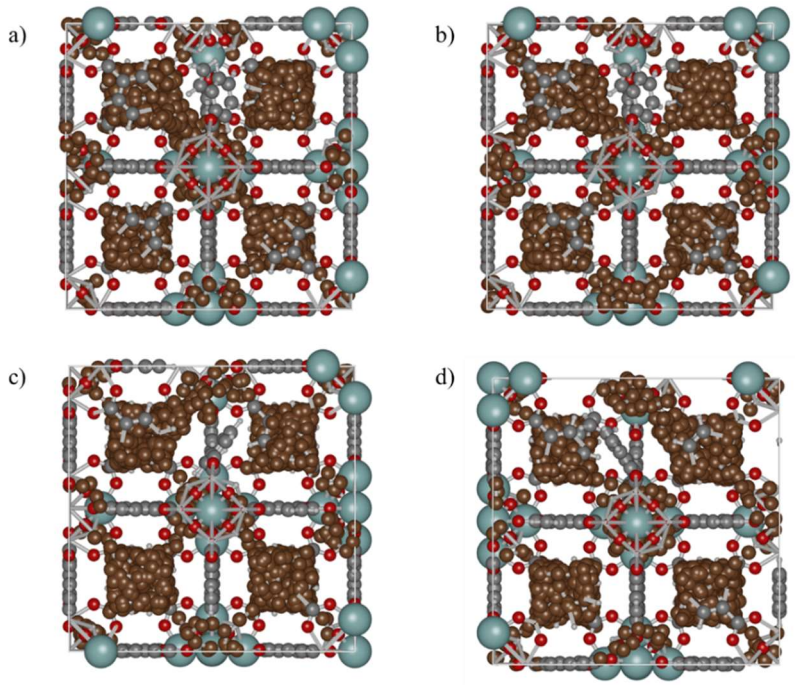

Figure 7. Simulation snapshot for (a) UiO-66, (b) UiO-66-2VBA, (c) UiO-66-3VBA, and (d) UiO-66-4VBA at 100kPa. The colors in the snapshot correspond to: linkers (grey), Zirconium atom (light blue), Oxygen atom (red) and ethylene gasses (brown)

Conclusion

We have successfully synthesized three functionalized, UiO-66 MOFs. The functionalization with different variations of vinyl benzoic acid did not disrupt the overall framework topology of the UiO-66(Zr) MOF. GCMC simulations provided an atomic-level understanding of ethylene gas adsorption in UiO-66, UiO-66-2VBA, UiO-66-3VBA, and UiO-66-4VBA at pressures ranging from 0 kPa to 100 kPa. The adsorption isotherm revealed the largest and most consistent ethylene loading in UiO-66-2VBA but did not differ significantly from the other MOFs studied. The carbon atoms in the functionalized linker and the Zr metal ion have the most interactions with ethylene gases. This was validated further by analyzing the simulation snapshots at 100kPa. Based on the findings, we determined that functionalization of UiO-66 MOF with vinyl benzoic acid will contribute towards more efficient ethylene gas adsorption and storage.

Acknowledgement

The authors would like to acknowledge the Ministry of Education (MOE) Malaysia. This research is supported by the Ministry of Education (MOE) Malaysia through Fundamental Research Grant Scheme (FRGS/1/2020/STG04/UPM/02/9). We are grateful to Dr. Felipe Gándara Barragan (ICMM, Madrid) for his support of global science activities.

References

1. Che Omar, S., Shaharudin, A., and Tumin, S.A. (2019). The status of the paddy and rice industry in Malaysia. *In Khazanah Research Institute*.
2. Saltveit, M.E. (1999). Effect of ethylene on quality of fresh fruits and vegetables. *Postharvest Biology and Technology,* 15: 279-292.
3. Sehaqui, H., Zhou, Q., and Berglund, L.A. (2011). High-porosity aerogels of high specific surface area prepared from nanofibrillated cellulose (NFC). *Composites Science and Technology,* 71: 1593-1599.
4. Golipour, H., Mokhtarani, B., Mafi, M., Moradi, A.V., and Godini, H.R. (2020). Experimental measurement for adsorption of ethylene and ethane gases on copper-exchanged zeolites 13X and 5A. *Journal of Chemical & Engineering Data,* 65:

3920-3932.

5. Cao, Z., Anjikar, N.D., and Yang, S. (2022). Small-pore zeolite membranes: A review of gas separation applications and membrane preparation. *Separations*, 9: 47.
6. Li, B., Wen, H.M., Zhou, W., and Chen, B. (2014). Porous metal-organic frameworks for gas storage and separation: what, how, and why? *The journal of physical chemistry letters,* 20: 3468-3479.
7. Zhang, B., Luo, Y., Kanyuck, K.M., Bauchan, G.R., Mowery, J.D., and Zavalij, P.Y. (2016). Development of metal-organic framework for gaseous plant hormone encapsulation to manage ripening of climacteric produce. *Journal of Agricultural and Food Chemistry,* 23: 5164-5170.
8. Grissom, T.G., Driscoll, D.M., Troya, D., Sapienza, N.S., Usov, P.M., Morris, A.J., and Morris, J.R. (2019). Molecular-level insight into CO_2 adsorption on the zirconium-based metal–organic framework, UiO-66: A combined spectroscopic and computational approach. *The Journal of Physical Chemistry C*, 22: 13731-13738.
9. Ethiraj, J., Albanese, E., Civalleri, B., Vitillo, J.G., Bonino, F., Chavan, S.M., Shearer, G.C., Lillerud, K.P., and Bordiga, S. (2014). Carbon dioxide adsorption in amine-functionalized mixed-ligand metal-organic frameworks of UiO-66 topology. *ChemSusChem,* 12: 3382-3388.
10. Le, V.N., Vo, T.K., Yoo, K.S., and Kim, J. (2021). Enhanced CO_2 adsorption performance on amino-defective UiO-66 with 4-amino benzoic acid as the defective linker *Separation and Purification Technology*, 274: 119079.
11. Zhao, W., Zhang, C., Yan, Z., Zhou, Y., Li, J., Xie, Y., Bai, L., Jiang, L., and Li F. (2017). Preparation, characterization, and performance evaluation of UiO-66 analogues as stationary phase in HPLC for the separation of substituted benzenes and polycyclic aromatic hydrocarbons. *PLoS One.*
12. Trousselet, F., Archereau, A.Y., Boutin, A., and Coudert, F. (2016). Heterometallic metal–organic frameworks of MOF-5 and UiO-66 families: Insight from computational chemistry. *Journal of Physical Chemistry C,* 120: 24885-24894.
13. Dassault Systèmes BIOVIA, B. W. *Release 2017; BIOVIA Pipeline Pilot*, *Release 2017;* Dassault Systèmes, San Diego, CA.
14. Rappe, A. K., Casewit, C. J., Colwell, K. S., Goddard, W. A., and Skiff, W. M. (1992). UFF, a full periodic table force field for molecular mechanics and molecular dynamics simulations. *Journal American Chemical Society*, 114: 10024,
15. Wilmer, C. E., Kim, K. C., and Snurr, R. Q. (2012). an extended charge equilibration method. *Journal of Physical Chemistry,* 3: 2506-2511.
16. Dubbeldam, D., Calero, S., Ellis, D.E., and Snurr, R.Q. (2016). RASPA: Molecular simulation software for adsorption and diffusion in flexible nanoporous materials. *Journal of Molecular Simulation,* 42: 81-101.
17. Savage, M., Yang, S., Suyetin, M., Bichoutskaia, E., Lewis, W., Blake, A.J., Barnett, S.A., and Schröder, M. A. (2014). Novel bismuth-based metal–organic framework for high volumetric methane and carbon dioxide adsorption. *Journal of Chemical European,* 20: 8024-8029.
18. Xia, X., Hu, G., Li, W., and Li, S. (2019). Understanding reduced CO_2 uptake of ionic liquid/metal organic framework (IL/MOF) composites. *Journal of Applied Nano Material,* 2: 6022-6029.
19. Anderson, R., Schweitzer, B., Wu, T., Carreon, M.A., and Gómez-Gualdrón, D.A. (2018). Molecular simulation insights on Xe/Kr separation in a set of nanoporous crystalline membranes. *Journal of Applied Material Interfaces,* 10: 582-592.
20. Avci, G., Velioglu, S., and Keskin, S. (2018). High-throughput screening of MOF adsorbents and membranes for H_2 purification and CO_2 capture. *Journal of Applied Material Interfaces,* 10: 33693-33706.
21. Rahmawati, I., Ediati, R., and Prasetyoko, D. (2014). Synthesis of UiO-66 using solvothermal method at high temperature. *Journal of Proceedings Series,* 1: 2354-6026.
22. Vakili, R., Xu, S., Al-Janabi, N., Gorgojo, P., Holmes, S.M., and Fan, X. (2018). Microwave-assisted synthesis of zirconium-based metal organic frameworks (MOFs): Optimization and gas

adsorption. *Microporous and Mesoporous Materials.* 260: 45-53.

23. The Ky, V., Le, V. N. N., Van, S., Mugeun, K., Daekeun, Y., Kye, S., Park, B., and Kim, J. (2020). Microwave-assisted continuous-flow synthesis of mixed-ligand UiO-66(Zr) frameworks and their application to toluene adsorption. *Journal of Industrial and Engineering Chemistry.* 86: 178-185.

Malaysian Journal of Analytical Sciences (MJAS)
Published by Malaysian Analytical Sciences Society

NANOCRYSTALLINE CELLULOSE EXTRACTED FROM DISCARDED CIGARETTE BUTTS

(Selulosa Nanokristal yang Diekstrak daripada Sisa Puntung Rokok)

Muhammad Hafiz Azlan, Khairatun Najwa Mohd Amin, and Noraziah Abu Yazid*

Faculty of Chemical & Process Engineering Technology, Universiti Malaysia Pahang Al-Sultan Abdullah, Lebuh Persiaran Tun Khalil Yaakob, 26300 Kuantan, Pahang, Malaysia

**Corresponding author: noraziahay@umpsa.edu.my*

Received: 3 November 2023; Accepted: 1 April 2024; Published: 29 June 2024

Abstract

The increase in cigarette consumption has led to significant accumulation of non-degradable cigarette butt (CB) waste worldwide. CBs, though small, contain both cellulose acetate and toxic tobacco substances, posing environmental risks. This includes water pollution and harm to aquatic life by releasing toxins from leachate into waterways. This study addresses the problem by exploring the extraction and hydrolysis of cellulose acetate from discarded CBs, converting it into nanocrystalline cellulose (NCC). Several conditions were examined during this study such as the ratio of water and ethanol for the extraction (1:1, 1:2, 1:3 v/v%) and the efficiency of acid hydrolysis. Analysis techniques including FTIR, TEM, ICP-MS, and XRD were employed. TEM results showed that sample C has the smallest diameter of nanocrystal cellulose with needle-like shape that corresponded to the XRD results that show the highest Crystallinity Index (CI) of 64.8% with 3.66 nm crystallite size. The treatments successfully removed toxic chemicals from the CBs that were not detected in the retained NCC using ICP-MS. The preliminary results obtained open an avenue to reuse the CB to produce environmentally friendly NCC that can be used widely in many applications fields.

Keywords: cigarette butts, nanocrystal, cellulose pulp, extraction, cellulose acetate

Abstrak

Peningkatan penggunaan rokok telah membawa kepada pengumpulan sisa pepejal rokok yang sukar untuk terurai di seluruh dunia. Walaupun saiz puntung rokok (CB) kecil, tetapi ia mengandungi asetat selulosa dan toksin tembakau yang menyebabkan masalah pencemaran. Ini termasuk pencemaran air yang mengancam kehidupan akuatik kesan daripada pelepasan toksin ke dalam salur air. Kajian ini mengatasi masalah tersebut dengan mengkaji kesan pengekstrakan dan hidrolisis selulosa asetat daripada CB, mengubahnya menjadi selulosa nanokristal (NCC). Beberapa keadaan telah dikaji seperti nisbah air dan etanol untuk pengekstrakan (1:1, 1:2, 1:3 v/v%) dan efisiensi hidrolisis asid. Teknik analisis termasuk FTIR, TEM, ICP-MS, dan XRD digunakan. Hasil TEM menunjukkan sampel C mempunyai diameter selulosa nanokristal terkecil dengan bentuk jarum yang sepadan dengan hasil XRD yang menunjukkan Indeks Kristaliniti (CI) tertinggi iaitu 64.8% dengan saiz kristal 3.66 nm. Rawatan yang dilakukan berjaya mengeluarkan bahan kimia beracun daripada CB yang dikesan menggunakan NCC yang dihasilkan menggunakan ICP-MS. Keputusan awal ini membuka peluang untuk mengguna semula CB untuk menghasilkan NCC mesra alam yang boleh digunakan secara meluas dalam pelbagai bidang aplikasi.

Kata kunci: puntung rokok, nanokristal, pulpa selulosa, pengekstrakan, selulosa asetat

Introduction

A cigarette butt (CB) acts as a filter to a cigarette. It filters the toxic substances contained in cigarettes before going through humans. CB is made up of cellulose acetate and rolled with paper. Cellulose acetate is extensively used in textiles, cigarette filters for absorbing vapors and collecting particulate smoke components, surface coatings and inks as an additive, and as a carrier in photographic negatives, motion picture film (celluloid), microfilm, microfiche, and audio tape [1]. The global market for cellulose acetate is expected to reach 1.05 million metric tons by 2017, with an anticipated price of $1.80 per pound, according to a new analysis by Global Industry Analysis [2].

CB littering is ubiquitous in urban life and can be found abundantly in most public places especially streets, beaches, and food stalls. Studies have consistently found that a substantial majority of smokers litter CB (76.7%–84%) [3]. Even though it is small, the accumulation of CB may lead to environmental problems. Apart from being not easily degraded, the discarded CB may contain harmful chemicals such as nicotine as the major toxic substance. A smoker gets between 1.4 and 2.2 mg of the chemicals in each cigarette, with polycyclic aromatic hydrocarbons, N-nitrosamines, and aromatic amines being the most effective carcinogens [4]. The biodegradability of cellulose acetate is still questionable as some researchers reported that natural organisms could not degrade cellulose acetate with a degree of substitution of greater than 1.5. Therefore, it is not degraded by itself thus creating a big problem to dispose of the CB and recycle them.

The filter used for a cigarette is composed of cellulose acetate which is not easily degradable and may lead to the accumulation of CB on the ground and the toxins leaching out into the groundwater [5]. Recently, there have been several initiatives taken to overcome this problem such as recycling CBs to produce supercapacitors, bricks, insecticides, chemical inhibitors, sound absorbing material [6], or cellulose pulp [5]. Toxic chemicals trapped in the CB filters that leaching out and dissolving into the water can cause considerable damage to the environment and various organisms [3]. Incinerating or landfilling are not the best methods to dispose of cigarette butts. It incurs more costs and is challenging to dispose waste that contains a lot of organic and toxic materials in landfills. Since many toxic compounds are released into the air when the waste is burned, incinerating CBs is also an unsustainable approach [4]. Recycling CB is problematic due to the toxic substances contained in the filter. Any mechanism to dispose of the filter needs to consider its impact on the environment and the feasibility of the methods. The current method has initiated recycling CB to produce nano crystalline cellulose (NCC) by using pure ethanol in the extraction. However, the maximum yield of cellulose acetate and NCC produced was not high [7]. Therefore, to increase the yield, the extraction solvent needs to be studied. It is known that ethanol can play a role in particle size and morphology, where a decrease in the aqueous solution's dielectric constant due to the addition of ethanol causes supersaturation, which in turn leads to the development of many homogenous nuclei and reduced average particle sizes [8]. Furthermore, instead of pure ethanol, aqueous ethanol can be an eco-friendly method for the extraction of cellulose [9].

Thus, this study aimed to use aqueous ethanol for the extraction of cellulose acetate from discarded CBs and convert it into nano-crystalline cellulose to reduce the environmental impact of discarded CBs. Apart from that, the heavy metals content in the recovered cellulose pulp was investigated to ensure safe usage when reused as other materials such as in biomaterial, catalysis, or polymer coating.

Materials and Methods

Materials

CBs were collected in public areas in Kuantan, Pahang. Ethanol (99.8%), sodium hydroxide pellets (NaOH), sulfuric acid (H_2SO_4), and sodium hypochlorite (NaOCl) were obtained from Merck (Malaysia). All chemicals were of analytical grade. Double distilled water was used for all experiments.

Sample preparation

Excess paper and tobacco were manually removed from the collected CB to ensure the toxic substance from the tobacco does not leach out during the extraction. Then

about 10 g of cleaned CBs were weighted prior to soaking and later, they were washed with water for 24 h. Following that, the water was drained, and the cleaned CBs were gathered.

Cellulose acetate extraction and isolation of nano-crystalline cellulose

The extraction method followed previous research [7] with a slight modification. Approximately 10 g of the washed CBs (1:10 w/v%) were extracted using water and ethanol at the ratios of 1:1, 1:2, and 1:3 (v/v%), respectively, for 24 h at room temperature. After the extraction, the solid materials were collected as cellulose acetate (CA-CB). The obtained CA-CB was bleached with 1.25 w/v% sodium hypochlorite for 6 h at room temperature. Following the bleaching procedure, the samples were dried and deacetylated for 24 hours at room temperature using 1 w/v% ethanolic NaOH. After mixing the samples, nano-crystalline cellulose (NCC-CB) was then isolated using 55 wt% of sulfuric acid at 45 °C for 45 minutes to remove the amorphous areas from the cellulose that had been produced. The percentage yield of the extracted cellulose from CB (Cel-CB) was determined using Equation (1).

$$\%\, Yield\ of\ Cel-CB = \frac{Weight\ of\ extracted\ Cel-CB(g)}{Weight\ of\ CB(g)} \times 100\% \quad (1)$$

Subsequently, NCC-CB suspension was diluted 20 times its original volume at room temperature using double-distilled water. This process was repeated 5 times. Then, the NCC-CB suspension was freeze dried at −60ºC for 72 h. A pestle and mortar were used to grind the resulting film (NCC-CB) to a powder and stored in sample vial for further analysis. The yield of NCC-CB was calculated using Equation (2).

$$\%\, Yield\ of\ NCC-CB = \frac{Weigh\ \ of\ NCC-CB\ isolated(g)}{Weigh\ \ of\ Cel-CB\ used(g)} \times 100\% \quad (2)$$

Characterization

The obtained cellulose powder (NCC-CB) was characterized based on the particle size, surface, crystal shape, morphology and elemental analysis using Particle Size Distribution, FTIR, TEM, XRD and ICP-MS. These instruments were used to identify the physical properties, chemical properties, and microstructure of the NCC-CB. XRD with radiation at 45kV and 40mA provides information about crystallinity and phase composition. The samples were scanned with a step size of 0.05° and a scan rate of three seconds per step. The crystallinity index of NCC and crystallite size were calculated by using Equation (3) and (4), respectively. TEM provides the photomicrograph of the dimensions and microstructure of NCC-CB using high resolution transmission electron microscopy (HRTEM, JEM-2011/JEOL). ImageJ software was used to analyze the dimension of the NCC from TEM image. The functional groups of NCC-CB were confirmed using Fourier transform Infrared spectroscopy (FTIR) within a range of 4000 – 500 cm^{-1}. The elemental analysis was conducted using ICP-MS Elan 9000 (Perkin-Elmer).

$$CI(\%) = \frac{I_{crys} - I_{am}}{I_{002}} \times 100\% \quad (3)$$

Where I_{crys} is the maximum intensity of diffraction at the highest peak around 20° to 22° angle and I_{am} is the minimum intensity of amorphous material around 18° angle. The crystallite size of the sample was calculated using Scherrer equation as in Equation (4):

$$Crystallite\ size\ (nm) = \frac{0.94\lambda}{\beta\ cos\theta} \quad (4)$$

Where λ is the wavelength at 0.154, β is the full width half maximum (FWHM), and θ is the corresponding Bragg angle [10].

Results and Discussion

Cellulose and nano-crystalline yield

Nano-crystalline Cellulose-Cigarette Butt (NCC-CB) was isolated from CB after the extraction with ethanolic sodium hydroxide, bleaching, deacetylation, and sulfuric acid hydrolysis. NCC-CB differs to Cel-CB in terms of amorphous region, whereby, in NCC-CB, the amorphous region is lesser when compared to Cel-CB. This is due to acidic hydrolysis. According to Table 1, sample A with the extraction ratio of water to ethanol 1:1 (v/v) obtained 98.76% of Cel-CB yield, sample B with the extraction ratio of 1:2 (v/v) gives 97.76% yield of Cel-CB and sample C with the extraction ratio of 1:3 (v/v) yielded 83.98% of Cel-CB. As a comparison, the yield of Cel-CB obtained by previous research [7] was at 60% with the extraction ratio of water to ethanol of 1:1 (v/v) which was lower than the yield obtained in the current study. On the other hand, for the yield of NCC-CB isolated using 55% wt. of sulfuric acid at 45 °C for 45 minutes, sample C shows the highest yield at 33.7%, followed by sample B at 24.4% and sample A at 15.1%. The yield of NCC-CB obtained from the previous study [7] was a bit higher than the current study which was at 29.4% when using an extraction ratio of 1:1 (v/v). However, the yield of NCC-CB in this study was 33.7%, was improved with extraction ratio 1:3 (v/v) which is higher than previous studies that yielded 29.4% from discarded cigarette butt with the usage of 99.8% ethanol extraction [7], 23.5% from corncob [11], and 15-20% from olive fiber [12]. It shows that when ethanol in the extraction ratio is increased, the yield of NCC increases. Based on Table 1, it can be concluded that the extraction ratio of water to ethanol at 1:1 (v/v) gives the best yield of Cel-CB at 98.76% and the extraction ratio of 1:3 gives the best yield of NCC-CB at 33.7%. The trend of NCC increased with decreasing of the yield of Cel-CB. The yield from the treatment in Sample B and C was also higher than the yield obtained by other studies using pineapple leaves (32.1%) and sugarcane bagasse (28.6%) as a source of nanocellulose [10].

Table 1. Yield of Cellulose (Cel-CB) and Nano-crystalline cellulose (NCC-CB) from Cigarette Butt

Sample	Ethanol to Water Ratio (v/v)	Yield of Cel-CB (%)	Yield of NCC-CB (%)
A	1:1	98.76	15.1
B	1:2	94.76	24.4
C	1:3	83.98	33.7

Aqueous dispersion and morphology of nanocrystalline cellulose: Correlogram of particle size

Dynamic Light Scattering (DLS) determines how randomly particles move when they undergo Brownian motion, and it is not applicable when a particle's motion is not random. Figure 1 shows the DLS measurement. From Figure 1, sample A has increased correlation at higher delay times between 100000-1000000μs which indicates sedimentation, whereas for Sample B, there is no sudden increase which indicates that there is a lower level of sedimentation happening in Sample B. In Sample C, there is an increase in correlation that happened earlier than in Sample A.

Particle Size Distribution (PSD)

The particle size distribution of nanocrystalline cellulose (NCC) from cigarette butt is shown in Figure 2. The size distribution in Sample A shows the largest size distribution in a range 100–1000 nm with 655.4 nm indicated microcrystalline size (MCC). While in Sample B and Sample C, the largest size distribution was in the range of 10–100 nm with 41.75 nm and 30.47 nm, respectively, indicating nano cellulose crystal (NCC). The formation of size differs by the extraction ratio of water to ethanol which is conducted in Sample A, B, and C. It shows that the treatments had improved the cellulose crystal size. The Polydispersity index (PdI) for Sample A, B and C were 0.859, 0.400 and 0.410, respectively. High reading of PdI may result from a sample containing large particles reflected in Sample A. Samples B and C have the lowest PdI which corresponds to Sadeghifar [13], their NCC extracted with HBr of 1M gives PdI of 0.41 reflected small particles. In conclusion,

the extraction ratio of 1:2 and 1:3 (v/v) used for samples B and C improved the size distribution of NCC and this corresponds to the yield of NCC in Table 1.

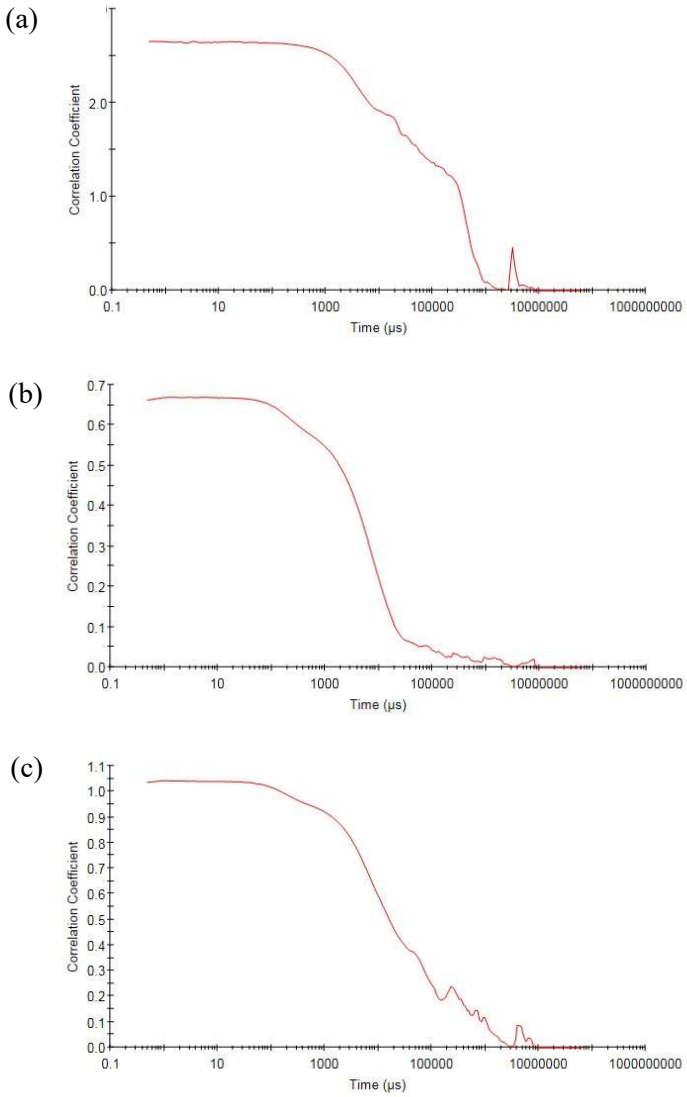

Figure 1. Dynamic light scattering (DLS) measurement of a) Sample A, b) Sample B and c) Sample C of NCC-DCB

Transmission electron microscope (TEM)

The crystallinity and morphology of the NCC-CB produced from this study were analyzed using TEM to analyze the nanometer size samples. Figure 3 shows the TEM micrograph for Sample A, B and C that varied the extraction ratio of water to ethanol 1:1, 1:2, and 1:3 (v/v), respectively. The TEM shows obtained nano-crystals cellulose resulting from sulfuric acid hydrolysis. The amorphous portion of cellulose microfibrils was predicted to be cleaved transversely by the acid hydrolysis treatment under regulated conditions, preserving the straight crystalline domains. Eventually, the treatment should cause the fibers' size to decrease from the micron to the nanometer scale [14]. Here it can be seen that the nanocrystals cellulose is rod in shape for Sample A and needle-like in shape for Sample B and C with a reduction in size due to the treatments, respectively. The observed behavior may be explained

by the fact that ethanol creates a layer and adsorbs more strongly than water on the surface, preventing agglomeration during crystallization [8]. The length and diameter range of Sample A is found to be in a micro size which corresponded to 50% of ethanol extraction, contrary to Sample B and C, where the size of the cellulose crystals is found to be in the nanometric range which corresponded to 66% and 75% of ethanol extraction. From Figure 3(b) and 3(c), the formation of nanocrystalline requires further extraction ratio to have complete shape and size of NCC as in other studies. However, other studies that used other sources of cellulose such as sugar palm fiber [15], pine wood and corncob [11] obtained smaller size than that was obtained in this study that due to higher exposure to more concentrated sulfuric acid (>60%) on the cellulose fiber. According to Yu [14], their nano-crystals diameter is in the range of 15–20 nm with different method of preparing NCC which only involves alkali treatment with NaOH, using aqueous chlorite to bleach, and acid hydrolysis with 10 $molL^{-1}$ of sulfuric acid. The size 170 nm in diameter nanocrystals were isolated from sugarcane bagasse which was extracted with 17.5% w/v of sodium hydroxide solution [16].

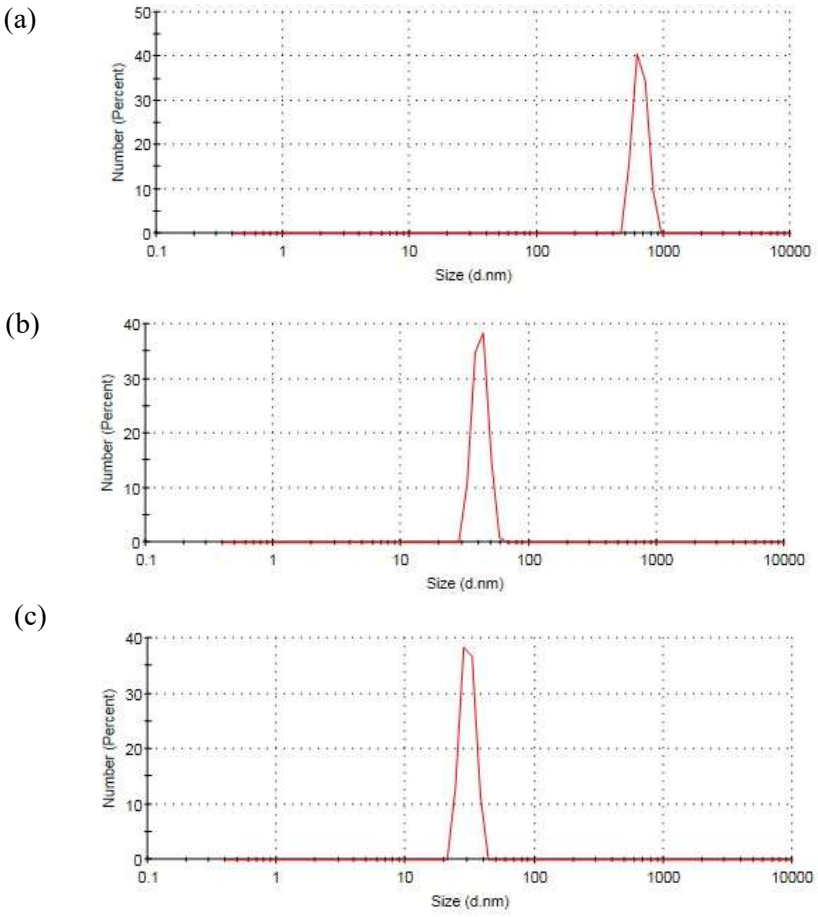

Figure 2. Particle size distribution of nano-crystalline from discarded cigarette butt for a) Sample A, b) Sample B and c) Sample C

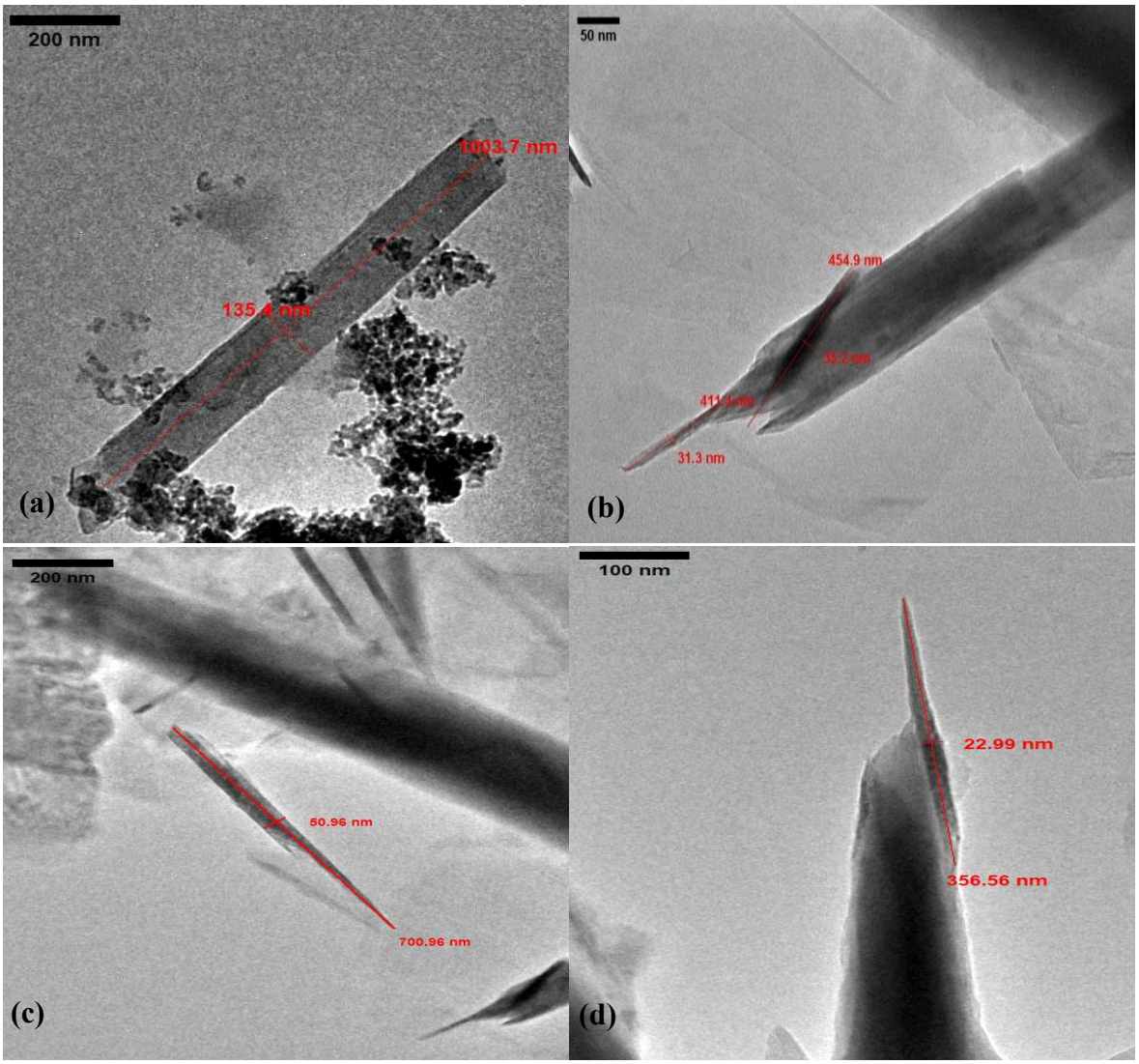

Figure 3. TEM image of nanocrystalline cellulose from a) Sample A; b and c) Sample B; and d) Sample C

The aspect ratio shown in Table 2 for this study indicated that the treatments did not interfere with the formation of the crystal. The aspect ratio is increasing as the ratio is increasing. The aspect ratio for treatment in Sample B and C exhibited more than ten (Table 2) which indicated that the isolated NCC has a mechanical stability for polymer composites synthesis corresponding to the minimal aspect ratio of more than ten to achieve optimal stress transmission during the fiber-matrix interaction[17].

Fourier-transform Infrared Spectroscopy (FTIR)

The successful isolation of the freeze-dried NCC–CB from cigarette butt was confirmed by FTIR. All three samples show a broad band at 3320 cm^{-1} in the absorbance regions of O–H with increasing intensities as the NCC yield increased with the treatment extraction ratio (Figure 4). The O-H stretching vibration of the O-H groups in cellulose molecules is shown by a broad band in the range of 3100 to 3600 cm^{-1} that is visible in the FTIR spectra of every sample. The spectra were compared with the cigarette butt extract without treatment that showed the two main absorbance regions at 3338 cm^{-1} and 1634 cm^{-1}, respectively, that indicate band for O–H and –NH group [18]. After the treatments for Sample A, B, and C there were no sign of C=O at

1743 cm^{-1} and –NH group as in untreated cigarette butt in the orange line in Figure 4. This shows that the treatments in this study can remove ketone and amine [7], [18]. The spectra of sample A, B and C show a C–H stretching band at 2890, 2880, 2894 cm^{-1}, respectively. Furthermore, a peak in band detected at 1363, 1368,1370 cm^{-1} is related to the bending vibration of the C–H and C–O bonds in the polysaccharide aromatic rings [19]. In addition, the absorption peak was linked to aromatic C–C in the plane symmetrical stretching vibration of aromatic rings seen in lignin at 1604 cm^{-1} in the untreated sample. These bands were no longer present in the FTIR spectra of the current NCC.

Table 2. The dimension and aspect ratio for sample with different extraction ratio treatment

Samples	*L*, length (nm)	*D*, diameter (nm)	Aspect ratio (*L*/*D*)
A	1003.7	135.4	7.413
B	454.9	35.2	12.923
	411.4	31.3	13.143
	700.3	50.9	13.731
C	356.6	23.0	15.504

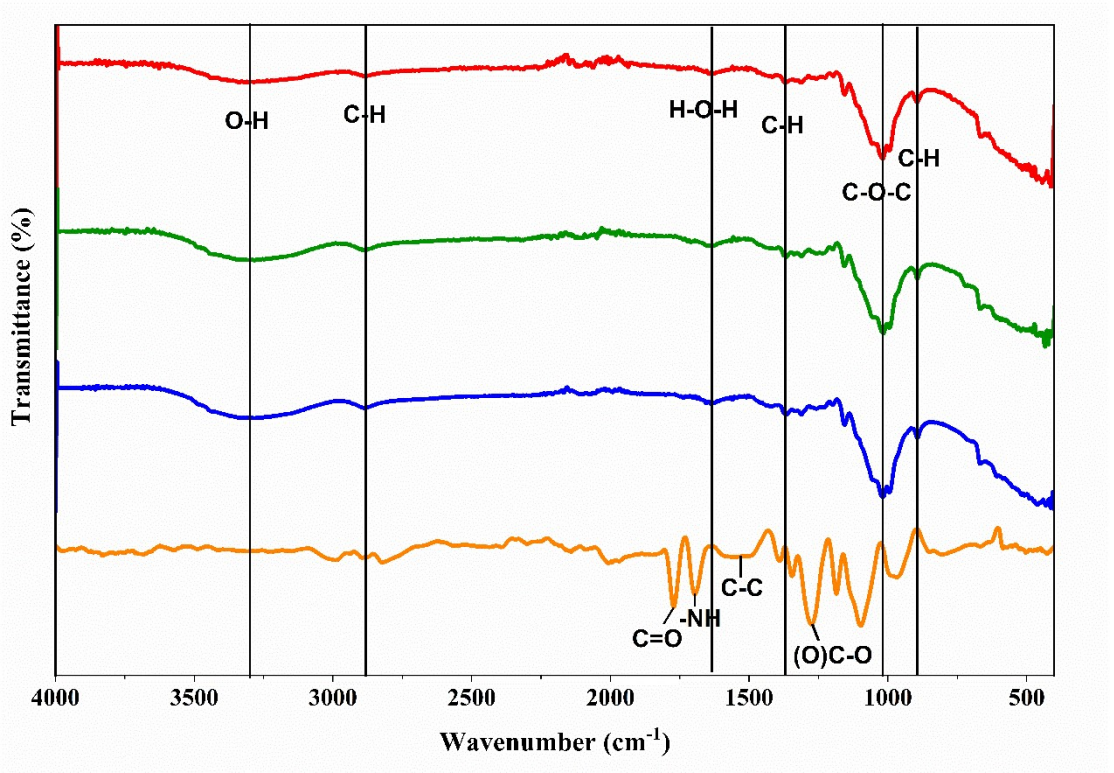

Figure 4. FTIR spectra of Sample A (red line), B (green line), C (blue line), and untreated cigarette butt (orange line)

Finally, the band peaks at 1016, 1018 and 1016 cm^{-1} for sample A, B and C respectively, due to the stretching vibration of the C–O–C pyranose ring, which is antisymmetric in phase. The most important absorption band is at 800–950 cm^{-1} (which is associated with the glycosidic linkages between glucose units in cellulose) [19] when comparing with the FTIR result obtained previously [7], 3320 cm^{-1} (O–H), 2900 cm^{-1} (C–H), 1646 cm^{-1} (H–O–H), 1437 cm^{-1} CH2, 1371 cm^{-1} (C–H), 1018 cm^{-1} (C–O–C) and 898 cm^{-1} (C–H) with the extraction of ethanol to water of 1:1 (v/v). This shows that the FTIR results for sample A, B and C have the

same absorption band to prove that it is NCC chemical structure, and the ratio of extraction did give little impact on FTIR results.

.

X-ray powder diffraction (XRD)

The XRD patterns of the NCC-CB in Sample A, B and C show a characteristic of cellulose III structure with a wide peak around 2θ = 12° (101), 20° (10$\bar{1}$), 22° (002) and 25° (111) (Figure 5) similar shape with other NCC obtained from cigarette butt [7]. After acid hydrolysis, the isolated NCC-CB Crystallinity Index (CI) and crystallite size were calculated using Equation 3 and 4, respectively as shown in Table 3 for sample A, B and C. This data is lower than the data obtained previously [7] using CBs as the cellulose source, which is 94.5% for NCC. However, for this study, the CI was increasing as the treatment increased the extraction ratio. When referring to the untreated cigarette butt, the CI was 28.26% which was due to the amorphous region in the cellulose being removed during the acid hydrolysis [7]. There is no significant difference between all three samples. Sample A had the highest peak is highest at 22° whereas Sample B and C recorded the highest peak at 20°. This is due to the conversion of cellulose I to cellulose III as the extraction ratio increased [20]. Sample C shows the highest crystallinity Index (CI), 64.8% with the smallest crystallite size 3.66 nm. This suggests that the extraction ratio does not have a negative effect on crystallite of cellulose. Further, an increase in the extraction ratio can be extended to obtain more CI.

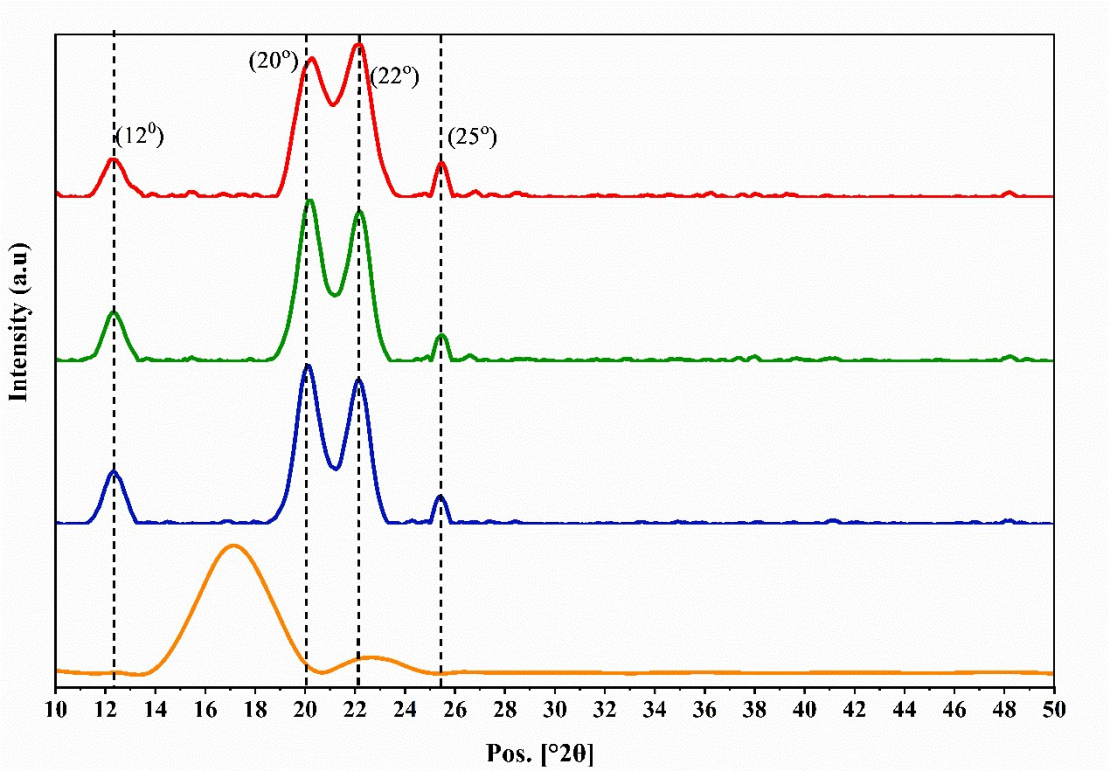

Figure 5. XRD results of Sample A (red line), B (green line), C (blue line), and untreated cigarette butt (orange line)

Table 3. Crystallinity index and crystallite size of nanocrystalline cellulose from cigarette butt

Sample	Crystallinity Index (%)	Crystallite Size (nm)
A	44.9	4.25
B	48.6	3.99
C	64.8	3.66

Inductively coupled plasma mass spectrometry (ICP-MS)

CB can contain toxic chemicals that come from cigarettes as it functions to filter the chemicals from getting into the human body. To reuse the CBs as a source of cellulose for NCC, the contents need to be examined. The metal contents in the powder NCC-CB were analyzed using Inductively Coupled Plasma Mass Spectrometry (ICP-MS) and compared with the previous study [18] as shown in Table 2. Based on Table 2, Sample A has most metal elements from the discarded CB due to the inappropriate extraction ratio during the isolation of the NCC-CB. Contrary to Sample B and Sample C, the metal contents were reduced and most of them were not traceable. The amount of heavy metal content reduced with increasing extraction ratio. This shows that the heavy metal contents in the cigarette butt can be removed, and this opens an avenue to recycle the waste in an environmentally safe way.

As the treatment ratio increased it improved the content in the CB and enhanced the CI of the isolated NCC from CB, and it is confirmed by the formation of the NCC-CB shown in Figure 3(b) and 3(c) for Sample B and Sample C. This shows that the samples contain high percentage of nano-crystals cellulose [21]. Apart from that, heavy metal contents in the discarded CB were removed successfully using all the extraction ratios, indicated by lead, nickel, copper, arsenic, cadmium, cobalt, manganese, and titanium were not traceable in all samples. However, further treatment needs to be done to remove or reduce other metals such as aluminum and iron [17].

Table 2. Elements analyzed by ICP-MS for Sample A, B, and C and compared with the metal leached from untreated cigarette butt [18]

	Concentration (ppm)			
Elements	**Sample A**	**Sample B**	**Sample C**	**Untreated Cigarette butt [18]**
Na	368	139	60.9	239
Mg	100	69.4	64.1	620
Al	1320	720	323	950
Pb	-	-	-	2.39
K	162	40.6	20.9	929
Ca	540	417	559	766
V	2.53	-	1.52	-
Cr	21.6	11.1	6.99	85
Fe	403	194	154	590
Ni	3.02	-	-	2.90
Cu	2.12	4.66	-	11
Zn	27.4	21.8	16	35.3
As	1.54	-	-	-
Ag	-	1.94	7.49	0.18
Cd	-	-	-	0.99
Co	-	-	-	0.04
Mn	-	-	-	178
Ti	-	-	-	106
Ba	-	-	-	48.7
Sr	-	-	-	39.6

Conclusion

In conclusion, reusing CB to isolate NCC can be a solution to the CB littering problem. The NCC can be used further in polymer industries. The NCC isolated in this study using water to ethanol of 1:3 (v/v) gives the best results of crystallinity index with 64.8%, polydispersity index of 0.40, and crystallite size 3.66 nm with needle-like shape showing the improvement in the treatment. The NCCs yield was considerably great between 24-34% and MCC yield was 15%, by only utilizing more aqueous ethanol (1:3 v/v), proving the preparation method was environmentally friendly. The

chemical structure of NCC in FTIR spectra of sample A, B and C present similar bands, indicating the same chemical structure for all the NCC. ICP-MS was conducted to determine the content of metal found in the samples and aluminum and iron were found to be the highest. Thus, further treatment needs to be done with aqueous ethanol (1:3 v/v) and sulfuric acid treatment to improve the NCC isolated from the CB to use in various application fields especially in polymer and medical. The results obtained here suggest that CB is capable of being one of the sources of cellulose to produce NCC with the advantage of being easily biodegradable and environmentally friendly.

Acknowledgement

The authors would like to acknowledge with an appreciation to the Ministry of Higher Education for providing financial support under Fundamental research grant FRGS-KPT (FRGS/1/2019/TK02/UMP/02/11) and Universiti Malaysia Pahang Al-Sultan Abdullah for additional financial support under UMP Research Grant (PGRS220307).

References

1. Rahman, N. H. A., Chieng, B. W., Ibrahim, N. A., and Rahman, N. A. (2017). Extraction and characterization of cellulose nanocrystals from tea leaf waste fibers. *Polymers*, 9(11): 588-599.
2. Fialho e Moraes, A. R., Pola, C. C., Bilck, A. P., Yamashita, F., Tronto, J., Medeiros, E. A. A., and Soares, N. F. F. (2017). Starch, cellulose acetate and polyester biodegradable sheets: Effect of composition and processing conditions. *Materials Science and Engineering C*, 78: 932-941.
3. Green, A. L. R., Putschew, A., and Nehls, T. (2014). Littered cigarette butts as a source of nicotine in urban waters. *Journal of Hydrology*, 519: 3466-3474.
4. Lee, W. and Lee, C. C. (2015). Developmental toxicity of cigarette butts – An underdeveloped issue. *Ecotoxicology and Environmental Safety*, 113: 362-368.
5. d'Heni Teixeira, M. B., Duarte, M. A. B., Raposo Garcez, L., Rubim, J. C., Gatti, T. H., and Suarez, P. A. Z. (2017). Process development for cigarette butts recycling into cellulose pulp. *Waste Management*, 60: 140-150.
6. Maderuelo-Sanz, R., Escobar, V. G., and Meneses-Rodríguez, J. M. (2018). Potential use of cigarette filters as sound porous absorber. *Applied Acoustics*, 129: 86-91.
7. Ogundare, S. A., Moodley, V., and van Zyl, W. E. (2017). Nanocrystalline cellulose isolated from discarded cigarette filters. *Carbohydrate Polymer*, 175: 273-281.
8. Shah, K., Gupta, K., and Sengupta, B. (2020). Role of ethanol on particle size and morphology during copper oxalate synthesis by precipitation-stripping. *Powder Technology*, 366: 230-238.
9. De Fenzo, A., Giordano, M., and Sansone, L. (2020). A clean process for obtaining high-quality cellulose acetate from cigarette butts. *Materials*, 13 (21): 1-13.
10. Sainorudin, M. H., Abdullah, N. A., Rani, M. S. A., Mohammad, M., Mahizan, M., Shadan, N., Abd Kadir, N. H., Yaakob, Z., El-Denglawey, A. and Alam, M. (2021). Structural characterization of microcrystalline and nanocrystalline cellulose from *Ananas comosus* L. leaves: Cytocompatibility and molecular docking studies. *Nanotechnology Reviews*, 10(1): 793-806.
11. Ditzel, F. I., Prestes, E., Carvalho, B. M., Demiate, I. M., and Pinheiro, L. A. (2017). Nanocrystalline cellulose extracted from pine wood and corncob. *Carbohydrate Polymer*, 157: 1577-1585.
12. Kian, L. K., Saba, N., Jawaid, M., Alothman, O. Y., and Fouad, H. (2020). Properties and characteristics of nanocrystalline cellulose isolated from olive fiber. *Carbohydrate Polymer*, 241: 1-7.
13. Sadeghifar, H., Filpponen, I., Clarke, S. P., Brougham, D. F., and Argyropoulos, D. S. (2011). Production of cellulose nanocrystals using hydrobromic acid and click reactions on their surface. *Journal of Material Science*, 46(22): 7344-7355.
14. Yu, X., Jiang, Y., Wu, Q., Wei, Z., Lin, X., and Chen, Y. (2021). Preparation and characterization of cellulose nanocrystal extraction from *Pennisetum hydridum* fertilized by municipal sewage sludge via sulfuric acid hydrolysis. *Frontier in Energy Research*, 9: 1-10.
15. Ilyas, R. A., Sapuan, S. M., and Ishak, M. R. (2018). Isolation and characterization of nanocrystalline cellulose from sugar palm fibres (*Arenga pinnata*). *Carbohydrate Polymer*, 181: 1038-1051.
16. Mandal, A., and Chakrabarty, D. (2011). Isolation of nanocellulose from waste sugarcane bagasse (SCB) and its characterization. *Carbohydrate*

Polymer, 86(3): 1291-1299.

17. Deepa, B., Abraham, E., Cordeiro, N., Mozetic, M., Mathew, A. P., Oksman, K., Faria, M., Thomas, S., Pothan, L. A. (2015). Utilization of various lignocellulosic biomass for the production of nanocellulose: a comparative study. *Cellulose*, 22(2): 1075-1090.
18. Mondal, N. K., Hajra, A., Chakraborty, D., Medda, S., Dey, U., and Kumar, J. (2015). Cigarette butt waste and its effective utilization towards larvicidal activity of Mosquito. *International Journal of Scientific Research in Environmental Sciences*, 3(1): 9-15.
19. Rahimi, M. K. S., Brown, R. J., Tsuzuki, T. and Rainey, T. J. (2016). A comparison of cellulose nanocrystals and cellulose nanofibres extracted from bagasse using acid and ball milling methods. *Advances in Natural Sciences: Nanoscience and Nanotechnology*, 7(3): 1-9.
20. Mittal, A., Katahira, R., Himmel, M. E., and Johnson, D. K. (2011). Effects of alkaline or liquid-ammonia treatment on crystalline cellulose: Changes in crystalline structure and effects on enzymatic digestibility. *Biotechnology for Biofuels*, 4: 41-57.
21. Haron, G. A. S., Mahmood, H., Noh, H., Goto, M., and Moniruzzaman, M. (2022). Cellulose nanocrystals preparation from microcrystalline cellulose using ionic liquid-DMSO binary mixture as a processing medium. *Journal of Molecular Liquid*, 346: 118208.

Malaysian Journal of Analytical Sciences (MJAS)
Published by Malaysian Analytical Sciences Society

SYNTHESIS AND CHARACTERISATION OF REUSABLE PVA-SODIUM ALGINATE-Ni CATALYST IN HECK REACTION

(Sintesis dan Pencirian Pemangkin yang Boleh Digunakan Semula dalam Tindak Balas Heck)

Norul Azilah Abdul Rahman[1,2], Nurul Afiqah Mohd Haris[1], Karimah Kassim[3], Mazni Musa[1], and Nur Rahimah Said[1*]

[1]*School of Chemistry and Environment, Universiti Teknologi MARA (UiTM), Cawangan Negeri Sembilan, Kampus Kuala Pilah, 72000 Kuala Pilah, Negeri Sembilan, Malaysia*
[2]*School of Chemistry and Environment, Faculty of Applied Sciences, Universiti Teknologi MARA (UiTM), 40450 Shah Alam, Selangor, Malaysia*
[3]*Institute of Science (IOS), Level 3, Block C, Kompleks Inspirasi, Universiti Teknologi MARA (UiTM), 40450 Shah Alam, Selangor, Malaysia*

[*]*Corresponding author: nurra1435@uitm.edu.my*

Received: 15 September 2023; Accepted: 18 April 2024; Published: 29 June 2024

Abstract

Heck reaction is a carbon-carbon coupling reaction that essential for the development of natural products, agrochemicals, optical devices and drugs. During the synthesised of chemicals, the presence of catalysts is important. Normally, the reaction is carried out with the presence of palladium metal as catalyst. However, it has disadvantages such as high toxicity and considerably expensive. Compared to palladium, nickel represent a low cost and environmental friendly type metal. Therefore, nickel is effective to replace the palladium in their application as catalyst in Heck reaction. This study produced a Polyvinyl alcohol-sodium alginate-Nickel (PVA-SA-Ni) catalyst by using one pot synthesis method in the ultrasound irradiation system. The benefits in producing a catalyst not only is cost effective but also its reusability properties due to the presence of PVA-SA as a support. The PVA-SA-Ni was successfully synthesised and characterised by using FTIR, XRD, FESEM-EDX and AAS. The catalytic performance and reusability of PVA-SA-Ni was investigated in Heck reaction between 1-bromo-4-nitrobenzene and styrene. The percentage conversion rate of reactant to product was determined by using GC-FID. The PVA-SA-Ni showed the best performance in Heck reaction with 74 % conversion by using 1 mmol % in the presence of K_2CO_3 as a base at a temperature of 165 °C, and DMA as solvent within 4 h of reaction time.

Keywords: polyvinyl alcohol, sodium alginate, nickel(II) catalyst, Heck reaction, reusable catalyst

Abstrak

Tindak balas heck ialah tindak balas gandingan karbon-karbon adalah penting untuk pembangunan produk semula jadi, agrokimia, peranti optik dan ubat-ubatan. Semasa bahan kimia disintesis, kehadiran pemangkin adalah penting. Biasanya, tindak balas dilakukan dengan kehadiran logam paladium sebagai mangkin. Walau bagaimanapun, ia mempunyai kelemahan seperti kadar toksik tinggi dan harga yang agak mahal. Berbanding dengan paladium, nikel dilihat sebagai jenis logam kos rendah dan mesra alam. Oleh itu, nikel berkesan untuk menggantikan paladium dalam penggunaannya sebagai pemangkin dalam tindak balas Heck. Kajian ini menghasilkan mangkin Polivinil Alkohol-natrium alginat-Nikel (PVA-SA-Ni) menggunakan kaedah sintesis satu pot

dalam sistem penyinaran ultrabunyi. Terdapat banyak faedah dalam menghasilkan pemangkin ini bukan sahaja efektif dari segi kos tetapi dilengkapi dengan sifat kebolehgunaan semula kerana kehadiran PVA sebagai sokongan. PVA-SA-Ni yang telah berjaya disintesis dicirikan menggunakan FTIR, XRD, FESEM-EDX dan AAS. Prestasi pemangkin dan kebolehgunaan semula PVA-SA-Ni telah disiasat dalam tindak balas Heck antara 1-bromo-4-nitrobenzene dengan stirena. Kadar penukaran peratus bahan tindak balas kepada produk ditentukan dengan menggunakan GC-FID. PVA-SA-Ni menunjukkan prestasi yang baik dalam tindak balas Heck dengan penukaran 74 % dengan menggunakan 1 mmol % pemangkin, kehadiran K_2CO_3 sebagai bes pada suhu 165 °C, dan DMA sebagai pelarut dalam masa 4 jam tindak balas.

Kata kunci: polivinil alkohol, natrium alginat, pemangkin nikel(II); tindak balas Heck, pemangkin yang boleh digunakan semula

Introduction

The Heck reaction is a common practical reaction used in the synthesis of natural compounds, agrochemicals, and medicines. Palladium (Pd) catalysts are commonly used in Heck reaction [1] because of their high catalytic activity, high stability, and the reaction can occur at low temperatures [2]. Nevertheless, the price of Pd metal is expensive and toxic that is harmful to the environment leading to its limitations in industrial applications. An alternative to replace the Pd metal is nickel catalyst. It is cheaper, low toxicity, and good in catalytic activity [3].

The catalytic performance of Ni type catalyst in the Heck reaction is comparable with Pd type catalyst. However, the homogenous Ni catalyst has difficulty separating from the product of Heck. Ni-phosphine ligand also has its drawbacks, whereby phosphine is not cheaper, toxic and needs inert condition because it is sensitive to water and oxygen. Heterogeneous Ni type catalyst is more preferable due to easy recovery at the end of reaction, recyclable, reduce waste of chemical and environmentally friendly [4].

The heterogeneous type of catalyst is designed by the presence of solid polymer support in the structure of catalyst. Amongst the polymers, biodegradable polymers such as chitosan (CS) [5], PVA [6] and sodium alginate (SA) [7] are gaining more attention due to their great advantages. For instance CS is an expensive polymer from polysaccharides, non-toxic, biodegradable, renewable and not soluble in common solvents [5]. Interestingly, CS have OH and NH_2 groups that function as chelating ligand to Ni and other metals [8]. Tang et al. [8] synthesized CS together with carbon nanotube (CNT) to support Ni (CS-CNT-Ni). Excellent catalytic activity of CS-CNT-Ni is reported giving 100% acetylene conversion at 160^{o}C. However, no study on recyclability was reported. Hajipour and Abolfathi [5] also synthesized CS with Ni and triazole (CS-triazole-Ni). The catalytic activity of CS-triazole-Ni was good at above 80% of conversion and the recyclability of catalyst is 5 times without any reduction in rate of conversion.

The PVA is also used as support for the synthesis of heterogeneous Ni type catalyst. PVA is non-toxic, biocompatibility, biodegradable and environmentally friendly [6]. Moreover, the presence of hydroxyl group in PVA structure cause it easy to dissolve in water [9] and also can function as ligand during the complexation [10]. Medjili, et al. [11] synthesized Ni supported catalyst with Cu, PVA and polyaniline (PANI). PVA-PANI-Ni-Cu catalyst was successfully used in removing methylene blue (94%) from 10^{-5} M initial concentration of dye. Lakhdari, et al. [6] also synthesis PVA-PANI-Ni-Cu. They applied the PVA-PANI-Ni-Cu in converting the toxic methanol to less harmful by-products, CO_2 and H_2O.

Sodium alginate (SA) is extracted from brown algae that contain polysaccharides. It is water soluble because it contains carboxyl (-COO^-) and hydroxyl (-OH) functional groups. The -COO^- and -OH functional group can coordinate with metal to form coordination complex. The SA will become a hydrogel when it is cross-link with $CaCl_2$ [12]. Qiao et al. [7] synthesized SA-Ni and used as catalyst for hydrogenation. SA-Ni catalyst has excellent catalytic activity in styrene hydrogenation where it successfully converts 99.9% styrene to ethylbenzene. It also can be reused up to 20 times without loss of initial activity.

Both PVA and SA have good interaction with metals. The properties of SA can be increased by blending with

PVA [13]. Knijnenburg, et al. [14] used PVA-SA to bind with Zn for fertilizer application. While Rahman et al. [15] synthesized PVA-SA-$PdCl_2$ for Heck reaction. The catalytic performance of PVA-SA-$PdCl_2$ for reaction of aryl halides with styrene gives an outstanding result of 100% conversion rate. In addition, the recyclability of PVA-SA-$PdCl_2$ is excellent which is over 11 cycles. PVA-SA as active metal site support has been found in many literatures. As noted, there are yet findings available that emphasising the applications of PVA-SA as polymer support for Ni catalysts. Hence, the current study aimed to synthesise polymer-supported Ni or PVA-SA-Ni catalysts employable in Heck reactions. Moreover, the recyclability and optimum reaction conditions of the catalyst in different parameters were determined. This is a fundamental study to determine the capability of synthesis polymer-supported Ni or PVA-SA-Ni as catalyst in Heck reaction.

Materials and Methods

Materials and instrumentation

Polyvinyl alcohol (PVA, 99+% hydrolysed) (Aldrich), sodium alginate (SA) (Sigma, medium viscosity), nickel(II) chloride ($NiCl_2$) (Aldrich, 99%), nitric acid (HNO_3)(R&M Chemicals, 65%), hydrogen peroxide (H_2O_2, 50%) (Bendosen), calcium chloride ($CaCl_2$) (Sigma Aldrich, 97%), distilled water, styrene (R&M Chemicals, 99%), 1-bromo-4-nitrobenzene (Aldrich, 99%), N,N-Dimethylacetamide (DMA) (R&M Chemicals, 99%), toluene (R&M Chemicals, 99.5%), potassium carbonate (K_2CO_3) (Fisher Scientific, 99.5%), methanol (Sigma-Aldrich, 99%) and sodium acetate (NaOAc) (Sigma-Aldrich) were purchased from standard commercial suppliers and used as received without further purification.

The characteristic of PVA-SA-Ni was characterized by using flame atomic absorption spectroscopy (FAAS), attenuated total reflection-Fourier transform infrared (ATR-FTIR), field emission scanning electron microscope-energy dispersive X-ray (FESEM-EDX), and X-ray diffraction (XRD). The Ni content in PVA-SA-Ni was measured by using FAAS (Perkin Elmer-AAnalyst 400) utilizing a flame approach. The spectra of samples were provided by ATR-FTIR (Perkin Elmer Spectrum 100) analysis and recorded in the range of 650 cm^{-1} to 4000 cm^{-1} by averaging 16 scans numbers at 4 cm^{-1} resolution.

The sample surface analysis was conducted utilizing FESEM-EDX (Hitachi, SU8220). The analysis using a Carl Zeiss electron microscope at 10 kV with 3 k magnification. Diffractogram of the samples by using XRD (Empyrean, PANanalytical). It was recorded over a 2-theta range of 2^o to 50^o by X-ray diffractometer with a angle of 0.02^o min^{-1}. The voltage and current were utilized at 40 kV and 20 mA respectively.

The percentages of conversion rate and turnover number (TON) of reactant determined the catalytic efficiency. The percentage conversion rate and percentage TON were calculated by using equation (1) and (2) below. The data was obtained from Gas Chromatography (GC) (Agilent Technologies, 7890A). The instrument was equipped with an HP-5 capillary column (15 m × 0.25 mm × 0.25 μm) with a flame ionization detector (GC-FID). The microliter samples were injected at 50 °C (held for 1 min) and the final temperature of 250 °C (held for 30 s). The temperature increased at a rate of 15 °C min^{-1}. The flow rate was set at 1.9162 mL min^{-1}.

$$\% \text{ conversion} = \frac{A_{initial} - A_{final}}{A_{final}} \times 100 \quad (1)$$

$$\% \text{ TON} = \frac{\% \text{ conversion}}{\% \text{ catalyst}} \quad (2)$$

Preparation of catalyst

In the preparation of $NiCl_2$ catalyst, the optimum parameter from previous study was used with 1 h ultrasonic synthesise time. The modification method was acquired from a study by Rahman et al. [15].

Catalytic testing

1-bromo-4-nitrobenzene reacts with styrene monomer to produce 1-bromo-4-styrylbenzene in Heck reaction. All chemicals: 1-bromo- 4-nitrobenzene (0.2000 g;1 mmol), styrene monomer (0.2083 g; 2 mmol), Na_2CO_3 (0.2500 g, 2.4 mmol), PVA-SA-Ni catalyst (1.0 mmol%) and DMA (10 mL) as solvents was mixed in a round bottle flask and refluxed at 165 ºC based on the boiling point of DMA solvent whilst being purge with the nitrogen gas

for 1 h. The conversion rate of crude products was analyzed by GC-FID. The Heck reactions were then studied with three parameters, including the effect of different reaction times, solvent, and bases.

Recyclability of catalyst

The catalyst was separated from the reaction mixture after reaction and washed with water and acetonitrile to remove salts and organic residual. The catalyst was then dried in a vacuum oven and subjected to use in a fresh new reaction.

Results and Discussion

Characterization of synthesized compound

This study successfully synthesized PVA-SA-Ni (Figure 1) by using a one-pot ultrasonic method. The color of PVA-SA-Ni obtained is pale green as shown in Figure 2 (transformed from white color of PVA-SA). The amount of Ni is 0.14615 % in 50 mg PVA-SA-Ni was determined by using AAS.

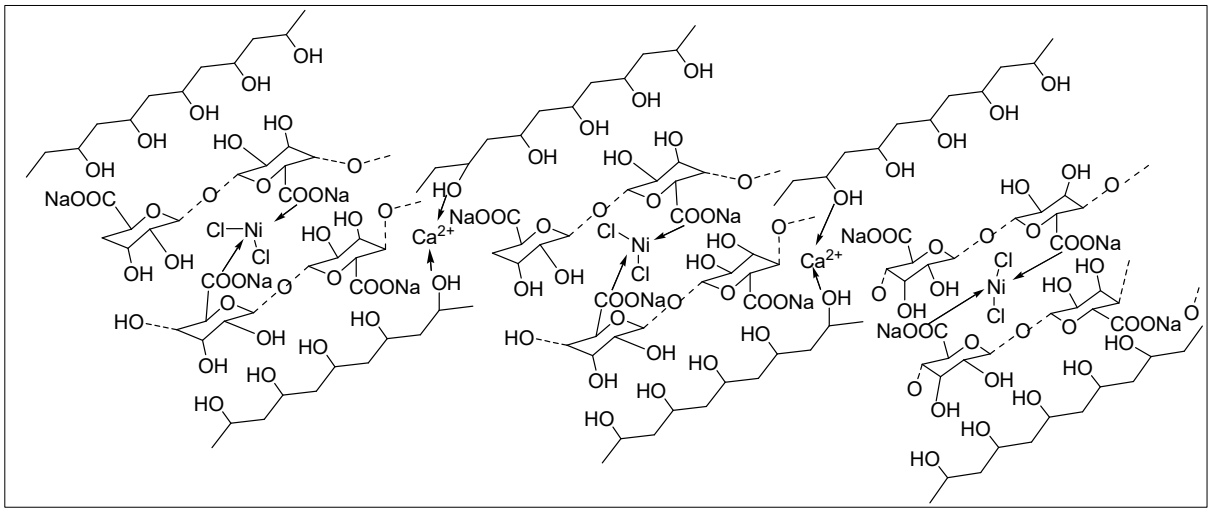

Figure 1. Structure of PVA-SA-Ni

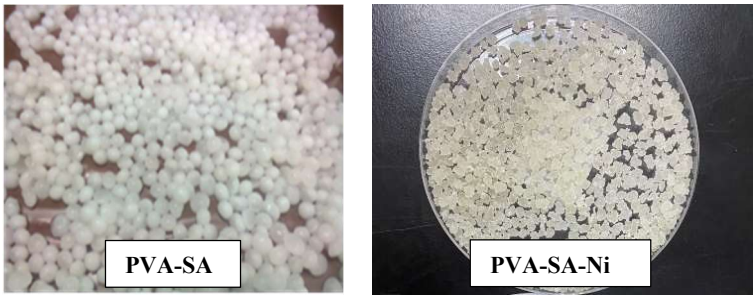

Figure 2. The images of PVA-SA and PVA-SA-Ni

The successful synthesis of PVA-SA-Ni catalyst was confirmed by using ATR-FTIR, FESEM-EDX and XRD. The functional group absorption bands of PVA-SA and PVA-SA-Ni using ATR-FTIR is summarized in Table 1 measured within 650 cm^{-1} to 4000 cm^{-1}. Based on Table 1, the functional group present in PVA-SA and PVA-SA-Ni catalyst is similar. This result showed that the PVA-SA structure was not altered during blending with $NiCl_2$ and only the position of functional group was affected [16].

Table 1 shows no significant changes for hydroxyl (-OH), alkyl (-CH_2 and -CH_3) and -CO groups. The -OH absorption bands appeared at 3345 cm^{-1} and 3355 cm^{-1} in both PVA-SA and PVA-SA-Ni catalyst due to presence of a large amount hydroxyl group in both

structure of PVA and SA [15]. The -CH_2 absorption bands of PVA-SA and PVA-SA-Ni appeared at 2920 cm^{-1} and 2924 cm^{-1}. The group of -CH_3 symmetry bending of PVA-SA and PVA-SA-Ni observed at 1320 cm^{-1} and 1333 cm^{-1}. While the absorption band of -CO visualized at 1085 cm^{-1} and 1086 cm^{-1}. Important absorption band is asymmetric and symmetric vibration of -C=O at 1636 cm^{-1} and 1429 cm^{-1} that moved to lower wavenumbers after complexation due to the interaction of $NiCl_2$ and -C=O from -COONa indicating the successful construction of PVA-SA-Ni catalyst [15, 17].

Table 1. The functional group of PVA-SA and PVA-SA-Ni

Functional Group	PVA-SA (cm^{-1})	PVA-SA-Ni (cm^{-1})
-OH stretching	3345	3355
-CH_2 stretching asymmetric	2920	2924
-C=O asymmetric stretching	1636	1616
-C=O symmetric stretching	1429	1423
-CH_3 symmetric bending	1320	1333
-C-O bending	1085	1086

The micrograph of outer surface and cross-section of PVA-SA and PVA-SA-Ni from FESEM (100x of magnification) is presented in Figure 3. The outer surface and cross section of PVA-SA beads in Figure 3 (A1) and Figure 3 (A2) had a rough and ridged surface. It has pores due to lumps stuck together. The presence of $NiCl_2$ in outer surface and cross section of PVA-SA-Ni Figure 3 (B1) and Figure (B2) caused modification on PVA-SA which resulted more pores on PVA-SA-Ni as compared to PVA-SA [16]. Based on Rahman et al. [15] study's every angle of pores allow catalytic reaction to occur by allowing diffusion of reactant and product utilised in the reaction that help in catalytic activity. The FESEM mapping of PVA-SA-Ni outer surface is shown in Figure 3 (**C1**) and cross-section in Figure 3 (**C2**) revealed that dispersion of Ni metal is homogenous over the whole mass of the beads through the binding process.

Meanwhile, the chemical composition of the PVA-SA and PVA-SA-Ni (Figure 4) was analysised by using an energy dispersive x-ray (EDX). The element present in PVA-SA was similar as reported by Rahman et al. [15] that contain element of carbon (C), oxygen (O), sodium (Na), calcium (Ca) and chlorine (Cl). In contrast, the PVA-SA-Ni detected contained 0.8 % mass of Ni atom. The crystalline phase in PVA-SA and PVA-SA-Ni was confirmed by using XRD as shown in Figure 5. Diffractogram of PVA-SA showed peaks appeared at 20° with shoulder similar to diffractogrom obtained by Sang Joon Lee, et al. [18]. Broad peaks obtained indicated the PVA-SA is in amorphous form similar to a study by Rahman, et al. [15]. In contrast with diffractogram of PVA-SA-Ni , the peaks at 20° is narrower and sharp, indicating that the presence of Ni promoted the crystallisation of PVA-SA [19]. While, peak of Ni at 44.4°, 51.7° and 76.4° [20] was not seen because the amount of Ni in PVA-SA-Ni is small based on data FAAS and EDX. From all the characterisation data of PVA-SA-Ni were sucessfully synthesised and the structure is illustrated in Figure 1.

Catalytic activity of PVA-SA-Ni in Heck reaction

The efficiency of PVA-SA-Ni as catalyst was tested in Heck reaction between styrene and 1-bromo-4-nitrobenzene. The study focused on optimizing the reaction condition and the results are summarized in Table 2. The initial test was conducted by using 1 mmol % of the PVA-SA-Ni catalyst, K_2CO_3 as base, DMA as solvent, reflux at 165 °C temperature based on DMA solvent boiling point with different times. The results are recorded at Entries 1-5.

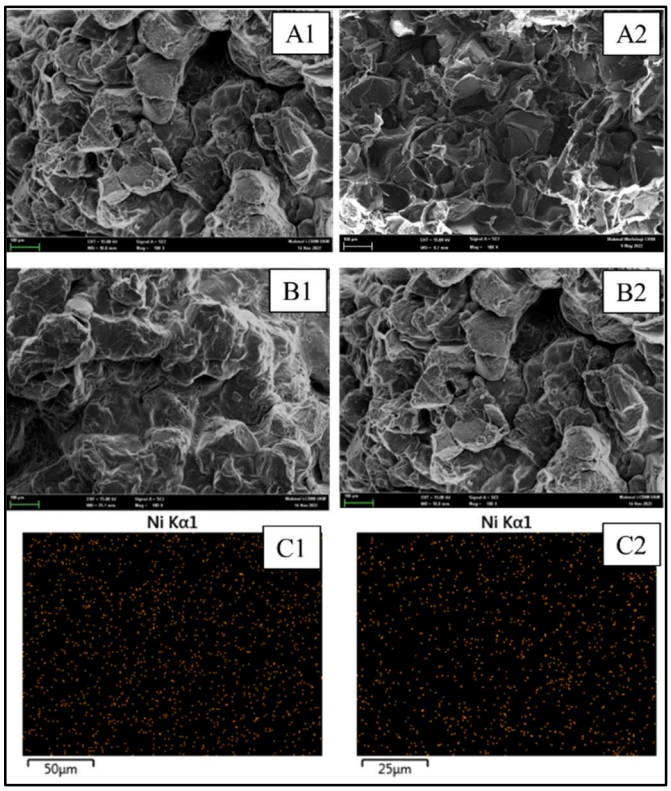

Figure 3. FESEM micrograph of PVA-SA (**A1** and **A2**), PVA-SA-Ni (**B1** and **B2**) and elemental mapping of Ni for PVA-SA-Ni (**C1** and **C2**)

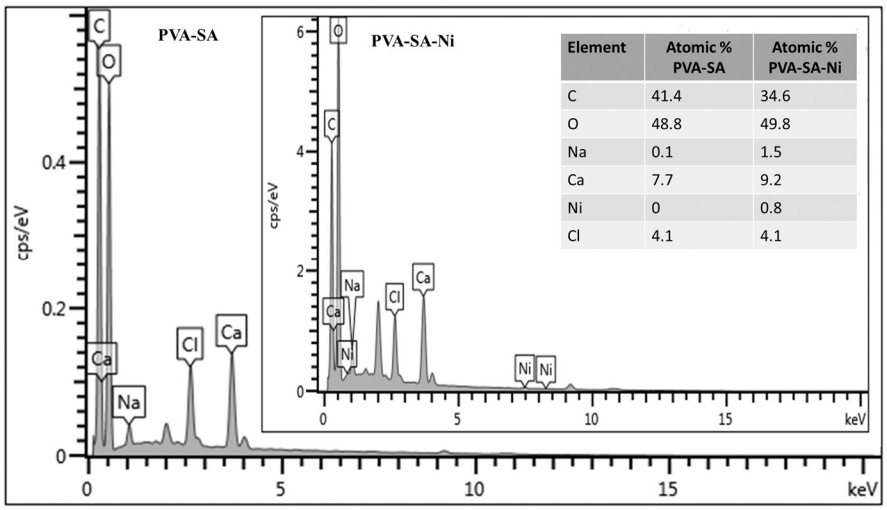

Element	Atomic % PVA-SA	Atomic % PVA-SA-Ni
C	41.4	34.6
O	48.8	49.8
Na	0.1	1.5
Ca	7.7	9.2
Ni	0	0.8
Cl	4.1	4.1

Figure 4. The EDX images of PVA-SA and PVA-SA-Ni

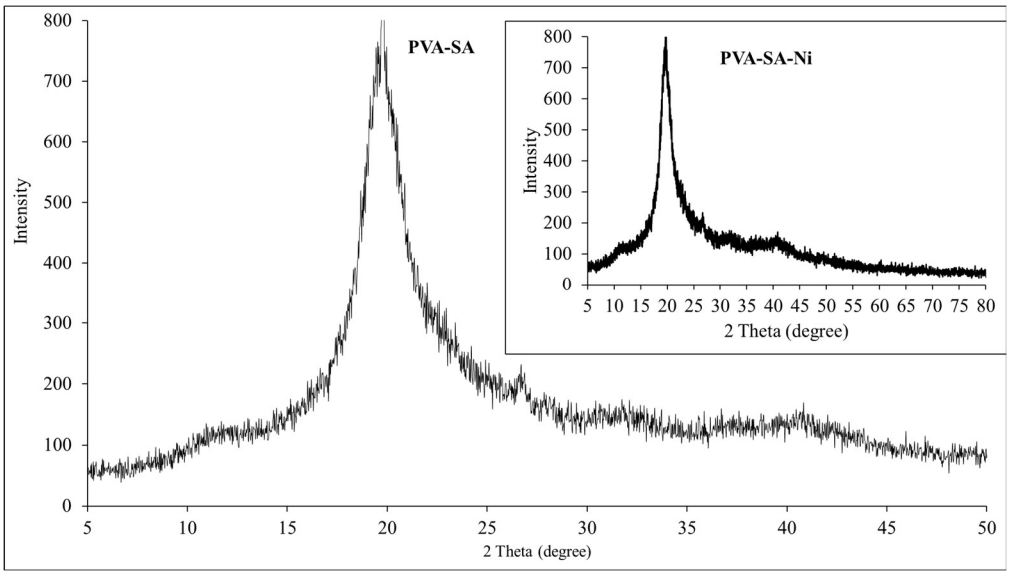

Figure 5. The diffractogram of PVA-SA and PVA-SA-Ni

The first 1 h of reaction, only 36% (Entry 1) of conversion rate was obtained. In order to confirm the substrates have sufficient time to convert to product, the reaction time was increased (Entries 2-5) [21]. Within 4 h of reaction times, 74% (Entry 4) of conversion rate was recorded. However, reaction time increase to 5 h showed no significant changes in conversion rate percentage because deactivation of catalyst caused by the reaction was too long [22]. Thus, 4 h was selected as optimum reaction time for future study in effect of bases, and solvents.

Catalytic activities also would increase by the presence of suitable bases. The function of base is to regenerate active complexes of catalyst by removing hydrogen halide from inactive catalyst complex [23]. In this study, K_2CO_3, Na_2CO_3 and NaOAc (Entries 4, 6-7) were used. The highest conversion rate percentage by using K_2CO_3 probably due to the solubility of base in solvent [21].

The effect of solvent in the catalytic activity has been studied by employing polar solvent DMA, 6.5 (Entry 4) and methanol, 6.1 (Entry 8) and non-polar solvent toluene (Entry 9). Based on Table 2, DMA was the most efficient solvent due to its higher basicity and nucleophilicity [24] as compared to methanol that is less polar. Toluene is not suitable in this catalytic activity due to its non-polar solvent.

From all the results obtained, used of 1 mmol% PVA-SA-Ni catalyst load gained the highest catalytic activity when K_2CO_3 acted as base, DMA as solvent, with temperature at 165 °C and time within 4 h were employed (Entry 4).

The parameter for entry 4 was used to pursue the recyclability study of PVA-SA-Ni catalyst. It is important to evaluate the ease separation of catalyst from reaction mixture. The catalyst was separated from reaction mixture by easy filtration step, wash, dried and used for next catalytic cycle. The reusability of PVA-SA-Ni was three times based on Entry 4, 10 and 11. In the 1st run, the conversion rate of the product was 74%. For the 2nd run, the conversion rate of product was 69%. However, for the 3rd run, the conversion rate obtained was 24% and the catalyst was denatured. The reusability of the heterogeneous catalyst was low maybe due to Ni leaching from FAAS analysis (59%). It is expected that this results in a loss of catalytic because in many cases showed low reusability and low catalytic activity due to the leaching [15].

Table 2. Optimisation of Heck cross-coupling reaction of PVA-SA-Ni (II) catalyst

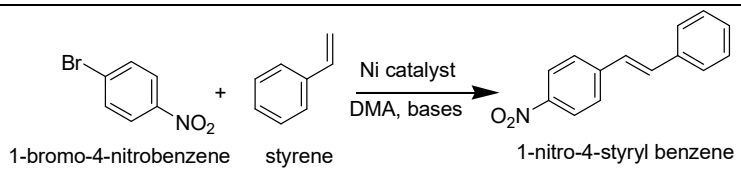

Entry	Base	Solvent	Time (h)	%Conversion
1	K_2CO_3	DMA	1	36
2	K_2CO_3	DMA	2	40
3	K_2CO_3	DMA	3	51
4	K_2CO_3	DMA	4	74
5	K_2CO_3	DMA	5	69
6	Na_2CO_3	DMA	4	6
7	NaOAc	DMA	4	43
8	K_2CO_3	Methanol	4	2
9	K_2CO_3	Toluene	4	-
10	K_2CO_3	DMA	4	69
11	K_2CO_3	DMA	4	24

*The catalytic study was conducted by using 1 mmol % of PVA-SA-Ni at reflux condition

The plausible reaction mechanisms involved in Heck reaction between 1-bromo-4-nitrobenzene and styrene is shown in Figure 6. The first step is started with the reduction of catalyst, complex $NiCl_2$-A to the catalytic active species Ni(0)-A with the presence of K_2CO_3, where A is PVA-SA polymer. The active species of Ni(0)-catalysed coupling reaction in five steps; (2) oxidative addition of 1-bromo-4-nitrobenzene to generate (a), (3) styrene insertion to form a π-alkene complex (b), (4) migratory insertion to produce σ-alkyl Ni complex (c), (5) rearrangement of the complex by internal rotation to generate (d), β-hydride elimination to release targeted product (e), and the addition of base to regenerate the catalyst by removing hydrogen halide (HX) from the inactive complex.

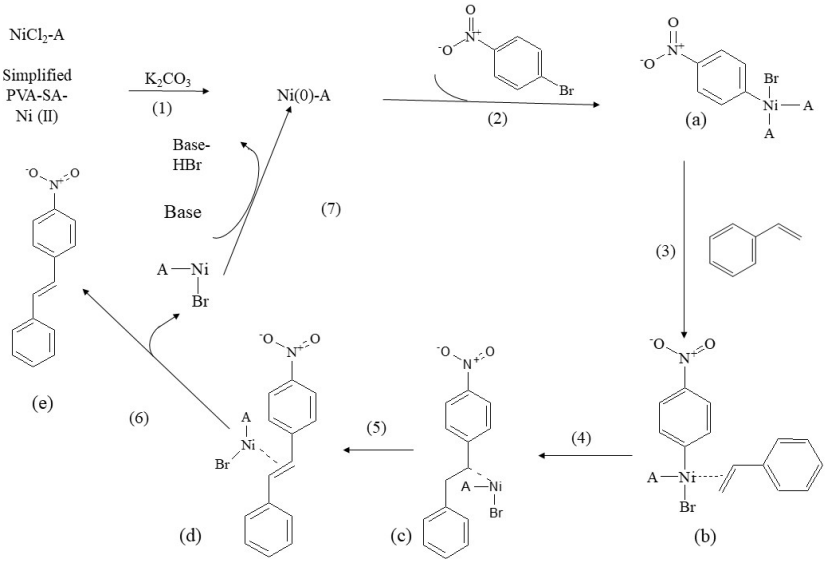

Figure 6. The proposed mechanism of Heck reaction in the presence of a PVA-SA-Ni as a catalyst

Conclusion

This study was successful in supporting $NiCl_2$ by using PVA-SA that form PVA-SA-Ni catalyst utilizing one pot ultrasonic method. The Ni loading in PVA-SA-Ni was 0.14615 % in 50 mg of catalyst. The successful synthesis PVA-SA-Ni was confirmed by using FAAS, ATR-FTIR, FESEM-EDX and XRD. The catalytic activity of catalyst in Heck reaction between 1-bromo-4-nitrobenzene and styrene was analyzed by using GC-FID gave 74% conversion rate at optimum condition. The optimum condition involved K_2CO_3 as base in DMA solvent at 165 °C and 4 h reaction time. The recyclability of catalyst is up to 3 cycles. Therefore, this study produced a novel green technique in preparing Ni catalyst that has potential for Heck reaction. However, study on the structure of catalysts improvement is needed by modification of parameter during synthesis to achieve high metal loading that influence conversion rate percentage and recyclability of catalyst. Further research on optimization of the synthesis parameters and exploring additional factors could potentially enhance the catalytic performance even more. Continuous improvement and refinement of the synthesis process are essential to maximize the efficiency and applicability of the catalyst.

Acknowledgement

This research was supported by FRGS/1/2019/STG01/UITM/02/6 from Ministry of Education Malaysia. The authors are grateful to the Universiti Teknologi MARA Cawangan Negeri Sembilan, Kampus Kuala Pilah for generously providing the research material, equipment, and instrument.

References

1. Hajipour, A. R., Khorsandi, Z., and Abeshtian, Z. (2019). Pd/Cu-free Heck and Sonogashira reactions using cobalt immobilized on in situ magnetic cross-linked chitosan fibers: A highly efficient and reusable catalyst. *Inorganic Chemistry Communications,* 107:107470.
2. Ghadiri, A. M., Farhang, M., Hassani, P., Salek, A., Ramezani, A. T., and Akbarzadeh, A. R. (2022). Recent advancements review Suzuki and Heck reactions catalyzed by metalloporphyrins. *Inorganic Chemistry Communications,* 149: 110359.
3. Daryanavard, M., Ataei, A., Rafiee, E., and Joshaghani, M. (2020). Ni (acac) 2/2, 6-bis (diphenylphosphino) pyridine/CuI: A highly efficient palladium-free homogeneous catalyst for the Sonogashira cross-coupling reaction. *Inorganic Chemistry Communications,* 122: 108274.
4. Bhakta, S., and Ghosh, T. (2021). Nickel nanocatalysis: An efficient tool for Heck reaction. *ChemCatChem,* 13(3): 828-835.
5. Hajipour, A. R., and Abolfathi, P. (2018). Chitosan‐supported Ni particles: an efficient nanocatalyst for direct amination of phenols. *Applied Organometallic Chemistry,* 32(4): e4273.
6. Lakhdari, D., Lakhdari, N., Laourari, I., Berchi, A., Park, Y., Vasseghian, Y., and Berkani, M. (2023). Bimetallic composite catalyst based on NiCu alloy supported on PVA/PANI film polymer for electrodegradation of methanol. *Journal of Industrial and Engineering Chemistry,* 124: 422-430.
7. Qiao, X., Niu, L., Zhang, H., Wen, X., Cao, Y., and Bai, G. (2017). Controllable fabrication of a novel porous Ni-alginate hybrid material for hydrogenation. *Applied Catalysis B: Environmental,* 218: 721-730.
8. Tang, S., Li, L., Cao, X., and Yang, Q. (2023). Ni-chitosan/carbon nanotube: An efficient biopolymer-inorganic catalyst for selective hydrogenation of acetylene. *Heliyon,* 9(2), e13523.
9. Soliman, T. S., Hessien, M. M., & Elkalashy, S. I. (2022). Structural, thermal, and optical properties of polyvinyl alcohol films doped with La2ZnOx nanoparticles. *Journal of Non-Crystalline Solids,* 580: 121405.
10. Xu, M., Zhao, J., Luo, C., Liu, Q., Zeng, M., Qi, C., Xia, R., Cao, X., and Wang, B. (2019). Catalysis mechanism of Pd (II)@ PVA membrane catalyst studied from the aspect of molecular level micro-defects by positron annihilation spectroscopy. *Radiation Physics and Chemistry,* 156: 128-136.
11. Medjili, C., Lakhdari, N., Lakhdari, D., Berchi, A., Osmani, N., Laourari, I., Vasseghian,Y., and Berkani, M. (2023). Synthesis of novel PANI/PVA-NiCu composite material for efficient removal of

organic dyes. *Chemosphere,* 313: 137427.

12. Sami, N. M., Elsayed, A. A., Ali, M. M. S., and Metwally, S. S. (2022). Ni-alginate hydrogel beads for establishing breakthrough curves of lead ions removal from aqueous solutions. *Environmental Science and Pollution Research,* 29(53): 80716-80726.
13. Rahman, N. A. A., Musa, M., Kassim, K., and Said, N. R. (2023). A review of the synthesis and modification of PVA-alginate as binder of metal atom. *Malaysian Journal of Analytical Sciences,* 27(2): 314-328.
14. Knijnenburg, J. T., Kasemsiri, P., Amornrantanaworn, K., Suwanree, S., Iamamornphan, W., Chindaprasirt, P., and Jetsrisuparb, K. (2021). Entrapment of nano-ZnO into alginate/polyvinyl alcohol beads with different crosslinking ions for fertilizer applications. *International Journal of Biological Macromolecules,* 181: 349-356.
15. Rahman, N. A. A., Shamsuddin, N. A. M., Musa, M., Alias, Y., Sharif, I., Mohamed, A. H., Kassim, K., and Said, N. R. (2023). One pot preparation of PVA-sodium alginate-$PdCl_2$ with excellent recyclability properties as a catalyst for Heck cross-coupling reactions. *Inorganic Chemistry Communications,* 155: 111035.
16. Isawi, H. (2020). Using zeolite/polyvinyl alcohol/sodium alginate nanocomposite beads for removal of some heavy metals from wastewater. *Arabian Journal of Chemistry,* 13(6): 5691-5716.
17. Du, Z., Liu, F., Xiao, C., Dan, Y., andJiang, L. (2021). Fabrication of poly (vinyl alcohol)/sodium alginate hydrogel beads and its application in photo-Fenton degradation of tetracycline. *Journal of Materials Science,* 56: 913-926.
18. Lee, S. J., Lim, H. W., and Park, S. H. (2021). Adsorptive seawater desalination using MOF-incorporated Cu-alginate/PVA beads: Ion removal efficiency and durability. *Chemosphere,* 268: 128797.
19. Bai, Z., Zhang, H., Zhu, H., Jiang, J., Zhang, D., Yu, Y., and Quan, F. (2023). PVA/sodium alginate multi-network aerogel fibers, incorporated with PEG and ZnO, exhibit enhanced temperature regulation, antibacterial, thermal conductivity, and thermal stability. *Carbohydrate Polymers,* 317: 121037.
20. Zhou, W., Xin, H., Yang, H., Du, X., Yang, R., Li, D., and Hu, C. (2018). The deoxygenation pathways of palmitic acid into hydrocarbons on silica-supported Ni12P5 and Ni2P catalysts. *Catalysts,* 8(4):153.
21. Soh, S. K. C., Jusoh, S. A., Yusof, M. S. M., Khairul, W. M., and Shamsuddin, M. (2018). The effect of bases, catalyst loading and reaction temperature on the catalytic evaluation of supported palladium(II) catalyst in the Mizoroki-Heck. *International Journal of Engineering and Technology,* 7: 467-469.
22. Argyle, M. D., and Bartholomew, C. H. (2015). Heterogeneous catalyst deactivation and regeneration: a review. *Catalysts,* 5(1): 145-269.
23. Shamsuddin, N. A. M., Rahman, N. A. A., Chandrasekaram, K., Alias, Y., and Said, N. R. (2021). Catalytic activity study of synthesised polystyrene-supported palladium (II)-hydrazone (CH_3) as catalyst in Heck reaction. *Malaysian Journal of Analytical Sciences,* 25(6): 987-997.
24. Shamsuddin, N. A. M., Badri, N. N. H. S., Rahman, N. A. A., and Said, N. R. (2021). Examining the effect of base, solvent and temperature in heck reaction with the presence of palladium (II)-hydrazone complexes. In *AIP Conference Proceedings,* 2332(1): 070002.

Malaysian Journal of Analytical Sciences (MJAS)
Published by Malaysian Analytical Sciences Society

METHANOGEN INHIBITOR EFFECT ON ANAEROBIC DEGRADATION OF 1,2-DICHLOROETHANE BY SUNGAI ULAR SEDIMENT

(Kesan Perencat Metanogen Terhadap Degradasi Anaerobik 1,2-Dikloroetana oleh Sedimen Sungai Ular)

Nur Intan Shaheera Nuralhuda, Muhammad Haikal Muhaimin Ariza Fattah, Nur Kholis Zulkifli, and Siti Hatijah Mortan*

Faculty of Chemical and Process Engineering Technology, Universiti Malaysia Pahang Al-Sultan Abdullah, Lebuh Persiaran Tun Khalil Yaakob, 26300 Kuantan, Pahang, Malaysia

**Corresponding author: hatijah@umpsa.edu.my*

Received: 30 October 2023; Accepted: 16 April 2024; Published: 29 June 2024

Abstract

The toxicity of industrial organohalides such as 1,2-dichloroethane (1,2−DCA) and their longevity in the environment has piqued the public's interest. Anaerobic degradation by Organohalide-Respiring Bacteria (OHRB) has emerged as one of the effective techniques in the removal or degradation of toxic organohalides. Meanwhile, it is typical for methanogenesis to occur within OHRB-dechlorinating bacteria microcosms. These methanogens will compete with the OHRB in the cultures for nutrients and electron donors such as hydrogen, limiting the OHRB's development and dechlorination activity. Methanogen inhibitors are used to remove methanogens from enrichment cultures. The objective of this study is to investigate the effect of methanogen inhibitors on the degradation rate of 1,2-dichloroethane (1,2-DCA) by Sungai Ular sediments. The concentration of 2-Bromoethanesulfonate (BES) as a methanogen inhibitor was varied from 1−25 mM and its effects on the 1,2-DCA degradation were monitored using gas chromatography (GC). Methane which is the methanogenesis product, was also monitored to evaluate the effectiveness of the inhibitor. The results indicated the microcosm treated with 25 mM BES demonstrated the fastest 1,2-DCA degradation at 0.61 µM/day. The amount of methane produced showed a decline in all the BES concentrations, with 25 mM BES demonstrating the lowest methane production at 0.2 ppm. Metagenomic data after the BES treatment also revealed a decrease in the methanogen's population from 42% to 0.007% and an increase in OHRBs population 5% to 69%. This study showed that the addition of a methanogen inhibitor can significantly increase the degradation rate of the chlorinated compound by inhibiting the growth of the methanogens.

Keywords: organohalide-respiring bacteria, methanogen inhibitors, dechlorination, methanogen, 1,2−dichloroethane

Abstrak

Ketoksikan organohalida industri seperti 1,2-dikloroetana (1,2−DCA) dan jangka hayatnya dalam alam sekitar telah menarik minat orang ramai. Degradasi anaerobik oleh bakteria pernafasan organohalida (OHRB) telah muncul sebagai salah satu teknik yang berkesan dalam penyingkiran atau degradasi organohalida toksik. Sementara itu, adalah tipikal untuk metanogenesis berlaku dalam mikrokosmos bakteria penyahklorinan OHRB. Metanogen ini akan bersaing dengan OHRB dalam kultur untuk nutrien dan penderma elektron seperti hidrogen, mengehadkan aktiviti pembangunan dan penyahklorinan OHRB. Perencat metanogen digunakan untuk mengeluarkan metanogen daripada kultur pengayaan. Objektif kajian ini adalah untuk menyiasat kesan perencat metanogen terhadap kadar degradasi 1,2-dikloroetana (1,2-DCA) oleh sedimen Sungai Ular. Kepekatan 2-Bromoetanasulfonat

(BES) sebagai perencat metanogen telah diubah daripada 1−25 mM dan kesannya terhadap degradasi 1,2-DCA dipantau menggunakan kromatografi gas (GC). Metana yang merupakan produk metanogenesis, juga dipantau untuk menilai keberkesanan perencat. Keputusan menunjukkan mikrokosmos yang dirawat dengan 25 mM BES menunjukkan degradasi 1,2-DCA terpantas pada 0.61 µM/hari. Jumlah metana yang dihasilkan menunjukkan penurunan dalam semua kepekatan BES, dengan 25 mM BES menunjukkan pengeluaran metana terendah pada 0.2 ppm. Data metagenomik selepas rawatan BES juga mendedahkan penurunan populasi metanogen daripada 42% kepada 25% dan peningkatan populasi OHRB 5% hingga 30%. Kajian ini menunjukkan bahawa penambahan perencat metanogen boleh meningkatkan kadar degradasi sebatian berklorin dengan ketara dengan menghalang pertumbuhan metanogen.

Kata kunci: bakteria penafas organohalida, perencat metanogen, penyahklorinan, metanogen, 1,2−dikloroetana

Introduction

Anthropogenic organohalide pollution of land and water (e.g., through the manufacturing and use of pesticides, dry-cleaning solvents, ozone-depleting refrigerants, and industrial degreasers) is ubiquitous and constitutes a serious risk due to its negative effects on human health and ecosystems [1]. Anthropogenic organohalogens have significantly damaged the environment as a result of their widespread usage and frequently unregulated disposal. The Stockholm Convention lists polyhalogenated pollutants as the majority of persistent organic pollutants with a serious impact on human, animal, and environmental health [2,3]. Much research has been conducted in order to better understand the microbial detoxification of anthropogenic organohalogens and to create viable bioremediation techniques [4,5].

Halogenated alkane with the common name ethyl chloride (chloroethane) is commonly used in the production of tetraethyllead (TEL), which is an additive for gasoline. The 1,2-dichloroethane (1,2-DCA) compound belongs to a category of chloroethanes that have two chloro groups replaced at positions 1 and 2. Vinyl chloride, which is used to create a range of plastic and vinyl items such as polyvinyl chloride (PVC) pipes, furniture and car upholstery, wall coverings, household goods, and vehicle parts, is the most prevalent usage of 1,2-DCA. When toxicity occurs, higher concentrations of 1,2-DCA can circulate throughout the body and bind to glutathione instead of being detoxified and removed because the biotransformation systems are saturated [6].

Anaerobic degradation by using OHRBs has emerged as one of the effective methods in the degradation of toxic chlorinated compounds which include 1,2-DCA. The OHRBs are found in several phyla including the Proteobacteria, Firmicutes and Chloroflexi [7]. Reductive dehalogenase enzymes, which is a special characteristic of OHRB, allow them to employ various organohalides as terminal electron acceptors and live in a variety of terrestrial and aquatic habitats. The capacity of OHRB to utilize organohalides as terminal electron acceptors to provide energy for growth offers a possible remedy for cleaning up polluted locations [8].

One of the common problems in the OHRBs bacterial communities is the presence of methanogens. Since methanogens are usually the dominant anaerobic bacteria in most reduced aquifers, the electron donor and substrate consumption by methanogens could be a rate-limiting factor for OHRBs during anaerobic degradation of halogenated compounds [9]. These methanogens will compete with the OHRB in the cultures for nutrients and electron donors such as hydrogen, which will slow down the growth of the OHRB and its dechlorination activity [10]. The effectiveness of dechlorination is limited when methanogens are present because they can outcompete OHRB for available electron sources and acceptors. Methanogen inhibitors are compounds that selectively target and inhibit the activity of methanogens. The activity of OHRBs will be increased and methanogen competition will be decreased by the addition of the methanogen inhibitor to the consortia containing OHRBs [9]. The aim of this study is to investigate the relationship between the dechlorination process of the Sungai Ular sediments and the methanogen inhibitor, specifically 2-Bromoethanesulfonate (BES).

Materials and Methods

Sample collection

Inocula was obtained from sediments collected at Sungai Ular (4.046821°N, 103.395601°W) in Kuantan, Pahang. The sediments were taken at 15 cm below the riverbank surface using sterile 50 mL Falcon tubes. The sampling tubes is immersed beneath the sediment, filled with

sediment, and completely closed before being brought to the surface. Exposure to air was strictly limited and the samples were transferred into the serum bottle within 24 hours.

Preparation of anaerobic medium

The anaerobic medium contained 0.2% (w/v) KH_2PO_4, 0.27 % (w/v) NH_4Cl, 1% (w/v) NaCl, 0.41% (w/v) $MgCl_2.6H_2O$, 0.52% (w/v) KCl, 0.15 % (w/v) $CaCl_2.2H_2O$, 0.7% (w/v) $ZnCl_2$, 0.8% (w/v) $MnCl_2.4H_2O$, 0.06% (w/v) H_3BO_3, 0.19% (w/v) CoCl2.6H_2O, 0.02 % (w/v) $CuCl_2.2H_2O$, 0.24% (w/v) $NiCl_2.6H_2O$, 0.36% (w/v) $Na_2MoO_4.2H_2O$, 0.02% (w/v) $FeCl_2.4H_2O$ and 0.0128% (w/v) nitriloacetic acid [11]. The medium was flushed with nitrogen for approximately 2 minutes before being sealed with a rubber stopper and aluminum crimp cap. The medium was then autoclaved for 20 minutes at 121°C. Sterile $NaHCO_3$ solution (1g/L), $Na_2S.9H_2O$ + L-cysteine solution (25mg/L) and vitamin cyanocobalamin solution (40 mg/L) were then added to the serum bottles before the inoculation of sediments.

Degradation of 1,2-DCA using methanogen inhibitor

Six g of sediment (wet weight) was inoculated to each 120 mL glass serum bottle containing 65 mL medium prepared above. 20 µM 1,2−DCA as the electron acceptor and overpressure H_2 at 0.4 bar as the electron donor were added to the serum bottles. The methanogen inhibitor, 2-bromoethanesulfonate (BES) at 1, 10 and 25 mM were then added to the consortia. Microcosms were prepared in triplicates for each BES concentration. The serum bottles were then incubated at 25 °C in dark static conditions.

Gas chromatography analysis

1,2−DCA, methane and other volatile organic compounds were detected and quantified by analyzing headspace taken from the serum flasks using gas chromatography coupled to a flame ionized detector (GC-FID). The analysis was carried out using DB−624 column (30m × 0.32mm with 0.25µm film thickness; Agilent Technologies). The oven, injector and detector temperatures were fixed at 150 °C, 250 °C and 260 °C, respectively for 25 minutes. 1 mL of the sample was taken from the headspace and then manually injected into GC-FID. Chromatographic peak areas obtained from the GC-FID were converted to corresponding 1,2−DCA concentrations.

Results and Discussion

1,2−DCA degradation

Figure 1 shows the concentration of 1,2−DCA in the Sungai Ular anaerobic bacterial culture at different concentrations of BES as methanogen inhibitor. Microcosm without any BES addition labeled as "No BES" was included as control. 20 µM of 1,2−DCA was added at day 0 and an additional 20µM of 1,2−DCA was added at day 32, after all the 1,2−DCA fully degraded in all tested microcosms. During the first addition of 1,2−DCA (day 0-32), 25 mM BES recorded the fastest 1,2−DCA degradation when compared to other added concentrations of BES. However, the control culture (No BES) demonstrates faster 1,2−DCA degradation than the 25 mM BES culture. Nonetheless, following the second addition of 1,2−DCA at day 32, 25 mM BES started to exhibit more rapid 1,2−DCA degradation than the control culture and other BES concentrations. 1 mM BES displays the slowest 1,2−DCA degradation followed by the control culture and 10 mM BES, respectively.

Figure 2(a) depicts the chromatogram profiles for 1,2−DCA at day 1 after the transfer while Figures 2(b) and 2(c) depict the chromatogram profiles of No BES and 25mM BES consortia after several days. As can be seen from those figures, 1,2−DCA partially degraded in consortia with No BES while it was completely degraded in 25mM BES consortia. This indicates that the addition of BES accelerated the degradation rate of 1,2−DCA. Similar outcomes were seen in a study by Lin et al. [9], where the inclusion of BES led to the maximum trichloroethylene (TCE) removal efficiency of 99.8%, while BES-free cultures only achieved 77.4% TCE removal.

In the first cycle (day 0−32), lower 1,2−DCA degradations in the cultures with BES addition when compared to control culture can be caused by several factors. The first factor could be caused by slower build-up of the dehalogenating OHRB communities as compared to methanogen populations [12]. During this time, methanogens competed for hydrogen and substrates with the OHRBs and contributed to the lag of 1,2−DCA degradation [13]. Aside from that, numerous studies also pointed out that sometimes, instead of limiting the growth of OHRBs, methanogens synthesized cyanocobalamin (vitamin B_{12}) which is a

niche co-factor in OHRBs growth [3,4]. However, at the second cycle of 1,2−DCA addition (day 52-66), higher BES concentrations contributed to a more positive impact on the dechlorination of 1,2−DCA. It is possible that during this period, the populations of OHRBs began to expand more quickly than those of methanogens. Thus, high concentrations of BES favor the dechlorination by OHRB and limiting the methanogens' activity. Aside from that, the redox potentials and dechlorination levels of the polychlorinated compounds itself appeared to be involved in their capacity to inhibit methanogenesis and promote reductive dechlorination [14].

Methane production

Figure 3 depicts the production of methane, which is the product of methanogenesis in the BES-treated and untreated cultures. As depicted in Figure 3, all the cultures showed methane increment from day 1 to day 32. After that, the amount of methane started to decrease in all BES-treated cultures except the without BES culture. This is in line with the 1,2−DCA degradations displayed in Figure 1, where lower dechlorination activities were observed during day 0−32. An increase in methane production indicates higher methanogen activities and thus limiting the dechlorination activities. However, from day 32−66, the methane concentrations started to drop in all the BES treated cultures and an increase in 1,2−DCA dechlorination was also observed. Higher concentrations of BES were discovered to give favorable benefits in the reduction of methane production with 25 mM BES demonstrating the lowest methane production, followed by 10 mM and 1 mM BES. Meanwhile, the methane in treatment cultures without BES keeps increasing and thus causing slower 1,2−DCA degradation in it. Furthermore, chromatogram profiles in Figure 2 demonstrate that consortia without BES addition (Figure 2b) produced higher levels of methane but slower degradation of 1,2−DCA than consortia that had 25mM of BES added into it (Figure 2c). Consortia supplemented with 25 mM BES (Figure 2c) exhibit lower methane production and after a few days, it totally degraded 1,2-DCA.

A similar trend was also observed in other studies on the degradation of trichloroethylene (TCE) by *Dehalococcoides* sp. in which the addition of 0.5 mM BES was found to improve the dechlorination rate of TCE [9]. However, this study did not particularly study the effect of BES at different concentrations. In another study that investigates the effect of BES concentrations (10–30 mM) on pentachlorophenol degradation that was carried out by Zhu et al., methane was hardly detected at BES concentrations as low as 10 mM, indicating complete inhibition of methanogens in their study [15]. Nevertheless, these two previous studies agree with this study where there is a synergistic association between the increased rate of halogenated chemical degradation and the reduced methane production caused by the addition of BES.

Microbial community compositions

Figure 4 illustrates the metagenomic data by 16S rRNA gene sequencing before (Figure 4a) and after the BES treatment (Figure 4b). In this figure, the identified OHRB were *Desulfobaccia, Desulfobacteria, Desulfomonillia, Desulfuromonadia, Desulfovibrionia, Shewanella* and *Desulfitobacteriia*); while the identified methanogens are *Methanomicrobia, Methanococci, Methanosarcinia* and *Methanobacteria*. Blue color indicates the presence of methanogens in the microbial communities of Sungai Ular sediments. The findings show that the total bacterial diversity decreased in the microcosm treated with BES. The relative abundance of methanogens in the microcosm decreased from 42% to 0.007%. Meanwhile, the relative abundance of OHRBs population increased from 5% to 69%. These results suggest that methanogen proliferation may be considerably inhibited by high BES concentrations.

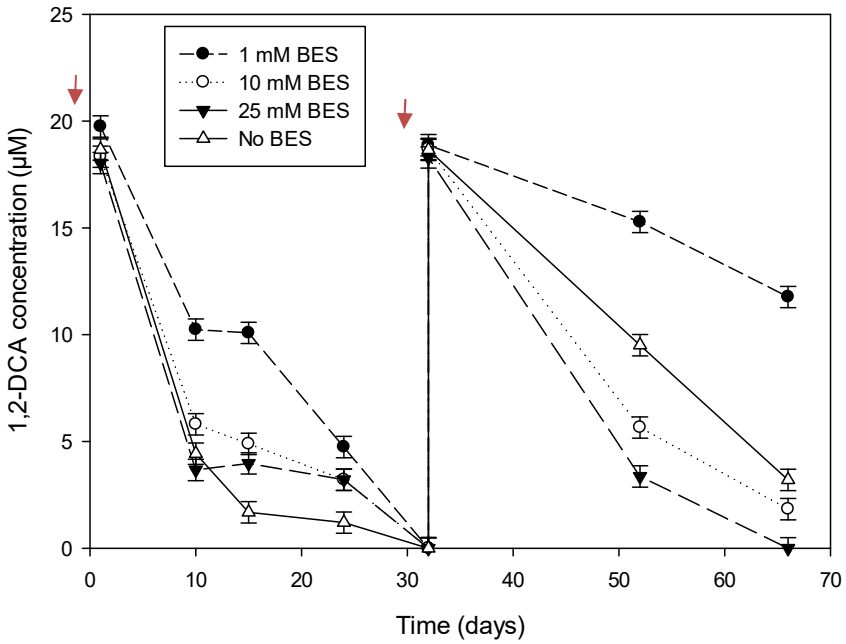

Figure 1. 1,2−DCA degradation at different BES concentrations by Sungai Ular sediments. Arrows (↓) indicate the addition of 1,2-DCA

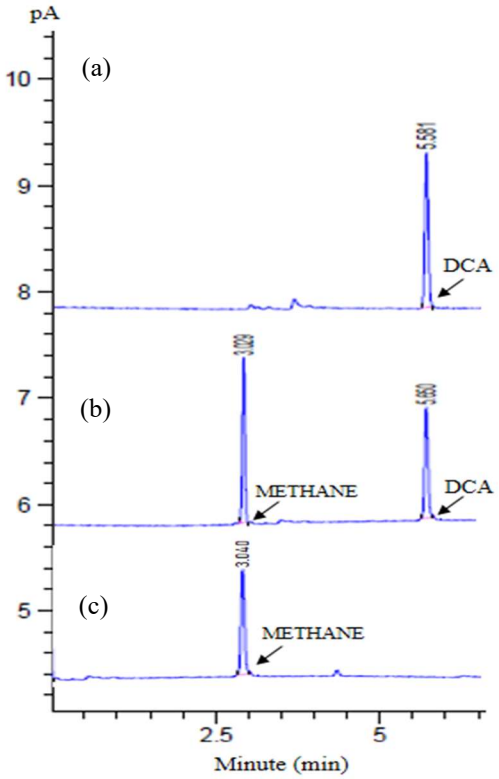

Figure 2. 1,2−DCA and methane chromatogram profile, (a) initial chromatogram of the consortia, (b) chromatogram of consortia with No BES treatment, (c) chromatogram of consortia with 25mM BES

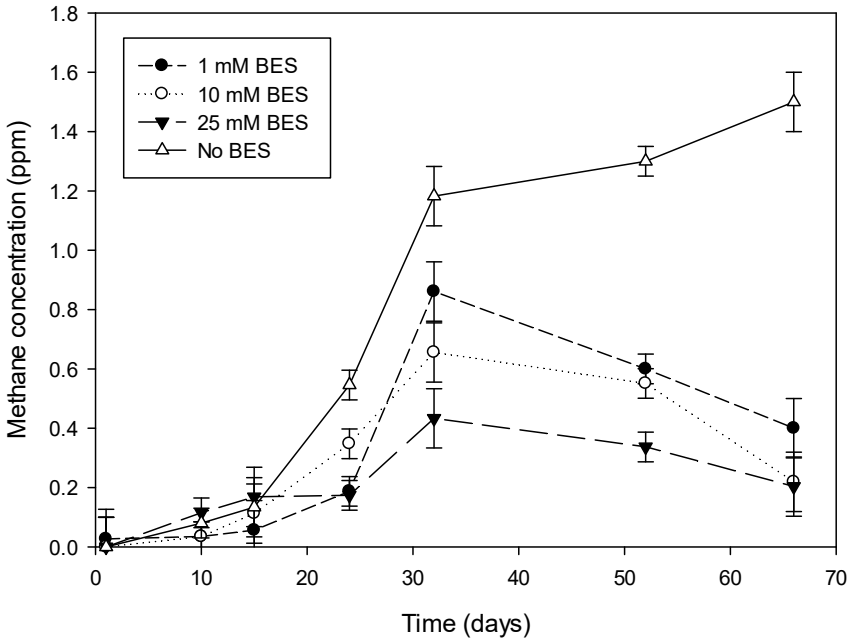

Figure 3. Methane concentration at different BES concentrations in Sungai Ular sediments

(a)

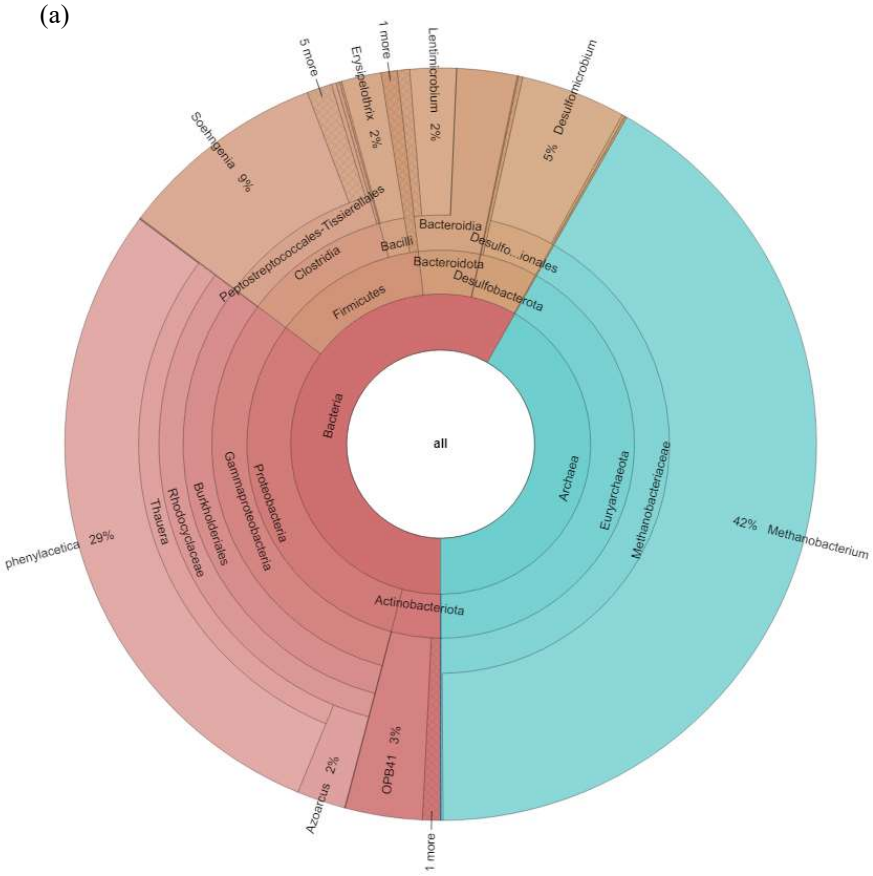

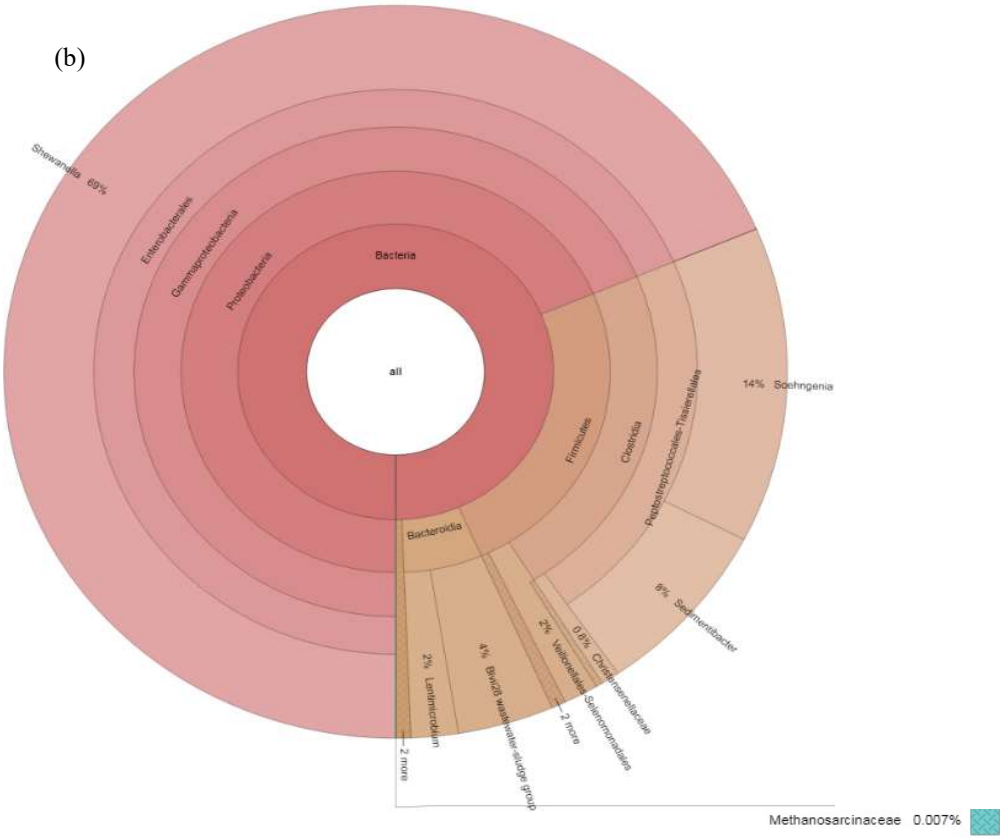

Figure 4. Bacterial communities in Sungai Ular sediments, (a) metagenomic data before the addition of BES, (b) metagenomic data after addition of 25 mM BES

Despite that, the synchronous relationship between methanogenesis and the anaerobic breakdown of halogenated substances remains incomprehensible [13,15]. Most studies on the effect of methanogen inhibitors on dechlorination were carried out in simple systems and its effect on largescale contaminated sites has never been tested. In addition, there are no definite studies concluding the negative impact of methanogens' presence on the dechlorinators population in the environment. The methanogens competition for nutrients and electron donors may hinder the OHRBs growth but simultaneously also provides a beneficial co-factor for OHRBs growth.

Conclusion

This study demonstrated that the degradation rate of 1,2–DCA was highly affected by different concentrations of BES. Higher 1,2–DCA degradation and lower methane production were found in the culture with higher BES concentration. The metagenomic data also supported the relationship between the BES concentrations with the methanogens and OHRBs population. Our results suggested a potential application for high concentrations of methanogen inhibitor in promoting faster degradation rates of chlorinated compounds.

Acknowledgement

This study is funded by the Ministry of Higher Education under Fundamental Research Grant Scheme (FRGS) No. FRGS/1/2019/TK02/UMP/02/23 (University reference RDU1901188) with additional financial support from Universiti Malaysia Pahang Al-Sultan Abdullah under Internal Research grant RDU1803114.

References

1. Renpenning, J. and Nijenhuis, I. (2016). Evaluation of the microbial reductive dehalogenation reaction using compound-specific stable isotope analysis (CSIA). Springer Berlin

Heidelberg, Berlin, Heidelberg: pp. 429-453.
2. Maillard, J., Schumacher, W., Vazquez, F., Regeard, C., Hagen, W.R. and Holliger, C. (2003). Characterization of the corrinoid iron-sulfur protein tetrachloroethene reductive dehalogenase of *Dehalobacter restrictus*. *Applied Environmental Microbiology,* 69(8): 4628-4638.
3. Rosell, M., Palau, J., Mortan, S.H., Caminal, G., Soler, A., Shouakar-Stash, O. and Marco-Urrea, E. (2019). Dual carbon - chlorine isotope fractionation during dichloroelimination of 1,1,2-trichloroethane by an enrichment culture containing *Dehalogenimonas* sp. *Science Total Environment,* 648: 422-429.
4. Häggblom, M.M. and Bossert, I.D. (2004). Halogenated organic compounds - a global perspective dehalogenation microb. process. Environmental Applied, Kluwer Academic Publishers, Boston: pp. 3-29.
5. Adrian, L. amd Löffler, F.E. (2016). Organohalide-respiring bacteria. Springer Berlin Heidelberg, Berlin, Heidelberg: pp. 3–6.
6. Maness, A.D., Bowman, K.S., Yan, J., Rainey, F.A. and Moe, W.M. (2012). *Dehalogenimonas* spp. can reductively dehalogenate high concentrations of 1,2-dichloroethane, 1,2-dichloropropane, and 1,1,2-trichloroethane. *AMB Express,* 2(1): 54.
7. Ritalahti, K.M., Amos, B.K., Sung, Y., Wu, Q., Koenigsberg, S.S. and Loffler, F.E. (2006). Quantitative PCR Targeting 16S rRNA and Reductive Dehalogenase Genes Simultaneously Monitors Multiple Dehalococcoides Strains. *Applied and Environmental Microbiology,* 72 (4): 2765–2774.
8. Jugder, B.E., Ertan, H., Bohl, S., Lee, M., Marquis, C.P. and Manefield, M. (2016). Organohalide respiring bacteria and reductive dehalogenases: Key tools in organohalide bioremediation. *Frontiers in Microbiology*, 7: 1-12.
9. Lin, W.H., Chien, C.C., Lu, C.W., Hou, D., Sheu, Y.T., Chen, S.C. and Kao C.M. (2021). Growth inhibition of methanogens for the enhancement of TCE dechlorination. *Science of the Total Environment,* 787(2021): 147648.
10. Hug, L.A. (2016). Diversity, evolution, and environmental distribution of reductive dehalogenase genes, in: organohalide-respiring bacteria. Springer Berlin Heidelberg, Berlin, Heidelberg: pp. 377-393.
11. Adrian, L., Szewzyk, U., Wecke, J. and Görisch, H. (2000). Bacterial dehalorespiration with chlorinated benzenes. *Nature*, 408(6812): 580-583.
12. Martín-González, L., Mortan, S.H., Rosell, M., Parladé, E., Martínez-Alonso, M., Gaju, N., Caminal, G., Adrian, L. and Marco-Urrea, E. (2015). Stable carbon isotope fractionation during 1,2-dichloropropane-to-propene transformation by an enrichment culture containing *Dehalogenimonas* strains and a dcpA gene. *Environmental Science & Technology*, 49(14): 8666-74.
13. Yuan, J., Li, S., Cheng, J., Guo, C., Shen, C., He, J., Yang, Y., Hu, P., Xu, J. and He, Y. (2021). Potential Role of methanogens in microbial reductive dechlorination of organic chlorinated pollutants *in situ, Environmental Science & Technology,* 55(9): 5917-5928.
14. Yu, Z. and Smith, G.B. (2000). Inhibition of methanogenesis by C1- and C2-polychlorinated aliphatic hydrocarbons. *Environmental Toxicology and Chemistry*, 19(9): 2212-2217.
15. Zhu, M., Feng, X., Qiu, G., Feng, J., Zhang, L., Brookes, P.C., Xu, J. and He, Y. (2019). Synchronous response in methanogenesis and anaerobic degradation of pentachlorophenol in flooded soil. *Journal of Hazardous Materials*, 374(2019): 258-266.

Malaysian Journal of Analytical Sciences (MJAS)
Published by Malaysian Analytical Sciences Society

INVESTIGATIONS ON THE INCLUSION OF BETULINIC ACID INTO CD-MOF-1 PERFORMED BY QUANTUM MECHANICS CALCULATIONS AND MOLECULAR DOCKING SIMULATION

(Kajian Kemasukan Asid Betulinik ke dalam CD-MOF-1 Melalui Pengiraan Mekanik Kuantum dan Simulasi Dok Molekul)

Saurelle Kenfack Tiofack[1,2], Mostafa Yousefzadeh Borzehandani[1], Patrice Kenfack Tsobnang[2], Muhammad Alif Mohamad Latif[1,3], Bimo Ario Tejo[1,3], Haslina Ahmad[1,3], Jean Ngoune[2], and Mohd Basyaruddin Abdul Rahman[1,3*]

[1]*Integrated Chemical BioPhysics Research, Faculty of Science, Universiti Putra Malaysia, Serdang 43400, Selangor, Malaysia.*
[2]*Department of Chemistry, University of Dschang, P. O. Box 67, Dschang, Cameroon*
[3]*Foundry of Reticular Materials for Sustainability, Institute of Nanoscience and Nanotechnology, Universiti Putra Malaysia, Serdang 43400, Selangor, Malaysia*

[*]*Corresponding author: basya@upm.edu.my*

Received: 5 February 2024; Accepted: 16 April 2024; Published: 29 June 2024

Abstract

In recent years, CycloDextrin Metal-Organic Frameworks (CD-MOFs) have been investigated to develop potential drug carriers and improve the solubility of some molecules by their encapsulation. Betulinic acid (BA) or 3β-hydroxy-lup-20(29)-en-28-oic acid is a pentacyclic triterpene of the lupane family which has a wide range of biological activities, and it is considered a promising candidate for clinical application but, its high hydrophobicity and limited aqueous solubility contribute to its poor bioavailability. In this work, we show through computational studies that CD-MOF-1 can strongly encapsulate betulinic acid molecules through hydrogen bond interactions. For this purpose, the optimized geometry of BA was implemented by the Density Functional Theory using the function of Becke, Lee, Yang, and Parr (DFT/B3LYP) method with a 6-31+G(d) basis set using the Gaussian09 program and GaussView 5.0 for visualization. We noticed that BA has a lower energy gap (Egap = 6.1615 eV) indicating that it is soft, less stable, more reactive, and polarizable. According to the map of electrostatic potential (MEP), the active site of betulinic acid is the carboxylic group and the latter molecule preferred electrophilic attacks. The molecular docking was performed using AutoDock Vina v1.1.2 program and Discovery Studio Visualizer 16.1. The best binding affinities of BA and CD-MOF-1 had the lowest values of -8.2 KCal/mol and -11.5 KCal/mol for the simple and the packed CDMOF-1 structure respectively. The docking revealed that BA bound in the hydrophobic cavities of CD-MOF-1 through hydrogen bonds interactions which are [CD-MOF-$1_{OH13\cdots O28}$BA (2.95 Å)], [CD-MOF-$1_{O13\cdots H30}$BA (2.54 Å)], and [CD-MOF-$1_{OH12\cdots H30}$BA (2.12 Å)] for the simplest structure and [CD-MOF-$1_{OH12A\cdots O28}$BA (3.00 Å)], [CD-MOF-$1_{H13A\cdots H30}$BA (2.72 Å)] and [CD-MOF-$1_{OH2A\cdots H30}$BA (2.66 Å)] for the packed structure 1×1×1. The packed CD-MOF-1 structure is the best with accurate results, this may be the factor of enhancement of betulinic acid solubility and bioavailability. The present theoretical results indicate the possibility of forming the host-guest inclusion complex between BA and CD-MOF-1 which may enhance the solubility of BA and then its efficiency for drug delivery.

Keywords: CD-MOF, betulinic acid, quantum mechanics, molecular docking, solubility

Abstrak

Kebelakangan ini, pembangunan kerangka kerja logam-organik siklodekstrin (CD-MOF) telah dikaji sebagai pembawa ubat yang berpotensi dan meningkatkan keterlarutan beberapa molekul melalui pengkapsulan mereka. Asid betulinik (BA) atau asid 3β-hidroksi-lup-20(29)-en-28-oik ialah triterpena pentasiklik daripada keluarga lupana yang mempunyai pelbagai aktiviti biologi, dan ia dianggap sebagai calon yang berpotensi untuk aplikasi klinikal, namun hidrofobisitinya yang tinggi dan keterlarutan dalam air yang terhad menyumbang kepada bioavailabilitinya yang lemah. Dalam kajian ini, kajian pengiraan menunjukkan bahawa CD-MOF-1 boleh memerangkap molekul asid betulinik dengan kuat melalui interaksi ikatan hidrogen. Untuk tujuan ini, geometri BA yang optimum telah dilaksanakan melalui kaedah Teori fungsi ketumpatan menggunakan fungsi Becke, Lee, Yang, dan Parr (DFT/B3LYP) dengan set asas 6-31+G(d) menggunakan program Gaussian09 dan GaussView 5.0 untuk visualisasi. Kami mendapati bahawa BA mempunyai jurang tenaga yang lebih rendah (Egap = 6.1615 eV) menunjukkan bahawa ia lembut, kurang stabil, lebih reaktif dan boleh dipolarisasi. Menurut peta potensi elektrostatik (MEP), tapak aktif asid betulinik ialah kumpulan karboksilik dan molekul terakhir lebih cenderung kepada serangan elektrofilik. Pendokkan molekul telah dilakukan menggunakan program AutoDock Vina v1.1.2 dan Discovery Studio Visualizer 16.1. Perkaitan pengikatan terbaik BA dan CD-MOF-1 mempunyai nilai terendah -8.2 KCal/mol dan -11.5 KCal/mol untuk struktur CDMOF-1 yang ringkas dan padat. Pendokkan mendedahkan bahawa BA terikat dalam rongga hidrofobik CD-MOF-1 melalui interaksi ikatan hidrogen iaitu [CD-MOF-$1_{OH13\cdots O28}$BA (2.95 Å)], [CD-MOF-$1_{O13\cdots H30}$BA (2.54 Å)], and [CD-MOF-$1_{OH12\cdots H30}$BA (2.12 Å)] untuk struktur paling ringkas dan [CD-MOF-$1_{OH12A\cdots O28}$BA (3.00 Å)], [CD-MOF-$1_{H13A\cdots H30}$BA (2.72 Å)] and [CD-MOF-$1_{OH2A\cdots H30}$BA (2.66 Å)] untuk struktur tersusun 1×1×1. Struktur CD-MOF-1 tersusun adalah yang terbaik dengan hasil yang tepat, yang berkemungkinan faktor peningkatan keterlarutan asid betulinik dan bioavailabiliti. Keputusan teori semasa menunjukkan kemungkinan pembentukan kompleks kemasukan hos antara BA dan CD-MOF-1 yang boleh meningkatkan keterlarutan BA dan kemudian kecekapannya untuk penghantaran ubat.

Kata kunci: CD-MOF, asid betulinik, mekanik kuantum, dok molekul, keterlarutan

Introduction

For millennia, natural products have been used as a source of natural bioactive compounds for the medication and treatment of various sicknesses [1]. Alkaloids, steroids, quinones, limonoids, flavonoids, as well as another significant component, terpenoids, are all being explored in medicine for their potential to improve health. Based on their chemical skeleton, terpenoids can be classified as monoterpenes, sesquiterpenes, diterpenes, triterpenoids, and steroids [2]. Triterpenes molecules, in particular, are the most abundant terpenoids and their study has increased dramatically during the last decade due to their different kinds of bioactivities [3], including liver protection, antioxidant, anti-cancer, immunomodulatory, anti-inflammatory, and anti-obesity [2, 4]. Betulinic acid is one of this family's most frequently studied compounds [3]. Indeed, betulinic acid (BA) or 3β-hydroxy-lup-20 (29)-en-28-oic acid is a pentacyclic triterpene of the lupane family isolated primally from the bark of white birch plants [5] (Figure 1). BA has a wide range of biological activities such as its cytotoxic, anti-inflammatory, antiviral (especially anti-HIV), antimalarial, anti-tumor, antibacterial, and antioxidant activities [6, 7]. Its first anticancer effect against melanoma was reported by Pisha et al. [8]. A main advantage of BA and its derivatives is that they are cytotoxic to different human tumor cells, while cytotoxicity is much lower in normal cells [9]. Many subsequent investigations have discovered that BA was demonstrated to be a very promising anticancer agent against various tumor cell lines such as breast, colon, lung, and brain [10, 11].

Therefore, betulinic acid is considered a promising candidate for clinical application [12, 13]. Despite its strong cytotoxic effect, BA exhibits low water solubility, characterized by high hydrophobicity leading to poor bioavailability [5, 10], it belongs to the Biopharmaceutics Classification System (BCS) class IV that is characterized by both low solubility and permeability [14]. To overcome these inconveniences, several approaches for improving the physicochemical and pharmacokinetic profile of the hydrophobic small drug molecules have been conducted such as cocrystallization, amorphous solid dispersions, liposomes, solubilization in co-solvents, complexation with β-cyclodextrin and nanoemulsions [6, 15, 16]. Although these approaches can enhance performance over pure drugs, they all have drawbacks, most of which

are linked to the drug's chemical stability and physical stability against crystallization [17].

A general approach to improve drug solubility can be demonstrated by incorporating such active molecules into appropriate Metal-Organic Frameworks (MOFs) [15]. Since 1999, when Yaghi et al. named materials connected by metal-ligand coordination as Metal-Organic Frameworks (MOFs), they have rapidly become a hot topic of research [18]. Indeed, MOFs are novel porous materials with ultrahigh surface areas, tunable pores, high crystallinity, designable crystal structures, permanent porosity, and abundant metal sites which have shown huge potential applications in various fields, including gas sorption and separation, catalysis, luminescence, biomedicine, environmental pollution, sensor, and so on [19-22]. In recent years, MOFs have been investigated for the encapsulation of organic or organometallic molecules as well as for the development of potential drug carriers [23]. To this end, they ensure the structural, chemical, and thermal stability of the active molecules through confinement in their pores and they experience rapid hydrolytic decomposition, resulting in the release of the drug molecule [15]. Recently, a concept of "edible" MOF named cyclodextrin metal-organic framework (CD-MOF) has been reported, it is synthesized by using γ-CD as an organic ligand, and low-toxic alkali metal potassium ions (K^+) as metal ions [24, 25]. CD-MOFs which have the empirical formula $[(C_{48}H_{80}O_{40})(KOH)_2]_n$ can be employed as a versatile host to encapsulate enough biological agents and convert crystal pharmaceuticals into molecular form, significantly increasing the solubility and bioavailability of poorly soluble drugs [26, 27].

One of the reasonable and helpful strategies in drug discovery is the quantitative structure-activity relationship (QSAR), which is important for the development and optimization of drug candidates as well as for improving their biological activities [28]. The development of a new medicine is a time-consuming, costly, difficult, and ineffective procedure that can take up to 15 years [29]. The concept of computational chemistry such as computer-aided drug design (CADD) has recently achieved a remarkable revolution in medicinal chemistry as well as the model for discovering pharmacologically interesting molecules [30]. This study aimed to investigate in silico, the inclusion of betulinic acid into CD-MOF-1 by quantum mechanics (QM) calculations, and molecular docking simulation, to indicate the possibility of forming the host-guest inclusion complex between BA and CD-MOF-1 which may enhance the solubility of BA and then its efficiency for drug delivery. To the best of our knowledge, this work has not yet been done in the literature, but it has been reported some similar work using protein as a receptor like myeloid differentiation 2 (MD2) [31], phospholipase A2 (PLA2) [32], human serum albumin (HSA) [33], and so on to show the biological properties of betulinic acid.

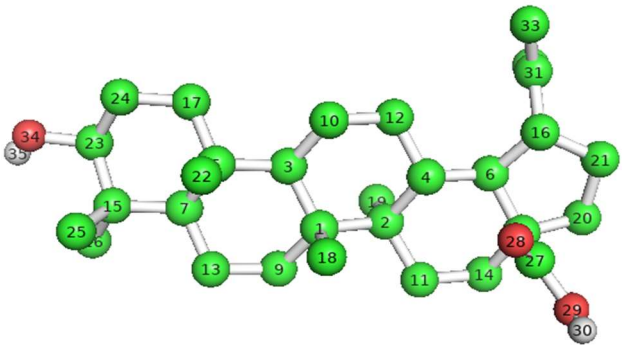

Figure 1. Molecular structure of betulinic acid retrieved after adding atomic partial charges based on B3LYP/6-31+G(d) level, (carbon atoms in green, oxygen atoms in red, and hydrogen atoms in grey)

Materials and Methods

Quantum mechanics (QM) calculations

Density functional theory (DFT) developed by Hohenberg and Kohn [34] and Kohn and Sham [35], is a method for calculating the electronic structures of molecules using the first principles of quantum

mechanics [29]. DFT calculations are a functional tool for determining the correct molecular structure corresponding to the lowest energy state at the potential energy surface. This approach is useful in exploring the structure-activity relationship since accurate molecular structure determination is required in this field. Researchers can utilize DFT calculations to obtain reliable information about molecules' electronic structure and properties, which can then predict their behavior in chemical reactions and interactions with other compounds [36]. In this study, all geometry optimizations were calculated by using the function of Becke, Lee, Yang, and Parr (B3LYP) with a basis set of 6-311+G(d). Atomic partial charges of CD-MOF-1 and betulinic acid were calculated by CHarges from ELectrostatic Potentials using a Grid-based (CHelpG) method based on B3LYP/6-31+G(d) level, the cluster structures used for those calculations are given in Figures 1 and 2 and their values in Tables 1 and 2 for betulinic acid and CDMOF-1 respectively. Thus, we were allowed to analyze some properties such as frontier molecular orbital (FMO) and molecular electrostatic map (MEP).

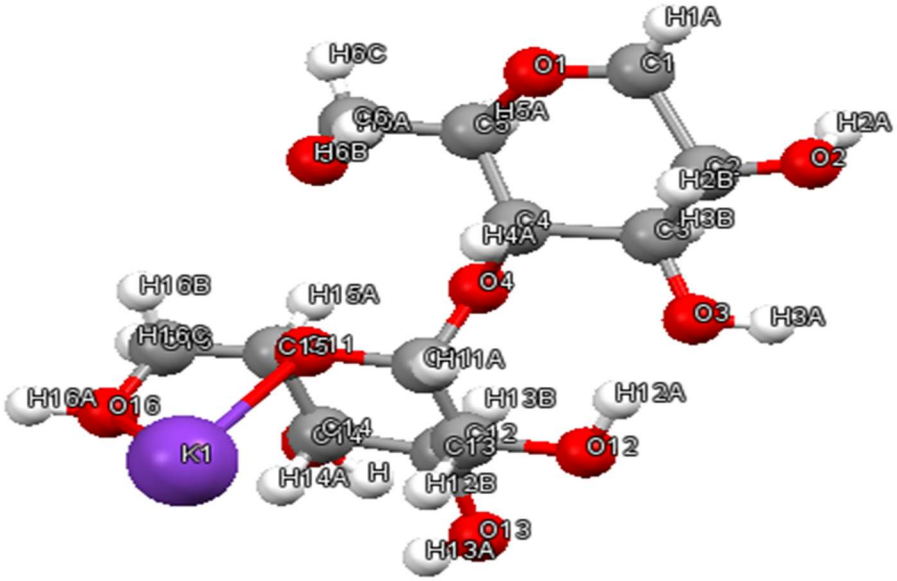

Figure 2. The cluster was created by cutting directly a piece of framework used for the calculation of atomic charges. One hydrogen (H) has been added to O14 to saturate the structure. (K, O, C, and H atoms are represented as light blue, red, grey, and white respectively)

Table 1. The partial atomic charge values of CD-MOF-1 as given by CHelpG calculation based on the B3LYP/6-31+G(d) method

Atoms	Charges	Atoms	Charges	Atoms	Charges
K1	0.070	C4	0.104	O13	-0.849
O1	-0.318	C5	0.434	H13A	0.480
C1	0.538	O6	-0.468	C13	0.254
O2	-0.701	H6A	0.375	O14	-0.616
H2A	0.492	C6	0.172	C14	0.341
C2	0.176	O11	-0.093	C15	-0.304
O3	-0.660	C11	-0.709	O16	-0.576
H3A	0.371	O12	-0.678	H16A	0.350
C3	0.472	H12A	0.333	C16	0.142
O4	-0.763	C12	0.605	H	0.418

Table 2. The partial atomic charge values of betulinic acid as given by CHelpG calculation based on the B3LYP/6-31+G(d) method

Atoms	Charges	Atoms	Charges	Atoms	Charges
C1	0.283	C13	-0.047	C25	- 0.177
C2	0.388	C14	-0.133	C26	-0.152
C3	0.181	C15	0.462	C27	0.728
C4	-0.249	C16	0.038	O28	-0.607
C5	0.098	C17	-0.191	O29	-0.603
C6	0.346	C18	-0.205	H30	0.409
C7	-0.058	C19	-0.191	C31	0.185
C8	-0.017	C20	0.081	C32	-0.052
C9	-0.072	C21	-0.118	C33	-0.182
C10	-0.030	C22	-0.134	O34	-0.759
C11	0.007	C23	0.305	H35	0.415
C12	-0.067	C24	0.054	Total	0.000

Molecular docking simulation: Receptor preparation

The CIF (crystallographic information files) of CD-MOF-1 was retrieved from the Cambridge Crystallographic Data Centre (CCDC) (https://www.ccdc.cam.ac.uk/structures/) using the reference code 773709 with the name catena-((μ8-γ-cyclodextrin)-di-potassium dihydroxyde) [37]. Atomic partial charges were added, then the AutoDock Tool was used to add hydrogen atoms and Kollman charges and the file has been saved in pdbqt format.

Ligand preparation

Betulinic acid molecule was obtained in Structure Data Format (sdf) from PubChem web platform (https://pubchem.ncbi.nlm.nih.gov/) in 3D conformation (CID 64971) and converted to the PDB file using OpenBabel software [38] of the Python Prescription (PyRx) suite, a virtual screening tool. Betulinic acid geometry was optimized, and atomic charges added, then, the preparation of the pdbqt file was done using the AutoDock Tool.

Molecular docking processes

Molecular docking simulations were carried out using the AutoDockTool 1.5.7 and AutoDock Vina v1.1.2 program. The number of points in the grid map of 42×46×40 Å was set to cover whole the framework spacing of 1.000 Å, which was centered at x = 12.971, y = 18.216, and z = 14.482. Grid-based energy evaluation methods combined with a Lamarckian Genetic Algorithm (LGA) were considered for pre-calculating grid maps according to the interatomic potentials of all-atom types present for each CD-MOF-1 pores and BA molecules. The docking has also been performed using the packed 1×1×1 CD-MOF-1 structure to have more accurate results. The exhaustiveness value was set as 8 to obtain an efficient binding conformation pose of the CD–MOF–drug complex. Using an AutoDock Vina, the docking analysis was performed, and the receptor-drug complex's binding affinity was observed as a negative score with a unit of kcal/mol and the same value for all 9 poses. Discovery Studio 16.1 software packages and Pymol were assisted to analyze and visualize the host-guest interactions.

Results and Discussion

Frontier molecular orbital (FMO) analysis

The most important orbitals in a molecule also called frontier molecular orbitals (FMOs) are the lowest unoccupied molecular orbital (LUMO), which can accept electrons, and the highest occupied molecular orbital (HOMO), which can donate electrons [36]. These orbitals are important for determining a compound's electrical properties, kinetic stability, optical polarizability, and chemical reactivity [29]. To understand the chemically reactive site of BA, the HOMO, and LUMO are obtained, where the negative region is presented in red and the positive one in green (Figure 3). As we can see from the given figure, HOMO is located over the alkene group, the cyclohexane and cyclopentane rings, which can be useful for donating electrons to the electrophilic sites of CD-MOF-1. On the other side, the formation of LUMO in the carboxylic group is important for accepting electrons given by

nucleophilic sites of CD-MOF-1.

The HOMO and LUMO energy values of betulinic acid were calculated as well as the global chemical parameters, like energy gap (Egap), ionization potential (I), electronic affinity (EA), chemical potential (μ), electronegativity (χ), chemical hardness (η), softness (S), electrophilicity (ω) and nucleophilicity (ε) according to equations (1 to 9) below (Table 3) [29].

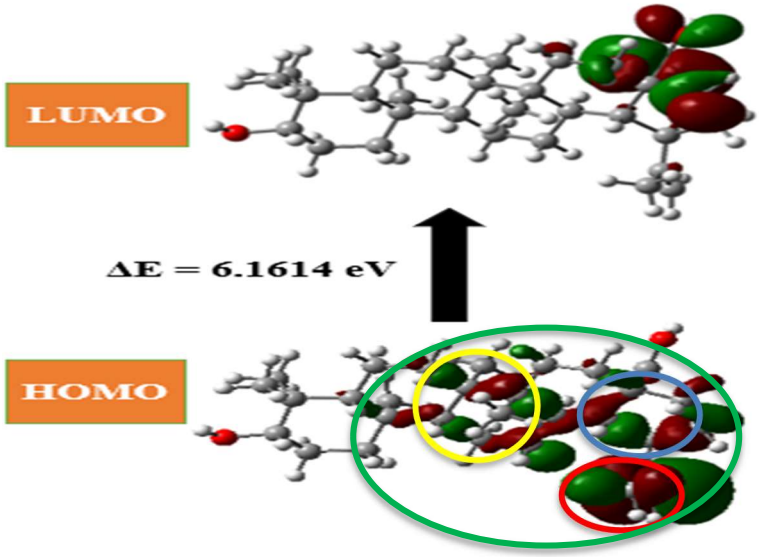

Figure 3. HOMO and LUMO orbitals of betulinic acid, the circles in green, yellow, blue, and red show the location of HOMO, cyclohexane, cyclopentane, and alkene groups respectively

Table 3. Electronic properties of betulinic acid based on B3LYP/6-31G+ (d)

Electronics properties	Values
E_{HOMO}	-6.5558 (eV)
E_{LUMO}	-0.3943 (eV)
Energy gap (E_{gap})	6.1615 (eV)
Ionization potential (I)	6.5558 (eV)
Electronic affinity (EA)	0.3943 (eV)
Electronegativity (χ)	3.4750 (eV)
Chemical potential (μ)	-3.4750 (eV)
Chemical hardness (η)	3.0807 (eV)
Chemical softness (S)	0.3246 (eV^{-1})
Electrophilicity (ω)	1.9599 (eV)
Nucleophilicity (ε)	0.5102 (eV^{-1})

The energy gap (Egap) was calculated by the difference of energy between the highest occupied molecular orbital (HOMO) and the lowest unoccupied molecular orbital (LUMO) shown in equation 1. For the molecular system containing π electrons, smaller Egap increases the mobility of π electrons to higher energy levels, with better energy distribution and higher reactivity [39]. According to Table 3, the value of Egap of betulinic acid is 6.1615 eV in the gas phase, which is less than 6.378 eV in water as reported by Khan et al. (2018). Khan et al. (2018) performed the DFT calculations of betulinic acid using the Solvation Model on Density (SMD) involving several solvents like water, dimethyl sulfoxide (DMSO), acetonitrile, n-octanol, chloroform [32]. That

model is called SMD, where the "D" stands for "density" to denote that the full solute electron density is used without defining partial atomic charges [40]. This means that betulinic acid is less stable and more reactive and its electrons can easily flow from the HOMO orbital to the empty LUMO orbital until reaching the equilibrium state.

The ionization potential (I) and electronic affinity (EA) are obtained from the reverse sign of the calculated energies of HOMO and LUMO as follows in equations 2 and 3 respectively.

$$Egap = ||E_{HOMO}|| - ||E_{LUMO}|| \quad (1)$$

$$I = -E_{HOMO} \quad (2)$$

$$EA = -E_{LUMO} \quad (3)$$

Electronegativity (χ) (equation 4) is a measure of an atom's ability to attract electrons towards itself in a chemical bond, it is a fundamental property of atoms that affects the nature of chemical bonding and the resulting properties of compounds. Electronic chemical potential (μ) (equation 5) which is the absolute reversed value of electronegativity means escaping the tendency of electron cloud from the ground state. Betulinic acid can be capable of forming polarized covalent bonds with other atoms having both relatively low electronegativity, such as alkali metals or alkaline earth metals, or strong electronegativity like the hydroxide group. The polarity of the bonds in the molecule can have effects on the physical properties of betulinic acid, such as solubility and polarizability, BA may tend to interact with other molecules with complementary electronic properties, which may affect its chemical reactivity.

$$\chi = \frac{I+EA}{2} \quad (4)$$

$$\mu = -\chi \quad (5)$$

Hardness (η) (equation 6) is a measure of the resistance of a molecule to electron transfer and is defined as the energy required to add or remove an electron from the molecule's HOMO or LUMO respectively. In order words, a molecule with a high hardness requires a large amount of energy to donate or accept an electron. On the other hand, softness (S) (equation 7) is the inverse of hardness and represents the ease with which a molecule can donate or accept electrons.

$$\eta = \frac{-Egap}{2} \quad (6)$$

$$S = \frac{1}{\eta} \quad (7)$$

The concept of hardness (η) and softness (S) is related to a compound's reactivity, so, to the energy gap of a molecule. As the energy gap increases, the molecule becomes harder (less soft), significantly less polarizable, and less reactive. The calculated values are 3.0807 eV and 0.3246 eV^{-1} for chemical hardness and softness respectively, as compared to 3.189 eV and 0.314 eV^{-1}. As shown above, betulinic acid has a smaller energy gap, so it is less soft, more reactive, and polarizable. The same behavior has been demonstrated by Muya and collaborators, they did the DFT calculations of betulinic acid using the continuum solvation model based on density (SMD) at B3LYP and M062X with 6-311 + G(d,p) basis sets, they conclude that betulinic acid appears soft and can interact with soft acceptor molecules [41].

Other important descriptors are the electrophilicity index (ω) and nucleophilicity (ε) used to describe the ability of a molecule or atom to accept or donate electrons in a chemical reaction. Electrophilicity refers to the tendency of a molecule to attract electrons, it is typically associated with electron-deficient species that have a partially positive charge and nucleophilicity refers to the tendency of a molecule to donate electrons, it is associated with electron-rich species that have a partially negative charge. Their values are defined as follows in equations 8 and 9:

$$\omega = \frac{\mu 2}{2\eta} \quad (8)$$

$$\varepsilon = \frac{1}{\omega} \quad (9)$$

Electrophilicity included both the ability of an electrophile to acquire additional electronic charge and a system's resistance to exchange electronic charge with the environment. Betulinic acid electrophilicity is 1.9599 eV at the B3LYP/6-31G+ (d), 1.48 eV at the B3LYP/6-31G(d) using SMD solvation model [32] and

1.15 eV at B3LYP/6-31G+ (d,p) and 1.19 eV at M062X/6-311 + G(d,p) using SMD model [41]. We notice that, with atomic partial charges, the electrophilicity value of BA increases at the B3LYP/6-31G+ (d). The electrophilicity character of betulinic acid proves that the active site of the latter molecule may be the carboxylic group.

Molecular electrostatic potential (MEP) and contours analyses

The MEP maps give an idea about the chemical reactivity of the compounds by determining electrophilic and nucleophilic attack regions in the molecule according to charge distributions [42]. The maps of electrostatic potential (MEPs) surfaces and contours were used to display the electron density on surfaces that surround the atoms within the molecules and sites for nucleophilic and electrophilic attacks. To predict the electrophilic and nucleophilic center of betulinic acid, MEP for optimized geometry was calculated at the DFT/B3LYP/6-31G+ (d). According to Figure 4a, potential decreases in the following order of colors red < orange < yellow < green < blue. Red and yellow regions indicate negative regions (rich electron) which promote nucleophilic site while the positive regions represented by the blue color promote electrophilic site. The green color represents a region of zero potential which indicates the neutral region [36]. In addition, MEP contours are more significant for illustrating the reactive nature of outermost orbital electrons (Figure 4b) [29]. The reactivity of betulinic acid is observed with red-colored contours and green lines show that electrons are not moving in the area. Figure 4 shows that the negative potentials are generated over the electronegative oxygen atom of the hydroxide group and the positive potentials are located in the oxygen atom of the carboxylic group. As shown above, for the molecular system containing π electrons, a smaller energy gap increases the mobility of π electrons to higher energy levels, which corroborates with MEPs showing that the carboxylic group of BA is preferred active site. This may be confirmed or not following this work by performing molecular docking simulation between betulinic acid and CD-MOF-1.

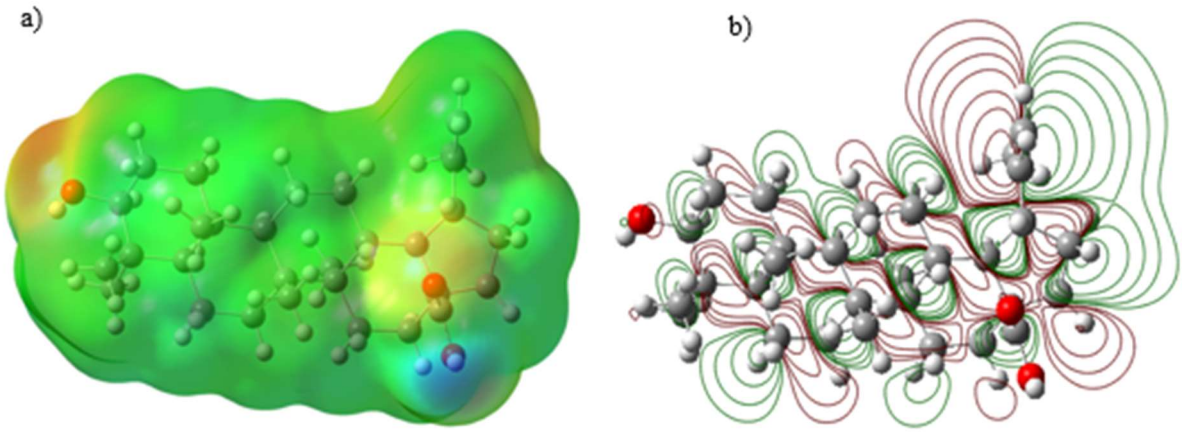

Figure 4. MEP of (a) surface and (b) contours of betulinic acid

Molecular docking analysis

CD-MOF has spherical voids with a diameter of 0.95 nm and pore size of 0.78 nm, which are body-centered cubic extended structures with surface areas of approximately 1200 m^2/g (Figure 5) [43]. The possible conformations of betulinic acid molecules were done by docking BA into CD-MOF-1, the hydrogen bond interactions are given in Table 4. The blind docking was done in triplicate and the binding affinity of all of the nine poses was -8.2 kcal/mol, the specific docking has also been performed thrice and the binding affinity varying between -8.2 and -8.1 kcal/mol, a very low difference. The best-docked conformation of betulinic acid, located in the center of the cyclodextrin pore has been analyzed by Discovery Studio as shown in Figure 6. We noticed that betulinic acid bound in the hydrophobic inner cavity of CD and its electrophilic side (carboxylic group) interacted with a hydrophilic outer surface of CD (constituted by D-glucopyranose units) and the nucleophilic side of BA (hydroxyl group) can just form

the unfavorable interaction. This confirms that the carboxylic group (COOH) of betulinic acid is its active site as predicted by the global descriptors and the MEPs. So, betulinic acid and CD-MOF-1 exhibit a stronger affinity examined by the hydrogen bond interactions, which means that CD-MOF-1 can stabilize BA against oxidation by tailoring its physical properties.

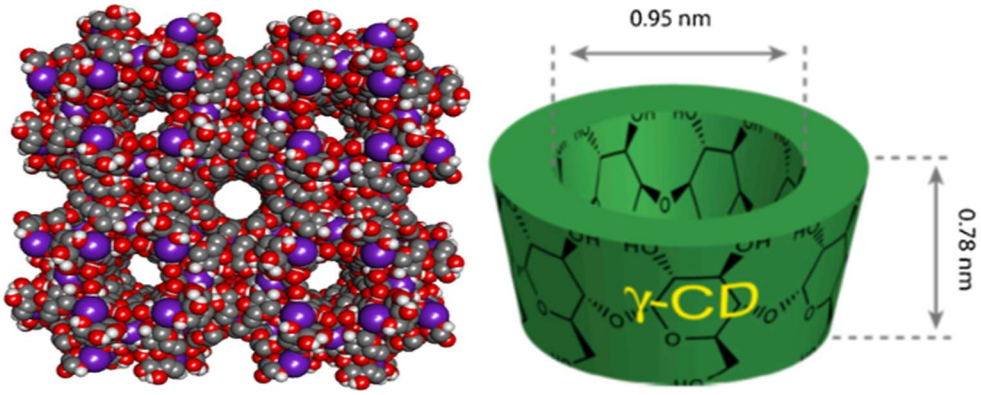

Figure 5. A space-filling representation of the extended solid-state structure, showing the $(\gamma CD)_6$ repeating motifs adopting a body-centered cubic packing arrangement (C gray, O red, K purple)

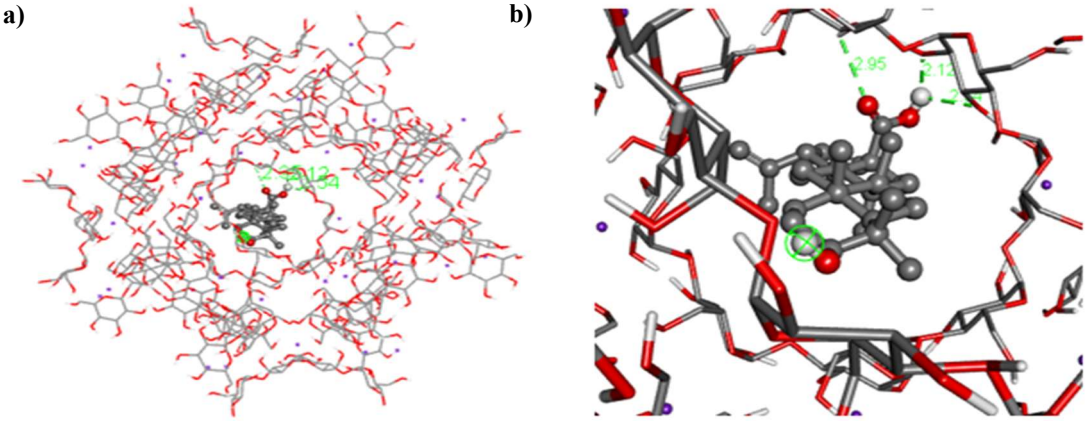

Figure 6. (a) The best binding affinity of BA into CD-MOF-1, (b) the zoom of the cyclodextrin pore where we have hydrogen bonds interactions, the green lines are hydrogen bonds between CD-MOF-1 and BA

Many researchers noticed that the drug candidate may be most effective when the binding energy is lowest and the number of H-bond donors with the receptor is largest [30]. Figure 6 shows three hydrogen bonds between BA and CD-MOF-1, which are [CD-MOF-$1_{OH13}\cdots_{O28}$BA (2.95 Å)], [CD-MOF-$1_{O13}\cdots_{H30}$BA (2.54 Å)], and [CD-MOF-$1_{OH12}\cdots_{H30}$BA (2.12 Å)]. So, CD-MOF-1 may be a good carrier of betulinic acid in drug delivery and can enhance its bioavailability and solubility, by improving its biological efficiency.

To have more accurateness, molecular docking simulation has also been done with the packed 1×1×1 of CD-MOF-1 structure, the binding affinities of the blind and specific docking of all of the nine poses were -11.3 kcal/mol more significant than -8.2 kcal/mol. All the poses are located in the cavities of the cyclodextrin, Figure 7 shows hydrogen interactions between BA and CD-MOF-1 which are [CD-MOF-$1_{OH12A}\cdots_{O28}$BA (3.00 Å)], [CD-MOF-$1_{H13A}\cdots_{H30}$BA (2.72 Å)] and [CD-MOF-$1_{OH2A}\cdots_{H30}$BA (2.66 Å)]. These interactions are not similar to the ones above, but they are longer and more significant in terms of energy and distance, so the CD-MOF-1 packed structure is the best to have accurate results.

The observed binding affinities in molecular docking studies provide valuable insights into the strength of interaction between betulinic acid and CDMOF-1, these binding affinities can have several implications for stabilizing betulinic acid against oxidation:

- Identification of stable binding interactions: High binding affinity often indicates strong and stable interactions between the ligand and receptor. In the context of stabilizing betulinic acid molecules against oxidation, this suggests that betulinic acid is tightly bound to CDMOF-1, which may shield it from interacting with oxidizing agents in the surrounding environment.
- Prevention of oxidation-induced conformational changes: Binding to the CDMOF-1 molecule in a specific conformation may prevent betulinic acid from adopting alternative conformations that are more susceptible to oxidation. By stabilizing betulinic acid in a particular orientation, CDMOF-1 may help shield vulnerable functional groups from oxidation.
- Design of antioxidant compounds: Insights gained from molecular docking studies can aid in the design of small molecules with enhanced antioxidant properties. By understanding the structural features that contribute to high binding affinity and stability against oxidation, we can modify betulinic acid or design novel molecules that better fulfill the desired criteria.

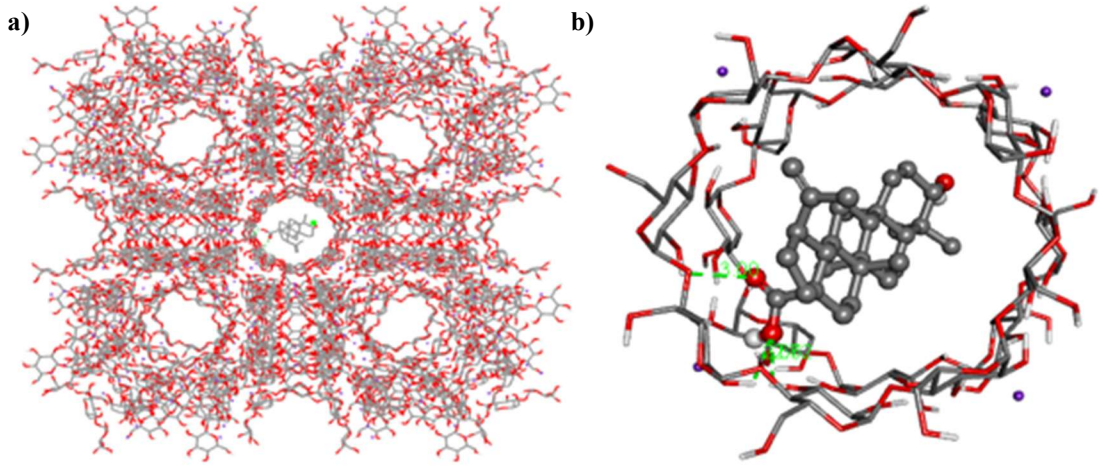

Figure 7. The best binding affinity of BA into CD-MOF-1 using the packed 1×1×1 structure of CD-MOF-1, the green lines are hydrogen bonds between CD-MOF-1 and BA

Table 4. Hydrogen bond interactions between CD-MOF-1 and betulinic acid

CD-MOF-1 Structure	**Hydrogen bond interactions between CD-MOF-1 and BA (Interaction distance)**		
Simple	CD-MOF-1_{OH13}··· $_{O28}$BA (2.95 Å)	CD-MOF-1_{O13} ···$_{H30}$BA (2.54 Å)	CD-MOF-1_{OH12} ··· $_{H30}$BA (2.12 Å)
Packed 1×1×1	CD-MOF-1_{OH12A} ···$_{O28}$BA (3.00 Å)	CD-MOF-1_{H13A} ··· $_{H30}$BA (2.72 Å)	CD-MOF-1_{OH2A} ··· $_{H30}$BA (2.66 Å)

Conclusion

CD-MOF-1 is a porous coordination compound, that exhibits many unique characteristics such as high surface area, high porosity, and tunability leading to numerous applications in many fields including drug delivery. In the present work, we have theoretically obtained the host-guest interactions between betulinic acid and CD-MOF-1 by performing QM calculation to understand the behavior of BA inside the CD-MOF-1, and molecular docking simulation to determine the best

binding affinity of BA into CD-MOF-1. The global descriptors such as energy gap, electronegativity, chemical hardness and softness, and electrophilicity show that betulinic acid has a smaller energy gap which involves less stability, more reactivity, and more polarizability. The MEPs map shows that the active site of betulinic acid is the carboxylic group and the latter molecule preferred electrophilic attacks. Molecular docking revealed that BA bound in the hydrophobic cavities of CD-MOF-1 through hydrogen bonds [CD-MOF-$1_{OH13\cdots O28}$BA (2.95 Å)], [CD-MOF-$1_{O13\cdots H30}$BA (2.54 Å)], and [CD-MOF-$1_{OH12\cdots H30}$BA (2.12 Å)] for the simplest structure and [CD-MOF-$1_{OH12A\cdots O28}$BA (3.00 Å)], [CD-MOF-$1_{H13A\cdots H30}$BA (2.72 Å)] and [CD-MOF-$1_{OH2A\cdots H30}$BA (2.66 Å)] for the packed structure 1×1×1. The packed CD-MOF-1 structure is the best with accurate results, this may be the factor of enhancement of betulinic acid solubility and bioavailability. So, CD-MOF-1 may be investigated and validated as an efficient carrier to enhance the solubility and bioavailability of betulinic acid. However, translating theoretical findings from molecular docking studies into practical applications can face several challenges and limitations such as accuracy of predictions, validation, flexibility and dynamics, solvent effects, chemical accessibility, and synthesis. In forthcoming research, the integration of molecular docking and molecular dynamic simulations unveils potential mechanisms governing binding affinities, enabling virtual observation. This integrated approach guides experimental synthesis and characterization validation from in vitro to preclinical studies, offering cost-effective methods to advance drug discovery, particularly in nanomedicine for cancer treatment, ensuring sustainable research practices.

Acknowledgment

This work was supported by the Malaysian Ministry of Higher Education under the Fundamental Research Grant Scheme, FRGS/1/2020/STG04/UPM/01/2 (Vot 5540441); the Organization for Women in Science for the Developing Word (OWSD) and the Swedish International Development Cooperation Agency (Sida). The authors also thank the Cambridge Crystallographic Data Centre for the FAIRE grant provided to the University of Dschang (Cameroon).

References

1. Zhong, Y., Liang, N., Yang, L. and Cheng, M.-S. (2021). Recent progress on betulinic acid and its derivatives as antitumor agents: A mini-review. *Chinese Journal of Natural Medicines,* 19(9): 641-647.
2. Zhao, P., Guan, M., Tang, W., Walayat, N., Ding, Y. and Liu, J. (2023). Structural diversity, fermentation production, bioactivities and applications of triterpenoids from several common medicinal fungi: Recent advances and future perspectives. *Fitoterapia*, 166 (1): 1-14.
3. Kozubek, M., Höhlich, L., Hoenke, S., Deigner, H.-P., Al-Harrasi, A. and Csuk, R. (2021). Apoptotic activity of substituted 3-O-acetyl-betulinic acid benzylamides. *European Journal of Medicinal Chemistry Reports,* 3(1): 1-8.
4. Azenha, I., Aniceto, J., Sequeira, S., Mendes, A. and Silva, C. (2020). Chromatographic separation of betulinic and oleanolic acids. *Separation and Purification Technology,* 235(1): 1-11.
5. Chen, C., Song, K., Zhang, Y., Chu, C., Fan, B., Song, Y., Huang, H. and Chen, G. (2021). Biotransformation of betulinic acid by Circinella muscae and Cunninghamella echinulata to discover anti-inflammatory derivatives. *Phytochemistry,* 182(1): 1-7.
6. Bravo-Alfaro, D. A., Ochoa-Rodríguez, L. R., Villaseñor-Ortega, F., Luna-Barcenas, G. and García, H. S. (2022). Self-nano emulsifying drug delivery system (SNEDDS) improves the oral bioavailability of betulinic acid. *Journal of Molecular Liquids,* 364(1): 1-12.
7. Pokornı, J., Olejníková, D., Frydrych, I., Lišková, B., Gurská, S., Benická, S., Šarek, J., Kotulová, J., Hajdúch, M., & Džubák, P. (2021). Substituted dienes prepared from betulinic acid–Synthesis, cytotoxicity, mechanism of action, and pharmacological parameters. *European Journal of Medicinal Chemistry,* 224(1): 1-18.
8. Pisha, E., Chai, H., Lee, I.-S., Chagwedera, T. E., Farnsworth, N. R., Cordell, G. A., Beecher, C. W., Fong, H. H., Kinghorn, A. D. and Brown, D. M. (1995). Discovery of betulinic acid as a selective inhibitor of human melanoma that functions by induction of apoptosis. *Nature medicine,* 1(10): 1046-1051.
9. Jiang, W., Liu, H., Liao, Q., Tang, T., Liu, J., Liu, Z., Xie, L. and Yan, J. (2021). Preparation of two metal-organic frameworks (K-β-CD-MOFs and Cs-

β-CD-MOFs) and the adsorption research of myricetin. *Polyhedron,* 196(1): 1-9.

10. Nicolov, M., Ghiulai, R. M., Voicu, M., Mioc, M., Duse, A. O., Roman, R., Ambrus, R., Zupko, I., Moaca, E. A. and Coricovac, D. E. (2019). Cocrystal formation of betulinic acid and ascorbic acid: Synthesis, physico-chemical assessment, antioxidant, and antiproliferative activity. *Frontiers in Chemistry,* 7(92): 1-11.
11. Zheng, L.-y., Zou, X., Wang, Y.-l., Zou, M., Ma, F., Wang, N., Li, J.-w., Wang, M.-s., Hung, H.-Y. and Wang, Q. (2022). Betulinic acid-nucleoside hybrid prevents acute alcohol-induced liver damage by promoting anti-oxidative stress and autophagy. *European Journal of Pharmacology,* 914(1): 1-13.
12. Boryczka, S., Bebenek, E., Jastrzebska, M., Kusz, J. and Zubko, M. (2012). Crystal structure of betulinic acid-DMSO solvate. *Zeitschrift für Kristallographie,* 227(6): 379-384.
13. Kutkowska, J., Strzadala, L. and Rapak, A. (2021). Hypoxia increases the apoptotic response to betulinic acid and betulin in human non-small cell lung cancer cells. *Chemico-Biological Interactions,* 333(1): 1-8.
14. Ghadi, R. and Dand, N. (2017). BCS class IV drugs: Highly notorious candidates for formulation development. *Journal of Controlled Release,* 248(1): 71-95.
15. Suresh, K., & Matzger, A. J. (2019). Enhanced drug delivery by the dissolution of amorphous drug encapsulated in a water unstable metal-organic framework (MOF). *Angewandte Chemie International Edition,* 58(47): 16790-16794.
16. Cheng, Z., Li, Y., Wang, K., Zhu, X., Tharkar, P., Shu, W., Zhang, T., Zeng, S., Zhu, L. and Murray, M. (2022). Compritol solid lipid nanoparticle formulations enhance the protective effect of betulinic acid derivatives in human Müller cells against oxidative injury. *Experimental Eye Research,* 215(1): 1-9.
17. Horvat, G., Pantić, M., Knez, Ž. and Novak, Z. (2018). Encapsulation and drug release of poorly water-soluble nifedipine from bio-carriers. *Journal of Non-Crystalline Solids,* 481(1): 486-493.
18. Li, H., Eddaoudi, M., O'Keeffe, M. and Yaghi, O. M. (1999). Design and synthesis of an exceptionally stable and highly porous metal-organic framework. *Nature,* 402(6759): 276-279.
19. Han, Z., Fan, X., Yu, S., Li, X., Wang, S. and Lu, L. (2022). Metal-organic frameworks (MOFs): A novel platform for laccase immobilization and application. *Journal of Environmental Chemical Engineering*, 10(1): 1-17.
20. Shan, Y., Zhang, G., Shi, Y. and Pang, H. (2023). Synthesis and catalytic application of defective MOF materials. *Cell Reports Physical Science,* 4(1): 1-44.
21. Haslina, A., Nur, A. Y., Khairulazhar, J. and Mohd, B. A. R. (2020). Ionothermal Synthesis of Zn-Based Metal-Organic Frameworks in Pyridinium Ionic Liquid. *Malaysian Journal of Analytical Sciences,* 24(2): 159-164.
22. Kamni, S. S., Kassim, K., Kassim, N. S. A. and Abidin, N. A. Z. (2021). Metal-organic frameworks as sorbent-based extraction: a review. *Malaysian Journal of Analytical Sciences,* 25(5): 791-807.
23. Balestri, D., Capucci, D., Demitri, N., Bacchi, A. and Pelagatti, P. (2017). Coordination-driven capture of nicotine inside a mesoporous MOF. *Materials,* 10(7): 1-12.
24. Hartlieb, K. J., Ferris, D. P., Holcroft, J. M., Kandela, I., Stern, C. L., Nassar, M. S., Botros, Y. Y. and Stoddart, J. F. (2017). Encapsulation of ibuprofen in CD-MOF and related bioavailability studies. *Molecular Pharmaceutics,* 14(5): 1831-1839.
25. Shen, M., Zhou, J., Elhadidy, M., Xianyu, Y., Feng, J., Liu, D. and Ding, T. (2022). Cyclodextrin metal-organic framework by ultrasound-assisted rapid synthesis for caffeic acid loading and antibacterial application. *Ultrasonics Sonochemistry,* 86(1): 1-10.
26. He, Y., Zhang, W., Guo, T., Zhang, G., Qin, W., Zhang, L., Wang, C., Zhu, W., Yang, M. and Hu, X. (2019). Drug nanoclusters formed in confined nano-cages of CD-MOF: dramatic enhancement of solubility and bioavailability of azilsartan. *Acta Pharmaceutica Sinica B,* 9(1): 97-106.
27. Zhou, Y., Zhao, Y., Niu, B., Luo, Q., Zhang, Y., Quan, G., Pan, X. and Wu, C. (2020). Cyclodextrin-based metal-organic frameworks for pulmonary delivery of curcumin with improved solubility and fine aerodynamic performance. *International Journal of Pharmaceutics,* 588(1): 1-8.
28. Mohammed, E.-R., EL FADILI, M., Mrabti, N. N., Zarougui, S. and Elhallaoui, M. (2022). QSAR,

molecular docking, ADMET properties in silico studies for a series of 7-propanamide benzoxaboroles as potent anti-cancer agents. *Chinese Journal of Analytical Chemistry,* 50(12): 1-11.

29. Badran, A.-S. and Ibrahim, M. A. (2023). Synthesis, spectral characterization, DFT, and in silico ADME studies of the novel pyrido [1, 2-a] benzimidazoles and pyrazolo [3, 4-b] pyridines. *Journal of Molecular Structure,* 1274(1): 1-14.
30. Ibrahim, M. and Uzairu, A. (2023). 2D-QSAR, molecular docking, drug-likeness, and ADMET/pharmacokinetic predictions of some non-small cell lung cancer therapeutic agents. *Journal of Taibah University Medical Sciences,* 18(2): 295-309.
31. Sabu, V., Peter, J., Sasidharan Nair, A. I. B., Krishnan, S., Sathyaseelan Suja, L. P., Helen, A. and Radhakrishna Pillai, G. (2019). Combinatorial action of triterpenoid, flavonoid, and alkaloid on inflammation. *Natural Product Communications,* 14(8): 1-9.
32. Khan, M. F., Nahar, N., Rashid, R. B., Chowdhury, A. and Rashid, M. A. (2018). Computational investigations of physicochemical, pharmacokinetic, toxicological properties and molecular docking of betulinic acid, a constituent of Corypha taliera (Roxb.) with Phospholipase A2 (PLA2). *BMC complementary and alternative medicine,* 18(1): 1-15.
33. Malleda, C., Ahalawat, N., Gokara, M. and Subramanyam, R. (2012). Molecular dynamics simulation studies of betulinic acid with human serum albumin. *Journal of Molecular Modeling,* 18(1): 2589-2597.
34. Hohenberg, P. and Kohn, W. (1964). Inhomogeneous electron gas. *Physical review,* 136(3B): 1-8.
35. Kohn, W., and Sham, L. J. (1965). Self-consistent equations including exchange and correlation effects. *Physical review,* 140(4A): 1-6.
36. Rajaraman, D., Anthony, L. A., Nethaji, P. and Vallangi, R. (2023). One-pot synthesis, NMR, quantum chemical approach, molecular docking studies, drug-likeness and in-silico ADMET prediction of novel 1-(2, 3-dihydrobenzo [b][1, 4] dioxin-6-yl)-2-(furan-2-yl)-4, 5-diphenyl-1H-imidazole derivatives. *Journal of Molecular Structure,* 1273(1): 1-11.
37. Agwupuye, J. A., Gber, T. E., Edet, H. O., Zeeshan, M., Batool, S., Duke, O. E., Adah, P. O., Odey, J. O. and Egbung, G. E. (2023). Molecular modeling, DFT studies, and biological evaluation of methyl 2, 8-dichloro-1, 2-dihydroquinoline-3-carboxylate. *Chemical Physics Impact,* 6(1): 1-11.
38. O'Boyle, N. M., Banck, M., James, C. A., Morley, C., Vandermeersch, T. and Hutchison, G. R. (2011). Open Babel: An open chemical toolbox. *Journal of Cheminformatics,* 3(1): 1-14.
39. Yousefzadeh Borzehandani, M., Abdulmalek, E., Abdul Rahman, M. B. and Mohammad Latif, M. A. (2021). First-principles investigation of dimethyl-functionalized MIL-53 (Al) metal-organic framework for adsorption and separation of xylene isomers. *Journal of Porous Materials,* 28(2): 579-591.
40. Marenich, A. V., Cramer, C. J. and Truhlar, D. G. (2009). Universal solvation model based on solute electron density and a continuum model of the solvent defined by the bulk dielectric constant and atomic surface tensions. *The Journal of Physical Chemistry B,* 113(18): 6378-6396.
41. Muya, J. T., Mwanangombo, D. T., Tsalu, P. V., Mpiana, P. T., Tshibangu, D. S.-T., & Chung, H. (2019). Conceptual DFT study of the chemical reactivity of four natural products with anti-sickling activity. *SN Applied Sciences,* 1(1): 1-18.
42. Ayşen, I., Çevik, U. A., Çelik, I., Bostancı, H. E., Karayel, A., Gündoğdu, G., Ince, U., Koçak, A., Özkay, Y., & Kaplancıklı, Z. A. (2022). Benzimidazole-hydrazone derivatives: Synthesis, in vitro anticancer, antimicrobial, antioxidant activities, in silico DFT and ADMET studies. *Journal of Molecular Structure,* 1270(1): 1-10.
43. Smaldone, R. A., Forgan, R. S., Furukawa, H., Gassensmith, J. J., Slawin, A. M., Yaghi O. M. and Fraser, J. S. (2010). Metal-organic frameworks from edible natural products. *Angewandte Chemie International Edition,* 49(46): 8630-8634.

Malaysian Journal of Analytical Sciences (MJAS)
Published by Malaysian Analytical Sciences Society

UNVEILING THE IMPACT OF BACTERIAL CELLULOSE DERIVED FROM NATA DE COCO AND SORBITOL ON BIOCOMPOSITE FILM PROPERTIES FOR POTENTIAL FOOD PACKAGING

(Menyingkap Kesan Selulosa Bakteria Diperoleh daripada Nata De Coco dan Sorbitol Terhadap Sifat-Sifat Filem Biokomposit Sebagai Bahan Pembungkus Makanan Alternatif)

Sharifah Fathiyah Sy Mohamad*, Nur Fikriyah Yaacob, and Intan Anak Ekong

Faculty of Chemical and Proces Engineering Technology, Universiti Malaysia Pahang Al-Sultan Abdullah Lebuh Persiaran Tun Khalil, Yaakob, 26300 Kuantan, Pahang, Malaysia

**Corresponding author: fathiyah@umpsa.edu.my*

Received: 10 October 2023; Accepted: 31 March 2024; Published: 29 June 2024

Abstract

The surge in plastic production in recent years has demonstrated the urgent need for eco-friendly alternatives. Bacterial cellulose (BC) has emerged as a promising candidate for replacing petroleum-based materials. However, the inherent rigidity, fragility, and brittleness of BC have posed formidable challenges, particularly in food packaging. This study investigates the impact of combining BC (1.0g, 2.5g, 5.0g, 7.5g, 10.0g) derived from nata de coco and sorbitol (0.5g, 1.0g, 1.5g, 2.0g, 2.5g) on the physical, mechanical, chemical, and thermal properties, as well as the surface morphology of the biocomposite films. Films were produced by varying BC and sorbitol quantities via the solvent casting method. Evaluations encompassed film thickness, moisture content, water solubility, mechanical characteristics, FTIR, TGA, and FE-SEM. Tensile strength increased with BC content but decreased with added sorbitol. FTIR confirmed the consistency of functional groups in the BC/Chitosan/Sorbitol biocomposite film with those in BC. TGA indicated improved thermal stability with increased BC and decreased sorbitol content. FE-SEM images revealed a smoother biocomposite film surface with sorbitol. The optimal composition was determined to be 10.0BC and 0.5S due to its low moisture content, low water solubility, high tensile strength, and minimal TGA weight loss. Overall, this study highlights the potential of BC/Chitosan/Sorbitol films as environmentally friendly and sustainable alternatives to traditional synthetic food packaging materials.

Keywords: bacterial cellulose, nata de coco, chitosan, sorbitol, biocomposite film

Abstrak

Peningkatan pengeluaran plastik dalam beberapa tahun kebelakangan ini telah menghasilkan keperluan mendesak untuk pembangunan pengganti plastik yang mesra alam. Dalam konteks ini, selulosa bakteria (SB) mempunyai potensi yang memberangsangkan sebagai pengganti bahan berasaskan petroleum. Walau bagaimanapun, ketegaran dan kerapuhan SB telah menimbulkan pelbagai cabaran, terutamanya dalam konteks kegunaannya sebagai pembungkus makanan. Dalam kajian ini, kami mengkaji kesan gabungan BC dan sorbitol terhadap sifat fizikal, mekanikal, kimia, termal, dan morfologi permukaan filem biokomposit berdasarkan BC. Filem-filem ini dihasilkan dengan mengubah kuantiti BC (1.0g, 2.5g, 5.0g, 7.5g, 10.0g) dan sorbitol (0.5g, 1.0g, 1.5g, 2.0g, 2.5g) menggunakan kaedah pelarut. Sampel filem yang terhasil dinilai berdasarkan ketebalan filem, kandungan lembapan, kelarutan dalam air, sifat-sifat mekanik, FTIR, TGA, dan FE-SEM. Hasil kajian menunjukkan bahawa nilai kekuatan regangan meningkat seiring dengan peningkatan BC, tetapi berkurangan apabila kepekatan sorbitol bertambah. FTIR

menunjukkan bahawa kumpulan berfungsi yang wujud dalam filem biokomposit BC/Chitosan/Sorbitol sepadan dengan kumpulan berfungsi BC. TGA pula mendedahkan bahawa kestabilan termal filem komposit meningkat dengan peningkatan BC dan penurunan sorbitol. Peningkatan kuantiti BC menyebabkan filem mengalami kehilangan berat yang minimum, tetapi apabila tahap sorbitol meningkat, filem mengalami kehilangan berat yang lebih besar FE-SEM menggambarkan bahawa permukaan filem komposit menjadi lebih licin dengan penambahan sorbitol. Komposisi optimum ditentukan sebagai 10.0BC dan 0.5S, disebabkan oleh kandungan lembapan yang rendah, kelarutan dalam air yang rendah, kekuatan regangan yang tinggi, dan kehilangan berat yang minima dalam TGA. Keseluruhannya, kajian ini membuktikan bahawa filem komposit berdasarkan BC mempunyai potensi untuk digunakan sebagai alternatif yang boleh dikompos secara biodegradasi dan mampan kepada bahan pembungkusan makanan sintetik tradisional.

Kata kunci: selulosa bakteria, nata de coco, kitosan, sorbitol, filem biokomposit

Introduction

The packaging industry plays a crucial role in the global economy, particularly in the food and beverage segment, which holds the majority market share of around 85% [1]. However, the reliance on conventional plastic packaging materials has led to significant environmental concerns due to their non-biodegradable nature [2]. The immense volume of plastic waste generated worldwide is expected to triple by 2060, surpassing one billion metric tons. Alarmingly, only a minimal fraction (9%) of this plastic waste is recycled, leading to exacerbated resource depletion, contributing to global warming, acidification, eutrophication, and posing risks to human health [3]. Consequently, there is an increasing global demand for environmentally friendly alternatives to traditional packaging materials. Traditional approaches to biodegradable food packaging, which use proteins, polysaccharides, and lipids from agricultural byproducts or synthetic biopolymers such as PLA and PHA, encounter significant challenges because of their reduced tensile strength and insufficient moisture and oxygen barriers. These properties are essential for preserving food safety and quality. Despite their eco-friendly nature, these methods struggle with scalability and cost-effectiveness, primarily due to the elevated price of raw materials, energy-intensive processing, and advanced equipment requirements [4]. Moreover, the environmental advantages of polymers, such as PLA, are mitigated by their dependence on industrial composting facilities, which are scarcely available. On the other hand, naturally degradable materials such as chitosan show promise but are plagued by sourcing and quality consistency issues [5]. These limitations highlight the urgent necessity for new, sustainable, and economically viable food packaging solutions that effectively balance environmental benefits with performance requirements for widespread commercial adoption.

In this context, Nata de coco (NDC) emerges as an environmentally sustainable and promising alternative to conventional plastic packaging materials, primarily due to its role as a BC source. BC, derived from Nata de coco, is a natural and renewable biopolymer primarily produced by *Acetobacter xylinum* through the fermentation of coconut water [6]. This unique production process involves the metabolic conversion of glucose found in coconut water, enriched with carbon and nitrogen, by *Acetobacter xylinum*, resulting in the extracellular production of cellulose as a valuable metabolite [7]. BC shares a chemical composition identical to plant cellulose but distinguishes itself by the absence of lignin or hemicelluloses, leading to superior physical characteristics compared to conventional plant cellulose [8]. Its high tensile strength and water-holding capacity make BC stronger, more resistant to breaking, and capable of absorbing more water. Furthermore, BC exhibits high purity and crystallinity, contributing to excellent transparency and barrier properties [9]. These properties make BC an attractive potential replacement for synthetic food packaging materials [10]. Nevertheless, despite its potential, using BC alone for food packaging applications is not ideal due to its natural brittleness when dried. Dried BC has a rigid and less pliable structure, resulting in a rough appearance and reduced flexibility. To overcome this limitation, BC is often combined with other biopolymers or plasticizers, such as chitosan or glycerol, to enhance its pliability, achieve a more plastic-like appearance, and improve overall properties while minimizing brittleness [11,12].

Chitosan, the second most abundant natural biopolymer after cellulose, is primarily sourced from the byproducts

of the shellfish industry [5]. It has demonstrated remarkable versatility in various applications, notably in food packaging, due to its non-toxicity, biodegradability, film-forming attributes, solubility, and inherent antimicrobial properties. Furthermore, chitosan and bacterial cellulose exhibit similar chemical structures and mutually complementary characteristics, fostering enhanced molecular interactions among their polysaccharide chains [13]. Consequently, chitosan emerges as a highly promising candidate for utilization as a filler in the production of BC-based films, offering the prospect of enhanced mechanical properties and film-forming capability [14]. In contrast to films composed solely of chitosan, BC/chitosan composite films present distinct advantages in terms of mechanical resilience, including improved thermal stability and reduced oxygen permeability, making chitosan a highly viable candidate for augmenting BC-based films [15].

Moreover, incorporating plasticizers such as sorbitol, recognized for its low molecular weight and non-volatile nature, into film formulations can significantly enhance their flexibility, elongation, and toughness, thereby effectively addressing the inherent brittleness of BC [16]. The materials can also reduce film stiffness and brittleness, enhance transparency, and decrease water vapor transmission rate. One commonly used plasticizer is sorbitol, which has a low molecular weight, non-volatile nature, and high boiling point. Sorbitol exhibits significant intermolecular interaction with polymers, reducing polymer strength while increasing flexibility and extensibility. It is a polyhydric alcohol monosaccharide molecule, also known as hexitol or glucitol, with a chemical formula of $C_6H_{14}O_6$ [17]. Incorporating sorbitol as a plasticizer into film formulations can influence film thickness, flexibility, density, and water content [15], offering a means to enhance the properties of BC and make it more suitable for food packaging applications.

In the past few years, numerous studies have explored the incorporation of BC and chitosan for food packaging applications [18–20]. BC showed a reinforcing effect and can improve the physical properties of whey protein concentrate films [21]. However, despite these advancements, comprehensive studies considering film formulations and interactions between BC from NDC, chitosan, and sorbitol are still lacking in the literature. Building on this gap of knowledge, this study aimed to investigate the impact of varying BC and sorbitol concentrations on the physical, mechanical, and thermal properties of BC-based biocomposite films for potential use in sustainable food packaging. The study aims to determine the ideal composition of BC and sorbitol that ensures low moisture content, high tensile strength, and improved thermal stability. This research is expected to contribute to the advancement of an environmentally friendly substitute for traditional plastic packaging materials.

Materials and Methods

Materials

1.5 kg of food-grade nata de coco (Brand: Desa Alpha, Manufactured by Rico Food Ind. Sdn. Bhd.) in the form of cubes was purchased from the local supermarket. Chitosan of medium molecular weight and sodium hydroxide were obtained from Sigma-Aldrich. Sorbitol and acetic acid were purchased from R&M Chemicals. All other chemicals used were of the analytical grade.

Purification of bacterial cellulose (BC) from nata de coco

The nata de coco cubes were thoroughly washed and soaked in distilled water twice daily for 10 days to ensure the pH reached 7. This step was done to neutralize the acidity and remove any impurities from the nata de coco cubes. After that, an alkaline treatment was performed by stirring the nata de coco cubes in 0.01 M NaOH at 80 °C for 90 min to remove any remaining bacterial cell debris, microorganisms, and other dissolved substances. Subsequently, the nata de coco cubes were washed multiple times with distilled water at room temperature until the pH reached 7 [22]. The purified nata de coco was then ground and mechanically blended for 1 hour using a kitchen blender (ProMix hand blender, Philips). The resulting BC slurry was collected and stored at room temperature for future use.

Preparation of BC/Chitosan/Sorbitol biocomposite films

The biocomposite films were prepared using a solvent casting method, following the procedure by Yanti et al. [23]. The film-forming solution consisted of BC suspension, chitosan, and sorbitol as plasticizers, as shown in Table 1. The chosen ranges for BC and sorbitol were established through preliminary experiments

aimed at identifying levels that yield films with flexibility and without brittleness, suitable for further testing and application. Chitosan solution was first prepared by dissolving 0.25g of chitosan powders in 25 mL of 1 %v/v acetic acid. All film formulations were homogenized using an ultrasonic homogenizer for 5 min with a pulse of 5 sec and amplitude of 60%. The resulting film solutions were then cast onto an acrylic mold (8 cm × 12 cm) and dried at 50 °C for 12 hours in an oven. The dried films were peeled off from the petri dishes and stored in zip-lock bags for further analysis. The biocomposite films were previously conditioned for 48 h at 25 °C and 54% RH before evaluating their physicochemical properties.

Table 1. Composition of BC and sorbitol in film formulations.

Sample Name	Bacterial Cellulose (g)	Sorbitol (g)
0.5S	10.00	0.50
1.0S	10.00	1.00
1.5S	10.00	1.50
2.0S	10.00	2.00
2.5S	10.00	2.50
1.0BC	1.00	0.50
2.5BC	2.50	0.50
5.0BC	5.00	0.50
7.5BC	7.50	0.50
10.0BC	10.00	0.50

Characterization of BC/Chitosan/Sorbitol films:

Film thickness

A digital micrometer (3109-25A, InSize, China) was used to measure the thickness of the formed film with an accuracy of 0.001 mm. The thickness of the film was measured at five different spots, and the average thickness was calculated and recorded.

Moisture content (MC)

Test specimens (2 cm × 2 cm) at three random positions of each film type were uniformly cut and placed on glass Petri dishes. The moisture content of the films was determined by drying test specimens in an oven at 105 °C for 24 h until a constant dry weight was obtained according to the method briefly explained by Azaza et al. [24]. The dry weight of the film was measured after drying, and the MC was calculated using Equation (1) below:

$$\text{Moisture Content (\%)} = \frac{\text{Initial sample weight (g)} - \text{Dried sample weight (g)}}{\text{Initial sample weight (g)}} \times 100 \quad (1)$$

Water solubility (WS)

The water solubility of the film was measured according to the method described by Lee et al. [25]. Briefly, to determine the initial dry weight, samples were cut to sizes (2 cm × 2 cm) in triplicate and dried at 105 °C for 24 hours. The dried films were then immersed in 50 mL of distilled water and stirred at room temperature for 24 hours at 100 rpm. After 24 hours, any remaining films were removed and dried at 105 °C for 24 hours to obtain the final dry weight. The percentage of water solubility in samples was calculated using the following Equation (2):

$$\text{Water Solubility (\%)} = \frac{\text{Dried sample weight (g)} - \text{Final dried sample weight (g)}}{\text{Dried sample weight (g)}} \times 100 \quad (2)$$

Mechanical properties

Tensile strength (TS) and elongation at break (EAB) of the film samples were measured according to the ASTM D882-00 method (ASTM., 2000) using a texture analyzer (Stable Micro Systems TA-XT plus, Surrey, UK). Each BC and BC/Chitosan/Sorbitol film was cut into a rectangular shape (10 cm × 1 cm). All the tests were carried out at least twice with different strips. TS was calculated using the following Equation (3):

$$TS = \frac{\text{Force Maximum (Fmax)}}{\text{Area (A)}} \quad (3)$$

where Fmax is the maximum load, and A is the cross-sectional area.

EAB was calculated using the following Equation (4):

$$EAB = \frac{\Delta L}{L_0} \times 100 \quad (4)$$

where ΔL is the film extension, and L_0 is the initial length of the film sample.

Structure by Fourier-transform infrared (FTIR)

The film samples were cut into small pieces (2 cm × 2 cm) and analyzed using an FTIR Spectrophotometer (Nicolet iS5, Thermo Fisher Scientific, USA). For each sample, 32 scans with a resolution of 4 cm^{-1} were collected over the wavenumber ranging from 600 – 4000 cm^{-1} in transmittance mode.

Thermogravimetric analysis (TGA)

TGA was carried out on selected film samples to evaluate their respective mass losses when it is subjected to continuous heating. TGA was performed using TGA Instrument Q500 V 6.7 (TA Instruments, USA) with a 10 °C/min heating rate from 25 to 600 °C under nitrogen gas purging with a flow rate of 40 ml/min.

Surface morphology by field emission scanning electron microscopy (FE-SEM)

The surface morphology of the pure BC and selected BC/Chitosan/Sorbitol films were visualized using a Field Emission Scanning Electron Microscope (FE-SEM) JEOL JSM 7800 F with an accelerating voltage of 15 kV.

Results and Discussion

Physical appearances of BC/Chitosan/Sorbitol films

The physical appearance of the films was evaluated by analyzing their opacity and transparency, as shown in Figure 1. The results indicated that the opacity of the pure BC film was nearly 100% due to the high concentration of BC fibers. The higher value of opacity signified smaller transparency. BC is a polymer composed of ultrafine nanofibrils that form a three-dimensional web-shaped structure, held together by intermolecular and intramolecular hydrogen bonding [26]. As the BC content increased, the film became rougher and less homogenous. Conversely, the addition of sorbitol improved homogenization and gave the film a smoother appearance due to its high hydrophilicity. These findings align with previous research by Wang et al. [27], which also observed a significant increase in film opacity with increasing BC concentrations from 0% to 10%.

Film thickness, moisture content, and water solubility

Table 2 presents valuable insights into the characteristics of the film formulations with varying proportions of bacterial cellulose and sorbitol. The thickness of these films ranged from 0.0384 to 0.2507 mm and can be adjusted by modifying the amounts of BC and sorbitol. The results suggest that adding BC and sorbitol can improve film thickness. The film with a greater sorbitol concentration (2.5S) formed a thicker (0.2526 mm) film than the film with a lower amount of BC and sorbitol (1.0BC), which produced a thinner (0.0718mm). These findings are comparable to similar reports on the effects of sorbitol on the characteristics of carrageenan edible film. Edible film features and basic material composition are two aspects that impact the thickness of edible film. As the sorbitol concentration increased, the edible coating showed a corresponding thickness increment. This is because when the total solids in the edible film solution increased, the formation of the edible film occurred. Therefore, the higher the concentration of sorbitol, the higher the thickness of the film due to the solid content and characteristics of sorbitol [28].

In contrast, the moisture content exhibited less significant variations upon the introduction of BC but demonstrated a substantial increase when sorbitol concentration was augmented, ranging from 4.82% to

89.51%. This phenomenon mirrors findings from a study by Ghamari et al. [29], which investigated active edible film based on milk proteins infused with Nigella sativa essential oil. The study emphasized the crucial role of sorbitol concentration in moisture content, highlighting that its increment can affect the hydrophilic nature of sorbitol. This is because sorbitol has hydroxyl groups in its structure that can actively form hydrogen bonding with water.

Furthermore, the water solubility of the films exhibited a notable decline, decreasing from 32.88% to 5.29%, as BC and sorbitol were incorporated in greater quantities. The reduction in water solubility can be attributed to the enlarged surface area resulting from BC and the formation of intermolecular interactions between the agar matrix and BC. These interactions enhance the cohesion of the biopolymer matrix, leading to decreased water solubility [27]. Therefore, it is evident that as the proportions of BC and sorbitol increased, the water solubility of the films decreased significantly, an essential property for their potential applications

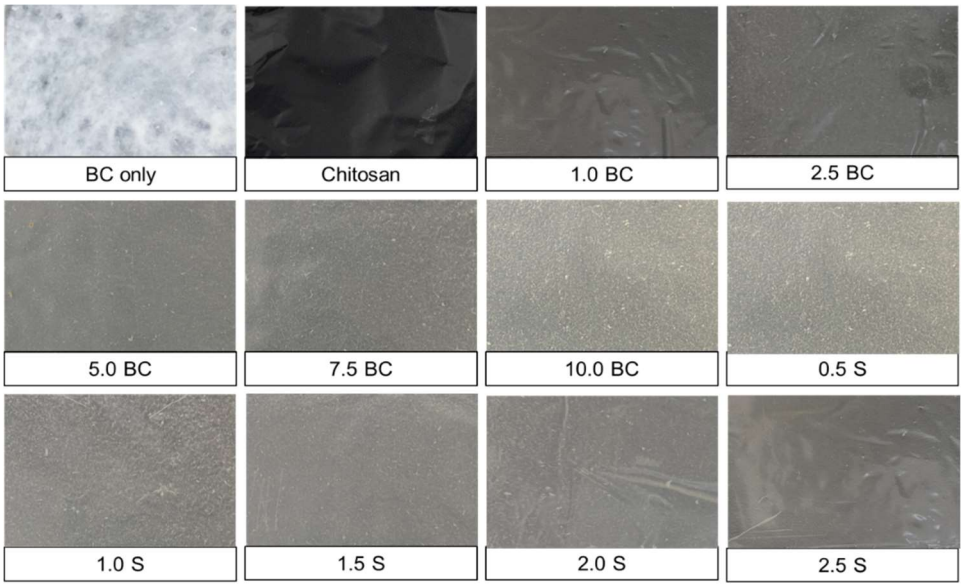

Figure 1. Visual appearances of BC/Chitosan/Sorbitol films. Digital photographs are taken under natural light to show color, transparency, and texture differences. No magnification was applied

Table 2. Thickness, moisture content, and water solubility of the BC/Chitosan/Sorbitol films

Sample Name	Thickness (mm)	Moisture Content (%)	Water Solubility (%)
BC	0.0384	8.31	64.88
0.5S	0.0822	58.57	8.87
1.0S	0.1620	66.76	6.93
1.5S	0.1580	74.72	5.29
2.0S	0.1896	89.51	18.60
2.5S	0.2526	78.42	19.21
1.0BC	0.0718	4.82	27.95
2.5BC	0.0774	11.32	26.98
5.0BC	0.0774	4.86	16.23
7.5BC	0.0760	8.37	32.63
10.0BC	0.0886	16.67	12.46

Fourier transform infrared (FTIR) spectroscopy

FTIR spectroscopy was employed to investigate the intricate chemical interactions occurring between BC and sorbitol. This analytical approach allowed for the observation of shifts and alterations in the intensity of characteristic peaks within the spectra, providing valuable insights into both the physical and chemical interaction between these substances and shedding light on their compatibility [30].

Figure 2 compares FTIR spectra between BC and BC/Chitosan/Sorbitol films, varying in the amounts of BC and sorbitol. Figure 2(a) notably highlights the characteristic peaks of BC present in all the samples. The broad absorption band in the 3200-3500 cm^{-1} range was attributed to the stretching vibrations of hydroxyl groups (-OH) of BC and sorbitol [31]. The existence of hydroxyl groups within BC facilitates the formation of different intermolecular and intramolecular hydrogen bonds. The establishment of these hydrogen bonds, both between molecules and within individual molecules, plays a fundamental role in shaping the physical characteristics of cellulosic materials [12]. Meanwhile, the peak around 2925 cm^{-1} corresponds to C-H stretching vibrations, while the peak at 1637 cm^{-1} can be attributed to the –CO group. The peaks at 1411 and 1314 cm^{-1} signify the –CH asymmetric deformation and –CH bending vibrations, which serve as critical signatures for samples with chitosan [32]. Furthermore, the peak around 1056 cm^{-1} corresponds to C–O symmetric stretching. In contrast, the presence of the hydroxyethyl group is indicated by the shift of the C-O-C stretching vibration peak to 888 cm^{-1} [15].

The introduction of sorbitol as a plasticizer induced a noticeable shift in the peak positions, transitioning from 3500 cm^{-1} (as observed in pure BC in Figure 2(b)) to lower wavenumbers, typically around 3300 cm^{-1}. This shift is primarily attributable to the formation of hydrogen bonding interactions involving BC, chitosan, and sorbitol [27]. Interestingly, the FTIR spectra of plasticized films (Figure 2(b)) displayed only marginal reductions in intensity. This observation suggests the presence of intermolecular interactions facilitated by the formation of hydrogen bonds. Consequently, it can be inferred that the plasticizer did not induce significant structural alterations in BC; instead, it engaged in cooperative interactions with the material.

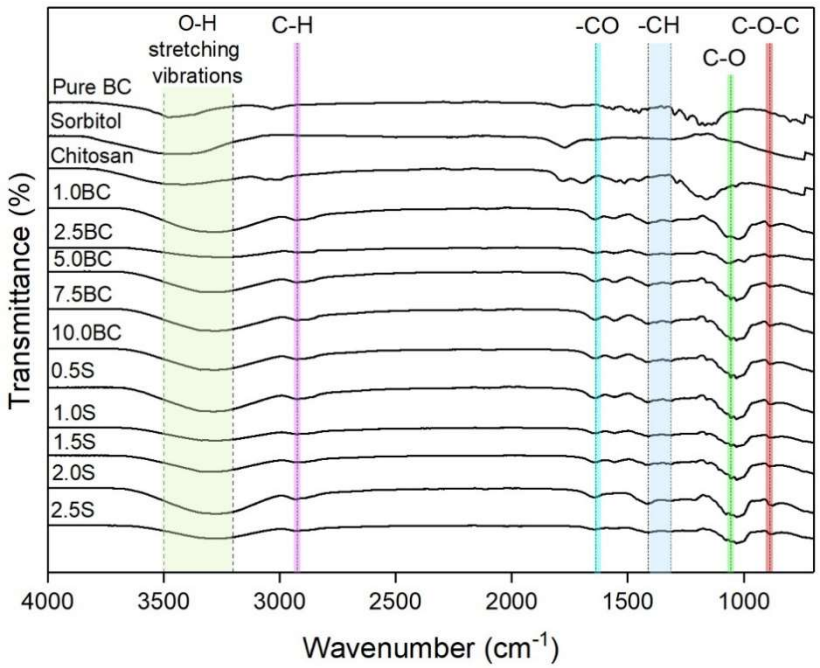

Figure 2. FTIR spectra for BC/Chitosan/Sorbitol films containing various amounts of BC and sorbitol

Mechanical properties

The evaluation of mechanical properties (Table 3), including tensile strength (TS), Young's modulus (YM), and elongation at break (EAB), is fundamental in assessing the potential of BC/sorbitol biocomposite films for food packaging applications. The control sample, which consisted solely of BC, served as the baseline for subsequent comparisons, recording a TS of 10.60 MPa, a YM of 629.91 MPa, and an EAB of 2.36%. As the BC concentration incrementally increased, these mechanical properties were affected. The findings align with previous analysis suggesting that a BC reinforcing effect within composite matrices can ultimately enhance the TS [33,34]. However, the phenomenon of agglomeration at higher BC concentrations observed in the 10.0BC formulation resulted in diminished TS, possibly due to impaired stress distribution [35]. On the other hand, adding sorbitol reduced the sample's YM due to its function as a plasticizer. Notably, the 2.5S formulation showed the lowest YM at 44.55 MPa, suggesting a significant improvement in film flexibility. This reduction aligns with theoretical expectations, where plasticizers weaken intermolecular hydrogen bonds in cellulose, thereby enhancing chain mobility and reducing stiffness [18].

Moreover, the YM analysis delineated a decrease with incremental BC and sorbitol additions. Initially, the BC-only films displayed considerable stiffness, a characteristic trait of materials with high crystallinity [23]. As BC concentrations were increased, stiffness initially rose due to the additional cellulose fibers reinforcing the structure of the films. However, similar to TS findings, excessive BC countered stiffness due to ineffective stress distribution within the matrix [35]. In contrast, the systematic addition of sorbitol to the film formulations markedly decreased the YM, reflecting its function as a plasticizer. For instance, the 2.5S formulation showed the lowest YM at 44.55 MPa, indicating substantial increases in film flexibility. This reduction in stiffness with added sorbitol supports the anticipated outcome where plasticizers disrupt hydrogen bonding within cellulose, thereby increasing chain mobility and decreasing material rigidity [36].

EAB further elucidates the ductility and adaptability of the films under strain. Initially, BC-only films displayed low EAB values, signifying limited elasticity, which is typical for rigid polymer matrices. As BC content was increased, there was a moderate increase in EAB, suggesting that higher levels of BC might slightly enhance the flexibility due to the distribution of stress across a denser network of cellulose fibers. On the other hand, increasing amounts of sorbitol had a more pronounced effect on EAB, substantially improving the stretchability of the films. Particularly, films with higher sorbitol content, such as the 2.5S sample, demonstrated significant increases in elongation capabilities. This behavior, indicative of enhanced film plasticity, highlights the efficacy of sorbitol in facilitating polymer chain slippage that induces more deformable film structures [36]. Such properties are desirable in packaging applications where material flexibility and resistance to breakage under load are essential.

Comparatively, the range of TS in this study, between 5.02 and 17.47 MPa, aligns closely with that of the modified BC films derived from sago liquid waste. However, it is noteworthy that the YM and EAB parameters observed in this study were slightly lower compared to those reported for modified BC derived from sago liquid waste. The modified BC displayed a YM range of 2.93-6.54 GPa and an EAB range of 10.27-29.67%, suggesting opportunities for further refinement of materials and tailored adjustments for specific applications.

Thermogravimetric analysis (TGA)

The thermal behavior of selected BC/Chitosan/Sorbitol films was investigated using TGA to unravel their thermal stability and degradation profiles. The obtained TGA curves and their first derivative (DTG) are depicted in Figure 3. DTG was the first-order differential of the TG curve; that is, the upward peaks in the DTG curve were consistent with the maximum weight loss of the TG curve. Notably, the findings unveiled an intriguing similarity in the thermal degradation behavior among all BC/Chitosan/Sorbitol films, aligning closely with the patterns observed in BC and sorbitol. The TGA curves revealed a multi-stage thermal degradation process, shedding light on the intricate transformations that occur within these materials when subjected to high temperatures [27]. Initially, a subtle weight loss, occurring around 100 °C, was linked to the evaporation

of water and the presence of residual acetic acid in the polymer matrix [33]. Subsequently, a distinct and substantial weight loss phase unfolded within the temperature range of 200 °C to 350 °C, marking the second thermal event that is closely associated with polymer decomposition [30]. It is worth noting that cellulose typically undergoes thermal degradation within the 300-450 °C temperature range. Incorporating chitosan and sorbitol into the film composition influenced the second stage of thermal degradation, with the primary thermal degradation step for chitosan and sorbitol initiating at approximately 300 °C [37]. Overall, the results regarding thermal stability suggest that the BC/Chitosan/Sorbitol biocomposite films remain stable when subjected to temperatures below 200 °C. As such, this biodegradable composite material is better suited for use with food products following sterilization or pasteurization processes.

Table 3. Tensile strength (TS), Young's modulus (YM), and elongation at break (EAB) of the BC/Chitosan/Sorbitol films

Sample Name	Tensile (MPa)	Young Modulus (MPa)	Elongation at Break (%)
BC	10.60±1.00	629.91	2.36±0.04
0.5S	41.08±2.58	1054.43	4.14±0.05
1.0S	14.95±1.09	426.03	3.71±0.64
1.5S	25.32±2.33	396.34	6.76±0.20
2.0S	15.32±0.76	248.37	6.47±0.04
2.5S	3.83±0.20	44.55	9.21±0.94
1.0BC	6.10±0.14	104.42	6.45 ± 0.05
2.5BC	19.20±0.38	255.99	8.60 ± 0.27
5.0BC	7.90±0.24	54.26	12.91 ± 0.09
7.5BC	20.65±0.85	318.89	11.29 ± 0.45
10.0BC	29.59 ±0.26	403.46	7.78 ± 0.63

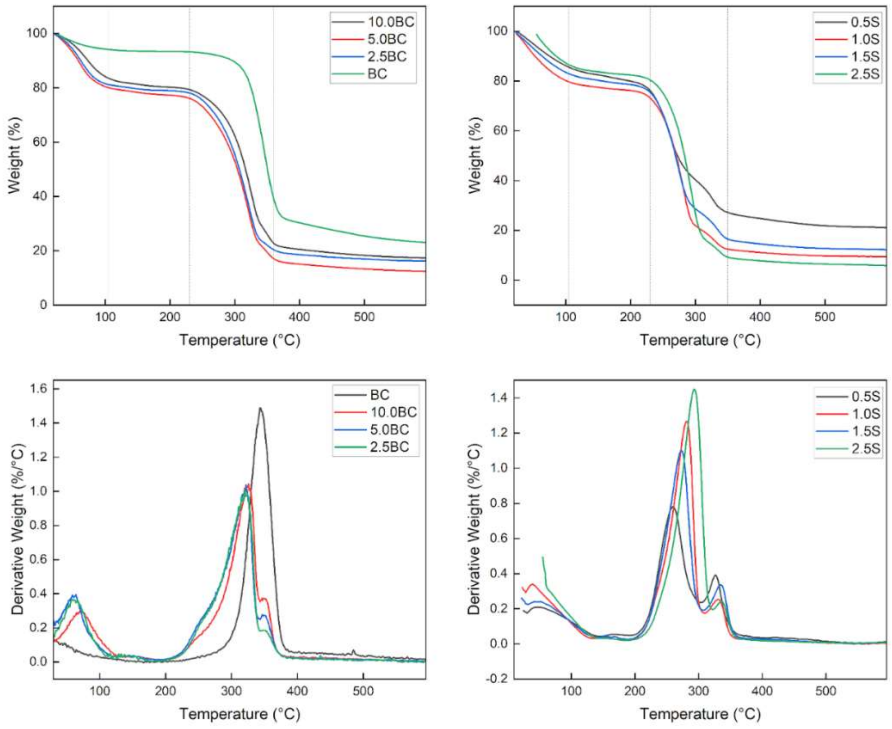

Figure 3. TG and DTG curves of selected BC/Chitosan/Sorbitol films

Morphology by FE-SEM

Figure 4 presents the surface morphology of pure BC film and selected BC/Chitosan/Sorbitol film samples (pure BC, 1.0BC, 10.0BC, 0.5S, 2.5S). The FE-SEM image of the pure BC film reveals the fibrous 3-D ultrafine networks of well-arranged nanofibers stabilized by hydrogen bonds existing in cellulose units [12,22]. However, the addition of sorbitol to the film formulation resulted in slightly smooth and homogeneous surfaces because of an even distribution of the material in the BC-based film [27]. Due to the hydrophilicity properties of sorbitol, an increase in the amount of plasticizer (from 0.5S to 2.5S) resulted in the least appearance of BC fibers and a wetter texture. In contrast, the 1.0BC film containing 0.5g of sorbitol had a dry texture but the same surface morphology.

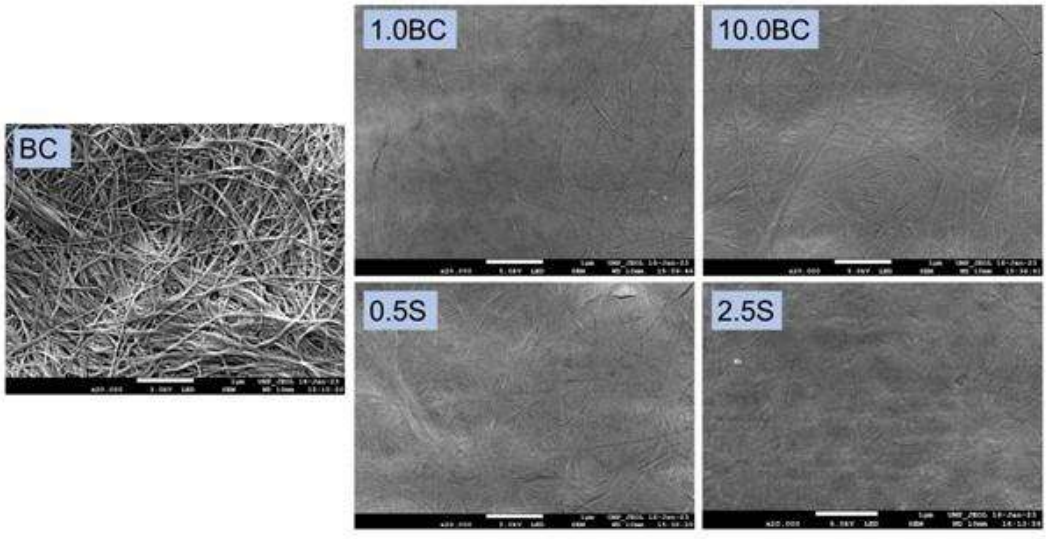

Figure 4. FE-SEM images of selected BC/Chitosan/Sorbitol films at 20000x magnifications

This study presents a comprehensive exploration of BC/Chitosan/Sorbitol films, which were developed using nata de coco as a key resource. Various amounts of BC and sorbitol were added to the films to improve their properties and compare their characterization. The results showed that an increase in BC content led to a significant improvement in the tensile strength, elongation at break, and thermal stability of the films due to hydrogen bonding interactions between the macromolecule chains of BC and the plasticizers. Conversely, the addition of sorbitol influenced moisture content and TGA weight loss. The optimum film composition emerged as 10.0BC and 0.5S, characterized by low moisture content, low water solubility, high tensile strength, and minimal TGA weight loss. These properties position this film as an excellent candidate for extended food packaging, offering a shield against physical, chemical, and biological contaminants while facilitating long-term content preservation. This research not only advances our understanding of biocomposite films but also underscores their potential in diverse applications, particularly in the realms of sustainability and food preservation.

The promising results of this study are anticipated to be the benchmark for future investigations into the incorporation of antimicrobial agents, natural dyes, and other natural plasticizers into the BC/Sorbitol matrix. Additionally, scale-up processes and lifecycle analyses will be crucial for assessing the commercial viability and environmental impact of these biocomposite films. Exploring these avenues will significantly contribute to the advancement of sustainable food packaging technologies.

Acknowledgment

The research was supported by the Fundamental Grant Research Scheme (FRGS/1/2018/ TK05/UMP/03/3) received from the Malaysian Ministry of Higher Education (MOHE).

References

1. Bharimalla, A.K., Deshmukh, S.P., Vigneshwaran, N., Patil, P.G. and Prasad, V. (2017). Nanocellulose-polymer composites for applications in food packaging: Current status, future prospects and challenges. *Polymer - Plastics Technology and Engineering*, 56: 805-23.
2. Moniri, M., Moghaddam, A.B., Azizi, S., Rahim, R.A., Ariff, A. Bin, Saad, W.Z. et al. (2017) Production and status of bacterial cellulose in biomedical engineering. *Nanomaterials*, 7: 1-26.
3. Nagtzaam, G., Geert, V.C., Steve, K. and Elena, K. (2023). Global plastic pollution and its regulation: History, trends, perspectives. Edward Elgar Publishing.
4. Gupta, I., Cherwoo, L., Bhatia, R. and Setia, H. (2022). Biopolymers: Implications and application in the food industry. *Biocatalysis and Agricultural Biotechnology*, 46: 102534.
5. Wang, H., Qian, J. and Ding, F. (2018). Emerging chitosan-based films for food packaging applications. *Journal Agriculture Food Chemistry,* 2018: 395-413.
6. Athirah Raihana Nor Aziz Hashim, N., Zakaria, J., Mohamad, S., Fathiyah Sy Mohamad, S. and Ab. Rahim, M.H. (2021) Effect of different treatment methods on the purification of bacterial cellulose produced from OPF juice by *Acetobacter xylinum*. *IOP Conference Series: Materials Science and Engineering*, 1092: 012058.
7. Kongruang, S. (2008) Bacterial cellulose production by *Acetobacter xylinum* strains from agricultural waste products. *Applied Biochemistry and Biotechnology*, 148: 245-56.
8. Amr, A. and Ibrahim, H. (2023). Bacterial cellulose: Biosynthesis and applications. *IntechOpen*, pp. 1-24.
9. Gan, M., Guo, C., Liao, W., Liu, X. and Wang, Q. (2023). Development and characterization of chitosan/bacterial cellulose/pullulan bilayer film with sustained release curcumin. *International Journal of Biological Macromolecules*, 34: 301-11.
10. Mishra, S., Singh, P.K., Pattnaik, R., Kumar, S., Ojha, S.K., Srichandan, H. (2022). Biochemistry, synthesis, and applications of bacterial cellulose: A review. *Frontier Bioengineering Biotechnology*, 2022: 780409
11. Vázquez, M., Velazquez, G. and Cazón, P. (2021). UV-shielding films of bacterial cellulose with glycerol and chitosan. Part 1: equilibrium moisture content and mechanical properties. *CYTA - Journal of Food*, 19: 105-114.
12. Rahman, M.A.A.A., Mohamad, S.F.S. and Mohamad, S. (2023). Development and characterization of bio-composite films made from bacterial cellulose derived from oil palm frond juice fermentation, chitosan and glycerol. *Trends in Sciences*, 20: 1-10.
13. Amorim, L.F.A., Mouro, C., Riool, M. and Gouveia, I.C. (2022). Antimicrobial food packaging based on prodigiosin-incorporated double-layered bacterial cellulose and chitosan composites. *Polymers*, 14: 20315.
14. Melro, E., Antunes, F.E., da Silva, G.J., Cruz, I., Ramos, P.E., Carvalho, F. et al. (2021). Chitosan films in food applications. Tuning film properties by changing acidic dissolution conditions. *Polymers*, 23: 1-12.
15. Mohammed, A.A.B.A., Hasan, Z., Omran, A.A.B., Elfaghi, A.M., Khattak, M.A., Ilyas, R.A. et al. (2023) Effect of various plasticizers in different concentrations on physical, thermal, mechanical, and structural properties of wheat starch-based films. *Polymers*, 15: 10063.
16. Maniglia, B.C., Tessaro, L., Ramos, A.P. and Tapia-Blácido, D.R. (2019). Which plasticizer is suitable for films based on babassu starch isolated by different methods? *Food Hydrocolloids*, 89:143-52.
17. Shahrampour, D. and Razavi, S.M.A. (2022). Physicochemical and structural properties of a bio-based antioxidant packaging film derived from *Eremurus luteus* root gum. *Materials Today Communications*, 33: 104756.
18. Indriyati, Dara, F., Primadona, I., Srikandace, Y. and Karina, M. (2021). Development of bacterial cellulose/chitosan films: structural, physicochemical and antimicrobial properties. *Journal of Polymer Research*, 28: 02328
19. Xu, Y., Liu, X., Jiang, Q., Yu, D., Xu, Y., Wang, B. et al. (2021). Development and properties of bacterial cellulose, curcumin, and chitosan composite biodegradable films for active packaging materials. *Carbohydrate Polymers*, 260: 117778.
20. Cazón, P., Velázquez, G. and Vázquez, M. (2019). Characterization of bacterial cellulose films combined with chitosan and polyvinyl alcohol:

Evaluation of mechanical and barrier properties. *Carbohydrate Polymers*, 216, 72-85.

21. Papadaki, A., Lappa, I.K., Manikas, A.C., Pastore Carbone, M.G., Natsia, A., Kachrimanidou, V. et al. (2024) Grafting bacterial cellulose nanowhiskers into whey protein/essential oil film composites: Effect on structure, essential oil release and antibacterial properties of films. *Food Hydrocolloids*, 147: 109374.
22. Nguyen, T.A. and Nguyen, X.C. (2022). Bacterial cellulose-based biofilm forming agent extracted from vietnamese nata-de-coco tree by ultrasonic vibration method: Structure and properties. *Journal of Chemistry*, 2022: 7502796.
23. Yanti, N.A., Ahmad, S.W., Ramadhan, L.O.A.N., Jamili, Muzuni, Walhidayah, T. et al. (2021). Properties and application of edible modified bacterial cellulose film based sago liquid waste as food packaging. *Polymers*, 13: 3570.
24. Azaza, Y. Ben, Hamdi, M., Charmette, C., van der lee, A., Jridi, M., Li, S. et al. (2023). Development and characterization of composite films based on chitosan and collagenous proteins from bluefin tuna: application for peeled shrimp preservation. *Cellulose*, 30: 373-395.
25. Lee, J.S., Lee, E. sil and Han, J. (2020). Enhancement of the water-resistance properties of an edible film prepared from mung bean starch via the incorporation of sunflower seed oil. *Scientific Reports*, 10: 1-15.
26. Mohamad, S., Abdullah, L.C., Jamari, S.S., Al Edrus, S.S.O., Aung, M.M. and Mohamad, S.F.S. (2022). Influence of drying method on the crystal structure and thermal property of oil palm frond juice-based bacterial cellulose. *Journal of Materials Science*, 57: 1462-1473.
27. Wang, X., Guo, C., Hao, W., Ullah, N., Chen, L., Li, Z. et al. (2018). Development and characterization of agar-based edible films reinforced with nano-bacterial cellulose. *International Journal of Biological Macromolecules*, 118: 722-730.
28. Rahmawati, M., Arief, M. and Satyantini, W.H. (2019). The effect of sorbitol addition on the characteristic of carrageenan edible film. *IOP Conference Series: Earth and Environmental Science*, 236: 12129.
29. Ghamari, M.A., Amiri, S., Rezazadeh-Bari, M. and Rezazad-Bari, L. (2022). Physical, mechanical, and antimicrobial properties of active edible film based on milk proteins incorporated with *Nigella sativa* essential oil. *Polymer Bulletin*, 79: 1097-1117.
30. Janik, W., Ledniowska, K., Nowotarski, M., Kudła, S., Knapczyk-Korczak, J., Stachewicz, U. et al. (2023). Chitosan-based films with alternative eco-friendly plasticizers: Preparation, physicochemical properties and stability. *Carbohydrate Polymers*, 301: 120277.
31. Pakoulev, A., Wang, Z. and Dlott, D.D. (2003). Vibrational relaxation and spectral evolution following ultrafast OH stretch excitation of water. *Chemical Physics Letters*, 371: 594-600.
32. Jia, Y., Wang, X., Huo, M., Zhai, X., Li, F. and Zhong, C. (2017). Preparation and characterization of a novel bacterial cellulose/chitosan bio-hydrogel. *Nanomaterials and Nanotechnology*, 7: 1-8.
33. Hasan, N.S.A., Mohamad, S., Mohamad, S.F.S., Arzmi, M.H. and Supian, N.N.I. (2023). Ex-situ development and characterization of composite film based on bacterial cellulose derived from oil palm frond juice and chitosan as food packaging. *Pertanika Journal of Science and Technology*, 31: 1173-1187.
34. Boey, J.Y., Lee, C.K. and Tay, G.S. (2022). Factors affecting mechanical properties of reinforced bioplastics: A review. *Polymers*, 14:183737.
35. Wang, B., Yang, D., Zhang, H.R., Huang, C., Xiong, L., Luo, J. et al. (2016). Preparation of esterified bacterial cellulose for improved mechanical properties and the microstructure of isotactic polypropylene/bacterial cellulose composites. *Polymers*, 8: 1-11.
36. Paudel, S., Regmi, S. and Janaswamy, S. (2023). Effect of glycerol and sorbitol on cellulose-based biodegradable films. *Food Packaging and Shelf Life*, 37: 101090.
37. Arief, M.D., Mubarak, A.S. and Pujiastuti, D.Y. (2021). The concentration of sorbitol on bioplastic cellulose based carrageenan waste on biodegradability and mechanical properties bioplastic. *IOP Conference Series: Earth and Environmental Science*, 679: 12013.

Malaysian Journal of Analytical Sciences (MJAS)
Published by Malaysian Analytical Sciences Society

GLYCEROL ACETYLATION INTO ACETINS OVER SnO_2-BASED BIMETALLIC OXIDE CATALYST

(Pengasetilan Gliserol kepada Asetin Menggunakan Mangkin Dwilogam Oksida Berasaskan SnO_2)

Ain Arisya Azami[1], Irmawati Ramli[1,2,3]*, Shera Farisya Mohamad Rasid[1,2], Muhammad Shamirul Khairul Lail[1], Mohd Rafein Zakaria[3], and Sarwat Iqbal[4]

[1]*Department of Chemistry, Faculty of Science, Universiti Putra Malaysia, 43400 UPM Serdang, Selangor, Malaysia*
[2]*Catalysis Science and Technology Research Centre (PutraCat), Faculty of Science, Universiti Putra Malaysia, 43400 UPM Serdang, Selangor, Malaysia*
[3]*Laboratory of Processing and Product Development, Institute of Plantation Studies, Universiti Putra Malaysia, 43400 UPM Serdang, Selangor, Malaysia*
[4]*Cardiff Catalysis Institute, School of Chemistry, Cardiff University, Main Building, Park Place, Cardiff CF10 3AT, United Kingdom*

**Corresponding author: irmawati@upm.edu.my*

Received: 12 October 2023; Accepted: 13 March 2024; Published: 29 June 2024

Abstract

Tin oxide-based bimetallic oxide catalysts, MO_x (MO_x = Al_2O_3, TiO_2, Y_2O_3) with a molar ratio of MO_x:SnO_2 of 1:1 was prepared by the solid-state method. X-ray diffraction (XRD) analysis showed that tin oxide, SnO_2, was present in all samples as a cassiterite phase with a tetragonal structure. The presence of other oxides, aluminum oxide (Al_2O_3), titanium oxide (TiO_2), yttrium oxide (Y_2O_3) in the respective Al_2O_3/SnO_2, TiO_2/SnO_2, Y_2O_3/SnO_2 were also identified and confirmed by X-ray fluorescence (XRF) analysis. A small exothermic peak at 480 °C and 750 °C in the differential thermal gravimetric (DTG) analysis revealed the oxidation of sub-oxide defects, took place which are very common in SnO_2-based samples. Further Fourier transform infrared spectroscopy (FTIR) analysis indicated the presence of Sn-O bonds, reflecting the abundance of tin-oxygen bonds in the materials. Acidity measurements by titration showed that both TiO_2/ SnO_2 and Y_2O_3/SnO_2 have the same acidity value of 0.23 mmol/g whereas Al_2O_3/SnO_2 and monoxide SnO_2 at 0.20 mmol/g. These catalysts were tested for the acetylation of glycerol to monoacetin (MA), diacetin (DA) and triacetin (TA) in a batch reactor at a molar ratio of glycerol: acetic acid of 1:6 w/v, a temperature of 100 °C, a reaction time of 2 h and a catalyst loading of 0.5 g. The tests showed complete conversion of glycerol by all catalysts, with the selective product being mainly MA, which was 64%, 62%, 57% and 43% for Al_2O_3/SnO_2, Y_2O_3/SnO_2, SnO_2 and TiO_2/SnO_2, respectively. The percentage selectivity of the more valuable products, DA + TA, was produced in the following order, TiO_2/SnO_2 > SnO_2 > Y_2O_3/SnO_2 > Al_2O_3/SnO_2 with 57%, 43%, 37%, and 35%, respectively. Further analysis of TiO_2/SnO_2 revealed that the catalyst not only had a high acidity, but also an increased BET surface area of 9.8 m^2/g compared to 8.6 m^2/g for SnO_2 when TiO_2 was incorporated into SnO_2. Analysis of the surface elements by energy dispersive X-ray spectroscopy (EDX) revealed a high surface oxygen content, which is consistent with the high acidity of the sample.

Keywords: glycerol acetylation, tin oxide, SnO_2-based bimetallic oxide, monoacetin, diacetin

Abstrak

Mangkin dwilogam oksida berasaskan timah oksida, MO_x (MO_x = Al_2O_3, TiO_2, Y_2O_3) dengan nisbah molar MO_x:SnO_2 pada 1:1 telah disediakan melalui kaedah keadaan pepejal. Analisis pembelauan sinar-X (XRD) menunjukkan timah oksida, SnO_2, hadir di dalam semua sampel sebagai fasa kasiterit dengan struktur tetragonal. Kehadiran oksida lain iaitu aluminum oksida (Al_2O_3), titanium oksida (TiO_2), itrium oksida (Y_2O_3) dalam Al_2O_3/SnO_2, TiO_2/SnO_2, Y_2O_3/SnO_2 masing-masing juga dikenal pasti dan disahkan oleh analisis pendarflor sinar-X (XRF). Puncak eksotermik kecil pada 480 °C dan 750 °C dalam analisis pembezaan gravimetrik terma (DTG) mendedahkan pengoksidaan kecacatan sub-oksida telah berlaku, iaitu kejadian yang biasa terjadi bagi sampel berasaskan SnO_2. Selanjutnya, analisis spektroskopi inframerah transformasi Fourier (FTIR) menunjukkan kehadiran ikatan Sn-O yang menterjemahkan limpahan ikatan timah-oksigen dalam bahan. Pengukuran keasidan secara penitratan menunjukkan kedua-dua TiO_2/SnO_2 dan Y_2O_3/SnO_2 mempunyai nilai keasidan yang sama iaitu 0.23 mmol/g, manakala Al_2O_3/SnO_2 dan monoksida SnO_2 pada 0.20 mmol/g. Semua mangkin telah diuji untuk pengasetilan gliserol kepada monoasetin (MA), diasetin (DA) dan triasetin (TA) dalam reaktor kelompok pada nisbah molar gliserol:asid asetik 1:6 b/i, suhu 100 °C, masa tindak balas 2 j dan muatan mangkin 0.5 g. Hasil ujian menunjukkan penukaran lengkap gliserol oleh semua mangkin, dengan pemilihan produk rata-ratanya MA iaitu 64%, 62%, 57% dan 43% bagi masing-masing Al_2O_3/SnO_2, Y_2O_3/SnO_2, SnO_2 dan TiO_2/SnO_2. Manakala penghasilan produk yang lebih bernilai iaitu DA + TA, adalah mengikut urutan $TiO_2/SnO_2 > SnO_2 > Y_2O_3/SnO_2 > Al_2O_3/SnO_2$ dengan masing-masing 57%, 43%, 37%, dan 35%. Analisis lanjutan terhadap TiO_2/SnO_2 mendedahkan bahawa mangkin ini bukan hanya mempunyai keasidan yang tinggi tetapi juga mempunyai peningkatan luas permukaan sebanyak 9.8 m^2/g berbanding 8.6 m^2/g bagi SnO_2, apabila TiO_2 digabungkan pada SnO_2. Analisis unsur permukaan oleh spektroskopi penyebaran tenaga sinar-X (EDX) menunjukkan kandungan oksigen permukaan yang tinggi, selaras dengan keasidan tinggi sampel berkenaan.

Kata kunci: pengasetilan gliserol, timah oksida, dwilogam oksida berasaskan SnO_2, monoasetin, diasetin

Introduction

Energy is a vital resource in the modern world and plays a role in a country's economic growth. With the world's population growing at an unprecedented rate, the demand for energy continues to rise. The transportation sector is the largest consumer of energy, with a growth rate of 1.5% per year [1]. Fossil fuels, which are non-renewable energy sources, account for about 90% of the transportation sector's energy consumption. The excessive use of fossil fuels has a significant impact on the environment, particularly in the form of greenhouse gas emissions and climate change. To reduce these impacts, the world is moving towards renewable energy sources such as wind, solar, hydro, geothermal and biodiesel, with the latter being the fastest growing industry.

In Malaysia, the 18 biodiesel plants in operation produced a total of 2.33 million tonnes of biodiesel in 2021 [2,3] and produced a total of 233,000 tonnes of glycerol as a by-product, i.e. about 10% for every tonne of biodiesel produced [3]. The biodiesel industry will continue to grow due to its renewability and reduction of CO_2 emissions compared to fossil fuels. Unfortunately, this also produces a considerable amount of glycerol, the limited use of which in the domestic industry will lead to waste disposal problems. Therefore, the catalytic conversion of glycerol into value-added products is an important issue for the sustainable production of biodiesel [4]. Currently, the acetylation of glycerol to acetins is the focus of interest, as acetins have multiple industrial applications, such as in cryogenics, cosmetics, as a fuel additive and as a raw material for biodegradable polyesters [5]. When glycerol reacts with an acetylating agent such as acetic acid or acetic anhydride, the reaction goes through a consecutive step. First, monoacetin (MA) is formed, which is later converted to diacetin (DA) and then to triacetin (TA), leading to a decrease in MA and an increase in DA and TA. This behavior was attributed to the protonation of the carbonyl oxygen atom of acetic acid and nucleophilic attack by glycerol to form an acylium ion intermediate on the surface of the catalyst, which favors subsequent nucleophilic attacks on the hydroxyl groups of glycerol. This requires a high density of acidic sites on the catalyst surface. Therefore, strongly acidic catalysts such as sulfuric acid, hydrofluoric acid and p-toluene sulfonic acid are used and have been shown to improve glycerol acetylation performance [6].

However, these acids are homogeneous catalysts, which leads to a difficult separation process and environmental problems in wastewater production [7]. Therefore, the development of an acidic solid catalyst for the acetylation of glycerol to acetins with excellent selectivity and high activity is highly desirable. Solid catalysts are attractive for this reaction because they can be easily separated from the reaction mixture, are reusable, and have the potential for higher catalytic

activity and selectivity. Solid catalysts are attractive for this reaction because they can be easily separated from the reaction mixture, are reusable, and have the potential for higher catalytic activity and selectivity. In addition, a solid catalyst can facilitate a chemical reaction by providing a surface for the reaction molecules to attach to and chemically convert into the desired product. Some common examples of solid catalysts are basic zeolites, alkaline earth metal oxides, hydrotalcites and carbon-based materials [25, 26].

The combination of metal oxides as acidic solid catalysts has shown great potential for the formation of bimetallic oxides, which have been reported for various reactions, such as Co_3O_4/SnO_2 [8] and TiO_2-ZrO_2 [9] in the acetalization of glycerol, Al_2O_3-ZrO_2 in the carboxylation of glycerol [10] and CaO-SnO_2 in the transesterification of soybean [12]. These metal oxides are cheap, abundant, effective and of great interest for heterogeneous catalysis due to their unique properties. As one of the leading tin producing countries in the world, Malaysia has diversified its tin industry away from mining and primary industries to manufacturing, services, and technology sectors. This diversification has reduced the country's reliance on tin exports. This work is therefore concerned with the research of tin oxide-based catalysts for the acetylation of glycerol, with the aim of improving their efficiency and selectivity while reducing their environmental impact. As mentioned earlier, the rationale behind this study is rooted in addressing the limitations of current strong acid catalysts which are effective but pose challenges in terms of separation processes and environmental concerns. At the same time, proper disposal of crude glycerol is imperative due to its salt, free fatty acids, and methanol content, which can contaminate soil and contribute to environmental problems. This underscores the significance of finding value-added uses for crude glycerol, particularly through the glycerol acetylation process. Several studies have shown that tin oxide is desirable as a stable and durable active site in heterogeneous catalysts [11, 12]. According to Xie and Zhao [12], the use of CaO-SnO_2 in the transesterification of soybean oil resulted in high generation of fatty acid methyl esters (FAME) with a yield of 83.9%, contributed by the acidic SnO_2, which improved the stability of the bimetallic oxide catalyst. Bewana et al. [8] concluded that the highest activity of Co_3O_4/SnO_2 (75:25) gave above 90% conversion of glycerol with 100% solketal selectivity. The catalyst was very stable and can be recycled for up to 6 cycles with little catalyst loss. Inspired by these works, a bimetallic oxide based on SnO_2 is synthesized by the solid-state method. Tin oxide is combined with metal oxide, MO_x = TiO_2, Al_2O_3, and Y_2O_3, in a molar ratio of MO_x:SnO_2 of 1:1. It has been reported that the MO_x used in this work exhibit high oxygen adsorption due to several oxygen vacancies. The acidic properties of these materials possess are utilized and employed in the acetylation of glycerol with acetic acid, as shown in Figure 1.

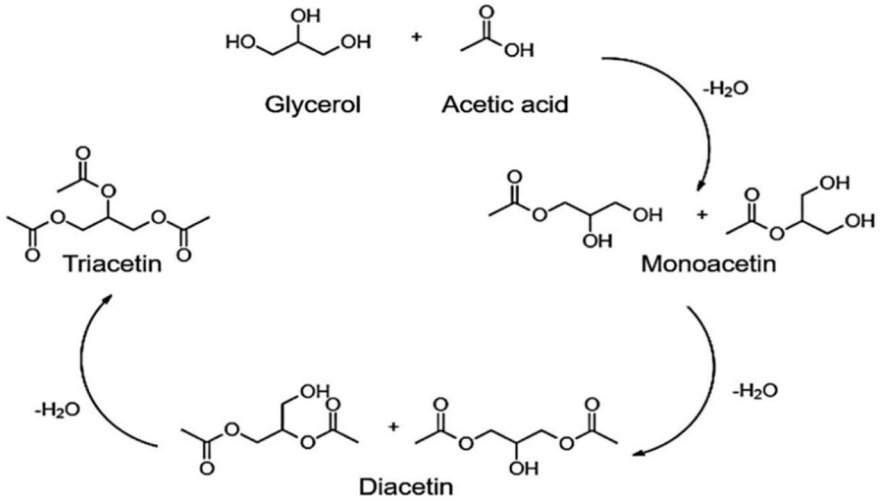

Figure 1. Acetylation of glycerol with acetic acid to produce monoacetin, diacetin, and triacetin

Materials and Methods

Materials

Anhydrous glycerol (99%), titanium dioxide, TiO_2 (98%), hydrochloric acid, HCl (99%), sodium hydroxide, NaOH (99%) and sodium chloride, NaCl (99.5%) were purchased from R&M Chemicals. Tin(IV) oxide, SnO_2 (99%), aluminum oxide, Al_2O_3 (99%), acetic acid, CH_3COOH (99.5%) and phenolphthalein (99%) were purchased from Systerm Chemicals. Yttrium oxide, Y_2O_3 (99.99%) was purchased from Sigma-Aldrich. All chemicals obtained were used without further purification.

Catalyst preparation

The SnO_2-based bimetallic oxide catalysts were synthesized through solid-state method [27]. A stoichiometric amount of TiO_2, SnO_2 in a 1:1 ratio was used. The measured chemical components were ground and well homogenized using a laboratory grade mortar and pestle. The grinding was maintained for a period of 30 minutes to allow proper intercalation of the Ti^{4+} and Sn^{4+} precursors. The precursor mixture was then calcined in a tubular furnace with a carbon dioxide flow at 400 °C for a duration of 2 hours at a heating rate of 5 °C /min. The calcined sample was named as TiO_2/SnO_2. The procedures for the solid-state synthesis of Al_2O_3 and Y_2O_3 with SnO_2 in a 1:1 ratio, respectively were repeated and the calcined samples were named Al_2O_3/SnO_2 and Y_2O_3/SnO_2. A monoxide SnO_2 was also prepared following the same procedures.

Catalyst characterisation

Thermal gravimetry analysis (TGA) and derivative thermogravimetry (DTG) were undertaken using Mettler Toledo 851e to determine the thermal stability of the synthesized catalysts. The sample was loaded into the sample pan and was heated from 50 to 900 ºC at a rate of 10 ºC min^{-1} under a continuous flow of nitrogen at 50 mL min^{-1}. The TGA provided information on absolute mass changes while the DTG focused on the rate of mass change as a function of temperature.

Fourier transform infrared spectroscopy (FTIR) spectra were obtained using a Perkin Elmer 1650 spectrometer. The sample was placed in the sample holder and inserted into the instrument with the spectroscopic range of 400 cm^{-1} to 4000 cm^{-1}. XRD measurements were obtained using a Shimadzu X-ray diffractometer model XRD 6000 using CuK_α radiation with a wavelength (λ) of 1.54 Å, scanning speed of 4º per minute, and operated at 30 kV and 15 mA. The patterns produced were compared to reference patterns supplied by the International Centre for Diffraction Data (ICDD).

Elemental composition and chemical compound analysis of the calcined SnO_2 and mixed oxide samples were conducted using Energy Dispersive X-ray Spectroscopy (EDX) attached to Scanning Electron Microscope (SEM) model JEOL, JSM6400 and using X-ray fluorescent (XRF), Shimadzu EDX-720, respectively. The surface morphology was delivered by the former analysis. Brunauer-Emmet-Teller (BET) surface areas were determined by N_2 absorption at -196 ºC using Thermo-Finnigan Sorptomatic 1990 series analyzer. Prior to the analysis, the sample was degassed at 150 ºC for 2 hours. The analysis was conducted at 5 different pressures along the isotherm before the results were converted to surface area measurements. While the Barret-Joyner-Halenda (BJH) method was used to calculate the pore volume and pore diameter of the samples from the desorption branch isotherm.

Acid titration

The necessary solutions were prepared in advance, with 0.1 M HCl prepared by diluting concentrated hydrochloric acid, HCl (99%) and 0.1 M NaOH prepared by diluting sodium hydroxide, NaOH (99 %). A phenolphthalein indicator solution was obtained by dissolving phenolphthalein powder in isopropanol. The catalyst powders, 0.1 g, were dispersed in a 20 ml NaOH solution, stirred for an hour, filtered, and the filtrate was added with phenolphthalein. The filtrate solution was then titrated with a HCl solution. Color change from pink to colorless was noted which signified the endpoint. These steps were repeated for three times for each catalyst to obtain average data.

Glycerol acetylation

The catalytic performance of the synthesized catalysts was carried out for the acetylation of glycerol to acetins in a laboratory batch reactor, as illustrated in Figure 2. The catalyst in powder form, 0.5g in weight, was introduced into a 250 mL round bottom flask. Glycerol and acetic acid (glycerol: acetic acid = 1:6 w/v) was carefully added and a magnetic bar was put into the mixture. A reflux condenser was fitted to the flask and

the flask was immersed in a silicon oil bath. The reaction was conducted at temperature of 100 °C for a duration of 2 hours under reflux conditions. The mixture was continuously stirred under a constant rate of 450 rpm. Upon completion of the reaction, the product was cooled down and subjected to centrifugation at 3000 rpm for 10 minutes. The catalyst was separated from the mixture using filter paper. To account for error bars and evaluate the statistical significance of the results, these procedures were repeated three times. The reaction products obtained were analyzed using gas chromatography coupled with a flame ionization detector (GC-FID) (Agilent 7890A), equipped with a DB Wax column (30 m × 0.25 mm ID × 0.25 µm). For internal standard and solvent, 1,3-butanediol and acetonitrile were utilized, respectively. A volume of approximately 1 µL of the final sample was injected into the column initially set at 80 °C for 3 minutes. Subsequently, the temperature was raised to 260 °C with a heating rate of 10 °C min^{-1}, and then at 300 °C, with a heating rate of 30 °C min^{-1}. The area of the peak was utilized for constructing the calibration curve and conducting quantification analysis. The total time required for GC-FID analysis was 22.3 minutes. Helium was employed as the carrier gas with a flow rate of 1.3 mL min^{-1}. The glycerol conversion and selectivity of MA, DA, and TA were calculated using the following equation.

$$\text{Glycerol conversion, \%} = \frac{Amount\ of\ glycerol\ converted}{Amount\ of\ glycerol\ fed}\ x\ 100 \quad (1)$$

$$\text{Selectivity, \%} = \frac{Amount\ of\ specific\ product\ formed}{Total\ amount\ of\ product\ formed}\ x\ 100 \quad (2)$$

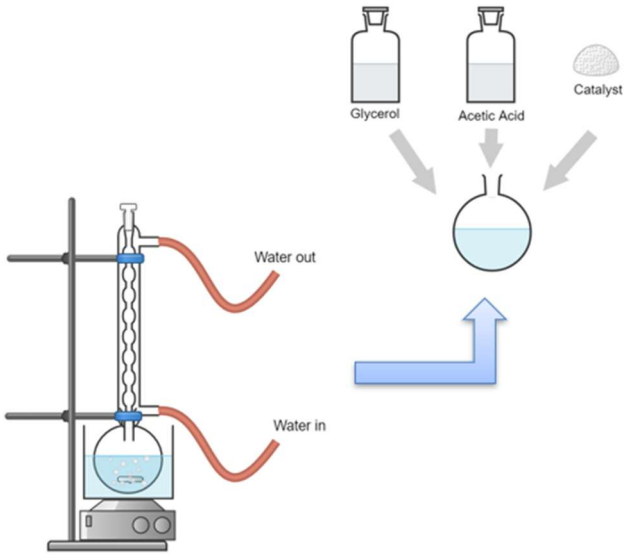

Figure 2. Experimental set up for glycerol acetylation process

Results and Discussion

The thermal properties of the mixed oxide catalysts, Al_2O_3/SnO_2, TiO_2/SnO_2, Y_2O_3/SnO_2 catalysts were investigated by thermogravimetric analysis and differential thermogravimetric analysis (TGA-DTG). The DTG is the derivative of the TGA curve and is displayed together with the TGA curve, Figure 3. The TGA weight loss from room temperature to 120 °C is likely due to the loss of adsorbed water molecules. A further loss of up to 400 °C could be due to the removal of hydroxyl groups (dehydroxylation) from the lattice [28]. These processes are accompanied by a weak endothermic peak on DTG profiles, with a maximum at 100 °C and 225 °C, respectively. It should be noted that the total loss due to bound and unbound water molecules was not recorded for all samples, except for Y_2O_3/SnO_2 and this was only for 0.25% [29]. The weight gain was observed in the TGA plot from 400 °C to 900 °C, with the differential thermogravimetric (DTG) curve revealing a small exothermic peak at about 480 °C and

750 °C. This phenomenon appears to be associated with the oxidation of sub-oxide defects. Oxygen defects are very common in SnO_2 due to oxygen vacancies where oxygen atoms are missing in the crystal lattice [13]. These vacancies can be caused by thermal treatment or by defects introduced during solid-state synthesis. These small exothermic peaks are accompanied by a small loss, 1%, corresponding to the removal of a certain amount of oxygen from the lattices, which leads to crystallization of the material [14].

The FTIR spectra of the SnO_2-based bimetallic oxides are displayed in Figure 4. The spectra of the mixed oxide showed no absorption band in the region of OH vibration (3000-4000 cm^{-1}), suggesting that the OH group could be removed during calcination at high temperature. A similar observation was made by Deshmukh and Kadam [15] who did not observe OH vibration in tin oxide treated with microwaves at high power. The SnO_2-based bimetallic oxides are typically a metal oxide compound consisting of tin (Sn), aluminum (Al), titanium (Ti), yttrium (Y) and oxygen (O) atoms in their respective mixtures. This observation confirms that these mixed oxides do not contain OH functional groups in their chemical structure, so there are no OH bonds to give rise to OH stretching or bending vibrations in the FTIR spectrum of SnO_2-based bimetallic oxides. An enlarged view of the FTIR spectra in the range of 400 to 700 cm^{-1} shows that the peaks at 610-630 cm^{-1} are due to the vibrations of the Sn-O terminal bonds and the peaks at 410-430 cm^{-1} are due to the vibrations of the O-Sn-O bridging bonds [14]. The well-defined absorption band indicates the presence of Sn-O bonds in the sample and reflects the abundance of tin-oxygen bonds in the materials. Nevertheless, the vibrations associated with Al-O, Ti-O and Y-O bonds should be observed in the FTIR spectra in the 400-700 cm^{-1} range, which are coincided with the vibrations of Sn-O.

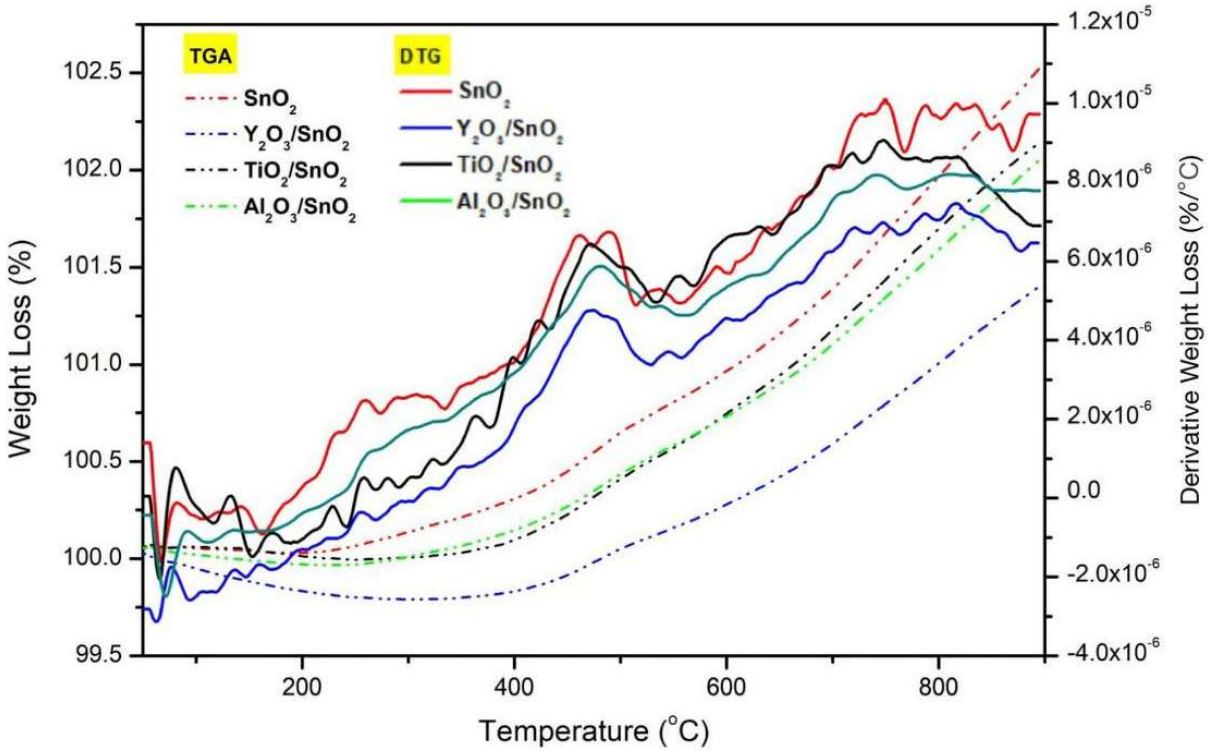

Figure 3. TGA-DTG curves for SnO_2-based bimetallic oxide catalysts

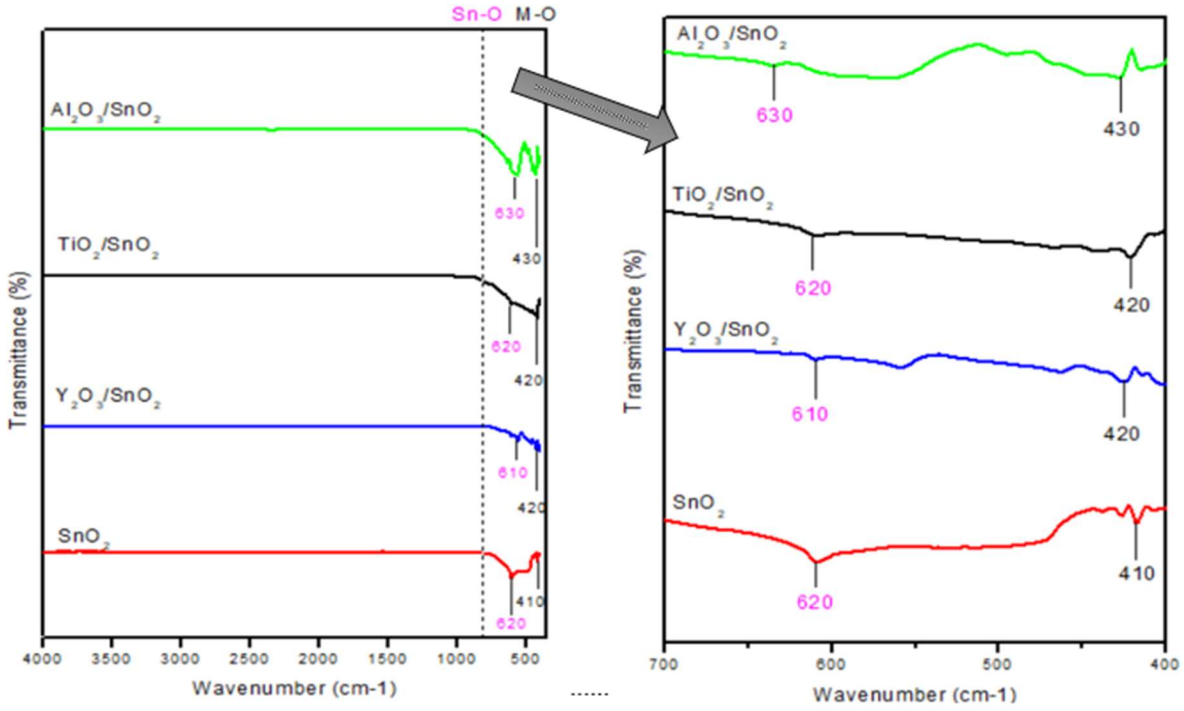

Figure 4. FTIR spectra of SnO_2-based bimetallic oxide catalysts.

The X-ray diffraction (XRD) patterns of the calcined catalysts are presented in Figure 5. For all materials, the main phase of tin oxide (SnO_2) cassiterite with a tetragonal structure was identified using ICDD file no. 98-010-5764, revealing distinct diffraction peaks at 2θ = 26.7°, 34.0°, 38.1°, 39.1°, 51.9°, 54.9°, 58.0°, 62.1°, 64.9°, 66.1°, 71.4°, and 78.9°. This indicates that the tin oxide species are present in all calcined catalysts and are in the form of a tetragonal phase, which is consistent with Bowles' report in 2021 [16]. The presence of other metal oxides, MO_x phases, Al_2O_3 (ICDD: 98-008-4608), TiO_2 anatase (ICDD: 98-004-0606), Y_2O_3 (ICDD: 98-003-5889), in the respective SnO_2-based bimetallic oxides was also detected. This is perhaps not surprising as the mixed oxide contains a stoichiometric amount of MOx and SnO_2 (MOx: SnO2 = 1:1). This is based on the preparation of the mixed oxide in the solid-state method, where one mole of MOx was mixed with one mole of SnO_2.

The apparent emergence of the sharp and intense peaks in all samples suggested that the obtained SnO_2-based mixed oxide was formed with a well-ordered crystal structure. A third phase of aluminium tin, $Al_{0.975}Sn_{0.025}$ (ICDD: 98-009-731), titanium tin oxide, $(Ti_{0.1}Sn_{0.9})O_2$ (ICDD: 98-005-7620) and yttrium stannide, YSn_2 (ICDD: 98-011-0094) was observed for all mixed oxide samples as Al_2O_3, TiO_2 and Y_2O_3 react with SnO_2 to form agglomerates of precipitates. Interestingly, a fourth phase, diyttrium distannate, $Y_2(Sn_2O_7)$ (ICDD: 98-003-9694) was observed in Y_2O_3/SnO_2. This is because the ionic radius of the ion Y^{3+} (93 pm) is larger than the ionic radius of the ion Sn^{4+} (71 pm). The ion Y^{3+} does not occupy the ion Sn^{4+} in the crystal lattice, instead Sn^{4+} tends to occupy the Y^{3+} site. As a result, the crystalline quality of the tin oxide was reduced. The opposite was true for TiO_2/SnO_2 and Al_2O_3/SnO_2, where both Al^{3+} (50 pm) and Ti^{4+} (61 pm) have a relatively smaller ionic radius than Sn^{4+}, which can be easily replaced the Sn^{4+} in the SnO_2 lattice. This substitution would disrupt the regular tin dioxide lattice. However, the composition of the resulting mixture depends on the extent of substitution and the ratio of TiO_2 and Al_2O_3 in the mixture. Since the substitution is limited (at a molar ratio of MOx: SnO_2 = 1:1), the regions of pure TiO_2 and Al_2O_3 are still present in the mixture, while the crystalline nature of SnO_2 has been preserved.

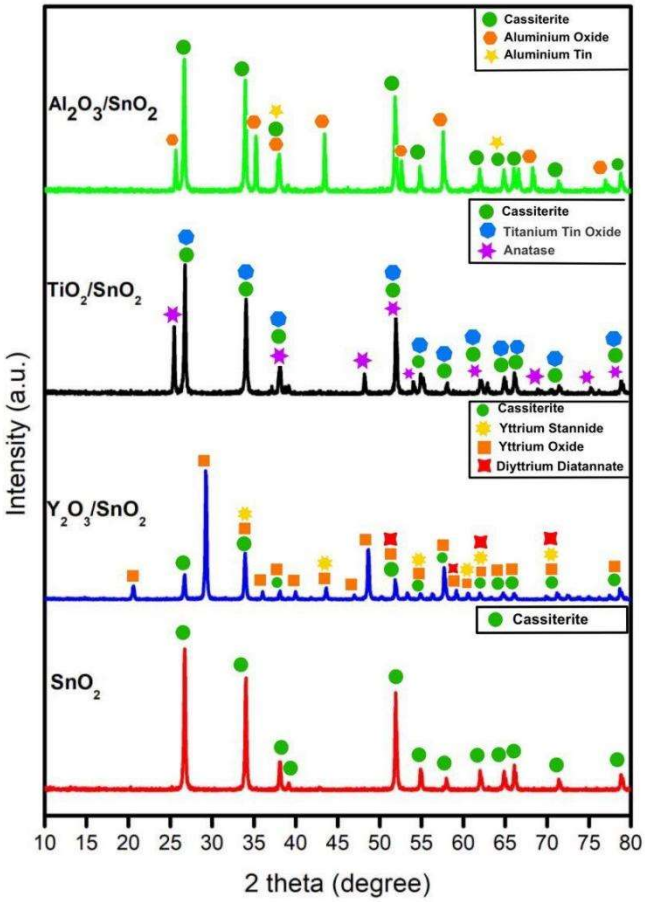

Figure 5. XRD profiles of SnO_2-based bimetallic oxide catalysts

XRF analysis was performed to determine the chemical composition of the catalysts. Table 1 shows the amount of metal oxide (MO_x) present in the catalyst samples in weight percent (wt.%). TiO_2/SnO_2 exhibits the chemical components of 47.8% TiO_2 and 51.4% SnO_2, which is closest to the 1:1 molar ratio. The Y_2O_3/SnO_2 has the lowest SnO_2 content (25.9 %) due to low occupation of the Y^{3+} crystal lattice by Sn^{4+}, which is consistent with the XRD analysis. The highest SnO_2 content (71.1%) is delivered by Al_2O_3/SnO_2, which is due to a larger SnO_2 occupation in the bimetallic oxide sample. The low weight percentage of Al_2O_3 in the Al_2O_3/SnO_2 mixture indicates that the substitution of Al_2O_3 into the SnO_2 lattice at a ratio of 1:1 may not be very efficient despite the smaller atomic radius of Al^{3+} compared to Sn^{4+}. This could be due to the different crystal structures of Al_2O_3 (hexagonal) and SnO_2 (rutile), which hinder the incorporation of Al_2O_3 into the SnO_2 lattice.

The acidity of the surface of the catalyst is a crucial factor affecting its activity. This acidity is attributed to the presence of Lewis acid sites on the surface of the metal oxide. The acid sites coordinate with electron-rich species of the carbonyl group of acetic acid and thereby activate it for the subsequent reaction with glycerol [34]. In this work, the acidic surface properties of the catalyst were investigated by titration after a displacement reaction. The attached free OH ions on the solid catalyst, previously dispersed in sodium hydroxide solution, were treated with acid to neutralize, and displace them from the surface by protonation. Table 1 shows the acidity measurements using the titration technique for SnO_2-based bimetallic oxide catalysts. The acidic sites are

associated with the surface tin cations [17] and the acidic character increases with the addition of MO_x = TiO_2 and Y_2O_3 (i.e. TiO_2/SnO_2 and Y_2O_3/SnO_2).

The SnO_2-based bimetallic oxide catalysts were investigated for the acetylation of glycerol to acetins. Figure 6 shows the catalytic performances of the prepared SnO_2-based bimetallic oxide catalysts expressed as glycerol conversion (GL) and selectivity to different acetins, namely monoacetin (MA), diacetin (DA), and triacetin (TA). As can be observed, after only 2 h of the process, all the glycerol present in the system was transformed to acetins, as 100% GL was achieved. This is not surprising, as it is known that the reaction of glycerol with acetic acid is an autocatalytic process that can convert glycerol to acetins even in the absence of a catalyst [18,19]. However, in the non-catalyzed process, the conversion rate of glycerol is low, about 9 % after 1 h of the reaction carried out at 80 °C [20]. Thus, in the presence of a catalyst, even a monoxide (SnO_2) showed a sufficient catalytic activity for glycerol conversion. The most important performance is the selectivity towards acetins, whereby during the 2 h reaction time at a temperature of 100 °C mainly a monosubstituted product, i.e. monoacetin (MA), was formed. The differences between the MA selectivity of SnO_2, Al_2O_3/SnO_2 and Y_2O_3/SnO_2 were not that significant. All these catalysts produced mainly MA (over 50%), and the selectivity for MA obtained after 2h of reaction time were 57%, 64% and 62%, respectively. For TiO_2/SnO_2, the selectivity to MA was lower compared to the other catalysts and was 43 %. While for the trisubstituted product (triacetin, TA) was formed in small amounts. SnO_2, Al_2O_3/SnO_2 and Y_2O_3/SnO_2 gave only about 1-2% TA selectivity. A study investigating the selectivity for substituted products at different reaction temperatures (80 °C and 110 °C) concluded that the higher reaction temperature (110 °C) promoted the formation of a mixture of products, with the conversion of MA to higher esters being significantly faster [21].

Table 1. XRF analysis and acidity measurements of SnO_2-based bimetallic oxide catalysts

Catalyst	Metal Oxide	Weight (wt.%)	Acidity (mmol/g)
TiO_2/ SnO_2	SnO_2	51.4	0.23
	TiO_2	47.8	
	Total	99.2	
Y_2O_3/SnO_2	SnO_2	25.9	0.23
	Y_2O_3	60.6	
	Total	86.5	
Al_2O_3/SnO_2	SnO_2	71.1	0.20
	Al_2O_3	27.8	
	Total	98.9	
SnO_2	SnO_2	98.0	0.20

In this work, TiO_2/SnO_2 showed the highest selectivity for TA at 8%, while the combined selectivity's for DA+TA showed that TiO_2/SnO_2 was the most active catalyst at 57%. TiO_2/SnO_2 provides an acidic site for activation of the carbonyl group of acetic acid, resulting in an acylium ion that is more susceptible to nucleophilic attack by the oxygen atom of the hydroxyl of glycerol [6, 18, 19]. Upon release of a water molecule, monoacetin (MA) is formed, which further reacts with acetic acid by a similar mechanism to form diacetin (DA) and triacetin (TA). The observed difference in selectivity for DA+TA between Y_2O_3/SnO_2 and TiO_2/SnO_2 catalysts, despite similar acidity (Table 1), could be due to differences in their acidic sites. Y_2O_3/SnO_2 may offer unique acidic sites that could influence the reaction pathways, exact mechanism, and effects on the formation of diacetin and triacetin compared to TiO_2/SnO_2.

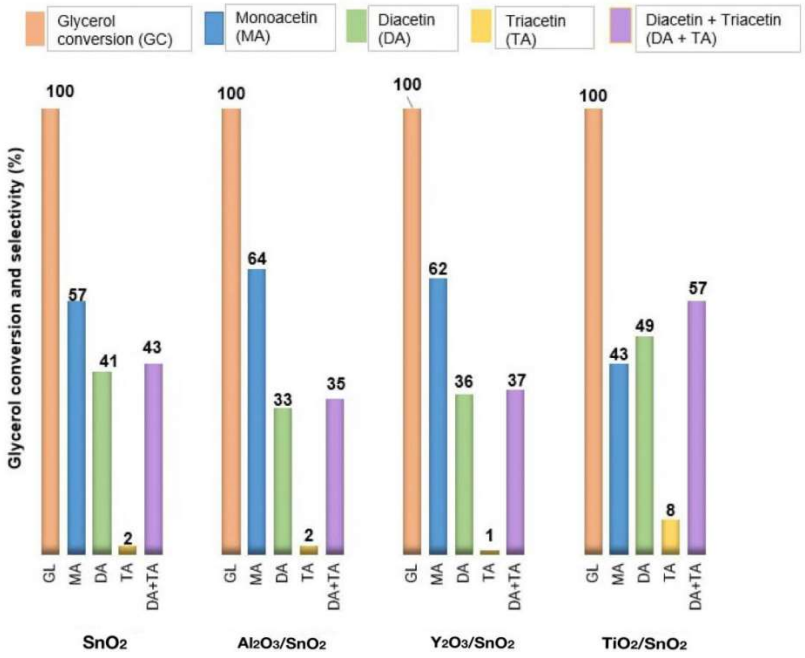

Figure 6. Glycerol conversion and product selectivity. Reaction conditions: glycerol to acetic acid molar ratio of 1:6, catalyst load 0.5 g, temperature 100 °C, time 2 h, and stirring rate 450 rpm. GL: Glycerol conversion, MA: monoacetin, DA: diacetin, TA: triacetin

The TiO_2/SnO_2 catalyst was further analyzed due to its promising catalytic activity in glycerol acetylation. The monometallic SnO_2 was also analyzed for comparison. Textural analysis of TiO_2/SnO_2 and SnO_2 by nitrogen adsorption-desorption showed a type IV isotherm (Figure 7 (a)), a typical feature of mesoporous materials, i.e. materials with a pore width between 2-50 nm [22]. The pore size distribution of both TiO_2/SnO_2 and SnO_2 is shown in Figure 7 (b). It is obvious that the pore size distribution of TiO_2/SnO_2 catalysts has a larger pore width compared to SnO_2 catalysts, while the pore volume of SnO_2 increases (Table 2). At the same time, TiO_2/SnO_2 shows a slightly higher BET surface area of 9.8 m^2/g compared to 8.6 m^2/g for SnO_2. Although the value of the changes is not significant, it shows that the addition of TiO_2 to SnO_2 affects its textural properties. Such a potent combination of suitable pore width and high acidity inherent in TiO_2/SnO_2 could enable more efficient selectivity of DA+TA in the glycerol acetylation process [35].

The morphology of TiO_2/SnO_2 was analysed with the SEM (see Figure 8). The catalyst exhibited a non-uniform particle shape similar to the morphology of the SnO_2 monoxide, indicating that the addition of TiO_2 did not affect the morphology of the tin oxide. Elemental analysis of the surface was performed using energy dispersive X-ray spectroscopy (EDX) and the analytical values are listed in Table 2. As can be seen in Figure 8, both TiO_2/SnO_2 and SnO_2 emit characteristic L-shell X-ray emission lines of tin, SnL. The atomic percentage of tin, calculated from the intensity of the SnL peaks relative to the other peaks, gave a value of 42.5 % Sn in SnO_2. This value decreased drastically for the mixed oxide TiO_2/SnO_2, with the heteroatom Sn accounting for 19.1 % and Ti for 12.7 %. The dominant atom in the bimetallic oxide was oxygen, based on the K-shell X-ray emission lines of oxygen, with a proportion of 66.3 %, which is higher than that of the monoxide SnO_2 at 56.1 %. These data demonstrate the efficiency of the solid-state mixture in increasing the surface oxygen in the bimetallic oxide. The immediate consequence of the high surface oxygen content was an increase in the surface acidity of the catalyst, which is consistent with the acidity measurement in Table 1. Therefore, TiO_2/SnO_2 provides a higher selectivity of DA + TA as it has a higher acidity that allows for a consecutive reaction of glycerol with acetic acid.

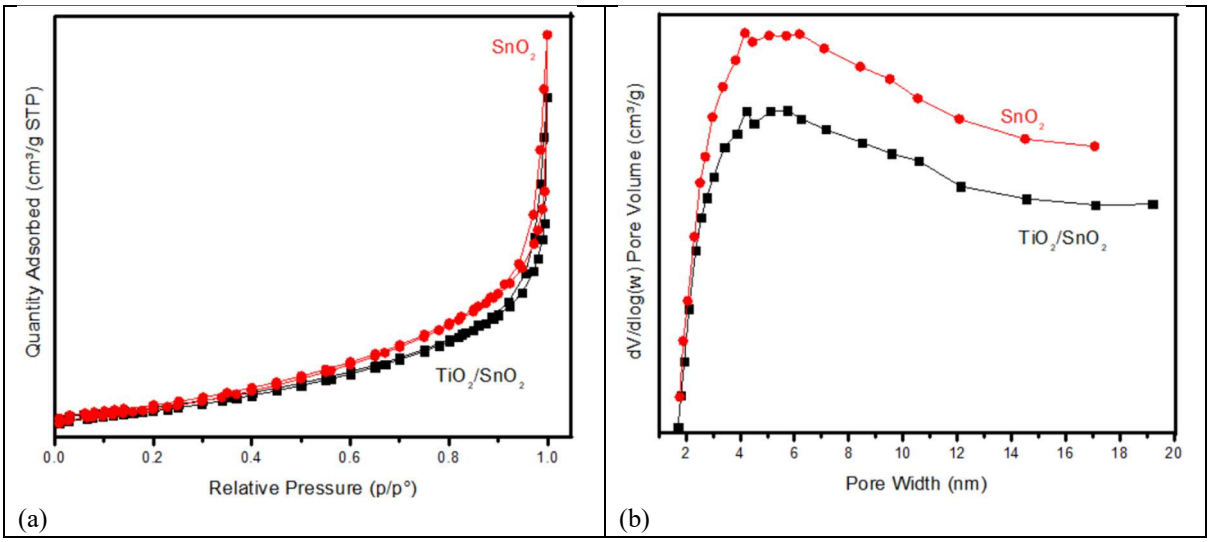

Figure 7. (a) N_2 adsorption–desorption isotherm and (b) pore size distributions of the synthesized TiO_2/SnO_2 and SnO_2 catalysts

Table 2. Textural and elemental analysis of SnO_2 and TiO_2/SnO_2 catalysts.

Catalyst	BET Surface Area ($m^2\ g^{-1}$)	Pore Volume (nm)	Pore Width (nm)	Element	Weight (%)	Atomic (%)
SnO_2	8.6	0.001829	4.9693	SnL	83.69	42.5
				OK	14.88	56.1
				Total	98.57	98.6
TiO_2/SnO_2	9.8	0.001783	5.0286	SnL	56.51	19.1
				OK	26.43	66.3
				TiK	15.14	12.7
				Total	98.08	98.1

SnL = Sn (Tin), OK = O (Oxygen), TiK = Ti (Titanium)

The catalytic activity of the TiO_2/SnO_2 catalyst was compared with a biomass-based catalyst (Biosolid) [5], (1Ag–10Cu-doped rice husk silica) [23], a mixed oxide-supported catalyst (MoO/TiO_2-ZrO_2) [24] and a zeolite catalyst (H-USY) [25] (Table 3). The summary shows that the reaction catalysed with TiO_2/SnO_2 gave better combined DA+TA production than other catalysts. In addition, the TiO_2/SnO_2 catalyst also yielded acetins at a lower reaction temperature (100 °C) than other catalysts, proving that the tin oxide-based catalyst promotes glycerol conversion and acetin selectivity. This is a very important result that should be highlighted as tin oxide is one of the most important minerals in Malaysia that has a high potential for use in the chemical industry

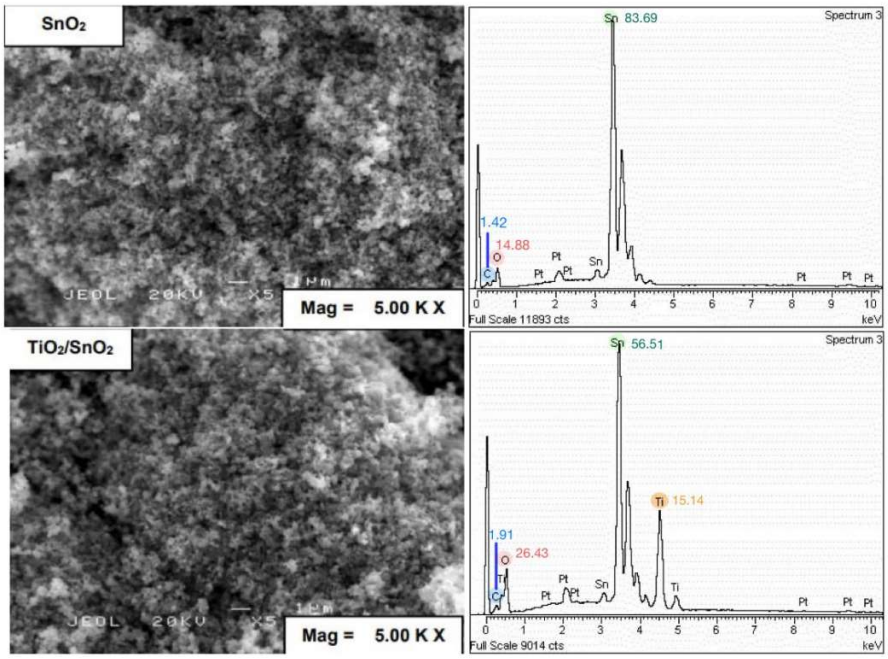

Figure 8. SEM image and EDX analysis of SnO_2 and TiO_2/SnO_2 catalysts. Carbon and platinum signals are attributed to the SEM carbon grid and platinum coating

Table 3. Comparison on glycerol acetylation into acetin

Catalyst	Reaction Parameters				GL (%)	Selectivity (%)				Reference
	T (ºC)	MR	CL	t (h)		MA	DA	TA	DA+TA	
TiO_2/SnO_2	100	1:6	10 wt.%	2	100	43	49	8	57	Present study
Biosolid	120	1:6	16 wt.%	2	100	47	48	6	54	[5]
1Ag–10Cu-doped rice husk silica	108	1:10	0.08 g	5	83.4	68.3	18.5	13.2	31.7	[23]
Zirconia-based: MoO/TiO_2-ZrO_2	120	1:6	5 wt.%	3	100	52	40	7	47	[24]
Zeolite-based: H-USY	110	1:9	-	4.5	78	74	21	6	27	[25]

GL = glycerol conversion, T = reaction temperature, MR = molar ratio glycerol: cetin, t = time, MA = monoacetin, DA = diacetin, TA = triacetin

Conclusion

Heterogeneous catalysts based on tin oxide, SnO_2, were investigated for the acetylation of glycerol acetylation with acetic acid to monoacetin (MA), diacetin (DA) and triacetin (TA). The catalyst was prepared by a solid-state method by adding metal oxide MO_x (MO_x = Al_2O_3, TiO_2, Y_2O_3) in a molar ratio of 1:1 to tin oxide. Monoxide SnO_2 was also prepared as a comparison. Remarkably, all catalysts used achieved complete conversion of glycerol, indicating their potential for acetylation reactions. However, glycerol was mainly converted to MA, as all catalysts showed. The selectivity towards DA and TA was rather low, except for TiO_2/ SnO_2, which showed a higher selectivity towards DA + TA (57 %) than other catalysts. Thus, TiO_2/ SnO_2 proves to be a compelling option for use as a heterogeneous

catalyst in glycerol acetylation. This innovative approach could effectively integrate tin oxide into the catalyst industry, increasing its versatility and value.

Acknowledgements

The authors deeply appreciate the Tin Industry (R&D) Board for providing the research funding (grant no 6300374). The Catalysis Science and Technology Research Centre (PutraCat) is also gratefully acknowledged.

References

1. International Energy Agency. (2023). Transport - Energy System. IEA. https://www.iea.org/energy-system/transport [Access online 20 April 2023].
2. Parveez, G.K.A., Kamil, N.N., Zawawi N.Z., Ong-Abdullah, M., Rasuddin R., Loh, S.K., Selvaduray, K.R., Hoong S.S., and Idris, Z. (2022). Oil palm economic performance in Malaysia and R&D progress in 2021. *Journal of Oil Palm Research*, 34(2): 185-218.
3. Armylisas, A.H.N., Hoong, S.S. and Tuan Ismail, T. (2023). Characterization of crude glycerol and glycerol pitch from palm-based residual biomass. *Biomass Conversion and Biorefinery*, 2023: 1-13.
4. Li, M., Alotaibi, M.K.H., Li, L., and Abomohra, A., (2022). Enhanced waste glycerol recycling by yeast for efficient biodiesel production: Towards waste biorefinery. *Biomass Bioenergy*, 159: 106410.
5. Bartoli, M., Zhu, C., Chae, M., and Bressler, D. C. (2019). Glycerol acetylation mediated by thermally hydrolysed biosolids-based material. *Catalysts*, 10(1): 5-19.
6. Nda-Umar, U.I., Ramli, I., Muhamad, E. N., Azri, N., Amadi, U. F., and Taufiq-Yap, Y. H. (2020). Influence of heterogeneous catalysts and reaction parameters on the acetylation of glycerol to acetin: A review. *Applied Sciences*, 10: 7155.
7. Shera Farisya, M. R., Irmawati, R., Shafizah, I. N., Taufiq-Yap, Y. H., Muhamad, E. N., Lee, S. L., and Salamun, N. (2021). Assessment on the effect of sulfuric acid concentration on physicochemical properties of sulfated-titania catalyst and glycerol acetylation performance. *Catalysts*, 11: 1542.
8. Bewana, S., Ndolomingo, M.J., Meijboom, R., Bingwa, N. (2021). Cobalt oxide promoted tin oxide catalysts for highly selective glycerol acetylation reaction. *Inorganic Chemistry Communications*, 128: 108578.
9. Sudarsanam, P., Mallesham, B., Prasad, A.N., Reddy, P.S., and Reddy, B.M. (2013). Synthesis of bio-additive fuels from acetalization of glycerol with benzaldehyde over molybdenum promoted green solid acid catalysts. *Fuel Processing Technology*, 106: 539-545.
10. Wang, D., Bai, D., Xiong, J., Chen, Z., Zhao, X., Wu, H., Shan, J., Wei, S., and Zhang, X. (2023). The atom-efficient production of glycerol carbonate via transesterification between dimethyl carbonate and glycerol over fluorinated Al_2O_3-ZrO_2 solid solution catalysts with suitable acidic-basic property. *Journal of Applied Catalysis A*: *General*, 665: 119370.
11. Safaripour, M., Saidi, M., Nodeh, H.R. (2023). Synthesis and application of barium tin oxide-reduced graphene oxide nanocomposite as a highly stable heterogeneous catalyst for the biodiesel production. *Journal of Renewable Energy*, 217: 119199.
12. Xie, W. and Zhao, L. (2013). Production of biodiesel by transesterification of soybean oil using calcium supported tin oxides as heterogeneous catalysts. *Energy Conversion and Management*, 76: 55-62.
13. Bhadane, M.S., Dahiwale, S.S., Sature, K.R.,Patil, B.J., Mandlik, N.T., Bhoraskar, V.N., Dhole, S.D. (2017). Synthesis and TSL properties of SnO_2:Eu nanophosphor for high gamma dosimetry. *Journal of Alloys and Compounds*, 695: 1918-1923.
14. Stefan, M., Leostean, C., Pana, O., Popa, A., Toloman, D., Macavei, S., Perhaita, I., Barbu-Tudoran, L., and Silipas, D. (2020). Interface tailoring of SnO_2-TiO_2 photocatalysts modified with anionic/cationic surfactants. *Journal of Material Sciences*, 55: 3279-3298.
15. Deshmukh, L. and Kadam, S.L. (2023). Effect of microwave annealing on tin oxide nanomaterials. *Materials Today: Proceedings*, 8:359.
16. Bowles, J.F.W. (2021). Encyclopedia of Geology. 2nd Edition. Academic Press, Colorado, USA: pp. 428- 441.
17. Lesafi, F.J., Pogrebnaya, T., and King'ondu, C.K. (2023). Mesoporous SnO_2-MoO_3 catalyst for diesel oxidative desulfurization: Impact of the SnO_2/MoO_3 ratio on catalytic efficiency. *Heliyon*, 9(8): 23-30.

18. Goscianska, J. and Malaika, A. (2019). A facile post-synthetic modification of ordered mesoporous carbon to get efficient catalysts for the formation of acetins. *Catalysis Today*, 357: 84-93.
19. Nda-Umar, U.I., Ramli, I., Muhamad, E.N., Taufiq-Yap, Y.H., and Azri, N. (2020). Synthesis and characterization of sulfonated carbon catalysts derived from biomass waste and its evaluation in glycerol acetylation. *Biomass Conversion and Biorefinery*, 12: 2045-2060.
20. Malaika A. and Kozlowski M. (2019). Glycerol conversion towards valuable fuel blending compounds with the assistance of SO_3H-functionalized carbon xerogels and spheres. *Fuel Processing Technology*, 184: 19- 26.
21. Malaika A., Mesjasz D., Kozlowski, M. (2023). Maximizing the selectivity to triacetin in glycerol acetylation through a plastic waste-derived carbon catalyst development and selection of a reaction unit. *Fuel,* 333(1): 126271.
22. Thommes, M., Kaneko, K., Neimark, A.V., Olivier, J.P., Rodriguez-Reinoso, F., Rouquerol, J., Sing, K.S.W. (2015). Physisorption of gases, with special reference to the evaluation of surface area and pore size distribution (IUPAC Technical Report). *Pure and Applied Chemistry*, 87(9-10): 1051-1069.
23. Ramalingam, R.J., T. Radhika, Adam, F., and Dolla, T.H. (2016). Acetylation of glycerol over bimetallic Ag–Cu doped rice husk silica based biomass catalyst for bio-fuel additives application. *International Journal of Industrial Chemistry*, 7: 187-194.
24. Abida, K., and Ali, A. (2022). A review on catalytic role of heterogeneous acidic catalysts during glycerol acetylation to yield acetins. *Journal of the Indian Chemical Society*, 99(1): 100459.
25. Hidayati, N., Sari, R. P., and Purnama, H. (2021). Catalysis of glycerol acetylation on solid acid catalyst: A review. *Jurnal Kimia Sains & Aplikasi*, 23(12): 414-423.
26. Ali, O. M., Mamat, R., Rasul, M. G., and Najafi, G. (2017). Chapter Eighteen - potential of biodiesel as fuel for diesel engine (M. G. Rasul, A. kalam Azad, & S. C. Sharma, Eds*.). Clean Energy for Sustainable Development Comparisons and Contrasts of New Approaches.* Academic Press: pp. 557-590.
27. Asiri, A.M., Adeosun, W.A., Khan, S.B., Alamry, K.A., Marwani, H.M., Zakeeruddin, S.M., Grätzel, M. (2022). Solid-state synthesis of $CdFe_2O_4$ binary catalyst for potential application in renewable hydrogen fuel generation, *Scientific Reports*, 22: 1632.
28. Stefan, M., Leostean, C., Pana, O., Popa, A., Toloman, D., Macavei, S., Perhaita, I., Barbu-Tudoran, L., Silipas, D. (2020). Interface tailoring of SnO_2-TiO_2 photocatalysts modified with anionic/cationic surfactants. *Journal of Materials Science*, 55: 3279-3298.
29. Bhadane, M. S., Dahiwale, S. S., Sature, K. R., Patil, B. J., Mandlik, N. T., Bhoraskar, V. N., and Dhole, S. D. (2017). Synthesis and TSL properties of SnO_2: Eu nanophosphor for high gamma dosimetry. *Journal of Alloys and Compounds,* 695: 1918-1923.
30. Künneth, C., Batra, R., Rossetti Jr, G. A., Ramprasad, R., and Kersch, A. (2019). Thermodynamics of phase stability and ferroelectricity from first principles. In Ferroelectricity in doped hafnium oxide: Materials, properties and devices.Woodhead Publishing: pp. 245-289.
31. Emmerich, K. (2010). Thermal analysis in the characterization and processing of industrial minerals. In G. E. Christidis (Ed.), Advances in the characterization of industrial minerals. European Mineralogical Union.
32. SciSpace - Question. (2023). Why does the intensity of the FTIR peak decrease due to the amount per unit volume? | 5 Answers from Research papers. https://typeset.io/questions/why-does-the-intensity-of-the-ftir-peak-decrease-due-to-the-26ei8ohjzr [Access online 6 January 2024]
33. Mufrodi, Z., Rochmadi, S., and Budiman, A. (2012). Chemical kinetics for synthesis of triacetin from biodiesel byproduct. *International Journal of Chemistry*, 4(2): 101.
34. Carr, R. T., Neurock, M., and Iglesia, E. (2011). Catalytic consequences of acid strength in the conversion of methanol to dimethyl ether. *Journal of Catalysis*, 278(1): 78-93.
35. Venkatesha, N. J., Bhat, Y. S., and Prakash, B. S. J. (2016). Volume accessibility of acid sites in modified montmorillonite and triacetin selectivity in acetylation of glycerol. *RSC Advances*, 6(51): 45819-45828.

Malaysian Journal of Analytical Sciences (MJAS)
Published by Malaysian Analytical Sciences Society

MICROPLASTIC POLLUTION IN MALAYSIA: STATUS AND CHALLENGES – A BRIEF OVERVIEW

(Pencemaran Mikroplastik di Malaysia: Status dan Cabaran – Suatu Tinjauan Ringkas)

Nurul Shahfiza Noor[1,2], Noorfatimah Yahaya[1,2], Nur Nadhirah Mohamad Zain[1,2], Nik Nur Syazni Nik Mohamed Kamal[1,2], Mohd Syahir Mansor[2,3], Mohd Yusmaidie Aziz[1,2], and Maisarah Nasution Waras[1,2*]

[1]*Department of Toxicology, Advanced Medical and Dental Institute (AMDI), Universiti Sains Malaysia, Bertam, 13200 Kepala Batas, Penang, Malaysia*
[2]*Advanced Management Liver Malignancies Research (Liver-ENRICH) Program, Advanced Medical and Dental Institute (AMDI), Universiti Sains Malaysia, Bertam, 13200 Kepala Batas, Penang, Malaysia*
[3]*Biomedical Imaging Department, Advanced Medical and Dental Institute (AMDI), Universiti Sains Malaysia, Bertam, 13200 Kepala Batas, Penang, Malaysia*

[*]*Corresponding author: maisarah.waras@usm.my*

Received: 3 April 2024; Accepted: 15 May 2024; Published: 29 June 2024

Abstract

Microplastics (MPs) are widespread and infiltrate the environment through unregulated use in diverse industrial processes such as the manufacturing of cleaning products, cosmetics, fertilizers, and pharmaceuticals, as well as from the degradation of larger plastic items. Due to this ubiquitous nature, combined with the fact that MPs possess the capacity for biomagnification within the food chain, MPs may constitute a major threat to human health. Hence, the scientific community and regulatory authorities are increasingly focusing their attention on this issue, leading to continuous developments in both legislation and the scientific literature concerning MPs. The review aims to provide an overview of the state-of-the-art occurrences of MPs, identification, detection, and quantification of MPs, degradation of MPs, and health effects of MPs from the perspective of Malaysia. A brief overview of the latest scientific research and recent developments on MPs (until the year 2024) will provide insights into the current understanding of MPs and their health implications. Furthermore, this review will serve as a valuable reference for further studies related to MPs in Malaysia and could help in informing future policy decisions.

Keywords: Microplastic, emerging contaminants, occurrence, analytical methods, degradation

Abstrak

Mikroplastik (MPs) adalah sebaran meluas dan meresap ke dalam alam sekitar melalui penggunaan yang tidak terkawal dalam pelbagai proses industri seperti pengilangan produk pembersihan, kosmetik, baja, dan farmaseutikal, serta daripada peluruhan bahan plastik yang lebih besar. Disebabkan sifatnya yang meluas ini, serta hakikat bahawa MPs mempunyai kapasiti untuk biomagnifikasi dalam rantaian makanan, MPs boleh menjadi ancaman besar kepada kesihatan manusia. Oleh itu, komuniti saintifik dan pihak berkuasa bagi pengawalan semakin memberi tumpuan kepada isu ini, yang membawa kepada perkembangan berterusan dalam perundangan dan literatur saintifik mengenai MPs. Tinjauan ini bertujuan untuk memberikan gambaran keseluruhan tentang kejadian MPs, pengenalpastian, pengesanan, dan pengukuran MPs, degradasi MPs, dan kesan kesihatan MPs dari perspektif Malaysia. Gambaran ringkas tentang penyelidikan saintifik terkini dan perkembangan terkini berkaitan dengan MPs (sehingga

tahun 2024) akan memberikan pemahaman semasa tentang MPs dan implikasinya kepada kesihatan. Selain itu, tinjauan ini boleh dijadikan sebagai rujukan yang berharga untuk kajian lanjutan berkaitan dengan MPs di Malaysia dan boleh membantu dalam membentuk keputusan dasar pada masa akan datang.

Kata kunci: mikroplastik, pencemar baharu, kemunculan, kaedah analisis, degradasi

Introduction

Microplastics (MPs) are scientifically defined as plastic fragments with sizes of less than 5 mm and are of different shapes, sizes, and polymer compositions [1]. MPs are further classified into two, which are primary and secondary MPs [2]. Primary MPs, including polyethylene (PE), polypropylene (PP), and polystyrene (PS) particles, are derived from many different sources [3], while secondary MPs originate through physical, chemical, and biological processes that lead to the breakdown of plastic debris [4, 5]. Researchers estimate that ten million metric tons of plastic waste and MPs enter the oceans every year and project that the total amount of plastic waste circulating the world's oceans will be 150 million tons by 2025 [6]. Malaysia has one of the largest plastic production industries globally comprising more than 1,300 plastic manufacturers. In 2016, Malaysia exported resin products with a total value of RM30 billion Malaysian Ringgits (RM) to plastic manufacturers worldwide [7]. The plastic industry in Malaysia is segmented into seven main sectors including agriculture, household products, packaging, construction, electronics, automotive, and others such as furniture and medical devices [7]. In Asia, the percentage of plastic in solid wastes generated in Malaysia ranks second after the Philippines [8]. In 2020, roughly 148,000 tons of plastic were used for food packaging in Malaysia [9]. Based on the Worldwide Fund (WWF) report, Malaysians are among the biggest per-capita plastic packaging users in South-East Asia and the region is responsible for more than half of the plastic litter in the world's oceans. It is reported too, that Malaysia produced 0.94 million tons of improperly disposed of plastic waste, of which 0.14 to 0.37 million tonnes may have potentially leaked into the ocean [10]. The country was thus, ranked the eighth-worst country responsible for mismanagement of plastic waste and third in the list of countries contributing most to marine plastic pollution [11].

MPs are ubiquitous, highly stable, have a long endurance, break up readily and have the potential to leach toxic plastic chemical additives. MPs can adsorb a variety of persistent organic environmental pollutants, thereby enhancing their bioavailability, toxicity, and dispersion [12, 13]. Then, it will eventually penetrate the food chain and might cause health problems such as endocrine disruption and gut inflammation when ingested by humans and other organisms [10, 14, 15]. Given the significant threat to posed by MPs pollution in Malaysia, this review aims to examine the updated status and challenges of MPs in Malaysia by discussing aspects such as MPs occurrence and distribution, uptake by aquatic organisms, degradation, effects on human health, and analytical methodologies for detection and analysis up to the year 2024. It is hoped that readers and researchers will benefit from this review by gaining a better understanding of MPs and by developing appropriate strategies for the management, mitigation, removal, and analysis of MPs.

Understanding MPs: Properties and Distribution

To effectively tackle this issue, a comprehensive understanding of MPs is crucial. This section will delve into the physical, chemical, and biological properties of MPs, exploring factors such as size, shape, polymer composition, and their potential for interaction with environmental pollutants. Following this, we will examine the abundance and distribution of MPs in Malaysia, focusing on data from various environmental compartments (e.g., rivers, coastal waters, and sediments).

Physical, chemical, and biological properties of MPs

Due to the degradation of MPs through processes such as oxidation, solar exposure, biofilm growth, and thermal aging [2], different physical properties of MPs have been reported [16, 17]. The degradation process breaks the particles into micro and nano-sized particles [17, 18], and facilitates their entry into living systems [19]. The shape of these polymeric particles plays a significant role in their interactions with biological systems in the aquatic environment. A study reported by Au et al. in 2015 [20] revealed that the toxic effect of polypropylene fibers on the amphipod *Hyalella azteca* was influenced by the particle shape. Additionally, the surface area of the MPs can be correlated to particle size. The alterations in the surface area of MPs particles are closely linked to their size, with surface ablation attributed to particle fragmentation [21]. Examples of shapes of MPs include microfibers, pellets, and fragments. The size can be whittled down by repeated filtration to provide the finest particles, the density can be from high to low density, colour can be varied, and

the fragmentation increases the surface area gradually.

In addition, MPs can exist in amorphous or semi-crystalline form [22]. The most common MPs polymer types found in the aquatic environment are polyethylene (25%), polyethylene terephthalate (16.5%), polyamide (12%), polypropylene (14%), polystyrene (8.5%), polyvinyl alcohol (6%), and polyvinyl chloride (2%) [15], [23], [24]. Polyethylene and polypropylene are semi-crystalline polymers, while polyvinyl chloride, polystyrene, and polyethylene terephthalate are amorphous polymers [21]. In general, plastic particles are resistant to microbial attack due to their high crystalline nature, thus posing challenges for the biodegradation process [25]. However, recent research has shown that various microorganisms, including bacteria and fungi, can contribute to the degradation of plastics [26, 27]. Other factors such as the soil conditions, the type of organisms involved, pre-treatment methods, polymer characteristics (e.g., mobility, toxicity, crystallinity, molecular weight, functional groups, substituents, and the presence of plasticizers or additives), as well as both biotic and abiotic conditions, are also vital factors in the biodegradation process [28].

Abundance and distribution of MPs in Malaysia

Examining the prevalence of microplastic pollution requires two-part approach where understanding both its abundance, which reflects the quantity of particles present, and its distribution, revealing the spatial extent and variability across various ecosystems. Learning the abundance and distribution of MPs is especially crucial for researchers to understand the sources and transportation pathways of these pollutants. Data of MPs abundance have yet to cover all waterway and terrestrial environments in Malaysia (Figure 1). However, the growing research is providing valuable insights. It is also important to note that the reported data are resulted from different methods and some studies reported the data with different unit.

As presented in Table 1, MPs are detected in estuarine, beaches, marine and freshwaters, coastal and offshore, agricultural soil, and air in various states of Malaysia. Sediments act as a sink for MPs, leading to higher concentrations compared to water. Therefore, many studies reported MPs abundance is higher in sediment than in surface water for Seberang Prai, Pulau Pinang and Setia Wetland, Terengganu (4000 pcs/kg and 5.97 items/g respectively). While in surface water, Seberang Prai was reported to have the highest abundance of MPs (1407 pcs/L) in Malaysia. MPs are detected higher in abundance in Seberang Prai than in Kuala Muda and Balik Pulau because of industrialization and urbanization intensity of the area. MPs have also been detected in agricultural soil in the Klang Valley, with concentrations ranging from 1.5-6.0 particles/kg. This suggests agricultural activities as a potential source of MPs pollution in soil [29]. Compared to other Asian countries, Malaysia has a lower MPs abundance in soil than China but higher than Bangladesh. Finally, only a few studies have measured MPs in Malaysian air, covering locations like Kuala Lumpur, Bangi, and Terengganu. Perlis was reported to have higher airborne MPs concentrations than Kuala Lumpur, possibly due to fewer buildings [30].

The scarcity of data, particularly regarding geographic coverage, restricts our complete understanding of the national picture of MPs pollution in Malaysia. While existing studies provide valuable insights, further research employing standardized methodologies is crucial. This research should encompass diverse environmental compartments (e.g., rivers, coastlines, remote areas) to obtain a more comprehensive understanding of MPs abundance and distribution. This information is essential for assessing the potential ecological and human health risks associated with MPs pollution in Malaysia.

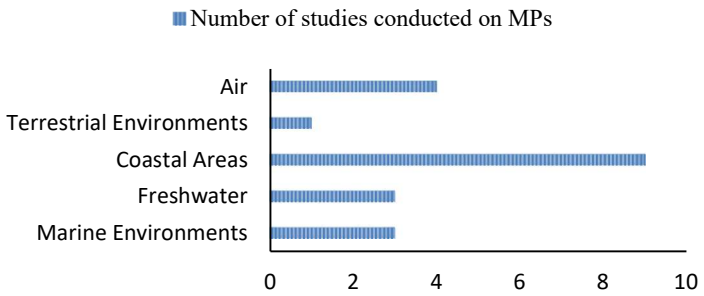

Figure 1. Number of studies conducted for abundance of MPs in Malaysia

Table 1. Abundance of MPs in Environmental Compartment in Malaysia

State	Location	Sample Type	Microplastics Concentration	Reference
Perlis	Timah Tasoh, Perlis	Air	983 ± 146 particles/m²/d	[30]
Pulau Pinang	Seberang Perai	Surface water	1407 ± 124.265 pcs/L	[31]
		Coastal bottom sediment	350 ± 25.892 pcs/kg	
		Estuarine sediment	4000 ± 29.174 pcs/kg	
	Penaga	Surface water	358 ± 50.991 pcs/L	
		Coastal bottom sediment	18.070 pcs/kg	
		Estuarine sediment	940 ± 15.773 pcs/kg	
	Balik Pulau	Surface water	273 ± 24.943 pcs/L	
		Coastal bottom sediment	255 ± 22.368 pcs/kg	
	Kuala Muda	Surface water	201 ± 21.214 pcs/L	
		Coastal bottom sediment	290 ± 24.505 pcs/kg	
		Estuarine sediment	430 ± 7.234 pcs/kg	
Selangor/Kuala Lumpur	Klang River estuary	Surface water	2.47 particles/L	[32]
	Langat River	Surface water	1464.8 items/L	[33]
	Sementa Man grove Area, Kapar	Sediment	-	[34]
	Bangi	Air	340 ± 30 MPs/m²/day	[35]
	Klang Valley	Soil	1.5–6.0 particles/kg	[29]
	Univerisit Teknologi Malaysia (Kuala Lumpur)	Air	97 - 775 particles/m² /day	[36]
Negeri Sembilan	Port Dickson	Surface water	4.65 particles/L	[37]
Johor	Skudai River	Surface water	360±60 particles/ per kg	[38]
	Tebrau River	Surface water	640±80 particles/ per kg	[38]
Pahang	Kuantan Port	Surface water	0.14–0.15 pcs/L	[39]
Kelantan	Kelantan Bay	Sediment	-	[40]
	Kelantan River	Surface water	179.6 items/L	[33]
Terengganu	Kuala Nerus	Surface water	0.13–0.69 pcs/L	[39]
	Terengganu estuary	Surface water	1687 particles/ m^{-3} and 1900 particles/ m^{-3} in estuary and offshore, respectively	[41]
	Sungai Dungun	Surface water	102.8 items/m^3	[42]
	Pulau Perhentian	Surface water	588.33 ± 111.77 items/L	[43]
	Pulau Redang	Surface water	314.67 ± 58.08 items/L	[43]
	Pulau Kapas	Surface water	359.8 ± 87.70 items/L	[43]

	Pulau Tenggol	Surface water	294.33 ± 101.64 items/L	[43]
	Setiu Wetland	Surface water	0.36 items/L	[44]
		Sediment	5.97 items/g	[44]
	Chagar Hutang	Air	274 ± 95 MPs/m^2/day	[35]
	Coastal area	Air	5476 ± 3796 MPs/m^2/ day	[45]
Sarawak	Miri River Estuary	Surface water	10.7 - 14.3 particles /L	[46]
		Sediment	283.7 - 456.2 particles/kg	[46]
	Miri Coast, NW Borneo	Sediment	83 - 327 particles/90g	[47]
	Pasir Pandak Beach	Sediment	60 - 328 items/m^2	
Sabah	Tanjung Aru Beach, Kota Kinabalu	Sediment	857 MPs/kg	[48]
	UMS ODEC Beach, Kota Kinabalu	Sediment	160 MPs/kg	[48]

Impacts of MPs Pollution

The presence of microplastics (MPs) in the environment poses significant threats to both aquatic ecosystems and human health. This section will explore the potential consequences of MPs pollution, focusing on two key areas, which are the uptake of aquatic organism and potential human health risks.

Uptake by aquatic organisms

Studies have shown that MPs have made their way into a range of organisms living in Malaysia's aquatic environments, including seafood. These minute plastic particles are ingested by organisms through both direct consumption and indirect trophic transfer mechanisms [1]. Planktonic creatures, larvae, invertebrates, and fish have all been found to have ingested MPs in Malaysian waters [1]. This alarming trend extends to commercial fish species in Malaysia, raising potential health risks for consumers [10].

The contamination of seafood with MPs poses significant threats to both food security and human health. Studies have revealed that commercially valuable fish and shellfish species are affected by MPs contamination [49]. For instance, an investigation discovered that 80% of sampled *Decapterus muroadsi* fish had ingested MPs resembling their natural prey, indicating a pathway for these particles to enter the human food chain. The presence of MPs in seafood is therefore a cause for concern regarding its potential health implications for consumers.

Beyond seafood, MPs have also been identified in other organisms inhabiting Malaysia's aquatic environments. A study in the Terengganu estuary and offshore waters of Malaysia detected MPs in seawater and zooplankton [41]. This widespread presence underscores the extensive contamination of MPs within Malaysia's marine ecosystem. Another study reported that marine species such as *Scapharca cornea*, cage cultured and wild *Lates calcarifer*, *Namalycastis sp*., and zooplankton have ingested MPs [50]. This suggests that MPs are found in Malaysia's aquatic environment and are being ingested by various wildlife species.

A study delved into the presence of MPs within commercially harvested marine fish off the northwestern coast of Malaysia's Peninsular region [51]. The study unveiled the presence of MPs in the digestive tracts of four distinct species of commercial marine fish: *Atule mate, Crenimugil seheli, Sardinella fimbriata*, and *Rastrelliger brachysoma*. This observation underscores

the potential risk of MPs infiltrating the human food chain through the consumption of contaminated fish. Another specific example of MPs ingestion by animals in Malaysia is the study conducted by Ratnam and Mohd Zanuri [52]. They found that blood cockles (*Tegillarca granosa*), a commonly consumed seafood in Malaysia, were contaminated with MPs in Kuala Juru, Pulau Pinang. This contamination poses a threat to seafood safety and potentially jeopardizes human health due to the potential toxicity of MPs.

Another study focused on the contamination of water bodies in Malaysia and its impact on marine organisms intended for human consumption [54]. The study found that commercial fish in seafood markets and abiotic sea products such as salts were contaminated with MPs. Marine organisms, including zooplankton, mussels, oysters, shrimp, and fish, were found to ingest MPs, further contributing to their presence in the human food chain. Efforts are underway to address the issue of MPs pollution in Malaysia. One study explored the possibility of polypropylene MPs degradation by bacteria isolated from Malaysian mangrove ecosystems [54]. Encouragingly, the study identified specific bacterial strains capable of breaking down polypropylene MPs, suggesting biodegradation as a potential remediation strategy.

The existence of MPs in seafood items presents challenges when assessing their health effects. The proportion of fiber-type MPs varies among different food items, and there are disparities between MPs levels in food and the adverse outcomes observed in animal studies [55]. Therefore, further research is imperative to gain a more comprehensive understanding of the potential health risks associated with consuming MPs in seafood [51, 59].

Effects of MPs exposure to human health

The potential health risks associated with MPs exposure in human is still under investigations. However, existing research suggested several possible pathways of exposure and potential health effects relevant to Malaysia. The primary route suggested is ingestion, often through the consumption of seafood as suggested earlier. Inadequate wastewater treatment facilities may also contribute to MPs contamination in drinking water (ingestion route) [56]. Exposure through inhalation route can occur when airborne MPs are respired, and dermal exposure is possible through personal care products and clothing containing MPs. The findings from cellular and animal experiments have demonstrated that MPs can impact various systems within the human body, including the digestive, respiratory, endocrine, reproductive, immune, and nervous systems.

Initially, when MPs are ingested, they can affect the digestive system, which may result in inflammation and subsequent gastrointestinal symptoms. These symptoms include abdominal pain, bloating, and alterations in bowel habits. MPs can also disrupt the balance of beneficial and harmful bacteria in the intestinal microbiome, contributing to gastrointestinal symptoms [57, 58]. Furthermore, MPs can serve as carriers for environmental toxic substances, such as bisphenol A (BPA), which can be absorbed into the body and cause health issues related to the endocrine and reproductive systems. Recent research even detected MPs in the placentas of pregnant women, emphasizing the need for further study on potential adverse effects [59].

In addition to their physical effects on the digestive system, MPs can also cause chemical toxicity by absorbing and accumulating environmental toxins such as heavy metals and polycyclic aromatic hydrocarbons [60]. These toxins can enter the body when MPs are ingested, leading to various gastrointestinal symptoms like nausea, vomiting, and abdominal pain. Both in vitro experiments with human cells and *in vivo* data from mice suggest that MPs can elicit adverse health effects, primarily through mechanisms involving inflammation, oxidative stress (resulting in increased production of reactive oxygen species), disturbances in lipid metabolism, gut microbiota imbalances, and neurotoxicity. For instance, exposure to certain MPs has been shown to increase the expression of inflammatory genes like Interleukin 6 (IL-6) and interleukin 8 (IL-8) in human cells [61]. Animal experiments have shown that MPs can disturb lipid metabolism in the liver, increase oxidative stress, affect acetylcholine esterase activity, and finally lead to intestinal microbiota

imbalances. Furthermore, exposure to MPs can exacerbate lipid-metabolism disturbances and inflammatory responses, especially in diabetic mice [62].

Concerning the immune system, accumulated exposure to MPs has been observed to induce chronic inflammation and homeostasis changes in animal experiments [63]. In addition, studies involving human lung cells have shown that MPs can activate innate immunity by regulating the expression of genes and proteins involved in the immune response [61]. Further research is required to fully understand the negative effects of MPs on the human immune system. Regarding the respiratory system, inhalation of MPs can lead to oxidative stress in the airways and lungs, resulting in respiratory symptoms such as coughing, sneezing, shortness of breath, and fatigue. Recent research has even linked nano-sized plastics to mitochondrial damage in human respiratory cells [64]. Finally, there is neurotoxicity induced by MPs has been reported in animal experiments, with findings showing that exposure to MPs can accumulate in the central nervous system, causing microglia activation and neuron damage [65]. This can lead to cognitive dysfunction, locomotor function changes and altered anticholinesterase activity in animals.

In conclusion, MPs have the potential to affect numerous systems in the human body. Even though many of the studies have been conducted on animals, further research is required to completely understand the degree of their effects and the mechanisms involved in humans. A complete understanding of these hazards and their long-term implications is still developing.

Analytical methodologies for determination of MPs

Effectively addressing MPs pollution requires reliable methods for their detection and analysis. This section will explore the various analytical methodologies currently employed to determine the presence and abundance of MPs in the environmental compartment, aquatic animal, and consumer products in Malaysia. Generally, the experimental design of MPs detection usually comprises of sample collection, sample preparation, sorting (physical characterization) and chemical characterization (Figure 2).

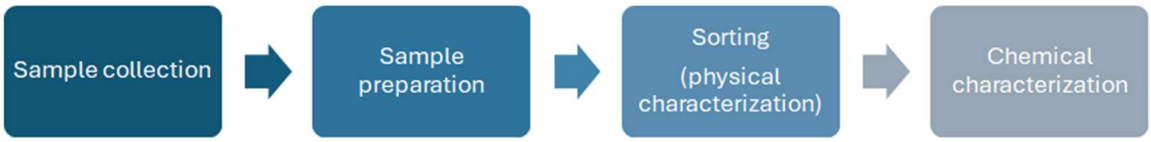

Figure 2. The general flow of MPs particles analysis

Sample collection

The technique to collect sample for MPs analysis in Malaysia depends on the type of sample itself and the purpose of the analysis (Table 2). For environment sample like marine water and sediment, the purpose was mostly to characterize and quantify the abundance of MPs particles in the environment or area selected. For instance, to quantify the extent of MPs in mangrove forest in Selangor, triplicate samples of sediment were collected from the surface of soil until 5 cm depth based on 50 cm x 50 cm quadrant [34]. Sampling quadrant was also adapted for sediment sample collection in Kota Kinabalu [48] and Pasir Pandak Beach [66]. For atmospheric MPs deposition, sample collection applied passive sampling technique[30, 45].

MPs are prevalent in marine environments and have been reported in commercial marine fish and other aquatic organism worldwide. For aquatic organism sample, like, bivalve or fishes, the purpose of the study is to investigate the digestion of those animals of the MPs particles polluted in the sampling area. Sample collection will either from the local area/market [67, 68, 69] or random collection by hand [70]. Processing of those animals will be dissection to obtain the guts, gills, and tissue. Sometimes, the whole organism was processed for the analysis of MPs particles itself. To analyse MPs particles in items like bottled water, fish meal products and personal products, these products were sourced from local market [71-74].

Table 2. Sample collection for different matrices in MPs particle analysis in Malaysia

Matrix	Sample Collection and Process
Surface water	Collection using stainless steel bucket and sampler [39, 46]
	Collection using water grab sampler [40]
Sediment	Collection using shovel [34]
	Collection using box corer [38]
	Collection using Ekman Grab sampler [40, 46]
	Collection using scoop [48]
Fishes	Caught at coordinated location [75]
	Purchases from local market [68]
Zooplankton	Collection by water pump [41]
Bivalve	Handpicked during low tide [70]
Sea cucumber	Random collection [76]
Products (dried fish, salt, canned sardine, bottled water, and fish meal product)	Purchased from Malaysian market [73, 74, 77, 78]
Human colectomy	Collection from patients who are scheduled to do colectomy. Specimen harvested after surgery [79]
Polychaete worm	Collection by hand [80]
Atmospheric deposition (air)	Collection through passive sampling in 24 h using a glass petri dish containing a glass microfibre filter paper [30, 45]

Sample preparation

After collection, the preparation of samples involves extraction of MPs from the sample matrices. Extraction of MPs includes manual sorting, density separation, filtration, and digestion method. Digestion process using acid or enzyme is needed for organic materials to dissolve. Digestion process is applied for matrices like fish, polychaete worm, and canned and dried fish. After digestion, some environment matrices apply density separation in sorting out the MPs particles. Density separation is applied through salt addition like sodium chloride (NaCl) or sodium iodide (NaI) or zinc chloride ($ZnCl_2$) [81]. Then, particles will be filtered by sieving through size exclusion or membrane filter. Filtered and separated MPs particles will be then characterized by physical and chemical characteristics.

Sorting (physical characterization)

After extraction, the isolated MPs are set for characterization to determine the particle size, shape, colour, surface texture and other characteristics to discriminate MPs from other particles (physical characterization). Then, this process is usually followed by identification of chemical composition such as the functional groups, molecular weight and structure, and degree of polymerization of polymers in MPs [82].

The goal of physical characterization is to do preliminary analysis to determine shape, size, and morphology of MPs collected [83]. In other words, the filtered MPs particles will be screened and distinguished from non-plastic before chemical characterization. Some main physical characterization techniques are visual inspection, laser diffraction particle size analysis and dynamic light scattering. For MPs analysis in Malaysia in this paper, the methods employed for physical characterization are visual analysis (Table 3). Visual analysis technique in physical characterization is applied for most type of samples such as environment (sediment and water), animals, (fishes and bivalve) and products (canned food, packed food, and bottled water) and personal products. The process of visual analysis consists of observing the MPs particles with naked eyes or with microscopes. Then, the particles will be classified and counted based on the shape, colour, and size [83]. Analysis with naked eyes only applies for greater size range of MPs particles (1-5 mm). On the other hand, microscope images that can provide the shape and the quantity of MPs particles. This technique

was seen used on MPs analysis 1-5 μm in size for all samples in Table 2. On the other hand, those MPs particles that are lacking distinct colours and shapes are sorted using SEM. In studies analysing MPs in dried fish, canned sardines, marine fishes, and human colectomy specimens [79], SEM was combined with EDX. This common approach provides elemental analysis, enabling the differentiation of inorganic MPs particles.

Chemical characterization

Determination of the composition of the detected and extracted MPs is crucial to assist the establishment of the methods for treating MPs pollution [84]. For MPs analyses in Malaysia, Fourier transform infrared spectroscopy (FTIR), Raman spectroscopy, and thermal analysis (Table 3).

Fourier transform infrared spectroscopy

Fourier transform infrared spectroscopy (FTIR) provides information about the functional groups present for MPs that are more than 20 μm in size [81]. It obtains chemical information of chemical bonds and functional group of samples through vibrational spectroscopy technique. FTIR is a non-invasive analysis that requires simple sample pre-treatment process. Also, it is also less vulnerable to interference from autofluorescence originating from plastic additives components [82]. Currently, FTIR is widely used for chemical characteristics of MPs analysis in Malaysia.

There are three analysis techniques of FTIR which are specular reflection, transmission and attenuated total reflection (ATR). The selection of the right techniques depends on the properties of the sample. ATR mode, for example, will be selected for samples that are thick or strong infra-red (IR) absorbent. MPs have been identified and characterized by ATR- FTIR for marine water [39], sediment samples [34, 39, 46, 66, 85] and personal products collected in Selangor [71]. Micro-FTIR is also growing technique in Malaysia for analysing MPs as small as 10 μm. Researchers have used it to study MPs not only in deposited atmospheric dusts, but also in human tissue samples (from colon surgery) and in zooplankton samples.

Raman spectroscopy

Raman spectroscopy is one of the widely used methods for identifying chemical composition of MPs. It works by analysing the frequency shift of light scattered from a sample due to the Raman effect. The frequency shift can determine the sample's vibrational modes and identify the chemical substances present. Raman spectroscopy is widely accepted for its many advantages including minimal sample damage, requirement of small sample sizes, potential for high throughput screening, and environmental friendliness (as reported by Huang et al. [82]).

In contrast to FTIR, Raman spectroscopy faces limitations when it comes to detecting for samples with fluorescence [82] . Besides, the Raman spectra generated by plastic additive within MPs and contaminants adhering to the particle surfaces may overlap with the Raman spectra of the plastic polymers itself. This interferes the function of Raman spectroscopy in identification of the MPs. A. Karami et al. [67] developed a time effective and low-cost protocol for sample preparation of MPs analysis in fish while protecting the integrity of the plastic polymers. Raman spectroscopy has been shown to be a reliable technique to identify MPs in dried fish, salt, and tropical shark species [68, 77, 86]. Raman spectroscopy can detect MPs greater than 10 μm in size, whereas micro-Raman spectroscopy offers higher resolutions, enabling detection up to 1 μm [83]. A. Karami et al. has successfully used micro-Raman to detect MPs in canned sardine and sprat products with size ranging from 190 to 3800 μm. Karbalei et al. detected MPs in commercial fish meal with particle size from 149-7800 μm [73].

Thermal analysis

Thermal analysis is a technique to study the functional change of temperature and time of a material [82]. Pyrolysis-GCMS (Py-GC/MS) is one of the classical methods for thermal analysis that was used for analysis of MPs in Polychaete worms in Setiu Wetlands [80]. Analysis with Py-GC/MS using a selective ion monitoring mode detected pyrolytic products and fragment ions associated with various polymers, including polyvinyl chloride, polypropylene, polyethylene, polyethylene terephthalate, polyamide,

and polymethylmethacrylate. The study demonstrated the valuable application of Py-GC/MS techniques for monitoring MPs, especially when dealing with analytical sample in large quantities. Usage of Py-GCMS must be complemented with optical techniques due to its inability to determine the number and other physical characteristic of the MPs extracted.

While the current analytical methods offer valuable insights, advancements in MPs analysis are constantly evolving. These advancements hold great promise for improving our understanding of MPs pollution in Malaysia. Currently, visual counting is a common method for quantifying MPs. However, this technique can be time-consuming and prone to human error. Emerging techniques, such as flow cytometry and microfluidics, offer the potential for automated, high-throughput analysis, allowing for more accurate quantification of MPs abundance in environmental samples [87, 88]. At the same time, there is a crucial need to identify the source of the MPs pollution for understanding their pathways into the environment and to develop effective mitigation plan. Advanced spectroscopic techniques, such as Raman spectroscopy coupled with multivariate analysis, can potentially be used to fingerprint the specific types of plastic present in MPs [89]. This information can help to identify the sources of plastic pollution, such as specific industries or consumer products.

As MPs research in Malaysia continues to grow, it is essential to establish standardized protocols for sample collection, preparation, and analysis across different research groups, as previously emphasized. This standardization will ensure data consistency and facilitate comparisons between studies conducted in various locations and by different researchers.

In conclusion, the analytical methods employed in Malaysia provide valuable insights into the presence and abundance of MPs in the environment. However, continuous advancements in MPs analysis offer exciting possibilities for the future. Techniques like flow cytometry and microfluidics hold promise for more accurate and automated MPs quantification, while advanced spectroscopy with chemometrics can help pinpoint the sources of plastic pollution. Moving forward, efforts to standardize sampling and analysis protocols across research groups in Malaysia are crucial for strengthening the nation's expertise in MPs analysis. By embracing these advancements and fostering a collaborative research environment, Malaysia can become a leader in tackling the challenge of MPs pollution.

Current challenges and data gaps

A report published by Minister of Science, Technology and Innovation (MOSTI) has revealed a roadmap plan to achieve towards zero single-use plastics in 2030 [7]. This plan highlighted the significant challenges hindering Malaysia’s efforts to achieve zero single-plastic use by 2030. These challenges include:

a) Limited public awareness: Many Malaysians lack sufficient knowledge about the environmental impact of single-use plastics and the benefits of alternatives.
b) Low recycling rate: The current recycling infrastructure struggles to handle the volume of plastic waste generated, leading to improper disposal and environmental pollution.
c) Cost factor: Biodegradable alternatives to single-use plastics are often more expensive, making it difficult for consumers and businesses to adopt them readily.
d) Enforcement difficulties: Effectively enforcing regulations against single-use plastics can be challenging due to limited resources and monitoring capabilities.
e) Waste management needs: Improvements are needed throughout the plastic waste management system, from collection and sorting to recycling and treatment facilities.

While these challenges are well-defined, several critical data gaps hinder the development of the targeted solutions. Table 4 described some of the data gaps that need to be addressed.

Table 3. Summary of common methods used in extraction, physical and chemical characterization of MPs

Matrix	Extraction Method	Physical Characterization Method	Analytical Instrument	References
Sediment	Density separation	SEM, spectroscopy, microscopy	FTIR, ATR-FTIR, μ-FTIR	[38, 46, 48]
Water	Filtration	SEM, microscopy	FTIR, ATR- FTIR, μ-FTIR	[33, 39, 42, 43]
Soil	Density separation followed by filtration	Microscope	FTIR	[29]
Air	Filtration	Stereomicroscope, selective fluorescent staining using Nile Red	μ-FTIR, ATR-FTIR	[35, 45]
Biota (tissues)	Digestion (chemical or enzymatic) followed by filtration	SEM, Stereomicroscope, FESEM-EDX	FTIR, μ-Raman spectroscopy, μ-FTIR, ATR-FTIR	[68, 69, 70]

Abbreviations: *FTIR=Fourier Transform Infrared Spectroscopy; μ-FTIR=Micro-FTIR; ATR-FTIR= Attenuated total reflectance-FTIR; FESEM-EDX=Field Emission Scanning Electron Microscopy-Energy Dispersive X-ray Spectroscopy; SEM=Scanning Electron Microscope*

Table 4. Data gap in MPs pollution in Malaysia

Area of Data Need	Specific Data Need	Importance for Addressing MPs Pollution
Sources of MPs pollution	Types and quantities of MPs from various industries	To identify major contributors of MPs to the environment
Distribution of MPs	Research on MPs abundance in rivers, coastal waters, and offshore environments throughout Malaysia should continue to cover the rest of the area which are not covered	To understand the spread and accumulation of MPs in different environments.
	Research on atmospheric MPs deposition should be further conducted	To understand the spread and accumulation of MPs in different environments
Impacts of MPs pollution	Potential pathways of microplastic ingestion (food, water)	To develop strategies to mitigate these risks
	Epidemiological studies on health effects of microplastic exposure.	To evaluate potential human health risks from microplastic contamination
	The presence of MPs in seafood and other products should be further examined covering all areas and types	To develop strategies to mitigate these risks

Conclusion

Microplastic pollution has emerged as a complex environmental challenge in Malaysia, with significant implications for both ecological health and human well-being. This review has examined the current understanding of MPs pollution in Malaysia, encompassing its abundance, potential impacts on biota and human health, and the analytical methods employed for its detection. The research conducted so far highlights the widespread presence of MPs in various environmental matrices in Malaysia, raising concerns about their potential ecological and human health risks. The potential for MPs to accumulate in the food chain and their ability to adsorb harmful pollutants necessitates further investigation t fully understand their long-term effects. Moving forward, addressing MPs pollution in Malaysia requires a comprehensive multi-pronged approach. This includes promoting the development and adoption of sustainable plastic production practices, coupled with effective waste management strategies to minimize plastic waste generation and improper disposal. Additionally, ongoing research efforts are crucial to develop efficient technologies for MPs detection, removal, and potential biodegradation. Public awareness campaigns are also essential to promote responsible plastic consumption and waste disposal practices among Malaysians. By implementing a combination of these strategies, Malaysia can play a leading role in combating MPs pollution and preserving its rich natural environment for future generations.

Acknowledgement

This study was supported by the Universiti Sains Malaysia, Short Term Grant with account code number: 304/CIPPT/6315592. This study also aligned with the mission and vision of the Advanced Management of Liver Malignancies Research Program 311.CIPPT.4119149 & 311.CIPPT.411988, Universiti Sains Malaysia.

References

1. Smith, M., Love, D. C., Rochman, C. M., and Neff, R. A. (2018). Microplastics in seafood and the implications for human health. *Current Environmental Health Reports*, 5(3): 375-386.
2. Andrady, A. L. (2017). The plastic in microplastics: A review. *Marine Pollution Bulletin*, 119(1): 12-22.
3. Horton, A. A., Walton, A., Spurgeon, D. J., Lahive, E., and Svendsen, C. (2017). Microplastics in freshwater and terrestrial environments: Evaluating the current understanding to identify the knowledge gaps and future research priorities. *Science of the Total Environment*, 586: 127-141.
4. Shim, W. J., Hong, S. H., and Eo, S. (2018). Marine microplastics: Abundance, distribution, and composition. In E. Zeng, (Ed.). Microplastics contamination in aquatic environments: An emerging matter of environmental urgency (pp. 1–26). Elsevier.
5. Ivar do Sul, J. A., Costa, M. F., and Fillmann, G. (2014). Microplastics in the Pelagic environment around oceanic islands of the Western Tropical Atlantic Ocean. *Water, Air, & Soil Pollution*, 225(7): 2004.
6. Landrigan, P. J., Stegeman, J. J., Fleming, L. E., Allemand, D., Anderson, D. M., Backer, L. C., Brucker-Davis, F., Chevalier, N., Corra, L., Czerucka, D., Bottein, M.-Y. D., Demeneix, B., Depledge, M., Deheyn, D. D., Dorman, C. J., Fénichel, P., Fisher, S., Gaill, F., Galgani, F., … Rampal, P. (2020). Human health and ocean pollution. *Annals of Global Health*, 86(1): 151.
7. MESTECC (2018). *Malaysia's Roadmap Towards Zero Single-Use Plastics 2018-2030*.
8. Moh, Y. C., and Abd Manaf, L. (2014). Overview of household solid waste recycling policy status and challenges in Malaysia. *Resources, Conservation and Recycling*, 82: 50-61.
9. The Star (2021, March 16). *Tackling increasing plastics pollution in Malaysia*. The Star.
10. Ma, Z., Ibrahim, Y. S., and Lee, Y. (2020). Microplastic pollution and health and relevance to the Malaysia's roadmap to zero single-use plastics 2018-2030. *Malaysian Journal Medicine Sciences*, 27(3): 1-6.
11. Meijer, L. J. J., Van Emmerik, T., Van Der Ent, R., Schmidt, C., and Lebreton, L. (2021). More than 1000 rivers account for 80% of global riverine plastic emissions into the ocean. *Science Advances*, 7(18): eaaz5803.

12. Adegoke, K. A., Adu, F. A., Oyebamiji, A. K., Bamisaye, A., Adigun, R. A., Olasoji, S. O., and Ogunjinmi, O. E. (2023). Microplastics toxicity, detection, and removal from water/wastewater. *Marine Pollution Bulletin*, 187: 114546.
13. Okoye, C. O., Addey, C. I., Oderinde, O., Okoro, J. O., Uwamungu, J. Y., Ikechukwu, C. K., Okeke, E. S., Ejeromedoghene, O., and Odii, E. C. (2022). Toxic chemicals and persistent organic pollutants associated with micro-and nanoplastics pollution. *Chemical Engineering Journal Advances*, 11: 100310.
14. Jin, Y., Xia, J., Pan, Z., Yang, J., Wang, W., and Fu, Z. (2018). Polystyrene microplastics induce microbiota dysbiosis and inflammation in the gut of adult zebrafish. *Environmental Pollution*, 235: 322-329.
15. Yang, C. Z., Yaniger, S. I., Jordan, V. C., Klein, D. J., and Bittner, G. D. (2011). Most plastic products release estrogenic chemicals: A potential health problem that can be solved. *Environmental Health Perspectives*, 119(7): 989-996.
16. Rouillon, M., and Taylor, M. P. (2016). Can field portable x-ray fluorescence (pXRF) produce high quality data for application in environmental contamination research? *Environmental Pollution*, 214: 255-264.
17. Lambert, S., and Wagner, M. (2016). Characterisation of nanoplastics during the degradation of polystyrene. *Chemosphere*, 145: 265-268.
18. El Hadri, H., Gigault, J., Maxit, B., Grassl, B., and Reynaud, S. (2020). Nanoplastic from mechanically degraded primary and secondary microplastics for environmental assessments. *NanoImpact*, 17(10): 100206.
19. Avio, C. G., Gorbi, S., and Regoli, F. (2017). Plastics and microplastics in the oceans: From emerging pollutants to emerged threat. *Marine Environmental Research*, 128: 2-11.
20. Au, S. Y., Bruce, T. F., Bridges, W. C., and Klaine, S. J. (2015). Responses of *Hyalella azteca* to acute and chronic microplastic exposures. *Environmental Toxicology and Chemistry*, 34(11): 2564-2572.
21. Crawford, C. B., and Quinn, B. (2017). Plastic production, waste and legislation in C. B. Crawford & B. B. T.-M. P. Quinn (Eds.), microplastics pollutants (pp. 39–56). Elsevier.
22. Ashrafy, A., Liza, A. A., Islam, M. N., Billah, M. M., Arafat, S. T., Rahman, M. M., and Rahman, S. M. (2023). Microplastics pollution: A brief review of its source and abundance in different aquatic ecosystems. *Journal of Hazardous Materials Advances*, 9: 100215.
23. Burns, E. E., and Boxall, A. B. A. (2018). Microplastics in the aquatic environment: Evidence for or against adverse impacts and major knowledge gaps. *Environmental Toxicology and Chemistry*, 37(11): 2776-2796.
24. Bond, T., Ferrandiz-Mas, V., Felipe-Sotelo, M., and van Sebille, E. (2018). The occurrence and degradation of aquatic plastic litter based on polymer physicochemical properties: A review. *Critical Reviews in Environmental Science and Technology*, 48(7-9): 685-722.
25. Mueller, R.-J. (2006). Biological degradation of synthetic polyesters—enzymes as potential catalysts for polyester recycling. *Process Biochemistry*, 41(10): 2124-2128.
26. Ren, L., Men, L., Zhang, Z., Guan, F., Tian, J., Wang, B., Wang, J., Zhang, Y., and Zhang, W. (2019). Biodegradation of polyethylene by *Enterobacter sp.* D1 from the guts of wax moth *Galleria mellonella. International Journal of Environmental Research and Public Health*, 16(11): 1941.
27. Jumaah, O. S. (2017). Screening of plastic degrading bacteria from dumped soil area. *IOSR Journal of Environmental Science, Toxicology and Food Technology*, 11(05): 93-98.
28. Ahmed, T., Shahid, M., Azeem, F., Rasul, I., Shah, A. A., Noman, M., Hameed, A., Manzoor, N., Manzoor, I., and Muhammad, S. (2018). Biodegradation of plastics: Current scenario and future prospects for environmental safety. *Environmental Science and Pollution Research*, 25(8): 7287-7298.
29. Praveena, S. M., Hisham, M. A. F. I., and Nafisyah, A. L. (2023). Microplastics pollution in agricultural farms soils: Preliminary findings from tropical environment (Klang Valley, Malaysia).

Environmental Monitoring and Assessment, 195(6): 650.

30. Hashim, H. A., Jamian, A., Yusuf, N. R., Naidu, S. Y., Paad, D. M., and Ishak, K. M. (2023). Evaluation of deposited atmospheric microplastic characteristic within Malaysia cities airshed. *Chemical Engineering Transactions*, 106: 1105-1110.
31. Tan, E., and Mohd Zanuri, N. B. (2023). Abundance and distribution of microplastics in tropical estuarine mangrove areas around Penang, Malaysia. *Frontiers in Marine Science*, 10: 1148804.
32. Zaki, M. R. M., Ying, P. X., Zainuddin, A. H., Razak, M. R., and Aris, A. Z. (2021). Occurrence, abundance, and distribution of microplastics pollution: An evidence in surface tropical water of Klang River Estuary, Malaysia. *Environmental Geochemistry and Health*, 43(9): 3733-3748.
33. Anuar, S. T., Abdullah, N. S., Yahya, N. K. E. M., Chin, T. T., Yusof, K. M. K. K., Mohamad, Y., Azmi, A. A., Jaafar, M., Mohamad, N., Khalik, W. M. A. W. M., and Ibrahim, Y. S. (2023). A multidimensional approach for microplastics monitoring in two major tropical river basins, Malaysia. *Environmental Research*, 227: 115717.
34. Barasarathi, J., P., A., C.U., E., and S.H., F. (2014). Microplastic abundance in selected mangrove forest in malaysia. *Proceeding of The ASEAN Conference on Science and Technology 2014*: pp. 18-20.
35. Hee, Y. Y., Hanif, N. M., Weston, K., Latif, M. T., Suratman, S., Rusli, M. U., and Mayes, A. G. (2023). Atmospheric microplastic transport and deposition to urban and pristine tropical locations in Southeast Asia. *Science of The Total Environment*, 902: 166153.
36. Afiq Daniel Azmi, M., Yasin, N. L. N. M., Norruwaida, J., Hasnatul, A. H., Dewika, M., and Sara, Y. Y. (2023). Analysis of suspended atmospheric microplastics size at different elevation in Universiti Teknologi Malaysia, Kuala Lumpur. *IOP Conference Series: Earth and Environmental Science*, 1144(1): 012009.
37. Zainuddin, A. H., Aris, A. Z., Zaki, M. R. M., Yusoff, F. M., and Wee, S. Y. (2022). Occurrence, potential sources and ecological risk estimation of microplastic towards coastal and estuarine zones in Malaysia. *Marine Pollution Bulletin*, 174: 113282.
38. Sharijan, S., Azman, S., and Mohd Said, M. I. (2018). Microplastics pollution in Skudai and Tebrau River, Malaysia. *Proceedings of 7th International Graduate Conference, Conference of Engineering, Science and Humanities*, pp. 16-18
39. Khalik, W. M. A. W. M., Ibrahim, Y. S., Tuan Anuar, S., Govindasamy, S., and Baharuddin, N. F. (2018). Microplastics analysis in Malaysian marine waters: A field study of Kuala Nerus and Kuantan. *Marine Pollution Bulletin*, 135: 451-457.
40. Saipolbahri, N., Anak Bitlus, M. L., Ismail, N. A., Fauzi, N. M., and Subki, N. S. (2020). Determination of microplastics in surface water and sediment of Kelantan Bay. *IOP Conference Series: Earth and Environmental Science*, 549(1): 012059.
41. Taha, Z. D., Md Amin, R., Anuar, S. T., Nasser, A. A. A., and Sohaimi, E. S. (2021). Microplastics in seawater and zooplankton: A case study from Terengganu estuary and offshore waters, Malaysia. *Science of the Total Environment*, 786: 147466
42. Yang Hwi, T., Ibrahim, Y. S., and Khalik, W. M. A. W. M. (2020). Microplastic abundance, distribution, and composition in Sungai Dungun, Terengganu, Malaysia. *Sains Malaysiana*, 49(7): 1479-1490.
43. Yusof, K. M. K. K., Anuar, S. T., Mohamad, Y., Jaafar, M., Mohamad, N., Bachok, Z., Mohamad, N., AND Ibrahim, Y. S. (2023). First evidence of microplastic pollution in the surface water of Malaysian Marine Park Islands, South China Sea during COVID-19. *Marine Pollution Bulletin*, 194: 115268.
44. Ibrahim, Y. S., Hamzah, S. R., Khalik, W. M. A. W. M., Ku Yusof, K. M. K., and Anuar, S. T. (2021). Spatiotemporal microplastic occurrence study of Setiu Wetland, South China Sea. *Science of The Total Environment*, 788: 147809.
45. Chenappan, N. K., Ibrahim, Y. S., Anuar, S. T., Yusof, K. M. K. K., Jaafar, M., Ahamad, F., Sulaiman, W. Z. W., and Mohamad, N. (2024). Quantification and characterization of airborne microplastics in the coastal area of Terengganu,

Malaysia. *Environmental Monitoring and Assessment*, 196(3): 1-15.

46. Liong, R. M. Y., Hadibarata, T., Yuniarto, A., Tang, K. H. D., and Khamidun, M. H. (2021). Microplastic occurrence in the water and sediment of Miri River Estuary, Borneo Island. *Water, Air, and Soil Pollution*, 232(8).
47. Alexander Tampang, A. M., and Mohan Viswanathan, P. (2022). Occurrence, distribution and sources of microplastics in beach sediments of Miri Coast, NW Borneo. *Chemosphere*, 305: 135368.
48. Zahari, N. Z., Vincent, S. D., Cleophas, F. N., Budin, K., and Sabullah, M. K. (2023). Abundance, distribution, and characterization of microplastics on two recreational beaches in Kota Kinabalu, Sabah, Malaysia. *Water (Switzerland)*, 15(15): 2681.
49. De-la-Torre, G. E. (2020). Microplastics: an emerging threat to food security and human health. *Journal of Food Science and Technology*, 57(5):1601-1608.
50. Sulaiman, R. N. R., Bakar, A. A., Ngadi, N., Kahar, I. N. S., Nordin, A. H., Ikram, M., and Nabgan, W. (2023). Microplastics in Malaysia's aquatic environment: Current overview and future perspectives. *Global Challenges*, 7(8): 2300047.
51. Foo, Y. H., Ratnam, S., Lim, E. V., Abdullah, M., Molenaar, V. J., Shau Hwai, A. T., Zhang, S., Li, H., and Mohd Zanuri, N. B. (2022). Microplastic ingestion by commercial marine fish from the seawater of Northwest Peninsular Malaysia. *PeerJ*, 10: e13181.
52. Ratnam, S., and Mohd Zanuri, N. B. (2022). Microplastic ingestion of blood cockles (*Tegillarca granosa*) in Kuala Juru, Pulau Pinang. *Journal of Survey in Fisheries Sciences*, 9(1): 97-115.
53. Usman, S., Abdull Razis, A. F., Shaari, K., Amal, M. N. A., Saad, M. Z., Mat Isa, N., ... and Ibrahim, M. A. (2020). Microplastics pollution as an invisible potential threat to food safety and security, policy challenges and the way forward. *International Journal of Environmental Research and Public Health,* 17(24): 9591.
54. Habib, S., Iruthayam, A., Shukor, M. Y. A., Alias, S. A., Smykla, J., and Yasid, N. A. (2020). Biodeterioration of untreated polypropylene microplastic particles by Antarctic bacteria. *Polymers*, 12(11): 2616.
55. Kwon, J. H., Kim, J. W., Pham, T. D., Tarafdar, A., Hong, S., Chun, S. H., Lee, S. H., Kang, D. Y., Kim, J. Y., Kim, S. Bin, and Jung, J. (2020). Microplastics in food: A review on analytical methods and challenges. *International Journal of Environmental Research and Public Health*, 17 (18): 1-23.
56. Yu, Q., Hu, X., Yang, B., Zhang, G., Wang, J., and Ling, W. (2020). Distribution, abundance and risks of microplastics in the environment. *Chemosphere*, 249: 126059.
57. Bouwmeester, H., C. H. Hollman, P., and J. B. Peters, R. (2015). Potential health impact of environmentally released micro- and nanoplastics in the human food production chain: Experiences from nanotoxicology. *Environmental Science & Technology*, 49(15): 8932-8947.
58. Abbasi, S., Moore, F., and Keshavarzi, B. (2021). PET-microplastics as a vector for polycyclic aromatic hydrocarbons in a simulated plant rhizosphere zone. *Environmental Technology and Innovation*, 21: 101370.
59. Ragusa, A., Svelato, A., Santacroce, C., Catalano, P., Notarstefano, V., Carnevali, O., Papa, F., Rongioletti, M. C. A., Baiocco, F., Draghi, S., D'Amore, E., Rinaldo, D., Matta, M., and Giorgini, E. (2021). Plasticenta: First evidence of microplastics in human placenta. *Environment International*, 146: 106274.
60. Lee, Y., Cho, J., Sohn, J., and Kim, C. (2023). Health effects of microplastic exposures: Current issues and perspectives in South Korea. *Yonsei Medical Journal*, 64(5): 301-308.
61. Forte, M., Iachetta, G., Tussellino, M., Carotenuto, R., Prisco, M., De Falco, M., Laforgia, V., and Valiante, S. (2016). Polystyrene nanoparticles internalization in human gastric adenocarcinoma cells. *Toxicology in Vitro*, 31: 126-136.
62. Liu, S., Wang, Z., Xiang, Q., Wu, B., Lv, W., and Xu, S. (2022). A comparative study in healthy and diabetic mice followed the exposure of polystyrene microplastics: Differential lipid metabolism and

inflammation reaction. *Ecotoxicology and Environmental Safety*, 244: 114031.

63. Détrée, C., and Gallardo-Escárate, C. (2018). Single and repetitive microplastics exposures induce immune system modulation and homeostasis alteration in the edible mussel *Mytilus galloprovincialis*. *Fish and Shellfish Immunology*, 83: 52-60.
64. Lin, S., Zhang, H., Wang, C., Su, X. L., Song, Y., Wu, P., Yang, Z., Wong, M. H., Cai, Z., and Zheng, C. (2022). Metabolomics reveal nanoplastic-induced mitochondrial damage in human liver and lung cells. *Environmental Science and Technology*, 56(17): 12483-12493.
65. Shan, S., Zhang, Y., Zhao, H., Zeng, T., and Zhao, X. (2022). Polystyrene nanoplastics penetrate across the blood-brain barrier and induce activation of microglia in the brain of mice. *Chemosphere*, 298: 134261.
66. Idrus, F. A., Roslan, N. S., and Harith, M. N. (2022). Occurrence of macro- and microplastics on Pasir Pandak Beach, Sarawak, Malaysia. *Jurnal Ilmiah Perikanan Dan Kelautan*, 14(2): 214-230.
67. Karami, A., Golieskardi, A., Choo, C. K., Romano, N., Ho, Y. Bin, and Salamatinia, B. (2017). A high-performance protocol for extraction of microplastics in fish. *Science of the Total Environment*, 578: 485-494.
68. Matupang, D. M., Zulkifli, H. I., Arnold, J., Lazim, A. M., Ghaffar, M. A., and Musa, S. M. (2023). Tropical sharks feasting on and swimming through microplastics: First evidence from Malaysia. *Marine Pollution Bulletin*, 189: 114762.
69. Jaafar, N., Azfaralariff, A., Musa, S. M., Mohamed, M., Yusoff, A. H., and Lazim, A. M. (2021). Occurrence, distribution and characteristics of microplastics in gastrointestinal tract and gills of commercial marine fish from Malaysia. *Science of the Total Environment*, 799: 149457.
70. Ibrahim, Y. S., Azmi, A. A., Abdul Shukor, S., Anuar, S. T., and Abdullah, S. A. (2016). Microplastics Ingestion by *Scapharca cornea* at Setiu Wetland, Terengganu, Malaysia. *Middle-East Journal of Scientific Research*, 24(6): 2129-2136.
71. Suardy, N. H., Tahrim, N. A., and Ramli, S. (2020). Analysis and characterization of microplastic from personal care products and surface water in Bangi, Selangor. *Sains Malaysiana*, 49(9): 2237-2249.
72. Praveena, S. M., Shaifuddin, S. N. M., and Akizuki, S. (2018). Exploration of microplastics from personal care and cosmetic products and its estimated emissions to marine environment: An Evidence from Malaysia. *Marine Pollution Bulletin*, 136: 135-140.
73. Karbalaei, S., Golieskardi, A., Watt, D. U., Boiret, M., Hanachi, P., Walker, T. R., and Karami, A. (2020). Analysis and inorganic composition of microplastics in commercial Malaysian fish meals. *Marine Pollution Bulletin*, 150: 110687.
74. Praveena, S. M., Shamsul Ariffin, N. I., and Nafisyah, A. L. (2022). Microplastics in Malaysian bottled water brands: Occurrence and potential human exposure. *Environmental Pollution*, 315: 120494.
75. Ibrahim, Y. Y. S., Rathnam, R. R., and Anuar, S. (2017). Isolation and characterisation of microplastic abundance in *Lates calcarifer* from Setiu Wetlands, Malaysia. *Malaysia Journal of Analytical Science*, 21(5): 1054-1064.
76. Jannah, M., Husin, M., Mazlan, N., Shalom, J., Shirwan, M., and Sani, A. (2021). Evaluation of microplastics ingested by sea cucumber *Stichopus horrens* in Pulau Pangkor, Perak, Malaysia. *Environmental Science and Pollution Research,* 28: 61592-61600.
77. Karami, A., Golieskardi, A., Ho, Y. Bin, Larat, V., and Salamatinia, B. (2017). microplastics in eviscerated flesh and excised organs of dried fish. *Scientific Reports*, 7(1): 5473.
78. Karami, A., Golieskardi, A., Choo, C. K., Larat, V., Karbalaei, S., and Salamatinia, B. (2018). Microplastic and mesoplastic contamination in canned sardines and sprats. *Science of the Total Environment*, 612: 1380-1386.
79. Ibrahim, Y. S., Tuan Anuar, S., Azmi, A. A., Wan Mohd Khalik, W. M. A., Lehata, S., Hamzah, S. R., Ismail, D., Ma, Z. F., Dzulkarnaen, A., Zakaria, Z., Mustaffa, N., Tuan Sharif, S. E., and Lee, Y. Y. (2021). Detection of microplastics in human colectomy specimens. *JGH Open*, 5(1): 116-121.
80. Anuar, S. T., Altarawnah, R. S., Mohd Ali, A. A., Lee, B. Q., Khalik, W. M. A. W. M., Yusof, K. M.

K. K., and Ibrahim, Y. S. (2022). Utilizing pyrolysis–gas chromatography/mass spectrometry for monitoring and analytical characterization of microplastics in polychaete worms. *Polymers*, 14(15): 3054.

81. Silva, A. B., Bastos, A. S., Justino, C. I. L., da Costa, J. P., Duarte, A. C., and Rocha-Santos, T. A. P. (2018). Microplastics in the environment: Challenges in analytical chemistry - a review. *Analytica Chimica Acta*, 1017: 1-19.
82. Huang, Z., Hu, B., and Wang, H. (2023). Analytical methods for microplastics in the environment: A review. *Environmental Chemistry Letters*, 21(1): 383-401.
83. Fu, W., Min, J., Jiang, W., Li, Y., and Zhang, W. (2020). Separation, characterization and identification of microplastics and nanoplastics in the environment. *Science of the Total Environment*, 721: 137561.
84. Song, Y. K., Hong, S. H., Jang, M., Han, G. M., Rani, M., Lee, J., and Shim, W. J. (2015). A comparison of microscopic and spectroscopic identification methods for analysis of microplastics in environmental samples. *Marine Pollution Bulletin*, 93(1-2): 202-209.
85. Matsuguma, Y., Takada, H., Kumata, H., Kanke, H., Sakurai, S., Suzuki, T., Itoh, M., Okazaki, Y., Boonyatumanond, R., Zakaria, M. P., Weerts, S., and Newman, B. (2017). Microplastics in sediment cores from Asia and Africa as indicators of temporal trends in plastic pollution. *Archives of Environmental Contamination and Toxicology*, 73(2): 230-239.
86. Karami, A., Golieskardi, A., Keong Choo, C., Larat, V., Galloway, T. S., and Salamatinia, B. (2017). The presence of microplastics in commercial salts from different countries. *Scientific Reports*, 7: 46173.
87. Zhang, Y., Zhang, M., & Fan, Y. (2023). Assessment of microplastics using microfluidic approach. *Environmental Geochemistry and Health*, 45(3): 1045-1052.
88. Tse, Y. T., Lo, H. S., Chan, S. M. N., and Sze, E. T. P. (2022). Flow cytometry as a rapid alternative to quantify small microplastics in environmental water samples. *Water,* 14(9): 1436.
89. Jin, N., Song, Y., Ma, R., Li, J., Li, G., and Zhang, D. (2022). Characterization and identification of microplastics using Raman spectroscopy coupled with multivariate analysis. *Analytica Chimica Acta*, 1197: 339519.

Malaysian Journal of Analytical Sciences (MJAS)
Published by Malaysian Analytical Sciences Society

SYNTHESIS AND MOLECULAR DOCKING SIMULATION OF CINNAMIC ACIDS DERIVATIVES AGAINSTS DENV2 NS2B/NS3

(Sintesis dan Simulasi Pengedokan Terbitan Asid Sinamik Terhadap DENV2 NS2B/NS3)

Nadia Mohamed Yusoff[1], Siti Nor Khadijah Addis[1], Nurul Huda Abdul Wahab[1,2], Fauziah Abdullah[3] and Asnuzilawati Asari[1,2,*]

[1]*Faculty of Science and Marine Environment, Universiti Malaysia Terengganu, 21030 Kuala Nerus, Terengganu, Malaysia*
[2]*Advanced Nano Materials (ANoMA) Research Group, Faculty of Science and Marine Environment, Universiti Malaysia Terengganu, 21030 Kuala Nerus, Terengganu, Malaysia*
[3]*Phytochemistry Programme, Natural Products Division, Forest Research Institute Malaysia (FRIM), 52109 Kepong, Selangor Darul Ehsan, Malaysia*

[*]*Corresponding author: asnu@umt.edu.my*

Received: 18 February 2024; Accepted: 23 April 2024; Published: 29 June 2024

Abstract

Dengue virus (DENV) is known as one of the serious global threats to human health since its emergence in the past few decades. However, clinically approved antiviral drugs are still not available for DENV treatment. The increased number of cases reported yearly had led to the on-going research in finding an effective drug for dengue. Cinnamic acid is a naturally occurring compound which consists of α, β-unsaturated carboxylic acid and is known for its wide pharmacological properties. Cinnamic acid derivatives such as caffeic acid are one of constituents in *Carica papaya* leaf which are used as a folk remedy for dengue. Recently, cinnamic acid was reported to show a potential against dengue virus. In this study, eight cinnamic acid derivatives were synthesized by incorporating cinnamic acid and amide moieties through the reaction of cinnamic acid with corresponding amines. All compounds were characterized by using ^{1}H and ^{13}C nuclear magnetic resonance (NMR), Fourier transform infrared (FTIR), mass spectrometry (MS) and CHN elemental analysis. Then, the synthesized compounds were simulated for molecular docking to investigate their binding affinity with the Wichapong homology protein model crystal structure, DENV-2 NS2B/NS3pro. The lower the value of FEB of a compound, the higher its binding affinity towards protein. The in-silico study revealed that compounds **6b1-6b4**, with *tert*-butyl substituents had the highest binding affinity and good interaction with DENV-2 NS2B/NS3 serine protease. This might be due to the presence of a *tert*-butyl moiety in the structure, which could interact with amino acid residue of protease, thereby increasing the binding interaction between the ligand and the protein. Compound **6b2** showed the lowest FEB value despite having less H-bond interactions as compared to compound **6b3**. This was probably due to the presence of more non-covalent interaction and closer bond distance which helped to enhance its binding stability. In summary, this study showed that cinnamic acid could be a promising candidate for the development of antiviral drugs to target DENV.

Keywords: cinnamic acid, synthesis, anti-dengue virus, docking

Abstrak

Virus denggi (DENV) telah dikenali sebagai salah satu ancaman global yang serius terhadap kesihatan manusia setelah

kemunculannya beberapa dekad yang lalu. Walau bagaimanapun, masih belum ada ubat antiviral yang diluluskan secara klinikal bagi rawatan DENV. Peningkatan jumlah kes yang dilaporkan setiap tahun telah membawa kepada penyelidikan yang berterusan dalam pencarian ubat yang berkesan untuk rawatan denggi. Asid sinamik adalah bahan semulajadi yang mempunyai kumpulan asid karbosilik α, β-tak tepu dan dikenali dengan pelbagai sifat farmakologinya. Asid sinamik seperti asid kafeik merupakan antara komposisi yang terkandung di dalam daun *Carica papaya* yang digunakan secara tradisional untuk rawatan denggi. Kebelakangan ini, asid sinamik telah dilapor menunjukkan potensi terhadap DENV. Di dalam kajian ini, lapan terbitan asid sinamik telah disintesis dengan menggabungkan asid sinamik dan amida melalui tindak balas asid sinamik dengan amina yang bersesuaian. Semua sebatian dicirikan dengan menggunakan 1H and ^{13}C Resonans Magnetik Nuklear (RMN), Inframerah Transformasi Fourier (FTIR), spektrometri jisim (MS) dan analisis unsur CHN. Sebatian yang disintesis kemudiannya disimulasikan menerusi pengedokan molekul bagi mengkaji keafinan pengikatan mereka bersama struktur kristal homologi protein Wichapong, DENV-2 NS2B/NS3pro. Kajian *in siliko* menunjukkan bahawa sebatian **6b1-6b4**, yang mengandungi kumpulan penukargantian *tert*-butil menunjukkan tenaga pengikatan yang tinggi dan interaksi yang baik dengan DENV-2 NS2B/NS3 serine protease. Ini mungkin disebabkan oleh kehadiran *tert*-butil dalam strukturnya, yang boleh berinteraksi dengan asid amino protein, dengan itu meningkatkan interaksi pengikatan antara ligan dan protein. Semakin rendah nilai FEB sebatian, semakin kuat ikatannya dengan enzim. Sebatian **6b2** menunjukkan nilai FEB terendah walaupun ia mempunyai kurang interaksi ikatan H-bond berbanding dengan sebatian **6b3,** dan ini mungkin disebabkan oleh kehadiran interaksi non-kovalen yang banyak dan jarak ikatan yang berdekatan telah membantu meningkatkan kestabilan ikatannya. Secara keseluruhannya, kajian ini menunjukkan bahawa sebatian asid sinamik berpotensi untuk pembangunan ubat-ubatan antiviral bagi merawat DENV.

Kata kunci: asid sinamik, sintesis, anti-denggi, pengedokan

Introduction

Dengue virus (DENV) is the most significant virus in the *Flaviviridae* family with the highest morbidity and mortality rates and has been a serious global threat in the past few decades [1]. The latest statistics from the World Health Organization (WHO) have shown an increasing trend of DENV infection throughout Malaysia with 127,407 reported cases in 2019 [2]. Despite this alarming issue, no current effective vaccine or antiviral treatment is available for treating dengue patients. Prevention against DENV infection by large depends on mosquito vectors control as well as the use of a natural remedy [3, 4, 5]. This underscores an urgent need to discover and develop a novel antiviral agent that is safe and effective in controlling dengue infection.

Cinnamic acid has gained a lot of interest due to its unique structure with great potential for pharmacological properties. It is a group of aromatic carboxylic acids which appear naturally in the plant kingdom. Cinnamic acids occur in all green plants as well as the reproductive organs of flowering plants [6]. Cinnamic acids with varied substitutions on the aryl ring and their esters have been identified in natural bee products, including honey and propolis [7]. It is also readily available from coffee beans, tea, cocoa, apples, tomatoes and cereals [8]. It is a safe and extensive source of material due to its natural and low toxicity properties.

Cinnamic acid and its related molecules have a variety of biological activities, such as anticancer, antimalarial, and antimicrobial [9, 10, 11]. Additionally, cinnamic acid was also reported to be an effective antiviral drug against Zika virus (ZIKV) by inhibiting RNA-dependent RNA polymerase (RdRp) activity at the post-entry stage of ZIKV replication cycle [12]. Cinnamic acid was also reported to have excellent activity against *Tobacco mosaic virus* (TMV) and Hepatitis C virus (HCV) [13,14]. Despite their rich medicinal tradition and remarkable biological activities, the antiviral activity of cinnamic acid related molecules against DENV infection remained underutilised for several decades. To our knowledge, cinnamic acid derivatives were first evaluated for their anti-dengue activity and were reported by Rees and co-workers in 2008. Zosteric acid (*para*-sulfoxy-cinnamic acid), derived from Zostera Marina and CF238, was found to exhibit the process of virus entry. It was suggested to entrap the virus on the surface of the cell in a non-permissive binding mode and prevent the fusion process of the virus into the cell [15]. Recently, a new cinnamic acid, 3-(2-chlrophenyl) acrylic acid was synthesised based on the structural scaffold found in *Carica papaya*, in which the extract was used as a folk remedy for dengue [16]. It was

reported that the compound showed higher inhibition activities against DENV2 NS2B-NS3 protease as compared to quercetin [17]. Arylcyanoacrylamide, aminobenzamide and α-ketomide were also reported to have a significant inhibitory effect on dengue protease NS2b/NS3 [18, 19, 20]. Due to this, this study aimed to develop a dengue inhibitor by incorporating cinnamic acid with amide, which has been reported to show potential towards DENV.

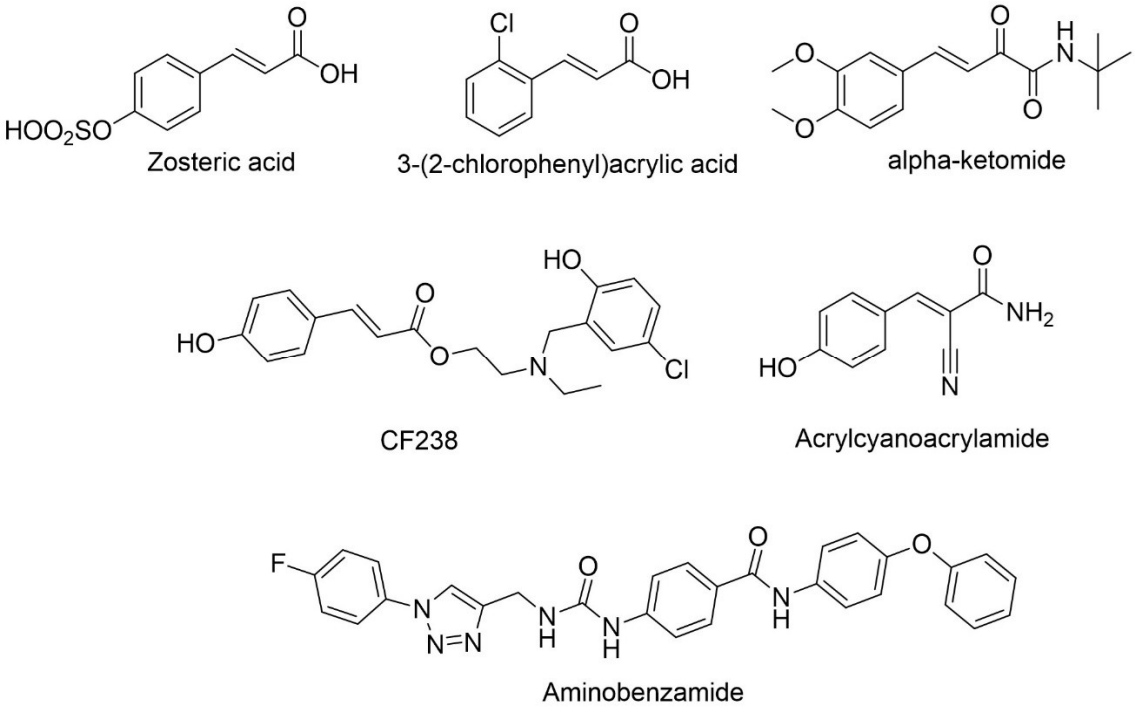

Figure 1. Structure of zosteric acid, CF238, 3-(2-chlorophenyl) acrylic acid, arylcyanoacrylamide, aminobenzamide and α-ketomide.

DENV is a single-stranded RNA genome which encodes a single open reading frame (5-C-prM-E-NS1-NS2A-NS2B-NS3-NS4A-NS4B-NS5-3) with three structural and seven non-structural proteins [21]. The N-terminal of NS3 is a trypsin-like serine protease, in which when combined with its co-factor (NS2B) it can cleave the viral polyprotein. Disruption of NS2B-NS3 protease inhibits viral replication [22]. This poses NS2B-NS3 protease of DENV-2 as a promising target for antiviral drug design [23]. The three catalytic triad amino acid residues present in NS3 serine proteases were His51, Asp75 and Ser135. The NS2B protease acted as an NS3 serine protease co-factor for an optimal catalytic activity [24]. The homology protein crystal structure generated by Wichapong et al. (2010) was used due to lack of DENV-2 NS2B/NS3 serine protease inhibitor-bound 3D structures. Moreover, some protease database structures were found to have missing amino acid residues [25].

In the selection of an effective medicine for patient, in addition to having a high biological activity, the targeted molecule must exhibit low toxicity and adhere to drug-like properties as outlined in Lipinski's Rule of Five. These properties, such as molecule size, hydrogen bonding characteristic and lipophilicity, play a crucial role in determine the permeability of molecule throughout the body [26]. Evaluation for these ADME (for absorption, distribution, metabolism, and excretion) parameter can be evaluated using SwissADME web tool [27].

In this study, eight cinnamic acid derivatives were synthesised, characterised, and subjected to molecular

docking simulations to investigate their binding interactions with the protein target of DENV-2 NS2B/NS3 protease. The drug-likeness parameter of compounds was calculated by using SwissADME.

Materials and Methods

Chemicals and instrumentations

The chemicals and solvents used were purchased from Sigma-Aldrich Co., Acros Organics, QRec and Merck Chemical Co. (Reagent Grade) and were used without further purification. Thin-layer chromatography (TLC) was performed on a plastic-backed pre-coated with silica gel plates (Merck silica gel, 60 F254), in the solvent system of ratio Hexane:ethylacetate (7:3). Completion of the reaction was determined by the appearance of product and disappearance of reactant spots under UV-fluorescence (λ_{max}= 254 nm), respectively. All reactions were carried out in heat-dried glassware under dry nitrogen atmosphere by using a ballon, unless otherwise stated. All liquids transferred were conducted by using standard cannula techniques. All spectral data were obtained on the following instruments: Attenuated total reflected-infrared (ATR-IR) spectra were recorded by using Perkin Elmer 100 spectrometer model at a spectral range of 4000—400 cm^{-1}. ^{1}H (400 MHz) and ^{13}C (100 MHz) Nuclear magnetic resonance spectra were obtained on Bruker Avance II 400 spectrometer and were reported in unit ppm on the δ scale. NMR analyses used DMSO-d_6 and TMS solvents as the internal standards. The data were analyzed by using Bruker TopSpin software package. The chemical shift was internally referenced to solvent DMSO-d_6 (^{1}H δ 2.50; ^{13}C δ 39.5). The mass spectrometer experiments were performed by using LCMS Orbitrap Discovery (Thermo Scientific), electrospray (ES) negative mode and the samples were dissolved in methanol.

Preparation of cinnamic acid derivatives

The cinnamate-amide derivatives (**6a1-6a4** and **6b1-6b4**) were synthesized according to the reported literature procedure with slight modifications [28]. A substituted cinnamic acid (2.0 mmol) was added to 15 mL tetrahydrofuran (THF) and treated with 1-(3-Dimethylaminopropyl)-3-ethylcarbodiimide hydrochloride (EDC.HCl) (3.0 mmol, 0.575g) under a nitrogen atmosphere. The solution was stirred at 0 ˚C for 30 min, and 2.0 mmol of amine was slowly added within 15 min. Then, the solution was stirred overnight at room temperature under nitrogen atmosphere. The completion of the reaction was monitored using TLC (Hexane: ethyl acetate, 7:3). The solvent was removed under reduced pressure, and the residue was treated with water and extracted with ethyl acetate. The organic extract was washed with 5% HCl solution, 5% $NaHCO_3$ solution and brine. The organic layer was dried over $MgSO_4$, filtered, and then evaporated under reduced pressure. The reactions are illustrated in Scheme 1.

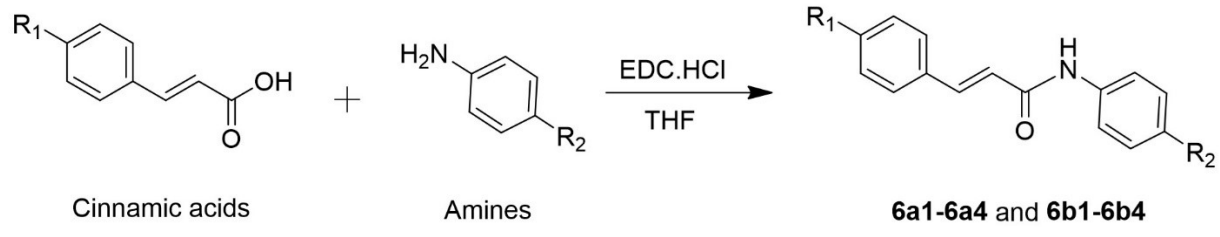

Scheme 1. Preparation of cinnamic acid amide derivatives (**6a1-6a4** and **6b1-6b4**)

3-(4-hydroxyphenyl)-N-4-phenylacrylamide (6a1)

Pale brownish powder (0.272g, 56.8%), m.p.156 ˚C (lit. 156 ˚C, [29]), compound **6a1** was prepared from the reaction of 4-hydroxycinnamic acid (0.33g, 2.0 mmol) with aniline (0.19g, 2.0 mmol) in the same manner as described in Scheme 1. Data analysis: ^{1}H NMR (400 MHz, DMSO-d_6): δ_H ppm, 10.12 (1H, s, NH), 9.98 (1H, s, OH), 7.67-7.75 (2H, m, H-ar), 7.48-7.56 (3H, m, H-ar and CH), 7.29-7.38 (2H, m, H-ar), 7.06 (1H, t, *J*= 8.0 Hz, H-ar), 6.86 (2H, d, *J*= 12.0 Hz,), 6.66 (1H, d, *J*= 16.0 Hz, CH); ^{13}C NMR (100 MHz, DMSO-d_6): δ_C ppm, 116.3 (2×CH-ar), 119.1 (=CH), 119.6 (2×CH-ar), 123.6 (CH-ar), 126.2 (Cq), 129.2 (2×CH-ar), 130.0 (2×CH-ar), 140.0 (Cq), 140.8 (=CH), 159.7 (C-O), 164.5 (C=O); FTIR (ATR, cm^{-1}): *v* 3317 (N-H, secondary amide), 3022 (O-H, phenol), 2922 (C-H, aromatic), 1651 (C=O), 1599 (N-H bend, secondary amide), 821 (C-H oop, aromatic); Found MS (ES, negative mode) $[M-H]^+$ 238.09 $C_{15}H_{12}NO_2$, requires 238.27. Anal. Calculated for $C_{15}H_{13}NO_2$: C, 75.30; H, 5.48; N, 5.85; Found: C, 73.55; H, 5.51; N, 5.24.

3-(4-hydroxyphenyl)-N-(4-methoxyphenyl) acrylamide (6a2)

Pale greenish-yellow powder (0.383g, 71.2%), m.p.167 ˚C, compound **6a2** was prepared from the reaction of 4-hydroxycinnamic acid (0.33g, 2.0 mmol) with 4-methoxyaniline (0.25g, 2 mmol) in the same manner as described in Scheme 1. Data analysis: ^{1}H NMR (400 MHz. DMSO-d_6): δ_H ppm, 10.00 (1H, s, NH), 9.97 (1H, s, OH), 7.65 (2H, d, *J*= 8.0 Hz, H-ar), 7.53 (1H, s, H-ar), 7.46 (2H, d, *J*= 8.0 Hz, H-ar), 6.92 (2H, d, *J*= 8.0 Hz, H-ar), 6.85 (2H, d, *J*= 8.0 Hz, H-ar), 6.63 (1H, d, *J*= 16.0 Hz, CH), 3.74 (3H, s, OCH3); ^{13}C NMR (100 MHz. DMSO-d_6): δ_C ppm, 55.6 (OCH_3), 114.4 (2×CH-ar), 116.3 (2×CH-ar), 119.2 (=CH), 121.1 (2×CH-ar), 126.3 (Cq), 129.9 (2×CH-ar), 133.1 (Cq), 140.3 (=CH), 155.6 (C-O), 159.6 (C-O), 164.1 (C=O); FTIR (ATR, cm^{-1}): *v* 3328 (N-H, secondary amide), 3066 (OH, phenol), 2946 (C-H, aromatic), 1679 (C=O), 1598 (N-H bend, secondary amide), 821 (C-H oop, aromatic); Found MS (ES, negative mode) $[M-H]^+$ 268.10 $C_{16}H_{13}NO_3$, requires 268.30. Anal. Calculated for $C_{16}H_{15}NO_3$: C, 71.36; H, 5.61; N, 5.20; Found: C, 68.45.15; H, 5.79; N, 4.79.

3-(4-hydroxyphenyl)-N-(4-methylphenyl) acrylamide (6a3)

Yellowish brown powder (0.306g, 60.5%), m.p. 167 ˚C [29], compound **6a3** was prepared from the reaction of 4-hydroxycinnamic acid (0.33g, 2.0 mmol) with 4-methylaniline (0.21g, 2 mmol) in the same manner as described in Scheme 1. Data analysis: ^{1}H NMR (400 MHz. DMSO-d6): δ_H ppm, 10.01 (1H, s, NH), 9.95 (1H, s, OH), 7.59 (2H, d, *J*= 8.0 Hz, H-ar), 7.48 (3H, t, *J*= 12.0 Hz, H-ar and CH), 7.13 (2H, d, *J*= 8.0 Hz, H-ar), 6.84 (2H, d, *J*= 8.0 Hz, H-ar), 6.62 (1H, d, *J*= 16.0 Hz, CH), 2.26 (3H, s, CH_3); ^{13}C NMR (100 MHz. DMSO-d_6): δ_C ppm, 20.9 (CH_3), 116.3 (2×CH-ar), 119.2 (=CH), 119.6 (2×CH-ar), 126.3 (Cq), 129.6 (2×CH-ar), 129.9 (2×CH-ar), 132.5 (Cq), 137.5 (Cq), 140.5 (=CH), 159.6 (C-O), 164.3 (C=O); FTIR (ATR, cm^{-1}): *v* 3250 (N-H, secondary amide), 3012 (O-H, phenol), 2920 (C-H, aromatic), 1653 (C=O), 1594 (N-H bend, secondary amide), 816 (C-H oop, aromatic); Found MS (ES, negative mode) $[M-H]^+$ 252.10 $C_{16}H_{14}NO_2$, requires 252.30. Anal. Calculated for $C_{16}H_{15}NO_2$: C, 75.87; H, 5.97; N, 5.53; Found: C, 68.45; H, 5.79; N, 4.79.

3-(4-hydroxyphenyl)-N-(4-chlorophenyl) acrylamide (6a4)

Yellow powder (0.352g, 64.0%), m.p. 187 ˚C [30], compound **6a4** was prepared from the reaction of 4-hydroxycinnamic acid (0.33g, 2.0 mmol) with 4-chloroaniline (0.26g, 2 mmol) in the same manner as described in Scheme 1. Data analysis: ^{1}H NMR (400 MHz. DMSO-d6): δ_H ppm, 10.12 (1H, s, NH), 9.98 (1H, s, OH), 7.72 (2H, d, *J*= 7.9 Hz, H-ar), 7.48-7.56 (2H, m, H-ar), 7.33 (2H, t, *J*= 7.7, 8.1 Hz, H-ar), 7.05 (1H, t, *J*= 7.4, 7.3 Hz, H-ar), 6.85 (2H, d, *J*= 8.4 Hz, H-ar), 6.66 (1H, d, *J*= 16.0 Hz, CH), 3.47 (1H, s, OH); ^{13}C NMR (100 MHz. DMSO-d_6): δ_C ppm, 116.3 (2×CH-ar), 118.7 (2×CH-ar), 121.1 (2×CH-ar), 127.1 (Cq), 129.1 (2×CH-ar), 130.1 (2×CH-ar), 138.9 (Cq), 141.2 (=CH), 159.8 (C-O), 164.6 (C=O); FTIR (ATR, cm^{-1}): *v* 3367 (N-H, secondary amide), 3112 (O-H, phenol), 2925 (C-H, aromatic), 1662 (C=O), 1594 (N-H bend, secondary amide), 826 (C-H oop, aromatic); Found MS (ES, negative mode) $[M-H]^+$ 272.05 $C_{15}H_{11}ClNO_2$, requires 272.72. Anal. Calculated for $C_{15}H_{12}ClNO_2$: C, 65.82; H, 4.42; N, 5.12; Found: C, 65.72; H, 4.83; N, 4.75.

3-(4-*tert*-butylphenyl)-N-4-phenylacrylamide (6b1)

Pale yellow powder (0.515g, 92%), m.p.142 ˚C [31], compound **6b1** was prepared from the reaction of 4-*tert*-butylcinnamic acid (0.41g, 2.0 mmol) with aniline (0.19g, 2.0 mmol) in the same manner as described in Scheme 1. Data analysis: ^{1}H NMR (400 MHz. DMSO-d_6): δ_H ppm, 10.23 (1H, s, NH), 7.74 (2H, d, *J*= 8.0 Hz, H-ar), 7.57 (3H, m, H-ar and CH), 7.46 (2H, d, *J*= 12.0 Hz), 7.34 (2H, t, *J*= 8.0 Hz, H-ar), 7.07 (1H, t, *J*= 8.0 Hz, H-ar), 6.84 (1H, d, *J*= 16.0 Hz, CH), 1.30 (9H, s, 3×CH_3), ^{13}C NMR (100 MHz. DMSO-d_6): δ_C ppm, 31.4 (3×CH_3), 35.0 (Cq), 119.7 (2×CH-ar), 121.9 (=CH), 123.7 (CH-ar), 126.3 (2×CH-ar), 128.0 (2×CH-ar), 129.2 (2×CH-ar), 132.5 (Cq), 139.8 (Cq), 140.5 (=CH), 153.1 (Cq), 164.2 (C=O); FTIR (ATR, cm^{-1}): *v* 3314 (N-H, secondary amide), 2953 (C-H, aromatic), 1662 (C=O), 1597 (N-H bend, secondary amide), 825 (C-H oop, aromatic); Found MS (ES, negative mode) [M−H]+ 278.06 $C_{19}H_{20}NO$, requires 278.38. Anal. Calculated for $C_{19}H_{21}NO$: C, 81.68; H, 7.58; N, 5.01; Found: C, 79.87; H, 7.17; N, 5.96.

3-(4-*tert*-butylphenyl)-N-(4-methoxyphenyl) acrylamide (6b2)

Brown solid (0.357g, 96.2%), m.p.175 ˚C [31], compound **6b2** was prepared from the reaction of 4-*tert*-butylcinnamic acid (0.41g, 2.0 mmol) with 4-methoxyaniline (0.25g, 2 mmol) in the same manner as described in Scheme 1. Data analysis: ^{1}H NMR (DMSO-d_6, 400 MHz): δ_H ppm, 10.09 (1H, s, NH), 7.62-7.65 (2H, d, *J*= 12.00 Hz, H-ar), 7.52-7.56 (3H, t, *J*= 8.00, 8.00 Hz, H-ar), 7.45-7.47 (2H, d, *J*= 8.00 Hz, H-ar), 6.91-6.93 (2H, d, *J*= 8.00 Hz, H-ar), 6.76-6.80 (1H, d, *J*= 16.00 Hz, CH), 3.74 (3H, s, CH_3), 1.28 (9H, s, 3×CH_3). ^{13}C NMR (DMSO-d_6, 100 MHz): δ_C ppm, 31.4 (3×CH_3), 35.0 (Cq), 55.6 (OCH_3), 114.4 (2×CH-ar), 121.1 (2×CH-ar), 122.0 (=CH), 126.3 (2×CH-ar), 127.9 (2×CH-ar), 132.5 (Cq), 133.0 (Cq), 139.9 (=CH), 152.9 (Cq), 155.7 (C-O), 163.7 (C=O); FTIR (ATR, cm^{-1}): *v* 3311 (N-H, secondary amide), 2954 (C-H, aromatic), 1660 (C=O), 1597 (N-H bend, secondary amide), 825 (C-H oop, aromatic); Found MS (ES, negative mode) [M−H]+ 308.17 $C_{20}H_{22}NO_2$, required 308.41. Anal. Calculated for $C_{20}H_{23}NO_2$: C, 77.64; H, 7.49; N, 4.53; Found: C, 78.85; H, 7.32; N, 5.31.

3-(4-*tert*-butylphenyl)-N-(4-methylphenyl) acrylamide (6b3)

Yellow solid powder (0.541g, 92.3%), m.p.135 ˚C, compound **6b3** was prepared from the reaction of 4-*tert*-butylcinnamic acid (0.41g, 2.0 mmol) with 4-methylaniline (0.21g, 2.0 mmol) in the same manner as described in Scheme 1. Data analysis: ^{1}H NMR (400 MHz. DMSO-d_6): δ_H ppm, 10.15 (1H, s, NH), 7.57-7.63 (5H, m, H-ar), 7.46 (2H, d, *J*= 8.0 Hz, H-ar), 7.14 (2H, d, *J*= 8.0 Hz, H-ar), 6.82 (1H, d, *J*= 16.0 Hz, CH), 2.27 (3H, s, CH_3), 1.28 (9H, s, 3×CH_3); ^{13}C NMR (100 MHz. DMSO-d_6): δ_C ppm 21.0 (CH_3), 31.4 (3×CH_3), 35.0 (Cq), 119.7 (2×CH-ar), 122.0 (=CH), 126.3 (2×CH-ar), 128.0 (2×CH-ar), 129.6 (2×CH-ar), 132.5 (Cq), 132.7 (Cq), 153.0 (Cq), 140.2 (=CH), 163.9 (C=O); FTIR (ATR, cm^{-1}): *v* 3245 (N-H, secondary amide), 2954 (C-H, aromatic), 1654 (C=O), 1605 (N-H bend, secondary amide), 816 (C-H oop, aromatic); Found MS (ES, negative mode) $[M-H]^+$ 292.17 $C_{20}H_{22}NO$, requires 292.41. Anal. Calculated for $C_{20}H_{23}NO$: C, 81.87; H, 7.90; N, 4.77; Found: C, 83.18; H, 7.64; N, 5.47.

3-(4-*tert*-butylphenyl)-N-(4-chlorophenyl) acrylamide (6b4)

Pale yellow solid powder (0.439g, 69.9%), m.p.135 ˚C, 6b4 was prepared from the reaction of 4-*tert*-butylcinnamic acid (0.41g, 2.0 mmol) with 4-chloroaniline (0.26g, 2.0 mmol) in the same manner as described in Scheme 1. Data analysis: ^{1}H NMR (400 MHz. DMSO-d_6): δ_H ppm, 10.37 (1H, s, NH), 7.75 (2H, d, *J*= 8.9 Hz, H-ar), 7.56-7.61 (3H, m, H-ar), 7.47 (2H, d, *J*= 8.4 Hz, H-ar), 7.39 (2H, d, *J*= 8.9 Hz, H-ar), 6.79 (1H, d, *J*= 15.7 Hz, CH), 1.30 (9H, s, 3×CH_3); ^{13}C NMR (100 MHz. DMSO-d_6): δ_C ppm 31.4 (3×CH_3), 35.0(Cq), 121.2 (2×CH-ar), 126.3 (2×CH-ar), 127.3 (=CH), 128.1 (2×CH-ar), 129.2 (2×CH-ar), 132.3 (2×Cq), 138.8 (Cq), 140.9 (=CH), 153.2 (Cq), 164.3 (C=O); FTIR (ATR, cm^{-1}): *v* 3318 (N-H, secondary amide), 2958 (C-H, aromatic), 1662 (C=O), 1594 (N-H bend, secondary amide), 824 (C-H oop, aromatic); Found MS (ES, negative mode) $[M-H]^+$ 312.12 $C_{19}H_{19}ClNO$, required 312.83. Anal. Calculated for $C_{19}H_{20}ClNO$: C, 72.72; H, 6.42; N, 4.46; Found: C, 72.02; H, 6.26; N, 5.23.

Molecular docking

The in-silico studies (molecular docking) were conducted to investigate the binding interactions of the synthesized compounds towards DENV-2 NS2B/NS3 protease and in search for the best orientation of ligand-protease complex with the lowest free energy of binding (FEB). This step served as a good tool to predict and match the desired binding site, understand possible conformation of the compounds and further clarify the binding interactions in the binding pocket [32].

Preparation of protein

The DENV non-structural protein homology model, NS2B/NS3pro with tetrapeptide inhibitor (Bz-Nle-Lys-Arg-Arg-H) developed by Wichapong and co-worker [33] was used as the protein target. This model was constructed based on DENV2 complex cofactor-protease and by using the crystal structure of NS2B/NS3pro West Nile Virus (WNV) as the template. Meanwhile, the coordinate was taken from DENV2 NS2b/NS3 crystal structure (PDBID: 2FOM). The NS2B/NS3pro was prepared as macromolecule prior to docking by using AutoDock 4.2 (www.autodock.scrips.edu). The protein was initially prepared by removing its inhibitor complex (Bz-Nle-Lys-Arg-Arg-H) by using Discovery Studio Client 2020 (www.accelrys.com). Both protein and ligand were prepared by using AutoDockTools 1.5.7. Kollmann charges were added to the protein structure while Gasteiger charge was added to the ligand. Both prepared protein and ligand were saved in pdbqt format file prior to docking simulation.

Preparation of ligand

The cinnamic acid derivatives were constructed in two-dimensional (2D) and three-dimensional (3D) structures and optimized by using ChemDraw Professional 16.0. The structures were saved in sdf format before being converted to pdb format.

Docking analysis

The docking simulation was performed by using AutoDock 4.2. In the positive control docking, extracted native ligand was re-docked into the binding sites of the protein. Coordinates of the redocked Bz-Nle-Lys-Arg-Arg-H were used as an active site of docking. The grid box size of dimension 60 × 60 × 60 Å in x, y, z coordinates and grid spacing of 0.375 Å were employed to cover the protein active site. The docking of ligands was applied with Lamarckian Genetics Algorithm (GA) search program to generate 100 runs. The re-docked results with the low root mean square deviation (RMSD) value of less than 2.0 Å were applied as the fix parameter for ligands simulation.

ADME properties

Lipinski's rule of five, also known as Pfizer rule is used in the prediction of a new compound to act as a drug molecule based on the membrane permeability and absorbance in the organism. The drug-likeness parameter of compounds was calculated by using a free access online server, SwissADME (http://swissadme.ch/)[27].

Results and Discussion

In this study, eight cinnamic acid amide derivatives were synthesized by the reaction of cinnamic acid with corresponding amine derivatives. EDC.HCl was used as a catalyst to produce cinnamic acid amide derivatives (**6a1-6a4** and **6b1-6b4**) in moderate to excellent yield (56.8-96.2%). Based on the literature, a common approach used to improve the reactivity of carboxyl group towards nucleophilic reagent is by employed a carbodiimide reaction [34, 35, 36]. The proposed plausible mechanism for the formation of cinnamic acid amide derivatives is shown in Figure 2.

The reaction starts with deprotonation of carboxylic group by EDC.HCl to form an active *O*-acylisourea intermediate. The highly electrophilic *O*-acylisourea intermediate is unstable and a good leaving group [35]. This intermediate was resonance stabilized, which then underwent a nucleophilic attack from amine to form an amide bond and removed urea by-product [36]. ^{1}H and ^{13}C NMR spectra of synthesized compounds were available in Supplementary material. The chemical shift for ^{1}H and ^{13}C NMR for **6a1-6a4** and **6b1-6b4** are tabulated in Table 1 and Table 2, respectively. The proton signal for N-H of all synthesized compounds was observed as a broad singlet at the downfield region of δ_H 10.00-10.23 ppm. Compared with the literature, the proton of N-H appeared at more downfield region [29,

30, 31]. This may be due to the temperature, concentration and solvent affecting the chemical shift of amide proton [37]. High intensity singlets of methyl and methoxy moieties in **6a1-6a4** were observed at δ_H 2.26 and 3.74 ppm, respectively. The electronegativity of oxygen attached to CH_3 in the methoxy group caused it to be more deshielded and their chemical shifted downfield, as compared to methyl moieties. A similar pattern was observed in ^{13}C NMR, whereby the signal for methoxy carbonyl appeared at a more upfield region (δ_C 20.9 ppm) than methyl carbonyl (δ_C 55.6 ppm). The chemical shift for C=O of amide appeared at the downfield region, 163.7-164.6 ppm. The position of C-O of methoxy (δ_C 155.6-155.7 ppm) than C-O of hydroxyl was observed at slightly upfield (δ_C 159.6 ppm—159.8 ppm) [37].

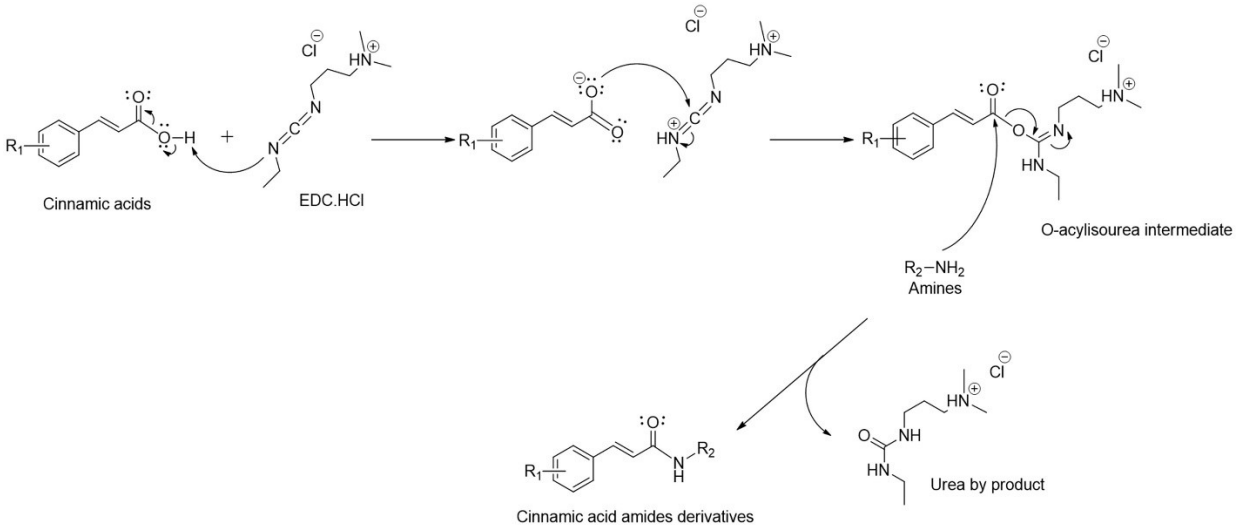

Figure 2. Plausible mechanism for the formation of cinnamic acid amide [35]

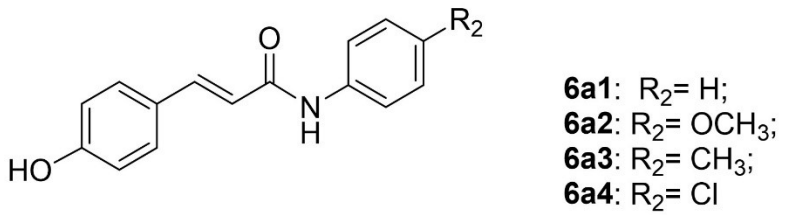

Figure 3. Structure of compounds **6a1-6a4**

Table 1. Chemical shift ^1H and ^{13}C NMR for compounds **6a1-6a4**

Comp.	Chemical Shift ^1H NMR (δ, ppm)				Chemical Shift ^{13}C NMR (δ, ppm)				
	OH	N-H	CH_3	OCH_3	C=O of amide	C-OH	C-OCH_3	CH_3	OCH_3
6a1	9.98 (s)	10.12 (s)	-	-	164.5	159.7	-	-	-
6a2	9.97 (s)	10.00 (s)	-	3.74 (s)	164.1	159.6	155.6	-	55.6
6a3	9.95 (s)	10.01 (s)	2.26 (s)	-	164.3	159.6	-	20.9	-
6a4	10.02 (s)	10.12 (s)	-	-	159.8	159.8	-	-	-

The proton signal for *tert*-butyl moieties in **6b1-6b4** appeared as singlet at δ_H 1.28 to 1.30 ppm, corresponding with literature [31]. The presence of three methyl groups in the moieties caused it to be more shielded and upfield compared to methoxy (δ_H 3.74 ppm) and single methyl moieties (δ_H 2.27 ppm) [37]. The same trend for the peak of moieties position was observed in ^{13}C NMR. The presence of carbon signal

between δ_C 34.9 to 35.0 ppm observed in ^{13}C NMR for **6b1-6b4**, and it is absence for **6a1-6a4**. This peak indicated the presence of quaternary carbon (Cq) of *tert*-butyl moieties presence in **6b1-6b4**. The chemical shift of proton and carbon for all compounds is very small, except for **6a4** and **6b4**. The proton signal for NH and carbon signal for carbonyl of amide in both **6a4** and **6b4** slightly shifted more downfield compared to other compounds. This might be due to the presence of an electronegative Cl at the para position of the aromatic ring, which caused an anisotropic effect on the ring and thus deshielded the proton of amide attached to the ring. Though the anistropic field diminishes with distance, the presence of the oxygen in the amide may also cause the NH proton to be more deshielded [37].

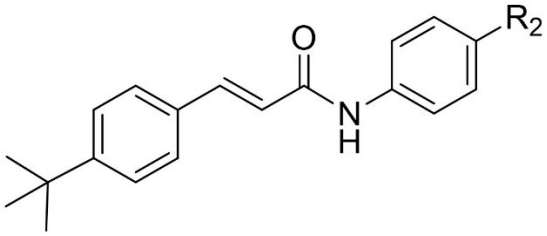

6b1: R_2= H;
6b2: R_2= OCH_3;
6b3: R_2= CH_3;
6b4: R_2= Cl

Figure 4. Structure of compounds **6b1-6b4**

Table 2. Chemical shift ^1H and ^{13}C NMR for compounds **6b1-6b4**

Comp.	Chemical Shift ^1H NMR (δ, ppm)				Chemical Shift ^{13}C NMR (δ, ppm)					
	$C(CH_3)_3$	N-H	CH_3	OCH_3	C=O of amide	$C(CH_3)_3$	Cq of $C(CH_3)_3$	C-OCH_3	CH_3	OCH_3
6b1	1.30 (s)	10.23 (s)	-	-	164.2	31.4	35.0	-	-	-
6b2	1.28 (s)	10.09 (s)	-	3.74 (s)	163.7	31.4	35.0	155.7	-	55.6
6b3	1.28 (s)	10.15 (s)	2.27 (s)	-	163.9	31.4	34.9	-	20.9	-
6b4	1.30 (s)	10.37 (s)	-	-	164.3	31.4	35.0	-	-	-

The FTIR spectrum of major functional groups for **6a1-6a4** and **6b1-6b4** are portrayed in Table 3. The absorption band of N-H bending vibration stretching for secondary amide was reported to generally appear at the range of 3370 to 3170 cm^{-1} [38]. The FTIR spectrum of synthesized compounds featured the absorption band of N-H stretching vibration at 3367 to 3245 cm^{-1} and the absorption band of N-H bending appears around 1594 to 1605 cm^{-1}, which implying the presence of secondary amine in the structure [37]. The high intensity of bands was due to the combination of N-H bending band with C-N stretching band. The presence of O-H in **6a1-6a4** could be observed by the presence of a broad O-H band within the range of 3022 to 3112 cm^{-1} [29]. A strong band of carbonyl C=O of amide stretching was observed around 1654 to 1662 cm^{-1}, corresponding with literature [29]. A prominent out-of-plane C-H bending vibrations band appeared at 808 to 869 cm^{-1} for all compounds attributed to a para-disubstituted aromatic compound, which were in rapport with its structures [37]. The spectral of compounds obtained agreed with the proposed structure.

Both theoretical values of synthesized compounds for MS and CHN analysis were calculated using ChemDraw Ultra 12.0. An electron spray ionization mass spectrometer (ESI) in negative mode was used to measure the mass-to-charge ratio (m/z) of the synthesized compounds in this study. The experimental m/z for all compounds agreed with the theoretical value. The elemental composition of a synthesized compound, including carbon, hydrogen, and nitrogen (CHN), provides essential information for chemical identification [39]. This study aimed to determine the molecular formula of **6a1-6a4** and **6b1-6b4** in the respect of theoretical versus the experimental results. However, the experimental results obtained show slightly different from the theoretical value. The percentage weight of carbon for **6a1**, **6a2**, and **6b1-6b4** varied slightly from the theoretical value by -1.75 to 2.91%. While the difference in nitrogen percentage from the theoretical value for **6a1** and **6b1-6b4** ranged

from -0.96 to 0.61%. These discrepancies may be attributed to the presence of solvents, which contribute to the calculation of weight percentage of experimental value. The theoretical values of oxygen showed good agreement with the experimental results for all compounds. However, the slight difference observed in the experimental nitrogen value compared to the theoretical value was maybe due to the presence of oxygen, leading to the generation of nitrogen oxide and resulting in a lower yield of nitrogen. It has also been suggested that the degree of variability in elemental result may be due to difference in the instrumental methods used for quantifying each element [40]. The data of CHN analysis are tabulated in Table 4.

Table 3. The IR absorption peaks for the synthesized compounds (**6a1-6a4** and **6b1-6b4**)

Group	Wavenumber (ν, cm^{-1})					
	N-H (secondary amide)	**OH (phenol)**	**C-H (aromatic)**	**C=O**	**N-H bend (secondary amide)**	**Out-of-plane C-H (aromatic)**
6a1	3317	3022	2922	1651	1599	821
6a2	3328	3066	2946	1654	1598	820
6a3	3250	3012	2920	1653	1598	816
6a4	3367	3112	2925	1662	1594	826
6b1	3314	-	2953	1662	1594	825
6b2	3311	-	2954	1660	1597	825
6b3	3245	-	2954	1654	1605	816
6b4	3318	-	2958	1662	1594	824

Table 4. The CHN data for the synthesized compound (**6a1-6a4** and **6b1-6b4**)

Element	Carbon		Hydrogen		Nitrogen	
	Theory (%)	**Experimental (%)**	**Theory (%)**	**Experimental (%)**	**Theory (%)**	**Experimental (%)**
6a1	75.30	73.55	5.48	5.51	5.85	5.24
6a2	71.36	68.45	5.61	5.79	5.20	4.79
6a3	75.87	76.03	5.97	5.59	5.53	5.31
6a4	65.82	65.72	4.42	4.83	5.12	4.75
6b1	81.68	79.87	7.58	7.17	5.01	5.96
6b2	77.64	78.85	7.49	7.32	4.53	5.31
6b3	81.87	83.18	7.90	7.64	4.77	5.47
6b4	72.72	72.02	6.42	6.23	4.46	5.23

In the positive control docking, the center of the grid box was determined by the center of Bz-Nle-Lys-Arg-Arg-H at 23.038, 3.372, -0.316 in the x, y and z coordinates, respectively. The Lamarckian genetic algorithm was employed with the covalent map parameter to constrain the molecular geometry of peptide inhibitor [41, 42].

The internal validation was done by re-docking tetrapeptide inhibitor (Bz-Nle-Lys-Arg-Arg-H) with RMSD value in the range of 1.5-2.0 Å, depending on ligand size, which indicating that the docking was able to reproduce native conformation [43]. The redocked tetrapeptide inhibitor to DENV2 NS2B/NS3pro was observed to have a similar conformation with an initial pose of the inhibitor with RMSD value 1.98 Å, as illustrated in Figure 5. The docking parameter obtained was utilized in docking simulations of ligand-DENV2-NS2b/NS3 protease study by using the synthesized compounds as ligand.

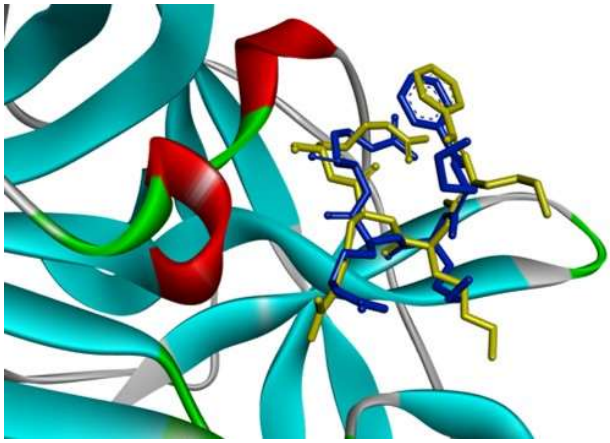

Figure 5. The overlay of the redocked Bz-Nle-Lys-Arg-Arg-H to DENV2 NS2B/NS3pro with RMSD of 1.61 Å Yellow: original; blue docked ligand conformation

The ligand-protein docking results based on free energy of binding (FEB) values and detailed type of interactions that occurred between the ligands and protease are shown in Table 5. Compounds with the lowest FEB were considered to have the strongest binding affinity towards DENV2 NS2b/NS3pro. All docked compounds displayed positive interaction with NS2b/NS3pro, with a binding energy of less than the peptide inhibitor. Generally, the difference between compounds **6a1-6a4** and **6b1-6b4** was the substitutes at the *para* position in the aromatic ring. The aromatic system with *para*-substituent with high electron density was reported to exhibit good activity against DENV2 NS2b/NS3 [18]. The *para*-substituted compounds possess an advantage in molecular interaction due to their optimal conformation, favorable electrostatic interactions, lower steric hindrance, π-π stacking and hydrophobic complementary [44].

Among the eight docked compounds, ligands with *tert*-butyl substituents had the lowest free binding energies, ranging from -6.69 kcal/mol to -7.72 kcal/mol. Compounds **6b2** and **6b3** were the top two hit compounds which showed the best result with minimum FEB values of -7.72 kcal/mol and -7.26 kcal/mol, respectively. The greater negative score binding free energy indicated a stronger binding affinity between the compound and enzyme, suggesting that the compounds have a higher probability of biological activity [45, 46]. The detailed ligand-binding site interaction in 2D structural views of compounds **6b2** and **6b3** are shown in Figure 6.

Table 5. The free energy of binding (FEB) of synthesized compounds

Compound	Free Binding Energy (kcal/mol)	Interaction	Type of Interaction	Bond Distance (Å)
6a1	-6.54	HIS B:51	H-Bond	2.07
		VAL B:52	π-Alkyl	5.35
		ASP B:129	H-Bond	1.92
		PHE B:130	H-Bond	2.47
		PRO B:132	H-Bond	4.17
		TYR B:161	π-π Stacked	1.79
6a2	-6.65	ILE B:36	π-Alkyl	3.89
		HIS B:51	H-Bond	2.03
		VAL B:52	π-Alkyl	5.36
		ASP B:129	H-Bond	1.88
		PHE B:130	H-Bond	2.56
		PRO B:132	H-Bond	1.91

		TYR B:161	π-π Stacked	4.13
6a3	-6.90	ILE B:36	Alkyl	5.37
			π-Alkyl	3.98
		VAL B:52	π-Alkyl	5.25
		ASP B:129	H-Bond	2.61
		PHE B:130	H-Bond	2.05
		PRO B:132	H-Bond	1.78
		TYR B:161	π-π Stacked	4.69
6a4	-7.03	ILE B:36	Alkyl	4.42
		HIS B:51	H-Bond	2.09
		VAL B:52	π-Alkyl	5.39
		ASP B:129	H-Bond	1.96
		PHE B:130	H-Bond	2.53
		PRO B:132	H-Bond	1.77
		TYR B:161	π-π Stacked	4.09
6b1	-6.69	HIS B:51	π-Cation	4.41
			π-π Stacked	3.73
		GLY B:151	H-Bond	2.06
6b2	-7.72	TRP B:50	π-Alkyl	5.08
		VAL B:72	Alkyl	4.82
		ILE A:86	Alkyl	4.03
		GLY B:153	H-Bond	2.06
		VAL B:154	π-Sigma	3.70
			Alkyl	4.21
			H-Bond	1.89
		VAL B:155	π-Alkyl	5.04
			Alkyl	5.13
6b3	7.26	TRP B:50	π-Alkyl	5.18
		HIS B:51	π- π Stacked	4.36
		ASP B:75	π-Anion	4.00
		GLY B:153	H-Bond	2.13
		TYR B:161	π- π Stacked	4.03
			π-Alkyl	4.00
6b4	-7.16	TRP B:50	π-Alkyl	5.19
		HIS B:51	π- π Stacked	4.38
		ASP B:75	π-Anion	4.00
		GLY B:153	H-Bond	2.14
		TYR B:161	π-Alkyl	4.14
			π- π Stacked	4.07
Positive control (Bz-Nle-Lys-Arg-Arg-H)	-5.21	-	-	-

Aside from the catalytic residue, involvement of amino acid residues, such as Val52, Val72, Pro132 and Tyr150 (in the NS3 domain) and Ile86, Gly151, Gly153 (in the NS2B cofactor domain) in ligand-protein interaction helped to contribute to the binding [47, 48]. The *tert*-butyl moiety of **6b2** and **6b3** formed an alkyl and π-alkyl interaction with Trp50 and Val72. Compound **6b2** and DENV2 NS2B/NS3pro complex showed H-bond interaction between O of amide with Gly153 and O of methoxy group with Val155. The methoxy group and *tert*-butyl substituents showed non-bonding interaction of alkyl and π-alkyl with Val72, Ile86 and Trp50. Although no interaction occurred with the catalytic triad residues (His51, Ser135 and Asp75), the binding of 6b2 to the active site of protease was stabilized through one H-bond with Gly153 and the support of non-covalent interaction with Trp50, Val72, Ile86, Val154, and Val155. [47].

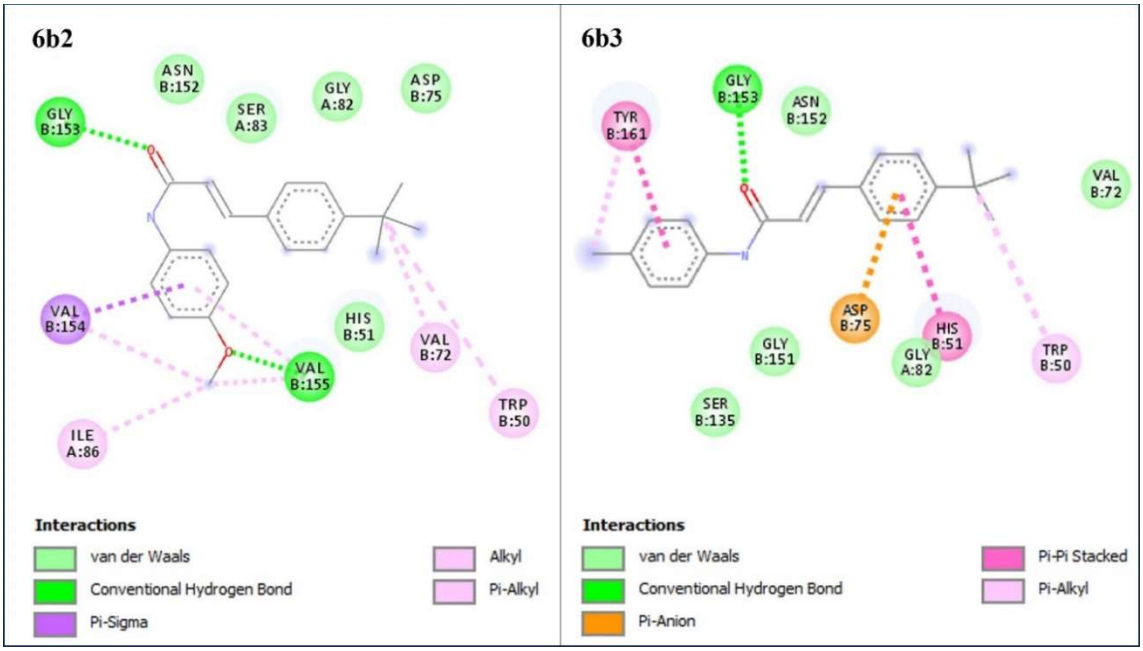

Figure 6. 2D protein-ligand interaction of **6b2** and **6b3** against NS2B/NS3pro

The docked pose showed that compound **6b3** formed one hydrogen bond interaction with Gly153 of NS3. The phenyl ring forms π-π stacking and π-anion with catalytic triad His51 and Asp75, respectively. The ligand also formed an interaction with Tyr161 and Trp50. Even though 6b3 interacted with two catalytic triad residues, its binding free energy was slightly higher than **6b2**. This might be due to a lack of non-covalent interaction to improve binding affinity for **6b3** as compared to **6b2**. The strength of hydrogen bonding increases as it gets closer to the geometry [49]. The distance of H-bond interaction between ligand-protein for **6b2** was 2.06 Å and 1.89 Å, which is less than in **6b3**. This made 6b2 bind more firmly to the protein, and thus its FEB value was more negative. ADME (absorption, distribution, metabolism, and excretion) describes the internal process of drug movement throughout the body. The ADME results for physiochemical properties of compounds **6b2** and **6b3** are tabulated in Table 6. The lipophilicity of drug candidate molecules was determined by the ratio of partition coefficient of n-octanol and water (log $P_{o/w}$), and its value should be less than 5 for it to have good absorption [50]. The number of H-Bond donors (HBD) needed to be less than 5 and H-Bond acceptors (HBA) should be less than 10 [51, 52].

Table 6. Physiochemical properties of compounds **6b2** and **6b3**

Properties	**The Top Two Hit Compounds**	
	6b2	**6b3**
Log S	-5.06	-5.29
Solubility	Moderately soluble	Moderately soluble
Heavy atoms	23	22
Number of rotatable bonds	6	5
Number of H-bond acceptors (HBA)	2	1
Number of H-bond donors (HBD)	1	1
Log $P_{o/w}$	3.51	3.45
TPSA ($Å^2$)	38.33	29.10

According to Kenny, elimination of HBD could lead to small increases in lipophilicity and improved permeability of the molecule [53]. Topological polar surface area (TPSA) score for a drug should be less than 130 $Å^2$, the solubility of the molecule log S, should not exceed more than 6 [54]. Both compounds were found to be within the acceptable range of drug-likeness parameter of compounds. An excessively high lipophilicity can contribute to the immobilization of the compound within a given layer [55]. Based on the ADME results, **6b2** and **6b3** were suggested to have moderate permeability against the cell barrier to be distributed to molecular targets.

Conclusion

In conclusion, the present work has demonstrated that eight cinnamic acid derivatives were successfully synthesised through the reaction of cinnamic acid with various amines. The molecular studies revealed a significant molecular interaction between the synthesised compounds and DENV2 NS2B/NS3 protease, which indicated their potential activity as a protease inhibitor. It was observed that both compounds with a hydroxyl group and *tert*-butyl substituents displayed a high binding affinity and good interaction with DENV-2 NS2B/NS3 serine protease as compared to the tetrapeptide inhibitor (Bz-Nle-Lys-Arg-Arg-H).

Amongst the eight compounds, **6b2** and **6b3** showed the best results with the minimum value of FEB. Compound **6b2** (-7.72 kcal/mol) exhibited the lowest FEB as compared to compound **6b3** (-7.26 kcal/mol). The number of ligand-protein interactions and their distance have an important influence on the FEB value. Although hydrogen bond is deemed as important in enhancing the ligand-protein binding affinity, the bond distance, and another types of interaction, such as non-bonding interaction could also help to compensate for enhancing the binding stability and binding affinity of the ligand. The ADME results showed that compounds **6b2** and **6b3** have the potential to serve as lead molecules and be developed as inhibitors for DENV2 NS2B/NS3pro to treat dengue. However, further validation through in-vitro and in-vivo analysis is required.

Acknowledgement

The authors would like to acknowledge the financial support from Ministry of Higher Education, Malaysia for Fundamental Research Grant Scheme FRGS 59580 (FRGS/1/2019/STG01/UMT/02/4). A sincere thanks to the Faculty of Science and Marine Environment, Universiti Malaysia Terengganu (UMT) for providing the research facilities.

References

1. Bhatt, S., Gething, P. W., Brady, O.J., Messina, J. P., Farlow, A. W., Moyes, C. L., Drake, J. M., Brownstein, J. S., Hoen, A. G., Sankoh, O., Myers, M. F., George, D. B., Jaenisch, T., Wint, G. R., Simmons, C. P., Scott, T. W., Farrar, J. J., and Hay, S. I. (2021). The global distribution and burden of dengue. *Nature*, 496 (7446): 504-507.
2. World Health Organization (WHO). (2019). Dengue and severe dengue. https://www.who.int/newsroom/fact-sheets/detail/dengue-and-severe-dengue. [Access online 25 November 2020].
3. Bere, A. W., Mulati, O., Kimotho, J., and Ng'ong'a, F. (2021). *Carica papaya* leaf extract silver synthesized nanoparticles inhibit dengue type 2 viral replication in vitro. *Pharmaceuticals*, 14(8): 718.
4. Wong, P. F., Wong, L. P., and AbuBakar, S. (2020). Diagnosis of severe dengue: challenges, needs an d opportunities. *Journal of Infection and Public He alth*, 13: 193-198.
5. Khan, M., Altamish, M., Samal, M., Srivastav, V., Insaf, A., Parveen, F., Akhtar, J., Krishnan, A., and Ahmad, S. (2023). Antiviral potential of traditional unani medicine with special emphasis on dengue: A review. *Current Drug Targets*, 24(17): 1317-1334.
6. Martin-Tanguy, J., Cabanne, F., Perdrizet, E., and Martin, C. (1978). The distribution of hydroxycinnamic acid amides in flowering plants. *Phytochemistry,* 17(11): 1927-1928.
7. Mohammadzadeh, S., Shariatpanahi, M., Hamedi, M., Ahmadkhaniha, R., Samadi, N., and Ostad, S. N. (2007). Chemical composition, oral toxicity, and antimicrobial activity of Iranian propolis. *Food Chemistry,* 103(4): 1097-1103.
8. Clifford, M. N. (1999). Chlorogenic acids and other

cinnamates – nature, occurrence, and dietary burden *Journal of the Science of Food and Agriculture*, 79(3): 362-372.

9. Fattah, A., Firdaus, and Soekamto, N. H. (2020). Synthesis of cinnamic acid derivative and bioactivity as an anticancer based on result quantitative structure relationship (QSAR) analysis. *Indonesia Chimica Acta,* 13(1): 23-29.
10. Seck, R., Mansaly, M., Gassama, A., Cave, C. and Cojean, S. (2018). Synthesis and antimalarial activity of cinnamic acid derivatives. *Journal of Chemical and Pharmaceutical Research,* 10(11): 1-8.
11. Silva, R. H., Andrade, A. C., Nóbrega, D. F., Castro, R. D. D., Pessôa, H. L., Rani, N., and de Sousa, D. P. (2019). Antimicrobial activity of 4-chlorocinnamic acid derivatives. *BioMed Research International,* 2019(1): 3941242.
12. Lee, S., Han, J. M., Kim, H., Kim, E., Jeong, T. S., Lee, W. S., and Cho, K. H. (2004). Synthesis of cinnamic acid derivatives and their inhibitory effects on LDL-oxidation, acyl-CoA:cholesterol acyltransferase-1 and -2 activity, and decrease of HDL-particle size. *Bioorganic and Medicinal Chemistry Letters*, 14(18): 4677-4681.
13. Gao, X., Tang, J., Liu, H., Liu, L., Kang, L., and Chen, W. (2018). Structure–activity relationship investigation of *tert*iary amine derivatives of cinnamic acid as acetylcholinesterase and butyrylcholinesterase inhibitors: compared with that of phenylpropionic acid, sorbic acid and hexanoic acid. *Journal of Enzyme Inhibition and Medicinal Chemistry*, 33(1): 519-524.
14. Zhang, J., Yang, J., Chang, X., Zhang, C., Zhou, H., and Liu, M. (2012). Ozagrel for acute ischemic stroke: A metaanalysis of data from randomized controlled trials. *Neurological Research*, 34(4): 346-353.
15. Rees, C.R., Costin, J.M., Fink, R.C., McMichael, M., Fontaine, K.A., Isern, S., and Michael, S. (2008). In vitro inhibition of dengue virus entry by p-sulfoxy-cinnamic acid and structurally related combinatorial chemistries. *Antiviral Research,* 80(2): 135-42.
16. Ahmad, N., Fazal, H., Ayaz, M., Abbasi, B. H., Mohammad, I., and Fazal, L. (2011). Dengue fever treatment with *Carica papaya* leaves extracts. *Asian Pacific Journal of Tropical Biomedicine*, 1(4): 330-333.
17. Ganji, L. R., Gandhi, L., Musturi, V., and Kanyalkar, M. (2020). Design, synthesis, and evaluation of different scaffold derivatives against NS2B-NS3 protease of dengue virus. *Medicinal Chemistry Research*, 30: 285-301.
18. Nitsche, C., Steuer, C., and Klein, C. D. (2011). Arylcyanoacrylamides as inhibitors of the dengue and West Niles virus proteases. *Bioorganic & Medicinal Chemistry*, 19(24): 7318-7337.
19. Aravapalli, S., Lai, H., Teramoto, T., Alliston, K. R ., Lushington, G. H., Ferguson, E. L., Padmanabha n, R., and Groutas, W. C. (2012). Inhibitors of den gue virus and West Nile virus proteases based on t he aminobenzamide scaffold. *Bioorganic & Medicinal Chemistry*, 20(13): 4140-4148.
20. Steuer C, GeGe C, Fischl W, Heinonen KH, Barten schlager R, Klein CD. (2011). Synthesis and biolog ical evaluation of α-ketoamides as inhibitors of the Dengue virus protease with antiviral activity in cell -culture. *Bioorganic & Medicinal Chemistry*, 19: 4 067-4074.
21. Leung, D., Schroder, K., White, H., Fang, N. X., Stoermer, M. J., Abbenante, G., Martin, J. L., Young, P. R., and Fairlie, D. P. (2001). Activity of recombinant dengue 2 virus NS3 protease in the presence of a truncated NS2B co-factor, small peptide substrates, and inhibitors. *Journal of Biological Chemistry*, 276(49): 45762-45771.
22. Chiu, M. W., Shih, H. M., Yang, T. H., and Yang, Y. L. (2007). The type 2 dengue virus envelope protein interacts with small ubiquitin-like modifier-1 (SUMO-1) conjugating enzyme 9 (Ubc9). *Journal of. Biomedical Science*, 14(3): 429-444.
23. Chen, W. N., Loscha, K. V., Nitsche, C., Graham, B., and Otting, G. (2014). The dengue virus NS2B-NS3 protease retains the closed conformation in the complex with BPTI. *FEBS Letters*, *588*(14): 2206-2211.
24. Tomlinson, S., Malmstrom, R., and Watowich, S. (2012). New approaches to structure-based discovery of dengue protease inhibitors. *Infectious Disorder - Drug Targets*, *9*(3): 327-343.
25. Preugschat, F., Yao, C. W., and Strauss, J. H. (1990).

In vitro processing of dengue virus type 2 nonstructural proteins NS2A, NS2B, and NS3. *Journal of Virology*, 64(9): 4364-4374.

26. Benet, L. Z., Hosey, C. M., Ursu, O., and Oprea, T. I. (2016). BDDCS, the rule of 5 and drug ability. *Advanced Drug Delivery Reviews*, 101: 89-98.
27. Daina, A., Michielin, O. and Zoete, V. (2017). SwissADME: A free web tool to evaluate pharmacokinetics, drug-likeness and medicinal chemistry friendliness of small molecules. *Scientific Reports,* **7**: 42717.
28. Chai, T., Zhao, X. B., Wang, W. F., Qiang, Y., Zhang, X. Y., and Yang, J. L. (2018). Design, synthesis of N-phenethyl cinnamide derivatives and their biological activities for the treatment of Alzheimer's disease: Antioxidant, beta-amyloid disaggregating, and rescue effects on memory loss. *Molecules*, 23(10): 2663.
29. Khatkar, A., Nanda, A., Kumar, P., and Narasimhan , B. (2017). Synthesis, antimicrobial evaluation and QSAR studies of p-coumaric acid derivatives. *Arab ian Journal of Chemistry*, 10: S3804-S3815.
30. Vishnoi, S., Agrawal, V., and Kasana, V. K. (2009). Synthesis and structure-activity relationships of su bstituted cinnamic acids and amide analogues: a ne w class of herbicides. *Journal of Agriculture and F ood Chemistry*, *57* (8): 3261-3265.
31. Doherty, E. M., Fotsch, C., Bo, Y., Chakrabarti, P. P ., Chen, N., Gavva, N., Han, N., Kelly, M. G., Kinc aid, J., Klionsky, L., Liu, Q., Ognyanov, V. I., Tami r, R., Wang, X., Zhu, J., Norman, M. H., and Trean or, J. J. S. (2005). Discovery of potent, orally avail able vanilloid receptor-1 antagonists. Structure-acti vity relationship of n-aryl cinnamides. *Journal of M edicinal Chemistry*, 48(1): 71-90.
32. Grinter, S. Z., and Zou, X. (2014). Challenges, applications, and recent advances of protein-ligand docking in structure-based drug design. *Molecules*, 19(7): 10150-10176.
33. Wichapong, K., Pianwanit, S., Sippl, W., and Kokpol, S. (2010). Homology modeling and molecular dynamics simulations of dengue virus NS2B/NS3 protease: Insight into molecular interaction. *Journal of Molecular Recognition*, 23(3): 283-300.
34. Valeur, E., and Bradley, M. (2009). Amide bond formation: Beyond the myth of coupling reagents, *Chemical Society Reviews*, 38: 606-631.
35. Kasprzak A, Zuchowska A, and Poplawska M. (2018). Functionalization of graphene: does organic chemistry matter? *Beilstein Journal of Organic Chemistry*, 14: 2018-2026.
36. Liew, K. M., Tagg, T., and Khairul, W. M. (2019). S ynthesis and characterization of N-analineferrocen ylamides via carbodiimide coupling. *Malaysian Jo urnal of Analytical Sciences*, 23(2): 189-196.
37. Lampman, G. M., Pavia, D. L., Kriz, G. S., and Vyvyan, J. R. (2010). Spectroscopy. International Edition, Brooks/Cole Cengage Learning, Canada; pp 15-198.
38. Brian C. Smith. Spectroscopy - Solution for Materials Analysis (2020). Multimedia Pharma Sciences, US, 35(1): pp. 10-15.
39. Itoh, N., Sato, A., Yamazaki, T., Numata, M., and Takatsu, A. (2013). Determination of the carbon, hydrogen and nitrogen contents of alanine and their uncertainties using the certified reference material l-alanine (NMIJ CRM 6011-a). *Analytical Sciences*, 29: 1209-1212.
40. Kuveke, R. E. H., Barwise, L., van Ingen, Y., Vashisth, K., Roberts, N., Chitnis, S. S., Dutton, J. L., Martin, C. D., and Melen, R. L. (2022). An international study evaluating elemental analysis. *ACS Central Science*, 8(7): 855-863.
41. Morris, G. M., Huey, R., Lindstrom, W., Sanner, M . F., Belew, R. K., Goodsell, D. S., and Olson, A. J. (2009), AutoDock4 and AutoDockTools4: Automat ed docking with selective receptor flexibility. *Journ al of Computational Science,* 30(16): 2785-2791.
42. Bianco, G., Forli, S., Goodsell, D. S., and Olson, A . J. (2016). Covalent docking using autodock: Two -point attractor and flexible side chain methods. *Pr otein Science*, 25(1): 295-301.
43. Hevener, K. E., Zhao, W., Ball, D. M., Babaoglu, K., Qi, J., White, S. W., and Lee, R. E. (2009). Validation of Molecular Docking Programs for Virtual Screening against Dihydropteroate Synthase. *Journal of Chemical Information and Modeling*, 49(2): 44-460.
44. Khalili, N. S. D., Khawory, M. H., Salin, N. H., Zakaria, I. I., Hariono, M., Mikhaylov, A. A., Kamarulzaman, E. E., A Wahab, H., Supratman, U.,

and Nurul Azmi, M. (2024). Synthesis and biological activity of imidazole phenazine derivatives as potential inhibitors for NS2b-NS3 dengue protease. *Heliyon*, 10(2): e24202.

45. Terefe, E. M., and Ghosh, A. (2022). Molecular docking, validation dynamics simulations, and pharmacokinetic prediction of pharmacokinetic prediction of phytochemicals isolated from *Croton dichogamus* against the HIV-1 reverse transcriptase. *Bioinformatics and Biology Insight*, 16: 1179322221125605.
46. Ivona, L. and Karelson, M. (2022). The impact of software used and the type of target protein on molecular docking accuracy. *Molecule*, 27(4): 9041.
47. Thioguanine Hariono, M., Choi, S. B., Roslim, R. F., Nawi, M. S., Tan, M. L., Kamarulzaman, E. E., Mohamed, N., Yusof, R., Othman, S., Abd Rahman, N., Othman, R., and Wahab, H. A. (2019). Thioguanine-based DENV-2 NS2B/NS3 protease inhibitors: Virtual screening, synthesis, biological evaluation and molecular modelling. *PloS one*, *14*(1): e0210869.
48. Purohit, P., Sahoo, S., Panda, M., Sahoo, P. S., and Meher, B. R. (2022). Targeting the DENV NS2B-NS3 protease with active antiviral phytocompounds: Structure-based virtual screening, molecular docking and molecular dynamic simulation studies. *Journal of Molecular Modeling*, 28(11): 365.
49. Anupurath, S., Rajaraman, V., Gunasekaran, S., Krishnan, A., Sreedevi, S. M., Vinod, S. M., Dakshinamoorthi, B. M., and Rajendran, K. (2021). Electrochemical investigation and molecular docking technique on the interaction of acridinedione dyes with water-soluble nonfluorophic simple amino acids. *ACS Omega*, 6: 30932-30941.
50. Lipinski, C. A. (2004). Lead- and drug-like compounds: the rule-of-five revolution. *Drug Discovery: Today Technologies,* 1(4): 337-341.
51. Vishvakarma, V.K., Patel, R., Kumari, K., and Sin gh P. (2017). Interaction between bovine serum alb umin and gemini surfactants using molecular docki ng characterization, *Information Sciences Letters*, 3 (2017): 1-9.
52. Veber, D. F., Johnson, S. R., Cheng, H. Y., Smith, B. R., Ward, K. W., and Kopple, K. D. (2002). Molecular properties that influence the oral bioavailability of drug candidates. *Journal of Medicinal Chemistry*, 45(12): 2615-2623.
53. Kenny P. W. (2022). Hydrogen-bond donors in drug design. *Journal of Medicinal Chemistry*, 65(21): 14261-14275.
54. Khan, S. A., Kumar, S., and Maqsood, A. M., (201 3). Virtual screening of molecular properties and bi oactivity score of boswellic acid derivatives in sear ch of potent anti-inflammatory lead molecule, *Inter national Journal of Interdisciplinary and Multidisc iplinary Studies*, 1: 8-12.
55. Halder, A. K., Moura and Cardeiro, M. N. D. S. (2018). QSAR modelling: A therapeutic patent review 2010-present. *Expert Opinion on Therapeutic Patents*, *28*(6): 467-476.

Malaysian Journal of Analytical Sciences (MJAS)
Published by Malaysian Analytical Sciences Society

FORMULATION AND EVALUATION OF BODY SCRUB USING PINEAPPLE WASTE AS NATURAL EXFOLIATOR

(Formulasi dan Penilaian Skrub Badan Menggunakan Sisa Nanas sebagai Pengelupas Semulajadi)

Nur Aisha Ahmi, and Siti Fatimah Sabran*

Department of Technology and Natural Resources, Faculty of Applied Sciences and Technology, Universiti Tun Hussein Onn Malaysia (Pagoh Campus), Pagoh Higher Education Hub, Muar, 84600, Johor, Malaysia

**Corresponding author: fatimahsb@uthm.edu.my*

Received: 6 January 2024; Accepted: 2 April 2024; Published: 29 June 2024

Abstract

The study explores potential of repurposing pineapple waste which known to contain antioxidants and bromelain as a body scrub to combat increasing amount of pineapple waste generated during pineapple production. The cream body scrub was formulated using varying concentrations of pineapple powder namely S0 (0%), S1 (3.5%), S2 (4.5%), and S3 (5.5%). The resulting formulations were evaluated for their physical and sensorial characteristics, including color, consistency, pH, viscosity, spreadability, foamability, odor, washability, grittiness, irritability, and exfoliation capability. Additionally, an online market survey was also conducted. Analysis showed that S0 had the highest pH value (7.97), viscosity (8120 cP), and spreadability (21411.71g). S1 with the lowest pineapple concentration exhibited the lowest irritancy (6.68) and the highest acceptance of pineapple body scrub with fragrance (6.48) and without fragrance (6.48), while S2 showed the highest acceptance for grittiness (6.45) and washability (7.18). S3 exhibited the highest foamability (2.1 mL within 30 minutes) and was the darkest (L=51.59±2.39) among other samples. The presence of pineapple powder is related to the exfoliation capacity of the body scrub (with a significant correlation, p <0.05). Body scrubs with 3.5% and 4.5% pineapple powder have the highest acceptance among respondents and are recommended for future research development.

Keywords: pineapple, waste, natural exfoliator, formulation, evaluation

Abstrak

Kajian ini meneroka potensi penggunaan semula sisa nanas yang diketahui untuk mengandungi antioksidan dan bromelain sebagai skrub badan untuk menangani peningkatan jumlah sisa nanas yang dihasilkan semasa pengeluaran nanas. Skrub badan krim diformulasikan menggunakan kepekatan serbuk nanas yang berbeza-beza iaitu S0 (0%), S1 (3.5%), S2 (4.5%), dan S3 (5.5%). Formulasi yang terhasil dinilai untuk ciri fizikal dan derianya, termasuk warna, ketekalan, pH, kelikatan, kebolehtebaran, kebolehbuih, bau, kebolehbasuh, kekasaran, kerengsaan, dan keupayaan pengelupasan. Selain itu, tinjauan pasaran dalam talian juga telah dilaksanakan. Analisis menunjukkan bahawa S0 mempunyai nilai pH tertinggi (7.97), kelikatan (8120 cP), dan kebolehtebaran (21411.71g). S1 dengan kepekatan nanas yang paling rendah menunjukkan kerengsaan yang paling rendah (6.68) dan penerimaan skrub badan nanas yang paling tinggi dengan pewangi (6.48) dan tanpa pewangi (6.48), manakala S2 menunjukkan penerimaan yang paling tinggi untuk kekasaran (6.45) dan kebolehbasuh (7.18). S3 mempamerkan kebolehbuih tertinggi (2.1 mL

dalam masa 30 minit) dan merupakan yang paling gelap (L=51.59±2.39) antara sampel lain. Kehadiran serbuk nanas adalah berkaitan dengan keupayaan pengelupasan skrub badan (dengan korelasi yang ketara, p <0.05). Skrub badan dengan serbuk nanas 3.5% dan 4.5% mempunyai penerimaan tertinggi dalam kalangan responden dan disyorkan untuk perkembangan kajian masa hadapan.

Kata kunci: nanas, sisa, pengelupas semula jadi, formulasi, penilaian

Introduction

According to Malaysian Pineapple Industry Board (MPIB), Malaysia has annually produced 400,000 to 600,000 metric tons of pineapple [1], accumulating 137, 550 tons of peel waste [2]. The waste has caused vast amount of pollution due to poor agro-waste management. The common way to manage the agro-waste is by discarding the waste via open burning, which releases harmful pollutants into the atmosphere, aggravating soil pollution, water pollution, and food contamination. Besides, waste is also dumped into the landfills, creating a breeding environment for disease outbreaks due to the presence of pests such as rats and flies. Due to the problems, alternative ways to reduce agro-waste from pineapple and its environmental impact are at urge. Pineapple waste has shown to contain high quantities of bioactive chemicals with antioxidant qualities and serves as a significant reservoir of bromelain protein [3]. The antioxidative nature of bromelain additionally aids in promoting skin health by combating oxidative stress [4]. Therefore, utilizing pineapple waste for a natural exfoliating body scrub is an excellent way to repurpose waste and reduce landfill contributions.

Body scrub is a type of physical exfoliator used to exfoliate dead skin and keep the pores of the skin clean from oil and grime [5]. Exfoliator helps boost blood circulation, thus providing revitalized and healthy-looking skin. Physical exfoliators can be sourced from natural exfoliants or synthetic exfoliants. Natural exfoliants refer to a list of non-exhaustive products such as seeds, nut shells, and grains, whereas synthetic exfoliators consist of particles such as polyethylene or polypropylene beads. However, synthetic exfoliators have caused microplastic pollution as they enter streams of waste water [6] and rise concern to marine ecosystems [7]. Hence, natural exfoliants made from pineapple peel and core would be more sustainable for the environment. The objectives of the study were to conduct market survey for development of pineapple body scrub, to formulate body scrub from the waste parts of pineapple which are peel and core and to evaluate its parameters, such as color, consistency, pH, viscosity, spreadability, foamability, odor, washability, grittiness, and irritability along with its exfoliation capability.

Materials and Methods

Formulation of pineapple body scrub

Pineapple wastes (peel and core) were collected from restaurants and fruit stalls nearby Muar, Johor. The pineapple wastes were washed and cut into smaller pieces [8]. The cut pineapples were dried using oven for 20 hours at 70 ℃. After that, the samples were ground and then sieved using sieved shaker (500 microns) to obtain uniform size of pineapple powder. The pineapple powder was weight to produce different concentrations which are 3.5g in 100g base cream (3.5%), 4.5g in 100g base cream (4.5%), and 5.5g in 100g base cream (5.5%). Base cream of pineapple body scrub was formulated with references to a previous study conducted by Hendrawati et al. [9]. Table 1 shows the formulation ingredients with percentage (%),

Table 1. Formulation ingredients for base scrub

Material	Weight (%)
Glycerin	15
Stearic acid	12
Cetyl alcohol	4
Trietanolamine	3
Isopropyl	2
Propylparabene	0.02
Distilled water, up to	100

The oil phase of the ingredients which are stearic acid and cetyl alcohol were mixed and melted in a beaker until it reached 70 ℃ in water bath. Then, as it was completely melted, the temperature was lowered to 65 ℃. As the temperature dropped, isopropyl and propyl

paraben were added to the oil phase mixture while stirring until it was homogenous. Then, the water phase ingredients such as glycerin and water were mixed and heated at 80 ℃ in a different beaker. It was then being cooled to 65 ℃ while triethanolamine was being slowly added. Both of the oil and water phase were mixed using hand mixer until a fine cream emulsion was produced. After that, the base cream was left to cool until the temperature dropped to 40 ℃ [9]. Different concentrations of pineapple powder which are 3.5%, 4.5%, and 5.5% were then added to the 100g base cream respectively with continuous stirring. The body scrubs were kept in airtight container. The body scrubs were labeled based on their concentrations as S0 (0%), S1 (3.5%), S2 (4.5%) and S3 (5.5%).

Evaluation of pineapple body scrub

The performance of the body scrubs was evaluated in two categories which were physical and sensorial characterization. The color, consistency, pH, viscosity, spreadability, and foamability for physical characterization, while odor, washability, grittiness, irritability, and exfoliation capability for sensorial characterization. The parameters of body scrubs were compared to the standard, previous study or commercialized product for a particular evaluation. In sensorial characterization, the acceptance level of body scrubs for odor with and without fragrance, grittiness, washability, irritability and overall acceptability were evaluated using 9-point hedonic scale, where 1 (extremely dislike), 2 (dislike very much), 3 (moderately dislike), 4 (slightly dislike), 5 (neither like nor dislike), 6 (slightly like), 7 (moderately like), 8 (like very much), and 9 (extremely like). The results were expressed in mean.

Color

In physical characterization, the color of the body scrubs was observed in petri dish at room temperature using MiniScan EZ portable spectrophotometer for eight days with two days interval. The results were displayed in L*a*b* reading, where L*, expressed lightness (100-0), a*, show the red-green field, where positive values for red, while negative values for green, (-128, +127), while *b, shows the blue-yellow field, where positive values for yellow, while negative values for green (-128, +127) [10]. The change of color was calculated using equation below.

$$\Delta E_{ab} = \sqrt{(L_2 - L_1)^2 + (a_2 - a_1)^2 + (b_2 - b_1)^2} \quad (1)$$

where, 0< ΔE < 1 = colour difference cannot be noticed, 1< ΔE < 2 = colour difference can be noticed by experienced observer, 2< ΔE < 3.5 = colour difference can be noticed by unexperienced observer, 3.5< ΔE < 5 = clear difference in colour can be noticed, and 5< ΔE = two different colours can be noticed

Consistency

The consistency was tested under microscope with 40x magnification for three parts of the body scrub which were the top, middle and bottom.

pH

The pH of the scrub was measured by utilizing Eutech Instruments pH 700 pH meter using a 1:9 ratio between sample and distilled water.

Viscosity

The viscosity was measured using Brookfield DV3T Rheometer, where the result would be displayed as centipoise (cP).

Spreadability

Spreadability was measured using a texture analyzer with stable micro systems, where a smaller force indicates higher spreadability [11].

Foamability

The foamability was measured by mixing one gram (g) of body scrub with five milliliters of water and observed for 30 minutes.

Irritability

The scrubs were applied to the skin and left on for 10 minutes. The irritability of the body scrub assessed using a 9-point hedonic scale, where a greater number signifies lesser irritability.

Exfoliation capability

The exfoliation capability of body scrubs was also

evaluated by calculating the colour changes before and after applying the body scrubs [12] using the Equation 1 above. The exfoliation capability of body scrub S0, S1, S2 and S3 was observed using the SPSS application one-way ANOVA test, where the factor observed was the concentration of pineapple powder. Meanwhile, other parameters were observed using descriptive analysis, where the results were expressed in mean or mean ± standard deviation.

Market survey of pineapple body scrub

An online market survey was conducted to gain information about market trends [13]. The online survey was performed through a Google Form questionnaires and distributed randomly through the WhatsApp application, which was expected to receive 100 to 200 responses, and the results obtained were analyzed and tabulated. The questionnaires consisted of three parts, Part 1: Demographic information, Part 2: Feedback on existing product, and Part 3: Interest and preferability in body scrub.

Results and Discussion

Pineapple body scrub product

The fresh pineapple that was obtained weighed about 2.86 kilograms (kg) while the dried and grinded pineapple was 336.78g. The moisture content of the dried pineapple was 11%. The moisture content of dried fruits should be around 10% to 15% to ensure safe storage [14]. The cream form of base cream was formulated and the concentration was mixed resulting to four concentrations, S0 (0%), S1 (3.5%), S2 (4.5%) and S3 (5.5%). Figure 1 shows the samples of body scrub.

Figure 1. Samples of body scrub

Analysis of body scrub product

In physical characterization, the color of body scrubs was determined using MiniScan EZ portable spectrophotometer, and S3 has the darkest color (L*= 51.59 ± 2.39) among all the other body scrubs, and it also has the highest color difference from the start and the end of the experiments with 5.28 differences. This is because, color formed usually affected by color of its constituent, therefore as S3 has the highest concentration of pineapple powder, it has the darkest color, while the lower pineapple concentration, the lighter the color. S0 has the lightest color (L= 68.49 ± 5.30) as it has no pineapple powder, and the base cream is quite white in color. Next, the consistency of body scrubs was observed after being left for a week, the result shows that all body scrubs were homogenous and consistent, as no separation of formulation was observed. The pH of body scrubs were examined in previous study to be around 6.29 to 7.61 [15]. The pH of body scrubs in this experiment ranges from 7.16 to 7.97. However, pH levels of all formulations still fell within the acceptable range for cosmetic products as outlined in accordance with SNI 16-4339-1996 which is from 4.5 to 8.0.

Next, the viscosity of body scrubs is in line ranges from 4660cP (S1) to 8120cP (S0), which is slightly lower than previous study [16], however still in line with SNI 16-4399-1996 standard for skin care which is about 2000-50000 cP [17]. The viscosity of body scrubs increases with pineapple powder concentration for S1, S2 and S3. As for spreadability, commercialized product has 23451.37g, making S2, having the most similar values to the standard commercialized product (Brand N),

though, the spreadability among other sample do not have huge differences, S0 has the highest spreadability with 21411.74g force, while S1 has the lowest spreadability as it has more force (24438.57g). Meanwhile, S3 has the highest foamability which is 2.1mL for 30 minutes and is equal to the commercialized product. In foamability, a trend can be observed where, the higher the pineapple powder concentration, the more foam is formed. Table 2, shows the result for parameters tested for physical characterization.

Table 2. Parameters of body scrub for physical characterizations

Attributes	Color	ΔEcolour	pH	Viscosity (cP)	Spreadability (g)	Foamability (mL/30mins)
Brand N	L= 64.09 ± 0.63 a = 3.78 ± 0.37 b = 9.49 ± 0.77	1.67	6.64	-	23451.37	2.1
S0	L= 68.49 ± 5.30 a = -0.06 ± 0.11 b = -0.86 ± 0.84	4.31	7.97	8120	21411.74	1.6
S1	L= 56.06 ± 2.40 a = 3.57 ± 0.11 b = 15.94 ± 1.69	3.63	7.48	4660	24438.57	1.8
S2	L= 54.64 ± 1.82 a = 4.28 ± 0.95 b = 17.01 ± 3.28	5.25	7.38	4760	23225.68	2.0
S3	L= 51.59 ± 2.39 a = 4.32 ± 0.74 b = 15.56 ± 3.07	5.58	7.16	5120	22509.14	2.1

According to 40 respondents, S0 has the lowest acceptance on both odor with fragrance (4.48) and odor without fragrance (4.55). This is most likely because, S0 lacks natural ingredient, which is the pineapple powder, allowing the respondents to directly smell the chemical ingredients in the base scrub. Meanwhile, S1 has the highest acceptance for both odor with fragrance (6.48) and odor without fragrance (5.50). There is no observable trend on odor, which is supported by previous study, where no significant difference was observed in acceptance of odor [9]. Next, S0 has the lowest acceptance on grittiness (4.60) as it has no pineapple powder. The body scrub with the highest acceptance on grittiness is S2 (6.45), which has 4.5% pineapple powder. This result is precisely the same as previous study, where body scrub with 4.5% concentration was the most preferable. This is because, scrubs that have higher than 5% of concentration may cause skin tissue to damage and cause dry skin [9]. Therefore, this shows that the respondents preferred mild grittiness as S3 with highest concentration of pineapple powder has the lowest acceptance (5.85) among body scrubs with pineapple powder, while S1 has 6.25 acceptance level. Next, S0 has the lowest washability acceptance (5.40) while S2 has the highest washability acceptance (7.18). S0 has the lowest washability as base cream has thick consistency [18]. Next, S1 with lowest pineapple concentrations (3.5%) has the highest acceptance for reaction of irritability, which indicates that the body scrub is non-irritant or has the least irritation (6.68). As the level of acceptance gradually decreases with increase of pineapple powder concentrations, thus S3 has the lowest acceptance on irritability (6.15). This indicates that the concentration 5.5% might be too harsh for respondents' skin. As the results, S1 and S2 has the highest overall acceptance (6.98), while S0 has the lowest overall acceptance (5.20). In Table 3, the results for sensorial characterization were shown.

Table 3. Level of acceptance for body scrubs in sensorial characterization

Sample	Odor With Fragrance	Odor Without Fragrance	Grittiness	Washability	Non-Irritant	Overall Acceptance
S0	4.48	4.55	4.60	5.40	6.40	5.20
S1	6.48	5.50	6.25	6.88	6.68	6.98
S2	6.30	4.93	6.45	6.63	6.63	6.98
S3	6.13	4.90	5.85	6.15	6.15	6.27

Next, the exfoliation capability of body scrubs of S0, S1, S2 and S3 were evaluated on 40 respondents. The capability was accessed by using SPSS one-way ANOVA, in which the factor that was being studied was the presence of pineapple powder, the null hypothesis was "presence of pineapple powder has no effect on exfoliation capability" and alternative hypothesis was "presence of pineapple powder has effect on exfoliation capability", where if the p >0.05, the null hypothesis is accepted. However, the exfoliation capacity shows that the significance value ($F_{3,116}$=6.612, p <0.05), thus indicating that the alternative hypothesis was accepted. As a result, adding an exfoliant, such as pineapple powder, contributes to the exfoliating capability of the body scrub as physical exfoliator should contain gritty particles. Table 4 shows the result of ANOVA exfoliation capability.

Table 4. ANOVA exfoliation capability of pineapple body scrub

Sample	Sum of Squares	df	Mean Square	F	Sig.
Between Groups	21.865	3	7.288	6.612	.000
Within Groups	127.863	116	1.102		
Total	149.728	119			

Market survey of pineapple body scrub

Results of 196 respondents were obtained from market survey, where 128 (65%) of the respondents are female and the remaining 68 (35%) are male. Most of the respondents used body care products, especially shower gel or body wash (84%) while about 80 respondents use body scrub. Respondents tend to choose their product based on brand (61%), especially a well-known brand, as they are more familiar with it [19]. In addition, respondents also purchased products by looking at its ingredients (54%). Given that, respondents wish to have more products with natural ingredients (25%) from existing body care products. Next, 108 respondents (55%) might be willing to try new products from new company especially if the price is within their budget. The future development of pineapple body scrub may be risky due to the lack of a brand. It is also not the essential body care product among respondents, but with appealing features such as natural ingredients and a fair price, there could potential for the product. Respondents preferred pump packaging (46%) compared to tube (39%) and jar packaging (14%). Pump packaging allows easier access to product and has good hygiene as buyers do not need to make direct contact with the product while using it. As for formulation of body scrub, half of the respondents preferred cream form (50%) compared to gel form (46%). Cream has higher physical stability which increases effectiveness of pineapple powder [20]. Cream form also has more moisturizing effect and lots of previous study has been done involving cream body scrub. Meanwhile, majority of respondents (60%) might be interested in pineapple body scrub, while 61 respondents (31%) were interested in pineapple body scrub products, where 77 respondents (39%) are willing to pay for RM10 - RM15 for 100g of pineapple body scrub. Hence, after conducting total cost spent for the experiment, it was observed that the pineapple body scrub can range at RM 5/100g without profit using ingredients and packaging preferred by the respondents. In Table 5, the results of the market survey are shown.

Table 5. Result for market survey based on majority of the respondents

Attributes	Result Based on Majority	Number of Respondents (%)
Gender	Female	128 (65)
Type of body care product used	Shower gel/Body wash	165(84)
Way of choosing body care product	Brand	119(61)
Suggestion of improvement for existing body care product	Natural ingredients	48(25)
Willingness to try new product	Maybe	108(55)
Preferred packaging for body scrub	Pump	85(46)
Preferred formulation for body scrub	Cream	98(50)
Interest in pineapple body scrub	Maybe	117(60)
Willingness to pay for pineapple body scrub	RM10-15	77(39)

Conclusion

The body scrub was formulated in cream form with pineapple waste as the natural exfoliator in pump packaging in accordance with the market survey. In the physical characterization test, S3 has the darkest color (L=51.59±2.39) and shows highest foamability (2.1mL within 30 minutes) among the body scrubs. The consistency is equal for all body scrubs. S0 has the highest pH value (7.97) among other samples, it also has highest viscosity (8120 cP) and highest spreadability (21411.74g). In sensorial characterization, the highest acceptance of pineapple body scrub for the odor with and without fragrance was S1, which is with fragrance (6.48) and without fragrance (5.50). S1 also showed the highest acceptance for nonirritant (6.68). S2 showed the highest acceptance for grittiness (6.45) and washability (7.18). S1 and S2 received the highest overall acceptance. The exfoliation capacity shows the significance value ($F_{3,116}=6.612$, $p<0.05$) between S0, S1, S2 and S3. In conclusion, the body scrub with pineapple waste as natural exfoliator was successfully developed and accepted among the respondents. Body scrubs with 3.5% and 4.5% pineapple powder concentrations are recommended for future development. Besides, it is recommended to observe the shelf-life of body scrub at different temperature for future consideration.

Acknowledgment

This research was supported by Universiti Tun Hussein Onn Malaysia (UTHM) under GPPS (Vot Q574).

References

1. Shah, M. F. (2023, July 6). New pineapple variety expected to increase Malaysia's yearly production, says MPIB. *The Star*.https://www.thestar.com.my/news/nation/2023/07/06/new-pineapple-variety-expected-to-increase-malaysia039s-yearly-production-says-mpib
2. Aili Hamzah, A. F., Hamzah, M. H., Che Man, H., Jamali, N. S., Siajam, S. I., and Ismail, M. H. (2021). Recent updates on the conversion of pineapple waste (*Ananas comosus*) to value-added products, future perspectives and challenges. *Agronomy,* 11(11): 2221.
3. Bansod, S. P., Parikh, J. K., and Sarangi, P. K. (2023). Pineapple peel waste valorization for extraction of bio-active compounds and protein: Microwave assisted method and Box Behnken design optimization. *Environmental Research,* 221: 115237.
4. Abbas, S., Shanbhag, T., and Kothare, A. (2021). Applications of bromelain from pineapple waste towards acne. *Saudi Journal of Biological Sciences,* 28(1): 1001-1009.
5. Packianathan, N., and Kandasamy, R. (2011). Skin care with herbal exfoliants. *Functional Plant Science and Biotechnology,* 5(1): 94-97.
6. Chang, M. (2015). Reducing microplastics from facial exfoliating cleansers in wastewater through treatment versus consumer product decisions. *Marine Pollution Bulletin,* 101(1): 330-333.
7. Arthur, C., and Baker, J. (2011*). Proceedings of the*

Second Research Workshop on Microplastic Marine Debris. National Oceanic and Atmospheric Administration Technical Memorandum NOS-OR&R-39. https://marinedebris.noaa.gov/sites/default/files/publications-files/TM_NOS-ORR_39.pdf

8. Asyikin, N., Zaki, M., and Fabilah, S. (2018). Quality retention of microwave dried pineapple peels and core. *Malaysian Journal of Chemical Engineering & Technology Journal*, 1: 1-7.
9. Hendrawati, Savitri, A. K., Fitriyati, N., and Mustika, A. A. (2019). Formulation of the body scrub cream containing moringa seed powder (*Moringa oleifera*) and its examination dermal acute irritation. *GEOMATE Journal,* 17(62): 244-249.
10. Mokrzycki, W., and Tatol, M. (2014). Color difference Delta E -A survey. *Machine Graphics and Vision,* 20(4):383-411
11. Schädle, C. N., Bader-Mittermaier, S., and Sanahuja, S. (2022). Characterization of reduced-fat mayonnaise and comparison of sensory perception, rheological, tribological, and textural analyses. *Foods,* 11(6): 806.
12. Matias, A. R., Ferreira, M., Costa, P., and Neto, P. (2015). Skin colour, skin redness and melanin biometric measurements: comparison study between Antera®3D, Mexameter® and Colorimeter®. *Skin Research and Technology,* 21(3): 346-362.
13. Al-Shatanawi, H. A., Osman, A., and Ab Halim, M. S. (2014). The importance of market research in implementing marketing programs. *International Journal of Academic Research in Economics and Management Sciences,* 3(2): 790.
14. Afolabi, I. S. (2014). Moisture migration and bulk nutrients interaction in a drying food systems: a review. *Food and Nutrition Sciences,* 5(8): 692-714.
15. Nieradko-Iwanicka, B., Dąbrowska, K., and Chodun, W. (2020). The pH of soaps, skin care products and cosmetics used in the period of COVID-19 pandemic. *Polish Journal of Public Health,* 130(1): 57-60.
16. Ervina, A., Santoso, J., Prasetyo, B. F., Setyaningsih, I., and Tarman, K. (2020). Formulation and characterization of body scrub using marine alga *Halimeda m*acroloba, chitosan and konjac flour. IOP Conference Series: *Earth and Environmental Science,* 414(1): 012004.
17. Standar National Indonesia (2017). *SNI 2016-4399-1996 (Tabir Surya) - Free Download PDF.* Kupdf.net. https://kupdf.net/download/sni-2016-4399-1996-tabir-surya_5af65742e2b6f52b79ea82cc_pdf
18. Hilda, D., Arini, A., and Nancy, C. D. (2021, January 16). formulation of body scrub cream from extract of Arabica green coffee (*Coffea arabica* L.) as antioxidant. Access www.atlantis-Press.com; Atlantis Press.
19. Sari Dewi, L. G. P., Edyanto, N., and Siagian, H. (2020). The effect of brand ambassador, brand image, and brand awareness on purchase decision of Pantene shampoo in Surabaya, Indonesia. *SHS Web of Conferences,* 76: 01023.
20. Putri, D. E., Djamil, R., and Faizatun, F. (2021). Body scrub containing virgin coconut oil, coffee grounds (*Coffea arabica* Linn) and carbon active coconut shell (*Cocos nucifera* L) as a moisturiser and a skin brightener. *Scripta Medica,* 52(1): 76-81.

Malaysian Journal of Analytical Sciences (MJAS)
Published by Malaysian Analytical Sciences Society

A REVIEW ON CONVERSION OF MICROPLASTICS INTO VALUE-ADDED PRODUCTS: CHALLENGES AND PERSPECTIVES

(Ulasan Tentang Penukaran Mikroplastik Kepada Produk Nilai Tambah: Cabaran dan Perspektif)

Nurul Mohd Ridzuan Afifah[1], Jennifer Janani Sathiaseelan[1], Seng Hon Kee[1], Tan Suet May Amelia[1], Wei Yien Lua[2], Nazli Aziz[4], Wan Mohd Afiq Wan Mohd Khalik[1,5], Sevakumaran Vigneswari[3], and Kesaven Bhubalan[1,3,5*]

[1]*Faculty of Science and Marine Environment, Universiti Malaysia Terengganu, 21030 Kuala Nerus, Terengganu, Malaysia*
[2]*Institute of Oceanography and Environment, Universiti Malaysia Terengganu, 21030 Kuala Nerus, Terengganu, Malaysia*
[3]*Institute of Climate Adaptation and Marine Biotechnology, Universiti Malaysia Terengganu, 21030 Kuala Nerus, Terengganu, Malaysia*
[4]*Faculty of Business, Economics, and Social Development, Universiti Malaysia Terengganu, 21030 Kuala Nerus, Terengganu, Malaysia*
[5]*Microplastic Research Interest Group, Universiti Malaysia Terengganu, 21030 Kuala Nerus, Terengganu, Malaysia*

**Correspondance: kesaven@umt.edu.my*

Received: 30 December 2023; Accepted: 31 March 2024; Published: 29 June 2024

Abstract

Microplastics have emerged as a pressing environmental concern, exerting profound impacts on ecosystems, water bodies, terrestrial landscapes, and human food sources. In light of the global plastic waste crisis, innovative strategies are being explored to manage and recycle plastic waste, with an emphasis on microplastics. Research endeavours aimed at transforming waste microplastics into valuable resources align seamlessly with circular economy principles. Microplastics can be collected using surface water sampling, air sampling, sediment sampling, soil sampling, shoreline sampling, as well as wastewater and effluent sampling. Microplastics can be chemically and physically characterised for composition selection and then converted using biological, chemical, and mechanical approaches. Biological conversion involves microbial activity and enzyme utilisation, chemical conversion involves chemically breaking down polymers into smaller molecules that can be used as feedstock for valuable materials, while mechanical conversion applies physical force to reduce polymer size. Both conventional and biodegradable plastics can undergo biological, chemical, and mechanical recycling to an extent to maintain their value and prevent the waste of non-renewable resources. However, there are challenges to overcome in the conversion of microplastics, including cost-effectiveness, scalability, environmental friendliness, and regulatory considerations. Appropriate macroplastic management and life cycle assessment analyses are still crucial for transitioning to a sustainable and circular economy.

Keywords: microplastics, conversion techniques, value-added products

Abstrak

Mikroplastik telah muncul sebagai kebimbangan alam sekitar yang mendesak, memberikan impak yang mendalam terhadap ekosistem, badan air, landskap terestrial, dan sumber makanan manusia. Dalam konteks krisis sisa plastik global, strategi inovatif sedang dikaji untuk mengurus dan mengitar semula sisa plastik, dengan penekanan pada mikroplastik. Usaha penyelidikan yang bertujuan untuk mengubah mikroplastik sisa menjadi sumber daya bernilai selari dengan prinsip ekonomi bulat. Mikroplastik boleh dikumpulkan melalui pengambilan sampel air permukaan, pengambilan sampel udara, pengambilan sampel sedimen, pengambilan sampel tanah, pengambilan sampel garis pantai, serta pengambilan sampel air sisa dan air buangan. Mikroplastik

boleh dicirikan secara kimia dan fizikal untuk pemilihan komposisi, dan kemudian diubah menggunakan pendekatan biologi, kimia, dan mekanikal. Penukaran biologi melibatkan aktiviti mikrob dan penggunaan enzim, penukaran kimia melibatkan pemecahan kimia polimer menjadi molekul yang lebih kecil yang boleh digunakan sebagai bahan mentah untuk bahan bernilai, manakala penukaran mekanikal menggunakan daya fizikal untuk mengurangkan saiz polimer. Plastik konvensional dan plastik terbiodegradasi boleh mengalami kitar semula biologi, kimia, dan mekanikal untuk mengekalkan nilai mereka dan mengelakkan pembaziran sumber tidak boleh diperbaharui. Walau bagaimanapun, terdapat cabaran yang perlu diatasi dalam penukaran mikroplastik, termasuk kos-efektif, skalabiliti, kemesraan alam sekitar, dan pertimbangan peraturan. Pengurusan makroplastik yang sesuai dan analisis penilaian kitar hidup masih penting untuk bergerak ke arah ekonomi lestari dan bulat.

Kata kunci: mikroplastik, teknik penukaran, produk bernilai tambah

Introduction

Microplastics have ubiquitously permeated the ecosystems of the planet, penetrating the atmosphere, water bodies, terrestrial regions, and even human food sources, signifying a critical predicament of global contamination [1-4]. Microplastics, small plastic particles less than 5 millimetres in size, are at the forefront of significant environmental concerns and thus have been intensively studied to understand their abundance, distribution, and sources [5-7]. The various sources of microplastics include fragmentation of larger plastic items, personal care products, textiles, industrial processes, and plastic resins used in manufacturing [8, 9]. In addition, the potential impacts of microplastics on aquatic organisms include feeding, growth, reproduction, as well as bioaccumulation of environmental pollutants from microplastic-pollutant complexes due to the vector ability of microplastics [10-13].

The persistence of microplastics in the environment and their potential to cause adverse ecological and health effects have escalated the search for sustainable solutions to address their accumulation. Research into the waste utilization of microplastics for value-added products is a new cutting-edge field being presently considered and expected to further intensify, staying abreast with the presence of multiple driving forces from international, national, environmental, economic, and social aspects [14]. The global plastic waste crisis has reached an annual microplastic waste generation of 3 million tonnes [15], leading to increased international and national interests, such as UNEP, in finding innovative ways to manage and recycle plastic waste, including microplastics [16]. Resource scarcity and the circular economy are also at the leading edge of the environmental drives propelling research in utilising waste plastics [17]. While the extraction of virgin materials and fossil fuels for manufacturing is resource-intensive and can contribute to environmental degradation, research into converting waste microplastics into value-added products can help to reduce resource consumption and thus align with the principles of the circular economy [18]. From an economic viewpoint, industrial opportunities arise from transforming microplastics into valuable materials, generating revenue from value-added products, reducing costs associated with waste disposal, and developing new markets for recycled materials [19, 20]. Consumer and industry demand for environmentally friendly and sustainable products is growing due to the plastic-free movement and public awareness of plastic pollution and environmental issues [21]. Additionally, the conversion of microplastics can occur through biological, chemical, and mechanical conversion techniques but research is lacking compared to macroplastics and conventional plastics [22].

Therefore, in the pressing quest to address global plastic pollution, the efficacy of converting conventional microplastics into value-added products presents a pivotal state-of-the-art juncture in sustainable resource management and environmental mitigation. This article reviews the collection, physical and chemical characterisation, biological, chemical, and mechanical conversion methods, potential value-added product applications, and environmental considerations associated with conventional microplastics.

Collection and characterisation of conventional microplastics

Supply chain management is essential for successful waste material manufacturing by coordinating the flow of materials from waste collection to final product manufacturing [23]. In other words, microplastic collection methods are vital for adequate material

supply in manufacturing and vary depending on the environment where microplastics are collected. In microplastic research, microplastics are commonly collected using manta trawl, grab sampling, and bulk water filtration targeting marine and freshwater [24, 25]. In general, major collection methods include surface water sampling, air sampling, sediment sampling, soil sampling, beach and shoreline sampling, wastewater and effluent sampling, and biota sampling (Table 1) [26-29]. Surface water sampling involves collecting water samples from rivers, lakes, and oceans, and filtering them to separate microplastics [27, 29]. Sediment sampling isolates microplastics from water bodies, while air sampling collects airborne particles [26, 30]. Biota sampling for microplastics has been used to examine organisms like fish and shellfish to determine ingestion occurrence or their ingestion rates on microplastics [29, 31]. Soil sampling extracts microplastics from sources like plastic mulch in agriculture or atmospheric deposition [28], while wastewater and effluent sampling at wastewater treatment plants provides insights into microplastic presence and fate in waste streams [32]. Additionally, beach and shoreline samplings involve manually picking up debris or using specialised devices to collect microplastics [33].

Table 1. The method types, advantages, and limitations of common collection approaches for microplastics

Methods	Advantages	Limitations	References
Surface water sampling	• Provides information on plastic distribution. • Comparatively simple and widely used.	• Restricted to surface-bound microplastics. • May underestimate the subsurface microplastic amount.	[24] [25] [29]
Air sampling	• Helps assess the microplastic amount in the atmosphere. • Non-invasive and can cover large areas.	• Difficult to distinguish microplastics from other particles. • Limited information on microplastic sources.	[26]
Sediment sampling	• Gives information on the accumulated history of plastic. • Allows study of buried microplastics.	• Time- and effort-consuming. • Sediment and benthos disturbance during sampling.	[30]
Soil sampling	• Gives information on plastic contamination of terrestrial ecosystems. • Can evaluate the uptake potential of plants.	• Microplastics might be mixed with natural particles. • Separating microplastics from organic matter is challenging. • Limited standardized protocols.	[28]
Beach and shoreline sampling	• Direct observation of shoreline plastic pollution. • Aids in understanding the ocean-to-land plastic transfer.	• Only a small portion of all marine microplastics are captured. • Limited to accessible shorelines. Microplastics may not be as noticeable if macroplastics are present.	[33]
Wastewater and effluent sampling	• Perspectives on plastic input from different sources. • Allows targeting of pollution sources.	• Variation in microplastic loads and types in different effluents. • Small particle detection in complicated matrices is difficult. • Limited data on microplastic fate after release.	[32]
Biota sampling	• Identifies potential harm that microplastics could cause to ecosystems. • Links plastic pollution to higher trophic levels.	• Invasive on living organisms. • Requires specialized techniques for extraction and analysis. • Limited species-specific data. Distinguishing environmental particles from ingested microplastics is challenging.	[31] [29]

Among the microplastic collection methods listed, air sampling and surface water sampling can be considered relatively clean and hygienic with less time and effort consumption, since air and water samplings mainly

involve collecting particles that are airborne, in marine, or freshwater environments, reducing the risk of direct contact with potentially contaminated materials. However, the process faces numerous challenges, such as microplastics from wastewater and effluent for conversion into food packaging or clinical applications may require additional treatment for consumer safety, the polymers making up microplastics contain chemical additives such as plasticizers, flame retardants, and antimicrobial agents. These additives need to be discarded priory the conversion process. The wide range and intricate nature of microplastics in terms of their types, shapes, sizes, colours, compositions, and additives pose challenges in their separation, classification, and characterization. In real environment, the low quality and purity of microplastic waste, potentially harboring contaminants like organic matter, metals, pathogens, and other pollutants, pose risks to the functionality and safety of the resultant products. Biota sampling involves not only contact with biological samples that may have been infected but also the dissection of living organisms [34, 35]. On the other hand, sediment sampling, soil sampling, beach and shoreline sampling, may have varying levels of cleanliness, hygienic conditions, and time and effort consumption (e.g., separation of sediment and microplastics) depending on the specific circumstances and precautions taken during the sampling process. Sample processing includes collection, transportation, storage, filtration, separation, and extraction techniques (Figure 1).

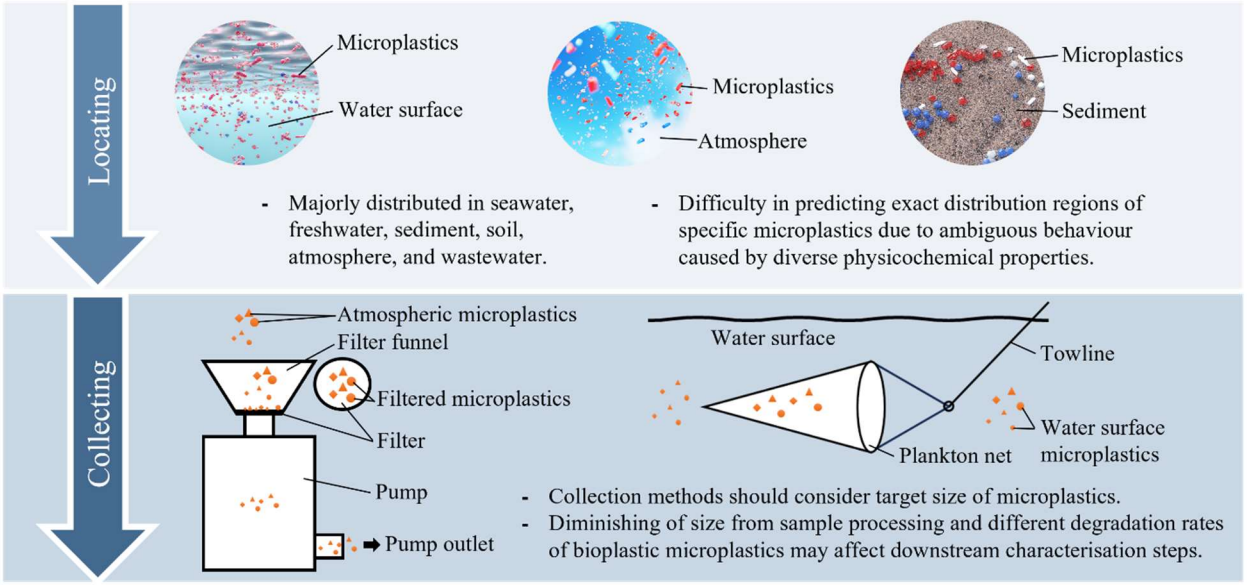

Figure 1. General conceptual illustration of collecting microplastics [26-29, 36-40]

In microplastic conversion to value-added products, additional microplastic characterisation steps are required to categorise or selectively collect microplastics according to their composition, using fluorescent spectroscopy, Fourier-transform infrared spectroscopy (FTIR), micro-Raman spectroscopy, mass spectrometry, chromatography, pressurized fluid extraction (PFE), density separation, and fluorescence microscopy via hydrophobic fluorochrome dye staining (e.g., Nile red staining) to verify the composition or properties of the collected microplastics. Presently, a blend of physical methods such as microscopy and chemical methods like spectroscopy is extensively employed for microplastic examination. This strategy reduces the occurrence of inaccurate positive and negative results. [41-44]. In plastics manufacturing, identical resin compositions are crucial for homogenous products as variations in these compositions can lead to defects, inconsistencies, or undesirable characteristics, affecting the appearance and performance of the final product [45, 46]. For industrial conversion of microplastics to value-added products, rapid collection and characterisation methods of high capacity are required to channel the microplastics to the appropriate manufacturing techniques and product types.

Physical characterisation

Physical characterization of plastic plays a significant role in determining and better understanding the properties of a plastic polymer including to determine the optimum surrounding condition to catalyse high-efficiency biodegradation of the plastic polymer and to ensure a higher quality and reliability of the plastic product that can adapt to a variety of applications. Due to the complicated nature and properties of the polymer, specific tests are required for each unique characteristic of each polymer and among the physical properties that are commonly tested and measured are comprising of mechanical properties such as flexural rigidity, tensile strength, hardness and wear and tear resistance [47]. Tensile strength of a plastic polymer is described and tested through the application of the maximum tensile stress before the polymer is fractured into fragments which are commonly utilized in load-bearing applications. According to Sola et al. [48], the tensile test is one of the commonly used mechanical tests in the industrial sector due to multiple factors such as relatively short, simple procedures and lack of in-depth requirements of research and development allowing industrial players to test for tensile strength without spending an extra cost for external services.

As the world has reached a point of a global boiling era as mentioned by the UN secretary general, studying the effect of heating of plastic to the polymer and its degradation properties have never been more relevant as the temperature of the global surface increasing at an alarming rate since the past decade [49] (Niranjan, 2023). Thermal-based analysis of polymers comprises a few analyses that are thermogravimetric analysis (TGA), differential thermal analysis (DTA), differential scanning calorimetry (DSC) and evolved gas analysis (EGA). As summarized by Ng et al. [50], TGA functions to analyse mainly the thermal stability, properties of composites and oxidative stabilities of polymer samples. The above-mentioned thermal analysis: DMA are reported to study the viscoelastic properties of polymeric samples that would further complement the TGA analysis. Another similar analysis that applies the thermal-based analysis is Melt Flow Index Measurement (MFI), which studies the process of thermoplastic polymers by measuring of flow of molten plastic [51]. This process is crucial for the application of moulding injection as well as extrusion processes.

Chemical characterisation

Polymers regardless of size have their respective monomers, linkages, reactive chains, or end-groups that determine their characteristics that could enable the creation of polymer networks reliably and repeatedly with desired features. Through chemical characterization, researchers can unveil surface functionalities, including oxidation, hydrophobicity, and adsorbed substances. Moreover, they can understand changes in polymer structure resulting from UV exposure, mechanical forces, and microbial activity. [52, 53]. There are many methods for identifying objects and determining their chemical composition as shown in Figure 2 [54]. SEM-EDS aids in quick differentiation between non-plastic and plastic pellets and can find microscopic particles that are missed by optical inspection. EDS was used to determine the qualitative elemental composition of the microplastic surface. In addition, tool plays a critical role in the identification of pollutants linked to microplastics, such as toxic metals. [55, 56].

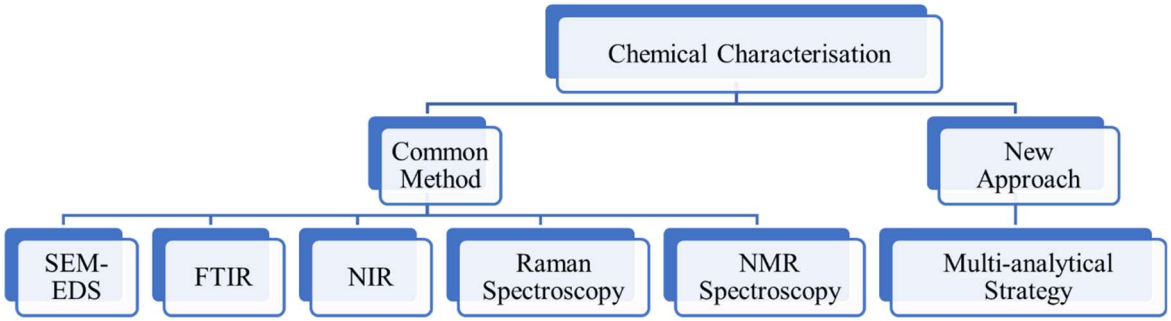

Figure 2. Methods in chemical characterisation

The most popular method for locating microplastics is Fourier-transform infrared (FTIR) which is typically used to determine the polymeric composition of the microparticles, while Raman spectroscopy since it is straightforward, reliable, and non-destructive [52, 57-59]. However, the detection of domain differences within a sub-micrometre region with traditional Raman or FTIR spectroscopy offers average chemical information at a bulk area with very limited spatial resolution, which may restrict the analysis of nanoplastics that are smaller than the spatial resolution [60, 61]. The use of hybrid approaches, namely atomic force microscopy-Raman (AFM-Raman) and AFM-IR techniques, have been considered to map and identify composites at the nanoscale on sample surfaces. AFM has the ability to function in various modes, such as contact mode, tapping mode, or phase mode, which are determined by the force feedback type and the probe's oscillation frequency. [62, 63]. Apart from that, NIR spectroscopy also can be used to characterize and differentiate microplastics and is capable of seeing deeper into the plastic compared to other spectroscopy methods [54, 64]. Quantitative ^{1}H NMR spectroscopy gives a way to identify microplastics both qualitatively and quantitatively which is also a cost-efficient, quick, and easy technology that provides a significant advantage over other detection techniques. In fact, this technique is non-destructive and non-invasive, eliminating the need for sample preparation or solvents. [65-67]. Thermal degradation of MPs has been discovered to be advantageous since it can simultaneously identify the type of polymer and detect chemical components, additives, and gases in the intricate formulation [68]. Thermal degradation includes pyrolysis as well as GC-MS where the product of pyrolysis (heating and melting of the microplastics) will undergo GC-MS for separation and detection of compounds present. This method has the capability to address certain drawbacks of spectroscopy approaches, including low detection limits, matrix interferences, and sample heterogeneity. [69, 70].

Analysis of MPs in environmental samples is hampered by microplastic contamination from the sampling and laboratory environments, which can affect both qualitative and quantitative determination that includes the most popular methods [71]. A series of newly created analytical protocols for the precise and selective detection of the polymers, along with specialized methods that include extraction of polymer using different solvents, hydrolytic depolymerization, purification, and quantification procedures that are tailored for condensation polymers, pyrolysis-gas chromatography-mass spectrometry (Py-GC/MS), and followed by physical characterization process [72]. ^{1}H NMR spectroscopy and the thermal desorption gas chromatography-mass spectrometry (TD-GC-MS) technology were used in a multi-analytical strategy to characterize the microplastics in different degradation times. Utilizing multiple strategies can surpass the limitations of each individual method, offering a more thorough and dependable insight into the characteristics of microplastics, including particle number, size, shape, mass, composition, and additives. [73, 74].

Conversion of conventional microplastics

As the development and applications of plastic have revolutionized the modern-day world, the constant increase in the usage of plastic in daily life has raised environmental concerns as plastic waste persists in the environment longer than intended. The valorisation of plastic waste, conventional plastic, shows a prospect in supporting the circular economy model [75]. Conversion of conventional microplastic to added value products takes the recycling principle to another level which is not just the recycling of the product itself but down to the monomer recycling of the said products through depolymerization of microplastic. Depolymerization of the polymer allows the monomeric products to be recycled to produce different yet environmentally friendly and economically valuable products closing the loop of recycling [76].

Research regarding the conversion of waste products to added value has been done extensively in the past decade as the valorisation of waste offers a prospective solution supporting the circular economy [77]. The waste-to-energy conversion technology involves the utilization of waste products to produce a variety of fuels that can be further used to generate other products and maintain a sustainable energy supply (Figure 3) [4]. Among the pathways discovered to increase the conversion of waste products into added value are biological, chemical, and mechanical pathways. Biological conversion utilizes the natural ability of microorganisms to further recycle the end-of-use plastic to produce simpler compounds that can be

recovered [78]. In addition, pyrolysis has gained popularity recently as the chemical pathway of conversion of plastic waste toward the production of gasoline, diesel and oils via heating of waste materials in the absence of oxygen [79]. Mechanical conversion of waste to value added products on the other hand, involves the change in the physical state of the waste products via the shredding and grinding process without altering the chemical or biological structure of the waste products [80].

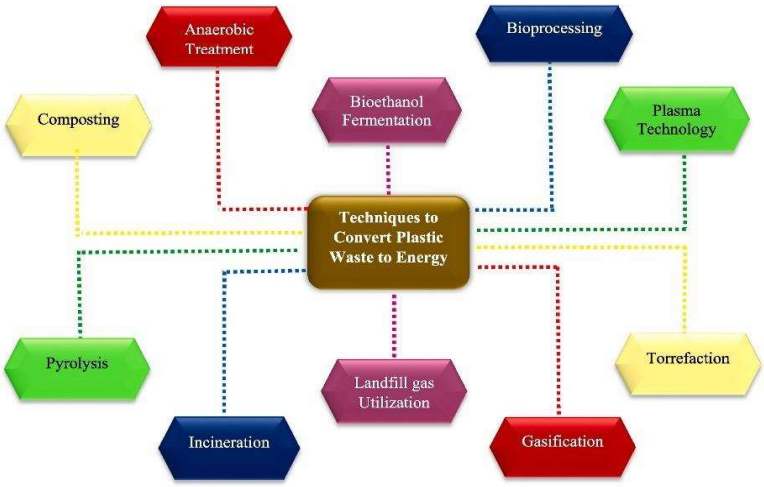

Figure 3. Techniques to convert plastic or microplastics waste to energy

Biological conversion

In general, the bioconversion of traditional biowaste such as agricultural, domestic, and industrial waste to value-added products comprises four primary conversion pathways, microbial, enzymatic, fermentation, and composting conversion pathways [81]. In this review, the valorisation of plastic waste through bioconversion pathways will be further explored. Biological conversion of plastic waste refers to the recent advances of innovative strategies for adding value to end-of-life plastic-based products by exploiting the fundamental abilities of the microbial factory [82]. Conventional petrol-based polymers are categorized into two groups depending on their chemical structure. The two categories of petrol-polymer are polymers that possess hydrolysable ester bonds and functional groups of esters and amides (PET and PUR) that have higher biodegradability compared to non-hydrolysable (PE, PS, PP, and PVC) which possess a stable carbon chain backbone [23, 78]. Recent advances in biological plastic conversion comprise two main elements: plastic-degrading microorganisms and enhancing enzymes for degradation. Both elements play a crucial part in the process of bioconversion of plastic to obtain the desired end-products. The efficiency and productivity of biological conversion of plastic waste into substrate depends on multiple factors such as the type of plastic-degrading microorganism used, depolymerization through enzymatic reactions and end-product value [23, 83].

Plastic-degrading microorganisms

Studies on the utilization of microorganisms in the degradation of plastic waste have been extensively done in the pursuit of a sustainable approach to plastic waste solutions. In a study conducted by Yoshida et al. [84], reported that *Ideonella sakaiensis* 201-F6 can produce enzymes with the ability to degrade PET into terephthalic acid (TPA) and ethylene glycol (EG) which can be assimilated for metabolic activity. It has been found that *I. sakaiensis* is capable of surviving on PET alone as a carbon source whilst utilizing two main enzymes that are PETase and MHETase [85, 86].

The genus *Pseudomonas* sp. is also among the most researched bacteria due to its versatility in degrading a wide range of polymers. A study conducted by Lee et al. [87] showed that *Pseudomonas aeruginosa* isolated from the guts of superworms exhibit biodegradability properties towards four synthetic plastics, PE, PS, PPS and PP with the fastest degradation on the PE type plastic. The terrestrial bacterium *Bacillus subtilis* possesses synthetic degrading abilities and has been

reported to efficiently degrade conventional plastic type PET with the rate of 9.26% in 30 days which supports biodegradation of conventional plastic through microbial factory [88]. To date, there are currently 949 microorganisms associated with plastic according to the plastic microbial biodegradation database (PMBD) [89].

Enzymatic depolymerization

Degradation of synthetic oligomers and polymers by enzymatic activity commonly involves two categories of enzymes that are hydrolases (e.g., esterases, lipases, cutinases, proteases) and oxidases (e.g., dehydrogenases, laccases) [90]. Depolymerization functions to chemically breakdown polymers from macromolecules to lower compounds of oligomers and monomers through the process of enzymatic activities such as hydrolysis, oxidation, or hydroxylation that will allow the reuse of these monomers through repolymerization process [78, 91]. For example, conventional plastic such as PP, PE, and PVC poses similar structure of C-C as the main chain that can be further turned into various type of fatty acids through the act of enzyme activity [75, 92, 93]. In a different study by Zhang et al. [94], conventional plastic PS can be converted into aromatic monomers, which leads to the oxidation of styrene epoxide catalyzed by the enzyme styrene monooxygenase (SMO) or styrene dioxygenase (SDO).

The biodegradation of PET employs a two-enzyme system which utilizes the PETase to hydrolyze PET into TPA, EG and MHET and MHETase enzyme to further hydrolyze MHET into TPA and EG [84, 86, 95]. To date, most PET-degrading enzymes have been found in two main genera of bacteria, *Pseudomonas sp.* and *Bacillus sp*. While other bacterial strains produce PET degrading enzymes such as *Brevibacillus parabrevis, Staphylococcus aureus, Streptococcus pyogenes* and *Clostridium thermocellum,* research studies have shown that the usage of microbial consortia comprising *Pseudomonas sp*. and *Bacillus sp.* have proven to have increased degradation efficiency of PET polymer [96, 97].

Chemical conversion

Chemical conversion or chemical upcycling approaches for converting conventional microplastics into value-added goods are gaining popularity as a potential solution to the world's plastic pollution problem. It involves a process that breaks down the polymers into smaller molecules which could then be used as a feedstock for a variety of valuable chemicals and materials. Microplastics are microscopic plastic particles, frequently less than five millimetres in size, found in a variety of environmental compartments such as oceans, rivers, and soil. Converting these microplastics into valuable materials has the potential to minimize their environmental impact while also providing economic rewards. This section briefly discusses the two techniques of chemical upcycling widely studied over the years.

Depolymerization

Depolymerization is a process where long polymer chains are broken down into small monomer units allowing new products to be synthesised using these monomers. Research was done to investigate the techniques of depolymerization such as using transition metals [98], enzymes [99], catalysts [100], electrocatalysis [101] and more. In 2012, a team of researchers used a PNP-Ru pincer complex (Ru-1, 0.1 mol %) as a catalyst to perform the first hydrogenative depolymerization of waste poly(propylene carbonate) (PPC) which yielded 1,2-propylenediol and methanol [102]. Besides, Mao et al. [101] reported the utilization of electrocatalytic upcycling of PET microplastics to formate, terephthalic acid and potassium sulphate using a novel catalyst Mn0.1Ni0.9Co2O4-δ rod-shaped fibre (RSFs) catalyst. Recently, enzymes are being used to facilitate the hydrolysis of amides, esters, or urethane bonds within microplastics, such as polyamides, polyesters, or polyurethanes, for the generation of monomers or oligomers, which can subsequently undergo analysis using techniques includes chromatography or spectroscopy. In addition, fungi are introduced to secrete various digestive enzymes and proteins that attach to the polymer surface, penetrate it, and degrade macromolecules into small organic compounds, such as carbon dioxide, water and methane [103, 104].

Pyrolysis

Pyrolysis is a thermochemical technique that decomposes waste materials into energy products such as liquid oil and gases in hypoxic conditions and at high operating temperatures ranging from 400 to 800°C [105, 106]. A myriad of studies has been

conducted on the conversion of microplastics to value-added products via the pyrolysis technique. Nabgan and coworkers [107] investigated the potential of utilizing microplastic wastes to produce value-added products using the pyrolysis-catalytic steam reforming technique. They synthesized the nano-catalyst, Ni-Pt/Ti-Al, and loaded it into the pyrolysis reactor before introducing the phenol-dissolved microplastics into the fixed-bed continuous flow quartz reactor at 500 – 700°C at standard atmospheric pressure. Several liquid oils were generated such as 1,2-bis(trimethylsilyl)benzene, bis(2-ethylhexyl) phthalate, cyclohexane-1,3-dione, 2-allylaminomethylene-5,5-dimethyl- and more. Agriculture is one of the largest plastic waste producers. The generated waste plastic mulching films are normally disposed of conventionally (incineration and landfilling) which introduces greenhouse gases and microplastics in the ecosystem [108]. Because of this Jung and coworkers [108] investigated the disposal of the mulching films through a CO_2-assisted catalytic pyrolysis. It was reported that hydrogen gas, short-chained and long-chained hydrocarbons were formed through thermal degradation of the mulching films. When a Ni/SiO_2 catalyst was used the hydrogen gas production skyrocketed to 100 times more. Furthermore, when CO_2 was introduced as a flow gas CO production was observed.

Gasification

Gasification is a technological process that converts any carbonaceous (carbon-based) raw material into synthesis gas (syngas). Gasification takes place in a gasifier, which is typically a high temperature/pressure vessel in which oxygen (or air) and steam come into direct contact with the coal or other feed material, resulting in a sequence of chemical processes that convert the feed to syngas and ash/slag (mineral wastes) [109]. The gasification of polypropylene was studied by Wang et al. [110]. They compared the effects of the presence of a catalyst with none. Expectedly, the catalyst (Ni/Al_2O_3) set-up has vastly improved the yield of H_2, CO, hydrocarbons and total syngas by 137%, 38.2%, 98.2%, and 44.1%, respectively. Not only that, Moghadam et al. [111] conducted a study on syngas production from palm kernel shells and polyethylene wastes via the gasification process. The paper reported that a co-gasification process under optimized conditions was able to yield 422.4 g/kg feedstock and 135.27 g/kg feedstock of syngas and H_2, respectively.

Mechanical conversion

Mechanical conversion is the mechanical force applied as a catalyst to reduce the molecular weight of the polymer [112]. Properties of plastics can be classified in terms of weight, hardness, tensile strength, thermal properties, electrical properties, and chemical properties [113] (Alauddin et al., 1995). Thus, breaking the plastic with external mechanical force could break and change those properties to some level. A study highlighted that mechanical conversion affects the structure of the polymer and reduces the quality of the product in terms of mechanical properties regardless of the type of the polymer [114]. Yet, mechanical recycling is a practical method for maintaining plastic's inherent worth, preventing the waste of non-renewable resources [115].

Grinding and milling techniques

Milling in general is a technique or process of cutting or grinding material using a rotary cutter and incorporates the conversion of mechanical energy into thermal energy and was the first technique to produce microplastic particles [116, 117]. The milling and grinding process is a crucial step before thermal conduction [118]. Meanwhile, a study by Eitzen et al [116] shows that longer cryogenic milling and pre-cooling duration could produce small particles of polystyrene (PS).

Cryogenic grinding with a wet-sieving technique could enable maximum yield of the polyvinyl chloride (PVC) and smaller microparticles could be obtained if the microparticles undergo 2 cycles of the grinding process [119]. There is also a new grinding technique that has been revealed which is the melt grinding technique that has the advantage of not having drying steps in the usual grinding technique where the time consumption was high [120]. Cryogenic milling and grinding are the processes that incorporate low temperatures to overcome the issue mentioned before such as heating despite milling or grinding conventional microplastic as each type of microplastic has respective characteristics that differ by physical and chemical properties. In conclusion, the grinding and milling technique is the early stage before the plastics are further proceeded for extrusion and injection moulding

as smaller plastics can be melted in large quantities in a shorter time compared to large plastics.

Extrusion and injection moulding

Injection moulding is a technique where injecting material into a mould with high temperature and pressure in a closed system [121], meanwhile, extrusion is a technique of pushing out a material through an opening with the help of an extruder [122]. The extrusion and injection moulding of conventional plastic can cause issues such as degradation of their features and usability arise when a combination of heat and mechanical shear affects the recycling of both post-industry and post-consumer plastics [123]. Changes in chain length and mechanical characteristics are a constant problem, even though the methods of degradation vary among polymers, especially upon thermal conduction [124]. For instance, the thermomechanical process results in a drastic reduction in poly (ethylene terephthalate) (PET) characteristics [125]. Also, polyolefins that include HDPE, LDPE, and PP shows varied mechanism; HDPE and LDPE have a high probability in chain branching, but PP has a high probability in chain scission upon extrusion [124, 126]. Extrusion is best for long, uniform products and is cost-effective for mass production. Injection moulding suits complex, irregular items with precision for custom orders. Unlike extrusion, it handles both thermoplastics and thermosets [127]. Figure 4 shows a combination of mechanical and chemical technique to convert plastic waste into value added products such as fuels.

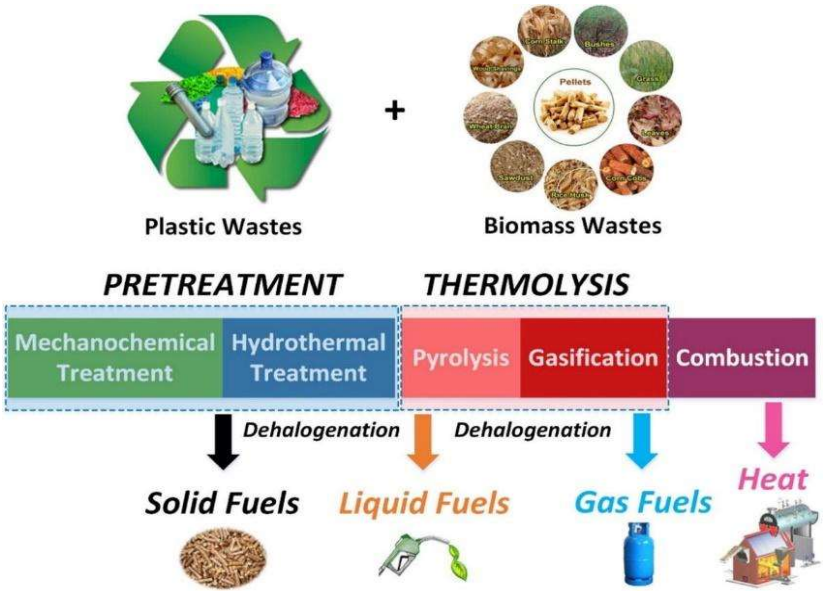

Figure 4. Mechanical and chemical treatment of valorisation of plastic waste

Potential applications of value-added products

The transformation of microplastics into value-added products requires consideration of material properties, process selection, waste utilisation, and environmental concerns. Material properties, such as composition, size, and shape, play a significant role in determining the suitability of waste materials for specific manufacturing processes [128], as well as the compatibility between waste materials and other components or additives for proper integration and performance since the properties of manufactured products should meet the required standards and specifications for their intended applications [129]. The selection of conversion and manufacturing processes is dependent on available resources and technologies, where process optimization and innovation are required to improve efficiency and sustainability. In microplastic research, the state-of-the-art focus has presently pivoted towards the waste utilisation, material properties, conversion process selection, and environmental implications of all types of microplastics [20, 106, 129]. These leading-edge endeavours underscore the imminent potential to transform microplastics into a range of valuable products, emphasizing the timeliness and urgency of such innovative pursuits.

Utilizing nature's process of breaking down complex compounds into simpler compounds mechanism in the innovative approach of recycling plastic waste has opened a new door towards plastic waste management. The biological approach to converting plastic waste through the coupled act of plastic-degrading bacteria and enzymatic degradation has shown promising results. For example, the intermediate produced from enzymatic reactions of PETase and MHETas can be used for further metabolic reactions, in PHA polymer production through microbial fermentation [78, 97, 130]. Enzymatic hydrolysis of plastic waste, including impurities from PLA-PET, is being researched as an eco-friendly method of bio-recycling plastic trash. Recent studies suggest an innovative hybrid approach merging thermal and electrochemical techniques to convert both plastic waste and biomass into exceptionally pure hydrogen and carbon nanotubes. Moreover, the method introduces a carbon capturing process using a molten salt, which can subsequently be transformed into valuable carbon nanotubes through electrochemical means powered by renewable energy sources. [131, 132].

Challenges associated with the conversion of microplastics to value-added products

Regulatory and policy considerations

Plastic is the main material used for packaging and textiles in various sectors. Excessive plastic usage has led to tremendous plastic waste generation. According to Tiwari et al. [133], the top three countries that produce the most plastic are in Asia within the Indo-Pacific region, namely India, China and the Philippines. Many countries have established regulations, action plans and policies to regulate and control plastic waste generation (Table 2) Despite many regulations that have been enforced, the accumulation of plastic usage at the rate of 25 million tonnes per year continues due to their persistence in the environment [134]. In addition, in certain countries, the mitigation plans and regulations are mostly focusing on plastics but not microplastics. Today's microplastic is a global issue since it can be found everywhere. Vectors for drugs in medical sectors and microbeads in beauty care products are known as primary microplastics, while secondary microplastics are tiny plastics deteriorated from primary microplastics [135, 136].

As a result of growing concern towards these tiny plastic particles, few countries have imposed national legislation to combat microplastic specifically (Table 3). All these plastic grains eventually end up in the ocean, posing major threats to the ecosystem, where they have been reported to be found in all levels of aquatic environments [137, 138]. Microplastics that are consumed by fish will eventually contaminate the human body through seafood consumption [139]. Consequently, this sparks a growing number of research and publications on the effects of microplastic towards fish and human beings. Kutralam-Muniasamy et al. [140] indicated that the actual consequences of microplastics are merely understood scientifically. In a recent study, Carrington [141] reported that microplastic has been detected in human blood for the first time. Although the impacts of microplastic in the human body are still being explored, a solution to substitute conventional plastic with an eco-friendlier alternative is urgently needed.

Fundamentally, reducing macroplastic usage through prohibition and restriction use of plastics will reduce the presence of microplastic in the ecosystem. However, Mitrano et al. [142] stated that it is unclear whether technical bans can help in the reduction of microplastic. They opined that proper macroplastic management is the ideal way to reduce microplastic as a transition towards a circular economy. An amendment to the government framework is suggested to focus on waste utilisation by repurposing and converting the waste into other products. Although many regulations were in place, microplastic pollution is hard to solve, so the focus should be concentrated on the utilisation of microplastic into value-added products, to address the circular economy concept and to comply with the Sustainable Development Goals 6, 7, 12, 13, 14, 15. We need specific guidelines, regulations and policies to regulate and control microplastic pollution, by regulating microplastic production, supporting microplastic conversion into value-added products, and encouraging a circular economy that reduces the usage of raw resources.

Table 2. Policies and regulations on plastic waste established by countries

Year	Country	Regulations
2016	India	Plastic Waste Management Rules (2016)
2008	China	China State Council had issued a Notice restricting the Production and Sale of Plastic Shopping Bags
2020	China	National Development and Reform Commission (NDRC) and the Ministry of Ecology and Environment (MEE) released an "Opinions on Further Strengthening the Control of Plastic Pollution
2022	Philippines	Extended Producer Responsibility Act (EPRA) 2022
2022	Philippines	Department of Environment and Natural Resources (2020) has banned the usage of unnecessary single-use plastics in offices under the National Solid Waste Management Commission.
2011	Italy	Banned traditional plastic bags and substituted them with biodegradable bags
2012	Sweden	Started to focus on the replacement of fossil-based raw materials with bio-based raw materials in their research and development needs
2013	Canada	Banned the usage of traditional plastic bags in Toronto
2023	United Arab Emirates (UAE)	Banned shopping bags that are not oxo-photodegradable.
2021	Australia	Published the National Plastics Plan 2021 to address and reduce plastic waste generation
2019	Scotland	Banned plastic cotton buds in 2019 and 2021, a ban was imposed on single-use plastic items
2018	Malaysia	Malaysia's Roadmap Towards Zero Single-use Plastics 2018-2030
2021	Malaysia	Ministry of Environment & Water (2021) published the Malaysia Plastic Sustainability Roadmap 2021-2030

References [143-150]

Table 3. Policies and regulations on microplastic established by countries

Year	Country	Regulations
2014	Netherlands	Ban the usage of microbeads in cosmetic products.
2015	United States (US)	Microbeads-Free Waters Act of 2015
2017	Canada	Microbeads in Toiletries Regulations 2017
2016	France	Law n° 2016-1087 for the recovery of biodiversity, nature and landscapes
2018	Italy	General Budget Law 2018 no. 205 of 27
2017	New Zealand	Waste Minimisation (Microbeads) Regulations 2017
1998	Sweden	Ordinance (1998: 944) on prohibitions, etc. in certain cases in connection with the handling, importation and export of chemical products
2017	England	Environmental Protection (Microbeads) Regulations 2017
2018	Scotland	Environmental Protection (Microbeads) Regulations 2018
2018	Wales	Environmental Protection (Microbeads) Regulations 2018
2018	Northern Ireland	Environmental Protection (Microbeads) Regulations 2018
2023	United States (US)	National Strategy to Prevent Plastic Pollution proposed by the United States Environmental Protection Agency

References [151-158]

Future directions and emerging trends

In the future, there is a need for standardised methodologies for microplastic analysis, quantification, and classification. The accurate characterisation of microplastics is crucial for appropriate categorisation and isolation of microplastics before downstream conversion processing, hence escalating future research is expected on the development of advanced techniques that allow for rapid and precise analysis of microplastics. For example, method improvisations on mechanical recycling and biodegradation optimisation through specific designs of microbial consortia or enzymes could recover high-quality conventional microplastics and accelerate the breakdown process of

biodegradable microplastics. As innovative conversion technologies emerge, future microplastic research could include the development and integration of circular economy models into broader frameworks that incorporate microplastic recovery, conversion, and reuse, thus reducing the dependence on virgin plastics. While future research expansion is expected on the conversion of conventional microplastics to biofuels, the simultaneous production of biodegradable microplastics and biofuels from renewable resources might also be considered. In addition, future regulatory frameworks are also expected to encompass both conventional and biodegradable microplastics, ensuring that products claiming to be biodegradable undergo rigorous testing to validate their claims before "green" or eco-friendly labels are permitted. Policymakers must collaborate with researchers and industries to develop effective waste management strategies that prevent microplastics from entering the environment. By embracing a multidisciplinary and holistic approach, international and national collaboration among researchers, industries, policymakers, governments, and non-governmental organizations is paramount for driving meaningful progress in microplastic research via the exchange of knowledge, resources, and expertise.

Conclusion

This study explores the potential of converting conventional microplastics into value-added products by comprehensively exploring the collection, characterisation (i.e., physical and chemical), conversion (i.e., biological, chemical, and mechanical) methods, providing valuable insights into the potential of mitigating microplastic pollution while deriving value from these materials. The physical and chemical characterisation of microplastics highlights the distinctive attributes of conventional microplastics to tailor suitable conversion approaches based on the various compositions of microplastics. Biological conversion is a promising avenue, as it shows the ability of microorganisms to degrade both types of microplastics, suggesting the potential for bioremediation of microplastic pollution. Chemical and mechanical conversion pathways also offer routes to synthesize value-added products such as biofuels from microplastic materials. Furthermore, the exploration of potential applications of value-added products derived from microplastics underlines their potential to contribute to the transition towards a more sustainable and circular economy. Regulatory and policy considerations are also crucial, as the conversion processes may be subject to varying regulations, requiring coordination and adaptive governance structures. Moreover, challenges in the conversion processes, such as technical constraints and economic feasibility, emphasise the need for continued research and development efforts. Collaboration between academia, industry, and policymakers is essential in mitigating plastic pollution and fostering circular economies.

Acknowledgement

Preparation of this review was supported by the Fundamental Research Grant Scheme (FGRS) awarded by Ministry of Higher Education of Malaysia, grant number FRGS/1/2022/STG01/UMT/02/1.

References

1. Gad, A. K., Toner, K., Benfield, M. C., and Midway, S. R. (2023). Microplastics in mainstem Mississippi River fishes. *Frontiers in Environmental Science*, 10: 1065583.
2. Harb, C., Pokhrel, N., and Foroutan, H. (2023). Quantification of the emission of atmospheric microplastics and nanoplastics via sea spray. *Environmental Science and Technology Letters*, 10(6): 513-519.
3. He, D., Bristow, K., Filipović, V., Lv, J., and He, H. (2020). Microplastics in terrestrial ecosystems: A scientometric analysis. *Sustainability*, 12(20): 8739.
4. Lee, H., Kunz, A., Shim, W. J., and Walther, B. A. (2019). Microplastic contamination of table salts from Taiwan, including a global review. *Scientific Reports*, 9(1): 10145.
5. Thornton Hampton, L. M., Brander, S. M., Coffin, S., Cole, M., Hermabessiere, L., Koelmans, A. A., and Rochman, C. M. (2022). Characterizing microplastic hazards: which concentration metrics and particle characteristics are most informative for understanding toxicity in aquatic organisms?. *Microplastics and Nanoplastics*, *2*(1): 20.
6. Kallenbach, E. M., Eriksen, T. E., Hurley, R. R., Jacobsen, D., Singdahl-Larsen, C., and Friberg, N.

(2022). Plastic recycling plant as a point source of microplastics to sediment and macroinvertebrates in a remote stream. *Microplastics and Nanoplastics*, 2(1): 26.

7. Li, J., Gao, F., Zhang, D., Cao, W., and Zhao, C. (2022). Zonal distribution characteristics of microplastics in the Southern Indian Ocean and the influence of Ocean current. *Journal of Marine Science and Engineering*, 10(2): 290.
8. Hernandez, L. M., Yousefi, N., and Tufenkji, N. (2017). Are there nanoplastics in your personal care products?. *Environmental Science & Technology Letters*, 4(7): 280-285.
9. McCormick, A. R., Hoellein, T. J., London, M. G., Hittie, J., Scott, J. W., and Kelly, J. J. (2016). Microplastic in surface waters of urban rivers: concentration, sources, and associated bacterial assemblages. *Ecosphere*, *7*(11): e01556.
10. Kang, T., Kim, D., and Oh, J. H. (2021). Ingestion of microplastics by free-living marine nematodes, especially Enoplolaimus spp., in Mallipo Beach, South Korea. *Plankton and Benthos Research*, 16(2): 109-117.
11. Koelmans, A. A. (2015). Modeling the role of microplastics in bioaccumulation of organic chemicals to marine aquatic organisms. A critical review. *Marine Anthropogenic Litter*, pp. 309-324.
12. Moyo, S. (2022). An enigma: A meta-analysis reveals the effect of ubiquitous microplastics on different taxa in aquatic systems. *Frontiers in Environmental Science*, 10: 999349.
13. Rades, M., Schubert, P., Wilke, T., and Reichert, J. (2022). Reef-building corals do not develop adaptive mechanisms to better cope with microplastics. *Frontiers in Marine Science*, 9: 863187.
14. Li, W., Zhao, W., Zhu, H., Li, Z. J., and Wang, W. (2023). State of the art in the photochemical degradation of (micro) plastics: from fundamental principles to catalysts and applications. *Journal of Materials Chemistry A*, 11(6): 2503-2527.
15. European Environment Agency. (2022). Microplastics from textiles: Towards a circular economy for textiles in Europe. Retrieved on 23 August 2023 from https://www.eea.europa.eu/publications/microplastics-from-textiles-towards-a
16. Galgani, L., Beiras, R., Galgani, F., Panti, C., and Borja, A. (2019). Impacts of marine litter. *Frontiers in Marine Science*, 6: 208.
17. Pacheco-Lopez, A., Lechtenberg, F., Somoza-Tornos, A., Graells, M., and Espuna, A. (2021). Economic and environmental assessment of plastic waste pyrolysis products and biofuels as substitutes for fossil-based fuels. *Frontiers in Energy Research*, 9: 676233.
18. Payne, J., McKeown, P., and Jones, M. D. (2019). A circular economy approach to plastic waste. *Polymer Degradation and Stability*, 165: 170-181.
19. Nabgan, W., Nabgan, B., Tuan Abdullah, T. A., Ikram, M., Jadhav, A. H., Jalil, A. A., and Ali, M. W. (2022). Highly active biphasic anatase-rutile Ni-Pd/TNPs nanocatalyst for the reforming and cracking reactions of microplastic waste dissolved in phenol. *ACS omega*, *7*(4): 3324-3340.
20. Vaccaro, P. A., Galvín, A. P., Ayuso, J., Lozano-Lunar, A., and López-Uceda, A. (2021). Pollutant potential of reinforced concrete made with recycled plastic fibres from food packaging waste. *Applied Sciences*, 11(17): 8102.
21. Dionela, T., Evangelista, A., Lansang, C. M., and Sato, M. V. U. (2022). Sustainable marketing: Studying the effects of environmental consciousness and involvement degree on purchasing behavior of consumers. *Journal of Business and Management Studies*, 4(1): 213-221.
22. Anand, U., Dey, S., Bontempi, E., Ducoli, S., Vethaak, A. D., Dey, A., and Federici, S. (2023). Biotechnological methods to remove microplastics: a review. *Environmental Chemistry Letters*, 21(3): 1787-1810.
23. Wu, H., Mehrabi, H., Naveed, N., and Karagiannidis, P. (2022). Impact of strategic control and supply chain management on recycled plastic additive manufacturing. *Journal of Cleaner Production*, 364: 132511.
24. Hale, R. C., Seeley, M. E., King, A. E., and Yu, L. H. (2022). Analytical chemistry of plastic debris: sampling, methods, and instrumentation. *Microplastic in the Environment: Pattern and Process*, pp. 17-67.
25. Hung, C., Klasios, N., Zhu, X., Sedlak, M., Sutton, R., and Rochman, C. M. (2021). Methods matter: methods for sampling microplastic and other anthropogenic particles and their implications for

monitoring and ecological risk assessment. *Integrated Environmental Assessment and Management*, 17(1): 282-291.

26. Hamilton, B. M., Jantunen, L., Bergmann, M., Vorkamp, K., Aherne, J., Magnusson, K., ... and Peeken, I. (2022). Microplastics in the atmosphere and cryosphere in the circumpolar North: a case for multicompartment monitoring. *Arctic Science*, 8(4): 1116-1126.
27. Khalik, W. M. A. W. M., Ibrahim, Y. S., Anuar, S. T., Govindasamy, S., and Baharuddin, N. F. (2018). Microplastics analysis in Malaysian marine waters: A field study of Kuala Nerus and Kuantan. *Marine Pollution Bulletin*, 135: 451-457.
28. Radford, F., Horton, A., Hudson, M., Shaw, P., and Williams, I. (2023). Agricultural soils and microplastics: Are biosolids the problem?. *Frontiers in Soil Science*, 2: 941837.
29. Taha, Z. D., Amin, R. M., Anuar, S. T., Nasser, A. A. A., and Sohaimi, E. S. (2021). Microplastics in seawater and zooplankton: A case study from Terengganu estuary and offshore waters, Malaysia. *Science of the Total Environment*, 786: 147466.
30. Lots, F. A., Behrens, P., Vijver, M. G., Horton, A. A., and Bosker, T. (2017). A large-scale investigation of microplastic contamination: abundance and characteristics of microplastics in European beach sediment. *Marine Pollution Bulletin*, 123(1-2): 219-226.
31. McNeish, R. E., Kim, L. H., Barrett, H. A., Mason, S. A., Kelly, J. J., and Hoellein, T. J. (2018). Microplastic in riverine fish is connected to species traits. *Scientific Reports*, 8(1): 11639.
32. Talvitie, J., Mikola, A., Koistinen, A., and Setälä, O. (2017). Solutions to microplastic pollution–removal of microplastics from wastewater effluent with advanced wastewater treatment technologies. *Water Research*, 123: 401-407.
33. Laglbauer, B. J., Franco-Santos, R. M., Andreu-Cazenave, M., Brunelli, L., Papadatou, M., Palatinus, A., ... and Deprez, T. (2014). Macrodebris and microplastics from beaches in Slovenia. *Marine Pollution Bulletin*, *89*(1-2): 356-366.
34. Zhou, C., and Wang, Y. (2020). Recent progress in the conversion of biomass wastes into functional materials for value-added applications. *Science and Technology of Advanced Materials*, 21(1): 787-804.
35. Lamichhane, G., Acharya, A., Marahatha, R., Modi, B., Paudel, R., Adhikari, A., ... and Parajuli, N. (2023). Microplastics in environment: global concern, challenges, and controlling measures. *International Journal of Environmental Science and Technology*, 20(4): 4673-4694.
36. Adhikari, S., Kelkar, V., Kumar, R., and Halden, R. U. (2022). Methods and challenges in the detection of microplastics and nanoplastics: a mini-review. *Polymer International*, 71(5): 543-551.
37. Sun, Y., Duan, C., Cao, N., Ding, C., Huang, Y., and Wang, J. (2022). Biodegradable and conventional microplastics exhibit distinct microbiome, functionality, and metabolome changes in soil. *Journal of Hazardous Materials*, 424: 127282.
38. Thakur, S., Chaudhary, J., Sharma, B., Verma, A., Tamulevicius, S., and Thakur, V. K. (2018). Sustainability of bioplastics: Opportunities and challenges. *Current Opinion in Green and Sustainable Chemistry,* 13: 68-75.
39. Wang, C., Yu, J., Lu, Y., Hua, D., Wang, X., and Zou, X. (2021). Biodegradable microplastics (BMPs): a new cause for concern?. *Environmental Science and Pollution Research*, 28: 66511-66518.
40. Weinstein, J. E., Dekle, J. L., Leads, R. R., and Hunter, R. A. (2020). Degradation of bio-based and biodegradable plastics in a salt marsh habitat: another potential source of microplastics in coastal waters. *Marine Pollution Bulletin*, 160: 111518.
41. Fuller, S., and Gautam, A. (2016). A procedure for measuring microplastics using pressurized fluid extraction. *Environmental Science and Technology*, 50(11): 5774-5780.
42. Maxwell S, H., Melinda K, F., and Matthew, G. (2020). Counterstaining to separate nile red-stained microplastic particles from terrestrial invertebrate biomass. *Environmental Science and Technology*, 54(9): 5580-5588.
43. Jin, M., Liu, J., Yu, J., Zhou, Q., Wu, W., Fu, L., ... and Karimi-Maleh, H. (2022). Current development and future challenges in microplastic detection techniques: A bibliometrics-based analysis and review. *Science Progress*, 105(4): 00368504221132151.

44. Shim, W. J., Hong, S. H., and Eo, S. E. (2017). Identification methods in microplastic analysis: a review. *Analytical Methods*, 9(9): 1384-1391.
45. Friedrich, K., Möllnitz, S., Holzschuster, S., Pomberger, R., Vollprecht, D., and Sarc, R. (2019). Benchmark analysis for plastic recyclates in Austrian waste management. *Detritus*, *9*(9): 105-112.
46. Schyns, Z. O., and Shaver, M. P. (2021). Mechanical recycling of packaging plastics: A review. *Macromolecular Rapid Communications,* 42(3): 2000415.
47. Hassan, T., Srivastwa, A. K., Sarkar, S., and Majumdar, G. (2022, February). Characterization of plastics and polymers: A comprehensive study. In *IOP Conference Series: Materials Science and Engineering*. IOP Publishing: p. 012033.
48. Sola, A., Chong, W. J., Simunec, D. P., Li, Y., Trinchi, A., Kyratzis, I. L., and Wen, C. (2023). Open challenges in tensile testing of additively manufactured polymers: A literature survey and a case study in fused filament fabrication. *Polymer Testing*, 117: 107859.
49. Niranjan, A. (2023, July 27). 'Era of global boiling has arrived', says UN chief as July set to be hottest month on record. The Guardian. https://www.theguardian.com/science/2023/jul/27/scientists-july-world-hottest-month-record-climate-temperatures
50. Ng, H. M., Saidi, N. M., Omar, F. S., Ramesh, K., Ramesh, S., and Bashir, S. (2002). Thermogravimetric analysis of polymers. *Encyclopedia of Polymer Science and Technology*, 2002: 1-29.
51. McKeen, L. (2012). The effect of sterilization on plastics and elastomers. William Andrew Publishing.
52. Danielsen, S. P. O., Beech, H. K., Wang, S., El-Zaatari, B. M., Wang, X., Sapir, L., Ouchi, T., Wang, Z., Johnson, P. N., Hu, Y., Lundberg, D. J., Stoychev, G., Craig, S. L., Johnson, J. A., Kalow, J. A., Olsen, B. D., and Rubinstein, M. (2021). Molecular characterization of polymer networks. *Chemical Reviews,* 121(8), 5042-5092.
53. Li, W., Luo, Y., and Pan, X. (2020). Identification and characterization methods for microplastics basing on spatial imaging in micro-/nanoscales. Microplastics in terrestrial environments: *Emerging Contaminants and Major Challenges*, 2020 : 25-37.
54. Tirkey, A., and Upadhyay, L. S. B. (2021). Microplastics: An overview on separation, identification, and characterization of microplastics. *Marine Pollution Bulletin,* 170: 112604.
55. Girão, A. V. (2022). SEM/EDS and optical microscopy analysis of microplastics. In handbook of microplastics in the environment. Cham: Springer International Publishing: pp. 57-78.
56. Ding, J., Li, J., Sun, C., Jiang, F., Ju, P., Qu, L., Zheng, Y., and He, C. (2018). Detection of microplastics in local marine organisms using a multi-technology system. *Analytical Methods,* 11(1): 78-87.
57. Dehaut, A., Hermabessiere, L., and Duflos, G. (2019). Current frontiers and recommendations for the study of microplastics in seafood. *TrAC Trends in Analytical Chemistry,* 116: 346-359.
58. Fytianos, G., Ioannidou, E., Thysiadou, A., Mitropoulos, A. C., and Kyzas, G. Z. (2021). Microplastics in mediterranean coastal countries: A recent overview. *Journal of Marine Science and Engineering*, 9(1): 98.
59. Renner, G., Schmidt, T. C., and Schram, J. (2017). A new chemometric approach for automatic identification of microplastics from environmental compartments based on FT-IR spectroscopy. *Analytical Chemistry,* 89(22): 12045-12053.
60. Lasch, P., and Naumann, D. (2006). Spatial resolution in infrared microspectroscopic imaging of tissues. *Biochimica et Biophysica Acta (BBA)-Biomembranes*, 1758(7): 814-829.
61. Miller, L. M., and Dumas, P. (2010). From structure to cellular mechanism with infrared microspectroscopy. *Current Opinion in Structural Biology*, 20(5): 649-656.
62. Fu, W., Min, J., Jiang, W., Li, Y., and Zhang, W. (2020). Separation, characterization and identification of microplastics and nanoplastics in the environment. *Science of the Total Environment*, 721: 137561.
63. Baruah, A., Sharma, A., Sharma, S., and Nagraik, R. (2022). An insight into different microplastic detection methods. *International Journal of Environmental Science and Technology*, 19(6): 5721-5730.

64. Blanco, M., and Villarroya, I. (2002). NIR spectroscopy: a rapid-response analytical tool. *TrAC Trends in Analytical Chemistry,* 21(4): 240-250.
65. Peez, N., Becker, J., Ehlers, S. M., Fritz, M., Fischer, C. B., Koop, J. H. E., Winkelmann, C., and Imhof, W. (2019). Quantitative analysis of PET microplastics in environmental model samples using quantitative ^{1}H-NMR spectroscopy: validation of an optimized and consistent sample clean-up method. *Analytical and Bioanalytical Chemistry,* 411(28): 7409-7418.
66. Peez, N., Janiska, M. C., and Imhof, W. (2019). The first application of quantitative ^{1}H NMR spectroscopy as a simple and fast method of identification and quantification of microplastic particles (PE, PET, and PS). *Analytical and Bioanalytical Chemistry*, 411(4): 823-833.
67. Huppertsberg, S., and Knepper, T. P. (2018). Instrumental analysis of microplastics—benefits and challenges. *Analytical and Bioanalytical Chemistry*, 410: 6343-6352.
68. Sridhar, A., Kannan, D., Kapoor, A., and Prabhakar, S. (2022). Extraction and detection methods of microplastics in food and marine systems: A critical review. *Chemosphere,* 286: 131653.
69. Fries, E., Dekiff, J. H., Willmeyer, J., Nuelle, M. T., Ebert, M., and Remy, D. (2013). Identification of polymer types and additives in marine microplastic particles using pyrolysis-GC/MS and scanning electron microscopy. *Environmental Science: Processes & Impacts,* 15(10): 1949-1956.
70. Akoueson, F., Chbib, C., Monchy, S., Paul-Pont, I., Doyen, P., Dehaut, A., and Duflos, G. (2021). Identification and quantification of plastic additives using pyrolysis-GC/MS: A review. *Science of the Total Environment,* 773: 145073.
71. La Nasa, J., Biale, G., Fabbri, D., and Modugno, F. (2020). A review on challenges and developments of analytical pyrolysis and other thermoanalytical techniques for the quali-quantitative determination of microplastics. *Journal of Analytical and Applied Pyrolysis,* 149: 104841.
72. Castelvetro, V., Corti, A., Biale, G., Ceccarini, A., Degano, I., La Nasa, J., Lomonaco, T., Manariti, A., Manco, E., Modugno, F., and Vinciguerra, V. (2021). New methodologies for the detection, identification, and quantification of microplastics and their environmental degradation by-products. *Environmental Science and Pollution Research,* 28(34): 46764-46780.
73. Giaganini, G., Cifelli, M., Biagini, D., Ghimenti, S., Corti, A., Castelvetro, V., Domenici, V., and Lomonaco, T. (2023). Multi-analytical approach to characterize the degradation of different types of microplastics: Identification and quantification of released organic compounds. *Molecules,* 28(3): 1382.
74. Adelugba, A., and Emenike, C. (2023). Comparative review of instrumental techniques and methods for the analysis of microplastics in agricultural matrices. *Microplastics,* 3(1): 1-21.
75. Ru, J., Huo, Y. and Yang, Y. (2020). Microbial degradation and valorization of plastic wastes. *Front Microbiology,* 2020: 442.
76. Thiyagarajan, S., Maaskant-Reilink, E., Ewing, T. A., Julsing, M. K., and van Haveren, J. (2022). Back-to-monomer recycling of polycondensation polymers: opportunities for chemicals and enzymes. *RSC Advances,* 12(2): 947-970.
77. Wierckx, N., Prieto, M. A., Pomposiello, P., de Lorenzo, V., O'Connor, K., and Blank, L. M. (2015). Plastic waste as a novel substrate for industrial biotechnology. *Microbial Biotechnology,* 8(6):900-903.
78. Mohanan, N., Montazer, Z., Sharma, P. K., and Levin, D. B. (2020). Microbial and enzymatic degradation of synthetic plastics. *Frontiers in Microbiology*, 11: 580709.
79. Papari, S., Bamdad, H., and Berruti, F. (2021). Pyrolytic conversion of plastic waste to value-added products and fuels: A review. *Materials,* 14(10): 2586.
80. Ragaert, K., Delva, L., and Van Geem, K. (2017). Mechanical and chemical recycling of solid plastic waste. *Waste Management,* 69 : 24-58.
81. Palve, A. M., Arukula, R., and Gupta, R. K. (2021). Bioconversion of biowastes for energy applications. *Sustainable Bioconversion of Waste to Value Added Products,* pp. 1-22.
82. Narancic, T., and O'Connor, K. E. (2017). Microbial biotechnology addressing the plastic waste disaster. *Microbial Biotechnology,* 10(5): 1232-1235.
83. Tamoor, M., Samak, N. A., Jia, Y., Mushtaq, M. U., Sher, H., Bibi, M. and Xing, J. (2021). Potential use of microbial enzymes for the

conversion of plastic waste into value-added products: a viable solution. *Frontier Microbiology,* 12: 777727.

84. Yoshida, S., Hiraga, K., Takehana, T., Taniguchi, I., Yamaji, H., Maeda, Y., Toyohara, K., Miyamoto, K., Kimura, Y. and Oda, K. (2016). A bacterium that degrades and assimilates poly(ethylene terephthalate). *Science,* 351(6278): 1196-1199.
85. Palm, G. J., Reisky, L., Böttcher, D., Müller, H., Michels, E. A. P., Walczak, M. C., Berndt, L., Weiss, M. S., Bornscheuer, U. T. and Weber, G. (2019). Structure of the plastic-degrading *Ideonella sakaiensis* MHETase bound to a substrate. *Nature Communication,* 10 : 1717.
86. Johnston, B., Adamus, G., Ekere, A. I., Kowalczuk, M., Tchuenbou-Magaia, F., and Radecka, I. (2022). Bioconversion of plastic waste based on mass full carbon backbone polymeric materials to value-added polyhydroxyalkanoates (PHAs). *Bioengineering,* 9(9): 432.
87. Lee, H. M., Kim, H. R., Jeon, E., Yu, H. C., Lee, S., Li, J., and Kim, D. H. (2020). Evaluation of the biodegradation efficiency of four various types of plastics by *Pseudomonas aeruginosa* isolated from the gut extract of superworms. *Microorganisms,* 8(9): 1341.
88. Vimala, P. P., and Mathew, L. (2016). Biodegradation of polyethylene using *Bacillus Subtilis*. *Procedia Technology,* 24: 232-239.
89. Gan, Z., and Zhang, H. (2019). PMBD: A comprehensive plastics microbial biodegradation database. *Database: The Journal of Biological Databases and Curation,* 2019: 1-11.
90. Atanasova, N., Stoitsova, S., Paunova-krasteva, T., and Kambourova, M. (2021). Plastic degradation by extremophilic bacteria. *International Journal of Molecular Sciences*, 12: 5610.
91. Nguyen, S. T., McLoughlin, E. A., Cox, J. H., Fors, B. P., and Knowles, R. R. (2021). Depolymerization of hydroxylated polymers via light-driven C–C bond cleavage. *Journal of the American Chemical Society,* 143(31): 12268-12277.
92. Gao. R. and Sun, C. (2021). A marine bacterial community capable of degrading poly(ethylene terephthalate) and polyethylene. *Journal of Hazardous Materials,* 416: 125928.
93. Wu, Z., Shi, W., Valencak, T. G., Zhang, Y., Liu, G., and Ren, D. (2023). Biodegradation of conventional plastics: Candidate organisms and potential mechanisms. *Science of The Total Environment,* 2023: 163908.
94. Zhang, M. Q., Wang, M., Sun, B., Hu, C., Xiao, D., and Ma, D. (2022). Catalytic strategies for upvaluing plastic wastes. *Chemistry,* 8(11): 2912-2923.
95. Taniguchi, I., Yoshida, S., Hiraga, K., Miyamoto, K., Kimura, Y., and Oda, K. (2019). Biodegradation of PET: Current status and application aspects. *ACS Catalysis,* 9(5): 4089-4105.
96. Roberts, C., Edwards, S., Vague, M., León-Zayas, R., Scheffer, H., Chan, G., Swartz, N. A., and Mellies, J. L. (2020). Environmental consortium containing *Pseudomonas* and *Bacillus* species synergistically degrades polyethylene terephthalate plastic. *mSphere,* 5(6): e01151-20.
97. Qi, X., Ma, Y., Chang, H., Li, B., Ding, M., and Yuan, Y. (2021). Evaluation of PET degradation using artificial microbial consortia. *Frontiers in Microbiology*, 12 : 778828.
98. Wang, C., and El-Sepelgy, O. (2021). Reductive depolymerization of plastics catalyzed with transition metal complexes. *Current Opinion in Green and Sustainable Chemistry*, 32: 100547.
99. Knott, B. C., Erickson, E., Allen, M. D., Gado, J. E., Graham, R., Kearns, F. L., Pardo, I., Topuzlu, E., Anderson, J. J., Austin, H. P., Dominick, G., Johnson, C. W., Rorrer, N. A., Szostkiewicz, C. J., Copié, V., Payne, C. M., Lee Woodcock, H., Donohoe, B. S., Beckham, G. T., and McGeehan, J. E. (2020). Characterization and engineering of a two-enzyme system for plastics depolymerization. *Proceedings of the National Academy of Sciences*, pp. 1-20.
100. Alberti, C., and Enthaler, S. (2020). Depolymerization of end-of-life poly(lactide) to lactide via zinc-catalysis. *Chemistry Select,* 5(46): 14759-14763.
101. Mao, Y., Fan, S., Li, X., Shi, J., Wang, M., Niu, Z., and Chen, G. (2023). Trash to treasure: Electrocatalytic upcycling of polyethylene terephthalate (PET) microplastic to value-added products by Mn0.1Ni0.9Co2O4-δ RSFs spinel. *Journal of Hazardous Materials,* 457(2023): 131743.

102. Han, Z., Rong, L., Wu, J., Zhang, L., Wang, Z., and Ding, K. (2012). Catalytic hydrogenation of cyclic carbonates: A practical approach from CO_2 and epoxides to methanol and diols. *Angewandte Chemie,* 124(52): 13218-13222.
103. Klein, S., Dimzon, I. K., Eubeler, J., and Knepper, T. P. (2018). Analysis, occurrence, and degradation of microplastics in the aqueous environment. *Freshwater Microplastics: Emerging Environmental Contaminants?*, pp. 51-67.
104. Al-Azzawi, M. S., Kefer, S., Weißer, J., Reichel, J., Schwaller, C., Glas, K., ... and Drewes, J. E. (2020). Validation of sample preparation methods for microplastic analysis in wastewater matrices—reproducibility and standardization. *Water,* 12(9): 2445.
105. Mahari, W. A. W., Kee, S. H., Foong, S. Y., Amelia, T. S. M., Bhubalan, K., Man, M., Yang, Y. F., Ong, H. C., Vithanage, M., Lam, S. S., and Sonne, C. (2022). Generating alternative fuel and bioplastics from medical plastic waste and waste frying oil using microwave co-pyrolysis combined with microbial fermentation. *Renewable and Sustainable Energy Reviews,* 153: 111790.
106. Akgül, A., Palmeiro-Sanchez, T., Lange, H., Magalhaes, D., Moore, S., Paiva, A., Kazanç, F., and Trubetskaya, A. (2022). Characterization of tars from the recycling of PHA bioplastic and synthetic plastics using fast pyrolysis. *Journal of Hazardous Materials,* 439: 129696.
107. Nabgan, W., Nabgan, B., Tuan Abdullah, T. A., Ikram, M., Jadhav, A. H., Ali, M. W., and Jalil, A. A. (2022). Hydrogen and value-added liquid fuel generation from pyrolysis-catalytic steam reforming conditions of microplastics waste dissolved in phenol over bifunctional Ni-Pt supported on Ti-Al nanocatalysts. *Catalysis Today,* 400–401: 35-48.
108. Jung, J. M., Cho, S. H., Jung, S., Lin, K. Y. A., Chen, W. H., Tsang, Y. F., and Kwon, E. E. (2022). Disposal of plastic mulching film through CO2-assisted catalytic pyrolysis as a strategic means for microplastic mitigation. *Journal of Hazardous Materials,* 430: 128454.
109. National Energy Technology Laboratory (n.d.). Gasification introduction. Retrieved from https://netl.doe.gov/research/Coal/energy-systems/gasification/gasifipedia/intro-to-gasification. [Accessed on 23/8/2023].
110. Wang, Z., Liu, X., Burra, K. G., Li, J., Zhang, M., Lei, T., and Gupta, A. K. (2021). Towards enhanced catalytic reactivity in CO2-assisted gasification of polypropylene. *Fuel,* 284: 119076.
111. Moghadam, R. A., Yusup, S., Uemura, Y., Chin, B. L. F., Lam, H. L., and Al Shoaibi, A. (2014). Syngas production from palm kernel shell and polyethylene waste blend in fluidized bed catalytic steam co-gasification process. *Energy,* 75: 40-44.
112. Lin, Y., Kouznetsova, T. B., and Craig, S. L. (2020). Mechanically gated degradable polymers. *Journal of the American Chemical Society,* 142(5): 2105-2109.
113. Alauddin, M., Choudhury, I. A., El Baradie, M. A., and Hashmi, M. S. J. (1995). Plastics and their machining: A review. *Journal of Materials Processing Technology,* 54(1–4): 40-46.
114. Zhou, J., Hsu, T. G., and Wang, J. (2023). Mechanochemical degradation and recycling of synthetic polymers. *In Angewandte Chemie - International Edition*, 62(27): 768.
115. Damayanti, D., Saputri, D. R., Marpaung, D. S. S., Yusupandi, F., Sanjaya, A., Simbolon, Y. M., Asmarani, W., Ulfa, M., and Wu, H. S. (2022). Current prospects for plastic waste treatment. *Polymers*, 14(15): 3133.
116. Eitzen, L., Paul, S., Braun, U., Altmann, K., Jekel, M., and Ruhl, A. S. (2019). The challenge in preparing particle suspensions for aquatic microplastic research. *Environmental Research*, 168: 490-495.
117. Kefer, S., Miesbauer, O., and Langowski, H. C. (2021). Environmental microplastic particles vs. engineered plastic microparticles—a comparative review. *Polymers,* 13(17): 2881.
118. Ramos, A., Monteiro, E., and Rouboa, A. (2022). Biomass pre-treatment techniques for the production of biofuels using thermal conversion methods – A review. *Energy Conversion and Management,* 270: 116271.
119. Lievens, S., Vervoort, E., Poma, G., Covaci, A., and Van Der Borght, M. (2023). A production and fractionation protocol for polyvinyl chloride microplastics. *Methods and Protocols*, 6(1): 15.
120. Nykamp, G., Carstensen, U., and Müller, B. W. (2002). Jet milling - A new technique for microparticle preparation. *International Journal of Pharmaceutics,* 242(1-2): 79-86.

121. Boey, J. Y., Lee, C. K., and Tay, G. S. (2022). Factors affecting mechanical properties of reinforced bioplastics: A review. *Polymers*, 14(18): 3737.
122. Sikora, J. W. (2008). Increasing the efficiency of the extrusion process. *Polymer Engineering & Science,* 48(9): 1678-1682.
123. Ragaert, K., Delva, L., and Van Geem, K. (2017). Mechanical and chemical recycling of solid plastic waste. *Waste Management,* 69: 24-58.
124. Schyns, Z. O., and Shaver, M. P. (2021). Mechanical recycling of packaging plastics: A review. *Macromolecular Rapid Communications,* 42(3), 2000415.
125. La Mantia, F. P., and Vinci, M. (1994). Recycling poly(ethyleneterephthalate). *Polymer Degradation and Stability,* 45(1): 121-125.
126. Vogt, B. D., Stokes, K. K., and Kumar, S. K. (2021). Why is recycling of postconsumer plastics so challenging? *ACS Applied Polymer Materials,* 3(9): 4325-4346.
127. Pfohl, P., Roth, C., Meyer, L., Heinemeyer, U., Gruendling, T., Lang, C., ... and Jessl, S. (2021). Microplastic extraction protocols can impact the polymer structure. *Microplastics and Nanoplastics*, 1: 1-13.
128. Imteaz, M. A., Arulrajah, A., and Maghool, F. (2020). Environmental and geotechnical suitability of recycling waste materials from plasterboard manufacturing. *Waste Management and Research,* 38(4): 383-391.
129. Almohana, A. I., Abdulwahid, M. Y., Galobardes, I., Mushtaq, J., and Almojil, S. F. (2022). Producing sustainable concrete with plastic waste: A review. *Environmental Challenges,* 9: 100626.
130. Rosenboom, J. G., Langer, R. and Traverso, G. (2022). Bioplastics for a circular economy. *Nature Review Materials,* 7: 117-137.
131. Maurya, A., Bhattacharya, A., and Khare, S. K. (2020). Enzymatic remediation of polyethylene terephthalate (PET)–based polymers for effective management of plastic wastes: an overview. *Frontiers in Bioengineering and Biotechnology,* 8: 602325.
132. Williams, J. M., Nitzsche, M. P., Bromberg, L., Qu, Z., Moment, A. J., Hatton, T. A., and Park, A. H. A. (2023). Hybrid thermo-electrochemical conversion of plastic wastes commingled with marine biomass to value-added products using renewable energy. *Energy and Environmental Science,* 16(12): 5805-5821.
133. Tiwari, R., Azad, N., Dutta, D., Yadav, B. R., and Kumar, S. (2023). A critical review and future perspective of plastic waste recycling. *Science of the Total Environment,* 2023: 163433.
134. Geyer, R., Jambeck, J. R., and Law, K. L. (2017). Production, use, and fate of all plastics ever made. *Science Advances,* 3(7): e1700782.
135. Cole, M., Lindeque, P., Halsband, C., and Galloway, T. S. (2011). Microplastics as contaminants in the marine environment: A review. *Marine Pollution Bulletin,* 62(12): 2588-2597.
136. González-Pleiter, M., Tamayo-Belda, M., Pulido-Reyes, G., Amariei, G., Leganés, F., Rosal, R., and Fernández-Piñas, F. (2019). Secondary nanoplastics released from a biodegradable microplastic severely impact freshwater environments. *Environmental Science: Nano,* 6(5): 1382-1392.
137. Ma, H., Pu, S., Liu, S., Bai, Y., Mandal, S., and Xing, B. (2020). Microplastics in aquatic environments: Toxicity to trigger ecological consequences. *Environmental Pollution,* 261: 114089.
138. Aragaw, T. A., and Mekonnen, B. A. (2021). Distribution and impact of microplastics in the aquatic systems: A review of ecotoxicological effects on biota. microplastic pollution. *Sustainable Textiles: Production, Processing, Manufacturing & Chemistry*. Springer Singapore: pp. 65-104.
139. Sequeira, I. F., Prata, J. C., da Costa, J. P., Duarte, A. C., and Rocha-Santos, T. (2020). Worldwide contamination of fish with microplastics: A brief global overview. *Marine Pollution Bulletin,* 160: 111681.
140. Kutralam-Muniasamy, G., Pérez-Guevara, F., Elizalde-Martínez, I., and Shruti, V. C. (2020). Review of current trends, advances and analytical challenges for microplastics contamination in Latin America. *Environmental Pollution,* 267: 115463.
141. Carrington, D. (2022, March 24). Microplastics found in human blood for first time. The Guardian. Retrieved from https://www.theguardian.com/environment/2022/

mar/24/microplastics-found-in-human-blood-for-first-time. [Accessed on 22 August 2023]

142. Mitrano, D. M., and Wohlleben, W. (2020). Microplastic regulation should be more precise to incentivize both innovation and environmental safety. *Nature Communications,* 11(1): 5324.
143. Poonacha, S. (2023, May 8). Plastic action in rural india with the alliance to end plastic waste. Retrieved from https://repurpose.global/blog/post/partnership-highlights-mobilizing-plastic-action-in-rural-india-with-the-alliance-to-end-plastic-waste. [Accessed on 22August 2023]
144. Liu, J., Yang, Y., An, L., Liu, Q., and Ding, J. (2021). The value of China's legislation on plastic pollution prevention in 2020. *Bulletin of Environmental Contamination and Toxicology,* 2021: 1-8.
145. Extended Producer Responsibility Act (EPRA). 2022. Retrieved from https://legacy.senate.gov.ph/republic_acts/ra%201898.pdf. [Accessed on 22 August 2023]
146. Solid Waste and Public Cleansing Management Act 2007 (Act 672).
147. Department of Agriculture, Water and the Environment. (2021). National Plastics Plan 2021.
148. Department of Environment and Natural Resources. (2020). National solid waste management commission.
149. Ministry of Energy, Science, Technology, Environment and Climate Change. (2018). Malaysia's roadmap towards zero single-use plastics 2018-2030: Towards a sustainable future.
150. Ministry of Environment and Water. (2021). Malaysia plastics sustainability roadmap 2021-2030: Catalysing sustainability and circularity towards a new plastics economy. Retrieved from https://ce.acsdsd.org/knowledge/the-malaysia-plastic-sustainability-roadmap-2021-2030-catalyzing-sustainability-and-circularity-towards-a-new-plastic-economy/. [Accessed on 22 August 2023]
151. GESAMP (2015). Sources, fate and effects of microplastics in the marine environment: a global assessment, London: International Maritime Organization.
152. Microbeads-Free Waters Act (2015)
153. OECD (2013 October 28). Policies for Bioplastics in the Context of a Bioeconomy, OECD Science, Technology and Industry Policy Papers, No. 10, OECD Publishing, Paris. Retrieved from http://dx.doi.org/10.1787/5k3xpf9rrw6d-en. [Accessed on 22 August 2023]
154. OECD (2020, June 4). Microbeads in cosmetics. The Oceans-Policy in practice.
155. OECD (2021). Policies to reduce microplastics pollution in water: Focus on textiles and tyres.
156. The Strait Times (2023, May 9). Malaysia to impose total ban on plastic bags by 2025. Retrieved from https://www.straitstimes.com/asia/se-asia/malaysia-to-impose-total-ban-on-plastic-bags-by-2025. [Accessed on 22 August 2023]
157. UNEP (2018). Legal limits on single-use plastics and microplastics: A global review of national laws and regulations. Retrieved from https://www.unep.org/resources/report/legal-limits-single-use-plastics-and-microplastics. [Accessed on 23 August 2023]
158. Xinhua (2020). China reveals plan to cut plastic use by 2025. China.org.cn. Retrieved from http://www.china.org.cn/china/2020-01/19/content_75629958.htm. [Accessed on 22 August 2023]

Malaysian Journal of Analytical Sciences (MJAS)
Published by Malaysian Analytical Sciences Society

INNOVATOVE ECO-FRIENDLY WOOD ADHESIVE FORMULATIONS: EXPLORING THE EFFICACY OF GELATINIZED CASSAVA STARCH AND POLYVINYL ALCOHOL CROSSLINKED WITH CITRIC ACID

(Formulasi Pelekat Kayu Mesra Alam: Inovatif Meneroka Keberkesanan Pati Ubi Kayu Bergelatin dan Alkohol Polivinil Berpaut Silang dengan Asid Sitrik)

Bima Prasetya Pancasakti, Danang Tri Hartanto, Vincent Sinarta, Masyta Dinda Riani, and Budhijanto*

Department of Chemical Engineering, Faculty of Engineering, Universitas Gadjah Mada, Jalan Grafika No. 2, Yogyakarta, Indonesia

Corresponding author budhijanto@ugm.ac.id

Received: 10 November 2023; Accepted: 31 March 2024; Published: 29 June 2024

Abstract

In an effort to develop eco-friendly bio-adhesives for wood applications, this study explores the effect of citric acid as a new cross-linking agent on the properties of a cassava starch/polyvinyl alcohol (PVA)-based wood bio-adhesive. The bio-adhesive was synthesized in a three-step process: first, the hydrolysis of cassava starch using hydrochloric acid, followed by the oxidation of cassava starch with ammonium persulfate, and finally, the polymerization of starch and PVA with citric acid. The reaction was conducted for 100 min in a three-neck flask, using a mercury stirrer at 70°C under atmospheric pressure. The amount of citric acid added to the adhesive was calculated based on the dry weight of the cassava starch, with percentages ranging from 0%, 0.5%, 1%, 1.5%, to 2%. The adhesive characteristics were then evaluated in line with the ASTM D906 wood adhesive standard. Tests were conducted to measure adhesive viscosity, solid content, dry and wet shear strengths, thermal stability, and surface morphology. Molecular changes resulting from the addition of citric acid were analyzed using Fourier transform infrared spectroscopy. This research demonstrated that the addition of citric acid improved the adhesive properties. Specifically, the addition of 2% citric acid (AD-CA2.0) produced optimal results across several analyses. These included a high viscosity reading of 2910 cP, dry and wet shear strengths of 1.21 MPa and 0.89 MPa, respectively, and high solid content of 36%.

Keywords: bio-adhesive, cassava starch, polyvinyl alcohol, citric acid, polymerization

Abstrak

Sebagai pengiktirafan mendapatkan bio-pelekat mesra alam untuk aplikasi kayu, kajian ini meneroka kesan asid sitrik sebagai agen penghubung silang baharu ke atas sifat-sifat bio-pelekat kayu berasaskan kanji ubi kayu/polivinil alkohol (PVA). Bio-pelekat disintesis melalui tiga langkah: hidrolisis kanji ubi kayu dengan asid hidroklorik (HCl), pengoksidaan kanji ubi kayu dengan ammonium persulfat ($(NH_4)_2S_2O_8$), dan pempolimeran kanji dan PVA dengan asid sitrik. Tindak balas dijalankan selama 100 minit dalam kelalang leher tiga dan pengacau merkuri pada suhu 70 °C dan tekanan atmosfera. Berdasarkan berat kering kanji ubi kayu, peratusan asid sitrik yang ditambahkan pada pelekat berbeza antara 0%, 0.5%, 1%, 1.5%, dan 2%. Selaras dengan piawaian pelekat kayu ASTM D906, kelikatan pelekat, kandungan pepejal, kekuatan ricih kering dan basah, kestabilan terma dan morfologi permukaan telah diuji. Perubahan molekul telah dianalisis menggunakan spektroskopi Fourier Transform Infrared (FTIR). Penyelidikan ini menunjukkan bahawa penambahan asid sitrik meningkatkan ciri pelekat. Penambahan 2% asid sitrik

(AD-CA2.0) mempunyai hasil yang optimum untuk beberapa analisis seperti kelikatan tinggi pada 2910 cP, kekuatan ricih kering dan basah pada 1.21 MPa dan 0.89 MPa, dan kandungan pepejal tinggi pada 36%.

Kata kunci: bio-pelekat, kanji ubi kayu, polivinil alkohol, asid sitrik, pempolimeran

Introduction

The global rise in human population has led to an escalating demand for wood furniture, which in turn has increased the consumption of wood adhesives, a pivotal component in the wood industry [1]. Numerous studies have underscored this trend, highlighting a significant annual increase in the demand for wood adhesives [2]. In industry, the capacity of an adhesive to combine two materials in a short amount of time is preferred because it is practical and simple [3, 4].

Wood adhesives are commonly produced by chemical reactions [5], with two main types being utilized in the industry: conventional and natural adhesives [6]. Conventional adhesives are typically derived from petroleum, a nonrenewable resource. Formaldehyde was one of the earliest standard adhesives used to bind wood pairs [7]. It continues to dominate the production of wood-based adhesives owing to its effectiveness, stability, and cost-efficiency [8]. For instance, the urea-formaldehyde adhesive, known for its superior water resistance, is commonly used for interior products, while the phenol-formaldehyde adhesive is preferred for exterior applications [9].

Empirical evidence supports the health risks associated with the use of conventional adhesives. Formaldehyde, a known carcinogen that is used to treat human organ systems [10], poses potential threats not only during the manufacturing process but also in the final products. This is because formaldehyde naturally occurs in wood products and its emissions are generated by the residual formaldehyde content of the resin. Exposure to formaldehyde can induce skin and lung irritation, genotoxicity, and cancer [11]. Additionally, formaldehyde emits volatile organic chemicals that cause significant risks to both humans and the environment [12].

Various investigations on bio-adhesives have been conducted as potential substitutes for petroleum-based adhesives in wood bonding. The objective is to mitigate the adverse effects of synthetic adhesives on both human health and the environment [13]. The raw ingredients for bio-adhesives are abundant and inexpensive resources found in nature. These included materials such as soy, tannins, lignin, gelatin, wood fibers, plant polymers, and starch [14, 15].

Cassava starch, a material rich in amylose and amylopectin, has been utilized as a raw ingredient for bioplastic and paper adhesives [16]. This suggests that cassava starch could potentially serve as a raw material for bio-adhesive production. However, wood panels constructed entirely of starch are currently too fragile for practical use [17]. The hydroxyl groups in starch chains are hydrophilic, causing the starch to quickly interact with water, resulting in poor moisture tolerance. Moreover, when exposed to sufficient moisture and heat, the starch undergoes gelatinization, absorbing water and swelling [18].

A solution to this issue is the addition of PVA to the bio-adhesive, which reduces the rate of water absorption and decreases starch swelling. In the meantime, to ensure effective binding between starch and PVA, a cross-linking agent is required. Previous studies have investigated the influence of cross-linking agents like PTSA and bio-oil on the quality of bio-adhesive materials [19], [20]. However, these agents have been found to reduce adhesive quality, highlighting the need for the development of improved cross-linking agents.

Citric acid, with its three functional carboxyl groups, holds promise as it can potentially form bonds with the hydroxyl groups in starch and PVA. Its incorporation as a cross-linking agent in cassava starch bio-adhesives has demonstrated improved water resistance and mechanical qualities [21]. Despite these promising results, no studies have been conducted to analyze the effects of citric acid on the adhesive properties of starch. This investigation, therefore, sought to fill this research gap by focusing on the performance of cassava starch and polyvinyl alcohol (PVA) using citric acid as the cross-linking agent. A range of tests were

carried out to assess the physical properties and structural changes of the bio-adhesive, including viscosity, dry and wet shear strengths, solid content, thermogravimetry, and Fourier transform infrared (FTIR) analyses.

Materials and Methods

Materials

This study utilized cassava starch purchased from PT. Budi Acid Jaya. PVA and sodium dodecyl sulfate (SDS) procured from CV. Gudang Kimia, Yogyakarta. Hydrochloric acid (HCl, 37%) and citric acid were obtained from the Chemical Reaction and Catalyst Laboratory, UGM, Yogyakarta. Ammonium persulfate ($(NH_4)_2S_2O_8$) was provided by the LPPT UGM (Yogyakarta). Wooden boards (*Tectona grandis*) were purchased from UD. Makmur Jaya, Yogyakarta.

Bio-adhesive synthesis

The bio-adhesive was prepared by dissolving 50 g of cassava starch in 100 mL of 0.5 M HCl. The solution was stirred for 15 min to ensure homogeneity, before being placed in a batch reactor for gelatinization. In this study, the reactor, designed using a three-necked flask and a mercury stirrer, was maintained at a temperature of 70 °C and 1 atm pressure. The stirrer was set to a speed of 500 rpm. After 10 min of gelatinization, 0.4 grams of $(NH_4)_2S_2O_8$ were added to the solution. In addition, 1 gram of SDS was added to the solution after the process had run for 30 minutes. Approximately 15 g of PVA dissolved in 50 mL of distilled water was added to the reactor. The process continued with adding citric acid at a certain concentration, and the reaction was carried out for 1 h. All procedures were repeated with citric acid concentrations of 0%, 1%, 1.5%, and 2% based on the weight of cassava starch. The schematic of bio-adhesive is provided in Figure 1.

Viscosity analysis

The viscosity of the adhesive was analyzed using the ASTM D1084 standard [22]. Approximately 200 mL of the adhesive solution was poured into a glass beaker for this experiment. The adhesive viscosity was measured using a DV-E Brookfield Viscometer. The solution viscosity results were displayed on the monitor.

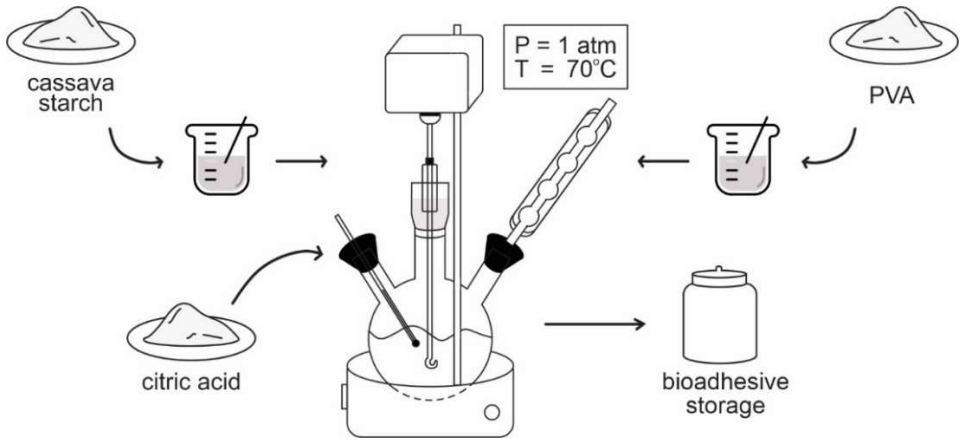

Figure 1. Schematic diagram of cassava starch bio-adhesive synthesis

Dry shear strength analysis

The dry shear strength was measured according to ASTM D906 [23] guidelines. Wood pieces measuring $30 \times 25 \times 2$ mm^3 were attached to the bio-adhesive and pressed under 3.27×10^{-2} N/mm^2 for 24 h before being stored at room temperature for seven days. The maximum bonding strength of the sample was determined at a speed of 2 mm/min using a universal testing machine in the Department of Chemical Engineering UGM. The shear strength of the adhesive was estimated using Equation (1).

$$\sigma_t = \frac{W}{A \times 1000} \quad (1)$$

Where σ_t is the shear strength of the adhesive (MPa),

W is the maximum force load (N), and A is the bonding area of the wood (mm^2). Dry strength analysis was conducted five times.

Wet shear strength analysis

The wet shear strength of the adhesive was calculated using the ASTM D1183 standard [24]. Identically sized wood pairs, already analyzed for dry shear strength, were bonded, and compressed under a pressure of 3.27×10^{-2} N/mm^2. After a day, the sample was submerged in distilled water for 24 h. Following this, the sample was dried and stored at room temperature at a relative humidity of 50%. Using a universal testing machine, we measured the maximum load of the sample at a testing speed of 2 mm/min. We used Equation 1 to calculate the wet shear strength. To ensure accuracy, we repeated this analysis five times and calculated the average of the results.

Solid content analysis

The solid content of the adhesive was determined according to ASTM-D2369 [25]. One gram of bio-adhesive was initially placed in a petri dish and heated at 110 °C ± 2.5 °C for an hour. After stabilizing the sample temperature using a desiccator for 10 min, we weighed the samples. We then used Equation 2 to determine the solid content of the adhesive.

$$S = \frac{w_2 - w_0}{w_1 - w_0} \times 100\% \quad (2)$$

Where S denotes the solid content of adhesive (%), w_0 signifies the mass of the petri dish (gram), w_1 is the mass of petri dish and sample before heating (gram), and w_2 is the mass of petri dish and sample after heating (gram). The solid content analysis was repeated three times.

Fourier transform infrared spectroscopy

The change in the functional groups in the adhesive because of the reaction process was investigated using a spectrophotometer FTIR Nicolet Is10 Mb 3000 from LPPT UGM in Yogyakarta, Indonesia. The spectral range of this study was between 650 and 4000 cm^{-1}, and 32 scans were recorded.

Thermogravimetry Analysis

Thermogravimetric analysis was performed at the Chemical Instrument Analysis Laboratory using a thermogravimetric analyzer (TA Instruments), housed in the DSC-60 Plus Shimadzu, Department of Chemical Engineering, Gadjah Mada University. The sample was dried in an oven at 60 °C for 3 h to obtain an adhesive powder with a size of 200 mesh or finer. The sample was placed in an alumina crucible, and another empty alumina crucible was used as a control. In an N_2 environment, the sample was gradually heated to 600 °C at a rate of 10 °C per min.

Adhesive morphology analysis

To analyze the morphology of the newly prepared adhesive, we used a Dino-Lite microscope AM8917 from the Department of Chemical Engineering, UGM and a scanning electron microscope (SEM) JSM-6510LA from LPPT, UGM. For the Dino-Lite microscope analysis, we placed the sample on a clean transparent glass. The light of the Dino-Lite microscope was turned on, and the magnification was adjusted to 500×. An image of the adhesive morphology was then captured for further analysis.

Results and Discussion

This study investigated the effects of citric acid addition on the quality of bio-adhesives made from cassava starch and PVA. The experiment varied the addition of citric acid between 0%, 0.5%, 1%, 1.5%, and 2%, based on the mass of cassava starch. The samples were labeled as AD-CA0 (blank sample), AD-CA0.5, AD-CA1.0, AD-CA1.5, and AD-CA2.0, according to their respective citric acid content. The experiment was conducted in a batch reactor system at 500 rpm.

In general, the synthesis of cassava starch bio-adhesives using citric acid involves a three-step process. The initial step involves hydrolysis and gelatinization of cassava starch using HCl. This process, carried out at 70 °C and 1 atm of pressure, breaks the glycosidic linkages in the starch to create an acid-thinned starch. The starch was then oxidized with ammonium persulfate $(NH_4)_2S_2O_8$) to produce carboxyl groups (–COOH). hydrolysis and oxidation mechanisms are shown in Figure 2.

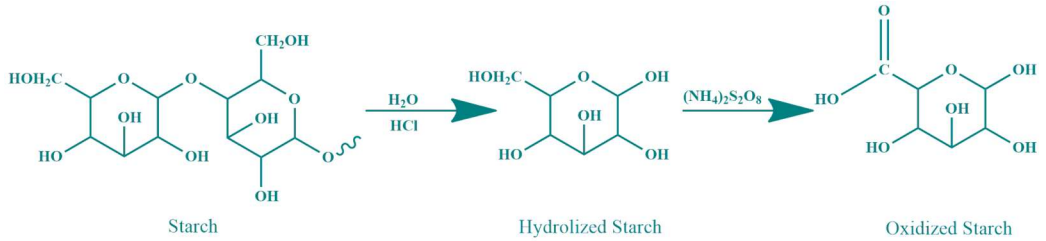

Figure 2. Reaction mechanism of cassava starch hydrolysis and oxidation

The carboxyl group of oxidized starch can form a bond with citric acid, which acts as a cross-linking agent. This bond formation gives rise to ester-starch. In addition, this oxidized molecule can induce retrogradation following gelatinization, a process where gelatinized starch reverts to its original form. Figure 3 illustrates the mechanism by which starch, and citric acid generate ester-starch.

Moreover, starch and PVA have the potential to form a bonding molecule known as ester starch/PVA. Figure 4 depicts the formation of bonding molecules between the starch and PVA using citric acid.

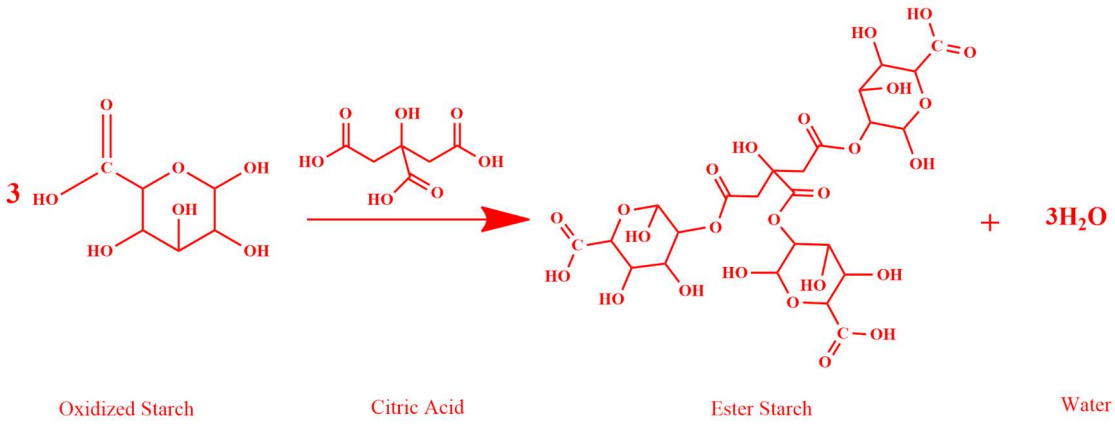

Figure 3. Reaction mechanism of ester starch synthesis

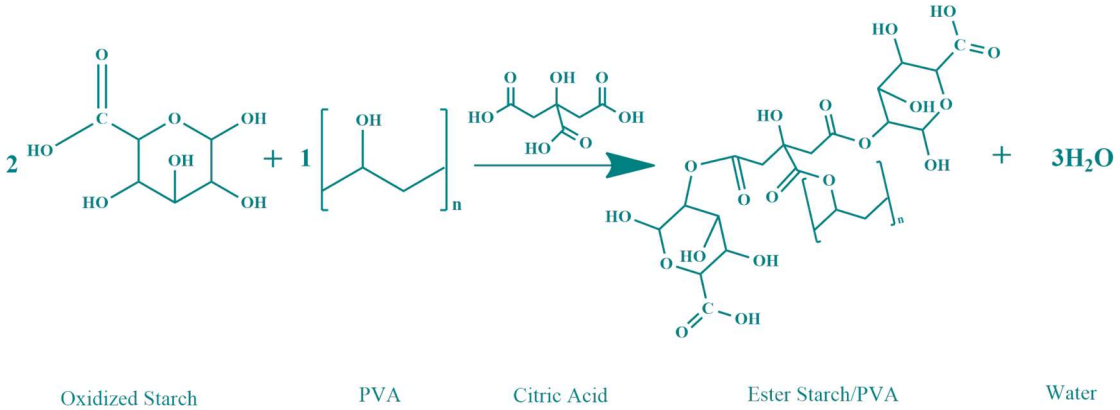

Figure 4. Reaction mechanism of ester starch/PVA synthesis

Viscosity analysis

The viscosity of each adhesive was measured to determine its physical properties. This characteristic is necessary as it greatly affects the adhesive capacity to coat wood surfaces. If the adhesive is too thick, it struggles to penetrate the wood pores, resulting in poor bonding. Conversely, a liquid adhesive fails to bond two pieces of wood together because it is rapidly absorbed by the wood pores. Figure 5 provides a visual example of this explanation.

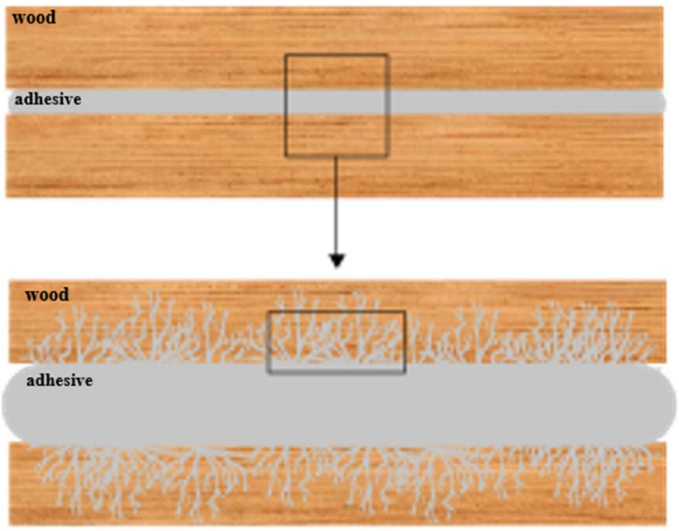

Figure 5. An illustration of bio-adhesive adsorption into the wood pores

In this experiment, viscosity was examined using a Brookfield Viscometer spindle. Given the nature of the adhesive as a non-Newtonian fluid, whose thickness fluctuates over time, the spindle was adjusted from its smallest to largest size and from its slowest to the fastest speed [26].

As shown in Figure 6, the adhesive viscosity increased with the addition of citric acid. The viscosity of AD-CA0, the reference sample without citric acid, was recorded at 1137 cP. Upon inclusion of 0.5% citric acid, the viscosity of AD-CA0.5 steadily increased to 1222 cP. The adhesive viscosity dramatically increased to 2312 cP and 2882 cP at concentrations of 1% (AD-CA1.0) and 1.5% (AD-CA1.5), respectively. Finally, adding 2% citric acid resulted in an adhesive viscosity of 2910 cP (AD-CA2.0).

This progressive increase in viscosity with the addition of citric acid underlines its role as a potent cross-linking agent that significantly influences adhesive properties. This is because the addition of citric acid to the adhesive greatly enhances the interaction of starch, PVA, and the cross-linker forming a polymer [27]. Citric acid, endowed with three carboxyl groups, functions as a bridging agent to enhance the number of hydrogen and covalent bonds between molecules. When citric acid is added to the mixture, its carboxyl groups react with the hydroxyl groups on starch and PVA to form a stable ester and reduce the mobility of the polymer chains. This polymerization process contributes to a denser solution, making the adhesive thicker and heavier. Therefore, higher concentrations of citric acid result in a more viscous adhesive.

Our results align with those of Kang et al. [28] and Wang et al. [29], who found that the addition of a cross-linking agent significantly increased polymer viscosity and enhanced adhesive mechanical properties. A comparison of our findings showed the consistency of cross-linker addition to the viscosity of the polymer. This finding also indicates that the concentration of citric acid as the cross-linker significantly contributes to the viscosity properties of the adhesive.

Dry and wet shear strength analysis

The shear strength of an adhesive is a crucial component that significantly influences its overall performance. The objective of this assessment was to determine the adhesive capacity to join two wood pieces. Additionally, we sought to determine how environmental factors affect the adhesive quality. Each sample was analyzed five times to confirm the accuracy of the data collected during this study. According to Figure 8, the adhesive strength was greater under dry conditions than that under wet conditions because water and starch share the same similar polarity properties. Therefore, the adhesive tends to dissolve in water easily, thereby reducing its bonding strength. The illustration of adhesive, wood, and water is shown in Figure 7.

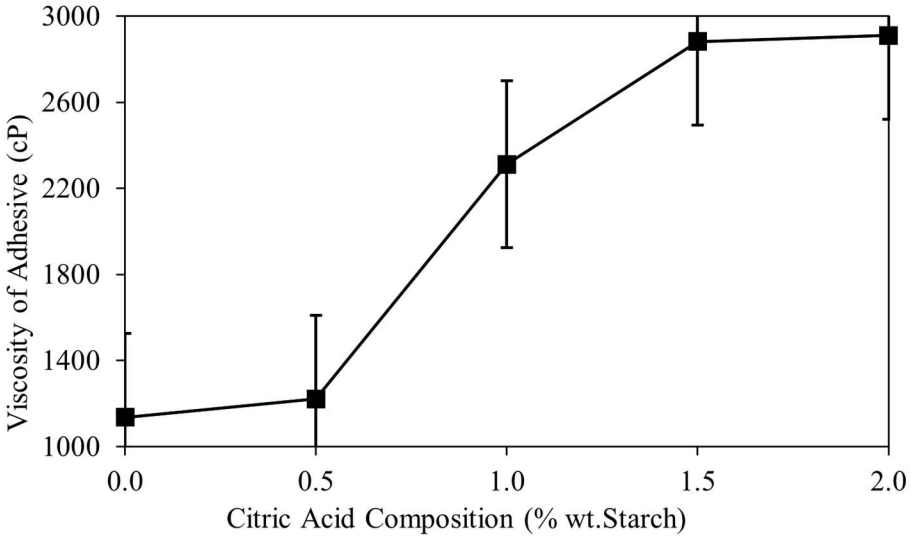

Figure 6. The viscosity of adhesive in various percentages of citric acid concentration

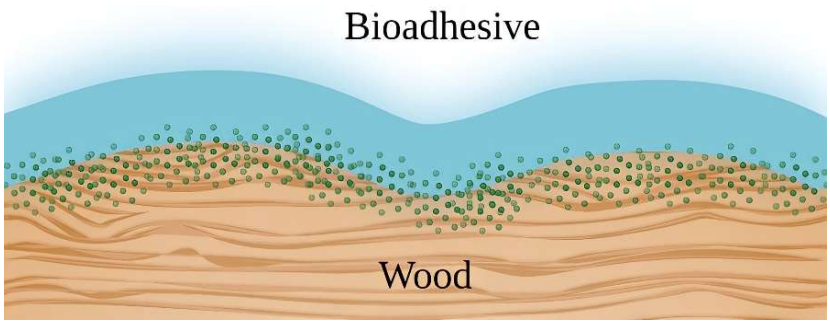

Figure 7. Illustration of the interaction between adhesive and water

An analysis of the shear stress demonstrated that the addition of citric acid significantly enhanced the adhesive's strength. In dry conditions, the reference sample (AD-CA0) exhibited a shear strength of 0.66 MPa. With citric acid addition, the shear strengths of samples AD-CA0.5, AD-CA1.0, and AD-CA1.5 increased progressively to 0.86 MPa, 1.02 MPa, and 1.16 MPa, respectively. AD-CA2.0 reached the highest dry shear strength with a value of 1.21 MPa. By contrast, under wet conditions, the reference sample (AD-CA0) recorded the lowest shear strength at 0.54 MPa. The shear strengths of samples AD-CA0.5, AD-CA1.0, and AD-CA1.5 reached 0.68 MPa, 0.70 MPa, and 0.84 MPa, respectively. The sample AD-CA2.0 demonstrated a maximum shear strength at 0.89 MPa.

Our findings echo those of Zhao [30] and Widyorini [31], who demonstrated that the addition of citric acid enhances polymer strength. The cross-linking reaction between citric acid and starch/PVA lowers the number of hydroxyl groups in the starch, thereby reducing the adhesive affinity for water and enhancing its resistance to moisture. However, when the adhesive is immersed in water, its bonding capability weakens owing to its similar polarity with water, making it more soluble and less resistant in wet conditions.

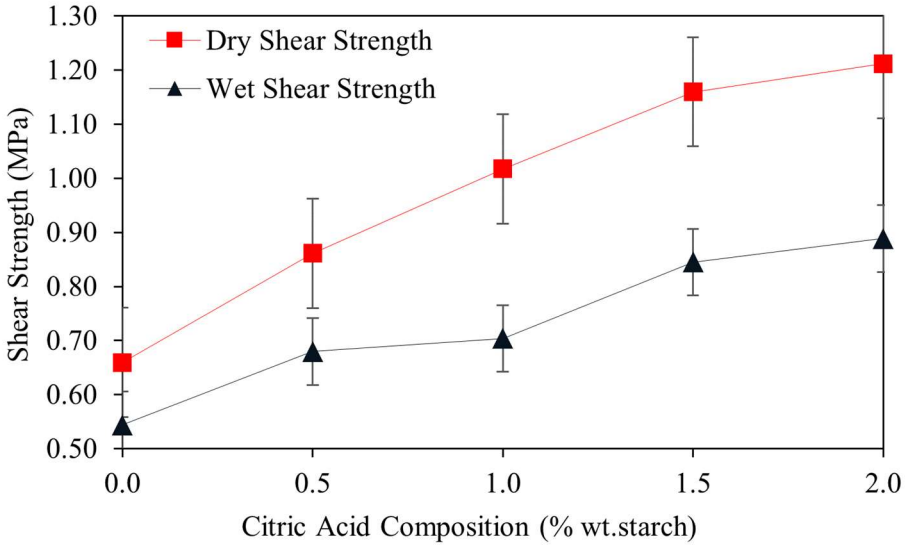

Figure 8. Dry and wet shear strength of adhesive in various percentages of citric acid concentration

Solid content analysis

The measurement of the adhesive's solid concentration is a critical step in determining the proportion of solid components. This analysis aids in evaluating the adhesive homogeneity and its ability to coat the substrate during the gluing process. Furthermore, determining the solid content provides insight into the adhesive's volatility level. This is crucial because high volatility can adversely affect the health of users. A well-balanced mixture of solid materials in the adhesive results in superior performance in terms of homogeneity and volatility [32].

In this study, we examined the solid content of the adhesive according to the ASTM D2369 standard. As illustrated in Figure 9, the addition of citric acid increased the adhesive's solid content. The solids made up 29% of the reference sample (AD-CA0). Upon adding citric acid, the percentage of solids rose to 33%, 34%, and 35% for samples AD-CA0.5, AD-CA1.0, and AD-CA1.5, respectively. Sample AD-CA2.0, with a 36% proportion of solids, included the highest percentage of solids.

This increase in solid content can be attributed to the bonding formed between cassava starch and polyvinyl alcohol owing to the addition of citric acid, thereby reducing the number of volatile components. Consequently, the reaction between citric acid and cassava starch/PVA increases the number of solid components. This observation aligns with a study conducted by Marquez [33], who discussed the potential of citric acid to modify adhesive properties and enhance the molecular solid weight of the adhesive. However, a high percentage of solids can hinder the adhesive performance owing to difficulties in application on wood. To ensure robust wood bonding, the adhesive needs to quickly coat the surface of the wood pores.

Fourier transform infrared spectroscopy

FTIR spectroscopy was performed to understand the structural modifications of the chemical molecules during the reaction. The molecular structures of

cassava starch, the 0% citric acid sample (AD-CA0), and the 2% citric acid sample (AD-CA2.0) were analyzed for comparison. Figure 10 illustrates the results of the analysis.

Figure 10 shows the alteration peak at 994 cm^{-1}. This implies that the strength of the C–O bonds in cassava starch was lower than that in the reference sample (AD-CA0). Additionally, the strength of the peak at 3262 cm^{-1} increased, indicating that the number of hydroxyl groups in each molecule of hydrolyzed starch increased. These modifications explain why cassava starch underwent hydrolysis during the procedure. Furthermore, the peak intensity at 1639 cm^{-1} for sample AD-CA0 increases, indicative of the creation of carboxyl functional groups (C=O) owing to oxidation. At 2942 cm^{-1}, the peak intensity increased as the fraction of carboxyl groups in AD-CA2.0 increases. This indicates that the sample underwent greater oxidation during polymerization.

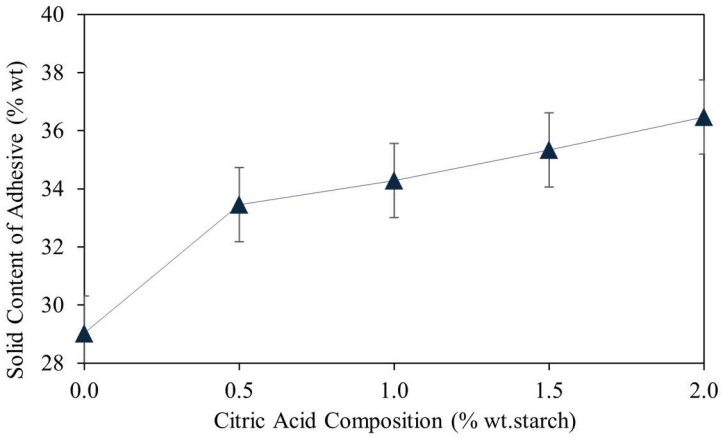

Figure 9. The solid content of adhesive in the various percentages of citric acid addition

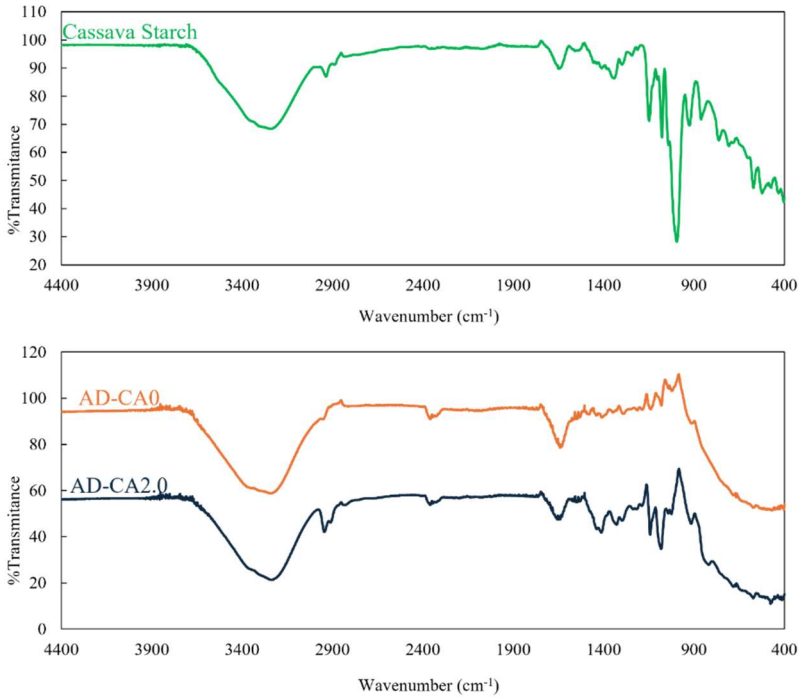

Figure 10. Infrared spectra of cassava starch, AD-CA0, and AD-CA2.0

Thermogravimetry analysis

Thermogravimetric analysis was performed to determine the thermal stability of the material. The thermal stabilities of both the reference sample (AD-CA0) and the sample with citric acid addition (AD-CA2.0) were examined across a temperature range between 0 °C and 600 °C. Figure 11 shows the results of thermogravimetric analysis. The mass loss of the reference sample (AD-CA0) and citric acid sample (AD-CA2.0) was separated into two stages based on this curve.

For the AD-CA0, the initial temperature degradation stage ranges from 0 °C to 100 °C, whereas the second stage spans from 100 °C to 600 °C. In the first stage, the sample experienced a weight loss of approximately 5%. This is attributed to the evaporation of water and monomers present in the adhesive. During the second stage, owing to the breakdown of hydrogen and covalent bonds in the adhesive, the weight progressively decreases until it reaches 600°C.

For the sample containing citric acid (AD-CA2.0), the first step of degradation occurred between 0 °C and 142 °C, and the second stage occurred between 142 °C and 600 °C. The initial stage saw a weight loss of about 7%, consistent with the evaporation of water and monomers as temperature increased. Owing to the dissolution of covalent bonds in the adhesive and the degradation of the adhesive leftovers, the mass loss rate decreased steadily during the second stage. This data suggests that the addition of citric acid can indeed enhance thermal stability of the adhesives.

Morphology analysis

A Dino-Lite microscope and a SEM were used to analyze adhesive surface morphology. This experiment was conducted to investigate the homogeneity of the adhesives. The adhesive morphology before (AD-CA0) and after (AD-CA2.0) citric acid addition was compared. As illustrated in Figure 12, the adhesive's surface became smoother with citric acid introduction. SEM analysis confirmed an increase in the adhesive's homogeneity following citric acid addition (Figure 13). This can be attributed to citric acid enhancing the likelihood of a reaction between cassava starch and PVA which made the homogeneity of adhesive increase.

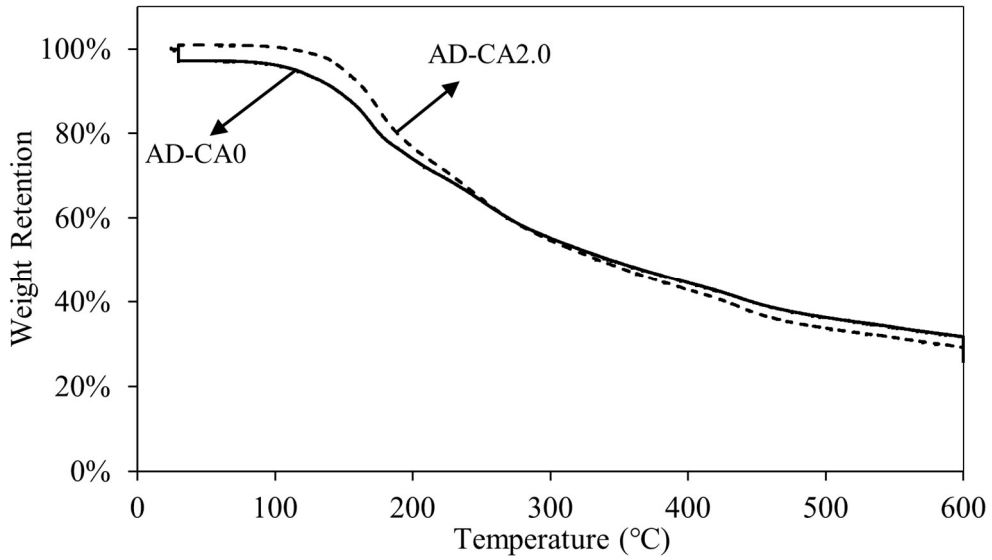

Figure 11. Thermogravimetric curves of citric AD-CA0 and AD-CA2.0

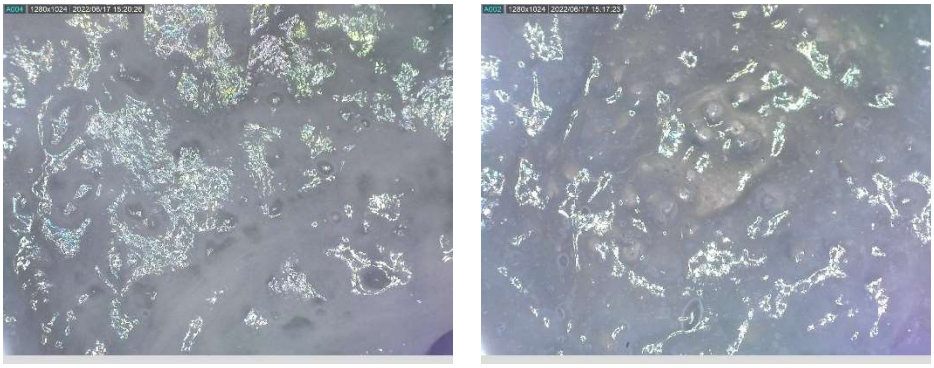

a b

Figure 12. The morphology of cassava starch/PVA adhesive before (a) and after (b) citric acid addition using dino-lite microscope

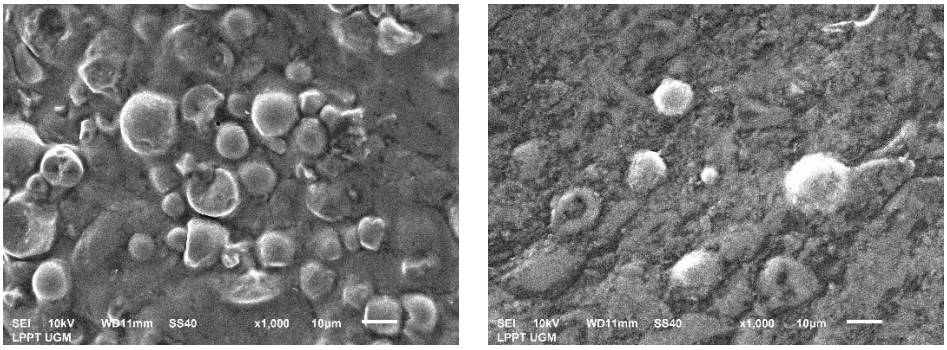

a b

Figure 13. The morphology of cassava starch/PVA adhesive before (a) and after (b) citric acid addition using scanning electron micrograph

Conclusion

Incorporating citric acid as a cross-linking agent considerably improved the quality of the cassava starch bio-adhesive. The physical attributes of the adhesive, such as viscosity, solid content, and dry and wet shear strengths, were improved with citric acid addition. Sample AD-CA2.0, with 2% citric acid, demonstrated the highest bond quality in this experiment, recording a viscosity of 2910 cP, and dry and wet shear strengths of 1.21 MPa and 0.89 MPa, respectively. Furthermore, the solid content of this sample was 36%. The adhesive underwent hydrolysis, oxidation, and polymerization according to FTIR measurements. Furthermore, the morphological study revealed that citric acid addition improved adhesive uniformity. These findings have opened up new avenues for further research to explore the long-term durability and environmental sustainability of cassava starch bio-adhesives modified with citric acid. Future studies could investigate the aging behavior of adhesive bonds under various environmental conditions, such as temperature and humidity fluctuations, to assess their performance over extended periods.

Acknowledgement

The funding of this research was supported by Faculty Research Grants 2021 from the Faculty of Engineering, Universitas Gadjah Mada.

References

1. Kaboorani, A., and Riedl, B. (2011). Effects of adding nano-clay on performance of polyvinyl acetate (PVA) as a wood adhesive. *Composites Part A: Applied Science and Manufacturing,* 42(8): 1031-1039.
2. Suci, N., and Arnellis, A. (2014). Model matematika kerusakan sumber daya hutan di Indonesia. *Journal of Mathematics UNP*, 2(1): 1-6.

3. Xu, Q., Wen, J., and Wang, Z. (2016). Preparation and properties of cassava starch-based wood adhesives. *BioResources,* 11(3): 6756-6767.
4. Jang, Y., Huang, J., and Li, K. (2011). A new formaldehyde-free wood adhesive from renewable materials. *International Journal of Adhesion and Adhesives*, 31(7): 754-759.
5. Buschow, K. J. (2001). Encyclopedia of materials: science and technology. Available: http://www.entwoodllc.com/PDF/wood adhesion mechanisms.pdf
6. Kumar, R. N., and Pizzi, A. (2019). Adhesives for wood and lignocellulosic materials. John Wiley & Sons.
7. Frihart, C. R. (2015). Introduction to special issue: wood adhesives: past, present, and future. *Forest Products Journal,* 65(1-2): 4-8.
8. Solt, P., Konnerth, J., Gindl-Altmutter, W., Kantner, W., Moser, J., Mitter, R., and van Herwijnen, H. W. (2019). Technological performance of formaldehyde-free adhesive alternatives for particleboard industry. *International Journal of Adhesion and Adhesives,* 94: 99-131.
9. Böhm, M., Salem, M. Z., and Srba, J. (2012). Formaldehyde emission monitoring from a variety of solid wood, plywood, blockboard and flooring products manufactured for building and furnishing materials. *Journal of Hazardous Materials,* 221: 68-79.
10. IARC (2006). Formaldehyde, 2-butoxyethanol and 1-tert-butoxypropan-2-ol. *IARC Monograph Evaluation Carcinogen Risks Human*, 88: 1-478.
11. Antov, P., Savov, V., and Neykov, N. (2020). Sustainable bio-based adhesives for eco-friendly wood composites. A review. *Wood Research,* 65(1): 51-62.
12. Li, K., Geng, X., Simonsen, J., and Karchesy, J. (2004). Novel wood adhesives from condensed tannins and polyethylenimine. *International Journal of Adhesion And Adhesives*, 24(4): 327-333.
13. Balgude, D., Sabnis, A., and Ghosh, S. K. (2017). Synthesis and characterization of cardanol based reactive polyamide for epoxy coating application. *Progress in Organic Coatings,* 104: 250-262.
14. Santosa, A. R. A., Zain, A. S., and Pancasakti, B. P. (2022). Analisis kuat tarik dan umur perekat poliamida berbasis gelatin dan asam adipat dengan variasi jumlah minyak sawit sebagai pemlastis. *Jurnal Teknik Kimia USU*, 11(2): 64-71.
15. Arias, A., Feijoo, G., and Moreira, M. T. (2021). Evaluation of starch as an environmental-friendly bioresource for the development of wood bioadhesives. *Molecules,* 26(15): 4526.
16. Graham, S., Craig, F., and Scott, S., (2011). *Organic Chemistry*, 11th edition. Hoboken, NJ: Wiley.
17. Lamaming, J., Heng, N. B., Owodunni, A. A., Lamaming, S. Z., Abd Khadir, N. K., Hashim, R., ... and Hiziroglu, S. (2020). Characterization of rubberwood particleboard made using carboxymethyl starch mixed with polyvinyl alcohol as adhesive. *Composites Part B: Engineering,* 183: 107731.
18. Garcia-Perez, M., Chaala, A., Pakdel, H., Kretschmer, D., Rodrigue, D., and Roy, C. (2006). Multiphase structure of bio-oils. *Energy & Fuels,* 20(1): 364-375.
19. Li, Z., Wang, J., Cheng, L., Gu, Z., Hong, Y., and Kowalczyk, A. (2014). Improving the performance of starch-based wood adhesive by using sodium dodecyl sulfate. *Carbohydrate Polymers,* 99: 579-583.
20. Haifa, M. H., Pancasakti, B. P., Budhijanto, B., Vincent, V., and Riani, M. D. (2022). Efek penambahan asam p-toluensulfonat (PTSA) dalam produksi perekat poliamida dari kitosan dan asam adipat. *Jurnal Sains dan Teknologi: Jurnal Keilmuan dan Aplikasi Teknologi Industri,* 22(1), 39-45.
21. Sun, J., Li, L., Cheng, H., and Huang, W. (2018). Preparation, characterization and properties of an organic siloxane-modified cassava starch-based wood adhesive. *The Journal of Adhesion,* 94(4): 278-293.
22. ASTM D1084 (2005). Standard test methods for viscosity of adhesives.
23. ASTM D906-98 (2010). Standard test method for strength properties of adhesives in two-ply wood construction in shear by tension loading.
24. ASTM D1183 (2011). Standard practices for resistance of adhesives to cyclic laboratory aging conditions (metal bonding committee).

25. ASTM D2369-20 (2020). Standard test method for volatile content of coatings.
26. Bird, R. B. (1993). The basic concepts in transport phenomena. *Chemical Engineering Education,* 27(2): 102-109.
27. Tam, K. C., Wu, X. Y., and Pelton, R. H. (1992). Viscometry—a useful tool for studying conformational changes of poly (N-isopropylacrylamide) in solutions. *Polymer,* 33(2): 436-438.
28. Kang, W., Zhang, H., Lu, Y., Yang, H., Zhu, T., Zhang, X., ... and Besembaevna, O. Z. (2019). Study on the enhanced viscosity mechanism of the cyclodextrin polymer and betaine-type amphiphilic polymer inclusion complex. *Journal of Molecular Liquids,* 296: 111792.
29. Wang, Z., Li, Z., Gu, Z., Hong, Y., & Cheng, L. (2012). Preparation, characterization and properties of starch-based wood adhesive. *Carbohydrate Polymers,* 88(2): 699-706.
30. Zhao, Z., Umemura, K., and Kanayama, K. (2016). Effects of the addition of citric acid on tannin-sucrose adhesive and physical properties of the particleboard. *BioResources,* 11(1): 1319-1333.
31. Widyorini, R., Umemura, K., Septiano, A., Soraya, D. K., Dewi, G. K., and Nugroho, W. D. (2018). Manufacture and properties of citric acid-bonded composite board made from salacca frond: Effects of maltodextrin addition, pressing temperature, and pressing method. *BioResources,* 13(4): 8662-8676.
32. Edalat, H., Faezipour, M., Thole, V., and Kamke, F. A. (2014). A new quantitative method for evaluation of adhesive penetration pattern in particulate wood-based composites: Elemental counting method. *Wood Science and Technology,* 48: 703-712.
33. Márquez, I., Paredes, N., Alarcia, F., and Velasco, J. I. (2022). Influence of acrylonitrile content on the adhesive properties of water-based acrylic pressure-sensitive adhesives. *Polymers,* 14(5): 909.

Malaysian Journal of Analytical Sciences (MJAS)
Published by Malaysian Analytical Sciences Society

EXPLORING DEEP EUTECTIC SOLVENTS AS A POTENTIAL SOLVENT FOR THE EXTRACTION OF FOOD ADDITIVE ALLURA RED IN FOOD TECHNOLOGY APPLICATION

(Mengeksplorasi Pelarut Eutektik Mendalam sebagai Pelarut Berpotensi untuk Pengekstrakan Pewarna Makanan Merah Allura dalam Aplikasi Teknologi Makanan)

Thanussha Elangovan[1], Nor Munira Hashim[1], Nurina Izzah Mohd Husani[1], Noorfatimah Yahaya[1], Farhanini Yusoff [2], and Nur Nadhirah Mohamad Zain[1*]

[1]*Department of Toxicology, Advanced Medical, and Dental Institute, Universiti Sains Malaysia, 13200 Kepala Batas, Penang, Malaysia.*
[2]*Faculty of Science and Marine Environment, Universiti Malaysia Terengganu, 21030 Kuala Terengganu, Terengganu, Malaysia.*

[*]*Corresponding author: nurnadhirah@usm.my*

Received: 4 January 2024; Accepted: 16 Apr 2024; Published: 29 June 2024

Abstract

In recent years, synthetic food dyes have gained significant popularity as additives, replacing natural dyes, with azo dyes comprising approximately 65% of the commercial dye market. However, concerns regarding the toxic effects of azo dyes used in food colouring have prompted the development of advanced analytical methods to detect them in various food matrices. These methods typically involve intricate pre-concentration processes, time-consuming steps, and the use of expensive instruments, thus emphasising the need for highly sensitive and selective approaches. Hence, this study aims to explore the application of deep eutectic solvent (DES) as a potential solvent for the extraction of Allura Red AC (ARAC). First, the synthesised magnetic nanoparticles functionalised with DES (silicone surfactant: dodecanoic acid) (SS: DoAc@Fe_3O_4) adsorbent was successfully characterised using attenuated total reflectance-Fourier transform infrared spectroscopy (ATR-FTIR) for the identification of functional bonds. This adsorbent was subsequently applied in the magnetic solid phase extraction (MSPE) technique to extract ARAC in soft drink samples. In contrast to pure Fe_3O_4 particles, the targeted ARAC can be easily adsorbed onto the SS: DoAc@Fe_3O_4 surface due to the formation of strong hydrophobic interaction between ARAC and the adsorbents, thus amplifying the extraction efficiency. Further optimisation was done via one-variable-at-a-time (OVAT) and Taguchi experimental design to determine the optimised condition for ARAC extraction. The OVAT analysis identified that using methanol: acetonitrile (1:1) as the desorption solvent, incorporating Na_2SO_4 to boost extraction efficiency, employing salt volume of 200 µL, and utilising a sample volume of 20 mL produced the most favourable outcomes. Meanwhile, the Taguchi experiments pinpointed the optimum conditions as pH 2, an adsorbent dosage of 25 mg, an extraction duration of 2 minutes, a desorption period of 3 minutes, and a desorption solvent volume of 400 µL. Under the optimised conditions, the R^2 value obtained was 0.999 while the limit of detection (LOD) and limit of quantification (LOQ) values were 0.1 mgL^{-1} and 0.4 mgL^{-1}, respectively. The studied ARAC also obtained relative recovery values between 80% to 111%. Therefore, it is safe to conclude that the newly proposed SS: DoAc@Fe_3O_4-based MSPE is an environmentally friendly, simple, affordable, and effective technique for the extraction of ARAC in drink samples.

Keywords: Allura red AC, deep eutectic solvents, dodecanoic acid, magnetic solid phase extraction, silicone surfactant

Abstrak

Kebelakangan ini, pewarna makanan sintetik semakin popular dan kerap digunakan sebagai bahan tambahan menggantikan pewarna semula jadi, dengan pewarna azo merangkumi kira-kira 65% daripada pasaran pewarna komersial. Walau bagaimanapun, kebimbangan mengenai kesan toksik pewarna azo yang digunakan dalam pewarna makanan telah mendorong pembangunan kaedah analisis lanjutan untuk mengesannya dalam pelbagai matriks makanan. Kaedah tersebut biasanya melibatkan proses pra-kepekatan yang rumit, prosedur yang memakan masa, dan penggunaan instrumen yang mahal, sekaligus menekankan keperluan untuk pendekatan yang sensitif dan terpilih. Oleh itu, kajian ini bertujuan untuk meneroka aplikasi pelarut eutektik mendalam (DES) untuk mengekstrak pewarna merah allura AC (ARAC). Pertama, penjerap zarah nano magnetik difungsikan dengan DES (surfaktan silikon:asid dodekanoik) (SS:DoAc@Fe_3O_4) telah berjaya disintesis dan dianalisis menggunakan spektroskopi transformasian Fourier inframerah dengan pantulan keseluruhan dikecilkan (ATR-FTIR) untuk mengenal pasti ikatan berfungsi. Bahan penjerap ini kemudiannya digunakan dalam teknik pengekstrakan fasa pepejal magnetik (MSPE) untuk mengekstrak ARAC dalam sampel minuman ringan. Berbeza dengan zarah Fe_3O_4 tulen, ARAC lebih mudah diserap ke permukaan SS:DoAc@Fe_3O_4 disebabkan oleh pembentukan interaksi hidrofobik yang kuat antara ARAC dan penjerap, sekaligus menguatkan kecekapan pengekstrakan. Pengoptimuman lanjut kemudiannya dilakukan melalui satu-pembolehubah-pada-satu-masa (OVAT) dan reka bentuk eksperimen Taguchi bagi menentukan keadaan optimum untuk pengekstrakan ARAC. Analisis OVAT mendapati bahawa penggunaan metanol:acetonitrile (1:1) sebagai pelarut penyahjerapan, penambahan garam untuk meningkatkan kecekapan pengekstrakan, penggunaan isipadu garam sebanyak 200 µL, dan penggunaan isipadu sampel 20 mL memberikan hasil yang paling baik. Sementara itu, eksperimen Taguchi menunjukkan keadaan optimum sebagai pH 2, dos penjerap sebanyak 25 mg, tempoh pengekstrakan selama 2 minit, tempoh penyahjerapan selama 3 minit, dan isipadu pelarut penyahjerapan sebanyak 400 µL. Dibawah keadaan yang dioptimumkan, nilai R^2 yang diperolehi adalah 0.999 manakala nilai had pengesanan (LOD) dan had kuantifikasi (LOQ) masing-masing adalah 0.1 mgL^{-1} dan 0.4 mgL^{-1}. ARAC yang dikaji juga memperoleh nilai pemulihan relatif antara 80% hingga 111%. Oleh itu, dapat disimpulkan bahawa MSPE berasaskan SS:DoAc@Fe_3O_4 yang dicadangkan adalah satu teknik mesra alam, mudah, berpatutan, dan berkesan untuk pengekstrakan ARAC dalam sampel minuman.

Kata kunci: Pewarna merah allura AC, pelarut eutektik mendalam, asid dodekanoik, pengekstrakan fasa pepejal magnetik, surfaktan silikon

Introduction

Food colourants, also known as pigments, encompass dyes or substances that impart colour to food and beverages. They are broadly utilised both in commercial food production and home cooking settings [1]. These colourants consist of diverse chemical substances added to food matrices, serving several purposes. They are employed to enrich or safeguard the sensory attributes of food items, which could otherwise be compromised or destroyed throughout the processes of manufacturing or storage [2]. Additionally, food colourants are employed in food technology applications to achieve the desired appearance and colour of the final product. The visual aspects are considered a vital role in the modern consumer's food choices, with colour being an integral part of food and beverages [3]. Over the past few years, a multitude of artificial food dyes have been introduced as an alternative to natural colourants. They are predominantly utilised to attain distinct attributes, such as enhanced visual appeal, intensified hues, increased colour stability, and uniformity [4, 5].

Synthetic food colourants offer several commercial benefits, such as affordability, resilience to light and pH changes, and excellent colour stability in comparison to natural colours [6]. These colourants are chemical compounds derived from coal tar derivatives, with many of them containing azo-group [7]. However, there are concerns in the market as some foods and beverages may contain unapproved synthetic colourants or excessive amounts of approved synthetic colourants [8]. Extensive research has revealed synthetic colourants as a significant contributor to food poisoning and can lead to severe health issues. It is also not safe to use approved synthetic colourants for the long term [9]. The use of unapproved colourants or the indiscriminate use of approved colourants is known to have adverse effects on animal and human health. There is a growing demand for the development of precise, accurate, sensitive, and selective analytical methods for the qualification and quantification of food colourants, owing to their extensive use in food manufacturing processes [10]. Among the synthetic dyes utilised in the food industry, azo dyes dominate the commercial dye market, accounting for about 65% of the share [11].

Azo dyes are synthetic organic colourants known for their vibrant and intense colours, making them popular additives in various food products. However, these dyes possess certain characteristics that warrant attention. They are typically resistant to aerobic conditions but can be metabolised by intestinal flora, leading to the formation of aromatic amines [12]. Such compounds have been associated with adverse effects on health, including headaches in adults, neurotoxicity, genotoxicity, and carcinogenic properties [13]. Most countries worldwide have taken measures to prohibit the usage of a significant number of azo dyes in food products as a response to the associated health concerns. Over the past few decades, strict regulations have been put in place to govern the use of azo dyes in both domestic food supplies and exports of various nations [14]. However, despite the presence of diverse regulatory frameworks, the overall approach is grounded in similar stages that demand well-established protocols for risk assessment.

Magnetic solid phase extraction (MSPE) has been developed based on traditional SPE [15]. In recent years, nano-magnetic materials have attracted much interest due to their unique size and physical properties. They possess a high surface area, resulting in greater adsorption capacity for analytes [16]. Because of their super-paramagnetic property, nanoparticles can be attracted by a magnet, but do not retain magnetism after the field is removed. Additionally, they do not agglomerate after the magnetic field is removed, thus not affecting sorption ability [17]. Meanwhile, the magnetic sorbent can be used repeatedly to enrich and separate the target analyte [18]. However, the naked Fe_3O_4 adsorbent is limited for selective analyte adsorption. Therefore, surface modification is necessary to design highly selective adsorbents to improve selectivity or affinity towards analytes [19]. Compared with traditional sample pre-treatment, MSPE offers many advantages, such as simplicity, low cost, and environmental friendliness, making it highly suitable for isolating and enriching target analytes from food samples [20]. The demand for environmentally friendly solvents has led to the adoption of ionic liquids (ILs) as replacements for traditional organic solvents, which are volatile and toxic. However, the green aspects of ILs have come under scrutiny due to their poor biocompatibility and biodegradability [21].

As a solution to this concern, deep eutectic solvents (DESs) have been introduced as a green alternative to ILs since 2004. DESs can be tailored to exhibit specific properties, such as hydrophobicity or hydrophilicity, providing the advantage of selectively extracting target compounds. This selectivity leads to higher purity and concentration of the emerging contaminants (ECs) obtained from the extraction process [22]. DESs can be easily modified by adjusting the composition of their components, making them adaptable to meet the specific demands of the extraction process. This versatility makes DESs well-suited as adsorbents for extracting or removing ECs in various matrices [23]. They offer numerous benefits, including high solvency, low toxicity, low environmental impact, biodegradability, and cost-effectiveness, as they are derived from renewable resources. Furthermore, DESs are easy to recycle without imposing negative effects on the environment.

Food analysis has become an exceptionally crucial procedure in ensuring the safety and quality of food products [24]. Furthermore, the adverse toxic effects linked to azo dyes employed for food colouring have spurred the advancement of exceptionally sensitive and selective analytical methods for their detection in various food matrices [25]. Despite the existence of many analytical methods previously studied, the majority of conventional methods, such as liquid-liquid extraction (LLE) and solid phase extraction (SPE), regrettably entail intricate pre-concentration, lengthy procedures, and the use of expensive equipment [26, 27]. An appropriate approach for preparing samples is imperative before conducting instrumental analysis, aiming to eliminate interferences arising from intricate food matrices that could potentially obstruct the chromatographic system. Hence, the development of green solvents has attracted significant interest in the demand for sustainable and green processes [28].

Based on our previous laboratory findings, a newly synthesised magnetic adsorbent named SS:DoAc@Fe_3O_4 using non-ionic silicone surfactant and dodecanoic acid as a DES in magnetic solid-phase extraction (MSPE) was reported as a reliable approach for the extraction of organophosphorus in honey and

vegetable samples. In this study, similar magnetic adsorbent is employed to explore the extraction performance towards Allura Red AC (ARAC) using the MSPE technique. The focus on ARAC is prompted by its extensive application as food colorant in the food industry. ARAC (E129), also known as Red 40, is an azo dye originally derived from petroleum with a dark red colour and water solubility. It serves as a food colouring substitute for amaranth and is commonly added to sodas, baby medicines, and cotton candy. In the United States, ARAC is the most frequently used food colouring in beverages, candy, popsicles, deli meats, cheeses, salmon, over-the-counter (OTC) medications, and liquid suspensions. This study explored the potential application of DES-based magnetic adsorbent, a novel adsorbent synthesised by Elencovan et al. in solid phase extraction methods for the determination of ARAC in food matrices [29]. Attenuated total reflectance-Fourier transform infrared spectroscopy (ATR-FTIR) analysis was conducted to confirm the successfully re-synthesised material. Then, the newly synthesised SS:DoAc@Fe_3O_4 adsorbent was applied in the MSPE technique. All the methods were optimised and validated for the analysis of ARAC in soft drink samples.

Materials and Methods

Chemicals and reagents

The food dye (ARAC) was purchased from R&M Chemicals (Essex, UK). Ultrapure water (18.2 MΩ/cm) supplied by the Sartorius Milli-Q system (Aubagne, Germany) was used to prepare the standard stock solution for ARAC at the concentration of 1000 mgL^{-1}. Daily preparation of the standard working solutions involved dilution of a sufficient quantity of the stock solutions with ultrapure water for the extraction analysis. Additionally, the stock solution for salt was created by dissolving the requisite amount of salt in ultrapure water to achieve a concentration of 25% (w/v). Miracle S240, a non-ionic silicone surfactant, was obtained from G-Planter (Johor, Malaysia) with the IUPAC designation of 3-[methyl-bis(trimethylsilyloxy) silyl]propan-1-ol;2-methyloxirane; oxirane. Sodium sulphate (Na_2SO_4) was purchased from Qrec (Chonburi, Thailand) while methanol and acetonitrile of HPLC grade were obtained from Fisher Scientific (Seoul, Korea). R&M Chemicals (Essex, UK), Friedemann Schmidt Chemicals (Parkwood, Australia), Sigma-Aldrich (Darmstadt, Germany), and Chemiz (Shah Alam, Malaysia) supplied the iron (II) chloride tetrahydrate ($FeCl_2.4H_2O$), iron (III) chloride hexahydrate ($FeCl_3.6H_2O$), ammonium hydroxide (25%), sodium hydroxide (NaOH), and hydrochloric acid (HCl), respectively. Absolute ethanol was purchased from Fisher Scientific (Seoul, Korea).

Instrumentation

Attenuated total reflectance-Fourier transform infrared spectroscopy (ATR-FTIR) was employed to identify the functional bonds present in the newly synthesised SS:DoAc-based DES. The spectra were examined using Fortier from Perkin Elmer USA in the 4000 to 600 cm^{-1} range. The Perkin Elmer Lambda 25 UV-Vis spectrophotometer was used to analyse the analytical response of ARAC. Meanwhile, the Minitab 2022 (v21.3.1) software was used to investigate the signal-to-noise ratios of the experimental parameters that were optimised for the MSPE technique via the Taguchi design of experiments.

Synthesis of SS:DoAc-based DES

The SS:DoAc-based DES used in this study was synthesised according to the procedure mentioned in Elencovan et al. [29]. The co-precipitation method was used to synthesise the SS:DoAc@Fe_3O_4 adsorbent. The DES was made by combining silicone surfactant (SS) as a hydrogen bond acceptor (HBA) and dodecanoic acid (DoAc) as a hydrogen bond donor (HBD) at a molar ratio composition of 1:5, respectively. A clear, homogeneous liquid of SS:DoAc-based DES was produced by heating the mixture at 70 °C for 15 min with continuous stirring. Then, 150 µL of DES was added to the mixture of 1.4576 g of $FeCl_2.4H_2O$ and 3.7306 g of $FeCl_3.6H_2O$. Subsequently, 75 mL of ultrapure water was incorporated into the mixture. The mixture underwent vigorous stirring using a magnetic stirrer for 30 minutes at 85 °C under nitrogen gas stream protection. Next, 10 mL of ammonium hydroxide (25%) was added dropwise to the mixture and agitated constantly for 60 minutes. The synthesised SS:DoAc@Fe_3O_4 adsorbent was later collected using an external magnet and rinsed repeatedly, alternating between ethanol and ultrapure water to ensure complete removal of any residual unreacted chemicals. Lastly, the isolated SS:DoAc@Fe_3O_4 adsorbent was placed to dry

in an oven for 24 hours at 80 °C.

Proposed SS:DoAc-based DES in MSPE technique

The magnetic solid-phase extraction (MSPE) method was conducted as described by Elencovan et al. with some modifications [29]. Firstly, 25 mg of SS:DoAc@Fe_3O_4 adsorbent was weighed precisely and incorporated into 10 ml of sample solution that was spiked with targeted analyte, followed by the addition of 800 µL of 25% (w/v) sodium sulfate (Na_2SO_4) to increase the ionic strength. The sample vial was vortexed for 2 minutes at 2500 rpm using a vortex mixer to promote the adsorption of the targeted analyte onto the SS:DoAc@Fe_3O_4 adsorbent. An external magnet was later used to isolate the SS:DoAc@Fe_3O_4 adsorbent and supernatant was discarded. Next, 700 µL of methanol:acetonitrile (1:1) acting as a desorption solvent was added to the isolated SS:DoAc@Fe_3O_4 adsorbent. The mixture underwent sonication for 2 minutes to facilitate the elution of the target dye analyte from the SS:DoAc@Fe_3O_4 adsorbent into the desorption solvent. Subsequently, the SS:DoAc@Fe_3O_4 adsorbent was separated using an external magnet and the desorption solvent was carefully retrieved with the aid of a micropipette tip and filtered using a 13 mm nylon syringe filter with a pore size of 45 µm. The final solution was then transferred into a 20 mL vial. Lastly, the desorption solvent containing the targeted analyte was subjected to UV-Vis spectrophotometry analysis for further identification and quantification.

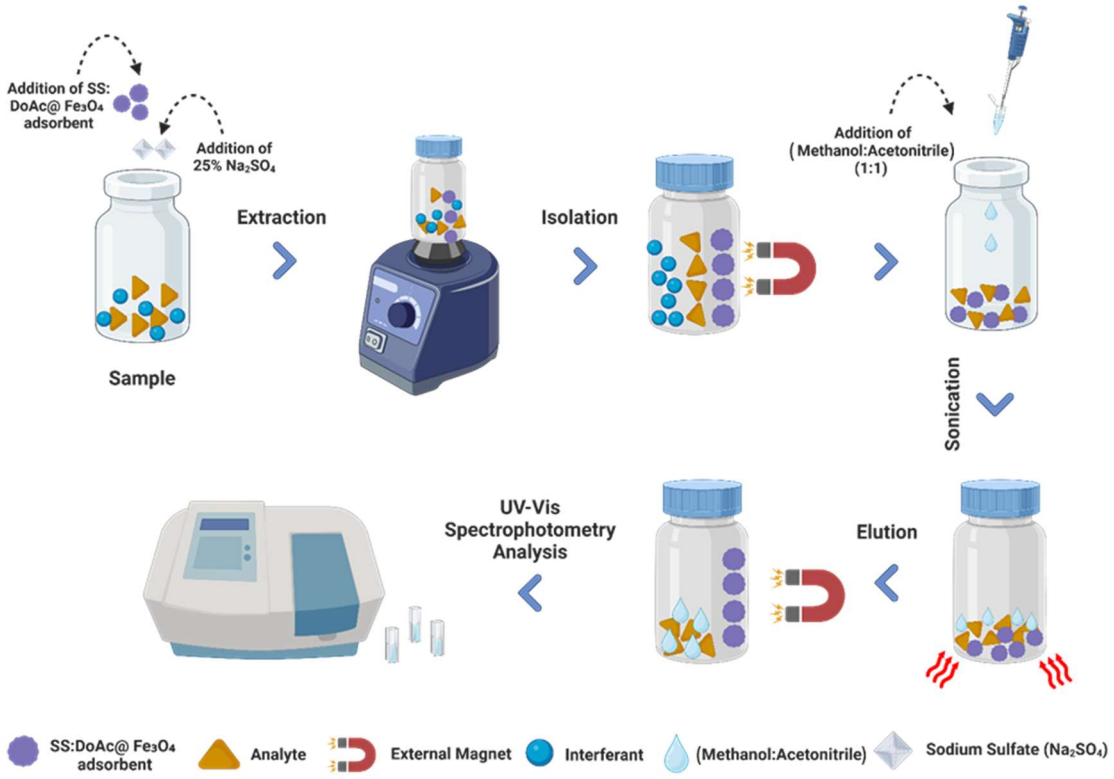

Figure 1. Schematic diagram of MSPE technique

Preliminary screening

A preliminary study was conducted via the MSPE approach to compare the performance of newly synthesised SS:DoAc@Fe_3O_4 adsorbent with control (Fe_3O_4 particles). Other extraction parameters included 25 mg of adsorbent, 10 mL of sample solution, 2 minutes of extraction time, 800 µL of 25% (w/v) Na_2SO_4, 700 mL of methanol:acetonitrile as desorption solvent, and 2 minutes of sonication. The adsorbent's performance in extracting ARAC was analysed using UV-Vis spectrophotometry at λ_{max}=501 nm.

Optimisation of MSPE technique via One-Variable-at-A-Time (OVAT) design of experiments

The OVAT (one-variable-at-a-time) design of experiments is a simple and straightforward approach in experimental design where one independent variable is varied while keeping all other variables constant. This method involves changing one factor at a time to observe its individual effect on the dependent variable. It is often used in the preliminary stages of research and allows researchers to quickly evaluate the impact of individual factors on a system without the complexity of considering interactions between multiple variables. In this study, in-depth analysis was conducted on the types of desorption solvent, addition of salt, volume of salt, volume of sample solution, and point zero charge as well as how they affect the extraction performance of the SS:DoAc-MSPE method. All experiments were conducted in triplicates (n=3). Four different types of desorption solvents, including methanol, acetonitrile, a 1:1 mixture of methanol and acetonitrile, and isopropanol, were evaluated in this study. To assess the effectiveness of target analyte extraction and recovery with and without the addition of salt, 25% (w/v) Na_2SO_4 was used to study the effect of salt. The effect of salt volume was investigated using volumes of 25% (w/v) Na_2SO_4 in the range of 200 to 800 µL. Different volumes of sample solution were investigated in this procedure ranging between 10 to 25 mL.

Point of zero charge

The points of zero charges (pzc) of the adsorbent were determined using this approach [18] where 25 mg of newly synthesised SS:DoAc@Fe_3O_4 adsorbent and control (Fe_3O_4 particles) were added to 10 mL solutions with pH levels of pH 2, 4, 6, 8, and 10, respectively. An orbital shaker was used to agitate the mixture for 24 hours. Subsequently, the final pH of the mixtures was determined using a pH meter and the graph of ΔpH versus the initial pH was plotted.

Optimisation of MSPE technique via Taguchi design of experiments

A process can be optimised using the Taguchi design of experiments method by identifying the crucial parameters that influence the output and determining the ideal levels of these parameters. This strategy uses the multi-variable at a time method, which is comparable to the conventional approach of OVAT. Five different parameters (pH of sample solution, mass of adsorbent (mg), extraction time (min), desorption time (min), and volume of desorption solvent (µL)) were analysed simultaneously where only one parameter was manipulated at a time whereas the rest were held constant. The extraction efficiency was assessed using the average of three replicate measurements (n=3), which were conducted for each parameter. Deionised water with 10 mgL^{-1} of ARAC was used to conduct the optimisation analysis. Spectrophotometric peak regions corresponding to the target dye wavelength were employed to analyse the effects of various factors on the effectiveness of the targeted dye's extraction. The effect of sample pH was studied at the range of pH 2, 4, 6, and 8. The SS:DoAc@Fe_3O_4 adsorbent ranging from 5 to 25 mg was also investigated. Additionally, the effect of extraction time was analysed for durations between 0.5 to 3 mins; the effect of desorption time was analysed for durations between 1 to 5 mins; and the effect of desorption solvent volume was analysed at the range of 400 to 700 µL. In this study, the extraction efficiency is the target property and should be maximised; thus, the favourable optimisation criterion is the larger-the-better (LTB) type of signal of noise.

Method validation

The linearity range, precision, limit of detection (LOD), limit of quantification (LOQ), recovery values, and matrix effect of the proposed SS:DoAc@Fe_3O_4-based MSPE approach was evaluated by conducting a range of tests on real matrix samples according to the International Council for Harmonisation of Technical Requirements of Pharmaceuticals for Human Use (ICH) guidelines [31].

Linearity

The linearity of the proposed DES in the MSPE method was examined by employing the optimised parameter conditions. Samples of soft drinks were spiked with various amounts of the standard dye analyte, ranging from 0.5 to 10 mgL^{-1}. A peak area following sample pre-treatment was applied to create a linear calibration curve with a coefficient of determination (R^2) close to 1.

Limit of detection (LOD) and limit of quantification (LOQ)

To assess the sensitivity of the proposed technique, the LOD and LOQ were calculated using the formulas in Eq. 1 and Eq. 2, respectively, where s is the standard deviation of ten replicate readings of the blank sample and b is the gradient of the calibration line [32].

$$\text{LOD} = \frac{3.3s}{b} \quad (1)$$

$$\text{LOQ} = \frac{10s}{b} \quad (2)$$

Precision analysis

The intra-day and inter-day precision at dye concentrations of 10 mgL^{-1} were measured to determine the precision of the proposed method. Both intra-day and inter-day precision analyses were conducted using three replicates (n=3). Prior to establishing the precision value, the standard deviation (SD) of the data was determined and provided in the form of percentage of relative standard deviation (%RSD). Subsequently, the SD and %RSD values were calculated using Eq. 3 and Eq. 4, respectively.

$$\text{SD} = \sqrt{\frac{\sum(x - \bar{x})^2}{n - 1}} \quad (3)$$

$$\text{RSD} = \frac{\text{SD}}{\bar{x}} \times 100 \quad (4)$$

where x is the outcomes of each run, n is the number of measurements, and $\bar{x}$ is the mean.

Recovery study

Three different dye concentrations were incorporated into the sample matrix to evaluate the accuracy of the suggested technique. The relative recovery (RR%) of dye was determined for each concentration level using three replicates (n=3) via Eq. (5).

$$\text{RR (\%)} = \frac{\text{Cs-Cu}}{\text{Co}} \text{ x } 100 \quad (5)$$

Where C_s is the dye concentration that has been spiked into the sample matrix, C_u is the dye concentration that has not been spiked into the sample matrix, and C_0 is the initial standard solution spiked into the sample matrix. In this study, the standard dye solution was spiked with dye at low, medium, and high concentrations (1, 3, and 10 mgL^{-1}) to analyse the drink samples.

Matrix effect

The process of co-extracting and co-eluting chemicals from actual matrix samples can have a significant impact on the spectrophotometry signals of dye. Therefore, Eq. (6) was used to study the matrix effect [33].

$$\text{Matrix effect (\%)} = \frac{(A_{M+S} - A_M)}{A_O} \text{ -1 x } 100 \quad (6)$$

Where A_{M+S} denotes the spectrophotometric response of the dye in a sample matrix that has been spiked, A_M denotes the spectrophotometric response of the dye in a sample matrix that has not been spiked, and A_O denotes the spectrophotometric response of the dye in a standard solution. A dye concentration of 10 mgL^{-1} was used to assess the matrix effect.

Real sample analysis

Commercial soft drinks were purchased from the local supermarket. First, an adequate amount of liquid drink sample was degassed for 10 minutes via sonication [34]. The liquid sample was later filtered through 0.45-µm nylon syringe filters, and 1.0 mL of the sample solution was taken and transferred into a 100-mL volumetric flask and diluted with ultrapure water [35]. Afterwards, the pH of the liquid samples was adjusted to 2 using 1 M hydrochloric acid. The MSPE technique was then applied to analyse the liquid samples.

Results and Discussion

Characterisation of DES

Figure 2 displays the FT-IR spectra of Fe_3O_4, SS:DoAc-based DES, and SS:DoAc@Fe_3O_4. The existence of the Fe-O stretching vibration at a frequency between 580 and 620 cm^{-1} serves as evidence for the successful formation of the Fe_3O_4 particles in spectra (a) and (b). The large absorption peak of approximately 3000 cm^{-1} in the Fe_3O_4 and SS:DoAc@Fe_3O_4 adsorbents indicated the existence of hydroxyl group (OH stretching). The Si−O−Si functional group of silicone surfactant (SS) is responsible for the stretching vibration in SS:DoAc@Fe_3O_4 materials at a wavenumber of around

1402 cm^{-1}. When Fe_3O_4 was coated with SS:DoAc-based DES, the C=O stretching band associated with the dodecanoic acid (DoAc) of SS:DoAc DES produced a wavenumber of 1622 cm^{-1}. These results are in line with the findings reported by previous studies [36, 37]. When compared to pure Fe_3O_4, the distinctive peaks of Si−O−Si stretch at 1402 cm^{-1} and C=O stretch at 1622 cm^{-1} established the success of the coating of SS:DoAc on Fe_3O_4. The attribution of the FT-IR spectra is summarised in Table 1. The FT-IR results denote the successful synthesis of the unique SS:DoAc@Fe_3O_4 material.

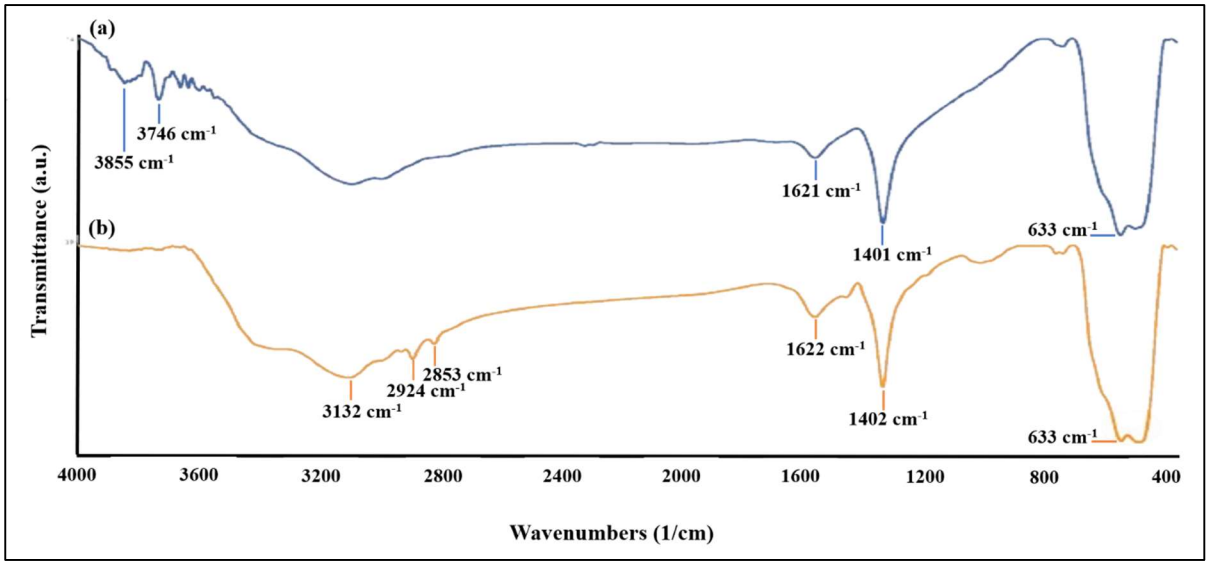

Figure 2. FT-IR spectra of (a) pure Fe_3O_4, (b) SS:DoAc@Fe_3O_4

Table 1. Main IR frequencies with assignments

	Wavenumber (cm^{-1})	
Assignment	**Fe_3O_4**	**SS:DoAc@Fe_3O_4**
OH stretching	3855	3132
Fe−O stretching vibration	633	633
Si−O−Si stretching	-	1402
C=O stretching	-	1622
C−H	3746	2924

Preliminary screening

An initial study was conducted using the MSPE technique with pure Fe_3O_4 particles and SS:DoAc@Fe_3O_4 adsorbent. As illustrated in Figure 3, the SS:DoAc@Fe_3O_4 adsorbent demonstrated a greater analytical response to dye extraction compared to pure Fe_3O_4 particles. This demonstrates that the coating of DES-based SS:DoAc on Fe_3O_4 particles enhanced the adsorbent's capacity for extraction. The extraction of the non-polar dye investigated in this study is facilitated by the hydrophobic SS:DoAc-based DES. Due to the strong hydrophobic interaction that developed between the target dye and the adsorbents, the target dye could be readily adsorbed onto the SS:DoAc@Fe_3O_4 surface. In the MSPE extraction technique, hydrophobic deep eutectic solvents (HDES) have been reported as an alternative to traditional extraction medium. HDES has been proven to be efficient absorbents with excellent CO_2 affinity and selectivity [38]. They are also efficient in removing hydrophobic compounds from aqueous samples [39]. Moreover, HDES has been utilised as an effective modification of inexpensive adsorbent for the extraction of pharmaceuticals and dyes [40]. Hence, the SS:DoAc@Fe_3O_4 adsorbent was preferred for further optimisation because the SS:DoAc-based DES coating could significantly enhance the extraction performance.

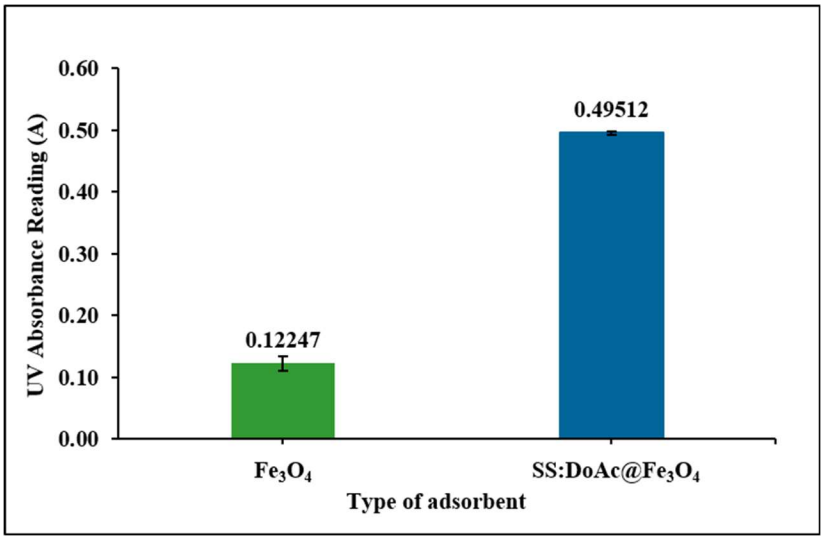

Figure 3. Type of adsorbent. (Condition: 10 mL of sample solution; 25 mg of adsorbent; 2 mins of extraction time; 800 µL of 25% (w/v) Na_2SO_4; 700 µL of methanol and 2 mins for desorption time), n=3

Optimisation of MSPE via OVAT design of experiments: Type of desorption solvent

The three frequently used organic solvents (methanol, acetonitrile, and methanol:acetonitrile (1:1) and isopropanol) with varied polarity were evaluated to determine their ability to elute the target dye to ensure the maximum recovery feasible. The results in Figure 4 show that the application of methanol:acetonitrile (1:1) as eluent resulted in the highest analytical signal, which was subsequently followed by methanol, acetonitrile, and isopropanol. The polarity and solvent characteristics of methanol and acetonitrile contribute to their efficacy as desorption solvents. Methanol is a polar-protic solvent, whereas acetonitrile is a polar-aprotic solvent and has a greater dipole moment. These two solvents are compatible with standard mobile phase additives and buffers and are completely miscible with water [41]. Methanol and acetonitrile, however, have been discovered to complement each other in terms of extraction efficiency. Both solvents can interact with non-polar compounds like ARAC due to their mid-polarity, making it easier to extract these compounds from food samples [42]. As a result, the target ARAC is more easily eluted from the SS:DoAc@Fe_3O_4 adsorbent into methanol:acetonitrile. Therefore, methanol: acetonitrile was chosen as a potential candidate for the desorption solvent in the forthcoming optimisation study.

Salt addition

The addition of salt was found beneficial in the extraction of ARAC because it enhances extraction efficiency by effectively separating dye molecules from the aqueous phase [43]. The recovery of the target analyte was favoured when salt was added to the sample solution due to the salting-out effect where it spiked the ionic strength of the aqueous matrix without causing additional reactions or chemical changes. This condition selectively reduced the analyte's solubility in the aqueous phase and increased the amount of analyte that could be adsorbed onto the SS:DoAc@Fe_3O_4 adsorbent [44]. Sodium sulfate (Na_2SO_4) is often used for salting out processes due to its properties where it is highly soluble in water and does not react with most compounds, making it an inert substance in this type of extraction. The effect of salt addition on the extraction performance was studied where sample solution added with salt was compared to sample solution without the addition of salt. The type of salt employed in this procedure is Na_2SO_4 with a concentration of 25% (w/v). In contrast to the standard sample solution, adding salt drastically increased the extraction yield, as shown in Figure 5. Therefore, 25% (w/v) of Na_2SO_4 was chosen for further investigation.

Volume of salt

The effect of salt volume was investigated by adding 25% (w/v) Na_2SO_4 at the range of 200 to 800 µL. As

depicted in Figure 6, the highest analytical response was the extraction yield obtained in 200 µL of 25% (w/v) Na_2SO_4. However, the extraction efficiency decreased with the addition of 800 µL of 25% (w/v) Na_2SO_4. This is due to the possibility of a salt-rich layer forming at the interface between the aqueous and organic phases, which potentially reduces the efficacy of the extraction method [45]. Thus, 200 µL of 25% (w/v) Na_2SO_4 was preferred for further investigation.

Volume of sample solution

The effect of sample solution volume was investigated with the range of 10 to 25 mL. As depicted in Figure 7, the highest analytical response was the extraction yield obtained in 20 mL of sample solution. A considerable amount of sample solution is necessary to obtain a higher pre-concentration factor [46]. The adsorption rate exhibited little impact for sample volumes between 10 and 20 mL but it drastically dropped between 20 and 25 mL (see Figure 7). This resulted from the use of high volume of sample solution, which may dilute the target analyte and minimise the efficacy of extraction and the analytical response of the method.

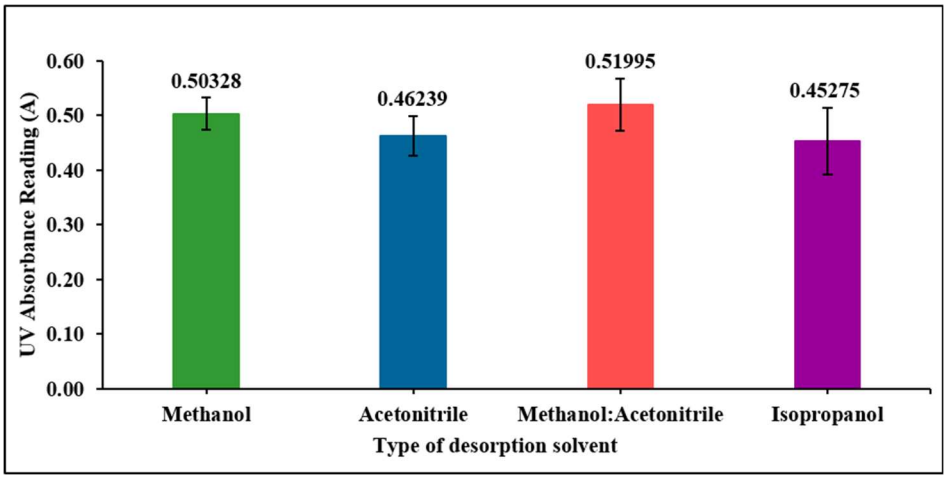

Figure 4. Effect of desorption solvent. (Condition: 10 mL of sample solution; 25 mg of adsorbent; 2 mins of extraction time; 800 µL of 25% (w/v) Na_2SO_4; and 2 mins for desorption time), n=3

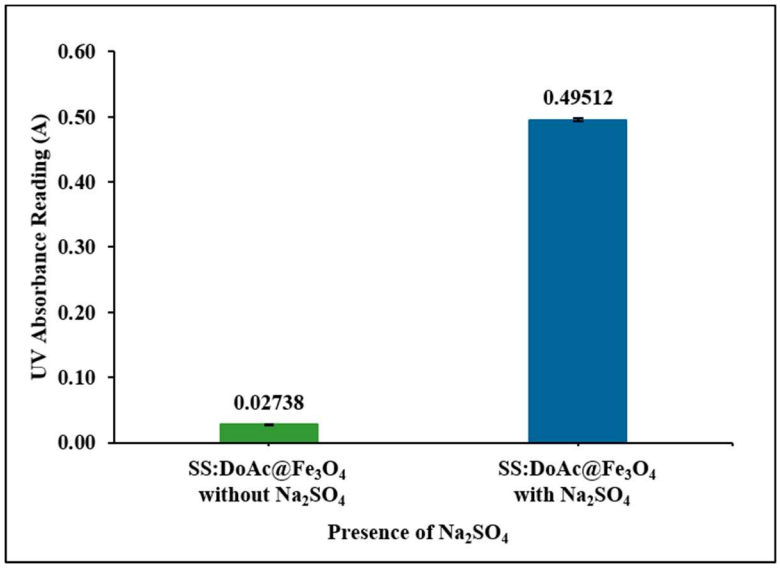

Figure 1. Effect of presence of Na_2SO_4. (Condition: 10 mL of sample solution, 25 mg of adsorbent; 2 mins of extraction time; 800 µL of 25% (w/v) Na_2SO_4; and 2 mins for desorption time), n=3

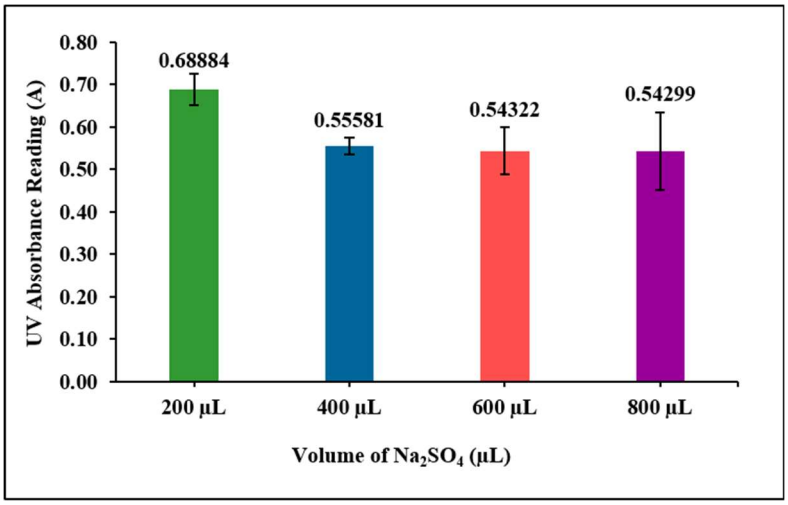

Figure 2. Effect of volume of Na_2SO_4. (Condition: 10 mL of sample solution, 25 mg of adsorbent; 2 mins of extraction time; and 2 mins for desorption time), n=3

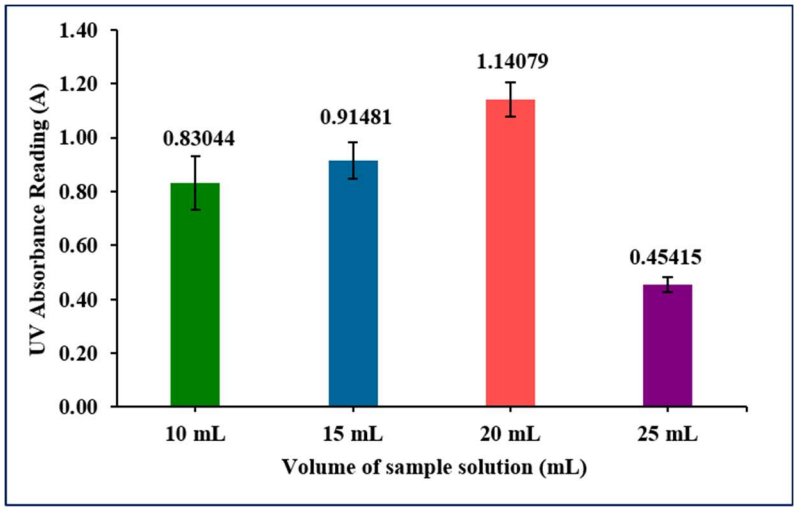

Figure 3. Effect of volume of sample solution. (Condition: 800 µL of 25% (w/v) Na_2SO_4, 25 mg of adsorbent; 2 mins of extraction time; and 2 mins for desorption time), n=3

Point of zero charge

The pH at which the net surface charge of the particles reaches zero is known as the point zero charge (pzc) of an adsorbent [47]. Determining the point of zero charge (pzc) of an adsorbent is crucial in adsorption studies. The surface of the adsorbent is positively charged whenever the solution's pH is lower than pzc. The surface may attract anions in this condition. However, if the pH of the solution is greater than pzc, the surface is negatively charged and may attract cations [48]. Figure 8 shows the Δ pH plotted against the initial pH graph. The pH value for zero-point charge of the SS:DoAc@Fe_3O_4 adsorbent was found to be at pH 2. Whereas the surface of SS:DoAc@Fe_3O_4 adsorbent became positively charged at pH level less than pH 2, making it feasible for anionic species like Allura Red AC to be adsorbed.

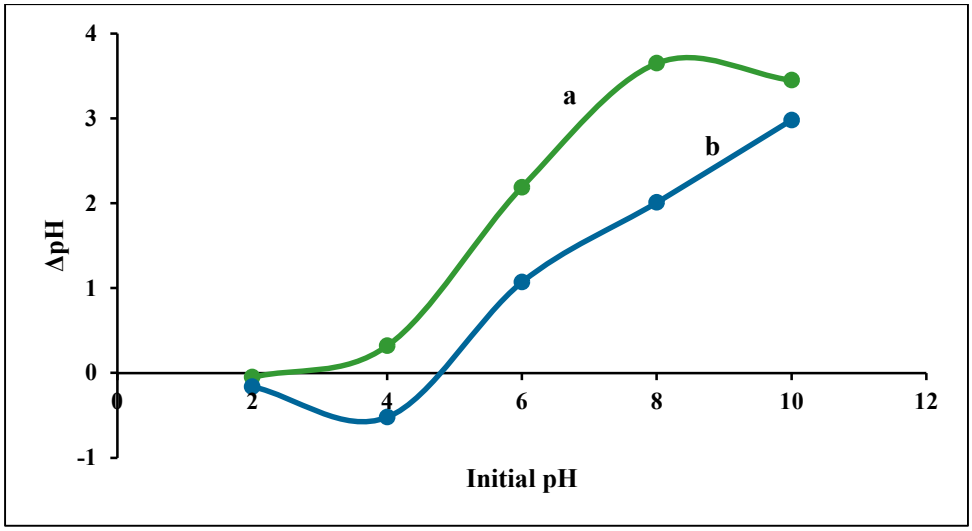

Figure 8. Point of zero charge of a) Fe_3O_4 and b) SS:DoAc@Fe_3O_4, (n=1)

Optimisation of MSPE technique via Taguchi design of experiments: pH of sample solution

The efficacy of the extraction is significantly affected by the pH of the sample solution by establishing the ionic state of any possible adsorbents, adsorbates, and other species in the sample [49]. The effect of sample pH was investigated with pH values ranging from 2 to 8. As shown in Figure 9, the extraction recovery of ARAC significantly increased in the pH range of 2 to 4 and decreased from 6 to 8. Given that the pKa of the target analyte, ARAC, is 11.4 and that 50% of this dye is protonated at the pH value of 11.4, the partial deprotonation of the phenol group for ARAC may be the cause of the decreased extraction of the analyte [50]. The results align with those reported by Yu and Fan who found that the adsorption rate of ARAC was higher at pH 2 or 3 but decreased as the pH increased from 3 to 7 [46]. Another study also mentioned that in an acidic solution (pH 2), the ARAC dye functions as an anionic dye molecule and two of its sulfonate (SO^{3-}) groups may be electrostatically attracted by protonated amino (NH^{2+}) groups. The maximum dye adsorption was seen at solution pH 2, which may be due to the electrostatic interaction between dye molecules and adsorption sites [51]. The target ARAC could be present as a stable acidic molecule with a greater affinity for adsorbents at pH 2, which resulted in the maximum extraction yield. As a result, pH 2 was selected as the appropriate pH for subsequent tests.

Mass of adsorbent

The quantity of adsorbent was optimised to achieve the highest extraction yield where different amounts of SS:DoAc@Fe_3O_4 in the range of 5 to 25 mg were investigated. As shown in Figure 9, the extraction recovery for the investigated ARAC rose exponentially with adsorbent mass up to 25 mg. The dosage of the adsorbent determines the amount of target dyes being adsorbed since it offers the sites needed to load the dyes. In this regard, more accessible sites are deemed advantageous for maximising extraction [49]. This agrees with Saha et al. who stated that surface area and the number of accessible adsorption sites increased as the mass of adsorbents increased in the extraction of Allura Red [51]. Therefore, 25 mg of the SS:DoAc@Fe_3O_4 adsorbent was established for the subsequent experiments.

Extraction time

According to Yu and Fan, the extraction method used in MSPE is based on a time-dependent equilibrium in which target molecule mass transfer rises with time until adsorption equilibrium is attained [46]. The period of time needed to establish extraction equilibrium is crucial for improving both the mass transfer and the interaction between the sample solution and the solvent [50]. The extraction time was examined between 0.5 and 3 mins in order to maximise the extraction yield. As seen in Figure 9, the analytical response elevated significantly in the first 2 mins. This could be prompted by the

powerful attraction forces between the dye molecules and the adsorbents. To achieve equilibrium, dye molecules quickly adsorb onto the adsorbents' exterior surfaces, followed by pore diffusion into their matrix [51]. Further prolongation of the extraction process notably after 2 mins demonstrates that the adsorption of ARAC dye onto the adsorbent did not show a significant progress, which could be related to back extraction [52]. Hence, 2 mins of extraction time was selected for forthcoming investigations.

Desorption time

The impact of desorption time was investigated between 1 and 5 mins. The results in Figure 9 show that 3 mins of sonication was sufficient to elute all the target ARAC from the adsorbent into methanol:acetonitrile (1:1). The analytical response increased gradually and declined after 3 mins of elution. According to Naing et al., prolonged sonication may have caused the target analytes to re-adsorb onto the adsorbent, thus decreasing the extraction yield [52]. Conversely, the adsorbents' magnetic properties allowed them to be quickly isolated from the sample solution in less than 2 mins using a powerful magnet as opposed to filtration or centrifugation [46]. Therefore, the optimal desorption time was established at 3 mins of sonication.

Desorption solvent volume

The impact of desorption solvent volume on the elution of target ARAC was also investigated to obtain the highest possible extraction yield. As shown in Figure 9, the analytical signal quickly decreased following the increasing volume of elution solvent. Methanol:acetonitrile (1:1) beyond 400 µL caused the target ARAC to be diluted in the solvent, which gradually reduced the spectrophotometric response. Desorption solvent volumes below 400 µL were not employed in this study because the remaining solvent obtained after the desorption process was insufficient to be subjected to UV-Vis spectrophotometry analysis. Subsequently, 400 µL of methanol:acetonitrile (1:1) was fixed to prepare for future optimisation.

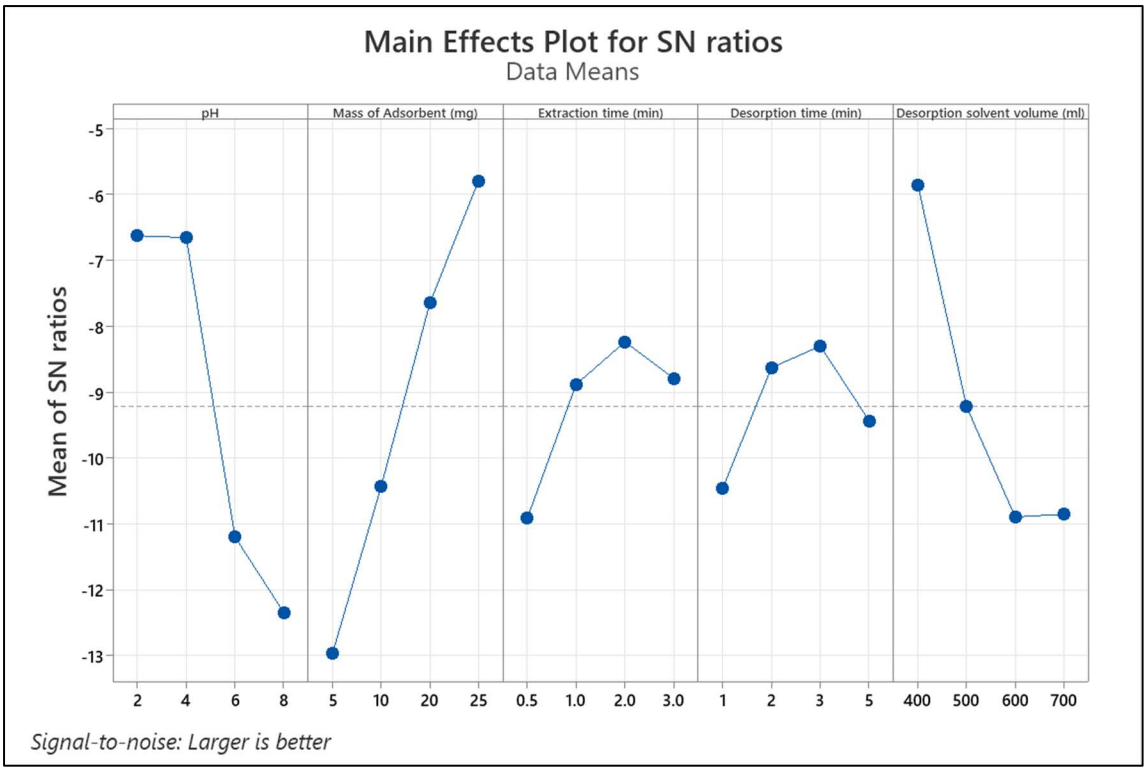

Figure 9. Signal-to-noise ratios involving sample pH; mass of adsorbent, extraction time, desorption time, desorption solvent volume

Method Validation

The proposed approach was implemented to monitor ARAC in soft drink samples to evaluate its feasibility. The calibration curve was plotted within the range of 0.3 to 10 mgL^{-1} for soft drinks samples under optimised experimental parameters. The coefficient of determination (R^2) derived from the linearity curve was 0.999. The LOD obtained was 0.1 mgL-1 and the LOQ was 0.4 mgL-1, and both values are lower compared to the maximum permitted level of ARAC in soft drinks. In accordance with Directive 94/36/EC from the European Parliament and Council, the highest acceptable concentration of ARAC in soft drinks is 100 mgL^{-1} [53]. The intra- and inter-precision values for the developed technique ranged between 5.05% and 5.37%, respectively. The matrix effect obtained is 4% across all investigated ARAC, indicating that the analysis of the soft drink samples had minimal effect on the recovery of ARAC. Table 2 provides a summary of the figure of merits.

Table 2. Analytical performance data of MSPE technique using SS:DoAc@Fe_3O_4 adsorbent

Assay	Allura Red AC
Linearity (mgL^{-1})	0.3 - 10
Coefficients of determination (R^2)	0.999
Intraprecision (%) (n=3)	5.05
Interprecision (%) (n=3)	5.37
LOD (mgL^{-1})	0.1
LOQ (mgL^{-1})	0.4
Matrix effect (%)	4

Real sample analysis

Samples of commercial soft drinks were subjected to the validated MSPE method using the SS:DoAc@Fe_3O_4 adsorbent. The samples were spiked with 1, 3, and 10 mgL^{-1} of the target ARAC to examine how the sample matrix affected the results. The recoveries obtained from soft drinks samples ranged from 80% to 111%. Table 3 lists the recovery values for the real sample.

Table 3. Relative recovery study of SS:DoAc@Fe_3O_4 based MSPE of ARAC in soft drink samples.

Analyte	Spiked (mgL^{-1})	% Recovery (% RSD, n = 3)		
		Sample A	Sample B	Sample C
Allura Red AC	0	nd	nd	nd
	1	111 (11.6)	101 (7.4)	93 (4.6)
	3	88 (9.2)	84 (6.2)	85 (1.1)
	10	80 (10.7)	83 (2.6)	90 (3.9)

Linear range: 0.3-10 mgL^{-1}

[a]nd-not detected.

[b]Mean of triplicate analysis.

[c]RSD-Relative standard deviation (n = 3)

Comparison with previous studies

As shown in Table 4, the developed method obtained lower LOD compared to those reported by dos Reis et al. [54]. Compared to other methods, the LOD obtained was slightly lower due to the instrument used in this study. UV-Vis has lower sensitivity compared to other instruments, such as HPLC. However, the result is comparable to other studies as the extraction time needed in this study was only one minute.

Table 4. Comparison of performance of ARAC extraction using various extraction techniques

Extraction Technique	Matrix	Instrument	LOD (mg L^{-1})	LOQ (mg L^{-1})	Extraction Time (min)	Reference
VA-SS-LPME	Confectioneries, beverages, drugs and syrups	UV-Vis spectrometer	0.051	0.172	2	[55]
LLE	Milk, meat and fish products, confections, wines, juices and beverages	HPLC-DAD	0.029	0.088	2 – 5 (based on samples)	[56]
MSPE	Paediatric syrup, colored sugar-coated chickpeas, and mineral water	HPLC-UV	0.05	0.1	5	[48]
LLE	Guava pulp	HPLC-DAD	15	30	0.5	[54]
MSPE	Soft drink	UV-Vis spectrometer	0.1	0.4	2	This study

Abbreviation: VA-SS-LPME: vortex assisted sequential-simultaneous liquid phase micro-extraction; LLE: liquid-liquid extraction; MSPE: magnetic solid phase extraction; HPLC-DAD: high performance liquid chromatography with diode array detector; HPLC-UV: high performance liquid chromatography with ultraviolet detector.

Conclusion

This study aimed to explore the application of SS:DoAc-based DES functionalised Fe_3O_4 (SS:DoAc@Fe_3O_4) adsorbents, which are inexpensive and environmentally benign solvents, to increase the effectiveness and sustainability of the extraction technique. The work was successful in demonstrating the feasibility and efficacy of SS:DoAc@Fe_3O_4 for the extraction of ARAC through an extensive experimental method and analysis. The results showed that the proposed adsorbent has higher extraction efficiency, high selectivity, and great reusability. Compared to unmodified Fe_3O_4 particles, the SS:DoAc-based DES functionalised Fe_3O_4 allowed for simple and quick separation of the adsorbent from the sample matrix. This was made possible by the strong hydrophobic interaction between ARAC and the SS:DoAc@Fe_3O_4 adsorbent.

Through a combination of OVAT and Taguchi design methodologies, we successfully optimised the extraction conditions for ARAC using magnetic solid phase extraction. The OVAT analysis revealed that having a methanol:acetonitrile (1:1) mixture as the desorption solvent, salt addition for enhanced extraction performance, salt volume of 200 µL, and a sample volume of 20 mL yielded optimal results. Meanwhile, Taguchi experiments determined the ideal conditions as pH 2, 25 mg of adsorbent dosage, 2 minutes of extraction time, 3 minutes of desorption time, and a desorption solvent volume of 400 µL. These findings enhance the current understanding of the extraction process and offer practical guidelines for maximising ARAC extraction efficiency. Under optimised experimental parameters, the studied ARAC derived the R^2 value of 0.999 for linearity curve while the LOD and LOQ were 0.1 mgL^{-1} and 0.4 mgL^{-1}, respectively. This infers that the developed MSPE approach capitalising on the SS:DoAc@Fe_3O_4 adsorbent is indeed an excellent tool for the analytical separation and identification of ARAC. The findings of this work significantly support the notion that DES-based MSPE is an extraction technique with high potential for the extraction of azo food dyes, hence providing new opportunities for efficient and sustainable dye analysis in the food industry. This research represents a significant advancement in the direction of more environmentally friendly and effective extraction techniques, making a substantial contribution to the overall development of green techniques for the analysis of food dyes.

Several suggestions for further research can be made based on the findings and conclusion deduced from this study. First, it is important to work on optimising the DES composition to find the best solvent system for a variety of azo food dyes. This can be accomplished by

experimenting with various molar ratios and DES component combinations. Moreover, examining the applicability of the suggested approach using other analytical tools, such as high-performance liquid chromatography (HPLC) and gas chromatography-mass spectrometry (GC-MS), can expand our knowledge in this specific field of study and improve its credibility. Investigating the application of DES-based MSPE to complex food matrices, like processed foods and different types of beverages, will also offer beneficial practical insights. For industrial implementation, it is essential to evaluate the scalability, viability, and compatibility of the process. Furthermore, it would be desirable to conduct an environmental impact assessment (EIA) to compare the sustainability and energy efficiency of DES-based MSPE to traditional approaches. These recommendations for future research must be taken into consideration to ensure consumer safety and environmental protection. This will help to promote effective and sustainable methods for food dye analysis in food technology applications.

Acknowledgement

The authors would like to express their deepest gratitude to the Universiti Sains Malaysia, Short-Term Grant with Project No: 304/CIPPT/6315811, and the Ministry of Higher Education Malaysia, for the Fundamental Research Grant Scheme (FRGS) with Project Code: FRGS/1/2021/STG04/USM/02/8. The authors are also thankful to the Advanced Medical and Dental Institute, Universiti Sains Malaysia, for the resources and facilities provided to aid in the successful completion of this project

References

1. Vega, E. N., Ciudad-Mulero, M., Fernández-Ruiz, V., Barros, L., and Morales, P. (2023). Natural sources of food colorants as potential substitutes for artificial additives. *Foods*, 12(22): 4102.
2. Luzardo-Ocampo, I., Ramírez-Jiménez, A. K., Yañez, J., Mojica, L., and Luna-Vital, D. A. (2021). Technological applications of natural colorants in food systems: A review. *Foods*, 10(3): 634.
3. Dey, S., and Nagababu, B. H. (2022c). Applications of food color and bio-preservatives in the food and its effect on human health. *Food Chemistry Advances*, 1: 19.
4. Nabi, B. G., Mukhtar, K., Ahmed, W., Manzoor, M. F., Ranjha, M. M. A. N., Kieliszek, M., Bhat, Z. F., and Aadil, R. M. (2023). Natural pigments: Anthocyanins, carotenoids, chlorophylls, and betalains as colorants in food products. *Food Bioscience,* 52: 102403.
5. Castro, T. A., Leite, B. S., Assunção, L. S., de Jesus Freitas, T., Colauto, N. B., Linde, G. A., Otero, D. M., Machado, B. A. S., and Ferreira Ribeiro, C. D. (2021). Red tomato products as an alternative to reduce synthetic dyes in the food industry: A review. *Molecules*, 26(23): 7125.
6. Dilrukshi, P. G. T., Munasinghe, H., Silva, A. B. G., and De Silva, P. G. S. M. (2019f). Identification of synthetic food colours in selected confectioneries and beverages in Jaffna District, Sri Lanka. *Journal of Food Quality*, 2019: 7453169.
7. John, A., Yang, H. H., Muhammad, S., Khan, Z. I., Yu, H., Luqman, M., Tofail, M., Hussain, M. I., and Awan, M. U. F. (2022). Cross talk between synthetic food colors (azo dyes), oral flora, and cardiovascular disorders. *Applied Sciences (Switzerland)*, 12(14): 7084.
8. Ntrallou, K., Gika, H., and Tsochatzis, E. (2020). Analytical and sample preparation techniques for the determination of food colorants in food matrices. *Foods*, 9(1): 58.
9. Silva, M. M., Reboredo, F. H., and Lidon, F. C. (2022i). Food colour additives: A synoptical overview on their chemical properties, applications in food products and health side effects. *Foods*, 11(3): 379.
10. Novais, C., Molina, A. K., Abreu, R. M. V., Santo-Buelga, C., Ferreira, I. C. F. R., Pereira, C., and Barros, L. (2022). Natural food colorants and preservatives: A review, a demand, and a challenge. *Journal of Agricultural and Food Chemistry,* 70(9): 7533.
11. Slama, H. Ben, Bouket, A. C., Pourhassan, Z., Alenezi, F. N., Silini, A., Cherif-Silini, H., Oszako, T., Luptakova, L., Golińska, P., and Belbahri, L. (2021k). Diversity of synthetic dyes from textile industries, discharge impacts and treatment methods. *Applied Sciences (Switzerland)*, 11(14): 6255.
12. Zafar, S., Bukhari, D. A., and Rehman, A. (2022l).

Azo dyes degradation by microorganisms – An efficient and sustainable approach. *Saudi Journal of Biological Sciences,* 29(12): 103437.

13. Kamali, M., Fazlpour, F., Karimi, F., Rezaee, A., Sadri, F., and Hosseini, S. F. (2023). A review of cytotoxic effects of azo dyes on brain-subregion. *Middle East Journal of Rehabilitation and Health Studies,* 10(2): 130751.
14. Barciela, P., Perez-Vazquez, A., and Prieto, M. A. (2023). Azo dyes in the food industry: Features, classification, toxicity, alternatives, and regulation. *Food and Chemical Toxicology*, 178: 113935.
15. Badawy, M. E. I., El-Nouby, M. A. M., Kimani, P. K., Lim, L. W., and Rabea, E. I. (2022). A review of the modern principles and applications of solid-phase extraction techniques in chromatographic analysis. *Analytical Sciences*, 38(12): 1457-1487.
16. Shen, Z., Kuang, Y., Zhou, S., Zheng, J., and Ouyang, G. (2023p). Preparation of magnetic adsorbent and its adsorption removal of pollutants: An overview. *TrAC - Trends in Analytical Chemistry,* 167: 117241.
17. Hu, M., Butt, H. J., Landfester, K., Bannwarth, M. B., Wooh, S., and Thérien-Aubin, H. (2019q). Shaping the assembly of superparamagnetic nanoparticles. *ACS Nano*, 13(3): 7783.
18. Zhang, M., Huang, G., Huang, J., Zhong, L., and Chen, W. (2017). Magnetic solid phase extraction with octahedral structured Fe3O4@SiO2@polydimethylsiloxane magnetic nanoparticles as the sorbent for determining benzene, toluene, ethylbenzene and xylenes in water samples. *RSC Advances*, 7(66): 07733e.
19. Rahnama, S., Shariati, S., and Divsar, F. (2021). Selective aptamer conjugation to silver-coated magnetite nanoparticles for magnetic solid-phase extraction of trace amounts of Pb2+ions. *RSC Advances*, 11(9): 4791.
20. Ibarra, I. S., Rodriguez, J. A., Galán-Vidal, C. A., Cepeda, A., and Miranda, J. M. (2015). Magnetic solid phase extraction applied to food analysis. *Journal of Chemistry*, 2015: 919414
21. de Jesus, S. S., and Maciel Filho, R. (2022). Are ionic liquids eco-friendly? *Renewable and Sustainable Energy Reviews*, 157: 112039.
22. Saini, R., Kumar, S., Sharma, A., Kumar, V., Sharma, R., Janghu, S., and Suthar, P. (2022). Deep eutectic solvents: The new generation sustainable and safe extraction systems for bioactive compounds in agri food sector: An update. *Journal of Food Processing and Preservation*, 46(10): 16250.
23. Ünlü, A. E., Arlkaya, A., and Takaç, S. (2019). Use of deep eutectic solvents as catalyst: A mini-review. *Green Processing and Synthesis*, 8(1): 355-372.
24. Bianchi, F., Giannetto, M., and Careri, M. (2018). Analytical systems and metrological traceability of measurement data in food control assessment. *TrAC Trends in Analytical Chemistry*, 107: 142-150.
25. Pay, R., Sharrock, A. V., Elder, R., Maré, A., Bracegirdle, J., Torres, D., Malone, N., Vorster, J., Kelly, L., Ryan, A., Josephy, P. D., Allen-Vercoe, E., Ackerley, D. F., Keyzers, R. A., and Harvey, J. E. (2023). Preparation, analysis and toxicity characterisation of the redox metabolites of the azo food dye tartrazine. *Food and Chemical Toxicology*, 182: 114193.
26. Emiroğlu, E., Yuvali, D., Sarp, G., Yilmaz, E., and Narin, İ. (2021). Magnetic solid phase extraction of erythrosine (E127) in pharmaceutical samples with Fe_3O_4/C-nanodots hybrid material prior to spectrophotometric analysis. *Microchemical Journal*, 170: 106766.
27. Liu, Q., Xu, Q., and Sun, W. (2021). Facile preparation of core-shell magnetic organic covalent framework via self-polymerization of two-in-one strategy as a magnetic solid-phase extraction adsorbent for determination of Rhodamine B in food samples. *Journal of Chromatography A*, 1657: 462566.
28. Reyes-Garcés, N., Gionfriddo, E., Gómez-Ríos, G. A., Alam, M. N., Boyacl, E., Bojko, B., Singh, V., Grandy, J., and Pawliszyn, J. (2018). Advances in solid phase microextraction and perspective on future directions. *Analytical Chemistry,* 90(1): 4502.
29. Elencovan, V., Yahaya, N., Raoov, M., and Zain, N. N. M. (2022). Exploring a novel silicone surfactant-based deep eutectic solvent functionalized magnetic iron particles for the extraction of organophosphorus pesticides in vegetable samples. *Food Chemistry*, 396: 133670.

30. Hashim, N. M., Mohamad, M., Kamal, N. N. S. N. M., Aziz, M. Y., Mohamad, S., Yahaya, N., and Zain, N. N. M. (2023). Revolutionizing drug removal: Green magnetic nanoparticles functionalized with hydrophobic deep eutectic solvents for anti-inflammatory drug adsorption. *Journal of Molecular Liquids*, 383: 122082.
31. International Conference Harmonisation. (1994). ICH guideline Q2(R2) on validation of analytical procedures. *Quality Guidelines*, 50(4): 99-108.
32. Shahriman, M. S., Ramachandran, M. R., Zain, N. N. M., Mohamad, S., Manan, N. S. A., and Yaman, S. M. (2018). Polyaniline-dicationic ionic liquid coated with magnetic nanoparticles composite for magnetic solid phase extraction of polycyclic aromatic hydrocarbons in environmental samples. *Talanta*, 178: 211-221.
33. Boon, Y. H., Mohamad Zain, N. N., Mohamad, S., Osman, H., and Raoov, M. (2019). Magnetic poly(β-cyclodextrin-ionic liquid) nanocomposites for micro-solid phase extraction of selected polycyclic aromatic hydrocarbons in rice samples prior to GC-FID analysis. *Food Chemistry*, 278: 322-332.
34. Mazdeh, F. Z., Khorrami, A. R., Moradi-Khatoonabadi, Z., Aftabdari, F. E., Ardekani, M. R. S., Moghaddam, G., and Hajimahmoodi, M. (2016). Determination of 8 synthetic food dyes by solid phase extraction and reversed-phase high performance liquid chromatography. *Tropical Journal of Pharmaceutical Research*, 15(1): 173-181.
35. Bişgin, A. T., Sürme, Y., Uçan, M., and Narin, İ. (2016). Solid-phase extraction and spectrophotometric determination of Allura Red (E129) in foodstuff, soft drink, syrup and energy drink samples: a comparison study. *International Journal of Food Science & Technology*, 51(11): 2367-2375.
36. Tavakoli, M., Hajimahmoodi, M., and Shemirani, F. (2014). Trace level monitoring of pesticides in water samples using fatty acid coated magnetic nanoparticles prior to GC-MS. *Analytical Methods*, *6*(9): 2988-2997.
37. Wang, J., Zhang, L., Xin, D., and Yang, Y. (2015). Dispersive micro-solid-phase extraction based on decanoic acid coated-Fe_3O_4 nanoparticles for HPLC analysis of phthalate esters in liquor samples. *Journal of Food Science*, 80(11): 13101.
38. Devi, M., Moral, R., Thakuria, S., Mitra, A., and Paul, S. (2023). Hydrophobic deep eutectic solvents as greener substitutes for conventional extraction media: examples and techniques. *ACS Omega*, 8(11): 7684.
39. Makoś, P., Przyjazny, A., and Boczkaj, G. (2018). Hydrophobic deep eutectic solvents as "green" extraction media for polycyclic aromatic hydrocarbons in aqueous samples. *Journal of Chromatography A*, 1570: 28-37.
40. Lawal, I. A., Klink, M., and Ndungu, P. (2019). Deep eutectic solvent as an efficient modifier of low-cost adsorbent for the removal of pharmaceuticals and dye. *Environmental Research*, 179: 108837.
41. Doppler, M., Kluger, B., Bueschl, C., Schneider, C., Krska, R., Delcambre, S., Hiller, K., Lemmens, M., and Schuhmacher, R. (2016). Stable isotope-assisted evaluation of different extraction solvents for untargeted metabolomics of plants. *International Journal of Molecular Sciences*, 17(7): 1017.
42. Moldoveanu, S., and David, V. (2022). Reversed-phase HPLC. *Essentials in Modern HPLC Separations* (pp. 341–419). Elsevier.
43. Bişgin, A. T. (2018). Cloud point extraction and spectrophotometric determination of Allura Red (E129) in foodstuffs. *Iğdır Üniversitesi Fen Bilimleri Enstitüsü Dergisi*, *8*(4): 397479.
44. Zhou, Q., Lei, M., Wu, Y., and Yuan, Y. (2017). Magnetic solid phase extraction of typical polycyclic aromatic hydrocarbons from environmental water samples with metal organic framework MIL-101 (Cr) modified zero valent iron nano-particles. *Journal of Chromatography A*, 1487: 22-29.
45. Pourreza, N., Rastegarzadeh, S., and Larki, A. (2011). Determination of Allura red in food samples after cloud point extraction using mixed micelles. *Food Chemistry*, 126(3): 158.
46. Yu, Y., and Fan, Z. (2016). Magnetic solid-phase extraction coupled with HPLC for the determination of Allura Red in food and beverage samples. *Food Additives and Contaminants - Part A Chemistry, Analysis, Control, Exposure and Risk*

Assessment, 33(10): 1231937.

47. Fiol, N., and Villaescusa, I. (2009). Determination of sorbent point zero charge: usefulness in sorption studies. *Environmental Chemistry Letters*, 7(1): 79-84.
48. Oymak, T., and Dural, E. (2022). Determination of Sunset Yellow, Allura Red, and Fast Green using a novel magnetic nanoadsorbent modified with *Elaeagnus angustifolia* based on magnetic solid-phase extraction by HPLC. *Brazilian Journal of Pharmaceutical Sciences*, 58: 20884.
49. Hamidi, S., Nemati, M., and Lotfipour, F. (2021). Simultaneous determination of synthetic dyes in gummy candy using novel mesoporous magnetic graphene oxide@zein aerogel followed by a high performance liquid chromatography-diode array detector. *Journal of Microbiology, Biotechnology and Food Sciences*, 11(3): 3785.
50. Piton, G. R., Augusto, K. K. L., Santos, D. A., and Fatibello-Filho, O. (2021). Spectrophotometric determination of Allura Red AC and tartrazine in food products using hydrophobic deep eutectic solvents as an environmentally sustainable micro-extractor. *Journal of the Brazilian Chemical Society*, *32*(3): 1-8.
51. Saha, T. K., Bishwas, R. K., Karmaker, S., and Islam, Z. (2020). Adsorption characteristics of Allura Red AC onto sawdust and hexadecylpyridinium bromide-treated sawdust in aqueous solution. *ACS Omega*, *5*(22): 1493.
52. Naing, N. N., Li, S. F. Y., and Lee, H. K. (2016). Micro-solid phase extraction followed by thermal extraction coupled with gas chromatography-mass selective detector for the determination of polybrominated diphenyl ethers in water. *Journal of Chromatography A*, 1458: 25-34.
53. Scientific Opinion on the re-evaluation of Allura Red AC (E 129) as a food additive. (2009). *EFSA Journal*, *7*(11): 1327.
54. dos Reis, M. F., Silva, F. A., Madureira, F., Vargas, E., Oliveira, L. M. F., and Lopes, R. P. (2021). Development and validation of a method for ionic dyes determination in guava fibrous matrix using reverse phase chromatography. *Journal of the Brazilian Chemical Society*, 32(11): 1-8.
55. Bişgin, A. T. (2024). Selective separation and determination strategy for monitoring E100, E127, E129 and E133 in foodstuffs: Vortex assisted sequential-simultaneous liquid phase micro-extraction. *Microchemical Journal*, 196: 109716.
56. Palianskikh, A. I., Sychik, S. I., Leschev, S. M., Pliashak, Y. M., Fiodarava, T. A., and Belyshava, L. L. (2022). Development and validation of the HPLC-DAD method for the quantification of 16 synthetic dyes in various foods and the use of liquid anion exchange extraction for qualitative expression determination. *Food Chemistry*, 369: 130947.

Malaysian Journal of Analytical Sciences (MJAS)
Published by Malaysian Analytical Sciences Society

AUTHENTICATION OF CLOVE LEAF OIL IN PRODUCTS (*Syzygium aromaticum* (L.) Merr. & L. M. Perry) USING GC-MS AND FTIR METHODS COMBINED WITH CHEMOMETRIC

Pengesahan Minyak Daun Cengkih (*Syzygium aromaticum* (L.) Merr. & L. M. Perry) dalam Produk Menggunakan Kaedah GC-MS dan FTIR Yang Digabungkan dengan Kemometri

Any Guntarti[1], Laela Hayu Nurani[1*], Putri Lestari[1], Citra Ariani Edityaningrum[1], Lalu Muhammad Irham[1], and Abdul Rohman[2,3]

[1]*Faculty of Pharmacy, Universitas Ahmad Dahlan Yogyakarta 55164, Indonesia*
[2]*Center of Excellence, Institute for Halal Industry and Systems, Universitas Gadjah Mada, Yogyakarta 55281, Indonesia*
[3]*Faculty of Pharmacy, Universitas Gajah Mada, Yogyakarta 55281, Indonesia*

[*]*Corresponding author: laela.farmasi@pharm.uad.ac.id*

Received: 24 January 2024; Accepted: 26 March 2024; Published: 29 June 2024

Abstract

The production cost and market demand for clove oil are significantly high due to its great commercial value and benefits. However, the extraction yield of clove oil is very low at around 1%, causing the act of adulteration of essential oils to reduce production costs. Therefore, this study aims to determine the addition of adulterants in essential oils using the authentication technique. The samples used are clove oil from dry leaf distillation, products A, B, and C on the market. The GC-MS and FTIR methods combined with PCA (Principal Component Analysis) and PLS (Partial Least Square) multivariate calibration analysis were selected in the authentication to detect clove oil adulteration. The constituent's presence in distilled clove oil from GC-MS analysis was eugenol (49.63%), β-Caryophyllene (28.25%), alpha-Humulene (8.92%), alpha-Copaene (2.15%), delta-Cadinene (1.61%), and Caryophyllene oxide (1.50%). Six concentrations were prepared for FT-IR analysis of clove leaf oil and turpentine oil mixture, which was estimated by PLS and PCA chemometrics. Turpentine oil was used as counterfeit, which was usually added to clove oil products. The PLS analysis of FTIR obtained optimized wavenumbers, 2960-2860 cm^{-1}. The equation y=0.9998x+0.0096 had an R^2 value of 0.9998, as well as RMSEC, RMSECV, and RMSEP values of 0.22%, 0.76%, and 1.20%, respectively. The PCA analysis can categorize the oil based on the main component types of distilled clove leaf oil, turpentine oil, and market oil, namely products A, B, and C. The results showed that product A oil was in the same quadrant as distilled clove leaf oil. Moreover, no clove leaf oil product had similar physical and chemical characteristics to turpentine oil.

Keywords: authentication, clove leaf oil, Fourier transform infrared, gas chromatography-mass spectrometry, turpentine oil

Abstrak

Minyak cengkih mempunyai nilai dan faedah komersial yang besar, pada masa ini permintaan untuk ketersediaan minyak cengkih di pasaran adalah sangat tinggi namun, hasil perahan minyak cengkih adalah sangat rendah, iaitu sekitar 1% dan mengakibatkan kos pengeluaran minyak cengkih yang agak tinggi. Ini menyebabkan pemalsuan minyak pati untuk mengurangkan kos pengeluaran

dan mengekalkan jumlah minyak pati. Satu teknik yang boleh digunakan untuk mengesan kehadiran bahan tiruan dalam minyak pati adalah melalui pengesahan. Kaedah GC-MS dan FTIR digabungkan dengan analisis penentukuran multivariat PCA (analisis prinsip utama) dan PLS (*partial least square*) telah dipilih dengan tujuan untuk mengesan tindakan pemalsuan pada minyak cengkih. Kandungan minyak daun cengkih suling daripada hasil analisis GC-MS iaitu eugenol 49.63% β-Caryophyllene 28.25%, alpha-Humulene 8.92%, alpha-Copaene 2.15%, delta-Cadiene 1.61% dan Caryophyllene oksida 1.50%. Analisis FT-IR dijalankan dengan membuat 6 siri kepekatan campuran minyak daun cengkih dan minyak turpentin dan kemudiannya dianalisis dengan kemometrik PLS dan PCA. Keputusan analisis PLS daripada FTIR menunjukkan bahawa nombor gelombang yang dioptimumkan ialah 2960-2860 cm^{-1}. Persamaan yang terhasil ialah y = 0.9998x + 0.0096 dengan nilai R^2 0.9998; Nilai RMSEC (0.22%; nilai RMSECV 0.76%; dan nilai RMSEP 1.20%. Hasil analisis PCA mampu mengklasifikasikan minyak berdasarkan jenis komponen utama minyak suling daun cengkih, minyak turpentin, dan minyak daun di pasaran (A, B, dan C), di mana minyak produk A berada dalam kuadran yang sama dengan minyak daun cengkih suling dan tiada produk minyak daun cengkih yang mempunyai ciri fizikal dan kimia yang serupa dengan minyak turpentin.

Kata kunci: pengesahan, inframerah transformasi Fourier, kromatografi gas-spektometri jisim, minyak daun cengkih, minyak terpentin

Introduction

Clove (*Syzygium aromaticum*) is a spices that has long been used in medicine and as a food preservative [1]. This plant is a natural source that contains many secondary metabolite compounds, namely phenolics such as eugenol, eugenol acetate, and gallic acid. Therefore, its leaf oil, namely clove oil, has great potential for applications in the pharmaceutical, cosmetic, food, and agricultural fields [2]. The main constituents in clove flower buds, stalks, and leaves are eugenol and β-caryophyllene [3]. Meanwhile, the essential oil content in clove leaves is 58.6% eugenol, 21.4% β-caryophyllene, 5.6% α-humulene, and 2.9% caryophyllene oxide [4].

Clove oil can be produced from flowers and stems, including leaves that have the highest economic value. The price range from various parts is not significantly different, making it a widely traded product. This makes the leaves more economically valued for their potential to be processed into oil [5].Currently, the market demand for clove is very high due to its great commercial value and benefits. However, the extraction yield is significantly low at around 1%, leading to a high cost of production. This has consequently caused the adulteration act of essential oils to reduce production costs [6]. According to Hong et al. [7], essential oil adulteration is a major problem in today's global market by mixing cheaper components of lower quality in high-value essential oils.

Detection of clove oil adulteration is carried out to ensure that the oil sold in the market meets the established quality standards. Meanwhile, a frequently used type of counterfeiting material is the addition of turpentine oil with the main component which can cause an increase in the α-pinene content. This will reduce the specific gravity and solubility value of the oil in alcohol and affect the odor [8]. Turpentine oil is widely selected as an adulterant in essential oils because it is relatively cheap, with a lighter and less polar fraction is lighter [9]. The technique that can be performed to detect the addition of counterfeiters in essential oils is authentication. This technique is conducted using GC-MS and FTIR methods, which will be analyzed with PCA (principal component analysis) and PLS (partial least square) multivariate calibration to detect counterfeiting of clove oil [10].

The technique commonly used for essential oil quality control is gas chromatography (GC) coupled with mass spectrometry (MS). This is because the detection of volatile compounds in essential oils can quickly, easily, and accurately be identified using the technique. In recent years, spectroscopic techniques with a PCA chemometrics approach have often been proposed as an alternative to chromatographic methods in detecting the adulteration of essential oils [11].

Another method commonly used is Fourier transforms infrared (FTIR) combined with multivariate calibration chemometrics PLS and PCA to detect specific functional group absorption [12]. The authentication of essential oils using the FTIR is carried out in the fingerprint area,

which is the characteristic of a compound with the spectrum and sample concentration entered in a one-step model [13]. In this study, the profile analysis of the chemical components of clove oil using GC-MS and FTIR methods was will be analyzed by multivariate calibration of PCA and PLS to authenticate clove oil products in the market.

Materials and Methods

Materials

The material used was dry clove leaves harvested in June 2022 from Green Herbal Yogyakarta Company. Fresh clove leaves were determined at the Ahmad Dahlan University Biology Laboratory by sending fresh whole samples, including leaves and stem, for accurate identification. Subsequently, the clove oil brands A, B, and C as samples were obtained from e-commerce (Shopee). Turpentine oil was obtained from PT. Syailendra Bumi Investama.

Tools

The tools used were a set of distillation tools, beakers, measuring pipettes, micropipettes, GC-MS Agilent 7890A instrument with specifications, capillary column type HP-5DB MSDB 5DB-5 (60 m x 250µm x 0.25µm), carrier gas used helium, injector temperature 250 °C with an injection volume of 0.2 µL, split ratio 1:200 with a split speed of 50 mL/minute and the initial temperature of 50 °C held for 2 minutes. The rate of increase is as follows 10 °C/minute to 99 °C, 2 °C/minute to 225 °C held for 20 minutes, and 5 °C/minute to 250 °C. The final temperature reached 250 °C. The detector used was Agilent 5975C MS with a mass range of 35-550.

The FTIR instrument used Thermo Scientific Nicolet iS10 with beam splitter using KBr and deuterated triglycine sulfate (DTGS) detector. The readings were taken at wavenumbers: 4000-650 cm^{-1}, resolution 8, and 32 scans.

Procedure: Clove leaf preparation

A 3 kg dried clove leaves obtained from Green Herbal Yogyakarta Company were dry-sorted, and the sizes were reduced by 2-3 cm.

Authentication method: Analysis using GC-MS with PCA chemometrics

Samples of clove oil, turpentine oil, and market products were put into 2 mL vials and placed sequentially in the sample container of the GC-MS device. The n-hexane solvent was also placed in a 2 mL vial in the last container. A total of 0.2 µL oil samples were automatically injected into the GC-MS using a syringe. After the injecting one sample, the syringe automatically washes and perform column cleaning. At the column cleaning stage, the GC-MS was run without inserting any sample. This process was repeated three times, and the samples were identified using MS. Subsequently, data were analyzed on GC-MS in the form of the relative area obtained from chromatogram results and m/z fragmentation of compounds.

Sample calibration and validation for FTIR with PCA and PLS chemometrics

A total of 7 concentrations was prepared for each oil in the form of distilled clove leaf oil (MC) 100%v/v, turpentine oil (MT) 100%v/v. Further concentration series (2 mL) were also prepared, namely MC:MT (90:10), (80:20), (70:30), (60:40), and (50:50) %v/v for calibration and validation. This was followed by the analysis of clove leaf oil, turpentine oil, as well as samples A, B, and C using an FTIR [12].

Data analysis: GC-MS data analysis of PCA chemometrics combination

GC-MS data in the relative area was collected by grouping the essential oil components with clove oil products on the market brands A, B, and C using PCA followed by biplot with MINITAB 20 software. This grouping was based on data diversity, which produces scree, score, loading plots, and biplot graphs [14].

FTIR data analysis of combined PLS and PCA chemometrics

The FTIR data were analyzed by multivariate calibration in MINITAB 20 program using PCA and PLS techniques for quantification. The original spectrum absorbance data, the spectrum with a preliminary process involving all absorption features, and part of the absorption data were processed according to the spectrum segmentation area. Subsequently, the

calculation of the RMSE value was obtained by squaring the subtraction of the actual value with the predicted value summed and divided by the number of data [15].

Results and Discussion

Component analysis of clove leaf oil

The analysis of clove leaf oil using the GC-MS method was applied to determine the oil component and the percentage of essential oil compound content. The method had a high sensitivity to quantitatively and qualitatively volatile compounds. Furthermore, it was a fast and accurate method for separating complex mixtures and producing data on the structure as well as the identity of organic compounds. In GC-MS, the AUC produced by the chromatogram was directly proportional to the concentration of the components contained in the sample. The number of essential oil components and their percentage levels were obtained from analysis with GC. This was followed by using MS to determine the type of compounds contained in clove leaf oil using spectra derived from NIST and WILEY libraries. Meanwhile, the chromatogram of GC separation results of clove leaf essential oil is presented in Figure 1.

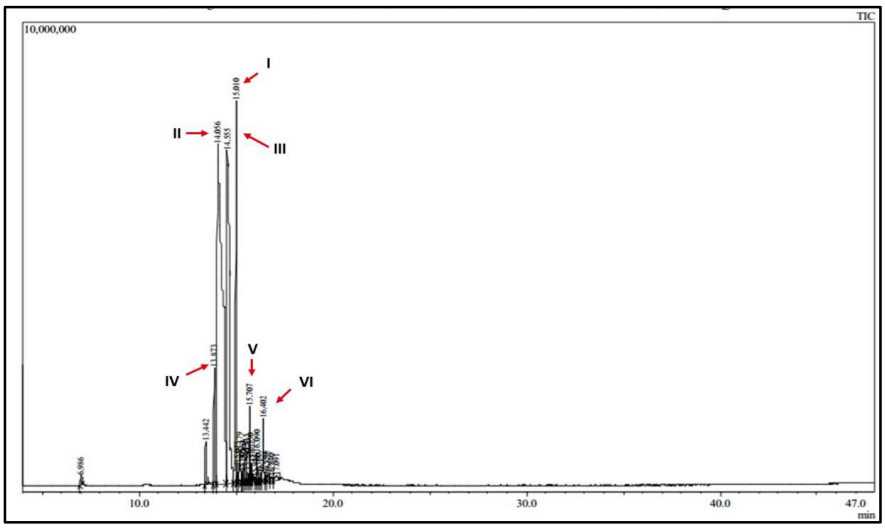

Figure 1. GC Chromatogram for clove leaf oil

Based on the chromatogram results of clove leaf oil in Figure 1, 25 chromatogram peaks were obtained, which showed the profile of the oil components. Subsequently, 6 main peaks were selected, each of which was estimated to contain eugenol (3-Allyl-6-methoxyphenol), trans-caryophyllene, α-humulene, α-copaene, δ-cadinene, and caryophyllene oxide. The component analysis of clove leaf essential oil was also replicated 3 times, and the results are presented in Table 1.

The results of the analysis using GC-MS method presented in Table 2 obtained the constituent components percentage of clove leaf oil, including eugenol (3-Allyl-6-methoxyphenol) (49.63±0.20) > trans-caryophyllene (28.25±0.22) > α-humulene (8.92±0.09) > α-copaene (2.15±0.04) > δ-cadinene (1.61±0.27) > caryophyllene oxide (1.50±0.05). There were also varying CV (Coefficient of Variation) values, with the smallest value of 0.40 in the eugenol compound. Meanwhile, the largest CV value of 16.92 was found in the δ-cadinene compound, which was caused by the large deviation between replications.

Analysis of clove leaf oil using GC-MS produced a retention time (tR) based on the separation results from GC. The mass spectra analysis was carried out using the base peak with the highest frequency in the spectrum, namely 100%, and Similarity Index (SI). Furthermore, to determine the closeness of the chemical structure of the essential oil components, the standard target was compared with the compound components in the spectra

by comparing the spectra of the NIST and WILEY 9.LIB libraries in the GC-MS software [16]. The detected compound was similar to the comparison data when the SI value approached 100% or above 90%. The analysis results in Table 2 showed that the detected clove leaf oil components had an SI value of >90%. Therefore, it can be concluded that the components of clove leaves were appropriate to the comparator spectra.

Table 1. The analysis results on the essential oil components of clove leave with GC-MS

No.	tR (minutes)	% Area	% Area±SD	CV (%)	SI	BM	Compound
I	14.056	49.49	49.63±0.20	0.40	97	164	eugenol
	14.058	49.54					
	14.080	49.86					
II	14.555	28.08	28.25±0.22	0.78	97	204	trans-caryophyllene
	14.555	28.17					
	14.556	28.50					
III	15.011	9.01	8.92±0.09	1.01	97	204	α-humulene
	15.011	8.91					
	15.011	8.83					
IV	13.873	2.19	2.15±0.04	1.68	95	204	α-copaene
	13.874	2.14					
	13.872	2.12					
V	15.707	1.30	1.61±0.27	16.92	95	204	δ-cadinene
	15.706	1.80					
	15.706	1.74					
VI	16.402	1.55	1.50±0.05	3.00	96	220	caryophyllene oxide
	16.404	1.50					
	16.403	1.46					

Note: SI = Similarity Index, MW = Molecular Weight

Table 2. The analysis results on the main components of clove leaf oil, turpentine oil, product A, B, and C

Oil Components	Percentage(%)				
	Clove Leaf Oil	Product A	Product B	Product C	Turpentine Oil
Eugenol	49.63±0.20	49.81±2.79	21.92±0.20	28.32±0.12	N/A
β-caryophyllene	28.5±0.12	32.49±0.14	19.97±0.12	12.83±0.02	N/A
α-humulene	8.92±0.09	10.43±0.03	10.03±0.05	3.13±0.45	N/A
α-copaene	2.16±0.04	1.58±0.03	1.71±0.07	0.57±0.01	N/A
δ-cadinene	1.61±0.27	0.53±0.02	3.30±0.02	1.21±0.26	N/A
Caryophyllene oxide	1.50±0.05	2.16±0.03	3.89±0.03	1.31±0.08	N/A
α-pinene	N/A	N/A	0.53±0.06	7.32±0.06	55.30±0.61
δ-carene	N/A	N/A	N/A	23.19±2.47	19.49±0.22
β-pinene	N/A	N/A	0.33±0.13	1.79±0.12	3.56±0.06
Camphene	N/A	N/A	N/A	N/A	2.533±0.17

Description; N/A= Not detected

Component profiles comparison of clove leaf oil, turpentine oil, and other clove leaf oil products in the market (A, B, and C)

This study used three types of clove leaf oil products from e-commerce (online shops) because the manufacturers were more varied. The selection of clove leaf oil products was based on predetermined criteria, namely clove leaf oil that was 100% pure from leaves and without mixture, within a price range of IDR 20,000-35,000, purchased by at least 100 buyers, and having a good store rating.

One type of clove leaf oil product had a certificate of analysis (CoA), namely product A. The CoA will show that the product has good quality and meets predetermined quality standards. This guaranteed the purity of the product and ensured no adulterants such as turpentine oil was contained. Meanwhile, products B and C do not have CoA and were suspected of adding adulterated oil because the price was very cheap with a large enough volume.

In this study, adulterated turpentine oil was obtained from Ddistillers (Syailendra Bumi Investama Company). a Central Java which has a CoA. Generally, turpentine oil is usually used as an adulterated oil because the price is relatively cheap, with a lighter and less polar fraction. However, the addition of turpentine oil can cause changes in the physicochemical properties of clove leaf oil, such as refractive index and specific gravity. This can also reduce the number of chemical components in the oil, thereby influencing the aroma of the oil. No derivatization was carried out in the analysis stage using GC-MS because the sample was a volatile compound.

Table 3. Functional group prediction results and vibration model of clove leaf oil and turpentine oil

Tape	Wavenumber (cm^{-1})			Functional Groups	Vibration Models	Intensity
	Clove Oil	Turpentine Oil	Reference [17, 18]			
1	3522	-	3000-3600	O-H (alcohol, acid, H bonding)	Hold out	Medium
2	2925	2953	3000-2840	C-H	Hold out	Strong
3	1637	1640	1667	C=C (para aromatic)	Buckling	Weak
4	1511	-	1600 and 1475; 1511 (eugenol acetate)	C=C (aromatic)	Hold out	Medium
5	1461	1462	1469	Methylene ($-CH_2-$)	Buckling	Medium
6	1451	1449	1446	Methyl ($-CH_3$)	Buckling	Medium
7	1265, 1231, 1204, 1181, 1147, and 1121	-	1300-1000	C-O (ether)	Hold out	Strong

The results presented in Table 3 showed that the largest component of clove leaf oil was eugenol. In the distilled clove leaf oil, eugenol was 49.63±0.20 > Product A (49.81±2.79) > Product C (28.32±0.12) > Product B

(21.92±0.20). Meanwhile, in the β-Caryophyllene compound, the content was Product A (32.48±0.14) > clove leaf oil (28.253±0.22) > Product B (19.97±0.12) > Product C (12.83±0.02). Eugenol is a phenolic compound and the largest component in clove oil, with a distinctive color and aroma in clove leaf oil, which can turn brown when in contact with air due to oxidation events. The previous study by Hasim et al. [4] related to the isolation of compound content in clove leaves showed that the eugenol component (58.6%) and β-Caryophyllene (21.4%) were obtained. Meanwhile, according to the Indonesian National Standard 06-2387-2006, the requirement for eugenol content in clove leaf oil is at least 78%, and β-Caryophyllene is a maximum of 17%. The concentration of eugenol and β-Caryophyllene levels can be different due to several factors, namely variations between seasons, soil conditions, growing areas, cultivation and harvesting processes of clove leaves, as well as distillation processes [19]. The component analysis of clove leaf oil, turpentine oil, as well as products A, B, and C, are shown in Table 2.

The alpha-pinene compound was turpentine oil's largest component (55.30±0.61), detected in products B and C with values of 0.53±0.06 and 7.32±0.06, respectively. The result of the component analysis in product B detected beta-pinene compound of 0.33±0.13, while C found delta-carene 23.19±2.47 and beta-pinene 1.793±0.12. Meanwhile, products B and C may contain adulterants, namely turpentine oil. Bhuiyan [20] analyzed compound components in clove leaf oil *Syzygium caryophyllatum* (L.) Alston species by GC-MS method and detected alpha-pinene compounds of 0.33% and beta-pinene of 0.45%. According to Oboh et al. [21], in a study related to the components in clove oil, the GC-MS method found alpha-pinene compounds and beta-pinene with values of 13.09% and 45.44% in *Eugenia aromatica Kuntze* species.

PCA of clove leaf oil with turpentine oil and market products

The PCA analysis was carried out by entering the AUC of pure clove oil components, the AUC of turpentine oil, pure clove leaf oil, as well as the AUC of products A, B, and C. This process was replicated three times to determine whether there were affecting factors. The location of the quadrants showed the similarity between the physicochemical properties of the constituent components of clove leaf oil.

PCA analysis was conducted using MINITAB 20 software, the latest version of MINITAB. The result of the analysis was a principal component (PC) that represented a large amount of variation in the initial data, where PC1 contained the most variance. The output of the PCA analysis of the component profiles of clove leaf oil, turpentine oil, as well as products A, B, and C are shown in Figure 2.

PCA analysis showed that each PC produced eigenvalue, proportion, and cumulative. The eigenvalue describes the variation explained by the data for each PC and the magnitude of the how much the variables on the formation of the matrix properties [22]. Proportion described the data variation for each influential PC with the number of original data variables. Meanwhile, the cumulative value describes the cumulative amount of proportion.

Figure 2 shows that the 16 PC generated corresponded to the number of variable data entered. The analysis results indicated that PCA can reduce the initial data with 16 PC variables and explained by 2 new variables (PC1 and PC2) to provide data information by 97%. This is revealed from the eigenvalue >1, close to zero, without effect, and was not correlated [23, 24]. Meanwhile, the score plot of the chemical components of clove oil, turpentine oil, and product oil is shown in Figure 3.

The score plot in PCA described a plot of two PC that provided information regarding the patterns present in the sample. The plot of the initial PC usually had the most variation in the data. The score plot displayed in this study was divided into 4 quadrants, where the plots of turpentine oil and products B and C oil were in different quadrants. Meanwhile, clove leaf oil and product A were in the same quadrant. This indicated that the closer the distance between plots, the closer the relationship among the samples analyzed [25].

Based on Figure 2, the main component of turpentine oil was in a different quadrant, located separately from the other oils analyzed. The product oil showed that the main components are not similar to the adulterated sample's. Meanwhile, product A and clove leaf oil are in the same quadrant, indicating that both samples had similar physical and chemical properties. Products B and C were in different quadrants from clove leaf oil but not with turpentine oil due to the presence of impurities or other oil mixtures. The results showed that the PCA chemometric method can be used to analyze or classify clove leaf oil with adulterants and products in the market.

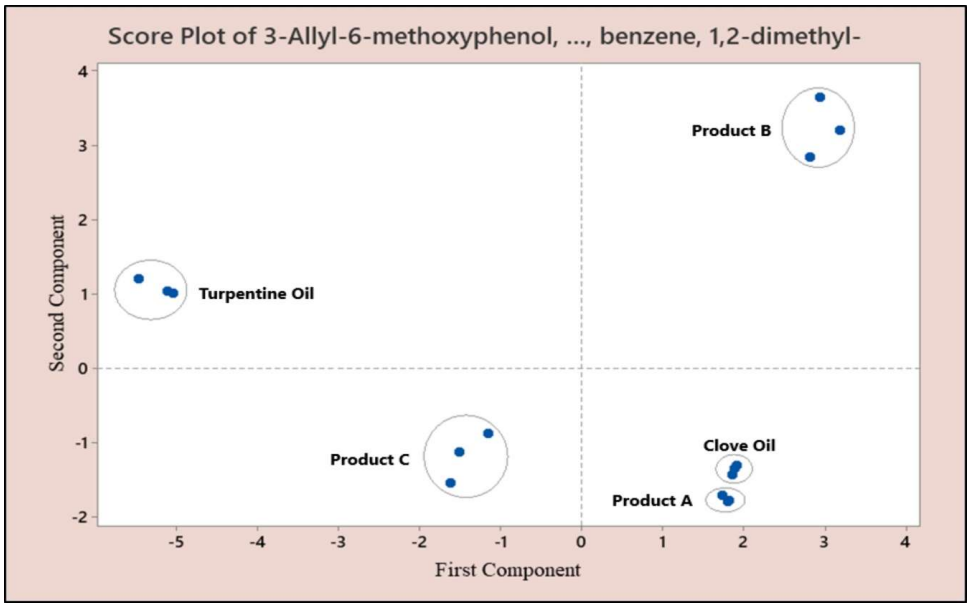

Figure 2. PCA plot scores from GC-MS of clove leaf oil, turpentine oil, product A, product B, and product C

Profile analysis of clove leaf essential oil by FTIR spectroscopy

The stages of analyzing the essential oil profile of clove leaves with the FTIR spectroscopy method were conducted using the functional groups. This was followed by the quantitative analysis with PLS and PCA.

Analysis of clove leaf essential oil by FTIR spectroscopy

FTIR spectroscopy is a widely used technique for essential oil authentication. This is because FTIR spectrophotometry can measure vibrations of functional groups as a consequence of electromagnetic radiation with the sample to produce a spectrum with fingerprinting properties [26]. Essential oils are volatile compounds consisting of a complex system of homogeneous mixtures of various compounds, and each species contains more than 100 constituents. Furthermore, essential oil fingerprint analysis can be used to distinguish species and chemotypes (common components) of different plants, representing a qualitative approach to the authentication and quality evaluation of essential oils [27, 28].

FTIR spectra can be distinguished from other compounds or samples based on wavenumber position, intensity, and the number of peaks [28]. The spectral analysis results of clove leaf oil and turpentine oil at wavenumbers between 4000 and 400 cm^{-1} are shown in Figure 3. The axis (x) is the wavenumber indicating the functional group, and the axis (y) is the absorption intensity [29]. The spectra analysis results showed that the infrared absorption peaks of both samples were at various wavenumbers. Further, Table 3 presented the predicted functional groups and vibrational models of clove leaf oil and turpentine oil.

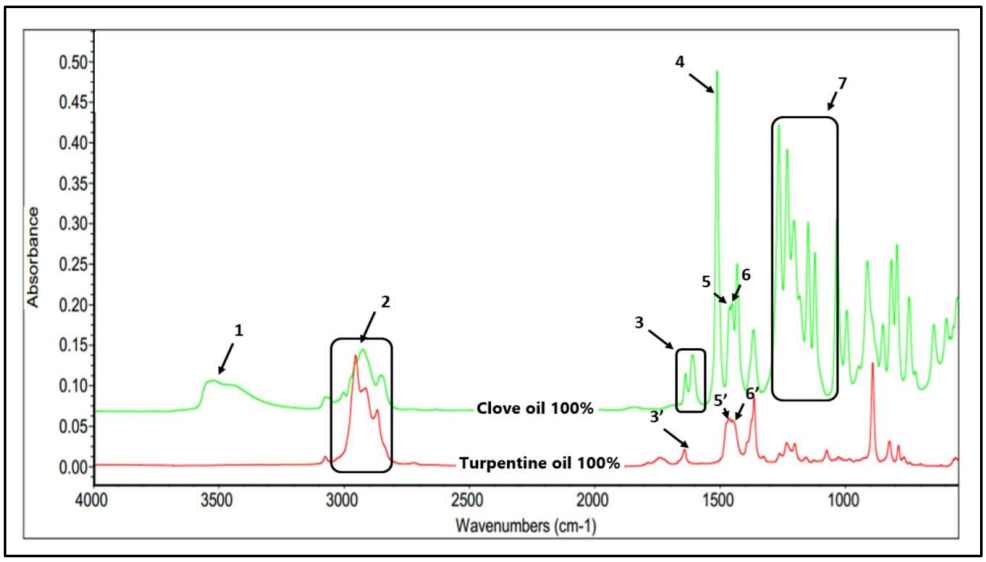

Figure 3. FTIR spectra of clove leaf oil and turpentine oil at wavenumbers 4000-600 cm^{-1}

The analysis results of the clove leaf oil functional groups in Table 3 showed a peak at wavenumber 3522 cm^{-1}, which was the O-H Phenol group with stretching vibrations. O-H groups typically at wavenumbers 3600-3000 cm^{-1}, as stated by Yang et al. [30] related to the analysis of eugenol compounds using FTIR instruments at wavenumbers obtained 3417 cm^{-1} with stretching vibrations. At wavenumber 2925 cm^{-1}, there was a C-H alkane functional group with stretching vibrations. Meanwhile, in turpentine oil at wavenumber 2953 cm^{-1}, the C-H alkane group will appear at 3000-2850 cm^{-1} [17]. At wavenumber 1511 cm^{-1}, an aromatic C=C functional group with the usual stretching vibrations. This indicated the presence of aromatic groups such as benzene in eugenol compounds, which were the main components of clove oil. The absorbance results in this study are 1637 cm^{-1} for the clove oil and 1640 cm^{-1} for turpentine oil, which is the C=C stretching vibration of the aromatic group [17]. Eugenol showed distinctive sharp peaks between 1640-1500 cm^{-1} of C=C aromatic because the functional groups of eugenols included double bonds. Therefore, these wavenumbers can provide unique spectral information with significant contributions to substance identification [31, 32, 33]. The FTIR spectra of clove oil and turpentine oil are shown in Figure 3.

In turpentine oil, the wavenumber 1640 cm^{-1} appeared, indicating the C=C alkene functional group with stretching vibrations, which showed the alkene group in the -pinene compound [34]. At 1461 cm^{-1} in clove oil and 1462 cm^{-1} in turpentine oil, there was a functional group (-CH_2-) with bending vibrations that usually appeared around the wavenumber 1465 cm^{-1} [17]. Furthermore, at wavenumbers 1451 cm^{-1} from clove, as well as 1449 cm^{-1} and 1363 cm^{-1} from turpentine oil, there was a bending vibration of the methyl group (-CH_3) [17]. The wavenumber of 1363 cm^{-1} in turpentine oil can indicate that α-pinena contains a gem-dimethyl group (C-(CH_3)$_2$) [34]. In clove leaf oil, wavenumbers 1265, 1231, 1204, 1181, 1147, and 1121 cm^{-1} contain C-O ether groups with stretching vibrations, which often appear at 1300-1000 cm^{-1} [17]. This wavenumber also indicated the presence of an ether group in the eugenol compound, such as C-O ether that appears at 1098 cm^{-1} [30]. The wavenumber 1300-1000 cm^{-1} not only described the C-O functional group but also explained the presence of CH_2 deformation vibrations in eugenol and eugenol acetate, besides C–C strain and C–H bending vibrations [18].

Based on the spectrum produced from clove leaf oil, the functional groups of the constituent components of clove leaf oil are eugenol and turpentine oil which contain α-pinene compounds. The wavenumber areas 1560-1480 cm^{-1}, 1814-1700 cm^{-1}, and 2954-2780 cm^{-1}

in clove leaf oil can be used in the PLS model developed for quantifying total eugenol [33]. The concentration series between clove oil and turpentine oil is presented in Figure 4. The peaks showed a variation in peak intensity in the difference in the concentration of clove oil and turpentine oil. Meanwhile, the variation in peak intensity during FTIR analysis indicates an effect that occurs when mixing clove leaf oil and turpentine oil.

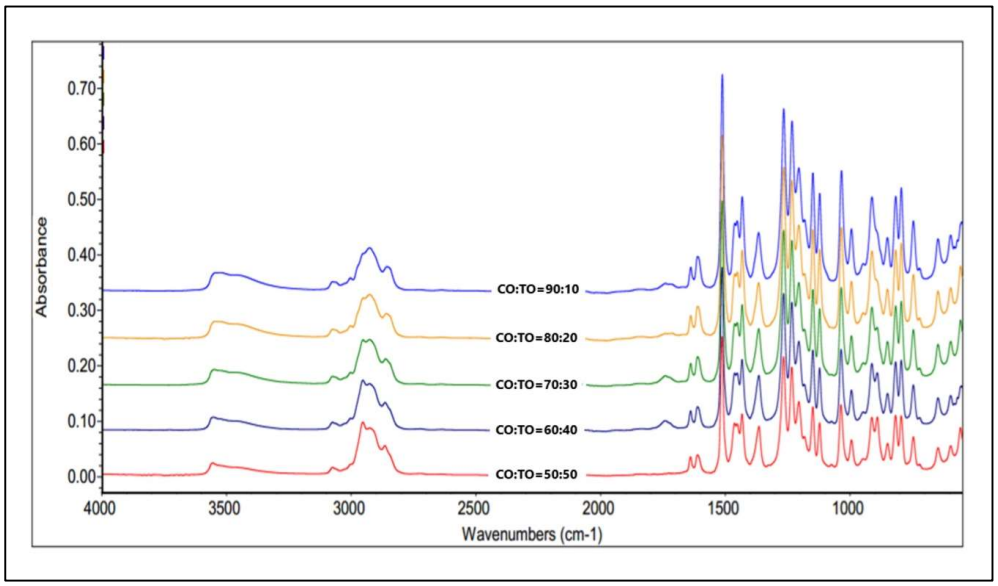

Figure 4. FTIR spectra of concentration series on clove leaf oil and turpentine oil at wavenumbers 4000-600 cm^{-1}

The absorbance results at each concentration ratio were used in the PLS and PCA chemometrics analysis. The FTIR spectra of clove leaf oil products A, B, and C circulating in the market are presented in Figure 5. Oil products were directly analyzed in the form of absorbance data using FTIR at wavenumbers 4000-400 cm^{-1}. The peak number of clove oil waves on the market is similar to that of the refined clove oil. However, there were differences in peaks indicating the OH functional group, namely products B and C, as shown in Table 4.

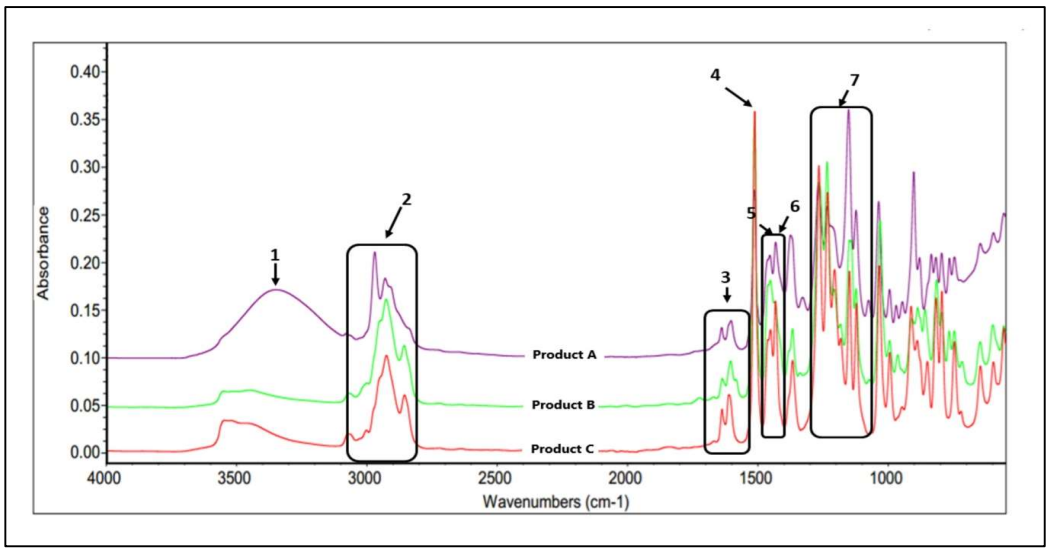

Figure 5. FTIR spectra of clove oil products in the market at wavenumbers 4000-600 cm^{-1}

Table 4. Prediction results on functional groups and vibration models of clove leaf oil products on the market

Tape	Wavenumber (cm^{-1})				Functional Groups	Vibration Models	Intensity
	Product A	Product B	Product C	Reference [17, 18]			
1	3350	-	-	3000-3600	O-H (alcohol, acid, H bonding)	hold out	Medium
2	2969	2925	2924	3000-2840	C-H	Hold out	Strong
3	1638	1636	1637	1667	C=C (para aromatic)	buckling	Weak
4	1513	1511	1511	1600 dan 1475; 1511 (eugenol acetate)	C=C (aromatic)	Hold out	Medium
5	1453	1451	1451	1469	Methylene ($-CH_2-$)	Buckling	Medium
6	1431	1433	1431	1446	Methyl ($-CH_3$)	Buckling	Medium
7	1267, 1233, 1151, 1122, and 1036	1264, 1233, 1182, 1248, 1141, and 1122	1265, 1232, 1205, 1148, 1121, and 1034	1300-1000	C-O (ether)	Hold out	Strong

Quantitative analysis with PLS

PLS regression is an analytical method that uses a linear combination of the predictor variables, not the original ones. In PLS, variables that show a high correlation with the response variable are given extra treatment because they will be more effective in the prediction process. In this method, a linear combination of predictor variables that were highly correlated with the response variable was selected to explain the existing variation. It was expected that only a few linear combinations of the predictor variables are needed to describe the majority of the variation [22].

PLS regression can be formed from a component that describes the correlation between x and y variables. Each component in the PLS regression was obtained by maximizing the covariance between the y variable and every possible linear function of the x variable. In an FTIR spectroscopy analysis, PLS is often used to extract information from complex spectra with overlapping peaks, impurities, and noise from FTIR spectroscopy instruments [35].

Before performing a PLS analysis, the first step was determining the wavenumber to be used for modelling calibration and validation by optimizing it. The wavenumber to be selected for optimization contains functional groups or fingerprint regions to determine the performance of the calibration model. It was also evaluated to provide a good correlation between the actual values of clove leaf oil, products A, B, and C oil, and turpentine oil to the predicted value using FTIR spectroscopy, expressed by the high coefficient of determination (R^2) close to 1. The R^2 value can be used to validate the accuracy parameter because R^2 describes the closeness of the predicted value to the actual value. Furthermore, the wavelength used during the analysis was selected based on the lowest error value in the calibration model, which was expressed by the Root Mean Standard Error of Calibration (RMSEC) [36, 29].

PLS connects two data matrices, x (actual value) and y (predicted value), with a linear multivariate model. The regression equation is used to find an expression that fits the data, where the linear regression equation model y=bx+a, y describes levels predicted with an FTIR spectrophotometer. The value of b is the slope of the straight line, x is the actual sample content, and a is the straight line intercept of the y-axis [37]. The optimization of wavenumber in clove oil is presented in Table 5.

Table 5. Wavenumber optimization for PLS multivariate calibration shows the relationship between the actual value (x-axis) and the predicted value (y-axis)

Wavenumber (cm^{-1})	Coefficient of Determination (R^2)	Regression Equation	RMSEC (%)
900-800	0.9991	y=0.9991x+0.0680	0.57
1300-1100	0.9908	y=0.9908x+0.7185	1.87
1400-1320	0.9955	y=0.9955x+0.3476	1.29
2900-2800	0.9993	y=0.9993x+0.0484	0.48
2960-2860	0.9998	y=0.9998x+0.0096	0.22

Multivariate calibration with the PLS method will provide relevant and specific spectral information based on the chemical properties of the calibration model at certain wavenumbers. Therefore, the selection of wavenumbers is based on optimization results which provide a linear relationship between the actual value and the predicted FTIR value [38]. As shown in Table 5, the wavenumbers used for calibration and validation of PLS modelling are 2960-2860 cm^{-1}. The relationship curve between the actual value (x-axis) and the predicted value (y-axis) of the calibration model is shown in Figure 7a.

The next process is calibration modelling at wavenumbers 2960-2860 cm^{-1}. The results, as shown in Figure 14 obtained the regression equation y=0.9998x+0.0096 and a coefficient of determination (R^2) of 0.9998. This indicated that the independent variable (x-axis) can explain 99.98% of the dependent variable (y-axis), with an RMSEC value of 0.22%. Meanwhile, the large value of the R^2 and the small RMSEC illustrate that the accuracy and precision of the developed model are acceptable.

The prediction model that has been made is evaluated using the cross-validation method by applying the leave-one-out technique. In this technique, one piece of data is deleted, and a new model is created with the remaining data. This validation is known as internal validation, where the parameter is the Root Mean Square Error of Cross Validation (RMSECV) value. Meanwhile, the validation result is said to be good when it produces a low RMSECV value, and the R^2 is close to 1. The curve of the relationship between the actual value (x-axis) and the predicted value (y-axis) using internal validation is shown in Figure 7b. Based on this curve, R^2 is 0.9992, and the RMSECV value is 0.76%, with a regression equation of y=0.9992x+1.5617. A small RMSECV value indicates that the error is getting smaller. Hence, the model built has better capabilities.

The next step is to carry out external validation to determine whether the validation model is applied to the new sample. Evaluation can be conducted by calculating the RMSEP value and the R^2. A low RMSEP value and an R^2 value close to 1 illustrate a successful creation of a regression model. The relationship curve between the actual value (x-axis) and the predicted value (y-axis) using external validation is shown in Figure 7c.

The R^2 obtained from the above curve is 0.9945, and the RMSEP value is 1.20%, with a regression equation of y=0.9945x+0.4918. The results of the external validation relationship curve, where the RMSEP value is getting smaller and the R^2 is close to 1, indicate that the validation model created can be applied to new samples.

Accuracy is expressed from R^2, where a value close to 1 illustrates that the relationship between the actual and

the predicted values is well formed, and the precision is improving. Precision was indicated by the smaller value of RMSEC, RMSECV, and RMSEP, showing that the model error was minimal. Based on several parameters, namely calibration, internal validation, and external validation, the value of $R^{2,}$ which was close to 1, showed better results. Meanwhile, smaller RMSEC, RMSECV, and RMSEP values described greater accuracy and higher precision in both models were made.

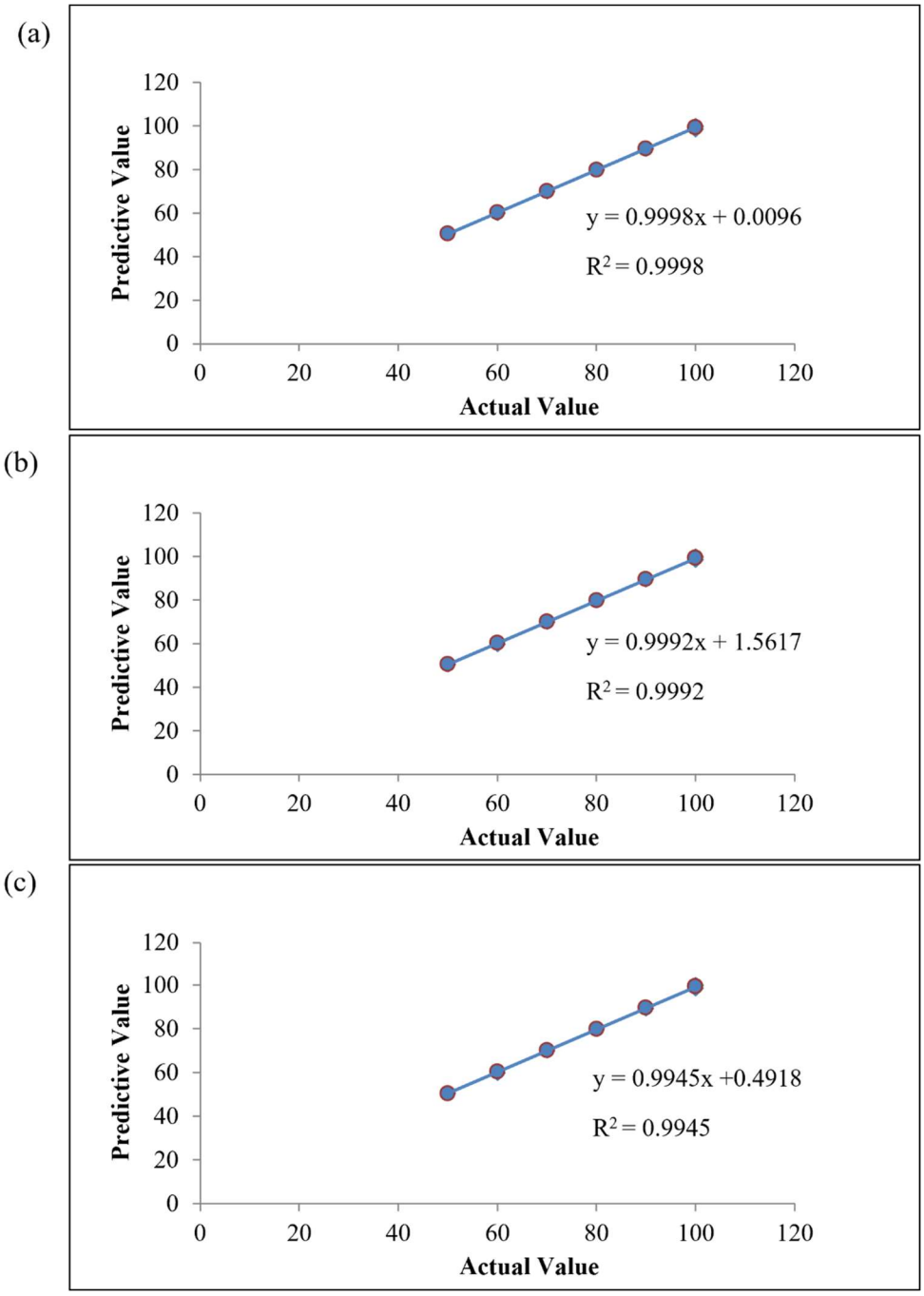

Figure 2. Relationship curves between actual values (x-axis) and predicted values (y-axis) of (a) calibration model, (b) internal validation model, and (c) external validation model at wavenumbers 2960-2860 cm^{-1}

Analysis with PCA

The FTIR spectra were analyzed using PCA, which is a data interpretation method that is performed by predicting data. This method reduces the number of variables in the matrix to generate new variables while retaining data information. The new variable is in the form of a score or main component [22]. PCA can reduce multivariate data when there is a correlation between variables. It also can be used for grouping data because samples with similar PC have similar Physicochemical properties [23].

The wavenumber that had been previously optimized was selected for PCA and used for quantitative analysis, namely 2960-2860 cm^{-1}. This wavenumber was selected for PCA modelling because of its ability to provide good separation of the samples to be evaluated, namely clove leaf oil, products A, B, and C oil, as well as turpentine oil as a forgery. The output of PCA analysis from FTIR is shown in Table 6. The results showed that analysis with PCA at wavenumbers 2960-2860 cm^{-1} reduced the initial data, namely 97 PC. This can be explained with three new variables, namely PC1, PC2, and PC3, capable of providing 100% data information. This can be seen from the eigenvalue>1, indicating that the data affect and correlate [24].

Table 6. Output PCA analysis of component profiles on the clove leaf essential oil, turpentine oil, product A, product B, and product C at wavenumbers of 2960-2860 cm^{-1}

Eigen analysis of the correction matrix											
Eigenvalue	82.235	17.151	4.552	0.054	0.008	0.001	0.000	0.000	0.000	0.000	0.000
Proportion	0.791	0.165	0.044	0.000	0.000	0.000	0.000	0.000	0.000	0.000	0.000
Cumulative	0.791	0.956	0.999	1.000	1.000	1.000	1.000	1.000	1.000	1.000	1.000
Eigenvalue	0.000	0.000	0.000	0.000	0.000	0.000	0.000	0.000	0.000	0.000	0.000
Proportion	0.000	0.000	0.000	0.000	0.000	0.000	0.000	0.000	0.000	0.000	0.000
Cumulative	1.000	1.000	1.000	1.000	1.000	1.000	1.000	1.000	1.000	1.000	1.000

A score plot comparison of clove oil and turpentine oil using PCA is shown in Figure 8a. The analysis with PCA showed that both samples are well separated, as indicated by the grouping in different quadrants, with a latent variable, namely the PCA score plot. Samples with the same PC values are similar in their physicochemical properties [39]. The grouping of pure clove leaf oil, products A, B, C, and turpentine oil was carried out. Three oil samples on the market claim to contain 100% pure clove leaf oil. The results of the PCA score plots in Figure 9b showed that 4 quadrants distinguish between clove leaf oil, turpentine oil, as well as products A, B, and C.

Based on the results of the score plot, product A oil was in the same quadrant as pure clove leaf oil. This is shown in the clove leaf oil profile analysis by GC-MS and using PCA chemometrics. These results indicated that product A had the same physical and chemical characteristics as clove leaf oil, while products B and C were in different quadrants. Based on this analysis results, PCA was successfully used to classify clove leaf oil, products A, B, and C, as well as turpentine oil. Meanwhile, future investigation regarding the main components in products A and B required further analysis such as using PCR.

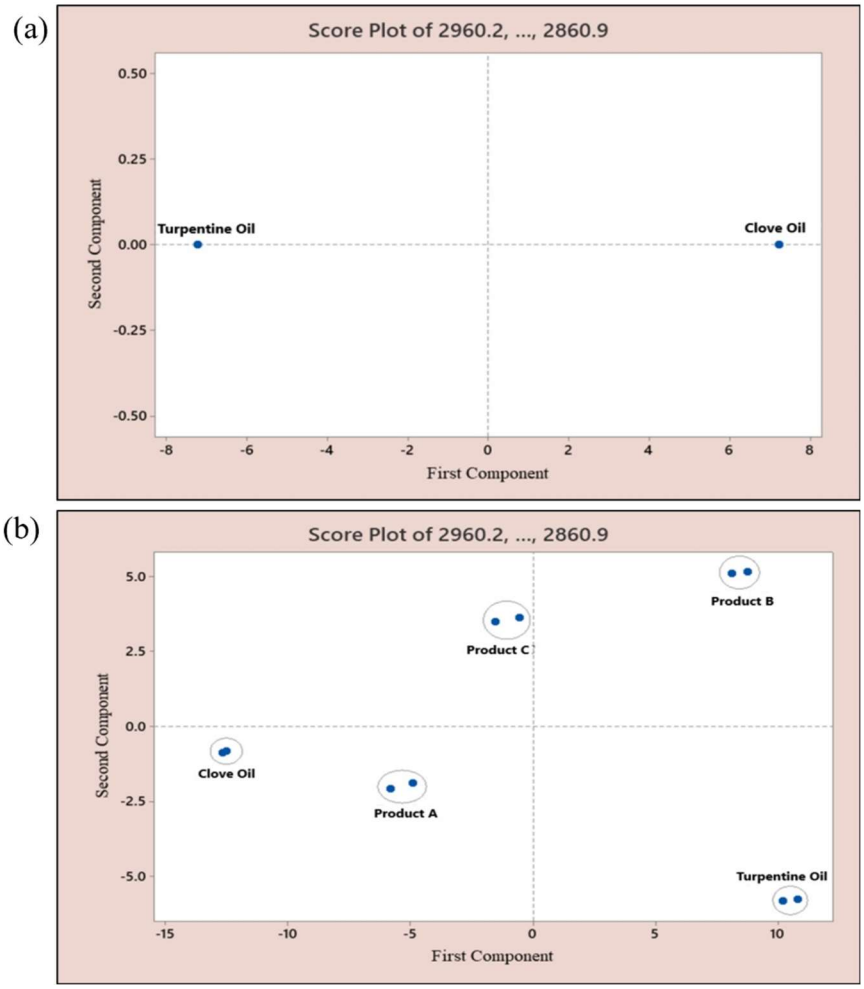

Figure 8. PCA Score Plot of FTIR (a) clove leaf oil and turpentine oil (b) clove leaf oil, turpentine oil and products A, B, C

Conclusion

The chemical components in the clove leaf oil were eugenol (3-Allyl-6-methoxyphenol), trans-Caryophyllene, alpha-Humulene, alpha-Copaene, delta-Cadinene, and Caryophyllene oxide. The results of grouping clove leaf oil using PCA based on the type of oil component showed that product A and distillate clove leaf oil were in the same quadrant. Therefore, both samples had similar physical and chemical properties. Clove leaf oil profile analysis using FTIR at wavenumbers 2960-2860 cm^{-1} with combined PLS yielded method validity results as indicated by R^2, RMSEC, RMSECV, and RMSEP values of 0.9998, 0.22%, 0.76%, and 1.20%, respectively. The results of PCA multivariate analysis showed that PCA can classify leaf oil, turpentine oil, and products A, B, and C. The authentication of oil products in the market, namely A, B, and C shows that no clove leaf oil products contain adulterated turpentine oil.

Acknowledgment

The authors are grateful for the funding provided by the Ahmad Dahlan University Study and Community Service Institute (LPPM) through a basic research study led by Prof. Dr. apt. Any Guntarti, M.Sc. Contract number: PD-101/SP3/LPPM-UAD/VII/2022.

References

1. Cortés-Rojas, D. F., de Souza, C. R. F. and Oliveira, W. P. (2014). Clove (Syzygium aromaticum): A

precious spice. *Asian Pacific Journal of Tropical Biomedicine*, 4(2): 90–96.

2. Neveu, V., Perez-Jiménez, J., Vos, F., Crespy, V., du Chaffaut, L., Mennen, L., Knox, C., Eisner, R., Cruz, J., Wishart, D. and Scalbert, A. (2010). Phenol-Explorer: an online comprehensive database on polyphenol contents in foods. *Database: The Journal of Biological Databases and Curation*, 2010: 1-9.
3. Gaylor, R., Michel, J., Thierry, D., Panja, R., Fanja, F. and Pascal, D. (2014). Bud, leaf and stem essential oil composition of Syzygium aromaticum from Madagascar, Indonesia and Zanzibar. *International Journal of Basic and Applied Sciences*, 3(3): 2473.
4. Hasim, F., Batubara, I. and Suparto, I. H. (2016). The potency of clove (Syzygium aromaticum) essential oil as slimming aromatherapy by in vivo assay. *International Journal of Pharma and Bio Sciences*, 7(1): 110-116.
5. Lutony, T. L. and Rahmayati, Y. (2002). Produksi dan perdagangan minyak atsiri. Penebar Swadaya, Jakarta.
6. Marincaş, O. and Feher, I. (2018). A new cost-effective approach for lavender essential oils quality assessment. *Industrial Crops and Products*, 125(9): 241-247.
7. Hong, E., Lee, S. Y., Jeong, J. Y., Park, J. M., Kim, B. H., Kwon, K. and Chun, H. S. (2017). Modern analytical methods for the detection of food fraud and adulteration by food category. *Journal of the Science of Food and Agriculture*, 97(12): 3877-3896.
8. Ma'mun. (2015). Identifikasi pemalsuan minyak nilam di Rantai Tataniaga. *Buletin Penelitian Tanaman Rempah dan Obat*, 14(2): 17-22.
9. Kurniawan, E., Sari, N. and Sulhatun, S. (2020). Ekstraksi sereh wangi menjadi minyak atsiri. *Jurnal Teknologi Kimia Unimal*, 9(2): 43.
10. Rohman, A. (2017). Physico-chemical properties, biological activities and authentication of cod liver oil. *Journal of Food and Pharmaceutical Sciences*, 5: 1-7.
11. Do, T. K. T., Hadji-Minaglou, F., Antoniotti, S. and Fernandez, X. (2015). Authenticity of essential oils. *TrAC - Trends in Analytical Chemistry*, 66(December): 146-157.
12. Rohman, A., Windarsih, A., Riyanto, S., Sudjadi, Shuhel Ahmad, S. A., Rosman, A. S. and Yusoff, F. M. (2016). Fourier transform infrared spectroscopy combined with multivariate calibrations for the authentication of avocado oil. *International Journal of Food Properties*, 19(3): 680-687.
13. Jaswir, I., Mirghani, M. E. S., Hassan, T. H. and Said, M. Z. M. (2003). Determination of lard in mixture of body fats of mutton and cow by fourier transform infrared spectroscopy. *Journal of Oleo Sciences*, 52(12): 633-638.
14. De Silva, C. C., Beckman, S. P., Liu, S. and Bowler, N. (2019). Principal component analysis (PCA) as a statistical tool for identifying key indicators of nuclear power plant cable insulation degradation. *Minerals, Metals and Materials Series*, 1227-1239.
15. Gontijo, L. C., Guimarães, E., Mitsutake, H., De Santana, F. B., Santos, D. Q. and Neto, W. B. (2014). Development and validation of PLS models for quantification of biodiesels content from waste frying oil in diesel by HATR-MIR. *Revista Virtual de Quimica*, 6(5): 1517-1528.
16. Guntarti, A., Rohman, A., Martono, S. and Yuswanto, D. A. (2016). Autentikasi lemak celeng dengan kromatografi gasspektroskopi gas-spektroskopi kemometrika pca (principle component analysis). *Prosiding Rakernas dan Pertemuan Ilmiah Tahunan Ikatan Apoteker Indonesia* 2016: 2541-474.
17. Pavia, D. L., Lampman, G. M., Kriz, G. S. and Vyvyan, J. R. (2010). *Introduction to Spectroscopy*. Brooks/Cole Cengage Learning, USA.
18. Wang, L. and Sung, W. (2011). Rapid evaluation and quantitative analysis of eugenol derivatives in essential oils and cosmetic formulations on human skin using attenuated total reflectance – infrared spectroscopy, 26: 43-52.
19. Khalil, A. A., Rahman, U. U., Khan, M. R., Sahar, A., Mehmood, T. and Khan, M. (2017). Essential oil eugenol: Sources, extraction techniques and nutraceutical perspectives. *RSC Advances*, 7(52): 32669-32681.
20. Bhuiyan, M. N. I., Begum, J., Nandi, N. C. and Akter, F. (2012). Constituents of the essential oil from leaves and buds of clove (Syzigium

caryophyllatum (L.) Alston). *African Journal of Plant Science*, 4(11): 451-454.

21. Oboh, G., Akinbola, I. A., Ademosun, A. O., Sanni, D. M., Odubanjo, O. V., Olasehinde, T. A. and Oyeleye, S. I. (2015). Essential oil from clove bud (*Eugenia aromatica* Kuntze) inhibit key enzymes relevant to the management of type-2 diabetes and some pro-oxidant induced lipid peroxidation in rats pancreas in vitro. *Journal of Oleo Science*, 64(7): 775-782.
22. Miller, J. N. and Miller, J. C. (2010). *Statistics and chemometrics for analytical chemistry sixth edition*. London: Pearson Education Limited.
23. Rohman, A. (2014). *Spektroskopi inframerah dan kemometrika untuk analisis farmasi.* Pustaka pelajar, Yogyakarta.
24. Yasin, H. and Asih Maruddani, D. I. (2016). Analisis faktor-faktor yang mempengaruhi persentase penduduk miskin di jawa tengah dengan metode geographically weighted principal components analysis (GWPCA) adaptive bandwidth. *Jurnal Gaussian*, 5(3): 487-496.
25. Nugraha, I., Utami, P. I. and Rahayu, W. S. (2018). Analisis asam lemak daging anjing pada bakso sapi menggunakan gas chromatography mass spectrometry (GCMS) yang dikombinasikan dengan PCA (principal component analysis). *Indonesian Journal of Halal*, 1(2): 117-124.
26. Yuliani, F., Riyanto, S. and Rohman, A. (2018). Application of ftir spectra combined with chemometrics for analysis of candlenut oil adulteration. *International Journal of Applied Pharmaceutics*, 10(5): 54-59.
27. Agatonovic-Kustrin, S., Ristivojevic, P., Gegechkori, V., Litvinova, T. M. and Morton, D. W. (2020). Essential oil quality and purity evaluation via FT-IR spectroscopy and pattern recognition techniques. *Applied Sciences (Switzerland)*, 10(20): 1-12.
28. Rohman, A. and Che Man, Y. B. (2012). Analysis of pig derivatives for halal authentication studies. *Food Reviews International*, 28(1): 97-112.
29. Guntarti, A. and Abidin, M. A. Z. (2018). Analisis lemak anjing dalam bakpao ayam menggunakan FTIR (Fourier Transform Infrared) dikombinasi kemometrika. *Media Farmasi: Jurnal Ilmu Farmasi*, 15(1): 34.
30. Yang, Z., Chai, Y., Zhou, D., Yao, X. and Ji, H. (2020). Mechanism for efficient separation of eugenol and eugenol acetate with β-cyclodextrin as a selective solvent. *Supramolecular Chemistry*, 31(12): 767-775.
31. de Oliveira, A. de N., Lima, E. T. L., de Oliveira, D. T., Angélica, R. S., Andrade, E. H. de A., Filho, G. N. da R. and do Nascimento, L. A. S. (2019). Acetylation of eugenol over 12-molybdophosphoric acid anchored in mesoporous silicate support synthesized from flint kaolin. *Materials*, 12(18): 2995.
32. Pramod, K., Suneesh, C. V., Shanavas, S., Ansari, S. H. and Ali, J. (2015). Unveiling the compatibility of eugenol with formulation excipients by systematic drug-excipient compatibility studies. *Journal of Analytical Science and Technology*, 6: 34.
33. Tarhan, İ. (2021). A robust method for simultaneous quantification of eugenol, eugenyl acetate, and β-caryophyllene in clove essential oil by vibrational spectroscopy. *Phytochemistry*, 191:112928.
34. Wijayati, N. (2016). *Biotransformasi alfa pinena dari minyak terpentin*. Unnes Press, Semarang.
35. Rohman, A., Irnawati and Riswanto, F. D. O. (2021). *Kemometrika*. Gadjah Mada University Press, Yogyakarta.
36. Dzulfianto, A., Riswanto, F. D. O. and Rohman, A. (2017). The employment of UV-spectroscopy combined with multivariate calibration for analysis of paracetamol, propyphenazone and caffeine. *Indonesian Journal of Pharmacy*, 28(4): 191-197.
37. Bingham, N. and Fry, J. M. (2010). *Regression Linear Models in Statistics*. Springer Undergraduate Mathematics Series, London.
38. Triyasmono, L., Riyanto, S. and Rohman, A. (2013). Determination of iodine value and acid value of red fruit oil by infrared spectroscopy and multivariate calibration. *International Food Research Journal*, 20(6): 3259-3263.
39. Guntarti, A., Martono, S., Yuswanto, A. and Rohman, A. (2015). FTIR spectroscopy in combination with chemometrics for analysis of wild boar meat in meatball formulation. *Asian Journal of Biochemistry*, 10(4): 165-172.

Malaysian Journal of Analytical Sciences (MJAS)
Published by Malaysian Analytical Sciences Society

SYNTHESIS OF TIN DOPED ZINC OXIDE (TZO) NANOWIRES: EFFECT ON DYE ADSORPTION

(Synthesis Zink Oksida Nanodawai Terdop Timah: Kesan Kepada Penjerapan Pewarna)

Nur Fairuz Rostan[1,2], Mohd Firdaus Malek[1,2,*], Maryam Mohammad[1,2,3], Nurul Zulaikha Mohd Zambri[1,2], Nurfatini Atiqrah Khairul Azhar[1,2], Zahidah Othman[1,2], Kevin Alvin Eswar[1,2,4], Irmaizatussyehdany Buniyamin[1,2], Noor Asnida Asli[1,2], Mohd Yusri Abdul Rahman[5], Mohamad Hafiz Mamat[6] and Mohamad Rusop Mahmood[1,6]

[1]NANO-SciTech Lab, Centre for Functional Materials and Nanotechnology, Institute of Science, Universiti Teknologi MARA, 40450 Shah Alam, Selangor, Malaysia
[2]Faculty of Applied Sciences, Universiti Teknologi MARA, 40450 Shah Alam, Selangor, Malaysia
[3]Department of Physics, Faculty of Applied Sciences, Universiti Teknologi MARA, Perak Branch, Tapah Campus, Tapah Road, 35400 Perak, Malaysia
[4]Faculty of Applied Sciences, Universiti Teknologi MARA, Sabah Branch Tawau Campus, 91032 Tawau, Malaysia
[5]Institute of Microengineering and Nanoelectronics, Universiti Kebangsaan Malaysia, 43600, Bangi, Selangor, Malaysia
[6]NANO-ElecTronic Centre, School of Electrical Engineering, College of Engineering, Universiti Teknologi MARA, 40450 Shah Alam, Selangor, Malaysia

[*]Corresponding author: mfmalek07@uitm.edu.my

Received: 19 September 2023; Accepted: 21 April 2024; Published: 29 June 2024

Abstract

In this study, pristine zinc oxide (ZnO) and tin doped zinc oxide (TZO) nanowires (NWs) had been synthesised on a fluorine doped tin oxide glass substrate via a microwave-assisted ultrasonic irradiation technique. This is a facile and rapid technique that combined ultrasonic irradiation technique during preparation of precursor solution with microwave assisted hydrothermal technique during synthesisation of nanowires. The ultrasonic irradiation technique helps to breakdown the agglomerated and large molecules inside the precursor solution mixture into smaller molecules. The microwave assisted technique helps to increase the temperature of the precursor solution from internal to external in shorter time through the increasing of interaction between molecules. It is important to produce a wide surface area of this material in the photoanode of dye-sensitive solar cells (DSSCs) configuration. Specifically, dye adsorption was an important aspect to grasp, as it can be reflected in the performance of the DSSC device. The concentrations of tin, Sn dopant were varied between 0.3 and 1.8 at.%. As-prepared ZnO and TZO NWs were analysed using field emission scanning electron microscopy and X-ray diffraction. Then, the samples that were soaked in N719 were analysed with ultraviolet-visible-near infrared spectroscopy. The (002) peak of pristine ZnO was regressed, and the identified (100) and (101) peaks of ZnO were slightly shifted towards higher degrees after the addition of Sn dopants. The surface morphology of TZO NWs had displayed a more uniform transformation, with the smallest crystallite size at 51 ± 11 nm (0.9 at.%) due to the enhanced surface area. Unfortunately, it continued to degenerate for concentrations ranging from 1.2 to 1.8 at.%. Urbach energy analysis also suggested that the lowest defect at 0.9 at.% TZO (76 meV) produced the highest crystallinity with a less disorderly thin film. These properties had upheld the dye adsorption and trapping in the ZnO-based thin film. Thus, TZO NWs were the most promising candidates as photoanodes in DSSCs.

Keywords: crystallinity, dye adsorption, microwave, zinc oxide, tin doped

Abstrak

Dalam kajian ini, zink oksida tulen dan zink oksida terdop timah nanodawai telah disintesis ke atas substrat kaca timah oksida terdop florin menggunakan teknik penyiaran ultrasonik bantuan mikrogelombang. Teknik mudah dan pantas ini merupakan hasil gabungan teknik penyiaran ultrasonik yang digunakan semasa proses penyediaan larutan prekursor dengan teknik hidroterma bantuan mikrogelombang yang digunakan semasa proses pensintesisan nanodawai. Teknik penyiaran ultrasonik dapat membantu penguraian molekul yang beraglomerat dan besar dalam campuran larutan prekursor menjadi molekul yang lebih kecil. Teknik bantuan mikrogelombang pula dapat meningkatkan suhu larutan prekursor dari dalaman ke luaran dalam masa yang singkat melalui peningkatan interaksi antara molekul. Penghasilan kawasan permukaan yang luas merupakan aspek yang amat penting bagi bahan fotoanod dalam konfigurasi sel suria pekaan pewarna. Secara khusus, penjerapan pewarna merupakan aspek penting kerana ia akan mencerminkan prestasi peranti sel suria pekaan pewarna. Kepekatan dopan timah telah divariasi dalam lingkungan 0.3 hingga 1.8 peratusan atom. Zink oksida tulen dan zink oksida terdop timah nanodawai yang tersedia telah dianalisis menggunakan mikroskopi elektron pengimbasan pancaran medan dan pembelauan sinar-X. Kemudian, sampel yang telah direndam dalam pewarna N719 dianalisis dengan spektroskopi ultralembayung-cahaya nampak-inframerah dekat. Puncak utama (002) pada zink oksida tulen telah susut dan puncak-puncak identiti melibatkan puncak (100), (002) dan (101) milik zink oksida telah beranjak ke arah yang tinggi setelah penambahan dopan timah. Morfologi permukaan zink oksida terdop timah nanodawai memperlihatkan perubahan ke arah keseragaman dengan saiz kristal paling kecil pada 51 ± 11 nm (0.9 peratusan atom) disebabkan kawasan permukaan dipertingkat, namun terus merosot pada julat kepekatan 1.2 – 1.8 peratusan atom. Analisis tenaga Urbach juga mencadangkan terdapat kecacatan terendah pada 0.9 peratusan atom zink oksida terdop timah (76 meV) dengan menghasilkan saput tipis yang berhabluran tertinggi dan kurang ketaktertiban. Sifat-sifat tersebut telah menyumbang kepada penjerapan pewarna dan pemerangkapan dalam saput nipis berasaskan zink oksida. Oleh itu, zink oksida terdop timah nanodawai adalah calon berpotensi menjadi fotoanod dalam sel suria pekaan pewarna.

Kata kunci: habluran, penjerapan pewarna, gelombang mikro, zink oksida, terdop timah

Introduction

Dye-sensitized solar cell (DSSC) is an emerging third-generation technology in the photovoltaic field. This alternative may provide cleaner and replenishable energy sources for future generations by reducing carbon footprints. The basic structure of DSSC consists of a substrate with a conductive layer, a photoanode, a dye, an electrolyte, and a cathode. Photoaode and cathode are also known as working electrodes and counter electrodes, respectively. According to Green et al.'s 61st version of the solar cell efficiency table, Ecole Polytechnique Fédérale de Lausanne (EPFL) recorded the most recent DSSC efficiency at 12.25% [1]. Compared to other types of third-generation emerging solar cells, DSSCs' efficiencies progressed in small steps. We identified the photoanode layer as one of the major factors that limited the efficiency of DSSCs. The most commonly used photoanode was titanium dioxide (TiO_2). The irregular electric channels in TiO_2 trigger issues, leading to recombination that significantly impacts solar cell performance [2, 3].

The other alternative to TiO_2 was an II-VI semiconductor combination of zinc and oxide from metal and chalcogen elements that can create vast application materials. Zinc oxide (ZnO) is a benign, abundantly available, and thermally stable material. Zinc oxide nanostructure can be found in zero dimensions as nanodots [4] or nanoparticles [5], one dimensions as nanowires (NWs) [6] or nanorods [7], two dimensions as nanosheets [8] or nanoplates [9] and three dimensions as nanoflakes [10] or nanoflowers [11]. Based on previous studies, there are a few approaches to grow one-dimension (1D) ZnO nanostructures that include chemical bath deposition [12], hydrothermal [13], wet chemistry [14], solvothermal [15] and water bath [16]. However, these methods require longer reaction times, complex processes, and high-end instruments. For instance, the study conducted by Dloo et al. have found that using the hydrothermal technique required more than 2 hours to synthesis ZnO NWs [17]. Syrrokostas and his team have utilised chemical bath deposition process for 7 hours to form ZnO NWs that achieved the desired morphology [18]. Other than that, Guo et al. has managed to grow ZnO NWs within 1.5 hours using microwave assisted hydrothermal process [19]. However, the synthesisation process was utilising modified commercial oven that could inject the precursor solution continuously during the reaction. Thus, a rapid and straight-forward technique would be beneficial to the current technology of ZnO NWs synthesis.

The porosity of the photoanode compound directly influences dye adsorption, conductivity, and charge

transport across the DSSC [20]. A branched ZnO photoanode has the advantage of increasing dye adsorption properties by filling the space between the NW structures [21]. Previous studies have found that tin, Sn has a compatible structure as it has a lower ionic radius (Sn^{4+} ion: 0.69 Å) compared to Zn^{2+} ion with an ionic radius of 0.74 Å [22]. Therefore, at low doping concentrations, the oxide lattice remains unaffected [23]. Besides, Sn helps to improve the surface properties by increasing the surface area of ZnO thin film via the formation of smaller crystallite sizes than pure ZnO [24]. The doping of Sn must be controlled (below 2 at.%) to prevent clumping undesired truncated cone-shaped nanostructure that can affect the quality of ZnO thin film [25]. Sn also has the ability to improve electrical conductivity in a ZnO photoanode by enhancing the carrier concentration by introducing double-charge carriers [26]. This situation is favourable to boost the efficiency of DSSC [22, 23]. This study had combined the environmental-friendly ultrasonic irradiation with rapid microwave assisted technique to synthesis pristine ZnO and tin doped ZnO (TZO) NWs. These 1D TZO NWs were synthesised by varying the dopant concentrations (atomic percentage, at.%) to identify the optimum properties for DSSC photoanode applications.

Materials and Methods

The procedures are categorised based on step-by-step processes involved to synthesis and analyse the properties of pristine ZnO and TZO thin film that grown on FTO glass substrate.

TZO NWs thin film growth

The FTO glass was specified into 0.11 cm thickness and 2 × 2 cm^2 sized substrates. Then, aluminium doped ZnO seed layer had deposited on oxide-free substrate using spin coating technique [27]. Followed by that, tin doped ZnO (TZO) NWs were grown via microwave-assisted ultrasonic irradiation method was carried out. An equimolar of 12.5 mM of zinc acetate dihydrate, $Zn(CH_3COO)_2 \cdot 2H_2O$; hexamethylenetetramine, $C_6H_{12}N_4$ (HMTA) and tin (IV) chloride pentahydrate, $SnCl_4 \cdot 5H_2O$ powder were used as precursor, stabiliser and dopant, respectively. The amount of Sn dopant was varied to 0.3 – 1.8 at.%. All the reagents were dissolved in a beaker filled with 1000 mL distilled water that acted as solvent or medium for the reaction. Then, the mixture solution was stirred at 80 ºC for 40 minutes to yield clear and homogeneous solution. Next, the mixture solution was sonicated at 50 ºC for 30 minutes using an ultrasonic water bath (Hwasin Technology Powersonic 405, 40kHz) and aged for 60 minutes at room temperature. After that, the mixture solution is continued to age at room temperature with stirring at speed of 3. The solution was poured into a Schott bottle. Then, the optimized seed layer-coated glass substrates were placed at the bottom of the Schott bottle with one substrate each. Afterward, the container was placed inside the microwave oven (SHARP 25 L Microwave Oven with Grill R754AST) which was set to power of 600 W and microwaved for 60 minutes. The excess nanostructures deposited on the substrates were rinsed with distilled water thoroughly. After that, the samples were annealed (hard-baked) in a preheated furnace at 500 ºC for 60 minutes. Finally, the samples were removed from furnace for fast cooling process and proceeded with further analyses. The as-prepared pristine ZnO and TZO NWs grown on FTO were characterised with X-ray diffraction (XRD) to investigate the crystal orientations and crystallinity of the samples. The XRD model used was PANalytical X'Pert PRO with Cu K-alpha radiation wavelength of 1.5419 Å. The crystallite size was calculated based on the Scherrer formula provided in Equation 1. The k in this equation was the Scherrer constant with the value of 0.94. The λ represented the X-ray wavelength (CuK_α = 1.5419 Å), β denoted as the line broadening at full width half maximum while θ was the Bragg's angle. β and θ were both measured in radians.

$$D = \frac{k\lambda}{\beta \cos\theta} \quad (1)$$

Additionally, dislocation line density (DLD) of the thin films represented the length of dislocation lines per unit volume of the crystal which can be determined using Equation 2.

$$\delta = \frac{1}{D^2} \quad (2)$$

Furthermore, the interplanar distance or known as d-spacing can be figured out by substituting θ, n and λ

which were Bragg's angle, order of diffraction and wavelength of X-rays, respectively. The order of diffraction usually was 1 for first order. Value of d-spacing can be obtained through the Bragg's law formula in Equation 3.

$$2d \sin\theta = n\lambda \quad (3)$$

Besides that, Field Emission Scanning Electron Microscope (FESEM) to identify the morphology and particle distributions. The FESEM model utilised was Analytical High Resolution Field Emission Scanning Electron Microscope Apreo 2S (Thermo Fischer Scientific). The surface morphology images of the samples were taken at 10 kV and 60 000x magnification. Further analyses were done using ultraviolet-visible-near infrared (UV-vis-NIR) spectroscopy to analyse the defects in the samples. The UV-vis-NIR model used was Carry 5000 Varian with the fixed spectral range of 300 – 1200 nm. The data from UV-vis-NIR were analysed to obtain the Urbach energy value. The absorption coefficient was fitted to exponential function of energy. The derived formula of Urbach energy involved in this study was listed in Equation 4 and 5. The most linear gradient of plotted ln α against photon energy (hv) was enabled the gaining of Urbach energy value.

$$\alpha = \alpha_0 \, exp\left(\frac{hv}{E_u}\right) \quad (4)$$

$$\ln\alpha = \left(\frac{1}{E_u}\right) hv + \ln\alpha_0 \quad (5)$$

Dye adsorption and desorption process

Dye loading process was performed on pristine ZnO and TZO NWs thin film in order to analyse the adsorption and desorption ability of the photoanode. Dye that has been chosen as the light sensitizer in this study was a ruthenium-based dye namely Di-tetrabutylammonium cis-bis (isothiocyanato) bis (2,2′-bipyridyl-4,4′-dicarboxylato) ruthenium (II) or also known as N719. 0.5 mM of ethanolic N719 dye solution was allowed to be stirred homogenously at room temperature before ready to be used. FTO glass substrate with each type of NWs photoanode were then soaked into the prepared solution for 24 hours. The soaked sample was picked up and dried from excess dye solution. Then, dye loading process was carried out to analyse the adsorb and desorb action of photoanode thin film. Equation 1 was used to measure the dye loading in photoanode. Dye loading of photoanode thin film was determined by the multiply of dye concentration and volume of solution which then divided by the electrode area. The unit for dye loading in Equation 6 was mol/cm^2 while M denoted as dye concentration in mol/L, volume, V in unit of L and A was the electrode area in cm^2. The size of area covered with electrode was controlled at 3.6 cm^2. The dye loading value was consistent for all pristine ZnO and TZO thin films which was 0.833 μmol/cm^2. The dye loading value was smaller compared to other studies due to the large dye exposed surface area.

$$Dye\ loading = \frac{M \times V}{A} \quad (6)$$

The FTO glass/ZnO SL/pristine ZnO or TZO NWs/N719 dye configuration was illustrated as in Figure 1. Next step was the samples were washed with ethanol during unloading process to study the desorption of the photoanode. The transmittance of dye adsorbed and desorbed for all samples were plotted and discussed further in Results and Discussion section.

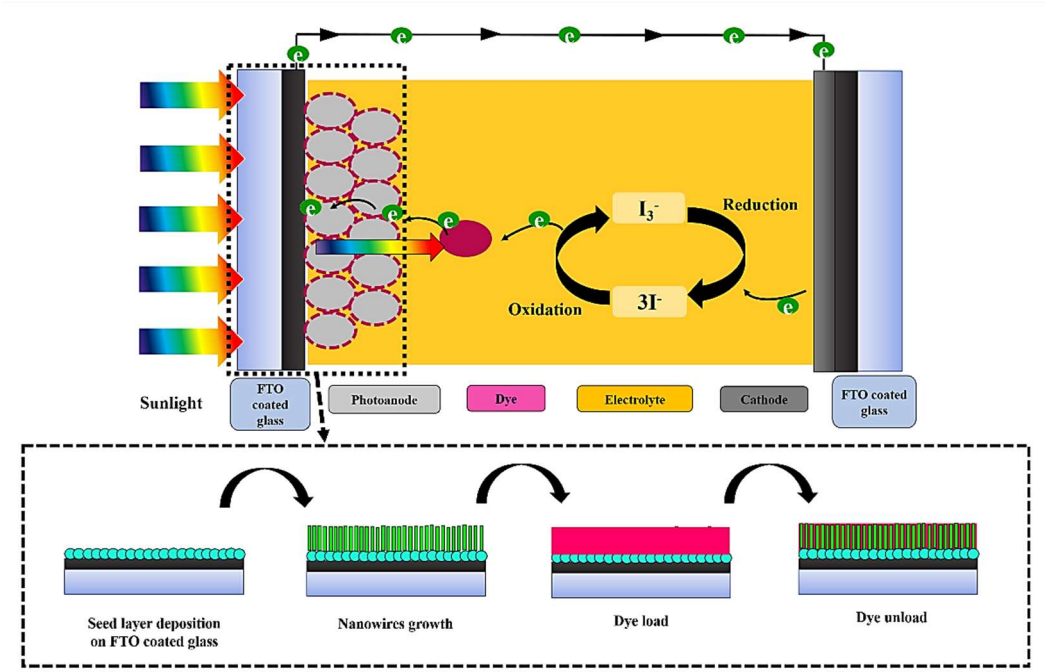

Figure 1. Stepwise processes that involved NWs photoanode formation and dye adsorb-desorb actions that build up DSSC configurations

Results and Discussion

This section presented the results and some elaboration based on physical and optical properties analysis that had been investigated on ZnO-based thin film. The analyses done were discussed in detailed based on each subtopic.

Crystal orientation and crystallinity analysis

The XRD pattern shown in Figure 2 (a) and Figure 2 (b) had indicated the hexagonal wurtzite structure with existence of peaks (100), (002), (101), (102), (110), (103) and (112) at 2θ of 32.29°, 34.96°, 38.35°, 52.11°, 57.06°, 62.17° and 66.26°. These peaks were the blueprints of pristine ZnO material according to JCPDS 00-036-1451. The small peak at 34.5° was belonged to FTO [28]. After the addition of Sn as dopants (0.3 – 1.8 at.%), the same peaks remained without any appearance of additional peak. After doped, the major peaks within the range of 30 – 40 degrees had slightly shifted to higher degree positions. Previous work on studying the effect of dopant concentration also had identified comparable tendency such as in this work [11]. This increment had suggested that there was shrinkage in d-spacing due to the consequence of compressive stress [29]. The slightly difference in atomic radii of Zn^{2+} ion with Sn^{4+} ion at 0.69 Å had shifted the 2θ crystal positions to relatively higher value [22]. The most dominant (002) peak that observable in pristine ZnO sample was suppressed and left with (101) as the most significant major peak after Sn dopant was added. This trend also can be noticed from earlier study by varying the Sn dopants in 2 – 8 wt.% [22]. The crystallite size and interplanar distance of pristine and all TZO samples had shown similar trends which indicated that both factors were closely related to each other. On the other hand, the FWHM and dislocation line density had the opposite relationship with the other two factors which mentioned before. These patterns can be seen from previous studies done by other researchers [29, 30].

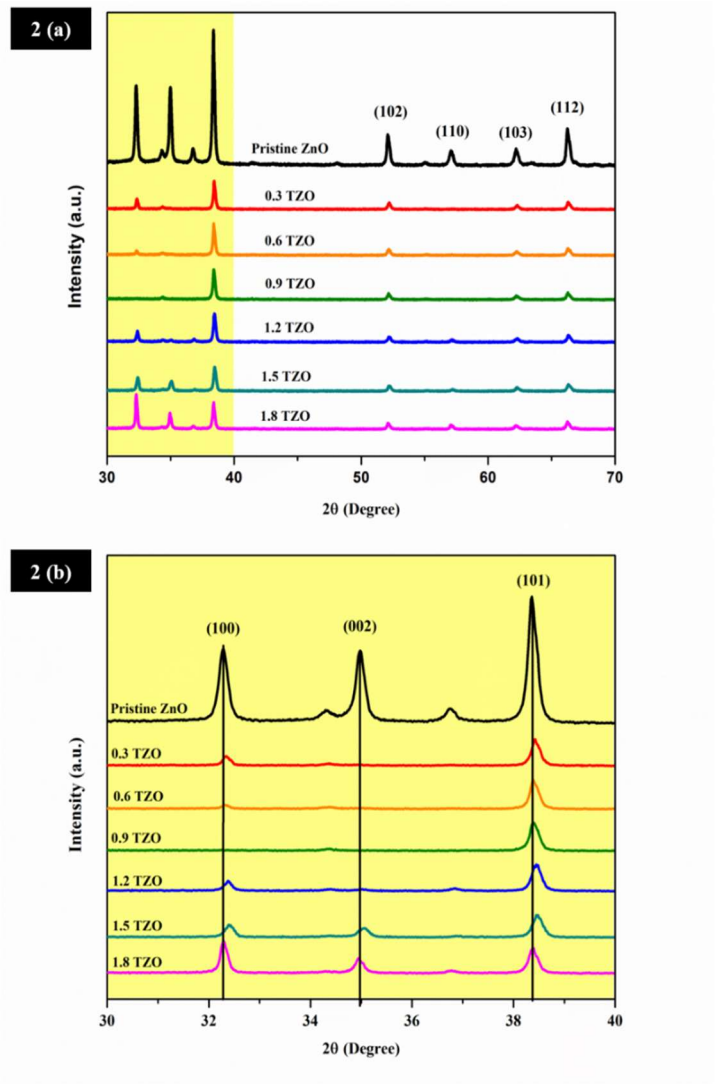

Figure 2. XRD patterns of pristine ZnO and various TZO samples within the range of (a) 30 – 70 degrees and (b) 30 – 40 degrees

Table 1. Crystallite size, dislocation line density and interplanar distance of pristine and varied TZO samples at (101) plane

Sample	FWHM (Degree)	Crystallite Size (nm)	Dislocation Line Density (E14 m^{-2})	Interplanar Distance (Å)
Pristine ZnO	0.214	41.09	5.92	2.347
0.3 TZO	0.223	39.44	6.43	2.340
0.6 TZO	0.203	43.32	5.33	2.344
0.9 TZO	0.214	41.09	5.92	2.344
1.2 TZO	0.232	37.91	6.96	2.341
1.5 TZO	0.244	36.05	7.70	2.340
1.8 TZO	0.223	39.43	6.43	2.345

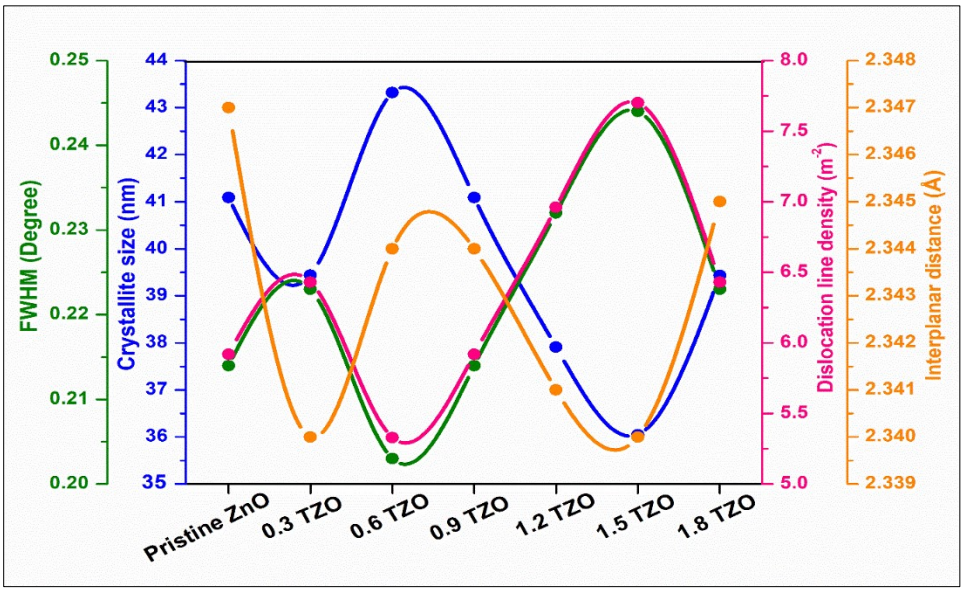

Figure 3. The crystallite size, dislocation line density and interplanar distance of pristine ZnO and varied TZO samples at (101) plane

Surface morphology and uniformity analysis

FESEM images had displayed pristine ZnO and TZO (0.3 – 1.8 at. %) NWs in Figure 4 (a – g). The particle size decreased and uniformity increased with the increment in Sn dopant concentration in ZnO to form nanowires. High in uniformity is one of the crucial aspects to produce decent morphological, optical and electrical properties. The smallest and most uniform TZO nanowire structures had displayed at 0.9 TZO (51 ± 11 nm). The introduction of Sn ions had changed the lattice of ZnO due to difference in ionic radius between Sn4+ ions (0.69 Å) and Zn^{2+} ions (0.74 Å) [22]. In contrary, after this point (1.2 at.% onwards), the nanowire structures started to show non-uniformity trend and become agglomerated and deformed. This phenomenon occurred due to Ostwald ripening effect which small crystals pick up the excess solute and amalgamate into large nanostructures [31]. This defect can be observed via FESEM surface images after excess Sn was doped (1.5 and 1.8 TZO). Previous researchers had suggested that the doping of tin must be restrained under 2 at.% to prevent clumping undesired truncated-cone shaped nanostructure which may disturb the quality of ZnO thin film [25]. Thus, this agglomerated nanostructures are expected to affect the resistivity and worsen the electrical properties of the photoanode thin film [25]. The summarised data on average particle size for all samples were tabulated in Table 2.

Defect analysis

Urbach energy indicates the degree of structural disorder, defects, and impurities in the material. High in Urbach energy translate into high defects density, more disorder and low in crystallinity. The defects can generate localised states that can traps carriers (electron and hole) and caused recombination. 0.9 TZO in Figure 5 had shown the lowest Urbach energy (76 meV) which reflected through the most uniform average particle size obtained in FESEM analysis and had achieved near lowest FWHM (0.214°) and dislocation line density (5.92 E14 m^{-2}). The Urbach energy values for all samples were tabulated in Table 3.

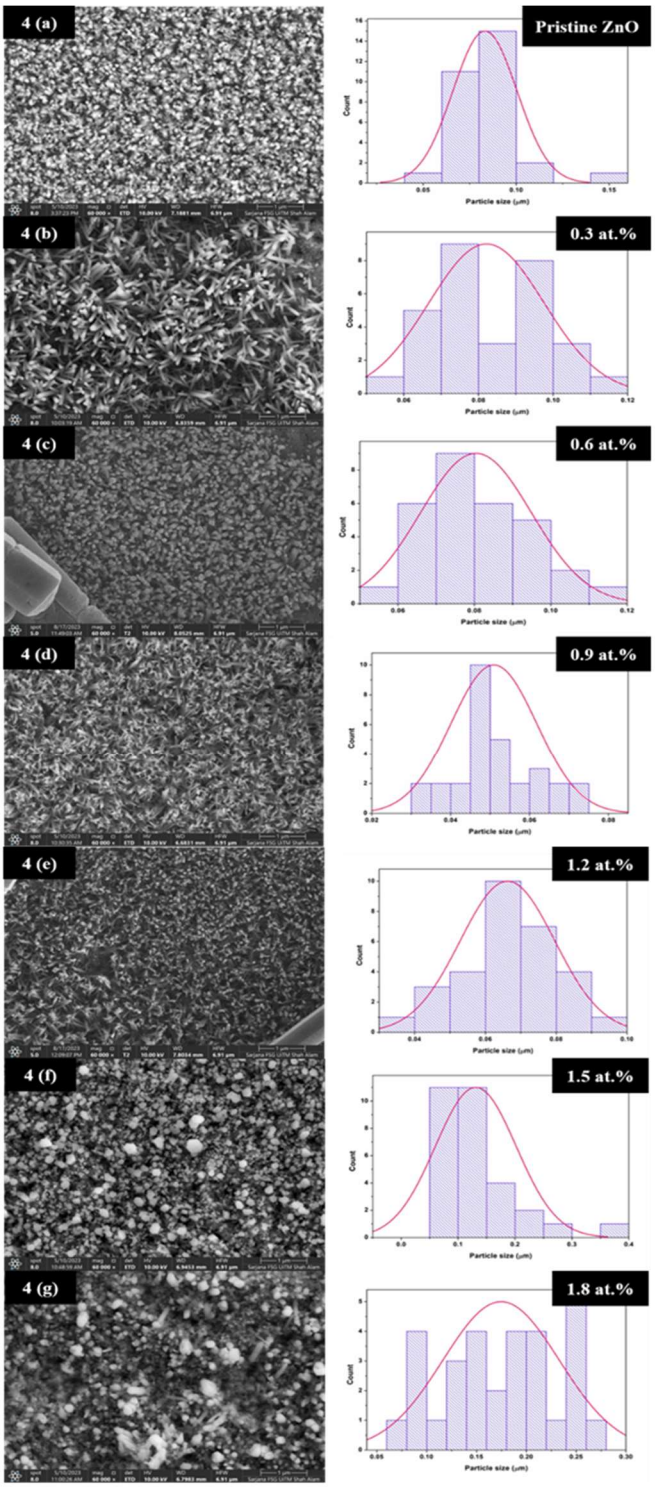

Figure 4. FESEM images and particle distributions of (a) pristine ZnO and (b – g) 0.3 – 1.8 at.% of TZO NWs

Table 2. The average particle size from particles distribution analysis in FESEM images for each sample

Label in Figure 4	Sample	Average Particle Size (nm)
(a)	Pristine ZnO	83 ± 17
(b)	0.3 TZO	82 ± 15
(c)	0.6 TZO	80 ± 14
(d)	0.9 TZO	51 ± 11
(e)	1.2 TZO	66 ± 13
(f)	1.5 TZO	131 ± 71
(g)	1.8 TZO	175 ± 58

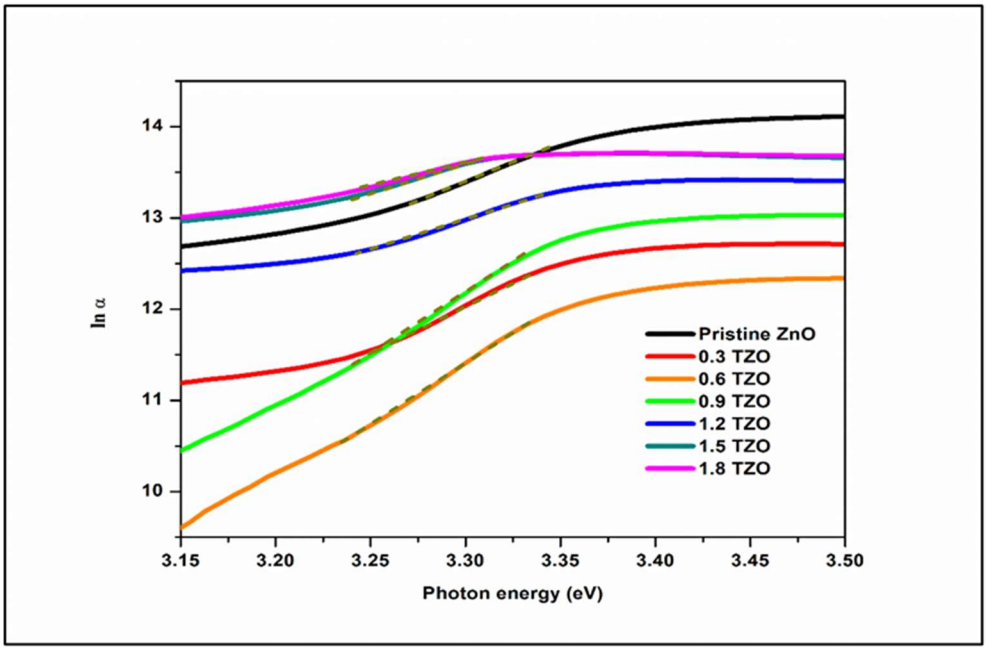

Figure 5. Plot of ln α against photon energy of pristine ZnO and 0.3 – 1.8 at.% of TZO NWs

Table 3. Urbach energy of pristine ZnO and 0.3 – 1.8 at.% of TZO NWs

Sample	Urbach Energy (meV)
Pristine ZnO	111
0.3 TZO	98
0.6 TZO	77
0.9 TZO	76
1.2 TZO	161
1.5 TZO	175
1.8 TZO	176

Dye adsorption and desorption analysis

From the plotted UV-vis-NIR graphs in Figure 6 (a – g) and the summarised data in Table 4 had found that the transmittance patterns of pristine ZnO was boosted with the helped of Sn dopants. This was due to the fact that Sn had successfully reduced the particle size as shown in FESEM images. However, the pattern had started to deteriorate after 1.2 TZO samples as the transmittance started to drop in respond to inhomogeneity of the NWs formation. For the dye adsorption ability, the transmittance of the window layer is reduced at the specific wavelengths corresponding to the dye's absorption peaks. The transmittance recorded by N719 dye was 13.50%. Numerous previous studies had discovered that this type of dye was one of the most promising and highly potential candidates for DSSC sensitiser application [32, 33]. The increased in the incident light absorbed by the dye molecules which resulted in a higher probability of generating electron-hole pairs. In this case, adsorbed dye molecules on ZnO nanostructures had maintained its adsorption even after desorption process (based on Table 4) was favourable for DSSC photoanode application. This strong bonding between dye molecules and metal oxide nanostructures were helpful for charge injection movement, dye functioning and generating the stability of solar cell performance [34]. There was not much difference in transmittance level during adsorption and desorption actions for pristine ZnO (1.25%), 0.3 TZO (2.71%), 1.2 TZO (2.21%), 1.5 TZO (5.28%) and 1.8 TZO (0.91%). This situation had established the dependability of better dye trapping character on the multiplane crystal orientation. The same pattern also displayed through less efficient dye trapping effect on 0.6 (7.79%) and 0.9 TZO (9.95%) due to much larger difference in trasnmittance before and after desorption process. This might due to the crystal growth leaned towards single plane (101). Less efficient dye trapping properties can be improved via application of buffer layer on top of the structure.

Table 4. The average transmittance within visible region (400 – 800 nm) of pristine ZnO and various TZO samples

Label in Figure 4	Sample	Average Transmittance (%)		
		As-prepared Sample	Dye Adsorbed (S1)	Dye Desorbed (S2)
(a)	Pristine ZnO	71.49	18.13	19.38
(b)	0.3 TZO	73.31	15.64	18.35
(c)	0.6 TZO	78.68	46.32	54.11
(d)	0.9 TZO	78.03	40.80	50.75
(e)	1.2 TZO	56.48	33.12	35.33
(f)	1.5 TZO	50.22	44.99	50.27
(g)	1.8 TZO	47.56	41.08	41.99

Conclusion

TZO nanowires with the desired properties were successfully synthesized using facile and ultrarapid microwave assisted ultrasonic irradiation technique. High uniformity, more crystalline, low defect, high transmittance and acceptable dye adsorption properties are the qualities can be found in 0.9 TZO thin film. Crystallinity can greatly influence the electrochemical stability of the thin film. The recombination will be suppressed if the defect level is low. Thus, this optimised TZO photoanode is expected to boost the efficiency and performance of DSSCs. Therefore, the fabrication of DSSCs is one of the ways to pave the pathway towards refining the future of renewable and clean energy generation.

Acknowledgement

All authors would like to highlight the appreciation towards Universiti Teknologi MARA (UiTM) for funding this project under Research Grant No. 600-RMC/GIP5/3 (020/2023) and 600-RMC/GPMCOE5/3 (106/2022). Besides that, we also would like to acknowledge the contributions by Faculty of Applied Sciences and NANO SciTech lab, Centre for Functional Materials & Nanotechnology, Institute of Science under UiTM.

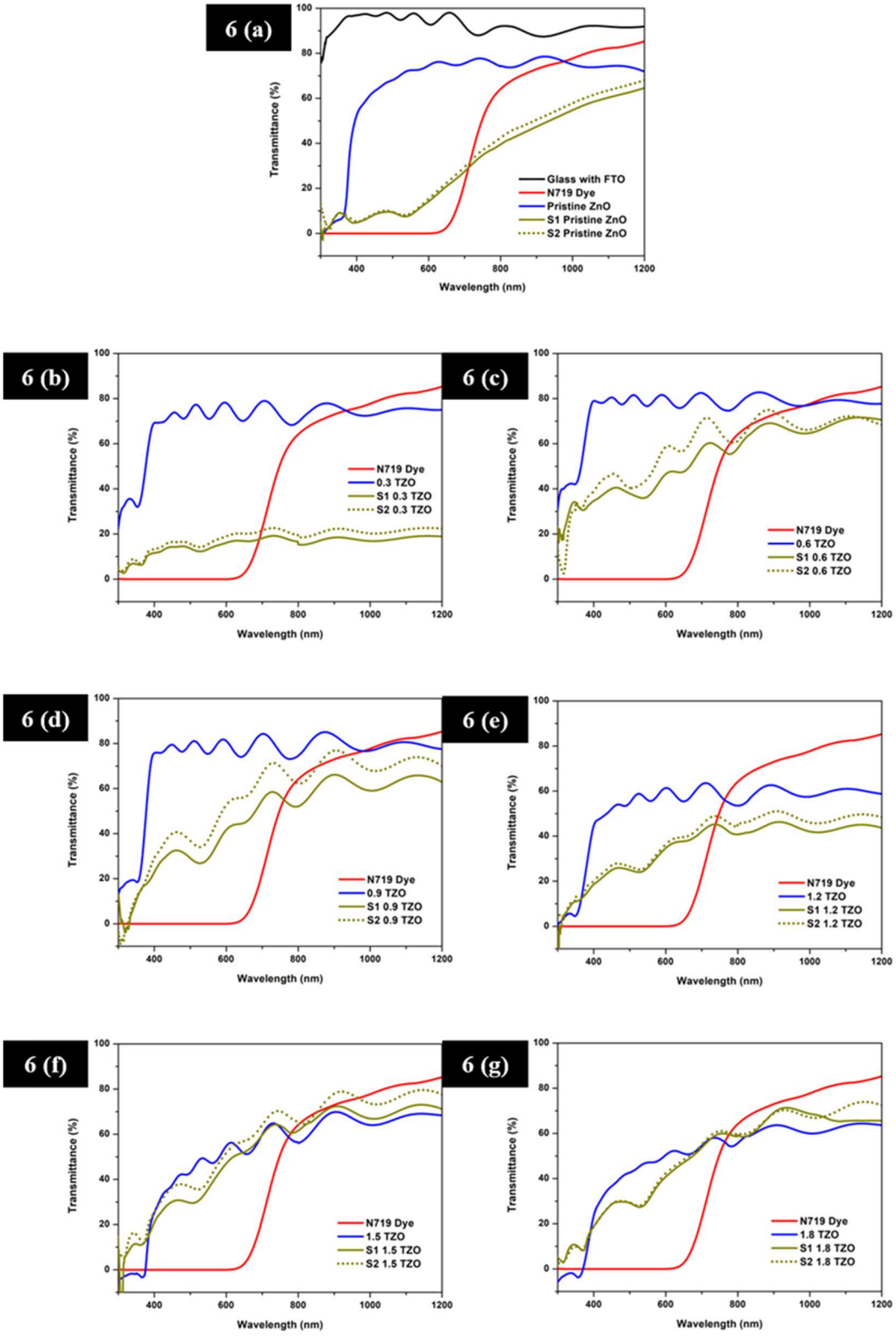

Figure 6. Transmittance of (a) pristine ZnO and (b – g) 0.3 – 1.8 at.% TZO NWs with dye adsorbed and desorbed plot

References

1. Green, M. A., Dunlop, E. D., Siefer, G., Yoshita, M., Kopidakis, N., Bothe, K., and Hao, X. (2023). Solar cell efficiency tables (Version 61). *Progress in Photovoltaics: Research and Applications*, 31(1): 3-16.
2. Mohammadian-Sarcheshmeh, H., Arazi, R., and Mazloum-Ardakani, M. (2020). Application of bifunctional photoanode materials in DSSCs: A review. *Renewable and Sustainable Energy Reviews*, 134: 110249.
3. Bhatti, K. A., Khan, M. I., Saleem, M., Alvi, F., Raza, R., and Rehman, S. (2019). Analysis of multilayer based TiO_2 and ZnO photoanodes for dye-sensitized solar cells. *Materials Research Express*, *6*(7): 075902.
4. Ramya, M., Nideep, T. K., Nampoori, V. P. N., and Kailasnath, M. (2021). Solvent assisted evolution and growth mechanism of zero to three dimensional ZnO nanostructures for dye sensitized solar cell applications. *Scientific Reports*, 11(1): 9.
5. Chen, H.-Y., Huang, B.-Y., Koo, H.-S., and Huang, M.-T. (2020). Characterization of dye-sensitized solar cells based on various $CaCO_3$-doped ZnO photoanodes prepared using wet powder mixing and grinding. *Optik*, 220: 164899.
6. Nikoobakht, B., Wang, X., Herzing, A., and Shi, J. (2013). Scalable synthesis and device integration of self-registered one-dimensional zinc oxide nanostructures and related materials. *Chemical Society Reviews*, 42(1): 342-365.
7. Fonseca, A. F. V. D., Siqueira, R. L., Landers, R., Ferrari, J. L., Marana, N. L., Sambrano, J. R., La Porta, F. D. A., and Schiavon, M. A. (2018). A theoretical and experimental investigation of Eu-doped ZnO nanorods and its application on dye sensitized solar cells. *Journal of Alloys and Compounds*, 739: 939-947.
8. Lin, C.-Y., Lai, Y.-H., Chen, H.-W., Chen, J.-G., Kung, C.-W., Vittal, R., and Ho, K.-C. (2011). Highly efficient dye-sensitized solar cell with a ZnO nanosheet-based photoanode. *Energy & Environmental Science*, 4(9): 3448-3455.
9. Kołodziejczak-Radzimska, A., and Jesionowski, T. (2014). Zinc oxide—from synthesis to application: A review. *Materials*, 7(4): 2833-2881.
10. Das, A., Wary, R. R., and Nair, R. G. (2020). Cu modified ZnO nanoflakes: An efficient visible light-driven photocatalyst and a promising photoanode for dye sensitized solar cell (DSSC). *Solid State Sciences*, 104: 106290.
11. Zhuang, S., Lu, M., Zhou, N., Zhou, L., Lin, D., Peng, Z., and Wu, Q. (2019). Cu modified ZnO nanoflowers as photoanode material for highly efficient dye sensitized solar cells. *Electrochimica Acta*, 294: 28-37.
12. Tayyaba, S., Ashraf, M. W., Tariq, M. I., Akhlaq, M., Balas, V. E., Wang, N., and Balas, M. M. (2020). Simulation, analysis, and characterization of calcium-doped ZnO nanostructures for dye-sensitized solar cells. *Energies*, 13(18): 4863.
13. Saboor, A., Shah, S. M., and Hussain, H. (2019). Band gap tuning and applications of ZnO nanorods in hybrid solar cell: Ag-doped verses Nd-doped ZnO nanorods. *Materials Science in Semiconductor Processing*, 93: 215-225.
14. Giannouli, M., Govatsi, K., Syrrokostas, G., Yannopoulos, S., and Leftheriotis, G. (2018). Factors Affecting the Power Conversion Efficiency in ZnO DSSCs: Nanowire vs. Nanoparticles. *Materials*, 11(3): 411.
15. Angaiah, S., Arunachalam, S., Murugadoss, V., and Vijayakumar, G. (2019). A Facile polyvinylpyrrolidone assisted solvothermal synthesis of zinc oxide nanowires and nanoparticles and their influence on the photovoltaic performance of dye sensitized solar cell. *ES Energy & Environment*, 4: 59-65.
16. Saleem, M., Farooq, W. A., Khan, M. I., Akhtar, M. N., Rehman, S. U., Ahmad, N., Khalid, M., Atif, M., Almutairi, M. A., and Irfan, M. (2019). Effect of ZnO Nanoparticles coating layers on top of ZnO nanowires for morphological, optical, and photovoltaic properties of dye-sensitized solar cells. *Micromachines*, 10(12): 819.
17. Dloo, A., Fazouan, N., and Atmani, E. H. (2023). Investigation of hydrothermal growth time and temperature for optimized ZnO nanowire arrays toward photovoltaics. *Surfaces and Interfaces*, 40: 103123.
18. Syrrokostas, G., Govatsi, K., and Yannopoulos, S. N. (2016). High-quality, reproducible ZnO nanowire arrays obtained by a multiparameter optimization of chemical bath deposition growth. *Crystal Growth & Design*, 16(4): 2140-2150.
19. Guo, H., Ding, R., Li, N., Hong, K., Liu, L., and Zhang, H. (2018). Defects controllable ZnO nanowire arrays by a hydrothermal growth method for dye-sensitized solar cells. *Physica E: Low-dimensional Systems and Nanostructures*, 2018: 105.
20. Zatirostami, A. (2021). Fabrication of dye-sensitized solar cells based on the composite TiO_2 nanoparticles/ZnO nanorods: Investigating the role of photoanode porosity. *Materials Today Communications*, 26: 102033.

21. Choudhury, B. D., Lin, C., Shawon, S. M. A. Z., Soliz-Martinez, J., Huq, H., and Uddin, M. J. (2021). A photoanode with hierarchical nanoforest TiO_2 structure and silver plasmonic nanoparticles for flexible dye sensitized solar cell. *Scientific Reports*, *11*(1)
22. Thirumoorthi, M., and Thomas Joseph Prakash, J. (2019). Doping effects on physical properties of (101) oriented tin zinc oxide thin films prepared by nebulizer spray pyrolysis method. *Materials Science and Engineering: B*, 248: 114402.
23. Nunes, V. F., Lima, F. M., Teixeira, E. S., Júnior, P. H. F. M., Almeida, A. F. L., and Freire, F. N. A. (2021). Effects of tin on the performance of ZnO photoanode for DSSC. *Matéria (Rio de Janeiro)*, *26*(4): 1312.
24. Khadtare, S., Pathan, H. M., Han, S.-H., and Park, J. (2021). Facile synthesis of binder free ZnO and its Indium, Tin doped materials for efficient dye sensitized solar cells. *Journal of Alloys and Compounds*, 872: 159722.
25. Xu, L., Zheng, G., Xian, F., and Su, J. (2019). The morphological evolution of ZnO thin films by Sn ions doping and its influence on the surface energy and photocatalytic activity. *Materials Chemistry and Physics*, 229: 215-225.
26. Saurdi, I., Mamat, M., Malek, M., and Rusop, M. (2014). Preparation of aligned ZnO nanorod arrays on Sn-doped ZnO thin films by sonicated sol-gel immersion fabricated for dye-sensitized solar cell. *Advances in Materials Science and Engineering,* 2014: 636725.
27. Mamat, M. H., Sahdan, M. Z., Khusaimi, Z., Ahmed, A. Z., Abdullah, S., and Rusop, M. (2010). Influence of doping concentrations on the aluminum doped zinc oxide thin films properties for ultraviolet photoconductive sensor applications. *Optical Materials*, 32(6): 696-699.
28. Magiswaran, K., Norizan, M. N., Mahmed, N., Mohamad, I. S., Idris, S. N., Sabri, M. F., Amin, N., Sandu, A. V., Vizureanu, P., Nabiałek, M., and Salleh, M. A. (2023). Controlling the layer thickness of zinc oxide photoanode and the dye-soaking time for an optimal-efficiency dye-sensitized solar cell. *Coatings*, 13(1): 20.
29. Khan, M. I., Naeem, M., Mustafa, G., Abubshait, S., Mahmood, A., Al-Masry, W., Al-Garadi, N., and Ramay, S. (2020). Synthesis and characterization of Co and Ga co-doped ZnO thin films as an electrode for dye sensitized solar cells. *Ceramics International*, 46: 127.
30. Bashir, M. B., Rajpar, A. H., Salih, E. Y., and Ahmed, E. M. (2023). Preparation and photovoltaic evaluation of CuO@Zn(Al)O-mixed metal oxides for dye sensitized solar cell. *Nanomaterials*, 13(5): 802.
31. Nanev, C. N. (2023). Thermodynamic and molecular-kinetic considerations of the initial growth of newly born crystals; crystal size distribution; dissolution of small crystals during ostwald ripening due to temperature changes. *Progress in Crystal Growth and Characterization of Materials*, 69(2): 100604.
32. Shalini, S., Balasundaraprabhu, R., Kumar, T. S., Prabavathy, N., Senthilarasu, S., and Prasanna, S. (2016). Status and outlook of sensitizers/dyes used in dye sensitized solar cells (DSSC): a review. *International Journal of Energy Research*, 40(10): 1303-1320.
33. Sekar, N., and Gehlot, V. Y. (2010). Metal complex dyes for dye-sensitized solar cells: Recent developments. *Resonance*, 15(9): 819-831.
34. Tomar, N., Agrawal, A., Dhaka, V. S., and Surolia, P. K. (2020). Ruthenium complexes based dye sensitized solar cells: Fundamentals and research trends. *Solar Energy*, 207: 59-76.

Malaysian Journal of Analytical Sciences (MJAS)
Published by Malaysian Analytical Sciences Society

MEMBRANE-PROTECTED MICRO-SOLID PHASE EXTRACTION OF CARCINOGENIC AROMATIC AMINES IN WATER SAMPLES PRIOR TO GC-FID ANALYSIS

(Pengekstrakan Fasa Pepejal Mikro Yang Dilindungi oleh Membran untuk Amin Aromatik Karsinogenik dalam Sampel Air dengan Analisis GC-FID)

Anjalee Pushpika Patabendi[1], Mohamad Shariff Shahriman[1], Hemavathy Surikumaran[2], Nur Nadhirah Mohamad Zain[3], Noorfatimah Yahaya[3], Faizah Mohammad Yunus[1], Usman Abdullahi Usman[4], Kavirajaa Pandian Sambasevam[5,6*], and Muggundha Raoov[1*]

[1]*Department of Chemistry, Faculty of Science, Universiti Malaya, 50603 Kuala Lumpur, Malaysia*
[2]*Faculty of Bioeconomic, Food and Health Sciences, Universiti Geomatika Malaysia, 54200 Kuala Lumpur, Malaysia*
[3]*Department of Toxicology, Advanced Medical & Dental Institute, Universiti Sains Malaysia, 13200 Pulau Pinang, Malaysia*
[4]*Department of Geology, Faculty of Science, University of Maiduguri, P.M.B 1069, Maiduguri, Borno State, Nigeria.*
[5]*Advanced Materials for Environmental Remediation (AMER), Faculty of Applied Sciences, Universiti Teknologi MARA, Cawangan Negeri Sembilan, Kampus Kuala Pilah, 72000 Kuala Pilah, Negeri Sembilan, Malaysia*
[6]*Electrochemical Material and Sensor (EMaS) Group, Universiti Teknologi MARA, Shah Alam, 40450, Selangor, Malaysia*

**Corresponding author: kavirajaa@uitm.edu.my, muggundha@um.edu.my*

Received: 17 February 2024; Accepted: 16 April 2024; Published: 29 June 2024

Abstract

A simple method to extract aromatic amines in environmental water samples was developed using β-cyclodextrin-toluene diisocyanate (β-CD-TDI) polymer enclosed with tea bag filter paper fashioned as a micro-solid phase extraction (μ-SPE) device combined with GC-FID. In this study, an efficient sorbent (β-CD-TDI polymer) was successfully synthesised and characterizaed for the microextraction of aromatic amines such as *p*-Toluidine, 4-chloroaniline, 2-naphthylamine, and 4-aminobiphenyl using FTIR, FESEM and TGA. Under optimized conditions (40 mg of β-CD-TDI polymer in 5 mL sample volume with 75 min extraction time and desorption with 300 μL of acetonitrile under 30s desorption time), β-CD-TDI polymer was proven to be an effective adsorbent for the extraction of aromatic amines in environmental water samples with a satisfactory percentage recovery achieved from 80 to 99%. All the studied analytes showed good linearity in the range of 5 to 500 μg L^{-1} and the correlation of determination (R^2) was from 0.9980 to 0.9990. The LODs obtained were from 1.67 to 3.18 μg L^{-1}, and LOQs were from 5.05 to 9.63 μg L^{-1}. This method gives precision values for both intra- and inter-day within accepted variable limits (<15% of RSD). The self-made cellulose-based μ-SPE device revealed that it can be simply prepared, easy to operate, reusable, cost-effective, reduce chemical consumption during extraction, and additionally speed up the extraction process, making it more efficient.

Keywords: μ-SPE, β-cyclodextrin-toluene diisocyanate, aromatic amines, GC-FID, environmental water

Abstrak

Satu kaedah mudah untuk mengekstrak amin aromatik dalam sampel air alam sekitar telah dibangunkan menggunakan polimer β-siklodextrin-toluen diisosiyanat (β-CD-TDI) yang dilingkungi dengan kertas penapis beg teh yang dihasilkan sebagai peranti pengekstrakan fasa pepejal mikro (μ-SPE) yang digabungkan dengan GC-FID. Dalam kajian ini, penyerap yang berkesan (polimer β-CD-TDI) berjaya disintesis dan dicirikan untuk pengeluaran mikro amin aromatik seperti p-Toluidin, 4-kloroanilin, 2-naftilamina, dan 4-aminobifenil menggunakan FTIR, FESEM, dan TGA. Di bawah syarat yang dioptimumkan (40 mg polimer β-CD-TDI dalam 5 mL isipadu sampel dengan masa pengekstrakan 75 minit dan desorpsi dengan 300 μL asetonitril dalam masa desorpsi 30 saat), polimer β-CD-TDI terbukti menjadi penjerap yang berkesan untuk pengekstrakan amin aromatik dalam sampel air alam sekitar dengan perolehan peratusan yang memuaskan mencapai dari 80 hingga 99 %. Semua analit yang dikaji menunjukkan lineariti yang baik dalam julat 5 hingga 500 μg L^{-1} dan korelasi penentuan (R^2) adalah dari 0.9980 hingga 0.9990. LOD yang diperolehi adalah dari 1.67 hingga 3.18 μg L^{-1}, dan LOQ adalah dari 5.05 hingga 9.63 μg L^{-1}. Kaedah ini memberikan nilai ketepatan untuk kedua-dua intraday dan inter-day dalam had batas variabel yang diterima (<15 % daripada RSD). Peranti μ-SPE berbahan selulosa buatan sendiri menunjukkan bahawa ia boleh disiapkan dengan mudah, mudah beroperasi, boleh digunakan semula, berkos rendah, mengurangkan penggunaan bahan kimia semasa pengekstrakan, dan tambahan pula mempercepatkan proses pengekstrakan, menjadikannya lebih cekap.

Kata Kunci: μ-SPE, β-siklodekstrin-toluena diisosiyanat, amin aromatik, GC-FID, air persekitaran

Introduction

Environmental pollution is the main concern today due to numerous fears caused by chemical contaminants to humans and other living beings with their high toxicity and widespread usage [1]. Among the number of organic pollutants found in the environment, aromatic amines (AAs) mainly gained the significant interest of researchers. Even in low concentrations, AAs negatively impact living organisms [2]. In recent years, aromatic amines have been used widely in high-in-demand developing sectors such as pharmaceuticals, pesticides, dyestuffs, and rubber industries. The production process, usage, and disposal of these products are the preliminary pathways aromatic amines enter into the environment. For instance, the hydrolysis of azo dyes and pesticides releases AAs directly into the water bodies.

Until now, more than 30 aromatic amines have been identified in the environment due to their thermodynamic stability, high polarity, and water solubility. Significant reactivity of amino groups enables them to be quite easily transported in and out of aquifers [3]. The United States Environmental Protection Agency (USEPA) and European Environmental Agency (EEA) have classified AAs as refractory organic materials as they are difficult to decompose by natural biological and chemical processes [4,5,6]. Therefore, reliable risk assessment of AAs is highly important, and the demand for trace level easy, efficient, and accurate analysis for various aromatic amines.

In addressing this matter, our current study focuses on a simple and cost-effective extraction technique to analyse these pollutants in water. To date, pollutant extraction using adsorbents is a highly favoured analytical technique and new sorbents are being widely studied using materials such as activated carbon powders and fibres, nanomaterials, paper mill sludge and cyclodextrin polymers [2]. Numerous cyclodextrin-based polymeric materials have been developed as sorbents for extracting environmental pollutants due to their eco-friendly nature and high regeneration value [4]. Cyclodextrins (CDs) are natural products obtained from the enzymatic degradation of starch. They are cyclic oligosaccharides built from (α-1,4)- linked D-glucopyranose units. CDs contain a hydrophobic interior and hydrophilic exterior in their torus structure. They have a structurally related series of macrocyclic oligosaccharides called α-, β-, and γ-CD [7]. Compared to other cyclodextrins, β-CD can form inclusion complexes with an extensive range of molecules through various interactions [8]. Besides, β-CD polymers are easy to synthesise, stable, water-insoluble, environment-friendly, and economical. Therefore, it is a good option for environmental-related applications.

The complexity of matrices, low concentrations of analytes in samples, and insufficient selectivity and

sensitivity in conventional methods commonly challenge the direct determination of aromatic amines in environmental samples. Therefore, the necessity for a simple and efficient sample preparation procedure arises constantly. Sample preparation is the conversion of complex sample matrices into an efficient analysable form via the elimination of interferences using separation and pre-concentration techniques [9]. Therefore, in analytical procedures, sample preparation can be expressed as critical and the most time-consuming step, which potentially could generate the highest error percentage on the work floor because it directly contributes to important analytical data such as the limit of detection (LOD), accuracy and precision [10]. Among the various sample preparation techniques, solid phase extraction (SPE) and liquid-liquid extraction (LLE) are the classical approaches for AAs. However, many disadvantages are associated with these classical methods, such as using a large volume of solvents, multi-step methodology, time-consuming extraction procedures, and difficulty in phase separation [11].

Recently, sample preparation has progressed towards a miniaturisation approach. Basheer and co-workers introduced an extraction technique using a small amount of sorbent packed inside a porous tea bag filter shaped like an envelope [12]. This technique is termed micro-solid phase extraction (μ-SPE) and has proven to be highly beneficial over classical extraction techniques. The method simultaneously provides better reproducibility, high accuracy, rapidity, high pre-concentration factor, and low consumption of organic solvents [13]. This miniaturised extraction technique has a growing interest in separation science due to its low cost, simplicity, and environmental compatibility compared to other commercial extraction techniques [14]. Hence in this research, the extraction of AAs from environmental water was studied using a similar μ-SPE technique. To our knowledge, β-cyclodextrin-toluene diisocyanate (β-CD-TDI), sorbent-based μ-SPE, is yet to be explored.

Typically, this study focuses on developing the μ-SPE method for four aromatic amines, namely 4-chloroaniline, 2-naphthylamine, 4-aminobiphenyl, and *o*-toluidine which are frequently found in environmental water samples and classified as carcinogens [15]. The study on the μ-SPE of AAs was conducted using polymeric sorbent (β-CD-TDI). β-CD-TDI was synthesised, characterised, and packed into a sealed porous cellulose-based envelope (teabag) prior to its application in the μ-SPE of AAs.

Materials and Methods

Materials and reagents

Commercially available β-CD [$(C_6H_{10}O_5)_7.3H_2O$] (molecular weight:1134.987 g mol^{-1}) was purchased from Calbiochem® (Calbiochem®, U.S.A.), and the linker 2,4-Toluene diisocyanate (TDI) (98%, v/v) was supplied by Sigma Aldrich (Aldrich, Buches SG, Switzerland). *N, N*-Dimethylformamide (DMF) (99.9%) was purchased from SeccoSolv® (Merck KGaA, 64271 Darmstadt, Germany). Analytes, *o*-toluidine, 4-chloroaniline, 2-naphthylamine, and 4-aminobiphenyl were purchased from Sigma Aldrich (St. Louis, MO, USA). Acetonitrile (ACN, HPLC grade, 99.9%), methanol (MeOH, HPLC grade, 99.9%), and n-hexane (HPLC grade, 95%) were acquired from Fisher Scientific, USA.

The individual standard stock solutions (200 mg L^{-1}) of four aromatic amines were prepared in 25 mL of MeOH and stored in the refrigerator at 4℃ to prevent degradation. The working standard mix was freshly prepared by diluting stock solutions with ultra-pure de-ionized water from the in-house Merk Milli-Q system. Cellulose-based heat sealable tea bag filter paper (Glatfelter brand) purchased from PCL Solutions (Pvt) Ltd, Sri Lanka.

Instrumentation analysis

Fourier transform infrared (FTIR) spectra were recorded on Perkin Elmer Spectrum 400 (Perkin Elmer, Waltham, MA, USA) in the range of 4000 to 400 cm^{-1} and resolution of 1 cm^{-1} using attenuated total reflectance (ATR) mode. Field emission scanning electron microscopy (FESEM) analyses were obtained using Hitachi SU8220 (Hitachi, Japan) with 1, 2, 10, and 50 μm magnifications under 1 and 2 kV voltages. Thermogravimetric analysis, TGA4000 (Perkin Elmer, USA) was used for thermal analysis of the synthesised polymer material where weight loss was measured for 10.0 mg of polymer using a linear temperature program at 10℃ min^{-1} within the temperature range of 50℃ to 900℃ under inert nitrogen atmosphere.

Chromatographic conditions

Separation and quantification of the selected AAs were performed on an Agilent 7890A gas chromatography

(GC) system equipped with an Agilent 5975C series flame ionization detector (Agilent, USA). The column used was the Agilent HP-5MS fused-silica capillary column (30 m x 0.32 mm, internal diameter, and film thickness: 0.25 µm). The following temperature program was used for the analysis of aromatic amines. Initially, the temperature was set to 60℃ for 1 min, then it was increased to 250℃ at the rate of 20℃ min^{-1} and held for 2 min. The total run time for GC-FID was 12.5 min. Nitrogen was used as the make-up gas (flow rate: 26.121 mL min^{-1}) and He as the carrier gas with a flow rate of 30 mL min^{-1} and pressure of 4.0 psi. The injector temperature was held at 300 °C with split-less mode, and the FID temperature was set to 300 °C. Quantitative calculations were made based on GC peak areas.

Preparation of materials: Synthesis of β-CD-TDI

The polymer was prepared according to the method referred to in the literature [16]. Firstly, 2.0 g of β-CD monomer (1.76 mmol) was added into 40 mL of anhydrous *N, N*-Dimethylformamide (DMF) solvent in a round bottom flask and flushed with nitrogen gas. Then 2.54 mL (17.6 mmol) of 2,4- toluene diisocyanate (TDI) crosslinking reagent was added dropwise into the solvent-β-CD system, with constant stirring at 700 rpm and heating at 80℃. The ratio of β-CD: TDI linker was 1: 10. The system was stirred and heated continuously for 24 hrs at the pre-set parameters. After completion, the reaction mixture was precipitated with excess acetone and allowed to settle for 10 min. This was done to remove excess solvent present in the reaction mixture. The mixture was then rinsed several times with acetone and de-ionized (DI) water to remove any unreacted starting materials. After rinsing, filtration was done using suction filtration, and the final product was dried in a vacuum desiccator for 48 hours prior to use [20].

Development of the µ-SPE device

The µ-SPE device consists of a porous membrane envelope filled with sorbent materials. In this study, cellulose-based tea bag filter paper was used as the porous membrane due to its high stability in the organic solvents and easy wettability. To prepare the µ-SPE device, the tea bag filter paper was cut into 1.5 cm x 1.8 cm rectangles, and 3 edges were heat-sealed. A glass pipette tip cut-off was used to insert 40 mg of β-CD-TDI polymer into pre-cleaned miniature tea bags (the variation of weights was less than 5%). The open ends were then heat-sealed to secure the sorbent content within the envelope. Each device was carefully weighed to ensure consistency in the preparation. The µ-SPE devices were soaked in acetone for 2 hrs to remove any organic impurities, followed by washing with DI water for another 2 hrs to remove any organic or inorganic impurities. For each washing step, 2 min vortex was used to achieve a better cleaning effect. Finally, the prepared device was stored in methanol until further use. Devices were pre-dried in the air before the extraction process. This method is highly cost-effective as 9 miniature devices could be prepared from one tea bag [14].

Micro-solid phase extraction procedure

A standard mixture of targeted AAs was extracted using the prepared µ-SPE device. For each extraction in a 20 mL sample vial, the µ-SPE device was placed into a 5.0 mL sample solution (pH 7.0) and agitated (100 rpm) for 75 min followed by a 1 min vortex (500 rpm) at room temperature. The device was removed with a pair of tweezers after extraction, transferred into a 5 mL sample vial, and dried in an oven at 80℃ for 15 min to remove trapped water. The analytes were eluted with acetonitrile (300.0 µL) using vortex for 30 s at 800 rpm. The eluent was then transferred into GC vials using 45 µm syringe filters. The extraction efficiency was subsequently analysed using GC-FID. The whole procedure is briefly illustrated in Figure 1.

Method validation

Method validation is an important process in analytical method development that provides evidence of whether the analytical process measures what is intended and is acceptable for its desired purpose. In the present study, optimised µ-SPE conditions for selected AAs were studied in terms of linearity, limits of detection (LOD), limits of quantification (LOQ), inter and intraday precision, and recovery.

Linearity

Linearity can be defined as the ability of the method to obtain signals proportional to the concentration of the analyte. Eight standards of different concentrations of aromatic amine mixtures were obtained by serial dilution from the stock solution. µ-SPE using optimised parameters was carried out for the prepared series of standards. The eluent was analysed using GC-FID, and the matrix match calibration plot for all four analytes

was prepared. The coefficient of determination for each plot was then calculated.

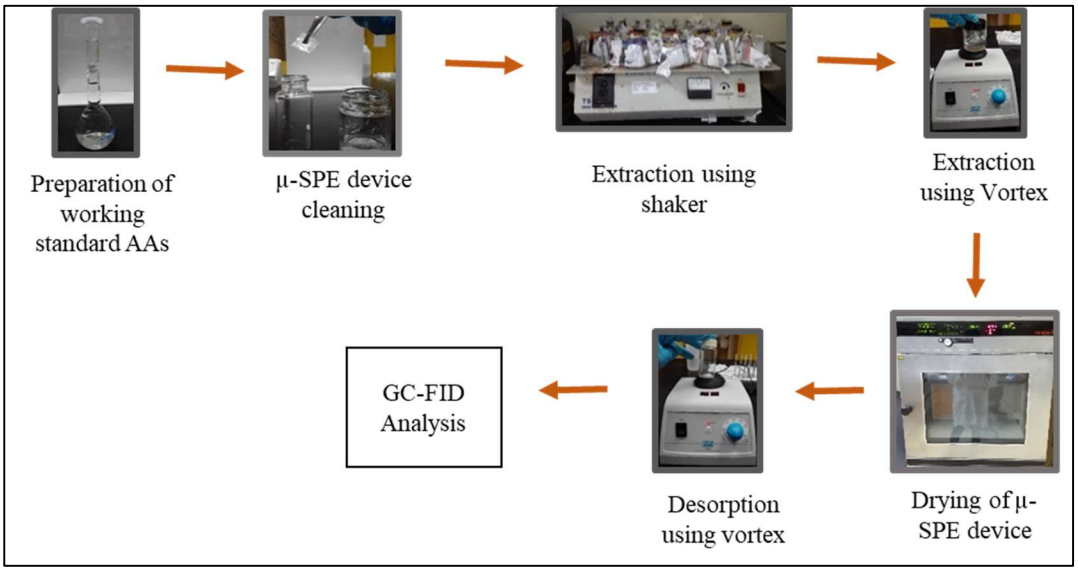

Figure 1. Schematic illustration of µ-SPE procedure for aromatic amines analysis

Limit of detection (LOD) and Limit of quantification (LOQ)

The limit of detection (LOD) can be defined as the lowest concentration of the target analyte, which could be detected by GC-FID with a certain confidence level and ought to be lower than the maximum residual limits (MRLs) in real samples. Meanwhile, the limit of quantification (LOQ) is the lowest concentration of an analyte that can be quantified with some degree of certainty. LOD and LOQ were calculated from equations 1 and 2**,** respectively.

$$LOD = 3.3 \times \frac{SD}{m} \quad (1)$$

$$LOQ = 10 \times \frac{SD}{m} \quad (2)$$

where m is the slope of the matrix match calibration plot and SD is the standard deviation of the blank residuals [17].

Pre-concentration factor (PF)

The pre-concentration factor is defined as the concentration ratio of the analyte in the enriched phase after extraction and the initial solution. This was calculated for each targeted analyte for the sample spike concentration of 200 µg L^{-1} using Equation 3.

$$PF = \frac{P_f}{P_i} \times \frac{V_i}{V_f} \quad (3)$$

P_f is the peak area of the analyte in the enriched extract after extraction, P_i is the peak area of the analyte in standard solution, V_i is the initial sample volume, and V_f is the desorption volume [18].

Matrix effect (ME)

The effect of interferences due to the co-extracting and co-eluting matrix substances can significantly influence the chromatographic signal of target analytes. The matrix effect can be calculated as the ratio of slopes of the standard and spiked calibration plots (equation 4).

$$ME = \frac{Slope\ of\ matrix\ matched\ calibration\ plot}{Slope\ of\ standard\ calibration\ plot} \quad (4)$$

Recovery

The recovery study was done by spiking a known concentration of analyte into the real samples. The spiking concentrations were chosen based on low, medium, and high concentrations for recoveries, i.e., 50.0, 75.0, and 100.0 µg L^{-1}, and the RSDs were determined using three different vials as triplicates ($n=3$). The percentage of recoveries (R %) for the real sample was calculated using Equation 5.

$$R\ \% = \frac{C_{observed} - C_{unfortified}}{C_{fortified}} \times 100\ \% \quad (5)$$

$C_{observed}$ is the concentration of AAs in the spiked sample, while $C_{unfortified}$ is the concentration of AAs in the unspiked sample. $C_{fortified}$ represents the initial spiking concentration [19].

Precision

Inter-day and intraday precisions of the developed technique were assessed by conducting extractions of 100.0 µg L^{-1} standard AAs mixture. Ten samples were tested for intraday precision, and inter-day precision was carried out on five consecutive days with five extractions per day. The results are presented as relative standard deviation (RSD %). Standard deviation (SD) and relative standard deviation (RSD %) were calculated using equations **6** and **7,** respectively.

$$SD = \sqrt{\frac{\sum(x - \tilde{x})^2}{n - 1}} \quad (6)$$

$$RSD\ \% = \frac{SD}{\tilde{x}} \times 100\ \% \quad (7)$$

where x is the observed result for the run, $\tilde{x}$ represents the mean value, and n is the number of measurements (repeatability) [19].

Reusability

The same µ-SPE devices were repeatedly used to determine the efficiency of reused polymers. Three of the 40 mg of β-CD-TDI polymer-packed tea bags were used for the extraction of 5.0 mL samples of AAs mixture (100.0 µg L^{-1}, pH 7.0). Extraction was done according to the optimised method. The same experiment was repeated for 8 additional cycles to study the reusability of the µ-SPE devices.

Real sample pre-treatment

To evaluate the applicability of the developed method, four different environmental water samples were analysed under optimized conditions. Tap water samples were collected from the working laboratory. Meanwhile, river water and lake water samples were collected in pre-cleaned amber glass bottles from the Pantai River, Malaysia, and Universiti Malaya (UM), Malaysia, respectively. Wastewater samples were collected from a cannel near the UM library. The collected water samples were filtered trice using 0.45 µm Millipore cellulose membrane filters right after sampling, and the pH was recorded. Finally, the filtered samples were covered with aluminium foil and stored in the refrigerator at 4℃ prior to analysis [9].

Results and Discussion

Synthesis and characterization of β-CD-TDI polymer: Mechanism of reaction

In the synthesis of cyclodextrin polymers, the use of diisocyanate as a cross-linking agent is a conventional direct reaction method. The reactions between β-CD and TDI were carried out at 80 °C for 24 hours. The polymerization mechanism follows the exothermic nucleophilic addition reaction as shown in Figure 2, where two electrons from OH- groups in β-CD donate to the C atom in the NCO- group of diisocyanate (Ar-aromatic ring structure). Thus, the double bond between N and C atoms breaks and forms 'urethane linkage' (-NH-C(=O)-O-) [13]. This polymerization reaction is popular among researchers working in this field due to its simplicity and high yields [16].

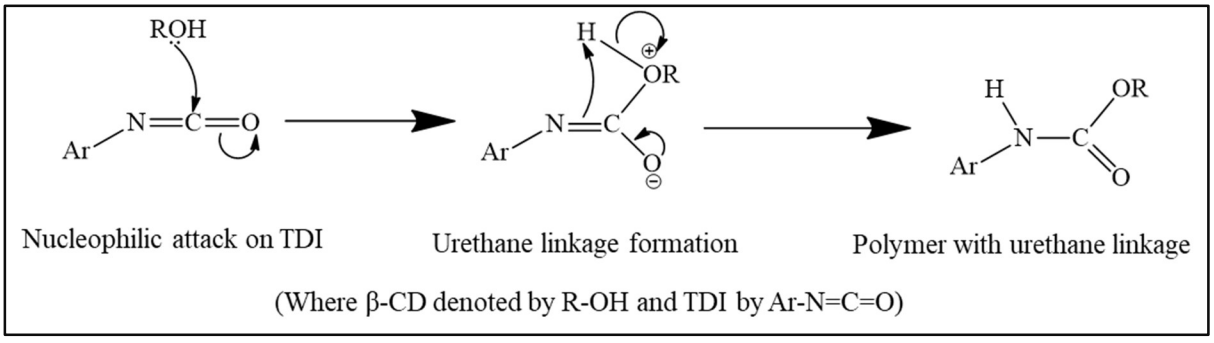

Figure 2. Proposed mechanism for the urethane linkage formation between β-CD and TDI

FTIR analysis

The spectrum of the β-CD-TDI polymer was compared with native β-CD and TDI spectra, as shown in Figure 3. In the spectrum of β-CD, the peaks at 1024 and 1080 cm^{-1} corresponded to C-OH stretching vibrations, while those at 3300-3400 cm^{-1} are attributed to -OH groups, the common functionalities in both native β-CD and TDI. However, in the β-CD-TDI spectrum, the absence of a peak around 2270 cm^{-1} (corresponding to the isocyanate group) and the appearance of stretching vibrations of carbamate linkage -NHCO at 1534 cm^{-1} indicates the completion of polymerization reaction [20]. Furthermore, the newly formed polymeric material (β-CD-TDI) exhibited peaks at 1600-1585 cm^{-1} and 1500-1400 cm^{-1} due to carbon-carbon stretching vibrations in the aromatic ring attached to TDI. The absorption band at 1221 cm^{-1} is attributed to the C-O-C characteristics of urethane linkage in the β-CD-TDI polymer [16]. These results confirm the successful polymerization of β-CD-TDI polymer.

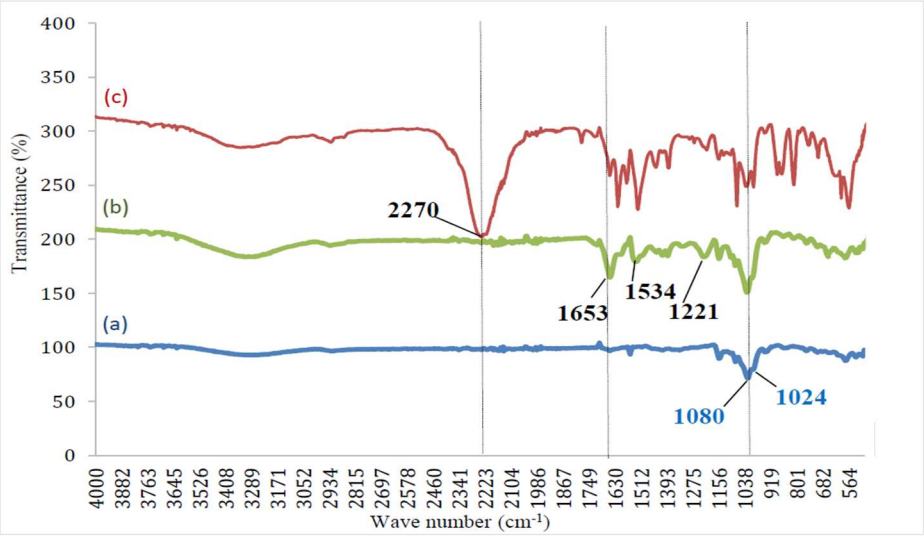

Figure 3. FTIR spectra of (a)β-CD, (b)β-CD-TDI polymer and (c)TDI

Morphology analysis

The polymer morphology analysis was carried out by FESEM analysis, and the results are given in Figure 4, illustrating both β-CD and β-CD-TDI images at different magnifications. FESEM images allow facile identification of irregularities on the surface of co-polymer materials [21]. The FESEM images of the β-cyclodextrin monomer shown in Figure 4 (a) have a smooth surface structure with deep cracks. The surface morphology of the β-CD-TDI polymer in Figure 4 (b) differs from the parent β-CD monomer. It records a non-smooth irregular surface with visible pore openings. Therefore, the results show that introducing the TDI linker to the β-CD has modified the surface characteristics of the polymer. Thus, it can be concluded that the synthesised polymer likely contains a more porous nature.

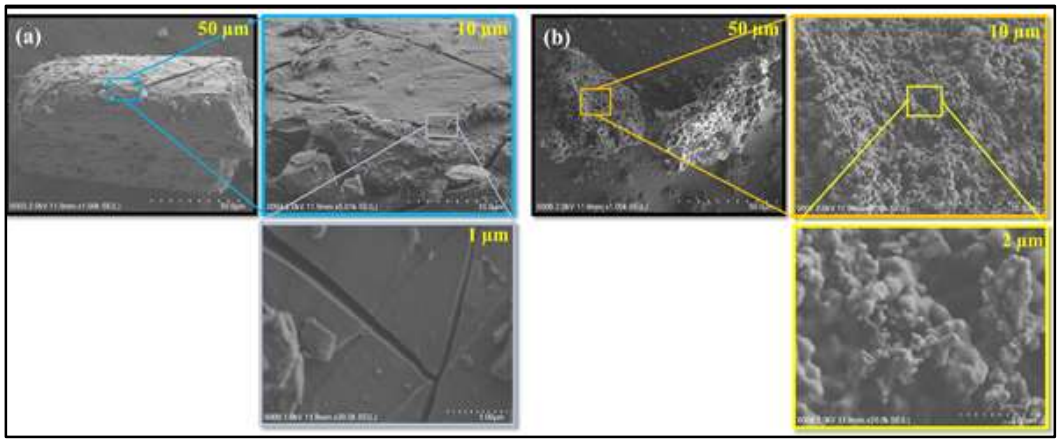

Figure 4. FESEM images 30k x magnification of (a) β-CD and (b)β-CD-TDI polymer

Thermal analysis

Thermal analysis is important in understanding the stability or function of the material at room temperature as well as in very high temperatures for extended periods. Besides, it is necessary to pre-determine the stability of the polymer during high-temperature applications. Polymer stability can be affected by various complex, interrelated phenomena, such as changes in the crystallinity of the bulk phase and polymer structure. Based on the TGA spectra of β-CD-TDI (Figure 5), the weight percentage reduction before 100 °C is around 8%. The evaporation of adsorbed moisture onto the polymer may cause a weight reduction [20, 22]. Further increment in temperature leads the polymer to lose weight as it degrades under the oxygenated environment. The polymer starts to degrade around 310 °C which is seen in the TGA curve. This higher weight loss is due to the cleavage of the urethane linkage and volatilization of the resultant product of decomposition [16]. It can be concluded from the thermal analysis data that the β-CD-TDI polymer is stable below 310℃ and can be used for high-temperature applications.

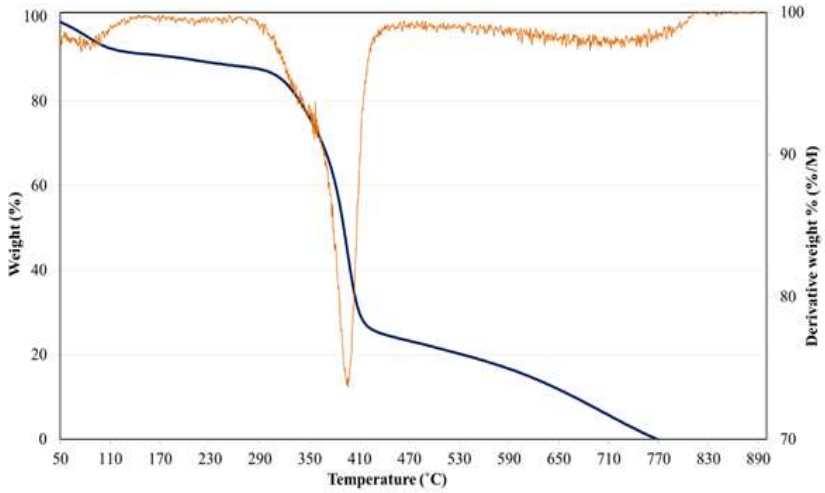

Figure 5. TGA analysis on weight (%) and derivative curves of β-CD-TDI polymer between 50 - 900℃

Optimization of micro-solid phase extraction (µ-SPE) parameters

Seven extraction parameters were selected to improve the performance of β-CD-TDI sorbent-based µ-SPE of aromatic amines. This includes optimising the type of desorption solvent, amount of adsorbent in the µ-SPE device, volume of desorption solvent, desorption time, sample volume, sample pH, and extraction time. The optimization procedure was started using an analyte concentration of 5.0 mg L^{-1}. All the optimizations were carried out in triplicates using GC-FID analysis.

Effect of types of desorption solvent

In the µ-SPE technique, the desorption step plays a vital role in desorbing maximum amounts of AAs from the β-CD-TDI polymer. Hence it is important to choose an appropriate desorption solvent that can provide optimum desorption efficiency. In this study, several organic solvents that were compatible with the GC system, namely methanol (MeOH), acetonitrile (ACN), and hexane, were explored. These solvents were chosen because the boiling point is lower than the analyte and for the GC system solvents that are easy to volatile are preferred [23]. Also, the wettability of the tea bag membrane, solubility of the analyte, and polarity of the solvents were considered. Due to the high porosity and fast water absorption of the cellulose-based tea bag filter paper, analytes could easily diffuse through and enhance the interactions with sorbent. Thus, the effect of tea bag material was neglected. Referring to Figure 6 (a), ACN was proven to yield the highest peak areas for all four analytes studied, whereas hexane showed the poorest elution capability. AAs are moderately polar compounds that form inclusion complexes with the β-CD-TDI during the extraction process [22]. Therefore, it may not be easily desorbed if the incorrect solvent is used. Hence, compared to non-polar solvents like hexane, polar solvents like methanol and acetonitrile were more suitable for the desorption of AAs. Among them, AAs were shown a strong affinity towards ACN, a moderately polar solvent, rather than β-CD-TDI achieving higher extraction efficiency. Therefore, ACN was chosen as the desorption solvent for further studies [14].

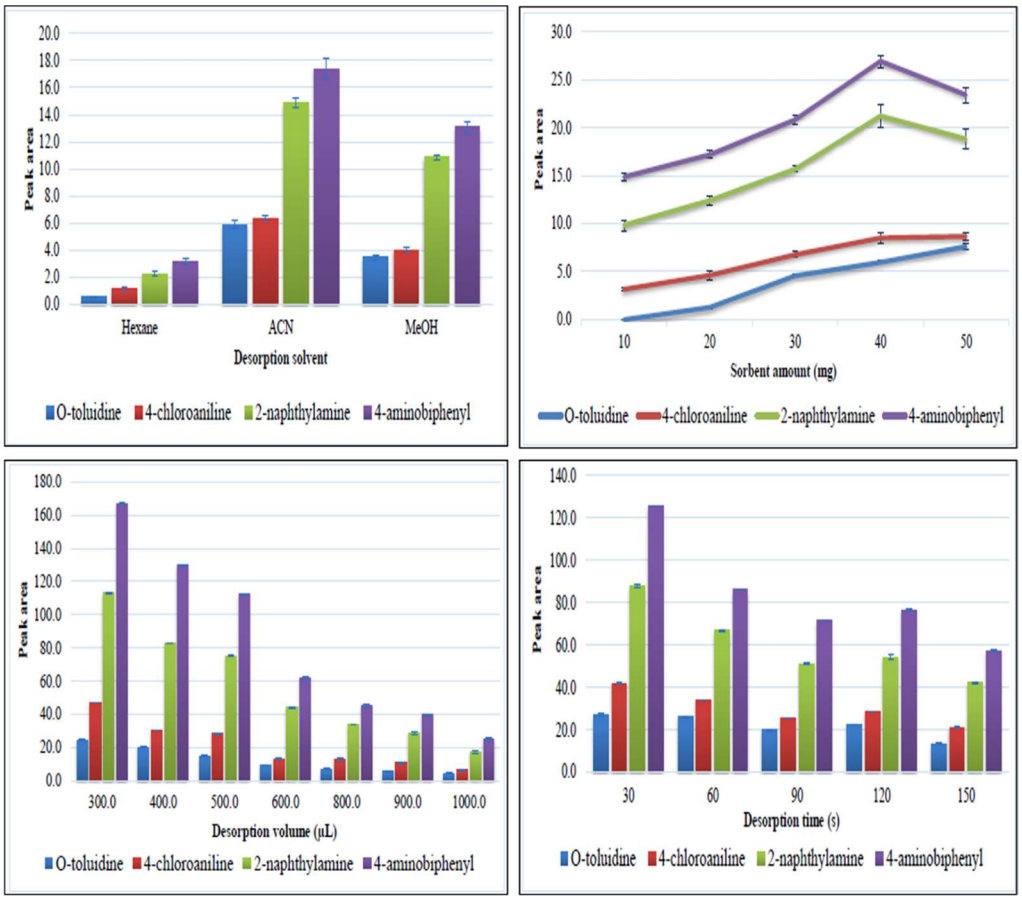

Figure 6. The effects of different types of desorption solvents (a), amount of adsorbent (b), volumes of desorption solvents (c) and different desorption times (d). (Extraction conditions: concentration of each AAs, 5 mg L-1; type of desorption solvent, hexane, MeOH and ACN; mass of β-CD-TDI, 10-50 mg; sample volume, 10 mL; extraction time, 30 min; desorption volume, 300 - 1000 µL and desorption time, 30- 150 s)

Effect of adsorbent amount

The effect of sorbent amount was observed using 10, 20, 30, 40, and 50 mg of polymer. According to Figure 6 (b), 40 mg of the β-CD-TDI polymer gave the largest peak area compared to other variables. Theoretically, the higher the amount of adsorbent used, the higher the concentration of analytes that can interact with polymer because of the increase in the surface area of the polymeric material. As the mass of the polymer increased from 10 - 40 mg, the peak area also increased, but beyond this point, there was no significant enhancement of the peak area for most of the analytes. This was due to the extraction of the maximum amount of analyte concentration from the solution; hence further increase in the mass of the adsorbent does not affect the extraction efficiency [16]. After 40 mg, a decrease in peak areas of some analytes may be due to steric hindrance or mobility disturbances occurring during analyte migration [14]. Thus, 40 mg of the β-CD-TDI polymer was chosen as the optimum amount for the extractions.

Effect of desorption volume

The effect of desorption solvent volume was studied in the range of 300.0 - 1000.0 µL. As observed in Figure 6 (c), 300.0 µL gave the highest peak area, and this micro-volume justifies the microextraction technique used in this study. This is probably due to the increasing dilution factor and the solubility of analytes in the aqueous phase the extraction step was increased which will lead to a decrease in the extraction efficiency. Thus, the smaller the volume is, the more concentrated the solvent becomes.100.0 and 200.0 µL were insufficient for desorption because those volumes were insufficient to make better contact with the prepared µ-SPE device. Therefore, 300 µL was selected as the optimum desorption volume for further studies.

Effect of desorption time

The effect of desorption time towards the extraction efficiency of AAs was investigated in the range of 30-150 s using a vortex (800 rpm). The observed results showed the best extraction efficiency was obtained at 30 s, as shown in Figure 6 (d). Beyond 30 s, when the time was increased, the peak area decreased as the equilibrium reaction of mass transfer moved to the opposite direction leading to the re-adsorption of analytes to the sorbent [14,24]. Thus, the 30 s desorption time was used in this study.

Effect of extraction volume

Sample volume also plays an important role in the extraction of AAs. Based on Figure 7 (a), when sample volume increases, the peak area also increases drastically, and 5.0 mL records the greatest value. When the volume of the sample increases up to 5.0 mL, proper dispersion of analytes occurs, leading to higher extraction efficiencies [25]. After reaching the maximum extraction efficiency, the binding sites of the sorbent are saturated with the targeted analytes; thus, further increase of volume will show a plateau. In contrast, the efficiency was decreasing, which may be due to migration difficulties between the sample solution and the surface of the sorbent [14]. Therefore, 5.0 mL was chosen as the optimal sample volume for this experiment.

Effect of sample pH

Sample pH plays a vital role in the extraction process because the degree of ionization and speciation of AAs depends on the pH of the solution. The effects of pH ranging from 2.0 - 9.0 were studied for the extraction of the selected AAs using β-CD-TDI as sorbent. It could be seen from Figure 7 (b) that the total amount of extractions improved significantly with the increase of pH from 2.0 to 7.0. The maximum peak area was found for pH 7.0, which was the natural pH of the aromatic amine mixture. Thereafter, the peak area decreased with an increase in pH until pH 9.0. The obtained results could be due to the sorption mechanism, which was probably dominated by the Van Der Waals forces, inclusion complex formation, л-л interactions, and hydrogen bonding between the β-CD-TDI and the aromatic amines [26]. Among these, inclusion complex formation plays a main role in the extraction [14]. When AAs were in the acidic medium, they were in ionic form, and due to that, the inclusion complex formation was low, whereas л-л interactions and hydrogen bonding may dominate. A higher pH (pH >7) also records the low capability of inclusion complex formation. However, higher chances for inclusion complex formation occur at pH 7, probably due to higher extraction efficiency. This is due to the neutral behaviour of AAs at the neutral pH [27]. Hence, pH 7.0 was selected as the optimum pH for the extractions.

Effect of extraction time

The effect of extraction time was another key parameter affecting the efficiency of extraction. In the µ-SPE technique, the mass transfer of AAs from the sample solution towards the polymeric sorbent is a time-dependent and equilibrium-based process rather than an exhaustive extraction process. The optimization for this parameter was carried out in the time range of 15 to 90 min using the shaker at 100 rpm and followed by a 1 min vortex at 500 rpm to provide better contact between the analyte solution and the polymer. The optimum time for the extraction was observed at 75 min (as shown in Figure 7 (c)), and the extraction efficiency was reduced after that point. Prolonged extraction decreases extraction performance due to a reverse equilibrium reaction [14,28]. Thus 75 min was selected as the optimum extraction time.

Reusability of µ-SPE device

The reusability of the prepared µ-SPE device was assessed through eight consecutive extraction cycles to check its extraction efficiency. Three µ-SPE devices were continuously reused to extract 100.0 µg L^{-1} standard AA solutions and then analyzed by GC-FID. According to the results, it was found that after five extractions, the response reduced significantly (> 25%), and the decreasing pattern continued, as shown in Figure 7 (d). Thus, this indicates that the µ-SPE device can be used only five times with no significant drop in performance. The non-reusability may be caused by the diffusion of oxygen and water into the polymer structure [21] and exposure to high agitation in a vortex where some amount of polymer might leach out from the teabag membrane after a few repetitions. Although the µ-SPE device cannot be reused more than five times, it still is low cost and records good reproducibility.

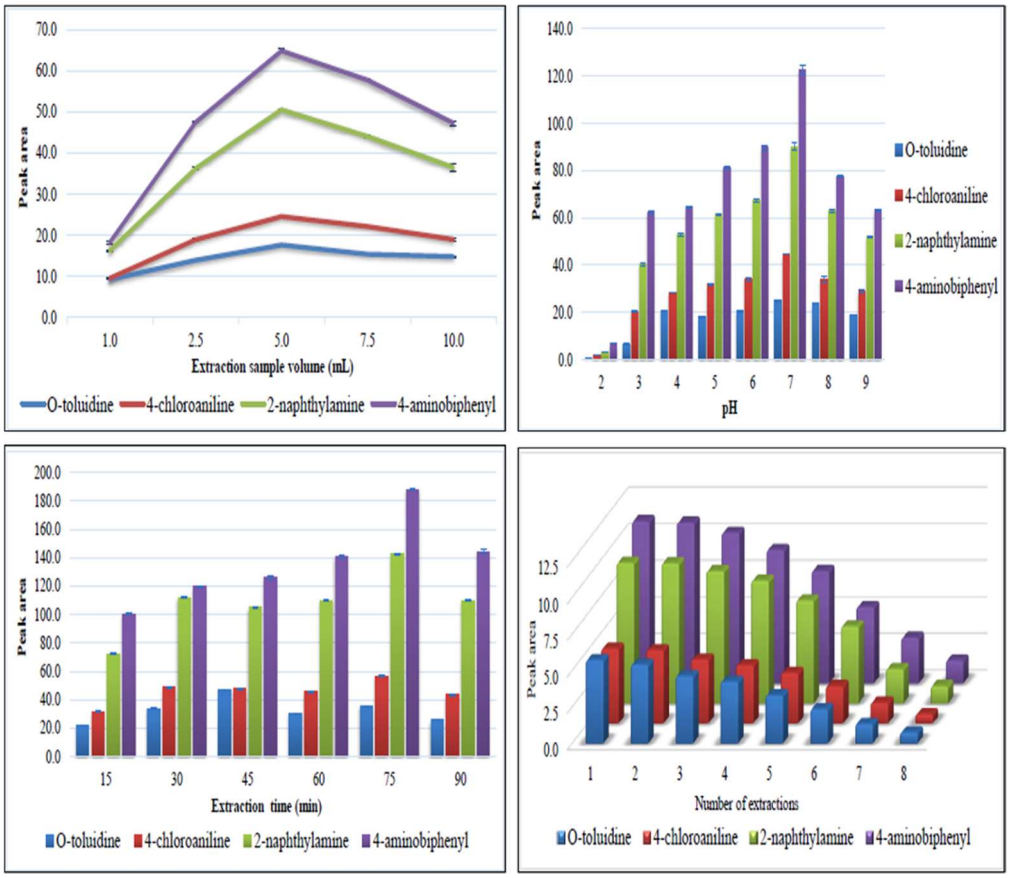

Figure 7. (a)The effects of different volumes of sample, (b)pH of sample, (c)extraction times and (d)reusability analysis of the µ-SPE device. (Extraction conditions: concentration of each AAs, 5 mg L-1; type of desorption solvent used :ACN; mass of β-CD-TDI, 40 mg; sample volume, 1 - 10 mL; extraction time, 15 - 90 min; desorption volume, 300 µL;desorption time, 30s and samples pH, 2-9)

Analytical performance of the proposed method

Method performance was analysed using the optimised parameters for μ-SPE of aromatic amines using β-CD-TDI. Under the optimised μ-SPE conditions, four selected aromatic amines were separated using GC-FID. A series of tests have been done to obtain the linear range, limits of detection, limits of quantification, and precision of the developed method. A series of spiked samples were extracted using the optimised μ-SPE method. The chromatographic data from GC-FID was used to prepare the calibration plots for each analyte (n=3). *o*-toluidine, 4-chloroaniline, and 2-naphthyl amine gave linear graphs between the ranges of 25.0 - 500.0 μg $L^{-1,}$ while 4-aminobiphenyl records the linear range of 5.0 - 500.0 μg L^{-1} for matrix match calibration. Based on matrix match calibration plots shown in Figure S2, the four aromatic amines gave linearity with a satisfactory coefficient of determination (R^2) ranging from 0.9980 to 0.9990. The results are tabulated in Table 1.

The lowest detection limits and limits of quantification for the developed method were calculated using the blank residue method. LOD values of the selected AAs for the proposed method as within the range of 1.67 - 3.18 μg L^{-1} and LOQs from 5.05 μg L^{-1} to 9.63 μg L^{-1}. The results of instrumental detection limits were found to be higher than method detection limits (*o*-toluidine: 215.70 μg L^{-1}, 4-chloroaniline: 289.54 μg L^{-1}, 2-naphthylamine: 219.21 μg L^{-1}, and 4-aminobiphenyl: 193.93 μg L^{-1}). Therefore, the developed method is sensitive enough to determine lower AA concentrations that cannot be detected by direct injection of AAs into the GC-FID. Furthermore, the obtained LOD values for the analytes (< 3.18 μg L^{-1}) were below the permissible levels suggested in the water. As mentioned earlier, the lowest possible concentration level for *o*-toluidine is 20 μg L^{-1} in ambient water (as indicated by USEPA), and the limit for 4-chloroaniline is 0.2 mg L^{-1} for domestic water and 28 μg L^{-1} according to the state drinking water guidelines of Florida [29,30]. According to USEPA, regional screening levels for chemical contaminants, 2-naphthylamine, is permitted up to 3.9 μg L^{-1} and 4-aminobiphenyl up to 3.0 μg L^{-1} in tap water [29].

The reproducibility of the optimised method was determined by intraday and inter-day precision studies. The samples were spiked with 100.0 μg L^{-1} standard AA mixture. The inter-day study was done on five consecutive days with 5 replicates per day, whereas 10 replicates were done on the same day to analyse intraday precision. Relative standard deviation (RSD) values for intraday ranged between 1.75% - 2.84%, and inter-day was 1.93% - 2.47%. The assessed values on precision were found to be within the variable limits of < 5% (different μ-SPE devices were able to produce reproducible results). Hence, the obtained results indicate that the developed μ-SPE method can be applied to determine trace levels of AAs with reproducible results. Moreover, pre-concentration factors for the target analytes were calculated from the ratios of the peak areas before and after the extraction of analytes. This was investigated to evaluate the extraction efficiency of the proposed μ-SPE method. As shown in Table 1, the extraction method provided moderately high pre-concentration factors ranging from 38 to 152. This may be due to the better mass transfer between the sorbent, β-CD-TDI, and sample solution facilitated by the continuous flow of sample solution via the cellulose teabag membrane [12].

Real samples analysis

The developed μ-SPE method was applied to real samples to determine the AA. The extractions were done under optimised conditions. Four water samples were collected inside UM premises: lake water from UM lake, water from Pantai River, tap water from the laboratory, and wastewater from the wastewater cannel. Samples were filtered twice using 0.45 μm Whatman filter papers to remove any possible particulates prior to extraction. The pH of the samples was tested prior to the analysis and adjusted accordingly. To study the matrix effect and recovery of the real samples, all four water samples were spiked with the analyte concentrations of 50.0, 75.0, and 100.0 μg L^{-1}. Simultaneously, the analysis of the blank samples was conducted for comparison purposes. The slopes of the standard and spiked calibration plots were compared through statistical testing to evaluate the effect of possible interferences from dissolved organic matter in real samples. As per the results tabulated in Table 1, a significant difference can be seen between the two slopes (ME > 0.05), which indicates the presence of interference from the sample matrix [24]. Therefore, the matrix match calibration plots were used for real sample analysis.

As illustrated in Table 2, recoveries of the aromatic amines for all the water samples were between 80 – 99% with % RSDs of 0.80 – 5.82%. The extraction recoveries for tap water ranged from 80 – 97% with % RSD values between 1.15 – 3.39%, for river water 80 – 95% (% RSD; 1.01 – 5.82%), lake water 81 – 99% (% RSD; 0.80 – 4.52%) and wastewater 80 – 99% (% RSD; 1.06 – 5.80%). The obtained results were within a satisfactory level. Typical chromatograms of lake water samples with and without spiking with aromatic amine standards (blank, 50.0, 75.0, and 100.0 μg L^{-1}) are demonstrated in Figure 8.

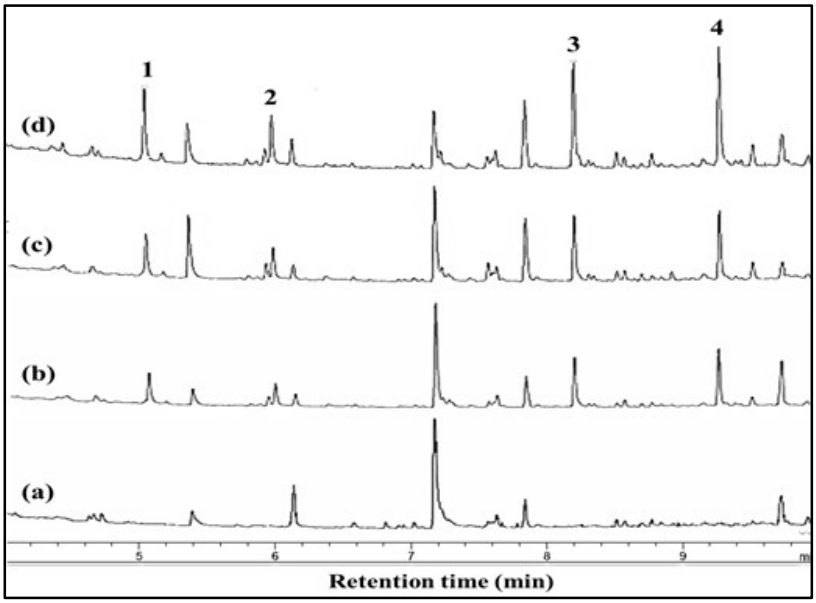

Figure 8. GC-FID chromatograms of unspiked lake water sample (a), lake water sample spiked with 50 μg L^{-1} AAs standard (b), lake water sample spiked with 75 μg L^{-1} AAs standard (c), and lake water sample spiked with 100 μg L^{-1} AAs standard (d). Analytes peak: o-toluidine (1), 4-chloroaniline (2), 2-naphthylamine (3), and 4-aminobiphenyl (4)

Table 1. Analytical performance data for the β-CD-TDI based μ-SPE method

Analytes	Regression Equation	Linear Range (μg L^{-1})	Coefficient of Determination (R^2)	RSD (%)		LOD (μg L^{-1})	LOQ (μg L^{-1})	Pre-Conc. Factor (PF)	Matrix Effect (ME)
				Inter-day (n=5)	Intra-day (n=10)				
***o*-toluidine**	Y = 0.0657x-0.4198		0.9990	2.18[a]	2.69[b]	2.66	8.07	38[d]	0.38
4-chloroaniline	Y = 0.0569x+0.3852	25- 500	0.9980	2.47[c]	2.68[c]	2.77	8.41	152	0.27
2-naphthylamine	Y = 0.1069x-0.3159		0.9983	2.06	2.84	3.18	9.63	102	0.24
4-aminobiphenyl	Y = 0.0882x+1.7317	5 - 500	0.9980	1.93	1.75	1.67	5.05	93	0.30

[a] Average of RSD % of five consecutive days

[b] Average of RSD % of ten different samples within a day

[c] Spiked with 100 μg L^{-1} standard AAs mixture

[d] Calculated for the concentration of 200 μg L^{-1}

Table 2. The relative recoveries and RSD of AAs in real water samples with spike concentrations of each analyte

Analyte	Average recovery (%) (% RSD, n = 3)				
	Spiked concentration (µg L^{-1})	Tap Water	River Water	Lake Water	Wastewater
***o*-toluidine**	0	N/D	N/D	N/D	N/D
	50	[a]90 [b](2.47)	87 (2.06)	82 (3.51)	83 (4.27)
	75	92 (2.29)	83 (3.03)	89 (3.95)	80 (5.80)
	100	96 (3.71)	93 (1.26)	99 (1.40)	99 (2.23)
4-chloroaniline	0	N/D	N/D	N/D	N/D
	50	84 (2.72)	82 (2.33)	88 (1.59)	83 (1.78)
	75	87 (3.39)	82 (5.08)	88 (4.52)	81 (4.45)
	100	97 (2.61)	85 (2.02)	87 (4.39)	94 (1.90)
2-naphthylamine	0	N/D	N/D	N/D	N/D
	50	90 (1.52)	86 (0.96)	84 (2.41)	80 (3.52)
	75	81 (1.15)	91 (1.01)	87 (2.20)	83 (3.32)
	100	96 (2.71)	95 (2.50)	97 (1.71)	96 (1.59)
4-aminobiphenyl	0	N/D	N/D	N/D	N/D
	50	80 (2.62)	80 (1.62)	81 (0.80)	(80 (1.62)
	75	82 (3.18)	83 (5.82)	81 (0.99)	81 (1.06)
	100	90 (1.79)	87 (5.18)	94 (2.15)	94 (1.77)

N/D – Not detected
[a] Average value from triplicate individual vial
[b] % RSD – Relative standard deviation (n=3)

Comparison study with other extraction methods

The analytical performances of the developed β-CD-TDI based µ-SPE method were compared with previously reported methods in Table 3. The obtained detection limits for the present work (1.67 – 3.18 µg L^{-1}) were lower than previous work that used LPME coupled with GC-FID [31] but were higher than the other methods. However, this method still provides a lower LOD value than the legally accepted lower limits proving its applicability for environmental water samples. The reproducibility results (< 5%) and percentage recoveries of the aromatic amines (80 – 99%) were within the acceptable range compared to other studies. Moreover, the current µ-SPE method is a cost-effective, simple, and green technique that consumed a lower sample volume (300 µL). Therefore, this method is beneficial over the other methods.

Table 3. Comparison of the proposed method with previous methods applied for the extraction of AAs in environmental water samples

Extraction Method	Sorbent	Analytical Method	Linear Range (µg L^{-1})	LOD (µg L^{-1})	Solvent Volume (µl)	Precision (% RSD)	Recovery (%)	Ref.
LPME	-	GC-FID	50 - 7000 90 - 10000	12 - 61	-	3.5 - 14.5	92 - 104	[32]
MSPE	PpPD/Fe_3O_4	GC-FID	0.05 - 100	0.007 - 0.01	250	< 5.9	93.0 - 99.8	[12]
SPE	β-CD-HMDI	HPLC-DAD	-	0.002 - 0.008	2000	3.5 - 9.2	38 - 108	[33]
SPE	C18 cartridge-SDS	HPLC-UV	3.1-125	1-4.5	3000	< 5.8	84.8 - 93.5	[34]
HS-SPME	PDMS-IL	GC-FID	0.005 - 0.5	0.001 - 0.1	-	3.5 - 8.5	83.3 - 95.0	[35]
Mixed Matrix Membrane Microextraction (MMMM)	MIP	HPLC-DAD	1 - 500	0.06 - 0.17	250	< 10	80 - 96	[9]
DLLME-SAP	DES-UA	HPLC-UV	-	0.07 - 0.11	40	2.9 - 6.2	85.1 - 99.9	[36]
µ-SPE	β-CD-TDI	GC-FID	25 - 500 5 - 500	1.67 - 3.18	300	< 5	80 - 99	This Method

BS-DLLME-binary solvent dispersive liquid-liquid microextraction; AALLME- Air assisted liquid-liquid microextraction; HS-SPME- Head-space solid-phase micro extraction; PDMS-IL-Poly(dimethylsiloxane)-ionic liquid; PpPD/Fe_3O_4-Poly(para-phenylenediamine) modified magnetic nanoparticles.

Conclusion

The synthesised β-CD-TDI polymer was packed inside the cellulose tea bag, successfully characterised by several analytical techniques, and applied as sorbent for the micro-solid phase extraction of aromatic amines combined with GC-FID analysis. Moreover, the self-made cellulose-based μ-SPE device revealed that it can be simply prepared, easy to operate, reusable, and cost-effective. This approach is environmentally friendly because this has reduced the consumption of organic solvents and sorbent. The method offers good repeatability and simple, rapid, and robust characteristics. The developed method was effectively applied to real water samples, including the lake, river, tap, and wastewater, with good sensitivity to analyse aromatic amines in aqueous samples and good reproducible results and better recoveries.

Acknowledgements

The authors wish to acknowledge the Ministry of Higher Education for the financial support provided through the Fundamental Research Grant Scheme (FRGS/1/2020/STG04/UM/02/9), as well as the Department of Chemistry and Faculty of Science at the University of Malaya for providing the necessary facilities.

Reference

1. Silva, C., e Silva, R., Figueiredo, A. T. d., and Alves, V. N. (2020). Magnetic solid-phase microextraction for lead detection in aqueous samples using magnetite nanoparticles. *Journal of the Brazilian Chemical Society*, 2020: 134.
   Zavareh, Siamak, Avanes, A., and Beiramyan, P. (2017). Effective and selective removal of aromatic amines from water by Cu^{2+}-treated chitosan/alumina nanocomposite. *Adsorption Science and Technology* 35 (1–2): 218-240.
2. Kim, Y. H., and Kim, K. H. (2013). An accurate and reliable analysis of trimethylamine using thermal desorption and gas chromatography–time of flight mass spectrometry. *Analytica Chimica Acta,* 780 (5): 46-54.
3. Zhao, Dong, Zhao, L., Zhu, C. S., Shen, X., Zhang, X., and Sha B. (2009). Comparative study of polymer containing β-cyclodextrin and –cooh for adsorption toward aniline, 1-naphthylamine and methylene blue. *Journal of Hazardous Materials*, 171(1–3): 241-46.
4. Sun, Yan, Liang, L., Zhao, X., Yu, L., Zhang, J., Shi, G., and Zhou, T. (2009). Determination of aromatic amines in water samples by capillary electrophoresis with amperometric detection. *Water Research*, 43 (1): 41-46.
5. USEPA (1982). Results of the nationwide urban runoff program, Water Planning Division, US Environmental Protection Agency 1982.
6. Szejtli, József (1998). Introduction and general overview of cyclodextrin chemistry. *Chemical Reviews* 98(5): 1743-1753.
7. Biedermann, F., and Schneider, H. J. (2016). Experimental binding energies in supramolecular complexes. *Chemical Reviews,* 116(9): 5216-5300.
8. Werner, J. (2020). Novel deep eutectic solvent-based ultrasounds-assisted dispersive liquid-liquid microextraction with solidification of the aqueous phase for HPLC-UV determination of aromatic amines in environmental samples. *Microchemical Journal,* 153: 104405.
9. Pawliszyn, J., and Lord, H. L. (2011). Handbook of Sample Preparation. *Handbook of Sample Preparation*, Wiley-Blackwell Publisher: 1-491.
10. Sajid, M. (2017). Porous membrane protected micro-solid-phase extraction: A review of features, advancements and applications. *Analytica Chimica Acta* 965 (5): 36-53.
11. Basheer, C., Han, G. C., Toh, M. H., and Hian, K. L. (2007). Application of porous membrane-protected micro-solid-phase extraction combined with HPLC for the analysis of acidic drugs in wastewater. *Analytical Chemistry* 79(17): 6845-6850.
12. Song, X., Li, J. Xu, S., Ying, R., Ma, J., Liao, C., Liu, D., Yu, J., and Chen, L. (2012). Determination of 16 polycyclic aromatic hydrocarbons in seawater using molecularly imprinted solid-phase extraction coupled with gas chromatography-mass spectrometry. *Talanta* 99(9): 75-82.
13. Nojavan,S., and Yazdanpanah, M. (2017). Micro-solid phase extraction of benzene, toluene, ethylbenzene and xylenes from aqueous solutions using water-insoluble β-cyclodextrin polymer as

sorbent. *Journal of Chromatography A,* 1525: 51-59.

14. Özkan, B. Ç., Merve F., Dotse S. C., and Sezgin B. (2019). Accurate and sensitive determination of harmful aromatic amine products of azo dyes in wastewater and textile samples by GC–MS after multivariate optimization of binary solvent dispersive liquid-liquid microextraction. *Microchemical Journal* 145(3): 84-89.
15. Anne, J. M., Boon, Y. H., Saad, B., Miskam, M., Yusoff, M. M., Shahriman, M. S., Zain, N. N. M., Lim, V. and Raoov, M. (2018). β-cyclodextrin conjugated bifunctional isocyanate linker polymer for enhanced removal of 2,4-dinitrophenol from environmental waters. *Royal Society Open Science* 5(8): 180942.
16. Sanagi, M. M., Susie L. L., Zalilah N., Dadan H., Wan Ibrahim, W. A., and Naim, A. A. (2009). Comparison of signal-to-noise, blank determination, and linear regression methods for the estimation of detection and quantification limits for volatile organic compounds by gas chromatography. *Journal of AOAC International* 92(6): 1833-1838.
17. Mukhtar, N. H., and Hong H. S. (2016). Carbonaceous nanomaterials immobilised mixed matrix membrane microextraction for the determination of polycyclic aromatic hydrocarbons in sewage pond water samples. *Analytica Chimica Acta* 931 (8): 57-63.
18. Peris-Vicente, J., Josep E. R., and Samuel C. B. (2015). Validation of analytical methods based on chromatographic techniques: An overview. *Analytical Separation Science,* 11: 1757-1808.
19. Raoov, M., Mohamad, S. and Abas, M. R., (2013). Synthesis and characterization of β-cyclodextrin functionalized ionic liquid polymer as a macroporous material for the removal of phenols and As(V). *International Journal of Molecular Sciences,* 15(1): 100-119.
20. Kvien, I., Tanem, B. S., and Oksman, K. (2005). Characterization of cellulose whiskers and their nanocomposites by atomic force and electron microscopy. *Biomacromolecules* 6(6): 3160-3165.
21. Bhaskar, M., Aruna, P., Ganeshjeevan, R. J., and Radhakrishnan, G. (2004). β-cyclodextrin-polyurethane polymer as solid phase extraction material for the analysis of carcinogenic aromatic amines. *Analytica Chimica Acta,* 509(1): 39-45.
22. Shahriman, Mohamad, Z. N. N., Mohamad, S., Abdul Manan, N. S., Yaman, S. M., Asman, S., and Raoov, M. (2018). Polyaniline modified magnetic nanoparticles coated with dicationic ionic liquid for effective removal of rhodamine B (RB) from aqueous solution. *RSC Advances*, 8(58): 33180-33192.
23. Pelden, T., Chongdee T., Panote T., and Proespichaya K. (2014). Tea bag filter paper as a novel protective membrane for micro-solid phase extraction of butachlor in aqueous samples. *Journal of Environmental Sciences and Health, Part B,* 49(7): 480-490.
24. Saraji, M., Boroujeni, M. K. and Bidgoli, A. A. H. (2011). Comparison of dispersive liquid-liquid microextraction and hollow fiber liquid-liquid-liquid microextraction for the determination of fentanyl, alfentanil, and sufentanil in water and biological fluids by high-performance liquid chromatography. *Analytical and Bioanalytical Chemistry,* 400(7): 2149-2158.
25. Premakumari, J. G., Allan G. R., A. Antony Muthu Prabhu, G. Venkatesh, V. K. Subramanian, and N. Rajendiran. (2011). Effect of solvents and pH on β-cyclodextrin inclusion complexation of 2,4-dihydroxyazobenzene and 4-hydroxyazobenzene. *Journal of Solution Chemistry,* 40(2): 327-347.
26. Leyva, E., Moctezuma, E., Strouse, J., and García-Garibay, M. A. (2001). Spectrometric and 2D NMR studies on the complexation of chlorophenols with cyclodextrins. *Journal of Inclusion Phenomena And Macrocyclic Chemistry,* 39(1-2): 41-46.
27. Yue, Mei E., Li, Q., Xu, J., and Jiang, T. F. (2016). Salt de-emulsification dispersive liquid-liquid microextraction and back-extraction combined with sweeping micellar electrokinetic capillary chromatography for detection of triazine herbicides in honey. *Food Analytical Methods,* 9(3): 699-705.
28. Pohanish, R. P. (2017). *Sittig's Handbook of Toxic and Hazardous Chemicals and Carcinogens*: pp. 1696-1717.
29. English, J. C., Virunya S. B., Gwendolyn L. B., and Clifton J. M. (2012). Establishing a total allowable

concentration of o-toluidine in drinking water incorporating early lifestage exposure and susceptibility. *Regulatory Toxicology and Pharmacology* 64(2): 269-284.

30. Reddy-Noone, K., Archana J., and Krishna K. V. (2007). Liquid-phase microextraction and GC for the determination of primary, secondary and tertiary aromatic amines as their iodo-derivatives. *Talanta,* 73 (4): 684-691.
31. Jiangning, C., Hongxia, Y., Ying, L., Wei, J., Jie, J., Junfeng, Z., and Zichun, H. (2004). Ecotoxicological evaluation of 4-aminobiphenyl using a test battery. *Ecotoxicology and Environmental Safety,* 58(1): 104-109.
32. Krause, R., Mamba, B., Bambo, M., and Malefetse, T. J. (2011). Cyclodextrin polymers: Synthesis and application in water treatment. *Cyclodextrin Chemistry and Physics*, 2011: 185-210.

deep eutectic solvent-based dispersive liquid-liquid microextraction followed by HPLC-UV. *Arabian Journal of Chemistry*, 15(6): 103783.

33. Rozaini, M. N. H., Semail, N. F., Saad, B., Kamaruzaman, S., Abdullah, W. N., Rahim, N. A., Miskam, M., Loh, S. H., and Yahaya, N. (2019). Molecularly imprinted silica gel incorporated with agarose polymer matrix as mixed matrix membrane for separation and preconcentration of sulfonamide antibiotics in water samples. *Talanta,* 199: 522-531.
34. Amiri, A., Baghayeri, M., and Nori, S. (2015). Magnetic solid-phase extraction using poly (para-phenylenediamine) modified with magnetic nanoparticles as adsorbent for analysis of monocyclic aromatic amines in water and urine samples. *Journal of Chromatography A,* 1415: 20-26.
35. Noormohammadi, F., Faraji, M., and Pourmohammad, M. (2022). Determination of aromatic amines in environmental water samples by

Malaysian Journal of Analytical Science (MJAS)

SYNTHESIS, CHARACTERIZATION AND BIOLOGICAL EVALUATION OF NOVEL THIAZOLIDINEDIONE DERIVATIVES AS EMERGING ANTIDIABETIC AGENTS

(Sintesis, Pencirian dan Penilaian Biologi Terbitan Novel Thiazolidinedion Sebagai Agen Antidiabetik yang Baru Muncul)

Shaik Munwar[1], M K Kathiravan1[*] and Ilango K[2*]

[1]*Department of Pharmaceutical Chemistry, SRM College of Pharmacy, SRM Institute of Science and Technology, Kattankulathur, Chengalpattu District-603203, Tamil Nadu, India*
[2]*Department of Pharmaceutical Chemistry, Tagore College of Pharmacy, Rathinamangalam, Chennai - 600 127, Tamil Nadu, India*

**Corresponding authors: ilangok67@gmail.com , kathirak@srmist.edu.in*

Received: 4 January 2024; Accepted: 32 March 2024; Published: 29 June 2024

Abstract

In the present research, derivatives of thiazolidinedione were synthesized and established as potent antidiabetic activity through *in vitro* alpha-amylase inhibition activity and *in vivo* animal experimentation. A total of 15 molecules were synthesized namely, SMI-IV-2, SMI-IV-4, SMI-IV-7, SMI-IV-9, SMI-IV-11, SMI-IV-15, SMI-IV-19, SMI-IV-22, SMI-IV-23, SMI-IV-28, SMI-IV-31, SMI-IV-32, SMI-IV-34, SMI-IV-41and SMI-IV-47. Thereafter, *in vitro* alpha amylase activity was carried out followed by *in vivo* animal study performed in STZ induced animal. Metformin was used as standard for result comparison. Furthermore, various biochemical parameters were analyzed. Initially, the novel thiazolidinedione derivatives were synthesized by the reaction between thiourea and chloroacetic acid and resulted first compound as 1,3-thiazolidine-2,4-dione which was further treated with pyridine-4-carbaldehydeand resulted (5*Z*)-5-[(pyridin-4-yl)methylidene]-1,3-thiazolidine-2,4-dione which was further reacted with acid chloride and aromatic aldehydes and resulted the derivatives of compound (5*Z*)-3-[(2*E*)-3-phenylprop-2-enoyl]-5-[(pyridin-4-yl) methylidene]-1,3-thiazolidine-2,4-dione which was named as SMI-IV. A total of five derivatives were selected based on *in vitro* and *in vivo* results and further characterized by melting point, thin layer chromatography, IR spectroscopy, ^{1}HNMR, ^{13}CNMR and mass spectra. *In vitro* alpha amylase study showed potent inhibition of alpha amylase activity by all the derivatives with dose dependent manner. Among the all derivatives, SMI-IV-4 showed IC50 value less than others (39.56%) and nearer to the standard (24.36%). *In vivo* animal experimentation was also revealed that derivative SMI-IV-4 significantly reduced the blood glucose level at 24 hours to 166 mg/dl when compared to the standard metformin (115 mg/dl). Overall results concluded that thiazolidinedione derivatives showed potent antidiabetic activity especially the derivatives viz. SMI-IV-4, SMI-IV-11, SMI-IV-22, SMI-IV-31, and SMI-IV-41 among them SMI-IV-4 showed more significance when compared to standard metformin.

Keywords: antidiabetic, *in vitro* assay, *in vivo* experiment, streptozotocin, spectroscopy, thiazolidinedione

Abstrak

Dalam penyelidikan ini, derivatif thiazolidinedion telah disintesis dan ditubuhkan sebagai aktiviti antidiabetik yang kuat melalui aktiviti perencatan alfa-amilase *in vitro* dan eksperimen haiwan *in vivo*. Sebanyak 15 molekul telah disintesis iaitu, SMI-IV-2, SMI-IV-4, SMI-IV-7, SMI-IV-9, SMI-IV-11, SMI-IV-15, SMI-IV-19, SMI-IV-22, SMI-IV-23, SMI-IV-28, SMI-IV-31, SMI-IV-32, SMI-IV-34, SMI-IV-41dan SMI-IV-47. Selepas itu, aktiviti amilase alfa *in vitro* telah dijalankan diikuti dengan kajian haiwan *in vivo* dilakukan dalam haiwan yang disebabkan oleh STZ. Metformin digunakan sebagai standard untuk perbandingan hasil. Tambahan pula, pelbagai parameter biokimia telah dianalisis.Pada mulanya, derivatif thiazolidinedion novel telah disintesis melalui tindak balas antara tiourea dan asid kloroasettik dan menghasilkan sebatian pertama sebagai 1,3-thiazolidine-2,4-dion yang kemudian dirawat dengan piridin-4-karbaldehid dan menghasilkan (5Z) -5- [(piridin-4-yl) metilliden]-1,3-thiazolidine-2,4-dion yang kemudiannya bertindak balas dengan asid klorida dan aldehid aromatik dan menghasilkan terbitan sebatian (5Z)-3-[(2E)-3-fenilprop-2-enoil]-5-[(piridin-4-il) metilliden]-1,3-thiazolidine-2,4-dion yang dinamakan sebagai SMI-IV. Sebanyak lima derivatif telah dipilih berdasarkan keputusan *in vitro* dan *in vivo* dan selanjutnya dicirikan oleh takat lebur, kromatografi lapisan nipis, spektroskopi IR, ^{1}HNMR, ^{13}CNMR dan spektrum jisim. Kajian *in vitro* alfa amilase menunjukkan perencatan kuat aktiviti alfa amilase oleh semua derivatif dengan cara bergantung kepada dos. Di antara semua derivatif, SMI-IV-4 menunjukkan nilai IC50 kurang daripada yang lain (39.56%) dan juga lebih hampir kepada standard (24.36%). Eksperimen haiwan *in vivo* juga mendedahkan bahawa terbitan SMI-IV-4 dengan ketara mengurangkan paras glukosa darah pada 24 jam kepada 166 mg/dl jika dibandingkan dengan metformin standard (115 mg/dl). Keputusan keseluruhan menyimpulkan bahawa derivatif thiazolidinedion menunjukkan aktiviti antidiabetik yang kuat terutamanya derivatif iaitu SMI-IV-4, SMI-IV-11, SMI-IV-22, SMI-IV-31, dan SMI-IV-41 antaranya SMI-IV-4 menunjukkan lebih ketara jika dibandingkan dengan larutan piawai metformin.

Kata kunci: antidiabetik, ujian *in vitro*, eksperimen *in vivo*, streptozotocin, spektroskopi, thiazolidinedion

Introduction

Diabetes mellitus (DM) is characterized by hyperglycemia, a complicated chronic disease that can develop when insulin production or action is impaired. Patients with this condition are at increased risk for macro- and microvascular consequences due to the chronic metabolic imbalance that characterizes it [1]. These difficulties, in turn, increase the likelihood of cardiovascular diseases (CVDs) and other hospitalizations that patients may have if they do not receive adequate care [2]. One of four plasma glucose (PG) criteria must be met for a clinical diagnosis of diabetes: (i) an elevated fasting plasma glucose (FPG) of more than 126 mg/dL; (ii) a 2-hour PG of more than 200 mg/dL during a 75-g oral glucose tolerance test (OGTT); (iii) an uncontrolled PG of more than 200 mg/dL accompanied by classic hyperglycemia symptoms; or (iv) a hemoglobin A1C level greater than 6.5% [3]. An American Diabetes Association report recently suggests that there might not be a suggested test for diagnosis. All people, regardless of weight, should start getting tested at 45 years of age [4]. People who have at least one extra risk factor for developing diabetes, are overweight or obese, and have diagnostic symptoms but are asymptomatic should still get tested [5].

Heterocyclic compounds with two heteroatoms incorporated into five-membered ring structures have significant biological efficacy. Thiazole is a fundamental structure found in the thiazolidine-2,4-dione, which is one of the physiologically active heterocyclic molecules [6]. Thiazolidine-4-one and thiazolidine-2-one is compounds that exhibit various functions and contain a carbonyl group at the 4th and 2nd positions, respectively. The presence of two carbonyl groups at the 2nd and 4th positions in the thiazole ring results in the formation of thiazolidine-2,4-dione. The substituents at positions 3 and 5 of the thiazolidine-2,4-dione structure are modifiable [7]. Peroxisome proliferator activated receptor-gamma is a nuclear receptor that plays a critical role in controlling gene expression linked to energy balance and lipid metabolism [8]. In the compound nucleus, PPARγ can limit the incidence of problems, increase insulin sensitivity, and boost lipocyte distinction. The glucose metabolism linked to insulin resistance can be controlled using thiazolidinediones (TZDs), which are PPARγ agonists with high affinity but no risk of

hypoglycemia [9]. There are now several medications that can be used to lower blood sugar levels in people with diabetes, including sulfonylureas and biguanides. Because of the serious adverse effects these medications caused, it is critical to find a new class of chemicals to address these issues [10].

Several TZDs like troglitazone, pioglitazone, and rosiglitazone are available in the market, but they are having severe side effects like idiosyncratic hepatotoxicity, fluid retention and weight gain. Furthermore, troglitazone and rosiglitazone were prohibited, and pioglitazone's label was revised due to risk of bladder cancer. Emerging strategies, guided by structural considerations of ligands, receptors and their interactions, offer the potential to create thiazolidinedione derivatives with diminished adverse effects [11]. Thereafter, many literatures were also reported that thiazolidine-2,4-dione derivatives are well known for diabetic management [12,13]. Therefore, detail structural characterization and synthesis of many thiazolidinedione derivatives are required for the development of small molecules as physiologically active agents as potent antidiabetic drugs.

Materials and Methods

Scheme and procedure: Below scheme-1 was highlighted the overall scheme of synthesis of compound-IV.

Step-I

A solution of 56.4g (0.6M) chloroacetic acid and 45.6g (0.6M) thiourea was dissolved in 60 mL of water in a 250 mL three-necked flask. After 15 minutes of stirring, white precipitates should have formed in the mixture. Once the contents of the flask were mixed, to dissolve the precipitates, 60 mL of strong hydrochloric acid was gradually added using the dropping funnel. The mixture was then refluxed for 10-12 hours at 100-110˚C while being stirred. White needle clusters formed from the flask's contents solidifying as they cooled. After removing any remaining hydrochloric acid, the product was filtered and rinsed with water before being dried. From ethanol, it was recrystallized.

Step-II preparation of compound-II:

After being refluxed for 6 hours and cooled, a solution containing 1,3-thiazolidine-2,4-dione molecule (I) (1.66 g, 0.005 mol), (pyridine-4-carbaldehyde 0.005 mol) in ethanol (15 mL), and 5 drops of glutathione (GAA) was prepared. The resulting solid was extracted from the methanol by filtering, drying, and recrystallization.

Step-III preparation of compound-III

A solution of brine, consisting of 36% aqueous sodium chloride, was mixed with 5g (0.038 mol) of sodium acetate trihydrate in 50 mL. On top of it, 0.025 mol of compound-II was added. Next, while the mixture was still at room temperature, 2 mL of acetyl chloride (0.028 mol) in 3mL of acetone was added drop wise with stirring. An additional hour was spent stirring the reaction mixture. The effervescence was stopped by adding saturated $NaHCO_3$ solution. A solution was acidified with concentrated hydrochloric acid. Compound III, which is sparingly soluble, washed out as a solid. It crystallized from a solvent solution consisting of MeOH, MeOH, and water after being filtered under suction.

Step-IV preparation of derivatives of compound-IV:

In a round bottom flask equimolar mixture of compound-III and substituted aromatic aldehydes were dissolved in ethanol and was subjected for reflux on a water bath for 3.30 min in the presence of few drops of acetic acid. The reaction mixture was later poured into ice-cold water and the solid formed was filtered out and dried. The derivatives of compound-IV were obtained then recrystallized from ethanol (Scheme-I). Thereafter, many derivatives were synthesized from compound-IV and their physicochemical properties were depicted in below Tables 1 to 6.

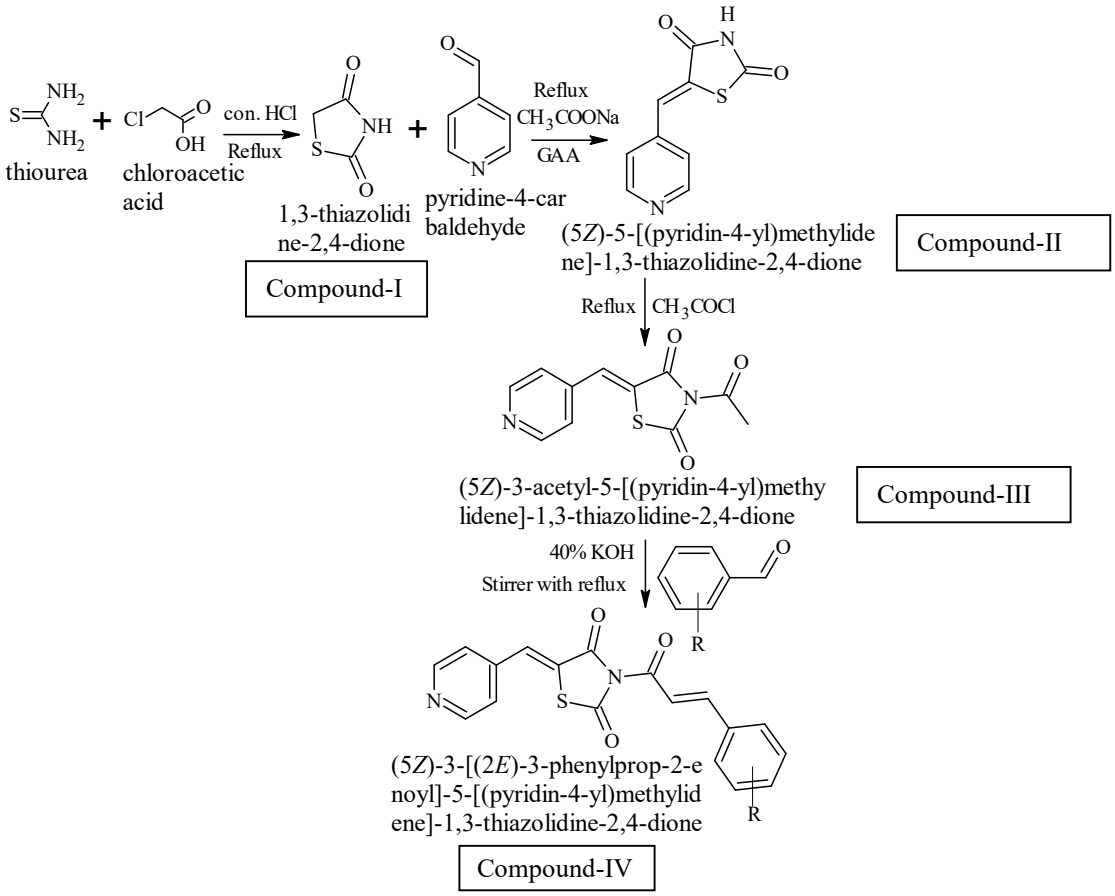

Scheme-1. Synthesis steps for compound-IV

Biological evaluation: *In vitro* α-amylase inhibitory assay

Minor adjustments were made to the standard procedure before the experiment was conducted. A 0.2 mL solution containing 0.01M $CaCl_2$ and 0.5M Tris-HCl buffer (pH 6.9) was used to suspend 2 mg of starch azure. The tubes with the substrate solution were pre-incubated at 37.5 °C for 15 minutes after 5 min of boiling. All the derivatives (SMI-IV) were dissolved in dimethyl sulfoxide (DMSO) and prepared the various concentrations (10, 20, 40, 60, 80, and 100 µg/mL) by added 0.2 mL of thiazolidinedione derivatives (SMI-IV) to the substrate solution in the tube, with a specific concentration. To the tube with the thiazolidinedione derivatives (SMI-IV) and additionally, 0.1 mL of porcine pancreatic amylase in Tris-HCl buffer (2 units/mL) was added to the substrate solution. We ran the reaction for 10 minutes at 37 °C. To halt the process, 0.5 mL of 50% acetic acid was added to each tube. Centrifuged at 3000 rpm for 5 minutes at 4 °C, the reaction mixture was strained. A spectrophotometer was used to measure the absorbance of the supernatant at 590 nm. The α-amylase inhibitory effects of the fifteen derivatives that were chosen were tested using the same approach. The standard medicine utilized was acarbose, which is known to inhibit α-amylase [12, 13].

***In vivo* anti-diabetic activity: Streptozotocin (STZ)-induced diabetes**

Male albino Wistar rats weighing 160±20 g and around 3-4 weeks old were obtained (Ethical Ref No: IAEC/Sangli/2023/74). Unless otherwise specified, all rats were housed in an animal housing facility under

typical circumstances, including an ideal temperature of 22 °C, relative humidity, and a 12-hour light/dark cycle. Before the trial began, all the rats spent four days becoming used to the lab environment. At a dosage of 60 mg/kg body weight, 80 albino Wistar rats that had fasted overnight and weighed 160 ± 20 g were injected with a solution of STZ that had been dissolved in Citrate buffer (0.1 M). A glucometer (Accu-Chek) was used to assess the animals' fasting blood glucose levels from the vein of their severed tails 48 hours after injection. Diabetic animals were defined as those with a fasting blood glucose level between 300 and 450 mg/dL, and 8 animals were randomly assigned to each experimental group (total 8 groups). Oral dosages of 250 mg/kg of thiazolidinedione derivatives (SMI-IV) were administered to each group using a fine-mesh solution of test samples made in 1% gum acacia. The typical dose of metformin used as an antidiabetic medication was 250 mg/kg of body weight. Blood samples were taken after 24 hrs from the animal's tail, 300 to 1440 minutes after they were treated with the test sample, reference medication. Body weights were determined followed by the blood serum was separated from the blood using centrifugation, which ran for 20 minutes at 3000 rpm. Total cholesterol, triglycerides, low-density lipoprotein (LDL), and low-density lipoprotein (HDL) were all estimated using commercially available kits. Serum insulin was determined using an enzyme-linked immunosorbent test (ELISA) kit. Whether it's a conventional medicine or a test chemical, that percentage of blood glucose reduction Graph Pad Prism was used to plot the blood glucose level (mg/dL) against time (min). To demonstrate the improvement in hyperglycemia, the area under the curve (AUC) between 0-300 and 0-1440 minutes was determined by comparing the AUC of the groups treated with the test substance and the standard treatment [14, 15].

Statistical analysis

Results were tabulated as mean ± SEM. Data was evaluated using one-way ANOVA followed by Dunnett's comparison. The differences were considered significant at $p \leq 0.05$.

Table 1. Physicochemical properties of compound-I, II, III

Sl. No	Parameter	Compound-I	Compound-II	Compound-III
1	Molecular formula	$C_3H_3NO_2S$	$C_9H_6N_2O_2S$	$C_{11}H_8N_2O_3S$
2	Molecular weight	117.22	206.21	248.25
3	Theoretical yield	8.65gm	8.32gm	8.14gm
4	Practical yield	8.32gm	8.14gm	7.88gm
5	% yield	96.18%	97.83%	96.80%
6	Melting point	120-122^0 C	126-128^0 C	130-132^0 C
7	Recrystallization solvent	Ethanol	Methanol	Methanol
8	Solvent for TLC	Chloroform: Methanol (9:1)	Chloroform: Methanol (9:1)	Chloroform: Methanol (9:1)
9	R_f value	0.90	0.84	0.96

Table 2. Physicochemical properties of derivatives of compound-IV

Sl. No	Parameter	SMI-IV-2	SMI-IV-4	SMI-IV-7
1	Molecular formula	$C_{18}H_{12}N_2O_4S$	$C_{18}H_{13}N_3O_4S$	$C_{18}H_{11}FN_2O_4S$
2	Molecular weight	352.36	367.39	370.35
3	Theoretical yield	1.10gm	1.10gm	1.10gm
4	Practical yield	0.98gm	0.87gm	0.91gm
5	% yield	89.09%	79.09%	82.72%
6	Melting point	128-130^0 C	130-132^0 C	132-134^0 C
7	Recrystallization solvent	Ethanol	Ethanol	Ethanol
8	Solvent for TLC	Chloroform: Methanol (9:1)	Chloroform: Methanol (9:1)	Chloroform: Methanol (9:1)
9	R_f Value	0.85	0.79	0.87

Table 3. Physicochemical properties of derivatives of compound-IV

Sl. No	Parameter	SMI-IV-9	SMI-IV-11	SMI-IV-15
1	Molecular formula	$C_{18}H_{12}N_2O_7S_2$	$C_{19}H_{14}N_2O_3S$	$C_{19}H_{13}N_3O_5S$
2	Molecular weight	432.42	350.39	395.39
3	Theoretical yield	1.10gm	1.10gm	1.10gm
4	Practical yield	1.02gm	0.97gm	1.01gm
5	% yield	92.72%	88.18%	91.81%
6	Melting point	124-126^{0}C	130-132^{0}C	136-138^{0}C
7	Recrystallization solvent	Ethanol	Ethanol	Ethanol
8	Solvent for TLC	Chloroform: Methanol (9:1)	Chloroform: Methanol (9:1)	Chloroform: Methanol (9:1)
9	R_f Value	0.82	0.90	0.88

Table 4. Physicochemical properties of derivatives of compound-IV

Sl. No	Parameter	SMI-IV-19	SMI-IV-22	SMI-IV-23
1	Molecular formula	$C_{20}H_{16}N_2O_3S$	$C_{19}H_{15}N_3O_3S$	$C_{18}H_{13}N_3O_4S$
2	Molecular weight	364.41	365.40	367.37
3	Theoretical yield	1.10gm	1.10gm	1.10gm
4	Practical yield	0.98gm	1.04gm	1.00gm
5	% yield	89.09%	94.54%	90.90%
6	Melting point	120-122^{0}C	122-124^{0}C	130-132^{0}C
7	Recrystallization solvent	Ethanol	Ethanol	Ethanol
8	Solvent for TLC	Chloroform: Methanol (9:1)	Chloroform: Methanol (9:1)	Chloroform: Methanol (9:1)
9	R_f Value	0.88	0.94	0.86

Table 5. Physicochemical properties of derivatives of compound-IV

Sl. No	Parameter	SMI-IV-28	SMI-IV-31	SMI-IV-32
1	Molecular formula	$C_{18}H_{12}N_4O_5S$	$C_{18}H_{11}ClN_2O_3S$	$C_{18}H_{11}ClN_2O_4S$
2	Molecular weight	396.37	370.80	386.80
3	Theoretical yield	1.10gm	1.10gm	1.10gm
4	Practical yield	0.99gm	1.02gm	0.99gm
5	% yield	90.00%	92.72%	90.00%
6	Melting point	118-120^{0}C	124-126^{0}C	122-124^{0}C
7	Recrystallization solvent	Ethanol	Ethanol	Ethanol
8	Solvent for TLC	Chloroform: Methanol (9:1)	Chloroform: Methanol (9:1)	Chloroform: Methanol (9:1)
9	R_f Value	0.91	0.89	0.72

Table 6. Physicochemical properties of derivatives of compound-IV

Sl. No	Parameter	SMI-IV-34	SMI-IV-41	SMI-IV-47
1	Molecular formula	$C_{18}H_{10}Cl_2N_2O_3S$	$C_{18}H_{10}F_2N_2O_3S$	$C_{18}H_{11}BrN_4O_5S$
2	Molecular weight	405.24	372.34	475.27
3	Theoretical yield	1.10gm	1.10gm	1.10gm
4	Practical yield	0.98gm	0.86gm	0.90gm
5	% yield	89.09%	78.18%	81.81%
6	Melting point	131-133^{0}C	125-127^{0}C	129-131^{0}C
7	Recrystallization solvent	Ethanol	Ethanol	Ethanol
8	Solvent for TLC	Chloroform: Methanol (9:1)	Chloroform: Methanol (9:1)	Chloroform: Methanol (9:1)
9	R_f Value	0.80	0.90	0.78

Results and Discussion

All the derivatives were experimented on potential antidiabetic activity and among them 5 derivatives were selected based on the result. Spectral Characterization of 5 selected derivatives of SMI-IV-4, 11, 22, 31 and 41 were characterized using spectroscopic techniques such as IR, ^{1}HNMR, ^{13}CNMR and mass spectral studies (data shown in supplementary file). All the data shown in Tables 7 to 10.

Table 7. FT-IR spectrum data of derivativesSMI-IV-4, 11, 22, 31, and 41

SMI-IV-4		SMI-IV-11		SMI-IV-22		SMI-IV-31		SMI-IV-41	
Wave number (cm^{-1})	**Functional Group Assigned**	**Wave number (cm^{-1})**	**Functional Group Assigned**	**Wave number (cm^{-1})**	**Functional Group Assigned**	**Wave number (cm^{-1})**	**Functional Group Assigned**	**Wave number (cm^{-1})**	**Functional Group Assigned**
3060-3150	-OH stretching	3000-3050	-N-H stretching	3000-3060	-N-H stretching	3000-3090	-N-H stretching	3040-3000	-N-H stretching
3010-3050	N-H stretching of 1^{0}amine	2850-2990	Aromatic C-H stretching	2850-2995	Aromatic C-H stretching	2900-2800	Aromatic - C-H stretching	2970-2850	Aromatic C-H stretching
3000-2950	N-H stretch 2° or 3° amine	2300-2410	Aliphatic C-H stretching	2300-2450	Aliphatic C-H stretching	2350-2500	Aliphatic C-H stretching	2390-2510	Aliphatic C-H stretching
2900-2850	Aromatic C-H stretching	1430 1450 1490	C = O stretching	1410 1420 1430	C = O stretching	1435 1440 1450	C = O stretching	1450 1460 1470	C = O stretching
2380	Aliphatic C-H stretching	700	CH_3 stretching	820	CH_3 stretching	690	-CH stretching	705	-CH stretching
1490	C = O stretching	1110	C-S stretching	1105	C-S stretching	1100	C-S stretching	1110	C-S stretching
800	-CH stretching					845	-C-Cl stretching	790	-C-F stretching
1090	C-S stretching								

Table 8. H^1 NMR spectrum data of derivativesSMI-IV-4, 11, 22, 31, and 41

SMI-IV-4		SMI-IV-11		SMI-IV-22		SMI-IV-31		SMI-IV-41	
δ Value in ppm	**Peak Assigned (Multiplicity)**	**δ Value in ppm**	**Peak Assigned (Multiplicity)**	**δ Value in ppm**	**Peak Assigned (Multiplicity)**	**δ Value in ppm**	**Peak Assigned (Multiplicity)**	**δ Value in ppm**	**Peak Assigned (Multiplicity)**
4.315	$-NH_2$ (2H)	4.0-4.2	$-NH_2$(2H)	3.8-4.5	$-NH_2$(2H)	2.0-2.3	-CH(3H)	2.4-3.2	-CH(3H)
2.60-3.35	-CH(3H)	1.95-3.7	$-CH_3$, 3CH (6H)	2.0-3.4	$-CH_3$, 3CH (6H)	6.6-8.0	Ar-H (multiplate)	6.7-8.9	Ar-H (multiplate)
6.5-9.5	Ar-H (multiplate) (7H)	6.6-8.3	Ar-H (multiplate)	6.6-8.8	Ar-H (multiplate)				
10.96	-OH (1H)								

Table 9. ^{13}CNMR spectrum data of derivativesSMI-IV-4, 11, 22, 31, and 41

SMI-IV-4		SMI-IV-11		SMI-IV-22		SMI-IV-31		SMI-IV-41	
Carbon's	**δ Value in ppm**	**Carbon's**	**δ Value in ppm**	**Carbon's**	**δ Value in ppm**	**Carbon's**	**δ Value in ppm**	**Carbon's**	**δ Value in ppm**
3C CH	32.35 40.10 74.25	1C $-CH_3$	33.45	1C $-CH_3$	33.50	3C CH	59.80 66.78 80.45	3C –CH	59.80 66.78 80.45
12C from Aromatic ring	110-150	3C CH	40.09 74.70 79.45	3C CH	40.09 74.70 79.75	12C from Aromatic ring	110-160	12C from Aromatic ring	115-145
3C from C=O	147.60 154.10 167.05	12C from Aromatic ring	110-150	12C from Aromatic ring	110-150	3C from C=O	166.96 177.40 179.45	3C from -C=O	148.25 162.33 167.05
		3C from C=O	153.10 167.05 168.02	3C from C=O	153.10 167.05 168.02				

Table 10. Mass spectrum of synthesized compounds

Parameters	SMI-IV-4	SMI-IV-11	SMI-IV-22	SMI-IV-31	SMI-IV-41
M^+ Peaks (m/z)	367.2	365.3	365.3	369.2	372.2
Base Peak	267.2	337.1	305.2	287.1	289.2
Molecular weight	367.2	365.3	365.3	369.2	372.2

***In vitro* alpha-amylase inhibition activity**

Alpha-amylase inhibition activity was carried out for all the derivatives of compound-IV but the selected 5 derivatives showed significant results when compared to standard acarbose. The IC_{50} value was less in standard (24.36) with greater inhibition of enzyme. The same trend followed with the derivatives. SMI-IV-4 showed less IC_{50} value among the derivatives and showed higher inhibition in 100 µg/mL than other derivatives. Table 11 showed the tabulated result where per cent inhibition was recorded in different concentrations.

Table 11. Alpha-amylase inhibitory effects of selected derivatives of compound-IV

Compounds	% of Inhibition at Different Concentration (µg/mL) of Various Derivatives						IC_{50} value (µg/mL)
	10	20	40	60	80	100	
SMI-IV-4	2.41	5.10	11.85	19.46	25.34	32.46	39.56±1.85
SMI-IV-11	2.98	6.18	14.10	20.97	24.75	29.34	66.94±1.94
SMI-IV-22	3.97	7.86	15.76	21.78	25.13	30.94	62.42±1.59
SMI-IV-31	3.64	7.10	15.40	22.55	26.71	31.70	55.40±1.65
SMI-IV-41	3.20	6.51	13.89	20.37	24.74	31.48	57.46±1.64
Standard Acarbose	4.58	9.12	20.34	29.74	36.74	42.58	24.36±1.52

Data replicated three times (n=3)

***In-vivo* anti-diabetic activity: Streptozotocin (STZ)-induced diabetes**

Male albino Wistar rats were used for the antidiabetic activity experimentation in STZ induced animals. In STZ-induced diabetic rats, a loss of β-cells leads to a significant shortage of insulin and, later, a fasting blood glucose level that is higher than usual. A thiazolidinedione derivative (SMI-IV) was administered to each animal. In case of body weight of the animals after 24 hours, control animals did not show much variation than initial (160.52g) but STZ induced animals showed elevated body weight (168.21 g) whereas STZ induced standard showed decreased in weight (154.10g) and the derivative SMI-IV-4 significant decreased in body weight (156.01g) (Table 12). Similar way, various other biochemical parameters viz. total cholesterol, triglycerides, LDL and HDL contents were estimated where similar results were revealed as earlier. Total cholesterol content was significantly lower by the SMI-IV-4, 101.12 mg/dL than STZ induced animals (203.44 mg/dL) which was near value of STZ induced standard drug (90.32 mg/dL). Similarly, the results were the same as triglycerides, LDL and HDL content (Table 13). Except for a notable decrease with thiazolidinedione derivatives (SMI-IV), results demonstrate moderate to low antihyperglycemic efficacy in blood glucose AUC in single dose animal trials. The thiazolidinedione derivative SMI-IV-4 significantly lowered the blood glucose level at 24 hours to 166 mg/dL when compared to the standard metformin (Table 14, 15).

Table 12. Determination of body weight of animals

	Initial (g)	After 24 hours (g)
Control	160.45±1.43	160.52± 1.23
STZ	160.36± 2.21	168.21± 2.21
STZ+ SMI-IV-4	161.12±2.20	156.01±1.04$^{\#*}$
STZ+ SMI-IV-11	160.38±1.36	158.22± 2.21$^{\#}$
STZ+ SMI-IV-22	159.30±1.41	157.67 ± 0.45$^{\#}$
STZ+ SMI-IV-31	161.04±0.05	159.66 ± 0.11
STZ+ SMI-IV-41	160.21±2.05	159.32 ± 1.03
STZ+ Metformin	159.36 ±1.28	154.10 ± 0.37$^{\#*}$

Values, mean ± SE; (n=8); *$p \leq 0.05$, **$p \leq 0.01$, compared with corresponding control values; $^{\#}$ when compared with standard, $^{\#\#}$when compared with STZ

Table 13. Determination of biochemical parameters after 24 hours

Parameters	Concentration (mg/dL)			
	Total Cholesterol	**Triglycerides**	**LDL**	**HDL**
Control	87.41± 0.43	76.22± 1.01	37.32± 2.41	33.41± 1.11
STZ	203.44±0.11**	168.34± 0.41**	148.32±0.32**	21.26± 0.21**
STZ+ SMI-IV-4	101.12± 0.20$^{\#\#}$	92.07± 1.06	56.82±1.46$^{\#\#}$	31.30± 1.03$^{\#\#}$
STZ+ SMI-IV-11	129.10± 1.36*	102.22± 0.22*	62.43± 2.56$^{\#\#}$	30.18± 2.01
STZ+ SMI-IV-22	120.39± 1.41*	111.01 ± 0.75*	74.40±2.41$^{*\#\#}$	29.12± 1.42
STZ+ SMI-IV-31	113.10± 1.57$^{*\#\#}$	99.06 ± 0.17$^{*\#\#}$	76.30±1.07$^{*\#\#}$	27.40± 0.48
STZ+ SMI-IV-41	116.03± 0.42$^{*\#\#}$	109.31 ± 0.36*	78.21± 0.65$^{\#\#}$	25.36± 0.71
STZ+ Metformin	90.32 ± 1.03$^{*\#\#}$	85.12 ± 1.33$^{*\#\#}$	48.20±0.11$^{*\#\#}$	35.61± 0.10$^{\#\#}$

Values, mean ± SE; (n=8); *$p \leq 0.05$, *$p \leq 0.01$; compared with corresponding control values, $^{\#}$ when compared with standard, $^{\#\#}$when compared with STZ.

In the present study, many derivatives were synthesized from thiazolidinedione compound-IV and evaluated for antidiabetic activity. There are many derivatives synthesized in which the best 15 derivatives were selected based on the properties and activity. *In vitro* alpha amylase enzyme inhibition activity was carried out. For glucose-stimulated insulin release in pancreatic beta cells, glucose metabolism is critical. Additionally, it has been suggested that stimulating enhanced glucose metabolism could enhance ATP synthesis in pancreatic β cells, which in turn could contribute to an increase in insulin release [16]. Many literatures were revealed earlier about *in vitro* alpha amylase inhibition activity as one of the mechanisms in controlling diabetics [17, 18]. The same method was followed in this investigation and revealed significant inhibition of alpha-amylase by the derivatives of thiazolidinedione. STZ was used as diabetic inducer in Wistar animals. One of the animal models of diabetes mellitus is diabetic rats generated by streptozotocin [19]. It has been widely utilized to cause diabetes in experimental rat models and is well known for its specific cytotoxicity to pancreatic islet beta cells. In STZ-induced diabetes, Metformin is frequently used as a standard antidiabetic medication to assess the effectiveness of various hypoglycemic medications [20]. In STZ-induced diabetic rats, a loss of β-cells leads to a significant shortage of insulin and, later, a fasting blood glucose level that is higher than usual. A thiazolidinedione derivative (SMI-IV) was administered to each animal. Except for a notable decrease with thiazolidinedione derivatives (SMI-IV), results demonstrate moderate to low antihyperglycemic efficacy in blood glucose AUC in single dose animal trials.

Table 14. Anti hyperglycemic activity of 5 best derivatives on STZ-induced diabetic rats at the dose of 250 mg/kg)

Compounds	Glucose Value in mg/dL					
	0 min	5 hours	10 hours	15 hours	20 hours	24 hours
Control	435±2.0	422±1.5	415±1.0	410±0.6	410±0.5	408±0.5
STZ	435.43± 1.2	442.22 ±0.32	457.09± 1.80	476.54 ±0.47	489.23 ±1.33	523.11± 0.51
STZ+ SMI-IV-4	433.2±1.2	390±1.0	345±1.2	290.32 ±0.8$^{\#\#,**}$	212±1.0$^{**\#\#}$	166.21±0.5$^{\#\#**\#}$
STZ+ SMI-IV-11	435.01±1.5	395±1.2	324±1.3	276±1.2	234±1.0$^{**\#}$	200±1.0$^{*\#}$
STZ+ SMI-IV-22	435.03±1.3	375±1.2	330±1.2	268±1.5	236±1.2$^{**\#}$	190±1.3$^{*\#}$
STZ+ SMI-IV-31	435±1.5	385±1.3	320±1.2	274±1.0	234±1.0$^{**\#}$	170±1.0$^{**\#}$
STZ+ SMI-IV-41	435±1.0	380±1.5	310±1.0	260.3±1.2$^{\#**\#\#}$	223.2±1.0**	180±1.0$^{\#\#**\#}$
STZ+ Metformin	433±1.2	210.3±1.0$^{*\#\#}$	160.1±1.0$^{**\#\#}$	146.7±1.0$^{**\#\#}$	140.3±1.0$^{**\#\#}$	115.4±1.0$^{**\#\#}$

Values, mean ± SE; *$p \leq 0.05$, **$p \leq 0.01$; compared with corresponding control values; $^{\#}$when compared with standard, $^{\#\#}$when compared to standard.

Table 15. Area under the curve (AUC) values

Compounds	Blood Glucose AUC	
	0 min	5 hours
Control	1.5462	1.5123
SMI-IV-4	0.7854	0.6524
SMI-IV-11	0.8913	0.8457
SMI-IV-22	0.8861	0.8261
SMI-IV-31	0.8758	0.7942
SMI-IV-41	0.8729	0.8134
Metformin	0.7828	0.4562

Conclusion

The study revealed that the synthesized novel derivatives of thiazolidinedione (SMI-IV) exhibited significant lowering of blood sugar in STZ induced albino Wistar rats. 15 derivates were synthesized from the compound IV and based on the practical yield, 5 derivatives were selected viz. SMI-IV-4, SMI-IV-11, SMI-IV-22, SMI-IV-31, and SMI-IV-41. All derivatives showed potent antidiabetic activity but among them, derivative SMI-IV-4 showed significant antidiabetic activity.

Acknowledgements

The authors acknowledge SRM College of Pharmacy for providing the facilities to carry out the work.

References

1. Sun, B., Luo, Z., and Zhou, J. (2021). Comprehensive elaboration of glycemic variability in diabetic macrovascular and microvascular complications. *Cardiovascular Diabetology,* 20: 1-13.

2. Battisti, N. M. L., Welch, C. A., Sweeting, M., de Belder, M., Deanfield, J., Weston, C., ... and Ring, A. (2022). Prevalence of cardiovascular disease in patients with potentially curable malignancies: a national registry dataset analysis. *Cardio Oncology,* 4(2): 238-253.
3. Sreedharan, R., Khanna, S., and Shaw, A. (2023). Perioperative glycemic management in adults presenting for elective cardiac and non-cardiac surgery. *Perioperative Medicine*, 12(1):13.
4. Lebovitz, H. E. (2019). Thiazolidinediones: the forgotten diabetes medications. *Current diabetes reports*, 19(12):151.
5. Consoli, A., and Formoso, G. (2013). Do thiazolidinediones still have a role in treatment of type 2 diabetes mellitus?. *Diabetes, Obesity and Metabolism,* 15(11): 967-977.
6. Bansal, G., Thanikachalam, P. V., Maurya, R. K., Chawla, P., and Ramamurthy, S. (2020). An overview on medicinal perspective of thiazolidine-2, 4-dione: A remarkable scaffold in the treatment of type 2 diabetes. *Journal of Advanced Research,* 23: 163-205.
7. Lončarić, M., Strelec, I., Pavić, V., Rastija, V., Karnaš, M., and Molnar, M. (2022). Green synthesis of thiazolidine-2, 4-dione derivatives and their lipoxygenase inhibition activity with QSAR and molecular docking studies. *Frontiers in Chemistry*, 10: 912822.
8. Christofides, A., Konstantinidou, E., Jani, C., and Boussiotis, V. A. (2021). The role of peroxisome proliferator-activated receptors (PPAR) in immune responses. *Metabolism,* 114: 154338.
9. Rizos, C. V., Elisaf, M., Mikhailidis, D. P., and Liberopoulos, E. N. (2009). How safe is the use of thiazolidinediones in clinical practice?. *Expert Opinion on Drug Safety*, 8(1): 15-32.
10. Alam, S., Sarker, M. M. R., Sultana, T. N., Chowdhury, M. N. R., Rashid, M. A., Chaity, N. I., ... and Mohamed, I. N. (2022). Antidiabetic phytochemicals from medicinal plants: prospective candidates for new drug discovery and development. *Frontiers in Endocrinology,* 13: 800714.
11. Khowdiary, M. (2022). Discovery potent of thiazolidinedione derivatives as antioxidiant, amylase inhibitor and antidiabetic agent. *Biomedicines,* 10(1):24.
12. Sameeh, M. Y., Khowdiary, M. M., Nassar, H. S., Abdelall, M. M., Amer, H. H., Hamed, A., and Elhenawy, A. A. (2022). Thiazolidinedione derivatives: *in silico, in vitro, in vivo*, antioxidant and anti-diabetic evaluation. *Molecules,* 27(3): 830.
13. Dastjerdi, Z. M., Namjoyan, F., and Azemi, M. E. (2015). Alpha amylase inhibition activity of some plants extract of Teucrium species. *European Journal of Biological Sciences,* 7(1): 26-31.
14. Das, K., Iyer, K. R., Orfali, R., Asdaq, S. M. B., Alotaibi, N. S., Alotaibi, F. S., ... and Ghoneim, M. (2023). *In silico* studies and evaluation of *in vitro* antidiabetic activity of berberine from ethanol seed extract of *Coscinium fenestratum* (Gaertn.) Colebr. *Journal of King Saud University-Science,* 35(5): 102666.
15. Rani, R., Dahiya, S., Dhingra, D., Dilbaghi, N., Kaushik, A., Kim, K. H., and Kumar, S. (2019). Antidiabetic activity enhancement in streptozotocin+ nicotinamide–induced diabetic rats through combinational polymeric nanoformulation. *International Journal of Nanomedicine,* 2019: 4383-4395.
16. Kahksha, Alam, O., Al-Keridis, L. A., Khan, J., Naaz, S., Alam, A., ... and Beg, M. A. (2023). Evaluation of antidiabetic effect of luteolin in STZ induced diabetic rats: Molecular docking, molecular dynamics, in vitro and in vivo studies. *Journal of Functional Biomaterials,* 14(3): 126.
17. Fu, Z., R Gilbert, E., and Liu, D. (2013). Regulation of insulin synthesis and secretion and pancreatic Beta-cell dysfunction in diabetes. *Current Diabetes Reviews,* 9(1): 25-53.
18. Sagbo, I. J., van de Venter, M., Koekemoer, T., and Bradley, G. (2018). *In vitro* antidiabetic activity and mechanism of action of *Brachylaena elliptica* (Thunb.) DC. *Evidence-Based Complementary and Alternative Medicine,* 2018(1): 4170372.
19. Ononamadu, C. J., Alhassan, A. J., Imam, A. A., Ibrahim, A., Ihegboro, G. O., Owolarafe, A. T., and Sule, M. S. (2019). *In vitro* and *in vivo* anti-diabetic and antioxidant activities of methanolic

leaf extracts of *Ocimum canum. Caspian Journal of Internal Medicine,* 10(2): 162.

20. Kottaisamy, C. P. D., Raj, D. S., Prasanth Kumar, V., and Sankaran, U. (2021). Experimental animal models for diabetes and its related complications—a review. *Laboratory Animal Research,* 37(1): 23.